

Habilitationsschrift
zur
Erlangung der Venia Legendi
für das Fach Physik
der
Ruprecht-Karls-Universität
Heidelberg

vorgelegt von
Sandro Marcel Wimberger
aus Passau
2011

Dynamik kalter Quantengase

Danksagung

Ich möchte all denen herzlichst danken, die zur erfolgreichen Fertigstellung der hier beschriebenen Arbeiten beigetragen haben:

zuallererst meiner Frau für die unermüdliche Unterstützung trotz aller Herausforderungen in den letzten Jahren und unserer Tochter Atena für die Kraft, die sie mir gibt,

meinen momentanen und ehemaligen Mitarbeitern, Frau Martina Abb, Frau Ghazal Tayebirad und den Herren Conrad Albrecht, Stephan Burkhardt, Rémy Dubertrand, Benedikt Herwerth, Anton Ivanov, Georgios Kordas, Niels Lörch, Michael Lubasch, Carlos Parra-Murillo, Tobias Paul, Patrick Plötz, Benedikt Probst, Torben Schell und Andrea Tomadin, die alle durch ihr Engagement viele Projekte getragen haben,

den Kollegen aus der Experimentalphysik, mit denen der Austausch und die Zusammenarbeit in den letzten Jahren eine Freude war, allen voran den Herren Ennio Arimondo, Rainer Leonhardt, Oliver Morsch, Markus Oberthaler und Mark Sadgrove,

den Kollegen aus der Theoretischen Physik, die immer anregende Vorschläge hatten, insbesondere den Herren Andreas Buchleitner, Pierfrancesco Buonsante, Italo Guarneri, Andrey Kolovsky, Hans Jürgen Korsch, Javier Madroñero, Riccardo Mannella, Florian Mintert, Scott Parkins, Stefano Ruffo, Peter Schlagheck und Dirk Witthaut,

Herrn Andreas Komnik, meinem Heidelberger Mentor, für viele wissenschaftliche Diskussionen und praktische Tipps; ihm und den Herren Klaus Hornberger und Michael Schmidt gebührt auch Dank für wertvolle Hinweise zur vorliegenden Schrift;

vielen Heidelberger Kollegen, insbesondere am Institut für Theoretische Physik und dessen Mitarbeitern, die alle mit Rat und Tat zur Seite standen und durch Ihre fortlaufende Unterstützung meiner Forschungsgruppe vieles erleichterten, und den Herren Maarten DeKieviet, Selim Jochim und Matthias Weidemüller für ihre kollegiale Hilfe bei der Organisation unseres Ruperto-Carola-Symposiums 2010 bzw. für die Ausrichtung des CQD-Kolloquiums.

Mein ganz besonderer Dank gilt Frau Gesine Heinzemann, Frau Sandra Klevansky, Herrn Matthias Bartelmann, Herrn Markus Oberthaler und Herrn Peter Schmelcher für den Aufbau und die hervorragende Leitung unserer Graduiertenschule für Fundamentale Physik, deren Existenz viele der hier vorgestellten Arbeiten erst ermöglichte.

Der Heidelberger Akademie der Wissenschaften danke ich für finanzielle und ideelle Unterstützung, der Deutschen Forschungsgemeinschaft und der Alexander von Humboldt-Stiftung für die Finanzierung einzelner Forschungsprojekte.

Inhaltsverzeichnis

1	Einleitung	11
1.1	Motivation	11
1.2	Optische Potentiale	12
1.3	Theoretische Modelle	13
1.3.1	Kalte atomare Gase	13
1.3.2	Bose-Einstein Kondensate in Molekularfeldnäherung	14
1.3.3	Bose-Hubbard Modell	15
2	Einführung in die Originalarbeiten	17
2.1	Lokalisierung und Quantenresonanzen in gekickten kalten Atomen . . .	17
2.1.1	Einfluss atomarer Wechselwirkung	18
2.1.2	Quantenresonanzen im semiklassischen Limes	19
2.1.3	Stabilisierung durch reguläre Strukturen im Phasenraum	20
2.1.4	Gerichteter Transport	22
2.1.5	Fraktale Fluktuationen als Signatur Dynamischer Lokalisierung	22
2.2	Interbandtunneln in gekippten periodischen Potentialen	23
2.2.1	Resonanzverstärktes Tunneln	24
2.2.2	Zeitaufgelöste Messung der Überlebenswahrscheinlichkeit . . .	25
2.2.3	Kontrolle des Zerfalls durch Phasenrauschen	27
2.2.4	Vielteilchen-Wannier-Stark-System	27
2.3	Quantenchaos in Vielteilchensystemen	29
2.3.1	Chaos verstärkt durch Unordnung	30
2.3.2	Fidelity-Maß zur Charakterisierung vermiedener Kreuzungen .	31
2.4	Dynamik im Doppeltopf	31
2.4.1	Kontrolle kollektiven Tunnelns	32
2.4.2	Verschränkungserzeugung im Bose-Hubbard-System	32
2.4.3	Stochastische Resonanz	33
2.5	Transport und Dynamik in offenen Vielteilchensystemen	34
3	Wissenschaftliche Kurzartikel (Letters)	37
3.1	Resonant nonlinear quantum transport for a periodically kicked Bose condensate	39
3.2	Ballistic and localized transport for the atom optics kicked rotor in the limit of a vanishing kicking period	43
3.3	Driven collective quantum tunneling of ultracold atoms in engineered optical lattices	47
3.4	Resonantly enhanced tunneling of Bose-Einstein condensates in periodic potentials	52

3.5	Many-body interband tunneling as a witness of complex dynamics in the Bose-Hubbard model	56
3.6	Dissipation induced coherence of a two-mode Bose-Einstein condensate	60
3.7	Time-resolved measurement of Landau-Zener tunneling in periodic potentials	64
3.8	Dynamical enhancement of spatial entanglement in massive particles . .	68
3.9	Engineering interband transport by time-dependent disorder	72
4	Wissenschaftliche Artikel	77
4.1	Delocalized and resonant quantum transport in nonlinear generalizations of the kicked rotor model	81
4.2	Experimental verification of a one-parameter scaling law for the quantum and classical resonances of the atom-optics kicked rotor	89
4.3	The role of quasi-momentum in the resonant dynamics of the atom-optics kicked rotor	96
4.4	Nonlinearity-induced destruction of resonant tunneling in the Wannier-Stark problem	105
4.5	Can quantum fractal fluctuations be observed in an atom-optics kicked rotor experiment?	110
4.6	Tunnelling rates for the nonlinear Wannier-Stark problem	125
4.7	Chaotic ratchet dynamics with cold atoms in a pair of pulsed optical lattices	137
4.8	Bose-Einstein condensates in accelerated double-periodic optical lattices: Coupling and crossing of resonances	144
4.9	Nonexponential decay of Bose-Einstein condensates: a numerical study based on the complex scaling method	155
4.10	Multifractal fluctuations in the survival probability of an open quantum system	161
4.11	Many-body Landau-Zener tunneling in the Bose-Hubbard model	170
4.12	Engineering many-body quantum dynamics by disorder	179
4.13	Resonant tunneling of Bose-Einstein condensates in optical lattices . . .	183
4.14	Mean-field dynamics of a two-mode Bose-Einstein condensate subject to noise and dissipation	198
4.15	Scaling law and stability for a noisy quantum system	203
4.16	Dissipation-induced coherence and stochastic resonance of an open two-mode Bose-Einstein condensate	207
4.17	Pseudo-classical theory for directed transport at quantum resonance . .	218
4.18	Pseudoclassical theory for fidelity of nearly resonant quantum rotors . .	231
4.19	Collapse and revival in inter-band oscillations of a two-band Bose-Hubbard model	235
4.20	Time-resolved measurement of Landau-Zener tunneling in different bases	241
4.21	Nonlinear resonant tunneling of Bose-Einstein condensates in tilted optical lattices	249
4.22	Detection of avoided crossings by fidelity	256
4.23	Engineering of Landau-Zener tunneling	263
4.24	Effective spin model for interband transport in a Wannier-Stark lattice system	270

4.25	Stückelberg-Interferometry with ultra-cold atoms	277
4.26	Beyond mean-field dynamics in open Bose-Hubbard chains	283
5	Eingeladene Buchbeiträge (Reviews)	291
5.1	Tunneling of ultracold atoms in time-independent potentials	293
5.2	A pseudo-classical method for the atom-optics kicked rotor: from theory to experiment and back	324
6	Nicht enthaltene Veröffentlichungen	385
	Literaturverzeichnis	387

Kapitel 1

Einleitung

1.1 Motivation

Noch vor etwa zwanzig Jahren hätte man nicht zu träumen gewagt, welche Möglichkeiten heutzutage moderne Experimente auf dem Gebiet der ultrakalten Quantengase bieten. Obwohl die untersuchten Objekte (Atome, schwach gebundene Moleküle) neutral sind, lassen sie sich in ihren externen und internen Freiheitsgraden mit hoher Präzision kontrollieren [1,2]. Dies erlaubt eine „bottom up“-Realisierung komplexer Systeme, wobei die Komplexität gezielt erhöht werden kann [3,4]. Letzteres wird beispielsweise erreicht durch das Einschalten der Wechselwirkung zwischen den Konstituenten, durch Erhöhung der Teilchenzahl bzw. durch Anlegen äußerer Potentiale in verschiedenen Formen und räumlichen Dimensionen. Dadurch lassen sich nicht nur wohlbekannte theoretische Modelle direkt im Labor testen, sondern man kann an gänzlich neue Szenarien der Quantenzustandskontrolle denken, die von der Systemsteuerung durch Ankopplung an geeignete Bäder (s. beispielsweise [5–9]) bis hin zu komplexen Hybridsystemen reichen, bei denen mehrere verschiedene quantenmechanische Freiheitsgrade gekoppelt werden (s. beispielsweise [10–13]).

Man könnte fast sagen, dass sich moderne quanten- und atomoptische Experimente die Methodik der Theorie zu eigen machen, indem sie die einzelnen Manifestationen eines komplexen Quantensystems Schritt für Schritt mit hoher Präzision synthetisieren. Die Aufgaben der theoretischen Physik lassen sich in diesem Zusammenhang wie folgt zusammenfassen: die untersuchten Systeme auf den verschiedenen mikroskopischen bis mesoskopischen Skalen zu verstehen; den Beitrag fundamentaler Einzel- bzw. Vielteilcheneffekte zu deuten; Komplexität zu quantifizieren (z. B. durch statistische Maße); und aus all den gewonnenen Erkenntnissen neue, interdisziplinäre Methoden, aber auch Vorschläge für neue Experimente zu erarbeiten. Insbesondere bei Anwesenheit äußerer Kräfte kann eine Trennung diverser Effekte schwierig sein. Mein Ziel ist es, genau dieses Wechselspiel zwischen induzierter Dynamik von innen (d.h. durch Vielteilchenkorrelationen) und von außen (durch explizite Zeitabhängigkeit oder Ankopplung an Rauschen oder Bäder) zu untersuchen. Erwartet werden neue emergente Eigenschaften komplexer Systeme, die sich sonst nicht unmittelbar aus dem Verhalten der unterschiedlichen Konstituenten ergäben. Besonders interessant sind Systeme unter zeitlich periodischem Antrieb und das dynamische Verhalten, welches über reine Dämpfungsdynamik hinausgeht und wesentliche Teile des quantenmechanischen Energiespektrums miteinschließt. Unsere Untersuchungen bauen soweit möglich auf drei Säulen. Erstens auf der theoretische Modellierung und auf analytischen Einsichten, zweitens auf der Weiterentwicklung fortgeschrittener numerischen Methoden und nicht zuletzt auf dem experimentellen

Fortschritt, der uns nicht nur als „Benchmark“ dient, sondern wiederum die ersten beiden Säulen stützt.

Im nächsten Abschnitt soll der Grundgedanke der experimentellen Realisierung von optischen Potentialen dargelegt werden. Die vorliegende Arbeit wird sich dann weitgehend auf das konkrete Szenario der Kontrolle kalter und ultrakalter atomarer Gase durch optische, zeitabhängige wie zeitunabhängige Kräfte konzentrieren. Die grundlegenden theoretischen Modelle zur Beschreibung der betrachteten Systeme werden kurz in Abschnitt 1.3 vorgestellt.

Kapitel 2 führt in die Originalarbeiten des Verfassers aus den letzten sieben Jahren ein [6, 14–50]. Ein Teil dieser Veröffentlichungen entstand in enger Zusammenarbeit mit den Kollegen aus der Experimentalphysik um Ennio Arimondo (Universität Pisa) und Rainer Leonhardt (Universität Auckland), und später direkt mit dem ehemaligen Studenten Mark Sadgrove (jetzt an der University of Electro-Communications, Tokyo). Der Großteil sind jedoch theoretische Arbeiten, die aus der Zusammenarbeit mit Kollegen im In- und Ausland und insbesondere mit meinen Mitarbeitern in Pisa und Heidelberg unter meiner Leitung hervorgingen. Die Originalarbeiten sind in der Form [14 | S. 39] zitiert, wobei sich die erste Ziffer auf das Literaturverzeichnis am Ende dieser Schrift bezieht, und die zweite die Seite angibt, ab der die entsprechende Publikation hier abgedruckt ist.

1.2 Optische Potentiale

Der Mechanismus, der einem optischen Potential zugrunde liegt, ist in Abbildung 1.1 schematisiert. Da ein Laserstrahl im (nah-)optischen Bereich schnell im Vergleich zu allen Zeitskalen der atomaren Schwerpunktbewegung oszilliert, ergibt sich ein zeitgemittelttes effektives Potential [51]. Durch eine entsprechend große Verstimmung Δ der Laserfrequenz von einem atomaren Übergang bleibt im Wesentlichen nur das Grundzustandsniveau (1 in Abbildung 1.1) besetzt. Bei gegebener räumlicher Intensitätsverteilung $I(\mathbf{r})$ des Laserstrahls ergibt sich folgendes konservatives Potential:

$$V(\mathbf{r}) \propto \hbar \Gamma \frac{\Gamma I(\mathbf{r})}{\Delta I_0}. \quad (1.1)$$

Γ^{-1} ist die Lebensdauer des angeregten elektronischen Zustandes (2 in Abbildung 1.1) und I_0 die Sättigungsintensität des Übergangs, die vom Dipolmatrixelement zwischen den Zuständen 1 und 2 und anderen Parametern abhängt [52–54]. $V(\mathbf{r})$ stellt eine ortsabhängige Energieverschiebung dar, die – je nach Vorzeichen der Verstimmung – positiv oder negativ sein kann. Es bestimmt also eine Potentiallandschaft für die Atome. Da die spontane Streuung aus dem oberen elektronischen Niveau proportional zu Δ^{-2} ist [52–54], sind für nicht zu kleine Verstimmungen dissipative Effekte vernachlässigbar, und es ergibt sich tatsächlich ein quasi konservatives Potential.

Neuere Experimente fangen einmal abgekühlte atomare Gase in sogenannten optischen Fallen (im Gegensatz zu Fallen, die auf magnetischen Feldern beruhen), die sehr flexibel einsetzbar sind [2, 52]. $V(\mathbf{r})$ stellt in diesem Fall ein durch einen starken Laser (mit hoher Intensität) erzeugtes Gaußsches Profil in transversaler Richtung dar, das rotationssymmetrisch ist. In axialer Richtung ergibt sich dagegen eine schwache Falle, die weitgehend homogen im Laserfokus über die relevanten räumlichen Skalen ist, vgl. die rechte Skizze in Abbildung 1.1.

Zusätzlich zum Fallenpotential kann man periodische Potentiale in einer, zwei oder drei Raumrichtungen anlegen, wobei sich unsere Arbeiten auf den Fall konzentrieren,

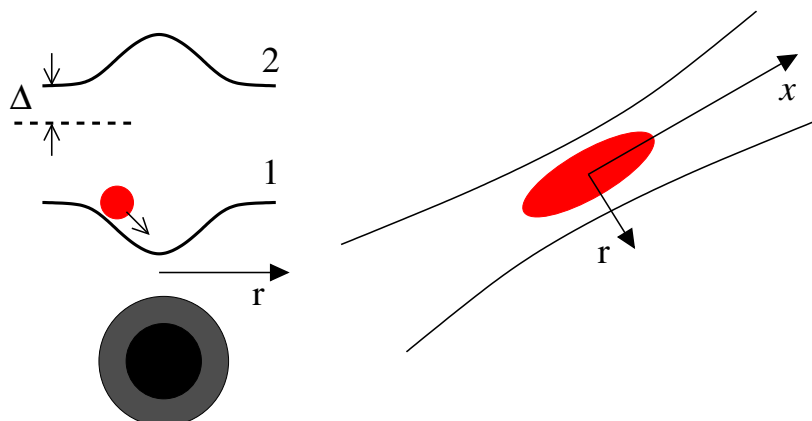


Abbildung 1.1: Ein starker Laserstrahl (links unten im Profil als dunkle Kreise) verschiebt die internen Energieniveaus 1 und 2 eines Atoms. Ist die Laserfrequenz wie im links gezeigten Fall kleiner als die atomare Resonanzfrequenz (mit Verstimmung $\Delta < 0$), ergibt sich ein attraktives Potential in Richtung maximaler Intensität für ein Atom im Grundzustand 1 (roter Punkt). Rechts ist ein Bose-Einstein-Kondensat (rote Ellipse) skizziert, das in radialer Richtung durch den Laserstrahl gefangen ist, wobei das Potential in axialer x -Richtung weitgehend homogen und konstant ist.

für den das periodische Gitter sich in longitudinaler Richtung ausdehnt, und die Atome in transversaler Richtung relativ stark gefangen sind. Dann spricht man vom sogenannten *quasi eindimensionalen* Regime. Das Gitter wird durch zusätzliche gegenläufige Strahlen erzeugt, die eine stehende Welle bilden [1]. Dabei kann man einerseits die Gitterkonstante über die Laserwellenlänge (für Δ im Rahmen der oben beschriebenen Einschränkungen) oder über eine Neigung der beiden Strahlachsen relativ zueinander einstellen [1]. Das statische, periodische Gitter kann man auch zeitlich ändern, sodass die Atome effektiv ein zeitabhängiges Potential spüren. Im Folgenden sind dabei vor allem zwei Realisierungen wichtig: zum einen ein beschleunigtes Gitter, was im beschleunigten Bezugssystem einer konstanten Stark-Kraft F oder $V_S(x) = Fx$ entspricht [55], und zum anderen ein Gitter, das zeitlich periodisch an- und abgeschaltet wird und somit einen großen Impulsübertrag auf die Atome durch diese Kraftstöße oder „Kicks“ bewirkt [56, 57].

1.3 Theoretische Modelle

Wir beschreiben nun drei grundlegende Modelle für kalte und ultrakalte atomare Systeme. Sie bilden die Basis für unsere theoretischen und experimentellen Untersuchungen, die im nächsten Kapitel zusammengefasst sind.

1.3.1 Kalte atomare Gase

Kalte Atome mit Temperaturen weit über der kritischen Temperatur, unterhalb derer sich ein Bose-Kondensat formt, werden üblicherweise in einer Kombination aus magnetischen und optischen Feldern gefangen. Dabei spielen – im Gegensatz zu den oben beschriebenen konservativen Fällen – dissipative Prozesse (bei kleiner Verstimmung Δ) eine entscheidende Rolle. In solchen sogenannten Magneto-Optischen-Fallen [54, 58]

werden Temperaturen erreicht, die einer Impulsverteilung entsprechen, die sich über mehrere Brillouin-Zonen in einem typischen optischen Gitter erstreckt. Detailphänomene wie zeitaufgelöste Bloch-Oszillationen innerhalb einer Brillouin-Zone sind damit nicht unmittelbar beobachtbar. Nichtsdestoweniger kann man durchaus interessante Experimente machen, solange z. B. dabei der Impulsübertrag groß im Vergleich zur anfänglichen Impulsverteilung ist. Diese atomaren Gase sind wegen der relativ großen mittleren Geschwindigkeiten sehr verdünnt, sodass die Wechselwirkung zwischen den einzelnen Atomen vernachlässigbar ist. Experimentelle Messungen sind daher üblicherweise Ensemblemessungen unabhängiger Teilchen, die mit einer Einteilchentheorie und anschließendem Ensemblemittel gut beschrieben werden [56, 57, 59–62]. In der in Abschnitt 2.1 behandelten Zeitentwicklung geklickter Atome ergibt sich dabei das Ensemble aus den Anfangsbedingungen, d.h. aus der Geschwindigkeitsverteilung der Atome zur Zeit $t = 0$.

1.3.2 Bose-Einstein Kondensate in Molekularfeldnäherung

Kühlt man bosonsche Atome unter ihre kritische Temperatur ab, kondensieren sie bevorzugt in den gleichen Zustand [63, 64]. Diesen Vorgang nennt man Bose-Einstein-Kondensation. Die entsprechenden Impulsverteilungen haben eine Breite, die typischerweise weit unterhalb der Breite einer Brillouin-Zone (in einem optischen Gitter) liegt, was natürlich entscheidend ist, um auch kleine Impulsveränderungen in einem weiterführenden Experiment zu messen. Die einfachste Näherung für die Gesamtwellenfunktion eines Systems aus N Atomen ist ein Produktansatz bestehend aus N Einteilchenwellenfunktionen (Hartree-Ansatz) [65]. Im Falle der Beschreibung eines Bose-Kondensates bei idealisierter Temperatur $T = 0$ führt dies auf eine Molekularfeldnäherung, die unter dem Namen Gross-Pitaevskii-Gleichung [66, 67] bekannt ist. Berücksichtigt man nur Zweiteilchenwechselwirkung und die Tatsache, dass bei sehr tiefen Temperaturen nur niederenergetische s -Wellen-Streuung zwischen den Atomen eine Rolle spielt, erhält man folgenden Vielteilchen-Hamilton-Operator:

$$\hat{H} = \int d\mathbf{r} \hat{\psi}^\dagger(\mathbf{r}, t) \left(-\frac{\hbar^2}{2m} \Delta + V(\mathbf{r}, t) + \frac{U_0}{2} \hat{\psi}^\dagger(\mathbf{r}, t) \hat{\psi}(\mathbf{r}, t) \right) \hat{\psi}(\mathbf{r}, t). \quad (1.2)$$

$V(\mathbf{r}, t)$ beschreibt ein Fallen- und Gitterpotential und die Wechselwirkungsstärke ist durch $U_0 = \frac{4\pi\hbar^2 a_s}{m}$ gegeben, wobei a_s die s -Wellen-Streulänge zwischen zwei Atomen und m die relative Masse im Streuprozess ist [2, 66, 67]. Der Hartree-Ansatz ergibt nun mit Hilfe des Variationsprinzips folgende *einzelne* Gross-Pitaevskii-Gleichung für das „optimale“ Einteilchenorbital $\phi(\mathbf{r}, t)$ [65, 66]:

$$i\hbar \frac{\partial}{\partial t} \phi(\mathbf{r}, t) = \left[-\frac{\hbar^2}{2m} \Delta + V(\mathbf{r}, t) + g|\phi(\mathbf{r}, t)|^2 \right] \phi(\mathbf{r}, t), \quad (1.3)$$

wobei für die Wechselwirkungskonstante $g = U_0 N$ mit der Gesamtteilchenzahl N gilt¹. Da wir allem voran an zeitabhängigen Potentialen (oder allgemeiner zeitabhängigen Hamilton-Operatoren) interessiert sind, gebe ich oben die zeitabhängige Version der Gross-Pitaevskii-Gleichung. Gerade in diesem Fall ist die Gleichung jedoch problematisch, da man von einer konstanten Gesamtteilchenzahl ausgeht und Anregungen des

¹Im Gegensatz zu vielen Autoren reskalieren wir die Wellenfunktion nicht mit \sqrt{N} , aus dem einfachen Grund, dass N ein experimenteller Parameter ist, der im direkten, quantitativen Vergleich mit experimentellen Daten angepasst werden kann (s. die Arbeiten [18 | S. 105] und [23 | S. 52]).

Kondensat von vorne herein vernachlässigt [65, 68]. Wir haben beispielsweise im Rahmen des diskreten Modells, das im nächsten Abschnitt eingeführt wird, genau aus diesem Grund Korrekturen zur diskreten Version der Gleichung (1.3) untersucht [48 | S. 283]. Trotzdem beschreibt die obige Gleichung relativ gut die Dynamik schwach wechselwirkender Kondensate, für die $g|\phi|^2$ klein im Vergleich zur kinetischen oder potentiellen Energie im System ist [1].

1.3.3 Bose-Hubbard Modell

Anstatt der extremen Vereinfachung, welche die Gross-Pitaevskii-Gleichung darstellt, kann man konzeptionell einen anderen Weg gehen und annehmen, dass man eine Basis aus Einteilchenwellenfunktionen $\{\chi_\ell(\mathbf{r})\}_\ell$ finden kann, die gut im Ort lokalisiert sind [69–71]. In dieser Basis kann man die Feldoperatoren $\hat{\psi}(\mathbf{r}, t)$ entwickeln

$$\hat{\psi}(\mathbf{r}, t) = \sum_\ell \chi_\ell(\mathbf{r}) \hat{a}_\ell(t), \quad (1.4)$$

und erhält statt kontinuierlich vom Ort abhängiger Felder Operatoren \hat{a}_ℓ , die nur an dem einen Gitterplatz wirken, an dem die Einteilchenwellenfunktionen im Wesentlichen lokalisiert sind. In der Sprache der zweiten Quantisierung ist \hat{a}_ℓ ein Vernichtungsoperator und sein Adjungiertes \hat{a}_ℓ^\dagger ein Erzeugungsoperator jeweils eines Bosons am Gitterplatz ℓ . In einer Raumdimension lautet dann der Hamilton-Operator dieses sogenannten Bose-Hubbard-Modells in seiner minimalen Form mit $\hat{n}_\ell = \hat{a}_\ell^\dagger \hat{a}_\ell$ und $\ell = 1 \dots L$ [2, 72]

$$\hat{H}_{\text{BH}} = -J \sum_{\ell=1}^{L-1} \left(\hat{a}_\ell^\dagger \hat{a}_{\ell+1} + h.c. \right) + \frac{U}{2} \sum_{\ell=1}^L \hat{n}_\ell (\hat{n}_\ell - 1). \quad (1.5)$$

Die konstanten Koeffizienten J und U ergeben sich aus den entsprechenden Matrixelementen des Einteilchen-Hamilton-Operators bzw. des Teilchenwechselwirkungsterms aus Gl. (1.2) in der Basis der sogenannten Wannier-Funktionen $\chi_\ell(x)$ [69–71]. Dieses „tight-binding“ Modell vernachlässigt die Dynamik innerhalb eines Potentialtopfs des Gitters. Notwendige Voraussetzung für seine Gültigkeit ist, dass das System gut durch stark lokalisierte Einteilchenmoden in den Gittertöpfen eines genügend tiefen periodischen Potentials beschrieben wird. Der Hamilton-Operator \hat{H}_{BH} ist der Ausgangspunkt einer ganzen Reihe von Arbeiten, die in den Abschnitten 2.2.4 und 2.3 zusammengefasst sind, wobei zusätzliche Terme hinzugenommen wurden, die von zufälligen Gitterplatzenergien [30 | S. 179] bis hin zu einer wesentlich komplexeren Zweibandversion von Gl. (1.5) [39 | S. 235] reichen. Zudem lässt sich ausgehend von \hat{H}_{BH} systematisch für große Teilchenzahlen eine diskrete nichtlineare Schrödinger-Gleichung ableiten, welche einen Molekularfeldlimes des Vielteilchensystems darstellt, der dann für die konkreten Szenarien aus Abschnitt 2.5 auf seine Gültigkeit getestet wurde [48 | S. 283].

Kapitel 2

Einführung in die Originalarbeiten

Dieses Kapitel führt in die im Anschluss abgedruckten Originalarbeiten des Autors ein. Es motiviert die Fragestellungen, hebt die Bedeutung der erzielten Forschungsergebnisse hervor und ordnet diese in knapper Form in ihren wissenschaftlichen Kontext ein. Auf die Verwendung von Formeln wird dabei weitgehend verzichtet.

Die Originalarbeiten sind untergliedert in Kurzartikel, reguläre Artikel und eingeladene Buchbeiträge. In den folgenden Kapiteln sind sie jeweils entsprechend ihrem Erscheinungsdatum angeordnet. Mein relativer Beitrag ist der Autorenenreihenfolge zu entnehmen, wobei ich in der Funktion des Betreuer von Abschlussarbeiten [73–80] oder des Ideengebers als Letztautor auftrete. In gemeinsamen Publikationen mit Kollegen aus der Experimentalphysik verantworte ich den Theorieteil.

Der Schwerpunkt meiner Arbeiten liegt in der Beschreibung gekickter Atome (Abschnitt 2.1) und der Realisierung des Wannier-Stark-Systems mit Bose-Einstein-Kondensaten (Abschnitt 2.2). Die wichtigsten Themenkomplexe hierzu sind in den Reviews [50 | S. 324] und [49 | S. 293] zusammengefasst. Einen neuen Anstoß zum Studium offener Vielteilchenquantensysteme geben unsere Arbeiten zur Stochastischen Resonanz im Doppeltopf (s. die Referenzen [6 | S. 60] und [35 | S. 207]), die wir momentan auf komplexere Systeme ausdehnen; vgl. dazu die Teilkapitel 2.4.3 und 2.5.

2.1 Lokalisierung und Quantenresonanzen in gekickten kalten Atomen

Der sogenannte „Kicked Rotor“ ist seit den siebziger Jahren ein etabliertes Standardmodell, um klassisches Chaos in niedrigdimensionalen Systemen zu untersuchen [81, 82]. Seine quantenmechanische Version als freier Rotor mit quantisiertem Drehimpuls, der zeitlich periodisch gekickt wird, zeigt ferner, dass das System für typische Parameter nach einer charakteristischen Zeit keine Energie mehr aus den Kicks absorbiert [83–85]. Dieses Phänomen ist unter dem Namen Dynamische Lokalisierung bekannt und ist ein Analogon [86, 87] der Anderson-Lokalisierung von Wellenpaketen in ungeordneten Potentialen [88, 89]. Seit fast zwanzig Jahren erfreut sich der quantisierte Kicked-Rotor reges Interesses, aus dem einfachen Grund, dass er sich mittels atomoptischen Methoden gut experimentell realisieren lässt [56, 90]. Dabei werden Atome in Magneto-Optischen Fallen abgekühlt (s. Abschnitt 1.3.1), und dann nach Abschalten der Falle mit einer stehende Welle gekickt, die periodisch mit einer extrem kurzer Rampe ein- und ausgeschaltet wird. Mit jedem Kick erfolgt eine Beugung der Impulsklassen der Atome durch das räumlich periodische Gitter in hohe Ordnungen (sogenanntes Raman-Nath-Regime

der Atomoptik [91, 92]).

Vor allem in den letzten zehn Jahren haben sich unter anderem zwei neue Forschungsschwerpunkte herauskristallisiert. Zum einen die Untersuchung von Lokalisierung und deren Zerstörung in einem System, das mit mehr als einer Frequenz gekickt wird (das entspricht mehreren Raumdimensionen im Anderson-Problem, vgl. die Referenzen [93–96]). Neben Lokalisierungsphänomenen werden zum anderen Resonanzeffekte studiert, die nur für spezielle Parameterkombinationen auftreten [84, 97–99]. Letztere Effekte sind zunächst quantenmechanischer Natur, wobei sich herausstellt, dass sie sich weitgehend auch durch ein pseudo-klassisches, effektives Modell [60, 100–104] verstehen lassen. Dieses Modell, das in den folgenden Abschnitten oft zitiert wird, hat den großen Vorteil hat, dass man im klassischen Phasenraum reguläre Strukturen identifizieren kann, die den Resonanzmoden entsprechen. Die Beschreibung des Systems vereinfacht sich dadurch erheblich gegenüber quantenmechanischer Analytik. Die experimentelle Herausforderung ist aber lange Zeit gewesen, die quantenresonante Bewegung, die ballistisch ist (d.h. der mittlere Impuls wächst linear mit der Zeit), gut zu messen. Mit einem Ensemble aus kalten Atomen können nur indirekte Spuren der Resonanzen beobachtet werden [17, 19, 61, 105–107], da die Resonanzbedingung vom anfänglichen Impuls (besser Quasiimpuls im räumlich periodischen Kick-Potential) der Atome abhängt [60, 100]. Nur wenn sich diese Anfangsbedingungen im Impulsraum gut kontrollieren lassen, kann man die rein ballistische Bewegung für die Resonanzen niedriger und hoher Ordnung auch schön sehen [108–111]. Die besten Daten liefern demnach Experimente mit Bose-Einstein-Kondensaten, die deshalb einen erheblichen, qualitativen Fortschritt in der experimentellen Kontrolle bedeuten [108, 109, 111–113].

Unser Beitrag während der letzten sieben Jahren erstreckt sich von der experimentellen Beobachtung, über den Ausbau der Theorie, um beispielsweise den Einfluss von atomaren Wechselwirkungen eines Bose-Einstein-Kondensates zu verstehen, bis hin zur Anwendung der Resonanzmoden, die, wie beispielsweise Abschnitt 2.1.4 zeigt, sehr robuste Arbeitspferde zur Realisierung anderer Phänomene sind.

2.1.1 Einfluss atomarer Wechselwirkung

Am einfachsten modelliert man interatomare Wechselwirkung durch einen nichtlinearen Term in einer effektiven Molekularfeldtheorie. Der Einfluss eines nichtlinearen Terms im Impulsraum, der kubisch in der Wellenfunktion ist, auf die Dynamik des Quanten-Kicked-Rotors wurde schon 1993 untersucht [114]. Dabei stand die Frage im Fokus, ob die Nichtlinearität die dynamische Lokalisierung zerstört. Experimente mit Kondensaten werden dagegen durch die Gross-Pitaevkii-Gleichung (1.3) beschrieben, wobei der kubisch nichtlineare Term lokal im Ortsraum ist. Da dadurch aber die Translationsinvarianz des Systems gebrochen wird (das effektive Potential ist nun nicht mehr periodisch, und folglich lässt sich das experimentelle Problem nicht mehr exakt auf einen Rotor mit periodischen Randbedingungen abbilden), sind entsprechende numerische Untersuchungen schwieriger. Auf der analytischen Seite scheint die Frage, welchen Einfluss eine räumliche Nichtlinearität auf die Lokalisierung hat, bis heute offen (s. z. B. [115]).

In einer ersten Studie [16 | S. 81] haben wir beide Arten von Nichtlinearitäten untersucht, wobei mein Beitrag hauptsächlich den Quantenresonanzen gilt. *Ab initio* numerische Rechnungen, in denen die Gleichung (1.3) für gegebene Anfangsbedingungen (z. B. ein Kondensat, das in einer dreidimensionalen Falle relaxiert wurde), zeitlich integriert wird, sind vor allem deshalb schwierig, da man dreidimensional rechnen muss, um den Effekt des nichtlinearen Terms wirklich quantitativ zu beschreiben [14 | S. 39].

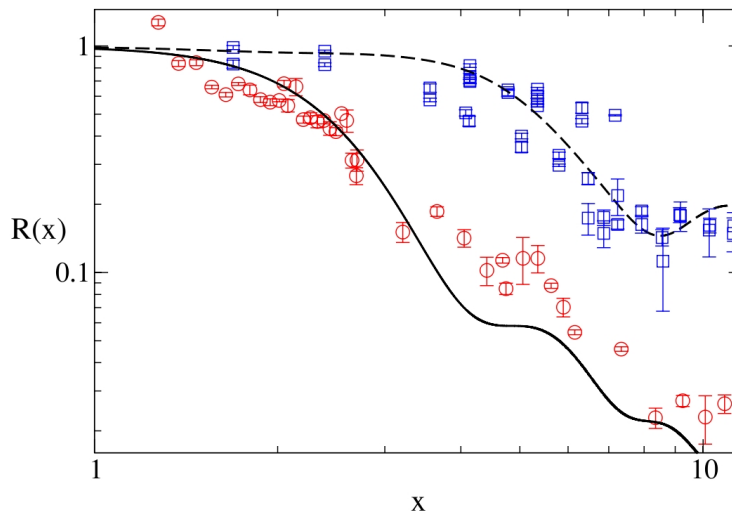


Abbildung 2.1: Ensemblegemittelte Energien aus Experimenten mit kalten Atomen in Nähe der Quantenresonanz (rote Kreise) und im Grenzfall $\tau \rightarrow 0$ (blaue Rechtecke) im Vergleich zu den theoretischen Vorhersagen (volle und gestrichelte Kurve). Die Energien sind dabei mit dem Wert bei $x \rightarrow 0$ reskaliert worden, woraus $R(x)$ folgt; $x = t\sqrt{|\varepsilon|k}$, wobei t die Anzahl der Kicks, k die Kickstärke und ε die Verstimmung der Kickperiode τ von der exakten Resonanzbedingung bzw. von $\tau = 0$ ist. Abbildung aus [19 | S. 96].

Effektive eindimensionale Modelle, wie auch von uns in [16 | S. 81] benutzt, machen üblicherweise Annahmen über die spezielle (zeitlich konstante!) Form der Wellenfunktion in radialer Richtung (senkrecht zur Kickachse), die sehr von den experimentellen Randbedingungen abhängen kann. In Ref. [14 | S. 39] zeigen wir für ein realistisches Szenario, dass eine schwache Wechselwirkung, wie sie durch die Gross-Pitaevkii-Gleichung gut beschrieben wird, nur einen kleinen Effekt während der anfänglichen Expansion des Kondensates hat, danach aber im Vergleich zu den Impulsüberträgen durch die Kicks vernachlässigbar wird. Mit anderen Worten führt gerade die schnelle Expansion zu einem Dichteabfall, der die Quantenresonanzen immun gegen die nichtlineare Störung macht. Unsere Vorhersagen, insbesondere auch für Resonanzen höherer Ordnung, wurden in einem Experiment mit einem Kondensat aus Natriumatomen am National Institute for Standards and Technology (NIST, USA) sehr schön bestätigt [108].

2.1.2 Quantenresonanzen im semiklassischen Limes

Gewisse Aspekte des NIST-Experiments [108] konnten wir mit Hilfe eines „alten“ Experimenttyps mit nur kalten Atomen vorwegnehmen. Die breite anfängliche Impulsverteilung macht zwar die direkte Beobachtung ballistischer Moden in Quantenresonanzbedingung unmöglich, aber unser pseudo-klassisches Modell [101] gibt eine genaue Theorie des Resonanzpeaks der mittleren Energie des atomaren Ensembles als Funktion der Kickperiode, der Zeit und der Kickstärke. Diese universelle Vorhersage des Peaks als Funktion nur einer einzigen Kombination der drei genannten Parameter konnte direkt im Experiment als Skalierungsfunktion nachgemessen werden [17 | S. 89]. Dabei stellten wir fest, dass eine kleine Abänderung der Theorie ausreicht, um auch den Grenzfall verschwindender Kickperiode zu beschreiben ($\tau \rightarrow 0$). Dieser unterscheidet sich vom üblichen semiklassischen Limes im Rotor, der zwei Grenzfälle braucht ($\tau \rightarrow 0$ und Kickstär-

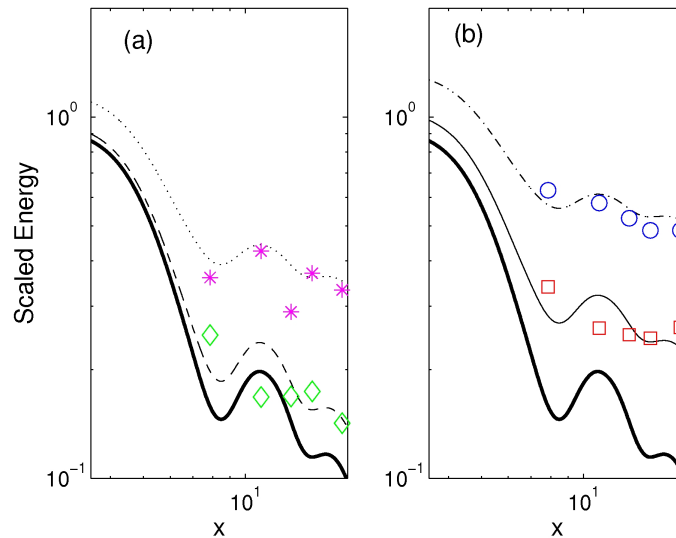


Abbildung 2.2: Ensemble-gemittelte Energien aus Experimenten mit kalten Atomen in Nähe einer Quantenresonanz (farbige Symbole) im Vergleich zu den theoretischen Vorhersagen ohne Rauschen (dicke Kurven) und relative Rauschstärken der Kickamplitude von 50% (gestrichelt), 100% (dünne Linie), 150% (gepunktet) und 200% (strichgepunktete Kurve). Die Energien sind dabei mit dem Wert bei $x \rightarrow 0$ reskaliert worden; $x = t\sqrt{|\varepsilon|k}$, wobei t die Anzahl der Kicks, k die Kickstärke und ε die Verstimmung der Periode von der exakten Resonanz ist. Abbildung leicht adaptiert aus [50 | S. 324].

ke $k \rightarrow \infty$), dadurch, dass bei uns die Kickstärke konstant gehalten wird. Damit lässt sich die Theorie, die im Rahmen der Quantenresonanzen entwickelt wurde, direkt auf den Fall $\tau \rightarrow 0$ übertragen [15 | S. 43]. Interessant ist dabei vor allem, dass die breite Anfangsimpulsverteilung in die pseudo-klassischen Gleichungen als (Breite \times Kickperiode) eingeht [101] und daher für kleine Perioden effektiv sehr schmal wird. Dies ermöglicht die Beobachtung ballistischen Transports auch direkt mit kalten Atomen zumindest bis zu einer Zeit, die das System braucht, um den endlichen Wert von τ aufzulösen [19 | S. 96]. Abbildung 2.1 zeigt die beiden Skalierungsfunktionen im Falle der Annäherung an eine Quantenresonanz (rote Datenpunkte), und des Grenzfalles $\tau \rightarrow 0$ (blaue Datenpunkte). Der von uns neu untersuchte Grenzfalle $\tau \rightarrow 0$ ist immer interessant, wenn man sonst eine sehr schmale Impulsverteilung braucht, um Effekte beobachten zu können. So basiert auch ein weiterer Vorschlag für ein Experiment, der am Ende des folgenden Abschnitts beschrieben wird, auf diesem Trick.

2.1.3 Stabilisierung durch reguläre Strukturen im Phasenraum

Amplitudenrauschen

In Experimenten mit periodischen optischen Gittern ist die Kalibrierung der Amplitude der stehenden Welle nicht ganz so gut möglich, und Unsicherheiten von etwa zehn Prozent der Amplitude sind die oft Regel (s. z. B. [17 | S. 89] und [1, 116]; Gründe sind unter anderem Amplitudenschwankungen von Experiment zu Experiment und die radiale Variation der Laserintensität, sodass nicht alle Atome dieselbe Amplitude wie im

Strahlzentrum spüren). Wir haben uns daher nach der Stabilität der Quantenresonanzen in Anwesenheit von Amplitudenrauschen [62, 117] gefragt und dabei festgestellt, dass diese äußerst robust sind (im Gegensatz zur Dynamischen Lokalisierung, die bei wachsendem Rauschen systematisch in Diffusion übergeht [118, 119]). Das Rauschen wurde dabei gezielt und kontrolliert im Experiment zugeführt, und deutliche Effekte sind erst bei etwa fünfzig Prozent Rauschstärke erkennbar [33 | S. 203]. Die beobachtete Stabilität der Dynamik lässt sich folgendermaßen erklären. Formal gesehen und qualitativ gesprochen sind die Bedingungen für das Auftreten von Quantenresonanzen nicht von der Kickstärke abhängig, sondern vor allem von der Periode der Kicks [50, 84, 97]. Unser pseudo-klassisches Bild kann auch auf den Fall von Rauschen erweitert werden, was zu einer neuen Skalierungsfunktion der mittleren Energie des atomaren Ensembles führt, die stark auf der regulären, pendelähnlichen Struktur der Resonanz im pseudo-klassischen Phasenraum basiert [33 | S. 203]. Das Rauschen bewirkt nun, dass Zustände nahe der Separatrix (welche Rotations- und Librationsbewegung trennt) mischen, und dadurch mehr Energie absorbiert wird als im Falle ohne Rauschen. Abhängig von der Rauschstärke werden also aus oszillierenden Pendelorbitalen mehr und mehr Rotationsorbitalen, was die Zunahme der Energie mit der Rauschstärke quantitativ erklärt, die in Abbildung 2.2 sichtbar ist.

Stabilitätsanalyse mittels der „Fidelity“

Eine dynamische Methode, um die Stabilität eines quantenmechanischen Systems zu charakterisieren, wurde erstmals 1984 von Peres vorgeschlagen [120]. Dabei wird derselbe Anfangszustand durch die Schrödinger-Gleichung zweimal propagiert, wobei aber in einem Fall ein Systemparameter leicht variiert wird. Das Stabilitätsmaß ist dann die sogenannte Fidelity, d.h. der Absolutbetrag des Hilbertraumüberlapps (des Skalarprodukts) der beiden gleichzeitigen Zustände als Funktion der Zeit. Die Fidelity wurde im Detail vor allem für Systeme untersucht, die im semiklassischen Limes chaotisch sind [121, 122]. Für (quasi-)reguläre Systeme – wie in unserem Fall der Pseudo-Klassik nahe der Quantenresonanzen – existiert bisher aber keine geschlossene Theorie. Intuitiv sollte aber klar sein, dass die schon im vorhergehenden Abschnitt beschriebenen Librationsorbitalen innerhalb einer stabilen klassischen Resonanzinsel ein periodisches Verhalten als Funktion der Zeit zeigen. Vergleicht man nun die Zeitentwicklung zweier Zustände, die mit leicht unterschiedlicher Geschwindigkeit oszillieren (bestimmt durch leicht unterschiedliche Kickstärken, was unser Fidelity-Parameter ist), sieht man tatsächlich zunächst einen Abfall der Fidelity von eins auf sehr kleine Werte, danach aber eine periodische Wiederkehr des Signals. Die Periode ergibt sich relativ einfach aus den beiden Oszillationsperioden der Einzelzustände, wie in Ref. [37 | S. 231] gezeigt wird. Interessant ist dabei, dass Zustände, die anfänglich genau mit dem stabilen Fixpunkt (dem Zentrum) der Resonanzinsel überlappen, auch bei der halben Periode ein Wiederkehren der Fidelity bewirken. Dies hat mit einer Symmetrie zu tun, welche einer Spiegelung des Drehwinkels um den Fixpunkt entspricht (vgl. auch [123]), und die schon bei leicht anderen Anfangsbedingungen gebrochen wird. Um den Unterschied zwischen diesen beiden Fällen zu sehen, bräuchte man deshalb sehr schmale Anfangsbedingungen im Impulsraum, die entweder durch ein hochverdünntes Bose-Einstein-Kondensat (ohne Wechselwirkung!) oder effektiv mittels des in Abschnitt 2.1.2 beschriebenen Tricks ($\tau \rightarrow 0$ anstatt nahresonanter Dynamik) erreicht werden können.

2.1.4 Gerichteter Transport

Eine direkte Anwendung der ballistischen Quantenresonanzmoden ist die Möglichkeit, durch sie gerichteten Transport (vulgo eine Quanten-Ratsche) zu realisieren. Vorschläge in dieser Richtung finden sich z. B. in [124–127]. Experimente im quantenresonanten Regime benutzen anstelle asymmetrischer Kickpotentiale leichter herzustellende, asymmetrische Anfangsbedingungen im Impulsraum [128, 129]. Unser Beitrag war es, eine einfache Erklärung für den im Experiment [128, 129] beobachteten Effekt zu geben, basierend auf unserer pseudo-klassischen Theorie [36 | S. 218]. Ferner erweiterten wir die Vorhersagen für exakte Resonanzbedingung auf kleine Verstimmungen um die Resonanz. Analog den in den vorherigen Abschnitten beschriebenen Skalierungsfunktionen für die Energie, lässt sich insbesondere eine neue Skalierungsfunktion des mittleren Impulses der Atome ableiten [36 | S. 218]. Der von uns beschriebene Ratschen-Effekt bei endlicher Verstimmung ist transient, d.h. er existiert, bis das System die Verstimmung bemerkt. Er hat aber den Vorteil, dass die Richtung des mittleren Impulses alleine durch die Verstimmung gesteuert werden kann (bei festen Anfangsbedingungen), und somit prinzipiell ein dynamischer Richtungswechsel möglich ist.

Neben den gerade erwähnten Quantenresonanz-Ratschen, lässt sich gerichteter Transport auch standardmäßig im Regime realisieren, in welchem die Dynamik des klassischen Rotors (jetzt nicht im pseudo-klassischen Sinne) chaotisch ist. Dazu bricht man üblicherweise sowohl eine räumliche als auch eine zeitliche Symmetrie des Problems [130–132]. In einer gemeinsamen Arbeit meiner ehemaligen Gruppe aus Pisa und Theoretikern aus Como schlugen wir in Analogie zu der Studie in Ref. [133] eine konkrete Implementierung mit nicht (oder schwach-) wechselwirkenden Atomen vor, in der sowohl beide Symmetrien gebrochen sind, als auch zusätzlich Dissipation auftritt. Die Symmetriebrechung erfolgt durch Doppelkicks mit zwei unterschiedlichen Kickperioden [134] durch zwei zueinander phasenversetzte optische Gitter, die aber die gleiche räumliche Periodizität aufweisen¹. Die relative Phase zwischen den Gittern bestimmt den Absolutwert und die Richtung des mittleren Impulses. Die Dissipation wird bewirkt durch absorbierenden Randbedingungen, die Impulsklassen außerhalb eines gewissen Fensters abschneiden. Der damit beobachtete Ratscheneffekt des Quantensystems ist dann zwar transient, da die Teilchen ja asymptotisch verloren gehen, aber sehr stabil gegenüber Parameterschwankungen, wie wir in Ref. [22 | S. 137] zeigen. Dasselbe Prinzip der absorbierenden Randbedingungen, die einer geschwindigkeitsabhängigen Selektion der Atome entsprechen, wie sie z. B. durch Raman-Übergänge realisierbar wäre [137], verwenden wir ferner in einem anderen Zusammenhang, der im nächsten Abschnitt kurz vorgestellt wird.

2.1.5 Fraktale Fluktuationen als Signatur Dynamischer Lokalisierung

Nachdem in den vorhergehenden Abschnitten die ballistischen Quantenresonanzmoden im Mittelpunkt standen, widmen wir uns nun dem Regime der Dynamischen Lokalisierung. Letztere kann auf verschiedene Weise charakterisiert werden: am besten durch *in situ* Messungen des Betragsquadrats der Wellenfunktion im Impulsraum [105], welche direkt den die Lokalisierung kennzeichnenden exponentiellen Abfall zeigt; aber auch durch die mittlere Energie des atomaren Ensembles, die nach einer transienten Zeit sättigt [105], was dem Einfrieren der Wellenfunktion in ihre exponentiell abfallende Form

¹Damals war die Phasenkontrolle doppelperiodischer Gitter, wie sie mittlerweile realisiert wurde [135, 136], noch nicht so einfach möglich.

entspricht. Eine weitere Methode besteht im Studium parametrischer Fluktuationen, die im lokalisierten Regime von der Größenordnung des Mittelwerts des Signals sind [138]. Letztere ist die Methode der Wahl in der Festkörperphysik, wo Lokalisierung vor allem durch Transportmessungen festgestellt werden kann.

Einer anderen Arbeit zum Quanten-Kicked-Rotor folgend [139], untersuchten wir dazu die Überlebenswahrscheinlichkeiten eines Ensembles von Anfangsbedingungen in einem Bereich im Impulsraum, der groß genug ist, um die Lokalisierung der Wellenfunktionen nicht wesentlich zu stören. Teile der Wellenfunktionen, die aus dem Bereich hinausreichen, werden abgeschnitten, was den Zerfall definiert, und dem im vorherigen Abschnitt besprochenen absorbierenden Randbedingungen entspricht. Wir wählten aber im Gegensatz zu früheren Untersuchungen die Kickperiode als Variationsparameter, als Funktion dessen die Fluktuationen der Überlebenswahrscheinlichkeit zu fester Zeit betrachtet werden. Das hat den einfachen Grund, dass die Periode im Experiment als Variable im Frequenzraum leichter kontrollierbar ist. Unsere theoretischen Ergebnisse, sowohl für einzelne Rotoren als auch für experimentell realisierbare Ensembles von Rotoren [20 | S. 110], übertragen nicht nur die früheren Resultate auf unseren Fall der Periodenvariation, sondern zeigen ferner, dass deutliche Signaturen der fraktalen Natur der parametrischen Fluktuationen schon bei relativ kurzen Kickzeiten beobachtet werden können; dazu ist jedoch eine hohe experimentelle Auflösung über mindestens eine Größenordnung der Kickperiode nötig. Zudem sollte der Einfluss von Quantenresonanzen hoher Ordnungen [84, 140], die dicht in jedem Intervall von Kickperioden liegen, möglichst ausgeschlossen werden. Letzteres ist eine Frage von Zeitskalen, denn Resonanzen hoher Ordnung machen sich erst bei extrem großen Kickzahlen bemerkbar [140]. Weitere detaillierte numerische Rechnungen und Analysen [27 | S. 161] weisen ferner auf eine bislang nicht näher untersuchte multifraktale Struktur der Fluktuationen hin; analoge komplexe Eigenschaften sind z. B. bekannt für Wellenfunktionen im kritischen Bereich eines Lokalisierung-Delokalisierungs-Übergangs [141]. Ob beide Phänomene zusammenhängen, und was die genaue Ursache der in Ref. [27 | S. 161] beobachteten Multifraktalität ist, sind offene Fragen.

2.2 Interbandtunneln in gekippten periodischen Potentialen

Ein altes Problem der Quantenmechanik ist die Dynamik eines Teilchens in einem periodischen Potential und unter Einfluss einer konstanten Kraft (z. B. eines Elektrons im Festkörpergitter bei Anlegen einer konstanten Spannung) [55, 142, 143]. Dieses sogenannte Wannier-Stark-System wurde schon in den neunziger Jahren mit kalten Atomen realisiert [144], was unter anderem die deutliche Messung von Bloch-Oszillationen ermöglichte [144, 145]. Auch Experimente mit Bose-Einstein-Kondensaten wurden von 1998 an gemacht [146, 147]. Letztere haben den Vorteil, dass nicht nur die Anfangsbedingungen im Impulsraum, sondern auch alle externen Potentiale sowie die Wechselwirkung zwischen den Teilchen mit hoher Präzision kontrollierbar sind [1]. Dies ist notwendig, um z. B. die Bloch-Oszillationen gut aufzulösen und den Einfluss der Wechselwirkung auf diese zu untersuchen [1, 147–149]. Für Experimente mit einem Kondensat aus Rubidiumatomen (^{87}Rb) ist die interatomare Wechselwirkung direkt durch eine Änderung der Streulänge in den Atom-Atom-Stößen schwer zu kontrollieren [150]. Ihr Effekt kann aber in einem gewissen Bereich durch das Einsperren des Kondensates in radialer Richtung, d.h. durch die Änderung der Teilchendichte, verstärkt werden [23 | S. 52]. In den im Folgenden beschriebenen Experimenten in Pisa war dies jedoch kein Hindernis, da wir entweder möglichst ohne Wechselwirkung arbeiteten oder deren schwache

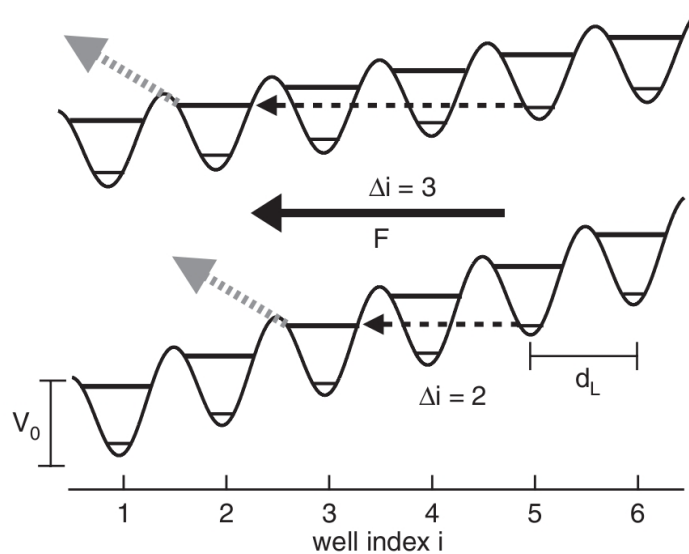


Abbildung 2.3: Skizze zum resonanten Tunneln in einem gekippten periodischen Potential mit Amplitude V_0 und Gitterkonstante d_L . Die eingezeichneten Zustände in den Gittertöpfen, die sogenannten Wannier-Stark-Zustände, bekommen durch die Tunnelkopplung eine endliche Zerfallsbreite. Diese Breiten sind für die dargestellten Fälle der Resonanz zwischen zwei Gitterplätzen mit Abstand $\Delta i = 2$ bzw. $\Delta i = 3$ stark erhöht, was durch die grauen Pfeile angegeben ist, die den Zerfall aus dem Gitter andeuten. Abbildung aus [23 | S. 52].

Wirkung gezielt durch resonantes Tunneln verstärken konnten.

2.2.1 Resonanzverstärktes Tunneln

Wie in Abbildung 2.3 für ein Einteilchenproblem skizziert, lässt sich der Transport in einem periodischen Potential erheblich verstärken, wenn man die konstante Stark-Kraft F so wählt, dass verschiedene Zustände in benachbarten Potentialtöpfen energetisch entarten [55]. Die Kopplung durch quantenmechanisches Tunneln führt dann zu vermiedenen Kreuzungen der Energieniveaus [55], deren Breite die Kopplungsstärke widerspiegelt. Da das System durch die Stark-Kraft an das energetische Kontinuum koppelt, ergeben sich derartige Kreuzungsszenarien in der komplexen Energieebene [143]. Mittels eigens entwickelter numerischer Methoden, wie der komplexen Skalierung zur Berechnung von Zerfallsraten [21 | S. 125] und einem Shooting-Suchverfahren [42 | S. 249], haben wir solche Szenarien für das nichtlineare Problem der Gross-Pitaevskii-Gleichung [151–153] untersucht, unter anderem auch in geneigten, doppelperiodischen Potentialen ([26 | S. 144] und [42 | S. 249]).

Während sich diese fundamentalen Studien auf eindimensionale Systeme beschränken, entwickelten wir eine hocheffiziente Methode zur direkten Integration der dreidimensionalen Gross-Pitaevskii-Gleichung (1.3) unter realistischen experimentellen Bedingungen [18 | S. 105], welche auch für die in Abschnitt 2.1.1 erwähnten Rechnungen eingesetzt wurde [14 | S. 39]. Unsere Vorhersagen zum Einfluss der Wechselwirkung auf die Zerfallsraten aus dem Grundzustandsband werden durch die in [23 | S. 52] und [31 | S. 183] beschriebenen Experimente bestens bestätigt. Der beobachtete Effekt des reso-

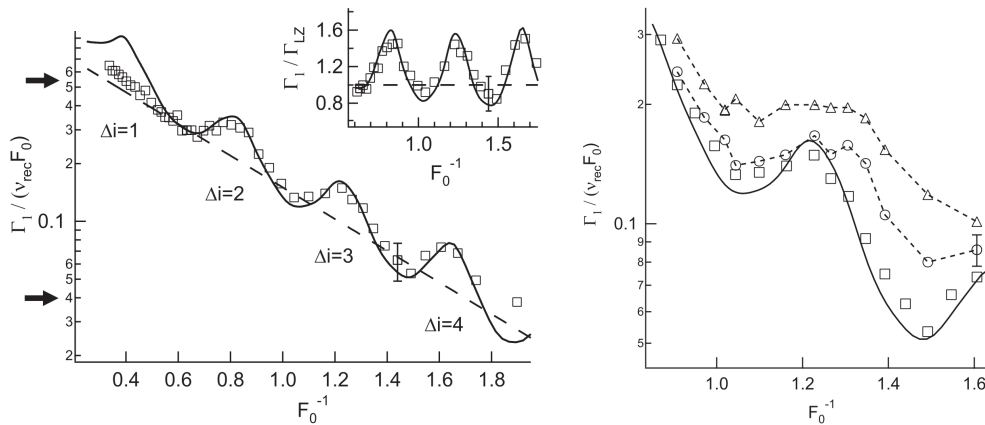


Abbildung 2.4: Experimentelle Messung der Zerfallsraten Γ_1 in einem gekippten periodischen Potential (Symbole) und theoretische Vorhersage (durchgezogene Linien). *Links*: Die Modulation auf der globalen exponentiellen Abhängigkeit der Raten von der inversen, dimensionslosen Stark-Kraft F_0^{-1} folgt aus der Resonanzbedingung zwischen den Zuständen in den Töpfen, welche zwei, drei und vier Gitterplätze voneinander entfernt liegen. Abweichungen bei großen und sehr kleinen Raten, im Bereich außerhalb der beiden Pfeile, sind durch experimentelle Probleme bedingt [23 | S. 52]. Die kleine Abbildung zeigt die Zerfallsrate relativ zur Vorhersage der Landau-Zener-Formel (s. Abschnitt 2.2.2 und z. B. [116]) welche die Resonanzen nicht berücksichtigt; letztere ist direkt als gestrichelte Linien in beiden Bildern zu sehen. *Rechts*: Abstoßende Wechselwirkung hebt systematisch die Zerfallsraten, zudem wird der Resonanzpeak ausgewaschen (Symbole mit steigender Teilchendichte von Rechtecken über Kreisen zu Pyramiden); beide Effekte konnten wir in der Arbeit [18 | S. 105] theoretisch vorhersagen. Abbildungen aus [23 | S. 52].

nanten Tunnels zwischen verschieden weit entfernten Nachbartöpfen kann mit oder ohne Wechselwirkung benutzt werden, um den Zerfall durch die Kippkraft stark zu beeinflussen. Wählt man beispielsweise einen experimentellen Arbeitspunkt zwischen einem Maximum (resonantes Tunneln) und einem Minimum („Antiresonanz“), führt eine kleiner Änderung der Kraft zu einer großen Variation der Raten (s. Abbildung 2.4). Eine solche Kontrolle des Transports durch resonantes Tunneln wurde bereits von Tsu und Esaki für ähnliche Systeme mit kleinerer Ausdehnung vorgeschlagen [154], wobei damals aber nicht mit der Präzision der Experimente mit ultrakalten Gasen gerechnet werden konnte [49 | S. 324].

2.2.2 Zeitaufgelöste Messung der Überlebenswahrscheinlichkeit

Wie das Arbeiten mit ultrakalten Atomen die direkte Beobachtung von Bloch-Oszillationen über lange Zeiten ermöglicht [148, 149], lässt sich auch der Zerfall aus dem Grundzustandsband des periodischen Potentials in Anwesenheit der Stark-Kraft mit feiner Zeitauflösung untersuchen. Die schmale Impulsbreite des Anfangszustandes verbessert dabei erste Messungen von Raizen und Mitarbeitern [116, 155] erheblich und macht die Stufenstruktur erst sichtbar, die aus der zeitlichen Trennung der Prozesse – Bloch-Oszillation bis zur Bandkante und Zerfall in der Nähe der Bandkante – folgt. Die Stufen haben dann eine endliche Breite, die der Breite des Wellenpakets im Impulsraum

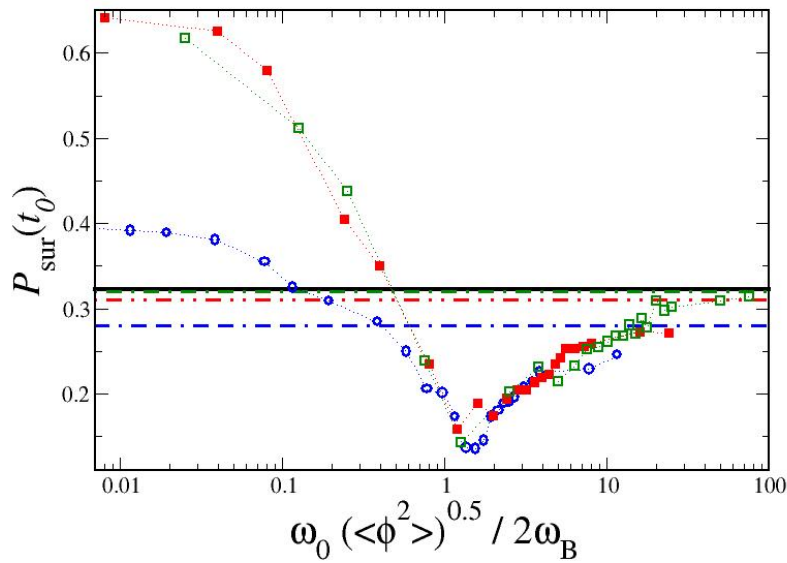


Abbildung 2.5: Überlebenswahrscheinlichkeiten nach sechs Bloch-Perioden $T_B = 2\pi/\omega_B$ als Funktion der skalierten Rauschfrequenz, bezogen auf das Referenzgitter, für das die Vorhersage als durchgezogene horizontale Linie gezeigt ist. Die Varianz des Rauschens variiert dabei von $\langle \phi^2 \rangle = 0.25$ (offene Kreise) über 1 (volle Rechtecke) bis 10 (offene Rechtecke). Für große Werte auf der x -Achse gehen die Daten in die Vorhersage des jeweiligen effektiven statischen Potentials über, das aus dem zeitlichen Mittel über die schnell variierende Phase folgt (durchbrochene Linien in gleicher Farbe wie entsprechende Symbole). Abbildung adaptiert aus [45 | S. 72].

entspricht [34 | S. 64]. Für den wechselwirkungsfreien Fall konnte die Gültigkeit einfacher Modelle getestet werden, welche die Interbandkopplung auf einen Landau-Zener-Übergang (beschrieben durch eine zwei mal zwei Matrix) im einfachperiodischen Potential [40 | S. 241] zurückführen. Abweichungen von den Vorhersagen dieser Modelle stammen unter anderem von Resonanzeffekten (s. vorhergehenden Abschnitt) oder der Tatsache, dass es sich im Wannier-Stark-Problem um eine zeitlich äquidistante Serie von Durchgängen durch vermiedene Kreuzungen handelt, vgl. [40 | S. 241] und [156, 157].

Interessant ist auch der Fall, wenn atomare Wechselwirkung eine Rolle spielt, die man unter Ausnutzung der zeitlichen Änderung der atomaren Dichte und von Resonanzeffekten verwenden kann, um starke Abweichungen von einem monoexponentiellen Zerfallsgesetz zu erhalten [28 | S. 155]. Aber auch ohne resonantes Tunneln erhält man nur asymptotisch das für den Einteilchenfall erwartete exponentielle Zerfallsgesetz, welches sich erst einstellt, wenn die Teilchendichte auf vernachlässigbare Werte abgefallen ist, vgl. [158] und [21 | S. 125]. Die Abweichungen vom globalen exponentiellen Zerfall sind zwar für die beispielsweise in Pisa hergestellten atomaren Dichten [31 | S. 183] schwach, und daher im Rahmen der Meßfehler schwer zu sehen, aber doch deutlich in den ansonsten realistischen numerischen Simulationen sichtbar [18 | S. 105].

2.2.3 Kontrolle des Zerfalls durch Phasenrauschen

Experimentell können heute standardmässig auch komplexere Potentiallandschaften realisiert werden [1, 2]. Ein Beispiel sind Doppelgitter, deren Gitterkonstanten entweder kommensurabel (üblicherweise sich um einen Faktor zwei oder vier unterscheiden [135]) oder inkommensurabel (im Rahmen der experimentellen Genauigkeit) [159, 160] sind. Während erstere eine Implementierung der von uns in [26 | S. 144] und [42 | S. 249] untersuchten Wannier-Stark-Systeme darstellen, sind inkommensurable Gitter interessant, um Lokalisierungsphänomene im statischen, pseudo-zufälligen Potential, das durch sie realisiert wird, zu untersuchen [161, 162].

Man kann sich fragen, wie sich nun eine zeitabhängige Unordnung auf die Dynamik in einem so veränderten Wannier-Stark-System auswirkt. Dazu betrachten wir den Fall zweier inkommensurabler Gitter, wobei das erste das in den vorhergehenden Abschnitten untersuchte Referenzsystem darstellt, das zweite aber einer zeitabhängigen Phasenverschiebung gegenüber dem ersten ausgesetzt ist. Für die Phasenverschiebung wählen wir einen stochastischen Prozess, um somit eine zeitabhängige Unordnung zu haben. Experimentell sollte eine solche dynamische Phasenverschiebung durch geeignete Modulatoren, die das Gitter kontrollieren, in einem weiten Parameterbereich herstellbar sein [1]. Insbesondere liefert die Wahl eines harmonischen Rauschens eine mittlere Energieskala, die man auf die Skalen des Referenzsystems abstimmen kann. Damit lässt sich nun der Zerfallsprozess aus dem Grundzustandsband des Referenzsystems zusätzlich kontrollieren. Das Ergebnis ist, dass sich das Signal (die Überlebenswahrscheinlichkeit zu fester Zeit) schön skalieren lässt, was die Universalität unserer Vorhersagen über einen weiten Parameterbereich hervorhebt. Abbildung 2.5 zeigt, dass bei geeigneter Reskalierung der mittleren Rauschfrequenz ω_0 mit der Varianz des Rauschens $\langle \phi^2 \rangle$ und der Bloch-Periode im Referenzgitter ω_B ein Minimum nahe dem universellen Wert 1 auftritt. Für größere Rauschfrequenzen gehen die Datenkurven in eine ebenfalls universelle Vorhersage für schnelles Rauschen über, wobei in diesem Fall ein Phasenmittel ein effektives statisches Potential ergibt, das nur von der Varianz $\langle \phi^2 \rangle$ abhängt [44 | S. 263]. Abweichungen vom universellen Verhalten treten bei zu kleinen Rauschfrequenzen auf, wenn einerseits die spektrale Breite des Rauschens wichtig wird, und andererseits die systemrelevanten Zeitskalen zu kurz sind, sodass sich die Details des Rauschens nicht mehr ausmitteln können [45 | S. 72].

2.2.4 Vielteilchen-Wannier-Stark-System

Die in den letzten Abschnitten vorgestellten Fragestellungen lassen sich auf den Fall tiefer Potentialgitter und starker interatomarer Wechselwirkung ausdehnen. Für tiefe Gitter kann man das ursprüngliche Kontinuumsproblem gut durch ein diskretes Modell beschreiben, dessen Grundstruktur oben in Abschnitt 1.3.3 eingeführt worden ist. Um Interbandkopplungen mitzunehmen, muss man das Bose-Hubbard-Modell natürlich erweitern und entsprechende Terme für die Stark-Kraft und das zweite Band mitberücksichtigen. Während das Einband-Modell mit Stark-Kraft in den Referenzen [72, 163–165] untersucht wurde, gibt es hauptsächlich nur Aussagen über Phasendiagramme der Grundzustandsmoden von Mehrbandmodellen ohne zusätzliche Kraft (s. beispielsweise [166–168]). Ein Zweibandmodell kann experimentell gut durch ein Übergitter realisiert werden, das aus zwei Gittern mit um einen Faktor zwei verschiedenen räumlichen Perioden gebildet wird [135]. Durch das zweite Gitter wird das Grundzustandsband in zwei Minibänder aufgespalten, die bei geeigneter Wahl der Gitteramplituden und -phasen energetisch gut von höheren Bändern getrennt sind [135, 169]. Für Füllfaktoren (An-

zahl der Bosonen geteilt durch die Zahl der Gitterplätze) um eins untersuchen wir dieses System unter Einfluss einer konstanten Stark-Kraft, wobei wir in zwei Schritten vorgehen:

Effektives Einbandmodell

Wir beginnen mit dem Studium eines aus dem vollen Zweibandmodell abgeleiteten effektiven Systems, das die Interbandkopplungsterme störungstheoretisch behandelt. Ausgehend von einer Besetzung rein im Grundzustandsband kann dadurch ein effektiver Hamilton-Operator für dieses Band abgeleitet werden, der absorbierende Terme enthält, welche den Zerfall ins angeregte Band perturbativ beschreiben. Letztere Terme wurden auf der Basis von Fermis Goldener Regel analytisch abgeleitet und dann am Ende in die Diagonalterme der Einband-Hamilton-Matrix eingesetzt. Dabei werden die Matrixelemente in der üblichen Fock-Basis im Ortsraum ausgedrückt, und somit erhält jeder Fock-Zustand seinen eigenen, von den jeweiligen Besetzungszahlen abhängigen Zerfallsterm [29 | S. 170]. Die exakte Diagonalisierung dieser effektiven Hamiltonschen Matrix ist für größere Systeme als für das volle Zweibandmodell möglich, wobei wir typischerweise Systeme bis zu zehn Bosonen in zehn Gitterplätzen betrachteten.

Unsere Ergebnisse bestätigen einerseits die Resultate zu den spektralen Eigenschaften des geschlossenen Einbandmodells [163, 164], erlauben aber darüber hinaus die Analyse der Zerfallsraten der Eigenzustände, die den Imaginärteilen der Eigenenergien entsprechen. Das überraschende Resultat ist, dass die Statistik dieser Zerfallsraten den Vorhersagen für den Zerfallsprozess eines *einzelnen Teilchens* in einem eindimensionalen, ungeordneten Gitter entspricht [24 | S. 56]. Dort tritt für genügend starke Unordnung Anderson-Lokalisierung auf, die auf eine Normalverteilung der Logarithmen der Zerfallsraten führt [170]; im Falle schwacher Unordnung, d.h. für Systemlängen klein oder vergleichbar mit der Lokalisierungslänge, erwartet man dagegen diffusiven Transport, aus dem eine Zerfallsratenverteilung folgt, die durch ein Potenzgesetz beschrieben wird (vgl. [171] und die darin enthaltenen Referenzen). Unser Vielteilchenmodell zeigt – bis auf systemspezifische Abweichungen – vergleichbare Statistiken, wobei hier die Teilchenwechselwirkung die Unordnung ersetzt [29 | S. 170]. Qualitativ gesprochen wirken also die restlichen Teilchen wie ein effektives Unordnungspotential für ein ausgezeichnetes Boson. Da es sich aber prinzipiell um ununterscheidbare Bosonen handelt, ist dieses Bild natürlich falsch und nur eine Hilfe zum Verständnis der beschriebenen Analogie. Um eine quantitative Interpretation zu geben, könnte man von der Matrixstruktur unseres Systems starten und diese mit üblichen Modellen aus der Theorie ungeordneter Systeme [172] vergleichen. Diese etwas technische Fragestellung wollen wir künftig weiter verfolgen.

Geschlossenes Zweibandmodell

In einem zweiten Schritt betrachteten wir das volle Zweibandmodell. Hier ergibt sich eine Vielzahl von Fragen, die man untersuchen kann. Im Gegensatz zum Einbandmodell besteht die Hamiltonsche Matrix nun aus zwei Teilen, die Zuständen entsprechen, die ausschließlich nur Besetzungen in einem der beiden Bänder haben, und einer großen Mehrheit von Zuständen, die zwischen dem oberen und unteren Band hybridisiert sind. Man kann dann – je nach Wahl der Parameter – starke Kopplungen in einem Teilbereich (z. B. in dem Teil, der dem unteren Band entspricht) haben und mehr oder weniger Einzelteilchendynamik im anderen Band. Darüberhinaus kann man die Interbandkopplungsterme durch die Stark-Kraft, aber auch durch die atomare Wechselwirkung einstellen.

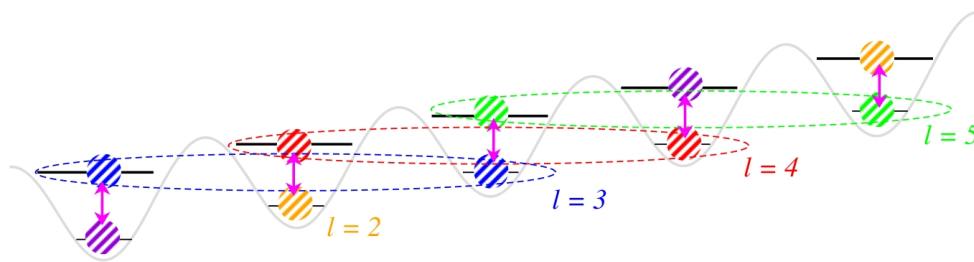


Abbildung 2.6: Veranschaulichung des effektiven Spinmodells mit jeweils zwei möglichen Spineinstellungen (innerhalb der gestrichelten Ellipsen), die den hybridisierten Zuständen des ursprünglichen Gittersystems entsprechen. Die Kopplung der Spins entlang der Kette bewirkt zunächst den Kollaps und das spätere „Revival“ der Interband- oder Spinoszillationen. Es ist der in Abbildung 2.3 gezeigte Fall von resonantem Tunneln zwischen jeweils übernächsten Nachbarn ($\Delta i = 2$) skizziert. Abbildung aus [46 | S. 270].

Startet man von einer schwachen Teilchenwechselwirkung, kann man die Resultate aus Abschnitt 2.2.1 reproduzieren, bei denen die Interbandkopplung durch eine resonante Stark-Kraft verstärkt wird. Der Unterschied besteht dann aber darin, dass unser Zweibandmodell an sich geschlossen ist, d.h. anstatt eines Transports ins Kontinuum sieht man Oszillationen in den Besetzungen der Bänder [47 | S. 277]. Für verschwindende Wechselwirkung sind solche resonanten Oszillationen perfekt, was mit der Rabi-Oszillation in einem Zweizustandssystem vergleichbar ist. Schaltet man schwache Wechselwirkung dazu, beobachtet man einen anfänglichen Zerfall der Oszillationen, aber auch eine Wiederkehr nach einer charakteristischen Periode, die hauptsächlich durch die Energieskala der wechselwirkungsinduzierten Interbandkopplung bestimmt ist [39 | S. 235]. Dieses Kollaps- und „Revival“-Phänomen lässt sich am besten dadurch verstehen, indem man – wie in Ref. [46 | S. 270] vorexerziert – das ursprüngliche System mit durchschnittlich einem Teilchen pro Gitterplatz auf eine Kette von Spins $1/2$ abbildet, wobei der besagte Wechselwirkungsterm der Atome zu einer Kopplung der Spins entlang der Kette führt. Wie in Abbildung 2.6 skizziert, entspricht dabei der untere Spinzustand einem Boson im unteren Niveau und der obere Spinzustand einem Boson im oberen Niveau des jeweils übernächsten Topfes. Der so erhaltene Hamilton-Operator für die Spins beschreibt ein eindimensionales Ising-Modell mit konstantem Magnetfeld, also ein analytisch lösbares Problem, aus dem eine analytische Abschätzung für die Wiederkehrzeit der Interbandoszillationen folgt [46 | S. 270]. Kollaps- und Revivalphänomene, die auf der starken Wechselwirkung zwischen den Atomen beruhen, wurden bereits im Experiment beobachtet [173, 174]. Im Gegensatz dazu ist bei uns der Oszillationseffekt durch die Stark-Kraft induziert und gewissermaßen durch die Wechselwirkung gestört, was zum Auftreten einer neuen Periode, eben der Revivalzeit, führt.

2.3 Quantenchaos in Vielteilchensystemen

Nicht nur niedrigdimensionale Quantensysteme wie der in Abschnitt 2.1 beschriebene Quanten-Kicked-Rotor zeigen komplexes dynamisches Verhalten, sondern natürlich auch Vielteilchensysteme. Während in ersteren der äußere Antrieb zu starken Kopplungen im Energieraum führt, können in letzteren die Teilchen-Teilchen-Wechselwirkung

und auch äußere Kräfte dazu beitragen, dass viele Zustände einer typischen Basis (beispielsweise der Fock-Zustände im Modell aus Gl. (1.5)) im Laufe der zeitlichen Entwicklung gekoppelt werden. Hochdimensionale Vielteilchensysteme charakterisiert man dabei am besten durch ihre spektralen Eigenschaften auf der Basis der sogenannten Bohigas-Giannoni-Schmit'schen Vermutung [87, 175], die besagt, dass komplexe Dynamik zu Statistiken führt, wie sie die Theorie von Zufallsmatrixen [176] vorhersagt. Ein übliches Maß dafür ist die Statistik der Energieabstände nächster Nachbarn im Spektrum, die anzeigen ob sich Energieniveaus als Funktion eines Kontrollparameters kreuzen (also nicht koppeln) oder als vermiedene Kreuzungen meiden (ein Zeichen von Kopplung zwischen den jeweiligen Niveaus). Ferner kann man die Verteilung der Breiten der vermiedenen Kreuzungen betrachten, die im Falle eines „quantenchaotischen“ Systems einer Gaußverteilung genügt [177], im Gegensatz zu einer sehr engen Verteilung (im Extremfall konstanter Kreuzungsbreiten einer δ -Verteilung), wie sie in regulären Systemen auftritt. Neben dem Spektrum lassen sich auch die Eigenfunktionen untersuchen [87, 176], z. B. projiziert auf eine typische Basis des Problems, wie der Fock-Basis [178] für das Modell aus Abschnitt 1.3.3.

Im Folgenden stellen wir Ergebnisse von Studien des Einband-Hubbard-Modells, s. Gl. (1.5), vor, wobei wir die meisten der gerade beschriebenen Maße zur Charakterisierung der Systemeigenschaften benutzen. Methodisch stellten wir ein neues Maß vor, um vermiedene Kreuzungen zu detektieren und weiter zu untersuchen. Diese in [43 | S. 256] eingeführte „Fidelity“ wurde bereits verwendet, um Phasenübergänge numerisch in Vielteilchenmodellen zu charakterisieren [179, 180]. Wir zeigten zusätzlich seine Eignung für das ganze Spektrum eines komplexen Systems.

2.3.1 Chaos verstärkt durch Unordnung

Als erstes widmen wir uns dem reinen Modell aus Abschnitt 1.3.3. Wie bereits in Ref. [178] gezeigt wurde, zeichnet sich dieses System durch verschiedene dynamische Regime aus: in den beiden Grenzfällen von entweder verschwindender Tunnelkopplung J oder verschwindender Wechselwirkung U ist es natürlich integrabel mit den bekannten Lösungen, z. B. der kosinus-förmigen Energiedispersion bei $U = 0$. Sind dagegen die Parameter so gewählt, dass beide Terme im Hamilton-Operator etwa gleich stark sind, also $J \approx Un$, wobei $n = N/L$ für den Füllfaktor (bei Teilchenzahl N und Systemlänge L) steht, zeigen die Unterräume des Problems, die sich aus der Berücksichtigung der Translationsinvarianz und möglicher Inversionssymmetrie ergeben, alle oben genannten Zeichen eines quantenchaotischen Verhaltens [178].

Da es experimentell schwierig ist, die aufgrund einer Symmetrie nicht koppelnden Bereiche zu trennen, untersuchten wir das Verhalten des um einen statischen Unordnungsterm erweiterten Hamilton-Operators aus Gl. (1.5). Die Unordnung hebt natürlich die Translationsinvarianz auf (wie auch die für bestimmte Quasiimpulse bestehende Inversionssymmetrie). Dadurch ergibt sich im Parameterbereich $J \approx Un \approx \Delta$, wobei Δ die Unordnungsstärke angibt, eine ähnliche Situation wie für Unterräume im Falle ohne Unordnung, nur jetzt *global* für das ganze Spektrum. Diese Tatsache macht sich in der zeitlichen Entwicklung sowohl im Impuls- als auch im Ortsraum bemerkbar, was als experimentelle Signatur der spektralen Eigenschaften messbar sein sollte, wie wir in der Arbeit [30 | S. 179] folgern.

2.3.2 Fidelity-Maß zur Charakterisierung vermiedener Kreuzungen

Wie oben erwähnt, zeigt sich der Charakter stark koppelnder Systeme nicht nur in den Eigenspektren, sondern auch in den Eigenfunktionen. Statt die Niveaudynamik als Funktion eines Kontrollparameters λ zu untersuchen, kann man auch die Eigenfunktionen über variiertes λ verfolgen, was am besten über den Überlapp der Eigenzustände zu jeweils festem Kontrollparameter geht. Der Absolutbetrag dieses Überlapps ist auch als Fidelity bekannt [181], die verwandt zur im Abschnitt 2.1.3 behandelten zeitabhängigen Größe ist, aber zunächst ein zeitunabhängiges Maß, basierend auf den *Eigenzuständen*, darstellt. Bei einer vermiedenen Kreuzung wird dieser Überlapp stark variieren, da der entsprechende Eigenzustand $|E(\lambda)\rangle$ durch die Kopplung an den anderen seinen Charakter ändert. Um einerseits eine Größe zu haben, die ein Maximum anstelle eines Minimums aufweist, und um andererseits die Abhängigkeit von der Parametervariation $\delta\lambda$ klein zu halten, definiert man am besten folgendes Maß

$$S_E(\lambda, \delta\lambda) = \frac{1 - |\langle E(\lambda) | E(\lambda + \delta\lambda) \rangle|}{(\delta\lambda)^2}. \quad (2.1)$$

Damit lassen sich nicht nur, wie beispielsweise in den Referenzen [179, 180] gezeigt, Phasenübergänge detektieren, sondern auch der spektrale Verlauf im allgemeinen charakterisieren [43 | S. 256]. In der numerischen Analyse von Daten bietet die Untersuchung von S_E verschiedene Vorteile. Erstens hat es sich als zuverlässiger Detektor von vermiedenen Kreuzungen herausgestellt, der somit als „Black Box“ universell einsetzbar ist. Zweitens kann man aus einer lokalen Untersuchung im Energieraum bereits Erkenntnisse über das Systemverhalten gewinnen, ohne eine globale spektrale Statistik von Niveauabständen machen zu müssen (letztere bedarf einer Vielzahl von Niveaus, um zuverlässige Statistiken zu erhalten). Dieser zweite Aspekt mag natürlich auch experimentell interessant sein, wenn man jeweils nur eine geringe Zahl von Energieniveaus aus mehreren Bereichen des Spektrums untersuchen und daraus bereits Signaturen komplexen oder regulären Verhaltens bekommen kann.

Da S_E nur jeweils zwei Zustände vergleicht, muss man sich fragen, was passiert, wenn sich mehrere Energieniveaus an einer vermiedenen Kreuzung nahekommen. Dies wurde in [43 | S. 256] für den Fall eines dritten, schwach mit den anderen beiden Zuständen gekoppelten Niveaus analytisch und für den Fall dreier stark gekoppelter Zustände numerisch untersucht. Dabei ergeben sich Korrekturen zu der Peakform der Maxima von S_E , die aber immer noch als solche aufgelöst werden können, solange sich mehrere stark gekoppelte Zustände sich nicht so nahe kommen, dass die Signalmaxima vollständig miteinander verschmelzen. Letzteres kann in quantenchaotischen Systeme auftreten, passiert aber erfahrungsgemäß selten (vgl. die in [43 | S. 256] untersuchten Systeme, z. B. die Einbandversion des bereits in Abschnitt 2.2.4 behandelten Hubbard-Modell mit konstanter Stark-Kraft [163–165]). In den gerade laufenden Untersuchungen des wegen der Abwesenheit einfacher globaler spektraler Eigenschaften weitaus schwieriger zu verstehenden Zweiband-Hubbard-Modells (s. Abschnitt 2.2.4) setzen wir das hier beschriebene Fidelity-Maß bereits erfolgreich ein, um lokale Niveaufenspaltungen durch Wechselwirkungsterme, z. B. im Bereich resonanten Tunnelns, zu untersuchen [182].

2.4 Dynamik im Doppeltopf

Bald nach den ersten Realisierungen eines Bose-Einstein-Kondensates aus ultrakalten Atomgasen [63, 64] wurde der mit einem Kondensat gefüllte Doppeltopf [183] einge-

hend theoretisch untersucht [65, 184–188]. Experimentell wird er implementiert durch die Überlagerung eines periodischen Gitters mit einer engen harmonischen Falle, vgl. beispielsweise die Referenzen [189, 190]. Eine einfache Abbildung der Molekularfeld-dynamik im Doppeltopf auf eine klassische Hamiltonsche Funktion, die ein Pendel beschreibt, bei dem die Pendellänge aber vom kanonischen Impuls abhängt, liefert verschiedene Regime oszillierender und rotierender Bewegung mit entsprechenden Orbits im Phasenraum [65, 187, 191]. Im sogenannten Josephson-Regime entsprechen zwei mögliche Bewegungen der Oszillation des Kondensates als ganzes vom einen in den anderen Topf bzw. dem Fall des sogenannten „self-trappings“, in dem das Kondensat in einem Topf verweilt [65, 189].

Wir haben das Doppeltopfproblem aus zwei Blickwinkeln untersucht. Zum einen haben wir uns der Frage gewidmet, wie man im geschlossenen Problem möglichst dynamisch zwischen den beiden Fällen im Josephson-Regime schalten kann, ohne die experimentelle Anfangssituation zu verändern, was z. B. in Ref. [189] geschah. Zum anderen dehnten wir die Fragestellung in zweierlei Hinsicht aus; nämlich auf Vielteilchenaspekte wie Verschränkungserzeugung durch einen periodischen Antrieb und auf das Problem eines Doppeltopfs, aus dem heraus Teilchen dissipieren können und zudem einem Phasenrauschen unterworfen sind. Die genannten Themen werden im Folgenden kurz vorgestellt.

2.4.1 Kontrolle kollektiven Tunnelns

Durch ein spezielles Design des Doppeltopfes kann man erreichen, dass die beiden Molekularfeldlösungen, die einem oszillierenden bzw. dem in einem Topf gefangenen Kondensat entsprechen, energetisch beinahe entartet sind. In unserem Vorschlag geschieht dies durch eine kleine periodische Modulation in jedem der beiden Töpfe [25 | S. 47]. Die beinahe Entartung über einen weiten Bereich der atomaren Wechselwirkungskonstante erlaubt dann relativ einfach, durch eine minimale zeitabhängige Veränderung der Barriere zwischen den Töpfen von einem Josephson-Regime ins andere zu schalten. Dabei lösten wir das statische Problem exakt durch Reduktion auf eine rechtwinklige Doppeltopfgeometrie ohne Modulation, woraus die Bedingungen für die minimale Barrierevariation abgeleitet werden konnten. Das dynamische Schaltverhalten wurde dann numerisch im Detail untersucht, vgl. Ref. [25 | S. 47].

2.4.2 Verschränkungserzeugung im Bose-Hubbard-System

Stellt man sich eine Situation mit einer tiefen periodischen Modulation vor, kann man nun auch das Bose-Hubbard-Modell mit einem Doppeltopf folgendermaßen verbinden: Zur Erzeugung und dem anschließenden Nachweis von Verschränkung im System entwickelten wir ein Szenario, das in Abbildung 2.7 skizziert ist: man startet im Grundzustand eines periodischen Gitters; dann treibt man das System, indem man die Gittertiefe leicht periodisch in der Zeit variiert, und zwar so, dass die Antriebsfrequenz energetisch einer Einteilchenanregung U entspricht; nachdem das System in einen quasi-stationären Zustand übergegangen ist, schaltet man den Antrieb ab und kurze Zeit später eine Barriere in der Mitte des Gitters hoch, sodass das System effektiv in zwei Teilsysteme separiert wird. Dadurch kann man übliche und einfache Verschränkungsmaße, die für zwei Subsysteme definiert sind [192, 193], anwenden. Das Einschalten der Barriere friert gewissermaßen die Kopplung zwischen den beiden Teilbereichen und auch die Verschränkungsdynamik ein. Jeder der zwei Teilbereiche enthält dann eine Superposi-

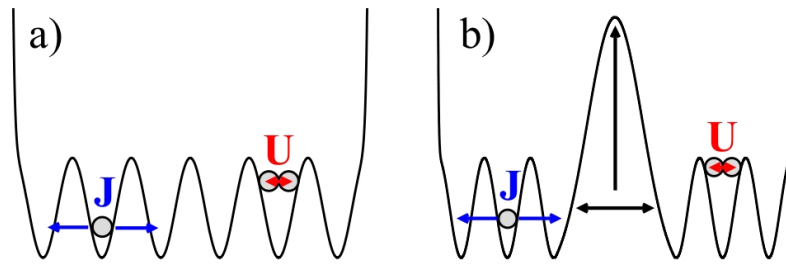


Abbildung 2.7: (a) Präparation des Systems in einem endlichen Gitter; eine periodische Modulation der Gitteramplitude führt zu einer zeitlichen Änderung der Kopplungskonstanten J und U des Hubbard-Modells aus Gl. (1.5). (b) Nach Abschalten der Modulation wird durch das Hochfahren der Barriere die Dynamik zwischen dem linken und rechten Teil der Barriere eingefroren, und man findet stark korrelierte Zustände in diesem „Doppeltopf“ vor. Abbildung aus [38 | S. 68].

tion verschiedener Teilchenzahlen, was formal bedeutet, dass die beiden Bereiche stark quantenmechanisch korreliert sind. Unsere Rechnungen zeigen, dass eine hohe und robuste Verschränkung in sogenannten postselektierten Zuständen (unter der Bedingung gleicher Teilchenzahl in beiden Teilbereichen) vorliegt [38 | S. 68]. Ein periodischer Antrieb ist also nicht nur nützlich zur Kontrolle der Dynamik (vgl. z. B. [194, 195]) oder zur Spektroskopie (vgl. z. B. [196]) in einem Vielteilchensystem, sondern auch zur kontrollierten Herstellung verschränkter Zustände, wie in anderen Zusammenhängen beispielsweise für zwei unterschiedliche Atomsorten in Ref. [194] oder an Hand eines einfacheren, reinen Zweitopfmodells in Ref. [197] gezeigt wird.

2.4.3 Stochastische Resonanz

Stochastische Resonanz tritt in den verschiedensten Kontexten in Erscheinung, in klassischen bis hin zu quantenmechanischen Systemen [198, 199]. Die Grundidee ist schlichtweg, dass die untersuchte Observable, in klassischen Systemen üblicherweise das sogenannte Signal-zu-Rausch-Verhältnis, ein Maximum bei einem endlichen Rauschwert aufweist. Mit anderen Worten tritt eine Signalverstärkung durch die Anwesenheit von Rauschen auf. Inspiriert von den experimentellen Möglichkeiten [1, 189, 190] untersuchten wir die Reaktion eines Kondensates in einem Doppeltopf auf Phasenrauschen und Teilchenverluste aus beiden Töpfen.

Unsere zentrale Observable ist dabei der Interferenzkontrast, der sich ergibt, wenn die Teilchen aus den zwei Töpfen nach Abschalten aller Potentiale interferieren. Dieser Kontrast ist in der Sprache der Bose-Hubbard-Moden aus Gl. (1.5) durch das Nichtdiagonalelement der reduzierten Einteilchendichtematrix für zwei Moden bzw. durch die folgende Operator-Korrelationsfunktion gegeben:

$$\alpha = \frac{2\langle \hat{a}_1^\dagger \hat{a}_2 \rangle}{\langle \hat{n}_1 + \hat{n}_2 \rangle}, \quad (2.2)$$

wobei wegen des Teilchenverlusts die Besetzungszahlen der Töpfe, $\langle \hat{n}_1 \rangle$ und $\langle \hat{n}_2 \rangle$, zeitabhängig sind. Im Rahmen dieses Zweimodenmodells kann man die Bewegungsgleichungen in der Molekularfeldnäherung auf die bekannten Bloch-Vektorgleichungen für

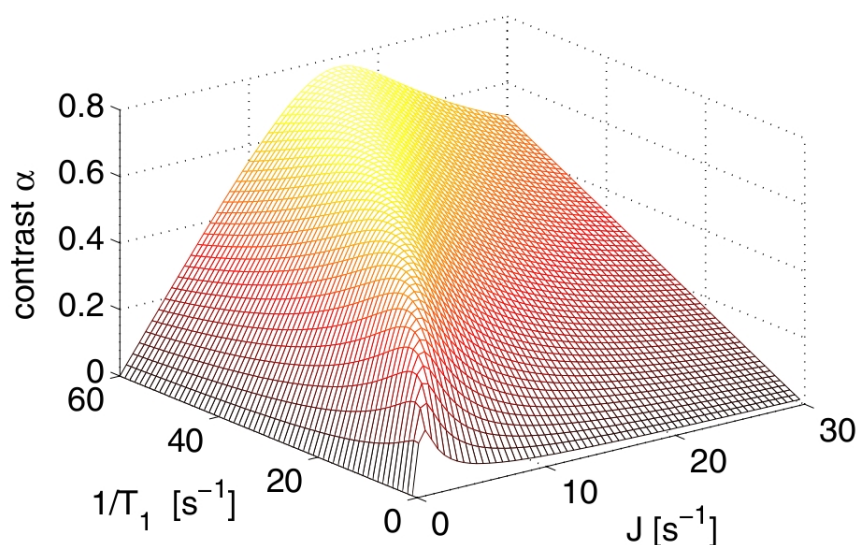


Abbildung 2.8: Phasenkontrast aus Gl. (2.2) als Funktion des Tunnelmatrixelements J und der Dissipationsrate T_1^{-1} bei verschwindender Wechselwirkung. Bei festem J sieht man deutlich ein Maximum im Kontrast bei endlicher Rate. Abbildung aus [6 | S. 60].

die Dynamik eines Spin-1/2-Systems abbilden. Dissipation und Rauschen führen dabei – wie im Problem der Kernspinresonanz [200] – zu den sogenannten T_1 und T_2 -Relaxationszeiten, und eine zusätzliche Gleichung beschreibt die zeitliche Abnahme der Teilchenzahl [6 | S. 60].

Interessant ist dabei die Rolle der Wechselwirkung. Bei verschwindender oder schwacher Wechselwirkung bildet sich nach einem kurzen Transienten ein quasi stationärer Zustand aus, in dem der oben definierte Phasenkontrast ein deutliches Maximum bei endlicher Zerfallszeit T_1 ausbildet, wie in Abbildung 2.8 zu sehen ist. Im Falle starker Wechselwirkung bleibt dagegen der beobachtete Stochastische-Resonanz-Effekt üblicherweise transient, d.h. verschwindet bei langen Zeiten. Im zeitlichen Verlauf des Phasenkontrastes zeigt sich aber – nach einer anfänglichen Abnahme – eine neuerliche Zunahme, die weitgehend ausbleibt, falls man entweder die Wechselwirkung oder die Dissipation ausschaltet. Mit andern Worten trägt die simultane Anwesenheit von Dissipation und Wechselwirkung zum Effekt bei. Ein gutes qualitatives Verständnis des Systemverhalten lässt sich aus der Molekularfelddynamik [32 | S. 198] ableiten. Daraus ergibt sich eine Schwelle für das minimale Produkt aus Wechselwirkungskonstante und Teilchenzahl, für die der Phasenkontrast merklich ansteigt. Diese ist verwandt mit der Schwelle für das Auftreten des „self-trappings“ im geschlossenen und ungestörten Doppelpotf [184, 185, 189, 190]. Vielteilchenrechnungen auf der Basis des Zweipotf-Hubbard-Modells bestätigen im Wesentlichen unsere Molekularfeldresultate, sind aber nötig, um Anregungen aus den Kondensatmoden zu beschreiben [35 | S. 207].

2.5 Transport und Dynamik in offenen Vielteilchensystemen

Das im vorhergehenden Abschnitt 2.4.3 beschriebene Problem lässt sich auf größere Systeme erweitern. Dies eröffnet eine Vielzahl neuer Fragestellungen. Schon methodisch gesehen kann man im Rahmen eines Einband-Hubbard-Modells nur relativ klei-

ne Systeme hinsichtlich der Zahl der Teilchen und der Gittertöpfe untersuchen. Damit stellt sich automatisch die Frage nach effizienten Rechenmethoden für geschlossene, vor allem aber auch offene Vielteilchensysteme. In ausgedehnten Systemen lässt sich dann konkret die zeitliche Entwicklung über das Gitter untersuchen, welche durch Dissipation und Phasenrauschen beeinflusst wird. Derartige Transportphänomene sind verwandt mit Untersuchungen aus der Festkörperphysik, und man spricht daran angelehnt in diesem Zusammenhang schon von „Atomtronics“ [201, 202].

Unser erster Schritt in die Richtung der Behandlung offener, ausgedehnter Vielteilchensysteme ist die systematische Weiterentwicklung numerischer Verfahren in Ref. [48 | S. 283]. Das System wird in Anlehnung an die Arbeiten [203, 204] durch ein gekoppeltes Gleichungssystem für die Erwartungswerte der reduzierten Ein- und Zweiteilchendichtematrixen geschrieben. Dieses Gleichungssystem erhält man aus der Entwicklung des Vielteilchenproblems in Korrelationsfunktionen von Erzeugungs- und Vernichtungsoperatoren, die wir in zweiter Ordnung abrechnen. Im Falle großer Teilchenzahl N ist diese Näherung gut und geht im Molekularfeldlimites für $N \rightarrow \infty$ in eine diskrete Gross-Pitaevskii-Gleichung auf dem Gitter über. Zusammen mit einer effektiven Beschreibung des offenen Systems durch eine Master-Gleichung können wir damit Transportphänomene in Gegenwart von Teilchendissipation und Phasenrauschen nahe am Molekularfeldlimites untersuchen. Die Mitnahme der Zweiteilchenkorrelationsfunktionen erlaubt aber auch Aussagen über die Fragmentierung eines Bose-Kondensats und die Stabilität der entsprechenden Molekularfeldlösungen. Durch geeignete Ankopplung an die Umgebung durch Rauschen und/oder Dissipation konnten wir dadurch bereits die Bildung stabiler (zumindest für experimentell relevante Zeitskalen) Strukturen wie eines soliton-ähnlichen Zustandes vorhersagen [48 | S. 283]. Unsere Ergebnisse entsprechen dabei für kleinere Systeme weitgehend den Daten aus einer Vielteilchenzeitentwicklung, die auf dem Einband-Hubbard-Modell basiert [48 | S. 283].

Dieses hochaktuelle Themenfeld beinhaltet natürlich noch viele offene Fragen. Momentan erweitern wir unsere bisherigen Studien in folgender Hinsicht. Wir streben an, die Kopplung an Bäder nicht nur perturbativ im Sinne der Master-Gleichung mitzunehmen, sondern die Bäder unter vereinfachenden Annahmen direkt in unseren Formalismus miteinzubauen. Damit lassen sich Szenarien wie Transport durch das Gitter von Bad zu Bad studieren, wie sie in der Festkörperphysik z. B. durch einzelne oder eine Kette von Quantenpunkten (vgl. die Referenzen [205, 206]) auftreten. Der Einfluss von Vielteilchenkorrelationen auf die mögliche Einstellung eines dynamischen Gleichgewichts ist dabei eine zentrale Frage. Dazu versuchen wir, unsere an die Molekularfeldtheorie angelehnte Methode weiter zu verallgemeinern, um Vielteilcheneffekte unter expliziter Mitnahme der Bäder besser behandeln zu können. Wir implementieren daher gerade eine Umformulierung in gekoppelte Gleichungssysteme von zeitgleichen und zeitunterschiedlichen Operatorkorrelationsfunktionen (Greensfunktionen), die – wie wir hoffen – zeitabhängige Phänomene realistischer beschreiben [207].

Kapitel 3

Wissenschaftliche Kurzartikel (Letters)

- **Resonant nonlinear quantum transport for a periodically kicked Bose condensate**
 S. Wimberger, R. Mannella, O. Morsch, and E. Arimondo,
 Physical Review Letters 94 (2005) 130404 39
- **Ballistic and localized transport for the atom-optics kicked rotor in the limit of vanishing kicking period**
 M. Sadgrove, S. Wimberger, S. Parkins, and R. Leonhardt,
 Physical Review Letters 94 (2005) 174103 43
- **Driven collective quantum tunneling of ultracold atoms in engineered optical lattices**
 R. Khomeriki, S. Ruffo, and S. Wimberger,
 Europhysics Letters 77 (2007) 40005 47
- **Resonantly enhanced tunneling of Bose–Einstein condensates in periodic potentials**
 C. Sias, A. Zenesini, H. Lignier, S. Wimberger, D. Ciampini, O. Morsch, and E. Arimondo, Physical Review Letters 98 (2007) 120403 52
- **Many-body interband tunneling as a witness for complex dynamics in the Bose-Hubbard model**
 A. Tomadin, R. Mannella, and S. Wimberger,
 Physical Review Letters 98 (2007) 130402 56
- **Dissipation induced coherence of a two-mode Bose-Einstein condensate**
 D. Witthaut, F. Trimborn, and S. Wimberger,
 Physical Review Letters 101 (2008) 200402 60
- **Time-resolved measurement of Landau–Zener tunneling in periodic potentials**
 A. Zenesini, H. Lignier, G. Tayebirad, J. Radogostowicz, D. Ciampini, R. Mannella, S. Wimberger, O. Morsch, and E. Arimondo,
 Physical Review Letters 103 (2009) 090403 64

- **Dynamical enhancement of spatial entanglement in massive particles**
M. Lubasch, F. Mintert, and S. Wimberger,
Physical Review Letters (2011) submitted68

- **Engineering interband transport by time-dependent disorder**
G. Tayebirad, R. Mannella, and S. Wimberger,
Physical Review Letters (2011) submitted72

Resonant Nonlinear Quantum Transport for a Periodically Kicked Bose Condensate

Sandro Wimberger, Riccardo Mannella, Oliver Morsch, and Ennio Arimondo

INFN, Dipartimento di Fisica E. Fermi, Università di Pisa, Largo Pontecorvo 3, 56127 Pisa, Italy

(Received 13 December 2004; published 8 April 2005)

Our realistic numerical results show that the fundamental and higher-order quantum resonances of the δ -kicked rotor are observable in state-of-the-art experiments with a Bose condensate in a shallow harmonic trap, kicked by a spatially periodic optical lattice. For stronger confinement, interaction-induced destruction of the resonant motion of the kicked harmonic oscillator is predicted.

DOI: 10.1103/PhysRevLett.94.130404

PACS numbers: 03.75.Lm, 02.70.Bf, 05.60.Gg, 32.80.-t

Dynamical systems that exchange significant energy with an external driving (time-dependent) field are paradigmatic objects for the study of complex evolutions with only a few degrees of freedom. In contrast to autonomous systems, where chaotic behavior can originate from many-body interactions, the complexity in driven systems arises from and can be controlled by the external field. An experimental setup where *both* types of complexity—many-body dynamics and external drive—are present is realizable and to a large degree controllable with state-of-the-art atom optical systems [1,2]. Good control over nontrivial dynamics is the necessary tool for manipulating quantum states in a desired way [3]. Controlled coherent evolution is the necessary ingredient for quantum computing schemes and, in particular, for algorithms which are based on a fast spreading over the Hilbert space of interest. Recently, ballistic expansion (i.e., linearly increasing momenta with time) was proposed to realize such quantum random walk algorithms [4].

In this Letter, we answer the question of whether ballistic resonant quantum transport can be realized with a periodically kicked Bose condensate. Cold dilute atomic gases have so far been used to realize many features of quantum chaos, such as dynamical localization [5] or dynamical tunneling [6]. To implement a fast spreading in momentum space, one can use quantum accelerator modes found recently [7], or the standard δ -kicked rotor (KR) which shows ballistic motion at the so-called quantum resonances [8]. The latter, however, are hard to realize if the initial conditions cannot be optimally controlled [9]. The preparation of a Bose condensate within a harmonic trap offers very well-defined initial momenta, necessary for observing ballistic motion for a substantial number of kicks.

We use the time-dependent Gross-Pitaevskii equation (GPE) [10] to describe a Bose-Einstein condensate in a harmonic confinement which is subject to a temporally and spatially periodic optical potential, created by a far detuned optical lattice. If the external potentials are not too strong, the GPE provides a good approximation of experiments with dilute Bose gases [11,12]. The GPE which we numerically integrate has the following form:

$$i\hbar \frac{\partial \psi(\vec{r}, t)}{\partial t} = \left[-\frac{\hbar^2 \nabla^2}{2M} + \frac{M\omega_x^2 x^2}{2} + \frac{M\omega_r^2 \rho^2}{2} + V_0 \cos(2k_L x) \sum_{m=-\infty}^{+\infty} F(t - mT) + gN |\psi(\vec{r}, t)|^2 \right] \psi(\vec{r}, t), \quad (1)$$

with $\rho^2 = y^2 + z^2$. $\psi(\vec{r}, t)$ represents the condensate wave function, and M is the atomic mass. The nonlinear coupling constant is given by $g = 4\pi\hbar^2 a/M$, N is the number of atoms in the condensate, a is the s -wave scattering length, and k_L is the wave vector of the laser creating the optical potential. In principle, an arbitrary pulse shape $F(t)$ may be realized, but here we restrict ourselves to a situation where the laser is switched on at time instants separated by T , with maximum amplitude V_0 and periodic pulse shape function $F(t)$ of unit amplitude and duration $\delta T \ll T$. Our system is then the nonlinear analogue of noninteracting cold atom experiments [5,9], which implement the KR model, and we can directly compare our results with the well-studied KR (for $\omega_x \rightarrow 0$) or with the kicked harmonic oscillator (KHO) [13] (for nonvanishing ω_x). The commonly used dimensionless kicking strength and kicking period of the KR are $k = (V_0/\hbar) \int_0^T dt F(t)$ and $\tau = 8TE_R/\hbar$, with the recoil energy $E_R = (\hbar k_L)^2/2M$ [9].

The GPE was numerically integrated using a finite difference propagator, adapted by a predictor-corrector loop to reliably evaluate the nonlinear interaction [14]. The external, time-dependent potential makes the integration challenging, in both time and computer memory. Typical integration times range from a few hours for a simplified 1D version of Eq. (1), to several weeks for the full 3D problem. For the 1D model, the motion is confined to the longitudinal (x) direction, and we use the renormalized nonlinear coupling parameter $g_{1D} = 2\hbar\omega_r a$, assuming a radial trapping frequency $\omega_r \gg \omega_x$ [15]. Experimentally, such a confinement is obtained using a cigar-shaped optical tube, as realized in the experiment of Moritz *et al.* [16]. The initial state inserted into (1) is the relaxed condensate wave function corresponding to the *experimental ground state* in a magnetic or optical trap. The ground state lies

between the cases of a Gaussian, for $g = 0$, and the Thomas-Fermi limit, which is essentially an inverted parabola, for large nonlinearity [10]. Its characteristic width σ_{p_x} in momentum space is determined by the nonlinearity. Increasing the nonlinearity in Eq. (1) leads to a smaller width σ_{p_x} of the initial state [10].

The dynamics of the system described by (1) depends sensitively on the relative strength of the three potentials, i.e., on the control parameters V_0 (for fixed pulse shape), ω_x , and g . Since the system absorbs energy from the optical lattice, we must at all times compare the kinetic energy with the (longitudinal) trap potential and the nonlinear term. If the latter two contributions are small, we can easily realize ballistic quantum motion, up to interaction times above which the trap potential is no longer negligible. On the other hand, we can tune the system to a situation where the trap crucially affects the dynamics, and we then have a realization of the KHO.

In the following, we show that the fundamental as well as higher-order quantum resonances (QR) of the KR can be observed in an experiment using a Bose condensate, in the presence of a shallow harmonic confinement. In the linear KR, the QRs occur at specific kick periods $T = T_T s/r$ (s, r integer) [8]. At the Talbot time $T = T_T$, the amplitudes of the wave function in momentum space exactly rephase between successive kicks for particular initial momenta ($p_{\text{init}} = 0$) [1,8]. The result is a maximal, i.e., perfectly phase-matched, absorption of energy from the kicks, leading to a ballistic spread of the wave packet [8,9]. Only signatures of the QRs at $T = T_T/2$ and $T = T_T$ have been

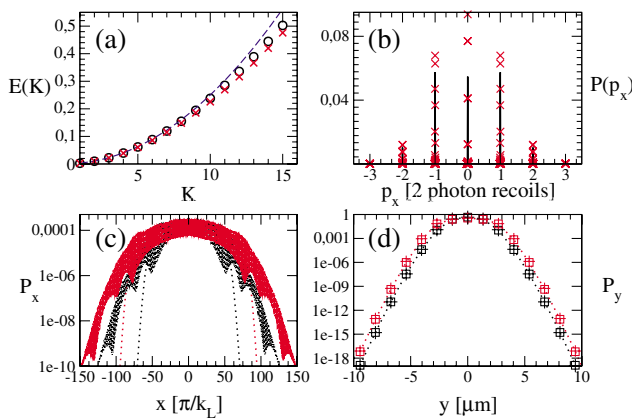


FIG. 1 (color online). (a) Kinetic energy (in units of $8E_R$) vs K , at $T = T_T$, $k = 0.1$ (pulse width $\delta T \approx 500$ ns, rise time 70 ns; $V_0/E_R \approx 8$, $\omega_x/2\pi = 10$ Hz, $\omega_r/2\pi = 100$ Hz, and $N = 10^4$ (circles), $N = 5 \times 10^4$ (crosses)). The linear KR evolution with $p_{\text{init}} = 0$ is shown by the dashed line. (b) Momentum distribution (2) after $K = 15$, $N = 10^4$ (solid line), $N = 5 \times 10^4$ (crosses). (c) The longitudinal (dotted line: $K = 0$; shaded area: $K = 15$) and (d) the transverse (dotted line: $K = 0$; squares: 7; pluses: 15) spatial distributions for $N = 10^4$ (thin distributions) and $N = 5 \times 10^4$ (broad distributions). The transverse dynamics is frozen due to the small effective nonlinearity.

observed up to now in experiments with essentially non-interacting atoms, because the initial momenta of the atoms could not be sufficiently controlled [9].

Figure 1 presents our results for the fundamental QR of the KR at the Talbot time for Rb atoms, $T = T_T = \pi\hbar/(2E_R) \approx 66.26 \mu\text{s}$, with $k_L \approx 8.1 \times 10^6 \text{ m}^{-1}$. Shown are the kinetic energy and the momentum distribution of the condensate along the longitudinal direction. The energy is computed from the momentum distribution, integrated over the transverse directions, i.e.,

$$E(K) = \frac{1}{2} \int dp_x p_x^2 P(p_x, K)$$

$$\text{with } P(p_x, K) \equiv \int dp_y dp_z |\psi(\vec{p}, t = KT)|^2, \quad (2)$$

where K denotes the number of kicks. We present also the integrated spatial distribution along the transverse direction [in y , or equivalently z , because of the radial symmetry in Eq. (1)]: $P_y(K) = \int dx dz |\psi(\vec{r}, t = KT)|^2$. As an example for higher-order QRs, which up to now have never been resolvable experimentally, Fig. 2 shows data for the resonance at $T = T_T/4$. For all the parameters studied, the

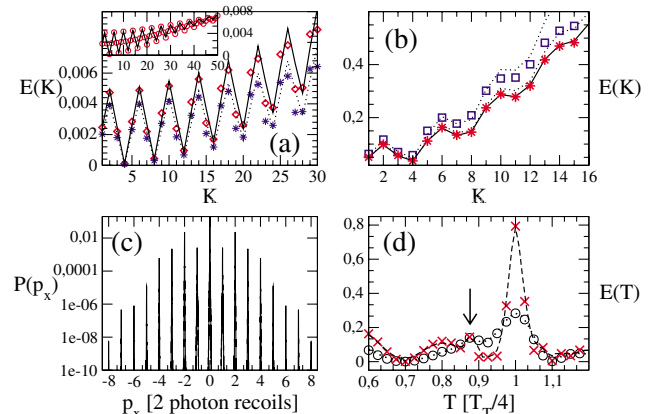


FIG. 2 (color online). Kinetic energies at $T = T_T/4$, same trap and pulse shape as in Fig. 1: (a) 1D, $N = 10^4$, $k = 0.1$ (red diamonds) and $k = 0.09$ (blue stars), and (b) $k = 0.45$ ($V_0/E_R \approx 42$), $N = 10^4$ (1D, solid line; 3D red stars), and 3D $k = 0.48$ ($V_0/E_R \approx 45$), $N = 10^3$ (squares). (c) Momentum distribution (2) for 3D with $k = 0.45$ after $K = 15$. (d) A scan of the kinetic energy vs T for the 1D case from (b), after $K = 10$ (circles) and $K = 20$ (red crosses), with the corresponding data for the linear KR (dotted and dashed lines). The resonance at $T = T_T/4$ manifests itself clearly, and a tiny peak of another higher-order resonance is marked by the arrow. The inset in (a) confirms the correspondence between our method (circles) and a 1D fast Fourier transform evolution of the linear KR (solid line) [a wave packet (circles) or an incoherent ensemble of plane waves (solid line) was evolved, respectively, with initial Gaussian momentum distribution— $\sigma_{p_x} = 0.026\hbar k_L$ — $k = 0.09$]. For comparison, the linear KR ($p_{\text{init}} = 0$) in (a) for $k = 0.1$ (solid line), $k = 0.09$ (dotted line), and (b) $k = 0.48$, $k = 0.45$ (dotted line).

ballistic quantum transport, with a quadratic growth $E(K) \propto K^2$, is clearly visible.

Deviations from the idealized ballistic motion arise because of the contributions of the trap potential and the nonlinearity. At long times, the expanding condensate feels the harmonic trap potential, and further acceleration is hindered by the trap. This effect is negligible for vanishing ω_x . Equating the longitudinal trap potential and the kinetic energy, and using $p_x \lesssim \pi k K \hbar k_L$ at $T = T_T$ [8,17], we estimate the kick number above which the trap dominates the dynamics as $K \sim 2k_L \sqrt{\hbar/M\omega_x} \approx 55$ for the parameters of Fig. 1. More crucial is the small but finite initial condensate momentum spread ($\sigma_{p_x} \ll 2\hbar k_L$ [1,2]), which, after a characteristic time $t^* \propto 1/\sigma_{p_x}$, leads to a linear increase of the energy $E(K) \propto K$ [17]. This crossover sets in at $K \approx 10$ in Fig. 1(a). For small σ_{p_x} , the condensate ground state extends over many lattice sites of the kicking potential, which in turn makes a smaller trap potential necessary for ideal ballistic motion. The interplay between these situations is illustrated in Fig. 3, where we systematically vary the number of atoms in the condensate. We stress that the effect of the nonlinearity manifests itself indirectly via its influence on the initial state, while the nonlinear interaction is negligible during the kick evolution at the QRs studied. This finding is quite surprising, remembering that the QRs correspond to exact phase revivals between kicks. On short time scales, however, the perturbation induced by the nonlinearity cannot accumulate a large enough dephasing, because even for the small

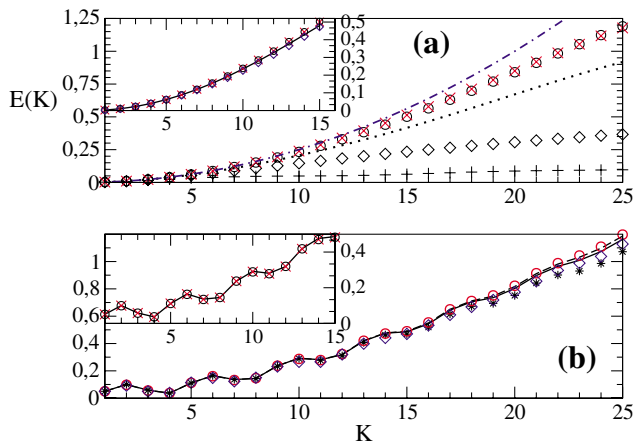


FIG. 3 (color online). Scan of the number of atoms (trap as in Fig. 1 if not stated otherwise): (a) for $T = T_T$, and 1D $N = 5 \times 10^3$ (crosses), $N = 10^4$ (circles), $N = 5 \times 10^4$ (diamonds), $N = 10^5$ (plusses); 3D in the inset for $N = 10^3$ (solid line), $N = 5 \times 10^3$ (crosses), $N = 10^4$ (circles), $N = 5 \times 10^4$ (diamonds). The dot-dashed line shows the analytical result $E(K) = k^2 K^2 / 4$ [linear KR, $p_{\text{init}} = 0$], and the dotted line 1D data for $\omega_x / 2\pi = 5$ Hz, and $N = 5 \times 10^4$. (b) $T = T_T / 4$, $k = 0.45$, 1D for $N = 10^2$ (stars), $N = 10^3$ (solid line), $N = 3 \times 10^3$ (dashed line), $N = 10^4$ (circles), $N = 5 \times 10^4$ (diamonds); 3D in the inset for $N = 10^3$ (solid line), $N = 5 \times 10^3$ (crosses), $N = 10^4$ (circles).

kick strength $k < 0.5$ it is at least 1 order of magnitude smaller than the kinetic energy. Our results are consistent with a simplified 1D model analysis of the QR, in the presence of a small nonlinear perturbation [18]. This analysis, however, could not account for the exact nonlinear wave packet evolution including the harmonic confinement.

We finally note that for a large number of atoms $N \geq 5 \times 10^4$ the results of our 1D model and the full 3D computations differ [cf. Fig. 3(a)] because initially the condensate substantially expands along the transverse directions. This is crucial for the realization of ballistic quantum transport, since for the same number of atoms in the condensate, the trap has less effect in the 3D as compared with the 1D case, but, on the other hand, σ_{p_x} in the 3D case is slightly larger. For the parameters of Fig. 3(a), the larger σ_{p_x} has a negligible influence, while the smaller initial spatial extension allows the ballistic motion to survive longer in the 3D than in the 1D case.

The nonlinearity manifests itself if we scan the kick period over the fundamental QR and plot the kinetic energy at fixed K . The resonance peak shows a slight asymmetry, which does not occur in the linear KR. The asymmetry decreases when (i) reducing the longitudinal confinement [solid line as compared with circles in Fig. 4(a)], or (ii) evolving the initial condensate state without the nonlinear term [pyramids in Fig. 4(a)]. Again the trap potential hides the influence of the nonlinearity, but the observed asymmetry originates from both perturbations of the usual KR. Any such perturbation is expected to introduce an asymmetric peak shape, following a semiclassical analysis

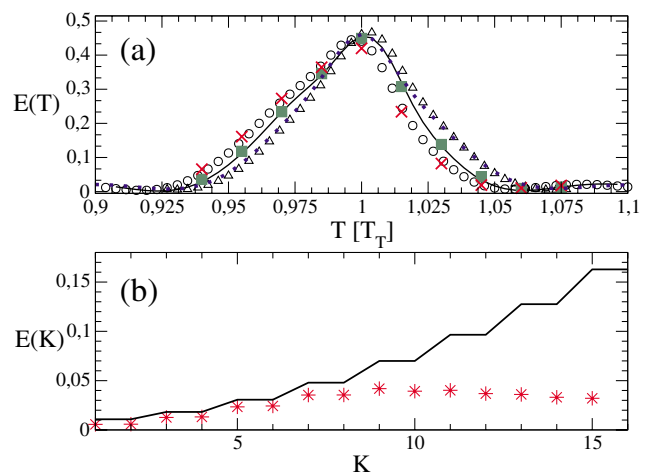


FIG. 4 (color online). (a) Scan of the kinetic energy vs T around $T = T_T$, parameters as in Fig. 1, in comparison with the linear KR (blue dots; $\sigma_{p_x} = 0.01\hbar k_L$), after $K = 14$; 1D ($N = 10^4$: circles; $\omega_x / 2\pi = 5$ Hz: solid line; $N = 0$ in kick evolution: pyramids), and 3D ($N = 10^4$: green squares; $N = 5 \times 10^4$: red crosses). (b) Kinetic energy of 3D KHO with $T = 250 \mu\text{s}$, $\omega_x / 2\pi = 1$ kHz, $\omega_T / 2\pi = 5$ kHz, and $k = 0.1$ for $N = 0$ (solid line) and $N = 100$ (stars).

specifically developed for the description of decoherence by spontaneous emission [17].

We can also tune our system described by the GPE (1) to the limit, in which the nonlinear interaction term becomes very important and even dominant for small kick strength. Experimentally such a situation can be realized either close to a Feshbach resonance (where the scattering length for two-body atomic collisions can increase by orders of magnitude [10]) or by simply increasing the strength of the harmonic confinement. The latter situation has been analyzed as a nonlinear generalization of the KHO in [11,19]. The analysis showed clear signatures of the nonlinearity in the resonant transport regime of the KHO, i.e., for $T\omega_x = 2\pi/r$ with $r = 3, 4, 6$, where the quantum transport is enhanced with respect to the classical one, much in the same way as at the QRs of the KR [13]. In the KR studied above, the total energy—corresponding to the chemical potential in the stationary case [10]—is almost entirely given by the kinetic energy obtained from the kicks. In the KHO, the energy distribution is very different: here the kinetic, the potential, and the self-energy (given by the nonlinear term) are of the same order of magnitude, which leads to a nonlinearity-induced redistribution of energy also to the transverse degrees of freedom.

Our numerical technique can be used to generalize the previous studies of the nonlinear KHO to the full 3D GPE, properly including the coupling of the transverse dimensions which is necessary for comparison with real-life experiments. Results on the KHO are presented in Fig. 4(b), where we observe the destruction of the resonant motion at $T\omega_x = \pi/2$ already for a small number of atoms $N = 100$, and after just a few kicks. In contrast to what was done in [11,19], the initial state need not be translated away from the classically stable origin in phase space. It suffices to use the relaxed ground state of the condensate to observe the impact of the now much stronger effective nonlinearity due to the strong harmonic confinement.

We have tested our data in different ways, making sure that our numerical codes produce stable results. In the 1D case and for $g_{1D} = 0$, we compared them either with analytical results for the linear KR [8] or with the much simpler evolution on a discrete grid, using a standard fast Fourier transform (FFT) [17,18]. The analytic growth rate of the kinetic energy for $p_{\text{init}} = 0$ at $T = T_T$ is shown in Fig. 1(a). For $T = T_T/4$, in the inset of Fig. 2(a), we compare both evolutions for up to $K = 50$ kicks. The FFT code does not take into account (i) the trap, (ii) the finite duration of the pulses, and (iii) the coherent evolution of the wave packet, which explains the tiny deviations for $K \geq 40$. The damping of the oscillations is due to the nonzero σ_{p_x} , an effect which was experimentally observed also for the antiresonance $T = T_T/2$ in [2], where the motion of the linear KR is perfectly periodic only for $p_{\text{init}} = 0$.

In summary, we presented the first (3 + 1)-dimensional treatment of a Bose condensate driven by an external temporally periodic force, which controls the dynamics of the system. Ballistic motion is shown to be realizable over a substantial number of kicks, even in the presence of a weak harmonic confinement. Within the framework of the 3D GPE, we have taken a first step towards the study of higher-dimensional chaos induced by the nonlinear coupling of the spatial dimensions, and future work will concentrate on situations where the transverse degrees of freedom significantly contribute to the dynamics.

This work was supported by MIUR, COFIN-2004, the Humboldt Foundation (Feodor-Lynen Program), the Scuola di Dottorato G. Galilei, and the ESF (CATS).

-
- [1] L. Deng *et al.*, Phys. Rev. Lett. **83**, 5407 (1999).
 - [2] G. J. Duffy, A. S. Mellish, K. J. Challis, and A. C. Wilson, Phys. Rev. A **70**, 041602(R) (2004).
 - [3] S. Pötting, M. Cramer, and P. Meystre, Phys. Rev. A **64**, 063613 (2001); J. Gong and P. Brumer, Phys. Rev. Lett. **88**, 203001 (2002).
 - [4] See, e.g., D. K. Wójcik and J. R. Dorfman, Phys. Rev. Lett. **90**, 230602 (2003); T. A. Brun, H. A. Carteret, and A. Ambainis, *ibid.* **91**, 130602 (2003).
 - [5] M. G. Raizen, Adv. At. Mol. Opt. Phys. **41**, 43 (1999).
 - [6] D. A. Steck, W. H. Oskay, and M. G. Raizen, Science **293**, 274 (2001); W. K. Hensinger *et al.*, Nature (London) **412**, 52 (2001).
 - [7] M. K. Oberthaler *et al.*, Phys. Rev. Lett. **83**, 4447 (1999).
 - [8] F. M. Izrailev, Phys. Rep. **196**, 299 (1990).
 - [9] W. H. Oskay *et al.*, Opt. Commun. **179**, 137 (2000); M. B. d'Arcy *et al.*, Phys. Rev. E **69**, 027201 (2004); G. Duffy *et al.*, *ibid.* **70**, 056206 (2004); S. Wimberger *et al.*, Phys. Rev. A (to be published).
 - [10] C. J. Pethick and H. Smith, *Bose-Einstein Condensation in Dilute Gases* (Cambridge University Press, Cambridge, 2002); L. Pitaevskii and S. Stringari, *Bose-Einstein Condensation* (Oxford University Press, Oxford, 2003).
 - [11] S. A. Gardiner *et al.*, Phys. Rev. A **62**, 023612 (2000).
 - [12] C. Zhang, J. Liu, M. G. Raizen, and Q. Niu, Phys. Rev. Lett. **92**, 054101 (2004); B. Mielck and R. Graham, J. Phys. A **37**, L581 (2004).
 - [13] G. M. Zaslavsky *et al.*, *Weak Chaos and Quasi-Regular Patterns* (Cambridge University Press, Cambridge, 1992); F. Borgonovi and L. Rebuzzini, Phys. Rev. E **52**, 2302 (1995); A. R. R. Carvalho and A. Buchleitner, Phys. Rev. Lett. **93**, 204101 (2004).
 - [14] E. Cerboneschi *et al.*, Phys. Lett. A **249**, 495 (1998).
 - [15] M. Olshanii, Phys. Rev. Lett. **81**, 938 (1998).
 - [16] H. Moritz, T. Stoferle, M. Köhl, and T. Esslinger, Phys. Rev. Lett. **91**, 250402 (2003).
 - [17] S. Wimberger, I. Guarneri, and S. Fishman, Nonlinearity **16**, 1381 (2003); Phys. Rev. Lett. **92**, 084102 (2004).
 - [18] L. Rebuzzini, S. Wimberger, and R. Artuso, Phys. Rev. E **71**, 036220 (2005).
 - [19] R. Artuso and L. Rebuzzini, Phys. Rev. E **66**, 017203 (2002).

Ballistic and Localized Transport for the Atom Optics Kicked Rotor in the Limit of a Vanishing Kicking Period

Mark Sadgrove,¹ Sandro Wimberger,² Scott Parkins,¹ and Rainer Leonhardt¹

¹Department of Physics, University of Auckland, Private Bag 92019, Auckland, New Zealand

²INFN and Dipartimento di Fisica E. Fermi, Università di Pisa, Largo Pontecorvo 3, 56127 Pisa, Italy
(Received 8 October 2004; published 4 May 2005)

We present mean energy measurements for the atom optics kicked rotor as the kicking period tends to zero. A narrow resonance is observed marked by quadratic energy growth, in parallel with a complete freezing of the energy absorption away from the resonance peak. Both phenomena are explained by classical means, taking proper account of the atoms' initial momentum distribution.

DOI: 10.1103/PhysRevLett.94.174103

PACS numbers: 05.45.Mt, 05.60.-k, 32.80.Qk, 42.50.Vk

The atom optics realization of the paradigmatic kicked rotor (KR) [1] allows the experimental study of uniquely quantum mechanical aspects of a fundamental, classically nonlinear system. Dynamical localization is perhaps the most celebrated quantum phenomenon observed in the quantum KR [1,2]; however, the phenomenon of quantum resonance, whereby some atoms experience enhanced energy growth (quadratic in the kick number) for well-defined kicking periods, has received renewed theoretical and experimental attention of late.

The possibility for quadratic energy growth to occur for the KR at quantum resonance has been known for some time [3]. The first experiments to observe phenomena related to quantum resonance employed the atom optics kicked rotor (AOKR) to study the momentum distributions of ensembles of kicked rotors [4], although the broad initial momentum distributions involved prohibited the observation of quadratic mean energy growth. Recent studies have shown that the quantum resonances, initially thought to be extremely sensitive quantum effects, can be described by classical means [5] and that, indeed, only linear growth in mean energy is expected at quantum resonance for experiments starting with a broad initial momentum distribution [5]. The experimental signatures of quantum resonant behavior prove to be robust with respect to decoherence by spontaneous emission [5,6], amplitude noise [7,8], and also to *large* perturbations of the kicking strength [9]. These counterintuitive findings make the quantum resonances a potential source for creating directed fast atoms, e.g., for the study of quantum random walks [10]. However, even for narrow initial atomic momentum distributions (i.e., those with standard deviation $\sigma_p < 2\hbar k_L$), true ballistic mean energy growth has only been observed convincingly for up to two kicks [11].

In this Letter, we present the first signatures of true ballistic peaks in the mean energy of a kicked atomic ensemble, with a relatively broad initial momentum distribution, but for an essentially classical regime. Our seemingly counterintuitive experimental results are explained by the same standard pendulum approximation [12] as used

to *classically* describe the structure of the quantum resonance peaks of the AOKR [5]. Additionally, we observe a regime in which an unexpected dynamical freezing effect occurs, which corresponds to atoms ceasing to absorb energy from the kicks. The close proximity, in terms of pulse period, of regimes of ballistic and frozen energy growth promises to allow fine control of atomic velocities.

We realize the AOKR by subjecting cold cesium atoms to a far detuned standing wave with spatial period π/k_L (k_L being the wave number of the kicking laser) and pulsed with a period T . Our system is described, in dimensionless units, by the Hamiltonian [13]

$$\mathcal{H}(t') = \frac{p^2}{2} + k \cos(x) \sum_{t=0}^N \delta(t' - t\tau), \quad (1)$$

where p is the atomic momentum in units of $2\hbar k_L$ (i.e., of two-photon recoils), x is the atomic position divided by $2k_L$, t' is time, and t is an integer which counts the kicks. Experimentally, we approximate δ kicks by pulses of width τ_p which are approximately rectangular in shape. We also define an effective Planck constant $\tau = 8\omega_r T$, where ω_r is the recoil frequency (associated with the energy change of a cesium atom after emission of a photon with $k_L = 7.37 \times 10^6 \text{ m}^{-1}$). The dimensionless parameter $k \approx V_0 \tau_p / \hbar$ (with V_0 the height of the optical potential) is the kick strength. By exploiting the spatial periodicity of the Hamiltonian, we can use Bloch's theorem to reduce the atomic dynamics along the x axis to that of a rotor on a circle, as described in [5,14]. Then, the one-kick propagator for a given atom is

$$\hat{U}_\beta = e^{-ik \cos(\hat{\theta})} e^{-i\tau(\hat{N} + \beta)^2/2}, \quad (2)$$

where $\theta = x \text{ mod}(2\pi)$, $\hat{N} = -id/d\theta$, and β is the quasimomentum (i.e., the noninteger part of p). To examine the limit as $\tau \rightarrow 0$, we can use the classical version of the mapping induced by the Hamiltonian (1). We define $J = \tau p$ and find

$$J_{t+1} = J_t + \tilde{k} \sin(\theta_{t+1}), \quad \theta_{t+1} = \theta_t + J_t, \quad (3)$$

where $\tilde{k} \equiv \tau k$ is the classical stochasticity parameter of the standard map [12]. Equation (3) implicitly contains the different quasimomentum classes which are vital to the description of quantum resonances [5]. In fact, (3) is equivalent to the ϵ -classical standard map developed in [5] to describe quantum resonance behavior when $\tau = 2\pi l + \epsilon$ for the special case where $l = 0$. Below, we will see that, in our case, the typically uniform initial distribution of quasimomenta [5,6] does *not* hinder ballistic motion at the observed resonance as $\tau \rightarrow 0$.

Assuming for simplicity an initially flat distribution of $p \in [0, 1)$, we have $J_0 = \tau\beta_0$ with β_0 uniformly distributed in $[0, 1)$. Since $J = \tau p$, the mean energy of the atomic ensemble at time t is given by $\langle E_{t,\tau} \rangle = \tau^{-2} \langle (\delta J_t)^2 \rangle / 2$, $\delta J_t = J_t - J_0$. As the initial conditions in phase space populate mainly the region close to $J_0 = 0$, we compute $\langle E_{t,\tau} \rangle$ for $\tau > 0$ by means of the pendulum approximation for the principal nonlinear resonance [12]. The motion is described (in *continuous* time) by $H_{\text{res}} = \frac{1}{2} \times (J')^2 + \tau k \cos(\theta)$, with the characteristic time for the motion in the resonant zone $t_{\text{res}} = (k\tau)^{-1/2}$ [12]. We remove τ from the Hamilton equations, by scaling momentum into $\bar{J} = J'/(k\tau)^{1/2}$ and time into t/t_{res} . This gives $\langle (\delta J_t)^2 \rangle = \langle (J'_t - J'_0)^2 \rangle \simeq k\tau G$, for an ensemble of orbits started inside the resonant zone. The function $G(x) \equiv \frac{\sqrt{k}}{2\pi\sqrt{\tau}} \int_0^{2\pi} d\theta_0 \times \int_0^{\sqrt{\tau/k}} dJ_0 \bar{J}(x, \theta_0, J_0)^2 \simeq \frac{1}{2\pi} \int_0^{2\pi} d\theta_0 \bar{J}(x, \theta_0, J_0 = 0)^2$ depends on the variable $x = t(k\tau)^{1/2}$ and weakly on k and τ , in *contrast* to the quantum resonant case studied in [5]. In Fig. 1, G is shown as a function of x . We see that G tends to a level $\alpha \approx 0.7$ as $x \rightarrow \infty$. This is because G is an average over nonlinear pendulum motions with a continuum of different periods, and therefore saturates to a

constant value for $x \geq 1$. The dependence of G on τ is negligibly small for $\tau \leq 1/k$, so that G can be viewed as a function of the scaling parameter x alone. We obtain as final result for the mean energy $\langle E_{t,\tau} \rangle \simeq \frac{\tau k}{2\tau^2} G$, and we can now derive two interesting limits.

First, as $x \rightarrow 0$, $G(x) \approx x^2/2$ leading to

$$\langle E_{t,\tau} \rangle_{\text{res}} = \frac{k^2 t^2}{4}. \quad (4)$$

This describes quadratic growth in mean energy, which occurs as exact resonance is approached. We note that, in the case of quantum resonances, ϵ -classical theory predicts only *linear* mean energy growth with the kick number at resonance [5]. This linear increase is induced by the contribution of most quasimomentum classes which lie *outside* the classical resonance island for $\tau = 2\pi\ell + \epsilon$ (ℓ integer). For small τ , almost all initial conditions (or quasimomenta) lie *within* the principal resonance island shown in the inset of Fig. 1.

Dividing $\langle E_{t,\tau} \rangle$ by its small x limit (4), we arrive at an elegant single-parameter scaling law for the energy ratio $\langle E_{t,\tau} \rangle / \langle E_{t,\tau} \rangle_{\text{res}} \simeq 2G(x)/x^2 \equiv R(x)$. The scaling function $R(x)$ describes the motion entirely for small τ , and specifically we see that, for τ fixed, ballistic motion occurs for $t \lesssim 1/\sqrt{k\tau}$, while for larger x , when G saturates to the value α , we obtain for $t \gg 1/\sqrt{k\tau}$ a second interesting limit:

$$\langle E_{t,\tau > 0} \rangle \simeq \frac{k}{2\tau} \alpha. \quad (5)$$

This result implies *dynamical freezing*—the ensemble's mean energy is independent of the kick number. This phenomenon is a *classical* effect in a system with a regular phase space (see inset of Fig. 1). It is distinct from dynamical localization, which is the *quantum* suppression of momentum diffusion for a chaotic phase space [2]. Experimentally, this freezing corresponds to the cessation of energy absorption from the kicks, similar to that which occurs at dynamical localization. The freezing is explained as the averaging over all trajectories which start at momenta close to zero and move with different frequencies about the fixed point of the map (3).

We now turn to the experimental verification of ballistic growth and dynamical freezing. In our experiments, we measured the mean energy of an atomic ensemble as τ was varied and for different kick numbers. Details of our experimental setup may be found in Ref. [7] and are summarized below. Using a standard six-beam magneto-optical trap, or MOT [15], we trap and cool cesium atoms typically to below $10 \mu\text{K}$. During an experiment, the trap is turned off and the atoms are subjected to pulses from an optical standing wave (created by a 150 mW, frequency stabilized diode laser) detuned 500 MHz from the $6S_{1/2}(F=4) \rightarrow 6P_{3/2}(F'=5)$ transition of cesium. Pulse durations of $\tau_p = 240$ and 320 ns were used for our experiments with

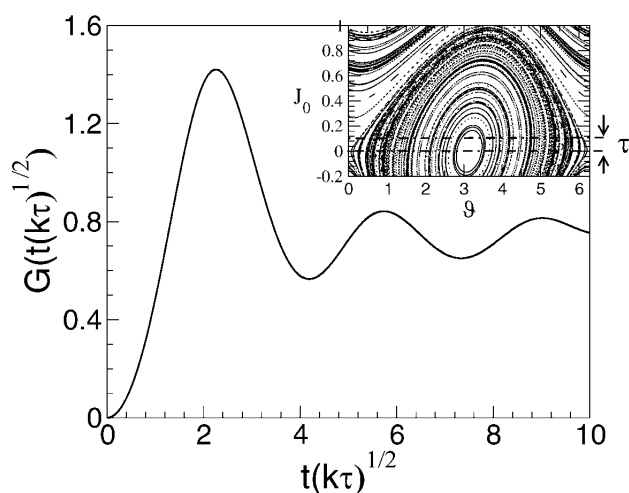


FIG. 1. The function G vs $x = t(k\tau)^{1/2}$ for $J_0 \in [0, 0.1)$. The inset shows a portion of the classical phase space of the map (3), for $\tau = 0.1$, $k = 2.5$. The dashed lines mark the position of the initial momenta, corresponding to a uniform distribution of quasimomenta in $[0, 1)$.

optical powers of $P = 20$ and 30 mW, respectively, and the atoms were subjected to at most 20 kicks. For these parameters, the effect of spontaneous emission is found to be negligible. The experimental momentum distribution of the atoms is found from a fluorescence image of the cloud using the standard time-of-flight technique [4,6,7], and the mean kinetic energy may be calculated from the second moment of this distribution. In order to probe the very narrow resonance predicted above as $\tau \rightarrow 0$, it was necessary to use very small pulse periods, leading to violations of the δ -kick assumption. Nonetheless, we found that finite pulse duration effects were negligible for our results due to the relatively low kick strengths, kick numbers, and kinetic energies involved [9,16]. We determine k using the method of Ref. [17], where the mean energy difference between one and two kicks for $\tau > 1$ is equated to the quasilinear value $k^2/4$ [12]. To predict the correct offset from zero energy of our measurements, it is still necessary to calculate the standard deviation σ_p of the initial experimental momentum distribution. This requires truncation of the wings of the experimental momentum distribution at some momentum so that the second moment calculation is not ruined by noise in the wings. Since the initial momentum distribution has considerable non-Gaussian wings, we inevitably underestimate the value of σ_p using this method. We estimate this systematic error to be less than 20% for the results presented here.

Figure 2 shows measured energies (circles) and classical data (solid lines) for a measured value of $k = 2.5 \pm 0.1$, and various kick numbers. The classical results are obtained from the dynamics generated by (3) for a Gaussian initial ensemble of 25 000 momenta $p = J/\tau$, with 200 uniformly distributed angles each. We have taken $\sigma_p = 8.4$ for our simulations, and the results can be compared

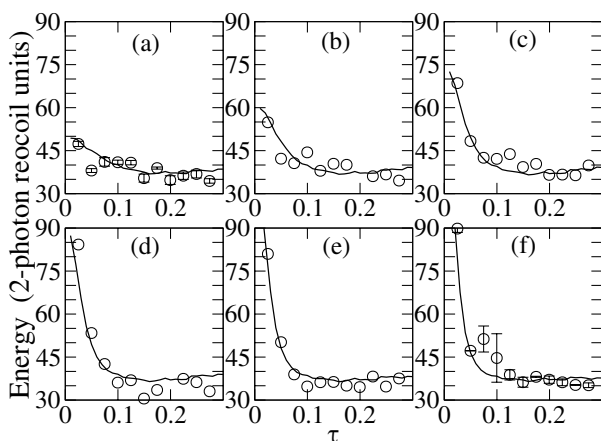


FIG. 2. Results from experiments (circles) and classical simulations (solid lines) showing energy vs τ for $k = 2.5$ and $t = 3, 4, 5, 6, 7, 8$ for panels (a)–(f), respectively. The error bars shown in (a) and (f) correspond to statistical fluctuations over three experimental shots (they do *not* take into account systematic effects such as power fluctuations of the kicking laser).

with the predictions of Eqs. (4) and (5) if the initial ensemble's energy is added to the analytic results [derived above for $p \in [0, 1]$]. Allowing for experimental uncertainties, excellent agreement is found between the measurements and our classical theory. In particular, a ballistic resonance peak is seen to exist and, although the vanishing resonant kicking period itself cannot be probed, the trend towards quadratic growth is clear in the data. The resonance is very narrow—much more so than the quantum resonances for the same parameters. Specifically, the half-width of the $\tau \rightarrow 0$ peak after five kicks is ~ 0.05 , whereas that for a quantum resonance peak for the same value of k would be ~ 0.4 [5]. The extremely fast compression of the resonance peak is characteristic of a quantum resonance which would be observed for a purely plane wave initial condition (e.g., for $p = 0$ at $\tau = 4\pi$). Hence, the peak width observed here shrinks even faster than at the quantum resonances observed in [6], for which a sub-Fourier peak width $\propto 1/t^2$ was predicted [5]. This makes the resonance as $\tau \rightarrow 0$ a sensitive phenomenon with the potential to be useful for making high-precision measurements. The results in Fig. 2 also demonstrate that dynamical freezing is occurring for $\tau > 0.1$. To observe this localization effect more convincingly, we chose a larger value of k and measured the mean energy of our atoms for up to 20 kicks. The results, shown in Fig. 3, are for a measured value of $k = 4.9 \pm 0.2$, with σ_p taken to be eight for the simulations. After 20 kicks, for $\tau > 0.1$, the mean energy of the atoms has not risen above the one-kick level. Again, excellent agreement is seen between experimental results and classical data. As a final test, we have compared our data with quantum simulations for $k = 4.9$, $\sigma_p = 8$. As shown in Fig. 4, the numerics and experimental measurements agree almost perfectly within the estimated errors. Above the threshold $\tau \geq 1/k$, the standard map enters the critical regime, which mainly affects the small subclass of extremely large momenta in our initial

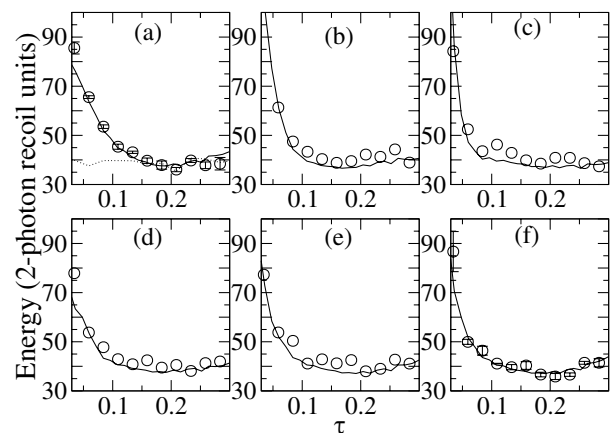


FIG. 3. Data as in Fig. 2, for $k = 4.9$ and $t = 3, 5, 7, 12, 16, 20$ for panels (a)–(f), respectively. The dotted line in (a) shows the measured energy after just one kick.

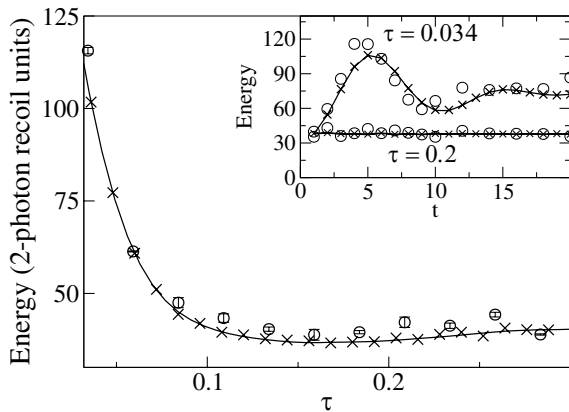


FIG. 4. Mean energy vs τ from experiments (circles) and from classical (crosses) and quantum simulations (using a Gaussian initial ensemble centered at $p = 0$; solid line) for $k = 4.9$, $\sigma_p = 8$, and $t = 5$. The inset shows how the energy varies with t for $\tau = 0.2$ and $\tau = 0.033$ ($T = 0.32 \mu\text{s}$, for which the δ -pulse approximation just remains valid for $t < 20$ [9,16]). We note the immediate onset of the freezing effect for $\tau = 0.2$; dynamical localization would set in on a time scale larger than one kick for this kick strength [2].

ensemble, lying outside the principal resonance island. Stronger deviations are expected in this region for very large interaction times ($t \gg 10$) [5]. The inset of Fig. 4 demonstrates the regimes of near-resonant and off-resonant energy growth explicitly by plotting energy against the kick number. The curve for $\tau = 0.033$ closely resembles the function G from Fig. 1, showing initial ballistic growth and saturation for $t \geq 2/\sqrt{k\tau} \approx 5$ kicks.

In conclusion, we have experimentally observed and theoretically explained the occurrence of ballistic, resonancelike transport in the limit of a vanishing kicking period for a broad initial ensemble of atomic momenta. The *quadratic* energy growth at this resonance has been verified in comparison with the *linear* growth of mean energy found at quantum resonance for comparable initial conditions [6,7]. For $\tau > 0$, a dynamical freezing effect, arising from the underlying regular classical dynamics, has been observed for up to 20 kicks in our experiment. These

phenomena, realized here for the first time, are of great interest for experimentally controlling fast (ballistic) and slow (frozen) atomic velocities [18].

We thank A. Buchleitner and S. Fishman for fruitful discussions. M.S. thanks the Tertiary Education Commission of New Zealand for support.

-
- [1] G. Casati *et al.*, in *Stochastic Behavior in Classical and Quantum Hamiltonian Systems*, edited by G. Casati and J. Ford (Springer, Berlin, 1979), p. 334.
 - [2] S. Fishman, in *Quantum Chaos*, Proceedings of the International School of Physics “Enrico Fermi,” Course CXIX, edited by G. Casati *et al.* (IOS, Amsterdam, 1993).
 - [3] F.M. Izrailev and D.L. Shepelyansky, *Sov. Phys. Dokl.* **24**, 996 (1979); F.M. Izrailev, *Phys. Rep.* **196**, 299 (1990).
 - [4] F.L. Moore *et al.*, *Phys. Rev. Lett.* **75**, 4598 (1995); W.H. Oskay *et al.*, *Opt. Commun.* **179**, 137 (2000).
 - [5] S. Wimberger, I. Guarneri, and S. Fishman, *Nonlinearity* **16**, 1381 (2003); *Phys. Rev. Lett.* **92**, 084102 (2004).
 - [6] M.B. d’Arcy *et al.*, *Phys. Rev. Lett.* **87**, 074102 (2001); *Phys. Rev. E* **69**, 027201 (2004).
 - [7] M. Sadgrove *et al.*, *Phys. Rev. E* **70**, 036217 (2004).
 - [8] S. Brouard and J. Plata, *J. Phys. A* **36**, 3745 (2003).
 - [9] S. Wimberger, Ph.D. thesis, University of Munich and Università degli Studi dell’Insubria, 2004 (<http://edoc.ub.uni-muenchen.de/archive/00001687/>).
 - [10] See, e.g., D.K. Wójcik and J.R. Dorfman, *Phys. Rev. Lett.* **90**, 230602 (2003); T.A. Brun, H.A. Carteret, and A. Ambainis, *ibid.* **91**, 130602 (2003).
 - [11] G. Duffy *et al.*, *Phys. Rev. E* **70**, 056206 (2004); L. Deng *et al.*, *Phys. Rev. Lett.* **83**, 5407 (1999).
 - [12] A.L. Lichtenberg and M.A. Leiberman, *Regular and Chaotic Dynamics* (Springer, Berlin, 1992).
 - [13] R. Graham, M. Schlautmann, and P. Zoller, *Phys. Rev. A* **45**, R19 (1992).
 - [14] C.F. Bharucha *et al.*, *Phys. Rev. E* **60**, 3881 (1999).
 - [15] C. Monroe *et al.*, *Phys. Rev. Lett.* **65**, 1571 (1990).
 - [16] R. Blümel, S. Fishman, and U. Smilansky, *J. Chem. Phys.* **84**, 2604 (1986).
 - [17] M. Sadgrove *et al.*, *Phys. Rev. E* **71**, 027201 (2005).
 - [18] S. Wimberger, M. Sadgrove, S. Parkins, and R. Leonhardt, physics/0502061 [*Phys. Rev. A* (to be published)].



Driven collective quantum tunneling of ultracold atoms in engineered optical lattices

R. KHOMERIKI^{1,2}, S. RUFFO¹ and S. WIMBERGER³

¹ *Dipartimento di Energetica “S. Stecco” and CSDC, Università di Firenze and INFN - Via S. Marta 3, 50139 Firenze, Italy*

² *Department of Exact and Natural Sciences, Tbilisi State University - 0128 Tbilisi, Georgia*

³ *CNR-INFN and Dipartimento di Fisica “E. Fermi”, Università degli Studi di Pisa - Largo Pontecorvo 3, 56127 Pisa, Italy*

received 28 September 2006; accepted in final form 19 December 2006

published online 6 February 2007

PACS 03.75.Lm – Tunneling, Josephson effect, Bose-Einstein condensates in periodic potentials, solitons, vortices, and topological excitations

PACS 74.50.+r – Tunneling phenomena; point contacts, weak links, Josephson effects

PACS 75.45.+j – Macroscopic quantum phenomena in magnetic systems

Abstract – Collective quantum tunneling of a Bose-Einstein condensate between two parts of an optical lattice separated by an energy barrier is theoretically investigated. We show that by a pulsewise change of the barrier height, it is possible to switch between a tunneling regime and a self-trapped one. This property of the system is explained by effectively reducing the nonlinear dynamics of the system to that of a particle moving in a double square well potential. The analysis is performed for both attractive and repulsive interatomic forces, and emphasizes the experimental relevance of our findings.

Copyright © EPLA, 2007

Since the first experimental discovery [1] of Macroscopic Quantum Tunneling, this phenomenon has been usually associated with the tunneling between different states of the system with no reference to a spatial energy barrier [2–5]. In Josephson junctions (JJ) one observes a tunneling escape from a metastable state [1]. Afterwards, similar realizations have been discovered in completely different physical systems, such as liquid helium [6] and nanomagnets [7]. Besides that, there are also several examples where macroscopic objects, such as vortices [8,9] or fluxons [10] in JJs, or magnetic domain walls [11], tunnel through a spatial potential barrier. This latter particle tunneling effect is hereafter referred to as Collective Quantum Tunneling (CQT).

Recently [12,13], following earlier theoretical predictions [14,15], it has been found that a Bose-Einstein Condensate (BEC) trapped in a harmonic-well potential of mesoscopic length behaves like a single JJ: for nonzero initial imbalance of the number of atoms in different wells, Josephson oscillations are present in the system, *i.e.* the condensate tunnels back and forth through the barrier displaying a CQT regime. The only difference with respect to superconducting JJ's is that, for large initial

imbalance, the condensate is mainly trapped in one of the wells, producing what is called Macroscopic Self-Trapping (MST).

Our aim in this Letter is to suggest the experimental realization of a BEC in an optical lattice, which is engineered in such a way to mimic two weakly coupled chains of JJ's (see fig. 1). Using such an experimental set-up, we demonstrate the feasibility of the efficient control of a switch between tunneling (CQT) and trapped (MST) states of the system. We show that our problem reduces to the Gross-Pitaevskii equation (GPE) [16] in a double square well, which displays very different properties from the previously considered double harmonic well potential [12,14,17–19]. Specifically, we show that for both attractive and repulsive nonlinearities the stationary solutions describing the CQT and MST regimes are characterized by very close energies in a wide range of values of the nonlinearity parameter. This property itself allows one to switch from the oscillatory tunneling regime to the trapped one and back via a simple pulselike adiabatic change of the energy barrier. Our results are broadly applicable and open the way to the experimental study of these phenomena in BEC dynamics.

R. Khomeriki *et al.*

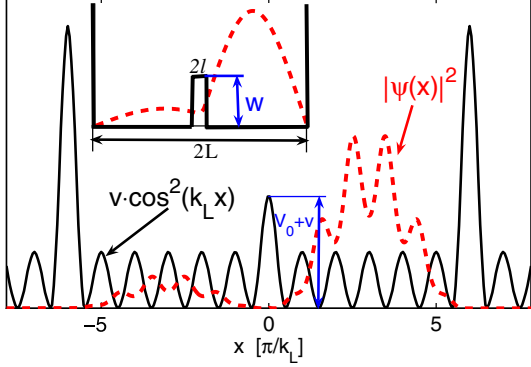


Fig. 1: Schematics of the suggested experimental setup. The optical lattice is supplemented with large energy barriers from both sides and a small one in the middle (solid curve). The condensate is initially loaded mainly into the right part of the optical lattice (the dashed line represents particle density). The inset shows the reduction of the problem to particle motion in a double-square-well potential (details are given in the text).

We start from the following, one-dimensional Hamiltonian of a BEC in an optical lattice:

$$i\hbar \frac{\partial \psi}{\partial t} = -\frac{\hbar^2}{2m} \frac{\partial^2 \psi}{\partial x^2} + V(x)\psi + \frac{2\hbar^2 a_s}{ma_{\perp}^2} |\psi|^2 \psi, \quad (1)$$

where m is the atomic mass, a_s the scattering length ($a_s < 0$ corresponds to attractive atom-atom interactions and $a_s > 0$ to repulsive interactions) and $a_{\perp} = \sqrt{\hbar/m\omega_{\perp}}$ is the transversal oscillation length, which implicitly takes into account the real three-dimensionality of the system [20], ω_{\perp} being the transversal frequency of the trap. The optical lattice potential is

$$V(x) = v \cos^2(k_L x) \quad \text{for } |k_L x| > \pi/2, \\ V(x) = (v + V_0) \cos^2(k_L x) \quad \text{for } |k_L x| < \pi/2, \quad (2)$$

where k_L is the wave number of the laser beams that create the optical lattice and V_0 is the height of the additional spatial energy barrier placed in the middle of the optical lattice. Besides that, Dirichlet boundary conditions with $\psi(\pm L) = 0$ are chosen in order to describe the large confining barriers at both ends of the BEC. These boundary conditions could be realized experimentally by an additional optical lattice with larger amplitude and larger lattice constant, as shown in fig. 1.

Introducing a dimensionless length scale $\tilde{x} = 2k_L x$ and time $\tilde{t} = E_B t/\hbar$, where $E_B = 8E_R = 4\hbar^2 k_L^2/m$ and E_R is the recoil energy [21], we can rewrite eq. (1) as follows:

$$i \frac{\partial \Psi}{\partial \tilde{t}} = -\frac{1}{2} \frac{\partial^2 \Psi}{\partial \tilde{x}^2} + \tilde{V}(\tilde{x})\Psi + g|\Psi|^2 \Psi, \quad (3)$$

where the normalized wave function, $\int |\Psi(\tilde{x}, \tilde{t})|^2 d\tilde{x} = 1$, is introduced [22]. The dimensionless potential \tilde{V} still has

the form (2) with the following dimensionless depths of the optical lattice

$$\tilde{v} = \frac{v}{E_B}, \quad \tilde{V}_0 = \frac{V_0}{E_B}, \quad g = \frac{Na_s}{k_L a_{\perp}^2}, \quad (4)$$

g being the dimensionless nonlinearity parameter and N the number of atoms.

We have performed numerical simulations of eq. (3) with 12 wells (6 wells on each side of the barrier as presented in fig. 1) and the parameters $\tilde{v} = 0.25$ (in physical units this means that the depth of the optical lattice is $v = 2E_R$), $\tilde{V}_0 = 0.15$ and we fix the nonlinearity to the value $g = -0.025$, *i.e.*, we choose attractive interactions. The dynamics is similar for repulsive interatomic forces (see the discussion below). The phenomenon we study in this letter does not depend significantly on the actual size of the system, if at least 3 lattice sites are present on each side of the barrier.

As seen from the top panel of fig. 2, the self-trapped state of the condensate persists until one applies the pulse-like time variation of the barrier displayed in the inset. After that action, the system makes a transition to the oscillating tunneling regime. The nature of these oscillations can be understood in terms of a two-mode approximation as was done in refs. [14,23], and in the limit of zero nonlinearity oscillations are Rabi-like. On the other hand, preparing the condensate in the oscillating tunneling regime (bottom graph in fig. 2) one can easily arrive at a self-trapping state by varying again the energy barrier in the middle as displayed in the inset. Let us mention that, as far as the energy of the barrier is changed adiabatically, the total energy of the condensate does not vary, *i.e.* the self-trapped and tunneling oscillatory regimes have the *same* energy. This is quite different from what happens in a double-harmonic-well potential [12,14,17–19]. The point is that, in the double-harmonic-well for $g < 0$, the asymmetric stationary solution is characterized by a smaller energy than the symmetric solution and this difference increases sharply with increasing nonlinearity. Hence, a significant energy injection is required in order to realize the transition between the two regimes; whilst in our case the transition is achieved by a simple pulsed variation of the energy barrier. Below we argue that this happens because our case effectively reduces to the case of a double-square-well potential (see the inset of fig. 1 and the reduction procedure below) for which asymmetric and symmetric stationary solutions carry almost the same energies in a wide range of the nonlinearity parameter.

Now we proceed to reducing eq. (3) to a Discrete NonLinear Schrödinger equation (DNLS). We discretize it via a tight-binding approximation [24–26], representing the wave function $\Psi(\tilde{x}, \tilde{t})$ as

$$\Psi(\tilde{x}, \tilde{t}) = \sum_j \phi_j(\tilde{t}) \varphi_j(\tilde{x}), \quad (5)$$

where $\varphi_j(\tilde{x})$ is a normalized isolated wave function in an optical lattice in the fully linear case $g = 0$ and could be

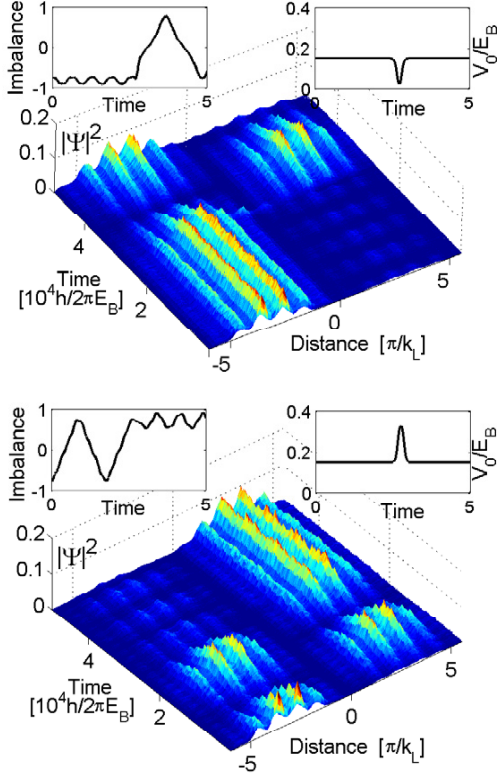


Fig. 2: Numerical simulations of eq. (3): the top graph represents the transition from a self-trapped (MST) state to a collective tunneling one (CQT), while the bottom graph shows the inverse process. The right insets in both graphs show the variation of the energy barrier necessary to realize the switching between the different regimes. The left insets display the time evolution of the atomic imbalance between the different sides of the barrier $z = \int_R |\Psi|^2 d\tilde{x} - \int_L |\Psi|^2 d\tilde{x}$, where \int_R and \int_L define the integrations over right and left sides of the barrier, respectively. The initial phase difference between the left and right sides of the barrier is zero in the top panel, while in the bottom panel the initial phase difference is taken equal to π . Time is scaled in units of $10^4 \hbar/2\pi E_B$ and space is scaled in terms of the lattice constant π/k_L .

expressed in terms of Wannier functions (see, *e.g.*, [27]). For clarity, we use here its approximation for a harmonic trap centered at the points $r_j = j\pi(|j| + 1/2)/|j|$ ($|j|$ varies from 1 to n). In the context of the evolution equation (3) $\varphi_j(\tilde{x})$ has the form

$$\varphi_j(\tilde{x}) = \left(\frac{\sqrt{\tilde{v}}}{\pi\sqrt{2}} \right)^{1/4} e^{-\sqrt{\tilde{v}}(\tilde{x}-r_j)^2/\sqrt{8}}, \quad (6)$$

for $|j| \neq 1$, and one should substitute \tilde{v} by $\tilde{v} + \tilde{V}_0$ in the above expression in order to get an approximate formula for the wave function for $|j| = 1$.

Assuming further that the overlap of the wave functions in neighboring sites is small, we get from (3) the following

DNLS equation for the sites $|j| \neq 1$:

$$i\hbar \frac{\partial \phi_j}{\partial t} = -Q(\phi_{j+1} + \phi_{j-1}) + U|\phi_j|^2 \phi_j, \quad (7)$$

while for $|j| = 1$ we have

$$i\hbar \frac{\partial \phi_{\pm 1}}{\partial t} = -Q\phi_{\pm 2} - Q_1\phi_{\mp 1} + U_1|\phi_{\pm 1}|^2 \phi_{\pm 1}, \quad (8)$$

where we assume pinned boundary conditions. The constants Q , Q_1 , U and U_1 are easily computed from the following expressions ($|j| \neq 0$)

$$\begin{aligned} Q &= - \int \left[\frac{\partial \varphi_j}{\partial \tilde{x}} \frac{\partial \varphi_{j+1}}{\partial \tilde{x}} + \tilde{v} \varphi_j \varphi_{j+1} \cos^2 \frac{\tilde{x}}{2} \right] d\tilde{x}, \\ Q_1 &= - \int \left[\frac{\partial \varphi_1}{\partial \tilde{x}} \frac{\partial \varphi_{-1}}{\partial \tilde{x}} + (\tilde{v} + \tilde{V}_0) \varphi_1 \varphi_{-1} \cos^2 \frac{\tilde{x}}{2} \right] d\tilde{x}, \\ U &= g \int \varphi_j^4 d\tilde{x} \simeq U_1 = g \int \varphi_{\pm 1}^4 d\tilde{x}. \end{aligned} \quad (9)$$

In order to characterize the solutions of eqs. (7) and (8), we follow the same procedure used in ref. [23], which goes through a continuum approximation and leads to the transformation $j \rightarrow \tilde{x}$ again. Assuming that $\phi_1 = \phi_{-1}$ we finally arrive at

$$\frac{i\hbar}{Q} \frac{\partial \phi}{\partial t} = - \frac{\partial^2 \phi}{\partial \tilde{x}^2} + W(\tilde{x})\phi + R|\phi|^2 \phi, \quad (10)$$

where $W(\tilde{x})$ is a double-square-well potential with a barrier height $w = 2(Q - Q_1)/Q$ and width $l = 1$, $\phi(\tilde{x}, \tilde{t})$ obeys pinned boundary conditions $\phi(\tilde{x} = \pm 2k_L L) = 0$ ($2L$ is the width of the double square well) and the nonlinearity parameter is given by $R = U/Q$.

Summarizing, we have reduced the initial problem, GPE with optical lattice and barrier potentials to a DNLS equation and then this latter again to a GPE with double-square-well potential. The reason for doing this, is to get rid of the optical lattice potential and to reduce our problem to the GPE with a double-square-well potential, for which one can easily find exact stationary solutions. They are sought as $\phi(\tilde{x}, \tilde{t}) = \Phi(\tilde{x}) \exp(-i\beta\tilde{t})$ with a real-valued function $\Phi(\tilde{x})$ found in terms of Jacobi elliptic functions [28], in the case of attractive atom-atom interactions $R < 0$

$$\begin{aligned} -L < \tilde{x} < -l &: \Phi = A \operatorname{cn}[\gamma_A(\tilde{x} + 2k_L L) - \mathbb{K}(k_A), k_A], \\ l < \tilde{x} < L &: \Phi = B \operatorname{cn}[\gamma_B(\tilde{x} - 2k_L L) + \mathbb{K}(k_B), k_B], \\ -l < \tilde{x} < l &: \Phi = C \operatorname{dn}[\gamma_C(\tilde{x} - \tilde{x}_0), k_C], \end{aligned} \quad (11)$$

with the parameters given in terms of the amplitudes by

$$\begin{aligned} \gamma_A^2 &= \beta + \frac{A^2}{|R|}, & k_A^2 &= \frac{A^2}{2(A^2 + |R|\beta)}, \\ \gamma_B^2 &= \beta + \frac{B^2}{|R|}, & k_B^2 &= \frac{B^2}{2(B^2 + |R|\beta)}, \\ \gamma_C^2 &= w - \beta - \frac{C^2}{2|R|}, & k_C^2 &= \frac{w - \beta - C^2/|R|}{w - \beta - C^2/2|R|}, \end{aligned}$$

R. Khomeriki *et al.*

while, in the case of repulsive interactions, $R > 0$, one obtains the stationary solution written in the form

$$\begin{aligned} -L < \tilde{x} < -l : \Phi &= A \operatorname{sn}[\gamma_A(\tilde{x} + 2k_L L), k_A], \\ l < \tilde{x} < L : \Phi &= B \operatorname{sn}[\gamma_B(\tilde{x} - 2k_L L), k_B], \\ -l < \tilde{x} < l : \Phi &= C/\operatorname{cn}[\gamma_C(\tilde{x} - \tilde{x}_0), k_C], \end{aligned} \quad (12)$$

where

$$\begin{aligned} \gamma_A^2 &= \beta - \frac{A^2}{2|R|}, & k_A^2 &= \frac{A^2}{2|R|\beta - A^2}, \\ \gamma_B^2 &= \beta - \frac{B^2}{2|R|}, & k_B^2 &= \frac{B^2}{2|R|\beta - B^2}, \\ \gamma_C^2 &= 2 \left(w - \beta + \frac{C^2}{|R|} \right), & k_C^2 &= \frac{w - \beta + C^2/2|R|}{w - \beta + C^2/|R|}. \end{aligned}$$

Here \mathbb{K} denotes the complete elliptic integral of the first kind, and, by construction, the above expressions verify the vanishing boundary values condition in $\tilde{x} = \pm 2k_L L$.

The solutions are then given in terms of five parameters $(A, B, C, \beta, \tilde{x}_0)$, which are determined by the four continuity conditions in $\tilde{x} = \pm l$ and the wave function normalization condition $\int d\tilde{x} \Phi^2(\tilde{x}) = 1$. In both cases, repulsive and attractive nonlinearities, one has a symmetric and an antisymmetric solution, and an additional asymmetric solution that appears above a given nonlinearity threshold value $|g_t| \approx 0.018$. In fig. 3, we plot the profiles of the lowest energy symmetric (attractive case, upper panel) and antisymmetric (repulsive case, lower panel) solution, the asymmetric solutions for both the repulsive and the attractive case, and, in the insets, the relative energy differences $\Delta E = 2(E_a - E_s)/E_a + E_s$ between the asymmetric (E_a) and the symmetric (E_s) case for attractive nonlinearities, while for repulsive nonlinearities E_s is replaced by the energy of the antisymmetric solution. Below $|g_t|$ the energy of the asymmetric solution joins those of the symmetric and antisymmetric ones, making $\Delta E = 0$. As seen from the insets of both panels, these energies are very close in the nonlinearity range $0.018 < |g| < 0.03$ (note that the numerical simulations presented in fig. 2 are made for $g = -0.025$) and hence it is easy to switch from the tunneling regime to the self-trapped state and back again.

As mentioned above, for small nonlinearities only the symmetric and antisymmetric solution exist. For large nonlinearities, according to an intuitive guess, the symmetric solution has lower energy than the asymmetric one for repulsive nonlinearities (the system prefers to be equally distributed on different sides of the barrier), whilst the asymmetric solution is energetically preferable (the system prefers to occupy mostly one of the sides of the barrier) in the case of attractive atomic interactions. For large nonlinearities the behavior of the double square well coincides with that of the double harmonic well, for which we direct the reader to ref. [17], where the energetic comparison and stability analysis of the above-mentioned solutions are given in full detail. However, we remark

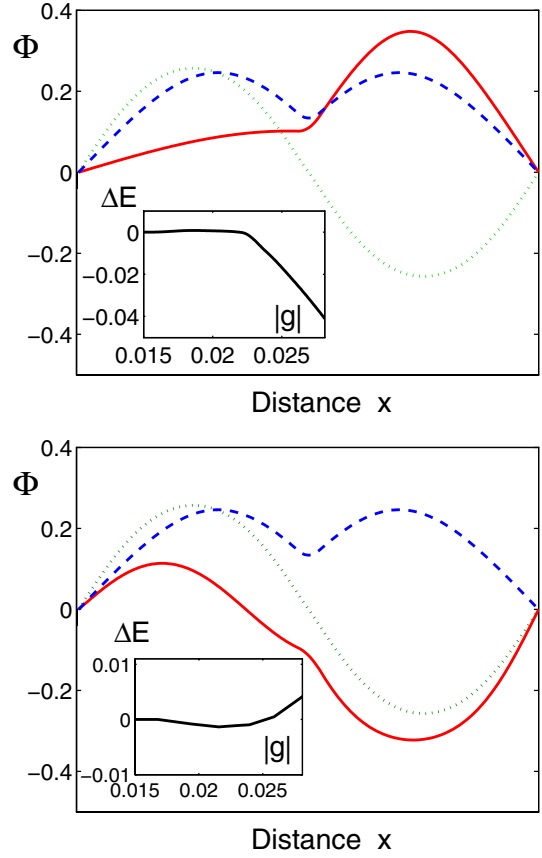


Fig. 3: Upper graph: Stationary profiles described by expressions (11) for attractive nonlinearities ($g = -0.025$): asymmetric solution (solid line), symmetric solution (dashed line), antisymmetric solution (dotted line). The inset shows the relative energy difference between the asymmetric and the symmetric stationary solution as a function of the nonlinearity parameter. Lower graph: Stationary profiles described by expressions (12) for repulsive nonlinearities ($g = 0.025$): asymmetric solution (solid line), symmetric solution (dashed line), antisymmetric solution (dotted line). The inset shows the relative energy difference between the asymmetric and the antisymmetric stationary solution as a function of the nonlinearity parameter.

once again that the behavior of the double-square-well potential differs from that of the double harmonic well [12,14,17–19] in the range of intermediate nonlinearities, where the energies of the symmetric and asymmetric solutions turn out to be very close to each other and the energetic ordering described for large nonlinearities is different.

In order to get an idea about a possible experimental realization of these effects, we choose ${}^7\text{Li}$, which is characterized by an attractive atom-atom interaction [29]. First of all we note that the confining harmonic potential along the optical lattice does not change the observed switching effect if the characteristic longitudinal oscillation length $a_{\parallel} = \sqrt{\hbar/m\omega_{\parallel}}$ of this potential (ω_{\parallel} being

the longitudinal confining frequency) is much larger than system size. In particular, for ${}^7\text{Li}$ this condition yields $\omega_{\parallel} < 2\pi \times 30 \text{ Hz}$. Then, with the realistic experimental parameters $\omega_{\perp} = 2\pi \times 30 \text{ Hz}$, $a_s = -1.4 \text{ nm}$, $k_L = 7.4 \cdot \mu\text{m}^{-1}$, from the formula for the nonlinearity $g = Na_s/a_{\perp}^2 2k_L$ one gets that the total atom number needed to access values of $|g|$ around 0.025 is $N \approx 10000$. While in case of ${}^{23}\text{Na}$ [30] with repulsive forces ($a_s = 4.9 \text{ nm}$), the atom number should be $N \approx 1000$. Increasing the number of wells (system size) n times, one should decrease the number of atoms n^2 times in order to observe the predicted effect. The optimal optical depth should be around $v = 0.25E_B$ and barrier height $V_0 = 0.15E_B$ (see eq. (2) for the definition of potential parameters). Increasing the potential barrier width the tunneling regime is suppressed and one should simultaneously decrease the potential barrier height in order to still observe the effect, keeping all the other parameters unchanged. The only restriction on the barrier width is that it should be much less than system size. Small fluctuations of the barrier parameters and position do not affect the predicted phenomenon. We note that in our numerical simulations, presented in fig. 1, the time is scaled in units of $10^4 \hbar/E_B$, where, let us remind, $E_B \equiv 4\hbar^2 k_L^2/m$.

To summarize, we predict the presence of a rich switching scenario from an oscillatory tunneling regime to a self-trapped one as a novel collective quantum tunneling (CQT) effect to be realized with ultracold atoms. We have shown that the problem effectively reduces to particle motion in a double-square-well potential, at variance with earlier studies dealing with double harmonic wells. This difference guarantees the possibility of a switch from an oscillatory tunneling to a self-trapped state via a pulse-like change of the central potential barrier. We have derived typical ranges of physical parameters, for both attractive and repulsive interatomic forces, in order to suggest a ready-to-implement experimental verification.

It is our pleasure to thank OLIVER MORSCH and ENNIO ARIMONDO for useful discussions. SR acknowledges financial support by the PRIN05-MIUR grant on *Dynamics and thermodynamics of systems with long-range interactions*, R.Kh. by the Marie-Curie international incoming fellowship award (MIF2-CT-2006-021328) and USA CRDF Award # GEP2-2848-TB-06, and SW by the Alexander von Humboldt foundation (Feodor-Lynen Program).

REFERENCES

- [1] VOSS R. F. and WEBB R. A., *Phys. Rev. Lett.*, **47** (1981) 265.
- [2] UEDA M. and LEGGETT A. J., *Phys. Rev. Lett.*, **80** (1998) 1576.
- [3] YU Y., HAN S., CHU XI., CHU SHIH-I. and WANG ZH., *Science*, **296** (2002) 889.
- [4] JIN X. Y. *et al.*, *Phys. Rev. Lett.*, **96** (2006) 177003.
- [5] BARONE A., KURIZKI G. and KOFMAN A. G., *Phys. Rev. Lett.*, **92** (2004) 200403.
- [6] HENDRY P. C., LAWSON N. S., MCCCLINTOCK P. V. E. and WILLIAMS C. D. H., *Phys. Rev. Lett.*, **60** (1988) 604.
- [7] THOMAS L., LIONTI F., BALLOU R., GATTESCHI D., SESSOLI R. and BARBARA B., *Nature*, **383** (1996) 145.
- [8] WALLRAFF A. *et al.*, *Nature*, **425** (2003) 155.
- [9] CLARKE J., *Nature*, **425** (2003) 133.
- [10] KIM JU H. and MOON K., *Phys. Rev. B*, **71** (2005) 104524.
- [11] BROOKE J., ROSENBAUM T. F. and AEPPLI G., *Nature*, **413** (2001) 610.
- [12] ALBIEZ M., GATI R., FOLLING J., HUNSMANN S., CRISTIANI M. and OBERTHALER M. K., *Phys. Rev. Lett.*, **95** (2005) 010402.
- [13] CATALIOTTI F. S., BURGER S., FORT C., MADDALONI P., MINARDI F., TROMBETTONI A., SMERZI A. and INGUSCIO M., *Science*, **293** (2001) 843.
- [14] SMERZI A., FANTONI S., GIOVANAZZI S. and SHENOY S. R., *Phys. Rev. Lett.*, **79** (1997) 4950; RAGHAVAN S., SMERZI A., FANTONI S. and SHENOY S. R., *Phys. Rev. A*, **59** (1999) 620.
- [15] FRANZOSI R., PENNA V. and ZECCHINA R., *Int. J. Mod. Phys. B*, **14** (2000) 943.
- [16] PITAEVSKII L. P., *Sov. Phys. JETP*, **13** (1961) 451; GROSS E. P., *Nuovo Climento*, **20** (1961) 454; *J. Math. Phys.*, **4** (1963) 195.
- [17] MONTINA A. and ARECCHI F. T., *Phys. Rev. A*, **66** (2002) 013605.
- [18] KAPITULA T. and KEVREKIDIS P. G., *Nonlinearity*, **18** (2005) 2491; KEVREKIDIS P. G. *et al.*, *Phys. Lett. A*, **340** (2005) 275.
- [19] ANDERLINI M. *et al.*, *J. Phys. B*, **39** (2006) S199.
- [20] BERGEMAN T., MOORE M. G. and OLSHANII M., *Phys. Rev. Lett.*, **91** (2003) 163201.
- [21] BLOCH I., *J. Phys. B*, **38** (2005) S629; MORSCH O. and OBERTHALER M., *Rev. Mod. Phys.*, **78** (2006) 179.
- [22] CARR L., HOLLAND M. J. and MALOMED B. A., *J. Phys. B*, **38** (2005) 3217; WIMBERGER S., SCHLAGHECK P. and MANNELLA R., *J. Phys. B*, **39** (2006) 729; SCHLAGHECK P. and PAUL T., *Phys. Rev. A*, **73** (2006) 023619.
- [23] KHOMERIKI R., LEON J. and RUFFO S., *Phys. Rev. Lett.*, **97** (2006) 143902.
- [24] SMERZI A. and TROMBETTONI A., *Phys. Rev. A*, **68** (2003) 023613.
- [25] SUKHORUKOV A. A., NESHEV D., KROLIKOWSKI W. and KIVSHAR Y. S., *Phys. Rev. Lett.*, **92** (2004) 093901.
- [26] ABLOWITZ M. J. and MUSSLIMANI Z. H., *Phys. Rev. Lett.*, **87** (2001) 254102; *Phys. Rev. E*, **65** (2002) 056618.
- [27] SLATER J. C., *Phys. Rev.*, **87** (1952) 807.
- [28] BYRD P. F. and FRIEDMAN M. D., *Handbook of Elliptic Integrals for Engineers and Physicists* (Springer, Berlin) 1954.
- [29] BRADLEY C. C., SACKETT C. A. and HULET R. G., *Phys. Rev. Lett.*, **78** (1997) 985.
- [30] DAVIS K. B. *et al.*, *Phys. Rev. Lett.*, **75** (1995) 3969.

Resonantly Enhanced Tunneling of Bose-Einstein Condensates in Periodic Potentials

C. Sias, A. Zenesini, H. Lignier, S. Wimberger, D. Ciampini, O. Morsch, and E. Arimondo

Dipartimento di Fisica "E. Fermi," CNR-INFM, Largo Pontecorvo 3, 56127 Pisa, Italy

(Received 22 December 2006; published 23 March 2007)

We report on measurements of resonantly enhanced tunneling of Bose-Einstein condensates loaded into an optical lattice. By controlling the initial conditions of our system we were able to observe resonant tunneling in the ground and the first two excited states of the lattice wells. We also investigated the effect of the intrinsic nonlinearity of the condensate on the tunneling resonances.

DOI: [10.1103/PhysRevLett.98.120403](https://doi.org/10.1103/PhysRevLett.98.120403)

PACS numbers: 03.65.Xp, 03.75.Lm

Resonantly enhanced tunneling (RET) is a quantum effect in which the probability for tunneling of a particle between two potential wells is increased when the quantized energies of the initial and final states of the process coincide. In spite of the fundamental nature of this effect [1] and the practical interest [2], it has been difficult to observe experimentally in solid state structures. Since the 1970s, much progress has been made in constructing solid state systems such as superlattices [3–5] and quantum wells [6] which enable the controlled observation of RET [7].

In recent years, ultracold atoms in optical lattices [8] have been increasingly used to simulate solid state systems. Optical lattices are easy to realize in the laboratory, and their parameters can be perfectly controlled both statically and dynamically. Also, more complicated potentials can be realized by adding further lattice beams [9]. This makes them attractive as model systems for crystal lattices, and in the past few years cold atoms and Bose-Einstein condensates (BECs) in optical lattices have been used to simulate phenomena such as Bloch oscillations [10] and the Mott insulator transition [11]. In this Letter we show that BECs in accelerated optical lattice potentials are ideally suited to studying RET. While in solid state measurements of RET only a few potential wells were used and the periodic structures had to be grown for each realization, in our experiment the condensate is distributed over several tens of wells and the parameters of the lattice can be freely chosen. Moreover, we are able to control the initial conditions of the system and thus observe RET in any chosen energy level and can also add nonlinearity to the system.

A schematic representation of RET is shown in Fig. 1. In a tilted periodic potential, atoms can escape by tunneling to the continuum via higher-lying levels. The tilt of the potential is proportional to the force F acting on the atoms, and in general the tunneling rate Γ_{LZ} can be calculated using the Landau-Zener formula [12]. However, when the tilt-induced energy difference $Fd_L\Delta i$ between wells i and $i + \Delta i$ matches the separation between two quantized energy levels, the tunneling probability is resonantly enhanced and the Landau-Zener formula no longer gives the correct result, as previously investigated in [13] for cold atoms in optical lattices. While for the parameters of our

experiment the enhancement over the Landau-Zener prediction was around a factor of 2 [see theoretical and experimental results of Fig. 2(a)], in general it can be several orders of magnitude.

The starting point of our experiments is a BEC of ^{87}Rb atoms, held in an optical dipole trap whose frequencies can be adjusted to realize a cigar-shaped condensate. The BECs are created using a hybrid approach in which evaporative cooling is initially effected in a magnetic time-orbiting potential (TOP) trap and subsequently in a crossed dipole trap. The dipole trap is realized using two intersecting Gaussian laser beams at 1030 nm wavelength and a power of around 1 W per beam focused to waists of $50\ \mu\text{m}$. After obtaining pure condensates of around 5×10^4 atoms the powers of the trap beams are adjusted in order to obtain an elongated condensate with the desired trap frequencies (≈ 20 Hz in the longitudinal direction and 80–250 Hz radially).

Subsequently, the BECs held in the dipole trap are loaded into an optical lattice created by two Gaussian laser beams ($\lambda = 852$ nm) with $120\ \mu\text{m}$ waist intersecting at an angle θ . The resulting periodic potential $V(x) = V_0 \sin^2(\pi x/d_L)$ has a lattice spacing $d_L = \lambda/(2 \sin(\theta/2))$ and its depth V_0 is measured in units of the recoil energy

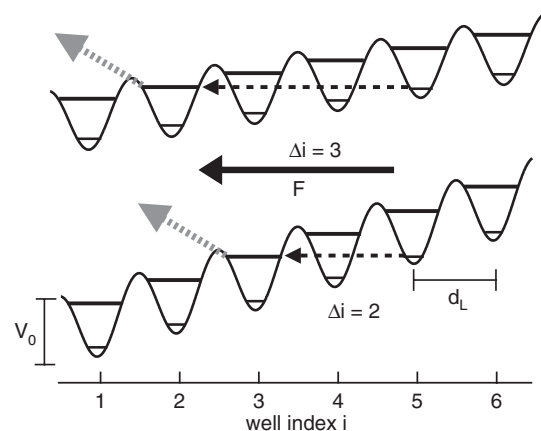


FIG. 1. Explanation of resonantly enhanced tunneling. Tunneling of atoms out of a tilted lattice is resonantly enhanced when the energy difference between lattice wells matches the distance between the energy levels in the wells.

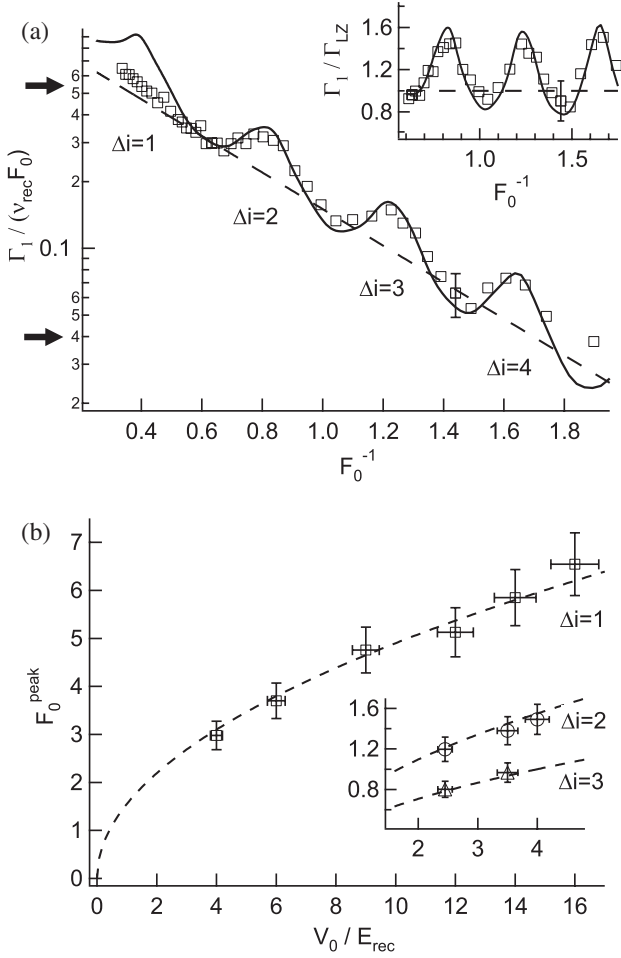


FIG. 2. Tunneling resonances in an accelerated optical lattice. (a) Tunneling resonances of the $n = 1$ lowest energy level for $V_0 = 2.5E_{\text{rec}}$. The arrows indicate the upper and lower limits for our precise measurement of Γ_n . Inset: Deviation from the Landau-Zener prediction. For clarity, in both graphs only one representative error bar is shown. (b) Positions of the $\Delta i = 1$ resonance peaks as a function of the lattice depth. Only data points for which the resonance is clearly visible [e.g., not $\Delta i = 1$ of (a)] are included. Inset: Positions of the peaks for $\Delta i = 2$ and 3.

$E_{\text{rec}} = \hbar^2 \pi^2 / (2m d_L^2)$, where m is the mass of the Rb atoms. In the present experiment, we used $d_L = 0.426 \mu\text{m}$ (for $V_0/E_{\text{rec}} = 6, 4, 9,$ and 16) and $d_L = 0.620 \mu\text{m}$ (for $V_0/E_{\text{rec}} = 2.5, 10, 12,$ and 14). By introducing a frequency difference $\Delta\nu$ between the two lattice beams (using acousto-optic modulators which also control the power of the beams), the optical lattice can be moved at a velocity $v = d_L \Delta\nu$ or accelerated with an acceleration $a = d_L (d\Delta\nu/dt)$.

A ramp from 0 to V_0 in around 1 ms loads the BEC adiabatically into the optical lattice [14]. For loading the ground-state levels, the lattice velocity is $v = 0$ during the ramp. For the first and second excited levels, during the ramp the lattice is moved at a finite velocity calculated

from the conservation of energy and quasimomentum [16]. Finally, the optical lattice is accelerated with acceleration a for an integer number of Bloch oscillation cycles. In the rest frame of the lattice, this results in a force $F = ma$ on the condensate. Atoms that are dragged along by the accelerated lattice acquire a larger final velocity than those that have undergone tunneling, and are spatially separated from the latter by releasing the BEC from the dipole trap and lattice at the end of the acceleration period and allowing it to fall under gravity for 5–20 ms. After the time of flight, the atoms are detected by absorptive imaging on a CCD camera using a resonant flash.

From the dragged fraction $N_{\text{drag}}/N_{\text{tot}}$, we then determine the tunneling rate Γ_n in the asymptotic decay law

$$N_{\text{drag}}(t) = N_{\text{tot}} \exp(-\Gamma_n t), \quad (1)$$

where the subscript n indicates the dependence of the tunneling rate on the local energy level n in which the atoms are initially prepared (ground state: $n = 1$, first excited state: $n = 2$, etc.). In the experiments reported in this work, the number of bound states in the wells was small (2–4, depending on the lattice depth), so after the first tunneling event, the probability for tunneling to the next bound state or the continuum was close to unity.

The resolution of our tunneling measurement is given by the minimum number of atoms that we can distinguish from the background noise in our CCD images, which varies between 500 and 1000 atoms, depending on the width of the observed region. With our condensate number, and taking into account the minimum acceleration time limited by the need to spatially separate the two fractions after time of flight and the maximum acceleration time limited by the field of view of the CCD camera, this results in a maximum $\Gamma_n/\nu_{\text{rec}}$ of ≈ 1 and a minimum of $\approx 1 \times 10^{-2}$, with the recoil frequency $\nu_{\text{rec}} = E_{\text{rec}}/\hbar$.

A typical plot of the tunneling rate Γ_1 out of the ground state as a function of F_0^{-1} (where $F_0 = F d_L / E_{\text{rec}}$ is the dimensionless force) in the linear regime is shown in Fig. 2(a). This regime is reached either by choosing small radial dipole trap frequencies or by releasing the BEC from the trap before the acceleration phase and thus letting it expand. In both cases, the density and hence the interaction energy of the BEC is reduced. Superimposed on the overall exponential decay of Γ_1/F_0 with F_0^{-1} , one clearly sees the resonant tunneling peaks corresponding to $\Delta i = 2, 3,$ and 4 (for this choice of parameters, the $\Delta i = 1$ peak lay outside our experimental resolution). In order to highlight the deviation from the Landau-Zener prediction, in the inset of Fig. 2(a) we plot $\Gamma_1/\Gamma_{\text{LZ}}$, where the Landau-Zener tunneling rate Γ_{LZ} is given by [12,16]

$$\Gamma_{\text{LZ}} = \nu_{\text{rec}} F_0 e^{-[\pi^2 (V_0/E_{\text{rec}})^2 / 32 F_0]}. \quad (2)$$

The experimental results are in good agreement with numerical solutions obtained by diagonalizing the Hamiltonian of the open decaying system [17,18]. Figure 2(b) sum-

marizes our results for the positions of the ground-state resonances $\Delta i = 1, 2$, and 3 as a function of the lattice depth together with a theoretical fit assuming the separation of the lowest energy levels to be

$$\Delta E = \alpha E_{\text{rec}} \sqrt{V_0/E_{\text{rec}}}. \quad (3)$$

Independently of Δi , the best fit is achieved for $\alpha = 1.5$, to be compared with $\alpha = 2$ for the harmonic oscillator approximation. A value $\alpha < 2$ is to be expected since our lattice wells only contain a few bound states and are, therefore, highly anharmonic.

Using BECs in optical lattices allows us to explore resonant tunneling in regimes that are difficult or even impossible to access in solid state systems. First, we can prepare the condensates in the excited levels of the lattice wells before the acceleration. Again, tunneling resonances are clearly visible, and the experimental results agree with theoretical calculations. The accessibility of higher energy levels allows us to experimentally determine the decay rates at resonance of two strongly coupled levels. Although our experimental resolution does not allow us to measure the decay rates in two different levels for the same set of parameters F_0 and V_0 , we are able to compare the ground and excited state decay rates Γ_1 and Γ_2 with the theoretical predictions for two different parameter sets, as shown in Fig. 3. This figure reveals the anticrossing of the decay rates of strongly coupled levels as a function of our control parameter F_0 . These results demonstrate a peculiar behavior of the Wannier-Stark states studied theoretically

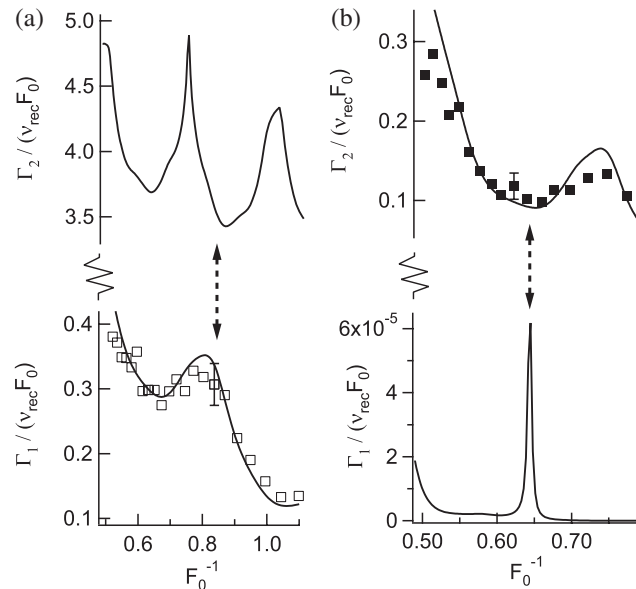


FIG. 3. Anticrossing scenario of the RET rates. (a) Theoretical plot of $\Gamma_{1,2}$ for $V_0 = 2.5E_{\text{rec}}$ with experimental points for Γ_1 . (b) Theoretical plot of $\Gamma_{1,2}$ for $V_0 = 10E_{\text{rec}}$ with experimental points for Γ_2 . For clarity, the vertical axes have been split and the Γ_n plotted on a linear scale, and only one representative error bar is shown.

[6,19] and more recently rephrased within a general context of crossings and anticrossings for the real and imaginary parts of the eigenvalues of non-Hermitian Hamiltonians [20]. Our data confirm the predictions of [17] that the anticrossings modify the decay rates of the two perturbing states in different ways.

Additionally, by exploiting the intrinsic nonlinearity of the condensate due to atom-atom interactions, we can study RET in the nonlinear regime, as simulated in [21]. In order to realize this regime, we carry out the acceleration experiments in radially tighter traps (radial frequency ≥ 100 Hz) and hence at larger condensate densities. Figure 4(a) shows the results for increasing values of the nonlinear parameter [22]

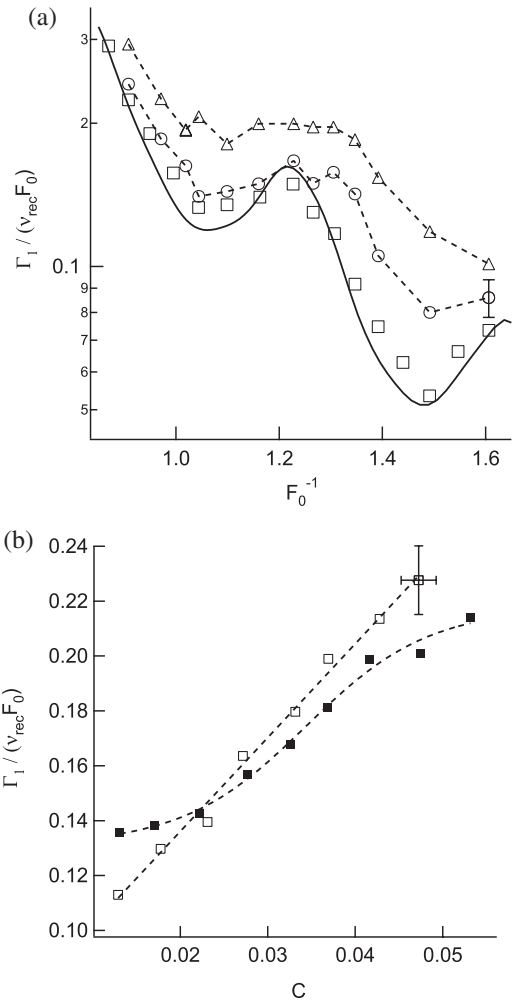


FIG. 4. Resonant tunneling in the nonlinear regime. (a) Resonance $\Delta i = 3$ for $V_0 = 2.5E_{\text{rec}}$ with $C = 0.024$ (squares), $C = 0.035$ (circles) and $C = 0.057$ (triangles). The solid line is the theoretical prediction for $C = 0$; the dashed lines are guides to the eye. (b) Dependence on C of the tunneling rate at the position of the peak $F_0^{-1} = 1.21$ (solid symbols) and of the trough $F_0^{-1} = 1.03$ (open symbols). The dashed lines are fits to guide the eye. For clarity, in (a) and (b) only one typical error bar is shown.

$$C = \frac{n_0 a_s d_L^2}{\pi}, \quad (4)$$

where n_0 is the peak condensate density and a_s the s -wave scattering length. Two effects are visible: First, the overall (off-resonant) level of Γ_1 increases linearly with C . This is in agreement with our earlier experiments on nonlinear Landau-Zener tunneling [22,23] and can be explained describing the condensate evolution within a nonlinearity-dependent effective potential $V_{\text{eff}} = V_0/(1 + 4C)$ [24]. Second, with increasing nonlinearity, the contrast of the RET peak is decreased and the peak eventually vanishes. This is confirmed by the different dependence on C of the on- and off-resonant values of Γ_1 [Fig. 4(b)]. We estimate that in order to significantly affect the resonant tunneling rate, the nonlinearity parameter has to be comparable to the width of the RET peak. This order-of-magnitude argument agrees with our observations.

Finally, we have experimentally tested the robustness of RET against a dephasing of the lattice wells induced by nonadiabatic loading of the BEC into the lattice in the nonlinear regime [15,25]. Even for completely dephased wells, the tunneling resonances survive.

In summary, we have measured resonantly enhanced tunneling of BECs in accelerated periodic potentials in a regime where the standard Landau-Zener description is not valid. Our results in the linear regime agree with numerical calculations, and the possibility to observe RET for arbitrary initial conditions and parameters of the periodic potential underlines the advantage of our system over solid state realizations. Furthermore, we have explored RET in the nonlinear regime and demonstrated that, as theoretically predicted, the tunneling resonances disappear for large values of the nonlinearity.

In the present setup the measurement of the tunneling rate is limited in its dynamic range by the detection geometry. A larger dynamic range can be realized by long-distance transport of BECs [26]. Our method for observing RET can also be generalized in order to study other regular or disordered potentials, the effects of noise and the presence of a thermal fraction in the condensate. Furthermore, one might exploit the tunneling resonances to explore the spatial decoherence processes and to perform precision measurements.

This work was supported by the European Community STREP Project OLAQUI, a MIUR-PRIN Project, the Sezione di Pisa dell'INFN, and the Feodor-Lynen Programme of the Alexander v. Humboldt Foundation. The authors would like to thank M. Cristiani, R. Mannella, and Y. Singh for assistance, A. Kolovsky for useful discussions, and S. Rolston for a critical reading of the manuscript.

- [1] D. Bohm, *Quantum Theory* (Dover Publications, New York, 1989), p. 286.
- [2] *Resonant Tunneling in Semiconductors*, edited by L. L. Chang, E. E. Mendez, and C. Tejedor (Plenum, New York, 1991).
- [3] L. L. Chang, L. Esaki, and R. Tsu, *Appl. Phys. Lett.* **24**, 593 (1974).
- [4] L. Esaki, *IEEE J. Quantum Electron.* **22**, 1611 (1986).
- [5] S. Glutsch, *Phys. Rev. B* **69**, 235317 (2004).
- [6] M. Wagner and H. Mizuta, *Phys. Rev. B* **48**, 14 393 (1993).
- [7] K. Leo, *High-Field Transport in Semiconductor Superlattices* (Springer, Berlin, 2003).
- [8] G. Grynberg and C. Robilliard, *Phys. Rep.* **355**, 335 (2001).
- [9] L. Santos, M. A. Baranov, J.I. Cirac, H.-U. Everts, H. Fehrmann, and M. Lewenstein, *Phys. Rev. Lett.* **93**, 030601 (2004).
- [10] O. Morsch and M. Oberthaler, *Rev. Mod. Phys.* **78**, 179 (2006), and references therein.
- [11] M. Greiner, O. Mandel, T. Esslinger, T. W. Hänsch, and I. Bloch, *Nature (London)* **415**, 39 (2002).
- [12] L. Landau, *Phys. Z. Sowjetunion* **1**, 88 (1932); **2**, 46 (1932); C. Zener, *Proc. R. Soc. A* **137**, 696 (1932).
- [13] C. F. Bharucha, K. W. Madison, P. R. Morrow, S. R. Wilkinson, B. Sundaram, and M. G. Raizen, *Phys. Rev. A* **55**, R857 (1997).
- [14] In the nonlinear regime, i.e., when the radial trap frequency is large and hence the interaction energy of the BEC is appreciable, the speed of the ramp has to be reduced and loading times can be as long as tens of milliseconds [15].
- [15] T. Gericke *et al.*, *cond-mat/0603590*.
- [16] E. Peik, M. B. Dahan, I. Bouchoule, Y. Castin, and C. Salomon, *Phys. Rev. A* **55**, 2989 (1997).
- [17] M. Glück, A. R. Kolovsky, and H. J. Korsch, *Phys. Rev. Lett.* **83**, 891 (1999).
- [18] M. Glück, A. R. Kolovsky, and H. J. Korsch, *Phys. Rep.* **366**, 103 (2002).
- [19] J. E. Avron, *Ann. Phys. (N.Y.)* **143**, 33 (1982).
- [20] F. Keck, H. J. Korsch, and S. Mossmann, *J. Phys. A* **36**, 2125 (2003).
- [21] S. Wimberger, R. Mannella, O. Morsch, E. Arimondo, A. R. Kolovsky, and A. Buchleitner, *Phys. Rev. A* **72**, 063610 (2005).
- [22] O. Morsch, J. H. Müller, M. Cristiani, D. Ciampini, and E. Arimondo, *Phys. Rev. Lett.* **87**, 140402 (2001).
- [23] M. Jona-Lasinio, O. Morsch, M. Cristiani, N. Malossi, J. H. Müller, E. Courtade, M. Anderlini, and E. Arimondo, *Phys. Rev. Lett.* **91**, 230406 (2003).
- [24] D. I. Choi and Q. Niu, *Phys. Rev. Lett.* **82**, 2022 (1999).
- [25] O. Morsch, J. H. Müller, D. Ciampini, M. Cristiani, P. B. Blakie, C. J. Williams, P. S. Julienne, and E. Arimondo, *Phys. Rev. A* **67**, 031603 (2003).
- [26] S. Schmid, G. Thalhammer, K. Winkler, L. Lang, and J. H. Denschlag, *New J. Phys.* **8**, 159 (2006).

Many-Body Interband Tunneling as a Witness of Complex Dynamics in the Bose-Hubbard Model

Andrea Tomadin,¹ Riccardo Mannella,¹ and Sandro Wimberger^{1,2}

¹*Dipartimento di Fisica, Università degli Studi di Pisa, Largo Pontecorvo 3, 56127 Pisa, Italy*

²*Dipartimento di Fisica del Politecnico, CNISM, C. Duca degli Abruzzi 24, 10129 Torino, Italy*

(Received 11 December 2006; published 27 March 2007)

A perturbative model is studied for the tunneling of many-particle states from the ground band to the first excited energy band, mimicking Landau-Zener decay for ultracold, spinless atoms in quasi-one-dimensional optical lattices subjected to a tunable tilting force. The distributions of the computed tunneling rates provide an independent and experimentally accessible signature of the regular-chaotic transition in the strongly correlated many-body dynamics of the ground band.

DOI: 10.1103/PhysRevLett.98.130402

PACS numbers: 03.65.Xp, 32.80.Pj, 05.45.Mt, 71.35.Lk

The experimental advances in atom and quantum optics allow the experimentalist to directly study a plethora of minimal models which have been developed to describe usually much more complex phenomena occurring in solid states [1–3]. Bose-Einstein condensates loaded into optical lattices, which perfectly realize spatially periodic potentials, are used, e.g., to implement the Wannier-Stark problem [4–6] as a paradigm of quantum transport where atoms move in a tilted lattice. Until now all experiments on the Wannier-Stark system with ultracold atoms have been performed in a regime where atom-atom interactions are either negligible [4] or reduce to an effective mean-field description [5,7]. State-of-the-art setups are, however, capable to achieve small filling factors of the order of 1 atom per lattice site [2]. Moreover, the atom-atom interactions can be tuned by the transversal confinement and by Feshbach resonances [3,8], resulting in strong interaction-induced correlations.

The regime of strong correlations in the Wannier-Stark system was addressed in [9,10], revealing the sensitive dependence of the system's dynamics on the Stark force F . The single-band Bose-Hubbard model of [9,10] is defined by the following Hamiltonian with the creation $\hat{a}_{l,1}^\dagger$, annihilation $\hat{a}_{l,1}$, and number operators $\hat{n}_{l,1}$ for the first band of a lattice $l = 1, \dots, L$:

$$\sum_l F l \hat{n}_{l,1} - \frac{J_1}{2} (\hat{a}_{l+1,1}^\dagger \hat{a}_{l,1} + \text{H.c.}) + \frac{U_1}{2} \hat{n}_{l,1} (\hat{n}_{l,1} - 1). \quad (1)$$

A transition from a regular dynamical (dominated by F) to a quantum chaotic regime (with comparable values of J_1 , U_1 , F) was found [9,10]. The transition was quantitatively studied using the distribution of the spacings between next nearest eigenenergies of the Hamiltonian (1). This analysis [9,10] verifies that the normalized level spacings $s \equiv \Delta E / \overline{\Delta E}$ obey a Poisson [$P(s) = \exp(-s)$] and a Wigner-Dyson (WD) [$P(s) = (s\pi/2) \exp(-\pi s^2/4)$] distribution in the regular and chaotic case, respectively, [11]. $P(s)$ and the cumulative distribution functions (CDFs) [$C(s) \equiv \int_0^s ds' P(s')$] are shown for typical cases in Fig. 1, where

we scanned F to emphasize the crossover between the regular and the chaotic regime. Statistical tests are also shown which confirm the analysis of [9,10] in a more systematic manner [12].

As shown in [9], the strong correlations in the quantum chaotic regime induce a fast and irreversible decay of the Bloch oscillations, which otherwise would persist in the ideal, noninteracting case. Therefore, the crossover between the two regimes discussed above could be measured in experiments by observing just the mean momentum as a function of time. Here we introduce a new, robust and hence also experimentally accessible prediction for this crossover. In the presence of strong interactions parametrized by U_1 , the single-band model should be extended to

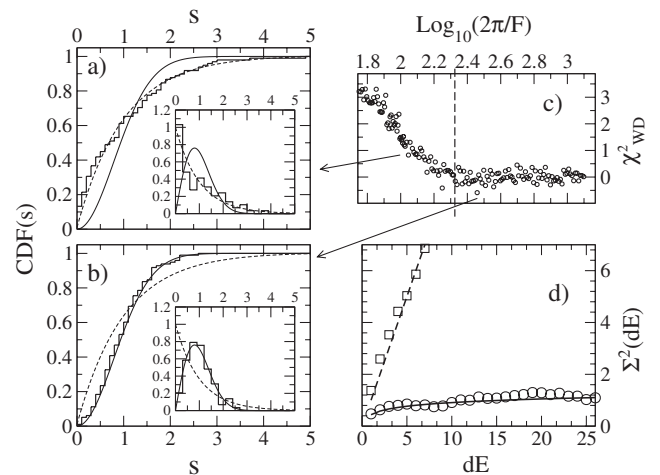


FIG. 1. (a),(b) CDF (stairs) and $P(s)$ (stairs in insets) for $N = 5$ atoms, $L = 8$, lattice depth $V = 10$ recoil energies (fixing $J_1 = 0.038$), $U_1 = 0.032$, $F \approx 0.063$ (a) and 0.021 (b), with WD (solid line) and Poisson distributions (dashed line). (c) χ^2 test with values close to zero for good WD statistics. The dashed line marks the transition to quantum chaos as F is tuned. (d) Variance of the number of levels in intervals of length dE (with normalized mean spacing), for the cases of (a) (squares) and (b) (circles), with the random matrix predictions for Poisson (dashed line) and WD (solid line) [11].

allow for interband transitions [13], as recently realized at $F = 0$ in experiments with fermionic interacting atoms [3]. Instead of using a numerically hardly tractable complete many-bands model, we introduce a perturbative decay of the many-particles modes in the ground band to a second energy band. Our novel approach to study the Landau-Zener-like tunneling between the first and the second band [1,5,7,14,15] leads to predictions for the expected decay rates and their statistical distributions. As we will show, the latter are drastically affected by the dynamics in the ground band, and they therefore provide a measurable witness for the regular-chaotic transition.

We first derive the individual decay rates of the dominating interband coupling channels. These decay rates will serve to effectively open the single-band model (1) for mimicking losses arising from the interband coupling. Our analysis starts from the following ‘‘unperturbed’’ Hamiltonian for the first two bands:

$$H_0 = \sum_{l=1}^L \left[\varepsilon_1 \hat{n}_{l,1} + \varepsilon_2 \hat{n}_{l,2} - \frac{J_2}{2} (\hat{a}_{l+1,2}^\dagger \hat{a}_{l,2} + \text{H.c.}) + F l (\hat{n}_{l,1} + \hat{n}_{l,2}) + \frac{U_1}{2} \hat{n}_{l,1} (\hat{n}_{l,1} - 1) \right]. \quad (2)$$

For a moment, we neglect the hopping in the lower band, where the single-particle Wannier functions [14] are more localized than in the upper band. In the latter we neglect the interactions, since initially only a few particles populate the excited levels. A closer analysis of the full two-bands system [12] shows that there are *two* dominating mechanisms that promote particles to the second band. The first one is a single-particle dipole coupling arising from the force term:

$$H_1 = FD \sum_l (\hat{a}_{l,2}^\dagger \hat{a}_{l,1} + \hat{a}_{l,1}^\dagger \hat{a}_{l,2}), \quad (3)$$

where D depends only on the lattice depth V (measured in recoil energies according to the definition in [7]). The second one is a many-body effect, describing two particles of the first band entering the second band together:

$$H_2 = \frac{U_\times}{2} \sum_{l=1}^L [\hat{a}_{l,2}^\dagger \hat{a}_{l,2}^\dagger \hat{a}_{l,1} \hat{a}_{l,1} + (1 \leftrightarrow 2)]. \quad (4)$$

The cross-band interaction is characterized by the parameter $U_\times \equiv \tilde{a}_s \int dx \chi_1^2 \chi_2^2 \simeq 0.5 U_1$ (for $V = 3, \dots, 10$) [12], for $U_1 \equiv \tilde{a}_s \int dx \chi_1^4$, with renormalized scattering length \tilde{a}_s [8,12] and the Wannier functions $\chi_{1,2}$ localized in each well for the first or second band. To justify the following perturbative approach, it is crucial to realize that the terms (3) and (4) must be small compared with the band gap $\Delta \equiv \varepsilon_2 - \varepsilon_1$ [not necessarily small with respect to the single-band terms in (1)], and indeed $FD, U_\times, U_1 \ll \Delta$ for the parameters considered here.

For the first perturbation, the decay channel of a given unperturbed Fock state labeled $|b\rangle$ (with a total number of

atoms N and n_h atoms in an arbitrary well h) is

$$|b; N\rangle \otimes |\text{vac}\rangle \rightarrow |b'; N-1\rangle \otimes |w\rangle, \quad n'_h = n_h - 1. \quad (5)$$

Here, $|w\rangle = \sum_{m=-\infty}^{+\infty} \mathcal{J}_{m-w} (|J_2|/F) \hat{a}_{m,2}^\dagger |\text{vac}\rangle$ is the single-particle eigenstate for the Wannier-Stark problem, localized around the site w in the second band, with the Bessel function of the first kind $\mathcal{J}_m(x)$ [14].

The expectation value of (3) for $|b; N\rangle$ of the first band, equal to the first-order $\delta E(b)$, is zero because the operator does not conserve the number of particles within the bands. The decay width at first order is given by the matrix element of the perturbation between the initial and final state according to Fermi’s golden rule, and only the first term in (3) gives a nonzero contribution [12]:

$$\langle k | \langle b' | \sum_{l=1}^L \hat{a}_{l,2}^\dagger \hat{a}_{l,1} | b \rangle | \text{vac} \rangle = \sum_{l=1}^L \mathcal{J}_{l-w} (|J_2|/F) \delta(n'_l, n_l - 1) \times \sqrt{n_l} \prod_{m \neq l} \delta(n'_m, n_m). \quad (6)$$

The $\delta(\cdot, \cdot)$ functions act as a selection rule for the Fock states that are coupled by the perturbation. The tunneling mechanism does not include any income of energy from an external source, so the initial and final energies $E_0(b) = \langle \text{vac} | \langle b | H_0 | b \rangle | \text{vac} \rangle$ and $E_0(b', w) = \langle w | \langle b' | H_0 | b' \rangle | w \rangle$, respectively, must be equal as required by the golden rule. The condition on the energy conservation is, however, relaxed to account for the uncertainty $\Delta E(b)$ of the unperturbed energy levels of the initial and final states in the lower band arising from the hopping in this band initially neglected in (2). A detailed derivation is given in [12], and here we only state the result:

$$\Delta E(b) = 2\pi (J_1/2)^2 \sum_{b'} \Delta E(b \rightarrow b') = 2\pi (J_1/2)^2 \sum_l \sum_{\Delta l = \pm 1} n_l^2 \delta(n_l + \Delta l + 1, n_l). \quad (7)$$

The level density $\rho(E, b)$ around the unperturbed energy $E_0(b)$ of a Fock state $|b\rangle$ is then approximated by a rectangular profile, of width $\Delta E(b)$ and unit area: $\rho(E, b) = \chi \{ |E - E_0(b)| \leq \Delta E(b)/2 \} / \Delta E(b)$. The relaxed energy conservation rule selects from (5) the set K of permitted decay channels (h, w) parametrized by the two indices h, w such that

$$E_0(b', w) - E_0(b) = \Delta - F(h-w) - U_1(n_h - 1) \in \left[-\frac{\Delta E(b) + \Delta E(b')}{2}, \frac{\Delta E(b) + \Delta E(b')}{2} \right]. \quad (8)$$

Hence the energy Δ required to promote a particle to the second band is supplied by the decrease of the interaction ($\propto U_1$) and by the work of the force ($\propto F$) exerted on the promoted particle.

The total width $\Gamma_1(b)$ for the decay via the allowed channels K is proportional to the square of the matrix element and to the level density $\rho(E, b)$:

$$\Gamma_1(b) = 2\pi(FD)^2 \sum_{(h,w) \in K} \left\{ \left| \mathcal{J}_{h-w} \left(\frac{|J_2|}{F} \right) \sqrt{n_h} \right|^2 \times \frac{1}{\Delta E(b)\Delta E(b')} \right\}. \quad (9)$$

$\mathcal{J}_m(x)$ significantly contributes only for $|m| \lesssim |x|$. If U_1 , $\Delta E(b) \ll \Delta$, the energy conservation is roughly given by $|\Delta| \simeq F(h-w)$. Requiring that the Bessel function in (9) is substantially larger than zero, we obtain the inequality $|\Delta| \leq |J_2|$. The last condition does not depend on F , since a twofold effect is at work: a stronger force produces a larger energy gain when a particle moves along the lattice, but the extension $|J_2/F|$ of the single-particle state shrinks. Therefore, increasing F results in an increased energy matching and a strongly reduced “geometrical” matching. For $3 < V < 26$, we have $|\Delta| - |J_2| > 1.0$ [12], such that the energy matching cannot be realized by just tuning the lattice depth. The decay can, however, be activated by an increase of the interactions, which can be experimentally achieved by acting on the transversal confining potential of a quasi-one-dimensional lattice, or by a Feshbach resonance [8]. In the calculations presented below, we augmented U_1 used in [9,10] by a factor of order 10, and as noted in the introduction, a similar increase of the interaction strength was used in the experiment to promote fermions to higher bands [3], in close analogy to the here-described field- and interaction-induced interband coupling of bosons.

The second term (4) is treated in a similar way, with the difference that two particles are promoted to the second band, and the position of the second single-particle state $|w'\rangle$ is an additional degree of freedom for the transition. The decay channels are

$$|b, N\rangle \otimes |\text{vac}\rangle \rightarrow |b', N-2\rangle \otimes |w, w'\rangle; \quad n'_h = n_h - 2. \quad (10)$$

The energy matching selects a set K of decay channels, parametrized by the three site indices h, w, w' :

$$\begin{aligned} & (h, w, w') \in K \quad \text{such that} \\ & E_0(b', w, w') - E_0(b) = 2\Delta - F(2h - w - w') \\ & \quad - U_1(2n_h - 3) \\ & \in \left[-\frac{\Delta E(b) + \Delta E(b')}{2}, \frac{\Delta E(b) + \Delta E(b')}{2} \right]. \end{aligned} \quad (11)$$

The computation of the matrix element yields [12]:

$$\begin{aligned} \Gamma_2(b) = 2\pi \left(\frac{U_\times}{2} \right)^2 \sum_{(h,w,w') \in K} & \left\{ \left| \mathcal{J}_{h-w} \left(\frac{|J_2|}{F} \right) \mathcal{J}_{h-w'} \left(\frac{|J_2|}{F} \right) \right|^2 \right. \\ & \left. \times 4n_h(n_h - 1) \frac{1}{\Delta E(b)\Delta E(b')} \right\}. \end{aligned} \quad (12)$$

With respect to (9), the additional degree of freedom w' results in a summation over all possible values of $w - w'$. This follows from the possibility to conserve the energy even if a particle is pushed far, if the other particle is pushed almost equally far in the opposite direction. Since the decay widths in (12) depend on the product of two (rapidly decaying) Bessel functions—again a geometrical matching condition—we apply the truncation $|w - w'| \leq |J_2/F|$, to reduce the formula to a finite form.

We can now compute the total width $\Gamma_F(b) = \Gamma_1(b) + \Gamma_2(b)$ defined by the two analyzed coupling processes for each basis state $|b\rangle$ of the single-band problem given in (1). The $\Gamma_F(b)$ are inserted as complex potentials in the diagonal of the single-band Hamiltonian matrix. After a gauge transform that recovers the translational invariance of the problem (see [10,12] for details), the latter matrix is used to compute the evolution operator over one Bloch period T_B , which is finally diagonalized to obtain its eigenphases $\exp(-iE_j T_B)$. Along with the statistics of the level spacings defined by $\text{Re}\{E_j\}$, Figs. 2 and 3 analyze the statistical distributions of the tunneling rates $\Gamma_j = -2 \text{Im}\{E_j\}$ for some paradigmatic cases. All rates are much smaller than unity, which *a posteriori* is fully consistent with our perturbative approach.

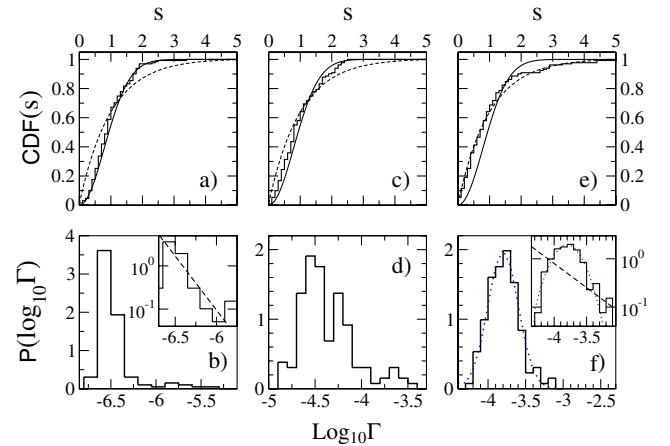


FIG. 2 (color online). (a),(c),(e) CDF from $\text{Re}\{E_j\}$ (stairs), together with WD (solid line) and Poisson predictions (dashed line). (b),(d),(f) Distributions of the logarithm of the rates. In (a),(b), (c),(d), (e),(f), $F \simeq 0.17, 0.31, 0.47$, respectively, with $(N, L) = (7, 6)$, $V = 3$, $U_1 = 0.2$ (fixing $U_\times \simeq 0.1$). In the regular regime (f), a log-normal distribution (dotted line) well fits the data, with a scaling $P(\Gamma) \propto \Gamma^{-x}$ for the largest Γ [dashed line in the inset of (f) with $x = 1$]. In the chaotic case, a global power-law behavior with $x \simeq 2$ is found [dashed line in the inset of (b)].

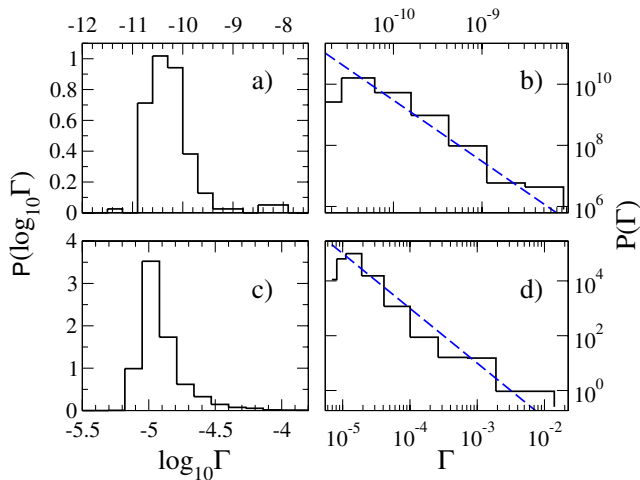


FIG. 3 (color online). (a),(c) Rate distributions in the chaotic regime with $F \approx 0.17$, $U_1 = 0.2$ ($U_\times \approx 0.1$), together with the corresponding *unscaled* $P(\Gamma)$ in (b),(d). In (a),(b) $(N, L) = (7, 6)$, $V = 4$, and in (c),(d) $(N, L) = (9, 8)$, $V = 3$. Power laws $P(\Gamma) \propto \Gamma^{-x}$ are found with $x \approx 2$ [dashed lines in (b),(d)].

To observe what happens at the regular-chaotic transition (cf. Fig. 1), we scan F in Fig. 2, and as F increases, the average decay increases by orders of magnitude, while the distributions broaden. The large increase of the rates is due to an improved energy matching, when F supplies the necessary energy to promote particles to the second band. For the parameters of Fig. 2, the single-particle Landau-Zener formula [14] gives $\Gamma_{LZ} = (F/2\pi) \times \exp[-\pi^2 \Delta^2 / (8F)] \sim 10^{-23}$, 10^{-12} , 10^{-8} for 2(b), 2(d), and 2(f). This huge variation, typical of semiclassical formulas, implies that there are possibly parameters for which our results are comparable to the single-particle prediction, but, in general, the many-particle effects *cannot* be neglected. Moreover, mean-field treatments of the Landau-Zener tunneling at best predict a shift of Γ [7,15], but cannot account for their distributions.

In the chaotic regime, the Fock states are strongly mixed by the dynamics [9,10,12] and a fast decaying Fock state can act as a privileged decay channel for *many* eigenstates. Many states then share similar rates, leading to thinner distributions. Therefore, the thinner distribution of Fig. 2(b) is a direct signature of the chaotic dynamics evidenced in 2(a), as compared with the regular case in 2(e) and 2(f). In Fig. 2(f), we found a good agreement with the expected log-normal distribution of decay rates [16] (or of the similarly behaving conductance [17]) in the regular regime. There the system shows nearly perfect Bloch oscillations [9], and the motion of the atoms is localized along the lattice [14]. We can even detect a qualitative crossover to a power law $P(\Gamma) \propto \Gamma^{-1}$ in the right tail of the distribution, as predicted from localization theory [16,18,19]. The distributions in Figs. 2(b) and 3 follow the expected power law for open quantum chaotic systems in the diffusive regime [18]. The exponents x are, however,

nonuniversal and depend on the opening of the system. In our case, the decay channels are defined by the interband coupling, which in a sense attaches “leads” to *all* lattice sites *within* the sample. Going along with the regular-to-chaotic transition in the lower band of our model [from Fig. 2(f) and 2(b), or to Fig. 3] the Γ distributions transform from a log normal to a power law with $x \approx 2$, in close analogy to the transition from Anderson-localized to diffusive dynamics in open disordered systems [18,20].

In summary, our perturbative opening of the single-band Wannier-Stark system allows one to study Landau-Zener-like interband tunneling within a many-body description of the dynamics of ultracold atoms. The statistical characterization of the tunneling rates (mean values and form of the distributions) provides clear and robust signatures of the regular-to-chaotic transition for future experiments. A more detailed analysis of the interband coupling in a full-blown model, in which at least two bands are completely included, calls for huge computational resources to access the complete quantum spectra. Nonetheless, our results are a first step in the direction of studies for which “horizontal” and “vertical” quantum transport along the lattice are simultaneously present and influence each other in a complex manner.

We thank the Centro di Calcolo, Dipartimento di Fisica, Università di Pisa, for providing CPU, and the Humboldt Foundation, MIUR-PRIN, and EU-OLAQUI for support.

- [1] O. Morsch *et al.*, *Rev. Mod. Phys.* **78**, 179 (2006).
- [2] M. Greiner *et al.*, *Nature (London)* **415**, 39 (2002); T. Stöferle *et al.*, *Phys. Rev. Lett.* **92**, 130403 (2004); S. Fölling *et al.*, *ibid.* **97**, 060403 (2006).
- [3] M. Köhl *et al.*, *Phys. Rev. Lett.* **94**, 080403 (2005).
- [4] M. BenDahan *et al.*, *Phys. Rev. Lett.* **76**, 4508 (1996); S.R. Wilkinson *et al.*, *ibid.* **76**, 4512 (1996); B.P. Anderson *et al.*, *Science* **282**, 1686 (1998).
- [5] O. Morsch *et al.*, *Phys. Rev. Lett.* **87**, 140402 (2001).
- [6] G. Roati *et al.*, *Phys. Rev. Lett.* **92**, 230402 (2004).
- [7] S. Wimberger *et al.*, *Phys. Rev. A* **72**, 063610 (2005).
- [8] T. Bergeman *et al.*, *Phys. Rev. Lett.* **91**, 163201 (2003).
- [9] A. Buchleitner *et al.*, *Phys. Rev. Lett.* **91**, 253002 (2003).
- [10] A.R. Kolovsky *et al.*, *Phys. Rev. E* **68**, 056213 (2003).
- [11] M.L. Mehta, *Random Matrices and the Statistical Theory of Energy Levels* (Academic, New York, 1991).
- [12] A. Tomadin, Master’s thesis, Università di Pisa, 2006.
- [13] V.W. Scarola *et al.*, *Phys. Rev. Lett.* **95**, 033003 (2005).
- [14] M. Glück *et al.*, *Phys. Rep.* **366**, 103 (2002).
- [15] B. Wu *et al.*, *Phys. Rev. A* **61**, 023402 (2000); O. Zobay *et al.*, *ibid.* **61**, 033603 (2000); S. Wimberger *et al.*, *J. Phys. B* **39**, 729 (2006).
- [16] M. Terraneo *et al.*, *Eur. Phys. J. B* **18**, 303 (2000).
- [17] C.W.J. Beenakker, *Rev. Mod. Phys.* **69**, 731 (1997).
- [18] T. Kottos, *J. Phys. A* **38**, 10761 (2005).
- [19] G. Casati *et al.*, *Phys. Rev. Lett.* **82**, 524 (1999); S. Wimberger *et al.*, *ibid.* **89**, 263601 (2002).
- [20] S. Wimberger *et al.*, *J. Phys. A* **34**, 7181 (2001).

Dissipation Induced Coherence of a Two-Mode Bose-Einstein Condensate

D. Witthaut,^{1,*} F. Trimborn,² and S. Wimberger³

¹*QUANTOP, Niels Bohr Institute, University of Copenhagen, DK-2100 Copenhagen, Denmark*

²*Institut für mathematische Physik, TU Braunschweig, D-38106 Braunschweig, Germany*

³*Institut für theoretische Physik, Universität Heidelberg, D-69120, Heidelberg, Germany*

(Received 10 July 2008; published 10 November 2008)

We discuss the dynamics of a Bose-Einstein condensate in a double-well trap subject to phase noise and particle loss. The phase coherence of a weakly interacting condensate as well as the response to an external driving show a pronounced stochastic resonance effect: Both quantities become maximal for a finite value of the dissipation rate matching the intrinsic time scales of the system. Even stronger effects are observed when dissipation acts in concurrence with strong interparticle interactions, restoring the purity of the condensate almost completely and increasing the phase coherence significantly.

DOI: 10.1103/PhysRevLett.101.200402

PACS numbers: 03.75.Lm, 03.65.Yz, 03.75.Gg

In our naive understanding thermal noise is generally distracting, hindering measurements and degrading coherences in quantum mechanics. A paradigmatic counterexample to this assertion is the effect of stochastic resonance (SR), where the response of a system to an external driving assumes its maximum in the presence of a finite amount of thermal noise, when the time scales of the noise and the driving match [1]. In this case the noise is strong enough to cause a large dynamical effect when it adds up constructively with the driving, whereas it is still weak enough not to make the dynamics completely random. By now, SR has been shown in a variety of systems, an overview is given in the review articles [2–5].

In addition to numerous examples in classical dynamics, SR has also been found in a variety of quantum systems (see [5] and references therein). Recently, there has been an increased interest in controlling and even exploiting dissipation in interacting many-body quantum systems. For instance, the entanglement in a spin chain assumes an SR-like maximum for a finite amount of thermal noise [6]. Furthermore, it has been shown that dissipative processes can be tailored to prepare arbitrary pure states for quantum computation and strongly correlated states of ultracold atoms [7] or to implement a universal set of quantum gates [8]. Actually, a recent experiment has even proven that strong inelastic collisions may inhibit particle losses and induce strong correlations in a quasi one-dimensional gas of ultracold atoms [9].

In this Letter we demonstrate the constructive effects of dissipation for an interacting many-particle quantum system realized by ultracold atoms in a double-well trap with biased particle dissipation. It is shown that a proper amount of dissipation maximizes the coherence of the two condensate modes in the fashion of the SR effect. In this case the particle loss is strong enough to significantly increase the condensate purity, whereas it is still weak enough not to dominate the complete dynamics. These effects are of considerable strength for realistic parameters, especially

in the case of strong interparticle interactions, and thus should be observable in ongoing experiments [10–13].

The unitary dynamics of ultracold atoms in a double-well trap is described by the two-mode Bose-Hubbard Hamiltonian [14–16]

$$\hat{H} = -J(\hat{a}_1^\dagger \hat{a}_2 + \hat{a}_2^\dagger \hat{a}_1) + \epsilon(\hat{n}_2 - \hat{n}_1) + \frac{U}{2}[\hat{n}_1(\hat{n}_1 - 1) + \hat{n}_2(\hat{n}_2 - 1)], \quad (1)$$

where \hat{a}_j and \hat{a}_j^\dagger are the bosonic annihilation and creation operators in the j th well and $\hat{n}_j = \hat{a}_j^\dagger \hat{a}_j$ are the number operators. In general we consider a biased double-well trap, where the ground state energies of the two wells differ by 2ϵ . We set $\hbar = 1$, thus measuring all energies in frequency units.

The main source of decoherence is phase noise due to elastic collisions with atoms in the thermal cloud [17,18] which effectively heats the system. The heating rate is fixed as $\gamma_p = 5 \text{ s}^{-1}$ in the following, which is a realistic value for the experiments in Heidelberg [10,11]. Methods to attenuate this source of decoherence were discussed only recently [19]. Amplitude noise, i.e., the exchange of particles with the thermal cloud due to inelastic scattering, drives the system to thermal equilibrium. However, this effect is usually much too weak to produce the effects discussed below in present experiments (cf. the discussion in [18]). In contrast, a strong and tunable source of dissipation can be implemented artificially by shining a resonant laser beam onto the trap, that removes atoms with the site-dependent rates γ_{aj} from the two wells $j = 1, 2$. Nontrivial effects of dissipation such as the stochastic resonance discussed below require strongly biased loss rates, i.e., $\gamma_{a1} \neq \gamma_{a2}$. For a laser beam focused on one of the wells an asymmetry of $f_a = (\gamma_{a2} - \gamma_{a1})/(\gamma_{a2} + \gamma_{a1}) = 0.5$ should be feasible. Thus we consider the dynamics generated by the master equation

$$\begin{aligned} \dot{\hat{\rho}} = & -i[\hat{H}, \hat{\rho}] - \frac{\gamma_p}{2} \sum_{j=1,2} (\hat{n}_j^2 \hat{\rho} + \hat{\rho} \hat{n}_j^2 - 2\hat{n}_j \hat{\rho} \hat{n}_j) \\ & - \frac{1}{2} \sum_{j=1,2} \gamma_{aj} (\hat{a}_j^\dagger \hat{a}_j \hat{\rho} + \hat{\rho} \hat{a}_j^\dagger \hat{a}_j - 2\hat{a}_j \hat{\rho} \hat{a}_j^\dagger). \end{aligned} \quad (2)$$

The macroscopic dynamics of the atomic cloud is well described by a mean-field approximation, considering only the expectation values $s_j = 2\text{tr}(\hat{L}_j \hat{\rho})$ of the angular momentum operators $\hat{L}_x = (\hat{a}_1^\dagger \hat{a}_2 + \hat{a}_2^\dagger \hat{a}_1)/2$, $\hat{L}_y = i(\hat{a}_1^\dagger \hat{a}_2 - \hat{a}_2^\dagger \hat{a}_1)/2$, $\hat{L}_z = (\hat{a}_2^\dagger \hat{a}_2 - \hat{a}_1^\dagger \hat{a}_1)/2$ and the particle number $n = \text{tr}[(\hat{n}_1 + \hat{n}_2)\hat{\rho}]$. The time evolution of the Bloch vector \mathbf{s} and the particle number is then given by [20]

$$\begin{aligned} \dot{s}_x &= -2\epsilon s_y - U s_y s_z - T_2^{-1} s_x, \\ \dot{s}_y &= 2J s_z + 2\epsilon s_x + U s_x s_z - T_2^{-1} s_y, \\ \dot{s}_z &= -2J s_y - T_1^{-1} s_z - T_1^{-1} f_a n, \\ \dot{n} &= -T_1^{-1} n - T_1^{-1} f_a s_z. \end{aligned} \quad (3)$$

As usual expectation values of products have been factorized in the U -dependent interaction terms to obtain a closed set of evolution equations [14–16], whereas the dissipation terms are exact. Furthermore, we have defined the transversal and longitudinal damping times by

$$T_1^{-1} = (\gamma_{a1} + \gamma_{a2})/2 \quad \text{and} \quad T_2^{-1} = \gamma_p + T_1^{-1}. \quad (4)$$

These equations of motion resemble the celebrated Bloch equations in nuclear magnetic resonance [21,22] with some subtle but nevertheless important differences. The longitudinal relaxation is now associated with particle loss and, more important, the dynamics is substantially altered by the interaction term [10,14,15].

In the following, we will show that a finite amount of dissipation induces a maximum of the coherence which can be understood as an SR effect. We have to distinguish between two different kinds of coherence, which will both be considered. First of all we consider the phase coherence between the two wells, which is measured by the average *contrast* in interference experiments as described in [10,11] and given by

$$\alpha = \frac{2|\langle \hat{a}_1^\dagger \hat{a}_2 \rangle|}{\langle \hat{n}_1 + \hat{n}_2 \rangle} = \frac{\sqrt{s_x^2 + s_y^2}}{n}. \quad (5)$$

Second, we will analyze how close the many-particle quantum state is to a pure Bose-Einstein condensate (BEC), which is a coherent state for the $SU(2)$ operator algebra [23]. This property is quantified by the purity $p = 2\text{tr}(\hat{\rho}_{\text{red}}^2) - 1 = |\mathbf{s}|^2/n^2$ of the reduced single-particle density matrix $\hat{\rho}_{\text{red}}$ cf. [16].

Let us first discuss the weakly interacting case, where the mean-field equations of motion (3) provide an excellent description of the dynamics, which is exact for $U = 0$. Obviously, only the trivial solution $\mathbf{s} = 0$ and $n = 0$ is a steady state in the strict sense. However, the system rapidly

relaxes to a quasisteady state of the form $\mathbf{s}(t) \sim \mathbf{s}_0 e^{-\kappa t}$ and $n(t) \sim n_0 e^{-\kappa t}$, where the internal dynamics is completely frozen out and all components of the Bloch vector and the particle number decay at the same rate κ . Figure 1 shows the contrast α for this quasisteady state as a function of the tunneling rate J and the dissipation rate $1/T_1$ for $U = 0$. For a fixed value of one of the parameters, say J , one observes a typical SR-like maximum of the contrast for a finite value of the dissipation rate $1/T_1$. In particular, the contrast is maximal if the time scales of the tunneling and the dissipation are matched according to $4J^2 \approx f_a T_1^{-1} (f_a T_1^{-1} + \gamma_p)$ [24]. This scenario is robust and not altered by weak interparticle interactions. Changes in the system parameters such as ϵ preserve the general shape of $\alpha(1/T_1, J)$ and the existence of a pronounced SR-like maximum. At the most, the function $\alpha(1/T_1, J)$ is stretched, shifting the position of the SR-like maximum.

The occurrence of a maximum of the contrast is explained by Fig. 2(b), where the results of a Monte Carlo wave function (MCWF) simulation [25] of the many-body dynamics are shown for three different values of J and $U = 0.1 \text{ s}^{-1}$. We have plotted a histogram of the probabilities to observe the relative population imbalance s_z/n and the relative phase ϕ in a single experimental run for three different values of the tunneling rate J after the system has relaxed to the quasisteady state. With increasing J , the atoms are distributed more equally between the two wells so that the single shot contrast increases. Within the mean-field description this is reflected by an increase of $\sqrt{s_x^2 + s_y^2}/|s|$ at the expense of $|s_z|$. However, this effect also makes the system more vulnerable to phase noise so that the relative phase of the two modes becomes more and more random and $|s|/n$ decreases. The average contrast (5) then assumes a maximum for intermediate values of J as shown in Fig. 2(a). In this example, the trap is assumed to be weakly biased, shifting the position of the SR-like maximum to a value of J which is more easily accessible in ongoing experiments [10,11].

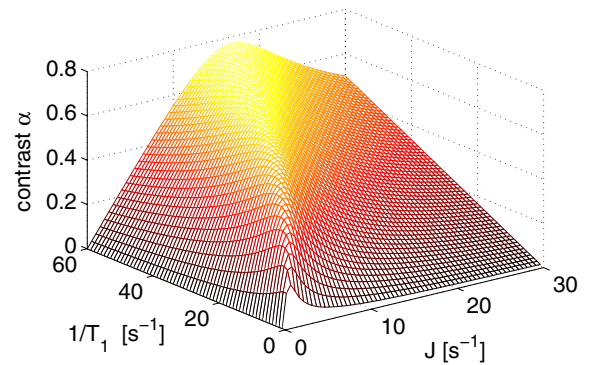


FIG. 1 (color online). Contrast α in the quasisteady state in dependence on the tunneling rate J and the dissipation rate $1/T_1$ for $U = 0$ and $\epsilon = 0$.

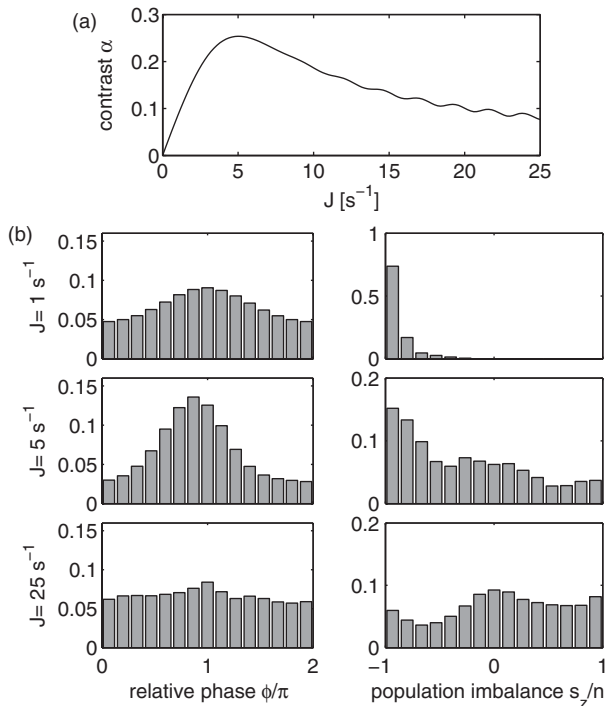


FIG. 2. (a) Average contrast α after $t = 1.5$ s starting from a pure BEC (i.e. a product state) with $s_z = n/2$ and $n(0) = 100$ particles in dependence on the tunneling rate J for $T_1 = 0.5$ s, $\epsilon = 10 \text{ s}^{-1}$, $U = 0.1 \text{ s}^{-1}$. (b) Histogram of the probabilities to measure the relative phase ϕ and the relative population imbalance s_z/n in a single experimental run after $t = 1.5$ s obtained from a MCWF simulation of the many-body dynamics.

So far we have demonstrated a SR of the contrast for a BEC in a static double-well trap with biased particle losses. We will now show that the system's response to a weak external driving also assumes a maximum for a finite dissipation rate—an effect which is conceptually closer to the common interpretation of stochastic resonance. We consider a weak driving of the tunneling rate $J(t) = J_0 + J_1 \cos(\omega t)$ at the resonance frequency $\omega = \sqrt{J_0^2 + \epsilon^2}$, where the amplitude is not more than $J_1/J_0 = 10\%$. This can be readily implemented in optical setups by varying the intensity of the counterpropagating lasers forming the optical lattice. Figure 3(a) shows the resulting dynamics for $T_1 = 0.5$ s and $J_0 = 1.5 \text{ s}^{-1}$. After a short transient period, the relative population imbalance $s_z(t)/n(t)$ oscillates approximately sinusoidally. The system response measured by the amplitude of these forced oscillations shows the familiar SR-like maximum as illustrated in Fig. 3(b). It should be detectable without major problems in ongoing experiments, in which the population imbalance s_z can be measured with a resolution of a few atoms [10,11]. A more detailed study of such a driven case of SR will be discussed in a forthcoming article [24].

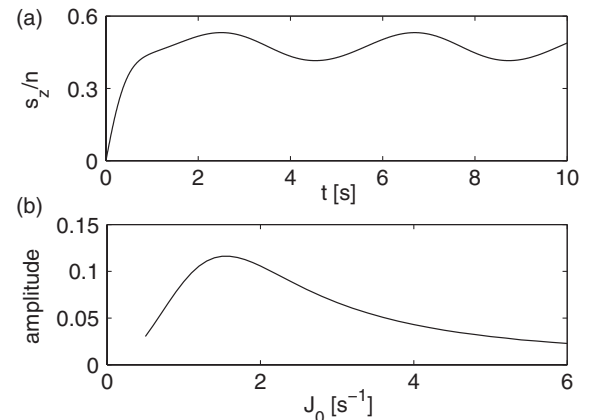


FIG. 3. (a) Oscillation of the relative population imbalance s_z/n of a weakly driven two-mode BEC for $J_0 = 1.5 \text{ s}^{-1}$, $T_1 = 0.5$ s and $\epsilon = 0$. (b) Amplitude of the oscillations in dependence on the tunneling rate J_0 .

Even more remarkable values of the coherences are observed in the case of strong interactions, which is experimentally most relevant and theoretically most profound. The interplay between interactions and dissipation significantly increases the coherences in comparison to situations where one of the two is weak or missing. An example for the dynamics of a strongly-interacting BEC is shown in Fig. 4 for an initially pure BEC with $s_z = n/2$, calculated both with the MCWF method and within the mean-field approximation (3). At first, the purity p and the contrast α drop rapidly due to the phase noise and the interactions cf. [16]. For intermediate times, however, the system relaxes to a nonlinear quasisteady state, which is a

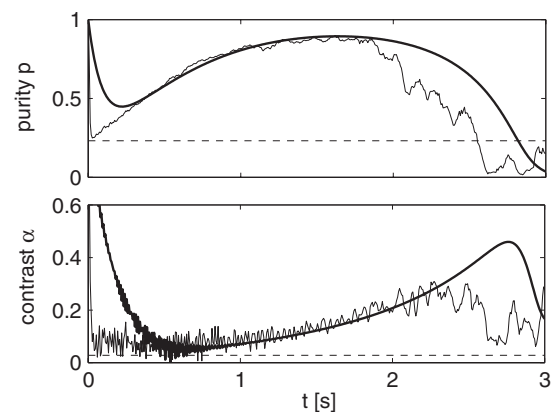


FIG. 4. Time evolution of the purity p and the contrast α for $J = U = 10 \text{ s}^{-1}$, $\epsilon = 0$, $T_1 = 0.5$ s. The initial state is a pure BEC with $s_z = n/2$ and $n(0) = 100$ particles. The results of a MCWF simulation averaged over 100 runs are plotted as a thin solid line while the mean-field results are plotted as a thick line. The dashed line shows the steady state values for $1/T_1 = 1/T_2 = 0$, i.e., without coupling to the environment.

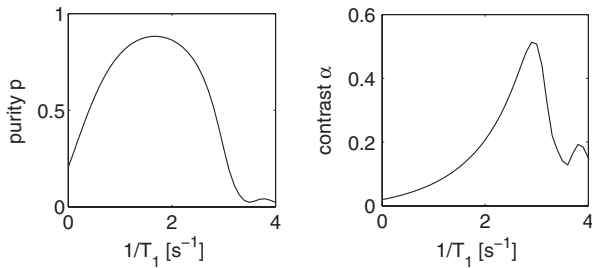


FIG. 5. Purity p and contrast α after $t = 2$ s in dependence on the dissipation rate $1/T_1$ calculated within the mean-field approximation for the same parameters as in Fig. 4.

nearly pure BEC mostly localized in the well with the smaller decay rate. Consequently, the purity p is restored almost completely and the contrast α is relatively large. In close analogy to the celebrated self-trapping effect [10,14,15], this quasisteady state exists only as long as the effective interaction strength $Un(t)$ is larger than a critical value given by [20,24]

$$U^2 n^2 \gtrsim 4J^2 - f_a^2 T_1^{-2}. \quad (6)$$

As the particle number n decays, this state ceases to exist so that the system relaxes to a linear quasisteady state with much smaller values of p and α as discussed above.

Moreover, the coherences at intermediate times are also larger than in an interacting, but nondissipative system. The dashed lines in Fig. 4 show the steady state values of the purity p and the contrast α for $1/T_1 = 1/T_2 = 0$, apart from occasional revivals due to the finite particle number. It is observed that the coherences are considerably smaller compared to the strongly-interacting open system. This loss of coherence can be understood by the fact that the interactions lead to an effective decoherence on the single-particle level [16], degrading α and p . This effect is mostly cured by the dissipation.

The behavior illustrated in Fig. 4 is universal, in the sense that the maxima of the purity and the contrast are present for all values of U and $1/T_1$ if only $Un(t=0)$ is well above the critical value (6) for the existence of the nonlinear quasisteady state. However, the maxima occur later if T_1 or U increase. The purity p and the contrast α after a fixed time $t = 2$ s are plotted in Fig. 5 in dependence on the dissipation rate $1/T_1$, showing pronounced maxima for finite values of $1/T_1$. For smaller dissipation rates, the maximum of the contrast has not been assumed yet while the system has already relaxed to the linear quasisteady state for larger values of $1/T_1$.

To summarize, we have shown that the coherence properties of a weakly and, in particular, also of a strongly interacting Bose-Einstein condensate in a double-well trap can be controlled by engineering the system's parameters

and dissipation simultaneously. An important conclusion is that the interplay of interactions and dissipation can drive the system to a state of maximum coherence, while both processes alone usually lead to a loss of coherence. Since the double-well BEC is nowadays routinely realized with nearly perfect control on atom-atom interactions and external potentials [10,11], we hope for an experimental verification and future extensions of the predicted stochastic resonance scheme.

We thank M.K. Oberthaler, J.R. Anglin, and A.S. Sørensen for stimulating discussions. This work was supported by the German Research Foundation (DFG) through the research fellowship program (Grant No. WI 3415/1) and the Heidelberg Graduate School of Fundamental Physics (Grant No. GSC 129/1) as well as the Studienstiftung des deutschen Volkes.

*dirk.witthaut@nbi.dk

- [1] R. Benzi *et al.*, *J. Phys. A* **14**, L453 (1981).
- [2] K. Wiesenfeld and F. Moss, *Nature (London)* **373**, 33 (1995).
- [3] M.I. Dykman *et al.*, *Nuovo Cimento D* **17**, 661 (1995).
- [4] L. Gammaioni *et al.*, *Rev. Mod. Phys.* **70**, 223 (1998).
- [5] T. Wellens *et al.*, *Rep. Prog. Phys.* **67**, 45 (2004).
- [6] S.F. Huelga and M.B. Plenio, *Phys. Rev. Lett.* **98**, 170601 (2007).
- [7] B. Kraus *et al.*, *Phys. Rev. A* **78**, 042307 (2008); S. Diehl *et al.*, *Nature Phys.* **4**, 878 (2008).
- [8] F. Verstraete *et al.*, arXiv:0803.1447.
- [9] N. Syassen *et al.*, *Science* **320**, 1329 (2008).
- [10] M. Albiez *et al.*, *Phys. Rev. Lett.* **95**, 010402 (2005).
- [11] R. Gati *et al.*, *Phys. Rev. Lett.* **96**, 130404 (2006); R. Gati *et al.*, *New J. Phys.* **8**, 189 (2006).
- [12] T. Schumm *et al.*, *Nature Phys.* **1**, 57 (2005).
- [13] S. Fölling *et al.*, *Nature (London)* **448**, 1029 (2007).
- [14] G.J. Milburn *et al.*, *Phys. Rev. A* **55**, 4318 (1997).
- [15] A. Smerzi *et al.*, *Phys. Rev. Lett.* **79**, 4950 (1997).
- [16] A. Vardi and J.R. Anglin, *Phys. Rev. Lett.* **86**, 568 (2001); J.R. Anglin and A. Vardi, *Phys. Rev. A* **64**, 013605 (2001).
- [17] J.R. Anglin, *Phys. Rev. Lett.* **79**, 6 (1997).
- [18] J. Ruostekoski and D.F. Walls, *Phys. Rev. A* **58**, R50 (1998).
- [19] Y. Khodorkovsky *et al.*, *Phys. Rev. Lett.* **100**, 220403 (2008).
- [20] F. Trimborn, D. Witthaut, and S. Wimberger, *J. Phys. B* **41**, 171001 (2008).
- [21] L. Viola *et al.*, *Phys. Rev. Lett.* **84**, 5466 (2000).
- [22] F. Bloch, *Phys. Rev.* **70**, 460 (1946).
- [23] F. Trimborn *et al.*, *Phys. Rev. A* **77**, 043631 (2008); arXiv:0802.1142.
- [24] D. Witthaut, F. Trimborn, and S. Wimberger (to be published).
- [25] J. Dalibard *et al.*, *Phys. Rev. Lett.* **68**, 580 (1992).

Time-Resolved Measurement of Landau-Zener Tunneling in Periodic Potentials

A. Zenesini,^{1,2} H. Lignier,¹ G. Tayebirad,³ J. Radogostowicz,^{1,2} D. Ciampini,^{1,2} R. Mannella,^{1,2} S. Wimberger,³ O. Morsch,¹ and E. Arimondo^{1,2}

¹CNR-INFM and Dipartimento di Fisica “E. Fermi,” Largo Pontecorvo 3, 56127 Pisa, Italy

²CNISM, Unità di Pisa, Largo Pontecorvo 3, 56127 Pisa, Italy

³Institut für theoretische Physik, Universität Heidelberg, D-69120, Heidelberg, Germany

(Received 19 March 2009; published 26 August 2009)

We report time-resolved measurements of Landau-Zener tunneling of Bose-Einstein condensates in accelerated optical lattices, clearly resolving the steplike time dependence of the band populations. Using different experimental protocols we were able to measure the tunneling probability both in the adiabatic and in the diabatic bases of the system. We also experimentally determine the contribution of the momentum width of the Bose condensates to the temporal width of the tunneling steps and discuss the implications for measuring the jump time in the Landau-Zener problem.

DOI: 10.1103/PhysRevLett.103.090403

PACS numbers: 03.65.Xp, 03.75.Lm

Tunneling is one of the most striking manifestations of quantum behavior and has been the subject of intense research in both fundamental and applied physics [1]. While tunneling *probabilities* can be calculated accurately and have an intuitive interpretation as statistical mean values of experimental outcomes, the concept of tunneling *time* and its computation are still the subject of debate even for simple systems [2,3]. The time it takes a quantum system to complete a tunneling event (which in the case of cross-barrier tunneling can be viewed as the time spent in a classically forbidden area) has been widely investigated and measured recently for electrons ionized by attosecond radiation [4]. It is related to the time required for a state to evolve to an orthogonal state, and an observation, i.e., a quantum mechanical projection on a particular basis, is required to distinguish one state from another [3]. The measured time depends both on the type of observation (e.g., a temporal modulation of the potential in the classically forbidden region [5]) and on the quantum mechanical basis used, as derived in [6] for Landau-Zener (LZ) tunneling [7,8], in which a quantum system tunnels across an energy gap at an avoided crossing of the system’s energy levels. Similarly to the tunneling time in real space, the LZ tunneling time measures the duration of the quantum mechanical evolution (which plays an important role, e.g., in quantum control [9]). In a given quantum basis for the LZ Hamiltonian, Vitanov [6] defined the “jump time” required to evolve a state to an orthogonal one, following previous works [10,11]. The role of the different bases was also emphasized by Berry [12], who introduced a super-adiabatic basis with a universal time evolution.

In this Letter we directly measure the dynamics of LZ tunneling. The tunneling process is frozen at different times by performing a projective quantum measurement on the states of a given basis. The jump time is then derived from the survival probability in the initial state as function of time [6]. In our experiments, backed up by numerical

simulations, we use ultracold atoms forming a Bose-Einstein condensate (BEC) inside an optical lattice [13,14].

For cold atoms, LZ tunneling in optical lattices was used [15,16] for detecting deviations from an exponential decay law at short times. In contrast to these experiments, our BEC has an initial width in momentum space that is much smaller than $p_B = 2p_{\text{rec}} = 2\pi\hbar/d_L$, the width of the first Brillouin zone of a periodic potential with lattice constant d_L . This enables us to observe the full dynamics for single or multiple LZ crossings [17], the only limitation being the initial momentum width of the condensates and nonlinear effects. Our experiments are similar to recent studies of LZ transitions in a solid-state artificial atom [18], but the high level of control over the light-induced periodic potential also allowed us to measure the tunneling dynamics in different eigenbases (adiabatic and diabatic).

In our experiments we created BECs of 5×10^4 ^{87}Rb atoms inside an optical dipole trap (mean trap frequency around 80 Hz). A one-dimensional optical lattice created by two counterpropagating, linearly polarized Gaussian beams was then superposed on the BEC by ramping up the power in the lattice beams in 100 ms. The wavelength of the lattice beams was $\lambda = 842$ nm, leading to a sinusoidal potential with lattice constant $d_L = \lambda/2$. A small variable frequency offset between the two beams introduced through the acousto-optic modulators in the setup allowed us to accelerate the lattice in a controlled fashion.

The time-resolved measurement of LZ tunneling was done [see Fig. 1(a)] by first loading the BEC into the ground state energy band of an optical lattice of depth V_0 . The lattice was then accelerated with acceleration a_{LZ} for a time t_{LZ} to a final velocity $v = a_{\text{LZ}}t_{\text{LZ}}$, resulting in a force F_{LZ} on the atoms in the lattice rest frame [19]. During t_{LZ} the quasimomentum of the BEC swept the Brillouin zone, and at multiples of half the Bloch time $T_B = 2\pi\hbar(Ma_{\text{LZ}}d_L)^{-1}$ (where M is the atomic mass), i.e., at times $t = (n + 1/2)T_B$ ($n = 0, 1, 2, \dots$) when the sys-

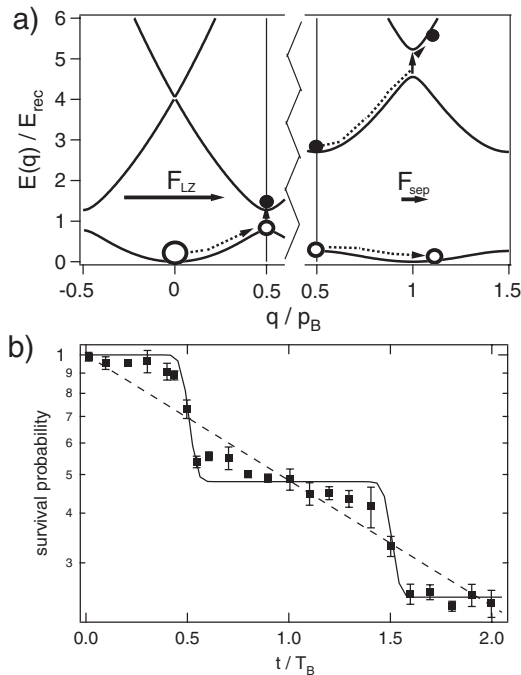


FIG. 1. Time-resolved measurement of LZ tunneling. (a) Experimental protocol [shown in the band-structure representation of energy $E(q)$ versus quasimomentum q]. Left: The lattice is accelerated, (partial) tunneling occurs. Right: The acceleration is then suddenly reduced and the lattice depth increased so as to freeze the instantaneous populations in the lowest two bands; finally, further acceleration is used to separate, and measure, these populations in momentum space. (b) Experimental results for $V_0 = 1E_{\text{rec}}$ and $F_0 = 0.383$ ($a_{\text{LZ}} = 13.52 \text{ ms}^{-2}$), giving $T_B = 0.826 \text{ ms}$. The solid and dashed lines are a numerical simulation of our experimental protocol and an exponential decay curve for our system's parameters, respectively.

tem was close to the Brillouin zone edge, tunneling to the upper band became increasingly likely. At $t = t_{\text{LZ}}$ the acceleration was abruptly reduced to $a_{\text{sep}} \ll a_{\text{LZ}}$ and the lattice depth was increased to V_{sep} in a time $t_{\text{ramp}} \ll T_B$. These values were chosen in such a way that at $t = t_{\text{LZ}}$ the probability for LZ tunneling from the lowest to the first excited energy band dropped from between ≈ 0.1 – 0.9 (depending on the initial parameters chosen) to less than ≈ 0.01 , while the tunneling probability from the first excited to the second excited band remained high at about 0.95 . This meant that at $t = t_{\text{LZ}}$ the tunneling process was effectively interrupted and for $t > t_{\text{LZ}}$ the measured survival probability $P(t) = N_0/N_{\text{tot}}$ (calculated from the number of atoms N_0 in the lowest band and the total number of atoms N_{tot}) reflected the instantaneous value $P(t = t_{\text{LZ}})$.

The lattice was then further accelerated for a time t_{sep} such that $a_{\text{sep}}t_{\text{sep}} \approx 2np_{\text{rec}}/M$ (typically $n = 2$ or 3). In this way, atoms in the lowest band were accelerated to a final velocity $v \approx 2np_{\text{rec}}/M$, while atoms that had tunneled to the first excited band before $t = t_{\text{LZ}}$ tunneled to

higher bands with a probability > 0.95 and were, therefore, no longer accelerated. At t_{sep} the lattice and dipole trap beams were suddenly switched off and the expanded atomic cloud was imaged after 23 ms . In these time-of-flight images the two velocity classes 0 and $2np_{\text{rec}}/M$ were well separated, from which N_0 and N_{tot} could be measured directly. Since the populations were “frozen” inside the energy bands of the lattice, which represent the adiabatic eigenstates of the system's Hamiltonian, this experiment effectively measured the time dependence of P_a in the adiabatic basis. A typical result is shown in Fig. 1(b). One clearly sees two “steps” at times $t = 0.5T_B$ and $t = 1.5T_B$, which correspond to the instants at which the atoms cross the Brillouin zone edges, where the lowest and first excited energy bands exhibit avoided crossings. For comparison, the result of a numerical simulation (integrating the linear Schrödinger equation for the experimental protocol) as well as an exponential decay as predicted by LZ theory are also shown.

The LZ tunneling probability can be calculated by considering a two-level system with the adiabatic Hamiltonian

$$H_a = H_d + V = \alpha t \sigma_z + \frac{\Delta E}{2} \sigma_x, \quad (1)$$

where σ_i are the Pauli matrices. The eigenstates of the diabatic Hamiltonian H_d , whose eigenenergies vary linearly in time, are mixed by the potential V characterized by the energy gap ΔE . Applying the Zener model [8] to our case of a BEC crossing the Brillouin zone edge leads to a band gap $\Delta E = V_0/2$ and to $\alpha = 2v_{\text{rec}}Ma_{\text{LZ}} = 2F_0E_{\text{rec}}^2/(\pi\hbar)$, with $E_{\text{rec}} = \hbar^2\pi^2/(2Md_L^2)$ the recoil energy and $F_0 = Ma_{\text{LZ}}d_L/E_{\text{rec}}$ the dimensionless force. The limiting value of the adiabatic and diabatic LZ survival probabilities (for t going from $-\infty$ to $+\infty$) in the eigenstates of H_a and H_d , respectively, is

$$P_a(t \rightarrow +\infty) = 1 - P_d(t \rightarrow +\infty) = 1 - P_{\text{LZ}}, \quad (2)$$

where the standard LZ tunneling probability is

$$P_{\text{LZ}} = e^{-\pi/\gamma} \quad (3)$$

with the adiabaticity parameter $\gamma = 4\hbar\alpha(\Delta E)^{-2}$ [20].

Figure 2(a) shows the first LZ tunneling step for different lattice depths V_0 , measured in units of E_{rec} at a given acceleration. The steps can be well fitted with a sigmoid function

$$P_a(t) = 1 - \frac{h}{1 + \exp[(t_0 - t)/\Delta t_{\text{LZ}}]}, \quad (4)$$

where t_0 is the position of the step (which can deviate slightly from the expected value of $0.5T_B$, e.g., due to a nonzero initial momentum of the condensate), h is the step height, and Δt_{LZ} represents the width of the step. Equations (2) and (3) correctly predict the height h of the step, as tested in the experiment for a variety of values of V_0 and F_0 [see Fig. 2(b)].

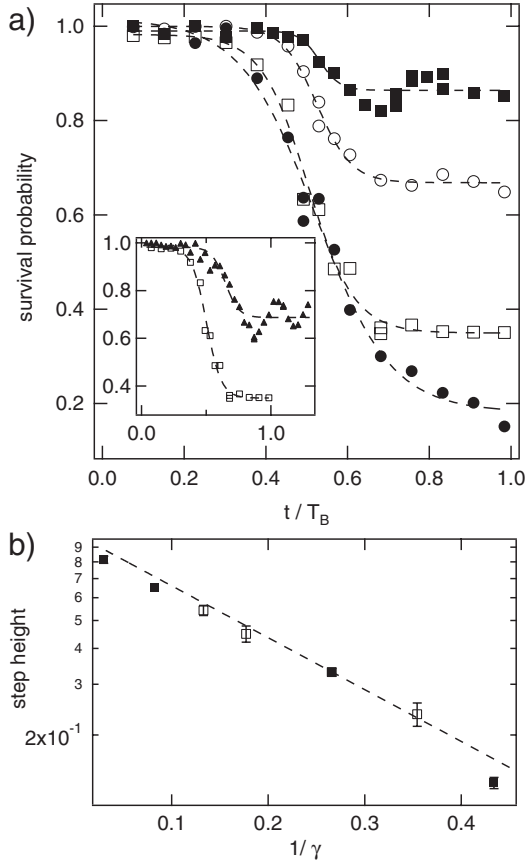


FIG. 2. (a) LZ survival probability in the adiabatic basis for a fixed force $F_0 = 1.197$ ($a_{LZ} = 42.25 \text{ ms}^{-2}$) and different lattice depths (filled squares: $V_0 = 2.3E_{\text{rec}}$; open circles: $V_0 = 1.8E_{\text{rec}}$; open squares: $V_0 = 1E_{\text{rec}}$; filled circles: $V_0 = 0.6E_{\text{rec}}$). The dashed lines are sigmoid fits to the experimental data. Inset: Survival probability in both the adiabatic (open squares) and diabatic (filled triangles) bases for $V_0 = 1E_{\text{rec}}$ and $F_0 = 1.197$. (b) Step height h as a function of the inverse adiabaticity parameter $1/\gamma$ for varying lattice depth and $F_0 = 1.197$ (open symbols), and for varying force with fixed $V_0 = 1.8E_{\text{rec}}$ (filled symbols). The dashed line is the prediction of Eq. (3) for the LZ tunneling probability.

While the experimental protocol described above measures the LZ tunneling probability in the *adiabatic basis*, it is possible to make analogous measurements in the *diabatic basis* of the unperturbed free-particle wave functions (plane waves with a quadratic energy-momentum dispersion relation) by abruptly switching off the lattice and the dipole trap after the first acceleration step (with the BEC initially prepared in the adiabatic basis, which, far away from the band gap, is almost equal to the diabatic basis). In this case, after a time-of-flight the number of atoms in the $v = 0$ and $v = 2p_{\text{rec}}/M$ velocity classes are measured and from these the survival probability in the $v = 0$ velocity class is calculated. The inset of Fig. 2(a) (filled triangles) shows such a measurement. Again, a step around $t = 0.5T_B$ is clearly seen, as well as strong oscillations for $t >$

$0.5T_B$. While weaker oscillations are also seen in the adiabatic basis [see Fig. 2(a) with $V_0 = 2.3E_{\text{rec}}$], they are much stronger and visible for a wider range of parameters in the diabatic basis [6]. These oscillations, also known as the Stokes phenomenon, are due to the discrepancy between the diabatic basis in which we measure the tunneling event and the ideal superadiabatic basis in which they are absent and the tunneling time is minimized [12]. They were also predicted for LZ tunneling in atomic Rydberg states [21] and experimentally observed in a wave-optical two-level system [22].

The widths Δt_{LZ} of the steps shown in Fig. 2(a) reflect the “jump time” for LZ tunneling $\Delta t_{LZ} = \Delta v_{LZ}/a_{LZ}$ during which the probability of finding the atoms in the lowest energy band goes from $P_a(t=0) = 1$ to its asymptotic LZ value $1 - P_{LZ}$. Vitanov [6] defines the jump time in the adiabatic basis as

$$\tau_a^{\text{jump}} = \frac{P_a(t = +\infty)}{P'_a(t = t_0)}, \quad (5)$$

where $P'_a(t = t_0)$ denotes the time derivative of the tunneling probability $P_a(t)$ evaluated at the crossing point of H_a . A sigmoidal function for $P_a(t)$ leads to $\tau_a^{\text{jump}} = 4\Delta t_{LZ}$. For large values of γ , which is the regime of our experiments, the theoretical jump time is given by

$$\tau_a^{\text{jump}} \approx T_B \frac{\Delta E}{4E_{\text{rec}}}. \quad (6)$$

This time, which coincides with the LZ traversal time of [10], is taken by the force to transfer the barrier energy to the system. It increases with ΔE and decreases with F_0 .

From our sigmoidal fits we retrieve $\tau_a^{\text{jump}}/T_B \approx 0.15\text{--}0.35$ (corresponding to absolute jump times between 50 and 200 μs), whereas the theoretical values for our experimental parameters are in the region of 0.1–0.15. This discrepancy is due to the fact that in our experiment the condensate does not occupy one single quasimomentum but is represented by a momentum distribution of width $\Delta p/p_B \gtrsim 0.1$ due to the finite number of lattice sites (around 50) it occupies and the effects of atom-atom interactions.

In order to test the dependence of Δt_{LZ} on Δp we created initial distributions of different widths using a dynamical instability [23]. The condensate was loaded into a lattice moving at a finite velocity corresponding to quasimomentum $q = -0.3p_B$ and held there for up to 3 ms. During this time the dynamical instability associated with the negative effective mass at that q led to an increase in Δp . After this preparatory stage, the LZ dynamics was measured as described above and Δt_{LZ} was extracted [see Fig. 3(a)]. As expected, Δt_{LZ} increases with Δp [Fig. 3(b)]. This was confirmed by a numerical integration of the Schrödinger equation in which Δp was varied by changing the initial trap frequency. The simulation also showed that

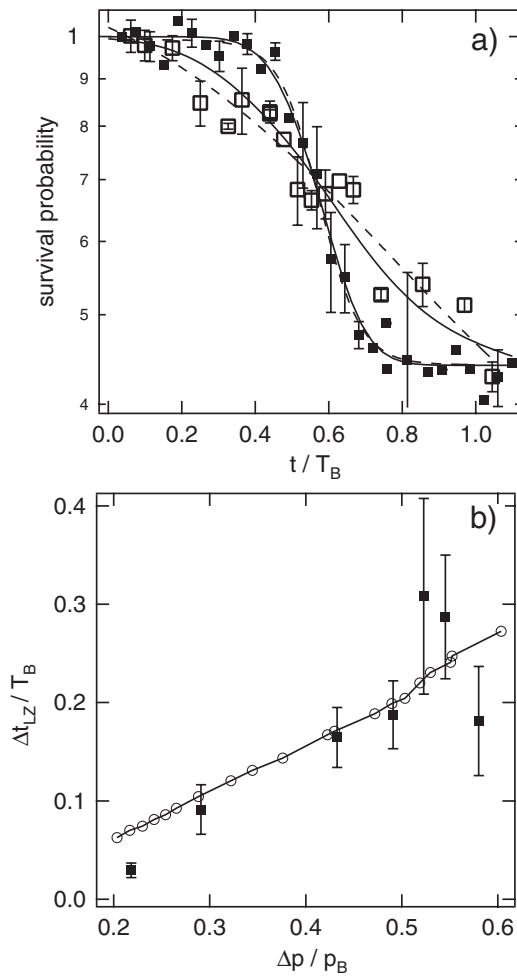


FIG. 3. LZ transition for different momentum widths of the condensate. (a) Survival probability for $\Delta p/p_B = 0.2$ (filled squares) and $\Delta p/p_B = 0.6$ (open squares). The solid and dashed lines are the results of a numerical simulation and of a sigmoid fit, respectively. (b) Step width Δt_{LZ} as a function of Δp . The open symbols (connected by a solid line for clarity) are the results of a numerical simulation.

for $\Delta p \rightarrow 0$, Δt_{LZ} remains finite and in that limit directly reflects the jump time given by Eq. (6).

In summary, we have measured the LZ dynamics of matter waves in an accelerated optical lattice in the adiabatic and diabatic bases. In both bases the steplike behavior as well as oscillations of the survival probability were clearly seen and agree with theoretical predictions. In future investigations one could reduce the initial momentum width, which currently limits the resolution of our experiment, by using, e.g., appropriate trap geometries or by controlling the nonlinearity through Feshbach resonances. This would enable a comparison with theoretical results related to the minimum time for a single LZ crossing limited by fundamental quantum (or wave, see [22]) mechanical properties [24]. Also, clearer observations of the short-time oscillations as seen in Fig. 2(a) should be

possible in this way. Our method can also be used to study multiple LZ crossings, e.g., in order to observe Stückelberg oscillations.

We gratefully acknowledge funding by the EU project “NAMEQUAM,” the CNISM “Progetto Innesco 2007,” and the Excellence Initiative by the German Research Foundation (DFG) through the Heidelberg Graduate School of Fundamental Physics (Grant No. GSC 129/1) and the Global Networks Mobility Measures. We thank M. Holthaus and T. Esslinger for discussions and comments on the manuscript.

- [1] M. Razavy, *Quantum Theory of Tunneling* (World Scientific, Singapore, 2003).
- [2] E. H. Hauge and J. A. Støvneng, *Rev. Mod. Phys.* **61**, 917 (1989); R. Landauer and Th. Martin, *ibid.* **66**, 217 (1994).
- [3] L. S. Schulman, *Lect. Notes Phys.* **734**, 107 (2007).
- [4] P. Eckle *et al.*, *Science* **322**, 1525 (2008).
- [5] M. Büttiker and R. Landauer, *Phys. Rev. Lett.* **49**, 1739 (1982).
- [6] N. V. Vitanov, *Phys. Rev. A* **59**, 988 (1999).
- [7] L. D. Landau, *Phys. Z. Sowjetunion* **2**, 46 (1932).
- [8] C. Zener, *Proc. R. Soc. A* **137**, 696 (1932).
- [9] J. M. Raimond, M. Brune, and S. Haroche, *Rev. Mod. Phys.* **73**, 565 (2001).
- [10] M. Büttiker and R. Landauer, *Adv. Solid State Phys.* **25**, 711 (1985); *IBM J. Res. Dev.* **30**, 451 (1986).
- [11] K. Mullen, E. Ben-Jacob, Y. Gefen, and Z. Schuss, *Phys. Rev. Lett.* **62**, 2543 (1989).
- [12] M. V. Berry, *Proc. R. Soc. A* **429**, 61 (1990); R. Lim and M. V. Berry, *J. Phys. A* **24**, 3255 (1991).
- [13] B. P. Anderson and M. A. Kasevich, *Science* **27**, 282 (1998).
- [14] O. Morsch, J. H. Müller, M. Cristiani, D. Ciampini, and E. Arimondo, *Phys. Rev. Lett.* **87**, 140402 (2001).
- [15] S. R. Wilkinson *et al.*, *Nature (London)* **387**, 575 (1997).
- [16] M. C. Fischer, B. Gutierrez-Medina, and M. G. Raizen, *Phys. Rev. Lett.* **87**, 040402 (2001).
- [17] S. Wimberger *et al.* [*Phys. Rev. A* **72**, 063610 (2005)] studied the influence of BEC atomic interactions on the nonexponential decay in LZ sequences.
- [18] D. M. Berns *et al.*, *Nature (London)* **455**, 51 (2008).
- [19] In all the experiments the dipole trap held the BEC against gravity during the lattice acceleration. As the dipole trap frequency in the lattice direction is only a few Hz, the assumption of translational symmetry is not significantly violated.
- [20] M. Holthaus [*J. Opt. B* **2**, 589 (2000)] derived a more refined Zener model for ultracold atoms in an optical lattice.
- [21] J. R. Rubbmark, M. M. Kash, M. G. Littman, and D. Kleppner, *Phys. Rev. A* **23**, 3107 (1981).
- [22] D. Bouwmeester *et al.*, *Phys. Rev. A* **51**, 646 (1995).
- [23] M. Cristiani *et al.*, *Opt. Express* **12**, 4 (2004).
- [24] M. Sillanpää, T. Lehtinen, A. Paila, Y. Makhlin, and P. Hakonen, *Phys. Rev. Lett.* **96**, 187002 (2006); T. Caneva *et al.*, arXiv:0902.4193.

Dynamical enhancement of spatial entanglement in massive particles

Michael Lubasch,¹ Florian Mintert,² and Sandro Wimberger³

¹Max-Planck-Institut für Quantenoptik, Hans-Kopfermann-Straße 1, 85748 Garching, Germany

²Albert-Ludwigs-Universität Freiburg, Freiburg Institute for Advanced Studies,

Albertstraße 19, Physikalisches Institut, Hermann-Herder-Straße 3, 79104 Freiburg, Germany

³Institut für Theoretische Physik, Universität Heidelberg, Philosophenweg 19, 69120 Heidelberg, Germany

(Dated: February 26, 2013)

We discuss dynamical enhancement of entanglement in a driven Bose-Hubbard model and find an enhancement of two orders of magnitude which is robust against fluctuations in experimental parameters.

Quantum coherence is often thought to be found only in very small systems or under artificial lab-conditions, since otherwise unavoidable environment coupling results in rapid loss of coherence. Whereas this holds quite generally, it holds in particular for many-body coherence, synonymous for entanglement. As recent experimental [1] and theoretical [2] evidence suggests, however, exceptions to this general rule exist. In particular coherent driving can compensate for the environment-induced loss of coherence and, thereby stabilize entanglement under conditions under which a static system would be completely separable [3, 4].

Such dynamically induced entanglement does not only hold the potential to influence macroscopically observable properties [5], but certainly also opens up new paths towards scalable quantum information processing which otherwise is limited through the unfavourably scaling dephasing times with the system size [6, 7]. However, our current understanding of dynamical enhancement of entanglement is still in its infancy.

In this Letter, we investigate the dynamical enhancement of entanglement between ultracold bosonic atoms stored in an optical lattice that gives rise to a spatially periodic potential created by two counterpropagating laser beams of wavelength λ and amplitude V_0 in one direction. A tight perpendicular confinement of strength V_\perp in the other two directions restricts the motion of the atoms to one dimension. In the deep lattice limit $V_0 \gg E_R$, where $E_R = \hbar^2 k^2 / 2m$ (with $k = 2\pi/\lambda$) is the recoil energy, and at sufficiently low temperatures, this system can be well described [8] in terms of the Bose-Hubbard Hamiltonian

$$\hat{H} = -J \sum_{l=1}^{L-1} (\hat{a}_l^\dagger \hat{a}_{l+1} + \hat{a}_{l+1}^\dagger \hat{a}_l) + \frac{U}{2} \sum_{l=1}^L \hat{n}_l (\hat{n}_l - 1) \quad (1)$$

where the creation operator \hat{a}_l^\dagger creates and the annihilation operator \hat{a}_l annihilates a boson at lattice site l . The tunneling parameter J and the on-site interaction U depend on the lattice parameters approximately [9] via

$$J/E_R = \frac{4}{\sqrt{\pi}} (V_0/E_R)^{\frac{3}{4}} e^{-2\sqrt{V_0/E_R}}, \quad \text{and} \quad (2)$$

$$U/E_R = \sqrt{\frac{8}{\pi}} k a_s (V_0 V_\perp^2 / E_R^3)^{\frac{1}{4}} \quad . \quad (3)$$

Whereas the lattice depth V_0 is typically time-independent, we will compare here the dynamics of such an autonomous system with its driven version [10], where V_0 is modulated temporally

$$V_0(t) = V \left(1 + dV \sin(\omega t) \right) . \quad (4)$$

As we will show, the temporal modulation of the tunneling parameter J and the on-site interaction U that results from this lattice depth modulation drives the atoms into a spatially strongly correlated, *i.e.* entangled state. For the verification of the entanglement properties, we envision a rapid separation of the few-body system into two parts, what can be realized by ramping up a potential barrier as depicted in Fig. 1.

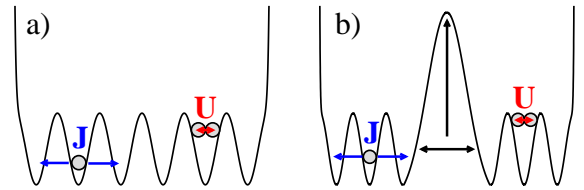


FIG. 1: (color online) a) The system is prepared in an entangled state. b) The system is split into two halves by raising the intermediate barrier. J is the kinetic term and U the on-site interaction in the Bose-Hubbard model (1).

This spatial separation effectively switches off the interaction between the two subsystems what freezes the entanglement dynamics. However, it also entails that each subsystem will typically *not* have a well-defined particle number. Whereas correlations in the particle number formally may imply entanglement, its experimental verification will be technically impossible because this would require the measurement of coherent superpositions of states with different numbers of massive particles [11]. Therefore, we will postselect [12] states with well-defined local particle number. We will focus in particular on those cases in which particles are split evenly between the two subsystems, since this is the case that occurs with highest probability, and this is also the case in which the highest entanglement can be achieved. Doing so, we obtain a clean notion of entanglement between

the two separated halves of the optical lattice where each half is filled with a fixed number of particles and can be addressed individually.

In the following we quantify the entanglement of the postselected states with the entropy of entanglement [6, 13] in the case of pure states and the negativity [14] in the case of mixed states. The entropy of entanglement is given by the von Neumann entropy of the reduced density matrix ϱ_r that is obtained through the partial trace over one subsystem of the entire many-body state, *i.e.* $E(\Psi) = -\text{Tr}\varrho_r \log_2 \varrho_r$. The negativity $N(\rho) = (\|\rho^{PT}\| - 1)/2$ of a mixed state ρ is defined in terms of the trace norm of the partially transposed density matrix ρ^{PT} .

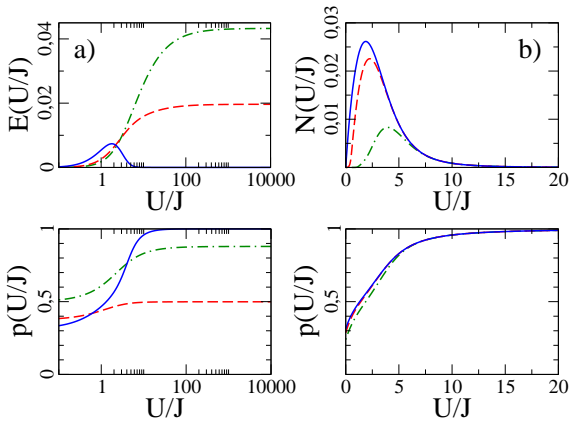


FIG. 2: (color online) a) Entropy of entanglement E and probability for successful postselection of evenly distributed number of bosons between the right and the left part of a $L = 6$ well Bose-Hubbard system. The overall particle number is $N = 6$ (solid blue), $N = 3$ (dashed red) and $N = 2$ (dash-dotted green). b) Negativity for the thermal state at temperature $T = 0$ nK (solid blue), $T = 40$ nK (dashed red) and $T = 80$ nK (dash-dotted green) for $N = 6$ particles.

Fig. 2a) depicts the ground state entanglement properties for the exemplary case of $L = 6$ wells filled with $N = 6, 3$ and 2 bosons, respectively. In all these cases the system features extremely low entanglement, which is also observed for different system sizes and particle numbers. The qualitative dependence of E on the parameter U/J is as expected: If the tunneling dominates the system dynamics, *i.e.* if $U/J \simeq 0$, the bosons populate the same single-particle states such that after postselection of local particle number the system is separable. For finite interaction U the bosons repel each other and establish correlations; therefore, E typically increases with U/J . There are, however, exceptions, like the case of unit filling (depicted in blue), where a separable, perfect Mott insulator [8, 9] develops for $U/J \rightarrow \infty$. This is also reflected in the fact that in this limit the bosons will always be separated in a balanced fashion between the left and right half of the system, whereas typically the probability

for this is smaller than unity.

Fig. 2 shows data for rather small fillings, but also the entanglement properties of the ground state for larger filling $N/L > 1$ can be inferred from this data since systems with $N + mL$ bosons (with integer m) behave qualitatively similar as the system with N bosons. That is, the maximal amount of entanglement in the ground state does typically not exceed the value of $E \approx 0.05$.

Assuming perfect ground state cooling is certainly a theoretical idealization, but also thermal excitation cannot enhance the entanglement as shown in Fig. 2b), where the negativity of the thermal state $\rho_{th} = \exp(-\hat{H}/k_B T)/Z$ is shown. The probability to find the bosons split evenly into left and right half decreases with increasing temperature, and the entanglement is even lower than for $T = 0$.

As we will see in the following, this is strongly contrasted by the behavior of the driven system. To be specific, we consider the experimental parameters: $V = 10 E_R$ and $V_{\perp} = 30 E_R$ as lattice depths, $dV = 0.2$ as lattice depth modulation, $\lambda = 842$ nm as the wave length of the laser, $a_s = 5.45$ nm as the scattering length and $m = 86.909 u$ as the mass of rubidium-87 [15]. As driving frequency, we chose $\omega = U/\hbar = 12862$ Hz, what corresponds to resonant driving in the Mott-insulating regime.

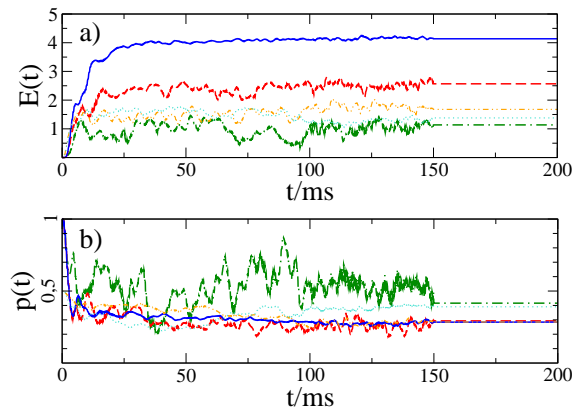


FIG. 3: (color online) Entropy of entanglement E and probability of successful postselection for the driven Bose-Hubbard Hamiltonian (4) with $L = 8 = N$ (solid blue), $L = 6 = N$ (dashed red), $L = 4 = N$ (dash-dotted green), $L = 6$ and $N = 5$ (thin dash-double-dotted orange), and $L = 6$ and $N = 7$ (thin dotted turquoise). At $t = 100$ ms the driving is stopped and at $t = 150$ ms the lattice depth is increased in order to freeze the entanglement dynamics.

Fig. 3 shows the dynamical enhancement of entanglement caused by the driving. We start with the ground state of the static system. After 100 ms the driving is switched off and after $t = 150$ ms the lattice depth is increased to $V_0 = 30 E_R$ in order to freeze the entanglement dynamics completely. Apparently, entanglement grows rather quickly once the driving is switched on. After

about 10 to 20 ms the increase slows down a bit, until entanglement saturates after $t \approx 50$ ms. From that time on, entanglement fluctuates around an average value due to the finite interactions in the system. Fig. 3 shows how these remaining fluctuations smooth out with growing system size. Whereas the saturation time turns out to depend crucially on the lattice depth modulation dV , the final values of entanglement seem not to. Thus, a larger modulation of the lattice depth can accelerate the entanglement generation; however, even very weak driving can yield the same enhancement of entanglement as strong driving.

Once entanglement is saturated, it can be preserved with the help of a potential barrier that separates the two entangled atomic ensembles as depicted in Fig. 1 and effectively switches off their mutual interaction. The small fluctuations around the average entanglement that persist for $t > 100$ ms can be stopped with an increase of the lattice depth, here at $t = 150$ ms.

As it can be seen in Fig. 3a) the attainable entanglement grows with increasing system size. This is as expected since larger systems can carry more entanglement. A concern, however, is that with increasing number of atoms, also the number of possible distributions of atoms between the two subsystems is growing, so that the probability to find an even distribution might decrease. This decrease is apparent in Fig. 3b), where the probability of an even distribution drops from $p = 0.33$ for 4 atoms to $p = 0.27$ for 5, 7 and 8 atoms. It also becomes apparent, however, that this decrease occurs in small systems, and that these probabilities become largely independent of the particle number for large N . Thus, one should expect to find evenly distributed particle numbers with substantial probability also in an experiment with significantly more bosons than a numerical simulation can handle.

In an experiment, certainly also the timing will be crucial. As Fig. 3 shows, the system evolves rapidly, and fluctuations in the durations of driving or ramping up the barrier that are comparable to system time scales will result in the generation of a mixed state which typically has reduced entanglement. The relevant time scale can be obtained from the fidelity $f(t, \Delta t) = |\langle \psi(t) | \psi(t + \Delta t) \rangle|^2$, where $|\psi(t)\rangle$ is the postselected system state after driving of duration t . The fidelity f is depicted in Fig. 4 for the exemplary case of $N = 6$ particles in a $L = 6$ site lattice. The width of the central peak (full width at half maximum) that determines the minimal required experimental precision reads in this case $\Delta t_m = 0.1$ ms. In a similar fashion, we can also estimate the required precision for all other experimental parameters, such as the potential V ($\Delta V_m = 0.08 E_R$), the perpendicular confinement V_\perp ($\Delta V_{\perp,m} = 0.12 E_R$), the amplitude of the driving dV ($\Delta dV_m = 0.016$) and the driving frequency ω ($\Delta \omega_m = 14.5$ Hz).

To estimate the impact of fluctuations of these parameters on the attainable entanglement, we have to con-

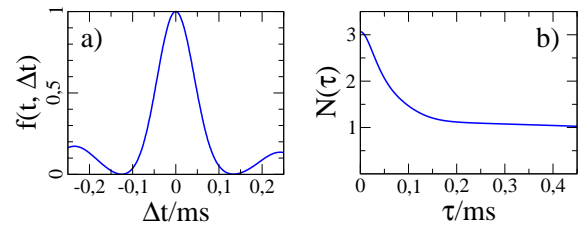


FIG. 4: a) Fidelity $f(t, \Delta t)$ at $t = 100$ ms for state preparation with imperfect timing. b) Negativity N of the mixed state (5) resulting from the measurement of the driven Bose-Hubbard Hamiltonian with $L = 6 = N$ at $t_0 = 100$ ms.

sider the mixed state that is obtained with many repetitions of the experiment with the fluctuating parameter taking different values at each repetition. To be specific, we focus on the inaccuracy in the duration of driving, and we assume that these durations are distributed according to a Gaussian centered around $t_0 = 100$ ms with a standard deviation τ . This gives rise to the mixed state

$$\rho(\tau) = \frac{1}{\tau\sqrt{2\pi}} \int_{-\infty}^{\infty} dt e^{-\frac{(t-t_0)^2}{2\tau^2}} |\psi(t)\rangle \langle \psi(t)|. \quad (5)$$

The negativity of this mixed state is depicted in Fig. 4b) as function of the inaccuracy τ of the duration of driving. For $\tau = 0$ ms, the situation reduces to the case of pure state entanglement as discussed above; but for finite τ entanglement is reduced significantly what is a very generic feature of mixed states. Besides this expected behavior, there are two features that should be stressed:

First, at $\tau = 0$ ms the first derivative of $N(\tau)$ vanishes, so that entanglement turns out to be insensitive to small timing errors. The second-order Taylor expansion reads $N(\tau) \approx 3.064 - 900(\tau/\text{ms})^2$. That is, timing errors below 0.01 ms imply a change in negativity of less than 3%.

Second, even in the presence of significantly larger timing errors there is still rather strong entanglement with $N(\tau) \simeq 1$, *i.e.* a value attained for a maximally entangled Bell pair!

In particular, this astonishing robustness against experimental fluctuations underpins that potential that driving offers as means to create entanglement as compared to engineered interactions.

As recent investigations on driven spin-systems suggest [4], the feature of dynamical enhancement of entanglement is not particular for the Bose-Hubbard system, but a rather generic feature, that is largely independent of detailed system properties. An advantage of the present bosonic system as compared to many spin-systems is that particle numbers can easily be varied in an experiment, what provides the means to study the generation of entanglement in the entire regime from rather small systems

through the mesoscopic domain, up to the semi-classical regime. In particular, observing the rise and decay of entanglement with increasing particle number will provide us with valuable insight in the emergence of classical behavior in large quantum systems.

M.L. thanks J. Eisert, M. B. Plenio and N. Schuch for very useful comments. S.W. acknowledges support by EMMI, DFG FOR760, and the Excellence Initiative through the Global Networks Mobility Measures, the Frontier Innovation Fonds and the HGSFP (DFG grant GSC 129/1). F.M. acknowledges financial support by DFG (MI 1245-1).

-
- [1] J. Estève *et al.*, Nature (London) **455**, 1216 (2008); M. F. Riedel *et al.*, Nature (London) **464**, 1170 (2010).
- [2] G. K. Brennen *et al.*, Phys. Rev. Lett. **82**, 1060 (1999); D. Jaksch *et al.*, Phys. Rev. Lett. **82**, 1975 (1999); T. Calarco *et al.*, Phys. Rev. A **61**, 022304 (2000); R. Ionicioiu and P. Zanardi, Phys. Rev. A **66**, 050301(R) (2002); J. Eisert *et al.*, Phys. Rev. Lett. **93**, 190402 (2004); S. Bose, arXiv:cond-mat/0610024.
- [3] C. E. Creffield, Phys. Rev. Lett. **99**, 110501 (2007); F. Galve, L. A. Pachón and D. Zueco, arXiv:1002.1923; J. Cai, G. G. Guerreschi and H. J. Briegel, Phys. Rev. Lett. **104**, 220502 (2010); J. Cai, S. Popescu and H. J. Briegel, Phys. Rev. E **82**, 021921 (2010).
- [4] F. Galve *et al.*, Phys. Rev. A **79**, 032332 (2009); J. Li and G. S. Paraoanu, New Jour. Phys. **11**, 113020 (2009).
- [5] S. Ghosh *et al.*, Nature (London) **425**, 48 (2003).
- [6] M. A. Nielsen and I. L. Chuang, *Quantum Computation and Quantum Information* (Cambridge Univ. Press, 2007).
- [7] H. Häffner, C. F. Roos and R. Blatt, Phys. Rep. **469**, 155 (2008).
- [8] M. P. A. Fisher *et al.*, Phys. Rev. B **40**, 546 (1989); D. Jaksch *et al.*, Phys. Rev. Lett. **81**, 3108 (1998); M. Greiner *et al.*, Nature (London) **415**, 39 (2002).
- [9] W. Zwerger, Jour. Opt. B **5**, S9 (2003); I. Bloch, J. Dalibard and W. Zwerger, Rev. Mod. Phys. **80**, 885 (2008).
- [10] T. Stöferle *et al.*, Phys. Rev. Lett. **92**, 130403 (2004).
- [11] H. M. Wiseman and J. A. Vaccaro, Phys. Rev. Lett. **91**, 097902 (2003); N. Schuch, F. Verstraete and J. I. Cirac, Phys. Rev. A **70**, 042310 (2004); M. R. Dowling, A. C. Doherty and H. M. Wiseman, Phys. Rev. A **73**, 052323 (2006).
- [12] Z. Y. Ou and L. Mandel, Phys. Rev. Lett. **61**, 50 (1988); Y. H. Shih and C. O. Alley, Phys. Rev. Lett. **61**, 2921 (1988); J. G. Rarity and P. R. Tapster, Phys. Rev. Lett. **64**, 2495 (1990); P. G. Kwiat *et al.*, Phys. Rev. Lett. **75**, 4337 (1995).
- [13] C. H. Bennett *et al.*, Phys. Rev. A **53**, 2046 (1996).
- [14] G. Vidal and R. F. Werner, Phys. Rev. A **65**, 032314 (2002).
- [15] C. Kollath *et al.*, Phys. Rev. Lett. **97**, 050402 (2006); A. Zenesini *et al.*, Phys. Rev. Lett. **102**, 100403 (2009); A. Zenesini *et al.*, Phys. Rev. Lett. **103**, 090403 (2009).

Engineering interband transport by time-dependent disorder

Ghazal Tayebirad,¹ Riccardo Mannella,² and Sandro Wimberger^{1,3}

¹*Institut für Theoretische Physik, Universität Heidelberg, Philosophenweg 19, 69120 Heidelberg, Germany*

²*Dipartimento di Fisica ‘E. Fermi’, Università di Pisa, Largo Pontecorvo 3, 56127 Pisa, Italy*

³*Heidelberg Center for Quantum Dynamics, Philosophenweg 12, 69120 Heidelberg, Germany*

(Dated: October 1, 2012)

We show how the evolution of atoms in a tilted lattice can be changed and controlled by phase noise on the lattice. Dependent on the characteristic parameters of the noise, the interband transport can either be suppressed or enhanced, which is of interest for high precision control in experimental realization with Bose-Einstein condensates. The effect of the noise on the interband coupling is summarized in a scaling plot stressing the universality of our results.

PACS numbers: 03.75.Lm, 37.10.Jk, 05.40.-a, 02.50.Ey

Ultracold atoms in optical lattices have opened a possibility to investigate effects which were not previously observable on ordinary matter crystals, at least not in such a controlled way, like Bloch oscillations, Wannier-Stark ladders, and Landau-Zener tunneling [1–7]. Loading Bose-Einstein condensates (BEC) into optical lattices provides an optimal control on different system parameters by optical means. More complicated potentials can be realized by adding further lattice beams [8, 9]. In fact, by superimposing laser beams from different directions and with different frequencies, it is possible to generate various lattice geometries [3, 9–11]. The question arises how to control the dynamics of particles by quasi-periodic potentials (possibly time-dependent or even stochastic ones). From the theoretical point of view, a variety of phenomena is expected to occur in these systems, such as Anderson localization [10, 12] and the quantum transition to the Bose glass phase originating from the interplay of interaction and spatial, but static disorder [11, 13].

In this Letter, we investigate the Landau-Zener tunneling of a BEC from the ground band of a lattice into higher bands and, finally, into the energetic continuum. We show that control on the interband coupling is not only achieved by varying the lattice parameters or the initial conditions [4, 6, 14], but also by additional noise which produces a time-dependent disordered potential. More specifically, we study the time evolution of the survival probability of a BEC loaded into a quasi-1D geometry built of a stochastic potential and a static Stark force. Our predictions demonstrate that stochastic noise can be used to engineer the interband transport without changing system intrinsic parameters.

We focus on the dynamics of a sufficiently dilute non-interacting BEC. In the absence of atom-atom interactions, the temporal evolution of a BEC in a tilted one-dimensional lattice is described by the single-particle Hamiltonian

$$H = -\frac{\hbar^2}{2M} \frac{d^2}{dx^2} + V_s(x, t) + Fx, \quad (1)$$

where M is the atomic mass and F the Stark force. $V_s(x, t)$ is a stochastic potential given by the following

time-dependent bichromatic lattice

$$V_s(x, t) = \alpha V \left\{ \sin^2 \left(\frac{\pi x}{d_L} \right) + \sin^2 \left(\frac{\pi x}{d'_L} + \phi(t) \right) \right\}. \quad (2)$$

It consists of two spatially periodic potentials with incommensurate spacings, d_L for the “reference” lattice and $d'_L = d_L(\sqrt{5} - 1)/2$ for the secondary lattice. The time-dependence of the second lattice arises because of the time-dependent stochastic phase $\phi(t)$. For constant ϕ , this is the system with a quasi-disordered lattice which was realized and described by Roati *et al.* [10]. The depths of the two lattices are considered to be comparable and for convenience equal amplitudes αV are chosen, where V is the lattice depth of the reference lattice and α is a renormalization factor (which will be defined below). The recoil energy $E_{\text{rec}} = p_{\text{rec}}^2/2M$, with $p_{\text{rec}} = \pi\hbar/d_L^2$, is the characteristic energy scale of the optical reference lattice [3], and $V_0 = V/E_{\text{rec}}$ and $F_0 = Fd_L/E_{\text{rec}}$ are dimensionless quantities in this energy unit. We assume a typical experimental situation [3, 4, 6], for which the initial state is a condensate’s wave function relaxed in a harmonic trap and then loaded adiabatically into the lattice given by $V_s(x, t = 0)$. The trap is shallow such that many lattice sites are initially populated by the condensate. It is turned off for the further time evolution.

For the original Wannier-Stark problem including just the first term on the r.h.s. of Eq. (2), the wave packet prepared in the ground band oscillates periodically in time with the Bloch period $T_B = 2\pi\hbar/(F_0 E_{\text{rec}})$ and frequency $\omega_B = 2\pi/T_B$ [15, 16]. However, for sufficiently large F , the BEC undergoes Landau-Zener tunneling after each Bloch period at the band edge, where the band gap has its smallest value [3, 17]. Such a phenomenon gives rise to a step-like structure in the time-resolved survival probability $P_{\text{sur}}(t)$ of the atoms in the ground band [6]. Following [4, 6, 17], we calculate $P_{\text{sur}}(t)$ in momentum space by projecting onto the support of the initial state: $P_{\text{sur}}(t) = \int_{-p_c}^{\infty} dp_x |\psi(p_x, t)|^2$. The upper bound can be safely extended to infinity since the tunneled wave packet moves into the direction of negative momenta [17]. The lower bound is given by the parameter p_c , which can be adapted to stabilize the results with respect to temporal fluctuations. While the true decay starts after a

traversal of half the Brillouin zone (the Brillouin zone has a width of $2p_{\text{rec}}$), we choose either $p_c = 3p_{\text{rec}}$ or $p_c = 5p_{\text{rec}}$, which effectively means that we measure the decay with a delay of T_B or $2T_B$ respectively. As long as the mean momentum evolves linearly in time with a variance significantly smaller than the width of the Brillouin zone, we can resort to the acceleration theorem [1, 16] to relate both ways of measuring. In the following, we introduce the type of stochastic process we use to generate $\phi(t)$ and show universal properties of the survival probability as a function of rescaled parameters.

In general, colored noise can be defined by a suitable spectral distribution. The simplest type can be produced by a harmonic oscillator of angular frequency ω_0 and damping rate Γ , driven by Gaussian white noise. The result is harmonic noise [18], which is represented by a two dimensional Gauss-Markov process taking the form of the following stochastic differential equations for $\phi(t)$:

$$\dot{\phi} = \nu \quad (3a)$$

$$\dot{\nu} = -2\Gamma\nu - \omega_0^2\phi + \xi(t). \quad (3b)$$

$\xi(t)$ is Gaussian white noise with $\langle \xi(t) \rangle = 0$, $\langle \xi(t)\xi(s) \rangle = 4\Gamma T\delta(t-s)$, and T measures the strength of the noise. Γ and ω_0 have the units of T_B^{-1} and ω_B respectively. For notational reasons, we express both of them in the unit of T_B^{-1} . The variance of the noise is given by $\langle \phi^2(t) \rangle = T/\omega_0^2$, where $\langle \cdot \rangle$ is a time average over a sufficiently large interval (in our simulations $\approx 20T_B$). The spectral distribution for the harmonic noise is

$$S(\omega) = \frac{2\Gamma T}{\pi(4\Gamma^2\omega^2 + (\omega^2 - \omega_0^2)^2)}. \quad (4)$$

This distribution incorporates two important regimes: (i) slowly-varying noise when the oscillation frequency is much less than the damping rate, i.e., $2\Gamma^2 \gg \omega_0^2$, and (ii) fast noise, when $2\Gamma^2 \ll \omega_0^2$. The spectral distributions corresponding to these limits are shown in the insets of Fig. 1. In the regime (i), the noise recovers the exponentially correlated noise [18, 19] with a Lorentzian-like distribution peaked around zero frequency (see Fig. 1(a)). The spectral distribution in the regime of fast noise (see Fig. 1(b)) peaks at $\tilde{\omega}_0 = \sqrt{\omega_0^2 - 2\Gamma^2}$ with a finite width $\Delta\tilde{\omega}_0 \approx 2\sqrt{\Gamma\sqrt{\omega_0^2 - \Gamma^2}}$. To control the evolution in the potential of Eq. (2) the most relevant noise realization is this latter regime (ii), for which the above mentioned energy scales can be matched with the scales of the original Wannier-Stark system.

For very fast noise, the particle effectively averages over the time-dependent potential. Assuming a Gaussian distribution of the fast varying phase with variance $\langle \phi^2 \rangle$ and integrating over the phase as random variable, an effective potential is calculated as

$$V_{\text{eff}}(x) = \alpha V \left\{ \sin^2 \left(\pi \frac{x}{d_L} \right) + \beta \sin^2 \left(\pi \frac{x}{d_L} \right) \right\}, \quad (5)$$

where $\beta = \exp(-2\langle \phi^2 \rangle)$. The effect of fast noise is hence to renormalize the amplitude of the second lattice by a

factor β . The parameter α is introduced to be able to compare better the dynamics in the potential given by Eq. (2) with the dynamics in the reference system, in which just $V(x) = V \sin^2(\pi x/d_L)$ is present. For this, α is chosen such that the following spatial standard deviations are equal: $\sigma(V(x)) = \sigma(V_{\text{eff}}(x))$, cf. ref. [14].

We study the temporal behavior of the survival probability $P_{\text{sur}}(t)$ in a broad range of noise parameters. We use a reference system with typical experimental values of $V_0 = 2.5$ (giving an average band gap $\Delta E \approx 2.5 E_{\text{rec}}$) and $F_0 = 1.5$ [4, 6]. ω_0 and Γ , are chosen in the range of $0.01/T_B$ and $300/T_B$, which covers both regimes of fast and slow noise. The stochastic nature makes it necessary to average the results over a sufficient number of statistical realizations. For the parameters investigated here, 20 realizations for fixed noise parameters turned out to well stabilize statistical fluctuations. The lattice parameters V_0 and F_0 can be adapted to fulfill the condition of resonantly enhanced tunneling (RET) in the reference system, i.e., $F_0 \approx n\Delta E/E_{\text{rec}}$, with an integer n [4, 15, 17], or away from this special condition (non-RET). Since at RET the transport from the ground band to higher bands is already enhanced by energetic quasi degeneracies [15], and the noise is likely to drive the system out of RET conditions, the decay probability is expected to degrade for typical parameters in this case [14]. For our non-RET conditions $V_0 = 2.5$ and $F_0 = 1.5$, it is shown in the following that a faster decay can be easily induced by harmonic noise, since there is no competition between the two effects (enhancement by RET and noise).

The stochastic potential $V_s(x, t)$ is determined by the spectral distributions $S(\omega)$ of the noise, which are depicted in the insets of Fig. 1(a) and (b) for the two different regimes of noise, respectively. For a small oscillation frequency $\omega_0 = 0.1/T_B$ compared with the damping rate $\Gamma = 5/T_B$, $S(\omega)$ has a very narrow peak at zero frequency. The phase itself is slowly varying with time in case (a), whilst it shows much faster fluctuations in case (b). The effect of the noise on the temporal evolution of $P_{\text{sur}}(t)$ is compared in Figs. 1(a) and (b) to the one for the noise-free reference system with its characteristic step-like structure (solid lines) [6, 17]. As seen, the harmonic noise tends to wash out the step structure after a few Bloch oscillations. Moreover, it leads to a systematic enhancement of the tunneling rate for the largest noise amplitude T in both cases (a,b). In the regime of fast noise (Fig. 1(b)) the tunneling rate is always enhanced with respect to the reference system, and here it is essentially independent of T (see also Fig. 3 below).

We find that, for a broad range of noise parameters, our main observable, the survival probability $P_{\text{sur}}(t_0)$ at fixed time t_0 , obeys a scaling relation as a function of *all* parameters. Our results are similar for various choices of $t_0 \gtrsim 4T_B$, and we stick in the following to $t_0 \approx 6T_B$, a typical experimental observation time reported, e.g., in [3]. In Fig. 2, the noise frequency ω_0 is varied by keeping the variance of the noise fixed. Rescaling now ω_0 by $2\omega_B$ and by the standard deviation of the noise $\sqrt{\langle \phi^2 \rangle}$,

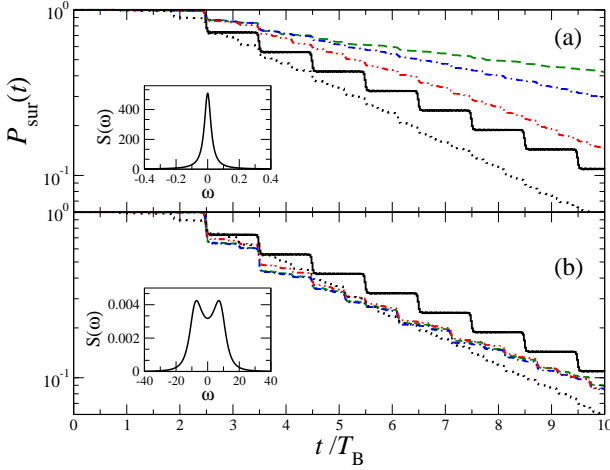


FIG. 1: (color online) $P_{\text{sur}}(t)$ $V_0 = 2.5$, $F_0 = 1.5$ in the presence of harmonic noise with $\Gamma = 5/T_B$, and $\omega_0 = 0.1/T_B$ (a) or $\omega_0 = 10/T_B$ (b) and for $T = 0.01/T_B^2$ (green dashed lines), $T = 1/T_B^2$ (blue dot-dashed lines), $T = 10/T_B^2$ (red dot-dot-dashed lines), and $T = 100/T_B^2$ (dotted lines). The result for the reference system is shown by the thick solid lines. The corresponding noise spectra $S(\omega)$ are given in the insets for the case of $T = 10/T_B^2$.

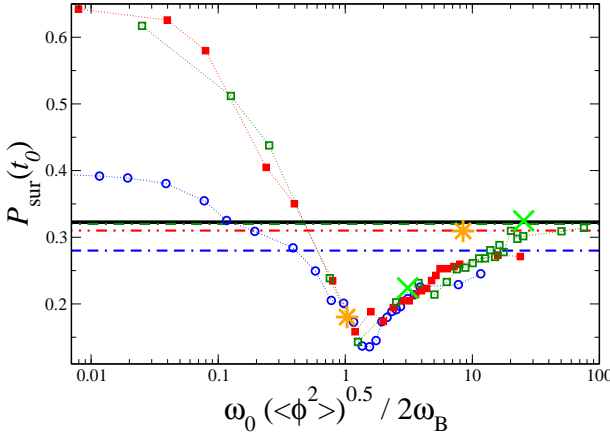


FIG. 2: (color online) $P_{\text{sur}}(t_0 \approx 6 T_B)$ for $V_0 = 2.5$, $F_0 = 1.5$, $\Gamma = 5/T_B$, for various (fixed) variances of the noise $\langle \phi^2 \rangle = 0.25$ (corresponding to $\alpha \approx 0.85$, open circles), 1 ($\alpha \approx 0.99$, filled squares), and 10 ($\alpha \approx 1$, open squares). For comparison we show $P_{\text{sur}}(t_0)$ for the respective effective models by the dashed, dash-dash-dotted, dot-dot-dashed, and dot-dashed lines (in the same order and color of the symbols), for the reference system (thick solid line), and calculated using a deterministically oscillating phase (described at the end of this Letter) with $A_d^2/2 \equiv T/\omega_0^2 = 1$ and $A_d^2/2 \equiv T/\omega_0^2 = 10$ for two values of $\omega_d \equiv \tilde{\omega}_0$ (large orange stars and green crosses respectively).

all the results of Fig. 2 show a similar behavior with a dip at around $\omega_0 \sqrt{\langle \phi^2 \rangle} \approx 2\omega_B = 2F_0 E_{\text{rec}}/\hbar$. First of all, this value of energy lies just above the average band gap, i.e., $2\hbar\omega_B \gtrsim \Delta E \approx 2.5 E_{\text{rec}}$, which turned out to be a necessary condition to observe the dip. Secondly, it implies that the optimal time scale of the noise is $T_B/2$ for observing an enhancement of the decay (i.e., a dip in Fig. 2). Intuitively, we expect such a dip for noise histories which facilitate the motion of the wave packet from the center of the Brillouin zone to the band edge. Once the wave packet has reached the band edge, it will easily fall into the next minimum along the band even in the absence of further activation; for a similar argument in noise-driven systems see, e.g., [20]. Dynamically speaking, $T_B/2$ is the time taken by the initial wave packet in the reference lattice, prepared at the center of the Brillouin zone, to reach the band edge. Hence the noise is most effective when its typical time scales are of the same order as $T_B/2$. Faster noise is less efficient again since it leads to the regime where the effective model applies, which has been introduced above. Indeed at very large ω_0 , $P_{\text{sur}}(t_0)$ lies in the vicinity of the corresponding value (shown by horizontal lines) calculated using the effective potential. The observed scaling relation drastically reduces the parameter dependence of the system. It helps predict and control the behavior of the survival probability by a simple choice of right combinations of the *a priori* many parameters ($F_0, V_0, \omega_0, \Gamma, T$).

Deviations from the scaling are expected when the noise frequency ω_0 becomes comparable with its spectral width, which is determined by Γ . This implies a crossover from the spectral distribution shown in Fig. 1(b) to the case of Fig. 1(a). Then the noisy phase changes slowly in time, and for $T \lesssim 10/T_B^2$ cannot assist the tunneling anymore, as observed in Fig. 1(a). Here $\omega_0 \sqrt{\langle \phi^2 \rangle} < \omega_B$ and the interband tunneling depends very much on the strength T of the noise, cf. Fig. 2. To better understand the regime where the scaling breaks down, it is helpful to study more explicitly the dependence on $\langle \phi^2 \rangle$, which is done in Fig. 3. Here we distinguish two cases: in (a) the data is produced as previously described by adapting α to compare with the reference system (α is calculated as a function of $\beta = \exp(-2\langle \phi^2 \rangle)$); in (b) we keep α fixed to understand the effect of the absolute value of the lattice depth (loosing, of course, the meaning of a reference system). The data collapses on a single curve described by the effective fast noise model of Eq. (5) (dashed lines in Fig. 3) for large frequencies $\omega_0^2/T \gtrsim 100$. The behavior of the various curves in (a) is similar (approximate scaling) for $1 < \omega_0^2/T < 100$, provided that $T \lesssim 1/T_B^2$. As shown also in Fig. 1(a), for a large $T \geq 100/T_B^2$ even the slowly varying noise is strong enough to enhance the decay below the value predicted for the static reference system. For the latter case, the scaling relation obviously is bound to fail. In Fig. 3(b), where we do not correct for the change in the relative height of the lattice amplitudes, the just described trends in (a) are shifted and the scaling is harder to appreciate (except for the very fast noise

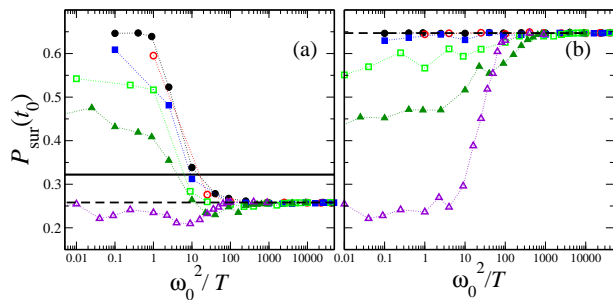


FIG. 3: (color online) $P_{\text{sur}}(t_0 \approx 6 T_B)$ for $V_0 = 2.5$, $F_0 = 1.5$ vs. $\langle \phi^2 \rangle^{-1} = \omega_0^2/T$: (a) adapted $\alpha \neq 1$; (b) fixed $\alpha = 1$. Other parameters: $\Gamma = 5/T_B$, and $T = 0.001/T_B^2$ (filled circles), $T = 0.01/T_B^2$ (open circles), $T = 0.1/T_B^2$ (filled squares), $T = 1/T_B^2$ (open squares), $T = 10/T_B^2$ (filled triangles) and $T = 100/T_B^2$ (open triangles). $P_{\text{sur}}(t_0)$ of the corresponding static reference system is shown by the solid line in (a) and for the effective model with $\beta = 1$ by the dashed lines in (a,b).

again, where our data always follows the expectation of the effective static model).

As a final benchmark for our calculations, we compare to a periodically oscillatory phase $\phi(t) = A_d \cos(\omega_d t + \varphi)$, with A_d being its amplitude and ω_d its oscillation frequency. To model random noise fluctuations the data are averaged over the parameter φ (picked randomly from a flat distribution). The spectral distribution of this function is given by $S_d(\omega) = \frac{A_d^2}{4\pi} \{\delta(\omega - \omega_d) + \delta(\omega + \omega_d)\}$. Practically, the delta functions gain a finite width $\Delta\omega_{\text{min}} = \frac{2\pi}{T_{\text{tot}}}$, where T_{tot} is the total numerical inte-

gration time. The spectral distribution of the harmonic noise in the fast noise regime, which very much peaks at $\tilde{\omega}_0$, is then comparable to the delta-like spectral distribution around ω_d of the oscillating noise. Therefore, for $\omega_d \approx \tilde{\omega}_0$ and $A_d = \sqrt{2T/\omega_0^2}$, the periodic phase (averaged over φ) has a similar effect as harmonic noise. Exemplary results are shown by the stars and crosses in Fig. 2 for $A_d^2/2 = 1$ and $A_d^2/2 = 10$, respectively. As expected, for large ω_0 , the star and the cross lie again on top of the prediction of the effective model.

a. Summary. We investigated the impact of noise on the Landau-Zener tunneling in a one-dimensional Wannier-Stark system. We motivated and derived an effective model (cf., Eq. (5)) which can be used as a benchmark to describe our results in the regime of fast oscillating noise. By a proper scaling of the data with parameters, we can universally characterize the effect of the noise. Our results show that time-dependent noise in a bichromatic lattice provides a further handle to control the transport to higher energy bands. We describe a first step towards the idea to push investigations of static into the realm of dynamical disorder [21]. A natural extension would be to study the case of the simultaneous presence of noise and atom-atom interactions, as done in Ref. [22] for a flat non-tilted potential, in our Wannier-Stark system.

b. Acknowledgments. We are very grateful to E. Arimondo and O. Morsch for inspiring discussions and for support by the Excellence Initiative through the HGSFP (grant number GSC 129/1), the Frontier Innovation Fund, and the Global Networks Mobility Measures.

-
- [1] M. BenDahan *et al.*, Phys. Rev. Lett. **76**, 4508 (1996).
[2] M. Raizen *et al.*, Phys. Today **50**, 30 (1997).
[3] O. Morsch and M. Oberthaler, Rev. Mod. Phys. **78**, 179 (2006).
[4] C. Sias *et al.*, Phys. Rev. Lett. **98**, 120403 (2007); A. Zenesini *et al.*, New J. Phys. **10**, 053038 (2008).
[5] M. Gustavsson *et al.*, Phys. Rev. Lett. **100**, 080404 (2008).
[6] A. Zenesini *et al.*, Phys. Rev. Lett. **103**, 090403 (2009); G. Tayebirad *et al.*, Phys. Rev. A **82**, 013633 (2010).
[7] J. G. Danzl *et al.*, Nature Phys. **6**, 265 (2010).
[8] L. Santos *et al.*, Phys. Rev. Lett. **93**, 030601 (2004); T. Schulte *et al.*, Phys. Rev. A **77**, 023610 (2008).
[9] T. Salger *et al.*, Phys. Rev. Lett. **99**, 190405 (2007); Science **326**, 1241 (2009).
[10] G. Roati *et al.*, Nature **453**, 895 (2008).
[11] B. Deissler *et al.*, Nature Phys. **6**, 354 (2010).
[12] J. Billy *et al.*, Nature **453**, 891 (2008).
[13] R. T. Scalettar, G. G. Batrouni, and G. T. Zimanyi, Phys. Rev. Lett. **66**, 3144 (1991); L. Fallani *et al.*, Phys. Rev. Lett. **98**, 130404 (2007); G. Roux *et al.*, Phys. Rev. A **78**, 023628 (2008).
[14] G. Tayebirad, R. Mannella, and S. Wimberger, Appl. Phys. B **102**, 489 (2011).
[15] M. Glück, A.R. Kolovsky, and H.J. Korsch, Phys. Rep. **366**, 103 (2002).
[16] M. Holthaus, J. Opt. B: Quantum Semiclassical Opt. **2**, 589 (2000).
[17] S. Wimberger *et al.*, Phys. Rev. A **72**, 63610 (2005).
[18] L. Schimansky-Geier and Ch. Zülicke. Z. Phys. B **79**, 452 (1990).
[19] G. E. Uhlenbeck and L. S. Ornstein, Phys. Rev. **36**, 823 (1930).
[20] D. G. Luchinsky and P. V. E. McClintock, Nature **389**, 463 (1997); T. Wellens, V. Shatokhin, and A. Buchleitner, Rep. Prog. Phys. **67**, 45 (2004).
[21] see, e.g., D. Burgarth, Eur. Phys. J. ST **151**, 147 (2007); C. K. Burrell, J. Eisert, and T. J. Osborne, Phys. Rev. A **80**, 052319 (2009).
[22] E. Lucioni *et al.*, preprint arXiv:1011.2362.

Kapitel 4

Wissenschaftliche Artikel

- **Delocalized and resonant quantum transport in nonlinear generalizations of the kicked rotor model**
 L. Rebuzzini, S. Wimberger, and R. Artuso,
 Physical Review E 71 (2005) 036220 81
- **Experimental verification of the one-parameter scaling law of the resonance peaks at quantum and “classical” resonance of the atom-optics δ -kicked rotor**
 S. Wimberger, M. Sadgrove, S. Parkins, and R. Leonhardt,
 Physical Review A 71 (2005) 053404 89
- **The role of quasi-momentum in the resonant dynamics of the atom-optics kicked rotor**
 S. Wimberger and M. Sadgrove,
 Journal of Physics A: Mathematical and General 38 (2005) 10549-10557 96
- **Nonlinearity induced destruction of resonant tunneling in the Wannier-Stark problem**
 S. Wimberger, R. Mannella, O. Morsch, E. Arimondo, A. R. Kolosvsky, and A. Buchleitner,
 Physical Review A 72 (2005) 063610 105
- **Can quantum fractal fluctuations be observed in an atom-optics kicked rotor experiment?**
 A. Tomadin, R. Mannella, and S. Wimberger,
 Journal of Physics A: Mathematical and General 39 (2006) 2477-2491 110
- **Tunnelling rates for the nonlinear Wannier-Stark problem**
 S. Wimberger, P. Schlagheck, and R. Mannella,
 Journal of Physics B: Atomic, Molecular and Optical Physics 39 (2006)
 729-740 125
- **Chaotic ratchet dynamics with cold atoms in a pair of pulsed optical lattices**
 G. Carlo, G. Benenti, G. Casati, S. Wimberger, O. Morsch, R. Mannella, and E. Arimondo,
 Physical Review A 74 (2006) 033617 137

- **Bose-Einstein condensates in accelerated double-periodic optical lattices: Coupling and crossing of resonances**
D. Witthaut, E. M. Graefe, S. Wimberger, and H. J. Korsch,
Physical Review A 75 (2007) 013617 144
- **Nonexponential decay of Bose-Einstein condensates: a numerical study based on the complex scaling method**
P. Schlagheck and S. Wimberger,
Applied Physics B: Lasers and Optics 86 (2007) 385-390 155
- **Multifractal fluctuations in the survival probability of an open quantum system**
A. Facchini, S. Wimberger, and A. Tomadin, Physica A 376 (2007) 266 161
- **Many-body Landau-Zener tunneling in the Bose-Hubbard model**
A. Tomadin, R. Mannella, and S. Wimberger,
Physical Review A 77 (2008) 013606 170
- **Engineering many-body quantum dynamics by disorder**
P. Buonsante and S. Wimberger,
Physical Review A 77 (2008) 041606 (R) 179
- **Resonant tunneling of Bose-Einstein condensates in optical lattices**
A. Zenesini, C. Sias, H. Lignier, Y. Singh, D. Ciampini, O. Morsch, R. Mannella,
E. Arimondo, A. Tomadin, and S. Wimberger,
New Journal of Physics 10 (2008) 053038 183
- **Mean-field dynamics of a two-mode Bose-Einstein condensate subject to noise and dissipation**
F. Trimborn, D. Witthaut, and S. Wimberger,
Journal of Physics B: Atomic, Molecular and Optical Physics 71 (2008)
171001 (FTC) 198
- **Scaling law and stability for a noisy quantum system**
M. Sadgrove, S. Wimberger, S. Parkins, and R. Leonhardt,
Physical Review E 78 (2008) 025206 (R) 203
- **Dissipation-induced coherence and stochastic resonance of an open two-mode Bose-Einstein condensate**
D. Witthaut, F. Trimborn, and S. Wimberger,
Physical Review A 79 (2009) 033621 207
- **Pseudo-classical theory for directed transport at quantum resonance**
M. Sadgrove and S. Wimberger,
New Journal of Physics 11 (2009) 083027 218
- **Pseudoclassical theory for fidelity of nearly resonant quantum rotors**
M. Abb, I. Guarneri, and S. Wimberger,
Physical Review E 80 (2009) 035206 (R) 231

- **Collapse and revival in inter-band oscillations of a two-band Bose-Hubbard model**
 P. Plötz, J. Madroñero, and S. Wimberger,
 Journal of Physics B: Atomic, Molecular and Optical Physics 43 (2010)
 081001 (FTC) 235
- **Time-resolved measurement of Landau-Zener tunneling in different bases**
 G. Tayebirad, A. Zenesini, D. Ciampini, R. Mannella, O. Morsch, E. Arimondo,
 N. Lörch, and S. Wimberger,
 Physical Review A 82 (2010) 013633 241
- **Nonlinear resonant tunneling of Bose-Einstein condensates in tilted optical lattices**
 K. Rapedius, C. Elsen, D. Witthaut, S. Wimberger, and K.-J. Korsch,
 Physical Review A 82 (2010) 063601 249
- **Detection of avoided crossings by fidelity**
 P. Plötz, M. Lubasch, and S. Wimberger,
 Physica A 390 (2011) 1363-1369 256
- **Engineering of Landau-Zener tunneling**
 G. Tayebirad, R. Mannella, and S. Wimberger,
 Applied Physics B: Lasers and Optics 102 (2011) 489-495 263
- **Effective spin model for interband transport in a Wannier-Stark lattice system**
 P. Plötz, P. Schlagheck, and S. Wimberger,
 European Physical Journal D (2011) in press, available online at
 DOI: 10.1140/epjd/e2010-10554-7 270
- **Stückelberg-Interferometry with ultra-cold atoms**
 P. Plötz and S. Wimberger,
 European Physical Journal D (2011) submitted 277
- **Beyond mean-field dynamics in open Bose-Hubbard chains**
 D. Witthaut, F. Trimborn, H. Hennig, G. Kordas, T. Geisel, and S. Wimberger,
 Physical Review A (2011) submitted 283

Delocalized and resonant quantum transport in nonlinear generalizations of the kicked rotor model

Laura Rebuzzini,¹ Sandro Wimberger,² and Roberto Artuso^{1,3,4}

¹*Center for Nonlinear and Complex Systems and Dipartimento di Fisica e Matematica, Università dell'Insubria, Via Valleggio 11, 22100 Como, Italy*

²*Dipartimento di Fisica E. Fermi, Università degli Studi di Pisa, Via Buonarroti 2, 56127 Pisa, Italy*

³*Unità di Como, Istituto Nazionale per la Fisica della Materia, Via Valleggio 11, 22100 Como, Italy*

⁴*Sezione di Milano, Istituto Nazionale di Fisica Nucleare, Via Celoria 16, 20133 Milano, Italy*

(Received 12 October 2004; published 24 March 2005)

We analyze the effects of a nonlinear cubic perturbation on the δ -kicked rotor. We consider two different models, in which the nonlinear term acts either in the position or in the momentum representation. We numerically investigate the modifications induced by the nonlinearity in the quantum transport in both localized and resonant regimes and a comparison between the results for the two models is presented. Analyzing the momentum distributions and the increase of the mean square momentum, we find that the quantum resonances asymptotically are very stable with respect to nonlinear perturbation of the rotor's phase evolution. For an intermittent time regime, the nonlinearity even enhances the resonant quantum transport, leading to superballistic motion.

DOI: 10.1103/PhysRevE.71.036220

PACS number(s): 05.45.-a, 03.65.Ta, 42.50.Vk

I. INTRODUCTION

Recent and ongoing experiments [1] have started to investigate the interplay between the many-body induced self-interaction in an ultracold atomic gas and an external driving induced by time-dependent optical potentials. The natural setup is to use a Bose-Einstein condensate of alkali-metal atoms, where the nonlinearity parameter can be tuned [2,3], and pulsed optical lattices can be used to impart momentum kicks to the atoms. For such a setup, the Gross-Pitaevskii (GP) equation [2,3] provides a good description of the system, as long as the nonlinearity is not too large, as a study of the stability of linearized excitations around the GP solution has shown [4,5].

In this paper, we analyze the evolution of a cubic nonlinear Schrödinger equation, as present in the GP model, under the perturbation of time-periodic δ kicks,

$$i \frac{\partial \psi}{\partial t} = \left[-\frac{1}{2} \frac{\partial^2}{\partial \vartheta^2} - u |\psi|^2 + k \cos(\vartheta) \sum_{t=0}^{+\infty} \delta(t' - t\tau) \right] \psi, \quad (1)$$

where ϑ and $n = -i\partial/\partial\vartheta$ are the position and the conjugated momentum of the system; we chose units such that $\hbar = 1$ and the motion is considered on a ring with periodic boundary conditions $\psi(\vartheta + 2\pi) = \psi(\vartheta)$. The parameters u and k are the nonlinearity coupling and the kicking strength, respectively.

In atom optics experiments, the δ -kicked rotor has been realized with an ensemble of laser-cooled, cold atoms [6], or recently also with an ultracold Bose-Einstein condensate [1], periodically driven with a standing wave of laser light. With the wave number of the laser k_L , the experimental variables are easily expressed in our units by noting that momentum is usually measured in two photon recoils ($2\hbar k_L$), and position in units of the inverse wave number of the standing wave ($1/2k_L$). Hence, the scaled variables ϑ, n and the physical ones ϑ', p' are related by $\vartheta = 2k_L \vartheta'$ and $n = p'/2k_L \hbar$ [7–9].

Our choice of units makes all the relevant quantities (including the ones plotted in figures) dimensionless.

Owing to the periodicity of the δ -kick perturbation, the time t is measured in number of periods τ and the evolution of the wave function of the system over a time interval τ is described by the operator $\hat{U}(\tau)$.

A cubic modification of linear Schrödinger dynamics for the δ -kicked rotor may be accomplished by two different models, both considered in the present paper. The correct way to approximate the evolution of the nonlinear Schrödinger equation is to evaluate the nonlinear term in the position representation [10]. In the following we will refer to this first model as model 1 (M1).

Since the Hamiltonian operator presents a time-dependent nonlinear part $u|\psi|^2\psi$, in the numerical integration of Eq. (1), the lowest order split method [11] is used and \hat{U} is approximated by the time-ordered product of evolution operators (Trotter-Kato discretization [12]) on small time steps τ/L (with L integer):

$$\hat{U}^{(1)}(\tau) = \hat{K} \hat{R}^{(1)}(\tau) \approx e^{-ik \cos(\hat{\vartheta})} \prod_{l=1}^L e^{-i\pi^2/L^2} e^{iu(\pi/L)|\psi(\hat{\vartheta}, l\tau/L)|^2}. \quad (2)$$

In the numerical simulations, we use a finite Fourier basis of dimension N : the discrete momentum eigenvalues lie on the lattice $p = (m - N/2)$ and the continuous angle variable is approximated by $\vartheta = (2\pi/N)(m - 1)$ with $m \in \mathbb{Z}, 1 \leq m \leq N$. Shifting between the coordinate and momentum representations, in the evaluation of the operator $\hat{R}^{(1)}(\tau)$, requires $2L$ fast Fourier transforms of N -dimensional vectors for each kick. In order to get stable numerical results, the splitting interval τ/L has to be reduced when increasing the nonlinear coupling constant u ; typical values of the number of steps

per period range between $L=80\,000$ and $5\,000\,000$. Therefore, investigating either the effects of strong nonlinearities or the dynamics of the system over long times is computationally quite expensive with M1.

A second model [known as the kicked nonlinear rotator and called in the following model 2 (M2)] was introduced in [13]. This model, being a much simpler variant of the kicked rotator (KR) model [14], allows one to perform faster and more efficient numerical computations.

The evolution operator over one period τ for M2 is given by

$$\hat{U}^{(2)}(\tau) = \hat{K}\hat{R}^{(2)}(\tau) \approx e^{-ik \cos(\hat{\vartheta})} e^{-i\tilde{m}^2/2} e^{i\tilde{u}\tau|\hat{\psi}_n|^2}, \quad (3)$$

where $\hat{\psi}_n$ indicates the n th component of the wave function of the system in the momentum representation. The change in the phase of each component $\hat{\psi}_n$ of the state vector, introduced by the nonlinear term between two kicks, is proportional to the amplitude of the component. In M1 instead, the phase acquired at each instant by the wave function involves all the Fourier components and the phase factor has as the n th Fourier component $(u/2\pi)\sum_m \hat{\psi}_{m+n}^* \hat{\psi}_m$. The two models coincide only if the wave function of the system is a plane wave of fixed momentum; in this case, the relation between the nonlinear coupling constants in M1 and M2 is $\tilde{u}=u/2\pi$.

Both models M1 and M2 are nonlinear generalizations of the KR and reduce to the KR in the limit $u \rightarrow 0$. Depending on the commensurability of the period τ of the δ -kick perturbation with 4π , the KR displays different regimes, deeply studied both theoretically [14–16] and experimentally [6,8]. The quantum resonant regime, corresponding to values of τ being rational multiples of 4π , is characterized by a ballistic transport: the mean energy of the system grows according to a parabolic law [15,17]. For generic irrational values of τ , the average energy grows linearly in time only within a characteristic time (break time), after which dynamical localization sets in and the diffusion is suppressed [16].

In this paper, we analyze in detail how the presence of the nonlinearity affects the general properties of transport in regimes that correspond to the localized (Sec. II, which is essentially a warm up exercise in which the results of [13] are reproduced and additional numerical results about prefactor scaling are presented) and resonant (Sec. III) ones of the KR. We focus our attention on the growth exponent of the mean energy and on how the diffusion coefficient or the rate of ballistic transport depends on the strength of the nonlinear coupling constant u . While in Secs. II and III we are dealing with the evolution of an initial state with fixed momentum, chosen at $n=0$, i.e., $\hat{\psi}_n(0)=\delta(0)$, Sec. IV is devoted to the effects of a finite spread of initial conditions as strongly suggested by state-of-the-art experiments using ultracold atoms [1,19].

The quantity we typically compute is the width of the momentum distribution of the system $\langle p^2(t) \rangle = \sum_{n=-\infty}^{+\infty} n^2 |\hat{\psi}_n|^2$, which gives the spreading of the wave packet over unperturbed levels or equivalently—apart from a constant factor 2—the expectation value of the energy. The time-averaged spreading $P^2(T) = (1/T) \sum_{t=1}^T \langle p^2(t) \rangle$ of the second moment has

been frequently used (see, e.g., [18]), as it preserves the exponent of the power-law growth, while smoothing out oscillations.

As pointed out in [13] the nonlinear shift is essential in determining dynamical features (providing for instance a mechanism for delocalization of the generic, irrational case), but when we deal with delocalized states it is typically quite small (e.g., for M2 the shift is proportional to $\tilde{u}/\Delta n$, where Δn is the width of the distribution over unperturbed states). So in general we may expect that, for moderate nonlinearities, the precise form of the shift does not alter in an essential way the nature of the asymptotic motion.

II. LOCALIZED REGIME

In this section, we consider the regime where the value of the period of the δ -kick perturbation is incommensurate with 4π . For better comparison we fix $\tau=1$ for all numerical computations shown in the following. The corresponding system in the $u \rightarrow 0$ limit is characterized by the phenomenon of dynamical localization [16] caused by quantum interference effects. Previous theoretical predictions and numerical simulations [13,20] indicate that, above a critical border $u_c \sim 2\pi$ for the nonlinear coupling constant, dynamical localization is destroyed. The delocalization takes place in the form of anomalous subdiffusion with an exponent of $2/5$: in [13] an asymptotic law $\langle p^2(t) \rangle \sim c(u)t^{2/5}$ [where $c(u) \sim u^{4/5}$] is predicted for both models; this is confirmed for both models by the data reported in Fig. 1. In Fig. 1(a) a bilogarithmic plot of the time-averaged second moment vs time is shown for increasing values of the nonlinear coupling constant u . In spite of large oscillations, both models fit the predicted asymptotic behavior with a power-law exponent equal to $2/5$. For nonlinear coupling larger than the critical border u_c , marked by the vertical line, the dependence of $c(u)$ vs u is confirmed for both models by Fig. 1(b). $\text{Log}_{10}[c(u)]$ is obtained by a one-parameter linear fitting of the logarithm of the second moment, once an anomalous diffusion exponent equal to $2/5$ is assumed.

The results obtained by calculating the evolution of the system with either M1 or M2, starting from the same state $\hat{\psi}_n(0)=\delta(0)$ and parameters, appear to be different on short time scales; nevertheless the two models share the same asymptotic behavior of the time evolution of the second moment and of the dependence of $c(u)$ vs u . The effect of the nonlinearity is the same for both models only at $t=1$, because of the common initial state. As explained in the Introduction, the way nonlinearity acts on the wave function is essentially different for M1 and M2, at least before the state becomes delocalized: so deviations are qualitatively expected for intermediate times, while we expect a closer analogy in the models' behavior in the asymptotic regime. Actually the close behavior exhibited by both models in Fig. 1 after a few time steps extends to more general features than the second moment: in Fig. 2 we provide a comparison between full distributions over momentum states for $u=10$.

We remark that nonlinearity-induced delocalization has recently been explored also in studying survival probability

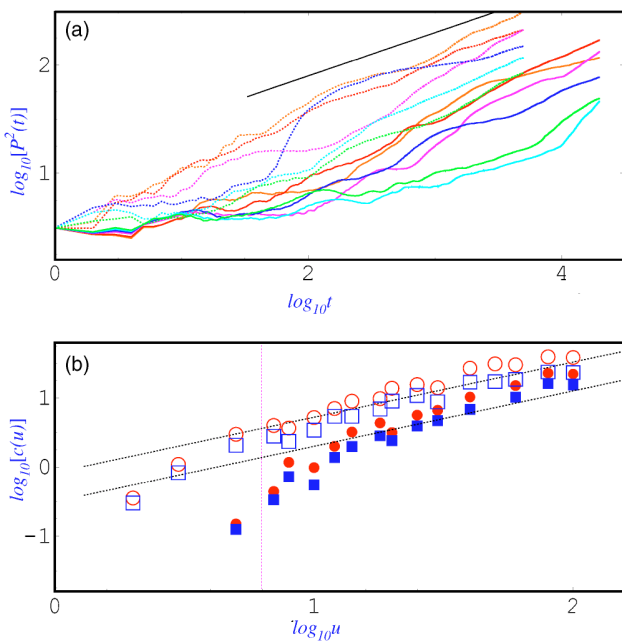


FIG. 1. (Color online) (a) Bilogarithmic plot of the time-averaged second moment vs time in the localized regime. Time is measured in number of periods. The dashed and full lines refer to M2 with $N=2^{17}$ and M1, with $N=2^9$ and $L=80\,000$, respectively. Values of $u=8,10,12,14,16,20$ are considered; generally higher nonlinearity values yield bigger spreading. The dashed line has the theoretically predicted slope $2/5$. The values of the parameters are $\tau=1$ and $k=2.5$; the initial state is $\hat{\psi}_n(0)=\delta(0)$. (b) The logarithm of the coefficient of the sub-diffusion as a function of $\log_{10}(u)$, for the second moment (circles) and its time average (squares). Empty and full symbols refer, respectively, to M1 and M2. The dashed lines show the predicted dependence $\sim u^{4/5}$.

on a finite momentum sample [21]: while the authors use M2 to cope with computational difficulties, our findings suggest that their results are probably relevant for true nonlinear Schrödinger equation dynamics too.

III. RESONANT REGIME

In this section, we examine in detail the response of the system to nonlinear perturbation in the resonant regime of the KR ($\tau=4\pi r/q$ with r,q relatively prime integers), characterized by a parabolic growth in time of the variance of the momentum distribution [15,17]. The value of τ is chosen equal to 4π , corresponding to the first fundamental quantum resonance of the KR.

In Fig. 3(a) a bilogarithmic plot of the time-averaged second moment of the momentum distribution for different values of the nonlinearity is shown. The nonlinear coupling constant u varies from 1 to 400. As already noticed [20], the resonant behavior survives even in the presence of nonlinearity, although generically the spreading is slowed with respect to the linear case. On asymptotically long time scales, resonant growth with a quadratic exponent is reached even for strong nonlinear perturbations, though we observe that the time needed to reach the asymptotic regime grows with

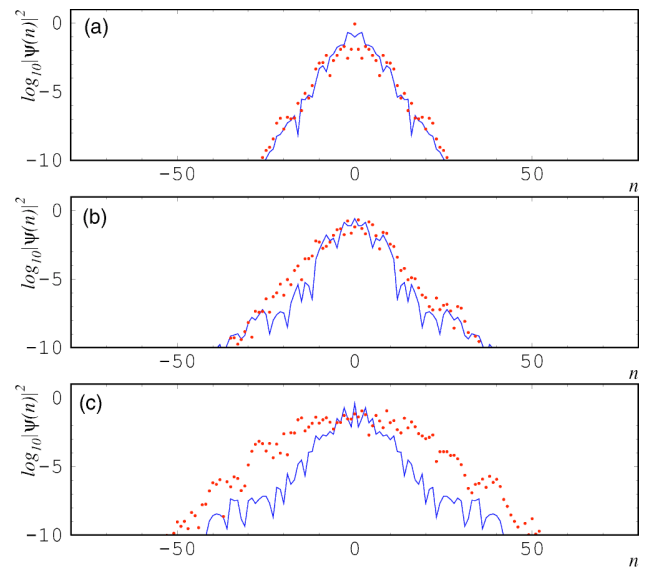


FIG. 2. Comparison between the momentum distributions for M1, circles, and M2, full line, after $t=10$ (a), 100 (b), and 1000 (c) kicks. The parameters are the same as in Fig. 1; the nonlinear coupling is fixed to the value $u=10$.

u . The results in Fig. 3(a) obtained from M2, shown in full lines, allow us now a more detailed analysis of the behavior of the system at quite long times. It can also be seen in Fig. 3(a) that the time evolution of the second moment of M1, shown with circle symbols, approaches the same asymptotic growth, even if some differences between the two models appear especially for large nonlinearity ($u \geq 50$).

The persistence of the resonant behavior in the presence of nonlinearity can be explained intuitively as follows. In the linear (i.e., $u=0$) resonant case the width of the momentum distribution increases linearly in time. Therefore, from the normalization condition, the probability amplitude to find the system in a momentum eigenstate n decays as $|\hat{\psi}_n|^2 \sim 1/\Delta n \sim 1/(\pi kt)$ [7,13]. The nonlinear phase shift $\pi u |\hat{\psi}_n|^2$ decreases with the same rate and its effects become irrelevant on long time scales, i.e., $t \gg (u/\pi k)\tau$.

Nevertheless, the nonlinearity affects the evolution of the second moment on smaller time scales $t \lesssim (u/\pi k)\tau$ and introduces a u dependence in the prefactor of the parabolic growth law $\langle p^2(t) \rangle \sim a(u)t^2$. Increasing nonlinear coupling manifests in a slower quadratic growth. In Fig. 3(b) the function $\Delta^{(\bar{i})}(t) = [\langle p^2(t) \rangle^{(\bar{i})} - \langle p^2(t) \rangle^{(0)}] / t^2$ is plotted for different values of the nonlinearity. Increasing asymptotic absolute values of $\Delta(t_{\max})$ give an estimate of the modifications in the transport induced by the nonlinearity. The coefficients a_{Δ} , calculated from the function $\Delta(t=t_{\max})$ with $t_{\max}=20\,000$, are shown in the inset of Fig. 4.

A detailed analysis of the dependence of the coefficient $a(u)$ of $\langle p^2(t) \rangle$ is presented in Fig. 4. The numerical calculation of $\log_{10}[a(u)]$ is obtained by a one-parameter linear fitting of the logarithm of the second moment vs the logarithm of time with a straight line of fixed slope 2. The fitting is performed on a time interval $\Delta t=200$; this rather small time interval was chosen in order to make a comparison between

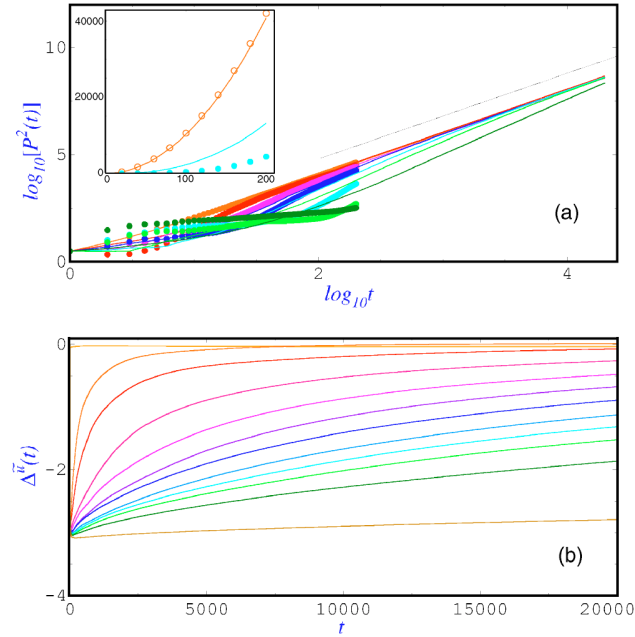


FIG. 3. (Color online) (a) Resonant growth of the time-averaged second moment vs time in the presence of nonlinearity, for $\tau=4\pi$ and $k=2.5$. The initial momentum distribution is $\hat{\psi}_n(0)=\delta(0)$. The symbols and the full lines refer to M2 with $N=2^{17}$ and M1 with $N=2^{10}$ and $L=5\,000\,000$, respectively. The straight black line shows the resonant asymptotic behavior t^2 . The values of the nonlinear parameter are $u=1, 5, 10, 20, 50, 100, 400$. The inset is a magnification for $u=1$ and 50 (lower part). A slight deviation between the two models can be seen for $u=50$. (b) The function $\Delta^{(\tilde{u})}(t)$ vs time for M2. Starting from above in the low $t < 5000$ region, the values of the nonlinear parameter are $\tilde{u}=0.1, 5, 10, 20, 30, 40, 50, 60, 70, 80, 100, 400$.

the results from both models (empty and full symbols refer to M1 and M2, respectively). The accordance between the two models is satisfying up to $u \lesssim 50$. For $u > 50$ the lowest order split method [11] to evaluate the Floquet operator in M1 becomes less stable and the numerical errors around the borders of the finite basis propagate faster.

Numerical data are compatible with an algebraic law $a(u) \approx k^2/[2(1+u/c)^\gamma]$, where γ is $4/5$ and c is a constant of the order of 10 (for the time-averaged moment the constant $k^2/2$ is substituted by $k^2/6$). This law has the required asymptotic behavior for $u \rightarrow 0$: in this limit $a(u)$ tends to the well-known value of the coefficient of the resonant KR, i.e., $a(0)=k^2/2$. In Fig. 4 the values of $a(0)$ are marked by arrows. For large values of u , $a(u)$ decreases for increasing nonlinearity with the inverse power law $\sim u^{-4/5}$. At the moment we have no explanation for the minimum observed in the intermediate region ($\log_{10} u \sim 0.85$).

Up to now, we discussed only the case of attractive interactions, i.e., $u > 0$. It turns out that the fundamental quantum resonance at $\tau=4\pi$ is insensitive to the sign of the nonlinearity as can be seen in the inset of Fig. 5. The same is true for the momentum distributions, which are not presented here. On the other hand, the next order resonance at $\tau=3\pi$ is sensitive to the sign of u . For $u < 0$ in Fig. 6(b), the momen-

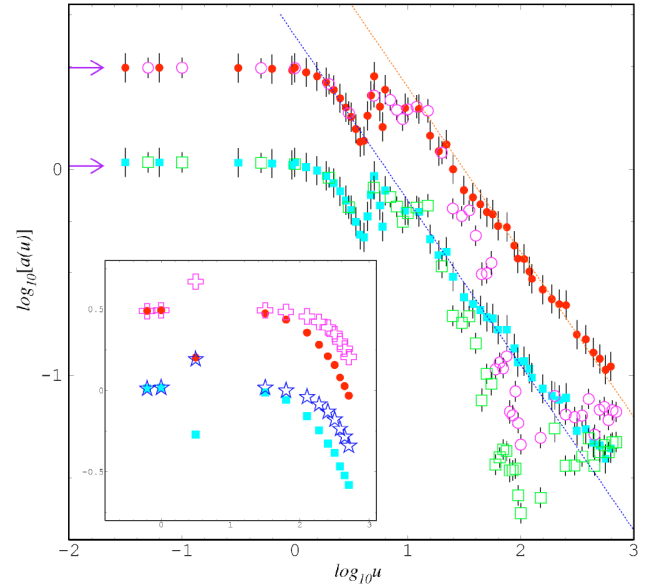


FIG. 4. (Color online) Bilogarithmic plot of the coefficient $a(u)$ of the quadratic growth of the second moment (circles) and its time average (squares) as a function of the nonlinear parameter u . Empty and full symbols refer to M1 and M2, respectively. The dashed lines show the algebraic behavior of $a(u)$ for large u with an exponent equal to $-4/5$. Notice that for $u \leq 1$ the coefficients approach the theoretical values of the KR model, marked by arrows. In the inset the empty symbols refer to a_Δ calculated using the function $\Delta(t=t_{\max})$ with $t_{\max}=20\,000$.

tum distribution is slightly different from $u > 0$. Asymptotically, however, the same ballistic growth of the mean square momentum is obtained. This means that the details of the effect of nonlinearity depend on the resonance type as far as the sign of u is concerned. This originates from the fact that while at the fundamental quantum resonances $\tau=4\pi m$ ($m > 0$ integer) the free evolution phase in the linear rotor is

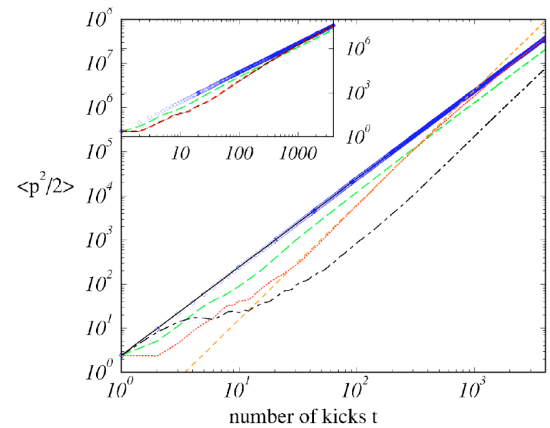


FIG. 5. Kinetic energy at the fundamental quantum resonance $\tau=4\pi$, $k=\pi$, $p_{\text{initial}}=0$, and nonlinearities $\tilde{u}=0$ (solid), -0.2 (diamonds), -1 (dashed), -10 (dotted), and -100 (dash-dotted). The short dashed line shows a superballistic increase proportional to $t^{2.6}$ for the case $\tilde{u}=-10$. The inset presents the results for $\tilde{u}=0.2, 1, 10$, and the case of $\tilde{u}=-10$ (thin solid line) for better comparison.

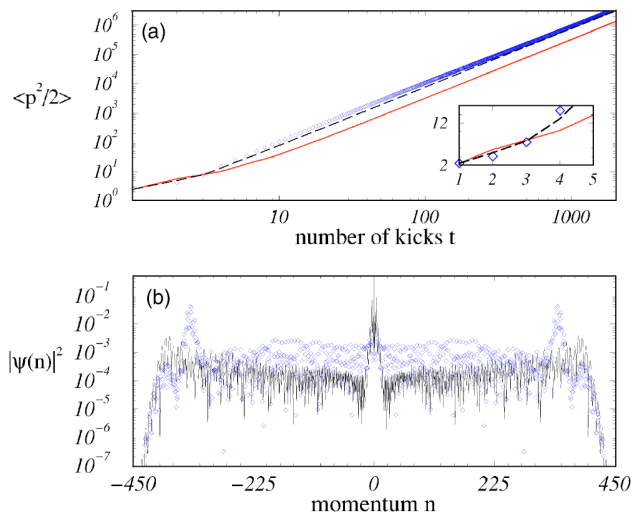


FIG. 6. (a) Kinetic energy as a function of the number of kicks, and (b) the corresponding momentum distributions after 200 kicks, for the quantum resonance $\tau=3\pi$. Same parameters as in Fig. 5, apart from the nonlinearity, which is $\tilde{u}=-0.2$ (diamonds) and 0.2 [(a) dotted, (b) solid]. In (a) we show also data for $u=0$ (dashed) for comparison, and the inset illustrates the opposite effect of the second and fourth kicks (the rephasing in momentum space occurs for the $u=0$ case only every second kick at $\tau=3\pi$) depending on the sign of \tilde{u} .

exactly 1, at higher order resonances there is a nontrivial phase evolution between two successive kicks. The inset of Fig. 6(a) highlights that $\langle p^2 \rangle/2$ either decreases or increases with respect to the case $u=0$ at the second and fourth kicks. This is related to the fact that at $\tau=3\pi$ the rephasing in momentum space occurs only every second kick, not between two successive kicks as at $\tau=4\pi$.

In Figs. 5 and 6 the time scales relevant for experiments ($t \lesssim 500$) are investigated (results refer to M2). In Fig. 5, we generically observe three regimes. (i) There is an initial stage, where the mean square momentum increases much more slowly than in the case $u=0$. This stage is followed by stage (ii) where the increase can be faster than ballistic, and the mean square momentum can even be larger for larger nonlinearity (see $|\tilde{u}|=10$ as compared to $|\tilde{u}|=1$ in Fig. 5).

The observed superballistic growth of the second moment of the momentum distribution is quite surprising, in particular, having in mind that such a growth is forbidden in the usual KR (i.e., $u=0$) [22]. The results in Fig. 5 are reminiscent of the observed superballistic spreading in one-dimensional tight-binding models [23]; however, here the superballistic behavior is caused by the *nonlinear* term in the time evolution, in contrast to the linear Hamiltonian models in [23]. In terms of the model studied in [23], the nonlinearity u would act as a finite size trapping region (cf. also [21]), outside of which the motion is ballistic (we already showed how nonlinearity does not essentially modify high n components).

The final stage (iii) we call the asymptotic regime, because there the growth exponent approaches the one for vanishing nonlinearity (only for $\tilde{u}=-100$ is this stage not yet reached in Fig. 5).

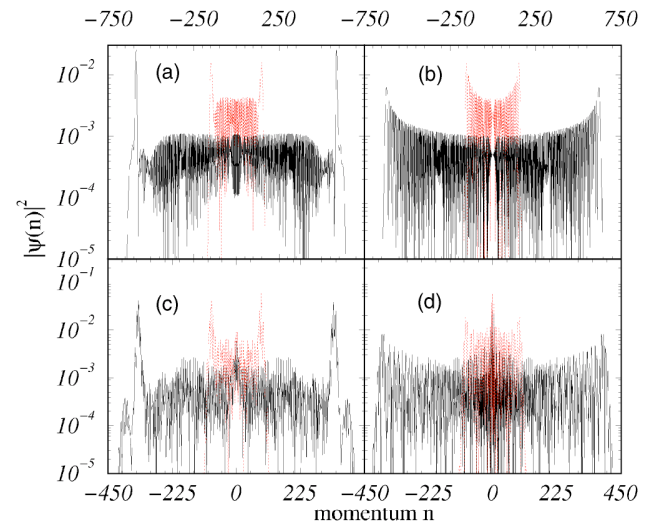


FIG. 7. Momentum distributions for zero initial momentum, $k=\pi$, $\tilde{u}=-0.2$ (a),(c) and $u=0$ (b),(d), and $\tau=4\pi$ (a),(b), $\tau=3\pi$ (c),(d). Note the stable peaks at the largest momenta in the case with small nonlinearity. The distributions are shown after 50 (dotted) and 200 (solid line) kicks in each panel.

In Fig. 6(b) we notice distinct peaks close to the very edge of the momentum distribution for $\tilde{u}=0.2$. Such peaks have been found for sufficiently large kicking strength $k \geq 2.5$ and corresponding $|\tilde{u}(k)|=0.2, \dots, 2$, and it turns out that they can be up to one order of magnitude higher than the maximum of the momentum distribution for the linear KR at the resonances $\tau=4\pi$ and 3π . Figure 7 compares the momentum distribution $|\hat{\psi}_n|^2$ at the fundamental quantum resonance $\tau=4\pi$, and at the resonance $\tau=3\pi$ for small nonlinearity $\tilde{u}=-0.2$ with the case of the linear KR. The distributions are shown after 50 and 200 kicks, respectively, to stress their evolution in time. For both resonances, we observe a very interesting feature, namely, the small nonlinearity sharpens the edge peaks, which move ballistically, i.e., with a speed that is proportional to the number of kicks t [we recall that when $u=0$ the distribution is characterized by a largest momentum component also moving according to a linear law $n_{\max}(t) \approx kt\pi/2$ [7]]. The peaks are more pronounced than in the linear case, and are remarkably stable, i.e., their height decreases very slowly with increasing number of kicks in Fig. 7(c), or even increases initially as in Fig. 7(a). While we focused our discussion on the model M2, the structure of the probability distribution is quite similar for M1 (see Fig. 8).

The intermediate time scaling properties look in this case more complex than in the kicked rotator dynamics in the presence of sticking accelerator modes, where the same exponent appears both in the classical and in the quantum cases (where a new modulation appears). Work is in progress to see whether there exist classical mappings that reproduce the peak dynamics we observe in the intermediate time quantum behavior [24].

IV. MOMENTUM DIFFUSION IN THE RESONANT REGIME

All the above results have been obtained for an initial state in the form of a plane wave of null momentum. In a

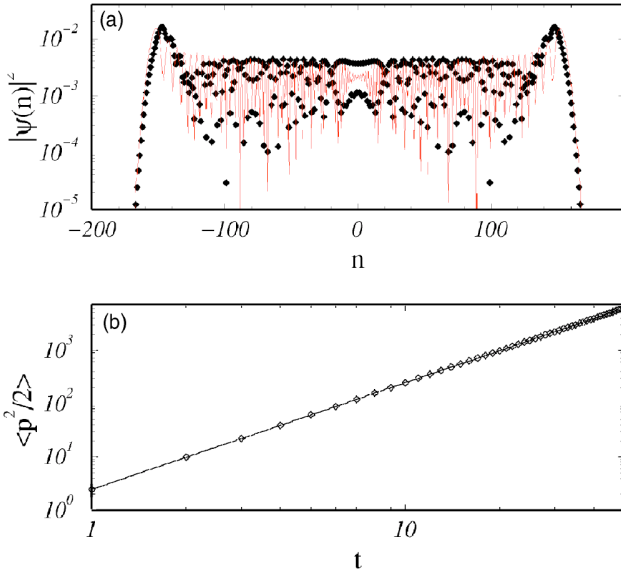


FIG. 8. (a) Momentum distribution after $t=50$ kicks, and (b) mean square momentum for $p_{\text{initial}}=0$, $u=-0.2$, $\tau=4\pi$, and $k=\pi$. Shown are the evolutions induced by M2 (diamonds) and by M1 (full lines).

typical experiment, one can create a Bose condensate with an initial spread of momentum which is much less than two photon recoils (which can be imparted as momentum kicks to the atoms by the kicking laser). We ask ourselves what happens if such a spread is taken into account. The momentum variable p , varying on a discrete lattice in the case of a single rotor, becomes a continuous variable. For the linear KR, the eigenvalues of \hat{p} can be written, distinguishing the integer and fractional parts (quasimomentum), as $p=[p]+\{p\}=n+\beta$. Owing to the conservation of quasimomentum β , the system dynamics can be decomposed into a bundle of rotors [26] (called in the following β rotors), each parameterized by a value of the quasimomentum, evolving incoherently with operators with the same functional form as Eqs. (2) and (3), in which \hat{n} is substituted by $\hat{n}+\hat{\beta}$. Such a decomposition is not easily accomplished when we introduce a nonlinear term in the dynamics. The general task we have to face becomes the study of a nonlinear evolution equation with periodic coefficients. This is a quite a complex problem that cannot be tackled in full generality, even though different approximation schemes have been proposed, e.g., by mapping the problem into a discrete lattice, which turns out to be useful if the wave function is expanded in a suitable set of localized functions related to the linear problem [27]. We generalize M2 in such a way that its linear limit is the evolution operator corresponding to a quasimomentum β (as formerly specified), and assume that each nonlinear β rotor evolves independently. In this way we study the influence of nonlinearity on realistic initial conditions in a highly simplified way, by means of a generalized M2 model: further work is obviously needed to check whether our findings extend to a full GP dynamics [28].

The quantum resonance phenomenon in the KR is strongly sensitive to the values of the parameters of the sys-

tem. The linear KR rotor ($u=0$) exhibits the quantum resonance only for a finite set of quasimomenta, i.e., $\beta=\beta^R=m/2p$ with $m<2p$ [7,15,26]. A slight deviation of the quasimomentum from β^R changes the evolution of the system completely. For values of $\beta\neq\beta^R$, after a transient regime, the suppression of the resonant growth of the energy of the linear β rotor through dynamical localization occurs; at fixed time t , only quasimomenta within an interval $\sim 1/t$ of β^R mimic the ballistic behavior proportional to t^2 and a rough estimate of the time up to which the quadratic growth of the β -rotor energy persists is $\bar{t}\sim 1/\Delta\beta$, where $\Delta\beta=|\beta-\beta^R|$ [7,25].

In the following, we investigate the mean square momentum distribution of the generalized M2 model, first (a) for a single β rotor with fixed quasimomentum, and then (b) for an incoherent ensemble of β rotors whose initial state in momentum space is a Gaussian distribution with zero mean and rms spreading $\Delta\beta=\sigma=0.01$. We choose $\tau=4\pi$, and the resonance condition is then met for $\beta^R=0$ and $\beta^R=1/2$. The case with $\beta^R=0$ fixed was considered in Sec. III. As in the localized regime, considered in Sec. II, the introduction of the nonlinearity causes a delocalization in the system with a nonresonant value of the quasimomentum ($\beta\neq\beta^R$). For small nonlinearities, the appearance of an anomalous asymptotic diffusion with an exponent of $2/5$, after the initial ballistic behavior, is confirmed by data of Fig. 9(a) for a β rotor with $\beta\approx 0.009$. On the contrary, greater nonlinear couplings ($u\geq 50$) introduce an excitation of diffusive type, starting from the first kicks. In Fig. 9(b) the quasimomentum of the β rotor is varied and u is kept fixed. The arrows mark the times \bar{t} , depending on the value of β , approximately bounding the region of the ballistic growth.

We then consider the dynamics of an incoherent ensemble of β rotors. The mean square displacement of the distribution is $\langle p^2(t) \rangle_\beta = \int d\beta \langle p_\beta^2(t) \rangle$. The average over β has been calculated using 5000 quasimomenta. In Fig. 10 the time evolution of the averaged second moment of the initially Gaussian wave packet is shown for M2. The behavior in the corresponding linear case of the KR is theoretically known (see Appendix A of [26]): for $u=0$, the kinetic energy of the system increases diffusively in time with a coefficient proportional to $k^2/4$, and dependent on the initial distribution of quasimomenta [7]. The presence of the nonlinearity manifests itself in a faster than linear growth, at least on short time intervals. After this transient regime, the asymptotic growth is expected to become approximately linear. The black straight line is drawn for better comparison. At fixed time t and assuming a uniform distribution of the quasimomenta, the resonant rotors whose quasimomenta lie within the interval $\Delta\beta$, enter in the average of $\langle p^2 \rangle_\beta$ with a contribution of $\sim t^\alpha$ and a weight $w\sim 1/t$, while the nonresonant rotors give a contribution of $(1-w)t^\gamma$. The exponents of the transport in the limit $t\rightarrow+\infty$ reach the values $\alpha(\infty)=2$ and $2/5\leq\gamma\leq 1$. Therefore, asymptotically in time, the global transport exponent reaches the value 1. In the inset of Fig. 10 the exponents of the algebraic growth of the second moment are plotted as a function of the nonlinear coupling constant \bar{u} . The fitting time interval is 1000 kicks. Full and open circles refer to 5000 and 500 quasimomenta of the initial Gaussian

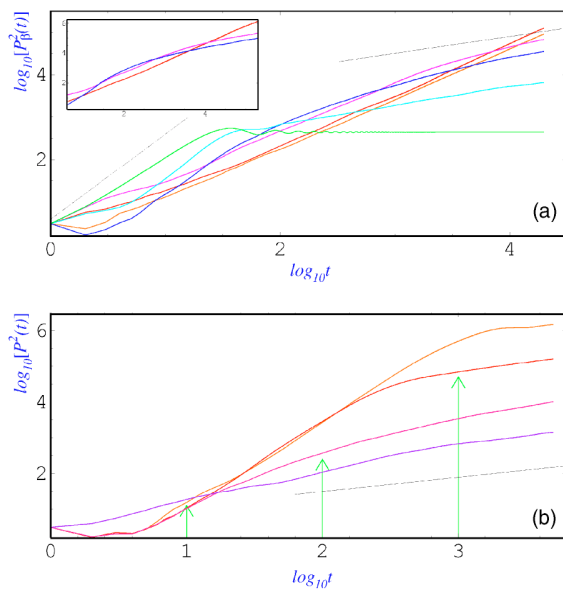


FIG. 9. (Color online) (a) Bilogarithmic plot of the second moment of a single β rotor with a fixed quasimomentum for increasing nonlinear coupling (from below, referring to high t values, $\bar{u} = 0, 1, 5, 10, 50, 100$). The two lines have slope 2 and $2/5$. Note that in the KR case ($u=0$), the localization occurs for time $t \geq 1/\beta$. The parameters are $\tau=4\pi$, $k=2.5$, and $N=2^{17}$. The initial state is an eigenfunction of the momentum with $n=0$ and $\beta=0.00946556$. In the inset the calculations are prolonged ten times. The unbounded growth for $\bar{u}=50, 100$ can be clearly seen. (b) The same as (a) with u fixed ($\bar{u}=5$) and variable β (from above, referring to high t values, $\beta=0.0001, 0.001, 0.01$, and 0.1). The arrows mark the times $1/\beta$.

distribution: a slight rise in the exponents can be noted on increasing the number of quasimomenta, because a greater number of them approach the value $\beta^R=0$, yielding the quadratic growth of the β -rotor energy. Note that the exponent approaches faster the value 1 for a uniform initial distribution of quasimomenta (stars), confirming the previous argument.

Figure 11 presents a closer look at the dynamics on a shorter time scale: the results refer to the case in which we found stable momentum peaks in Fig. 7. Part of the peak is still preserved for the used spread $\Delta\beta \approx 0.01$, which can be realized in state-of-the-art experiments [1,19]. After about 15 kicks, more weight lies, however, now in the center of the distribution made up of rotors which do not exactly satisfy the rephasing condition due to nonzero quasimomenta. Also the increase of the mean square momentum, which is averaged incoherently over all the independently evolved initial conditions, is then not any more quadratic but closer to linear (see inset in Fig. 11), as was found in the case of a uniform initial distribution of quasimomenta for the $u=0$ case [7,25]. The mean square momentum still increases much faster than for nonresonant values of the kicking period τ , where dynamical localization occurs. The latter may be destroyed by the nonlinearity but the above observed growth of $\langle p^2 \rangle / 2 \propto t^{2/5}$ (cf. Sec. II) is much slower than linear. On short time scales thus quantum resonance is very robust with respect to nonlinear perturbations. If our incoherent superposition

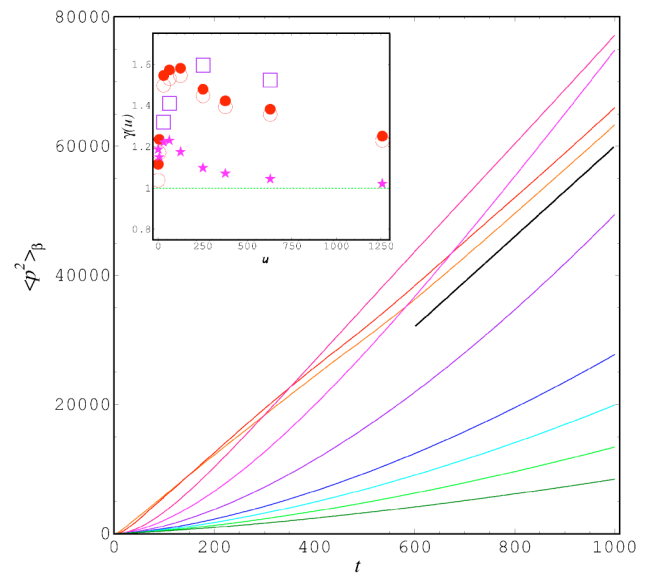


FIG. 10. (Color online) Average over 5000 quasimomenta of the second moment of the distribution vs time for M2; $\tau=4\pi$ and $k=2.5$. Starting from below (referring to high t values) $\bar{u} = 200, 100, 60, 40, 20, 0, 1, 5, 10$; the initial wave packet in Fourier space is a Gaussian distribution centered at $n=0$ with rms $\sigma=0.01$. The inset shows the power-law exponents of the second moment as a function of \bar{u} . The fitting is performed on time intervals $\Delta t = 1000$ (circles) and 6000 (squares). Open symbols refer to 500 quasimomenta. Stars refer to a uniform distribution of quasimomenta.

model is correct after some initial stage, the ballistic motion should cease but the dynamics will show the influence of the ballistic quantum resonant transport.

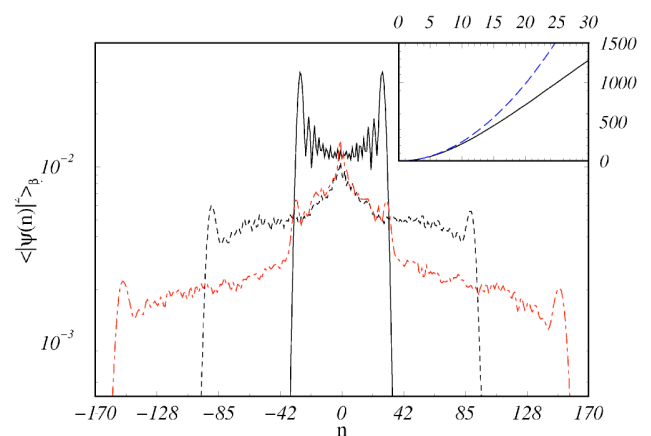


FIG. 11. Momentum distribution after $t=10$ (solid), 30 (dashed), and 50 kicks (dash-dotted), for the same parameters as in Fig. 7(a), but incoherently averaged over independently evolved initial conditions (Gaussian initial momentum distribution with rms $\sigma=0.01$ centred around $n=0$). The inset shows the corresponding $\langle p^2 \rangle_{\beta} / 2$ as a function of the number of kicks for $\bar{u}=-0.2$ (solid) and $u=0$ (dashed).

V. CONCLUSIONS

In summary, we have numerically analyzed in great detail the quantum transport occurring in two nonlinear generalizations of the famous δ -kicked rotor model, with a cubic nonlinearity as present in the Gross-Pitaevskii equation. We confirm previous results in the regime of localized transport, and show the validity of the predictions of [13] for a wide range of nonlinear coupling strengths. In addition, we found that the quantum resonances of the kicked rotor are very stable with respect to the nonlinear phase perturbation, which loses its effect in the asymptotic limit of large interaction times with periodic driving. Surprising phenomena like pronounced peaks in the momentum distributions at quantum resonance and superballistic intermittent growth of the mean square momentum have been found. Both phenomena are caused by cubic nonlinearity in the evolution, which shows that the analyzed models bear a rich dynamical behavior in parameter space.

Experimental work on the kicked rotor using a Bose-Einstein condensate [1] has mostly concentrated on the short time behavior at quantum resonance or on the so-called antiresonance, where the motion is exactly periodic in the case $u=0$. But an experimental observation of the ballistic quantum resonance dynamics up to 10,...,30 kicks seems possible

[28], for small enough kicking strength k so as to avoid a too fast spread in momentum space which cannot be monitored by standard time-of-flight detection [7,8]. Our results are fully consistent with the few published experimental data, which show that both resonant and antiresonant dynamics essentially survive the presence of small nonlinearities, apart from other effects which damp, for instance, the periodic oscillations at the antiresonance. Such effects are, e.g., the uncertainty of the center of the initial momentum distribution, and fluctuations in the experimental kicking strength [1].

ACKNOWLEDGMENTS

L.R. and R.A. acknowledge partial support from the MIUR-PRIN project “Order and Chaos in Nonlinear Extended Systems: Coherent Structures, Weak Stochasticity and Anomalous Transport,” and the INFM Advanced Project “Weak Chaos: Theory and Applications.” S.W. thanks Professor Ken Taylor for his hospitality and financial support at the Queen’s University of Belfast, where part of the present work originated. Enlightening discussions with Professor E. Arimondo and O. Morsch on the experimental possibilities and with R. Mannella on Lévy statistics are gratefully acknowledged.

-
- [1] L. Deng *et al.*, Phys. Rev. Lett. **83**, 5407 (1999); G. Duffy *et al.*, cond-mat/0401346; cond-mat/0406545.
- [2] C. J. Pethick and H. Smith, *Bose-Einstein Condensation in Dilute Gases*, (Cambridge University Press, Cambridge, U.K., 2002).
- [3] F. Dalfovo *et al.*, Rev. Mod. Phys. **71**, 463 (1999).
- [4] C. Zhang *et al.*, Phys. Rev. Lett. **92**, 054101 (2004).
- [5] S. A. Gardiner *et al.*, Phys. Rev. A **62**, 023612 (2000).
- [6] F. L. Moore *et al.*, Phys. Rev. Lett. **75**, 4598 (1995); H. Ammann *et al.*, *ibid.* **80**, 4111 (1998); J. Ringot *et al.*, *ibid.* **85**, 2741 (2000); M. B. d’Arcy *et al.*, *ibid.* **87**, 074102 (2001); M. P. Sadgrove *et al.*, e-print quant-ph/0401161.
- [7] S. Wimberger, I. Guarneri, and S. Fishman, Nonlinearity **16**, 1381 (2003).
- [8] M. B. d’Arcy *et al.*, Phys. Rev. E **69**, 027201 (2004).
- [9] D. A. Steck *et al.*, Phys. Rev. E **62**, 3461 (2000).
- [10] F. Benvenuto *et al.*, Phys. Rev. A **44**, R3423 (1991).
- [11] See, e.g., A. D. Bandrauk and H. Shen, J. Chem. Phys. **99**, 1185 (1993).
- [12] M. Reed and B. Simon, *Functional Analysis* (Academic Press, San Diego, 1980).
- [13] D. Shepelyansky, Phys. Rev. Lett. **70**, 1787 (1993).
- [14] G. Casati *et al.*, in *Stochastic Behavior in Classical and Quantum Hamiltonian Systems* edited by G. Casati and J. Ford (Springer-Verlag, Berlin, 1979), p. 334.
- [15] F. M. Izrailev, Phys. Rep. **196**, 299 (1990).
- [16] B. V. Chirikov, in *Chaos and Quantum Physics*, edited by M. J. Giannoni, A. Voros, and J. Zinn-Justin (North-Holland, Amsterdam, 1991).
- [17] F. M. Izrailev and D. L. Shepelyansky, Dokl. Akad. Nauk SSSR **249**, 1103 (1979); Teor. Mat. Fiz. **43**, 417 (1980).
- [18] R. Artuso and L. Rebuzzini, Phys. Rev. E **66**, 017203 (2002).
- [19] See, e.g., also O. Morsch *et al.*, Phys. Rev. Lett. **87**, 140402 (2001).
- [20] R. Artuso and L. Rebuzzini, Phys. Rev. E **68**, 036221 (2003).
- [21] T. Kottos and M. Weiss, Phys. Rev. Lett. **93**, 190604 (2004).
- [22] G. Casati *et al.*, Phys. Rev. A **34**, 1413 (1986).
- [23] L. Hufnagel *et al.*, Phys. Rev. E **64**, 012301 (2001).
- [24] M. Stefancich *et al.*, Phys. Rev. E **57**, 6625 (1998).
- [25] S. Wimberger, I. Guarneri, and S. Fishman, Phys. Rev. Lett. **92**, 084102 (2004).
- [26] S. Fishman, I. Guarneri, and L. Rebuzzini, J. Stat. Phys. **110**, 911 (2003).
- [27] G. L. Alfimov *et al.*, Phys. Rev. E **66**, 046608 (2002).
- [28] S. Wimberger, R. Mannella, O. Morsch, and E. Arimondo, Phys. Rev. Lett. cond-mat/0501565.

Experimental verification of a one-parameter scaling law for the quantum and “classical” resonances of the atom-optics kicked rotor

Sandro Wimberger,¹ Mark Sadgrove,² Scott Parkins,² and Rainer Leonhardt²

¹*Dipartimento di Fisica E. Fermi, Università di Pisa, Largo Pontecorvo 3, 56127 Pisa, Italy*

²*Department of Physics, University of Auckland, Private Bag 92019, Auckland, New Zealand*

(Received 11 February 2005; published 12 May 2005)

We present experimental measurements of the mean energy in the vicinity of the first and second quantum resonances of the atom-optics kicked rotor for a number of different experimental parameters. Our data are rescaled and compared with the one-parameter (ϵ) classical scaling function developed to describe the quantum resonance peaks. Additionally, experimental data are presented for the “classical” resonance which occurs in the limit as the kicking period goes to zero. This resonance is found to be analogous to the quantum resonances, and a similar one-parameter classical scaling function is derived, and found to match our experimental results. The widths of the quantum and classical resonance peaks are compared, and their sub-Fourier nature examined.

DOI: 10.1103/PhysRevA.71.053404

PACS number(s): 42.50.Vk, 75.40.Gb, 05.45.Mt, 05.60.-k

I. INTRODUCTION

The heart of experimentally testing and controlling classical and quantum systems often lies in the introduction of an external periodic driving force [1–3]. The driving probes system-specific properties, the knowledge of which allows one, in turn, to understand and to optimally control the system at hand. In particular, driven systems often exhibit resonancelike behavior if the external driving frequency matches the natural frequency of the unperturbed system.

Typical nonlinear classical systems are resonant for only a finite interaction time since the driving itself forces the system to gain energy and hence drift out of resonance. Only if the natural frequencies are independent of the energy, as for the linear (harmonic) oscillator, the system can absorb energy on resonance indefinitely. In the quantum world, the situation may be different by virtue of the unperturbed system possibly having a discrete energy spectrum. If this spectrum shows an appropriate scaling in the excitation quantum number, resonant motion can persist forever.

A simple example of such a system is provided by the free rotor, whose energy spectrum scales quadratically in the excitation quantum number (due to periodic boundary conditions for the motion on the circle). Kicking the rotor periodically in time with a frequency commensurable with the energy difference of two neighboring levels leads to perfectly resonant driving. These so-called quantum resonances of the well-studied kicked rotor (KR) [4] have been known theoretically for some time [5], but the first traces of this example of frequency-matched driving have only recently come to light in experiments with cold atoms [6,7]. Such experiments [7] and theoretical studies [8,9] have also shown the surprisingly robust nature of these resonances in the presence of noise and perturbations.

Experimentally, the quantum resonances of the KR are hard to detect for two principal reasons. First, only a relatively small proportion of atoms are kicked resonantly for the following reason: ideally, the atomic motion is along a line, which introduces an additional parameter, namely, the non-

integer part of the atomic momentum, i.e., the atom’s quasimomentum. Treating the atoms independently, their motion can be mapped onto the circle owing to the spatial periodicity of the standing wave, which makes the quasimomentum a constant of the motion. However, only some values of quasimomentum allow resonant driving to occur [5]. All other values induce a dephasing in the evolution which hinders the resonant kicking of the atoms (see Sec. III for details). Second, if an atom is kicked resonantly it moves extremely quickly; in fact its energy grows quadratically in time (so-called ballistic propagation). These fast atoms quickly escape any fixed experimental detection window after a sufficiently large number of kicks [6,7].

In this paper, we report experimental data which show the behavior of a typical experimental ensemble of cold atoms under resonant driving. Our main observable is the mean energy of the atomic ensemble measured after a fixed number of kicks and scanned over the resonant kicking frequency or period. We verify a recently derived single-parameter scaling law of the resonant peak seen when scanning the energy vs the period [8,10,11]. The scaling law allows us to clearly resolve the resonance peak structure because it reduces the dynamics to a *stationary* and experimentally robust signature of the quantum resonant motion.

After a short review of our experimental setup in Sec. II and the theoretical treatment of the atom-optics kicked rotor close to quantum resonance in Sec. III, we present experimental data for the mean energies around the first two fundamental quantum resonances of the kicked atom. From these data, we extract the afore mentioned scaling law in Sec. IV. The effect of the quasimomentum (as a typical quantum variable) on the motion disappears in the classical limit of the kicked rotor, when the kicking period approaches zero [5,12]. In the latter case, the rotor is constantly driven, and a ballistic motion occurs for *all* members of the atomic ensemble [13]. Both phenomena, the quantum and the “classical” (for vanishing kicking period) resonance, are related to one another by a purely classical theory developed previously for the quantum resonance peaks [8,10,11].

In Sec. V we focus on the first direct comparison of the behavior of the ensemble averaged energies in the case of the “classical” and the quantum resonance. In particular, the sub-Fourier scaling of the resonance peaks in the mean energy as a function of the kick number is discussed. The latter makes both types of resonances studied here a potential source of high-precision measurements of system-specific parameters.

II. EXPERIMENTAL SETUP

Our experimental system is a realization of the paradigmatic kicked rotor model [14,15], whose relevance lies in the fact that it shows the basic features of a complex dynamical system, and it may be used to locally (in energy) approximate much more complicated systems, such as microwave-driven Rydberg atoms [16], or an ion in a particle accelerator [1,17].

Our experiments utilize a cloud of about 10^5 cold cesium atoms, provided by a standard six beam magneto-optical trap (MOT) [18]. The typical momentum spread of the atomic sample lies between four and eight two-photon recoils. The shape of the initial momentum distribution is well approximated by a Gaussian with standard deviation $\sigma_p \approx (4-8) \times 2\hbar k_L$, centered at zero momentum [19], although significant non-Gaussian tails can exist [13]. The width is measured in units of two-photon recoils, corresponding to the wavelength of the kicking laser $\lambda_L = 2\pi/k_L$. The fractional parts in these units of the initial momenta, i.e., the quasimomentum discussed below, are practically uniformly distributed in the fundamental Brillouin zone defined by the periodic kick potential [10].

As shown in Fig. 1, the atoms interact with a pulsed, far-detuned optical standing wave which is created by retroreflecting the light from a 150 mW (slave) diode laser which is injection locked to a lower-power (master) diode laser at a wavelength of $\lambda_L = 852$ nm. Power fluctuations were minimal during the experiments performed here ($\sim 1\%$) although larger drifts occurred over the course of many experimental runs. Accurate pulse timing is achieved using a custom-built programmable pulse generator (PPG) to gate an acousto-optic modulator (AOM) which is programmed by a computer running the RTLINUX™ operating system kernel [20] which controls the timing of the experimental sequence (aside from the pulse train itself). Experimentally, we approximate δ kicks by pulses of width τ_p which are approximately rectangular in shape. The lowest value of τ_p used in our experiments was 240 ns and the highest was 480 ns. For the experiments reported here, the effect of the finite width of the kicking pulses [19,22] turns out to be negligible, since fairly small numbers of kicks (fewer than 20) and low kicking strengths are used. In the case where the $\tau \rightarrow 0$ limit is being investigated experimentally, the δ -kick assumption is clearly not valid [13,21]. This restricts us to a minimum period $\tau = 320$ ns, for $\tau_p = 240$ ns, in our study of the “classical” resonance peaks.

In a typical experimental run, the cooled atoms were released from the MOT and subjected to up to 16 standing wave pulses, then allowed to expand for an additional free drift time in order to resolve the atomic momenta. After this

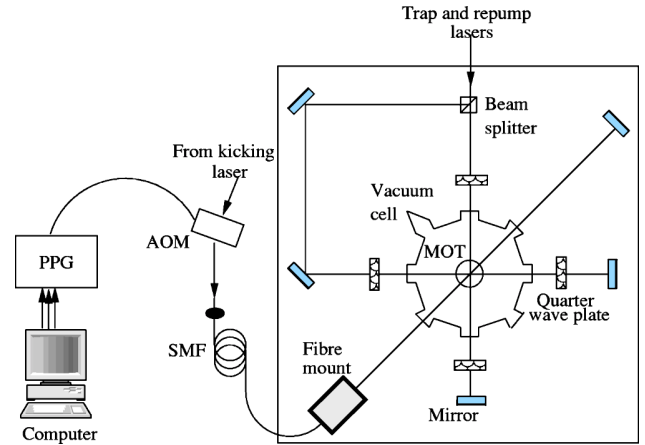


FIG. 1. Schematic diagram of our experimental setup. A standard six-beam magneto-optical trap (MOT) of about 10^5 Cs atoms is formed inside a vacuum cell at the intersection of three retroreflected “trapping” beams [vertical beams and (anti-)Helmholtz coils are not shown]. A standing wave is formed across the cloud of atoms by retroreflecting light from a “kicking laser,” which is transported to the MOT by means of a single-mode fiber (SMF). This light is pulsed on and off by an acousto-optic modulator (AOM) which is gated by a programmable pulse generator (PPG). The PPG’s pulse train is uploaded from a computer, which also controls the timing of the experiment (e.g., when the trapping AOM and anti-Helmholtz coils are turned on and off).

expansion time, the trapping beam is switched on and the atoms are frozen in space by optical molasses. A charge-coupled device image of the resulting fluorescence is recorded and used to infer the momentum distribution of the atoms using standard time-of-flight techniques [6]. The mean energy of the atomic ensemble may then be inferred by calculating the second moment of the experimental momentum distribution.

Kicking laser powers of up to 30 mW were employed, and detunings from the $6S_{1/2}(F=4) \rightarrow 6P_{3/2}(F'=5)$ transition of cesium of 500 MHz and 1 GHz were used for the classical and quantum resonance scans, respectively. These parameters produced spontaneous emission rates of $< 0.5\%$ per kick for the quantum resonance scans, which was low enough to ensure that the structure of the peaks was not affected for the low kick numbers used here.

III. ϵ CLASSICAL DYNAMICS NEAR THE FUNDAMENTAL QUANTUM RESONANCES

We now consider the theoretical treatment of the atom-optics kicked rotor near quantum resonance. The Hamiltonian that generates the time evolution of the atomic wave function is (in dimensionless form) [6,14]

$$H(t') = \frac{p^2}{2} + k \cos(z) \sum_{t=0}^N \delta(t' - t\tau), \quad (1)$$

where p is the atomic momentum in units of $2\hbar k_L$ (i.e., of two-photon recoils), z is the atomic position in units of $2k_L$, t' is time, and t is an integer that counts the kicks. In our

units, the kicking period τ may also be viewed as a scaled Planck constant as defined by the equation $\tau=8E_R T/\hbar$, where $E_R=\hbar^2 k_L^2/2M$ is the recoil energy (associated with the energy change of a cesium atom of mass M after emission of a photon of wavelength $\lambda_L=2\pi/k_L=852$ nm). The dimensionless parameter k is the kicking strength of the system and is proportional to the kicking laser intensity.

An atom periodically kicked in space and time is described by a wave packet $\psi(z)$ decomposed into 2π -periodic Bloch states $\psi_\beta(z)$, that is,

$$\psi(z) = \int_0^1 d\beta \exp(i\beta z) \psi_\beta(z), \quad (2)$$

where β is the quasimomentum (i.e., the fractional part of the momentum p). Quasimomentum is conserved in the evolution generated by Eq. (1), so the different Bloch states in Eq. (2) evolve independently of each other, whereby their momenta can change only by integers by virtue of the kicks. For any given quasimomentum, the dynamics is formally equivalent to that of a rotor (moving on a circle) whose one-period Floquet operator is given by

$$\hat{U}_\beta = e^{-ik \cos(\hat{\theta})} e^{-i\tau(\hat{N} + \beta)^2/2}, \quad (3)$$

where $\theta=z \bmod(2\pi)$, and $\hat{N}=-id/d\theta$ is the angular momentum operator. From Eq. (3) we can immediately derive the two necessary conditions for quantum resonant motion: if $\tau=2\pi r/q$ (r, q integers) then the atomic motion may show asymptotic quadratic growth in energy so long as $\beta=m/2r$, $0 \leq m \leq 2r$, m integer at the same time. Under these conditions the Floquet operator (3) is also periodic in momentum space, with the integer period q . As in previous experimental studies [6], we focus on the first two fundamental quantum resonances $q=1, 2$, for which the amplitudes of Bloch waves with $\beta=1/2$ for $q=2$, and $\beta=0, 1/2$ for $q=1$ at momentum states separated by $q \times 2\hbar k_L$ exactly rephase after each kick. The rephasing condition enforces ballistic propagation of the corresponding states in momentum space, so their energy grows quadratically in time. The remaining Bloch components of the original wave packet (2), with β not in the resonant class, exchange energy with the kicking laser in a quasiperiodic manner. The competition between the resonant and the nonresonant subclasses of Bloch states (between ballistic and quasiperiodic propagation) leads to *linear* growth of the total mean energy $E \approx k^2 t/4$ obtained by incoherently averaging over the continuous set of quasimomenta which constitute the atomic ensemble [8,10,11].

For $q=1, 2$, we write $\tau=2\pi\ell + \epsilon$, where ϵ denotes the detuning from the exact resonance and $\ell=1, 2$. As shown in [10,11], the Floquet operator (3), can then be rewritten as

$$\hat{U}_\beta(t) = e^{-i\tilde{k} \cos(\hat{\theta})/|\epsilon|} e^{-i\hat{I}_\beta^2/|\epsilon|}, \quad (4)$$

with $\tilde{k}=k|\epsilon|$, $\hat{I}_\beta=|\epsilon|\hat{N}$ as rescaled momentum, and

$$\hat{H}_\beta(\hat{I}, t) = \frac{1}{2} \text{sgn}(\epsilon) \hat{I}^2 + \hat{I}(\pi\ell + \tau\beta). \quad (5)$$

Introducing the new variables $J=\pm I + \pi\ell + \tau\beta$, $\vartheta=\theta + \pi[1 - \text{sgn}(\epsilon)]/2$, where \pm denotes the sign of $\epsilon=\text{sgn}(\epsilon)$, the quan-

tum evolution can be approximated by the ϵ classical standard map derived in [10,11,23]:

$$J_{t+1} = J_t + \tilde{k} \sin(\vartheta_{t+1}), \quad \vartheta_{t+1} = \vartheta_t + J_t \quad (6)$$

for $\tilde{k} \ll 1$. J_t implicitly contains the quasimomentum β , which defines the initial conditions in momentum in the phase space generated by the map (6) [8].

For small $|\epsilon|$, the ϵ classical dynamics is quasi-integrable, and the growth of the energy is dominated by the principal ϵ classical resonant island around $J=2\pi$ [1]. The latter island is populated only by the values of β that are close to the resonant ones, while the nonresonant quasimomenta correspond to initial conditions outside the nonlinear resonance island [8,10,11]. Moreover, at any time t , the ratio between the energy and its value at $\epsilon=0$ is a scaling function of the *single* variable

$$x = t\sqrt{k|\epsilon|}. \quad (7)$$

The scaling function (which was explicitly derived in [8,10,11]) is

$$\frac{\langle E_{t,\epsilon} \rangle}{\langle E_{t,0} \rangle} \approx R(x) \equiv 1 - \Psi_0(x) + \frac{4}{\pi x} G(x), \quad (8)$$

with the functions

$$\Phi_0(x) \equiv \frac{2}{\pi} \int_0^x ds \frac{\sin^2(s)}{s^2},$$

and

$$G(x) \approx \frac{1}{8\pi} \int_0^{2\pi} d\theta_0 \int_{-2}^2 dJ_0 \bar{J}(x, \theta_0, J_0)^2.$$

$\bar{J} \equiv J/\sqrt{k}$ is the momentum of the pendulum approximation to the dynamics generated around the stable fixed point of (6), rescaled to unit coupling parameter (see [8,10,11] for details).

The one-parameter scaling law (8) allows us to deduce the shape and the parameter dependence of the resonance peaks elegantly from the experimental data, which in the unscaled form is shown in Figs. 2 and 3 for $\tau=2\pi$ and 4π , respectively.

IV. EXPERIMENTAL VERIFICATION OF THE SCALING LAW AT QUANTUM RESONANCE

We have used the data obtained for various scans of the mean energy vs the kicking period around the quantum resonances $\tau=2\pi$ and 4π , and for kick numbers $t=5, 10, 15$ to extract the ratio $\langle E_{t,\epsilon} \rangle / \langle E_{t,0} \rangle$. We subtract from the numerator the initial energy of the atomic ensemble with the characteristic width in momentum space σ_p . The contribution of $\sigma_p^2/2$ to the energy must be subtracted because the derivation of the scaling function $R(x)$ assumed an initial atomic momentum distribution in the unit interval $[0, 1]$ [10], corresponding to a uniform distribution of quasimomenta $\beta \equiv p_0 \in [0, 1]$. Since the maximum of the resonance peak $\langle E_{t,\epsilon=0} \rangle$ is experimentally the most unstable parameter (due to the early loss

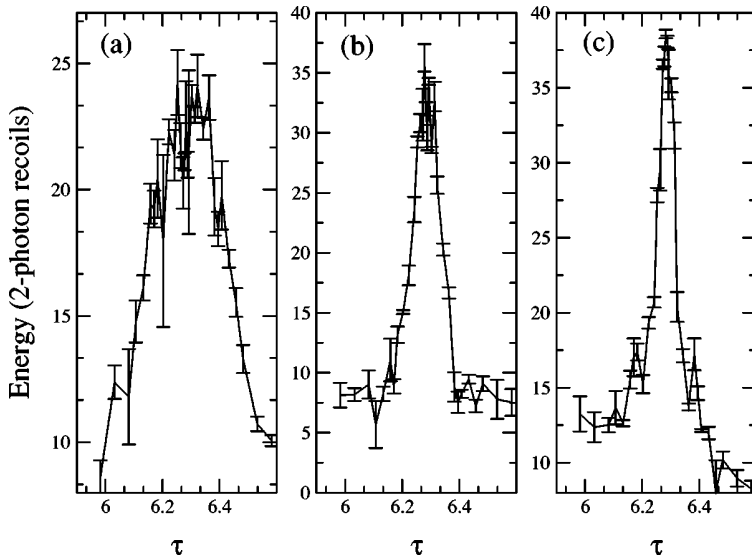


FIG. 2. Experimentally measured mean energies around the first quantum resonance at $\tau = 2\pi$ after (a) 5, (b) 10, and (c) 15 kicks. Error bars show an average over three independent experiments. The kicking strength and initial momentum standard deviation were measured to be $k=4.1\pm 0.6$ and $\sigma_p=5.9\pm 0.2$, respectively. Note that the estimated errors in these parameters do not take into account systematic drifts which take place over the course of experimental runs. The solid line joins the experimental points to aid the eye.

of the fastest resonant atoms from the experimental detection window [6–8]), we use the theoretical value $\langle E_{i,0} \rangle - \sigma_p^2/2 = k^2 t/4$ to rescale our experimental data, rather than the height of the experimental peak itself. Results are presented in Figs. 4 and 5 for $\tau=2\pi$ and 4π respectively. We see very good agreement between the theoretical scaling function $R(x)$ from Eq. (8) and our experimental data. Despite the relatively large experimental errors due to the uncertainty in the determination of σ_p (see discussion below), the data show the characteristic structure, and also the oscillations arising from the contribution of the function $G(x)$ at large $x \geq 8$. These oscillations arise from the averaged contributions of the initial conditions $\bar{J}_0 \in (-2, 2)$ within the principal nonlinear resonance island, which evolve with different frequencies around the corresponding elliptic fixed point of the map (6). The quasimomentum classes contributing to $G(x)$ are thus the near-resonant values, while the nonresonant values contribute to the function $1 - \Phi_0(x)$, which saturates to a constant for large x [8,10,11].

We fitted k and σ_p for each data set and then used these fitted parameters to scale our data. In the case of the $\tau=2\pi$ data, the best-fit value of k was found to be 4.5 compared to the independently measured value of $k=4.1\pm 0.6$. For the $\tau=4\pi$ data, the best fit value of k was 5.2 compared with a measured value of $k=5\pm 0.5$. The corresponding fitted values of σ_p were 5 and 5.2 two-photon recoils, respectively, which differ from the measured values of 4.53 ± 0.02 and 4.3 ± 0.2 . This difference is due to the systematic error involved in determining σ_p from the experimental initial momentum distribution (as discussed in [13]). In particular this distribution may have noisy exponential wings [19] which must be truncated in order to reliably extract the second moment leading to an underestimation of the true initial momentum spread.

It is interesting to note that in Figs. 2 and 3, there is noticeable asymmetry in the resonance peaks. This degree of asymmetry is not predicted by the standard ϵ classical theory and its precise cause has not yet been ascertained. However, the asymmetry most likely stems from one or more systematic experimental effects, including the effect of small

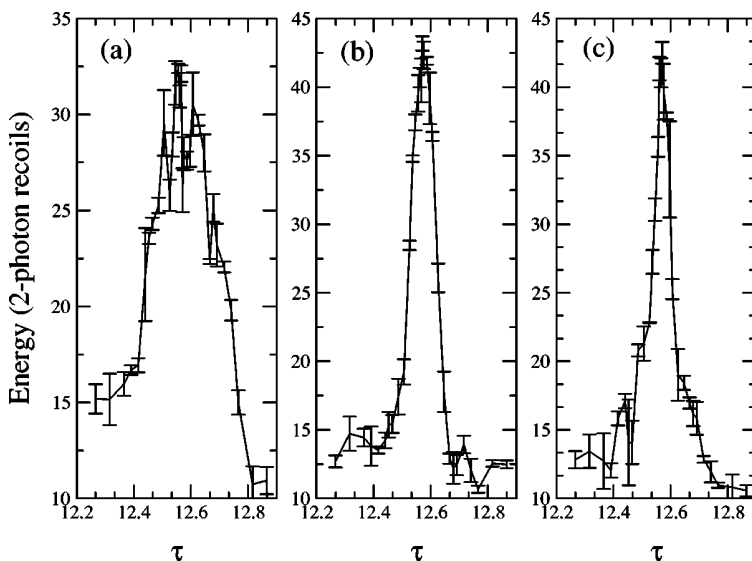


FIG. 3. Experimentally measured mean energies around the second quantum resonance at $\tau = 4\pi$ for (a) 5; (b) 10, and (c) 15 kicks. The kicking strength and initial momentum standard deviation were measured to be $k=5.0\pm 0.5$ and $\sigma_p=6.3\pm 0.1$, respectively. Error bars as in Fig. 2. We note both in this figure and in Fig. 2 that the resonances exhibit some asymmetry, which is thought to be of purely experimental origin (see the discussion in Sec. IV).

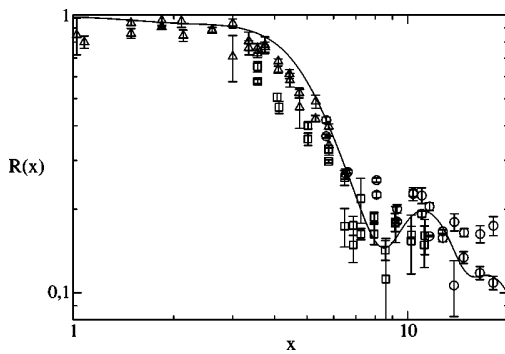


FIG. 4. Experimental mean energies around $\tau=2\pi$ taken from Fig. 2 and rescaled as $(\langle E_{t,\epsilon} \rangle - \sigma_p^2/2)/(tk^2/4)$. Triangles are for $t=5$, squares for $t=10$, and circles for $t=15$. Error bars represent statistical fluctuations over three experiments, and do not take into account fluctuations in k or σ_p . The solid line shows the numerically evaluated scaling function $R(x)$ of Eq. (8). We note that, for 10 and 15 kicks, data for $|\epsilon| < 0.03$ have been omitted due to our inability to accurately resolve atomic energies for fast atoms this close to resonance. Experimental data for both positive and negative values of ϵ are plotted. We would like to note the good correspondence between the ϵ classical prediction and the experimental data for over one order of magnitude in the scaling variable x .

amounts of spontaneous emission ($<0.5\%$ chance per kick for the quantum resonance scans) and also from the slightly lesser time of flight experienced by atoms for positive as opposed to negative ϵ . Asymmetry of the peaks has also been noted in other experiments probing the structure of the quantum resonances [24]. In any case, this asymmetry does not prevent us from observing the structure of the quantum resonances, but leads to a slightly enhanced scatter of the experimental data points in Figs. 4 and 5.

V. CLASSICAL LIMIT OF VANISHING KICKING PERIOD

In spite of the intrinsically quantum nature of the quantum resonances as an example of perfectly frequency-matched driving, the method reviewed in Sec. III allows us to map the

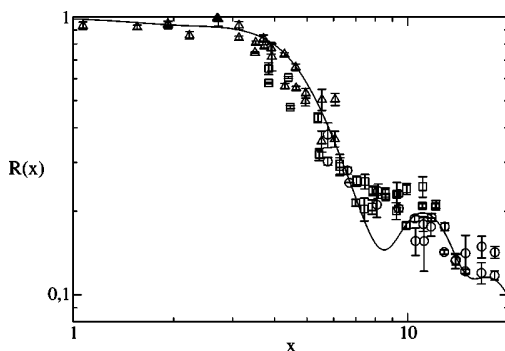


FIG. 5. Scaled experimental mean energies around $\tau=4\pi$ taken from Fig. 3; triangles are for $t=5$, squares for $t=10$, and circles for $t=15$ kicks. The solid line shows the scaling function $R(x)$ from Eq. (8). Again, for 10 and 15 kicks, data too close to resonance, i.e., for $|\epsilon| < 0.03$, have been omitted.

quantum dynamics onto a purely classical map given by (6). The latter map is formally equivalent to the usual standard map, which describes the classical limit of the quantum KR when the kicking period tends to zero [12]:

$$J_{t+1} = J_t + \tilde{k} \sin(\theta_{t+1}), \quad \theta_{t+1} = \theta_t + J_t, \quad (9)$$

now with $J = \tau p = \tau(n + \beta)$ and $\tilde{k} = k\tau$. Because of the analogy between the maps (6) and (9), we expect a scaling law for the mean energy also in the limit $\tau \rightarrow 0$. Since $\tau \rightarrow 0$, all quasimomentum subclasses contribute now similarly to the energy growth, and the averaged energy is given only by the initial conditions within the principal nonlinear resonance island (see [13] for details)

$$\langle E_{t,\tau} \rangle \approx \tau^{-2} \langle (J_t)^2 \rangle / 2 \approx k/2 \tau G_{cl}(x), \quad (10)$$

with

$$G_{cl}(x) \equiv \frac{\sqrt{k}}{2\pi\sqrt{\tau}} \int_0^{2\pi} d\theta_0 \int_0^{\sqrt{\pi k}} dJ_0 \bar{J}(x, \theta_0, J_0)^2 \\ \approx \frac{1}{2\pi} \int_0^{2\pi} d\theta_0 \bar{J}(x, \theta_0, J_0 = 0)^2, \quad (11)$$

which depends on the variable $x = t(k\tau)^{1/2}$ [which, given that $\tau = \epsilon$ for the classical resonance, is the same as the scaling variable given in Eq. (7)] and weakly on k and τ , in *contrast* to the quantum resonant case studied in Sec. III. The dependence of G_{cl} on τ is negligibly small for $\tau \lesssim 1/k$, so that in practice G_{cl} can be viewed as a function of the scaling parameter x alone.

For the ratio $\langle E_{t,\tau} \rangle / \langle E_{t,0} \rangle$ we then arrive at the scaling function

$$\frac{\langle E_{t,\tau} \rangle}{\langle E_{t,0} \rangle} \approx R_{cl}(x) \equiv \frac{2}{x^2} G_{cl}(x), \quad (12)$$

which in the limit of vanishing τ tends to unity, since $G_{cl}(x) \approx x^2/2$ for small x [8,13]. Our result (10) describes *quadratic* growth in mean energy as $\tau \rightarrow 0$. We note again that in the case of quantum resonances, ϵ classical theory predicts only *linear* mean energy growth with kick number at quantum resonance [10,11]. This linear increase is induced by the contribution of most quasimomentum classes which lie *outside* the classical resonance island. For $\tau \rightarrow 0$, almost all initial conditions (or quasimomenta) lie *within* the principal resonance island, which leads to the ballistic growth for the *averaged* ensemble energy (10).

For finite $\tau > 0$ and $t^2 k \gg 1/\tau$, we obtain from (10)

$$\langle E_{t,\tau > 0} \rangle \approx \frac{k}{2\tau} \alpha, \quad (13)$$

since G_{cl} saturates to the value $\alpha \approx 0.7$ for large x . Within the stated parameter range, this result implies dynamical freezing—the ensemble's mean energy is independent of kick number. This phenomenon is a classical effect in a system with a regular phase space, and was observed in [13] for the first time. It is distinct from dynamical localization which is the quantum suppression of momentum diffusion for a chaotic phase space [4,12]. Experimentally, the freezing ef-

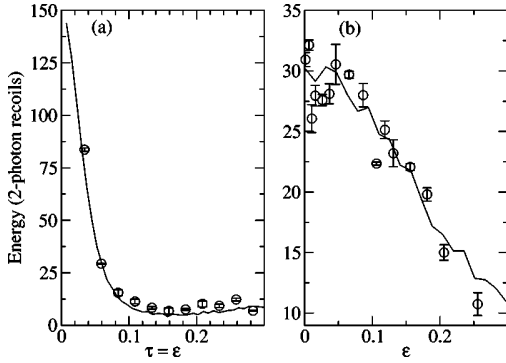


FIG. 6. (a) Circles show experimentally measured mean energies as $\tau \rightarrow 0$ after 5 kicks. The measured value of k is 4.9 ± 0.2 . The solid line is classical data for $k=4.9$, as generated by the map (9), using practically the same initial momentum distribution as in the experiment. The thermal energy $\sigma_p^2/2$ has been subtracted to facilitate comparison with the quantum resonance curve in (b). In (b), circles show experimental data after 5 kicks near the second quantum resonance for positive $\epsilon = \tau - 4\pi$ and the experimental parameters are as given for Fig. 3. The thermal energy $\sigma_p^2/2$ has been subtracted. The solid line shows ϵ classical data as generated by the map (6).

fect corresponds to the cessation of energy absorption from the kicks, similar (but different in origin) to that which occurs at dynamical localization. The freezing may be explained as the averaging over all trajectories which start at momenta close to zero, and move with different frequencies about the principal elliptic fixed point of the map (9).

From Eq. (12), we immediately see that for the “classical” resonance $\tau \rightarrow 0$, the resonant peak width scales in time like $(kt^2)^{-1}$, as at the quantum resonances studied in Secs. III and IV. However, the tails of the classical resonance peak decay faster (proportionally to $1/x^2$) than those at quantum resonance [proportionally to $1/x$; cf. Eq. (8)]. This very fast shrinking of both types of resonance peaks is compared in Figs. 6 and 7.

Both types of these sensitive resonance peaks may serve as an experimental tool for determining or calibrating parameters in a very precise manner. Additionally, we note that the quadratic scaling in time at the quantum resonances and the “classical” resonance, respectively, is much faster and hence much more sensitive than the sub-Fourier resonances detected in a similar context by Szriftgizer and co-workers [25]. A detailed study of the quantum energy spectrum of the kicked atoms close to the two types of resonances is under way to clarify the origin of the observed sub-Fourier scaling of the resonance peaks.

Finally, we have plotted rescaled experimental data for the $\tau \rightarrow 0$ resonance against the scaling function of Eq. (12), as seen in Fig. 8. The scaling was performed using the fitted parameters as given in Figs. 6 and 7. We note that it is more difficult to extract the scaling from experimental data in the classical case, as opposed to the quantum case, because the peak of the extremely narrow resonance is difficult to probe. This leads to a larger uncertainty in the scaled energy and the points appear somewhat more scattered than those in Figs. 4 and 5. However, the points clearly agree much better with

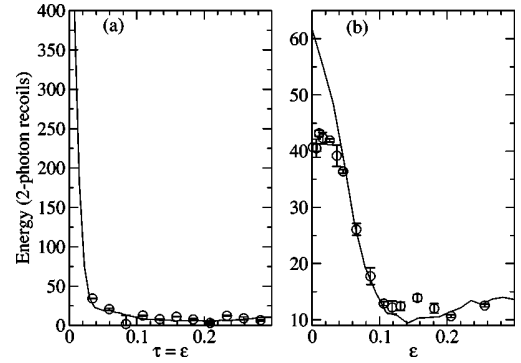


FIG. 7. (a) Circles show experimental data as $\tau \rightarrow 0$ for 10 kicks. The other experimental parameters are the same as those given for Fig. 6(a). The circles in (b) show experimental data once again for the second quantum resonance after 10 kicks this time. Other experimental parameters are the same as those given for Fig. 6(b). We note that for the quantum resonance in (b), the simulation and experimental results differ most markedly near the resonance peak. In this region ($\epsilon \leq 0.03$), some fast, resonant atoms are being lost from the experimental viewing area leading to a lower energy growth rate than predicted theoretically (see discussion in Secs. I and II). Note that in (a) it is not possible to probe low values of $\tau = \epsilon$ due to the finite width of the pulses.

the classical scaling function from (12) than the ϵ classical scaling function (8) which is shown in Fig. 8 as a dash-dotted line. The clearly different scaling of the quantum and the “classical” resonant peaks goes along with the same rates at which the peaks become narrower with time in a sub-Fourier manner.

VI. CONCLUSIONS

In summary, we have experimentally confirmed a theoretically predicted one-parameter scaling law for the resonance peaks in the mean energy of a periodically kicked cold

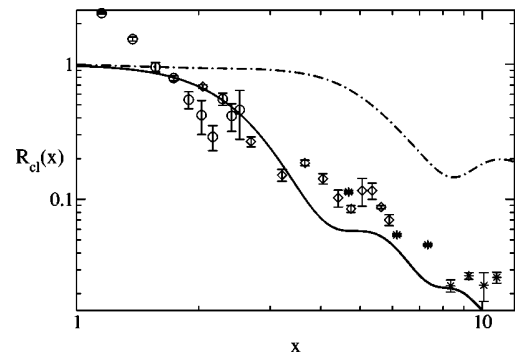


FIG. 8. Rescaled experimental mean energies for $\tau = 0.033 - 0.284$ (corresponding to $0.32 - 2.75 \mu\text{s}$). The data are for $k=4.9$ with $t=3$ (circles), 7 (diamonds), and 16 (stars). Error bars indicate statistical fluctuations over three experiments, and do not include variations in k or σ_p . The solid line shows the classical scaling function of Eq. (12). The dash-dotted line shows the scaling function from Eq. (8) (valid for the quantum resonances) for comparison.

atomic ensemble. This scaling of the resonant peaks is universal, in the sense that it reduces the dependence from all the system's parameters to just one combination of such variables. Furthermore, the scaling theory works in principle for arbitrary initial momentum distributions. In particular, it is valid for the experimentally relevant uniformly distributed quasimomenta at the fundamental quantum resonances of the kicked atoms. In the classical limit of vanishing kicking period, the dependence on quasimomentum, as an intrinsic quantum variable, disappears entirely, leading to a simpler version of the scaling law. The discussed scaling of the experimental data offers one the possibility to clearly observe the quantum and "classical" resonant peak structures over more than one order of magnitude in the scaling variable. Furthermore, its sensitive dependence on the system's parameters may be useful for high-precision calibration and measurements.

It will be of great interest to clarify whether a similar universal scaling law can be found for other time-dependent systems, such as the close-to-resonant dynamics of the kicked harmonic oscillator [26], or the driven Harper model [27,28]. As with the atom-optics kicked rotor, both of the latter systems may be readily realized in laboratory experiments [29,30].

ACKNOWLEDGMENTS

M.S. thanks T. Mullins for his assistance in the laboratory prior to these experiments and acknowledges support from the Tertiary Education Commission of New Zealand, Grant No. 03131. S.W. warmly thanks Professor Ennio Arimondo and Dr. Andreas Buchleitner for useful discussions and logistical support, and acknowledges funding by the Alexander von Humboldt Foundation and the Scuola di Dottorato di G. Galilei della Università di Pisa.

- [1] A. L. Lichtenberg and M. A. Lieberman, *Regular and Chaotic Dynamics* (Springer, Berlin, 1992).
- [2] J. E. Bayfield, *Quantum Evolution: An Introduction to Time-Dependent Quantum Mechanics* (Wiley, New York, 1999).
- [3] W. Demtröder, *Laser Spectroscopy: Basic Concepts and Instrumentation* (Springer, Berlin, 2003).
- [4] G. Casati *et al.*, in *Stochastic Behavior in Classical and Quantum Hamiltonian Systems*, edited by G. Casati and J. Ford (Springer, Berlin, 1979), p. 334.
- [5] F. M. Izrailev and D. L. Shepelyansky, *Sov. Phys. Dokl.* **24**, 996 (1979); F. M. Izrailev, *Phys. Rep.* **196**, 299 (1999).
- [6] W. H. Oskay *et al.*, *Opt. Commun.* **179**, 137 (2000); M. E. K. Williams *et al.*, *J. Opt. B: Quantum Semiclassical Opt.* **6**, 28 (2004); G. Duffy *et al.*, *Phys. Rev. E* **70**, 056206 (2004).
- [7] M. B. d'Arcy *et al.*, *Phys. Rev. Lett.* **87**, 074102 (2001); *Phys. Rev. E* **69**, 027201 (2004); M. Sadgrove *et al.*, *ibid.* **70**, 036217 (2004).
- [8] S. Wimberger, Ph.D. thesis, University of Munich and Università degli Studi dell' Insubria, 2004, available at <http://edoc.ub.uni-muenchen.de/archive/00001687/>
- [9] S. Wimberger, R. Mannella, O. Morsch, and E. Arimondo, *Phys. Rev. Lett.* **94**, 130404 (2005); L. Rebuzzini, S. Wimberger, and R. Artuso, *Phys. Rev. E* **71**, 036220 (2005).
- [10] S. Wimberger, I. Guarneri, and S. Fishman, *Nonlinearity* **16**, 1381 (2003).
- [11] S. Wimberger, I. Guarneri, and S. Fishman, *Phys. Rev. Lett.* **92**, 084102 (2004).
- [12] S. Fishman, in *Quantum Chaos*, Proceedings of the International School of Physics "Enrico Fermi", Course CXIX, edited by G. Casati *et al.* (IOS, Amsterdam, 1993).
- [13] M. Sadgrove, S. Wimberger, S. Parkins, and R. Leonhardt, *Phys. Rev. Lett.* (to be published).
- [14] R. Graham, M. Schlautmann, and P. Zoller, *Phys. Rev. A* **45**, R19 (1992).
- [15] F. L. Moore *et al.*, *Phys. Rev. Lett.* **75**, 4598 (1995).
- [16] G. Casati, I. Guarneri, and D. Shepelyansky, *IEEE J. Quantum Electron.* **24**, 1420 (1988); S. Wimberger and A. Buchleitner, *J. Phys. A* **34**, 7181 (2001).
- [17] B. V. Chirikov, *Phys. Rep.* **52**, 263 (1979).
- [18] C. Monroe, W. Swann, H. Robinson, and C. Wieman, *Phys. Rev. Lett.* **65**, 1571 (1990).
- [19] B. G. Klappauf, W. H. Oskay, D. A. Steck, and M. G. Raizen, *Physica D* **131**, 78 (1999).
- [20] FSMLabs Inc., http://www.fsmlabs.com/products/rtlinuxpro/rtlinuxpro_faq.html
- [21] M. Sadgrove, T. Mullins, S. Parkins, and R. Leonhardt, *Phys. Rev. E* **71**, 027201 (2005).
- [22] R. Blümel, S. Fishman, and U. Smilansky, *J. Chem. Phys.* **84**, 2604 (1986).
- [23] S. Fishman, I. Guarneri, and L. Rebuzzini, *J. Stat. Phys.* **110**, 911 (2003); *Phys. Rev. Lett.* **89**, 084101 (2002).
- [24] M. Hoogerland, S. Wayper, and W. Simpson (unpublished).
- [25] P. Szriftgiser, J. Ringot, D. Delande, and J. C. Garreau, *Phys. Rev. Lett.* **89**, 224101 (2002); H. Lignier, J. C. Garreau, P. Szriftgiser, and D. Delande, *Europhys. Lett.* **69**, 327 (2005).
- [26] G. M. Zaslavsky *et al.*, *Weak Chaos and Quasi-Regular Patterns* (Cambridge University Press, Cambridge, U.K., 1992); D. Shepelyansky and C. Sire, *Europhys. Lett.* **20**, 95 (1992); F. Borgonovi and L. Rebuzzini, *Phys. Rev. E* **52**, 2302 (1995); A. R. R. Carvalho and A. Buchleitner, *Phys. Rev. Lett.* **93**, 204101 (2004).
- [27] P. Leboeuf, J. Kurchan, M. Feingold, and D. P. Arovas, *Phys. Rev. Lett.* **65**, 3076 (1990); T. Geisel, R. Ketzmerick, and G. Petschel, *ibid.* **66**, 1651 (1991); R. Artuso *et al.*, *ibid.* **69**, 3302 (1992); I. Guarneri and F. Borgonovi, *J. Phys. A* **26**, 119 (1993); I. Dana, *Phys. Rev. E* **52**, 466 (1995).
- [28] O. Brodier, P. Schlagheck, and D. Ullmo, *Phys. Rev. Lett.* **87**, 064101 (2001); A. R. Kolovsky and H. J. Korsch, *Phys. Rev. E* **68**, 046202 (2003).
- [29] H.-J. Stöckmann, *Quantum Chaos: An Introduction* (Cambridge University Press, Cambridge, U.K., 1999); T. M. Fromhold *et al.*, *Nature (London)* **428**, 726 (2004).
- [30] S. A. Gardiner, J. I. Cirac, and P. Zoller, *Phys. Rev. Lett.* **79**, 4790 (1997); S. A. Gardiner *et al.*, *Phys. Rev. A* **62**, 023612 (2000).

The role of quasi-momentum in the resonant dynamics of the atom-optics kicked rotor

Sandro Wimberger¹ and Mark Sadgrove²

¹ CNR-INFM and Dipartimento di Fisica Enrico Fermi, Università di Pisa, Largo Pontecorvo 3, 56127 Pisa, Italy

² Department of Physics, University of Auckland, Private Bag 92019, Auckland, New Zealand

E-mail: saw@pks.mpg.de

Received 20 May 2005, in final form 15 August 2005

Published 22 November 2005

Online at stacks.iop.org/JPhysA/38/10549

Abstract

We examine the effect of the initial atomic momentum distribution on the dynamics of the atom-optical realization of the quantum kicked rotor. The atoms are kicked by a pulsed optical lattice, the periodicity of which implies that quasi-momentum is conserved in the transport problem. We study and compare experimentally and theoretically two resonant limits of the kicked rotor: in the vicinity of the quantum resonances and in the semiclassical limit of the vanishing kicking period. It is found that for the *same* experimental distribution of quasi-momenta, significant deviations from the kicked rotor model are induced close to quantum resonance, while close to the classical resonance (i.e. for a small kicking period) the effect of the quasi-momentum vanishes.

PACS numbers: 42.50.Vk, 32.80.Qk, 05.45.Mt, 05.60.–k

1. Introduction

The past decade has brought fascinating advances in the preparation and control of single particles [1]. Atoms can now be cooled down to a level where the effect of a single photon recoil can be measured experimentally [2]. Single atom dynamics can thus be controlled with a high precision by introducing an external field in the form of an optical potential [3, 4].

A particular example of such a system, the atom-optics kicked rotor, has shed light on interesting and paradigmatic quantum effects including dynamical localization [3] and quantum resonance [5–8]. In all such experiments, control of the initial conditions in phase space is essential. In particular, the impact of different momentum classes on the dynamics near quantum resonance was explained recently [9, 10]. The atoms are kicked by a spatially periodic potential which is pulsed on at a certain frequency. As dictated by the standard Bloch theory, the spatial periodicity implies that the quasi-momentum for the centre-of-mass

motion of each atom is conserved during the evolution. Quasi-momentum is an intrinsically quantum variable which arises due to the translational symmetry of the problem [11]. Since experiments with cold atoms typically use a broad, continuous distribution of quasi-momenta, the experimental data represent a result averaged over this initial distribution [9, 10, 12, 13].

The averaging over different momentum classes leads to significant deviations from the standard δ -kicked rotor model [14, 15] which typically does not consider the additional control parameter introduced by the quasi-momentum. Such deviations have been experimentally observed, in particular at quantum resonance [9] and have been explained theoretically by means of a new pseudo-classical model introduced in [16] and applied to the usual δ -kicked rotor in [10, 17].

In this paper, we use the same theoretical formalism to expose the innate similarities and surprising differences between the limit in which the exact quantum resonant driving is approached and the limit of vanishing kicking period. The former limit can be described using the pseudo-classical model from [10, 17] (with an effective Planck constant defined by the detuning from exact resonance), whilst the latter limit is the usual classical limit of the kicked rotor (with the scaled kicking period as the effective Planck constant). Our theoretical analysis of the experimental data focuses on the role of the quasi-momentum, which proves to be quite different in the two ‘classical’ limits studied here.

2. The atom-optics kicked rotor

We consider a system of caesium atoms in an optical standing wave (with wave number k_L) which is δ -pulsed with period τ . For sufficiently large detuning from the atomic absorption line, the Hamiltonian for an atom is given by [18]

$$H(t') = \frac{p^2}{2} + k \cos(z) \sum_{t=0}^N \delta(t' - t\tau), \quad (1)$$

where p is the atomic momentum in units of $2\hbar k_L$ (i.e., in units of two-photon recoils), z is the atomic position in units of $2k_L$, t' is time and t is the kick number. The scaled kicking period τ is defined by the equation $\tau = 8E_R T/\hbar$, where $E_R = \hbar^2 k_L^2 / 2M$ is the recoil energy (associated with the energy change of a caesium atom of mass M after emission of a photon of wavelength $\lambda_L = 2\pi/k_L = 852$ nm). The kicking strength of the system is given by $k = V_0\tau/\hbar$ where V_0 is the maximum potential depth created by the optical standing wave [3, 18].

Experimentally, momentum kicks are delivered to the atoms by an optical lattice which is created by a 150 mW diode laser injection locked to a lower power feedback stabilized source at 852 nm. Kicking laser powers of up to 30 mW were employed for detunings of 500 MHz from the $6S_{1/2}(F = 4) \rightarrow 6P_{3/2}(F' = 5)$ transition of caesium. For the experimental results presented in this paper, the average energy of the atomic ensemble was measured after up to 20 kicks. To control the pulse timing, a custom-built programmable pulse generator was employed to gate an acousto-optic modulator which controlled the amount of kicking light reaching the atomic sample. Timing of the experiment was controlled by a real-time, software based computer system with a latency on the order of 10 μ s.

For the classical resonance experiments reported here, the kicking pulse width was 320 ns, whilst for the quantum resonance results, a 480 ns pulse width was used. In the classical limit of vanishing kicking period, the δ -kick approximation is violated in the experiment (although for the small kick numbers and kicking strengths used here, our results do not show deviations from the δ -kick theory [19–21]). As a consequence, it is possible to probe the dynamics at

exact *quantum* resonance, but not at the exact classical limit, since the pulse period τ should always exceed the pulse width to ensure a reliable approximation to δ -pulses.

The experimental sequence ran as follows: atoms were released from the magneto-optical trap [2] and then kicked by a series of light pulses. A free expansion time of 12 ms was then allowed followed by ‘freezing’ of the atomic motion in optical molasses and subsequent CCD imaging of the resultant atomic cloud [8]. Mean energies are extracted from the raw data by calculating the second moment of the experimentally measured momentum distribution of the atoms’ centre-of-mass motion.

By exploiting the spatial periodicity of the Hamiltonian (1), the atomic dynamics along the z -axis can be reduced to that of a rotor on a circle by Bloch’s theorem [10]. This introduces the additional parameter $\beta \in [0, 1)$ which represents the atomic quasi-momentum—a constant of the motion by Bloch’s theorem. The fractional part of the physical momentum p in the units given above corresponds to the quasi-momentum which is practically uniformly distributed in the fundamental Brillouin zone defined by the periodic kick potential [10]. The one-kick propagation operator for a given atom is [10]

$$\hat{U}_\beta = e^{-ik \cos(\hat{\theta})} e^{-i\tau(\hat{N}+\beta)^2/2}, \quad (2)$$

where $\theta = x \bmod(2\pi)$, and $\hat{N} = -id/d\theta$ is the angular momentum operator with periodic boundary conditions.

3. Unifying classical description of quantum and classical resonance

The quantum dynamics in the two semiclassical limits studied here is approximated by the following map [12, 17]:

$$I_{t+1} = I_t + \tilde{k} \sin(\theta_{t+1}), \quad \theta_{t+1} = \theta_t \pm I_t + \ell\pi + \tau\beta \bmod(2\pi), \quad (3)$$

where $\tau = 2\pi\ell + \epsilon$ and $\tilde{k} = k|\epsilon|$, and $\ell = 0, 1, 2$ (\pm is the sign of ϵ , and for $\ell = 0$ only $+$ is allowed). The above map is similar to the well-studied standard map [22] augmented by the term $\tau\beta$ which accounts for the experimental quasi-momentum distribution. Changing variables to $J = \pm I + \ell\pi + \tau\beta$, $\vartheta = \theta + \pi(1 - \text{sign}(\epsilon))/2$ formally gives the true standard map

$$J_{t+1} = J_t + \tilde{k} \sin(\vartheta_{t+1}), \quad \vartheta_{t+1} = \vartheta_t + J_t. \quad (4)$$

The mean energy is calculated using the formula

$$\langle E_{t,\epsilon} \rangle = \epsilon^{-2} \langle I_t^2 \rangle / 2 = \epsilon^{-2} \langle \delta J_t^2 \rangle / 2, \quad \delta J_t = J_t - J_0. \quad (5)$$

Although the map (4) is not explicitly dependent on the additional β -dependent term, we note that the initial conditions in momentum space are given by $J_0 = \pm I_0 + \pi\ell + \tau\beta$, i.e., they are defined by the initial choice of quasi-momentum β .

Two *a priori* quite different regimes are described by either of the two maps (3) or (4): firstly that for $\ell = 0$ and $\tau \rightarrow 0$, and secondly that for $\ell > 0$, $\tau \rightarrow 2\pi\ell$, for the integer ℓ . In the case where $\ell = 0$ we have $\epsilon = \tau$ and $J = \tau p$, with the physical momentum p in units of two-photon recoils [12]. For the integer $\ell > 0$, the map in (4) approximates the dynamics near the fundamental quantum resonances occurring at $\tau = 2\pi\ell$. As shown in [10, 17], the one-kick propagator (2) may be rewritten in the form

$$\hat{U}_\beta(t) = e^{-i\tilde{k} \cos(\hat{\theta})/|\epsilon|} e^{-i\hat{H}_\beta/|\epsilon|}, \quad (6)$$

where $\epsilon = \tau - 2\pi\ell$, $\tilde{k} = |\epsilon|k$, $\hat{I} = |\epsilon|\hat{N}$ and $\hat{H}_\beta = \frac{1}{2} \text{sign}(\epsilon)\hat{I}^2 + \hat{I}(\pi\ell + \tau\beta)$. Considering $|\epsilon|$ to be an effective Planck constant, we see that the map given in equation (3) approximates the dynamics induced by (2) in both classical limits for $\epsilon \rightarrow 0$.

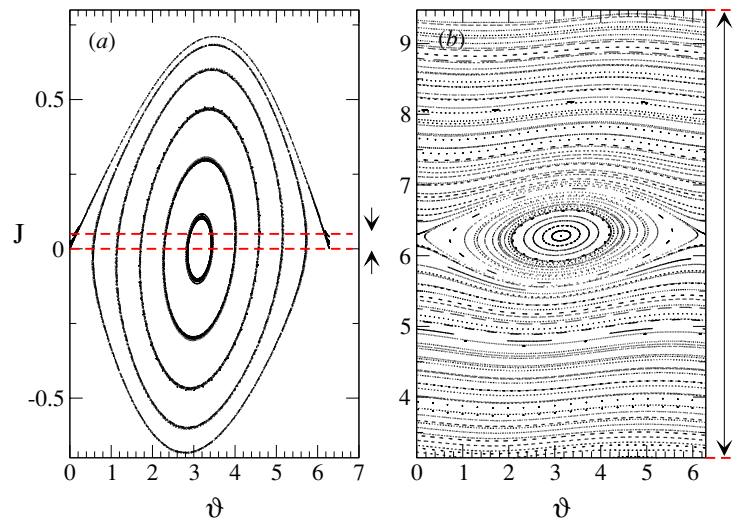


Figure 1. A phase-space portrait generated by the map (4) for $k = 2.5$ and $\epsilon = 0.05$. The initial angles θ_0 were uniformly distributed in $[0, 2\pi)$ whilst the initial momenta J_0 were taken from uniform distributions on the two different intervals $[0, \epsilon)$ (a) and $[\pi, 3\pi + \epsilon)$ (b) as shown by the arrows in both figures. Note that the phase space is 2π -periodic along the J -axis.

Figure 1 demonstrates the essential difference between the two semiclassical limits studied here. In the case where $\ell = 0$ (see figure 1(a)), a uniform quasi-momentum distribution on $[0, 1)$ leads to the initial momenta J_0 being uniformly distributed on the interval $[0, \sigma_p \epsilon)$, where σ_p is the characteristic width of the initial atomic momentum distribution in units of two-photon recoils. Therefore, for $\sigma_p \sim 1$, the initial momenta lie entirely within the region of phase space dominated by the nonlinear resonance island of the standard map. For $\ell = 1$ (see figure 1(b)), and the *same* uniform quasi-momentum distribution, the initial momenta populate the full unit cell $[\pi, 3\pi)$ in the periodic phase space which encompasses not only the nonlinear resonance island at $J = 2\pi$, but also regular ‘rotation’ motion beyond it. Therefore the same experimental quasi-momentum distribution leads to different behaviour of the atomic ensemble in the two limits of $\ell = 0$ and $\ell \neq 0$.

On the basis of the maps (3) and (4), useful results were previously derived for the analysis of experimental data [12, 17]. These results may be summarized by the following single-parameter scaling functions which differ for the two limits of interest here. For $\ell = 0$, the scaling function of the mean energy close to $\epsilon = \tau = 0$ is given by

$$\frac{\langle E_{t,\tau} \rangle}{\langle E_{t,0} \rangle} \approx R_{\text{cl}}(x) \equiv \frac{2}{x^2} G_{\text{cl}}(x), \quad (7)$$

with $x = t\sqrt{k|\epsilon|}$ and the function G_{cl} defined by

$$G_{\text{cl}}(x) \approx \frac{1}{2\pi} \int_0^{2\pi} d\theta_0 \bar{J}(x, \theta_0, J_0 = 0)^2, \quad (8)$$

where $\bar{J} \equiv J/\sqrt{k}$ is the momentum of the pendulum approximation to the dynamics generated by the map of equation (3) as defined previously in [10, 17].

For $\ell > 0$, we have instead close to $\epsilon = 0$

$$\frac{\langle E_{t,\epsilon} \rangle}{\langle E_{t,0} \rangle} \approx R_q(x) \equiv 1 - \Phi_0(x) + \frac{4}{\pi x} G_q(x), \quad (9)$$

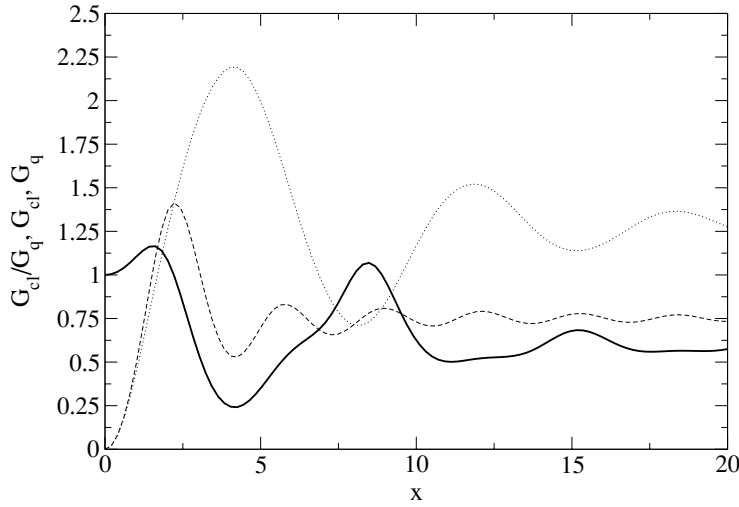


Figure 2. The ratio $G_{\text{cl}}/G_{\text{q}}$ (solid line) is shown along with the functions G_{cl} (dashed line) and G_{q} (dotted line) themselves. The ratio saturates to a constant for a large x after initial oscillations, as the classical and quantum resonance peaks decay at the same rate. The differences between the two scaling functions arise due to the different initial conditions in phase space in the classical and ϵ -classical limits (see figure 1).

with different functions Φ_0 and G_q . In this case, we have

$$G_q(x) \approx \frac{1}{8\pi} \int_0^{2\pi} d\theta_0 \int_{-2}^2 dJ_0 \bar{J}(x, \theta_0, J_0)^2. \quad (10)$$

The difference between the two scaling functions G_{cl} and G_{q} may be seen in figure 2 where the ratio of the two functions is plotted along with the functions themselves. Although the functions have the same slope for small x , their forms differ in general and for a large x , the ratio saturates to a constant less than 1. The difference in the saturation values of the two G functions arises from the different initial conditions in the phase space of map (3) which apply in the classical and ϵ -classical limits.

In the following section, we compare experimental data for the two different cases $\ell = 0$ and $\ell = 1, 2$ guided by the theoretical results reviewed in the present section.

4. Experimental versus theoretical results

In figure 3, experimentally measured energies close to the classical and quantum resonances are plotted against the kick number. In both plots of this figure, the observed oscillatory behaviour may be understood in terms of the pendulum approximation to the dynamics of the map (4) as embodied by the functions $G_{\text{cl}}(x)$ or $G_{\text{q}}(x)$ [10, 12, 17, 23]. For small times ($t < 5$ for the data in figure 3(a)), the energy growth near the classical resonance is *ballistic*, i.e., the energy grows quadratically in time.

We note that ballistic motion is also predicted to occur at quantum resonance for an atomic ensemble with a very narrow initial momentum distribution [24, 25]. But the broad initial momentum distribution present in cold atom experiments as discussed here, typically leads to a uniform distribution of all possible values of quasi-momentum [9, 10]. In terms of the classical model reviewed in the previous section, these experimental initial conditions correspond to initial momenta distributed over the full phase-space cell, as shown in figure 1(b). The majority of the atoms obey rotational motion with almost constant energies (see figure 1(b)), whilst only a small sub-class follows the motion inside the nonlinear resonance

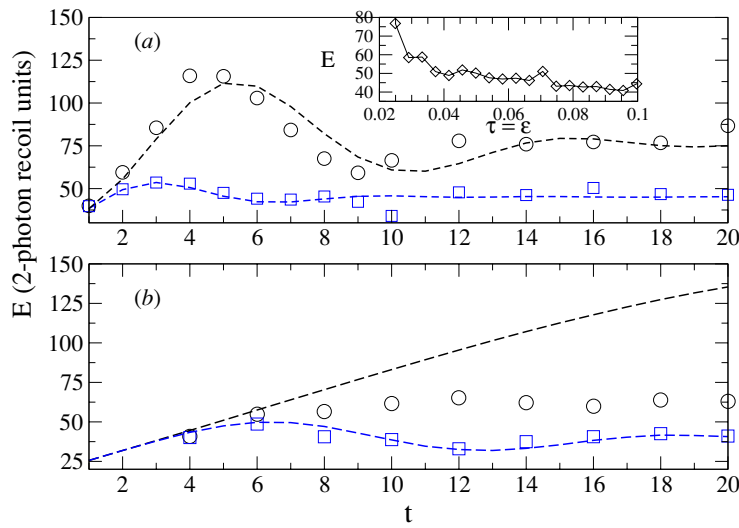


Figure 3. Experimental measurements of the mean energy as a function of kick number for $k \approx 5$, taken for small values of the detuning ϵ in the limits $\tau \rightarrow 0$ (a) and $\epsilon \rightarrow 0$ for $\ell = 1$ (b). In particular, we have (a) $\epsilon = 0.033$ (circles) and $\epsilon \approx 0.08$ (squares), and (b) $|\epsilon| \lesssim 0.005$ (circles) and $\epsilon \approx 0.08$ (squares), along with classical simulations using the map (4) (dashed lines). We note the oscillatory nature of the energy curve for finite detuning ϵ , which may be viewed as a consequence of the dynamics represented by the phase spaces in figure 1. The inset in (a) shows a detailed experimental scan of the classical resonance peak as $\tau = \epsilon \rightarrow 0$, for $k \approx 2.5$ and after $t = 5$ kicks.

island, which for a finite time (depending on the detuning ϵ) supports ballistic energy growth [10, 17].

The connection between the dynamics in the classical limit and that for a quantum particle starting from a momentum eigenstate is found in the term $\tau\beta$ in the map (3). We see that this term may become zero in either of the following limits: $\tau \rightarrow 0$ or $\beta \rightarrow 0$. In both cases, the effect is to regain ballistic energy growth. The inset in figure 3(a) shows a detailed scan of the mean energy near the classical resonance as $\tau \rightarrow 0$ which emphasizes the rapid energy growth seen in this regime associated with the ballistic classical resonance.

Figure 3(b) shows mean-energy measurements at exact quantum resonance (circles) and for $\epsilon \approx 0.08$ along with ϵ -classical simulation results (dashed lines). For *the same experimental momentum distribution*, only linear mean-energy growth is predicted to occur at exact quantum resonance. Additionally, the data shown here demonstrate a practical problem which arises from the uniform distribution of quasi-momenta over the first Brillouin zone. Because only the quasi-momentum classes $\beta \approx 1/2$ (for $\ell = 1$) and $\beta \approx 0, 1/2$ (for $\ell = 2$) experience quantum resonant dynamics [9, 10, 15], only a small number of resonant atoms are responsible for the linear growth of the ensemble mean energy. The measurement of the mean energy at exact quantum resonance is therefore experimentally very challenging since the signal-to-noise ratio is low for the small population of resonant atoms [5, 7, 9, 10]. This is the most likely cause of the apparent saturation of energy growth in the quantum resonance case as seen in figure 3(b) where the experimental mean energy (circles) noticeably deviates from the expected linear growth (dashed line). Indeed, an inspection of the experimental momentum distributions for the on-resonance data reveals that the characteristic ballistic wings associated with resonant atoms [9] are not resolved for kick numbers greater than about 6 in these experiments.

By comparison with the data in figure 3(a) for the classical resonance, we see that, even though the maximum energy is much larger than that measured at quantum resonance for the

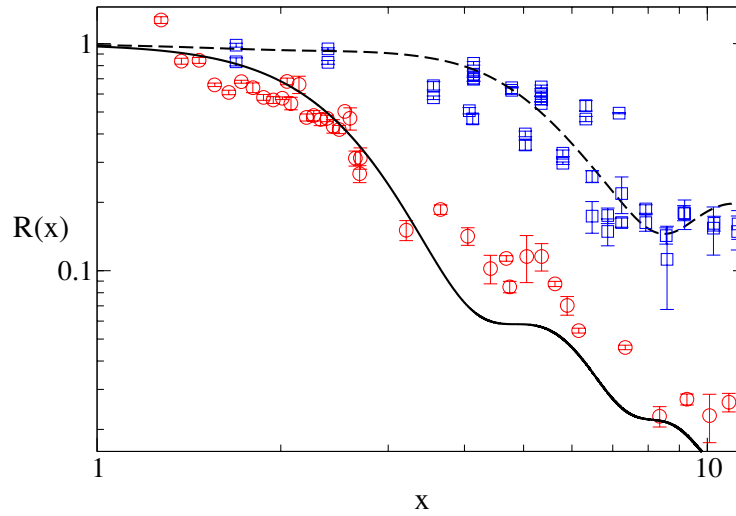


Figure 4. Rescaled experimental mean energies near classical resonance (circles), and the quantum resonances at $\tau = 2\pi$ and 4π (squares). In particular, the circles for $x \lesssim 3$ are rescaled data from the inset of figure 3(a). The mean energies have been scaled by the theoretical peak height of the resonances, i.e., by $k^2 t^2/4$ for the classical resonance [12] and $k^2 t/4$ for the quantum resonance data [10, 17]. The scaling functions for the classical (7) and quantum resonances (9) are shown as a solid line and a dashed line, respectively. The narrower width of the classical resonance peak is immediately apparent. This figure also shows the utility of the scaling function of data which is meaningful in the scaled units even for a wide range of the three parameters: here for $k \approx 2.5$ and $k \approx 5$ ($\ell = 0$) and $k = 5$ ($\ell = 1, 2$), $0.033 \leq \epsilon \leq 0.1$ ($\ell = 0$) and $0.03 \leq \epsilon < 0.3$ ($\ell = 1, 2$) and $3 \leq t \leq 16$. Error bars represent statistical fluctuations over three independent experiments.

same number of kicks, the initial quadratic mean-energy growth can easily be resolved since practically the *entire atomic ensemble* experiences resonant energy growth in this regime. This is precisely because as τ tends to zero, the β dependence of the map (3) is removed as the term $\tau\beta$ vanishes at the same rate as τ .

Finally, figure 4 shows rescaled data from experimental measurements for various experimental parameters with $\ell = 0$ (circles) and $\ell = 1, 2$ (squares). The data taken in the classical case ($\ell = 0$) fall on or close to the classical scaling function (solid line in figure 3) and that, likewise, the data taken for $\ell = 1, 2$ falls on or near the quantum scaling curve (dash-dotted line). The narrower nature of the classical resonance peak is emphasized by this plot. The dense set of points (circles) shown for $x \lesssim 3$ in the classical case come from the data shown in the inset of figure 3(a). These data provide a detailed confirmation of the classical scaling function's validity for smaller values of x than previously observed experimentally [23]. Somewhat surprisingly, it is found that the δ -kicked rotor theory holds even in a regime of x for which the spacing between kicking pulses is comparable to the width of the pulses themselves [12]. The smallest value of the kicking period τ for which the δ -kicked model remained valid in these experiments was $\tau = 0.033$ which, for a kicking strength $k \approx 5$ and $t = 5$, corresponds to $x \approx 2$. For the larger x , the data points show more scatter because of systematic fluctuations in the initial momentum spread and the difficulty in observing the peak very close to resonance for a larger number of kicks [23].

5. Conclusion

We have demonstrated the effect of averaging over a uniform quasi-momentum distribution in two different semiclassical limits of the atom-optics kicked rotor. For the *same* experimental

quasi-momentum distribution, the true classical limit gives rise to *ballistic* energy growth whereas in the pseudo-classical limit approximating quantum resonance only linear growth occurs.

This difference is explained by considering the inclusion of the quasi-momentum-dependent term $\tau\beta$ in the theoretical description. If this term approaches zero, which may be accomplished either by performing the classical limit $\tau \rightarrow 0$ or starting with a very narrow momentum distribution such as that provided by a Bose–Einstein condensate [25], ballistic energy growth is recovered. However, for standard atom-optics kicked rotor experiments using cold atoms only linear energy growth is predicted at quantum resonance since the quasi-momentum β is uniformly distributed in the entire Brillouin zone.

The classical theory of section 3 of the near resonant dynamics thus unifies the description of quantum and classical resonance behaviour of the atom-optics kicked rotor, and is elegantly summarized by two classical one-parameter scaling laws for the classical and quantum resonance peaks. These laws are very useful for a detailed analysis of experimental results in regimes in which measurements are limited by the signal-to-noise ratio.

Acknowledgments

The authors would like to thank Rainer Leonhardt and Scott Parkins for helpful discussions. Additionally, we are grateful to Andreas Buchleitner and Javier Madroñero for their hospitality and logistical support at the Max Planck Institute for the Physics of Complex Systems in Dresden. MS was supported by The Tertiary Education Commission of New Zealand. SW thanks the organizers of the International Workshop on ‘Aspects of Quantum Chaotic Scattering’ (Dresden, 2005) for providing a stimulating atmosphere and partial financial support, as well as the Alexander von Humboldt Foundation (the Feodor-Lynen Program) for funding.

References

- [1] See, e.g., Varcoe B T H, Brattke S, Weidinger M and Walther H 2000 *Nature* **403** 743
McKeever J, Boca A, Boozer A D, Buck J R and Kimble H J 2003 *Nature* **425** 268
Maunz P, Puppe T, Schuster I, Syassen N, Pinkse P W H and Rempe G 2004 *Nature* **428** 50
Riebe M *et al* 2004 *Nature* **429** 734
Barrett M D *et al* 2004 *Nature* **429** 737
Schrader D, Dotsenko I, Khudaverdyan M, Miroshnychenko Y, Rauschenbeutel A and Meschede D 2004 *Phys. Rev. Lett.* **93** 150501
- [2] Monroe C, Swann W, Robinson H and Wieman C 1990 *Phys. Rev. Lett.* **65** 1571
- [3] Moore F L, Robinson J C, Bharucha C F, Sundaram B and Raizen M G 1995 *Phys. Rev. Lett.* **75** 4598
- [4] Anderson B P and Kasevich M A 1998 *Science* **282** 1686
Steck D A, Oskay W H and Raizen M G 2001 *Science* **293** 274
Hensinger W K *et al* 2001 *Nature* **412** 52
Greiner M, Mandel O, Esslinger T, Hänsch T W and Bloch I 2002 *Nature* **415** 39
- [5] Oskay W H, Steck D A, Milner V, Klappauf B G and Raizen M G 2000 *Opt. Commun.* **179** 137
- [6] d’Arcy M B, Godun R M, Oberthaler M K, Cassettari D and Summy G S 2001 *Phys. Rev. Lett.* **87** 074102
- [7] d’Arcy M B, Godun R M, Oberthaler M K, Summy G S, Burnett K and Gardiner S A 2001 *Phys. Rev. E* **64** 056233
- [8] Sadgrove M, Hilliard A, Mullins T, Parkins S and Leonhardt R 2004 *Phys. Rev. E* **70** 036217
- [9] d’Arcy M B, Godun R M, Summy G S, Guarneri I, Wimberger S, Fishman S and Buchleitner A 2004 *Phys. Rev. E* **69** 027201
- [10] Wimberger S, Guarneri I and Fishman S 2003 *Nonlinearity* **16** 1381
- [11] Ashcroft N W and Mermin N D 1976 *Solid State Physics* (Philadelphia, PA: Holt, Rinehart and Winston)
- [12] Sadgrove M, Wimberger S, Parkins S and Leonhardt R 2005 *Phys. Rev. Lett.* **94** 174103

- [13] Bharucha C F, Robinson J C, Moore F L, Sundaram B, Niu Q and Raizen M G 1999 *Phys. Rev. E* **60** 3881
- [14] Casati G, Chirikov B V, Izrailev F and Ford J 1979 *Stochastic Behavior in Classical and Quantum Hamiltonian Systems* ed G Casati and J Ford (Berlin: Springer)
- Fishman S 1993 *Quantum Chaos: Proc. Int. School of Physics 'Enrico Fermi' CXIX* ed G Casati *et al* (Amsterdam: IOS)
- [15] Izrailev F M 1990 *Phys. Rep.* **196** 299
- [16] Fishman S, Guarneri I and Rebuzzini L 2002 *Phys. Rev. Lett.* **89** 084101
- Fishman S, Guarneri I and Rebuzzini L 2003 *J. Stat. Phys.* **110** 911
- [17] Wimberger S, Guarneri I and Fishman S 2004 *Phys. Rev. Lett.* **92** 084102
- [18] Graham R, Schlautmann M and Zoller P 1992 *Phys. Rev. A* **45** R19
- [19] Sadgrove M, Mullins T, Parkins S and Leonhardt R 2005 *Phys. Rev. E* **71** 027201
- [20] Blümel R, Fishman S and Smilansky U 1986 *J. Chem. Phys.* **84** 2604
- [21] Klappauf B G, Oskay W H, Steck D A and Raizen M G 1998 *Physica D* **131** 78
- [22] Chirikov B V 1979 *Phys. Rep.* **52** 264
- [23] Wimberger S, Sadgrove M, Parkins S and Leonhardt R 2005 *Phys. Rev. A* **71** 053404
- [24] Duffy G, Parkins S, Müller T, Sadgrove M, Leonhardt R and Wilson A C 2004 *Phys. Rev. E* **70** 056206
- [25] Wimberger S, Mannella R, Morsch O and Arimondo E 2005 *Phys. Rev. Lett.* **94** 130404
- Rebuzzini L, Wimberger S and Artuso R 2005 *Phys. Rev. E* **71** 036220

Nonlinearity-induced destruction of resonant tunneling in the Wannier-Stark problem

S. Wimberger,¹ R. Mannella,¹ O. Morsch,¹ E. Arimondo,¹ A. R. Kolovsky,^{2,3} and A. Buchleitner²

¹*Dipartimento di Fisica E. Fermi, CNR-INFM, Università di Pisa, Largo Pontecorvo 3, 56127 Pisa, Italy*

²*Max-Planck-Institut für Physik komplexer Systeme, Nöthnitzer Str. 38, 01187 Dresden, Germany*

³*Kirensky Institute of Physics, 660036 Krasnoyarsk, Russia*

(Received 9 June 2005; published 12 December 2005)

We present detailed numerical results on the dynamics of a Bose-Einstein condensate in a tilted periodic optical lattice over many Bloch periods. We show that an increasing atom-atom interaction systematically affects coherent tunneling, and eventually destroys the *resonant* tunneling peaks.

DOI: [10.1103/PhysRevA.72.063610](https://doi.org/10.1103/PhysRevA.72.063610)

PACS number(s): 03.75.Lm, 03.65.Xp, 05.60.Gg

Experiments with cold and ultracold atoms made it possible in the last decade to prepare and control the center-of-mass motion of atoms with unprecedented precision. Many toy models of either many-body solid state physics [1–5] or of simple Hamiltonian systems, whose complexity arises from an external driving force [6], were realized with the exceptional control offered by static or time-dependent optical potentials.

Particularly Bose-Einstein condensates (BECs) whose initial momentum spread can be adjusted in width and absolute position have proved to be an extremely helpful experimental tool [3,4,7–9]. In addition, a BEC offers interesting new features originating from the intrinsic interactions between the atoms. Examples of such effects are new quantum phases [10], solitonlike motion [11], the occurrence of energetic or dynamical instabilities in condensates [7,9,12,13], or the decay and subsequent revival of Bloch oscillations (BOs) [14].

We focus on the evolution of a BEC loaded into a one-dimensional lattice and subjected to an additional static force F , which is most easily realized and controlled by accelerating the optical lattice [1,3]. In previous experiments, a BEC was accelerated to allow for a single crossing of the Brillouin zone (BZ), and two effects were observed: for large accelerations, an enhanced tunneling probability from the ground state band to the first excited band due to the atom-atom interaction was measured [3,8]. Secondly, for smaller accelerations (where tunneling is negligible) signatures of a dynamical instability in the BEC were observed [9,15]. By contrast, here we investigate the dynamics of a BEC performing many Bloch oscillations (BO), and we ask ourselves how the atom-atom interaction affects tunneling for a *sequence* of BZ crossings. In particular, we scan F to study the impact of the atom-atom interaction on resonantly enhanced tunneling (RET), for which the standard Landau-Zener prediction is modified even in the absence of interactions [16]. The RET leads to a faster decay of the Wannier states trapped in the potential wells. With the survival probability and the recurrence probability [see Eqs. (4) and (6) below] we present two consistent measures for the nonlinear RET which define clear experimental signatures of the destruction of the coherent tunneling process inside the periodic potential.

If we neglect interactions for a moment, our system will be described by the Hamiltonian

$$H = -\frac{\hbar^2}{2M} \frac{d^2}{dx^2} + V \sin^2\left(\frac{\pi x}{d_L}\right) + Fx. \quad (1)$$

Here d_L is the spatial period of the optical lattice with maximal amplitude V , and M the atomic mass. Equation (1) defines the well-known Wannier-Stark problem, which gives rise to BO with period $T_{\text{Bloch}} = \hbar/d_L F$ (\hbar is Planck's constant). If tunneling is small, we can view the system as moving at a constant speed in momentum space within the fundamental BZ. At the zone edge, most of the wave packet is reflected (giving rise to BO) while a small part can tunnel across the first band gap to the next higher-lying energy band and then escape quickly by successive tunneling events across the smaller (higher) band gaps. Landau-Zener theory predicts a decay rate [16]

$$\Gamma(F) \propto F e^{-b/F}, \quad (2)$$

where b is proportional to the square of the energy gaps. Equation (2) is modified by RET which occurs when two Wannier-Stark levels in neighboring potential wells are coupled strongly due to their accidental degeneracy. The RET results in pronounced peaks in the tunneling rates, e.g., as a function of $1/F$, on top of the global exponential decay described by Eq. (2) [16]. In this paper we investigate the impact of the effective shift of the Wannier-Stark levels by a nonlinear interaction term.

For the linear problem (1), the decay rates have been measured previously in the regime of short lifetimes in the ground state band (of the order of 100 μs), where $\Gamma(F)$ is essentially smooth [17]. Since RET is a coherent quantum effect, the peaks should be sensitively affected by the atom-atom interaction, which can be varied experimentally by changing either the density of the BEC or through the atom-atom scattering potential via a Feshbach resonance [18]. Our results are a consequence of *many* sequential Landau-Zener events, and they show the destruction of a RET peak with increasing interaction strength, in a regime which is experimentally accessible.

We use a fully 3D Gross-Pitaevskii equation (GPE) [19] to describe the temporal evolution of a BEC which is subject to realistic potentials

$$i\hbar \frac{\partial}{\partial t} \psi(\vec{r}, t) = \left[-\frac{\hbar^2}{2M} \nabla^2 + \frac{1}{2} M (\omega_x^2 x^2 + \omega_r^2 \rho^2) + V \sin^2\left(\frac{\pi x}{d_L}\right) + Fx + gN |\psi(\vec{r}, t)|^2 \right] \psi(\vec{r}, t). \quad (3)$$

$\psi(\vec{r}, t)$ represents the condensate wave function, and the frequencies ω_x and ω_r characterize the longitudinal and transverse harmonic confinement (here with cylindrical symmetry $\rho = \sqrt{y^2 + z^2}$). We fixed $d_L = 1.56 \mu\text{m}$ and $V/E_R = 5$ for our computations, with the recoil energy $E_R = p_R^2/2M$ for $p_R = \hbar\pi/d_L$, and the recoil period $T_R = \hbar/E_R$. The above values for d_L and V were realized in the experiments reported in Refs. [3,8,9] based on two laser beams propagating at an angle different from π . In Eq. (3), the nonlinear coupling constant is given by $g = 4\pi\hbar^2 a_s/M$, where a_s is the s -wave scattering length and N the number of atoms in the BEC [19,20]. The dimensionless nonlinearity $C = gn_0/(8E_R)$ is computed from the peak density of the initial state of the condensate, with $C = 0.027 - 0.31$ for the experimentally investigated range of Ref. [3], and with $C = 0.5$ reached in Ref. [21]. Here we focus on $C > 0$, but report briefly also on attractive interactions with $C < 0$. The latter case leads to a fundamentally different behavior of the system because the collapse of the condensate introduces an additional time scale, which for experimentally relevant parameters is of the order of 10 msec [18,22] (slightly longer than $T_{\text{Bloch}} = 1.8 - 3.0$ msec here).

The GPE (3) is numerically integrated using finite difference propagation, adapted by a predictor-corrector estimate to reliably evaluate the nonlinear interaction [19]. Since our system is essentially the problem of a constantly accelerated particle for the part of the wave function which has tunneled out of the first BZ already, one must be careful with the application of absorbing boundary conditions or complex coordinate methods [23,24]. To avoid any spurious effects due to the fast spreading, we use a large numerical basis. In this way, we fully cover the 3D expansion of the entire wave packet, including its tunneled tail, without the use of non-Hermitian potentials. The initial state propagated by Eq. (3) is the relaxed condensate wave function, adiabatically loaded into the confining potential given by the harmonic trap and the optical lattice (with $F = 0$). Approximate analytic forms of the relaxed state are found, e.g., in Ref. [25], but we used an imaginary time propagation to reliably compute the initial state for $C > 0$.

The linear decay rates for noninteracting atoms in the optical lattice are computed from the spectrum of the 1D Wannier-Stark problem of Eq. (1) using, e.g., the method of Ref. [16]. Those linear rates are plotted in Fig. 1. The maxima in the rates occur when $Fd_L m$ (with m integer) is close to the difference between the first two energy bands (averaged over the BZ) of the $F = 0$ problem [16]. The actual peaks are slightly shifted with respect to the above estimate (marked by arrows in the inset of Fig. 1), owing to a field-induced level shift [16].

Experimentally, the most easily measurable quantity is the momentum distribution of the BEC obtained from a free expansion after the evolution inside the lattice. From the mo-

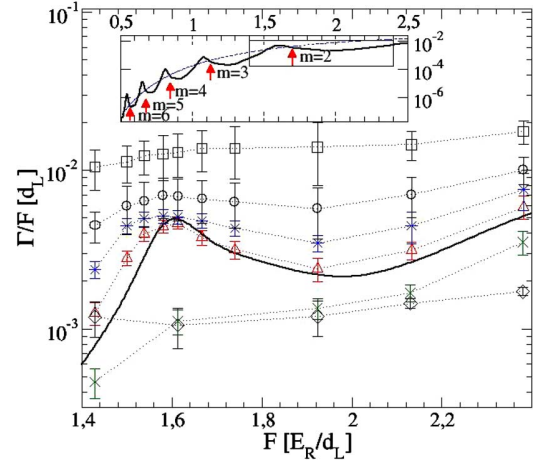


FIG. 1. (Color online) Tunneling rates obtained by exponential fits to data of $P_{\text{sur}}(t)$ as the solid-line fits in Fig. 3. Here the peak in the box in the inset is scanned locally, while globally the rates follow an exponential law (dashed line in the inset). $C = -0.31$ (diamonds), $C = -0.065$ (crosses), $C = 0$ (solid line), $C = 0.027$ (pyramids), $C = 0.065$ (stars), $C = 0.12$ (circles), $C = 0.31$ (squares). The “error” bars interpolate different exponential fits such as the dot-dashed ones in Fig. 3. The arrows in the inset mark the peak positions as predicted by the simple argument stated in the text.

mentum distribution we determine the survival probability by projection of the evolved state $\psi(\vec{p}, t)$ onto the support of the initial state

$$P_{\text{sur}}(t) \equiv \int_{-p_c}^{p_c} dp_x \left(\int dp_y dp_z |\psi(\vec{p}, t)|^2 \right), \quad (4)$$

where $p_c \geq 3p_R$ is a good choice since three momentum peaks are initially significantly populated, corresponding to $-2p_R, 0, 2p_R$ [3,25].

Figure 2 shows the initial population in momentum space [inset in (a)] as compared with the population after 10 BO periods, for both the linear and the nonlinear case. The increase of $C > 0$ has two effects: firstly, it enhances the tunneling for the first few crossings of the BZ. Secondly, it scrambles the out-coupled part of the wave function (see Fig. 2 and its complement in Fig. 4 below), as previously observed in Refs. [2,3,5]. The change in the momentum distributions after various Landau-Zener events is a manifestation of the intrinsic instability of the nonlinear GPE dynamics [9,12].

Instead of studying the details of the distributions shown in Fig. 2, we will focus on the temporal decay of the survival probability in the following. Figure 3 presents $P_{\text{sur}}(t)$, which for the linear case has an exponential form (apart from the $t \rightarrow 0$ limit [26])

$$P_{\text{sur}}(t) \sim e^{-t\Gamma/\hbar}, \quad (5)$$

with the characteristic exponent Γ . The temporal behavior of P_{sur} depends significantly on C . For $C = \pm 0.31$, we observe clear deviations from a purely exponential decay, as present for small C . A *repulsive* nonlinearity initially enhances the tunneling more than after about five crossings of the BZ (see

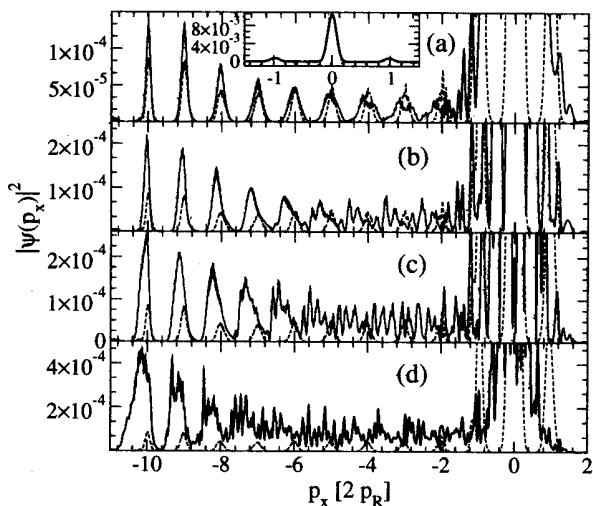


FIG. 2. Momentum distributions after 10 BOs, for $T_R/T_{\text{Bloch}}=1.428$. $C=0$ (dotted) compared with (a) $C=0.027$ (full line; the inset shows the corresponding $t=0$ distribution), (b) $C=0.065$, (c) $C=0.12$, and (d) $C=0.31$.

fits to data in Fig. 3). This deviation from the monoexponential behavior means that the tunneling events occurring at different integer multiples of the Bloch period are correlated by the presence of the nonlinearity. Since the remaining density becomes smaller, the impact of the nonlinearity becomes less. The result is that the rate Γ is defined only locally in time, and its value systematically decreases as time increases.

An *attractive* interaction can stabilize the system at the RET peak, which is shown for $C=-0.31$ in Fig. 3(b). For optimal comparison, we chose the same initial state (for $C=+0.31$) which then was evolved for $F \neq 0$ with $C=-0.31$. Such a scenario could be realized by a sudden

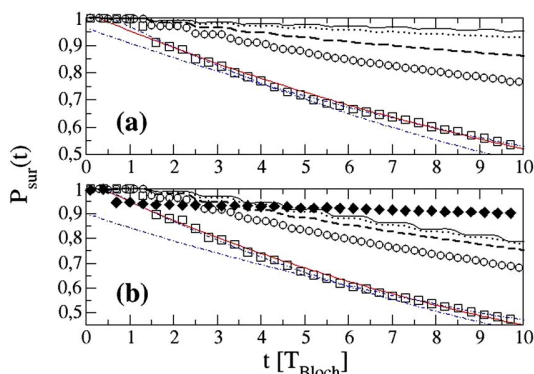


FIG. 3. (Color online) $P_{\text{sur}}(t)$ for (a) $T_R/T_{\text{Bloch}}=1.428$ and (b) 1.613 (the peak maximum in Fig. 1). C is scanned from -0.31 [diamonds in (b) only], 0 (solid line), 0.027 (dotted line), 0.065 (dashed line), 0.12 (circles), to 0.31 (squares). The gray/red solid lines show global exponential fits to the $C=0.31$ data, while the dot-dashed lines show exponential fits for small and large t , respectively. From those fits, the rates in Fig. 1 and their systematical variation in time are obtained. The step-like structures reflect the periodic BO and are correlated with the dephased oscillations in Fig. 4.

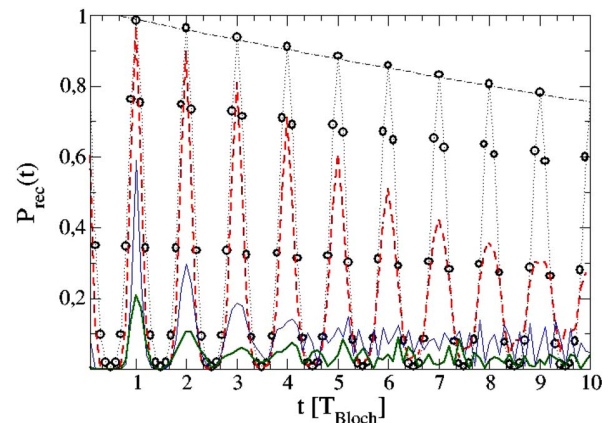


FIG. 4. (Color online) $P_{\text{rec}}(t)$ for the data shown in Fig. 3(b) with $C=0$ (circles), 0.027 (dashed), 0.12 (thin line), and 0.31 (thick line). The dot-dashed line presents an exponential fit to the maxima of the $C=0$ data.

change of the sign of the scattering length through a Feshbach resonance [18]. This result is consistent with studies of simpler models, where a resonance state can be stabilized at system-specific strengths of the nonlinearity [24,27].

The impact of the nonlinearity on the dynamical evolution of the “closed” system confined to the fundamental BZ can be studied with the help of the recurrence probability [17], defined by the autocorrelation

$$P_{\text{rec}}(t) \equiv |\langle \psi(t) | \psi(t=0) \rangle|^2. \quad (6)$$

The BO manifest themselves as the periodic oscillations in $P_{\text{rec}}(t)$ plotted in Fig. 4. These oscillations are less and less pronounced with increasing C , in much the same way as the momentum peaks are washed out when the band edge is crossed in the regime of instability [9]. In contrast to the survival probability, P_{rec} is a phase sensitive measure, and therefore it shows—in addition to the temporal decay—the dephasing of the BO due to the nonlinearity. For $C=0$, the recurrence maxima decay in time with the same rate as $P_{\text{sur}}(t)$, which offers an alternative method for extracting Γ . For $C \neq 0$, P_{rec} can be integrated over time, and the rates are extractable by the approximate proportionality between the integrated area and the inverse decay rate [recalling that $\int dt f(t) \exp(-t\Gamma) \sim 1/\Gamma$ to leading order, for a periodic function $f(t)$]. The latter approach works because we can determine the linear rate from a direct fit to P_{rec} and then compare the ratio of the linear and the nonlinear area (denoted by A_0 and A_C). This rough estimate $\Gamma_C \sim \Gamma_0 A_0 / A_C$ agrees within 25% with the rate extracted from the fits to the data of Fig. 3. The estimate could be improved if we knew the analytic form of the function $f(t)$, and it breaks down for large C , when the periodic oscillations in P_{rec} are destroyed.

Having introduced two methods to extract the tunneling rates, we scan the parameter F across a RET peak of the globally exponential curve $\Gamma(1/F)$ (see Fig. 1). The scanned range in F corresponds to values of lattice accelerations between 0.99 and 1.65 ms^{-2} , which are standard in experiments [3,9].

A repulsive nonlinearity particularly affects the wings of the peak and, for small C , much less the peak maximum. The global increase of Γ with increasing C is qualitatively predicted in Ref. [28], with enhanced *single* Landau-Zener crossing probabilities induced by the effective reduction of the energy gap due to the nonlinearity. The left and right-most points in Fig. 1 are in the regime where an amended version of Eq. (2) indeed applies [28], and here Γ/F is approximately proportional to C . However, near the peak, the rates do not follow a simple scaling law as a function of C , and the argumentation of Ref. [28] does not apply.

For $C < 0$ we also observe the destruction of the RET peak. For $C = -0.065$, the BEC clearly stabilizes in the potential wells, whilst for $C = -0.31$ the situation is more complicated (see Fig. 1). The precise dynamics of the system is governed by the two separate time scales for tunneling and collapse, which strongly depend on parameters in the sensitive RET regime.

In an experiment, ω_x can either be set to zero or decreased to $\omega_x/2\pi \approx 1$ Hz to realize a quasi-1D *nonlinear* Wannier-Stark problem. We verified that letting ω_x tend to zero for the evolution with $F \neq 0$, or applying a small finite ω_x gives the same results for the BO cycles studied here. Furthermore, for $0 < C \leq 0.05$, using the renormalized nonlinearity of Ref. [20] we observed that a 1D version of Eq. (3) reproduces well the 3D data. If $|C|$ is larger, the nonlinearity couples the

longitudinal and transverse degrees of freedom, which affects the dynamics of a real BEC in a nontrivial way [19]. The 1D computations are feasible up to 100 Bloch periods, and this would allow one to extract the tunneling rates more reliably. The effect of the nonlinearity is, however, hardly visible for $0 < C < 0.05$, and quantitative predictions for a broad range of C relied on 3D computations.

To summarize, we observed and quantified the deformation and destruction of the RET peaks due to interactions in a BEC in an accelerated optical lattice. Our results complement ongoing studies of interaction-induced processes such as dynamical instabilities or the decay and subsequent revival of BO. In the regime of small nonlinearity, where dynamical instabilities are not fully developed, the survival and recurrence probabilities experience an exponential decay modified by the condensate nonlinearity. The temporal decay of these observables remains a useful indicator also for large nonlinearity, even if the resonant structure in the tunneling rate is washed out.

We thank M. Cristiani and D. Ciampini for helpful discussions and the Humboldt Foundation (Feodor-Lynen Program), the MIUR (COFIN-2004), the EU (Specific Targeted Research Project OLAQUI), the ESF (European network activity QUDEDIS), and the DFG (Priority Program 1116) for financial support.

-
- [1] M. BenDahan, E. Peik, J. Reichel, Y. Castin, and C. Salomon, *Phys. Rev. Lett.* **76**, 4508 (1996); S. R. Wilkinson, C. F. Bharucha, K. W. Madison, Qian Niu, and M. G. Raizen, *ibid.* **76**, 4512 (1996).
- [2] B. P. Anderson and M. A. Kasevich, *Science* **282**, 1686 (1998).
- [3] O. Morsch, J. H. Müller, M. Cristiani, D. Ciampini, and E. Arimondo, *Phys. Rev. Lett.* **87**, 140402 (2001); M. Cristiani, O. Morsch, J. H. Müller, D. Ciampini, and E. Arimondo, *Phys. Rev. A* **65**, 063612 (2002).
- [4] J. Hecker-Denschlag, J. E. Simsarian, H. Häffner, C. McKenzie, A. Browaeys, D. Cho, K. Helmerson, S. L. Rolston, and W. D. Phillips, *J. Phys. B* **35**, 3095 (2002).
- [5] G. Roati, E. de Mirandes, F. Ferlaino, H. Ott, G. Modugno, and M. Inguscio, *Phys. Rev. Lett.* **92**, 230402 (2004).
- [6] M. G. Raizen, *Adv. At., Mol., Opt. Phys.* **41**, 43 (1999); D. A. Steck, W. H. Oskay, and M. G. Raizen, *Science* **293**, 274 (2001); W. K. Hensinger, H. Häffner, A. Browaeys, N. R. Heckenberg, K. Helmerson, C. McKenzie, G. J. Milburn, W. D. Phillips, S. L. Rolston, H. Rubensztein-Dunlop, and B. Upcroft, *Nature (London)* **412**, 52 (2001).
- [7] L. Fallani, L. De Sarlo, J. E. Lye, M. Modugno, R. Saers, C. Fort, and M. Inguscio, *Phys. Rev. Lett.* **93**, 140406 (2004).
- [8] M. Jona-Lasinio, O. Morsch, M. Cristiani, N. Malossi, J. H. Müller, E. Courtade, M. Anderlini, and E. Arimondo, *Phys. Rev. Lett.* **91**, 230406 (2003).
- [9] M. Cristiani, O. Morsch, N. Malossi, M. Jona-Lasinio, M. Anderlini, E. Courtade, and E. Arimondo, *Opt. Express* **12**, 4 (2004).
- [10] M. Greiner, O. Mandel, T. Esslinger, T. W. Hänsch, and I. Bloch, *Nature (London)* **415**, 39 (2002).
- [11] B. Eiermann, Th. Anker, M. Albiez, M. Taglieber, P. Treutlein, K.-P. Marzlin, and M. K. Oberthaler, *Phys. Rev. Lett.* **92**, 230401 (2004).
- [12] B. Wu and Q. Niu, *New J. Phys.* **5**, 104 (2003).
- [13] Y. Zheng, M. Kostrun, and J. Javanainen, *Phys. Rev. Lett.* **93**, 230401 (2004).
- [14] A. R. Kolovsky, *Phys. Rev. Lett.* **90**, 213002 (2003); A. Buchleitner and A. R. Kolovsky, *ibid.* **91**, 253002 (2003); Q. Thommen, J. C. Garreau, and V. Zehle, *ibid.* **91**, 210405 (2003).
- [15] Instability at the band edge has also been studied using a different experimental protocol in Ref. [7].
- [16] M. Glück, A. R. Kolovsky, and H. J. Korsch, *Phys. Rev. Lett.* **83**, 891 (1999); *Phys. Rep.* **366**, 103 (2002).
- [17] C. F. Bharucha, K. W. Madison, P. R. Morrow, S. R. Wilkinson, B. Sundaram, and M. G. Raizen, *Phys. Rev. A* **55**, R857 (1997).
- [18] J. L. Roberts, N. R. Claussen, S. L. Cornish, E. A. Donley, E. A. Cornell, and C. E. Wieman, *Phys. Rev. Lett.* **86**, 4211 (2001).
- [19] E. Cerboneschi, R. Mannella, E. Arimondo, and L. Salasnich, *Phys. Lett. A* **249**, 495 (1998); S. Wimberger, R. Mannella, O. Morsch, and E. Arimondo, *Phys. Rev. Lett.* **94**, 130404 (2005).
- [20] M. Olshanii, *Phys. Rev. Lett.* **81**, 938 (1998).
- [21] N. Gemelke, E. Sarajilic, Y. Bidet, S. Hong, and S. Chu, *cond-mat/0504311*.

- [22] S. Wüster, J. J. Hope, and C. M. Savage, *Phys. Rev. A* **71**, 033604 (2005).
- [23] T. Paul, K. Richter, and P. Schlagheck, *Phys. Rev. Lett.* **94**, 020404 (2005).
- [24] P. Schlagheck and T. Paul, *cond-mat/0402089*; N. Moiseyev, and L. S. Cederbaum, *cond-mat/0406189*.
- [25] P. Pedri, L. Pitaevskii, S. Stringari, C. Fort, S. Burger, F. S. Cataliotti, P. Maddaloni, F. Minardi, and M. Inguscio, *Phys. Rev. Lett.* **87**, 220401 (2001).
- [26] S. R. Wilkinson, C. F. Bharucha, M. C. Fischer, K. W. Madison, P. R. Morrow, Q. Niu, B. Sundaram, and M. G. Raizen, *Nature (London)* **387**, 575 (1997).
- [27] D. Witthaut, S. Mossmann, and H. J. Korsch, *J. Phys. A* **38**, 1777 (2005).
- [28] D. I. Choi and Q. Niu, *Phys. Rev. Lett.* **82**, 2022 (1999); O. Zobay and B. M. Garraway, *Phys. Rev. A* **61**, 033603 (2000).

Can quantum fractal fluctuations be observed in an atom-optics kicked rotor experiment?

Andrea Tomadin^{1,2}, Riccardo Mannella² and Sandro Wimberger²

¹ Scuola Normale Superiore, Piazza dei Cavalieri 7, I-56126 Pisa

² CNR-INFM and Dipartimento di Fisica ‘Enrico Fermi’, Università degli Studi di Pisa, Largo Pontecorvo 3, I-56127 Pisa

E-mail: saw@df.unipi.it

Received 1 December 2005, in final form 25 January 2006

Published 22 February 2006

Online at stacks.iop.org/JPhysA/39/2477

Abstract

We investigate the parametric fluctuations in the quantum survival probability of an open version of the δ -kicked rotor model in the deep quantum regime. Spectral arguments (Guarneri I and Terraneo M 2001 *Phys. Rev. E* **65** 015203(R)) predict the existence of parametric fractal fluctuations owing to the strong dynamical localization of the eigenstates of the kicked rotor. We discuss the possibility of observing such dynamically-induced fractality in the quantum survival probability as a function of the kicking period for the atom-optics realization of the kicked rotor. The influence of the atoms' initial momentum distribution is studied as well as the dependence of the expected fractal dimension on finite-size effects of the experiment, such as finite detection windows and short measurement times. Our results show that clear signatures of fractality could be observed in experiments with cold atoms subjected to periodically flashed optical lattices, which offer an excellent control on interaction times and the initial atomic ensemble.

PACS numbers: 05.45.Mt, 42.50.Vk, 05.60.Gg

(Some figures in this article are in colour only in the electronic version)

1. Introduction

Experiments with cold atoms nowadays offer unique possibilities for the study of single particle motion and collective particle dynamics in tailored optical or magnetic potentials. The atomic centre-of-mass motion can be prepared and controlled with unprecedented precision, what allows experimentalists to realize and study many toy models of condensed matter physics [1]. Since in experiments with cold atomic gases noise and perturbations can be driven to a

minimum, which often is indeed negligible, such set-ups offer a great advantage with respect to solid-state realizations.

In this paper, we discuss the possibility of observing sensitive quantum effects which manifest in a fractal variation of a transport function with respect to a well-tunable control parameter. Similar fractal fluctuations of the transmission probability across solid-state samples have been measured recently [2] in systems whose underlying classical phase space typically contains mixed regular-chaotic structures. Most features of these experiments can be understood semiclassically as a consequence of the phase space topology [3–5]. However, the precise origin of the observed fractal conductance fluctuations in these experiments is not yet fully understood [6], and, in fact, various theoretical models [7, 8] predict fractal conductance fluctuations for mesoscopic devices. Our aim is to design a concrete experimental scenario in which parametric fractal fluctuations could be measured with high precision cold-atom set-ups. In such experiments the cross-over between mixed and completely chaotic classical dynamics can be scanned easily [9–11], and hence fractal transmission probabilities could be measured in a regime where classical or semiclassical arguments do not apply.

As was shown by Guarneri and Terraneo [7], fractal fluctuations in the transmission probability of a quantum scattering problem arise naturally as a consequence of the spectral properties of the system. The two essential conditions on the spectrum are (i) a power-law distribution of decay widths and (ii) uncorrelated real parts of the energy spectrum. Moreover, various eigenstates have to contribute together to the decay, a fact which is expressed formally by requiring that (iii) the average decay width is much larger than the mean level spacing. Based on these conditions, the theory of [7] explained the occurrence of quantum fractal fluctuations in the δ -kicked rotor model in the deep quantum realm [12], where semiclassical arguments cannot explain the occurrence of fractality.

In this paper we study a similar dynamical situation as in [12], yet with important modifications which fully account for the actual experimental realization of the kicked rotor. Using either cold or ultracold atomic gases, the kicked rotor is realized by preparing a cloud of atoms with a small spread of initial momenta, which is then subjected to a one-dimensional optical lattice potential, flashed periodically in time [13]. Let us call k_L the wave number of the optical lattice, $\tilde{\tau}$ the flashing period (‘kicking’ period), \tilde{p} the momentum of the single atom, \tilde{x} its centre-of-mass position, V_0 the maximum potential depth, and M is the atomic mass. It is convenient to adopt rescaled units by noting that $p_R = \hbar k_L$ is the photon recoil momentum and $E_R = (\hbar k_L)^2/2M$ is the recoil energy [9, 11, 14]. So we define $p = \tilde{p}/2p_R$, $x = \tilde{x} \cdot 2k_L$, $\tau = \tilde{\tau} \cdot 8E_R/\hbar$. The kicking strength of the lattice is expressed by $k = V_0/(8E_R)$. The Hamiltonian now reads in dimensionless units [15]

$$\hat{H}(t') = \frac{p^2}{2} + k \cos x \sum_{t=1}^{\infty} \delta(t' - t\tau). \quad (1)$$

Owing to the δ -interaction of the potential with the atoms, the time evolution operator between kicks can be explicitly written in a factorized form, extremely convenient for numeric simulations. The derivation of the one-period evolution operator exploits the spatial periodicity of the potential by Bloch’s theorem [11, 16]. This defines the *quasimomentum* β as a constant of the motion, the value of which is the fractional part of the physical momentum p in dimensionless units $p = n + \beta$ ($n \in \mathbb{N}$). Since β is a conserved quantum number, p can be labelled using its integer part n only. The spatial coordinate is then substituted by $\theta = x \bmod (2\pi)$ and the momentum operator by $\hat{\mathcal{N}} = -i\partial/\partial\theta$ with periodic boundary conditions. The one-kick propagation operator for a fixed quasimomentum β is thus given by [16]

$$\hat{\mathcal{U}}_{\beta} = e^{-ik \cos(\hat{\theta})} e^{-i\tau(\hat{\mathcal{N}}+\beta)^2/2}. \quad (2)$$

In close analogy to the transport problem across a solid-state sample, we follow [12] to define the quantum survival probability as the fraction of the atomic ensemble which stays within a specified region of momenta while applying absorbing boundary conditions at the ‘sample’ edges. If we call $\psi(n)$ the wave function in momentum space and $n_1 < n_2$ the edges of the system, absorbing boundary conditions are implemented by the prescription $\psi(n) \equiv 0$ if $n \leq n_1$ or $n \geq n_2$. This truncation is carried out after *each* kick. This procedure mimics the escape of atoms out of the spatial region where the dynamics induced by the Hamiltonian (1) takes place. If we denote by \hat{P} the projection operator on the interval $]n_1, n_2[$ the survival probability after t kicks is

$$P_{\text{surv}}(\tau; t) = \|(\hat{P}\hat{U}_\beta)^t \psi(n, 0; \tau)\|^2. \quad (3)$$

We will show in the following that signatures of fractality in the survival probability could be observed in modern atom-optical experiments, where the initial atomic ensemble has a finite, non-zero width in momentum space. In contrast to the work of [12], where the initial quasimomentum is scanned to arrive at the parametric observable $P_{\text{surv}}(\beta)$, we investigate the behaviour of $P_{\text{surv}}(\tau)$ as a function of the best controllable parameter in the experiment, namely the time τ which elapses between two successive kicks [10, 14, 17, 18].

After a brief review of the results of Guarneri and Terraneo [7] applied to the dynamically localized kicked rotor (section 2), we discuss in section 3 our choices of the system parameters, which are guided by the experimental possibilities as well as the conditions stated in [7]. Our central results on the occurrence of fractal survival probabilities are presented for the limit of long-interaction times (section 4) as well as for experimentally accessible initial momentum distribution and interaction times (section 5). Section 6 finally concludes the paper.

2. Conditions for fractal fluctuations of the survival probability

Without *a priori* assumptions on the integrability or chaoticity properties of the classical analogue of the quantum system of interest, Guarneri and Terraneo [7] showed that fractal conductance fluctuations occur if certain conditions on the quantum spectrum of the open system are fulfilled.

The first condition, (i) a power-law distribution of the decay widths, is indeed present in the weakly opened quantum kicked rotor [19]. We verified this by diagonalizing the one-kick evolution operator \hat{U}_β , after representing it in the basis of momentum states. The matrix was cut at the positions n_1 and n_2 to mimic the required absorbing boundary conditions.

If either of the two cut-offs (n_1 or n_2) is chosen sufficiently large, the shape of the wave function in momentum space supports an exponential tail, independent of the evolution time (after a short transit time $\propto k^2$ at which dynamical localization has fully developed [20, 21]). For such a situation in the localized regime, the probability density of decay widths was found to be $\rho(\Gamma) \propto \Gamma^{-1}$ over more than 10 orders of magnitude in Γ , consistent with previous studies [5, 19, 22–24]. If, on the other hand, n_1 and n_2 were decreased, dynamical localization is gradually destroyed and the distribution deforms continuously, giving more weight to larger widths and less to the very small ones. Such a deformation was observed in the analogous context of ionization rates of microwave-driven hydrogen Rydberg atoms [24]. Our choice of n_1 and n_2 represents a compromise between the maximum width of typical experimental detection windows in momentum space and a guaranteed dynamically localized momentum distribution over a substantial interval of momenta. In the next section, we state the precise values of n_1 and n_2 which we investigated in this paper.

In the regime of strong dynamical localization, the quasienergy spectrum of the δ -kicked rotor has a Poisson-like statistics [25]. Under the same conditions as stated above on the

cut-off values n_1 and n_2 , this property of the real parts of the quasienergy spectrum remains even when the system is opened [22, 26]. Hence, also the second requirement for fractality of [7], that (ii) the energy spectrum consists of uncorrelated sequences, is fulfilled in good approximation for the opened δ -kicked rotor in the presence of dynamical localization.

The third condition stated in [7] is that the opening of the system is weak, but still sufficient to guarantee that (iii) the average decay width is much larger than the mean level spacing. For our choice of parameters and cut-off values n_1 and n_2 , also this condition of overlapping ‘resonance peaks’ is fulfilled, as we verified numerically from the quasienergy spectrum of the truncated matrix representation of \hat{U}_β .

As exercised in [7], the conditions (i)–(iii) are sufficient to guarantee self-affine fluctuations in the quantum survival probability, with a predicted fractal dimension D_f which is related to the exponent of the width distribution $\rho(\Gamma) \propto \Gamma^{-\alpha}$ by the following general formula $D_f = 1 + \alpha/2 \approx 1.5$ for $\alpha \approx 1$.

We repeat that parametric fractal fluctuations in the survival probability of dynamically localized kicked rotor have already been found in [12], before their origin could be explained in [7]. In this work, however, we scan a different parameter than the one used in [12], which corresponded to quasimomentum. Here we use the kicking period τ as control parameter, which can be much better controlled in state-of-the-art experiments [10, 14, 17, 18] than the initial value of momentum [11, 18, 27–29]. On the other hand, the use of τ confronts us with a new problem which is discussed in the following section.

3. Choice of parameters

3.1. Dynamical localization and classical chaos

For our analysis the value of the kicking strength k was chosen in the range 2–6, or $k\tau = 2.8$ –8.4, going along with the transition from local to global chaos with increasing k in this range [20, 21]. For our choice of kicking periods $\tau \equiv \hbar_{\text{eff}} > 1$ [20, 21], classical trajectories wandering about hierarchical structures of the classical phase space will not have a quantum analogue because those structures are too small to be resolved by the wave function. This means that the observed fluctuations indeed arise from quantum localization effects and not from a semiclassical diffusion process.

3.2. The kicking period as control parameter

As reviewed in section 2, the sufficient conditions for the occurrence of fractal fluctuations are fulfilled for choices of τ for which the δ -kicked rotor exhibits dynamically localized behaviour. However, besides dynamical localization the quantum δ -kicked rotor supports ‘quantum resonant’ motion for specific values of τ and quasimomentum β [20, 30]. Our goal is to avoid as much as possible the impact of the quantum resonances on the dynamics, such that we can clearly identify the origin of the fractality of the survival probabilities. Since the parameter we scanned is the kicking period τ , we verified that no signatures of quantum resonances are found in the analysed small range of τ and for the applied, finite kick numbers.

The quantum kicked rotor shows ballistic growth of momentum, shortly a *quantum resonance*, if

$$\tau \in \{4\pi s/q; s, q \in \mathbb{N}\}, \quad \beta \in \{m/2s, 0 \leq m < s; m, s \in \mathbb{N}\}, \quad (4)$$

and in these cases the time dependence of energy on the number of kicks is [20, 30]

$$E(t; \tau) = \eta t^2 + \mathcal{O}(t), \quad \text{with } \eta \simeq (k/q)^{2q}. \quad (5)$$

The denominator q in the rational factor of τ is called the *order* of the resonance. The set containing all the resonances has zero Lebesgue measure in any interval of kicking periods, but we do care about it because the dependence on τ of the survival probability $P_{\text{surv}}(\tau; t)$ is continuous for a fixed, finite number of kicks and the fluctuations we want to observe should be caused by dynamical localization and not by quantum resonances. The preceding growth estimate (5) establishes that a resonance is suppressed for a time that increases more than exponentially with its order. One way to avoid contributions from the resonances is to use a judicious choice of the range of τ and sampling grid G used for numerical simulations or experiments. We chose

$$G = \{\tau_i = \tau_0 + i \cdot \delta\tau, i \in \{0, \dots, m-1\}\}, \quad \text{with } m = 10^4, \quad (6)$$

where the value of $\tau_0/4\pi$ is a fraction of the golden mean:

$$\frac{\tau_0}{4\pi} = \frac{14}{10} \frac{s}{q} (\sqrt{5} - 1), \quad s = 6142, \quad q = 95\,403, \quad \frac{s}{q} - \frac{1}{4\pi(\sqrt{5} - 1)} < 10^{-11}. \quad (7)$$

For $\delta\tau = 9.98 \times 10^{-7}$, also all other grid points in G are incommensurable to 4π up to the used significant digits. We verified that the lowest order resonance in the range $[\tau_{\text{min}}, \tau_{\text{max}}] \approx [1.4, 1.41]$ has $q = 107$ and that there is no crowding of resonances of order $q \leq 2000$ anywhere in this interval. Since we are not going to use times longer than 10^4 kicks in our simulations, and kicking strength of order unity, the quadratic term is suppressed dramatically by the coefficient η in (5), for all occurring resonances $q \geq 107$. Finally, we explicitly checked throughout the simulations that localization is at work by inspecting the average energy and, for selected values of τ , the shape of the wave function in momentum space, which shows a characteristic exponential decrease as explained below in section 3.3.

We also tried a quantitative approach for the choice of the grid along the τ axis. If some resonance were important, any numerical selection method could detect it and prefer grids with points away from the quantum resonances. Our method is based on the maximization in the ‘grids space’ of a function $F(G(\tau_0, \delta\tau))$ that adds a contribution from each resonance, up to a maximum order, within a given interval, and this contribution is the larger the farther the resonance position in τ (see equation (4)) is from the nearest point of the grid. This means that a ‘higher mark’ is achieved by the grids whose points are away from the resonances. Formally we defined

$$\begin{aligned} S &= \{4\pi s/q\} \cap \{q \leq q_{\text{max}}\} \cap [\tau_{\text{min}}, \tau_{\text{max}}] \\ F(G(\tau_0, \delta\tau)) &= \sum_{\tau_r \in S} f_r(\min\{|\tau_r - \tau_g|; \tau_g \in G\}), \\ f_r^{(0)}(\Delta\tau) &= \Delta\tau; \quad f_r^{(1)}(\Delta\tau) = \Delta\tau^2; \quad f_r^{(3)}(\Delta\tau) = \Delta\tau/q_r. \end{aligned}$$

Different definitions of the weight function $f_r(\Delta\tau)$ allow us to give more weight to resonances with smaller $q \gtrsim 107$ (i.e., to those which influence the time evolution of a wider neighbourhood along the τ axis). Of course, this programme requires detailed knowledge of the dynamics near the high-order resonances of $q \geq 107$, but this goal has not been theoretically accomplished yet. None of our weight functions could resolve the presence of a resonance by a sharp minimum when applied to a specific grid.

As a consequence of our choice of the interval of kicking periods and grid points in this interval, no signatures of quantum resonances are expected to manifest for interaction times of up to 10^4 kicks.

3.3. The opening of the system

The probability decay arises from the open geometry of our system, which is implemented mathematically by imposing absorbing boundary conditions in momentum space [12]. This means that

$$\psi(n) \equiv 0 \quad \text{if } n \leq n_1 < 0 \quad \text{or} \quad n \geq n_2 > 0.$$

The requirement on the boundaries is that they must guarantee dynamical localization (see section 2). This happens if the wave function on the boundaries is ‘so’ small that the kicking potential cannot spread a ‘substantial’ part of the wave function out of the boundaries. The compatibility of the values of the parameters involved— t, k, n_1, n_2 —is checked using a consequence of the conditions that grant a fractional dimension of the graph of the survival probability (see section 2). This consequence is that the square of the wave function decreases with time *keeping its shape constant*, in the limited momentum lattice representing the open system.

Let us recall that the typical shape of a one-dimensional localized wave function is exponential, extending in a region intermediate between the support of the initial state in momentum space and the absorbing boundary. In a linear-logarithmic plot the wave function is (apart from erratic fluctuations around its mean decrease) a line in this intermediate region; constancy of the shape means constancy of the steepness of the line. This criterion, which is in fact a localization criterion, was used as a prerequisite for all our simulations. If the boundaries are too far away from the initial state, the decay is extremely slow (a consequence of strong dynamical localization). To avoid long waiting times (which are hard to reach experimentally), asymmetric boundaries have been used, with $1 \approx |n_1| \ll |n_2|$, and a statistical initial ensemble of orbits at $t = 0$ with $p = 0$ and randomly distributed phases θ , i.e., $\psi(n; t = 0) \equiv \delta_{n,0}$. The wave function in momentum space $\psi(n; t)$ then evolves to a shape which is asymmetric with respect to $n = 0$. On the side where the cut-off is closer to the origin, the wave function does not decrease exponentially, and in a linear-logarithmic plot the momentum distribution shows a broad and smooth maximum, while at $n = 0$ a sharp peak would be present if we choose $1 \gg |n_1| \approx |n_2|$. Although the exponential decrease on the side of the larger cut-off n_2 is influenced by the opening at n_1 , the shape indeed remains constant for a sufficiently large number of kicks in a range $[\bar{n}, n_2]$, where the precise value of $\bar{n} \approx 50, \dots, 100$ depends on the choice of n_1 .

4. Numerical results for fixed quasimomentum

The central result of this paper is the computation and fractal analysis of the survival probability $P_{\text{surv}}(\tau; t, \beta, k, n_1, n_2)$ as a function of τ , while the other parameters are fixed for each curve. Our fractal analysis comprehends the computation of (a) the box-counting dimension [7, 31], (b) a variational algorithm dimension [31], together with the calculation of the (c) correlations, and (d) variances of the graph $P_{\text{surv}}(\tau)$. Several curves are computed with different choices of parameters. Our results are essentially independent of quasimomentum β and the applied boundaries n_1 and n_2 , whose choice is guided by the considerations stated in section 3.3.

Numerical algorithms, of course, do not distinguish the origin of the irregular profile of a fractal graph. To make sure that the observed fractality is actually produced by quantum effects, we verified that the increase of k in the range 2–6 (for $\tau \gtrsim 1.4$) is accompanied by a monotonic increase of the fractal dimension. This is a *signature* of fractality owing to dynamical localization of a weakly open quantum system. As k reaches a certain saturation value $k_{\text{sat}} \approx 4.5$ (where $k\tau > 5$ exceeds the global chaos border [20, 21] and quantum chaos is

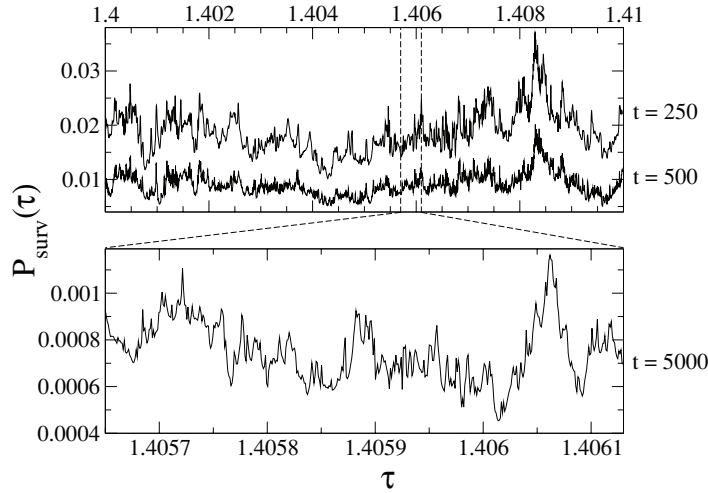


Figure 1. The survival probability as a function of τ for $k = 5$, $\beta = 0$, $n_1 = -1$, $n_2 = 200$ and different kick numbers t . The magnification in the lower panel shows that, as t increases, self-affine fluctuations occur on finer and finer scales in τ .

fully developed) we verified that the fractal dimension ceases its substantial growth observed in the range $k = 2$ – 4.5 .

At fixed kick number t , the survival probability is in principle a smooth function of τ on a sufficiently small scale $\delta\tau$. After a grid in τ is chosen, fractality is expected to increase as t increases due to the appearance of fluctuations on finer and finer scales. A finer grid requires a longer time to yield a ‘fractal graph’ down to finer scales, because it takes longer for the fluctuations to appear on a scale smaller than the grid resolution. This scenario, where fractality is generated by ‘dynamical intrusion’, is exemplified in figure 1 where the survival probability in the localized regime is shown after various interaction times. The calculation of the fractal dimension as a function of time shows a monotonic increase from unity up to a value between 1.6 and 1.7.

We computed the survival probability $P_{\text{surv}}(\tau)$ for various interaction times of up to 10^4 kicks. The latter value is much larger than the kick numbers of the order 100 typically realized in state-of-the-art experiments [9, 32]. Nevertheless, the monotonic behaviour in time can itself be used as an important signature of fractality. In figure 2(a)–(c) the profile of $P_{\text{surv}}(\tau; t)$ is shown along with a small, yet representative part of three successive magnifications over two orders of magnitude in the kicking period τ . The real parts of the quasienergy spectrum are presented in figure 2(d)–(f) in the same ranges of τ . The visibly avoided crossings are a consequence of quantum chaotic dynamics and their ubiquitous presence on different scales in τ naturally compares to the self-affine fluctuations of the survival probability. This comparison highlights the fact that the observed fractality is indeed a consequence of quantum chaos.

The box-counting plot in figure 3(a) shows the number of adjacent squares $N(\delta)$ of width δ along the τ axis necessary to box all points of the curve from figure 2(a). The scaling law $N(\delta) \sim \delta^{-D_f}$ thus determines the fractal dimension D_f . The variational method (b) is a substantial refinement of the box-counting which typically gives more reliable results [31]. It involves the division of the fully analysed τ interval in R subintervals, and the total variation of the curve on groups of $2l$ adjacent subintervals is computed. The average of these quantities is called $V_R(l)$ and the value of R which gives the best scaling of the form $V_R(l) \sim l^{-D_f}$ is used. In addition to the direct fractal analysis of $P_{\text{surv}}(\tau)$, we computed the autocorrelations and the

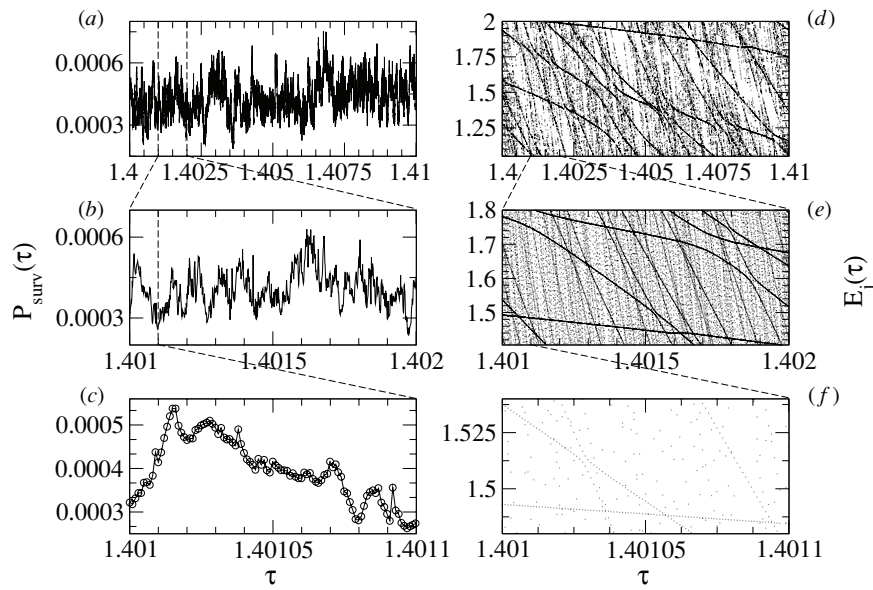


Figure 2. (a), (b), (c) show the survival probability of figure 1 after $t = 10^4$ kicks at different magnifications. For the same parameters, (d), (e), (f) show the real parts of the quasienergies as a function of τ (obtained as the eigenphases of the evolution operator (2), which was represented in the basis of momentum states as a finite matrix in the range $n \in]n_1, n_2[$ and then diagonalized). We see that the fluctuations on finer and finer scales are accompanied by ubiquitous avoided crossings in the eigenvalue spectrum (note that for better visibility in (d)–(f) only a small part of the full spectral range $[-\pi, \pi]$ is shown).

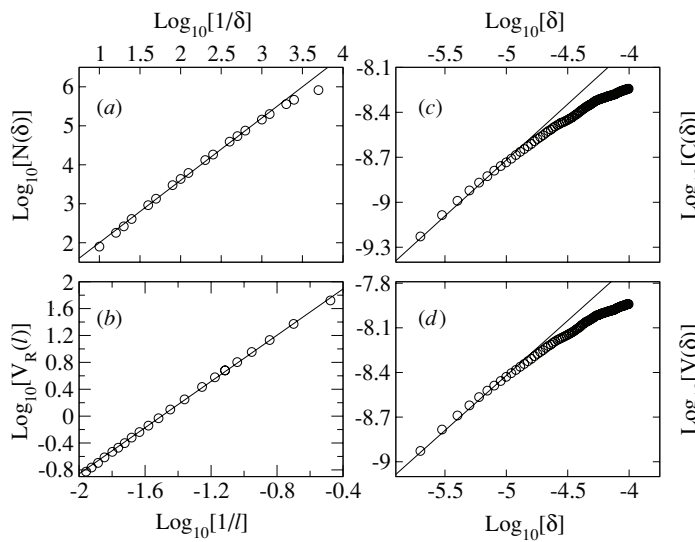


Figure 3. Fractal analysis of the survival probability from figure 2(a) using the following methods: (a) box counting, (b) variational method, (c) correlations, (d) variances. The exponents of the fits (solid lines) are $D_f = 1.6$ (a) and 1.7 (b), $a_{\text{corr}} = 0.8$ (c) and $a_{\text{var}} = 0.8$ (d).

variances of the fluctuating graphs. The correlations $C(\Delta\tau) = \langle P_{\text{surv}}(\tau) \cdot P_{\text{surv}}(\tau + \Delta\tau) \rangle_{\tau}$ are shown in figure 3(c), the variances $V(\Delta\tau) = \langle |P_{\text{surv}}(\tau + \Delta\tau) - P_{\text{surv}}(\tau)|^2 \rangle_{\tau}$ in figure 3(d).

Table 1. Fractal analysis of the survival probabilities after 10^4 kicks. $D_{f,bc}$ states to box counting dimension, while $D_{f,v}$ is obtained via the variational method. a_{corr} and a_{var} are the exponents of the fits to the correlations and variances, respectively. The estimated uncertainty derived from our fits (over finite ranges between one and two orders of magnitude of the power-law scaling, as e.g. in figure 3) is ± 0.1 for the fractal dimensions as well as the exponents.

k	β	n_1	n_2	$D_{f,bc}$	$D_{f,v}$	a_{corr}	a_{var}
2.0	0.0	-1	200	1.1	1.2	1.5	1.6
3.5	0.0	-1	200	1.3	1.4	1.0	1.0
4.0	0.0	-1	200	1.4	1.5	0.8	0.8
4.5	0.0	-1	200	1.5	1.6	0.8	0.8
5.0	0.0	-1	200	1.6	1.7	0.8	0.8
5.0	0.33	-1	200	1.6	1.7	0.8	0.8
5.0	0.38	-1	200	1.6	1.7	0.8	0.8
5.0	0.0	-1	250	1.6	1.7	0.8	0.7
5.0	0.0	-1	300	1.6	1.7	0.8	0.7
6.0	0.0	-1	300	1.6	1.7	0.8	0.7

Recalling the power-law scaling of $\rho(\Gamma)$ (see section 2), we can check the following set of relations:

$$\rho(\Gamma) \sim \Gamma^{-\alpha} \quad \Rightarrow \quad D_f \approx 1 + \alpha/2, \quad (8)$$

and

$$C(\Delta\tau) - C(0) \sim \Delta\tau^a, \quad V(\Delta\tau) \sim \Delta\tau^a \quad \text{with} \quad D_f = 2 - a/2,$$

in the presence of the numerically confirmed identity between the temporal decay exponent of $P_{\text{surv}}(t) \propto t^{-a}$ and the exponent of the correlations [12, 22]. These relations can be used as alternative and independent routes to the determination of the fractal dimension D_f . This follows from the fractional Brownian motion nature of $P_{\text{surv}}(\tau)$, which itself originates from the spectral properties of the opened δ -kicked rotor [7], and which determines the $\Delta\tau \rightarrow 0$ properties of statistical quantities such as correlations and variances [33].

Table 1 reports the fractal dimensions which were obtained by the above four methods. $D_{f,bc}$ and $D_{f,v}$ are the box counting and the variational dimension, respectively, while the exponents of the correlations and variances are denoted as a_{corr} and a_{var} . The table highlights the features already mentioned, i.e., the increase of D_f for increasing the kicking strength k and its basic independence of quasimomentum and the chosen cutoffs. The fractal dimension saturates for $k \geq k_{\text{sat}} \approx 4.5$. We verified this saturation with a series of simulations conducted for 13 values of $k \in [2, 6]$ (not all shown in table 1).

The obtained four independent methods of our fractal analysis (summarized in table 1) give fairly consistent results with each other, with an estimated precision of ± 0.1 . A systematical underestimation by box-counting method is observed, but also expected [31] when applying it to curves with $D \approx 1.5$.

For our choice of the grid in τ (see equation (6)) we noticed by inspecting the correlations and variances that, for $k \approx 5$, not all the fluctuations of the true curve are resolved by our grid. This yielded systematically smaller and meaningless values for a , a problem which does not affect the box counting and variational method that do not depend so critically upon the values of neighbouring points of the analysed graph. Augmenting the resolution of our grid in τ on a test interval $[\tau_0, \tau_0 + 10^3 \delta\tau]$ (cf equation (7) for the definition of τ_0 and $\delta\tau$) we nevertheless were able to estimate the exponents of the correlations and the variances for $k \geq 5$ and $n_2 \geq 250$ shown in table 1.

As a final test of our hypothesis that no trace of quantum resonances can be observed for the chosen interval in τ and our maximal interaction time of 10^4 kicks, we analysed the survival probability for $k = 5$ for two different quasimomenta $\beta \approx 1/3$ and $\beta = 0.378\,942\,469\,767\,714$ (stated as 0.33 and 0.38, respectively, in table 1). The latter value was chosen as a fraction of the golden mean to avoid any resonance condition in β (see equation (4)). As can be seen from table 1, no dependence on quasimomentum is found for the dynamically localized regime ($k = 5$).

In this section we presented a full-featured analysis of the fractal dimension of the survival probability $P_{\text{surv}}(\tau)$, studied the dependence on the parameters t and k and observed how these dependences provide systematical signatures of fractality caused by quantum effects. We found that $P_{\text{surv}}(\tau)$ is indeed fractal over a substantial range of scales, and its dimension can be estimated between 1.6 and 1.7. These numbers are stable when varying the initial quasimomentum (which is a constant of the motion) and the selected locations of the cut-offs n_1 and n_2 . Having in mind that the numerical determination of the fractal dimension of a graph bears some finite error (with estimated absolute uncertainty of about ± 0.1 for the data in table 1), our results are consistent with the fractal dimension 1.5 found for fixed $\tau = 1.4$ in the scan of quasimomentum [12] (figure 4 in [12] indeed seems to imply a similar systematic error as our data for the fractal dimension). Even if we scanned a different parameter than used in [12], the theory of [7] is independent of the chosen scanning variable, as long as the spectral premises reviewed in section 2 are fulfilled. The tendency towards a slightly larger fractal dimension in our data could, however, be related to the distribution of decay widths, whose precise form is sensitive to the chosen values of n_1 and n_2 (see [24] and discussion in section 2). Hence a slight deviation of our results from those of [12] is not surprising, since the finite-size effect of the boundary conditions may be different depending on whether τ or β is used as a scanning parameter [12].

5. Signatures of fractality for realistic experimental conditions

5.1. Experimental control of parameters

To realize an experiment where the fractal dimension of the survival probability, as studied in the preceding section, can be measured, it is necessary to address some principal problems of atom-optics kicked rotor experiments.

Control over the kicking strength k is granted with a precision of a few per cent [11, 14]. Anyway, table 1 tells us that a variation of k of the order up to 25% is not crucial. Time is one of the best controlled experimental parameters, and this feature makes it an ideal candidate for implementing an experiment to search for fractal fluctuations. Kicking periods between about hundred nanoseconds and a few hundred microseconds are available, with a maximal precision of a few nanoseconds [10, 14, 17, 18]. For caesium atoms, this range corresponds to dimensionless kicking periods (see section 1) $\tau \approx 10^{-2} \dots 18$, and a maximal precision of $\delta\tau \gtrsim 10^{-4}$. This precision implies that about 100 points could be scanned in our analysed interval in τ , which would be sufficient for a rough, qualitative verification of our predictions.

Any experiment will have a finite detection window of observable momentum classes. The actual width of this window is typically determined by the imaging resolution and by the minimal signal-to-noise ratio of the measurement device [9, 14, 27]. The detection window also determines a maximum interaction time after which the detection of a constantly decreasing atomic ensemble (due to the open boundary conditions) becomes meaningless. In other words, the maximum number of kicks is limited by the precision disposable in the determination of the final momentum distribution. Correspondingly, in our results reported below we choose the

minimal kicking strength $k = 4.5$ where the fractal dimension starts to saturate (see section 4) and a maximum interaction time of 500 kicks. The latter implies that we can choose a wider grid in τ because very fine structures do not develop for interaction times $t \leq 500$. We used $\delta\tau' = 10\delta\tau$, $\tau'_0 = \tau_0$ and $m' = m/10$ (cf equation (7)). A problem will certainly be the realization of our idealized absorbing boundary conditions at specific momentum classes of the atoms. Here methods using, for instance, external cutting potentials—such as so-called radio-frequency knives [34] or equally operating additional lasers—could be thought of.

5.2. The experimental initial ensemble

To approach real experimental scenarios, we shall analyse the survival probability for a smaller number of kicks of order 100 [9, 32] and take into account an initial spread of quasimomentum among the ensemble of cold atoms [16, 27].

For a typical ensemble of cold atoms, the momentum distribution is Gaussian-like, with a width exceeding that of the Brillouin zone $2\hbar k_L$, equal to 1 in our dimensionless units [9–11, 14, 27, 28, 32]. Folding produces approximately a uniform distribution in the entire Brillouin zone, i.e., a uniform distribution of quasimomenta with a width of $\Delta\beta = 1$ [16]. Using atoms in the Bose–Einstein condensate phase as initial ensemble allows the experimentalist a much better control over the width of the quasimomentum distribution [35]. Values of $\Delta\beta \lesssim 0.05$ have been realized in this context [18, 29, 36]. Letting the condensate expand a little before the actual kicking evolution, allows one to reduce the atom–atom interactions to negligible values, with only slight changes in $\Delta\beta$ [36]. As a consequence, the survival probability, experimentally measured by counting the number of atoms contained within the finite detection window, would be the result of an average of many *independent* survival probabilities with different values of quasimomentum. The independence of probabilities follows from the independent dynamics of the atoms [9–11, 14, 27, 28, 36], while the coherent evolution of a single atoms is still essential for the observed behaviour.

We computed $P_{\text{surv}}(\tau; \beta)$ for different ranges of β , and then averaged the resulting curves to arrive at $\langle P_{\text{surv}}(\tau; \beta) \rangle_\beta$. Figure 4 investigates the effect of averaging over β on the fractal dimension. The survival probabilities for two fixed β are shown, together with the average for a uniform distribution of 10^3 values of $\beta \in [0, 0.01]$. Figure 4(a) shows that the average curve is quite smooth on large scales, but nevertheless presents fluctuations on finer resolutions, with a fractal dimension substantially larger than unity. We verified that, by decreasing the number of atoms in the ensemble, the dimension steadily increases. We encounter a signature of fractality, which experiments could detect even far from the idealized limit of the one-atom dynamics. That is, the fluctuating behaviours of the averaged curves is a direct consequence of fluctuations of single β curves.

Figures 5(a) and (b) show the average survival probability for ensembles with the same number of β values but with different, larger widths $\Delta\beta$ of the initial quasimomentum distribution. Wider distributions are smoother on large scales and are not drawn in figure 5(a) because they could not be appreciated by eye when compared to curves for $\Delta\beta = 0.010$ and 0.025. The magnification in (b) shows that the fluctuations exhibit smaller excursions. A fractal analysis (see figure 5(c)) by the variational method shows that the dimension D_f remains in all cases larger than unity and, moreover, does *not* vary monotonically as $\Delta\beta$ is increased.

We interpret our results for finite $\Delta\beta$ in the following way: while a small range $\Delta\beta$ tends to wash out the fractal behaviour of the curves with one fixed β , an average over larger ranges $\Delta\beta$ tends to lift the fractal dimension again. This line follows nicely from the prediction

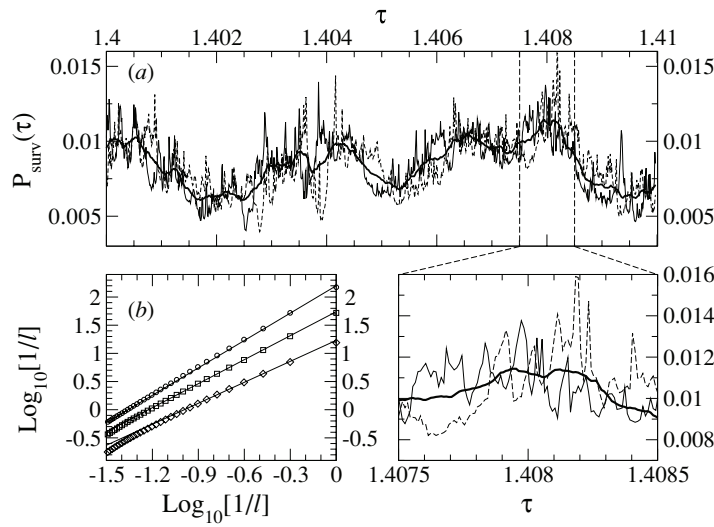


Figure 4. (a) shows two survival probabilities for fixed $\beta \approx 0.006554$ and $\beta \approx 0.002009$ together with an average of 10^3 β values equally distributed in $[0, 0.01]$ at $t = 500, k = 4.5, n_1 = -1, n_2 = 200$. The average curve (thick) is smoother but its fractional dimension is nevertheless greater than unity. (b) shows the fractal analysis by the variational method for $\beta \approx 0.006554$ (circles) that yields $D_f \approx 1.6$, for the average of $10^3 \beta \in [0, 0.01]$ (diamonds) with $D_f \approx 1.2$, and for the average of only 10 values of β in the same interval (squares) that gives the intermediate value of $D_f \approx 1.4$.

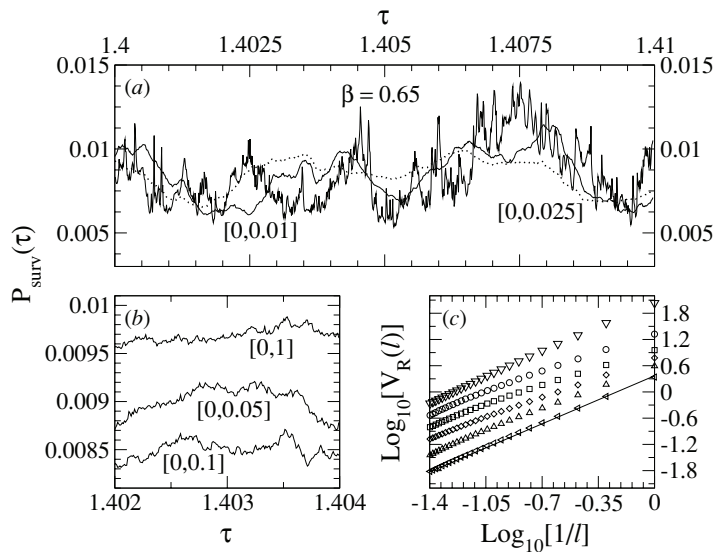


Figure 5. (a) average of the survival probability (for $k = 4.5$ and after 500 kicks) over 10^3 values of β uniformly distributed in $[0, 0.01]$ (solid) and $[0, 0.025]$ (dotted) together with a survival probability for a fixed value $\beta \approx 0.65$. (b) Same as (a) for 10^3 values of β uniformly distributed in the shown intervals. (c) Fractal analysis by the variational method for the survival probabilities shown in (a), (b). The fractal dimensions are obtained by linear fits (shown only for $\Delta\beta = 1$) through the symbols $D_f \approx 1.6$ (inverse pyramids, $\beta \approx 0.65$), 1.2 (circles, $\beta \in [0, 0.01]$), 1.2 (squares, $\beta \in [0, 0.025]$), 1.3 (diamonds, $\beta \in [0, 0.05]$), 1.4 (pyramids, $\beta \in [0, 0.1]$), and 1.5 (left triangles, $\beta \in [0, 1]$).

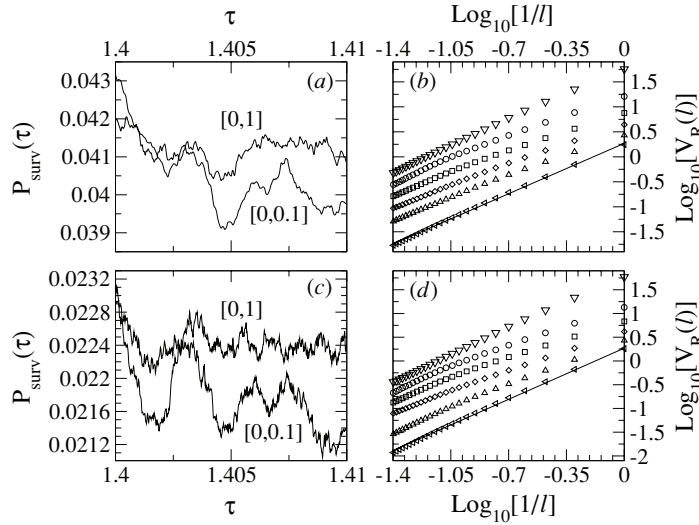


Figure 6. (a), (c) average of the survival probability over 10^3 values of β uniformly distributed in $[0, 0.1]$ and $[0, 1]$, after (a) 100 and (c) 200 kicks and for $k = 4.5$. The enhancement of self-affine fluctuations with time is clearly visible. (b) and (d) show the fractal analysis by the variational method for (a) and (b), respectively, corresponding to $\beta \approx 0.65$ (inverse pyramids), or 10^3 values of β uniformly distributed in $[0.01]$ (circles), $[0, 0.25]$ (squares), $[0, 0.05]$ (diamonds), $[0, 0.1]$ (pyramids), $[0, 1]$ (left triangles). The fractal dimensions are $D_f \approx 1.5, 1.2, 1.1, 1.2, 1.2, 1.4$ in (b) and $1.6, 1.2, 1.1, 1.2, 1.3, 1.5$ in (d) for increasing width of the β distribution.

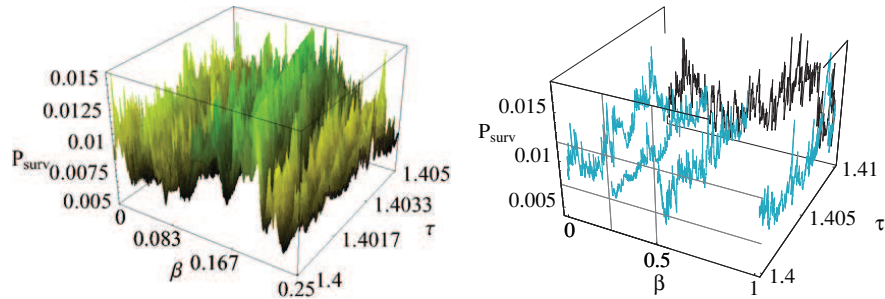


Figure 7. On the left panel the survival probability as a function of β and τ is shown after 500 kicks, for $k = 4.5$, $n_1 = -1$ and $n_2 = 200$. Slices of the graph $P_{\text{surv}}(\beta, \tau)$ are shown on the right panel. The thick lines represent the survival probability as a function of τ that is analysed in section 4 (we have used 10^3 similar curves to compute the incoherent average which is the experimental observable, as explained in section 5.2). The thin curve lying in the plane orthogonal to the τ axis is the survival probability $P_{\text{surv}}(\beta)$ as a function of the quasimomentum β such as studied in [12].

of [7] where it is argued that fractality can arise from superimposing non-fractal patterns on appropriate scales of the scanned variable [22, 26].

Figure 6 repeats the analysis of figure 5 for $t = 100$ (a), (b) and $t = 200$ (c), (d). The fractal dimension of each average survival probability for a definite value of $\Delta\beta$ is seen to be a monotonic function of time, what points out once more the dynamical origin of the analysed fluctuations. This contrasts the dependence of the fractal dimension on $\Delta\beta$ at a fixed time, which is non-monotonic, because averaging both washes out the fluctuations of the single curves for small $\Delta\beta \lesssim 0.1$, while it creates new ones by superimposition for $\Delta\beta \gtrsim 0.1$.

From a more general perspective, the survival probability $P_{\text{surv}}(\beta, \tau)$ can be seen as a surface lying over the plane spanned by the two variables τ and β . In [12] $P_{\text{surv}}(\beta, \tau)$ was analysed at fixed τ using β as a scanning parameter, i.e., a slice of the surface parallel to the β axis was analysed. In section 4 we studied the ‘orthogonal’ problem of fixed β , using τ as a scanning variable. Averaging over β can be interpreted as a ‘column density’, i.e., $P_{\text{surv}}(\beta, \tau)$ integrated over the β degree of freedom. The resulting averaged curve is the observable experimentally accessible as discussed in this section. Looking at figure 7, our results can thus be interpreted geometrically: the fractal behaviour of the slices $P_{\text{surv}}(\tau; \beta = \text{constant})$ is to a large extent preserved by the average over a typical experimental spread in β .

6. Conclusions

We considered the quantum kicked rotor, a paradigmatic model of quantum chaos, which describes the time evolution of noninteracting cold atoms in periodically flashed optical lattices. Imposing absorbing boundary conditions allows one to probe the transport properties of the system, and in particular to define the survival probability of atoms on a finite region in momentum space. For fixed kick numbers, the quantum survival probability depends sensitively on the parameters of the system, and a self-affine structure of the survival probability P_{surv} is predicted, as either the kicking period or quasimomentum is scanned.

Instead of using the initial quasimomentum β as control parameter, as done in the numerical simulations of [12], we used the kicking period τ as scan parameter, which is much better controllable experimentally. We verified the fractal nature of the graph of the survival probability $P_{\text{surv}}(\tau)$ in the dynamically localized regime, and obtained a fractal dimension $D_f \approx 1.6 \pm 0.1$ for large but finite interaction times, for which quantum resonances do not manifest.

Any experimental set-up prepares cold atoms with a finite spread in quasimomentum. The experimental observable is then the average of the survival probabilities over the quasimomentum distribution. We reproduced this observable by computing the incoherent average $\langle P_{\text{surv}}(\tau) \rangle_\beta$, and found that the fractal dimension of the average remains substantially larger than unity, even for shorter interaction times of a few hundred kicks.

We conclude that the fractality in the survival probability induced by quantum chaos is an unexpectedly robust feature and in spite of many challenging aspects (see section 5) could be observed in a future atom-optics experiment. Apart from the experimental verification of fractal fluctuations of purely quantum origin, a remaining open problem is whether a universal scaling law for the fractal dimension could be found as a function of *both* parameters τ and β , including quantitative predictions for the here computed averages $\langle P_{\text{surv}}(\tau, \beta) \rangle_\beta$ over a finite range of β .

Acknowledgments

We thank Emil Persson for bringing the variational method for the fractality analysis (see [31]) to our attention. SW acknowledges support by the Alexander von Humboldt Foundation (Feodor–Lynen Program) and is grateful to Italo Guarneri for a profound introduction to the field of ‘quantum fractals’.

References

- [1] Ben Dahan M, Peik E, Reichel J, Castin Y and Salomon C 1996 *Phys. Rev. Lett.* **76** 4508
 Wilkinson S R, Bharucha C F, Madison K W, Niu Q and Raizen M G 1996 *Phys. Rev. Lett.* **76** 4512

- Morsch O, Müller J H, Cristiani M, Ciampini D and Arimondo E 2001 *Phys. Rev. Lett.* **87** 140402
- Cataliotti F S *et al* 2001 *Science* **293** 843
- Greiner M, Mandel O, Esslinger T, Hänsch T W and Bloch I 2002 *Nature* **415** 39
- Roati G, de Mirandes E, Ferlaino F, Ott H, Modugno G and Inguscio M 2004 *Phys. Rev. Lett.* **92** 230402
- Paredes B *et al* 2004 *Nature* **429** 277
- Greiner M, Regal C A and Jin D S 2005 *Phys. Rev. Lett.* **94** 070403
- Albiez M, Gati R, Fölling J, Hunsmann S, Cristiani M and Oberthaler M K 2005 *Phys. Rev. Lett.* **95** 010402
- [2] Hegger H, Huckstein B, Hecker K, Janssen M, Freimuth A, Reckziegel G and Tuzinski R 1996 *Phys. Rev. Lett.* **77** 3885
- Micolich A P *et al* 1998 *J. Phys.: Condens. Matter* **10** 1339
- Crook R, Smith C G, Graham A C, Farrer I, Beere H E and Ritchie D A 2003 *Phys. Rev. Lett.* **91** 246803
- Micolich A P *et al* 2001 *Phys. Rev. Lett.* **87** 036802
- [3] Sachrajda A S, Ketzmerick R, Gould C, Feng Y, Kelly P J, Delage A and Wasilewski Z 1998 *Phys. Rev. Lett.* **80** 1948
- [4] Ketzmerick R 1996 *Phys. Rev. B* **54** 10841
- Huckstein B, Ketzmerick R and Lewenkopf C H 2000 *Phys. Rev. Lett.* **84** 5504
- Weingartner B, Rotter S and Burgdörfer J 2005 *Phys. Rev. B* **72** 115342
- [5] Hufnagel L, Ketzmerick R and Weiss M 2001 *Europhys. Lett.* **54** 703
- [6] Micolich A P *et al* 2004 *Phys. Rev. B* **70** 085302
- [7] Guarneri I and Terraneo M 2001 *Phys. Rev. E* **65** 015203(R)
- [8] Budiyo A and Nakamura K 2003 *Chaos Solitons Fractals* **17** 89
- Louis E and Verges J A 2000 *Phys. Rev.* **61** 13014
- [9] Klappauf B G, Oskay W H, Steck D A and Raizen M G 1999 *Physica D* **131** 78
- [10] Sadgrove M, Wimberger S, Parkins S and Leonhardt R 2005 *Phys. Rev. Lett.* **94** 174103
- [11] Bharucha C F, Robinson J C, Moore F C, Sundaram B, Niu Q and Raizen M G 1999 *Phys. Rev. E* **60** 3881
- [12] Benenti G, Casati G, Guarneri I and Terraneo M 2001 *Phys. Rev. Lett.* **87** 014101
- [13] Moore F L, Robinson J C, Bharucha C F, Sundaram B and Raizen M G 1995 *Phys. Rev. Lett.* **75** 4598
- [14] d'Arcy M B, Godun R M, Oberthaler M K, Summy G S, Burnett K and Gardiner S A 2001 *Phys. Rev. E* **64** 056233
- [15] Graham R, Schlautmann M and Zoller P 1992 *Phys. Rev. A* **45** R19
- [16] Wimberger S, Guarneri I and Fishman S 2003 *Nonlinearity* **16** 1381
- [17] Oskay W H, Steck D A and Raizen M G 2003 *Chaos Solitons Fractals* **16** 409
- [18] Ryu C, Andersen M, Vaziri A, d'Arcy M B, Grossman J M, Helmerson K and Phillips W D 2005 in preparation
- [19] Casati G, Maspero G and Shepelyansky D L 1999 *Phys. Rev. Lett.* **82** 524
- [20] Izrailev F M 1990 *Phys. Rep.* **196** 299
- [21] Fishman S 1993 *Quantum Chaos: Proceedings of the International School of Physics 'E. Fermi' CXIX* ed G Casati, I Guarneri and U Smilansky (Amsterdam: IOS)
- [22] Terraneo M 2001 *PhD Thesis* Università degli Studi di Milano
- [23] Titov M and Fyodorov Y 2000 *Phys. Rev. B* **61** 2444
- Terraneo M and Guarneri I 2000 *Eur. Phys. J. B* **18** 303
- Steinbach F, Ossipov A, Kottos T and Geisel T 2000 *Phys. Rev. Lett.* **85** 4426
- [24] Wimberger S, Krug A and Buchleitner A 2002 *Phys. Rev. Lett.* **89** 263601
- [25] Feingold M, Fishman S, Gempel D R and Prange R 1985 *Phys. Rev. B* **31** 6852
- [26] Guarneri I, Terraneo M and Wimberger S unpublished
- [27] d'Arcy M B, Godun R M, Summy G S, Guarneri I, Wimberger S, Fishman S and Buchleitner A 2004 *Phys. Rev. E* **69** 027201
- [28] Wimberger S, Sadgrove M, Parkins S and Leonhardt R 2005 *Phys. Rev. A* **71** 053404
- Wimberger S and Sadgrove M 2005 *J. Phys. A: Math. Gen.* **38** 10549
- [29] Duffy G J, Mellish A S, Challis K J and Wilson A C 2004 *Phys. Rev. A* **70** R041602
- [30] Izrailev F M and Shepelyansky D L 1980 *Theor. Math. Phys.* **43** 353
- [31] Dubuc B, Quiniou J F, Roques-Carnes C, Tricot C and Zucker S W 1989 *Phys. Rev. A* **39** 1500
- [32] Schlunk S, d'Arcy M B, Gardiner S A and Summy G S 2003 *Phys. Rev. Lett.* **90** 124102
- [33] Mandelbrot B B 1982 *The Fractal Geometry of Nature* (San Francisco: Freeman)
- [34] Stock S, Hadzibabic Z, Battelier B, Cheneau M and Dalibard J 2005 *Phys. Rev. Lett.* **95** 190403 and references therein
- [35] Wimberger S, Mannella R, Morsch O and Arimondo E 2005 *Phys. Rev. Lett.* **94** 130404
- [36] Duffy G J, Parkins S, Muller T, Sadgrove M, Leonhardt R and Wilson A C 2004 *Phys. Rev. E* **70** 056206

Tunnelling rates for the nonlinear Wannier–Stark problem

Sandro Wimberger¹, Peter Schlagheck² and Riccardo Mannella¹

¹ Dipartimento di Fisica Enrico Fermi and CNR-INFM, Università degli Studi di Pisa, Largo Pontecorvo 3, I-56127 Pisa, Italy

² Institut für Theoretische Physik, Universität Regensburg, D-93040 Regensburg, Germany

E-mail: saw@df.unipi.it

Received 18 October 2005, in final form 4 December 2005

Published 16 January 2006

Online at stacks.iop.org/JPhysB/39/729

Abstract

We present a method to numerically compute accurate tunnelling rates for a Bose–Einstein condensate which is described by the nonlinear Gross–Pitaevskii equation. Our method is based on a sophisticated real-time integration of the complex-scaled Gross–Pitaevskii equation, and it is capable of finding the stationary eigenvalues for the Wannier–Stark problem. We show that even weak nonlinearities have significant effects in the vicinity of very sensitive resonant tunnelling peaks, which occur in the rates as a function of the Stark field amplitude. The mean-field interaction induces a broadening and a shift of the peaks, and the latter is explained by an analytic perturbation theory.

(Some figures in this article are in colour only in the electronic version)

1. Introduction

Quantum dynamics often is intriguing and counter-intuitive. A prominent example thereof is the localization of a wave packet in a spatially periodic lattice induced by an additional static force: the force can turn an extended Bloch wave (which is a solution of the Schrödinger equation with a periodic potential [1]) to a wave packet which oscillates periodically in (momentum) space [1]. While conceptually simple, this well-known Wannier–Stark problem is complicated from the mathematical point of view because the system is open, i.e., unbounded, and any initially prepared state will, in the course of time evolution, decay via tunnelling out of the periodic potential wells [2, 3].

Starting from the Bloch bands of the unperturbed problem (i.e., without the static field $F = 0$), the decay can be attributed to tunnelling from the ground-state band to the first excited energy band. The celebrated Landau–Zener theory predicts an exponential decay rate (see, for instance, [4, 5] for introductory reviews):

$$\Gamma(F) \propto F e^{-\frac{b}{F}}, \quad (1)$$

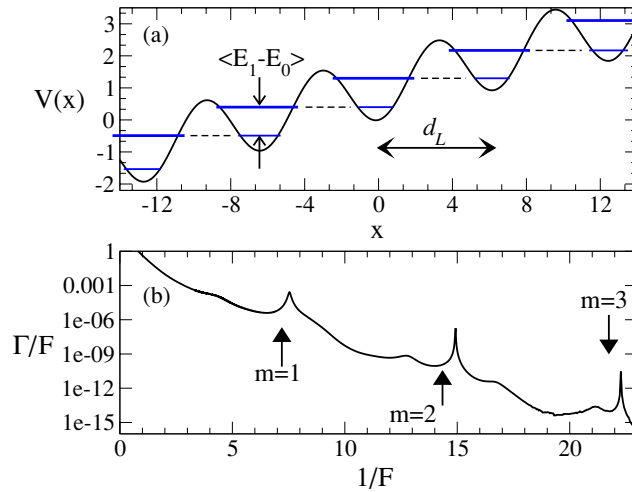


Figure 1. (a) Schematic sketch of nearly degenerate Wannier–Stark levels (thin line: ground-state levels; thick line: first excited levels in each well) in a potential of the form $V(x) = V_0 \sin^2(x/2) + Fx$. (b) Tunnelling rates Γ for $V_0 = 2$ as a function of the inverse Stark field amplitude $1/F$. The resonant tunnelling leads to the pronounced peaks, which lie approximately at $F \approx \langle E_1 - E_0 \rangle / (2\pi m)$ (with the integer m). These estimates (marked by the arrows) are slightly modified by field-induced level shifts.

where b is proportional to the square of the energy gap between the two lowest energy bands. For experiments with cold atoms, i.e., the scenario on which we focus in this paper, the wave packet decays very quickly by successive tunnelling events, once it has tunneled across the first band gap. This is due to the much smaller gaps of the higher energy bands in a sinusoidal potential [6, 7]. The Landau–Zener formula (1) cannot account for the interaction of the Wannier–Stark levels at adjacent potential wells. Between such adjacent lattice sites nearly degenerate Wannier–Stark levels repel each other, which leads to a strong enhancement of the tunnelling decay. These resonant tunnelling events result in pronounced peaks in the rates as a function of the inverse field amplitude $1/F$, on top of the of the global exponential decay described by (1) [5, 8].

Figure 1(a) shows two Wannier–Stark levels on each lattice site. The levels within either of the two ladders are separated by mFd_L in energy, where $d_L \equiv 2\pi$ denotes the lattice period and the integer m counts the number of sites in between two energy levels of the same ladder [1, 2]. The decay rates for non-interacting particles in the periodic potential $V(x) = V_0 \sin^2(x/2) + Fx$ can be computed from the Wannier–Stark spectrum, e.g., by using the numerical method described in [5]. Figure 1(b) presents the rate Γ as a function of $1/F$. The maxima occur when mFd_L is close to the difference in energy $\langle E_1 - E_0 \rangle$ between the first two energy bands (averaged over the fundamental Brillouin zone in momentum space) of the unperturbed ($F = 0$) problem [5, 9]. The actual peak positions are slightly shifted with respect to this simplified estimate (marked by arrows in figure 1(b)), owing to a field-induced level shift close to the avoided crossings of the levels [8].

Exceptional experimental control is possible nowadays with Bose–Einstein condensates (BEC) whose initial conditions in coordinate and momentum space can be adjusted with unprecedented precision. With the help of a BEC, sensitive tunnelling phenomena were studied in time-dependent systems [10], as well as in static potentials [11]. Here we are interested in tunnelling in the Wannier–Stark problem where the impact of the intrinsic atom–atom interactions in the BEC has been studied in several recent experiments [7, 12–14].

In those experiments, the difficulty in understanding quantum transport processes, such as coherent tunnelling, originates from the complex interplay between classical transport in the underlying phase space, quantum interference effects and the many-particle interactions.

In a typical experiment with a BEC, where the number of atoms in the condensate is large and the atom–atom interaction is rather small, the Gross–Pitaevskii equation (GPE) describes the condensate in very good approximation [15]. Recently, some of us proposed a concrete experimental scenario to measure the impact of a mean-field interaction potential (which in the GPE takes into account of the atomic collisions) on the tunnelling in the Wannier–Stark problem [16]. More specifically, the interaction-induced modification of the resonant tunnelling peaks was studied, and it was found that the peaks (such as those in figure 1(b)) are washed out for a large enough—but still experimentally feasible—interaction strength. As discussed in [16], for a finite mean-field nonlinearity, the concept of decay rates is not as well defined as in the case of non-interacting particles. The reason is that the weight of the nonlinear term, which is proportional to the condensate density, varies in time. Hence, the probability that an initially prepared state will stay in the preparation region does not follow a simple exponential law. In other words, the nonlinear interaction decreases as the condensate escapes via tunnelling and, as a consequence, the decay rates can be defined only locally in time.

In this paper, we want to discuss how the problem of defining proper decay rates can be solved. One way to define a time-independent, global tunnelling rate is to renormalize the density of the condensate in the preparation region (e.g., in the central potential well of the periodic lattice) continuously, such that the average density remains constant in time. For experimentally realizable nonlinearities [7, 12, 13, 17], this approach results in a mono-exponential decay of the survival probability, and in consequence in a reasonable definition of the decay rate. The corresponding resonance states are characterized by their stationary asymptotics, much in the same way as the stationary solutions of a linear scattering problem (i.e., described by the linear Schrödinger equation) [5]. We solve numerically the well-posed problem of finding the resonance states, using the method of complex scaling. The theoretical background to treat the nonlinear interaction in the GPE in a consistent way was recently laid in [18]. We use a modified version of this method, with crucial extensions on the algorithmic side, which proved necessary to stabilize the computations for more complicated potentials than the single-well potential exemplarily treated in [18].

We review the defining equations of the nonlinear Wannier–Stark problem and the complex-scaling technique of [18] in the following section 2, where we also describe our numerical algorithm in detail (cf subsection 2.2). Section 3 presents our central results on the decay rates in the vicinity of the resonant tunnelling peaks for experimentally relevant nonlinearities. Section 4 finally concludes the paper.

2. The nonlinear Wannier–Stark problem

We use the one-dimensional GPE to model the temporal evolution of a BEC loaded into a spatially periodic optical lattice potential and subjected to an additional static force F :

$$i \frac{\partial}{\partial t} \psi(x, t) = \left[-\frac{1}{2} \frac{\partial^2}{\partial x^2} + V_0 \sin^2 \left(\frac{x}{2} \right) + Fx + g |\psi(x, t)|^2 \right] \psi(x, t). \quad (2)$$

$\psi(x, t)$ represents the condensate wavefunction, and we used the dimensionless quantities $V_0 = V_{\text{SI}}/E_{\text{B}}$, $F = F_{\text{SI}}d_{\text{L}}/(2\pi E_{\text{B}})$, $g = g_{\text{SI}}d_{\text{L}}N/(2\pi E_{\text{B}})$. The characteristic length scale is the lattice period d_{L} , i.e., $x = x_{\text{SI}}2\pi/d_{\text{L}}$, the Bloch energy is $E_{\text{B}} = (\pi\hbar/d_{\text{L}})^2/M$, with atomic mass M , the number of atoms N and the (from three to one spatial dimensions) rescaled

nonlinearity parameter g_{SI} (see [19] for a definition of g_{SI} , where also the regime of validity of the one-dimensional approximation is discussed in detail).

Since $V(x) = V_0 \sin^2(x/2) + Fx \rightarrow -\infty$ for $x \rightarrow -\infty$, any state initially prepared in the optical lattice will escape via tunnelling. We search for the resonance state ψ_g which solves the stationary version of equation (2)

$$H[\psi_g]\psi_g = E_g\psi_g, \quad (3)$$

for the eigenvalue $E_g = \mu_g - i\Gamma_g/2$, and the Hamiltonian

$$H[\psi] = -\frac{1}{2}\frac{\partial^2}{\partial x^2} + V(x) + g|\psi(x)|^2. \quad (4)$$

To render the problem posed by equation (3) meaningful, we demand that the condensate wavefunction remains normalized around the initially prepared state, i.e., around $x \approx 0$:

$$\int_{-x_n}^{x_n} dx |\psi_g(x)|^2 = 1. \quad (5)$$

The boundaries x_n must be chosen in a reasonable way, and we chose $x_n = \pi$ (so the probability to stay in the central well around $x = 0$ remains one [20]). We verified that slightly different choices of the boundary $\pi \lesssim x_n < 3\pi/2$ led to eigenvalues which did not change on the significant digits given in section 3.

We discuss now the renormalization condition (5) and its consequences. In practice such a condition may be realized by the presence of a source term which constantly supplies a condensate flow [21]. Experimentally such a scenario could be achieved by constantly reloading the central well with coherent BEC matter. Transport experiments of such kind could be realized with the help of optical tweezers [22], atomic conveyer belts [23] or microscopic guides for ultracold atoms [24]. Any realization may introduce additional modifications in the temporal evolution of the decaying system, which go beyond our simplified assumption of renormalization. Such modifications, e.g., the relaxation of added particles in the periodic lattice potential, depend on the specific realization. We expect, however, that the asymptotic decay will be hardly affected by such processes, the time scales of which should be relatively short and of the order of the period of oscillations in the potential wells.

On the other hand, if the condensate wavefunction tunnels out of the central well without sudden changes of its shape, the time-dependent atomic population $N(t)$ inside the well decays according to the relation [18, 25]

$$\frac{dN(t)}{dt} = -\Gamma_{g(t)}N(t). \quad (6)$$

Assuming that the decay rate adiabatically adjusts itself to the time-dependent value $\Gamma_{g(t)}$, with $g(t) \propto N(t)$, equation (6) can be solved for a given initial number of atoms $N(0)$ in the condensate. Knowing the ‘local’ rates $\Gamma_{g(t)}$ for $0 \leq |g| \leq |g(0)|$ allows us then to compute the actual survival probability in the central well, which in [16] was obtained differently by a brute force integration of the time-dependent GPE (2).

We emphasize that the setup studied in [16] bears some crucial differences to the problem posed here, which is based on condition (5). In [16], the short-time behaviour of the relaxed ground state (for $F = 0$ in the periodic potential and in the presence of additional harmonic confinements) was predicted for the three-dimensional Wannier–Stark problem. The approach presented here is capable of determining, via equation (6), the decay only for *single* resonance states according to the above arguments. Although such resonance states are typically distributed over many lattice sites, they do not provide a prediction for the decay of a general initial state (which could be composed of contributions from many adjacent wells), simply because the superposition principle does not apply for the nonlinear GPE (2).

In this paper, we want to compute *directly* the precise decay rates Γ_g of a single resonance state using the complex-scaling method, which is described in the following subsection.

2.1. Complex scaling

For the linear problem with $g = 0$, one of the standard techniques to compute resonance states numerically is the complex-scaling method (which goes back to [26], and is reviewed, for instance, in [27]). Applying the renormalization condition (5) allows us to use this method to find the stationary eigenstates and the corresponding eigenvalues; see equation (3). Without this condition, the nonlinear interaction term would vary in time, and a stationary state would not exist because of the tunnelling decay.

An additional problem when dealing with the nonlinear term in the GPE arises from the method of complex scaling itself. The problem of defining the complex conjugate of the wavefunction $\psi(x)$ is described in [18, 28], and was solved in [18]. Usually, the scaling transformation is defined as follows:

$$\psi(x) \rightarrow \psi^\theta(x) \equiv \hat{R}(\theta)\psi(x) \equiv e^{i\theta/2}\psi(x e^{i\theta}), \quad (7)$$

where the pre-factor is just a phase depending on the dimensionality of the problem (here we treat only the one-dimensional case). θ is a real rotation angle, and the eigenvalues should not depend on it [26, 27], which is a useful fact for testing convergence. To evaluate the nonlinear term $|\psi|^2 = \psi^*\psi$ away from the real coordinate (or x) axis, we need to define a generalized complex conjugate $\bar{\psi}$ which reduces to $\bar{\psi}(x) = \psi(x)^*$ for $x \in \mathbb{R}$. Applying the complex-scaling transformation to $\bar{\psi}$

$$\overline{\psi(x)} \rightarrow \overline{\psi^\theta}(x) \equiv \hat{R}(\theta)\overline{\psi}(x) \equiv e^{i\theta/2}\overline{\psi}(x e^{i\theta}), \quad (8)$$

we see that $\overline{\psi^\theta}$ can be obtained from ψ^θ via the relation:

$$\overline{\psi^\theta}(x) = \hat{R}(\theta)(\hat{R}(-\theta)\psi^\theta)^*(x). \quad (9)$$

The analytic continuation of equation (3) to the complex domain can now be stated as

$$H^\theta[\psi_g^\theta]\psi_g^\theta = E_g\psi_g^\theta, \quad (10)$$

with

$$H^\theta[\psi_g^\theta] = -\frac{1}{2}\frac{\partial^2}{\partial x^2} e^{-i2\theta} + V(x e^{i\theta}) + g_\theta \overline{\psi_g^\theta}(x)\psi_g^\theta(x). \quad (11)$$

The nonlinear interaction strength is defined here as $g_\theta = g e^{-i\theta}$ to compensate for the two identical phase factors $e^{i\theta/2}$ of ψ^θ and $\overline{\psi^\theta}$.

2.2. Numerical solution and propagation algorithm

In the linear case with $g = 0$, the complex eigenvalue problem of the form (10) is usually solved by representing the complex-scaled Hamiltonian in a suitable basis and final matrix diagonalization [29]. For $g \neq 0$, the corresponding problem to find the eigenvalues can be solved only by implicit methods, since $H^\theta[\psi^\theta]$ explicitly depends on the wavefunction.

We solved equation (10) by searching for the ground-state solution in a self-consistent manner. Starting with an initial guess for the wavefunction $\psi^\theta(x, t = 0)$, we evolved in real time the grid representation of $\psi^\theta(x, t)$, i.e.,

$$\psi^\theta(x, t) = \sum_{j=-n}^n c_j(t)\chi_j(x), \quad (12)$$

with the box functions

$$\chi_j(x) = \begin{cases} 1/\Delta_x, & |x/\Delta_x - j| < 1/2 \\ 0, & \text{otherwise,} \end{cases} \quad (13)$$

and a suitable grid spacing Δ_x .

The time propagation was performed by a sequential application of two different integration methods. First, we used a sequence of Crank–Nicholson steps [30], i.e.,

$$(1 + iH^\theta \Delta t/2)\psi^\theta(x, t + \Delta t/2) = (1 - iH^\theta \Delta t/2)\psi^\theta(x, t - \Delta t/2). \quad (14)$$

The Crank–Nicholson method has the advantage of preserving the norm of the wavefunction, but the disadvantage is that it treats all modes equally. Since we are interested in the ground state, we iterated in a second stage the explicit relation

$$\psi^\theta(x, t + \Delta t) = (1 - iH^\theta[\psi^\theta]\Delta t)\psi^\theta(x, t). \quad (15)$$

The latter method, which still corresponds to a real-time integration of the complex scaled Gross–Pitaevskii equation, tends to suppress the higher modes [30] and leads to a faster stabilization of the numerical solution of equation (10) in comparison with the Crank–Nicholson method (14). For *each* time step $t \mapsto t + \Delta t$, we self-consistently solved equation (15) by using the left-hand side of equation (15) to approximate the nonlinear term $g_\theta \bar{\psi}^\theta \psi^\theta$. Three to five such self-consistent iterations proved sufficient for a stable and reliable time propagation. The second derivative appearing in H^θ was approximated by a finite difference representation (in other words we applied the ‘forward time centred space’ representation [30] to solve the GPE). This leads to a tridiagonal Hamiltonian matrix, which significantly simplifies the implementation of both propagators (14) and (15).

For evaluating $\bar{\psi}^\theta(x, t)$, we used the method described in detail in [18], which produced reliable numerical results also for our Wannier–Stark problem. Briefly speaking, we represent $\psi^\theta(x, t)$ in a basis set of Gaussians with increasing variance for increasing $|x|$. The Gaussian basis is thus well behaved at the boundaries of our grid, which allows us a numerically stable back-rotation to the real domain in x . At the end, $\bar{\psi}^\theta(x, t)$ is re-expressed again in the grid basis. The necessary matrix–vector multiplications are fast since the number of vectors in the Gaussian set can typically be chosen much smaller than the number of grid points in the spatial domain. Furthermore, the transformation matrices are effectively banded, which reduces the numerical effort (note that we computed $\bar{\psi}^\theta(x, t)$ from $\psi^\theta(x, t)$ for *each* time step $t \mapsto t + \Delta t$ to ensure stable convergence).

3. Results and discussion

In the following, we present our results on the tunnelling rates of resonance states (cf equation (10)) in the Wannier–Stark problem as sketched in figure 1(a). Without loss of generality we kept fixed the potential depth $V_0 = 2$ in equation (2), which corresponds to an optical lattice with a maximal amplitude of 16 photon recoil energies [6, 7]. We were particularly interested in studying the impact of the nonlinear term in equation (2) on the resonant tunnelling peaks of figure 1(b). Using the method described in the previous section we chose $\theta = 0.01, \dots, 0.02$ (where we found stable eigenvalues which are not dependent on θ in this range), and a grid spacing $\Delta_x = 0.02, \dots, 0.05$ for $-100 \leq x \leq 100$. The integration time step was $\Delta t = 2.5 \times 10^{-3}$ for $|g| < 0.2$ and reduced to $\Delta t = 2 \times 10^{-3}$ for larger $|g| \geq 0.2$ and the region of small $F < 0.2$, while the maximal integration time for finding one eigenvalue was $t_{\max} = 300$.

As expected, it is very difficult to find the correct eigenvalue close to a resonant tunnelling peak because of two reasons: (i) the rates Γ vary dramatically around the peak due to the close

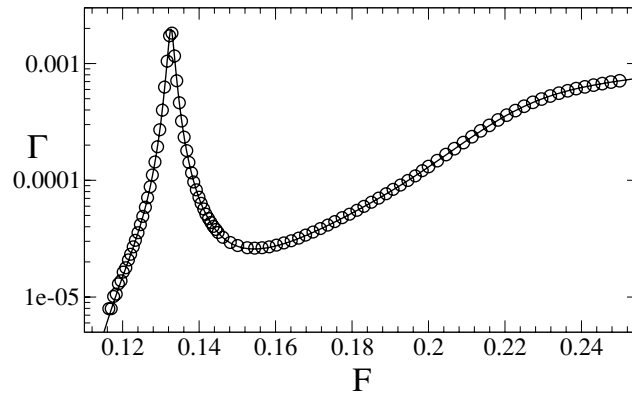


Figure 2. Comparison between the tunnelling rates around the first resonant tunnelling peak from figure 1(b), obtained for $g = 0$ by direct diagonalization of the problem (solid line) and by our complex-scaling algorithm (circles).

degeneracy of the Wannier–Stark levels in adjacent wells, and (ii) the rates are rather small $10^{-13} < \Gamma \lesssim 2 \times 10^{-3}$ at small fields $0.05 < F < 0.2$.

Therefore, we focused on the first (i.e., with $m = 1$) peak in figure 1(b), where the rates remain $\Gamma \gtrsim 10^{-5}$. Moreover, we improved the stability of the integration by starting with parameters in a stable regime (where we easily found stable, fast converging eigenvalues) and adiabatically changing the two parameters F and g into less stable parameter regimes. In our case, for $V_0 = 2$, the stable regime is above $F > 0.25$ for not too large nonlinearities $|g| \lesssim 0.5$ (with optimal stability properties for $g = 0$).

We tested our results in three different and independent ways. First, we compared them for $g = 0$ with the spectra of the linear Wannier–Stark problem, which can be computed by a standard diagonalization of $H_{g=0}^\theta$ [5, 29]. Figure 2 shows the good agreement between the data set obtained by our integration of the complex scaled, linear version of equation (2) and the data presented already in figure 1(b).

Secondly, for moderate nonlinearities $|g| \leq 0.5$, we computed for the *unscaled* problem (2) the survival probability

$$P_{\text{sur}}(t) \equiv \int_{-p_c}^{\infty} dp |\hat{\psi}(p, t)|^2 \approx N(t), \quad (16)$$

with $p_c \gtrsim 3$ photon recoils (such as to cover the support in momentum space of the initial state prepared in the spatially periodic lattice potential). $P_{\text{sur}}(t)$ was introduced for the Wannier–Stark problem in [16] and characterizes the out-coupled loss in momentum space, which corresponds to the part of the condensate which has tunneled through the potential. We integrated equation (2) constantly applying the renormalization condition (5) and computed the survival probability (16) with the wavefunction

$$\hat{\psi}(p, t) \approx \frac{\hat{\psi}_{\text{renorm}}(p, t)}{\prod_{j=1}^K \int_{-\pi}^{\pi} dx |\psi(x, jt/K)|^2},$$

for the discretized times jt/K ($j = 1, 2, \dots, K$) and large $K \in \mathbb{N}$. Here $\psi(x, jt/K)$ denotes the propagated wavefunction immediately before applying the renormalization ($\psi(x, jt/K)$ is renormalized afterwards and propagated up to time $(j+1)t/K$). $\hat{\psi}_{\text{renorm}}(p, t)$ represents the Fourier transform of the renormalized wavefunction at the end of the complete propagation. The decay rates Γ_{fit} were obtained by a direct mono-exponential fit to the temporal decay of

Table 1. Comparison between the tunnelling rates for $V_0 = 2$ obtained by the complex-scaling method (Γ_{CS}) and by the integration of the GPE (Γ_{fit} ; integration time up to 100 Bloch periods; the integration was performed on a large grid that covered the full extension of the tunnelled and subsequently accelerated part of the wavefunction, without the use of any cutoff or absorbing boundary conditions). Because of the restriction in the integration time, Γ_{fit} carries the shown error, whilst the complex-scaling method allows us to compute the rates Γ_{CS} with an absolute accuracy of at least 10^{-6} for $F \geq 0.15$, and 10^{-5} for F down to $\gtrsim 0.12$.

g	F	Γ_{fit}	Γ_{CS}
0	0.5	$1.94 \pm 0.01 \times 10^{-2}$	1.941×10^{-2}
0.1	0.5	$2.18 \pm 0.01 \times 10^{-2}$	2.180×10^{-2}
0	0.25	$7.2 \pm 0.1 \times 10^{-4}$	7.2×10^{-4}
0.1	0.25	$8.4 \pm 0.1 \times 10^{-4}$	8.4×10^{-4}
0.2	0.25	$9.7 \pm 0.1 \times 10^{-4}$	9.7×10^{-4}
0.25	0.25	$1.04 \pm 0.02 \times 10^{-3}$	1.04×10^{-3}
0.5	0.25	$1.45 \pm 0.03 \times 10^{-3}$	1.48×10^{-3}
0.2	0.15	$3.0 \pm 0.2 \times 10^{-5}$	2.9×10^{-5}
0.2	0.13125	$5.7 \pm 0.3 \times 10^{-5}$	5.7×10^{-5}

$P_{\text{sur}}(t)$. Table 1 highlights the good agreement with the rates computed by the complex-scaling method.

As a final test of our results, we constantly monitored the quality of the computed eigenvalues by evaluating $|(H^\theta[\psi^\theta] - E)\psi^\theta|$, which in all cases had to be $\lesssim 10^{-8}$ for not rejecting the eigenvalue. This boundary was chosen such as to be more than two orders of magnitude smaller than the smallest tunnelling rates which we computed.

Our central results are reported now in figure 3. There we observe two effects which are induced by the presence of the nonlinear interaction term in equation (2): (I) the resonant tunnelling peak shifts systematically with increasing g as a function of the Stark field amplitude F ; (II) the peak width slightly increases as $|g|$ increases away from zero.

The slight broadening goes along with a small increase in the height of the peaks with increasing nonlinearity g . Such a destabilization of the condensate for $g > 0$, more precisely of the decay in the survival probability $P_{\text{sur}}(t)$, has already been observed in [16]. The ratio of the difference in the height and the difference in the peak width (measured at the half of the peak height, see figure 3) is roughly constant as a function of the nonlinearity $0 < g \lesssim 0.25$. The broadening and the change in height of the peak are caused by two different but simultaneously acting mechanisms. The nonlinear mean-field term in equation (2) partially lifts the degeneracy of the Wannier–Stark levels (as sketched in figure 1(a)) by smearing them out. This qualitatively explains the slight broadening of the peak with increasing $|g|$. In addition, the peak maximum becomes systematically larger as g increases in figure 3 because the condensate is destabilized (stabilized) by an increasingly repulsive (attractive) nonlinearity.

The shift of the peak maximum can be estimated by first-order perturbation theory, which predicts the following shift in energy of the levels with respect to the linear case with $g = 0$:

$$\Delta E \approx g \int_{-x_c}^{x_c} dx |\psi_g|^2 |\psi_{g=0}|^2. \quad (17)$$

For the moderate nonlinearities realized in experiments [7, 17, 31], i.e., $|g| \lesssim 0.5$, the overlap integral is nearly independent of g , and the major contribution comes from the

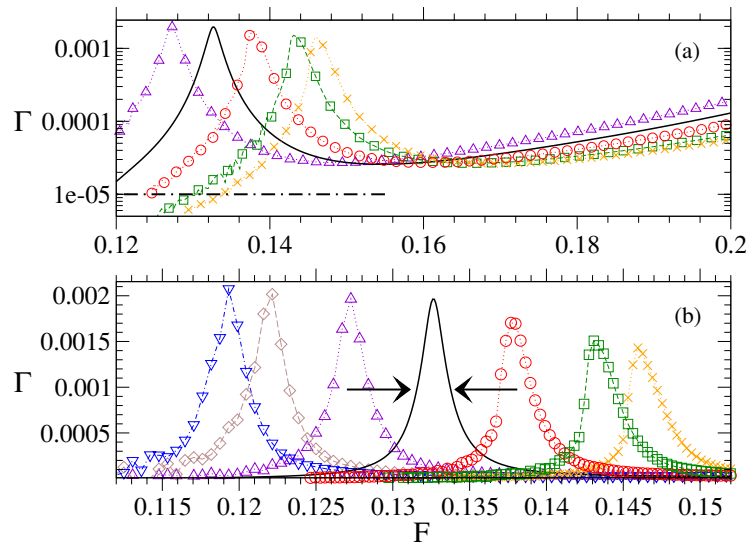


Figure 3. Decay rates Γ obtained for $V_0 = 2$ and the range of nonlinearities $-0.25 \leq g \leq 0.25$ as a function of the Stark field amplitude F ((a) logarithmic and (b) linear scale on the y -axis): $g = -0.25$ (crosses), $g = -0.2$ (squares), -0.1 (circles), 0 (solid line), 0.1 (pyramids), 0.2 (diamonds; only in (b)) and 0.25 (inverse pyramids; only in (b)). The nonlinearity systematically shifts the peak centres and slightly broadens the peaks. Their width we defined as the full peak width at half maximum, which is marked by the arrows in (b) for the $g = 0$ peak. The dot-dashed line in (a) shows the lower bound for converged $\Gamma \gtrsim 10^{-5}$ on the left-hand side of the resonant tunnelling peaks, i.e., for very small $F \lesssim 0.12$, where convergence is very hard to achieve even at small $g \simeq 0.1$ (in this parameter range, i.e., at the left-hand side of the peaks where Γ changes abruptly by about two orders of magnitude, the propagation according to equations (14) and (15) becomes unstable).

central potential well where the condensate is localized initially. Hence, we approximate further

$$\Delta E \approx g \int_{-\pi}^{\pi} dx |\psi_{g=0}|^4, \quad (18)$$

which in turn leads to a shift in the position on the F -axis corresponding to $\Delta E \approx 2\pi \Delta F$. Taking into consideration that the probability in the central well remains normalized (condition from equation (5)), equation (18) corresponds to the energy shift induced by the nonlinearity which was baptized ‘frequency pulling’ in [32], because it leads to a phase dispersion of the Bloch oscillations in the wells. With (18) we arrive at the general result that the following ratio is approximately constant:

$$\frac{2\pi \Delta F}{|g|} \approx \int_{-\pi}^{\pi} dx |\psi_{g=0}|^4 \approx 0.37. \quad (19)$$

This estimate proved to be valid with a maximal relative deviation of less than 18% with respect to the shifts observed in figure 3. Since the integral $\int_{-\pi}^{\pi} dx |\psi_g|^4$ is constant up to the third digit for all $|g| \leq 0.25$, we conclude that the first-order perturbation correction is not enough to describe the shifts more quantitatively.

While a repulsive mean field ($g > 0$) enhances the tunnelling rate far away from the $g = 0$ peak, an attractive interaction ($g < 0$) stabilizes the decay sufficiently far away from all the peaks. This is the case, e.g., for $F > 0.16$ in figure 3(a), where Γ systematically decreases with decreasing g . The symmetric displacement of the peak with respect to the sign of g reflects the symmetry of the Bloch band model, in which tunnelling from the first excited band

back to the ground band can be interpreted as the converse process but with a sign change in g [13]. The same qualitative behaviour of enhancement ($g > 0$) and stabilization ($g < 0$) was observed in the short-time evolution of the three-dimensional Wannier–Stark problem [16]. Apart from the conceptual difficulty of decomposing a solution of the nonlinear GPE (2) into contributions from many adjacent wells (see discussion in section 2), the observed washing out of the peak structure in [16] is a direct consequence of an effectively moving peak as $|g|$ diminishes monotonously (cf figure 3) with decreasing density in the wells.

To conclude this section, we briefly compare our results to other recent works which investigated the impact of a mean-field interaction of the GPE type on quantum mechanical decay processes. We emphasize, however, that such a comparison can only be qualitative, since such works [25, 28, 33, 34] typically treat much simpler model potentials than our Wannier–Stark problem with close level degeneracies. The common feature of our work and the results presented in [25, 28, 33, 34] is that an increasing nonlinearity typically enhances the decay in the one-dimensional problem. Systematical shifts in the chemical potential of resonance states (induced by the interaction term) were analytically studied in [34] for a delta-shell potential. Such shifts correspond to our perturbative estimate in equations (18) and (19).

Particularly, we compared the results obtained from our method (see section 2) with the description of [28] where a nonlinear equation was introduced which differs from ours (see equation (11)) in the treatment of the nonlinear term. In [28], the nonlinearity is of the form $g_\theta(\psi^\theta)^3$, and we found that such a nonlinear term leads to *different* decay rates than those we computed from either our complex-scaling method or from the real-time integration of the unscaled GPE (2) and subsequent fits to $P_{\text{sur}}(t)$. We conclude that a treatment based on complex scaling—for a condensate within the standard GPE description and generally complex-valued wavefunctions—makes it necessary to use the explicit form of ψ^θ as presented in section 2.

There is a growing literature of works on Landau–Zener tunnelling in the presence of a mean-field nonlinearity and its impact on the Bloch oscillation problem; see, e.g., [13, 35]. In such works, a similar systematical stabilization (for $g < 0$) or destabilization (for $g > 0$) was predicted (and also measured, see [13]) for a *single* Landau–Zener tunnelling event with various approximative models. This corresponds to our results on the decay rates which describe directly the initial decay of the condensate via tunnelling, i.e., the behaviour of $P_{\text{sur}}(t)$ at short times that are not much larger than one Bloch period. At and close to the resonant tunnelling peaks the problem is, however, more subtle because of the strong interaction of Wannier–Stark levels (see figure 1(a)), and such a case was not treated in [13, 35].

4. Conclusion

To summarize, we presented a method to numerically compute precise decay rates for tunnelling problems within the framework of the Gross–Pitaevskii equation. We adapted and improved the technique developed by one of us in [18] for the more complicated scenario of resonant tunnelling in the Wannier–Stark problem. We showed that the mean-field nonlinearity leads to experimentally observable modifications in the tunnelling of resonance states from the periodical potential wells, even in a regime where the kinetic and the periodic potential terms still dominate the dynamics. The broadening and the shift of the resonant tunnelling peaks define clear signatures for nonlinearity-induced effects.

Our method can be extended—with further system-specific improvements in the propagation algorithm—to treat even more complicated problems appearing in experiments with Bose condensates, e.g., the transport of coherent matter within atomic wave guides.

Finally, we can readily extend the proposed method to three spatial dimensions, with the only drawback of much larger numerical effort.

Acknowledgments

SW is very grateful to Ennio Arimondo and Oliver Morsch for valuable discussions on the experimental feasibility of the nonlinear Wannier–Stark system, and acknowledges support from the Alexander von Humboldt Foundation (Feodor–Lynen Program).

References

- [1] Kittel C 1996 *Introduction to Solid State Physics* (New York: Wiley)
- [2] Nenciu G 1991 *Rev. Mod. Phys.* **63** 91
- [3] Grecchi V and Sacchetti A 1997 *Phys. Rev. Lett.* **78** 4474
- [4] Holthaus M 2000 *J. Opt. B* **2** 589
- [5] Glück M, Kolovsky A R and Korsch H J 2002 *Phys. Rep.* **366** 103
- [6] Kolovsky A R and Korsch H J 2004 *Int. J. Mod. Phys. B* **18** 1235
- [7] Cristiani M, Morsch O, Müller J H, Ciampini D and Arimondo E 2002 *Phys. Rev. A* **66** 021601
Morsch O, Müller J H, Cristiani M, Ciampini D and Arimondo E 2001 *Phys. Rev. Lett.* **87** 140402
- [8] Glück M, Kolovsky A R and Korsch H J 1999 *Phys. Rev. Lett.* **83** 891
- [9] Glutsch S 2004 *Phys. Rev. B* **89** 235317
- [10] Steck D A, Oskay W H and Raizen M G 2001 *Science* **293** 274
Hensinger W K *et al* 2001 *Nature* **412** 52
Averbukh V, Osovski S and Moiseyev N 2002 *Phys. Rev. Lett.* **89** 253201
- [11] Greiner M, Mandel O, Esslinger T, Hänsch T W and Bloch I 2002 *Nature* **415** 39
- [12] Anderson B P and Kasevich M A 1998 *Science* **282** 1686
- [13] Jona-Lasinio M, Morsch O, Cristiani M, Malossi N, Müller J H, Courtade E, Anderlini M and Arimondo E 2003 *Phys. Rev. Lett.* **91** 230406
Jona-Lasinio M, Morsch O, Cristiani M, Arimondo E and Menotti C 2005 *Preprint cond-mat/0501572*
- [14] Roati G, de Mirandes E, Ferlaino F, Ott H, Modugno G and Inguscio M 2004 *Phys. Rev. Lett.* **92** 230402
- [15] Pethick C J and Smith H 2002 *Bose–Einstein Condensation in Dilute Gases* (Cambridge: Cambridge University Press)
Pitaevskii L and Stringari S 2003 *Bose–Einstein Condensation* (Oxford: Oxford University Press)
- [16] Wimberger S, Mannella R, Morsch O, Arimondo E, Kolovsky A R and Buchleitner A 2005 *Phys. Rev. A* **72** 063610
- [17] Gemelke N, Sarajlic E, Bidet Y, Hong S and Chu S 2005 *Preprint cond-mat/0504311*
- [18] Schlagheck P and Paul T 2004 *Preprint cond-mat/0402089* (*Phys. Rev. A*, submitted)
- [19] Olshanii M 1998 *Phys. Rev. Lett.* **81** 938
- [20] Krämer M, Menotti C, Pitaevskii L and Stringari S 2003 *Eur. Phys. J D* **27** 247
- [21] Paul T, Richter K and Schlagheck P 2005 *Phys. Rev. Lett.* **94** 020404
- [22] Gustavson T L, Chikkatur A P, Leanhardt A E, Görlitz A, Gupta S, Pritchard D E and Ketterle W 2002 *Phys. Rev. Lett.* **88** 020401
- [23] Hänsel W, Reichel J, Hommelhoff P and Hänsch T W 2001 *Phys. Rev. Lett.* **86** 608
- [24] Folman R, Krüger O, Schiedmayer J, Denschlag J and Henkel C 2003 *Adv. At. Mol. Opt. Phys.* **48** 263
- [25] Carr L D, Holland M J and Malomed B A 2005 *J. Phys. B: At. Mol. Opt. Phys.* **38** 3217
- [26] Baslev E and Combes J M 1971 *Math. Phys.* **22** 280
- [27] Kukulin V I, Krasnopo'sky V M and Horáček J 1989 *Theory of Resonances* (Dordrecht: Kluwer)
Moiseyev N 1998 *Phys. Rep.* **302** 211
- [28] Moiseyev N and Cederbaum L S 2005 *Phys. Rev. A* **72** 033605
- [29] Maquet A, Chu S I and Reinhardt W P 1983 *Phys. Rev. A* **27** 2946
Buchleitner A, Gremaud B and Delande D 1994 *J. Phys. B: At. Mol. Opt. Phys.* **27** 2663
- [30] Press W H, Flannery B P, Teukolsky S A and Vetterling W T 1989 *Numerical Recipes* (Cambridge: Cambridge University Press)
- [31] Robkerts J L, Claussen N R, Cornish S L, Donley E A, Cornell E A and Wieman C E 2001 *Phys. Rev. Lett.* **86** 4211
- [32] Thommen Q, Garreau J C and Zehnlé V 2003 *Phys. Rev. Lett.* **91** 210405

-
- [33] Moiseyev N, Carr L D, Malomed B A and Band Y B 2004 *J. Phys. B: At. Mol. Opt. Phys.* **37** L193
Adhikari S K 2005 *J. Phys. B: At. Mol. Opt. Phys.* **38** 579
- [34] Witthaut D, Mossmann S and Korsch H J 2005 *J. Phys. A: Math. Gen.* **38** 1777
- [35] Choi D I and Niu Q 1999 *Phys. Rev. Lett.* **82** 2022
Zobay O and Garraway B M 2000 *Phys. Rev. A* **61** 033603
Wu B and Niu Q 2000 *Phys. Rev. A* **61** 23402
Wu B and Niu Q 2000 *New J. Phys.* **5** 104
Konotop V V, Kevrekidis P G and Salerno M 2005 *Phys. Rev. A* **72** 023611

Chaotic ratchet dynamics with cold atoms in a pair of pulsed optical lattices

Gabriel G. Carlo,^{1,2} Giuliano Benenti,^{1,3} Giulio Casati,^{1,3,4} Sandro Wimberger,⁵ Oliver Morsch,⁵ Riccardo Mannella,⁵ and Ennio Arimondo⁵

¹Center for Nonlinear and Complex Systems, Università degli Studi dell'Insubria, Via Valleggio 11, 22100 Como, Italy

²Departamento de Física, Comisión Nacional de Energía Atómica, Avenida del Libertador 8250, 1429 Buenos Aires, Argentina

³Istituto Nazionale di Fisica Nucleare, Sezione di Milano and CNISM, and CNR-INFN, Via Celoria 16, 20133 Milano, Italy

⁴Department of Physics, National University of Singapore, Singapore 117542, Republic of Singapore

⁵CNR-INFN and Dipartimento di Fisica "Enrico Fermi," Università degli Studi di Pisa, Largo Pontecorvo 3, 56127 Pisa, Italy

(Received 29 May 2006; published 22 September 2006)

We present a very simple model for realizing directed transport with cold atoms in a pair of periodically flashed optical lattices. The origin of this ratchet effect is explained and its robustness demonstrated under imperfections typical of cold atom experiments. We conclude that our model offers a clear-cut way to implement directed transport in an atom optical experiment.

DOI: [10.1103/PhysRevA.74.033617](https://doi.org/10.1103/PhysRevA.74.033617)

PACS number(s): 03.75.Be, 05.45.Mt, 05.40.Jc, 32.80.Pj

I. INTRODUCTION

The atom optics realization of the paradigmatic kicked rotor (KR) [1] presents the possibility to study experimentally unique quantum mechanical aspects of a fundamental, classically nonlinear system. Dynamical Localization is perhaps the most celebrated quantum phenomenon observed in the quantum KR [1,2], but many other interesting features of the KR have been studied theoretically and experimentally [3,4]. Very recently, applications of modified KR models have been designed which allow for a controlled, directed motion of particles in momentum space [5,6].

The atom-optics kicked rotor (AOKR) is realized by subjecting cold atoms [3,4] or a Bose condensate [7–10] to a far detuned standing wave with spatial period π/k_L (k_L being the wave number of the kicking laser) and pulsed with period τ . The AOKR is described, in dimensionless units, by the Hamiltonian [11]

$$\mathcal{H}(t) = \frac{p^2}{2} + k \cos(x) \sum_{n=0}^{\infty} \delta(t - nT), \quad (1)$$

where p is the atomic momentum in units of $2\hbar k_L$ (i.e., of two-photon recoil momenta), x is the atomic position divided by $2k_L$, t is time, and n is an integer which counts the kicks. Experimentally, δ kicks are approximated by pulses of width τ_p which are approximately rectangular in shape. We also define an effective Planck's constant $\hbar_{\text{eff}} = T = 8E_R\tau/\hbar$, where $E_R = (\hbar k_L)^2/2M$ is the recoil energy (acquired by an atom after emission of a photon with wave number k_L). The dimensionless parameter $k \approx V_0\tau_p/\hbar$ is the kicking strength of the system (with V_0 the height of the optical lattice creating the kicking potential).

In this paper, we propose a ratchet which could be realized experimentally by adding to the standard AOKR dynamics defined by Eq. (1) a second kicking potential (applied in a synchronized way with respect to the first one). The application of a second kicking potential to the atom has some analogy with the double AOKR investigated in Ref. [12], because in both cases a sequence of two kicks is applied to the atoms. In the present investigation a spatial shift

of the second kick potential is also included. We show that this is sufficient to produce the ratchet effect. Moreover, we consider the effects of a particle escape mechanism similar to evaporative cooling [13]. More precisely, we study an open system with absorbing boundary conditions. If $\psi(p)$ is the wave function in momentum space, absorbing boundary conditions are implemented by the prescription $\psi(p) \equiv 0$ if $p \leq -p_c$ or $p \geq p_c$. Such absorbing boundary conditions could be realized experimentally using, e.g., velocity selective Raman transitions, which change the internal states of the atoms, and hence let them escape from the states of interest [14], or by other state selective methods [15]. Such a scenario of losing the faster atoms with momenta exceeding p_c , is analogous to evaporative cooling of cold atoms [13]. The time scale of the applied absorption mechanism should be of the order of the kicking period T to allow for a steady loss of atoms during the system's evolution.

We point out that, as shown below, in our model the ratchet phenomenon is also present in the Hamiltonian limit without escape of particles. On the other hand, it is interesting to investigate the particle escape mechanism because it models the evaporative cooling process natural in cold atoms experiments. Moreover, its introduction is relevant in order to analyze the stability of our proposed ratchet mechanism after that atoms excited to higher and higher velocities by chaotic diffusion are eventually lost. Finally, particle escape may allow the unprecedented experimental observation of a quantum phase space distribution located on an underlying classical fractal set.

In state-of-the-art atom optics experiments, control over the kicking strength k (or, equivalently over the laser power delivered to the atoms) is achieved with a precision of a few percent [4]. Kicking strengths in the range 1–7 correspond to standing wave amplitudes of about 80–600 E_R for rubidium atoms (and assuming a rectangular pulse shape with a width of 500 ns). Below we will be interested in the parameter region of small kicking periods $T \lesssim 1$, and hence it is important to note that time is one of the best controlled experimental parameters, and kicking periods between about one hundred nanoseconds and a few hundred microseconds are available, with a maximal precision of a few tens of nano-

seconds [4,16,17]. For cesium atoms, this range corresponds to dimensionless kicking periods $T \approx 10^{-2} - 20$, and a maximal precision of $\delta T \approx 10^{-3}$ [17]. Atom optics experiments may be performed on two different atomic samples: laser cooled atoms and Bose-Einstein condensates. The main difference is the initial width Δp_0 in momentum. For laser cooled atoms and in the best conditions, the initial width in momentum corresponds to a few two-photon recoils units. For Bose-Einstein condensates Δp_0 between 0.01 and 0.05 can be realized [7,8,10,18]. Bose-Einstein condensates experience a nonlinear potential associated with the atom-atom interaction. However, letting the condensate expand a little before the actual kicking evolution allows one to reduce the atom-atom interactions to negligible values, with only slight changes in Δp_0 [7]. The present analysis focuses on a sample of laser cooled atoms with a large initial momentum distribution. In fact, this condition is more favorable for the realization of the ratchet discussed in this paper, because the sample explores a larger region of the classical phase space and therefore exploits the structure of phase space (a strange repeller, in the classical limit) induced by the evaporative cooling process.

The paper is organized as follows. Section II analyzes the AOKR model and its evolution in phase space under the double kicking perturbation. Section III investigates different imperfections associated with the experimental realization. For instance, a deep optical potential is required for laser-cooled atoms, and in such conditions spontaneous emissions become a non-negligible issue. In addition, fluctuations in the laser power and other sources of noise are included in the analysis. The final Sec. IV concludes with an outlook discussing the role of nonlinearity as present in experiments using a Bose-Einstein condensate.

II. MODEL AND PROPERTIES

In this section we introduce a kicked system that shows directed transport and in which the direction of the current can be controlled. This is done in a very simple way, we just have to duplicate the series of kicks in Eq. (1) in a convenient fashion. This simplicity is essential for an efficient experimental implementation with cold atoms.

We consider a particle moving in one dimension [$x \in (-\infty, +\infty)$] in a periodically kicked potential. The Hamiltonian reads

$$\mathcal{H}_2(t) = \frac{p^2}{2} + V_{\phi,\xi}(x,t),$$

$$V_{\phi,\xi} = k \sum_{n=-\infty}^{+\infty} [\delta(t - nT)\cos(x) + \delta(t - nT - \xi)\cos(x - \phi)],$$
(2)

where T is the kicking period. In fact, we propose an asymmetric kicking sequence. This is made out of two series of kicks with the same spatial and temporal periods, 2π and $T = 2\pi/\omega$, but shifted by a phase ϕ ($0 \leq \phi < 2\pi$) and a time ξ

($0 \leq \xi < T$). Due to the spatial periodicity of the kicking potential $V_{\phi,\xi}$, the one-cycle evolution (Floquet) operator

$$\hat{U} = e^{-i(T-\xi)\hat{p}^2/2} e^{-ik \cos(\hat{x}-\phi)} e^{-i\xi\hat{p}^2/2} e^{-ik \cos(\hat{x})}$$
(3)

induced by the Hamiltonian of Eq. (2) commutes with spatial translations by multiples of 2π . As is well known from Bloch theory, this implies conservation of the quasimomentum β , defined as the fractional part of the momentum p ($0 \leq \beta < 1$) [19]. For a given value of the quasimomentum, the wave function of the system is a Bloch wave, of the form $e^{i\beta x} \psi_\beta(x)$, where $\psi_\beta(x)$ is a function of period 2π . A generic wave function can then be written as a superposition of Bloch waves $\psi(x) = \int_0^1 d\beta e^{i\beta x} \psi_\beta(x)$.

Introducing the rescaled momentum variable $I = Tp$, one can see that classical dynamics of model (2) depends on the scaling parameter $K = kT$ (not on k and T separately). The classical limit corresponds to $\hbar_{\text{eff}} = T \rightarrow 0$, while keeping $K = \hbar_{\text{eff}} k$ constant.

In order to simulate the evaporative cooling process in the quantum model we consider the projection over a subspace corresponding to the quantum levels that are below p_c (in absolute value). In practice, this is implemented at each kick: if we denote by \hat{P} the projection operator on the interval $]-p_c, p_c[$, the wave function after n kicks is then given by

$$\psi(p,n) = (\hat{P}\hat{U})^n \psi(p,0).$$
(4)

Note that quasimomentum is still a conserved quantity. In the classical case, we consider lost the particles that reach momentum p such that $|p| > p_c$.

We have checked in our numerical simulations that the dependence of the ratchet current on the cutoff value p_c is weak, provided that $p_c \gg k$. Therefore, the ratchet current in this regime turns out to be close to the current obtained in the Hamiltonian limit $p_c \rightarrow \infty$. On the other hand, the particle escape mechanism strongly affects the phase space structure, leading, in the classical limit, to the setting in of a strange repeller.

In the numerical simulations reported in this paper, we fix $K=7$, corresponding to the classically chaotic regime, $\xi = T/3$, and $p_c \hbar_{\text{eff}} = 15.2$. The initial state is given by a uniform mixture of the momentum states inside the interval $p \hbar_{\text{eff}} \in [-1, 1]$. Once the quasi-momentum is fixed, the number of momentum states in this interval is $\propto 1/\hbar_{\text{eff}}$. Moreover, we average numerical data over 10^3 randomly chosen quasimomenta. Classical averages are constructed from 10^7 initial conditions randomly and uniformly distributed inside the region $x \in [0, 2\pi)$, $I = pT \in [-1, 1]$. Note that with these initial conditions and the above parameter values we are left with approximately 35% of the initial number of particles at time $n = t/T = 10$ and 10% at $n = 20$.

The appearance of a strange repeller in our model in the classical limit is shown in the phase space portrait of Fig. 1 (a), obtained for $\phi = \pi/2$ at $n = 20$. The three panels of Fig. 1 correspond, from (a) to (c), to the classical Poincaré section and the quantum Husimi function at $\hbar_{\text{eff}} \approx 0.16$ and $\hbar_{\text{eff}} \approx 1$. We can see a good agreement between the classical and the quantum phase space portraits. Quantum fluctuations smooth

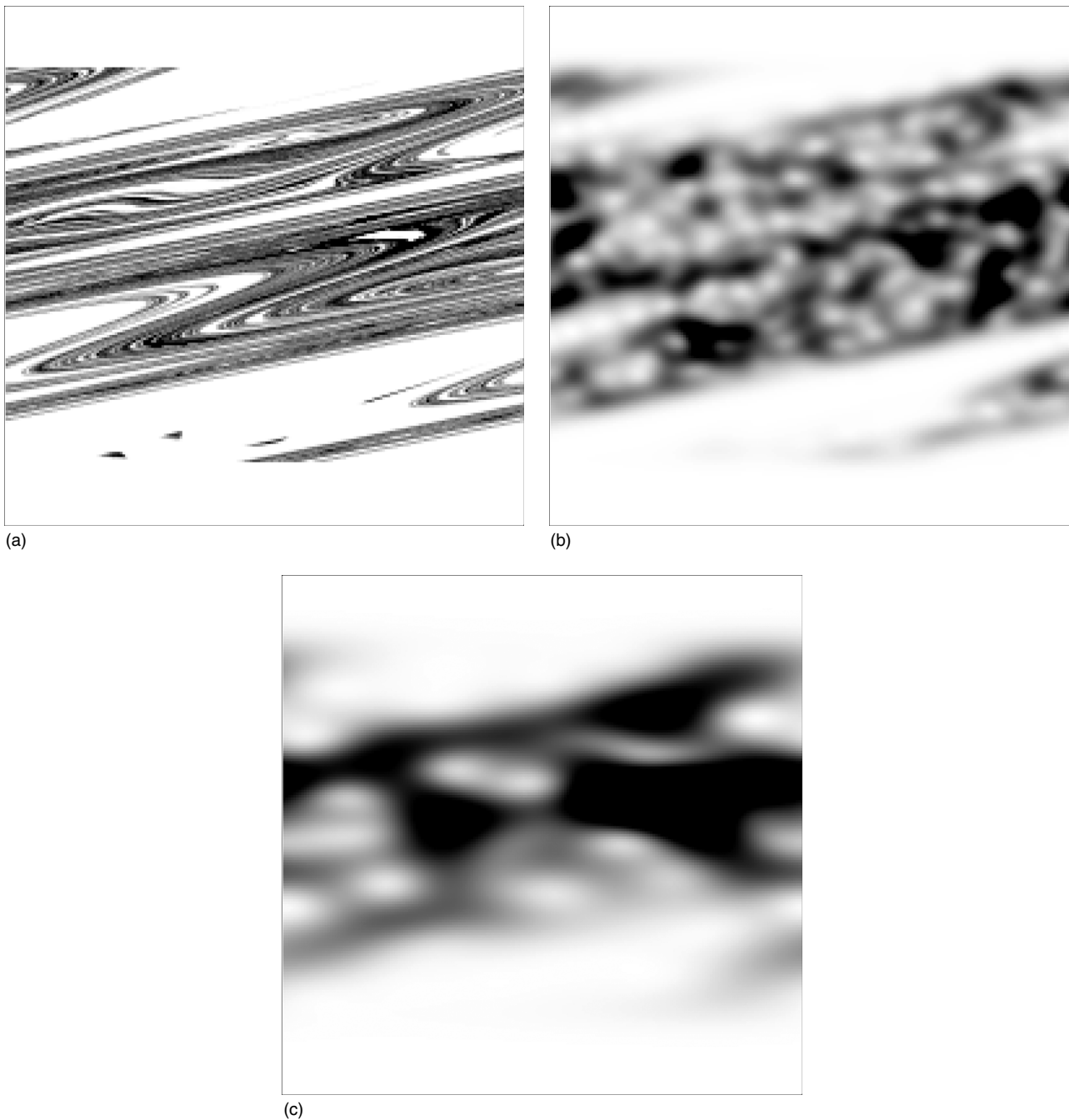


FIG. 1. Phase space pictures for $\phi = \pi/2$, at $n=20$: classical Poincaré sections (a) and quantum Husimi functions at $\hbar_{\text{eff}} \approx 0.16$ (b) and $\hbar_{\text{eff}} \approx 1$ (c). The displayed region is given by $I=pT \in [-20, 20]$ (vertical axis) and $x \in [0, 2\pi)$ (horizontal axis). Note that, to draw the attractor, x is taken modulus 2π . The brightness is inversely proportional to the density: black (white) regions correspond to maximal (zero) density.

the fractal structure of the classical repeller on the scale of Planck's cell [20]. In the quantum case the values of $\hbar_{\text{eff}} \approx 0.16$ and $\hbar_{\text{eff}} \approx 1$ considered here (and suitable for a realistic experimental implementation) are not sufficiently small to resolve the fractal structure at small scales. However, the Husimi function shows clear similarities with the underlying classical probability distribution. Even for $\hbar_{\text{eff}} = T \approx 1$ the major features of the classical repeller (i.e., width in phase space and asymmetry) are visible. Parameter values and evo-

lution time are suitable for the experimental measurement of the quantum probability distribution located on the underlying classical strange repeller. This is important because the appearance of strange sets (attractors or repellers) is a distinctive feature of open chaotic systems.

The repeller in Fig. 1 is strongly asymmetric, suggesting directed transport, that is, $\langle p \rangle \neq 0$. This is confirmed by the numerical data of Fig. 2, where $\langle p \rangle$ is shown as a function of the time n .

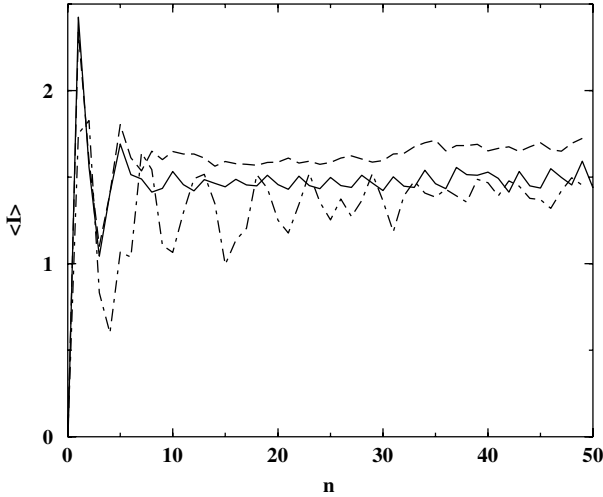


FIG. 2. Average rescaled momentum $\langle I \rangle = \langle p \rangle T$ as a function of the discrete time n , for the same parameter values as in Fig. 1. The solid curve corresponds to the classical case, while the dashed curve corresponds to quantum results for $\hbar_{\text{eff}} \approx 0.16$ and the dot-dashed one to $\hbar_{\text{eff}} \approx 1$.

We can explain the origin of the directed current present in our system by following the approach developed in Ref. [21]. We have a classical time evolution given by

$$\ddot{x} + f_{\phi, \xi}(x, t) = 0, \quad (5)$$

where $f_{\phi, \xi}(x, t) = \partial V_{\phi, \xi}(x, t) / \partial x$. To this equation we add a particle escape process consisting of cutting out the orbits that exceed a given value of the momentum $p = \dot{x}$. We are interested in symmetry transformations that leave Eq. (5) invariant but change the sign of p . In fact, if we assume that our system is chaotic we can generate for each orbit its p -reversed partner, which will explore the whole region embedding the chaotic trajectories. This amounts to saying that, being essentially equivalent, both orbits (and all of them) should have zero average momentum. If these symmetries are absent it is natural to conclude that a net p (i.e., different from zero) can be generated. Thus, breaking all possible symmetries of this kind constitutes a good method to engineer ratchet systems. As the particle escape process introduced above is symmetrical with respect to p , we can neglect it in the following reasoning. It is worth mentioning that all the symmetry considerations developed in this section translate almost immediately to the quantum case.

There are two general ways to change the sign of p :

$$(I) \quad x \rightarrow -x + \alpha, \quad t \rightarrow t + \gamma$$

and

$$(II) \quad x \rightarrow x + \alpha, \quad t \rightarrow -t + \gamma.$$

In order to leave Eq. (5) unchanged we need that $f_{\phi, \xi}(x, t) = -f_{\phi, \xi}(-x + \alpha, t + \gamma)$ holds for (I), since $\ddot{x} \rightarrow -\ddot{x}$ under this transformation. If we apply twice transformation (I) we obtain $f_{\phi, \xi}(x + \alpha/2, t) = f_{\phi, \xi}(x + \alpha/2, t + 2\gamma)$. Since $f_{\phi, \xi}(x, t)$ is assumed to be bounded and periodic with zero mean, both in x and t , γ can only be an integer multiple of $T/2$ (including the

$\gamma=0$ case). In turn, there are no restrictions on α . On the other hand, for (II) we need $f_{\phi, \xi}(x, t) = +f_{\phi, \xi}(x + \alpha, -t + \gamma)$ (with a plus sign since now \ddot{x} keeps its original sign). By applying twice transformation (II) we obtain $f_{\phi, \xi}(x, t + \gamma/2) = f_{\phi, \xi}(x + 2\alpha, t + \gamma/2)$. Following the same reasoning as before, α is fixed to integer multiples of π (including $\alpha=0$) while there are no restrictions on γ . Note that (I) and (II) are the only two symmetries that should be broken in order to find directed transport. Our choice of the potential (2) guarantees the possibility to break both of them.

In fact, we have that $f_{\phi, \xi}(x, t) = k \sum_{n=-\infty}^{+\infty} [-\delta(t - nT) \sin(x) - \delta(t - nT - \xi) \sin(x - \phi)]$, and in the case of symmetry (I) we require that $f_{\phi, \xi}(x, t) = -f_{\phi, \xi}(-x + \alpha, t + \gamma)$. We can take $\gamma=0$ without loss of generality since we only have a sum of delta functions in t , i.e., the sign change of f induced by symmetry (I) can only come from the first part of the transformation ($x \rightarrow -x + \alpha$). Therefore, we arrive at the conditions $\sin(-x + \alpha) = -\sin(x)$ and $\sin(-x + \alpha - \phi) = -\sin(x - \phi)$. These two conditions lead to $\alpha = l2\pi$ and $\alpha = l'2\pi + 2\phi$, with l and l' integers, and cannot be fulfilled together, except for $\phi=0$ or $\phi=\pi$. Therefore, symmetry (I) is broken when $\phi \neq 0, \pi$.

In the case of symmetry (II), if we take α an odd multiple of π then the sign of $f_{\phi, \xi}$ changes. Then, we are only left with α being an even multiple of π , i.e., we can take $\alpha=0$ without loss of generality. Moreover, we notice that if $\phi=0$ and $\alpha=0$ both kicks become the same in x and therefore symmetry (II) holds for any ξ , taking $\gamma=\xi$. On the other hand, considering $\phi \neq 0$ we arrive at the conditions $\sum_{n=-\infty}^{+\infty} \delta(-t + \gamma - nT) = \sum_{n=-\infty}^{+\infty} \delta(t - nT)$ and $\sum_{n=-\infty}^{+\infty} \delta(-t + \gamma - nT - \xi) = \sum_{n=-\infty}^{+\infty} \delta(t - \xi)$, which imply $\gamma = lT$ and $\gamma = l'T + 2\xi$, with l and l' integers. We conclude that, if $\phi \neq 0$, symmetry (II) is broken when $\xi \neq 0, T/2$.

In summary, both symmetries (I) and (II) are broken for $\phi \neq 0, \pi$ and $\xi \neq 0, T/2$. Hence two series of kicks are sufficient to observe the ratchet effect, provided that these kicks are shifted both in space and in time, the shift in space being different from half wavelength and the shift in time being different from half period.

It is interesting to remark that current reversal can be engineered in a very simple way, by taking $\tilde{\phi} = -\phi$ instead of ϕ in Eq. (2). Indeed, Eq. (5) is left unchanged when $x \rightarrow -x$, $t \rightarrow t$, and $\phi \rightarrow \tilde{\phi} = -\phi$, while this transformation changes the sign of p . We can see current inversion in Fig. 3, both in the classical and in the quantum case, when $\phi = \pi/2 \rightarrow \tilde{\phi} = -\pi/2$. Note that $\langle p \rangle = 0$ at $\phi=0$, in agreement with the above symmetry considerations.

III. STABILITY OF THE RATCHET EFFECT UNDER IMPERFECTIONS

The purpose of this section is to study the robustness of the ratchet effect introduced in this paper in the presence of typical sources of noise in cold-atom experiments. For the large kicking strengths needed to guarantee clear signatures of a chaotic repeller, spontaneous emission during the flashing of the optical lattice cannot be ruled out [3]. Spontaneous emission can be effectively modeled by random jumps in quasimomentum [19]. We test the influence of such random

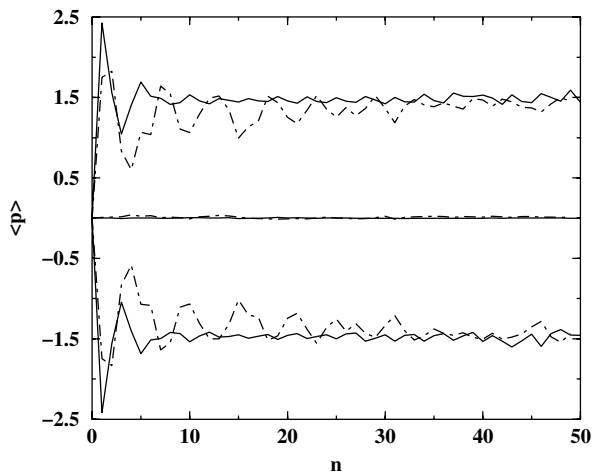


FIG. 3. Average momentum $\langle p \rangle$ as a function of n , for $\phi = \pi/2$ (positive values), $\phi = 0$ (zero values), and $\phi = -\pi/2$ (negative values). Both the classical (solid curves) and the quantum case (dot-dashed curves, $\hbar_{\text{eff}} \approx 1$) are shown. Note that at $\phi = 0$ quantum and classical curves are almost superimposed.

changes in quasimomentum on the results presented in the previous section. That is to say, we repeat the previous calculations but letting at any kick the quasimomentum randomly change with a probability of 0, 0.2, and 0.5 (see Fig. 4). In practice, it may jump to any possible value in the Brillouin zone with those probabilities. As can be seen, this additional randomness even helps to reduce fluctuations, and when the jump probability is different from zero there is a better convergence towards the classical result.

We now investigate how different kind of errors affect the value of the ratchet current. More precisely, we compute the average current $\langle p \rangle_{\text{av}}$, obtained after averaging $\langle p \rangle$ in the time interval $10 \leq n \leq 20$, as a function of the noise strengths associated to different noise sources.

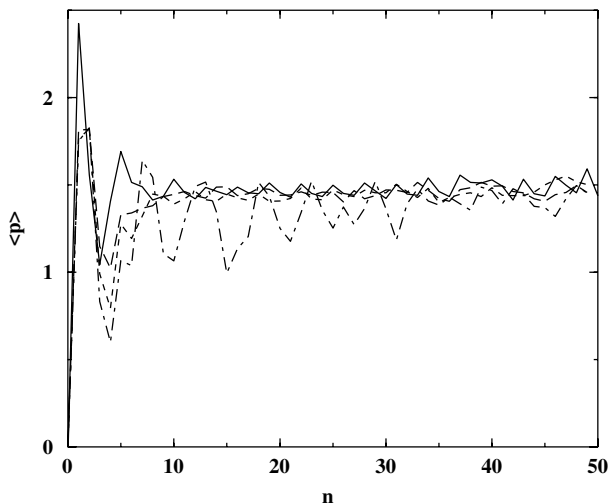


FIG. 4. Average momentum $\langle p \rangle$ as a function of the discrete time n , for the same parameters as in Fig. 2, at $\hbar_{\text{eff}} \approx 1$. At each kick, the quasimomentum can jump to any other possible value with probabilities 0 (dot-dashed curve), 0.2 (dashed curve), and 0.5 (long dashed curve). The solid curve corresponds to the classical case.

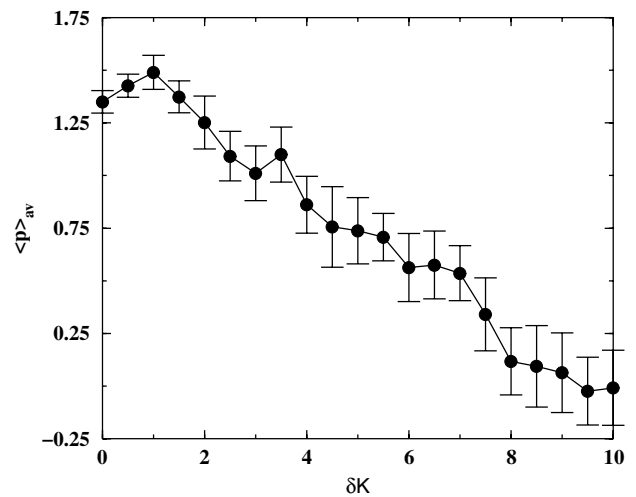


FIG. 5. Average current $\langle p \rangle_{\text{av}}$ as a function of the noise δK in the kick strength K , for parameter values as in Fig. 2, at $\hbar_{\text{eff}} \approx 1$.

First of all, we consider the effects of fluctuations in the kicking strength. This is simulated by memoryless random errors of size δK in the value of K : the kicking strength K_n at time n is given by $K_n = K + (\delta K)_n$ where the noise value $(\delta K)_n$ is randomly drawn from a uniform distribution in the interval $[-\delta K, \delta K]$. It can be seen in Fig. 5 that the ratchet effect is stable up to approximately $\delta K \approx 2$, corresponding to a relative amplitude noise of $\delta K/K \approx 0.3$.

Since the ratchet mechanism described in the previous section works the better the smaller we choose $\hbar_{\text{eff}} = T$, we consider possible fluctuations in the kicking period [16] arising from the problem of controlling strong but narrow pulses in time with a high repetition rate. We model these imperfections as random and memoryless fluctuations in the period between consecutive kicks. This takes into account the fact that the timing of the kicks can suffer from uncontrollable variations. As we can see from Fig. 6, stability is quite sat-

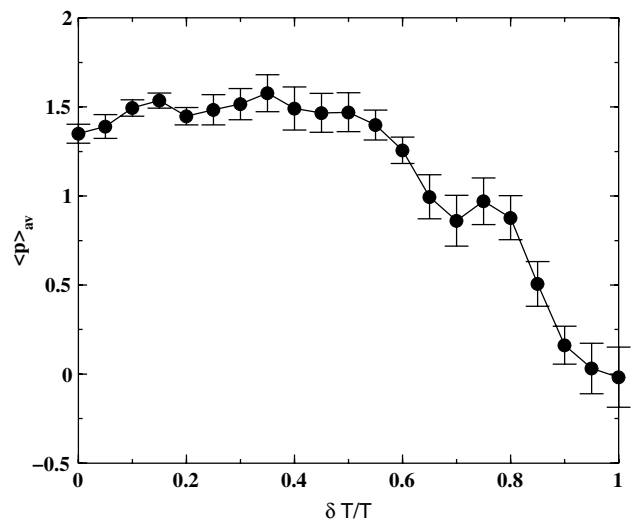


FIG. 6. Average current $\langle p \rangle_{\text{av}}$ as a function of the relative error $\delta T/T$ in the kicking period T , for parameter values as in Fig. 5.

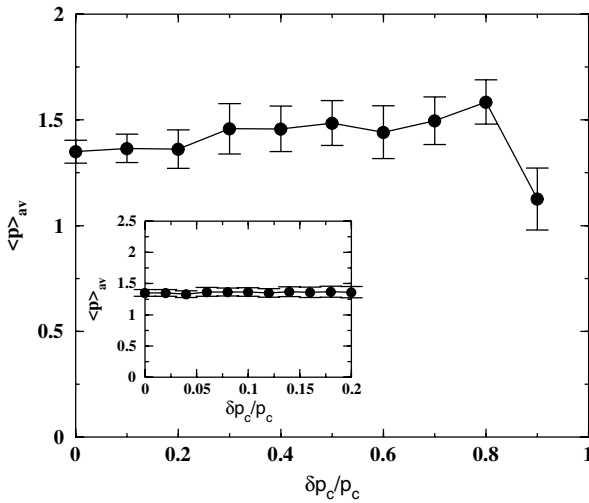


FIG. 7. Average current $\langle p \rangle_{av}$ as a function of the relative error $\delta p_c / p_c$ in the cutoff momentum p_c , for parameter values as in Fig. 5. A magnification of the figure for small values of $\delta p_c / p_c$ is shown in the inset.

isfactory when $\delta T / T \approx 0.5$, where δT is the size of the fluctuations and $T \approx 1$.

Finally, we consider the effect of an imprecision in the p_c selection. This is modeled by random memoryless variations of the cutoff value $(p_c)_n$ used at time n : $(p_c)_n = p_c + (\delta p_c)_n$, with $(\delta p_c)_n \in [-\delta p_c, \delta p_c]$. Again the ratchet effect proves to be robust, as can be deduced from Fig. 7. The results of this

figure are in agreement with the previous observation that the dependence of the ratchet current $\langle p \rangle$ on the cutoff value p_c is weak (under the condition $p_c \gg k$).

IV. CONCLUSIONS

Considering a realistic experimental scenario, we showed that a ratchet effect—induced by a combination of a two-kick sequence as applied to an open system—is observable in an atom-optics kicked rotor experiment. We also checked the robustness of the ratcheted atomic evolution under reasonable noise conditions.

An interesting perspective would be to study the ratchet dynamics in a kicked Bose-Einstein condensate. Strong kicks may, however, lead to thermal excitations out of equilibrium and destroy the condensate, rendering the description by the usually applied Gross-Pitaevskii equation meaningless [22]. We have verified that the ratchet evolution is preserved in the presence of typical experimental nonlinearities. However, a full treatment of a strongly kicked Bose-Einstein condensate remains a challenge for future work.

ACKNOWLEDGMENTS

We gratefully acknowledge support by the MIUR COFIN-2004 and 2005, the EU Specific Targeted Research Project OLAQUI, and the Alexander von Humboldt Foundation (Feodor-Lynen Program). G.G.C. gratefully acknowledges support by Conicet (Argentina).

- [1] G. Casati, B. Chirikov, J. Ford, and F. Izrailev, in *Stochastic Behavior in Classical and Quantum Hamiltonian Systems*, edited by G. Casati and J. Ford (Springer, Berlin, 1979), p. 334.
- [2] S. Fishman, in *Quantum Chaos, School "E. Fermi" CXIX*, edited by G. Casati, I. Guarneri, and U. Smilansky (IOS, Amsterdam, 1993).
- [3] F. L. Moore, J. C. Robinson, C. F. Bharucha, B. Sundaram, and M. G. Raizen, *Phys. Rev. Lett.* **75**, 4598 (1995); H. Ammann, R. Gray, I. Shvarchuck, and N. Christensen, *ibid.* **80**, 4111 (1998); J. Ringot, P. Szriftgiser, J. C. Garreau, and D. Delande, *ibid.* **85**, 2741 (2000); M. B. d'Arcy, R. M. Godun, G. S. Summy, I. Guarneri, S. Wimberger, S. Fishman, and A. Buchleitner, *Phys. Rev. E* **69**, 027201 (2004); S. A. Wayper, W. Simpson, and M. D. Hoogerland, quant-ph/0602081 (unpublished); J. F. Kanem, S. Maneshi, M. Partlow, M. Spanner, and S. M. Steinberg, quant-ph/0604110 (unpublished).
- [4] C. F. Bharucha, J. C. Robinson, F. L. Moore, B. Sundaram, Q. Niu, and M. G. Raizen, *Phys. Rev. E* **60**, 3881 (1999); M. Sadgrove, S. Wimberger, S. Parkins, and R. Leonhardt, *Phys. Rev. Lett.* **94**, 174103 (2005).
- [5] G. G. Carlo, G. Benenti, G. Casati, and D. L. Shepelyansky, *Phys. Rev. Lett.* **94**, 164101 (2005).
- [6] T. S. Monteiro, P. A. Dando, N. A. C. Hutchings, and M. R. Isherwood, *Phys. Rev. Lett.* **89**, 194102 (2002); T. Jonckheere, M. R. Isherwood, and T. S. Monteiro, *ibid.* **91**, 253003 (2003); E. Lundh and M. Wallin, *ibid.* **94**, 110603 (2005).
- [7] G. J. Duffy, S. Parkins, T. Muller, M. Sadgrove, R. Leonhardt, and A. C. Wilson, *Phys. Rev. E* **70**, 056206 (2004).
- [8] G. J. Duffy, A. S. Mellish, K. J. Challis, and A. C. Wilson, *Phys. Rev. A* **70**, 041602(R) (2004).
- [9] S. Wimberger, R. Mannella, O. Morsch, and E. Arimondo, *Phys. Rev. Lett.* **94**, 130404 (2005).
- [10] C. Ryu, M. F. Andersen, A. Vaziri, M. B. d'Arcy, J. M. Grossman, K. Helmerson, and W. D. Phillips, *Phys. Rev. Lett.* **96**, 160403 (2006).
- [11] R. Graham, M. Schlautmann, and P. Zoller, *Phys. Rev. A* **45**, R19 (1992).
- [12] P. H. Jones, M. M. Stocklin, G. Hur, and T. S. Monteiro, *Phys. Rev. Lett.* **93**, 223002 (2004); G. Hur, C. E. Creffield, P. H. Jones, and T. S. Monteiro, *Phys. Rev. A* **72**, 013403 (2005); H. Lignier, J. Chabé, D. Delande, J. C. Garreau, and P. Szriftgiser, *Phys. Rev. Lett.* **95**, 234101 (2005).
- [13] W. Ketterle, D. S. Durfee, and D. M. Stamper-Kurn, in *Bose-Einstein Condensation in Atomic Gases*, Proceedings of the International School of Physics "Enrico Fermi," Course CXL edited by M. Inguscio, S. Stringari, and C. E. Wieman (IOS Press, Amsterdam, 1999), pp. 67–176.
- [14] M. Kasevich, D. S. Weiss, E. Riis, K. Moler, S. Kasapi, and S. Chu, *Phys. Rev. Lett.* **66**, 2297 (1991).
- [15] S. Stock, Z. Hadzibabic, B. Battelier, M. Cheneau, and J. Dali-

- bard, Phys. Rev. Lett. **95**, 190403 (2005), and references therein.
- [16] W. H. Oskay, D. A. Steck, and M. G. Raizen, Chaos, Chaos, Solitons Fractals **16**, 409 (2003).
- [17] S. Wimberger and M. Sadgrove, J. Phys. A **38**, 10549 (2005).
- [18] A. Browaeys, H. Häffner, C. McKenzie, S. L. Rolston, K. Helmerson, and W. D. Phillips, Phys. Rev. A **72**, 053605 (2005).
- [19] S. Wimberger, I. Guarneri, and S. Fishman, Nonlinearity **16**, 1381 (2003).
- [20] T. Dittrich and R. Graham, Ann. Phys. (N.Y.) **200**, 363 (1990).
- [21] S. Flach, O. Yevtushenko, and Y. Zolotaryuk, Phys. Rev. Lett. **84**, 2358 (2000); O. Yevtushenko, S. Flach, and K. Richter, Phys. Rev. E **61**, 7215 (2000).
- [22] S. A. Gardiner, D. Jaksch, R. Dum, J. I. Cirac, and P. Zoller, Phys. Rev. A **62**, 023612 (2000); C. Zhang, J. Liu, M. G. Raizen, and Q. Niu, Phys. Rev. Lett. **92**, 054101 (2004).

PHYSICAL REVIEW A 75, 013617 (2007)

Bose-Einstein condensates in accelerated double-periodic optical lattices: Coupling and crossing of resonances

D. Witthaut,^{1,*} E. M. Graefe,¹ S. Wimberger,^{2,3} and H. J. Korsch¹¹*Fachbereich Physik, TU Kaiserslautern, D-67653 Kaiserslautern, Germany*²*Dipartimento di Fisica Enrico Fermi and CNR-INFM, Università degli Studi di Pisa, Largo Pontecorvo 3, I-56127 Pisa, Italy*³*CNISM, Dipartimento di Fisica del Politecnico, Corso Duca degli Abruzzi 24, 10129 Torino, Italy*

(Received 27 September 2006; published 16 January 2007)

We study the properties of coupled linear and nonlinear resonances. The fundamental phenomena and the level crossing scenarios are introduced for a nonlinear two-level system with one decaying state, describing the dynamics of a Bose-Einstein condensate in a mean-field approximation (Gross-Pitaevskii or nonlinear Schrödinger equation). An important application of the discussed concepts is the dynamics of a condensate in tilted optical lattices. In particular the properties of resonance eigenstates in double-periodic lattices are discussed, in the linear case as well as within mean-field theory. The decay is strongly altered, if an additional period-doubled lattice is introduced. Our analytic study is supported by numerical computations of nonlinear resonance states, and future applications of our findings for experiments with ultracold atoms are discussed.

DOI: [10.1103/PhysRevA.75.013617](https://doi.org/10.1103/PhysRevA.75.013617)

PACS number(s): 03.75.Lm, 03.65.Nk, 03.65.Xp

I. INTRODUCTION

In the last decade, the advance of atom and quantum optics has made it possible to realize and to study the evolution of the center-of-mass motion on scales ranging from the microscopic (single particle) to the macroscopic (many-particle) realm [1,2]. In a typical experiment with ultracold atoms, interactions can either be made negligibly small or reduced to a mean-field effect on the evolution of the macroscopic order parameter of a Bose-Einstein condensate (see, e.g., [2,3] and references therein). The latter approach results in an effective nonlinear Schrödinger equation, the following Gross-Pitaevskii equation:

$$\left(-\frac{\hbar^2}{2m} \frac{\partial^2}{\partial x^2} + V(x) + g|\psi(x,t)|^2 \right) \psi(x,t) = i \hbar \frac{\partial \psi(x,t)}{\partial t}, \quad (1)$$

that describes the dynamics of the macroscopic wave function (or of the order parameter) of a Bose-Einstein condensate (BEC) for zero temperature [3]. This mean-field description has proved to be extremely successful and reliable for most recent experiments. The nonlinearity of the equation leads to a variety of surprising phenomena, which are present even in a simple nonlinear two-level system. Self-trapping of a BEC in a double-well trap was observed experimentally only recently [4]. The self-trapping transition manifests itself in the appearance of novel nonlinear eigenstates [5]. The appearance and disappearance of nonlinear eigenstates may also lead to a breakdown of adiabaticity and nonlinear Zener tunneling [6–8].

In the present paper, we investigate nonlinear quantum dynamics in decaying systems. Up to now, only relatively few papers have studied nonlinear and non-Hermitian quantum dynamics, discussing self-stabilizing, shifting, and broadening of nonlinear resonances [9–13]. Here we focus on the coupling of nonlinear resonances in nonlinear, non-

Hermitian level crossing scenarios. Our first object of investigation, the nonlinear two-level system with one decaying level, offers analytic access to this subject. The eigenvalues and eigenstates of its linear counterpart show some interesting features, such as exceptional crossing scenarios [14].

A very natural experimental setup leading to nonlinear dynamics and decay is the dynamics of a Bose-Einstein condensate in a tilted or accelerated optical lattice, corresponding to the Wannier-Stark scenario of solid-state physics [16].

The decay dynamics in a nonlinear Wannier-Stark system was recently discussed in [12,13]. It was shown that a nonlinear mean-field interaction can destroy resonant tunneling. In this paper, we extend these studies to a double-periodic optical lattice. The decay dynamics in this system shows some interesting features even in the linear case, such as a splitting of resonant tunneling peaks. The different types of non-Hermitian crossing scenarios can be observed in dependence on the system parameters.

The paper is organized as follows: first of all we review some important results about the crossing scenarios in the non-Hermitian two-level system in the linear (Sec. II) and the nonlinear (Sec. III) case. The double-periodic Wannier-Stark system is introduced and analyzed in Sec. IV. Nonlinear Wannier-Stark resonances for a doubly periodic lattice are presented in Sec. V. A discussion of interesting experimental applications of our findings follows in Sec. VI.

II. CROSSING SCENARIOS OF RESONANCES IN LINEAR QUANTUM MECHANICS

We prepare for the full discussion of nonlinear resonance states as solutions of Eq. (1) by reviewing some essential properties of the simpler linear case. First of all, we want to illustrate the different types of possible curve crossing scenarios for non-Hermitian systems. To start with, we briefly review a simple and instructive model system, a two-level Hamiltonian with one decaying level [14,15]:

*Electronic address: witthaut@physik.uni-kl.de

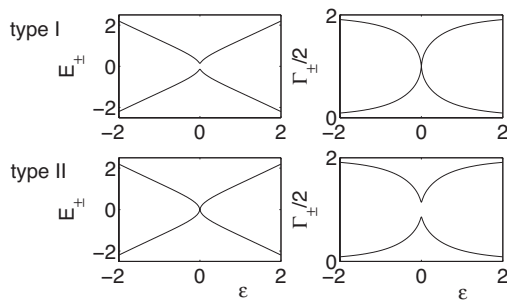


FIG. 1. Real (left) and imaginary (right) part of the eigenvalues (3) as a function of ϵ for $\gamma=1$. A type-I crossing is found for $v=1.01 > \gamma$ (upper figures), a type-II crossing is found for $v=0.99 < \gamma$ (lower figures).

$$H_2 = \begin{pmatrix} +\epsilon - 2i\gamma & v \\ v & -\epsilon \end{pmatrix} \quad (2)$$

with $\epsilon, v, \gamma \in \mathbb{R}$, and $\gamma \geq 0$. In this approach it is assumed that one of the bare states decays with rate γ , while the decay is negligible for the other one. The mean energy of the two bare states is set to zero, the energy difference is given by 2ϵ . The two states are coupled with strength v . A different, non-Hermitian two-level Hamiltonian was previously discussed by Berry [17].

The eigenvalues of the non-Hermitian Hamiltonian (2) are given by

$$\mathcal{E}_{\pm} = -i\gamma \pm \sqrt{(\epsilon - i\gamma)^2 + v^2} = E_{\pm} - i\Gamma_{\pm}/2. \quad (3)$$

Both real and imaginary part of the eigenvalues are different for $\epsilon \neq 0$. (Anti)crossings of the real and imaginary part are found only in the critical plane $\epsilon=0$. The exceptional line $v = \pm\gamma$ separates the critical plane into different regions: (i) For $|v| > \gamma$ the imaginary parts of the eigenvalues coincide, $\Gamma_+ = \Gamma_- = 2\gamma$, while the real parts differ. This case is denoted as a type-I crossing. (ii) For $|v| < \gamma$ the real parts of the eigenvalues coincide, $E_+ = E_- = 0$, while the imaginary parts differ. This case is denoted as a type-II crossing. (iii) The eigenvalues are fully degenerate, $\mathcal{E}_+ = \mathcal{E}_-$, along the critical lines $v = \pm\gamma$.

The two different crossing types are illustrated in Fig. 1. For a type-I crossing, i.e., $|v| > \gamma$, the imaginary parts of the eigenvalues cross while the real parts anticross. For a type-II crossing, i.e., $|v| < \gamma$, it is the other way around. Physically this crossing describes a resonantly enhanced tunneling (RET) effect: the decay rate of the lower state increases significantly if this state is energetically close or equal to the decaying upper level.

In view of the discussion of Wannier-Stark resonances in period-doubled lattices in the following sections we want to introduce another model system. We assume that the bare states split up into two states, where the energies of the stable bare states differ slightly by 2δ . Each stable state mainly couples to one of the decaying states, while all other couplings are assumed to be weak. We consider the Hamiltonian

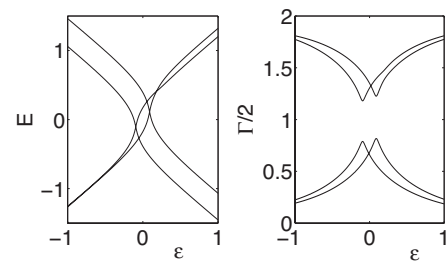


FIG. 2. Real (left) and imaginary (right) part of the eigenvalues of the four-level Hamiltonian (4) as a function of ϵ for $\gamma=1$, $v=0.98$, $w=0.04$, and $\delta=0.2$.

$$H_4 = \begin{pmatrix} H_2 + A & W \\ W & H_2 - A \end{pmatrix} \quad (4)$$

with the two-level Hamiltonian H_2 defined in Eq. (2) and

$$A = \delta \begin{pmatrix} 0 & 0 \\ 0 & 1 \end{pmatrix}, \quad W = w \begin{pmatrix} 1 & 1 \\ 1 & 1 \end{pmatrix}. \quad (5)$$

Figure 2 shows the eigenvalues of this Hamiltonian in dependence of the on-site energies ϵ . One observes that the resonance peak splits up into two peaks. Two possibilities for resonant tunneling, i.e., two type-II crossings, are found instead of just one. This crossing scenario is robust against small variations of the coupling w as long as $w \ll v$ is fulfilled. A nonvanishing coupling w causes a slight asymmetry of the two crossings. For $v > \gamma$ one has two type-I crossings instead, i.e., the imaginary parts of the eigenvalues cross while the real parts anticross.

The change of a system parameter, e.g., the strength of the Stark field F in the Wannier-Stark system discussed in Sec. IV, will typically affect the bare state energies ϵ as well as the decay rate γ and the coupling strengths. Therefore we consider a variety of the four-level Hamiltonian (4), the parameters of which are functions of the external field F :

$$\begin{aligned} \epsilon &= -F/2 + 0.1, \\ \gamma &= Fe^{-1/F}, \\ v &= 0.05Fe^{-1/2F}, \\ w &= 0.01Fe^{-1/2F}. \end{aligned} \quad (6)$$

The exponential scaling of the decay rate γ is well known from standard Landau-Zener theory (see, e.g., [18]). The dependence of the bare state energies and the coupling coefficients on F were analyzed in detail for a two-ladder system in [19]. It was shown that the Wannier-Stark spectrum is accurately described assuming that the parameters scale as in Eq. (6). The actual values of coefficients in Eq. (6) are chosen in an *ad hoc* manner for illustration only. The resulting decay rates are illustrated in Fig. 3. For $\delta=0.02$, we find two type-II crossings. With increasing δ , the crossing on the right changes its form and becomes a type-I crossing. Such a crossing scenario is naturally realized for Wannier-Stark

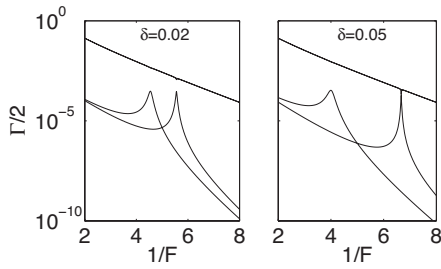


FIG. 3. Imaginary part of the eigenvalues of the four-level Hamiltonian (4) as a function of $1/F$ and $\delta=0.02$ (left) and $\delta=0.05$ (right). See text for details.

resonances in double-periodic lattices, as will be shown in Fig. 9 below.

III. NONLINEAR NON-HERMITIAN CROSSING SCENARIOS

The linear non-Hermitian two-level system described in Sec. II neglects any particle interaction. Including this interaction in a mean-field description according to the Gross-Pitaevskii equation (1) yields a nonlinear non-Hermitian two-level system [20], described by the Hamiltonian

$$H_{\text{mf}} = \begin{pmatrix} \epsilon + 2c|\psi_1|^2 - 2i\gamma & v \\ v & -\epsilon + 2c|\psi_2|^2 \end{pmatrix}, \quad (7)$$

where the nonlinearity parameter c is proportional to the parameter g in the Gross-Pitaevskii equation (1). The nonlinear eigenstates are then defined as the self-consistent solutions of the time-independent Gross-Pitaevskii equation

$$H_{\text{mf}} \begin{pmatrix} \psi_1 \\ \psi_2 \end{pmatrix} = \mu \begin{pmatrix} \psi_1 \\ \psi_2 \end{pmatrix}. \quad (8)$$

The nonlinear eigenstates crucially depend on the normalization of the state vector, which is fixed as $|\psi_1|^2 + |\psi_2|^2 = 1$ throughout this section. For convenience we symmetrize the nonlinear Hamiltonian (7) by subtracting a constant energy term $c(|\psi_1|^2 + |\psi_2|^2)$. The Gross-Pitaevskii equation (8) then reads

$$\begin{pmatrix} \epsilon + c\kappa - 2i\gamma & v \\ v & -\epsilon - c\kappa \end{pmatrix} \begin{pmatrix} \psi_1 \\ \psi_2 \end{pmatrix} = \mu \begin{pmatrix} \psi_1 \\ \psi_2 \end{pmatrix} \quad (9)$$

with $\kappa = |\psi_1|^2 - |\psi_2|^2$. The self-consistent solutions of this nonlinear equation define the nonlinear eigenstates and eigenvalues.

Note that the nonlinear eigenstates are not connected to stationary solutions of the time-dependent system, if the chemical potential turns out to be complex, since the dynamics depends crucially on the normalization of the state vector, which is not constant for a complex valued chemical potential. After some algebraic manipulation one can show that the nonlinear eigenstates, i.e., the solutions of Eq. (9), are given by the real roots of the equation

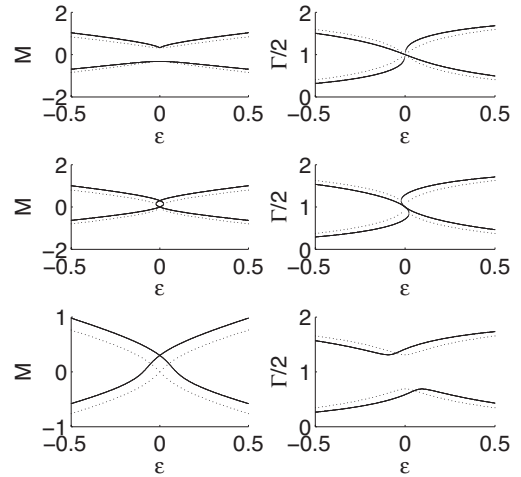


FIG. 4. Real (left) and imaginary (right) part of the eigenvalues (9) as a function of ϵ for $\gamma=1.00$, $c=0.3$, and $v=1.05 > \gamma$ (upper figures), $v=1.00 = \gamma$ (middle figures), $v=0.95 < \gamma$ (lower figures). The linear levels ($c=0$) are plotted as dotted lines for comparison.

$$(c^2 + \gamma^2)\kappa^4 + 2c\epsilon\kappa^3 + (v^2 + \epsilon^2 - \gamma^2 - c^2)\kappa^2 - 2c\epsilon\kappa - \epsilon^2 = 0. \quad (10)$$

Depending on the parameters, there are two or four real roots and each of them is connected to a complex eigenvalue by

$$\mu = c + \epsilon/\kappa - i\gamma(1 + \kappa) = M - i\Gamma/2. \quad (11)$$

For $\epsilon \rightarrow \pm\infty$, the linear term dominates and one has only two eigenvalues. For $\epsilon=0$, $\kappa=0$ is a double degenerate solution of Eq. (10). For $\gamma < v$ these states are connected to the common linear (anti)symmetric eigenstates, while this is not the case for $\gamma > v$. In the following we consider the crossing scenario of the eigenvalues in dependence on ϵ for different fixed values of the other parameters.

The nonlinear eigenstates of a two-level system are well known for the Hermitian case $\gamma=0$ [6,7,21]. Novel eigenstates emerge with broken symmetry if the nonlinearity exceeds a critical value, $|c| > c_{\text{cr}} = v$, which is given by the coupling strength v which corresponds to half of the gap between the linear levels at $\epsilon=0$. The levels show looped structures around $\epsilon=0$ with a width $|\epsilon| \leq (c^{2/3} - v^{2/3})^{3/2}$.

Let us first discuss the effect of a weak nonlinearity. Figure 4 shows the eigenvalues for a relatively weak nonlinearity in comparison with the linear case $c=0$. The size of the gaps is not altered by the nonlinearity, which leads to the important fact that the nonlinearity does *not* influence the crossing type. Nevertheless, it changes the shape of the levels. For a type-I crossing, the real part of the upper level is sharpened while the one of the lower level is flattened, which is well known for $\gamma=0$ [6]. For a type-II crossing the effect is basically the same, but is accompanied by a shift of the crossing point from $\mu=0$ to $\mu=c$ and the lower level is stretched to this point. The imaginary parts bend slightly to the left. At the exceptional point additional eigenvalues emerge in a narrow interval around $\epsilon=0$

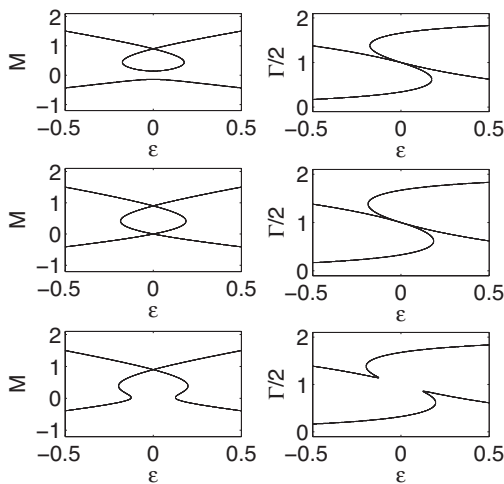


FIG. 5. Real (left) and imaginary (right) part of the eigenvalues (9) as a function of ϵ for $\gamma=1.00$, $c=0.9$, and $v=1.01 > \gamma$ (upper figures), $v=1.00 = \gamma$ (middle figures), $v=0.99 < \gamma$ (lower figures).

In general, the presence of moderate decay facilitates the formation of novel eigenstates. Figure 5 shows the nonlinear levels for $c=0.9$, which is slightly below the critical value $c_{cr}=v$ for $\gamma=0$. For a type-I crossing, $v > \gamma$, the real parts show a familiar loop. The imaginary parts cross as usual, showing an additional S-shaped structure. In fact, the critical nonlinearity for the emergence of looped levels is decreased to

$$c_{cr} = \sqrt{v^2 - \gamma^2}, \quad (12)$$

which can be seen by analyzing the behavior of the polynomial (10) for $\epsilon=0$. At the exceptional point $v = \gamma$, the critical nonlinearity tends to zero and there are additional eigenstates even in the case of arbitrary weak nonlinearity. For a type-II crossing, $v < \gamma$, the imaginary parts anticross and the real parts cross in a manner which can be understood as a destruction of the loop at its lower edge. The crossing appears at the former crossing point of the loop at $\epsilon=0$ and $\mu=c \neq 0$. In the nondecaying case, $\gamma=0$, novel eigenstates first emerge at the point of the avoided crossing at $\epsilon=0$. This remains true for a type-I crossing, $v > \gamma$. For a type-II crossing, $v < \gamma$, however, novel eigenvalues emerge, again in an S-shaped structure around some nonzero value of ϵ .

Concluding this section, a weak nonlinearity does not alter the crossing type, however, it deforms the levels in a characteristic manner. For a type-II crossing the real parts cross at $\mu=c \neq 0$. At the exceptional point novel eigenstates emerge, even for small nonlinearities. The presence of decay facilitates the formation of novel eigenstates for stronger nonlinearities. For type-I crossings, loops appear if $|c| > c_{cr} = \sqrt{v^2 - \gamma^2}$. For a type-II crossing the additional eigenstates emerge around some nonzero value of ϵ forming a double-S structure. If the sign of the nonlinearity is changed, the levels interchange their behavior, i.e., the real parts are mirrored at the ϵ axis, the imaginary parts at the Γ axis.

IV. WANNIER-STARK RESONANCES IN DOUBLE-PERIODIC LATTICES

A. Fundamentals of the linear Wannier-Stark system

A prime example for resonances and resonant tunneling is the (linear) Wannier-Stark problem described by the Hamiltonian

$$H_{WS} = -\frac{1}{2} \frac{\partial^2}{\partial x^2} + V(x) + Fx \quad (13)$$

with a periodic potential $V(x+d)=V(x)$. We use rescaled units in which $\hbar=M=1$. The Wannier-Stark problem was already discussed in the early days of quantum mechanics in the context of electrons in solids under the influence of an external electric field [22]. Coherent dynamics of electrons in semiconductor superlattices were observed not until the 1990s. Experiments showed Bloch oscillations for “weak” electric fields and decay for stronger fields [23,24]. The Wannier-Stark system is furthermore realized for the propagation of light pulses in thermo-optically biased coupled waveguides. Bloch oscillations as well as decay could thus be observed directly in real space [25]. On the other hand, recent experiments with cold atoms and Bose-Einstein condensates in optical lattices offer some considerable advantages [2,26–28]. Scattering by lattice defects or impurities is absent and experimental parameters can be tuned in a wide range. The periodic potential is generated by a standing laser beam and thus simply cosine shaped.

Let us briefly review some fundamentals of Wannier-Stark resonances, which are defined by the eigenvalue equation

$$H_{WS} \Psi_{\alpha,n}(x) = \mathcal{E}_{\alpha,n} \Psi_{\alpha,n}(x). \quad (14)$$

Here, α is the ladder index and $n \in \mathbb{Z}$ labels the lattice sites. The Wannier-Stark Hamiltonian (13) is non-Hermitian due to the boundary condition: A wave packet will eventually decay towards $x \rightarrow -\infty$. In fact, it has been shown that the spectrum of the Hamiltonian is continuous with embedded resonances [29]. Thus the resonance eigenenergies are complex, $\mathcal{E}_{\alpha,n} = E_{\alpha,n} - i\Gamma_{\alpha}/2$, where the imaginary part Γ gives the decay rate. The Wannier-Stark Hamiltonian has one important symmetry, it is invariant under a simultaneous spatial translation over a lattice period d and an energy shift dF . This symmetry is expressed by the commutation relation

$$[H_{WS}, T_m] = -mdFT_m, \quad (15)$$

where T_m is the translation operator over m lattice periods. Now it is easy to see that the Wannier-Stark resonances from one ladder α are related by a simple translation,

$$\begin{aligned} H_{WS} T_m \Psi_{\alpha,n}(x) &= T_m H_{WS} \Psi_{\alpha,n}(x) + [H_{WS}, T_m] \Psi_{\alpha,n}(x) \\ &= (\mathcal{E}_{\alpha,n} - mdF) T_m \Psi_{\alpha,n}(x). \end{aligned} \quad (16)$$

Thus the discrete spectrum is arranged in the form of the so-called Wannier-Stark ladders,

$$\Psi_{\alpha,n}(x) = \Psi_{\alpha,0}(x - nd),$$

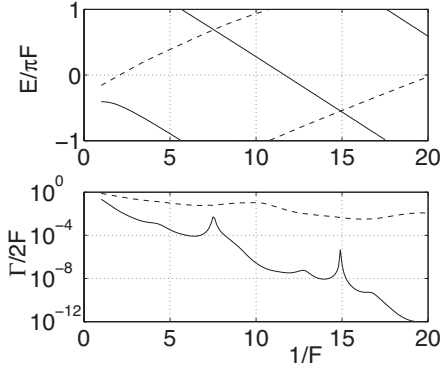


FIG. 6. Eigenenergies (upper panel) and decay rates (lower panel) of the two most stable Wannier-Stark ladders for the potential $V(x)=\cos x$.

$$\mathcal{E}_{\alpha,n} = E_{\alpha,0} + n d F - i \Gamma_{\alpha} / 2. \quad (17)$$

The different ladders are labeled by $\alpha=0,1,2,\dots$. An efficient method to calculate the resonance eigenstates was introduced in [30], a recent review can be found in [31].

The decay rate Γ_{α} is the same for all resonances in one ladder. In general, the decay rate scales as $\Gamma \sim F \exp(-\pi \Delta E^2 / F)$, where ΔE is the energy gap between the Bloch bands of the periodic potential. This result can be deduced from Landau-Zener theory [18,19]. However, one observes peaks of the decay rate on top due to resonant tunneling. For example, the decay rate of the two most stable resonances for the periodic potential $V(x)=\cos x$ is plotted as a function of the inverse field strength $1/F$ in Fig. 6. RET takes place when a state of a lower ladder with energy $\mathcal{E}_{\alpha,n}$ gets in resonance with a state of a higher ladder at a different site, i.e., $E_{\alpha,n} = E_{\alpha',n'}$. The decay rate of the lower ladder is significantly increased as it couples resonantly to a higher ladder with a higher decay rate. For example, the pronounced peak in the ground ladder decay rate (i.e., $\alpha=0$) at $F \approx 1/7$ corresponds to the resonance $\alpha=0 \leftrightarrow \alpha'=1$ and $n'=n-1$.

B. Double-periodic lattices

Now we turn to the main subject of the present paper. We consider a double-periodic potential $V(x)$ consisting of a major optical lattice of period d plus an additional shallow lattice of double period,

$$V(x) = V_0 [\sin^2(\pi x/d) + \delta \sin^2(\pi x/2d + \phi/2)]. \quad (18)$$

Rescaling the spatial coordinate as $x' = 2\pi x/d$ and neglecting a constant potential offset, we can rewrite the periodic potential as

$$V(x) = -\frac{V_0}{2} [\cos(x) + \delta \cos(x/2 + \phi)]. \quad (19)$$

The relative phase of the two lattices is denoted by ϕ .

Due to the additional lattice each Bloch band splits up into two minibands [34], and each Wannier-Stark ladder splits up into two miniladders, as proved in the following. The symmetries of the Hamiltonian are given by the commutation relations

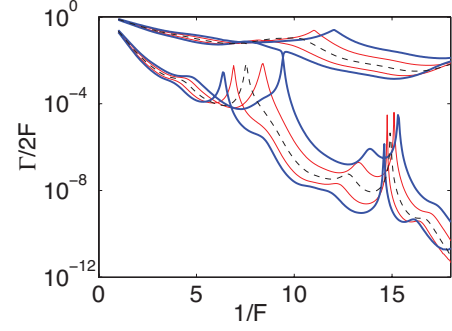


FIG. 7. (Color online) Resonant tunneling in a double-periodic Wannier-Stark system. Decay rates of the four most stable resonance for $V_0=2$, $\phi=0$, and $\delta=0$ (dashed black line), $\delta=0.05$ (thin red lines), and $\delta=0.1$ (thick blue lines).

$$[H, T_{2m}] = -2mdFT_{2m},$$

$$[H, T_{2m+1}G] = -(2m+1)dFT_{2m+1}, \quad (20)$$

where T_m is the translation operator over m lattice periods and the operator G inverts the sign of δ in all following terms. Then it is easy to see that the Wannier-Stark states of one ladder are related by a translation over an even number of lattice periods, or by a translation over an odd number of lattice periods plus an inversion of the sign of δ ,

$$HT_{2m}\Psi_{\alpha,n}(x) = [\mathcal{E}_{\alpha,n}(\delta) - 2mdF]T_{2m}\Psi_{\alpha,n}(x),$$

$$HT_{2m+1}G\Psi_{\alpha,n}(x) = [\mathcal{E}_{\alpha,n}(-\delta) - (2m+1)dF]T_{2m+1}G\Psi_{\alpha,n}(x). \quad (21)$$

Furthermore, it can be shown that the energy offset $\mathcal{E}_{\alpha,0}$ is antisymmetric in δ ,

$$\mathcal{E}_{\alpha,0}(-\delta) = -\mathcal{E}_{\alpha,0}(\delta). \quad (22)$$

Thus the Wannier-Stark ladders split up into two miniladders, each with an energy offset $2\mathcal{E}_{\alpha}(\delta)$:

$$\mathcal{E}_{\alpha,2n} = \mathcal{E}_{\alpha}(\delta) + 2ndF,$$

$$\mathcal{E}_{\alpha,2n+1} = -\mathcal{E}_{\alpha}(\delta) + (2n+1)dF. \quad (23)$$

A similar proof is given in [32] within the tight-binding approximation.

The decay of the Wannier-Stark resonances is seriously influenced by the additional period-doubled potential. Figure 7 shows the decay rate Γ as a function of the inverse field strength $1/F$ for $V_0=2$, $\phi=0$, $\delta=0.05$, and $\delta=0.1$, respectively. The decay rate of the single-periodic lattice $\delta=0$ is also plotted for comparison. As all Wannier-Stark ladders split up into two miniladders, so does the decay rate Γ . The general scaling of Γ with F remains the same for both miniladders, while the RET peaks are seriously altered. The peaks split up into two, where the height of the subpeaks increases significantly. This effect is mostly pronounced for the major resonance at $F \approx 1/7$. The explanation of the splitting is straightforward: In Fig. 8, the thick blue lines represent the energy levels of the two most stable Wannier-Stark

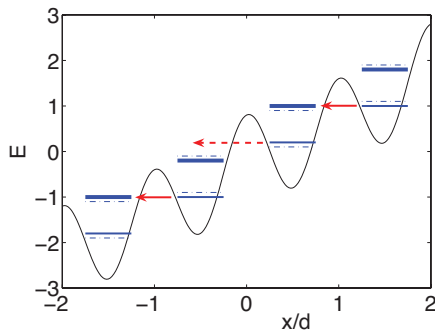


FIG. 8. (Color online) Explanation of resonantly enhanced tunneling (RET). See text for details.

ladders. Due to the period-doubled potential they are alternately shifted up or down with respect to the unperturbed level ($\delta=0$, dash-dotted lines). The decay rate Γ is resonantly enhanced when two energy levels of different ladders are degenerate, as indicated by the solid red arrow. However, for $\delta \neq 0$, the two miniladders are in resonance with higher ladders for different values of the field strength F due to the alternating energy shift. In Fig. 8, for example, one of the miniladders is off resonance (indicated by the broken arrow) while the other one is in resonance (solid arrow). If the field strength is lowered, the off-resonant ladder will get into resonance at another value of F .

With increasing amplitude δ of the second double-periodic lattice, the splitting of the resonant tunneling peaks clearly becomes more pronounced as one can see in Fig. 7. Another (not so intuitive) effect is that the additional lattice can also alter the crossing type. For $\delta=0.1$ one observes a crossing of the decay rates at $F \approx 1/9.5$ due to resonant tunneling instead of an anticrossing. This effect is further illustrated in Fig. 9. The real and the imaginary part of the resonance eigenenergies are plotted in the vicinity of one of the RET peaks (cf. Fig. 7). For $\delta=0.075$, one observes a familiar RET peak, i.e., a type-II curve crossing. For $\delta=0.08$, however, the crossing type is altered from type II to type I. The decay rate of one miniladder crosses the decay rate of one excited miniladder. Correspondingly, the real parts anticross. A diabolic point, where real and imaginary part are degener-

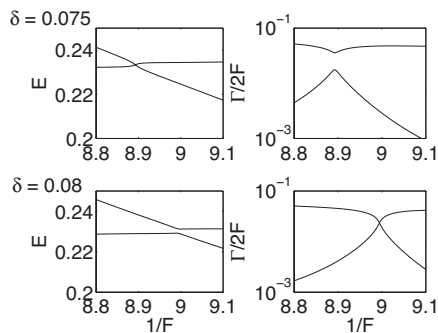


FIG. 9. (Anti)Crossing of the real and the imaginary part of two eigenenergies of the Wannier-Stark resonances in a double-periodic Wannier-Stark system for $V_0=2$, $\phi=0$, and $\delta=0.075$ (upper panels), $\delta=0.08$ (lower panels).

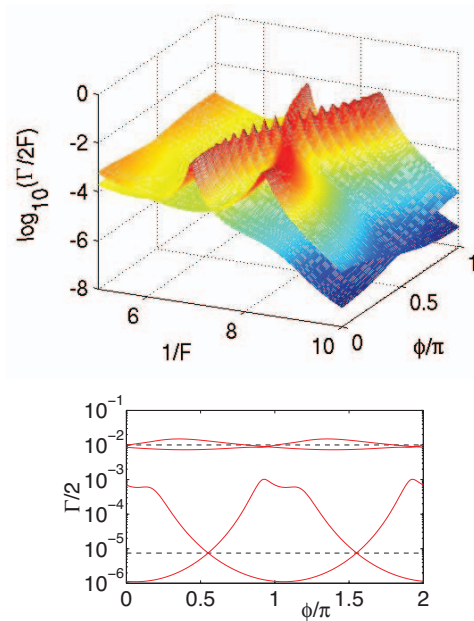


FIG. 10. (Color online) Upper panel: Decay rates of the two most stable resonances as a function of the relative phase ϕ and the inverse field strength $1/F$ for $V_0=2$ and $\delta=0.05$. Lower panel: For fixed Stark field $F=0.12$.

ate, is found at $\delta=0.0772$ and $F=1/8.937$ for $\phi=0$. If we consider the relative phase ϕ as another free parameter, the set of diabolic points is a one-dimensional subset of the three-dimensional parameter space (δ, F, ϕ) ; the diabolic crossing has co-dimension 1.

C. Output control by the relative phase

Up to now, we have shown that the RET peaks split up, whereby the splitting increases with the amplitude δ of the additional lattice. Furthermore, the decay depends crucially on the relative phase ϕ of the lattices. Figure 10 shows the decay rate of the two lowest miniladders in dependence of the relative phase ϕ and the inverse field strength $1/F$ for $V_0=2$ and $\delta=0.05$. The splitting of the RET peaks is maximal for $\phi=0$. It becomes zero for $\phi \approx 0.55\pi$, where the decay rates of the two miniladders degenerate again.

Despite the fact that the additional lattice is much weaker than the single-periodic one ($\delta=0.05$), it can seriously affect the decay properties. Changing the relative phase ϕ of the two lattices, the decay rate of the two lowest miniladders may vary over several orders of magnitude. This is further illustrated in the lower panel of Fig. 10, where the decay rate is plotted for a fixed value of $F=0.12$. The decay rate for the single-periodic case $\delta=0$ is also plotted for comparison. This strong effect is caused by the shift of the RET peak position F_{res} in dependence of ϕ shown in the upper panel of Fig. 10. Fixing the field strength F at an appropriate value, one can tune the system in and out of resonance solely by a variation of the phase ϕ . In the example in Fig. 10, we have chosen the field strength so that $F=0.12 \approx F_{\text{res}}$ for $\phi=0$. Changing the phase to $\phi=0.55\pi$ shifts the RET peak to $F_{\text{res}}=0.134$. As

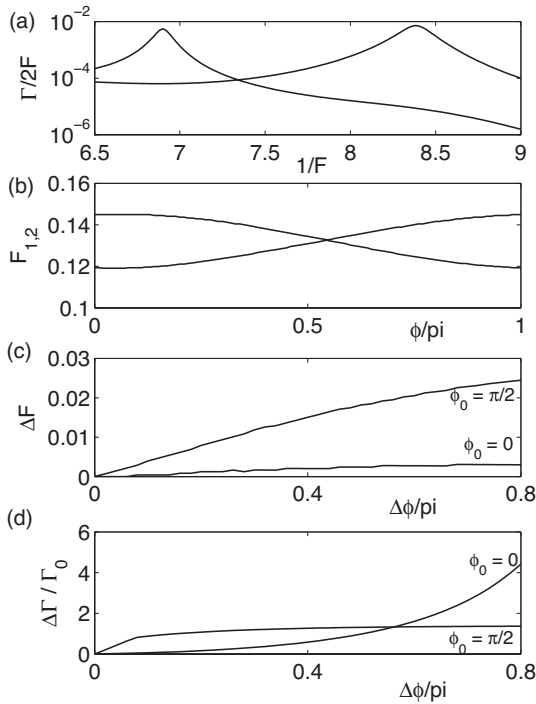


FIG. 11. Effects of fluctuations of the relative phase ϕ . (a) Decay rate of the two most stable resonances for $V_0=2$, $\delta=0$, and $\phi=0$. (b) Position $F_{1,2}$ of the RET peaks vs the relative phase ϕ . (c) Uncertainty ΔF of the positions of the RET peaks vs fluctuation $\Delta\phi$ of the phase. (d) Relative fluctuation $\Delta\Gamma/\Gamma_0$ of the decay rate for $F=1/8$ vs $\Delta\phi$.

the field strength F remains fixed, the system is tuned out of resonance and the decay rate drops by orders of magnitude. The decay rate as a function of the phase, $\Gamma(\phi)$, is π periodic. This can be seen as follows: Shifting the phase by an amount of π and the position by 2π leaves the Wannier-Stark Hamiltonian (13) with the potential (19) invariant up to a real constant. Since a spatial translation by 2π just exchanges the two miniladders as shown above, so does a phase shift by π .

The sensitive dependence on the relative phase ϕ might be very useful for the design and control of future experiments with double-periodic optical lattices. A complete stabilization of the relative phase of the two lattices will be hard to achieve and fluctuations will play an important role. Yet, Ritt *et al.* have realized a new technique based on Fourier synthesis to control two (or even more) optical lattices with different spatial harmonics [33]. In the following, we will discuss the effects on the decay rates of the Wannier-Stark resonance in some detail. The strongest effects are found in the vicinity of the RET peaks, on which we focus in our present discussion.

Figure 11(a) again presents the decay rate as a function of the inverse field strength $1/F$ for $V_0=2$ and a weak additional lattice with $\delta=0.05$ and $\phi=0$. For the given parameters, we find RET peaks at $F_1 \approx 1/6.9$ and $F_2 \approx 1/8.4$. Figure 11(b) shows the position $F_{1,2}$ of the two resonant tunneling peaks in dependence of the relative phase ϕ . The positions vary in an interval of width $\Delta F \approx 1/40$.

In a real-life experiment, it is difficult to exactly control the relative phase of two independent standing waves. Therefore we study also the influence of random-phase fluctuations. If we assume that the phase ϕ fluctuates in an interval of width $\Delta\phi$ around the desired value ϕ_0 , $\phi \in [\phi_0 - \Delta\phi/2, \phi_0 + \Delta\phi/2]$, the positions of the resonant tunneling peaks will also fluctuate in an interval of width ΔF . Figure 11(c) shows how the width ΔF depends on the strength of the phase fluctuations $\Delta\phi$ for $\phi_0=0$ and $\phi_0=\pi/2$. The fluctuations are rather weak for $\phi_0=0$, where the RET peaks have maximum distance. For a given value of the external field F , the decay rates Γ fluctuate in an interval of width $\Delta\Gamma$. Figure 11(d) shows the relative strength of the fluctuation, $\Delta\Gamma/\Gamma_0$ vs the phase fluctuations $\Delta\phi$ for the most stable resonance for an external field $F=1/8$ and $\phi_0=0$ or $\phi_0=\pi/2$, respectively. The relative uncertainty of the decay rate becomes greater than unity already for small fluctuations of the phase ϕ . Nevertheless, the noise induced shift and change in height of the RET peaks is small considering the absolute change of the decay rates around the RET peaks of about two orders of magnitude.

However, it is also possible to exploit the sensitive dependence on the phase ϕ , if it can be accurately controlled. For instance, it could be possible to rapidly tune the output of a pulsed atom laser. An example will be discussed in detail in Sec. VI.

V. NONLINEAR WANNIER-STARK RESONANCES IN DOUBLE-PERIODIC OPTICAL LATTICES

A method to obtain accurate, nonlinear Wannier-Stark resonances was proposed recently in [13], and we use a similar approach to numerically compute decay rates of the nonlinear version of the Wannier-Stark introduced in Sec. IV B above. In contrast to the case studied in [13], the computations based on the Gross-Pitaevskii equation (1) in the presence of a two-period optical lattice are more difficult, since the algorithm needs to discriminate between the two miniband solutions which are quite close in energy (cf. Figs. 6 and 7). In particular, for very small Stark fields, it is hard to obtain convergence. In the following, we concentrate therefore on RET peaks at fields as large as possible, and one trick to shift the peaks to such values is to use *attractive* interactions, i.e., negative nonlinearities ($g < 0$). Figure 12 presents a set of RET peaks for different values of the nonlinearity g .

The nonlinearity induced a shift of both RET peaks (corresponding to the two minibands) and also a systematic stabilization (i.e., smaller heights) can be observed, as predicted by similar results for the usual, one-band Wannier-Stark system [13]. This is analyzed in more detail in Fig. 13, where the peak positions F_{res} and the height of the peaks Γ_{res} are plotted in dependence of g .

The stabilization of the Wannier-Stark states by an attractive nonlinearity is shown in the upper panel. An asymmetry of the two peaks is observed already in the linear case $g=0$: The left peak is slightly higher than the right one, i.e., the peak decay rate is larger for *smaller* external fields F . This phenomenon becomes even more pronounced in the nonlinear case $g < 0$. The stabilization by an attractive nonlinearity (cf. [13]) is stronger for the right peak.

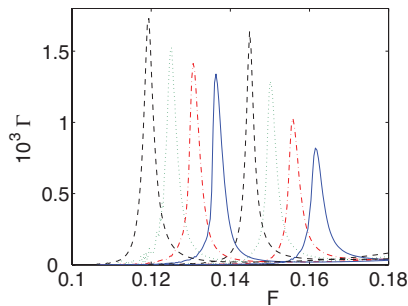


FIG. 12. (Color online) Decay rates of nonlinear Wannier-Stark resonances in double periodic optical lattices with $V_0=2$, $\delta=0.05$, $\phi=0$, and $g=0$ (dashed black line), $g=-0.1$ (dotted green line), $g=-0.2$ (dash-dotted red line), and $g=-0.3$ (solid blue line), respectively.

The peak positions shown in the lower panel of Fig. 13 vary linearly with g , which can be derived in a perturbative approach. As discussed above, resonant tunneling is observed when a state of a lower ladder get in resonance with a state in a higher ladder at a different site, $E_{\alpha,n}=E_{\alpha',n'}$. Here we consider only the states in the ground ladder, which are localized in a single potential well. First-order perturbation theory with respect to the linear case $g=0$ predicts that their energy is shifted by the amount [13]

$$\Delta E_{0,0} \approx g \int_{-\pi}^{+\pi} |\psi_{0,0}^{(0)}(x)|^4 dx, \quad (24)$$

where the superscript (0) refers to the linear case $g=0$. The shift ΔF of the RET peaks then follows from the modified resonance condition

$$E_{0,n}^{(0)} + \Delta E_{0,n} = E_{\alpha',n'}^{(0)} + n' d \Delta F. \quad (25)$$

Evaluating the integral in Eq. (24) and setting $n'=n-1$ one finds

$$\Delta F = -\frac{0.36}{2\pi} g \quad (26)$$

for the peak shift plotted in Fig. 13. Both peaks are shifted equally, so that the distance of the peaks remains constant.

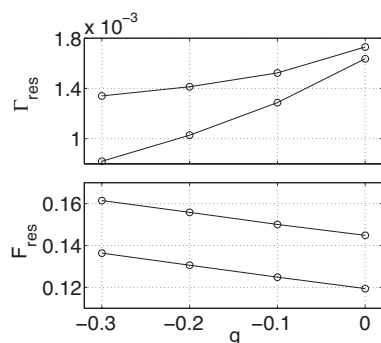


FIG. 13. Shift of the RET peaks. Shown is the position F_{res} of the RET peaks (lower panel) and the resonant decay rate Γ_{res} (upper panel) in dependence of the nonlinearity g .

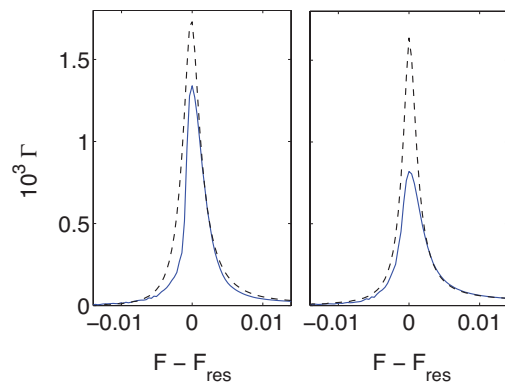


FIG. 14. (Color online) Asymmetry of the nonlinear RET peaks. Shown is the decay rate $\Gamma(F)$ of the two peaks (left and right) around the respective peak positions F_{res} for $g=0$ (black dashed line) and $g=-0.3$ (solid blue line).

Furthermore, the shape of the RET peaks becomes asymmetric in the nonlinear case. This is shown in Fig. 14, where we have plotted a magnification of the decay rate $\Gamma(F)$ around the respective positions of the RET peaks for $g=-0.3$ and $g=0$. In comparison to the linear case, the peak is bent to the left for an attractive nonlinearity. This asymmetry is a general feature of nonlinear eigenstates in open systems. It is already present for the nonlinear two-level system as shown in Fig. 4. A similar incline of resonant curves is also important for nonlinear resonant transport. The curves can even bend over for strong nonlinearities leading to a bistable behavior as shown in [35].

VI. DYNAMICS

In this section, we discuss the dynamics of an initially localized matter wave, e.g., a Gaussian wave packet in the tilted double-periodic optical lattice (19). In one of the first experiments on the macroscopic dynamics of BECs in optical lattices it was shown that such a system shows a coherent pulsed output [28]. An explanation in terms of truncated Wannier-Stark resonances can be found in [36]. The amplitude of the pulsed output is given by the decay rate of the Wannier-Stark resonances.

First of all, we illustrate how the sensitive dependence on the phase can be used to tune a pulsed atom laser. As a proof of principle, we just consider the *linear* ($g=0$) evolution. In contrast to the previous sections we consider a weaker potential, $V_0=0.8$, so that decay is generally stronger. We numerically integrate the Schrödinger equation for an initially Gaussian wave packet

$$\psi(x, t=0) = \frac{1}{(2\pi)^{1/4} \sigma^{1/2}} \exp[-(x-x_0)^2/4\sigma^2] \quad (27)$$

with width $\sigma=5\pi$. Figure 15 shows the density $|\psi(x, t)|^2$ in a grey-scale plot for a single periodic lattice ($\delta=0$). A pulsed output forms due to the external field. The pulses are accelerated just as classical particles. The first three strong pulses emerge from excited ladders. The output strength of the other

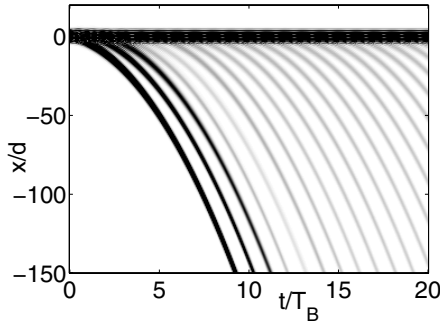


FIG. 15. Pulsed output from a tilted optical lattice for $V_0=0.8$, $F=1/18$ and $\delta=0$, $g=0$. Shown is the atomic density $|\psi(x,t)|^2$ in a grey-scale plot.

pulses from the ground ladder can be controlled to a large extent in the double-periodic case by the relative phase ϕ . As already shown in Fig. 10, the decay rate varies strongly with the relative phase of the two lattices. The effect on the pulsed output is shown in Fig. 16, where the density is plotted for $t=14T_B$ for three different lattice setups.

For $\delta=0.2$ and $\phi=0$, a RET peak of type I is found in the second miniladder at $F=1/18$. Thus decay from this miniladder is strongly enhanced in comparison to the single-periodic lattice $\delta=0$. Note that the pulsed output will stop as soon as the population in the second miniladder has decayed. In contrast, the pulsed output is strongly suppressed for a relative phase $\phi=\pi/2$, where RET does not play a role for the given field strength.

In order to measure the performance of this output switch more qualitatively, we define the fidelity

$$f = \frac{P_{\text{out}}(\phi_0=0)}{P_{\text{out}}(\phi_0=\pi/2)}, \quad (28)$$

where P_{out} measures the integrated density of the pulsed output for a certain value ϕ_0 of the relative phase of the two optical lattices. The output is switched on for $\phi_0=0$ and it is switched off for $\phi_0=\pi/2$. We measure the output density P_{out} at $t=14T_B$, where we neglect the first three strong pulses

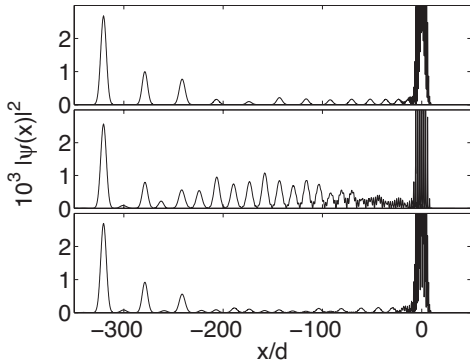


FIG. 16. Pulsed output from a tilted optical lattice for $g=0$. Shown is the atomic density for $t=14T_B$ for $\delta=0$ (top), $\delta=0.2$ and $\phi=0$ (middle), and $\delta=0.2$ and $\phi=\pi/2$ (bottom).

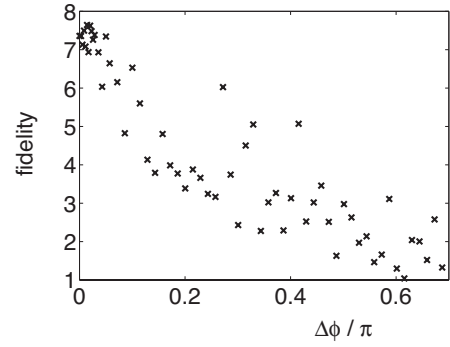


FIG. 17. Fidelity of the output switch in dependence of the standard deviation $\Delta\phi$ of the phase fluctuations.

as they are due to the initial population of excited Bloch bands. Then one has

$$P = \int_{-230d}^{-30d} |\psi(x)|^2 dx. \quad (29)$$

For the parameters used in Fig. 16, we find a fidelity of $F=7.4$, i.e., the output for $\phi_0=0$ is enhanced by a factor of 7.4 in comparison to $\phi_0=\pi/2$.

However, in a real experimental setup the phase ϕ will fluctuate around the desired value. This is mainly due to mechanical perturbations, thus fluctuations with very high frequencies are unlikely, while fluctuations with small frequencies up to some kHz can be controlled by an active stabilization. Thus we assume that the power spectrum of the phase fluctuations has a maximum at intermediate values in the kHz regime. This is comparable to the Bloch frequency $\omega_B=2\pi/T_B$, as the Bloch period is about one millisecond in a typical experiment [28]. Exemplarily, we consider fluctuations with a Gaussian power spectrum with mean ω_B and width $\omega_B/4$. In the following we analyze the pulsed output in dependence of the strength of the fluctuations. Figure 17 shows the fidelity of the output in dependence of the standard deviation $\Delta\phi=[\langle(\phi-\phi_0)^2\rangle]^{1/2}$ of the fluctuations for the same parameters as in Fig. 16. One observes that the fidelity drops to 1 (no switching effect) for a standard deviation of $\Delta\phi \approx 0.6\pi$. A reduction of the fluctuations below this value is in principle possible today, however, only with a great technical effort. As a consequence, an output switching seems feasible in double periodic lattices.

VII. CONCLUSION AND OUTLOOK

In the present paper we have studied the interplay between decay and a nonlinear mean-field potential describing the atom-atom interactions in a dilute Bose-Einstein condensate.

As an illustrative model we have investigated a two-level systems with one decaying level, which can be treated analytically. In the linear case, one has to distinguish two types of level crossings, either the real parts anticross while the imaginary parts of the eigenvalues cross (type I) or the other way around (type II). Both real and imaginary parts are de-

generate at the exceptional point, where the bare state decay rate equals the coupling strength. A weak nonlinearity does *not* alter the crossing type, however, it *deforms* the levels in a characteristic manner. For example, it leads to a bending of the peaks in the decay rates. Novel nonlinear eigenstates emerge for a stronger nonlinearity, where the critical nonlinearity is decreased in the presence of decay. Looped levels appear for type-I crossings, while the additional eigenstates emerge in a double-S structure for a type-II crossing. At the exceptional point novel eigenstates emerge, even for small nonlinearities.

An experimental setup where both decay and nonlinearity play an important role is the dynamics of Bose-Einstein condensates in accelerated optical lattices. In particular, we have analyzed the decay in a double-periodic lattice, where a weak period-doubled potential is superimposed onto the fundamental lattice. These results will be of interest for controlling transport of ultracold atoms in future and ongoing experiments [37].

The decay rate in a double-periodic Wannier-Stark system depends sensitively on the system parameters, such as the relative amplitudes of the lattices and the relative phase, which can be varied over a wide range. In particular, the resonant tunneling peaks of the decay rate $\Gamma(F)$ split up into

two subpeaks. Varying the system parameters one can tune these peaks and even achieve a crossover from a type-II crossing to a type-I crossing. This could be crucial for future experiments since a robust control of the relative phase is hard to realize. One can, however, also exploit this sensitive dependence in order to implement a fast output switch for a pulsed atom laser. A weak nonlinear mean-field potential describing the atom-atom interactions in a Bose-Einstein condensate of ultracold atoms has two major effects: The resonant tunneling peaks are shifted. This shift can lead to a stabilization against decay. Furthermore, it leads to a bending of the peaks as predicted by the nonlinear non-Hermitian two-level system.

ACKNOWLEDGMENTS

We thank Peter Schlagheck for fruitful and inspiring discussions. D.W. acknowledges support from the Studienstiftung des deutschen Volkes and the Deutsche Forschungsgemeinschaft via the Graduiertenkolleg 792. S.W. acknowledges support from the Alexander von Humboldt Foundation (Feodor-Lynen Program).

-
- [1] M. Scully and G. Rempe, *Adv. At., Mol., Opt. Phys.* **53**, 1 (2006).
 - [2] O. Morsch and M. Oberthaler, *Rev. Mod. Phys.* **78**, 179 (2006).
 - [3] L. Pitaevskii and S. Stringari, *Bose-Einstein Condensation* (Oxford University Press, Oxford, 2003).
 - [4] M. Albiez, R. Gati, J. Fölling, S. Hunsmann, M. Cristiani, and M. K. Oberthaler, *Phys. Rev. Lett.* **95**, 010402 (2005).
 - [5] A. Smerzi, S. Fantoni, S. Giovanazzi, and S. R. Shenoy, *Phys. Rev. Lett.* **79**, 4950 (1997).
 - [6] Biao Wu and Qian Niu, *Phys. Rev. A* **61**, 023402 (2000).
 - [7] J. Liu, B. Wu, and Q. Niu, *Phys. Rev. Lett.* **90**, 170404 (2003).
 - [8] D. Witthaut, E. M. Graefe, and H. J. Korsch, *Phys. Rev. A* **73**, 063609 (2006).
 - [9] N. Moiseyev, L. D. Carr, B. A. Malomed, and Y. B. Band, *J. Phys. B* **37**, L193 (2004).
 - [10] P. Schlagheck and T. Paul, *Phys. Rev. A* **73**, 023619 (2006).
 - [11] D. Witthaut, S. Mossmann, and H. J. Korsch, *J. Phys. A* **38**, 1777 (2005).
 - [12] S. Wimberger, R. Mannella, O. Morsch, E. Arimondo, A. Kolovsky, and A. Buchleitner, *Phys. Rev. A* **72**, 063610 (2005).
 - [13] S. Wimberger, P. Schlagheck, and R. Mannella, *J. Phys. B* **39**, 729 (2006).
 - [14] F. Keck, H. J. Korsch, and S. Mossmann, *J. Phys. A* **36**, 2125 (2003).
 - [15] J. E. Avron, *Ann. Phys. (N.Y.)* **143**, 33 (1982).
 - [16] G. Nenciu, *Rev. Mod. Phys.* **63**, 91 (1991).
 - [17] M. V. Berry and M. Wilkinson, *Proc. R. Soc. London, Ser. A* **392**, 15 (1984).
 - [18] M. Holthaus, *J. Opt. B: Quantum Semiclassical Opt.* **2**, 589 (2000).
 - [19] M. Glück, A. R. Kolovsky, and H. J. Korsch, *J. Opt. B: Quantum Semiclassical Opt.* **2**, 694 (2000).
 - [20] E. M. Graefe and H. J. Korsch, *Czech. J. Phys.* **56**, 1007 (2006).
 - [21] J. Liu, D. Choi, B. Wu, and Q. Niu, *Phys. Rev. A* **66**, 023404 (2002).
 - [22] F. Bloch, *Z. Phys.* **52**, 555 (1928).
 - [23] J. Feldmann, K. Leo, J. Shah, D. A. B. Miller, J. E. Cunningham, T. Meier, G. von Plessen, A. Schulze, P. Thomas, and S. Schmitt-Rink, *Phys. Rev. B* **46**, 7252 (1992).
 - [24] K. Leo, *High-Field Transport in Semiconductor Superlattices* (Springer, Berlin, 2003).
 - [25] T. Pertsch, P. Dannberg, W. Elflein, A. Bräuer, and F. Lederer, *Phys. Rev. Lett.* **83**, 4752 (1999); J. A. Morales, E. Deumens, and Y. Öhrn, *J. Math. Phys.* **40**, 766 (1999); R. Sapienza, P. Costantino, D. Wiersma, M. Ghulinyan, C. J. Oton, and L. Pavesi, *Phys. Rev. Lett.* **91**, 263902 (2003); M. Ghulinyan, C. J. Oton, Z. Gaburro, L. Pavesi, C. Toninelli, and D. S. Wiersma, *ibid.* **94**, 127401 (2005); H. Trompeter, T. Pertsch, F. Lederer, D. Michaelis, U. Streppel, A. Brauer, and U. Peschel, *ibid.* **96**, 023901 (2006).
 - [26] M. Ben Dahan, E. Peik, J. Reichel, Y. Castin, and C. Salomon, *Phys. Rev. Lett.* **76**, 4508 (1996); S. R. Wilkinson, C. F. Bharucha, K. W. Madison, Q. Niu, and M. G. Raizen, *ibid.* **76**, 4512 (1996); E. Peik, M. Ben Dahan, I. Bouchoule, Y. Castin, and C. Salomon, *Phys. Rev. A* **55**, 2989 (1997).
 - [27] O. Morsch, J. H. Müller, M. Cristiani, D. Ciampini, and E. Arimondo, *Phys. Rev. Lett.* **87**, 140402 (2001); G. Roati, E. de Mirandes, F. Ferlaino, H. Ott, G. Modugno, and M. Inguscio, *ibid.* **92**, 230402 (2004).
 - [28] B. P. Anderson and M. A. Kasevich, *Science* **282**, 1686 (2000).

BOSE-EINSTEIN CONDENSATES IN ACCELERATED...

PHYSICAL REVIEW A **75**, 013617 (2007)

- (1998).
- [29] J. Zak, Phys. Rev. Lett. **20**, 1477 (1968); G. H. Wannier, Phys. Rev. **181**, 1364 (1969); J. Zak, *ibid.* **181**, 1366 (1969); J. E. Avron, J. Zak, A. Grossmann, and L. Gunther, J. Math. Phys. **18**, 918 (1977).
- [30] M. Glück, A. R. Kolovsky, and H. J. Korsch, J. Phys. A **32**, L49 (1999).
- [31] M. Glück, A. R. Kolovsky, and H. J. Korsch, Phys. Rep. **366**, 103 (2002).
- [32] B. M. Breid, D. Witthaut, and H. J. Korsch, New J. Phys. **8**, 110 (2006).
- [33] M. Weitz, G. Cennini, G. Ritt, and C. Geckeler, Phys. Rev. A **70**, 043414 (2004); G. Ritt, C. Geckeler, T. Salger, G. Cennini, and M. Weitz, e-print cond-mat/0512018.
- [34] S. Glutsch and F. Bechstedt, Phys. Rev. B **57**, 11887 (1998).
- [35] T. Paul, K. Richter, and P. Schlagheck, Phys. Rev. Lett. **94**, 020404 (2005); K. Rapedius, D. Witthaut, and H. J. Korsch, Phys. Rev. A **73**, 033608 (2006).
- [36] M. Glück, F. Keck, and H. J. Korsch, Phys. Rev. A **66**, 043418 (2002).
- [37] C. Sias, A. Zenesini, H. Lignier, S. Wimberger, D. Ciampini, O. Morsch, and E. Arimondo (unpublished).

P. SCHLAGHECK^{1,✉}
S. WIMBERGER²

Nonexponential decay of Bose–Einstein condensates: a numerical study based on the complex scaling method

¹ Institut für Theoretische Physik, Universität Regensburg, 93040 Regensburg, Germany

² Dipartimento di Fisica Enrico Fermi and CNR-INFM, Università degli Studi di Pisa, Largo Pontecorvo 3, 56127 Pisa, Italy

Received: 31 July 2006

Published online: 6 December 2006 • © Springer-Verlag 2006

ABSTRACT We study the decay dynamics of an interacting Bose–Einstein condensate in the presence of a metastable trapping potential from which the condensate can escape via tunneling through finite barriers. The time-dependent decay process is reproduced by means of the instantaneous decay rates of the condensate at a given population of the quasi-bound state, which are calculated with the method of complex scaling. Both for the case of a double-barrier potential as well as for the case of a tilted periodic potential, we find pronounced deviations from a monoexponential decay behavior, which would generally be expected in the absence of the atom–atom interaction.

PACS 03.75.Lm; 03.65.Xp; 03.75.Kk

1 Introduction

With the advent of optical lattices [1–3] and ‘atom chips’ [4, 5], it became possible to probe the transport properties of a Bose–Einstein condensate in the mesoscopic regime. The unprecedented degree of experimental control in these systems led to the observation of Bloch oscillations [6, 7], the guided and free propagation of condensates through waveguide structures [8, 9], the transport of condensates with ‘optical tweezers’ [10], as well as the realization of Josephson junctions [11] and matter-wave interferometry [12], to mention just a few examples. Those experiments typically involve rather small trapping potentials, with length scales that can be of the order of a few microns. In such geometries, decay mechanisms of the condensate become a relevant issue. On the one hand, the condensed state is, at finite atom densities, subject to depletion, which is caused by the interaction with the thermal cloud and by three-body collisions. On the other hand, the condensate can escape from the trapping potential by tunneling through its barriers if the chemical potential of the condensed atoms exceeds the background potential in the free space outside the trap. In that case, the self-consistent mean-

field state of the condensate is no longer bound, but rather corresponds to a metastable ‘resonance’ state, in a similar way as, for example, doubly excited electronic states in the helium atom [13].

From the theoretical point of view, various methods were used [14–19] to tackle the problem of how to treat ‘resonances’, i.e. stationary states that describe the escape of population from an open confinement potential, in the context of Bose–Einstein condensates. For linear systems, it is well known that this task is most conveniently accomplished by applying the method of ‘complex scaling’ (or ‘complex rotation’) [20–23]. This technique essentially amounts to the complex dilations $\mathbf{r} \mapsto \mathbf{r}e^{i\theta}$ and $-i\nabla \mapsto -i\nabla e^{-i\theta}$ of the position and momentum operators in the Hamiltonian that describes the quantum system under study. This transformation leads to a non-Hermitian Hamiltonian with a complex eigenvalue spectrum the continuous part of which is rotated to the lower half of the complex energy plane. Resonances, i.e. decaying states with eigenvalues corresponding to poles of the resolvent below the real energy axis, are thereby uncovered and can be calculated using standard diagonalization techniques for complex matrices. This approach is essentially exact, in the sense that no a priori approximations are introduced in the complex dilation procedure. Positions and widths of resonances can therefore be calculated with high precision by means of the complex scaling procedure [22, 23].

The generalization of this approach to Bose–Einstein condensates was recently accomplished in our previous studies [18, 19], where we applied the complex scaling transformation to the nonlinear Gross–Pitaevskii equation that describes the mean-field dynamics of the condensate. In contrast to an alternative approach proposed by Moiseyev and Cederbaum [17], we explicitly took into account the complex nature of the wavefunction of the resonance state, which leads to a considerable complication of the problem due to the resulting nonanalyticity of the interaction term in the Gross–Pitaevskii equation. We showed in [18] how this complication can be tackled and how quasi-bound resonance states of the condensate can be calculated by means of a real-time propagation approach based on the complex scaled Gross–Pitaevskii Hamiltonian.

✉ Fax: +49 941 943 4382,

E-mail: peter.schlagheck@physik.uni-regensburg.de

In this paper, we apply this method in order to calculate specific time-dependent decay processes of the condensate. Instead of a direct numerical integration of the time-dependent Gross–Pitaevskii equation (which is rather computationally intensive in CPU time for the evolution time scales under consideration), we compute, with complex scaling, the decay rates of the quasi-bound state of the condensate at various values for the effective interaction strength (which would be proportional to the number of atoms that are populating this quasi-bound state at a given instance of time). Then we integrate, on the basis of this information, a simple rate equation that directly describes the decay of the quasi-bound population. This approach is comparatively efficient, avoids the introduction of artificial complex potentials at the grid boundaries in order to absorb the outgoing population (see e.g. [14]), and provides physical insight that could be used to control the decay process in a similar way as for macroscopic tunneling of condensates in double-well potentials (e.g. [24, 25]).

The paper is organized as follows. In Sect. 2, we establish the general relation between resonance states of the stationary Gross–Pitaevskii equation and the actual time-dependent decay process of the condensate. We furthermore discuss how such resonance states can be calculated by the method of complex scaling, as was described in more detail in [18]. Section 3 contains the numerical results that we obtain for two paradigmatic examples of metastable confinement configurations: a harmonic trapping potential with Gaussian envelopes, and a tilted periodic lattice. We calculate the time-dependent decay of the condensate, which is, in both cases, characterized by a pronounced nonexponential nature.

2 The nonlinear complex scaling approach

We consider a Bose–Einstein condensate that is confined within a cylindrical matter-wave guide with transverse frequency ω_{\perp} and evolves in the presence of a longitudinal potential $V(x)$. In the ‘one-dimensional mean-field regime’ [26] (where the confinement is strong enough to inhibit transverse excitations within the waveguide, but not as strong as to enter the Tonks–Girardeau regime [27]), the dynamics of the condensate is described by the one-dimensional time-dependent Gross–Pitaevskii equation

$$i \frac{\partial}{\partial t} \psi(x, t) = \left(-\frac{1}{2} \frac{\partial^2}{\partial x^2} + V(x) + g_0 |\psi(x, t)|^2 \right) \psi(x, t), \quad (1)$$

where x denotes the coordinate along the waveguide. The longitudinal potential $V(x)$ is assumed to provide a local harmonic confinement with trapping frequency ω_{\parallel} , from which the condensate can escape via tunneling through finite barriers. Dimensionless variables, defined by setting $\hbar = m = \omega_{\parallel} = 1$, are used throughout this paper. This means that we express all length scales (including the coordinate x) in units of $a_{\parallel} = \sqrt{\hbar/(m\omega_{\parallel})}$, all energy scales in units of $\hbar\omega_{\parallel}$, and all time scales in units of ω_{\parallel}^{-1} . The effective one-dimensional interaction strength is, in these units, given by $g_0 = 2a_s\omega_{\perp}$, where a_s denotes the s -wave scattering length of the atoms [27].

For the description of our theoretical approach, we specifically focus in the following on the double-barrier potential

$$V(x) = \frac{1}{2} x^2 \exp(-\alpha x^2), \quad (2)$$

with $\alpha = 0.1$, which could be experimentally realized, e.g. with red- and blue-detuned laser beams that are tightly focused onto the waveguide. Obviously, $V(x)$ does not exhibit any bound state, and the eigenspectrum of the linear (noninteracting) Hamiltonian operator is fully continuous. There exist, however, quasi-bound states which are localized in the well around $x = 0$ and which give rise to resonances in the energy spectrum (corresponding to complex poles of the scattering matrix). In the case of noninteracting atoms ($g_0 = 0$), such resonance states are described by time-dependent wavefunctions of the form $\psi(x, t) = \psi(x) \exp(-iEt)$, where $\psi(x)$ satisfies the stationary Schrödinger equation for the complex eigenvalue $E = \mu - i\Gamma/2$ and exhibits outgoing (Siegert) boundary conditions [28] $\psi(x) \rightarrow \psi_0 \exp(ik|x|)$, with $\text{Re}(k) > 0$ for $x \rightarrow \pm\infty$. This latter property expresses the fact that the wavefunction of the decaying state is characterized by a finite current of atoms that propagate away from the well.

As a consequence, the atomic population inside the well decays exponentially according to $\propto \exp(-\Gamma t)$ if the system is initially prepared in the energetically lowest resonance state. It is quite obvious that this is no longer true in the nonlinear case of interacting atoms ($g_0 \neq 0$). There, the tunnel coupling through the barriers explicitly depends, via the nonlinear term in the Gross–Pitaevskii equation, on the local atomic density, which in turn induces a temporal variation of the decay rate Γ . We therefore naturally obtain, as was also pointed out in [29], a nonexponential decay of the atomic density, the reproduction of which is the central aim of this paper.

Despite this complication, a description of the decay process of the interacting condensate in terms of instantaneous quasi-bound states can nevertheless be justified if the rate Γ characterizing the temporal variation of the density inside the well is rather small compared to the chemical potential (which should generally be the case if the condensate escapes via tunneling through finite barriers). In such a quasi-stationary situation, we can employ an adiabatic ansatz where the condensate is assumed to remain always in the energetically lowest (and most stable) resonance state associated with a given instantaneous density $|\psi(x, t)|^2$. This resonance state is formally defined, together with its associated complex eigenvalue $E_g = \mu_g - i\Gamma_g/2$, by the self-consistent solution of the nonlinear stationary equation

$$H(\psi_g) \psi_g(x) = E_g \psi_g(x), \quad (3)$$

with

$$H(\psi) \equiv -\frac{1}{2} \frac{\partial^2}{\partial x^2} + V(x) + g |\psi(x)|^2. \quad (4)$$

$\psi_g(x)$ is normalized according to the condition

$$\mathcal{N}[\psi_g] \equiv \int_{-\infty}^{\infty} |\psi_g(x)|^2 w(x) dx = 1. \quad (5)$$

Here $w(x)$ represents a weight function that measures the population inside the well. For the double-barrier potential (2), a natural choice for this weight function would be $w(x) = \theta(a-x)\theta(x+a)$, where $a \equiv 1/\sqrt{\alpha}$ corresponds to the maximum of the potential and $\theta(x)$ denotes the Heaviside step function.

In addition, $\psi_g(x)$ should also satisfy outgoing boundary conditions, which would imply an asymptotic behavior of the form $\psi_g(x) \propto \exp[i \int^x k(x') dx']$ for large $x \rightarrow \infty$ (and a similar one for $x \rightarrow -\infty$), where the spatial dependence of the effective wavenumber $k(x)$ accounts for the smooth variation of the self-consistent potential in (4). It was pointed out in [18] that this condition can only be fulfilled in an approximate way up to a given maximum spatial distance x_c at which the interaction energy $g|\psi_g(x)|^2$ starts to exceed the chemical potential μ . For $x > x_c$, the self-consistent quasi-bound state would formally encounter a singularity, which reflects the fact that explicit time dependence is expected beyond that critical distance.

On the basis of these resonance states, we can now formulate the adiabatic ansatz for $\psi(x, t)$ as

$$\psi(x, t) = \sqrt{N_0} \psi_{g(t)}(x) \exp\left(-i \int_0^t E_{g(t')} dt'\right). \quad (6)$$

Here the effective time-dependent interaction strength is given by $g(t) \equiv g_0 N(t)$, where $N(t)$ denotes the time-dependent population inside the well, defined by

$$N(t) \equiv \int_{-\infty}^{\infty} |\psi(x, t)|^2 w(x) dx. \quad (7)$$

Using the normalization condition (5) of the resonance state and taking into account the fact that its eigenvalue $E_g = \mu_g - i\Gamma_g/2$ is complex, one can straightforwardly derive the implicit expression

$$N(t) = N_0 \exp\left(-\int_0^t \Gamma_{g(t')} dt'\right) \quad (8)$$

for the quasi-bound population of the condensate, which can also be formulated in terms of the ordinary differential equation

$$\frac{dN}{dt} = -\Gamma_{g(t)} N(t), \quad (9)$$

with the initial condition $N(0) = N_0$. The time-dependent decay process of the condensate can therefore be entirely reproduced with comparatively little numerical effort if the decay rates $\Gamma_{g(t)}$ of the instantaneous quasi-bound states $\psi_{g(t)}(x)$ are known.

As was described in detail in [18], the calculation of the decay rates can be achieved by the method of complex scaling. This technique essentially amounts to the application of the nonunitary mapping

$$\psi(x) \mapsto \psi^{(\theta)}(x) \equiv R_\theta \psi(x) = e^{i\theta/2} \psi(x e^{i\theta}) \quad (10)$$

to the wavefunction $\psi(x)$, which corresponds to the complex dilation $x \mapsto x e^{i\theta}$ of the position operator. Applying this transformation to the linear stationary Schrödinger equation $H_0 \psi = E \psi$ – with H_0 being defined through (4) via $H_0 \equiv H(\psi = 0)$ – yields the complex stationary equation

$$H_0^{(\theta)} \psi^{(\theta)}(x) = E \psi^{(\theta)}(x), \quad (11)$$

with the complex scaled Hamiltonian

$$H_0^{(\theta)} \equiv R_\theta H_0 R_\theta^{-1} = -\frac{1}{2} e^{-2i\theta} \frac{\partial^2}{\partial x^2} + V(x e^{i\theta}). \quad (12)$$

The spectral properties of this non-Hermitian Hamiltonian are widely discussed in the literature on complex scaling [20–23]: while bound states of the original Hamiltonian H_0 (which are absent in our particular case) remain bound after the complex dilation (as long as $|\theta| < \pi/4$), the continuum states are ‘rotated’ in the complex energy plane, in such a way that their eigenvalues are located along the axis $E = \epsilon e^{-2i\theta}$ with real positive ϵ . This rotation uncovers the spectral resonances of the system, which correspond to the poles of the analytical continuation of the Green function $G = (E - H_0 + i\delta)^{-1}$ to the lower half of the complex energy plane. Those resonances turn into discrete complex eigenvalues $E_n = \mu_n - i\Gamma_n/2$ under complex dilation, and are represented by normalizable eigenfunctions that can be straightforwardly calculated by diagonalizing $H_0^{(\theta)}$ in any numerical basis.

The generalization of this approach to the nonlinear case would be comparatively straightforward if the replacement $|\psi(x)|^2 \rightarrow [\psi(x)]^2$ in the nonlinear Gross–Pitaevskii Hamiltonian (4) could be justified. For this particular case, the implementation of the complex scaling technique was explained in detail in [17]. In reality, however, the wavefunction of the resonance state is intrinsically complex due to the outgoing boundary conditions (i.e. $\psi(x) \propto \exp(ik|x|)$ for $|x| \rightarrow \infty$), and the resulting nonanalyticity in the Hamiltonian (4) introduces a major complication of the problem. Formally, a second analytic wavefunction $\bar{\psi}$ needs to be introduced, which coincides with the complex conjugate of ψ on the real axis, i.e.

$$\bar{\psi}(x) \equiv \psi^*(x) \quad \text{for real } x, \quad (13)$$

and which is independently transformed under the nonunitary dilation operator R_θ , i.e.

$$\bar{\psi}(x) \mapsto \bar{\psi}^{(\theta)}(x) \equiv R_\theta \bar{\psi}(x) = e^{i\theta/2} \bar{\psi}(x e^{i\theta}). \quad (14)$$

The analytic continuation of the stationary Gross–Pitaevskii equation to the complex domain then yields

$$H^{(\theta)}(\psi) \psi^{(\theta)}(x) = E \psi^{(\theta)}(x), \quad (15)$$

where the complex scaled nonlinear Hamiltonian is given by

$$H^{(\theta)}(\psi) = H_0^{(\theta)} + g e^{-i\theta} \bar{\psi}^{(\theta)}(x) \psi^{(\theta)}(x). \quad (16)$$

The lowest resonance state of the condensate can be calculated by a real-time propagation approach [18], i.e. by numerically propagating $\psi^{(\theta)}$ under the time-dependent Gross–Pitaevskii equation

$$i \frac{\partial}{\partial \tau} \psi_\tau^{(\theta)}(x) = H^{(\theta)}(\psi_\tau) \psi_\tau^{(\theta)}(x), \quad (17)$$

in the complex scaled system, where τ represents a fictitious numerical ‘time’ parameter (which is unrelated to the physical time evolution in the actual decay process). In practice, $\psi_\tau^{(\theta)}(x)$ is expanded on a spatial grid, and an implicit finite-difference scheme is employed to carry out the mapping $\psi_\tau^{(\theta)} \mapsto \psi_{\tau+\delta\tau}^{(\theta)}$ for small time steps $\delta\tau$. If $\psi_\tau^{(\theta)}$ is renormalized after each propagation step in order to satisfy the condition (5), the integration of (17) necessarily converges to the most stable resonance state of the complex scaled Hamiltonian, which corresponds to the quasi-bound state with the smallest decay rate [30].

The major numerical difficulty in this approach lies in the evaluation of the nonlinear term in the complex scaled Hamiltonian (16). Indeed, $\overline{\psi}^{(\theta)}(x)$ is not identical to $[\psi^{(\theta)}(x)]^*$, the complex conjugate of $\psi^{(\theta)}(x)$, and needs to be evaluated according to the relation

$$\overline{\psi}^{(\theta)}(x) = R_\theta \left(\overline{R_{-\theta} \psi^{(\theta)}} \right) (x), \quad (18)$$

which requires explicit backward and forward rotations of the complex scaled condensate wavefunction. In practice, these rotations (which are also used to evaluate the normalization condition (5)) are numerically performed by mapping the grid representation of the wavefunction into a nonorthogonal set of analytic Gaussian orbitals $\phi_\nu(x)$ that are centered around different positions along the grid, and by using a transformation matrix that contains the overlap integrals $\int \phi_\nu(x) e^{i\theta} \phi_{\nu'}(x) dx$ as elements (see [18] for more details). Such an operation, however, is known to be potentially unstable [31] and requires great care in the numerical implementation. It is therefore not obvious to which extent unlimited precision in the decay rates of the quasi-bound states can be achieved within this nonlinear complex scaling approach.

3 Calculation of time-dependent decay processes

3.1 Double-barrier potential

Despite this latter complication, we find that the chemical potentials and decay rates of the self-consistent quasi-bound states of the double-barrier potential (2) can be calculated in this way with rather good accuracy, even in the case of very strong nonlinearities where the resonance level lies close the barrier height of $V(x)$. This was explicitly verified in [18] by comparing the resulting values for μ_g and Γ_g with the ones that are obtained from an alternative approach, which was based on the real-time propagation of the original (i.e. unscaled) Gross–Pitaevskii equation in the presence of absorbing boundaries. Good agreement was generally found between the two approaches [18].

The chemical potentials and decay rates of the lowest resonance state are plotted in Fig. 1 as a function of the effective interaction strength g . Quite intuitively μ_g increases with increasing g due to the presence of the mean-field interaction energy in the nonlinear Gross–Pitaevskii Hamiltonian. This increase of the chemical potential results in a dramatic enhancement of the decay rate Γ_g , which can be explained by the fact that the effective imaginary action integral that semiclassically determines the tunneling rate through the barriers is appreciably reduced with increasing energy. It was pointed out

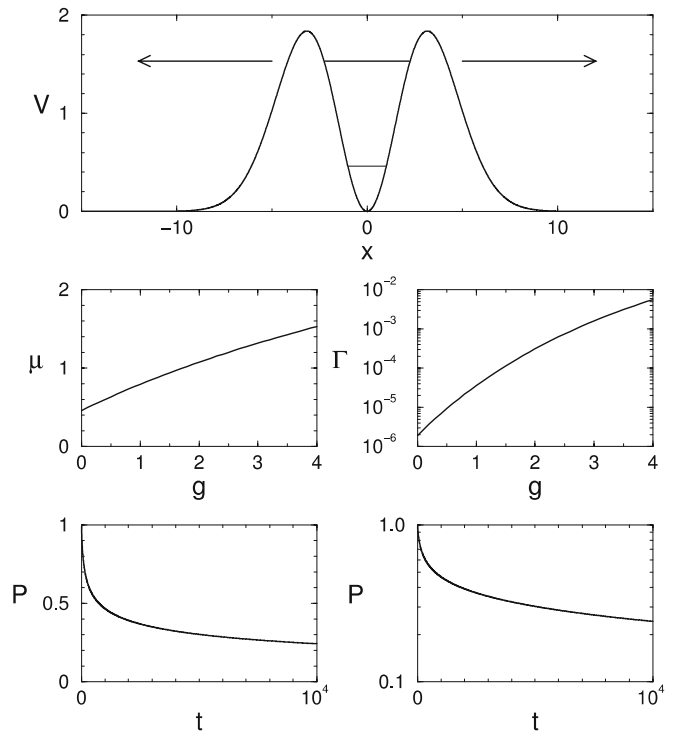


FIGURE 1 Decay of a Bose–Einstein condensate in the double-barrier potential. The *upper panel* shows the potential (2) together with the chemical potential of the initial quasi-bound state of the condensate (*thick horizontal line*), which corresponds to the initial value $g(t=0) \equiv g_0 N(t=0) = 4$ of the effective interaction strength. During the decay process, the chemical potential decreases with time, due to the reduced interaction energy, and approaches the level of the noninteracting quasi-bound state (*thin horizontal line in the upper panel*). This decrease of μ is accompanied by a strong reduction of the decay rate Γ , which can be seen in the *two middle panels* where μ and Γ are plotted as a function of g . As a consequence, a pronouncedly nonexponential decay of the quasi-bound population $P(t) \equiv N(t)/N(t=0)$ is obtained from integrating the equation $dN/dt = -\Gamma(N)N$, which is displayed in the *two lower panels* (where P is plotted vs. t on a linear and a logarithmic scale, respectively)

in [14, 16, 18] that an attractive interaction between the atoms leads to a stabilization of the resonance state, i.e. to a reduction of the chemical potential to values below $\mu = 0$, where the associated decay rate would vanish. For the double-barrier potential under consideration, this stabilization process would occur at $g \simeq -1.1$.

With this information, we can now quantitatively reproduce the time-dependent decay process of the condensate by means of the integration of the rate equation (9). For this purpose, we use the values of the decay rates that are calculated with the complex scaling method at the equidistant interaction strengths $g = 0, 0.1, 0.2, \dots$, and employ a cubic interpolation to obtain intermediate values of Γ . As initial value of the effective interaction strength, we consider $g(t=0) = 4$, where the chemical potential of the quasi-bound state lies already rather close to the barrier height of the potential. In the specific case of a condensate of ^{87}Rb atoms that encounters the longitudinal and transverse confinement frequencies $\omega_{\parallel} = \omega_{\perp} = 2\pi \times 10^3$ Hz, this would imply that about $N(0) = 4/g_0 \simeq 100$ atoms are initially localized in the single well [32].

The result of the integration is displayed in the two lower panels of Fig. 1. We see a clearly nonexponential decay of the bound population, which reflects the fact that the decay rate

decreases with decreasing interaction strength g . As a consequence, a rather large number of atoms leave the trap during the first 1000 units of the evolution time, while the remaining part of the condensate becomes stabilized and decays, for asymptotically large times, with the rate $\Gamma_0 \simeq 2 \times 10^{-6}$ of the noninteracting quasi-bound state. In the example of a ^{87}Rb condensate in a confinement with trapping frequency $\omega_{\parallel} = 2\pi \times 10^3$ Hz, the above characteristic time scale of the nonexponential behavior would correspond to $t \sim 100$ ms, which is of experimental relevance.

3.2 Tilted periodic potential

Nonexponential features can also be observed in the presence of relatively small interaction strengths, namely if the confinement potential permits the possibility of resonant tunneling. This is, for instance, the case for the tilted periodic potential

$$V(x) = \sin^2(x/2) + Fx \quad (19)$$

that is experimentally realized with optical lattices [1–3] or, within the atom chip context, by means of periodic sequences of microfabricated wires [33]. In this nonlinear Wannier–Stark system, the possibility of resonant tunneling arises if the local ground state of one of the wells is nearly degenerate with the first excited state of the adjacent well. As was pointed out in [29], this near-degeneracy would give rise to a significant enhancement of the condensate’s decay rate.

As in our previous study [19], we assume that the condensate is initially confined within a single well of the lattice. The method of complex scaling can again be used to calculate the chemical potential and decay rate of the self-consistent quasi-bound state in the presence of the interaction, even though the tilted potential (19) leads to an asymptotic spatial behavior of the continuum states that is substantially different from the previous double-barrier problem. As was described in detail in [19], additional complications arise in this potential (such as the existence of many different self-consistent resonance states with identical decay rates) and technical modifications need to be implemented in order to achieve good convergence of the real-time propagation method. In analogy with the double-barrier potential, the weight function that characterizes the bound population inside the well according to (5) is given by $w(x) = \theta(\pi - x)\theta(x + \pi)$.

The resonance-enhanced decay process of the condensate in this tilted lattice is displayed in Fig. 2, for the tilt strength $F = 0.1412$ at which the level of the noninteracting local ground state in each well lies slightly above the level of the first excited state in the adjacent well on the left-hand side. As initial value for the nonlinearity, we consider $g(t = 0) = -0.25$, which would correspond to an attractive interaction between the atoms (which could be realized, for example, by using condensates with ^7Li atoms or by applying Feshbach tuning techniques [34]). This attractive nonlinearity lowers the chemical potential of the self-consistent quasi-bound state in such a way that it becomes shifted below the level of the first excited (noninteracting) state in the adjacent well. During the time evolution, the loss of population leads to an increase of the chemical potential, which, at about $t \simeq 2500$ time units, approaches the resonance. At

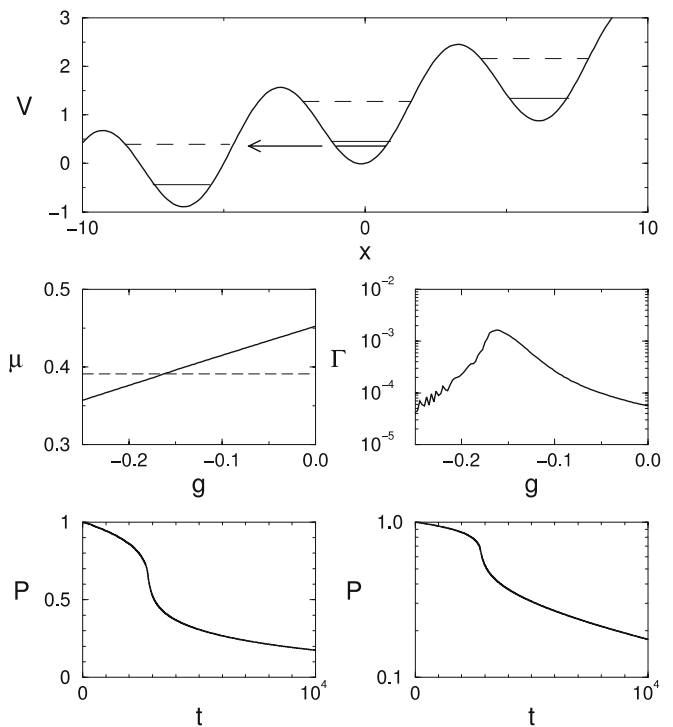


FIGURE 2 Decay of a Bose–Einstein condensate in the tilted periodic potential (19) with $F = 0.1412$. The atomic cloud is assumed to be entirely localized within a single well of the lattice, and decays via tunneling through the barrier on the left-hand side of the well. This decay process can be substantially accelerated in the case of resonant tunneling, i.e. if the chemical potential of the condensate matches the energy of the first excited (noninteracting) state of the adjacent well (*dashed horizontal lines*; the *thin solid lines* mark the noninteracting ground levels of the wells). In contrast to the case of the double-barrier potential, we consider here a relatively weak and attractive initial interaction strength, $g(0) = -0.25$, which leads to an initial chemical potential that lies slightly below the level of this excited state (*thick horizontal line in the upper panel*). The time evolution of the quasi-bound population $P(t) = N(t)/N(0)$, shown in the *two lower panels*, clearly displays the characteristic signature of an intermediate resonant tunneling process. Note that the wiggles in the decay rates at large $|g|$ (*middle right panel*), which arise from numerical inaccuracies, do not leave significant traces in the time evolution of $P(t)$

that point, the decay rate becomes drastically increased resulting in a significant escape of atoms from the well. As a consequence, the chemical potential of the quasi-bound state quickly moves out of resonance, and the decay rate again becomes reduced.

The time evolution of the condensate was again calculated by integrating the rate equation (9), using decay rates that were calculated with the complex scaling method at the equidistant values $g = 0, -0.0025, -0.005, \dots$ of the interaction strength. The accuracy with which these decay rates could be calculated was not as good as in the case of the double-barrier potential [18], which is clearly reflected by the appearance of wiggles on the left-hand side in the middle right panel of Fig. 2. These artificial fluctuations of Γ , however, leave no significant traces in the actual time-dependent decay process, as is clearly seen in the lower two panels of Fig. 2.

This intermediate ‘burst’ of atoms should be readily observable within existing experimental setups based on optical lattices or atom chips. By imposing a rather weak transverse confinement, the one-dimensional interaction strength (given by $g_0 = 2a_s \hbar \omega_{\perp}$ [27]) can be appreciably reduced, which

should allow one to suppress effects beyond the mean-field description of the condensate, and additional longitudinal potentials can, as in the experiment on tunneling in a double well potential [35], be employed to prepare the condensate in a single well of the lattice. Obviously, the attractive interaction between the atoms is not a necessary condition for this nonexponential decay phenomenon: indeed, the same effect could be induced with a repulsively interacting species at slightly weaker tilt strengths F , where the noninteracting ground state of the well lies slightly below the first excited level of the adjacent well. In both cases of attractive and repulsive interaction, the intermediate enhancement of the decay rate should clearly manifest in the time-of-flight image of the condensate after the decay process, which would display a pronounced peak due to the effect of resonant tunneling.

4 Conclusion

In summary, we studied the time-dependent decay of Bose–Einstein condensates in mesoscopic trapping potentials that permit escape by tunneling through finite barriers. The decay process of the condensate was reproduced by integrating a simple rate equation for the quasi-bound population, using instantaneous decay rates that were computed by means of the method of complex scaling. This approach is rather efficient as compared to a direct numerical integration of the time-dependent Gross–Pitaevskii equation, and provides additional insight into the mechanisms that underly the decay of the condensate. Though only applied to one-dimensional configurations, the complex scaling approach can be straightforwardly generalized to three-dimensional decay problems, and might furthermore represent a convenient conceptual framework for treating resonances of the nonlinear Gross–Pitaevskii equation from the mathematical point of view.

With this approach, we calculated the decay of a Bose–Einstein condensate in a double-barrier potential [14, 16, 18] as well as in a tilted periodic potential [19, 29]. For this latter case, we found a strong intermediate enhancement of the tunneling rate, which arises due to a near-degeneracy with a quasi-bound state in another well of the periodic potential. This enhancement leads to a pronounced deviation from an exponential behavior of the condensate’s escape dynamics, which could be controlled by suitable time-dependent variations of the tilt field, in a similar way as for macroscopic tunneling in double-well potentials [24, 25] and for nonlinear resonant transport through atomic quantum dots [36]. Such non-exponential effects should be readily observable in present-day state-of-the-art experiments on interacting matter waves in mesoscopic trapping potentials [3, 11, 12, 33, 35, 37].

ACKNOWLEDGEMENTS SW acknowledges support from the Alexander von Humboldt Foundation (Feodor-Lynen Program).

REFERENCES

- J. Hecker Denschlag, J.E. Simsarian, H. Häffner, C. McKenzie, A. Browaeys, D. Cho, K. Helmerson, S.L. Rolston, W.D. Phillips, *J. Phys. B* **35**, 3095 (2002)
- I. Bloch, *J. Phys. B* **38**, S629 (2005)
- O. Morsch, M. Oberthaler, *Rev. Mod. Phys.* **78**, 179 (2006)
- R. Folman, P. Krüger, D. Cassettari, B. Hessmo, T. Maier, J. Schmiedmayer, *Phys. Rev. Lett.* **84**, 4749 (2000)
- R. Folman, P. Krüger, J. Denschlag, C. Henkel, J. Schmiedmayer, *Adv. At. Mol. Opt. Phys.* **48**, 263 (2003)
- B.P. Anderson, M.A. Kasevich, *Science* **282**, 1686 (1998)
- O. Morsch, J.H. Müller, M. Cristiani, D. Ciampini, E. Arimondo, *Phys. Rev. Lett.* **87**, 140402 (2001)
- H. Ott, J. Fortagh, G. Schlotterbeck, A. Grossmann, C. Zimmermann, *Phys. Rev. Lett.* **87**, 230401 (2001)
- W. Hänsel, J. Reichel, P. Hommelhoff, T.W. Hänsch, *Phys. Rev. Lett.* **86**, 608 (2001)
- T.L. Gustavson, A.P. Chikkatur, A.E. Leanhardt, A. Görlitz, S. Gupta, D.E. Pritchard, W. Ketterle, *Phys. Rev. Lett.* **88**, 020401 (2002)
- M. Albiez, R. Gati, J. Fölling, S. Hunsmann, M. Cristiani, M.K. Oberthaler, *Phys. Rev. Lett.* **95**, 010402 (2005)
- T. Schumm, S. Hofferberth, L.M. Andersson, S. Wildermuth, S. Groth, I. Bar-Joseph, J. Schmiedmayer, P. Krüger, *Nature Phys.* **1**, 57 (2005)
- H. Friedrich, *Theoretical Atomic Physics*, 2nd edn. (Springer, Berlin, 1994)
- N. Moiseyev, L.D. Carr, B.A. Malomed, Y.B. Band, *J. Phys. B* **37**, L193 (2004)
- D. Witthaut, S. Mossmann, H.J. Korsch, *J. Phys. A* **38**, 1777 (2005)
- L.D. Carr, M.J. Holland, B.A. Malomed, *J. Phys. B* **38**, 3217 (2005)
- N. Moiseyev, L.S. Cederbaum, *Phys. Rev. A* **72**, 033605 (2005)
- P. Schlagheck, T. Paul, *Phys. Rev. A* **73**, 023619 (2006)
- S. Wimberger, P. Schlagheck, R. Mannella, *J. Phys. B* **39**, 729 (2006)
- E. Balslev, J.M. Combes, *Commun. Math. Phys.* **22**, 280 (1971)
- B. Simon, *Ann. Math.* **97**, 247 (1973)
- W.P. Reinhardt, *Ann. Rev. Phys. Chem.* **33**, 223 (1982)
- N. Moiseyev, *Phys. Rep.* **302**, 212 (1998)
- A. Smerzi, S. Fantoni, S. Giovanazzi, S.R. Shenoy, *Phys. Rev. Lett.* **79**, 4950 (1997)
- C. Weiss, T. Jinasundera, *Phys. Rev. A* **72**, 053626 (2005)
- C. Menotti, S. Stringari, *Phys. Rev. A* **66**, 043610 (2002)
- M. Olshanii, *Phys. Rev. Lett.* **81**, 938 (1998)
- A.J.F. Siegert, *Phys. Rev.* **56**, 750 (1939)
- S. Wimberger, R. Mannella, O. Morsch, E. Arimondo, A. Kolovsky, A. Buchleitner, *Phys. Rev. A* **72**, 063610 (2005)
- We neglect here the fact that there also exist ‘long-lived’ *continuum states* in the open system under consideration, the decay rates of which can be comparable to or smaller than that of the energetically lowest quasi-bound state. In practice, the unwanted convergence into such continuum states can be avoided by starting with an initial wavefunction that is rather close to the quasi-bound state to be calculated
- A. Buchleitner, B. Grémaud, D. Delande, *J. Phys. B* **27**, 2663 (1994)
- The number of atoms in the well can be enhanced by choosing a weaker transverse confinement, e.g. $\omega_{\perp} = 10^2$ Hz, for which one would obtain $N(0) \simeq 1000$ atoms. In that case, however, three-dimensional calculations ought to be performed in order to make reliable quantitative predictions for the decay process
- A. Günther, S. Kraft, M. Kemmler, D. Koelle, R. Kleiner, C. Zimmermann, J. Fortágh, *Phys. Rev. Lett.* **95**, 170405 (2005)
- C.J. Pethick, H. Smith, *Bose–Einstein Condensation in Dilute Gases* (University Press, Cambridge, 2002)
- T. Anker, M. Albiez, R. Gati, S. Hunsmann, B. Eiermann, A. Trombettoni, M.K. Oberthaler, *Phys. Rev. Lett.* **94**, 020403 (2005)
- T. Paul, K. Richter, P. Schlagheck, *Phys. Rev. Lett.* **94**, 020404 (2005)
- R. Gati, B. Hemmerling, J. Fölling, M. Albiez, M.K. Oberthaler, *Phys. Rev. Lett.* **96**, 130404 (2006)

Available online at www.sciencedirect.com

Physica A 376 (2007) 266–274

PHYSICA Awww.elsevier.com/locate/physa

Multifractal fluctuations in the survival probability of an open quantum system

Angelo Facchini^{a,*}, Sandro Wimberger^b, Andrea Tomadin^{b,c}^aCenter for the Study of Complex Systems, University of Siena, Via Tommaso Pendola 37, I-53100 Siena, Italy^bCNR-INFN and Dipartimento di Fisica “Enrico Fermi”, Università degli Studi di Pisa, Largo Pontecorvo 3, I-56127 Pisa, Italy^cScuola Normale Superiore, Piazza dei Cavalieri 7, I-56126 Pisa, Italy

Received 31 May 2006; received in revised form 24 September 2006

Available online 27 October 2006

Abstract

We predict a multifractal behavior of transport in the deep quantum regime for the opened δ -kicked rotor model. Our analysis focuses on intermediate and large scale correlations in the transport signal and generalizes previously found parametric *mono*-fractal fluctuations in the quantum survival probability on small scales.

© 2006 Elsevier B.V. All rights reserved.

Keywords: Quantum transport; Fractals; Time series analysis; Multifractals

1. Introduction

Multifractal analysis of fluctuating signals is a widely applied method to characterize complexity on many scales in classical dynamics [1], or in the analysis of a given time series (without any a priori knowledge on the underlying dynamical system which generated the series) [2].

On the quantum level, multifractal behavior was found in the scaling of eigenfunctions in solid-state transport problems [3]. As far as we know, there have been, however, very few attempts to use the method of multifractal analysis to directly characterize transport properties such as conductance (across a solid state sample) or the survival probability (in open, decaying systems). Often it is indirectly argued that the multifractal structure of the wave functions at critical points (at the crossover between the localized and the extended regime) imprints itself on the scaling of transport coefficients [4]. Other works found a fractal scaling of *local* transport quantities, such as hopping amplitudes [5] or two-point correlations [6]. At criticality [6] predicts, e.g., a multifractal scaling of the two-point conductance between two small interior probes within the transporting sample.

In this paper, we directly study the fluctuations properties of a *global* conductance like quantity in a regime of *strong localization* (Anderson or dynamical localization in our context of quantum dynamical systems). The studied quantity is the survival probability of an open, classically chaotic system, which in the deep quantum

*Corresponding author.

E-mail address: a.facchini@unisi.it (A. Facchini).

realm was found to obey a monofractal scaling if certain conditions on the quantum eigenvalue spectrum are fulfilled [7,8]. In particular, the distribution of decay rates of the weakly opened system needs to obey a power-law with an exponent $\gamma \sim -1$, which translates into an analytic prediction for the corresponding box counting dimension (of the survival probability as a function of a proper scan parameter): $D_{BC} \simeq 2 - |\gamma|/2$.

A more detailed, yet preliminary numerical analysis of the decay rate distribution for our model system (to be introduced below) has found that two scaling regions can be identified [9]. While for small rates the probability density function $\rho(\Gamma)$ scales as Γ^{-1} , at larger scales it turns to $\Gamma^{-3/2}$ —which is expected for strongly transmitting channels from various models for transport through disordered systems [10]. Here, we ask ourselves whether this prediction of a smooth variation in the scaling of the monofractal behavior (induced by the smoothly changing exponent γ) can be generalized to characterize the fluctuations on many scales using from the very beginning the technique of multifractal analysis. Before we present our findings on the multifractal scaling of the parametric fluctuations of the survival probability, we introduce the kicked rotor system and our numerical algorithm for the multifractal analysis in the subsequent two sections.

2. Our transport model and the central observable

The δ -kicked rotor is a widely studied, paradigmatic toy model of classical and quantum dynamical theory [12,13]. Using either cold or ultracold atomic gases, the kicked rotor is realised experimentally by preparing a cloud of atoms with a small spread of initial momenta, which is then subjected to a one-dimensional optical lattice potential, flashed periodically in time [14]. In good approximation, the Hamiltonian for the experimental realization of the rotor on the line (in one spatial dimension) reads in dimensionless units [14]

$$\hat{H}(t) = \frac{p^2}{2} + k \cos x \sum_{t=1}^{\infty} \delta(t' - t\tau). \quad (1)$$

The derivation of the one-period quantum evolution operator exploits the spatial periodicity of the potential by Bloch's theorem [15]. This defines quasimomentum β as a constant of the motion, the value of which is the fractional part of the physical momentum p in dimensionless units $p = n + \beta$ ($n \in \mathbb{N}$). Since β is a conserved quantum number, p can be labelled using its integer part n only. The spatial coordinate is then substituted by $\theta = x \bmod (2\pi)$ and the quantum momentum operator by $\hat{\mathcal{N}} = -i\partial/\partial\theta$ with periodic boundary conditions. The one-kick quantum propagation operator for a fixed β is thus given by [15]

$$\hat{\mathcal{U}}_{\beta} = e^{-ik \cos(\hat{\theta})} e^{-i\tau(\hat{\mathcal{N}} + \beta)^2/2}. \quad (2)$$

In close analogy to the transport problem across a solid-state sample, we follow [8,11] to define the quantum survival probability as the fraction of the atomic ensemble which stays within a specified region of momenta while applying absorbing boundary conditions at the “sample” edges. If we call $\psi(n)$ the wave function in momentum space and $n_1 < n_2$ the edges of the system, absorbing boundary conditions are implemented by setting $\psi(n) \equiv 0$ if $n \leq n_1 \equiv -1$ or $n \geq n_2 \equiv 251$. This truncation is carried out after each kick, and it mimics the escape of atoms out of the spatial region where the dynamics induced by the Hamiltonian (1) takes place. If we denote by \hat{P} the projection operator on the interval $]n_1, n_2[$ the survival probability after t kicks is

$$P_{\text{sur}}(t) = \|(\hat{P}\hat{\mathcal{U}}_{\beta})^t \psi(n, 0)\|^2. \quad (3)$$

The early studies of the fluctuation properties of P_{sur} focused on its parametric dependence on the quasimomentum β [9,11]. While β is hard to control experimentally on a range of many scales (with a typical uncertainty of 0.1 in experiments with an initial ensemble of *ultra*-cold atoms [16]), some of us recently proposed to investigate the parametric fluctuations as a function of the kicking period τ (see Eq. (1)), which can be easily controlled on many scales in the experimental realization of the model even with laser-cooled (just “cold”) atoms [8].

In Fig. 1 we present the survival probability P_{sur} of the opened kicked rotor in the deep quantum regime (i.e., at kicking periods $\tau \equiv \hbar_{\text{eff}} > 1$ [13]) as a function of the two different scan parameters β and τ . The global oscillation with a period of the order 1 in Fig. 1(a) originates from the β -dependent phase term $\mathcal{N}\beta$ in the evolution operator (2), and can be understood qualitatively by remembering the Bloch band structure of the

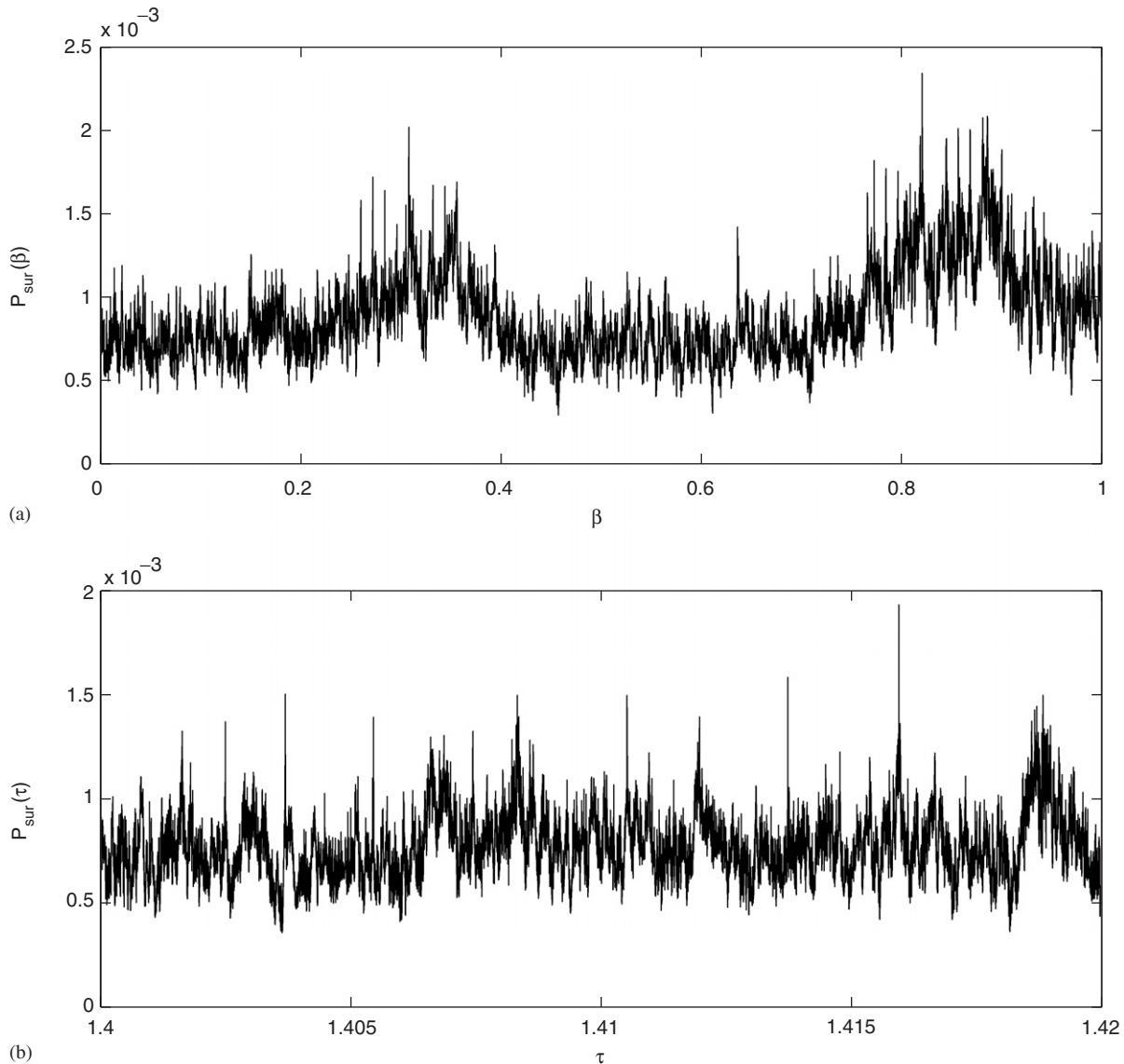


Fig. 1. The series $P_{\text{sur}}(\beta)$ (a) and $P_{\text{sur}}(\tau)$ (b) after an interaction time of $t = 6000$ kicks. Other parameters are $k = 5$, and $\tau = 1.4$ in (a) and $\beta = 0$ in (b), respectively. Both sequences extend over 10^5 sampling points along the shown intervals.

corresponding quasienergy spectrum as a function of β [13]. No such oscillating trend is found for the graph as a function of the kicking period. Nonetheless, in the following, we use a well developed variation of the standard multifractal algorithm, which intrinsically takes account of such global, yet irrelevant trends in the signal function P_{sur} . The basic features of the *MultiFractal Detrended Fluctuation Analysis* (MF-DFA) [18] are now explained before we present our central results which indicate the multifractal scaling of data sets as the ones shown in Fig. 1.

3. Multifractal detrended fluctuation analysis

The MF-DFA is a generalization of the DFA method originally proposed by Ref. [17], and it is extensively described in Ref. [18]. In the recent years it was used, for instance, to investigate the nonlinear properties of nonstationary series of wind speed records [19], electro-cardiograms [20], and financial time series [21].

The method consists of five steps. First the series $\{x_i\}_{i=1}^N$ is integrated to give the profile function

$$y(k) = \sum_{i=1}^k (x_i - \bar{x}), \quad (4)$$

where \bar{x} is the average value of x_i . The profile can be considered as a random walk, which makes a jump to the right if $x_i - \bar{x}$ is positive or to the left side if $x_i - \bar{x}$ is negative. In order to analyze the fluctuations, the profile is divided into $N_s = \text{int}(N/s)$ nonoverlapping segments of length s , and, since usually N is not an integer multiple of s , to avoid the cutting of the last part of the series, the procedure is repeated backwards starting from the end to the beginning of the data set. In each segment v we subtract the local polynomial trend of order k and we compute the variance

$$F^2(v, s) = \frac{1}{s} \sum_{i=1}^s \{y[(v-1)s + i] - y_v^k(i)\}^2 \quad (5)$$

for $v = 1, \dots, N_s$, and

$$F^2(v, s) = \frac{1}{s} \sum_{i=1}^s \{y[N - (v - N_s)s + i] - y_v^k(i)\}^2, \quad (6)$$

with $v = N_s + 1, \dots, 2N_s$ for the backward direction. The order of the polynomial defines the order of the MF-DFA too, therefore we may speak about MF-DFA(1), MF-DFA(2), \dots , MF-DFA(k).

The fourth step consists on the averaging of all segments to obtain the q th order fluctuation function for segments of size s

$$F_q(s) = \left\{ \frac{1}{2N_s} \sum_{v=1}^{2N_s} [F^2(v, s)]^{q/2} \right\}^{1/q}. \quad (7)$$

In the last step we determine the scaling behavior of the fluctuation function by analyzing the log–log plots of $F_q(s)$ versus s for each value of q . If the series is long-range correlated $F_q(s)$ increases for large s as a power law

$$F_q(s) \sim s^{h(q)}. \quad (8)$$

Since the number of segments becomes too small for very large scales ($s > N_s/4$), we usually exclude these scales for the fitting procedure to determine $h(q)$. The MF-DFA reduces to the standard DFA for $q = 2$, while the scaling exponent $h(q)$ can be related to the standard multifractal analysis considering stationary time series, in which $h(2)$ is identical to the Hurst exponent H , therefore, $h(q)$ can be considered a generalized Hurst exponent. Monofractal series indeed show a very weak or no dependence of $h(q)$ on q . By example, for monofractal series as white noise, the generalized Hurst exponent is $H = \frac{1}{2}$ for all q . On the contrary, for multifractal time series, $h(q)$ is a function of q and this dependence influences the multifractality of the process. Referring to the formalism of the partition function

$$Z_q(s) = \sum_{v=1}^{N_s} |y_{vs} - y_{(v-1)s}|^q \sim s^{\tau(q)} \quad (9)$$

where $\tau(q)$ is the Renyi exponent, to which the $h(q)$ is related by

$$\tau(q) = 1 - qh(q). \quad (10)$$

Now we are able to use the formalism of the multifractal spectrum [22] $f(\alpha)$ to characterize the data set

$$\begin{aligned} \alpha &= \frac{d\tau(q)}{dq} = h(q) + q \frac{dh(q)}{dq}, \\ f(\alpha) &= q\alpha - \tau(q) = q[\alpha - h(q)] + 1. \end{aligned} \quad (11)$$

The generalized dimensions are expressed as a function of $\tau(q)$ or $h(q)$ [23]

$$D_q = \frac{\tau(q)}{q-1} = \frac{qh(q) - 1}{q-1}, \quad (12)$$

which cannot be straightforwardly defined for $q = 0$ and $q = 1$.

If the signal is multifractal, the spectrum $f(\alpha)$ has approximately the form of an inverted parabola. As significant parameters for its characterization we considered the point α_M corresponding to the maximum of $f(\alpha)$, and its width W_α considered for a fixed q interval. In other words, α_M represents the α value at which is situated the “statistically most significant part” of the time series (i.e, the subsets with maximum fractal dimension among all subsets of the series). The width W_α is related to the dependence on $h(q)$ from q . The stronger this dependence, the wider is the fractal spectrum (cf., Eq. (11)).

4. Results

We performed a MF-DFA of order $k = 1$ on data sets produced by scanning the β or τ parameter, respectively, over 10^5 data points, and considering different interaction times from $t = 250$ to $t = 10\,000$ kicks. The analysis performed with higher order ($k = 2$ and 3) polynomial detrending for some of the series produced basically the same results. Furthermore, we tested our numerical algorithm on a monofractal time series (white noise) and a well known multifractal process (binomial multifractal model [24]). For these two test series we reproduce the known analytical results, with a precision better than 1%.

A full analysis for $t = 6000$ (see Fig. 1) is shown in Figs. 2 and 3 for the β and τ scanned series, respectively. Tables 1 and 2 collect the multifractal parameters α_M and W_α , which were computed for $t = 250 \dots 10\,000$. Analogously to Ref. [25], we defined W_α as the width of the parabolic form of $f(\alpha)$ between the points corresponding to $q = -3$ and $q = 3$.

Fig. 2(a) shows the scaling behavior of the fluctuation function $F_q(s)$, with $q \in [-5, 5]$. Here, s represents the index of the scanning parameter β , while the fit was performed in the zone $\log(s) \in [1.6, 2.7]$ (corresponding to $s \in [40, 500]$). In Fig. 2(b) we report the dependence of $h(q)$ on q , revealing the multifractal nature of the data set. In order to better characterize the multifractality and to highlight how it changes among the different analyzed series, we have computed the MF spectrum $f(\alpha)$ (cf. Fig. 2(c)). Fig. 2(d) shows the variation of the multifractal parameters for the different interaction times considered. After a fast decrease, both the parameters tend to converge around the values $\alpha_M = 1.29$ and $W_\alpha = 0.2$ (see also Table 1). Very similar results were obtained for the τ scanned series (cf., Fig. 3 and Table 2). Comparing the values of Tables 1 and 2 we can say that both the τ and the β scanned series have essentially the same multifractality.

Even if we cannot a priori predict the asymptotic similarity between the two series of τ and β , we can a posteriori interpret this result: both parameters enter not equally yet similarly in the *phase* of the second factor on the right of Eq. (2). As a consequence, the restriction of β to the unit interval does make no difference to the, in principle, unboundedness of τ (in fact, to avoid different dynamical properties of the system, τ was chosen in a restricted window too, cf. Ref. [8]).

In general, two types of multifractality can be distinguished, and both of them require different scaling exponents for small and large fluctuations. (I) The multifractality can be due to the broad probability density function for the values, and (II) it can also be due to different long-range correlations for small and large fluctuations. The simplest way to distinguish between the mentioned two cases is to perform the analysis on a randomly reshuffled series. The shuffling destroys all the correlations, and the series with multifractals of type (II) will exhibit a monofractal behavior with $h_{\text{shuf}}(q) = 0.5$ and $W_\alpha = 0$. On the contrary, multifractality of type (I) is not affected by the shuffling procedure. If both (I) and (II) are present the series will show a weaker multifractality than the original one.

We applied the shuffling procedure to the series showed in Fig. 1. The procedure destroyed the multifractality of both series since for both the sequences we obtained $h(q) = 0.51 \pm 0.01$ for $q \in [-5, 5]$. The dependence on q was so weak that we were not able to compute any reliable $f(\alpha)$ spectrum, which, in this case, can be considered singular, i.e., with $W_\alpha \approx 0$.

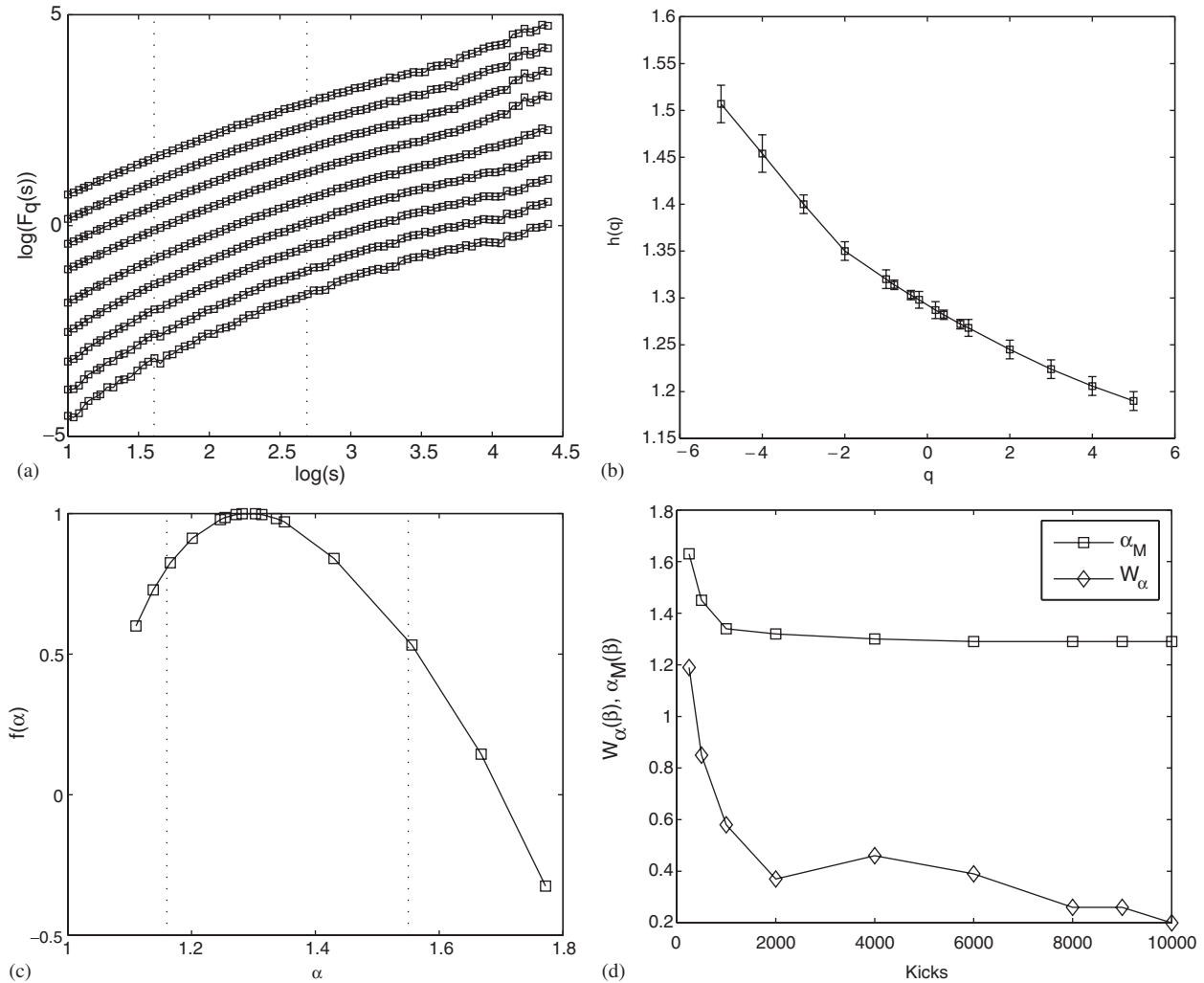


Fig. 2. (a) The decimal logarithm of the fluctuation function $F_q(s)$ for $q \in [-5, 5]$ for the β scanned series after an interaction time of 6000 kicks. The fitting procedure was performed in the zone $\log(s) \in [1.6, 2.7]$ (corresponding to $s \in [40, 500]$). The curves were vertically shifted for better reading; (b) the spectrum of the generalized Hurst exponents $h(q)$; its strong dependence on q indicates the multifractal behavior. The error bars show the uncertainty arising from the fits to the curves in (a); (c) the $f(\alpha)$ spectrum with $\alpha_M = 1.29$ and $W_\alpha = 0.39$. The dotted lines indicate the α interval used to compute W_α ; (d) the multifractal parameters α_M and W_α as a function of the interaction time. After a strong, initial variation, the value α_M shows a saturation towards the value $\alpha_M \approx 1.3$. The width W_α shows approximately the same behavior, and tends to saturate towards the value $W_\alpha \approx 0.2$.

5. Conclusions

We studied the quantum kicked rotor, a paradigmatic model of quantum chaos, which describes the time evolution of cold atoms in periodically flashed optical lattices. Imposing absorbing boundary conditions allows one to probe the transport properties of the system, here expressed by the survival probability on a finite region in momentum space. For a fixed interaction time, the quantum survival probability depends sensitively on the parameters of the system, and our application of the detrended multifractal method shows that *clear signatures of a multifractal scaling of the survival probability* are found, as either the kicking period or quasimomentum is scanned. Our results generalize the previously predicted *mono-fractal* structure of the signal [7,8,11], by characterizing long-range correlations in the parametric fluctuations. In agreement with the monotonic increase of the box counting dimension with the interaction time t and its saturation after $t \gtrsim 5000$

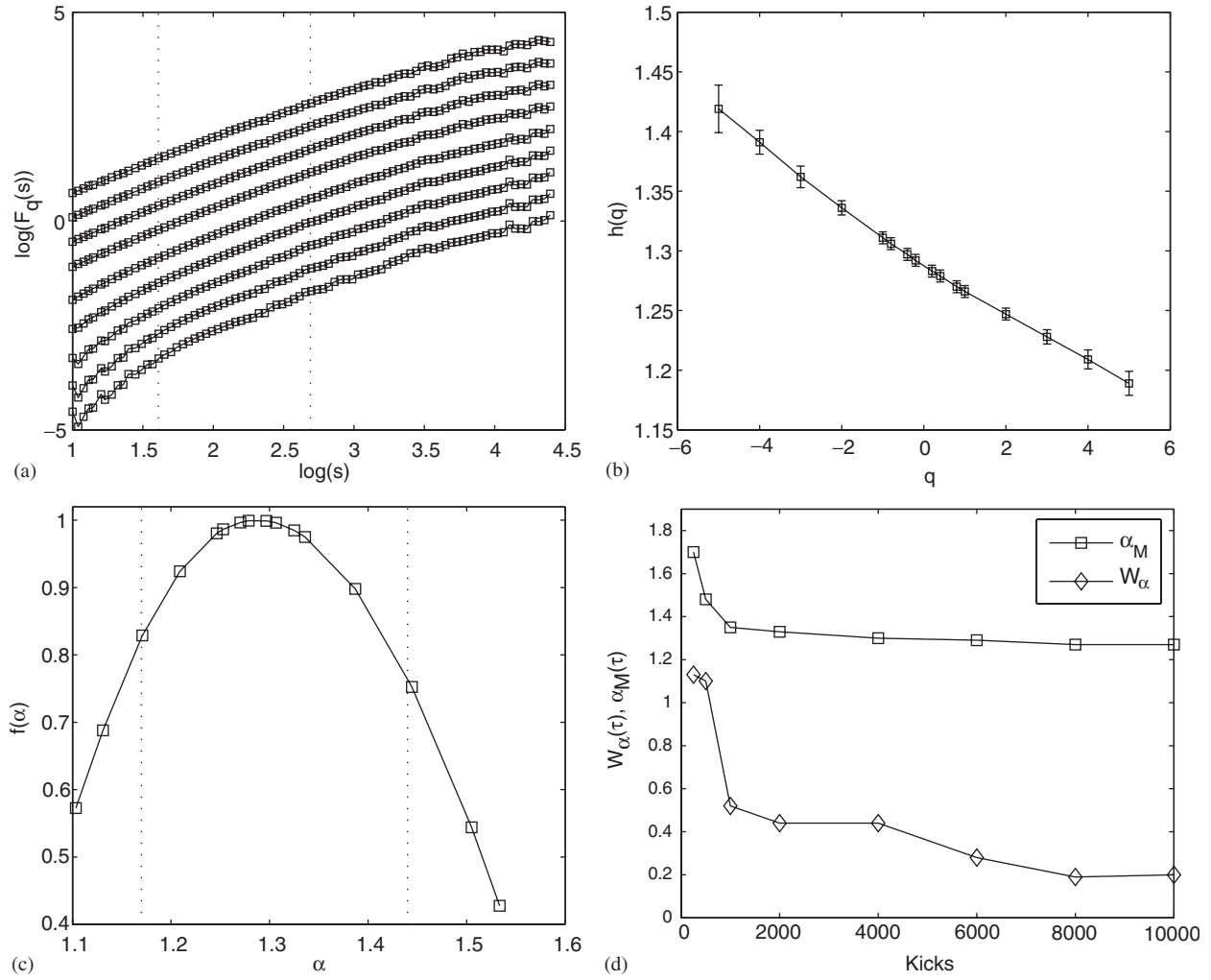


Fig. 3. (a) The decimal logarithm of $F_q(s)$ with $q \in [-5, 5]$ for the τ scanned series with $t = 6000$. The fitting procedure was performed in the zone $\log(s) \in [1.6, 2.7]$ (corresponding to $s \in [40, 500]$); (b) the spectrum of the generalized Hurst exponents $h(q)$; (c) the $f(\alpha)$ spectrum with $\alpha_M = 1.29$ and $W_\alpha = 0.28$; (d) the variation of the multifractal parameters α_M and W_α with the interaction time. α_M shows a saturation towards the value $\alpha_M \approx 1.3$, while W_α tends to saturate around the value $W_\alpha \approx 0.2$.

Table 1
Multifractal parameters of the β -scanned data sets for different interaction times

	α_M	W_α
$t = 250$	1.63	1.19
$t = 500$	1.45	0.85
$t = 1000$	1.34	0.58
$t = 2000$	1.32	0.37
$t = 4000$	1.30	0.46
$t = 6000$	1.29	0.39
$t = 8000$	1.29	0.26
$t = 10000$	1.29	0.20

The estimated error due to the fitting procedure described in Section 3 is about ± 0.02 for α_M and ± 0.05 for W_α .

Table 2
Multifractal parameters of the β -scanned data sets for different interaction times

	α_M	W_x
$t = 250$	1.70	1.13
$t = 500$	1.48	1.12
$t = 1000$	1.35	0.9
$t = 2000$	1.33	0.52
$t = 4000$	1.30	0.44
$t = 6000$	1.29	0.28
$t = 8000$	1.27	0.19
$t = 10\,000$	1.27	0.20

The estimated error due to the fitting procedure described in Section 3 is about ± 0.02 for α_M and ± 0.05 for W_x .

observed in Ref. [8], we found a systematically decreasing value for the maximum α_M of the MF spectrum and of its widths W_M . Both of these two values also tend to saturate for $t \gtrsim 5000$.

Future work along the lines of Ref. [8] will be devoted to check in detail whether traces of the here predicted multifractality could be observed under real-life experimental conditions (e.g., for short interaction times and finite resolutions in the scanning parameter [8]).

Acknowledgments

S.W. acknowledges support by the Alexander von Humboldt Foundation (Feodor-Lynen Program) and is grateful to Carlos Viviescas and Andreas Buchleitner for their hospitality at the Max Planck Institute for the Physics of Complex Systems (Dresden) where part of this work has been done. A.F. is grateful to Holger Kantz and Nikolay Vitanov for their support and important suggestions. Furthermore we thank Riccardo Mannella for his helpful advice on the numerical procedure.

References

- [1] E. Ott, *Chaos in Dynamical Systems*, Cambridge University Press, Cambridge, 1993.
- [2] H. Kantz, T. Schreiber, *Nonlinear Time Series Analysis*, Cambridge University Press, Cambridge, 1997.
- [3] L. Pietronero, A.P. Siebesma, E. Tosatti, M. Zannetti, *Phys. Rev. B* 36 (1987) 5635;
M. Schreiber, H. Grussbach, *Phys. Rev. Lett.* 67 (1991) 607 and refs. therein.
- [4] L. Schweitzer, P. Markoř, *Phys. Rev. Lett.* 95 (2005) 256805;
J.A. Méndez-Bermidez, T. Kottos, *Phys. Rev. B* 72 (2005) 064108 and refs. therein.
- [5] R. Berkovitz, J.W. Kantelhardt, Y. Avishai, S. Havlin, A. Bunde, *Phys. Rev. B* 63 (2001) 085102.
- [6] M. Janssen, M. Metzler, M.R. Zirnbauer, *Phys. Rev. B* 59 (1999) 15636.
- [7] I. Guarneri, M. Terraneo, *Phys. Rev. E* 65 (2001) 015203(R).
- [8] A. Tomadin, R. Mannella, S. Wimberger, *J. Phys. A* 39 (2006) 2477.
- [9] M. Terraneo, Ph.D. Thesis, Università degli Studi di Milano 2001; I. Guarneri, M. Terraneo, S. Wimberger, unpublished.
- [10] F. Borgonovi, I. Guarneri, D.L. Shepelyansky, *Phys. Rev. A* 43 (1991) 4517;
S. Wimberger, A. Krug, A. Buchleitner, *Phys. Rev. Lett.* 89 (2002) 263601;
A. Ossipov, T. Kottos, T. Geisel, *Europhys. Lett.* 62 (2003) 719;
S.E. Skipetrov, B.A. van Tiggelen, *Phys. Rev. Lett.* 96 (2006) 043902.
- [11] G. Benenti, G. Casati, I. Guarneri, M. Terraneo, *Phys. Rev. Lett.* 87 (2001) 014101.
- [12] B.V. Chirikov, *Phys. Rep.* 52 (1979) 263.
- [13] F.M. Izrailev, *Phys. Rep.* 196 (1990) 299.
- [14] F.L. Moore, J.C. Robinson, C.F. Bharucha, B. Sundaram, M.G. Raizen, *Phys. Rev. Lett.* 75 (1995) 4598;
H. Ammann, R. Gray, I. Shvarchuck, N. Christensen, *Phys. Rev. Lett.* 80 (1998) 4111;
J. Ringot, P. Szriftgiser, J.C. Garreau, D. Delande, *Phys. Rev. Lett.* 85 (2000) 2741;
M. Sadgrove, S. Wimberger, S. Parkins, R. Leonhardt, *Phys. Rev. Lett.* 94 (2005) 174103;
M.B. d’Arcy, et al., *Phys. Rev. E* 69 (2004) 027201.
- [15] S. Wimberger, I. Guarneri, S. Fishman, *Nonlinearity* 16 (2003) 1381.

- [16] G.J. Duffy, S. Parkins, T. Muller, M. Sadgrove, R. Leonhardt, A.C. Wilson, *Phys. Rev. E* 70 (2004) 056206, better control of the quasimomentum was recently realized by a method described in C. Ryu et al., *Phys. Rev. Lett.* 96 (2006) 160403.
- [17] C.K. Peng, S.V. Buldriev, S. Havlin, M. Simons, H.E. Stanley, A.L. Goldberger, *Phys. Rev. E* 49 (1999) 1685.
- [18] J.W. Kantelhardt, S.A. Zschiegner, E. Koscielny-Bunde, S. Havlin, A. Bunde, H.E. Stanley, *Physica A* 316 (2002) 87.
- [19] R.K. Kavasseri, R. Nagarajan, *Chaos Solitons Fractals* 24 (2005) 165–173.
- [20] D. Makowieca, R. Galaska, A. Dudkowska, A. Rynkiewicz, M. Zwierza, *Physica A* 369 (2006) 632.
- [21] J.W. Lee, K.E. Lee, P.A. Rikvold, *Physica A* 364 (2006) 355–361.
- [22] R. Benzi, G. Paladin, G. Parisi, A. Vulpiani, *J. Phys. A* 17 (1984) 3521;
G. Paladin, A. Vulpiani, *Phys. Rep.* 156 (1987) 147;
J.L. McCauley, *Chaos, Dynamics, and Fractals: An Algorithmic Approach to Deterministic Chaos*, Cambridge University Press, Cambridge, 1994.
- [23] N.K. Vitanov, K. Sakai, E.D. Yankulova, *J. Theor. Appl. Mech.* 35 (2005) 2.
- [24] J. Feder, *Fractals*, Plenum Press, New York, 1988.
- [25] R.B. Govindan, H. Kantz, *Europhys. Lett.* 68 (2004) 184.

PHYSICAL REVIEW A 77, 013606 (2008)

Many-body Landau-Zener tunneling in the Bose-Hubbard modelAndrea Tomadin,¹ Riccardo Mannella,² and Sandro Wimberger^{3,*}¹*Scuola Normale Superiore, Piazza dei Cavalieri 7, I-56126 Pisa, Italy*²*Dipartimento di Fisica "Enrico Fermi," Università degli Studi di Pisa, Largo Pontecorvo 3, I-56127 Pisa, Italy*³*Institut für Theoretische Physik, Universität Heidelberg, Philosophenweg 19, D-69120 Heidelberg, Germany*

(Received 16 July 2007; published 7 January 2008)

We study a model for ultracold, spinless atoms in quasi-one-dimensional optical lattices and subjected to a tunable tilting force. Statistical tests are employed to *quantitatively* characterize the spectrum of the Floquet-Bloch operator of the system along the transition from the regular to the quantum chaotic regime. Moreover, we perturbatively include the coupling of the one-band model to the second energy band. This allows us to study the Landau-Zener interband tunneling within a truly many-body description of ultracold atoms. The distributions of the computed tunneling rates provide an independent and experimentally accessible signature of the regular-chaotic transition.

DOI: [10.1103/PhysRevA.77.013606](https://doi.org/10.1103/PhysRevA.77.013606)

PACS number(s): 03.75.Lm, 03.65.Yz, 05.60.Gg, 68.65.-k

I. INTRODUCTION

Bose-Einstein condensates loaded into optical lattices, which perfectly realize spatially periodic potentials, represent an exciting field of research in the sense that many simplified toy models of condensed matter physics can be studied in an exceptionally clean manner [1]. This is achieved by modern means of atom and quantum optics that allow the experimentalist an unprecedented control of initial conditions in coordinate and momentum space and also of the desired dynamics [1,2].

A paradigm of quantum transport on the microscopic scale is the Wannier-Stark (WS) problem, where particles move in a tilted, but otherwise spatially periodic potential. The famous Bloch oscillations and related phenomena, such as interband tunneling, were observed in experiments with quasiparticles in superlattices [3], with light in optical nonlinear media [4], and in great detail also with ultracold atoms moving in optical lattices [1,5–8]. All experimental studies based on the latter realization were performed in a regime where atom-atom interactions are either negligible [5] or they reduce to a perturbative mean-field effect [6–8].

The regime of strong correlations in the WS system, in which interactions cannot be reduced to a mean-field model or even dominate the evolution has been addressed only theoretically up to now [9–12]. State-of-the-art experiments are, however, capable of getting into a regime of filling factors (i.e., of atoms per lattice site) of the order one, where interaction-induced correlations are crucial [13,14].

Motivated by the experimental progress, we extend previous studies of the asymmetric triple well [15] and of the WS problem [9–11]. In the present work we give a more comprehensive and quantitative account of our findings briefly reported in [16]. In Sec. II we introduce our two-bands Bose-Hubbard (BH) model and focus on the dynamics within the first band of the optical lattice. In contrast to the vast literature which focuses on regimes around Mott-insulator-like phase transitions in the absence of an additional Stark force,

see, e.g., [17–22], we concentrate on the BH model in the superfluid realm and in the presence of a static tilt. We characterize the transition between the regular and the chaotic realm of the quantum spectra by a quantitative and systematic analysis based on statistical tests. In Sec. III we perturbatively include the decay to the second band via Landau-Zener-like tunneling processes. The quantum spectrum of the latter, nonunitary problem is analyzed in Sec. IV and found to essentially reproduce the properties of the purely one-band approximation down to rather small lattice depths. The resulting decay rates for the interband tunneling strongly depend on the many-particle nature of the problem and are found to correlate with the transition to the quantum chaotic regime. As a consequence, signatures of many-body quantum chaos are predicted to be accessible to experiments with ultracold atoms over a broad range of parameters, in both “horizontal” transport along the lattice and in interband “vertical” transport. Our results are finally summarized in Sec. V.

II. SPECTRAL ANALYSIS OF THE ONE-BAND BOSE-HUBBARD MODEL

We briefly review the general Hamiltonian for a system of spinless, interacting atoms in a quasi-one-dimensional optical lattice subjected to a tunable tilting force F . We start out with the purely periodic problem, $F=0$, in an optical potential of spacing a , recoil momentum $k_L=\pi/a$, and typical kinetic energy $E_R=k_L/2m$. The optical potential and the kinetic energy form the single-particle Bloch Hamiltonian,

$$H_1(x) = -\frac{\Delta}{2m} - V \cos\left(\frac{2\pi x}{a}\right). \quad (1)$$

The eigenfunctions are the Bloch waves ψ , labeled by the quasimomentum k and the band index α [23], with dispersion law $E_{k,\alpha}$. In Appendix A we explain how to use the single-particle solutions $\psi_{k,\alpha}$ to build a set of localized orbitals $\chi_{\ell,\alpha}$ called Wannier functions (WF). In the limit of deep lattices, the orbital $\chi_{\ell,\alpha}$ goes to the wave function of the α th excited level for an harmonic potential centered on the ℓ -lattice site. We use the WF to expand the field of the ultracold bosons,

*s.wimberger@thphys.uni-heidelberg.de

$$\hat{\phi}(x) = \sum_{\alpha} \sum_{\ell} \chi_{\ell,\alpha}(x) \hat{a}_{\ell\alpha}. \quad (2)$$

Then we introduce a Stark force F that tilts the optical potential and a zero-range interaction between the atoms, parametrized by the scattering length a_S . In a quasi-one-dimensional optical lattice—as realizable in experiments [14]—the scattering length is derived from the true three-dimensional scattering length via a renormalization that accounts for the transverse confinement of the atomic wave functions [14] and the physical dimension is then $[a_S]=L^{-1}$. The Hamiltonian in the second quantization is written as

$$\hat{H} = \int \hat{\phi}^{\dagger}(x) [H_{\text{one}}(x) + Fx] \hat{\phi}(x) dx + \frac{1}{2} \frac{4\pi a_S}{m} \int \hat{\phi}^{\dagger}(x) \hat{\phi}^{\dagger}(x) \hat{\phi}(x) \hat{\phi}(x) dx. \quad (3)$$

Substituting the expansion equation (2) into Eq. (3) we obtain the Hamiltonian in terms of the creation and annihilation operators $\hat{a}_{\ell,\alpha}^{\dagger}$, $\hat{a}_{\ell,\alpha}$, for a particle in the ℓ th site and the α th energy band of the lattice. The number operator is $\hat{n}_{\ell,\alpha} = \hat{a}_{\ell,\alpha}^{\dagger} \hat{a}_{\ell,\alpha}$. We restrict the analysis to the first two bands, which can be addressed by experiments [24] and that can be handled numerically without great difficulties. The coefficients of the Hamiltonian are given by integrals involving the WF: the exact computation of the WF outlined in Appendix A motivates the selection of the operators that are most relevant for $V \geq E_R$. We are left with the on-site energy $\hat{a}_{\ell,\alpha}^{\dagger} \hat{a}_{\ell,\alpha}$, the kinetic energy $\hat{a}_{\ell+1,\alpha}^{\dagger} \hat{a}_{\ell,\alpha}$, and the on-site interaction between atoms in the same band $\hat{n}_{\ell,\alpha}(\hat{n}_{\ell,\alpha}-1)$ [25], for $\alpha \in \{1, 2\}$. Moreover, we have on-site interaction between atoms in different bands $\hat{n}_{\ell,1} \hat{n}_{\ell,2}$ and two transition operators $\hat{a}_{\ell,2}^{\dagger} \hat{a}_{\ell,1}$, $\hat{a}_{\ell,1}^{\dagger} \hat{a}_{\ell,2}$ that are the subject of a detailed analysis in Sec. III.

The dimension D_H of the Hilbert space spanned by the Fock states $|\vec{n}\rangle$ (defined in Appendix B), for a system of N bosons distributed over L lattice sites, occupying up to the second band of the periodic potential, is given by the combinatorial formula $D_H = (N+2L-1)!/N!(2L-1)!$. The typical number of lattice sites in experiments is $L \lesssim 100$ and the filling factor N/L is of order unity [13,14], such that the exponential increase of D_H with the system size limits any exact numerical approach to smaller systems, where we impose the cyclic boundary conditions $\hat{a}_{L,\alpha} = \hat{a}_{0,\alpha}$. The implementation of these conditions requires the system to be translationally invariant. The Stark potential Fx , however, spoils the periodicity of the Bloch Hamiltonian equation (1) and produces localized WS eigenstates instead of traveling Bloch waves [23]. We follow [10] and proceed to eliminate the Stark potential from the Hamiltonian by changing to the interaction representation (IR) with respect to $\hat{H}_S = F \int \hat{\phi}^{\dagger} x \hat{\phi} dx = aF \sum_{\ell=1}^L \sum_{\alpha} \ell \hat{n}_{\ell,\alpha}$. The Hamiltonian in the IR, $\hat{H}(t) = e^{-i\hat{H}_S t} \hat{H} e^{i\hat{H}_S t}$, is time dependent, and the problem becomes conceptually more complicated.

We rescale the energies by E_R , the lengths by a , the momenta by k_L , and we make the substitutions $F \leftarrow FE_R/a$, $\chi \leftarrow \chi/\sqrt{a}$. The on-site energies ε_{α} and the hopping amplitudes

J_{α} are given in Eq. (A3). The interaction coefficients W_{α} , W_{\times} , are proportional to the coupling constant $W = 4\pi a_S/amE_R$ and are given in Eq. (A5). The ‘‘dipole’’ coefficient d_F is given in Eq. (A6). The Hamiltonian of Eq. (3), restricted to the first two bands of the lattice, finally reads, in the IR, as

$$\hat{H}(t) = \sum_{\ell=1}^L \left(\varepsilon_1 \hat{n}_{\ell,1} - \frac{1}{2} J_1 e^{iFt} \hat{a}_{\ell+1,1}^{\dagger} \hat{a}_{\ell,1} + \text{H.c.} \right. \\ \left. + \frac{1}{2} W_1 \hat{n}_{\ell,1} (\hat{n}_{\ell,1} - 1) + (1 \rightarrow 2) + 2W_{\times} \hat{n}_{\ell,1} \hat{n}_{\ell,2} \right. \\ \left. + Fd_F (\hat{a}_{\ell,2}^{\dagger} \hat{a}_{\ell,1} + \text{H.c.}) + \frac{1}{2} W_{\times} (\hat{a}_{\ell,1}^{\dagger} \hat{a}_{\ell,1}^{\dagger} \hat{a}_{\ell,2} \hat{a}_{\ell,2} + \text{H.c.}) \right). \quad (4)$$

In the IR the Hamiltonian is again symmetric for discrete translations in space and it has lost the time independence but it is periodic with the Bloch period $T_B = 2\pi/F$. We assume that the initial state, for $F=0$, is superfluid, characterized by the delocalization of the atoms over the entire lattice. The critical conditions on the parameters, that enforce the superfluid phase in the present context [17] is $W_1/J_1 \leq 5.8$. Following [9], in the present section we set the lattice depth $V \simeq 5$, which gives $J_1 \simeq 0.038$ and the interaction coefficient $W \simeq 0.016$, with $W_1 = 0.032$.

The object of the subsequent study is the evolution operator up to the Bloch period $\hat{U}_{\text{FB}} = \text{exp}(-\int_0^{T_B} i\hat{H}(t) dt)$, called Floquet-Bloch (FB) operator [10]. The caret over exp indicates that it is time ordered. The results presented in the following confirm and extend the results of [10]. The discrete translational symmetry of the Hamiltonian entails that the FB operator is a block-diagonal matrix in the basis of Eq. (B2), labeled by a many-body quasimomentum κ . The dynamics of the atoms in the lattice is complex because many vectors take part in the time evolution of an arbitrary initial state. The strong mixing of the basis vectors in time means that the evolution of a state is not bound to a small subspace of the total Hilbert space (contrary to [18]), but, after a Bloch period, the initial state spreads over the entire Hilbert subspace with definite quasimomentum (e.g., $\kappa=0$). This is evidenced by the dependence on F of the quasienergies E_j , obtained from the eigenvalues $\text{exp}(-iE_j T_B)$ of the FB operator.

In Fig. 1 we show the quasienergy spectrum as the ‘‘control parameter’’ F is varied. In the limit $F \rightarrow 0$, we recover the standard BH model (the analysis of the FB spectrum is here, however, not useful since the Bloch period tends to infinity). In the regime where the atomic interactions are negligible with respect to the lattice potential, the single particle Bloch picture is adequate and the spectrum is simply a finite band. For $F \geq 0.1$ the single-particle WS ladder is found, i.e., a fan of energy levels $E_m(F) \simeq 2\pi mF$, m integer. Since the interactions are nonzero, the levels are split up and the first-order perturbative effect on the ladder was computed in [11]. The central WS rung is split into levels which are proportional to the interaction energies of many atoms in a site, $W_1 n(n-1)$, $n=1, \dots, 4$. Since the level splittings have the common factor W_1 , a collapse and revival of quasimomentum oscillations

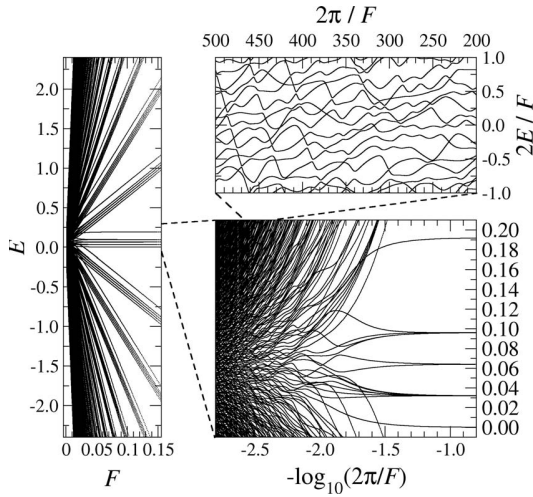


FIG. 1. The quasienergy levels E of the FB operator for a system with $N=4$, $L=5$, in the subspace with $\kappa=0$. The WS ladder is seen on the left-hand panel, the perturbative splitting of the first rung is magnified in the lower panel. In the upper panel a single linear function of $1/F$ is added to $2E/F$ to eliminate an overall winding trend, and allow a better visibility of the avoided crossings. The parameters of the Hamiltonian are $J_1=0.038$, $W_1=0.032$, as used also in the subsequent figures.

(the Fock space version of the single-particle Bloch oscillations) was predicted for this parameter range in [11]. On the contrary, an irreversible decay of the quasimomentum oscillations was found in the range $F \approx W_1$ [9], where avoided crossings dominate the spectrum. These are directly, experimentally observable consequences of the complex level structure presented in Fig. 1. The presence of avoided crossings means that a strong mixing of the Fock states is necessary to build the eigenstates of the system, and no set of quantum numbers can be assigned to individual levels as F varies. In the region of parameters where the energy scales of the system are comparable in magnitude, we can characterize the spectrum in terms of the statistical distribution of the quasienergy spacing and by statistical measures for the eigenfunctions. The latter have been intensively studied in [26]. In the following, we concentrate on the statistical behavior of the quasienergies, which is closely linked to the behavior of the open system studied in Sec. III.

The probability $\mathbf{P}(s)ds$ that the magnitude of a given interval spacing $s_j = \Delta E_j / \langle \Delta E_j \rangle$ is in $[s, s+ds]$ is given by the Poisson distribution $\mathbf{P}(s) = \exp(-s)$ [27] for an uncorrelated spectrum in the regular regime. Strongly correlated quantum spectra, corresponding to the chaotic regime in our many-particle model, are well modeled by the Wigner-Dyson (WD) distribution for a circular orthogonal ensemble of random matrices [27], $\mathbf{P}(s) = \pi s \exp(-\pi s^2/4)/2$. In Fig. 2 the probability distribution and the cumulative distribution function (CDF) of the quasienergy spacing are shown for two paradigmatic values of F . The presence of avoided crossings in the chaotic case $\log_{10}(2\pi/F) \approx 2.4$ shows up as a depletion of small quasienergy spacing, and the probability to find a level crossing vanishes.

We improved the statistical description of the quasienergy spectrum with further analyses, shown in Fig. 3. In the panel

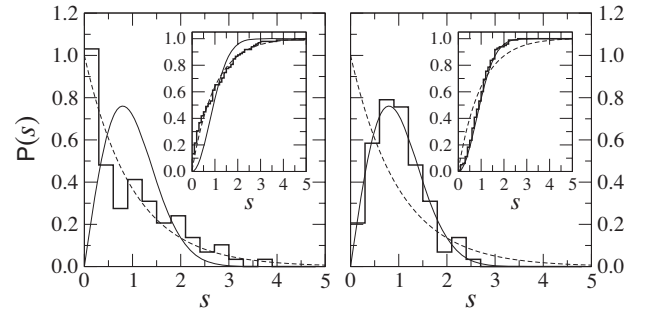


FIG. 2. The distribution $\mathbf{P}(s)$ and the CDF (insets) for the quasienergy spacing (stairs), the WD (solid), and the Poisson distribution (dashed). The parameters are $N=5$, $L=8$, $\log_{10}(2\pi/F) \approx 2.0$ (left-hand side, regular) and 2.4 (right-hand side, chaotic).

(a) we quantify the convergence of the quasienergy spacing distribution to the WD profile, thus filling the gap between the two pictures of Fig. 2. We computed the FB operator for several values of F and confronted each spectrum with the WD distribution using a modified χ^2 test, computed as follows. Each sequence of levels spacing's was algorithmically binned to leave $5 \leq O_b \leq 10$ "observed" spacing in each bin $b=1, \dots, N_b$ [28]. The "expected" values E_b are the integrals of the theoretical distributions over the bins and the sum $Q = \sum_b (O_b - E_b)^2 / E_b$ was calculated. The values of Q are distributed according to a χ^2 distribution with $N_b - 1$ degrees of freedom and mean $N_b - 1$. The renormalized variable

$$\chi^2 = \log_{10}[Q/(N_b - 1)] \quad (5)$$

is thus appropriate to compare several data sets, each binned optimally and independently. For $F \leq 0.025$, χ^2 is in the range $[-0.5, 0.5]$ (in the bulk of the original χ^2 distributions before the transformation of Eq. (5) was performed), and the

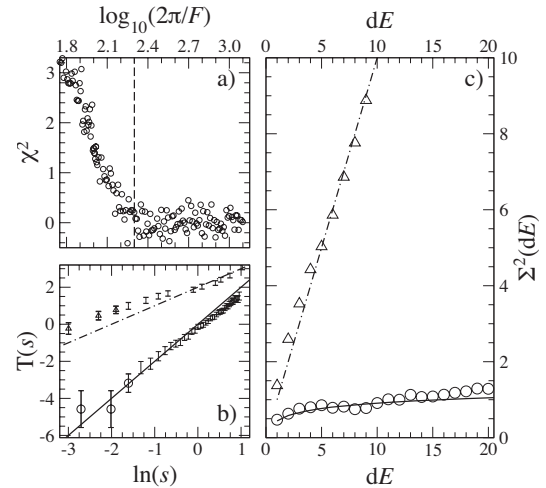


FIG. 3. Statistical tests applied to the system of Fig. 2. (a) χ^2 -like test of Eq. (5). (b) T test, and (c) variance of number of levels (with mean spacing normalized to 1), for the chaotic (circles) and the regular (pyramids) case. In both panels the solid and dotted-dashed lines are the theoretical predictions for the WD and Poisson statistics of energy levels, respectively.

correspondent distribution of the spacing is well described by a WD profile. As the external force increases and the parameter $2\pi/F$ diminishes, the larger values of χ^2 (lying in the tails of the original χ^2 distributions) indicate that the spectrum is not well characterized by a WD distribution. The condition for the regular-chaotic transition can be directly read off from the quantitative statistical test results and corresponds, e.g., to $\log_{10}(2\pi/F) \approx 2.3$.

We found that the profile of the quasienergy spacing distribution changes smoothly, but we used two statistical tests introduced in [29] [Eqs. (27) and (29) therein] to show that the Poisson and WD statistics are clearly identified at the borders of the transition. Figure 3(b) shows the explicit results for the T function of [29] whose predicted linear scaling $T \sim \ln s$ for the Poisson and $T \sim 2 \ln s$ for the WD expectation is confirmed. In Fig. 3(c) we show the variance $\Sigma^2(dE)$ [30] of the number of levels $N(E, E+dE)$ found in a finite energy interval dE :

$$\Sigma^2(dE) \equiv \langle [N(E, E+dE) - \bar{N}dE]^2 \rangle_E, \quad (6)$$

where the average is taken over all the energies and we rescaled the spectrum so that the average number of levels per unit of energy \bar{N} is equal to unity. A linear and logarithmic scaling is predicted for a Poisson and WD-like spectra, respectively. The logarithmic behavior clearly prevails over all energy ranges for the chaotic spectrum, only apart from oscillations which are indeed typical for samples of finite size (see [30] for details).

III. INTERBAND COUPLING IN THE MANY-BODY REGIME

We develop a perturbative analysis of the two-bands system of Eq. (4). We consider the many-body dynamics within the ground band and the perturbative action of the operators that couple the Fock states of the ground band to states in the second band. As a consequence of the interband terms each Fock state $|\vec{n}\rangle$ (see Appendix B) suffers an energy shift $\delta E(\vec{n}) - i\Gamma_F(\vec{n})/2$, where $\Gamma_F(\vec{n})$ is its decay width. The Hamiltonian is modified accordingly and becomes a non-Hermitian effective Hamiltonian for the ground band, that yields a non-unitary FB operator. In the following, we compute the set of decay widths. In the next section we then study the spectrum of this new FB operator.

We first define a basis of unperturbed states. We choose to neglect the hopping in the lower band, where the WF are more strongly localized, so an unperturbed state projected on the Hilbert space of N particles in the ground band is a Fock state $|\vec{n}; N\rangle$. In the second band we neglect the interactions, since in the perturbative approach only a few particles (one or two in the following) populate the excited levels. So an unperturbed state projected on the second band is the solution of the one-particle WS problem [18,23], i.e., a localized wave function centered at site w , written with the Bessel function $\mathcal{J}_m(x)$ as

$$|w\rangle = \sum_{\ell=-\infty}^{+\infty} \mathcal{J}_{\ell-w}(-J_2/F) \hat{a}_{\ell,2} |\text{vac}\rangle. \quad (7)$$

We approximate the Hilbert space of the system as the tensor product of the spaces of the two bands and the entanglement between the ground and the excited particles is neglected. Then an unperturbed state with one or two promoted particles is of the form $|\vec{n}; N-1\rangle \otimes |w\rangle$ or $|\vec{n}; N-2\rangle \otimes |w, w'\rangle$, respectively. In the following, the occupation number $n_{\ell,1}$ for the ℓ th site in the ground band is written as n_ℓ .

The Hamiltonian equation (4) contains two mechanisms that promote particles to the second band. The first is a single-particle effect, a consequence of the external force, proportional to the dipole coupling d_F between the WF of different bands. The Hamiltonian of the perturbation is

$$\hat{H}_1 = Fd_F \sum_{\ell} (\hat{a}_{\ell,2}^\dagger \hat{a}_{\ell,1} + \hat{a}_{\ell,1}^\dagger \hat{a}_{\ell,2}). \quad (8)$$

The second perturbation is a many-body effect, describing two particles of the first band that collide and transform their interaction energy into kinetic energy, entering the second band together,

$$\hat{H}_2 = \frac{1}{2} W_{\times} \sum_{\ell=1}^L (\hat{a}_{\ell,2}^\dagger \hat{a}_{\ell,2}^\dagger \hat{a}_{\ell,1} \hat{a}_{\ell,1} + \text{H.c.}). \quad (9)$$

The expectation value of \hat{H}_1 , \hat{H}_2 on the unperturbed states, equal to the first-order energy shift $-i\Gamma_F(\sigma)/2$, is zero because the operators do not conserve the number of particles n_α within the bands.

Let us focus on \hat{H}_1 and compute its matrix element for the channel,

$$|\vec{n}; N\rangle \otimes |\text{vac}\rangle \rightarrow |\vec{n}'; N-1\rangle \otimes |w\rangle, \quad n'_h = n_h - 1. \quad (10)$$

The decay width at first order is given by Fermi's golden rule and only the first term in Eq. (8) gives nonzero contribution for the channel of Eq. (10). Our result for the matrix element is

$$\begin{aligned} & \langle k | \langle \vec{n}' | \sum_{\ell=1}^L (\hat{a}_{\ell,2}^\dagger \hat{a}_{\ell,1}) | \vec{n} \rangle | \text{vac} \rangle \\ &= \sum_{\ell=1}^L \mathcal{J}_{\ell-w}(-J_2/F) \delta(n'_\ell, n_\ell - 1) \sqrt{n_\ell} \prod_{m \neq \ell} \delta(n'_m, n_m). \end{aligned} \quad (11)$$

The Kronecker $\delta(\dots, \dots)$ functions act as a selection rule for the Fock states that are coupled by the perturbation. The tunneling mechanism does not include any income of energy from an external source, so the initial and final energies,

$$\begin{aligned} E_0(\vec{n}) &= \langle \text{vac} | \langle \vec{n} | \hat{H}_0 | \vec{n} \rangle | \text{vac} \rangle, \\ E_0(\vec{n}', w) &= \langle w | \langle \vec{n}' | \hat{H}_0 | \vec{n}' \rangle | w \rangle, \end{aligned} \quad (12)$$

must be equal as required by the golden rule. The condition on the energy conservation is relaxed to account for the uncertainty $\Delta E(\vec{n})$ of the unperturbed energy levels of the initial

and final states. The energy uncertainty and the level density function $\rho(E, \vec{n})$ are derived from the perturbative action of the hopping operator of the first band that has been neglected so far. We postpone the computation of these quantities to the end of the present section. The relaxed energy conservation rule selects from Eq. (11) the set K of permitted decay channels (h, w) parametrized by the two indices h, w such that:

$$E_0(\vec{n}', w) - E_0(\vec{n}) = \varepsilon_2 - \varepsilon_1 - F(h - w) - W_1(n_h - 1) \in \left[-\frac{\Delta E(\vec{n}) + \Delta E(\vec{n}')}{2}, \frac{\Delta E(\vec{n}) + \Delta E(\vec{n}')}{2} \right]. \quad (13)$$

The last equation means that the energy $\varepsilon_2 - \varepsilon_1$ required to promote a particle to the second band is supplied by the decrease of the repulsion energy (proportional to W) and by the work of the force (proportional to F) exerted on the promoted particle.

The total width $\Gamma_1(\vec{n})$ for the decay via the allowed channels K , is proportional to the square of the matrix element and to the level density $\rho(E, \vec{n})$ given below in Eq. (22). We arrive at

$$\Gamma_1(\vec{n}) = 2\pi F^2 d_F^2 \sum_{(h,w) \in K} \left(|\mathcal{J}_{h-w}(-J_2/F) \sqrt{n_h}|^2 \frac{1}{\Delta E(\vec{n}) \Delta E(\vec{n}')} \right). \quad (14)$$

The perturbation \hat{H}_2 is treated in a similar way, with the difference that two particles are promoted to the second band, and the position of the second Stark state $|w'\rangle$ is an additional degree of freedom for the transition. The decay channels are

$$|n, N\rangle \otimes |\text{vac}\rangle \rightarrow |\vec{n}'; N-2\rangle \otimes |w\rangle, \quad n'_h = n_h - 2. \quad (15)$$

The approximate energy matching equation selects a set K of possible decay channels, parametrized by the three site indices (h, w, w') ,

$$(h, w, w') \in K \text{ s.t. } E_0(\vec{n}', w, w') - E_0(\vec{n}) = 2(\varepsilon_2 - \varepsilon_1) - F(2h - w - w') - W_1(2n_h - 3) \in \left[-\frac{\Delta E(\vec{n}) + \Delta E(\vec{n}')}{2}, \frac{\Delta E(\vec{n}) + \Delta E(\vec{n}')}{2} \right]. \quad (16)$$

We state the result for the decay width

$$\Gamma_2(\vec{n}) = \frac{1}{2} \pi W_\times^2 \sum_{(h,w,w') \in K} \left(|\mathcal{J}_{h-w}(-J_2/F) \mathcal{J}_{h-w'}(-J_2/F)|^2 \times 4n_h(n_h - 1) \frac{1}{\Delta E(\vec{n}) \Delta E(\vec{n}')} \right). \quad (17)$$

With respect to Eq. (14), the additional degree of freedom w' results in an extra summation extended over the (infinite) possible values of the difference $w - w'$. This follows from the possibility to conserve the energy even if a particle is

pushed very far, if the other particle is pushed almost equally far in the opposite direction. Since the decay width equation (17) depends on the product of two (rapidly decaying) Bessel functions we apply the truncation $|w - w'| \leq |J_2/F|$, to reduce the formula to a finite form.

Now we conclude the computation and derive the energy broadening $\Delta E(\vec{n})$ of the Fock states in the ground band necessary to implement the conditions of Eqs. (13) and (16). In the ground band, the unperturbed Hamiltonian consists only of the on-site interaction operator

$$\hat{H}_0 = \frac{1}{2} W_1 \sum_{\ell} \hat{n}_{\ell,1} (\hat{n}_{\ell,1} - 1).$$

In the case of a single particle in a periodic potential, the use of first-order perturbation theory is wrong, as the second order of the perturbation theory diverges because of the exact degeneracy in energy of neighboring sites, entailed by the translational symmetry of the lattice. On the contrary, in the present case, the unperturbed Hamiltonian is just a rough approximation of the true Hamiltonian of the system and the remaining operators are supposed to remove the degeneracy, since the translational symmetry is broken by the external field in the WS picture. The perturbation Hamiltonian is given by

$$\hat{H}_h = -\frac{1}{2} J_1 \sum_{\ell} (\hat{a}_{\ell+1,1}^\dagger \hat{a}_{\ell,1} + \text{H.c.}), \quad (18)$$

and its matrix elements between Fock states are

$$\begin{aligned} \langle \vec{n}' | \hat{H}_h | \vec{n} \rangle &= -\frac{1}{2} J_1 \sum_{\ell=1}^L \sum_{\Delta \ell = \pm 1} \prod_{m \neq \ell} \sqrt{n_{\ell,1}} \sqrt{n_{\ell+\Delta \ell,1} + 1} \\ &\times \delta(n'_{m,1}, n_{m,1}) \delta(n'_{\ell,1}, n_{\ell,1} - 1) \\ &\times \delta(n'_{\ell+\Delta \ell,1}, n_{\ell+\Delta \ell,1} + 1). \end{aligned} \quad (19)$$

Transitions are allowed between Fock states that differ for one boson in two adjacent holes $m, m + \Delta m$. The transition channels are written as $|\vec{n}\rangle \rightarrow |\vec{n}'\rangle$, with $\vec{n}'_{m,1} = \vec{n}_{m,1} - 1$ and $\vec{n}'_{m+\Delta m,1} = \vec{n}_{m+\Delta m,1} + 1$, and must fulfill the condition of the energy conservation

$$E_0(\vec{n}') - E_0(\vec{n}) = W_1(n_{m+\Delta m,1} - n_{m,1} + 1) \equiv 0. \quad (20)$$

The total uncertainty is obtained by adding up the contributions from all the transitions and the summation over the allowed channels can be recast in a summation over the lattice sites. Using the golden rule, each Fock state is attributed the following energy uncertainty:

$$\begin{aligned} \Delta E(\vec{n}) &= \frac{1}{2} \pi J_1^2 \sum_{\vec{n}'} \Delta E(\vec{n} \rightarrow \vec{n}') \\ &= \frac{1}{2} \pi J_1^2 \sum_{\ell} \sum_{\Delta \ell = \pm 1} n_{\ell,1}^2 \delta(n_{\ell+\Delta \ell,1} + 1, n_{\ell,1}). \end{aligned} \quad (21)$$

Finally, the level density $\rho(E, \vec{n})$ around the unperturbed energy $E_0(\vec{n})$ of a Fock state $|\vec{n}\rangle$ is approximated by a rectangular profile, of width $\Delta E(\vec{n})$ and area unity

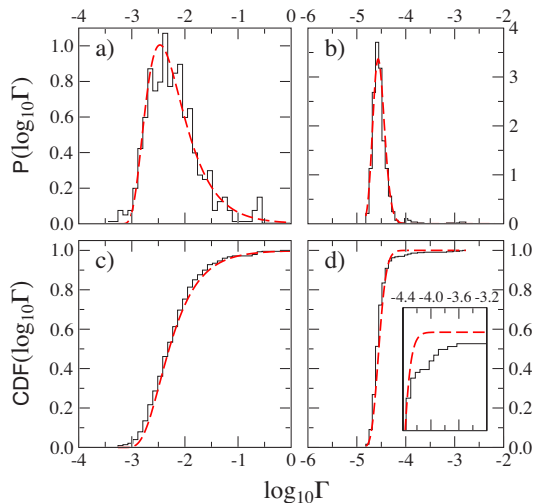


FIG. 4. (Color online) (a,b) The probability distribution \mathbf{P} and (c,d) the CDF for the logarithm of the decay widths Γ in the regular regime [(a,c) with $\log_{10}(2\pi/F) \approx 1.5$] and in the chaotic regime [(b,d) with $\log_{10}(2\pi/F) \approx 2.1$]. The size of the system is $N=8$, $L=7$. The dashed line is the fit with a log-normal distribution. The inset in panel (d) shows that the log-normal is not appropriate to fit the tails of the distributions in the chaotic regime. Here and in the following figures, $V=1.5$, $\varepsilon_2-\varepsilon_1=2.63$, $J_1=0.22$, $J_2=-1.0$, $W_1=0.2$, $W_\times=0.1$, $d_F=-0.2$.

$$\rho(E, \vec{n}) = \chi \{ |E - E_0(\vec{n})| \leq \Delta E(\vec{n})/2 \} / \Delta E(\vec{n}). \quad (22)$$

IV. RESULTS OF THE PERTURBATIVE OPENING OF THE ONE-BAND SYSTEM

The total width $\Gamma_F = \Gamma_1 + \Gamma_2$ is now added to the single-band Hamiltonian as a complex shift. Given the translational symmetry of this Hamiltonian, we added the shift to the diagonal in the representation of the cyclic basis $|\sigma\kappa\rangle$ in Eq. (B2), as $-i\Gamma_F(\sigma)/2$. The eigenvalues of the FB operator are no longer unitary and the quasienergy E_j has a complex part $-i\Gamma_j/2$. We analyzed the decay rates Γ_j along with the quasienergy spacing's statistics to study how the dynamics within the first band influences the coupling to the second band. We reported the distribution $\mathbf{P}(\Gamma)$ in [16]. Here we refine our analysis and we first focus on $\mathbf{P}(\Lambda)$, with $\Lambda = \log_{10}\Gamma$, shown in Fig. 4 for some paradigmatic cases. The widths are much smaller than unity, consistently with a perturbative approach of the system, yet the lattice potential is only $V=1.5E_R$ to increase the spread of the Stark state in the second band. Moreover, the decay channels are activated by an increase of the interaction energy, which can be experimentally achieved by acting on the transversal confining potential [31] of the quasi-one-dimensional lattice, or by a Feshbach resonance [14]. In this section, $W \approx 0.02$ used in [9] is multiplied by a factor of order 10, a value that is still well within the experimental possibilities [14,32].

In Fig. 4 we compare the distribution of the decay widths for two values of F that belong to the regular (a,c) and the chaotic region (b,d). The difference in the average decay width $\langle \Lambda \rangle$ is due to the improved energy matching provided

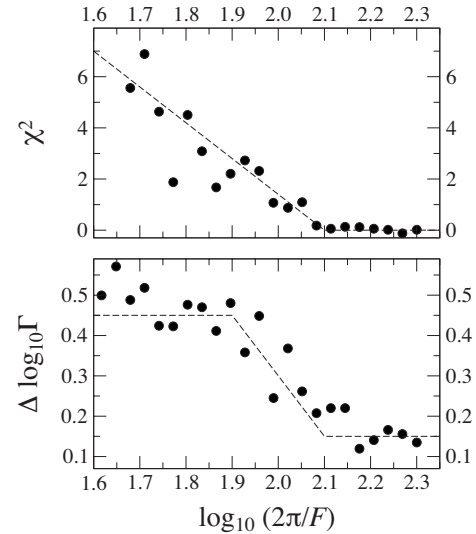


FIG. 5. (Upper panel) The χ^2 -like test for the quasienergy spacing s and (lower panel) the spread of the distribution of the decay widths Γ . The size of the system is $N=8$, $L=7$. The dashed lines are a guide to the eye and suggest that the transition to the chaotic regime can be appreciated by looking at both, the real and the imaginary parts of the FB eigenvalues.

by a stronger external field F , that supplies the necessary energy to promote particles to the second band. For the parameters of Fig. 4, the single-particle Landau-Zener formula [23] gives $\Gamma_{LZ} = F/(2\pi) \exp[-\pi^2(\varepsilon_2 - \varepsilon_1)^2/(8F)] \sim 10^{-20}$, 10^{-75} for (a,b). Then we see that there are regimes where the many-body interactions affect substantially the single-particle tunneling rates and *cannot* be neglected. Moreover, even mean-field treatments of the Landau-Zener tunneling [8,33] cannot account for several decay channels.

The *bulks* of the distributions, both in the regular and in the chaotic regime, are appropriately fit by a log-normal profile $\mathbf{P}(\Lambda) \propto \exp\{-[\ln(\Lambda - \Lambda_{\min})]^2/2\Delta\Lambda^2\}/(\Lambda - \Lambda_{\min})$. We notice that the spread $\Delta\Lambda$ is reduced in the chaotic case, where the Fock states are strongly mixed by the dynamics and a fast decaying Fock state (in the $|\sigma\kappa\rangle$ representation) could be a privileged decay channel for *many* eigenstates of the system. Many eigenstates then shared similar decay widths and their statistical distribution would be thinner. Following this reasoning, we interpret the thinner distributions found in the panels (b) and (d) of Fig. 4 as a signature of the strongly correlated dynamics.

This picture is supported by Fig. 5, where the dependence on F of the spread $\Delta\Lambda$ (lower panel) is confronted with the regular-chaotic transition evidenced by the χ^2 -like test of Eq. (5) (upper panel). The shrinking of the decay widths distribution goes along with the transition, though the precise determination of a transition point is precluded by a substantial amount of noise. The finite size of the samples that can be managed numerically accounts for the noise, as we verified that the profile becomes sharper while increasing the size of the system. Moreover, since the average decay width decreases with smaller F , we need a more precise and hence a more time-expensive numerical computation to determine $\Delta\Lambda$ as we enter the chaotic regime.

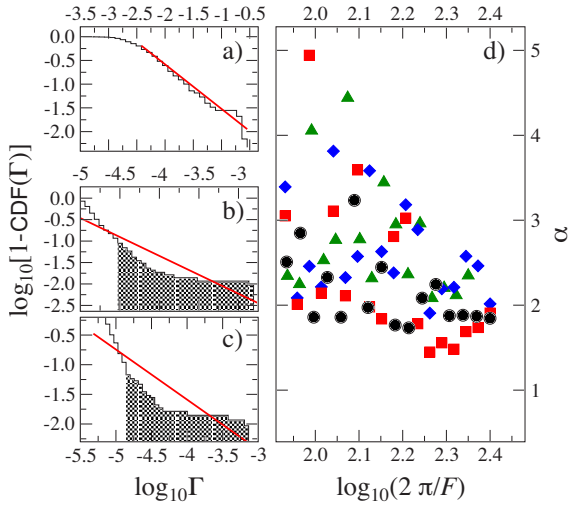


FIG. 6. (Color online) (a)–(c) Left-hand side of Eq. (23) in the regular (a) and in the chaotic regime (b,c), for a system with $N=8$, $L=7$. The dashed area in panels (b,c) shows the part of the histogram where the total amount of points is about 40, less than 10% of the full sample. The red solid line is the linear fit to the profile in the scaling region. (d) The exponent of the power law $\mathbf{P}(\Gamma) \sim \Gamma^{-\alpha}$ as obtained from the linear fits shown in (a)–(c), for $N=8$, $L=7$ (black circles), $N=8$, $L=5$ (red squares), $N=7$, $L=8$ (blue diamonds), $N=7$, $L=5$ (green pyramids). To show together different data sets we horizontally translated the first by +0.1 and the last by -0.05 .

Finally, we found in [16] that the tails of the distributions in the chaotic case follow the expected power law for the diffusive regime of an open quantum chaotic system. In our case, the opening of the ground band subsystem is defined by the interband coupling, which in a sense attaches “leads” to all lattice sites within the sample. Indeed, the inset of Fig. 4(d) shows that the log-normal is not a good fit to the tails in the chaotic regime: the distributions transform to a power law $\mathbf{P}(\Gamma) \sim \Gamma^{-\alpha}$ in close analogy to the transition from Anderson localized to diffusive dynamics in open disordered systems [34,35]. In particular we found $\alpha \approx 2$, in accordance with the general results of [36]. In Fig. 6, panel (d) we show that this value is indeed peculiar to the chaotic regime, and strong fluctuations with F mean that the exponent α is not defined within the transition region. Here we evaluate the integrated profile

$$1 - \text{CDF}(\Gamma) \sim 1 - \int \Gamma \mathbf{P}(\Gamma') d\Gamma' \sim \Gamma^{1-\alpha}, \quad (23)$$

and fit the latter to reduce the statistical fluctuations due to the finiteness of our samples. The finite-size effects are more relevant in the chaotic case [panels (b) and (c)], because the reduced spread of the distribution makes the fit sensible to the few points that fall in the further part of the tail (shaded in the pictures). The largest analyzed sample has only ≈ 400 energy levels, yet the uncertainty on $\alpha \approx 2$ on the chaotic side of the transition is less than 10%.

V. CONCLUSIONS

We studied the problem of a many-body atomic system in a tilted optical lattice, using a statistical analysis of the com-

plete quantum spectrum. We extended previous work [9,10,16] and verified thoroughly the transition from a regular to a quantum chaotic spectrum, found in [10] as the Stark field is varied. The transition takes place when the tunneling amplitude in the lattice becomes comparable to the interaction energy of the atoms. In this regime it is not possible to find a set of quantum numbers that decompose the spectrum into subspaces not mixed by a change of the Stark field. Because of the strong mixing of the energy eigenstates, many avoided crossings are found in the spectrum and the statistical analysis of the energy spacing’s show a characteristic depletion of small spacing’s—a signature of quantum chaos.

We derived a reasonable two-band model, on the basis of which we opened the ground band subsystem by a perturbative coupling of the Fock states to excited Stark states. We obtained the set of decay rates from the complex-valued quasienergies of the FB operator. We analyzed the real part of the quasienergies and verified that the transition from the regular to the chaotic regime is still visible and not much modified with respect to the one-band system. Moreover, we analyzed the statistical distribution of the imaginary part of the quasienergies, i.e., the decay rates of the states in the ground band. We found that the distributions of the decay rates become thinner as the regular-chaotic transition is crossed. We believe that thinner distributions of the decay rates are a signature of the complex dynamics, where a few strongly decaying states act as leading decay channels. The statistical characterization of the tunneling rates could be used to compute the expected atomic current from the ground band to the excited band of the lattice, thus providing an experimental probe for the regular-chaotic transition. Time-dependent observables could possibly be computed also with advanced mean-field techniques as reported in Ref. [37], as long as no full spectral information of the many-body system is wanted.

Of course, a deeper investigation is desirable to understand on quantitative grounds the full interplay of the dynamics within the first band and the decay toward higher bands, and a more detailed analysis of the interband coupling will be worthwhile in a full-blown model in which at least two bands are completely included. Our results are a step in this direction of studies of regimes in which both “horizontal” and “vertical” quantum transport are simultaneously present and influence each other in a complex manner.

ACKNOWLEDGMENTS

The authors thank Alexey Ponomarev, Gregor Veble, and Andrey Kolovsky for lively discussions on the Wannier-Stark system and quantum chaos and Yan Fyodorov for bringing attention to Ref. [36]. The authors are grateful to the Centro di Calcolo, Dipartimento di Fisica, Università di Pisa, for providing CPU and kind assistance, and for support by MIUR-PRIN and EU-OLAQUI. One of the authors (S.W.) furthermore acknowledges support within the framework of the Excellence Initiative by the German Research Foundation (DFG) through the Heidelberg Graduate School of Fundamental Physics (Grant No. GSC 129/1).

APPENDIX A: COMPUTATION OF THE COEFFICIENTS OF THE MANY-BODY HAMILTONIAN

The coefficients of the Hamiltonian equation (4) are given by integrals of the WF $\chi_{\ell,\alpha}$, once the expansion of Eq. (2) is substituted into Eq. (3). The WF are defined as

$$\psi_{k,\alpha}(x) = \sqrt{\frac{1}{2\pi}} \sum_{\ell} e^{i\pi\ell k} \chi_{\ell,\alpha}(x). \quad (\text{A1})$$

From the definition it follows that $\chi_{\ell,\alpha}(x) = \chi_{\alpha}(x - \ell a)$, so that all the Bloch waves for a band can be computed starting from a *single* Wannier function χ_{α} . We computed the WF following the method introduced in [38]. A Bloch wave is factorized as $\psi_{k,\alpha}(x) = e^{ikx} u_{k,\alpha}$, where the periodic function $u_{k,\alpha}(x) = u_{k,\alpha}(x+a)$ is expanded in a truncated basis of momenta using multiples of $2\pi j/a$ only,

$$u_{k,\alpha}(x) = \sum_{j=-Q}^{Q-1} u_j(\alpha, k) \frac{1}{\sqrt{a}} e^{i2jx}. \quad (\text{A2})$$

Using a gauge transform ($p \rightarrow -i\partial_x + k$), an effective Hamiltonian for the periodic $u_{k,\alpha}$ is derived from Eq. (1). We solved the effective Schrödinger equation as a linear system for $u_j(k, \alpha)$ with dispersion law $E_{k,\alpha}$ as eigenvalues. We obtained the on-site energies and the hopping amplitudes from the Fourier transform of $E_{k,\alpha}$

$$\varepsilon_{\alpha} = \frac{1}{2} \int_{-1}^{+1} E_{k,\alpha} dk, \quad J_{\alpha} = - \int_{-1}^{+1} E_{k,\alpha} e^{i\pi k} dk. \quad (\text{A3})$$

The WF is finally computed from the inversion of Eq. (A1). The relative phase of the eigenvectors $u_j(k, \alpha)$, for different quasimomenta, is not unique. For the simple case of a sinusoidal lattice potential, the correct choice of the phases can be inferred from [38],

$$u_j(k, 1) \rightarrow |u_j(k, 1)|, \quad u_j(k, 2) \rightarrow |u_j(k, 2)| \text{sgn}(2j + k). \quad (\text{A4})$$

This phase choice guarantees the correct inversion symmetry $\chi_{\alpha}(-x) = (-1)^{\alpha-1} \chi_{\alpha}(x)$ of the WF of the first and of the second band, respectively. The interaction coefficients for Eq. (4) read as

$$W_{\alpha} = W \int_{-\infty}^{\infty} \chi_{\alpha}^4 dx, \quad W_{\times} = W \int_{-\infty}^{\infty} \chi_1^2 \chi_2^2 dx. \quad (\text{A5})$$

The WF are an orthogonal set of functions, so that different bands are decoupled in the one-body dynamics. The tilting potential Fx has nonvanishing ‘‘dipole’’ matrix elements that couples adjacent bands,

$$d_F = \int_{-\infty}^{\infty} \chi_1(x) x \chi_2(x) dx. \quad (\text{A6})$$

APPENDIX B: COMPUTATION OF THE FLOQUET-BLOCH OPERATOR

The Fock states $|\vec{n}\rangle$ are defined by the sequence of occupation numbers $\{n_{\ell,\alpha}\}_{\ell=1}^L$ for the L sites of the lattice, in each band α . The cyclic boundary conditions, $n_{0,\alpha} = n_{L,\alpha}$ allow us to define a shift operator \hat{S} [10] that translates the occupation numbers of a Fock state $|n\rangle$,

$$\hat{S}^m |n\rangle = |\dots, n_{1-m,\alpha}, \dots, n_{L-m,\alpha}, \dots\rangle. \quad (\text{B1})$$

The operator \hat{S} naturally decomposes the Fock space into equivalence classes of vectors generated by repeated application of \hat{S} onto a ‘‘seed’’ vector $|\sigma\rangle$ with $M(\sigma) \leq L$ such that $\hat{S}^{M(\sigma)} |n\rangle = |n\rangle$ for all the vectors $|n\rangle$ in the class. A new basis $|\sigma\kappa\rangle$ can be introduced for which the many-body quasimomentum $\kappa = j/M(\sigma)$ [$0 \leq j < M(\sigma)$], supplies a convenient label

$$|\sigma\kappa\rangle = \frac{1}{\sqrt{M(\sigma)}} \sum_{\ell=1}^{M(\sigma)} e^{i2\pi\kappa\ell} \hat{S}^{\ell} |\sigma\rangle. \quad (\text{B2})$$

The cyclic basis decomposes the Hamiltonian equation (4) into a block form that transfers to the FB operator, whence $\hat{U}_{\text{FB}} = \oplus_{j=1}^L \hat{U}_{\text{FB}}(\kappa = j/L)$ with the obvious advantage that we can diagonalize separately each block of dimension $D \leq D_H/L$. This decomposition not only leads to a substantial numerical simplification but is also of dynamical relevance [10]. Moreover, we exploited that the Hamiltonian matrix is *sparse* and we verified that the fraction of the nonzero entries is $4.0 \times D^{-1.1}$ in the limit of large Hilbert spaces $D \gg 1$.

The column c of the FB operator coincides with the column of the coefficients of the basis state of index c , evolved in time up to one Bloch period. We used a fourth-order Runge-Kutta time integrator with adaptive step size, tuned in precision by the upper bound ε of the estimated one-step error [28]. The value of ε was chosen to suppress, up to T_B , the well-known exponential instability of the Runge-Kutta method applied to the Schrödinger equation. The quantity $Q(E, E') \equiv (\sum_i |E_i - E'_i|^2 / D^2)^{1/2}$ was used to compare different spectra $\{E\}$, $\{E'\}$, and we verified the consistency of our computations, finding a power-law self-convergence $Q(E^{(r)}, E^{(r-1)}) \propto \varepsilon_r^{1.2}$ for a sequence of tests with increasing required precision, $\{\varepsilon_r\}_r \rightarrow 0$. The achieved precision scales with CPU time t as $Q \propto t^{-6.1}$. A precision up to 10^{-11} was necessary to reliably compute the small complex part in the eigenvalues of the FB operator, analyzed in Sec. IV.

- [1] J. Hecker Denschlag, J. E. Simsarian, H. Häffner, C. McKenzie, A. Browaeys, D. Cho, K. Helmerson, S. L. Rolston, and W. D. Phillips, *J. Phys. B* **35**, 3095 (2002); I. Bloch, *ibid.* **38**, S629 (2005); O. Morsch and M. Oberthaler, *Rev. Mod. Phys.* **78**, 179 (2006).
- [2] M. Scully and G. Rempe, *Advances in Atomic, Molecular, and Optical Physics* (Academic, Amsterdam, 2006), Vol. 53.
- [3] E. E. Mendez, F. Agullo-Rueda, and J. M. Hong, *Phys. Rev. Lett.* **60**, 2426 (1988); J. Feldmann, K. Leo, J. Shah, D. A. B. Miller, J. E. Cunningham, T. Meier, G. von Plessen, A. Schulze, P. Thomas, and S. Schmitt-Rink, *Phys. Rev. B* **46**, 7252 (1992); K. Leo, *High-Field Transport in Semiconductor Superlattices* (Springer, Berlin, 2003).
- [4] T. Pertsch, P. Dannberg, W. Elflein, A. Bräuer, and F. Lederer, *Phys. Rev. Lett.* **83**, 4752 (1999); R. Morandotti, U. Peschel, J. S. Aitchison, H. S. Eisenberg, and Y. Silberberg, *ibid.* **83**, 4756 (1999); M. Ghulinyan, C. J. Oton, Z. Gaburro, L. Pavesi, C. Toninelli, and D. S. Wiersma, *ibid.* **94**, 127401 (2005).
- [5] M. Ben Dahan, E. Peik, J. Reichel, Y. Castin, and C. Salomon, *Phys. Rev. Lett.* **76**, 4508 (1996); S. R. Wilkinson, C. F. Bharucha, K. W. Madison, Q. Niu, and M. G. Raizen, *ibid.* **76**, 4512 (1996); B. P. Anderson and M. A. Kasevich, *Science* **282**, 1686 (1998).
- [6] O. Morsch, M. Cristiani, J. H. Müller, D. Ciampini, and E. Arimondo, *Phys. Rev. A* **66**, 021601(R) (2002); O. Morsch, J. H. Müller, M. Cristiani, D. Ciampini, and E. Arimondo, *Phys. Rev. Lett.* **87**, 140402 (2001).
- [7] G. Roati, E. de Mirandes, F. Ferlaino, H. Ott, G. Modugno, and M. Inguscio, *Phys. Rev. Lett.* **92**, 230402 (2004).
- [8] C. Sias, A. Zenesini, H. Lignier, S. Wimberger, D. Ciampini, O. Morsch, and E. Arimondo, *Phys. Rev. Lett.* **98**, 120403 (2007).
- [9] A. Buchleitner and A. R. Kolovsky, *Phys. Rev. Lett.* **91**, 253002 (2003).
- [10] A. R. Kolovsky and A. Buchleitner, *Phys. Rev. E* **68**, 056213 (2003).
- [11] A. R. Kolovsky, *Phys. Rev. Lett.* **90**, 213002 (2003).
- [12] A. V. Ponomarev, J. Madroñero, A. R. Kolovsky, and A. Buchleitner, *Phys. Rev. Lett.* **96**, 050404 (2006).
- [13] M. Greiner, O. Mandel, T. Esslinger, T. W. Hänsch, and I. Bloch, *Nature (London)* **415**, 39 (2002); O. Mandel, M. Greiner, A. Widera, T. Rom, T. W. Hänsch, and I. Bloch, *ibid.* **425**, 937 (2003); F. Gerbier, S. Fölling, A. Widera, O. Mandel, and I. Bloch, *Phys. Rev. Lett.* **96**, 090401 (2006).
- [14] I. Bloch, J. Dalibard, and W. Zwerger, *Rev. Mod. Phys.* (to be published), e-print arXiv:0704.3011v1.
- [15] P. Buonsante, R. Franzosi, and V. Penna, *Phys. Rev. Lett.* **90**, 050404 (2003); *J. Phys. B* **37**, S229 (2004); M. Hiller, T. Kottos, and T. Geisel, *Phys. Rev. A* **73**, 061604(R) (2006).
- [16] A. Tomadin, R. Mannella, and S. Wimberger, *Phys. Rev. Lett.* **98**, 130402 (2007).
- [17] M. P. A. Fisher, P. B. Weichman, G. Grinstein, and D. S. Fisher, *Phys. Rev. B* **40**, 546 (1989).
- [18] S. Sachdev, K. Sengupta, and S. M. Girvin, *Phys. Rev. B* **66**, 075128 (2002).
- [19] V. W. Scarola and S. Das Sarma, *Phys. Rev. Lett.* **95**, 033003 (2005).
- [20] W. Zwerger, *J. Opt. B: Quantum Semiclassical Opt.* **5**, S9 (2003); R. Roth and K. Burnett, *ibid.* **5**, S50 (2003); M. Rigol and A. Muramatsu, *Phys. Rev. Lett.* **93**, 230404 (2004); A. M. Rey, G. Pupillo, C. W. Clark, and C. J. Williams, *Phys. Rev. A* **72**, 033616 (2005); G. Mazzarella, S. M. Giampaolo, and F. Illuminati, *ibid.* **73**, 013625 (2006).
- [21] S. R. Clark and D. Jaksch, *New J. Phys.* **8**, 160 (2006); M. Hild, F. Schmitt, and R. Roth, *J. Phys. B* **39**, 4547 (2006).
- [22] O. E. Alon, A. I. Streltsov, and L. S. Cederbaum, *Phys. Rev. Lett.* **95**, 030405 (2005); **97**, 230403 (2006).
- [23] M. Glück, A. R. Kolovsky, and H. J. Korsch, *Phys. Rep.* **366**, 103 (2002).
- [24] T. Müller, S. Fölling, A. Widera, and I. Bloch, *Phys. Rev. Lett.* **99**, 200405 (2007).
- [25] D. Jaksch, C. Bruder, J. I. Cirac, C. W. Gardiner, and P. Zoller, *Phys. Rev. Lett.* **81**, 3108 (1998).
- [26] A. R. Kolovsky and A. Buchleitner, *Europhys. Lett.* **68**, 632 (2004); A. R. Kolovsky, *New J. Phys.* **8**, 197 (2006).
- [27] F. Haake, *Quantum Signatures of Chaos* (Springer, Berlin, 2001).
- [28] W. H. Press, S. A. Teukolsky, W. T. Vetterling, and B. P. Flannery, *Numerical Recipes* (Cambridge University Press, Cambridge, 1993).
- [29] T. Prosen and M. Robnik, *J. Phys. A* **26**, 2371 (1993).
- [30] M. Mehta, *Random Matrices and the Statistical Theory of Energy Levels* (Academic, New York, 1991).
- [31] T. Bergeman, M. G. Moore, and M. Olshanii, *Phys. Rev. Lett.* **91**, 163201 (2003).
- [32] M. Köhl, H. Moritz, T. Stöferle, K. Günter, and T. Esslinger, *Phys. Rev. Lett.* **94**, 080403 (2005).
- [33] S. Wimberger, R. Mannella, O. Morsch, E. Arimondo, A. R. Kolovsky, and A. Buchleitner, *Phys. Rev. A* **72**, 063610 (2005); S. Wimberger, P. Schlagheck, and R. Mannella, *J. Phys. B* **39**, 729 (2006); D. Witthaut, E. M. Graefe, and H. J. Korsch, *Phys. Rev. A* **73**, 063609 (2006); D. Witthaut, E. M. Graefe, S. Wimberger, and H. J. Korsch, *ibid.* **75**, 013617 (2007).
- [34] T. Kottos, *J. Phys. A* **38**, 10761 (2005).
- [35] S. Wimberger and A. Buchleitner, *J. Phys. A* **34**, 7181 (2001); S. Wimberger, A. Krug, and A. Buchleitner, *Phys. Rev. Lett.* **89**, 263601 (2002).
- [36] Y. V. Fyodorov and H. Sommers, *JETP Lett.* **63**, 1026 (1996).
- [37] A. I. Streltsov, O. E. Alon, and L. S. Cederbaum, *Phys. Rev. Lett.* **99**, 030402 (2007).
- [38] J. C. Slater, *Phys. Rev.* **87**, 807 (1952).

PHYSICAL REVIEW A 77, 041606(R) (2008)

Engineering many-body quantum dynamics by disorderPierfrancesco Buonsante¹ and Sandro Wimberger^{1,2}¹*CNISM – Dipartimento di Fisica, Politecnico di Torino, Corso Duca degli Abruzzi 24, 10129 Torino, Italy*²*Institut für Theoretische Physik, Universität Heidelberg, Philosophenweg 19, 69120 Heidelberg, Germany*

(Received 1 June 2007; published 15 April 2008)

Going beyond the currently investigated regimes in experiments on quantum transport of ultracold atoms in disordered potentials, we predict a crossover between regular and quantum-chaotic dynamics when varying the strength of disorder. Our spectral approach is based on the Bose-Hubbard model describing interacting atoms in deep random potentials. The predicted crossover from localized to diffusive dynamics depends on the *simultaneous* presence of interactions and disorder and can be verified in the laboratory by monitoring the evolution of typical experimental initial states.

DOI: [10.1103/PhysRevA.77.041606](https://doi.org/10.1103/PhysRevA.77.041606)

PACS number(s): 03.75.Kk, 05.45.Mt, 61.43.-j, 71.35.Lk

While well-controlled experiments in solid-state systems are lacking, the recent advances in atom and quantum optics allow the experimentalist to study minimal models where single-particle dynamics, many-body interactions, and disorder can be engineered at will. Ultracold bosons or fermions loaded into optical lattices, which realize spatially periodic potentials [1], are optimally suited to study, e.g., quantum transport across disorder potentials and possible manifestations of Anderson localization in the mean-field regime [2,3]. Moreover, modern experiments reach the regime of strong atom-atom correlations to investigate many-body quantum effects such as interaction-driven phase transitions [1,4] or interaction-induced changes of Landau-Zener tunneling rates [5,6].

The Bose-Hubbard model well describes ultracold bosons in periodic lattices at small fillings (where a mean-field theory is obviously bound to fail) and not too shallow lattice depths [1,4,7,8]. A recent study of an open Bose-Hubbard system [6] furthermore showed that many-body interactions lead to similar decay-rate distributions as predicted for single-particle transport in disordered potentials. More precisely, interactions in a many-body system can substitute for disorder in the diffusive regime of quantum transport [6].

Here we show how to engineer the dynamical properties of a many-body Bose-Hubbard system by varying the strength of static disorder. We predict that, for an intermediate regime of disorder strength, the system shows clear signature of *global* quantum chaos. The latter is quantified by spectral measures of quantum chaos [6–10] and transport [11–13]. Complexity arises in our systems from the *simultaneous* presence of atom-atom interactions and disorder.

We consider a disordered Bose-Hubbard system on a one-dimensional (1D) lattice [14] comprising L sites, defined by the Hamiltonian

$$H = \sum_{\ell=1}^L [U a_{\ell}^{\dagger 2} a_{\ell}^2 - J(e^{i\theta} a_{\ell}^{\dagger} a_{\ell+1} + \text{H.c.}) + \epsilon_{\ell} a_{\ell}^{\dagger} a_{\ell}]. \quad (1)$$

The operators a_{ℓ}^{\dagger} , a_{ℓ} create and destroy bosons at lattice site ℓ , respectively. The random on-site potentials, $\{\epsilon_{\ell}\}$, are chosen from a box distribution in $[-\epsilon/2, \epsilon/2]$. The deterministic Peierls phase θ in the kinetic term corresponds to a finite (angular) momentum of the lattice or, equivalently, to the

presence of a (effective) magnetic potential [15], and mathematically to imposing different boundary conditions, *twisted* as opposed to simply periodic, onto the standard model, Eq. (1) with $\theta=0$ [13]. Phases could be controlled experimentally as described in [16], while the periodic boundary conditions assumed for Eq. (1) in the following could be implemented in optical ring lattices [16,17]. The effects of $\{\epsilon_{\ell}\}$ and θ are in some sense complementary. This can be understood switching to the Fock basis of the quasi-momentum (QM) operators $b_{\kappa} = L^{-1/2} \sum_{\ell} a_{\ell} e^{i2\pi\ell\kappa/L}$ [8,18], diagonalizing the kinetic term in Eq. (1). In this reciprocal basis, the interaction term is block-diagonal, the blocks being labeled by the total QM $= \sum_{\kappa} \kappa b_{\kappa}^{\dagger} b_{\kappa} \text{ mod}(L)$, where the mod operation guarantees a QM in the unit interval. Conversely, the local potential term, $\{\epsilon_{\ell}\}$, couples blocks of different QM, since it corresponds to a sum of nonlocal operators $b_{\kappa}^{\dagger} b_{\eta}$ [18]. Any such operator couples blocks whose total QM differs by $(\kappa - \eta)$ units, and since $b_{\kappa}^{\dagger} b_{\kappa}$ is a number operator, the coupling within each block reduces to a trivial constant. Hence $\{\epsilon_{\ell}\}$ induces interblock couplings, while θ affects the diagonal blocks of fixed QM.

We are interested in the global dynamics generated by Eq. (1). Our approach to characterize the quantum transport in the system is twofold: first, we study the spectral properties of Eq. (1), and second, we present results of the time-evolution of initial states which are not eigenstates of Eq. (1). The evolution of typical experimental observables, such as the spatial population and the mean momentum of the condensate particles [1,3,4], allows one to directly probe the here predicted diffusion-localization transition (DLT). In contrast to [19], we do not just focus on the regime of small disorder $\epsilon \ll J$, and we include θ to generalize the assumed periodic boundary conditions.

For the case without disorder and filling factors of order one, a crossover between regular and quantum chaotic spectra was predicted in [8] when varying the ratio U/J . Quantum chaotic spectra are identified by their statistics, more precisely the distribution $P(s)$ of the normalized level spacings $s \equiv \Delta E / \overline{\Delta E}$ follows a Wigner-Dyson (WD) distribution [8]. Also by adding a linear force to the Hamiltonian, a transition between regular and chaotic motion can be identified by a crossover from Poisson to WD statistics [6,7], corresponding to a regime of strong (Stark) localization or of

PIERFRANCESCO BUONSANTE AND SANDRO WIMBERGER

PHYSICAL REVIEW A 77, 041606(R) (2008)

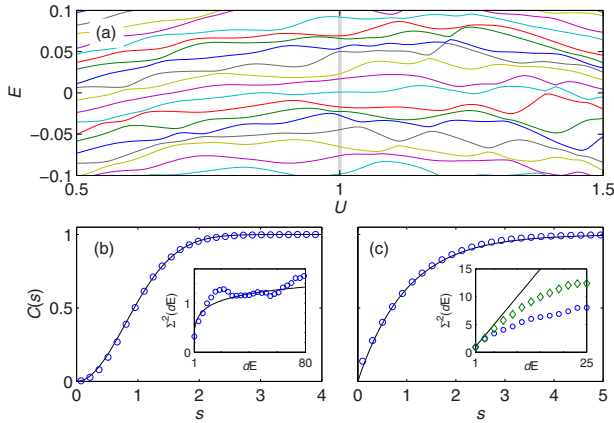


FIG. 1. (Color online) (a) Sector of the spectrum in the band center as a function of U , for $N=3, L=15, J=1$, and $\theta \approx 0.119$ for $\epsilon=1$ (a linear function of U was added to E to eliminate an overall trend). (b) $C(s)$ (obtained from collecting levels of 25 disorder realizations) and Σ^2 (for one realization in the inset) at $U=1$, corresponding to the WD prediction (solid lines). (c) Same as in (b) but for a regular case with $N=3, L=15$ (\circ), 20 (\diamond), $U=1=J$, and $\epsilon=10, \theta=0$, together with the Poisson predictions (solid lines).

quantum chaos, respectively. Based on translational invariance, most previous results [6–8] concern a subset of states with constant (conserved) QM. Since in the experiment it is generally hard to focus on a subset of states taking part in the dynamical evolution, it is desirable and more general to search for *global* quantum chaos, which is not just restricted to independent subsets of the system’s eigenvalue spectrum, e.g., corresponding to constant QM. Disorder (which cannot be completely avoided in any real system) naturally breaks the translation invariance [19], and we will show that the dynamics of a dilute boson system (induced by its spectral properties) can be controlled by the combined action of atom-atom interactions and the random potential in Eq. (1).

For a complex spreading of the system’s eigenfunctions in the eigenbases of the integrable cases ($J=0=\epsilon$) and ($U=0=\epsilon$), the energy scales defined by the terms in Eq. (1) should be roughly of the same order of magnitude, i.e., $J \sim U \sim \epsilon$. For such a situation and small filling, we indeed found clear signatures of *global* quantum chaos in the system. Our results are shown in Fig. 1, which collects avoided crossing scenarios of the energy levels (a), the cumulative distribution $C(s) \equiv \int_0^s ds' P(s')$, and the number variance Σ^2 of the energy levels (which measures the long-range correlations in the spectrum [10]) in 1(b) and 1(c). Both $C(s)$ and Σ^2 agree well with the WD predictions for a Gaussian orthogonal ensemble of random matrices [7–10]. Residual symmetries of Eq. (1) (e.g., a reflection symmetry for special values of the number of atoms N and the system size L [8]) can be destroyed by $\theta \neq 0$.

Our results of Figs. 1 and 2 depend on the procedure chosen to unfold the energy spectrum (i.e., to make the density of states approximately constant), which is necessary to compare to the normalized theoretical predictions [8,10]. We used a rescaling of the levels by the numerically obtained local density of the raw data, which is independent of further assumptions on the original level density. Choosing a small

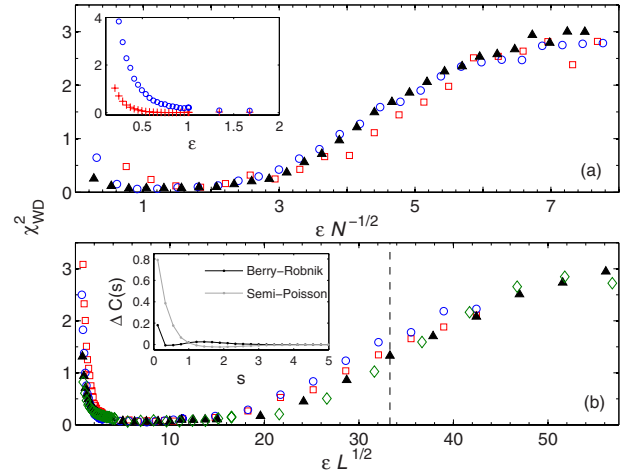


FIG. 2. (Color online) (a) and (b) χ^2 statistical test [23] (with values close to zero for good WD statistics) as a function of the *scaled* disorder parameter, for (a) $L=15$ and $N=2$ (\square), 3 (\circ), 4 (\blacktriangle), and (b) for $N=4$ and $L=8$ (\square), 10 (\circ), 14 (\blacktriangle), 17 (\diamond), at $J=1=U, \theta=0$. The inset in (a) shows a zoom of $N=3$ for small ϵ , $\theta=0$ (\circ) and $\theta=0.119$ ($+$). Each data point is averaged over 20 disorder realizations. The inset in (b) shows the relative deviation for the marked point in the crossover regime (dashed line) from two heuristic interpolating laws between WD and Poisson: Semi-Poisson (gray) [21] and Berry-Robnik [22] (black). As expected [21,22], correspondence is not perfect with either of those laws, but the Berry-Robnik lies closer overall.

window (over 5–10 levels) for computing the local average permits an optimal match on smaller scales, while larger windows (over 20–40 levels) are chosen to compute the number variance. Our analysis considered all levels of a given spectrum at fixed parameters, and we checked that excluding levels at the band edges does not change our results, as long as we stay in the dilute limit of $UN/L \leq 1$.

For $\epsilon \leq 0.5$ and $\epsilon \gg 1$, we observed a trend towards globally regular dynamics, a consequence of good, yet not perfect Poisson statistics. In the limit $\epsilon \rightarrow 0$, the various QM blocks uncouple, and as exercised in [6–8] one has to concentrate just on one of these blocks in the spectral analysis. Any small $\epsilon \neq 0$, however, destroys the translation invariance, making an analysis of the *full* spectrum quite intricate. We therefore concentrate for a moment on the case of large disorder. As shown in Fig. 1(c), this limit is well-characterized by a Poisson distribution. This result is expected, since the eigenstates become pinned at the randomly distributed minima of the potential, leading to a small residual overlap between them. Of course, for finite U and L , such a localization cannot be perfect [14]. Indeed, we observe a better correspondence in our system with the Poisson prediction [see inset of Fig. 1(c)] for smaller fillings, consistent with single-particle localization theory [20]. This trend was observed when increasing $L < 20$ at fixed $N=3$ and 4 , or when decreasing $1 < N \leq 4$ at fixed $10 < L < 20$.

The DLT occurs for all data sets shown in Fig. 2 at a critical value $\epsilon_{cr} \approx 4$. We characterize this crossover by a χ^2 statistical test [23], which measures the deviation from WD. The saturation of our χ^2_{WD} measure for large ϵ , at the right of

ENGINEERING MANY-BODY QUANTUM DYNAMICS BY ...

PHYSICAL REVIEW A 77, 041606(R) (2008)

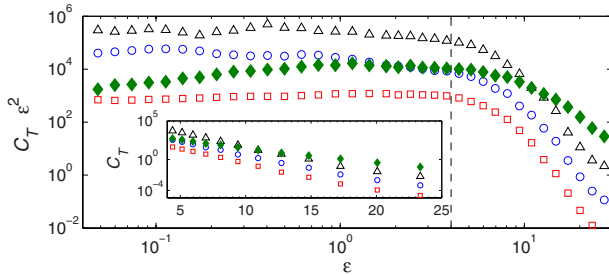


FIG. 3. (Color online) Level curvature C_T as a function of the disorder strength for $N=2$ (\square), 3 (\circ), 4 (\triangle), and $J=1=U$, $\theta=0$, $L=15$. Two different scalings are chosen to highlight the DLT around the dashed line. Increasing the filling (particularly for $N=4$, $L=10$, shown as closed diamonds) leads to deviations from the single-particle scalings for both small and large disorder.

the graphs in Fig. 2, signals the convergence to a Poisson distribution, an example of which is explicitly shown in Fig. 1(c). For fixed N and L , ϵ_{cr} scales linearly with $U=J$, as expected since our Hamiltonian in Eq. (1) is scale invariant for a given realization of disorder (i.e., $U=J$ defines the energy scale for ϵ). At fixed $U=J$, the crossover to the localized regime depends on the filling, and our results from Fig. 2 suggest the following functional form $\chi_{WD}^2(x)$, with $x \equiv \epsilon\sqrt{L/N}$, in the range $\epsilon \approx 4-15$. It is numerically hard to obtain a full scaling function for interacting systems with larger N and L , since it is necessary to diagonalize the full system, not just one QM block as in [6–8].

Interestingly, our spectral analysis of Figs. 1 and 2 does not show a dependence on θ in the localized regime ($\epsilon \geq 4$), while especially for $\epsilon \leq 1$ [see inset of Fig. 2(a)] both couplings by $\theta \neq 0$ and by $\epsilon \neq 0$ can conspire to enhance the quantum chaotic properties of the *full* spectrum (i.e., not only of a subblock of fixed QM). We therefore can use, to some extent, both parameters as independent handles to change the *global* spectral properties.

The dependence of the spectrum on the choice of the boundary conditions defined by θ is reminiscent of the Thouless conductance, another prominent measure to characterize the transition between extended and localized states [12]. We computed the Thouless conductance, which essentially is given by the curvature $C_T \equiv \langle |d^2E/d\theta^2| \rangle \approx \langle |2[E(\theta) - E(0)]/\theta^2| \rangle$, for $\theta \rightarrow 0$ [11,13], which was geometrically averaged [11] over the full spectrum and 40 realizations of disorder. Our results are shown in Fig. 3. In contrast to the distributions of nearest level spacings, where the small but finite mixing of QM blocks at $\epsilon \rightarrow 0$ does not allow one to characterize well the true type of dynamical regime, the curvature is a *local* property of the spectrum. Hence in the diffusive limit $\epsilon \rightarrow 0$, we find the expected divergence $C_T \propto \epsilon^{-\alpha}$, with $\alpha \approx 2-1.8$ ($N=2-4$, $L=15$) and $\alpha \approx 1.3$ ($N=4$, $L=10$). In analogy to Fig. 2, the crossover between the diffusive (quantum chaotic) and the localized regime sets in at $\epsilon_{cr} \approx 4$. For $\epsilon \geq 4$, our results confirm an exponential scaling (typical of finite-size localized systems) $C_T \propto \exp(-\text{const } \epsilon^\beta)$, with $\beta \approx 0.8$ ($N=2-4$, $L=15$) and $\beta \approx 0.5$ ($N=4$, $L=10$). The systematic deviation of both exponents from the single-particle predictions ($\alpha=2$ and β

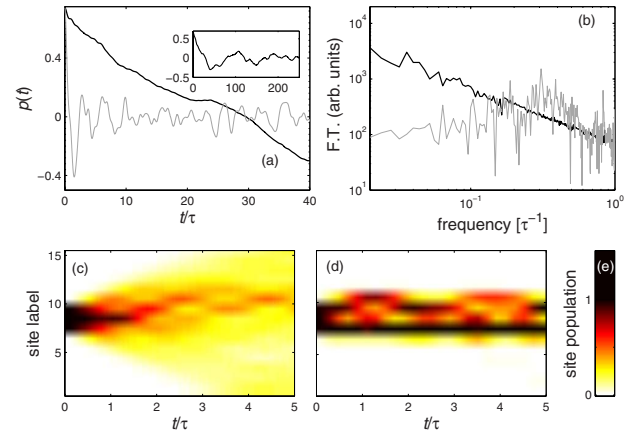


FIG. 4. (Color online) (a) $p(t)$ for a three particle initial state with fixed QM, for $L=15$, $J=1=U$, $\theta=0$, and (b) Fourier transforms of the curves from (a), for $\epsilon=1$ (thick lines) and $\epsilon=10$ (thin gray lines). The evolution of the well populations for a box initial state of $N=3$ atoms in real space is shown in (c) for $\epsilon=2$ and in (d) for $\epsilon=10$ [same parameters as in (a), color code defined in (e)]. The time unit is $\tau=2\pi\hbar/J[E_R] \approx 15$ ms [7], for a lattice constant of the order 412 nm and a lattice depth of ten recoil energies E_R for ^{87}Rb atoms [1,4]. The inset in (a) highlights the slow decay for $\epsilon=1$.

$=1$ [11]) with increasing filling factor highlights the structural change of the level dynamics in the presence of atom-atom interactions.

In the following, we focus on experimentally observable consequences of the spectral analysis presented so far. Figure 4 shows the temporal evolution of initial states, typically prepared in experiments with Bose-Einstein condensates. Panel (a) presents the mean momentum on the lattice [7,13,19], defined as

$$p(t) \equiv \frac{1}{2iN} \langle \psi(t) | \sum_{\ell} (a_{\ell}^{\dagger} a_{\ell-1} - \text{H.c.}) | \psi(t) \rangle$$

$$= \frac{1}{N} \langle \psi(t) | \sum_{\kappa} \sin\left(\frac{2\pi\kappa}{L}\right) b_{\kappa}^{\dagger} b_{\kappa} | \psi(t) \rangle, \quad (2)$$

in the direct and reciprocal space, respectively, for $|\psi(t=0)\rangle = (b_{\kappa}^{\dagger})^N |0\rangle / \sqrt{N!}$, with $\kappa=2$. For strong disorder, the momentum decays almost instantaneously to zero, and is further characterized by small, random fluctuations. The quantum chaotic behavior for $\epsilon=1$ is visible in the strongly correlated large-scale fluctuations, characterized by a slowly, algebraically decaying Fourier transform of the time series $p(t)$, cf. Fig. 4(b). The latter implies a large number of modes being present in the evolution of $p(t)$, a standard signature of complex dynamics [24]. Complex transport behavior was predicted also in [25] by analyzing the power spectrum of oscillations in a three-well system. In contrast to Figs. 4(a) and 4(b), Figs. 4(c) and 4(d) show the real space dynamics of a box-distributed initial state with one atom in wells $\ell=7, 8$, and 9 and none elsewhere. While the chaotic mixing of all wells dominates for $\epsilon=2$, in the localized regime $\epsilon=10$ we observe the expected strong pinning at the random minima of the potential [particularly in the seventh well in Fig. 4(d)].

PIERFRANCESCO BUONSANTE AND SANDRO WIMBERGER

PHYSICAL REVIEW A **77**, 041606(R) (2008)

The fluctuations in the latter case arise from our finite values of U and L . For a typical realization of $\{\epsilon_\ell\}$, the evolution will be asymmetric as seen in Fig. 4(c), which allows one to distinguish it from the $\epsilon=0$ case. Equivalently, while for $\epsilon=0$ QM is conserved, for $\epsilon\neq 0$ QM starts to deviate from its initial value, which is 0 for the data in Figs. 4(c) and 4(d). Figure 4 presents the limits of fully developed global quantum chaos (without any residual symmetry in the system) and strong localization. Yet, the crossover between the two regimes is systematic, and as exemplified, even the evolution of single, reduced experimental observables of our many-body problem can be used to directly visualize the change in the quantum spectra analyzed in Figs. 1–3. Of experimental relevance is in particular the difference in the short-time evolution of $p(t)$ for experimental detection times < 1 s.

In summary, we showed how one can scan between the different dynamical regimes of the Bose-Hubbard system, characterized by global quantum chaos and by essentially localized bosons, by varying the strength of static disorder. The dynamics of initial states which are far from eigenstates

of the system could be used as a clear experimental signature of this crossover. Moreover, our analysis of the many-body level curvatures opens a new link to transport problems in mesoscopic solids [11,12] and photonic lattices [26], where global chaotic properties are accessible by conductance measurements. As adumbrated in [9], the here presented, extended, and unifying characterization of the spectral properties of a disordered many-body problem may be useful to obtain, for instance, experimentally accessible estimates for the localization properties for such complex systems. However, the necessary scaling arguments [12] as a function of N and L make such an approach challenging for up-to-date computational resources.

P.B. acknowledges support by the *Lagrange Project-CRT* Foundation and S.W. within the Excellence Initiative by the DFG through the Heidelberg Graduate School of Fundamental Physics (Grant No. GSC 129/1). We are grateful to A. Montorsi, V. Penna, P. Schlagheck, and G. Veble for useful discussions.

-
- [1] O. Morsch and M. Oberthaler, *Rev. Mod. Phys.* **78**, 179 (2006); I. Bloch *et al.*, e-print arXiv:0704.3011, *Rev. Mod. Phys.* (to be published).
- [2] See, e.g., T. Paul, P. Schlagheck, P. Leboeuf, and N. Pavloff, *Phys. Rev. Lett.* **98**, 210602 (2007); B. Shapiro, *Phys. Rev. Lett.* **99**, 060602 (2007).
- [3] J. E. Lye *et al.*, *Phys. Rev. Lett.* **95**, 070401 (2005); D. Clément *et al.*, *Phys. Rev. Lett.* **95**, 170409 (2005); C. Ford *et al.*, *Phys. Rev. Lett.* **95**, 170410 (2005); T. Schulte *et al.*, *Phys. Rev. Lett.* **95**, 170411 (2005); L. Fallani, J. E. Lye, V. Guarnera, C. Fort, and M. Inguscio, *Phys. Rev. Lett.* **98**, 130404 (2007).
- [4] M. Greiner *et al.*, *Nature (London)* **415**, 39 (2002); T. Stöferle, H. Moritz, C. Schori, M. Kohl, and T. Esslinger, *Phys. Rev. Lett.* **92**, 130403 (2004).
- [5] M. Köhl, H. Moritz, T. Stöferle, K. Günter, and T. Esslinger, *Phys. Rev. Lett.* **94**, 080403 (2005).
- [6] A. Tomadin, R. Mannella, and S. Wimberger, *Phys. Rev. Lett.* **98**, 130402 (2007); *Phys. Rev. A* **77**, 013606 (2008).
- [7] A. Buchleitner and A. R. Kolovsky, *Phys. Rev. Lett.* **91**, 253002 (2003).
- [8] A. R. Kolovsky and A. Buchleitner, *Europhys. Lett.* **68**, 632 (2004).
- [9] D. Weinmann *et al.*, *J. Phys. I* **7**, 1559 (1997).
- [10] G. Montambaux, D. Poilblanc, J. Bellissard, and C. Sire, *Phys. Rev. Lett.* **70**, 497 (1993).
- [11] G. Casati, I. Guarneri, F. M. Izrailev, L. Molinari, and K. Zyczkowski, *Phys. Rev. Lett.* **72**, 2697 (1994); D. Braun, E. Hofstetter, G. Montambaux, and A. MacKinnon, *Phys. Rev. B* **55**, 7557 (1997).
- [12] B. Kramer and A. MacKinnon, *Rep. Prog. Phys.* **56**, 1469 (1993).
- [13] B. S. Shastry and B. Sutherland, *Phys. Rev. Lett.* **65**, 243 (1990); R. Roth and K. Burnett, *Phys. Rev. A* **67**, 031602(R) (2003).
- [14] R. T. Scalettar, G. G. Batrouni, and G. T. Zimanyi, *Phys. Rev. Lett.* **66**, 3144 (1991).
- [15] See, e.g., A. M. Rey, K. Burnett, I. I. Satija, and C. W. Clark, *Phys. Rev. A* **75**, 063616 (2007).
- [16] L. Amico, A. Osterloh, and F. Cataliotti, *Phys. Rev. Lett.* **95**, 063201 (2005).
- [17] B. Mieck and R. Graham, *J. Phys. A* **37**, L581 (2004); E. Courtade, O. Houde, J. F. Clement, P. Verkerk, and D. Hennequin, *Phys. Rev. A* **74**, 031403(R) (2006).
- [18] P. Buonsante, V. Penna, and A. Vezzani, *Phys. Rev. A* **72**, 043620 (2005).
- [19] A. R. Kolovsky, *New J. Phys.* **8**, 197 (2006).
- [20] M. Feingold, S. Fishman, D. R. Grempel, and R. E. Prange, *Phys. Rev. B* **31**, 6852 (1985).
- [21] S. N. Evangelou and J.-L. Pichard, *Phys. Rev. Lett.* **84**, 1643 (2000).
- [22] T. Prosen and M. Robnik, *J. Phys. A* **26**, 2371 (1993).
- [23] W. H. Press *et al.*, *Numerical Recipes* (Cambridge University Press, Cambridge, England, 1993).
- [24] See, e.g., L. E. Reichl, *The Transition to Chaos* (Springer, New York, 2004). R. Blümel and U. Smilansky, *Phys. Rev. Lett.* **60**, 477 (1988).
- [25] D.-W. Wang, M. D. Lukin, and E. Demler, *Phys. Rev. Lett.* **92**, 076802 (2004).
- [26] T. Schwartz *et al.*, *Nature (London)* **446**, 52 (2007).

New Journal of Physics

The open-access journal for physics

Resonant tunneling of Bose–Einstein condensates in optical lattices

**Alessandro Zenesini^{1,3}, Carlo Sias^{1,2}, Hans Lignier^{1,2},
Yeshpal Singh¹, Donatella Ciampini^{1,3}, Oliver Morsch^{1,2},
Riccardo Mannella^{1,3}, Ennio Arimondo^{1,2,3}, Andrea Tomadin⁴
and Sandro Wimberger^{5,6}**

¹ Dipartimento di Fisica Enrico Fermi, Università degli Studi di Pisa,
Largo Pontecorvo 3, I-56127 Pisa, Italy

² CNR-INFM, Largo Pontecorvo 3, I-56127 Pisa, Italy

³ CNISM Unità di Pisa, Largo Pontecorvo 3, I-56127 Pisa, Italy

⁴ Scuola Normale Superiore, Piazza dei Cavalieri 7, I-56126 Pisa, Italy

⁵ Institut für Theoretische Physik, Universität Heidelberg, Philosophenweg 19,
D-69120 Heidelberg, Germany

E-mail: s.wimberger@thphys.uni-heidelberg.de

New Journal of Physics **10** (2008) 053038 (15pp)

Received 22 December 2007

Published 29 May 2008

Online at <http://www.njp.org/>

doi:10.1088/1367-2630/10/5/053038

Abstract. In this paper, we present the theoretical as well as experimental results on resonantly enhanced tunneling of Bose–Einstein condensates in optical lattices both in the linear case and for small nonlinearities. Our results demonstrate the usefulness of condensates in optical lattices for simulating Hamiltonians originally used for describing solid-state phenomena.

⁶ Author to whom any correspondence should be addressed.

Contents

1. Introduction	2
2. Theoretical description	3
2.1. Single-particle RET	3
2.2. Interacting BEC dynamics	6
3. Experimental results	8
3.1. The linear regime	10
3.2. The nonlinear regime	11
4. Conclusions and outlook	13
Acknowledgments	13
References	13

1. Introduction

In the last decade, the experimental techniques used in atom and quantum optics have made it possible to control the external and internal degrees of freedom of ultracold atoms with a very high degree of precision. Thus, ultracold bosons or fermions loaded into optical lattices are optimal realizations of lattice models proposed and studied in the context of solid-state physics. Bose–Einstein condensates (BECs), for instance, have been used to simulate phenomena such as Bloch oscillations in tilted periodic potentials [1]–[6] and to study quantum phase transitions driven by atom–atom interactions [7].

Up to now most of the quantum transport phenomena investigated with BECs within periodic optical lattices have focused on the atomic motion in the ground state band of the periodic lattice. Only a few experiments have examined the quantum transport associated with interband transitions ‘vertical’ in the energy space. Interband transitions were induced by additional electromagnetic fields, as in the case of the spectroscopy of Wannier–Stark levels [8], or by quantum tunneling between the bands. Tunneling between otherwise uncoupled energy bands occurs when the bands are coupled by an additional force, which can be a static Stark force (tilting the otherwise periodic lattice) [6], or also by strong atom–atom interactions as observed for fermions in [9] and discussed for bosons in [10]. The quantum tunneling between the ground and the first excited bands is particularly pronounced in the presence of degeneracies of the single-well energy levels within the optical lattice leading to resonantly enhanced tunneling (RET). RET is a quantum effect in which the probability for tunneling of a particle between two potential wells is increased when the energies of the initial and final states of the process coincide. Owing to the fundamental nature of this effect and the practical interest [11], in the last few years much progress has been made in constructing solid state systems such as superlattices [12]–[15], quantum wells [16] and waveguide arrays [17] which enable the controlled observation of RET. RET has also been examined theoretically for ultracold atoms trapped in an optical lattice [18]–[21].

RET-like effects have been observed in a number of experiments to date. In [22], resonant tunneling was observed for cold atoms trapped by an optical lattice when an applied magnetic field produced a Zeeman splitting of the energy levels. At certain values of the applied magnetic field, the states in the up-shifting and down-shifting energy levels were tuned into resonance with one another. This led to RET drastically altering the quantum dynamics of the system

and producing a modulation of the magnetization and lifetime of the atoms trapped by the optical lattice. Resonant tunneling has been observed in a Mott insulator within an optical lattice, where a finite amount of energy given by the on-site interaction energy is required to create a particle–hole excitation [23]. Tunneling of the atoms is therefore suppressed. If the lattice potential is tilted by application of a potential gradient, RET is allowed whenever the energy difference between neighboring lattice sites due to the potential gradient matches the on-site interaction energy. The corresponding nonlinear effect in a Mott insulator allowed Fölling *et al* [24] to observe two-atom RET, and RET in the presence of many-body coherences was theoretically analyzed in [25]. We reported very precise RET measurements for BECs in [26]. The condensates were loaded into a one-dimensional (1D) optical lattice and subjected to an additional Stark force, optimally implemented and controlled by accelerating the lattice.

In this paper, we report additional investigations on RET for a BEC in a 1D optical lattice applying the high-level control elaborated in our previous work. The experimental data presented here concentrates on the regime of parameters for which the Stark force dominates the dynamics of the condensate. Our precise control of the experimental parameters (lattice depth, interaction strength, and the flexibility of the choice of the initially populated band) enables us to measure the RET decay of the ground band and the first two excited energy bands in a wide range of experimental conditions. Moreover, we study the impact of atom–atom interactions on the RET process. All these features extend previous experimental studies on Landau–Zener tunneling for ultracold atoms in periodic potentials [3, 4, 27, 28]. A theoretical description complements our experimental work.

The paper is organized as follows. Section 2.1 collects the necessary theoretical tools to describe our experiments, whereas section 2.2 introduces the RET modifications produced by the atom–atom interactions. Section 3.1 presents our experimental data in the linear tunneling regime, i.e. in the absence of atom–atom interactions. The effect of the latter is investigated in section 3.2, before we discuss and summarize our results in section 4.

2. Theoretical description

2.1. Single-particle RET

Neglecting for a moment atom–atom interactions in a BEC, our system is described by the following Hamiltonian:

$$H = -\frac{\hbar^2}{2M} \frac{d^2}{dx^2} + V_0 \sin^2 \left(\frac{\pi x}{d_L} \right) + Fx, \quad (1)$$

where V_0 is the depth of the optical lattice, d_L its spatial period, and M the atomic mass of rubidium 87. This Hamiltonian defines the well-known Wannier–Stark problem [19, 29, 30].

For small Stark forces F , one can picture the evolution of a momentum eigenstate induced by equation (1) as an oscillatory motion in the ground energy band of the periodic lattice. These Bloch oscillations with period $T_{\text{Bloch}} = h/d_L F$, where h is Planck’s constant, were observed for cold and ultracold atoms in optical lattices [6].

At stronger forces, a wave packet prepared in the ground state band has a significant probability to tunnel at the band edge (where the band gap Δ is minimal) to the first excited band. For a single tunneling event, such a probability is best estimated by Landau–Zener theory

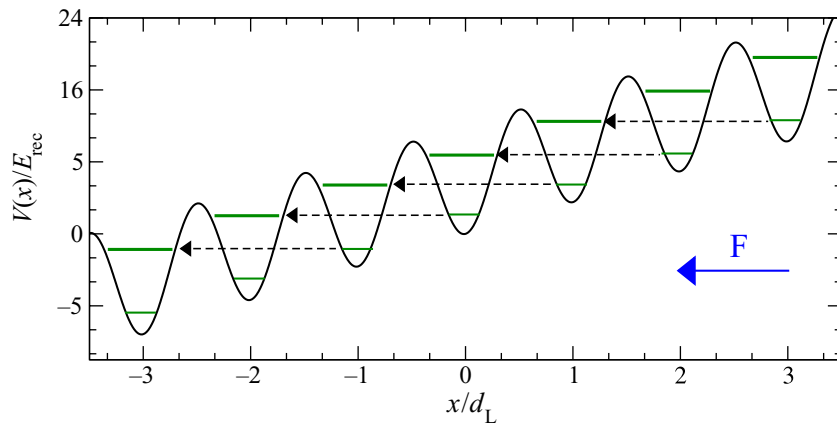


Figure 1. Schematic of the RET process between second nearest neighboring wells, i.e. for $\Delta i = 2$. The tunneling of atoms is resonantly enhanced when the energy difference between lattice wells matches the separation between the energy levels in different potential wells.

as [30]

$$P_{LZ} = e^{-\pi^2(\Delta/E_{\text{rec}})^2/(8F_0)}, \quad (2)$$

with the recoil energy $E_{\text{rec}} = (\hbar\pi/d_L)^2/2M$ and $F_0 \equiv Fd_L/E_{\text{rec}}$. The decay rate—owing to a sequence of Landau–Zener tunneling events—is then obtained by multiplying P_{LZ} with the Bloch frequency [19]

$$\Gamma_{LZ} = \nu_{\text{rec}} F_0 e^{-\pi^2(\Delta/E_{\text{rec}})^2/(8F_0)}, \quad (3)$$

where the recoil frequency is given by $\nu_{\text{rec}} = E_{\text{rec}}/\hbar$.

The actual decay rates can dramatically deviate from equation (3) when two Wannier–Stark levels in different potentials wells are strongly coupled owing to an accidental degeneracy. By imposing an energy resonance between the Wannier–Stark levels in different wells of an optical lattice shifted by the potential of the external force, one finds that these degeneracies occur at the values F at which $Fd_L\Delta i$ (Δi integer) is close to the mean band gap between two coupled bands of the $F = 0$ problem [15, 19]. The actual peak positions are slightly shifted with respect to this simplified estimate, because the Wannier–Stark levels in the potential wells are only approximately defined by the averaged band gap of the $F = 0$ problem, a consequence of field-induced level shifts [19]. The RET process based on the $n = 1$ and 2 levels of the Wannier–Stark ladder is sketched in figure 1.

The modification of the level decay rate by the presence of a degeneracy may be described by a simple model of a two-level Hamiltonian with energy splitting 2ϵ and one decaying level [31, 32]

$$H = \begin{bmatrix} \epsilon - i\gamma & v \\ v & -\epsilon \end{bmatrix}. \quad (4)$$

In this approach it is assumed that the upper bare state decays with rate γ , whereas the decay is negligible for the other one. The two states are coupled with strength v . The eigenvalues of the non-hermitian Hamiltonian of equation (4) are given by

$$\mathcal{E}_{\pm} = -i\gamma \pm \sqrt{(\epsilon - i\gamma)^2 + v^2} = E_{\pm} - i\Gamma_{\pm}/2. \quad (5)$$

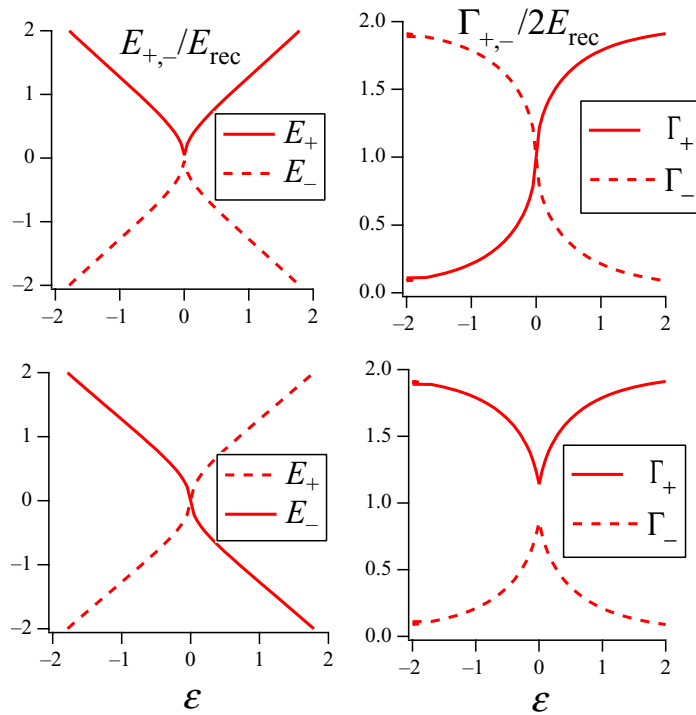


Figure 2. Real (left) and imaginary (right) part of the eigenvalues of equation (5) as a function of ϵ for $\gamma = 1$, measured in units of E_{rec} . A type-I crossing is found for $v = 1.01 E_{\text{rec}}$ (upper plots), and a type-II crossing is found for $v = 0.99 E_{\text{rec}}$ (lower plots).

Real and imaginary part of the eigenvalues are different for $\epsilon \neq 0$, but crossings or anticrossings of the real and imaginary part are found at the critical value $\epsilon = 0$ where two different scenarios take place. For $|v| \geq \gamma$, at $\epsilon = 0$ the imaginary parts of the eigenvalues coincide, $\Gamma_+ = \Gamma_- = 2\gamma$, whereas the real parts differ. In this case, denoted as type-I crossing, the imaginary parts of the eigenvalues cross while the real parts anti-cross, as shown in the upper plots of figure 2. For $|v| \leq \gamma$, at $\epsilon = 0$ the real parts of the eigenvalues coincide, $E_+ = E_- = 0$, whereas the imaginary parts differ. In this case, denoted as type-II crossing, the eigenvalues anticross whereas the real parts cross, as shown in the lower plots of figure 2. Type-II crossing corresponds to the RET phenomenon: if the lower state is energetically close or equal to the decaying upper level, the decay rate of the lower state increases significantly. In addition, the upper state experiences a resonantly stabilized tunneling (RST) with a decrease of its decay rate.

For non-interacting atoms described by equation (1), we can easily diagonalize an opened version of our Hamiltonian [18, 19], [33]–[35] to obtain the true resonance eigenstates and eigenenergies of our decaying system. Figure 3(a) shows the crossing and anticrossings for the real parts of the eigenenergies associated with a configuration investigated experimentally as a function of the experimental control parameter, the Stark force. It may be noticed that the type-II crossings are typically encountered for our problem of decay from lower bands. The associated Wannier–Stark states decay with rates are shown in figure 3(b) as a function of the dimensionless parameter F_0 . The strong modulations on top of the global exponential decrease arise from the RET processes originated by the type-II crossings.

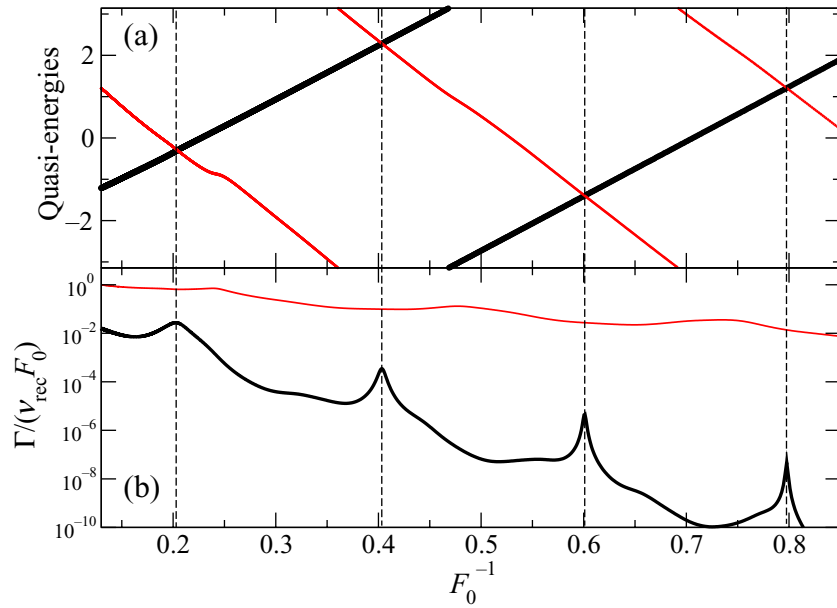


Figure 3. (a) Real part of the eigenenergies and (b) decay rates for a lattice depth of $V_0/E_{\text{rec}} = 10$ and the Hamiltonian from equation (1). The eigenenergies and the decay rates are associated with two Wannier–Stark ladders or, equivalently, with two energy bands: ground (thick black lines) and first excited states (thin red lines). The maxima of the ground-state decay rates correspond to $\Delta i = 1, 2, 3$ and 4.

2.2. Interacting BEC dynamics

In this section, we discuss the effect of atom–atom interactions in the BEC and how to effectively model them for a quantitative description of the experiment. We focus on a parameter regime where the Stark force essentially dominates the dynamics of the condensate. Here the quantum tunneling between the energy bands is significant and most easily detected experimentally. The critical field values for which such excitations are relevant can be estimated by comparing, for instance, the potential energy difference between neighboring wells, Fd_L , with the coupling parameters of the many-body Bose–Hubbard model, i.e. the hopping constant J and the interaction constant U [6]. These parameters are plotted in figure 4 for typical experimental parameters as a function of the lattice depth V_0 .

Our theoretical and experimental analyses will exclude the regime of $F_0 \leq J/E_{\text{rec}}$ where a quantum chaotic system is realized [36]–[39]. The origin of quantum chaos, i.e. of the strongly force-dependent, nonperturbative mixing of energy levels can be understood as a consequence of the interaction-induced lifting of the degeneracy of the multiparticle Wannier–Stark levels in the crossover regime from Bloch to Wannier spectra, making nearby levels strongly interact, for comparable magnitudes of hopping matrix elements and Stark shifts.

For the regime of $F_0 \gg J/E_{\text{rec}}$ studied here, the effect of weak interactions is just a perturbative shifting and a small splitting of many-body energy levels [33, 39]. As a consequence, we can use a global mean-field description based on the Gross–Pitaevskii equation [40] to simulate the temporal evolution of a BEC wavefunction $\psi(\vec{r}, t)$ subjected to a

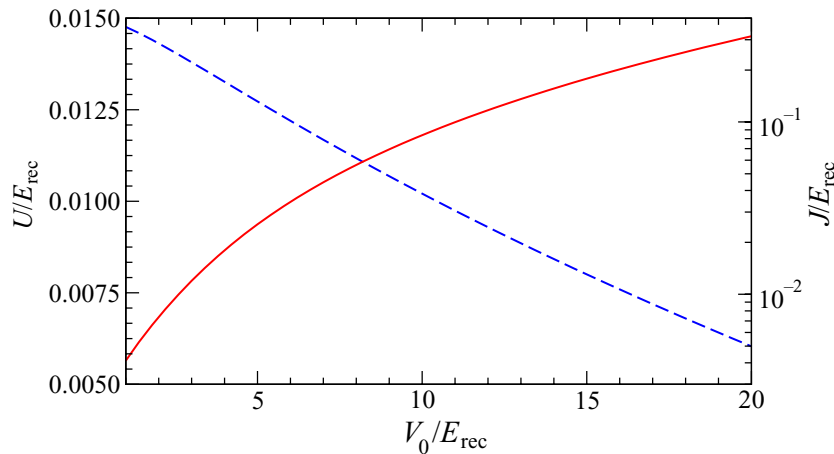


Figure 4. Hopping parameter J (dashed line) and on-site interaction constant U (solid line) of a 1D Bose–Hubbard model as a function of the depth of the optical lattice. U is computed for rubidium 87 and for typical experimental parameters, i.e. lattice spacing $d_L = 620$ nm, and radial confinement frequency $\omega_r/2\pi = 250$ Hz, using the projection to a quasi-1D situation of [41].

realistic potential

$$i\hbar \frac{\partial}{\partial t} \psi(\vec{r}, t) = \left[-\frac{\hbar^2}{2M} \nabla^2 + \frac{1}{2} M (\omega_x^2 x^2 + \omega_r^2 \rho^2) + V_0 \sin^2 \left(\frac{\pi x}{d_L} \right) + Fx + g |\psi(\vec{r}, t)|^2 \right] \psi(\vec{r}, t). \quad (6)$$

The frequencies ω_x and ω_r characterize the longitudinal and transverse harmonic confinement (with cylindrical symmetry of the optical dipole trap: $\rho = \sqrt{y^2 + z^2}$, cf section 3). The atom–atom interactions are modeled by the nonlinear term in equation (6), with the nonlinear coupling constant given by $g = 4\pi\hbar^2 a_s/M$, where a_s is the s-wave scattering length [40]. Later, we will use the dimensionless nonlinearity parameter $C = gn_0/(8E_{\text{rec}})$ [4, 6], which is computed from the peak density n_0 of the initial state of the condensate, to describe the experimentally relevant nonlinear couplings $C \approx 0.01, \dots, 0.06$. In the Thomas–Fermi regime of the condensate [40], for given ω_x and ω_r the density n , and therefore C , is proportional to $N^{2/5}$ where N is the number of atoms in the condensate.

The Gross–Pitaevskii equation (6) is numerically integrated using finite difference propagation, amended by predictor–corrector loops to reliably evolve the nonlinear interaction term [42]. To avoid any spurious effects owing to the fast spreading of the wavefunctions, we use a large numerical basis, especially in the longitudinal direction. In this way, we fully cover the 3D expansion of the entire wave packet, including its tunneled tail, without the use of non-Hermitian potentials. The initial state propagated by equation (6) is the relaxed condensate wavefunction, adiabatically loaded into the confining potential given by the harmonic trap and the optical lattice (at $F = 0$).

In order to have access to the decay rates in the experiment, one needs to measure the temporal evolution of the probability of the condensate to remain in the energy band in which it has been prepared initially. As proposed in [21], such a survival probability is best measured in momentum space, since, experimentally, the most easily measurable quantity is the momentum

distribution of the condensate obtained from a free expansion after the evolution inside the lattice. From the momentum distributions we determine the survival probability by projection of the evolved state $\psi(\vec{p}, t)$ onto the support of the initial state:

$$P_{\text{sur}}(t) \equiv \int_{-p_c}^{p_c} dp_x \left(\int dp_y dp_z |\psi(\vec{p}, t)|^2 \right). \quad (7)$$

A good choice is $p_c \geq 3p_R$ since typically three momentum peaks are initially significantly populated when loading the condensate adiabatically into the periodic lattice, and they correspond to $-2p_R, 0, 2p_R$ [3, 4, 6]. For $g = 0$, the individual tunneling events occurring when the condensate crossed the band edge are independent, and hence $P_{\text{sur}}(t)$ has a purely exponential form (apart from the $t \rightarrow 0$ limit [43]). When the nonlinear interaction term is present, the density decays with time too. As a consequence, the rates Γ are at best defined locally in time, and in the presence of RET even a sharp non-exponential decay is possible, as discussed in [35, 44]. Nevertheless, for the short evolution times and the weak nonlinear coupling strengths C that are experimentally accessible, the decay of the condensate can be well fitted by an exponential law [26, 45]

$$P_{\text{sur}}(t) = P_{\text{sur}}(t = 0) \exp(-\Gamma_n t) = \exp(-\Gamma_n t), \quad (8)$$

with rates Γ_n for the band $n = 1$ (ground band), 2 (first excited band), 3 (second excited band), in which the atoms are initially prepared.

Before we discuss our experimental set-up and present our data on linear and nonlinear tunneling, we come back to the RET peaks discussed above, cf figure 1. These peaks, which are predicted to occur for the single-particle motion studied in section 2.1, will be affected by the nonlinear interaction term of equation (6). A shift of the RET peaks in energy or in the position of the Stark force, as predicted in [33] for much larger parameters C , is negligible for our nonlinearities $C < 0.06$, for which such a shift would correspond to the extremely small amount of $\Delta F_0 < 5 \times 10^{-4}$ [33]. The RET peaks, however, originate from an exact matching of energy levels in neighboring potential wells, and hence they are very sensitive to slight perturbations. We may estimate the necessary perturbation by the nonlinear term in equation (6) by comparing the width of the RET peaks of a band n (which essentially is determined by the decay width Γ_{n+1} of the band into which the atoms tunnel) with the energy scale of the nonlinearity. In the experiment, we can easily reach nonlinearities corresponding to this order-of-magnitude argument, and the consequences will be discussed in section 3.2 below.

3. Experimental results

The starting point of the measurements presented in this paper is the creation of a BEC of ^{87}Rb atoms. This is realized starting from a cloud of atoms trapped in a 3D magneto-optical trap (MOT) and then loaded in a pure-magnetic time-orbital potential (TOP) trap after a molasses stage for sub-Doppler cooling. In order to achieve condensation, evaporative cooling is performed first in the TOP trap and then in an all-optical dipolar trap, where the atoms are transferred once they have a temperature of few microkelvin. A BEC of up to 5×10^4 atoms then forms in the optical trap. The dipolar trap is realized with two off-resonant Gaussian laser beams focused to waists of $50 \mu\text{m}$, having a wavelength $\lambda = 1030 \text{ nm}$, and mutually detuned by $\sim 220 \text{ MHz}$ in order to avoid interference. The aspect ratio of the trap can be varied through the power of the laser beams, which is up to 1 W each and actively controlled by a feedback

loop. This feedback loop permits us to decrease the intensity noise on the beams and to improve reproducibility during the data collection.

After the creation of the condensate, the trap frequencies are adiabatically varied in order to confine the BECs in a cigar-shaped trap, with a longitudinal frequency of ~ 20 Hz and radial frequency in the range 80–250 Hz. The BECs are then loaded into a 1D optical lattice oriented along the weak direction of the dipolar trap. The lattice is created by optical interference of two linearly polarized Gaussian laser beams ($\lambda = 852$ nm) focused to a waist of $120 \mu\text{m}$ and intersecting with an angle θ . The lattice spacing is then $d_L = \lambda/(2\sin(\theta/2))$. The lattice depth V_0 is controlled through the laser intensity, and will be expressed in units of the recoil energy E_{rec} . The measurements presented in the paper were taken for different values of the lattice depth and of the lattice spacing: $V_0/E_{\text{rec}} = 6, 4, 9, 16$ with $d_L = 0.426 \mu\text{m}$, and $V_0/E_{\text{rec}} = 2.5, 10, 12, 14$ with $d_L = 0.620 \mu\text{m}$. Each lattice beam passes through an acousto-optic modulator (AOM) in order to control its power and hence the lattice depth. Moreover, by varying the radio-frequency driving one of the two AOMs, it is possible to create a detuning $\Delta\nu$ between the two lattice beams. This causes a displacement in time of the lattice in the laboratory frame. Within this frame, it is possible to make the lattice move at a velocity $v = d_L \Delta\nu$, or to accelerate it with an acceleration $a = d_L (d\Delta\nu/dt)$.

The lattice is usually loaded in 1 ms to avoid excitations to higher bands, and the atoms occupy the fundamental band if they have zero group velocity in the lattice rest frame during the loading phase. However, if the lattice is loaded with a constant velocity, the atoms can occupy one of the excited bands if the energy and quasi-momentum are conserved [1]. Furthermore, when the lattice is accelerated, the atoms are subjected to a force $F = ma$ in the rest frame of the lattice: this corresponds to the experimental realization of the Hamiltonian (1). The applied force F is chosen in order to minimize the growth of dynamical instabilities, as explored in [46].

In order to measure the tunneling rate Γ_n for BECs initially loaded into the n th band of the optical lattice (ground state: $n = 1$, first excited state: $n = 2$, etc), the lattice is accelerated with acceleration a for an integer number of Bloch oscillation cycles. During this acceleration time, atoms are most likely to tunnel to upper bands when the condensate quasi-momentum is close to the edge of the Brillouin zone. Atoms that do not tunnel to a higher band and are, therefore, ‘dragged along’ by the accelerated lattice acquire a larger final velocity than those that have undergone tunneling. They are spatially separated from the latter by releasing the BEC from the dipole trap and lattice at the end of the acceleration period and allowing it to expand and to fall under gravity for 5–20 ms. After the time-of-flight, the atoms are detected by absorptive imaging on a CCD camera using a resonant flash.

From the dragged fraction $N_{\text{drag}}/N_{\text{tot}}$, we then determine the tunneling rate Γ_n by imposing the asymptotic decay law

$$N_{\text{drag}}(t) = N_{\text{tot}} \exp(-\Gamma_n t), \quad (9)$$

where the subscript n indicates the dependence of the tunneling rate on the local energy level n in which the atoms are initially prepared. Our measurement of Γ_n based on the dragged fraction relies on the fact that for the lattice depths used in our experiments the number of bound states in the wells was small (2–4, depending on the lattice depth), so after the first tunneling event, the probability for tunneling to the next bound state or the continuum was close to unity. This explains why we observe type-II crossings, corresponding to $\gamma > |v|$ in the model discussed in section 2.1.

The way in which we measure the tunneling rate also determines the achievable resolution of our method. This is given by the minimum number of atoms that we can distinguish reliably

from the background noise in our CCD images, which varies between 500 and 1000 atoms, depending on the width of the observed region. With our condensate number, and taking into account the minimum acceleration time limited by the need to spatially separate the two fractions after time-of-flight and the maximum acceleration time limited by the field of view of the CCD camera, this results in a maximum $\Gamma_n/\nu_{\text{rec}}$ of ≈ 1 and a minimum of $\approx 1 \times 10^{-2}$.

3.1. The linear regime

Although the finite and positive scattering length of the ^{87}Rb atoms in our BECs means that the linear Hamiltonian of equation (1) is never exactly realized in our experiments, we can approximate a non-interacting BEC by keeping the condensate density low. In that case, the interaction energy can be made much smaller than all the other energy scales of the system (recoil energy, band width, gap width) and hence negligible for our purposes. A low density can be achieved by using a weak trap with small trap frequencies and/or a small atom number in the BEC. Alternatively, one can also allow the BEC to expand freely for a short time (typically less than a millisecond, to avoid excessive dropping under gravity) before performing the lattice acceleration.

Figure 5 shows the results of experiments with low-density condensates for which the nonlinearity parameter C was less than $\approx 1 \times 10^{-2}$, which in this work we define to be the limit of the linear regime. In each plot, the tunneling rate Γ_n out of the n th band (in our experiments we were able to study the cases $n = 1, 2$ and 3) is shown as a function of F_0^{-1} . Superimposed on the overall exponential decay of Γ_n/F_0 with F_0^{-1} , one clearly sees the resonant tunneling peaks corresponding to the various resonances $\Delta i = 1, 2, 3, 4$. Which of the resonances were visible in any given experiment depended on the choice of lattice parameters and the finite experimental resolution. The limit $n = 3$ for the highest band we could explore was given by the maximum lattice depth achievable.

The inset in figure 5(a) shows the tunneling resonances in the lowest energy band for a different value of the lattice depth V_0 . One clearly sees that the positions of the resonances are shifted according to the variation in the energy levels. Figure 6(a) shows the positions F_0^{res} of the $\Delta i = 1$ resonances as a function of the lattice depth. For deep enough lattices, these positions agree perfectly with the results of a numerical simulation (see figure 6(a)) and can also be approximately calculated by making a harmonic approximation in the lattice wells, which predicts a separation of the two lowest energy levels ($n = 1$ and 2) of

$$\Delta E_{2-1} = 2E_{\text{rec}} \sqrt{\frac{V_0}{E_{\text{rec}}}}. \quad (10)$$

The resonance condition $\Delta E_{2-1} = F^{\text{res}} d_1 \Delta i$ can then be used to calculate the resonance position F^{res} . Our experimental results of figure 5(a) are well fitted by this formula if the factor 2 in the expression for ΔE_{2-1} is replaced by ≈ 1.5 . This discrepancy with the theoretical prediction is to be expected since the anharmonicity of the potential wells reduces the actual energy separation of the levels compared to the harmonic case. While we were not able to measure the tunneling resonances in two *different* bands for the *same* lattice depth, we could measure the resonances in one single band and compare our results with the theoretically predicted resonances in an adjacent band [26]. This allowed us to confirm that in our experiments a resonance peak in one band always coincided with an anti-peak or trough in

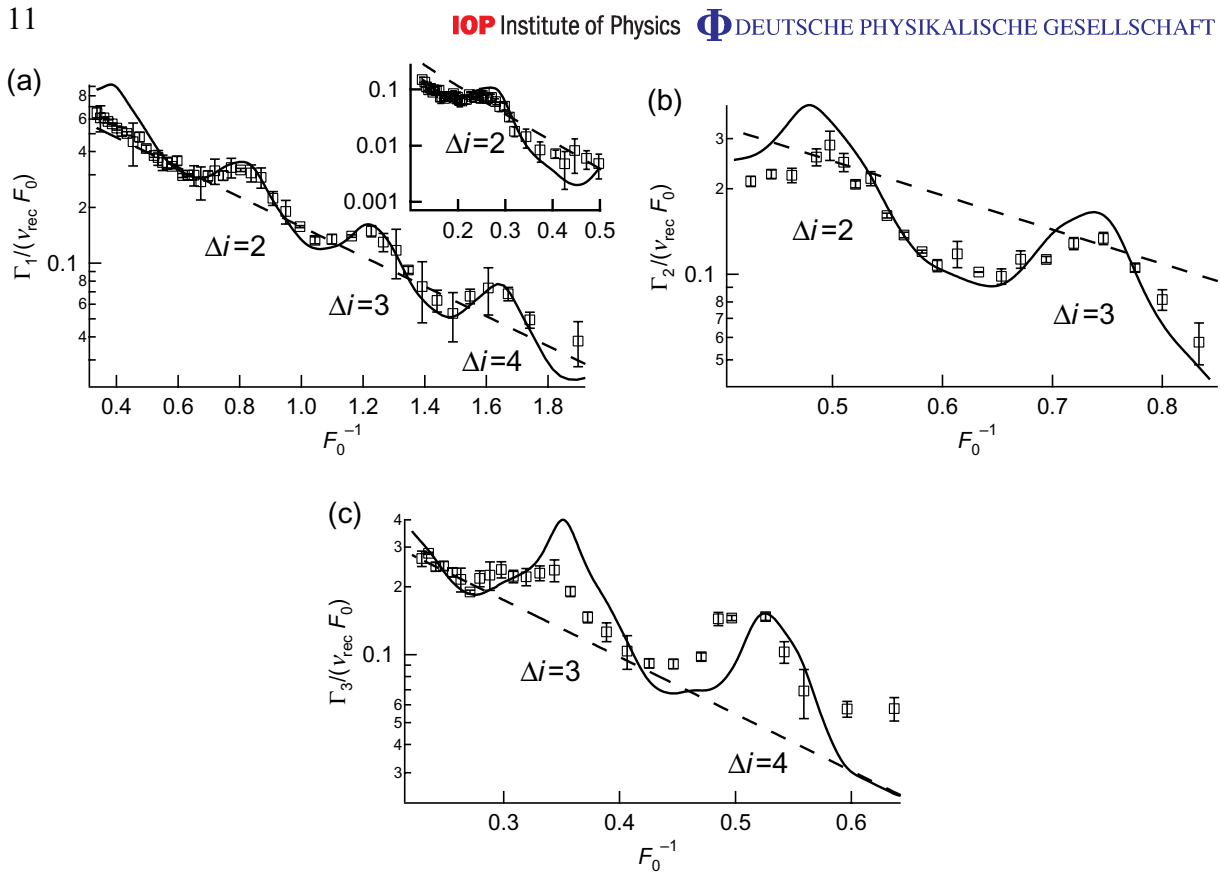


Figure 5. Resonant tunneling in the linear regime. Shown here are the tunneling rates from the three lowest energy bands of the lattice as a function of the normalized inverse force F_0^{-1} for lattice depths (a) $V_0/E_{\text{rec}} = 2.45$ (insert: $V_0/E_{\text{rec}} = 6$), (b) $V_0/E_{\text{rec}} = 10$ and (c) $V_0/E_{\text{rec}} = 23$. Note the different scales on the horizontal axes.

the adjacent band, which agrees with our interpretation in terms of a type-II crossing (see section 2.1).

We also studied the dependence of the widths of the tunneling resonances on the lattice depth. Physically, this width is determined by the width of the state to which the atoms tunnel and hence should decrease with increasing lattice depth. For instance, for tunneling from the ground state band $n = 1$, the resonance width should reflect the width of the first excited band $n = 2$. Figure 6 shows the results of our measurements. For large lattice depths, the resonance width decreases as expected, whereas for shallow lattices the behavior is more complicated. This is also reflected in the numerical simulations.

3.2. The nonlinear regime

In order to enter the regime for which $C \gtrsim 1 \times 10^{-2}$, we carry out the acceleration experiments in radially tighter traps (radial frequency $\gtrsim 100$ Hz) and hence at larger condensate densities. Figure 7 shows the $\Delta i = 2$ and 3 resonance peaks of the ground state band ($n = 1$) for increasing values of C , starting from the linear case and going up to $C \approx 3 \times 10^{-2}$. As the nonlinearity increases, two effects occur. Firstly, the overall (off-resonant) level of Γ_1 increases linearly with C . This is in agreement with our earlier experiments on nonlinear Landau–Zener tunneling

12

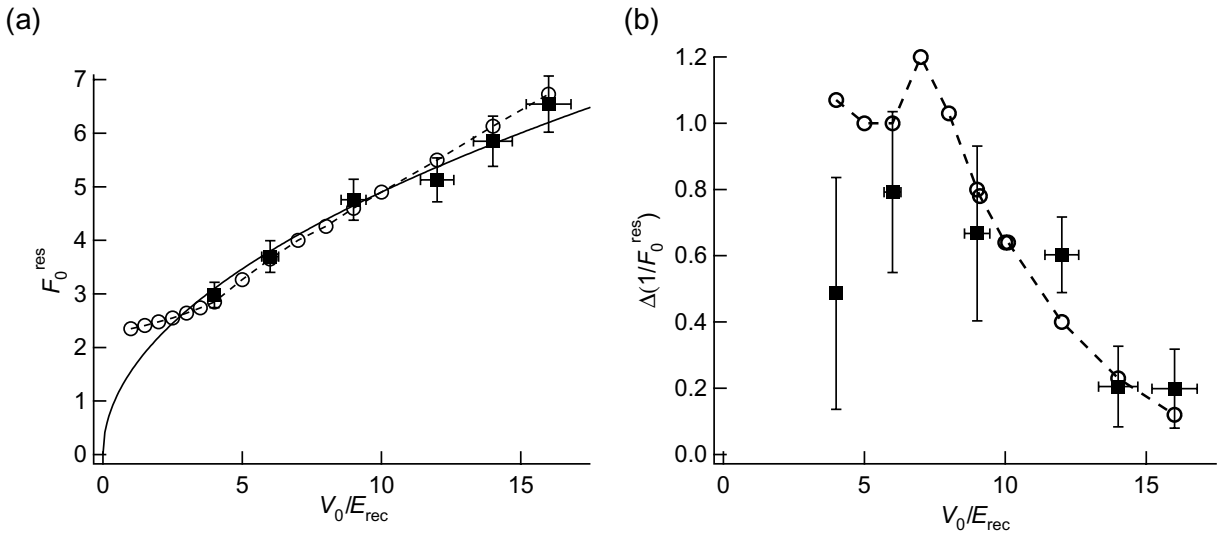
IOP Institute of Physics Φ DEUTSCHE PHYSIKALISCHE GESELLSCHAFT

Figure 6. Positions (a) and widths (b) of the tunneling resonances with $\Delta i = 1$ in the lowest energy band as a function of the lattice depth. In (a), the solid line is the theoretical prediction based on the harmonic oscillator approximation, modified as described in the main text. In (a) and (b), the open symbols connected by the dashed line are the results of a numerical simulation.

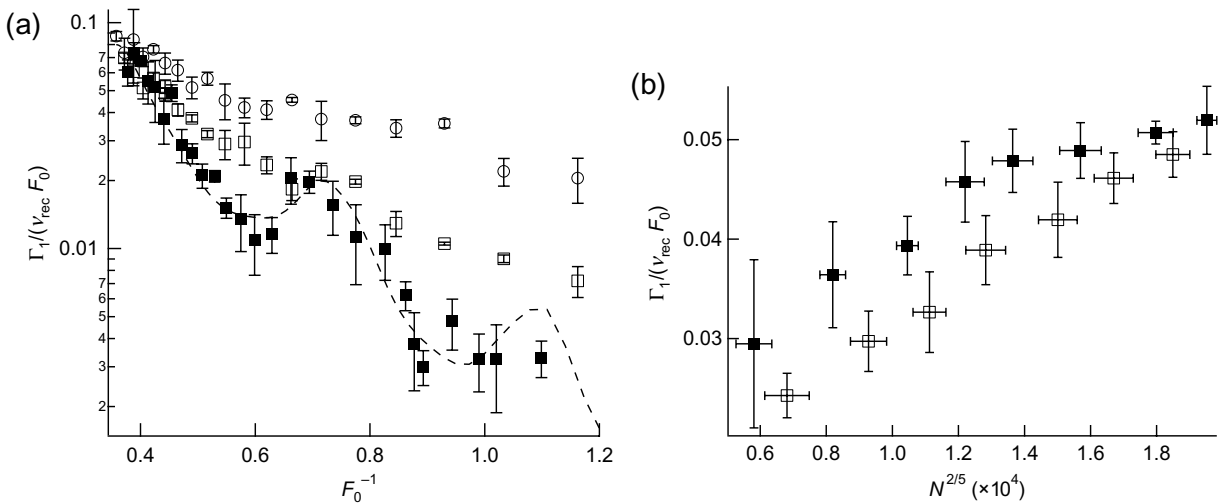


Figure 7. Resonant tunneling in the nonlinear regime. (a) The tunneling rates for $\Delta i = 2$ from the lowest energy band of the optical lattice as a function of the normalized inverse force F_0^{-1} for a lattice depth $V_0/E_{\text{rec}} = 3.5$ and different values of $C \approx 0.01, 0.022$ and 0.033 from bottom to top. The dashed line is the theoretical prediction in the linear regime. As the nonlinearity increases, the overall tunneling rate increases and the resonance peak becomes less pronounced. (b) Dependence on the condensate atom number N of the tunneling rate at the position of the peak $F_0^{-1} = 0.71$ (solid symbols) and of the through $F_0^{-1} = 0.60$ (open symbols) for $V_0/E_{\text{rec}} = 3.0$.

[3, 28] and can be explained describing the condensate evolution within a nonlinearity-dependent effective potential $V_{\text{eff}} = V_0/(1+4C)$ [47]. Secondly, with increasing nonlinearity, the contrast of the RET peak is decreased and the peak eventually vanishes, as is also evident from the different on-resonance and off-resonance dependence of the tunneling rate as a function of the atom number N (and hence the nonlinearity), as seen in figure 7(b). This is in agreement with the theoretical discussion of section 2.

As mentioned in section 2.2, the critical value of C for which the nonlinearity significantly affects the resonance peak should be given by the width of the resonance peak itself. For the parameters of figures 5(a) and 7(a) and the RET peak with $\Delta i = 2$, the typical width Γ_2 of the decaying state to which the atoms tunnel is of the order of 0.2, . . . , 0.5, expressed in units of E_{rec} . Since C reflects the nonlinearity expressed in units of $8 \times E_{\text{rec}}$, this means that we expect to see substantial deviations from the linear behavior when $C \gtrsim 0.025, \dots, 0.06$. Experimentally, we confirm that this threshold is a good estimate for the onset of the destruction of the RET peak, which is observed to occur around $C = 0.02$ in figure 7(a).

4. Conclusions and outlook

In this paper, we have studied the RET of BECs in optical lattices both theoretically and experimentally. Our results show that ultracold atoms in periodic potentials are well suited to simulating and exploring basic quantum mechanical processes which are also the subject of active investigations in the solid state physics community, such as Bloch oscillations [48]–[51] and Zener tunneling [52, 53]. Compared to solid-state experiments, our approach offers the advantage of a large flexibility in the experimental parameters and the possibility to add a nonlinearity in a controlled way.

The experimental set-up presented in this paper also opens up the possibility to explore different regimes, such as the strongly interacting regime for $J \simeq U \gtrsim F_0$ [38, 39]. Another interesting aspect to be studied in the nonlinear regime is the limit in which the fraction of atoms undergoing tunneling is either very large (i.e. very few atoms remain in the initial band) or very small. In both limits, deviations from the Gross–Pitaevskii equation, which presupposes a mean-field approximation for all the bands involved, are expected [54].

Acknowledgments

This work was supported by the European STREP Project OLAQUI, a MIUR PRIN-2005 Project, and the Sezione di Pisa dell’INFN. SW acknowledges support from the Alexander von Humboldt Foundation (Feodor-Lynen Program 2004–2006) and within the framework of the Excellence Initiative by the German Research Foundation (DFG) through the Heidelberg Graduate School of Fundamental Physics (grant number GSC 129/1), as well as a travel grant from CNISM Unità di Pisa. We thank Matteo Cristiani for assistance, and Lincoln Carr, Andrey Kolovsky, Hans-Jürgen Korsch and Peter Schlagheck for enlightening discussions.

References

- [1] BenDahan M, Peik E, Reichel J, Castin Y and Salomon C 1996 *Phys. Rev. Lett.* **76** 4508
- [2] Raizen M, Salomon C and Niu Q 1997 *Phys. Today* **50** 30
- [3] Morsch O, Müller J H, Cristiani M, Ciampini D and Arimondo E 2001 *Phys. Rev. Lett.* **87** 140402

- [4] Cristiani M, Morsch O, Müller J H, Ciampini D and Arimondo E 2002 *Phys. Rev. A* **66** 021601
- [5] Roati G, de Mirandes E, Ferlaino F, Ott H, Modugno G and Inguscio M 2004 *Phys. Rev. Lett.* **92** 230402
- [6] Morsch O and Oberthaler M 2006 *Rev. Mod. Phys.* **78** 179
- [7] Bloch I, Dalibard J and Zwerger W 2007 *Rev. Mod. Phys.* at press (*Preprint* 0704.3011)
- [8] Wilkinson S R, Bharucha C F, Madison K W, Niu Q and Raizen M G 1996 *Phys. Rev. Lett.* **76** 4512
- [9] Köhl M, Moritz H, Stöferle T, Günter K and Esslinger T 2005 *Phys. Rev. Lett.* **94** 080403
- [10] Lee C, Ostrovskaya E A and Kivshar Y S 2007 *J. Phys. B: At. Mol. Opt. Phys.* **40** 4235
- [11] Chang L L, Mendez E E and Tejedor C (ed) 1991 *Resonant Tunneling in Semiconductors* (New York: Plenum)
- [12] Chang L L, Esaki L and Tsu R 1974 *Appl. Phys. Lett.* **24** 593
- [13] Esaki L 1986 *IEEE J. Quantum Electron.* **22** 1611
- [14] Leo K 2003 *High-Field Transport in Semiconductor Superlattices* (Berlin: Springer)
- [15] Glutsch S 2004 *Phys. Rev. B* **69** 235317
- [16] Wagner M and Mizuta H 1993 *Phys. Rev. B* **48** 14393
- [17] Rosam B, Leo K, Glück M, Keck F, Korsch H J, Zimmer F and Köhler K 2003 *Phys. Rev. B* **68** 125301
- [18] Glück M, Kolovsky A R and Korsch H J 1999 *Phys. Rev. Lett.* **83** 891
- [19] Glück M, Kolovsky A R and Korsch H J 2002 *Phys. Rep.* **366** 103
- [20] Dounas-Frazer D R, Hermundstad A M and Carr L 2007 *Phys. Rev. Lett.* **99** 200402
- [21] Wimberger S, Mannella R, Morsch O, Arimondo E, Kolovsky A R and Buchleitner A 2005 *Phys. Rev. A* **72** 063610
- [22] Teo B K, Guest J R and Raithel G 2002 *Phys. Rev. Lett.* **88** 173001
- [23] Greiner M, Mandel O, Esslinger T, Hänsch T W and Bloch I 2002 *Nature* **415** 39
- [24] Fölling S, Trotzky S, Cheinet P, Feld M, Saers R, Widera A, Müller T and Bloch I 2007 *Nature* **448** 1029
- [25] Lee C, Fu L B and Kivshar Y S 2008 *Europhys. Lett.* **81** 60006
- [26] Sias C, Zenesini A, Lignier H, Wimberger S, Ciampini C, Morsch O and Arimondo E 2007 *Phys. Rev. Lett.* **98** 120403
- [27] Bharucha C F, Madison K W, Morrow P R, Wilkinson S R, Sundaram B and Raizen M G 1997 *Phys. Rev. A* **55** R857
- [28] Jona-Lasinio M, Morsch O, Cristiani M, Malossi N, Müller J H, Courtade E, Anderlini M and Arimondo E 2003 *Phys. Rev. Lett.* **91** 230406
- [29] Nenciu G 1991 *Rev. Mod. Phys.* **63** 91
- [30] Holthaus M 2000 *J. Opt. B: Quantum Semiclass. Opt.* **2** 589
- [31] Avron J E 1982 *Ann. Phys.* **143** 33
- [32] Keck F, Korsch H-J and Mossmann S 2003 *J. Phys. A: Math. Gen.* **36** 2125
- [33] Wimberger S, Schlagheck P and Mannella R 2006 *J. Phys. B: At. Mol. Opt. Phys.* **39** 729
- [34] Witthaut D, Graefe E M, Wimberger S and Korsch H J 2007 *Phys. Rev. A* **75** 013617
- [35] Schlagheck P and Wimberger S 2007 *Appl. Phys. B* **86** 385
- [36] Buchleitner A and Kolovsky A R 2003 *Phys. Rev. Lett.* **91** 253002
- [37] Thommen Q, Garreau J C and Zehnle V 2003 *Phys. Rev. Lett.* **91** 210405
- [38] Tomadin A, Mannella R and Wimberger S 2007 *Phys. Rev. Lett.* **98** 130402
- [39] Tomadin A, Mannella R and Wimberger S 2008 *Phys. Rev. A* **77** 013606
- [40] Pethick C J and Smith H 2002 *Bose–Einstein Condensation in Dilute Gases* (Cambridge: Cambridge University Press)
- Pitaevskii L and Stringari S 2003 *Bose–Einstein Condensation* (Oxford: Oxford University Press)
- [41] Bergeman T, Moore M G and Olshanii M 2003 *Phys. Rev. Lett.* **91** 16320
- [42] Cerboneschi E, Mannella R, Arimondo E and Salasnich L 1998 *Phys. Lett. A* **249** 495
- Wimberger S, Mannella R, Morsch O and Arimondo E 2005 *Phys. Rev. Lett.* **94** 130404
- [43] Wilkinson S R, Bharucha C F, Fischer M C, Madison K W, Morro P R, Niu Q, Sundaram B and Raizen M G 1997 *Nature* **387** 575
- [44] Carr L D, Holland M J and Malomed B A 2005 *J. Phys. B: At. Mol. Opt. Phys.* **38** 3217

- [45] Wimberger S, Ciampini C, Morsch O, Mannella R and Arimondo E 2007 *J. Phys.: Conf. Ser.* **67** 012060
- [46] Cristiani M, Morsch O, Malossi N, Jona-Lasinio M, Anderlini M, Courtade E and Arimondo E 2004 *Opt. Express* **12** 4
- [47] Choi D I and Niu Q 1999 *Phys. Rev. Lett.* **82** 2022
- [48] Feldmann J, Leo K, Shah J, Miller D A B, Cunningham J E, Meier T, von Plessen G, Schulze A, Thomas P and Schmitt-Rink S 1992 *Phys. Rev. B* **46** R7252
- [49] Waschke C, Roskos H G, Schwedler R, Leo K, Kurz K and Köhler K 1993 *Phys. Rev. Lett.* **70** 3319
- [50] Pertsch T, Dannberg P, Elflein W, Bräuer A and Lederer F 1999 *Phys. Rev. Lett.* **83** 4752
- [51] Morandotti R, Peschel U, Aitchison J S, Eisenberg H S and Silberberg Y 1999 *Phys. Rev. Lett.* **83** 4756
- [52] Ghulinyan M, Oton J C, Gaburro Z, Pavesi L, Toninelli C and Wiersma D S 2005 *Phys. Rev. Lett.* **94** 127401
- [53] Trompeter H, Pertsch T, Lederer F, Michaelis D, Streppel U, Bräuer A and Peschel U 2006 *Phys. Rev. Lett.* **96** 023901
- [54] Shchesnovich V S and Konotop V V 2007 *Phys. Rev. A* **75** 063628

FAST TRACK COMMUNICATION

Mean-field dynamics of a two-mode Bose–Einstein condensate subject to noise and dissipation

F Trimborn¹, D Witthaut² and S Wimberger³¹ Institut für mathematische Physik, TU Braunschweig, D-38106 Braunschweig, Germany² QUANTOP, Niels Bohr Institute, University of Copenhagen, DK-2100 Copenhagen, Denmark³ Institut für theoretische Physik, Universität Heidelberg, D-69120, Heidelberg, GermanyE-mail: dirk.witthaut@nbi.dk

Received 23 July 2008

Published 26 August 2008

Online at stacks.iop.org/JPhysB/41/171001**Abstract**

We discuss the dynamics of an open two-mode Bose–Hubbard system subject to phase noise and particle dissipation. Starting from the full many-body dynamics described by a master equation the mean-field limit is derived resulting in an effective non-Hermitian (discrete) Gross–Pitaevskii equation which has been introduced only phenomenologically up to now. The familiar mean-field phase-space structure is substantially altered by the dissipation. In particular, the character of the fixed points shows an abrupt transition from elliptic or hyperbolic to attractive or repulsive, respectively. This reflects the metastable behaviour of the corresponding many-body system which surprisingly also leads to a significant increase of the purity of the condensate. A comparison of the mean-field approximation to simulations of the full master equation using the Monte Carlo wavefunction method shows an excellent agreement for wide parameter ranges.

(Some figures in this article are in colour only in the electronic version)

The physics of ultracold atoms in optical lattices has made enormous progress in the last decade, as it is an excellent model system for a variety of fields such as nonlinear dynamics or condensed matter physics [1, 2]. Although this seems to be an inherent many-particle problem, the dynamics of the macroscopic wavefunction is remarkably well reproduced by the (discrete) Gross–Pitaevskii equation (GPE) if the system undergoes a Bose–Einstein condensation (BEC) [3]. Recently, there has been an increased theoretical [4–8] as well as experimental [9] interest in the dynamics of these systems coupled to the environment. In particular, the effects of particle loss have been discussed in several theoretical communications resorting to an effective non-Hermitian mean-field description introduced phenomenologically to analyse resonances, transport and localization effects [10–16].

In this communication, we want to illuminate the origin and give a convincing motivation of this approach.

Starting from a master equation describing the full many-body dynamics including phase noise and particle loss we derive a generalized, non-Hermitian GPE. Due to the decay the structure of the resulting dynamics abruptly changes introducing repulsive and attractive fixed points. Unlike the dissipation-free case there are no longer oscillations around the fixed points, such that irreversible transitions between the former self-trapping fixed points are possible. This reflects the metastable behaviour of the open many-particle system and gives rise to a significant purification of the BEC by the dissipation which will be explained here. The validity of the presented approximation is tested by a comparison to full quantum many-body calculations, showing that the mean-field approximation provides an excellent description of the system. To integrate the effective description by a non-Hermitian GPE into well-known concepts from the theory of open quantum systems, we discuss their relation

to the quantum jump approach [17, 18], demonstrating that they provide a well-suited tool to analyse the short-time as well as the long-time behaviour of the open many-particle system.

In particular, we consider the dynamics of ultracold atoms in an open double-well trap which is not only an extremely popular model system, but also has several recent experimental realizations [19–22]. The unitary part of the dynamics is described by the Bose–Hubbard-type Hamiltonian

$$\hat{H} = -J(\hat{a}_1^\dagger \hat{a}_2 + \hat{a}_2^\dagger \hat{a}_1) + \epsilon_1 \hat{n}_1 + \epsilon_2 \hat{n}_2 + \frac{U}{2}(\hat{a}_1^{\dagger 2} \hat{a}_1^2 + \hat{a}_2^{\dagger 2} \hat{a}_2^2), \quad (1)$$

where \hat{a}_j and \hat{a}_j^\dagger are the bosonic annihilation and creation operators in mode j and $\hat{n}_j = \hat{a}_j^\dagger \hat{a}_j$ is the corresponding number operator. We set $\hbar = 1$, thus measuring all energies in frequency units. In order to analyse the dynamics in the Bloch representation we transform the Hamiltonian using the collective operators

$$\begin{aligned} \hat{L}_x &= \frac{1}{2}(\hat{a}_1^\dagger \hat{a}_2 + \hat{a}_2^\dagger \hat{a}_1), & \hat{L}_y &= \frac{i}{2}(\hat{a}_1^\dagger \hat{a}_2 - \hat{a}_2^\dagger \hat{a}_1), \\ \hat{L}_z &= \frac{1}{2}(\hat{a}_2^\dagger \hat{a}_2 - \hat{a}_1^\dagger \hat{a}_1), \end{aligned} \quad (2)$$

which form an angular momentum algebra $su(2)$ with rotational quantum number $N/2$ [6, 23–25]. With these definitions the Hamiltonian (1) can be rewritten as

$$\hat{H} = -2J\hat{L}_x + 2\epsilon\hat{L}_z + U\hat{L}_z^2, \quad (3)$$

with $2\epsilon = \epsilon_1 - \epsilon_2$ up to terms which only depend on the total number of atoms. The macroscopic dynamics of the atomic cloud is well described within a mean-field approximation, only considering the expectation values of the angular momentum operators $\ell_j = \langle \hat{L}_j \rangle$ and the particle number $n = \langle \hat{n}_1 + \hat{n}_2 \rangle$ [6, 23, 24].

Here we consider the dissipative extension of this system. The main source of decoherence in current experiments is phase noise due to elastic collision with atoms in the thermal cloud [4, 5] which effectively heats the system, leaving the particle number invariant. Only recently, methods to tame this source of decoherence were discussed in [30, 31]. In this communication, we focus on the effects of particle loss at constant rates γ_{aj} in the two wells $j = 1, 2$. Such a loss is not only of fundamental interest but can be adapted in current experiments without greater difficulties by removing atoms with a focused resonant laser beam or by inducing a radio frequency transition to an untrapped internal state [26]. All parameters used here lie in realistic ranges for ongoing experiments [19, 20].

The master equation description including both phase noise and particle loss is well established [27] and routinely used in the context of photon fields. Thus we consider the dynamics generated by the master equation

$$\begin{aligned} \dot{\hat{\rho}} &= -i[\hat{H}, \hat{\rho}] - \frac{\gamma_p}{2} \sum_{j=1,2} (\hat{n}_j^2 \hat{\rho} + \hat{\rho} \hat{n}_j^2 - 2\hat{n}_j \hat{\rho} \hat{n}_j) \\ &\quad - \frac{1}{2} \sum_{j=1,2} \gamma_{aj} (\hat{a}_j^\dagger \hat{a}_j \hat{\rho} + \hat{\rho} \hat{a}_j^\dagger \hat{a}_j - 2\hat{a}_j \hat{\rho} \hat{a}_j^\dagger). \end{aligned} \quad (4)$$

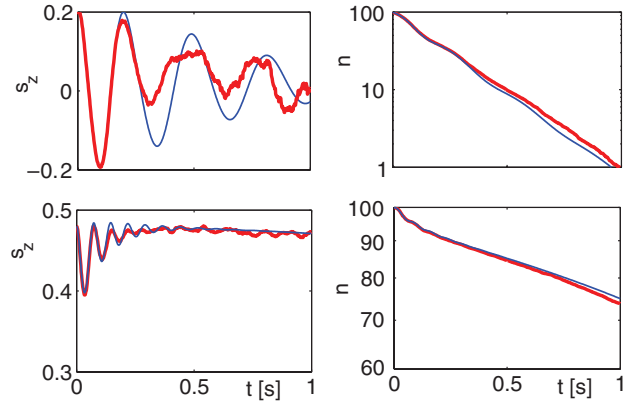


Figure 1. Comparison of the mean-field approximation (thin blue line) with the full many-particle dynamics calculated with the MCWF method (thick red line) for $J = 10 \text{ s}^{-1}$, $U = 1 \text{ s}^{-1}$, $\gamma_p = 3 \text{ s}^{-1}$ and $\gamma_{a2} = 5 \text{ s}^{-1}$. The initial state was assumed to be a pure BEC (i.e. a product state) with $\mathbf{s} = (0.46, 0, 0.2)$ (a) and $\mathbf{s} = (0.14, 0, 0.48)$ (b), respectively, and $n = 100$ particles.

The evolution equations for the expectation values of the angular momentum operators (2) can be calculated starting from the master equation via $\dot{\ell}_j = \text{tr}(\hat{L}_j \dot{\hat{\rho}})$ with $j = x, y, z$. This yields the exact result

$$\begin{aligned} \dot{\ell}_x &= -2\epsilon\ell_y - 2U(\ell_y\ell_z + \Delta_{yz}) - T_2^{-1}\ell_x, \\ \dot{\ell}_y &= 2J\ell_z + 2\epsilon\ell_x + 2U(\ell_x\ell_z + J_{xz}) - T_2^{-1}\ell_y, \\ \dot{\ell}_z &= -2J\ell_y - T_1^{-1}\ell_z - T_1^{-1}f_a n/2, \\ \dot{n} &= -T_1^{-1}n - 2T_1^{-1}f_a\ell_z, \end{aligned} \quad (5)$$

where we have defined the transversal T_1^{-1} and longitudinal T_2^{-1} damping rates by

$$T_1^{-1} = (\gamma_{a1} + \gamma_{a2})/2 \quad \text{and} \quad T_2^{-1} = \gamma_p + T_1^{-1} \quad (6)$$

and the asymmetry of the loss rates by $f_a = (\gamma_{a2} - \gamma_{a1})/(\gamma_{a1} + \gamma_{a2})$. In the non-interacting case $U = 0$, these equations of motion resemble the Bloch equations in nuclear magnetic resonance [28], except for the fact that the ‘equilibrium’ value of the population imbalance ℓ_z is given by $-f_a n/2$ and therefore depends on the decreasing expectation value of the total particle number n .

The exact equations of motion (5) still include the covariances $\Delta_{jk} = \langle \hat{L}_j \hat{L}_k + \hat{L}_k \hat{L}_j \rangle / 2 - \langle \hat{L}_j \rangle \langle \hat{L}_k \rangle$. The approximation of second-order moments by products of expectation values, such that $\Delta_{jk} \approx 0$ yields the well-known mean-field description. This truncation is valid in the macroscopic limit, since the covariances vanish as $1/n$ if the many-particle quantum state is close to a pure BEC. Here and in the following we depict the rescaled variables $s_j = \ell_j/n$, thus renormalizing to separate the decay of the particle number n from the internal dynamics.

The benefit of the mean-field approximation is illustrated in figure 1, where it is compared to the full many-particle quantum dynamics calculated with the Monte Carlo wavefunction (MCWF) method [17, 18]. The trajectory in figure 1(a) was launched at $\mathbf{s} = (0.46, 0, 0.2)$ with a moderate population imbalance, thus performing Josephson oscillations [19]. The amplitude is damped because of the

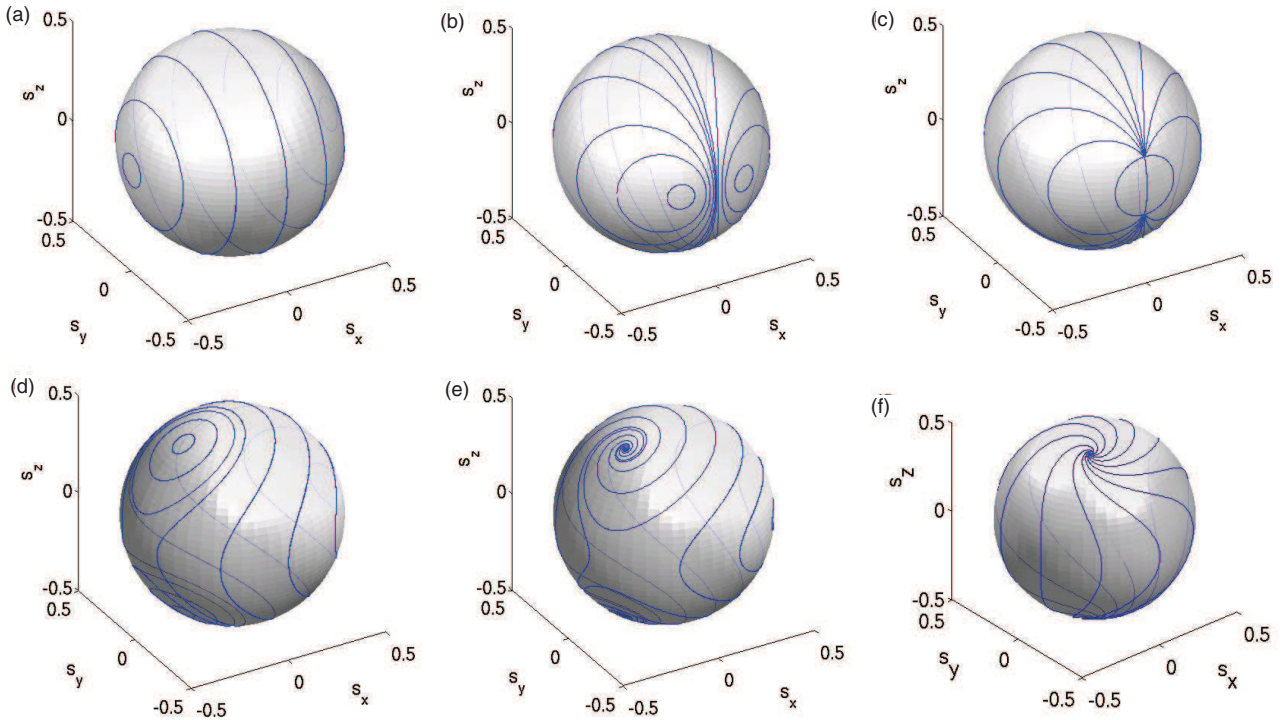


Figure 2. Mean-field dynamics for the non-interacting case $g = 0$ (upper row) and for a fixed interaction strength $g = 4 \text{ s}^{-1}$ (lower row) in dependence of the decay rate ($\gamma = 0$ for (a) and (d), $\gamma = 1.9 \text{ s}^{-1}$ for (b), $\gamma = 2.1 \text{ s}^{-1}$ for (c), $\gamma = 1 \text{ s}^{-1}$ for (e) and $\gamma = 4 \text{ s}^{-1}$ for (f)), for all figures holds $J = 1 \text{ s}^{-1}$ and $\epsilon = 0$.

phase noise, while the oscillation period increases as the effective macroscopic interaction strength $g(t) := Un(t)$ decreases. The decay of the particle number $n(t)$ is also strongly modulated by the oscillations of the population imbalance. The trajectory in figure 1(b) was launched at $s = (0.14, 0, 0.48)$ in the self-trapping region. The residual oscillations are rapidly damped out and the system relaxes to a quasi-steady state on the shown time scale. The particle number decreases slowly and non-exponentially, since the condensate is mostly localized in the non-decaying potential well, cf also [15]. All these features of the dynamics are well reproduced by the mean-field description, and the decay of the particle number is accurately predicted. Strong deviations are only expected in the vicinity of unstable fixed points of the mean-field dynamics, which can be nearly cured within the framework of phase-space distributions [25].

In order to explore the genuine effects of particle loss, phase noise is neglected ($\gamma_p = 0$) in the following. In this case, the dynamics can be further simplified and one can easily show that the particle number coincides with the magnitude of the Bloch vector $\sqrt{\ell_x^2 + \ell_y^2 + \ell_z^2} = n/2$, which we can use to reformulate the mean-field dynamics by an effective non-Hermitian GPE

$$i \frac{d}{dt} \begin{pmatrix} \psi_1 \\ \psi_2 \end{pmatrix} = \begin{pmatrix} \tilde{\epsilon}_1 + U|\psi_1|^2 & -J \\ -J & \tilde{\epsilon}_2 + U|\psi_2|^2 \end{pmatrix} \begin{pmatrix} \psi_1 \\ \psi_2 \end{pmatrix} \quad (7)$$

with complex on-site energies $\tilde{\epsilon}_j = \epsilon_j - i\gamma_{aj}/2$. The equivalence to the Bloch vector description is established via

the identification

$$\begin{aligned} \ell_x &= \frac{1}{2}(\psi_1^* \psi_2 + \psi_2^* \psi_1), & \ell_y &= \frac{1}{2i}(\psi_2^* \psi_1 - \psi_1^* \psi_2), \\ \ell_z &= \frac{1}{2}(|\psi_2|^2 - |\psi_1|^2) \end{aligned} \quad (8)$$

and $n = |\psi_1|^2 + |\psi_2|^2$. In this effective description a loss of particles is represented by a loss of normalization.

We now consider the dynamics for a fixed value of the macroscopic interaction strength $g = Un = \text{const.}$ in the special case $\gamma_{a1} =: \gamma$ and $\gamma_{a2} = 0$. Even though the restriction to a fixed interaction constant seems to be artificial, it reveals the effects of the particle loss on the structure of the mean-field phase space and especially the character of the fixed points most clearly. Moreover, the dynamics under a fixed interaction constant correspond to the periods of the constant particle number between two loss processes in the quantum jumps picture [17, 18]. Therefore this treatment provides a well-suited description of the short-time as well as the long-time behaviour. Note that the more general case $\gamma_{a1} \neq 0$ and $\gamma_{a2} \neq 0$ does not lead to a fundamentally different dynamical behaviour since only the difference of the decay rates influences the internal dynamics. However, the expectation value of the particle number n and thereby also the effective interaction strength $g(t)$ decrease faster.

The resulting dynamics of the Bloch vector is illustrated in figure 2. The upper row (a)–(c) shows the phase space for the linear case, $U = 0$, where the mean-field approximation is exact. Without loss one recovers the famous Josephson

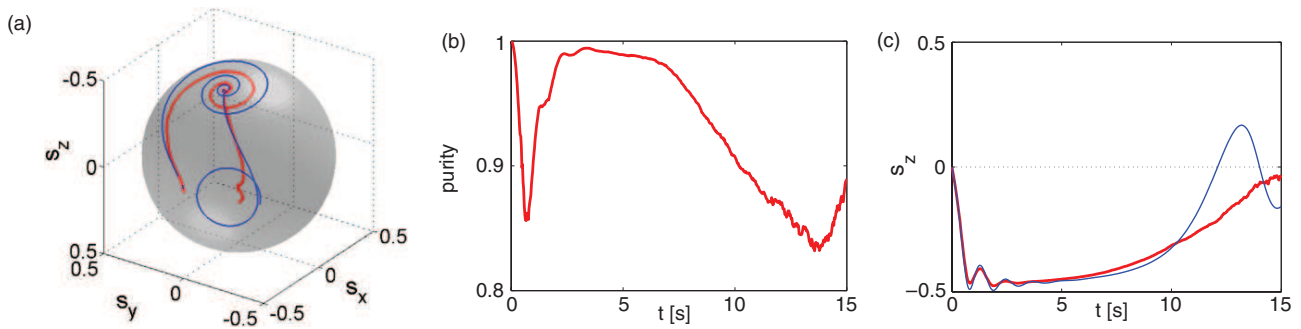


Figure 3. Comparison of the many-particle dynamics (thick red line) to the mean-field approximation (thin blue line) for an initially pure BEC, with $\mathbf{s} = (-0.5, 0, 0)$ and $n(0) = 200$ particles: dynamics of the Bloch vector \mathbf{s} (a), evolution of the purity of the BEC (b) and evolution of the population imbalance s_z (c). The system initially relaxes to a nonlinear quasi-steady state with a purity of almost one which is then lost as $n(t)$ decreases. Parameters are chosen as $J = 1 \text{ s}^{-1}$, $Un(0) = 10 \text{ s}^{-1}$, $T_1 = 1 \text{ s}$ and $f_a = 1$.

oscillations (a). An analysis of the fixed points for the dissipative dynamics shows the emergence of two regimes depending on the amplitude of the loss rate. For weak losses, $|\gamma| \leq 2J$, the fixed points are given by

$$\mathbf{s}_{\pm}^J = \begin{pmatrix} \pm \left[\frac{1}{4} - \left(\frac{\gamma}{4J} \right)^2 \right]^{\frac{1}{2}} \\ -\frac{\gamma}{4J} \\ 0 \end{pmatrix}. \quad (9)$$

While the fixed points remain elliptic and the population is still equally distributed, the fixed points are no longer symmetric, since the relative phase between them decreases (b). This behaviour can be qualitatively understood within the analogy to Josephson junctions: the weak decay induces an asymmetry between the wells leading to a continuous particle stream to the first well. At the fixed points this effect is compensated by the Josephson current $I_J \propto Js_y$ requiring $s_y \neq 0$.

For stronger decay rates, $|\gamma| \geq 2J$, the two fixed points are given by

$$\mathbf{s}_{\pm}^D = \begin{pmatrix} 0 \\ -\frac{J}{\gamma} \\ \pm \left[\frac{1}{4} - \left(\frac{J^2}{\gamma^2} \right)^{\frac{1}{2}} \right] \end{pmatrix}. \quad (10)$$

Above the critical value $|\gamma| = 2J$ the character of the two fixed points changes abruptly from elliptic into an attractive and a repulsive one as shown in figure 2(c). The maximal Josephson current is no longer sufficient to compensate the current induced by the decay leading to a population excess in the non-decaying site. This explains the population imbalance in the fixed points which increases with ascending decay rates.

In the strongly interacting case without dissipation one observes the splitting of one of the elliptic fixed points into two novel elliptic and one hyperbolic fixed point—this is the famous self-trapping effect [19, 23, 24]. The critical interaction strength for the occurrence of this bifurcation is lowered in the presence of dissipation to $g^2 = U^2 n^2 \geq 4J^2 - \gamma^2$. In the subcritical regime for $\gamma < 2J$ and $Un \leq 4J^2 - \gamma^2$, we find oscillations around the same fixed points \mathbf{s}_{\pm}^J as in the non-interacting, but dissipative case (9). However, these are now distorted (not shown in the figure). In the overcritical regime $g = Un > \sqrt{4J^2 + \gamma^2}$ and for a weak decay $\gamma < 2J$

one rediscovers a generalized self-trapping effect. As a result of the dissipative process, one elliptic fixed point now bifurcates into an attractive and a repulsive fixed point (in contrast to the two elliptic ones) and one hyperbolic one (cf figure 2(e)). The novel fixed points are located at

$$\mathbf{s}_{\pm}^{\pi} = \frac{1}{\gamma^2 + g^2} \begin{pmatrix} -gJ \\ -\gamma J \\ \pm \sqrt{(\gamma^2 + g^2) \left(\frac{\gamma^2 + g^2}{4} - J^2 \right)} \end{pmatrix}. \quad (11)$$

For stronger decay rates, $\gamma \geq 2J$, the hyperbolic and the elliptic fixed point \mathbf{s}_{\pm}^J (9) meet and annihilate themselves as illustrated in figure 2(f). Their disappearance is accompanied by the complete disintegration of periodic orbits.

Let us finally discuss the implication of this phase-space structure. We especially focus on the emergence of the attractive fixed point since it is stable and therefore strongly influences the many-body quantum dynamics. Figure 3 shows the dynamics of the rescaled Bloch vector \mathbf{s} comparing results of a MCWF simulation (solid red line) to the mean-field approximation (thin blue line). The given parameters correspond to the situations illustrated in figure 2(b) or (e), respectively, depending on the value of the macroscopic interaction strength $g(t) = Un(t)$. The Bloch vector first relaxes to the attractive fixed point illustrated in figure 2(e). The contraction of the mean-field trajectories to the attractive fixed point manifests itself by a convergence towards a pure BEC, which is the state of tightest localization in phase space [25]. This is illustrated in figure 3(b) where we have plotted the purity $\mathcal{P} := 2 \text{tr}(\rho_{\text{red}}^2) - 1$ of the reduced single-particle density matrix ρ_{red} . $\mathcal{P} = 1$ indicating a pure BEC [6]. However, the attractive fixed point is lost as $g(t) = Un(t)$ decreases, and thus the Bloch vector departs again. This behaviour is very well predicted by the mean-field approximation already for the modest atom number in the simulation. The mean-field trajectory then converges to the limit cycle shown in figure 2(b). However, as the atoms are so rapidly lost nearly no particles remain to follow the limit cycle predicted by mean-field theory. This transition effect between different fixed points is closely related to the quantum-state diffusion in and out of a metastable state, which can be observed in optical

bistability (see, e.g., [32]). Note, however, that the system considered here irretrievably departs from the metastable self-trapping state because the fixed point is lost as $n(t)$ decreases.

In summary, we have derived a mean-field approximation for a dissipative two-mode BEC, starting from the full many-body dynamics described by a master equation including phase noise and particle losses. This treatment puts the so far phenomenological description of open systems via non-Hermitian GPEs on a firm footing and paves the way for a variety of future applications in particular because the extension to an arbitrary number of modes is straightforward.

An analysis of the resulting equations for a fixed interaction constant g shows that not only the critical value for the self-trapping bifurcation is lowered but also the character of the fixed points abruptly changes to attractive and repulsive, such that one of them becomes unstable. Taking into account the decline of the interaction constant $g(t)$ due to the particle losses, the system initially converges to the attractive fixed point, but then suddenly jumps to a Josephson oscillation as soon as $g(t)$ falls below the critical value. This effect is understood as a manifestation of the metastable behaviour of the many-particle system and leads to a significant increase of the purity of the quantum state compared to the dissipation-free case.

The comparison to numerical results for the many-particle system obtained via the Monte Carlo wavefunction method shows that the approach presented here is an excellent approximation to the full many-body dynamics already for a modest initial number of atoms. Thus it provides an excellent basis for a further analysis of the interplay between dissipation and interaction [31]. Likewise the embedding into the more general concept of mean-field description [33] will be the subject of future research.

Acknowledgments

This work has been supported by the German Research Foundation (DFG) through the research fellowship program (grant no WI 3415/1) and the Heidelberg Graduate School of Fundamental Physics (grant no GSC 129/1), as well as the Studienstiftung des deutschen Volkes. We thank H J Korsch, E M Graefe and A Niederle for stimulating discussions.

References

- [1] Morsch O and Oberthaler M 2006 *Rev. Mod. Phys.* **78** 179
- [2] Madroñero J *et al* 2006 *Adv. At. Mol. Opt. Phys.* **53** 33
- [3] Pitaevskii L and Stringari S 2003 *Bose–Einstein Condensation* (Oxford: Oxford University Press)
- [4] Anglin J R 1997 *Phys. Rev. Lett.* **79** 6
- [5] Ruostekoski J and Walls D F 1998 *Phys. Rev. A* **58** R50
- [6] Vardi A and Anglin J R 2001 *Phys. Rev. Lett.* **86** 568
- [7] Anglin J R and Vardi A 2001 *Phys. Rev. A* **64** 013605
- [8] Ponomarev A V, Madroñero J, Kolovsky A R and Buchleitner A 2006 *Phys. Rev. Lett.* **96** 050404
- [9] Wang W, Fu L B and Yi X X 2007 *Phys. Rev. A* **75** 045601
- [10] Syassen N, Bauer D M, Lettner M, Volz T, Dietze D, Garcia-Ripoll D D, Cirac J I, Remppe G and Dürr S 2008 *Science* **320** 1329
- [11] Moiseyev N and Cederbaum L S 2005 *Phys. Rev. A* **72** 033605
- [12] Schlagheck P and Paul T 2006 *Phys. Rev. A* **73** 023619
- [13] Witthaut D, Graefe E M, Wimberger S and Korsch H J 2006 *Phys. Rev. A* **75** 013617
- [14] Livi R, Franzosi R and Oppo G L 2006 *Phys. Rev. Lett.* **97** 060401
- [15] Hiller M, Kottos T and Ossipov A 2006 *Phys. Rev. A* **73** 063625
- [16] Schlagheck P and Wimberger S 2007 *Appl. Phys. B* **86** 385
- [17] Graefe E M, Korsch H J and Niederle A 2008 arXiv:0807.1777
- [18] Dalibard J, Castin Y and Mølmer K 1992 *Phys. Rev. Lett.* **68** 580
- [19] Carmichael H J 1993 *An Open Systems Approach to Quantum Optics* (Berlin: Springer)
- [20] Albiez M, Gati R, Fölling J, Hunsmann S, Cristiani M and Oberthaler M K 2005 *Phys. Rev. Lett.* **95** 010402
- [21] Gati R, Hemmerling B, Fölling F, Albiez M and Oberthaler M K 2006 *Phys. Rev. Lett.* **96** 130404
- [22] Gati R, Esteve J, Hemmerling B, Ottenstein T B, Appmeier J, Weller A and Oberthaler M K 2006 *New J. Phys.* **8** 189
- [23] Schumm T, Hofferberth S, Andersson L M, Wildermuth S, Groth S, Bar-Joseph I, Schmiedmayer J and Krüger P 2005 *Nature Phys.* **1** 57
- [24] Fölling S, Trotzky S, Cheinet P, Feld M, Saers R, Widera A, Müller T and Bloch I 2007 *Nature* **448** 1029
- [25] Milburn G J, Corney J, Wright E M and Walls D F 1997 *Phys. Rev. A* **55** 4318
- [26] Smerzi A, Fantoni S, Giovanazzi S and Shenoy S R 1997 *Phys. Rev. Lett.* **79** 4950
- [27] Trimborn F, Witthaut D and Korsch H J 2008 *Phys. Rev. A* **77** 043631
- [28] Trimborn F, Witthaut D and Korsch H J 2008 *Preprint* arXiv:0802.1142
- [29] Bloch I, Hänsch T W and Esslinger T 1999 *Phys. Rev. Lett.* **82** 3008
- [30] Gardiner C W and Zoller P 2004 *Quantum Noise* (Berlin: Springer Series in Synergetics)
- [31] Bloch F 1946 *Phys. Rev.* **70** 460
- [32] Tikhonenkov I, Anglin J R and Vardi A 2007 *Phys. Rev. A* **75** 013613
- [33] Khodorkovsky Y, Kurizki G and Vardi A 2008 *Phys. Rev. Lett.* **100** 220403
- [34] Witthaut D, Trimborn F and Wimberger S 2008 in preparation
- [35] Rigo M, Alber G, Mota-Furtado F and O'Mahony P F 1997 *Phys. Rev. A* **55** 1665
- [36] Duffield N G and Werner R F 1992 *Rev. Math. Phys.* **4** 383

PHYSICAL REVIEW E **78**, 025206(R) (2008)**Scaling law and stability for a noisy quantum system**Mark Sadgrove,¹ Sandro Wimberger,² Scott Parkins,³ and Rainer Leonhardt³¹*CREST, Japan Science and Technology Agency, Kawaguchi, Saitama 332-0012, Japan*²*Institut für Theoretische Physik, Universität Heidelberg, Philosophenweg 19, 69120 Heidelberg, Germany*³*Physics Department, The University of Auckland, Private Bag 92019, Auckland, New Zealand*

(Received 16 May 2008; published 27 August 2008)

We show that a scaling law exists for the near-resonant dynamics of cold kicked atoms in the presence of a randomly fluctuating pulse amplitude. Analysis of a quasiclassical phase-space representation of the quantum system with noise allows a new scaling law to be deduced. The scaling law and associated stability are confirmed by comparison with quantum simulations and experimental data.

DOI: [10.1103/PhysRevE.78.025206](https://doi.org/10.1103/PhysRevE.78.025206)

PACS number(s): 05.45.Mt, 03.65.Yz, 05.60.Gg

Coherent quantum phenomena may now be routinely observed in ultracold neutral atoms manipulated by light fields detuned from atomic resonance. The unprecedented control of atomic dynamics afforded by these atom-optical techniques has impacted a number of fields significantly in the last decade. In practical terms, the realization of cold-atom fountain atomic clocks and atom interferometers is very important for precision measurements and metrology in general [1]. Other promising applications include the manipulation of atoms in optical lattices [2] with possible applications to quantum computing [3].

Aside from such practical applications, atom optics has also offered the means to create ideal experimental implementations of model systems, in particular, the quantum kicked rotor known in this realization as the atom optics kicked rotor. The system and its variants have been studied by a number of groups worldwide [4–8] due to the ease of observing such quintessential quantum phenomena as dynamical localization [9] and dynamical quantum resonance [10]. Recent interest in the quantum resonance phenomenon comes not only from a fundamental perspective, but also from the useful features of the resonance behavior. For example, it has been shown that the resonance peaks exhibit sub-Fourier resonance scaling [7,8], opening the possibility of faster than Fourier signal detection using the resonance phenomenon [5]. Additionally, our work has great relevance to similar proposals for precision measurements of the atomic recoil frequency [11].

The cloud hanging over all planned implementations of quantum technologies, is that of *decoherence* [12]—interaction with environmental degrees of freedom which leads to irreversible loss of phase coherence in quantum systems. In atom-optics systems, decoherence typically arises due to spontaneous emission and timing and amplitude fluctuations in lasers. Typically, decoherence must be treated statistically, and its effect is only made plain by simulating quantum master equations. However, in the case of the quantum kicked rotor, some progress has been made in treating the response to spontaneous emission decoherence through a quasiclassical scaling theory [13]. In this case the dynamics of kicked atoms near a fundamental quantum resonance, dependent ostensibly on four parameters (kick number, strength, period, and spontaneous emission rate) is reduced to a stationary function of two scaled time variables, with a closed analytical form. The presence of this scaling belies the

fact that moderate noise typically destroys quantum correlations and it might be thought that the scaling function in the presence of spontaneous emission is an isolated case where decoherence is analytically tractable. However, here we show that a scaling exists in the same system in the presence of amplitude fluctuations. Most remarkably, the fundamentally quantum decoherence process can be visualized with a classical phase-space picture here. The noise changes the topology of the phase space in a way that makes clear which parameter regimes will exhibit robustness to decoherence.

It is important to note that amplitude noise induced destruction of quantum correlations has been proven for non-quantum resonance conditions [14]. This naturally leads to the assumption that away from exact quantum resonance, amplitude fluctuations will rapidly induce quantum decoherence. The contrary was proved by a recent experiment [15], but the cause of the stability near quantum resonance has remained opaque. We derive in the following a thorough theoretical understanding of this robustness based on a semi-classical scaling approach. Our theory compares very well with measurements of near-resonant motion.

Experimentally, we realize a kicked atom system with noise by overlapping an optical standing wave with a sample of cold atoms and pulsing the potential periodically. The height of the potential can be controlled by adjusting the optical power transmitted through an acousto-optic modulator. The system with amplitude noise may be represented by the Hamiltonian [16]

$$H(t') = \frac{p^2}{2} + k \cos(z) \sum_{s=0}^{t'-1} (1 + R_s) \delta(t' - \tau - s), \quad (1)$$

where p is the atomic momentum in units of $2\hbar k_L$, z is the atomic position scaled by $2k_L$, t' is time, and t is the total number of kicks. Amplitude noise enters in the factors R_s , which are random numbers distributed uniformly on the interval $[-L/2, +L/2]$, where L is a noise level between 0 and 2. The scaled kicking period τ is defined by the equation $\tau = 8\omega_r T$, where $\omega_r = \hbar k_L^2 / 2M$ is the recoil energy. The kicking strength is proportional to the optical standing wave intensity, and its measured value was $k \approx 4.3$ or $k \approx 2.8$ for the two separate sets of experimental data considered here. The kicking strength varied by about 10% across the atomic sample.

SADGROVE *et al.*PHYSICAL REVIEW E **78**, 025206(R) (2008)

In our experiments, a sample of cold Cs atoms was prepared in a standard magneto-optical trap (MOT) [15]. The atom ensemble had an initial width in momentum of up to $\sigma_p/(2\hbar k_L) \approx 8$. They were released from the trap and exposed to either 5 or 20 periodic pulses of width 480 ns from an optical standing wave detuned by 0.5 GHz from atomic resonance. For the 20 kicks experiments (with $k \approx 2.8$) the presence of spontaneous emission at a rate of 2.5% per kick led to a slight lifting and broadening of the resonance peaks. We corrected for the broadening by subtracting an additional small, empirically determined constant from the off-resonant energies in this case. Atoms were then allowed to evolve freely for 12 ms before applying the MOT beams and imaging the resultant fluorescence on a charge-coupled device camera. In this way, the momentum distribution of the atoms was calculated allowing a comparison with theoretical predictions. It has been shown that for pulse periods τ equal to integer multiples of 2π (so-called fundamental quantum resonances) a semiclassical map may be used to describe the quantum dynamics [13]. We define a detuning $\epsilon = \tau - 2\pi\ell$ which measures how far the pulse period is from the ℓ th fundamental quantum resonance, and define new scaled momenta and position variables $J_s = |\epsilon|p_s + \pi\ell + \tau\beta$ (where p_s is the atomic momentum in units of $2\hbar k_L$ at kick s and β is the noninteger quasimomentum) and $\theta = z + \pi[1 - \text{sgn}(\epsilon)]/2 \bmod(2\pi)$. Then the pseudoclassical standard map with amplitude fluctuations is (see [13,15])

$$J_{s+1} = J_s + \epsilon k(1 + R_s)\sin(\theta_{s+1}), \quad \theta_{s+1} = \theta_s + J_s. \quad (2)$$

We now proceed to investigate how the mean energy at exact quantum resonance is affected by *amplitude noise*. To do this we need to find the average over all amplitude noise realizations (and later initial conditions θ_0, J_0) of the equation

$$E_t(k_1, \dots, k_t) = \frac{1}{2|\epsilon|^2} (J_t - J_0)^2 \xrightarrow{\epsilon \rightarrow 0} \frac{1}{2} \left[\sum_{s=0}^{t-1} k_{s+1} \sin(\theta_0 + sJ_0) \right]^2,$$

where we have used an expansion given in [13]. The noise average is given by $\langle E_t(k_1, \dots, k_t) \rangle_{R_j} = \prod_{j=1}^t \frac{1}{L} \int_{-L/2}^{L/2} dR_j E_t(k_1, \dots, k_t)$. Since the series $\{k_s = k(1 + R_s)\}$ is a series of independent random variables, this expression simplifies greatly. Noting that $\langle R_j \rangle = 0$ and $\langle R_j R_i \rangle = 0$, $j \neq i$, we need only retain the following terms of E_t in the integrand:

$$\left[\sum_{s=0}^{t-1} \sin(\theta_0 + sJ_0) \right]^2 + \left[\sum_{s=0}^{t-1} R_s \sin(\theta_0 + sJ_0) \right]^2. \quad (3)$$

We note in addition that $\langle [\sum_{s=0}^{t-1} R_s \sin(\theta_0 + sJ_0)]^2 \rangle = \frac{L^2}{12} \sum_{s=0}^{t-1} \sin^2(\theta_0 + sJ_0)$, where we have used the fact that $(1/L^t) \int_{-L/2}^{L/2} dR_1 \dots dR_t R_s^2 = L^2/12$. Averaging over initial conditions (θ_0, J_0) gives, with $\theta_0 \in [0, 2\pi]$ and $J_0 \in [\pi\ell, \pi\ell + \tau]$ corresponding to a uniform quasimomentum distribution in the unit interval (see [13]),

$$\langle \langle E_{t,L} \rangle \rangle = \frac{k^2}{4} t \left(1 + \frac{L^2}{12} \right), \quad (4)$$

where we have used the fact that the averages over both terms in Eq. (3) evaluate to $t/2$. (This result was also given in Ref. [17] from a purely quantum argument.) Figure 1

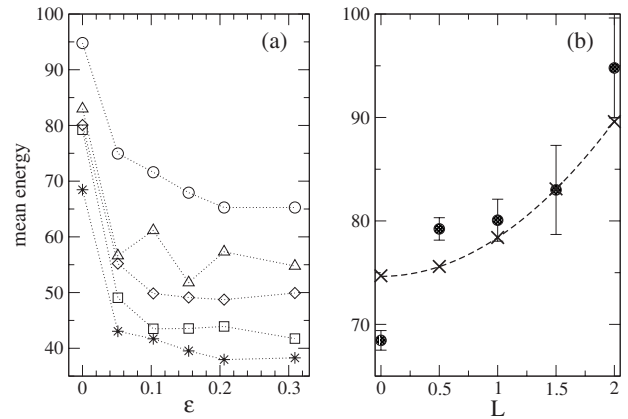


FIG. 1. (a) Experimental measurements of quantum resonance peaks as a function of ϵ for noise levels $L=0$ (\star), $L=0.5$ (\square), $L=1.0$ (\diamond), $L=1.5$ (\triangle), and $L=2.0$ (\circ). (b) Points show experimentally measured peak energies (circles), whilst the dashed line shows the theoretical formula Eq. (4). Crosses show simulation energies, which exactly agree with the theory. Sample error bars are plotted from shot-to-shot measurements, not taking into account systematic uncertainties in the absolute value of k .

shows experimental data compared with simulation results and Eq. (4), demonstrating good agreement between all three. Shot-to-shot errors were found not to vary with ϵ and the given error bars are estimates calculated from the standard error over ten energy measurements at a kicking period of $58 \mu\text{s}$. The discrepancy between theory and experiment in the $L=0$ case is due to the difficulty in measuring the high momentum components, a problem which is ameliorated by the addition of noise [6,15].

We now show how the scaling law introduced in [13] can be modified to take amplitude noise into account. We start with the pseudoclassical scaling function [13]

$$\frac{\langle E_{t,L,\epsilon} \rangle}{\langle E_{t,0} \rangle} \equiv R(t, k, \epsilon) \approx H(x) \equiv 1 - \Phi_0(x) + \frac{4}{\pi x} G(x), \quad (5)$$

where $x = t\sqrt{k|\epsilon|}$ and $\langle E_{t,0} \rangle = k^2 t/4$ is the mean peak energy. The functions Φ_0 and G are evaluated numerically, and the reader is referred to Ref. [13] for details.

For $L > 0$, we generally expect a loss of the scaling in all the variables ϵ, k, t, L due to higher correlations in the evolution of the classical map (2), neglected above when deriving Eq. (4). Remarkably, however, by observing the type of change in topology of the pseudoclassical phase space when increasing ϵ , as depicted in Fig. 2, we can nevertheless accurately estimate the change of energy growth in the presence of noise for small ϵ (for which the semiclassical approach is valid for long experimental time evolutions). Noise is well known to enhance diffusion along nonlinear resonances in the first place [18]. Therefore, we expect the major contribution of energy enhancement around the separatrix region of pseudoclassical phase space, which separates the two different topologies that give rise to the contributions G and Φ_0 to the scaling function [13]. Since G describes bounded librating pendulum motion within the principal resonance zone, local changes of that motion due to noise

SCALING LAW AND STABILITY FOR A NOISY QUANTUM ...

PHYSICAL REVIEW E 78, 025206(R) (2008)

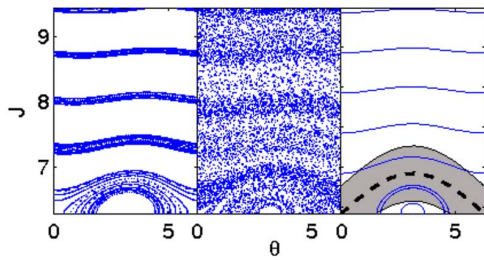


FIG. 2. (Color online) Phase-space diagrams showing the effect of amplitude noise on the pseudoclassical map (2). Left panel: without noise. Middle panel: noise level $L=1.5$. Right panel: pendulum trajectories for various initial conditions. The separatrix is shown by a thick, dashed line. The gray shaded area shows a region of $\pm\langle\Delta J_{\text{res}}^2\rangle$ for $L=1.5$ about the separatrix, demonstrating the trajectories which lead to the correction in Eq. (7).

will be small. The largest perturbation comes from classical trajectories moving close to the separatrix which is washed out due to the fluctuations of k (see Fig. 2). In this region, trajectories can actually perform rotating motion now, where at $L=0$ they would still be bounded to the resonance. The increase of energy arising from those trajectories can be estimated by considering the area in phase space covered by them, as shown for $L=1.5$ in Fig. 2. Since the width of the principal resonance is given by $\Delta J_{\text{res}} \approx 4\sqrt{k\epsilon}$, the relative change in weight of rotating orbits is given by

$$\frac{1}{2\pi} \frac{\langle\Delta J_{\text{res}}^2\rangle - \Delta J_{\text{res}}^2}{\Delta J_{\text{res}}^2} \approx \frac{L}{8\pi}. \quad (6)$$

The noise-averaged standard deviation is $\langle\Delta J_{\text{res}}^2\rangle \approx (1 + L/4)\Delta J_{\text{res}}^2$ by a simple integration. With this result we can now add the additional energy of rotating trajectories to the scaling function from Eq. (4), by adding a term $L/(8\pi)\Phi(x)$. Dividing now the true energies by the result at exact quantum resonance and $L=0$, we finally arrive at the new scaling function for finite noise,

$$\begin{aligned} \frac{\langle\langle E_{t,\epsilon} \rangle\rangle}{\frac{1}{4}k^2t} &\equiv \mathcal{R}(t,\epsilon,k,L) \approx \mathcal{H}(x,L) \\ &\equiv 1 + \frac{L^2}{12} - [1 - L/(8\pi)]\Phi_0(x) + \frac{4}{\pi x}G(x). \end{aligned} \quad (7)$$

Our derivation of Eq. (7) is thus analogous to the noise-free case, taking into account, however, the main contribution of heating due to noise. Higher-order correlations and heating of the librating modes are neglected. We note that the principle changes to the phase space which give rise to this scaling are readily seen in Fig. 2. In essentials, the scaling function reduces a complicated quantum system which includes decoherence to the dynamics of the pendulum.

Inspection of Eq. (7) reveals some interesting features as seen in Fig. 3. Firstly, because Φ_0 saturates to 1 and $G(x)$ is small for small values of x , the small x behavior is largely unchanged in the scaling function. Essentially, the zero-noise scaling function is merely displaced upwards for small t, k ,

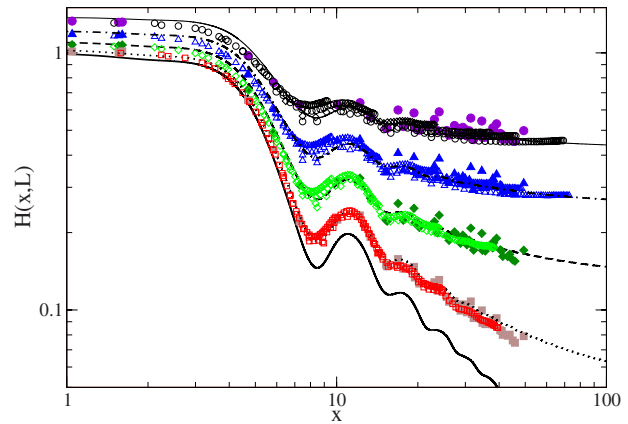


FIG. 3. (Color online) Theoretical scaling function for $L=0$ (thick solid line), $L=0.5$ (dotted line), $L=1.0$ (dashed line), $L=1.5$ (dot-dashed line) and $L=2.0$ (thin line). Simulation data is also shown, rescaled by the factor $\frac{1}{4}k^2t$, for $L=0.5$ (\square), $L=1.0$ (\diamond), $L=1.5$ (\triangle), and $L=2.0$ (\circ). Open symbols are produced for fixed $k=2.8$, varying $\epsilon \in [10^{-3}, 0.1]$, $t \in [20, 150]$, while filled symbols represent data for randomly chosen values of $k \in [1, 10]$, $\epsilon \in [10^{-3}, 0.1]$, $t \in [2, 150]$.

or ϵ . Experimentally, this means that as long as $x = t\sqrt{k\epsilon} \lesssim 4$ (e.g., take $t=20$, $k=0.1$ and scan over ϵ for any noise value), the resonance peak will not be broadened. This fact is important for proposed precision experiments such as [11] where experimenters need to know how much tolerance the resonance width has to naturally occurring laser power fluctuations. Secondly, for large x the scaling function is significantly changed with the offset being much greater, corresponding to real broadening of the peak and reduction of peak visibility.

A comparison of the theory with simulation results is shown in Fig. 3. It may be seen that the scaling function reproduces the broad shape of the quantum simulations over a large spectrum of parameters. Each point in Fig. 3 is obtained by averaging over 50 000 initial conditions, each of which is subject to kick-to-kick amplitude fluctuations. Although our statistics are good, there is still a non-negligible scatter in the simulation data which decreased systematically when augmenting the number of initial conditions averaged to obtain the final energy. The experimental data from Fig. 1(a) and additional new data sets have been plotted in Fig. 4. The experimentally measured energies are obtained as an ensemble average over the total number of atoms and are rescaled by subtracting the mean initial energy of the ensemble $\sigma_p^2/4$ and then dividing by the energy at the peak maximum for $L=0$. The estimated error bars shown in Fig. 4 represent shot-to-shot fluctuations over different noise realizations calculated as for Fig. 1.

In summary, we have derived and tested a generalized scaling function for the quantum resonance peaks in the presence of noise. The theory shows broad agreement with both quantum simulations and experimental results. Most importantly it illuminates new facts about the response of quantum resonance to noise—in particular, the stability of motion near to quantum resonance is revealed to be due to the unexpected

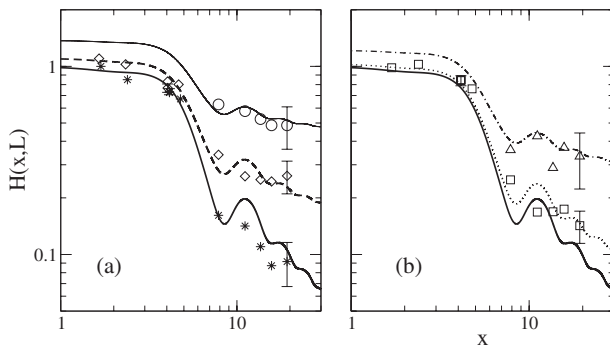

SADGROVE *et al.*PHYSICAL REVIEW E **78**, 025206(R) (2008)

FIG. 4. Theoretical scaling function of Eq. (7) (as shown in Fig. 3) is compared with rescaled experimental data (as, e.g., from Fig. 1). Shown are data across more than one order of magnitude in the scaling variable x for (a) $L=0$ (\star), $L=1.0$ (\diamond), and $L=2.0$ (\circ) and (b) $L=0.5$ (\square) and $L=1.5$ (\triangle). Theoretical curves are shown with the same line styles as in Fig. 3. Note that for $x < 5$ the data comes from separate five kick experiments, and the error bars are the same size as the plotted points. Sample error bars are calculated as described in the caption of Fig. 1. Data for $|\epsilon| > 0.15$ is excluded since the pseudoclassical theory breaks down in this region.

persistence of scaling laws in the noisy system. Although the effect of amplitude noise is to modify and even destroy quantum correlations, the effect near to quantum resonance can be understood precisely in terms of the noise-induced changes to the epsilon-classical phase space. Hence, quantum decoherence may be understood by a quasiclassical analysis in the system studied here. The robust nature of the scaling for small x allows us to predict parameter families of t , τ , and k for which noise will have a minimal effect on the quantum resonance, and surprisingly we find that for small enough x , the quantum resonance peak shape is entirely unaffected by noise (although a displacement in energy occurs). The exploration of quantum systems which exhibit resistance to noise is of great importance for the future of quantum technologies. Analytical methods for determining the response of a system to noise and perturbations, as done here and in a different context in [19], are valuable because they offer insight on the stability of quantum motion which simulations cannot readily provide.

The authors acknowledge support within the Excellence Initiative by the DFG through the Heidelberg Graduate School of Fundamental Physics (Grant No. GSC 129/1) and thank Shmuel Fishman for stimulating discussions.

- [1] *Atom Interferometry*, edited by P. R. Berman (Academic, New York, 1997); S. L. Rolston and W. D. Phillips, *Nature (London)* **416**, 219 (2002).
- [2] O. Morsch and M. Oberthaler, *Rev. Mod. Phys.* **78**, 179 (2006).
- [3] G. K. Brennen, C. M. Caves, P. S. Jessen, and I. H. Deutsch, *Phys. Rev. Lett.* **82**, 1060 (1999); T. Calarco, U. Dorner, P. Julienne, C. Williams, and P. Zoller, *Phys. Rev. A* **70**, 012306 (2004).
- [4] F. L. Moore, J. C. Robinson, C. F. Bharucha, B. Sundaram, and M. G. Raizen, *Phys. Rev. Lett.* **75**, 4598 (1995); H. Ammann, R. Gray, I. Shvachuck, and N. Christensen, *ibid.* **80**, 4111 (1998); G. Duffy *et al.*, *Phys. Rev. E* **70**, 056206 (2004); P. H. Jones, M. Goonasekera, D. R. Meacher, T. Jonckheere, and T. S. Monteiro, *Phys. Rev. Lett.* **98**, 073002 (2007); I. Dana, V. Ramareddy, I. Talukdar, and G. S. Summy, *ibid.* **100**, 024103 (2008).
- [5] P. Szriftgiser, J. Ringot, D. Delande, and J. C. Garreau, *Phys. Rev. Lett.* **89**, 224101 (2002); H. Lignier, J. C. Garreau, P. Szriftgiser, and D. Delande, *Europhys. Lett.* **69**, 327 (2005).
- [6] M. B. d'Arcy, R. M. Godun, M. K. Oberthaler, D. Cassettari, and G. S. Summy, *Phys. Rev. Lett.* **87**, 074102 (2001); *Phys. Rev. E* **69**, 027201 (2004); C. Ryu *et al.*, *Phys. Rev. Lett.* **96**, 160403 (2006); J. F. Kanem, S. Maneshi, M. Partlow, M. Spanner, and A. M. Steinberg, *ibid.* **98**, 083004 (2007).
- [7] S. Wimberger, M. Sadgrove, S. Parkins, and R. Leonhardt, *Phys. Rev. A* **71**, 053404 (2005).
- [8] M. Sadgrove, S. Wimberger, S. Parkins, and R. Leonhardt, *Phys. Rev. Lett.* **94**, 174103 (2005).
- [9] S. Fishman, in *Quantum Chaos, School "E. Fermi" CXIX*, edited by G. Casati *et al.* (IOS, Amsterdam, 1993).
- [10] F. M. Izrailev, *Phys. Rep.* **196**, 299 (1990).
- [11] A. Tonyushkin, S. Wu, and M. Prentiss, e-print arXiv:0803.4153v1.
- [12] See, e.g., the recent review by K. Hornberger, e-print arXiv:quant-ph/0612118, and references therein.
- [13] S. Wimberger, I. Guarneri, and S. Fishman, *Nonlinearity* **16**, 1381 (2003).
- [14] V. Milner, D. A. Steck, W. H. Oskay, and M. G. Raizen, *Phys. Rev. E* **61**, 7223 (2000); D. A. Steck, V. Milner, W. H. Oskay, and M. G. Raizen, *ibid.* **62**, 3461 (2000).
- [15] M. Sadgrove, A. Hilliard, T. Mullins, S. Parkins, and R. Leonhardt, *Phys. Rev. E* **70**, 036217 (2004).
- [16] R. Graham, M. Schlautmann, and P. Zoller, *Phys. Rev. A* **45**, R19 (1992).
- [17] S. Brouard and J. Plata, *J. Phys. A* **36**, 3745 (2003).
- [18] A. L. Lichtenberg and M. A. Leiberman, *Regular and Chaotic Dynamics* (Springer, Berlin, 1992).
- [19] J. Chabé *et al.*, *Phys. Rev. Lett.* **97**, 264101 (2006).

 Selected for a **Viewpoint** in *Physics*
PHYSICAL REVIEW A **79**, 033621 (2009)

Dissipation-induced coherence and stochastic resonance of an open two-mode Bose-Einstein condensate

D. Witthaut,^{1,*} F. Trimborn,² and S. Wimberger³

¹*QUANTOP, Niels Bohr Institute, University of Copenhagen, DK-2100 Copenhagen, Denmark*

²*Institut für Mathematische Physik, TU Braunschweig, D-38106 Braunschweig, Germany*

³*Institut für Theoretische Physik, Universität Heidelberg, D-69120 Heidelberg, Germany*

(Received 27 October 2008; published 23 March 2009)

We discuss the dynamics of a Bose-Einstein condensate in a double-well trap subject to phase noise and particle loss. The phase coherence of a weakly interacting condensate, experimentally measured via the contrast in an interference experiment, as well as the response to an external driving becomes maximal for a finite value of the dissipation rate matching the intrinsic time scales of the system. This can be understood as a stochastic resonance of the many-particle system. Even stronger effects are observed when dissipation acts in concurrence with strong interparticle interactions, restoring the purity of the condensate almost completely and increasing the phase coherence significantly. Our theoretical results are backed by Monte Carlo simulations, which show a good qualitative agreement and provide a microscopic explanation for the observed stochastic resonance effect.

DOI: [10.1103/PhysRevA.79.033621](https://doi.org/10.1103/PhysRevA.79.033621)

PACS number(s): 03.75.Lm, 03.75.Gg, 03.65.Yz

I. INTRODUCTION

Stochastic resonance (SR) is a strongly surprising yet very general effect in nonlinear dynamical systems. Against our naive understanding, the response of a system to an external driving can be facilitated if an appropriate amount of noise is added. In fact, the maximum of the response—the stochastic resonance—is found if the time scale of the noise matches an intrinsic time scale of the system. The effect was first described for strongly damped classical systems such as the overdamped particle in a driven double-well trap. In this case the noise is strong enough to induce the transition between the wells, whereas it is still weak enough not to randomize the dynamics completely. The particle will then hop to and fro almost deterministically if the average transition time between the wells due to the noise equals half of the driving period [1]. By now, a stochastic resonance has been shown in a variety of systems; an overview can be found in the review articles [2–5]. In addition to numerous examples in classical dynamics, stochastic resonance has also been found in a variety of quantum systems (see, e.g., [5–11]).

Recently, there has been an increased interest in the effects of dissipation and the possibilities to control these in interacting many-body quantum systems. For instance, the entanglement in a spin chain assumes an SR-like maximum for a finite amount of thermal noise [12]. Methods to attenuate phase noise for an open two-mode Bose-Einstein condensate (BEC) were discussed in [13], and the effects of particle loss on the spin squeezing of such a system were analyzed in [14]. Furthermore, it has been shown that dissipative processes can be tailored to prepare arbitrary pure states for quantum computation and strongly correlated states of ultracold atoms [15,16] or to implement a universal set of quantum gates [17]. Actually, a recent experiment has even proven that strong inelastic collisions may inhibit particle

losses and induce strong correlations in a quasi-one-dimensional (quasi-1D) gas of ultracold atoms [18,19].

In the present paper, we investigate the effects of noise and dissipation for a BEC in a double-well trap. The essential idea has been introduced in a recent letter [20], and here we extend the discussion to a detailed analysis of the predicted SR phenomenon. The setup under consideration has been experimentally realized by several groups only in the last few years [21–26]. Ultracold atoms in optical potentials have the enormous advantage that they allow us to observe the quantum dynamics of an interacting many-particle system *in situ*. Thus they serve as excellent model systems, bringing together aspects of nonlinear dynamics, solid-state physics, and the theory of open quantum systems. Here we show that the coherence of the two condensate modes assumes a maximum in the fashion of the stochastic resonance effect for a finite dissipation rate, which matches the time scales of the intrinsic dynamics. In this case the particle loss is strong enough to significantly increase the condensate purity, whereas it is still weak enough not to dominate the dynamics completely. Similarly the response to an external driving is increased if a proper amount of dissipation is present. Even more remarkable results are found when dissipation acts in concurrence with strong interparticle interactions, leading to an almost complete revival of the purity of the BEC. These effects are of considerable strength for realistic parameters and thus should be readily observable in ongoing experiments.

This paper is organized as follows. First, we introduce the theoretical description of the open two-mode Bose-Hubbard system. We discuss the main sources of noise and dissipation and derive the corresponding mean-field approximation of the many-particle system. The resulting dynamics for weak interparticle interactions is analyzed in Sec. III. It is shown that the phase contrast between the two modes assumes an SR-like maximum if the time scales of tunneling and dissipation are matched. This result is explained within the mean-field approximation as well as for the underlying many-

*dirk.witthaut@nbi.dk

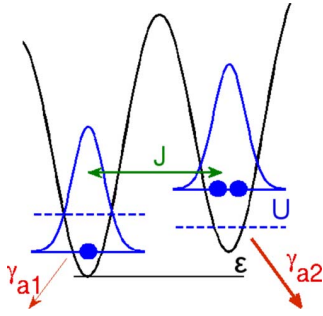


FIG. 1. (Color online) The open double-well trap considered in the present paper.

particle quantum dynamics with Monte Carlo simulations backing up the approximative results. The response of the open system to an external driving is discussed in Sec. IV. The amplitude of the forced oscillation also shows a pronounced stochastic resonance effect. Section V then investigates the case of a strongly interacting BEC, which is a problem of both fundamental theoretical interest as well as high experimental relevance. The interplay between interactions and dissipation can restore the purity of the condensate almost completely and significantly increase the phase coherence in comparison with situations where one of the two is weak or missing. This counterintuitive effect is robust and can be explained by the appearance of novel nonlinear eigenstates.

II. NOISE AND DISSIPATION IN A TRAPPED BEC

The basic setup under consideration is depicted in Fig. 1. Ultracold atoms are confined in a double-well trap that can be realized, e.g., by superimposing an optical lattice with an optical dipole trap [21–23], in a bichromatic optical lattice [24,25], or on an atom chip [26]. We consider the case of a deep but tight trap, which is tuned such that only one mode in each well is bounded and thus significantly populated. All scattering solutions of the model form a continuum of unbound modes which adds up to the heat bath (see below) [27]. One major assumption in the derivation of this model is that the level spacing between the trap modes is significantly larger than the self-energy of the atom-atom interactions in the trap: $UN \ll \hbar \omega_{\text{trap}}$. For a typical trap frequency around 100 Hz, this restricts the atom number to a few hundreds. Note that this model is not compatible to the Thomas-Fermi approximation, where the many-body interaction dominates the kinetic energy. Likewise, it is not directly applicable to the case of two weakly coupled 1D quasicondensates [28,29] due to the excitation of longitudinal modes.

The unitary dynamics of the atoms is then described by the two-mode Bose-Hubbard Hamiltonian [30–33],

$$\hat{H} = -J(\hat{a}_1^\dagger \hat{a}_2 + \hat{a}_2^\dagger \hat{a}_1) + \epsilon_2 \hat{n}_2 + \epsilon_1 \hat{n}_1 + \frac{U}{2} [\hat{n}_1(\hat{n}_1 - 1) + \hat{n}_2(\hat{n}_2 - 1)], \quad (1)$$

which describes both the dynamics of the condensed fraction, as well as the noncondensate, but nevertheless trapped

atoms. The operators \hat{a}_j and \hat{a}_j^\dagger are the bosonic annihilation and creation operators in mode j and $\hat{n}_j = \hat{a}_j^\dagger \hat{a}_j$ is the corresponding number operator. Furthermore, J denotes the tunneling matrix element between the wells, U denotes the interaction strength, and ϵ_j denotes the on-site energy of the j th well. We set $\hbar = 1$, thus measuring all energies in frequency units.

In order to clarify the algebraic structure of the model and to analyze the dynamics in the Bloch representation we introduce the collective operators,

$$\begin{aligned} \hat{L}_x &= \frac{1}{2}(\hat{a}_1^\dagger \hat{a}_2 + \hat{a}_2^\dagger \hat{a}_1), \\ \hat{L}_y &= \frac{i}{2}(\hat{a}_1^\dagger \hat{a}_2 - \hat{a}_2^\dagger \hat{a}_1), \\ \hat{L}_z &= \frac{1}{2}(\hat{a}_2^\dagger \hat{a}_2 - \hat{a}_1^\dagger \hat{a}_1), \end{aligned} \quad (2)$$

which form an angular-momentum algebra $\text{su}(2)$ with quantum number $\ell = N/2$ [30–35], where N is the actual particle number. Hamiltonian (1) then can be rewritten as

$$\hat{H} = -2J\hat{L}_x + 2\epsilon\hat{L}_z + U\hat{L}_z^2 \quad (3)$$

up to terms only depending on the total number of atoms. Here, $\epsilon = \epsilon_2 - \epsilon_1$ denotes the difference of the on-site energies of the two wells.

A model for noise and dissipation in a deep trapping potential has been derived by Anglin [27] and later extended by Ruostekoski and Walls [36] to the case of two weakly coupled modes. The dissipation of energy is described by the coupling to a thermal reservoir consisting of noncondensate modes. The dynamics is then given by the master equation,

$$\begin{aligned} \dot{\hat{\rho}} &= -i[\hat{H}, \hat{\rho}] - \frac{\gamma_p}{2} \sum_{j=1,2} (\hat{n}_j^2 \hat{\rho} + \hat{\rho} \hat{n}_j^2 - 2\hat{n}_j \hat{\rho} \hat{n}_j) \\ &\quad - \frac{\gamma_{\text{in}}}{2} \sum_{j=1,2;\pm} (\hat{C}_{j\pm}^\dagger \hat{C}_{j\pm} \hat{\rho} + \hat{\rho} \hat{C}_{j\pm}^\dagger \hat{C}_{j\pm} - 2\hat{C}_{j\pm} \hat{\rho} \hat{C}_{j\pm}^\dagger) \end{aligned} \quad (4)$$

with the Lindblad operators

$$\hat{C}_{j+} = \hat{a}_j^\dagger$$

and

$$\hat{C}_{j-} = e^{\beta/2(\epsilon_j - \mu + U\hat{n}_j)} \hat{a}_j, \quad (5)$$

describing growth and depletion of the condensate.

Let us briefly discuss the effects of the noise and dissipation terms. The second term $\sim \gamma_p$ in Eq. (4) describes phase noise due to elastic collisions with the background gas atoms. It is usually the dominating contribution, effectively heating the system, but leaving the total particle number invariant. If only phase noise is present, the system relaxes to an equilibrium state where all coherences are lost and all Dicke states $|n_1, N-n_1\rangle \sim \hat{a}_1^{\dagger n_1} \hat{a}_2^{\dagger N-n_1} |0, 0\rangle$ are equally populated,

$$\langle n_1, N - n_1 | \hat{\rho} | n'_1, N - n'_1 \rangle = \frac{1}{N+1} \delta_{n_1, n'_1}, \quad (6)$$

as long as $J \neq 0$ [37,38]. This corresponds to a thermal state of infinite temperature with $\langle \hat{\mathbf{L}} \rangle = \mathbf{0}$. The remaining terms $\sim \gamma_{\text{in}}$ in the master equation [Eq. (4)] describe amplitude noise, i.e., the growth and depletion of the condensate due to inelastic collisions with the background gas. In contrast to phase noise, amplitude noise heats *and* cools the system. If both amplitude and phase noise are present, the system will relax to the proper thermal state with a density operator $\hat{\rho} \propto \exp[-\beta(\hat{H} - \mu\hat{n})]$ [27].

In current experiments amplitude noise and dissipation are usually extremely weak in comparison to phase noise [36], if it is not introduced artificially as for example by forced evaporative cooling during the preparation of the BEC. For example, phase noise damps Josephson oscillations on a time scale of a few hundred milliseconds in the experiments, while less than 10% of the atoms are lost during a 30 s experiment [21–23]. This is much too weak to produce significant effects, such that the terms describing the particle exchange with the background gas in Eq. (4) can be neglected, $\gamma_{\text{in}} \approx 0$.

However, nontrivial effects of dissipation such as the stochastic resonance discussed below require strong, tunable, and biased loss rates. A well-controllable source of dissipation can be implemented artificially by shining a resonant laser beam onto the trap, which removes atoms with the site-dependent rates γ_{aj} from the two wells $j=1,2$. For such a laser beam focused on one of the wells an asymmetry of $f_a = (\gamma_{a2} - \gamma_{a1}) / (\gamma_{a2} + \gamma_{a1}) = 0.5$ should be feasible. In magnetic trapping potentials, a similar effect can also be achieved by a forced rf transition to an untrapped magnetic substate [39].

Therefore the above master equation must be extended to take into account the single-particle losses. The additional term describing the particle loss is well established and routinely used in the context of photon fields [38]. In the following we will thus consider the dynamics generated by the master equation:

$$\begin{aligned} \dot{\hat{\rho}} = & -i[\hat{H}, \hat{\rho}] - \frac{\gamma_p}{2} \sum_{j=1,2} (\hat{n}_j^2 \hat{\rho} + \hat{\rho} \hat{n}_j^2 - 2\hat{n}_j \hat{\rho} \hat{n}_j) \\ & - \frac{1}{2} \sum_{j=1,2} \gamma_{aj} (\hat{a}_j^\dagger \hat{a}_j \hat{\rho} + \hat{\rho} \hat{a}_j^\dagger \hat{a}_j - 2\hat{a}_j \hat{\rho} \hat{a}_j^\dagger). \end{aligned} \quad (7)$$

The macroscopic dynamics of the atomic cloud is to a very good approximation [32,33,40] described by a mean-field approximation, considering only the expectation values $s_j(t) = 2 \text{tr}[\hat{L}_j \hat{\rho}(t)]$ of the angular-momentum operators [Eq. (2)] and the particle number $n(t) = \text{tr}[(\hat{n}_1 + \hat{n}_2) \hat{\rho}(t)]$. The evolution equations for the Bloch vector $\mathbf{s} = (s_x, s_y, s_z)$ are then calculated starting from the master equation via $\dot{s}_j = 2 \text{tr}[\hat{L}_j \dot{\hat{\rho}}]$ with the exact result (cf. [40]),

$$\dot{s}_x = -2\epsilon s_y - U(s_y s_z + \Delta_{yz}) - T_2^{-1} s_x,$$

$$\dot{s}_y = 2J s_z + 2\epsilon s_x + U(s_x s_z + \Delta_{xz}) - T_2^{-1} s_y,$$

$$\dot{s}_z = -2J s_y - T_1^{-1} s_z - T_1^{-1} f_a s_z,$$

$$\dot{n} = -T_1^{-1} n - T_1^{-1} f_a s_z, \quad (8)$$

where we have defined the transversal and longitudinal damping times by

$$T_1^{-1} = (\gamma_{a1} + \gamma_{a2})/2 \quad \text{and} \quad T_2^{-1} = \gamma_p + T_1^{-1}. \quad (9)$$

These equations of motion resemble the celebrated Bloch equations in nuclear-magnetic resonance [41,42], with some subtle but nevertheless important differences. The longitudinal relaxation is now associated with particle loss and, more important, the dynamics is substantially altered by the U -dependent interaction term [21,30,31].

The exact equations of motion (8) still include the covariances

$$\Delta_{jk} = \langle \hat{L}_j \hat{L}_k + \hat{L}_k \hat{L}_j \rangle - 2\langle \hat{L}_j \rangle \langle \hat{L}_k \rangle. \quad (10)$$

The celebrated mean-field description is now obtained by approximating the second-order moments by products of expectation values such that $\Delta_{jk} \approx 0$ [30–33].

In the following, we will show that a finite amount of dissipation induces a maximum of the coherence which can be understood as a stochastic resonance effect. In this discussion we have to distinguish between two different kinds of coherence, which will both be considered in the following. First of all we consider the phase coherence between the two wells, which is measured by the average *contrast* in interference experiments as described in [21–23] and given by

$$\alpha(t) = \frac{2|\langle \hat{a}_1^\dagger \hat{a}_2 \rangle|}{\langle \hat{n}_1 + \hat{n}_2 \rangle} = \frac{\sqrt{s_x(t)^2 + s_y(t)^2}}{n(t)}. \quad (11)$$

Second, we will analyze how close the many-particle quantum state is to a pure Bose-Einstein condensate. This property is quantified by the purity

$$p = 2 \text{tr}(\hat{\rho}_{\text{red}}^2) - 1 \quad (12)$$

of the reduced single-particle density matrix [32,33,35,43],

$$\hat{\rho}_{\text{red}} = \frac{1}{N} \begin{pmatrix} \langle \hat{a}_1^\dagger \hat{a}_1 \rangle & \langle \hat{a}_1^\dagger \hat{a}_2 \rangle \\ \langle \hat{a}_2^\dagger \hat{a}_1 \rangle & \langle \hat{a}_2^\dagger \hat{a}_2 \rangle \end{pmatrix}. \quad (13)$$

One can easily show that the purity is related to the Bloch vector \mathbf{s} by $p = |\mathbf{s}|^2 / n^2$. A pure BEC, corresponding to a product state, is, of course, characterized by $p=1$. For smaller values of p , there is a growing amount of trapped but non-condensate atoms. This depletion of the BEC results from the many-particle interactions, which destroy the macroscopic product state. However, in leading order these do not lead to scattering to the background gas or to higher unpopulated modes, respectively (cf. [27,36]).

III. DISSIPATION-INDUCED COHERENCE IN A WEAKLY INTERACTING BEC

In this section, we show that a proper amount of dissipation can indeed increase the phase coherence (11) of a two-mode BEC similar to the stochastic resonance effect. For simplicity, we start with the linear case $U=0$, where the

WITTHAUT, TRIMBORN, AND WIMBERGER

PHYSICAL REVIEW A 79, 033621 (2009)

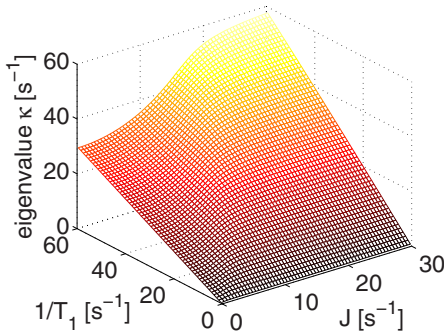


FIG. 2. (Color online) Decay rate κ of the quasi-steady-state (14) as a function of the tunneling rate J and the dissipation rate $1/T_1$ for $\gamma_p=5 \text{ s}^{-1}$ and $U=\epsilon=0$.

mean-field equations of motion for the expectation values [Eq. (8)] are exact. The linear equations resemble the Bloch equations for driven nuclear spins in the rotating wave approximation [42], which are known to show a pronounced stochastic resonance effect [41]: the amplitude of forced oscillations of the spins given by s_y assumes a maximum for a finite value of the relaxation rates T_1^{-1} and T_2^{-1} , provided these are coupled. For the two-mode BEC considered here this is automatically the case as given by Eq. (9). Thus we also expect a maximum of the steady-state value of the phase coherence (11) for a finite value of T_1^{-1} .

Let us now determine the steady-state value of the contrast (11) which quantifies the phase coherence of the two wells as a function of the system parameters and the relaxation rates. Obviously, the only steady state in the strict sense is given by $\mathbf{s}=\mathbf{0}$ and $n=0$, corresponding to a completely empty trap. However, the system rapidly relaxes to a quasi-steady-state where the internal dynamics is completely frozen out and all components of the Bloch vector and the particle number decay at the same rate,

$$\mathbf{s}(t) = \mathbf{s}_0 e^{-\kappa t}, \quad n(t) = n_0 e^{-\kappa t}. \quad (14)$$

Substituting this ansatz into the equations of motion (8), the quasi-steady-state is determined by the eigenvalue equation,

$$\mathbf{M} \begin{pmatrix} s_{x0} \\ s_{y0} \\ s_{z0} \\ n_0 \end{pmatrix} = \kappa \begin{pmatrix} s_{x0} \\ s_{y0} \\ s_{z0} \\ n_0 \end{pmatrix} \quad (15)$$

with the matrix

$$\mathbf{M} = \begin{pmatrix} T_2^{-1} & 2\epsilon & 0 & 0 \\ -2\epsilon & T_2^{-1} & -2J & 0 \\ 0 & 2J & T_1^{-1} & f_a T_1^{-1} \\ 0 & 0 & f_a T_1^{-1} & T_1^{-1} \end{pmatrix}, \quad (16)$$

which is readily solved numerically.

Figure 2 depicts the smallest real eigenvalue κ corresponding to the most stable quasi-steady-state as a function of J and $1/T_1$ for the noninteracting case and $\epsilon=0$. It determines the basic time scale of the system and is essentially proportional to the dissipation rate T^{-1} .

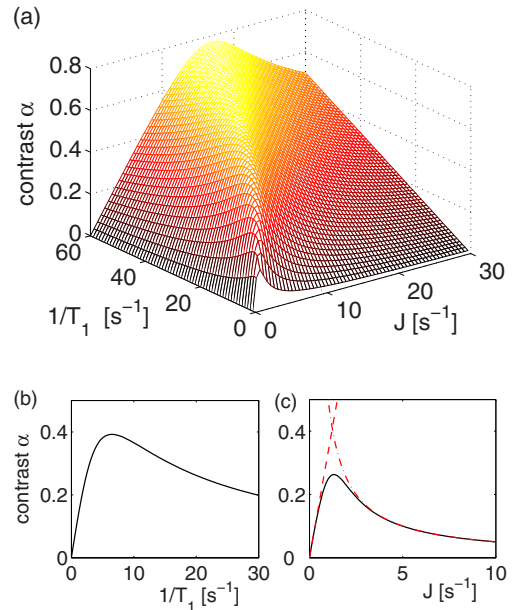


FIG. 3. (Color online) Contrast α of the quasi-steady-state (14) as a function of the tunneling rate J and the dissipation rate $1/T_1$ (a) for $\gamma_p=5 \text{ s}^{-1}$ and $U=\epsilon=0$ and (b) for a fixed value of the tunneling rate $J=2 \text{ s}^{-1}$ and (c) a fixed value of the dissipation rate $1/T_1=2 \text{ s}^{-1}$. The dashed-dotted red lines represent the approximations [Eq. (19)] for small and large values of J .

Figure 3 shows the resulting values of the contrast α as a function of the dissipation rate T_1^{-1} and the tunneling rate J for $U=\epsilon=0$ and $\gamma_p=5 \text{ s}^{-1}$. For a fixed value of one of the parameters, say J , one observes a typical SR-like maximum of the contrast for a finite value of the dissipation rate $1/T_1$ as shown in part (b) of the figure. In particular, the contrast is maximal if the time scales of the tunneling and the dissipation are matched according to

$$4J^2 \approx f_a^2 T_1^{-2} + f_a \gamma_p T_1^{-1}. \quad (17)$$

Furthermore, the contrast $\alpha(J)$ shows a similar maximum for a finite value of the tunneling rate J when the dissipation rate is fixed as shown in Fig. 3(c). Contrary to our intuition this shows that an increase in the coupling of two modes can indeed *reduce* their phase coherence.

In the special case $\epsilon=0$, illustrated in Fig. 3, one can solve the eigenvalue problem [Eq. (15)] exactly. In this case one has $s_x=0$ and the contrast α is related to the eigenvalue κ by

$$\alpha = \frac{2J(T_1^{-1} - \kappa)}{f_a T_1^{-1}(T_2^{-1} - \kappa)}. \quad (18)$$

Evaluating the roots of the characteristic polynomial to determine κ leads to an algebraic equation of third order which can be solved analytically. The resulting expressions are quite lengthy, but the limits for small and large values of the tunneling rate are readily obtained as

$$\alpha \approx \frac{2J}{T_2^{-1} - (1 - f_a)T_1^{-1}} \quad \text{for } J \ll T_1^{-1},$$

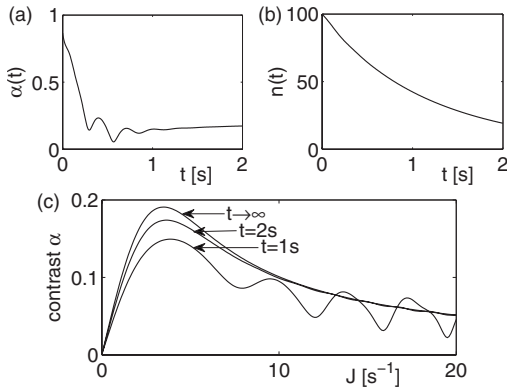


FIG. 4. Relaxation to the quasi-steady-state for $\gamma_p=5 \text{ s}^{-1}$, $T_1^{-1}=1 \text{ s}^{-1}$, $\epsilon=10 \text{ s}^{-1}$, and $U=0$. (a) Relaxation of the contrast $\alpha(t)$ for $J=4 \text{ s}^{-1}$. (b) Decay of the particle number $n(t)$ for $J=4 \text{ s}^{-1}$. (c) Development of the SR maximum of the contrast $\alpha(J)$.

$$\alpha \approx \frac{f_a T_1^{-1}}{2J} \quad \text{for } J \gg T_1^{-1}. \quad (19)$$

These approximations are plotted as dashed red lines in Fig. 3(c). Their intersection given by Eq. (17) gives a very good approximation for the position of the SR-like maximum of the contrast $\alpha(J)$.

An important experimental issue is the question whether the quasi-steady-state is reached fast enough, such that the typical SR-like curve of the contrast as shown in Fig. 3 can be observed while still enough atoms are left in the trap. To answer this question, we integrate the equations of motion (8) starting from a pure BEC with $\mathbf{s}(0)/n(0) = (\sqrt{3}/2, 0, 1/2)$ and $n(0)=100$ particles. Figure 4(a) shows the relaxation of the contrast for $J=4 \text{ s}^{-1}$ and $T_1=1 \text{ s}$. The steady-state value is nearly reached after $t=1 \text{ s}$ when still 40% of the atoms are left in the trap. Figure 4(b) shows the development of the contrast $\alpha(J)$ in time. It is observed that the characteristic SR-like maximum is already well developed after 1 s, where roughly half of the atoms are lost. Thus we conclude that the SR-like maximum of the contrast should be observable in ongoing experiments.

The stochastic resonance effect introduced above is robust and generally not altered by changes in the system parameters or in the presence of weak interparticle interactions. For instance, a change in the bias ϵ of the on-site energies of the two wells preserves the general shape of $\alpha(1/T_1, J)$ shown in Fig. 3 and especially the existence of a pronounced SR-like maximum. At most, the function $\alpha(1/T_1, J)$ is stretched, shifting the position of the SR-like maximum. This shift is

illustrated in Fig. 5(a) where we have plotted the contrast as a function of J for the dissipation rate $T_1^{-1}=2 \text{ s}^{-1}$ and different values of ϵ . Thus, this effect provides a useful tool to shift the maximum to values of J , which are easier accessible in ongoing experiments.

Similarly, the position of the maximum of the coherence $\alpha(J)$ is shifted in the presence of weak interparticle interactions. An interacting BEC will usually not show a simple exponential decay of form (14) because the instantaneous decay rate depends on the effective interaction strength $Un(t)$, which also decreases [44–46]. However, the discussion of quasi-steady-states and instantaneous decay rates is still useful if the decay is weak. In this case the system can follow the quasi-steady-states adiabatically and the decay of the population is given by

$$\frac{dn(t)}{dt} = -\kappa(n(t))n(t)$$

and

$$\frac{ds(t)}{dt} = -\kappa(n(t))s(t), \quad (20)$$

in good approximation. Substituting this ansatz into the equations of motion (8) yields four coupled nonlinear algebraic equations, which can be disentangled with a little algebra. For a given number of particles n , the instantaneous decay rate κ is obtained by solving the fourth-order algebraic equation,

$$[(\kappa - T_2^{-1})^2 + (Un)^2(\kappa - T_1^{-1})^2][(\kappa - T_1^{-1})^2 - f_a^2 T_1^{-2}] + 4J^2 f_a^2 T_1^{-2} (\kappa - T_1^{-1})(\kappa - T_2^{-1}) = 0. \quad (21)$$

The Bloch vector for the corresponding quasi-steady-state is then given by

$$s_{x0} = \frac{\kappa - T_1^{-1}(\kappa - T_1^{-1})^2 - f_a^2 T_1^{-2}}{\kappa - T_2^{-1}(\kappa - T_1^{-1})^2 - f_a^2 T_1^{-2}} Un^2, \\ s_{y0} = \frac{(\kappa - T_1^{-1})^2 - f_a^2 T_1^{-2}}{2Jf_a T_1^{-1}} n, \\ s_{z0} = \frac{\kappa - T_1^{-1}}{f_a T_1^{-1}} n. \quad (22)$$

The fourth-order equation [Eq. (21)] yields four solutions for the decay rate κ . Discarding unphysical values, one finds either one or three quasi-steady-states. This appearance of novel nonlinear stationary states has been discussed in detail

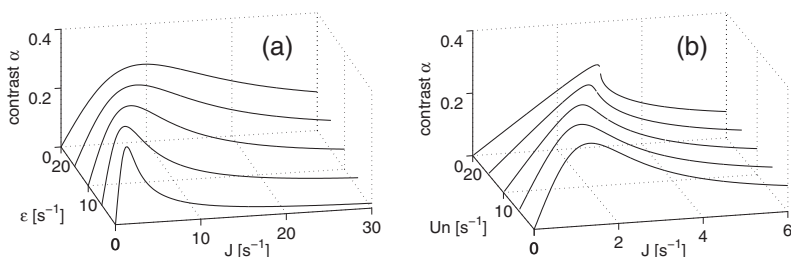


FIG. 5. Steady state values of the contrast α as a function of the tunneling rate (a) for $U=0$ and different values of the energy bias ϵ and (b) as a function of the effective interaction strength $g=Un$ for $\epsilon=0$. The remaining parameters are $\gamma_p=5 \text{ s}^{-1}$ and $T_1^{-1}=2 \text{ s}^{-1}$.

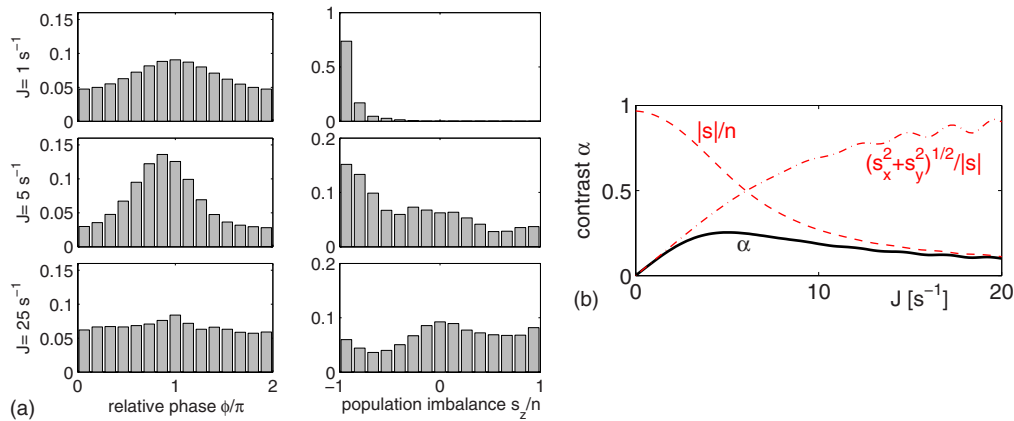


FIG. 6. (Color online) (a) Histogram of the probabilities to measure the relative phase ϕ and the relative population imbalance s_z in a single experimental run after $t=1.5$ s obtained from a MCWF simulation of the many-body dynamics. The initial state was chosen as a pure BEC (i.e., a product state) with $s_z=n/2$ and $n(0)=100$ particles and the remaining parameters are $\gamma_p=5 \text{ s}^{-1}$, $T_1=0.5 \text{ s}$, $\epsilon=10 \text{ s}^{-1}$, and $U=0.1 \text{ s}^{-1}$. (b) Average contrast $\alpha=\sqrt{s_x^2+s_y^2}/n$ (solid black line) after $t=1.5$ s compared to $\sqrt{s_x^2+s_y^2}/|s|$ and $|s|/n$ (dashed red lines).

in the context of nonlinear Landau-Zener tunneling [44–50] and nonlinear transport [51,52].

The resulting contrast $\alpha(J)$ in a quasi-steady-state is shown in Fig. 5(b) for different values of the effective interaction constant $g=Un$. One observes that the position of the SR-like maximum of the contrast is shifted to larger values of the tunneling rate, while the height remains unchanged. Furthermore the shape of the stochastic resonance curve $\alpha(J)$ is altered, becoming flatter for $J < J_{\max}$ and steeper for $J > J_{\max}$. For even larger values of the interaction constant Un one finds a bifurcation into three distinct quasi-steady-states as introduced above. This case will be discussed in detail in Sec. V.

The reasons for the occurrence of an SR-like maximum of the contrast in terms of the underlying many-particle dynamics are illustrated in Fig. 6. To obtain these results we have simulated the dynamics generated by the master equation [Eq. (7)] using the Monte Carlo wave-function (MCWF) method [53–55] averaging over 100 quantum trajectories. For a given particle number n , the probabilities P to obtain the population imbalance s_z and the relative phase ϕ in a projective measurement are thereby given by

$$P(s_z) = \text{tr}(|s_z\rangle\langle s_z|\hat{\rho})$$

and

$$P(\phi) = \text{tr}(|\phi\rangle\langle\phi|\hat{\rho}), \quad (23)$$

where the \hat{L}_z eigenstates

$$|s_z\rangle = |n/2 - s_z, n/2 + s_z\rangle$$

with

$$s_z = -n/2, -n/2 + 1, \dots, n/2 \quad (24)$$

and the phase eigenstates

$$|\phi\rangle := \frac{1}{\sqrt{n+1}} \sum_{s_z=-n/2}^{+n/2} e^{i\phi s_z} |s_z\rangle$$

with

$$\phi = 0, 2\pi \frac{1}{n+1}, \dots, 2\pi \frac{n}{n+1} \quad (25)$$

each form a complete basis.

Part (a) of Fig. 6 shows a histogram of the probabilities to observe the relative population imbalance s_z/n and the relative phase ϕ in a single experimental run for three different values of the tunneling rate J after the system has relaxed to the quasi-steady-state. With increasing J , the atoms are distributed more equally between the two wells so that the single shot contrast increases. Within the mean-field description this is reflected by an increase in $\sqrt{s_x^2+s_y^2}/|s|$ at the expense of $|s_z|/|s|$ [cf. part (b) of the figure]. However, this effect also makes the system more vulnerable to phase noise so that the relative phase of the two modes becomes more and more random and $|s|/n$ decreases. The average contrast (11) then assumes a maximum for intermediate values of J as shown in part (b) of the figure.

IV. STOCHASTIC RESONANCE OF A DRIVEN BEC

So far we have demonstrated a stochastic resonance of the contrast for a BEC in a static double-well trap with biased particle losses. In the following we will show that the system's response to a weak external driving also assumes a maximum for a finite dissipation rate—an effect which is conceptually closer to the common interpretation of stochastic resonance. From a mathematical viewpoint, however, one can rather relate the *undriven* case discussed above to the stochastic resonance effect in nuclear-magnetic resonance [41]. In fact, the Bloch equations for the magnetization have constant coefficients in the rotating wave approximation and should thus be compared to the undriven equations of motion (8).

Let us consider the response of the system to a weak sinusoidal driving of the tunneling rate

$$J(t) = J_0 + J_1 \cos(\omega t) \quad (26)$$

at the resonance frequency $\omega = \sqrt{J_0^2 + \epsilon^2}$, while the amplitude of the driving is small and fixed as $J_1/J_0=10\%$. A variation

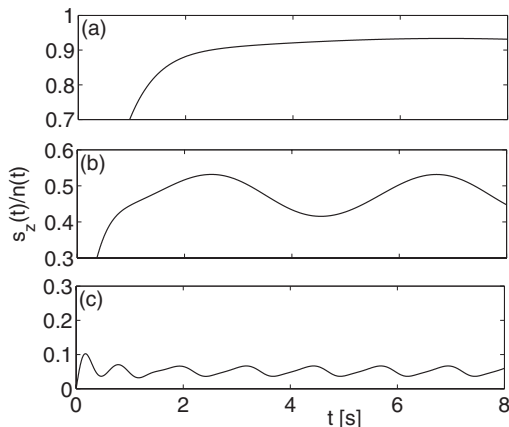


FIG. 7. Dynamics of the relative population imbalance $s_z(t)/n(t)$ in a weakly driven double-well trap for three different values of the tunneling rate: (a) $J_0=0.5 \text{ s}^{-1}$, (b) $J_0=1.5 \text{ s}^{-1}$, and (c) $J_0=5 \text{ s}^{-1}$. The amplitude of the forced oscillations is maximal for intermediate values of J_0 as shown in part (b). The remaining parameters are $T_1^{-1}=2 \text{ s}^{-1}$, $U=0$, $\epsilon=0$, $\gamma_p=5 \text{ s}^{-1}$, and $J_1/J_0=10\%$. Please note the different scalings.

in J can be realized in a quite simple way in an optical setup [21–23], where the tunneling barrier between the two wells is given by an optical lattice formed by two counterpropagating laser beams. A variation in the intensity of the laser beams then directly results in a variation in the tunneling rate J . Figure 7 shows the resulting dynamics for $T_1=0.5 \text{ s}$ and three different values of J_0 and $U=0$. After a short transient period, the relative population imbalance $s_z(t)/n(t)$ oscillates approximately sinusoidally. One clearly observes that the response, i.e., the amplitude of the forced oscillations, assumes a maximum for intermediate values of J_0 matching the external time scale of the dissipation given by T_1^{-1} .

For a detailed quantitative analysis of this stochastic resonance effect, we evaluate the amplitude of the oscillation based on a linear-response argument for $U=0$. In the following, we will use a complex notation for notational convenience, while only the real part is physically significant. The equations of motion (8) are then rewritten in matrix form as

$$\frac{d}{dt} \begin{pmatrix} \mathbf{s} \\ n \end{pmatrix} = (\mathbf{M}_0 + \mathbf{M}_1 e^{i\omega t}) \begin{pmatrix} \mathbf{s} \\ n \end{pmatrix}. \quad (27)$$

The matrices M_0 and M_1 are defined by

$$\mathbf{M}_0 = \begin{pmatrix} T_2^{-1} & 2\epsilon_0 & 0 & 0 \\ -2\epsilon_0 & T_2^{-1} & -2J_0 & 0 \\ 0 & 2J_0 & T_1^{-1} & f_a T_1^{-1} \\ 0 & 0 & f_a T_1^{-1} & T_1^{-1} \end{pmatrix} \quad (28)$$

and

$$\mathbf{M}_1 = \begin{pmatrix} 0 & 0 & 0 & 0 \\ 0 & 0 & -2J_1 & 0 \\ 0 & 2J_1 & 0 & 0 \\ 0 & 0 & 0 & 0 \end{pmatrix}. \quad (29)$$

As before we consider the dynamics after all transient oscillations have died out, assuming that $\mathbf{s}(t)$ as well as $n(t)$ decay

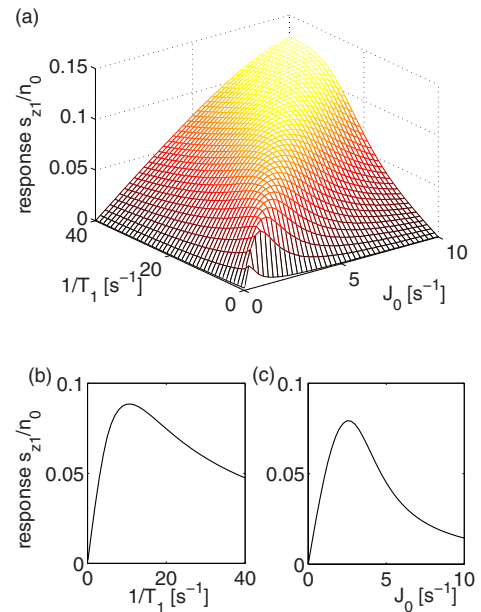


FIG. 8. (Color online) (a) Response [amplitude of the oscillations of $s_z(t)/n(t)$] of a weakly driven double-well trap vs T_1^{-1} and J_0 calculated within linear-response theory. (b) For a fixed value of the tunneling rate $J_0=2.5 \text{ s}^{-1}$. (c) For a fixed value of the dissipation rate $T_1^{-1}=2 \text{ s}^{-1}$. The remaining parameters are $U=0$, $\epsilon=0$, $\gamma_p=5 \text{ s}^{-1}$, and $J_1/J_0=10\%$.

exponentially at the same rate. However, we now also have an oscillating contribution so that we make the ansatz,

$$\begin{aligned} \mathbf{s}(t) &= (\mathbf{s}_0 + \mathbf{s}_1 e^{i\omega t}) e^{-\kappa t}, \\ n(t) &= (n_0 + n_1 e^{i\omega t}) e^{-\kappa t}. \end{aligned} \quad (30)$$

The amplitude of the oscillations, i.e., the system response, is thus directly given by \mathbf{s}_1/n_0 . Substituting this ansatz in the equations of motion and dividing by $e^{-\kappa t}$ yields

$$\begin{aligned} -\kappa \begin{pmatrix} \mathbf{s}_0 \\ n_0 \end{pmatrix} + (i\omega - \kappa) \begin{pmatrix} \mathbf{s}_1 \\ n_1 \end{pmatrix} e^{i\omega t} \\ = [\mathbf{M}_0 + \mathbf{M}_1 e^{i\omega t}] \left[\begin{pmatrix} \mathbf{s}_0 \\ n_0 \end{pmatrix} + \begin{pmatrix} \mathbf{s}_0 \\ n_0 \end{pmatrix} e^{i\omega t} \right]. \end{aligned} \quad (31)$$

Neglecting the higher order terms $\sim e^{2i\omega t}$ in a linear-response approximation and dividing Eq. (33) in the time-dependent and the time-independent parts yields the equations

$$[-\mathbf{M}_0 + (i\omega - \kappa)] \begin{pmatrix} \mathbf{s}_1 \\ n_1 \end{pmatrix} = \mathbf{M}_1 \begin{pmatrix} \mathbf{s}_0 \\ n_0 \end{pmatrix} \quad (32)$$

and Eq. (15), which determine \mathbf{s}_1 and n_1 . The resulting values of the system response are shown in Fig. 8. One observes the characteristic signatures of a stochastic resonance: if one of the two parameters J_0 and T_1 is fixed, the response assumes a maximum for a finite value of the remaining parameter as shown in parts (b) and (c) of the figure. Part (a) shows that this maximum is assumed if the external (T_1^{-1}) and the internal (J_0) timescales are matched similar to the undriven

WITTHAUT, TRIMBORN, AND WIMBERGER

PHYSICAL REVIEW A 79, 033621 (2009)

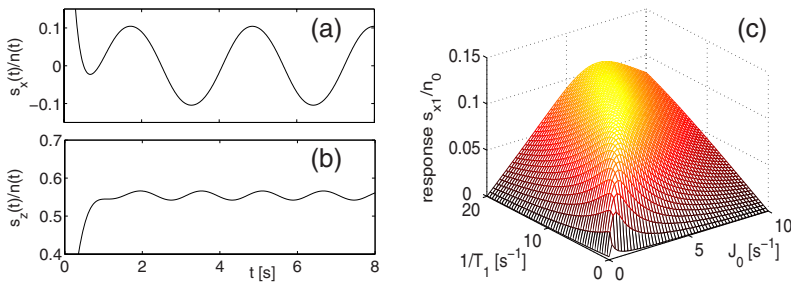


FIG. 9. (Color online) Dynamics of the coherence (a) $s_x(t)/n(t)$ and the relative population imbalance (b) $s_z(t)/n(t)$ for a double-well trap with a driven energy bias ϵ for $J_0=2 \text{ s}^{-1}$ and $T_1^{-1}=4 \text{ s}^{-1}$. (c) Response [amplitude of the oscillations of $s_x(t)/n(t)$] vs T_1^{-1} and J_0 calculated within linear-response theory. The remaining parameters are $U=0$, $\epsilon_1=1 \text{ s}^{-1}$, and $\gamma_p=5 \text{ s}^{-1}$.

case illustrated in Fig. 3. Let us stress that this scenario is again not fundamentally altered in the case of weak interactions as numerically tested but not shown here.

A different situation arises if the energy bias is driven instead of the tunneling rate J such that

$$\epsilon(t) = \epsilon_1 \cos(\omega t). \quad (33)$$

As above we can evaluate the amplitude of the forced oscillations within the linear-response theory, however, with

$$\mathbf{M}_1 = \begin{pmatrix} 0 & -2\epsilon_1 & 0 & 0 \\ 2\epsilon_1 & 0 & 0 & 0 \\ 0 & 0 & 0 & 0 \\ 0 & 0 & 0 & 0 \end{pmatrix}. \quad (34)$$

Solving Eqs. (32) and (15) then yields $s_{1y}=s_{1z}=0$. Remarkably, a driving of the energy bias does not affect the population imbalance in leading order. Only the first component of the Bloch vector s_x , and thus also the contrast α , is strongly affected.

This is illustrated in Figs. 9(a) and 9(b) where the relative population imbalance $s_z(t)/n(t)$ and the first component of the Bloch vector $s_x(t)/n(t)$ are plotted for $J_0=2 \text{ s}^{-1}$, $T_1^{-1}=4 \text{ s}^{-1}$, and $\epsilon_1=1 \text{ s}^{-1}$. The coherence oscillates strongly at the fundamental frequency ω , while the population imbalance oscillates only with a tiny amplitude at the second-harmonic frequency 2ω . The oscillation amplitude of the coherence then again shows the familiar SR-like dependence on the parameters J_0 and T_1 as illustrated in Fig. 9(c).

V. DISSIPATION-INDUCED COHERENCE IN A STRONGLY INTERACTING BEC

Let us finally discuss the case of strong interactions, which is experimentally most relevant and theoretically most profound. This is the regime of the current experiments [21–23], which confirm the theoretical predictions using the two-mode approximation (1) extremely well. However, the model assumes that the ground-state properties of the individual potentials are only slightly affected by the interactions, such that the condition $UN \ll \hbar\omega_{\text{trap}}$ discussed above must be fulfilled. Moreover, the results presented here are not directly applicable to the case of extended trapping potentials, where longitudinal excitations cause dephasing and a loss of purity.

An example for the dynamics of a strongly interacting BEC is shown in Fig. 10(a) for an initially pure BEC with $s_z=n/2$, calculated both with the MCWF method and within

the mean-field approximation (8). One observes that the purity p and the contrast α first drop rapidly due to the phase noise and, more importantly, due to the interactions. This is an effect well known from the nondissipative system and can be attributed to a dynamical instability which also leads to the breakdown of the mean-field approximation [32,33,35,56]. However, a surprising effect is found at intermediate times: the purity p is restored almost completely and the contrast α is slightly increasing.

Most interestingly, the observed values of the purity and the coherence are much larger than in the cases where one of the two effects—interactions and dissipation—is missing. The time evolutions for these two cases are also shown in Fig. 10. In the case of no interactions both purity and coherence rapidly drop to values of almost zero and do not revive. This case has been discussed in detail in Sec. III. In the interacting case without dissipation one observes regular revivals, which are artifacts of the small particle number in the simulation and become less pronounced with increasing par-

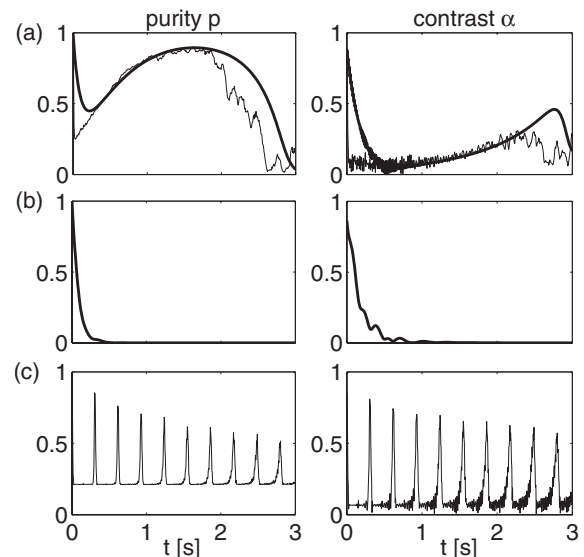


FIG. 10. (a) Time evolution of the purity p and the contrast α for $J=U=10 \text{ s}^{-1}$, $\epsilon=0$, and $T_1=0.5 \text{ s}$. (b) Time evolution without interactions ($U=0$) and (c) without dissipation ($1/T_1=1/T_2=0$) for comparison. The occasional revivals are artifacts of the small particle number. The initial state is a pure BEC with $s_z=n/2$ and $n(0)=100$ particles. The results of a MCWF simulation averaged over 100 runs are plotted as a thin solid line in (a) and (c), while the mean-field results are plotted as a thick line in (a) and (b). Note that the mean-field approximation is exact in case (b), whereas it breaks down in case (c) and is thus not shown (cf. [32,35]).

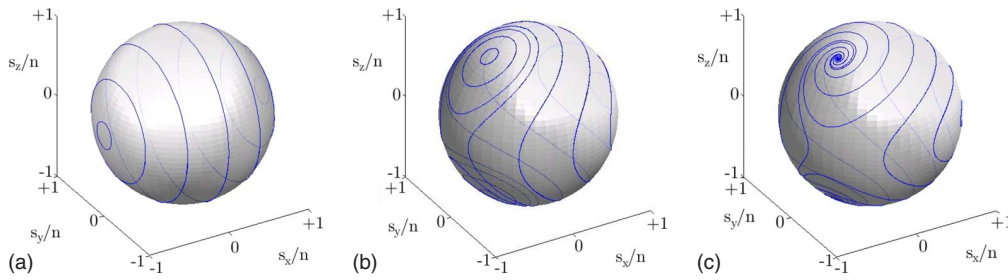


FIG. 11. (Color online) Mean-field dynamics (a) without interactions and dissipation, (b) with interactions $Un=40 \text{ s}^{-1}$, and (c) with interactions and dissipation $\gamma_a=10 \text{ s}^{-1}$. The remaining parameters are $J=10 \text{ s}^{-1}$ and $\epsilon=0$. To increase the visibility we have plotted the rescaled Bloch vector \mathbf{s}/n and we have artificially fixed the particle number so that $n=\text{const}$.

title number. Apart from these occasional revivals, however, the purity and the coherence relax to values which are much smaller than in the interacting and dissipative case.

The surprising repurification of a strongly interacting BEC by particle dissipation can be understood within a semiclassical phase-space picture. In order to visualize the effects of particle loss, we have plotted the “classical” phase-space structure generated by the Bloch equation [Eq. (8)] for $\gamma_p=0$ in Fig. 11 without interactions and dissipation (a), with interactions (b), and with both (c). For illustrative purposes, we have plotted the rescaled Bloch vector \mathbf{s}/n and have artificially fixed the particle number so that $n=\text{const}$. Since we are interested only in the short-time dynamics of the Bloch vector and not in the decay of the particle number on longer time scales, this is an appropriate treatment. Moreover, in the quantum jump picture this approximation corresponds to the periods of constant particle number between two loss processes [40,53,55].

Parts (a) and (b) of the figure show the phase-space structure without dissipation and $Un=0$ and $Un=4J$, respectively. One observes the familiar self-trapping bifurcation of the fixed points for $Un > 2J$ [31,32]. The phase-space structure is significantly altered in the presence of particle loss as shown in part (c). The most important consequence is the occurrence of an attractive and a repulsive fixed point instead of the elliptic fixed points in the dissipation-free case [40].

In the course of time the system will thus relax to the attractive stationary state illustrated Fig. 11(c). A many-particle quantum state can now be represented by a quasidistribution function on this classical phase space, for instance, the Husimi Q function [34,35]. In this picture, a pure BEC is represented by a maximally localized distribution function and the loss of purity corresponds to a broadening or distortion of the Q function. The existence of an attractive fixed point clearly leads to the contraction of a phase-space distribution function and thus to a repurification of the many-particle quantum state as observed in Fig. 10(a).

However, this nonlinear stationary state exists only as long as the particle number exceeds a critical value given by (cf. [40])

$$U^2 n^2 \geq 4J^2 - J_a^2 T_1^{-2}. \quad (35)$$

As particles are slowly lost from the trap, the particle number eventually falls below the critical value. For this reason the attractive fixed point vanishes and the purity drops to the

values expected for the linear case $U=0$. Since the attractive fixed point tends toward the equator maximizing $s_x/|\mathbf{s}|$, the contrast assumes a maximum just before the disappearance of the attractive fixed point, while the purity is still large. In Fig. 10(a) this happens after approximately 2.5 s.

The surprising effect of the repurification of a BEC is extremely robust—it is present as long as condition (35) is satisfied. A variation in the system parameters does not destroy or significantly weaken the effect, it only changes the time scales of this relaxation process. Figure 12 compares the time evolution of the purity and the contrast for three different values of the particle loss rate T_1^{-1} . With increasing losses, the nonlinear stationary state is reached much faster but is also lost earlier. One can thus maximize the purity or the contrast at a given point of time by engineering the loss rate. This effect is further illustrated in Fig. 13, where the purity and the contrast after 2 s of propagation are shown in dependence of the loss rate T_1^{-1} . Both curves assume a maximum for a certain finite value of T_1^{-1} .

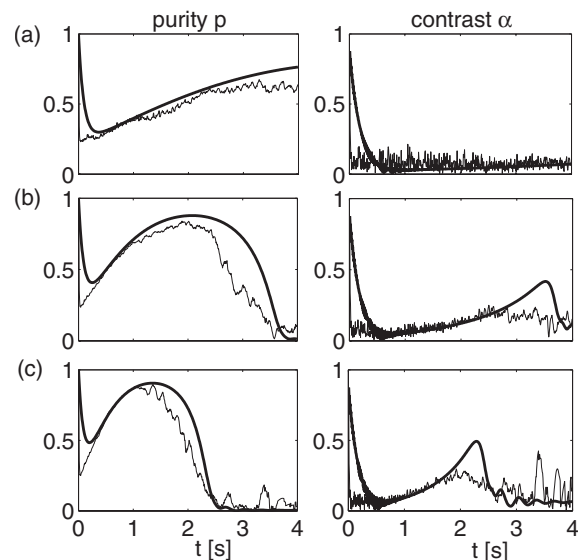


FIG. 12. Time evolution of the purity p and the contrast α for $J=U=10 \text{ s}^{-1}$, $\epsilon=0$, and (a) $1/T_1=0.5 \text{ s}^{-1}$, (b) $1/T_1=1.5 \text{ s}^{-1}$, and (c) $1/T_1=2.5 \text{ s}^{-1}$. The initial state is a pure BEC with $s_z=n/2$ and $n(0)=100$ particles. The results of a MCWF simulation averaged over 100 runs are plotted as a thin solid line, while the mean-field results are plotted as a thick line.

WITTHAUT, TRIMBORN, AND WIMBERGER

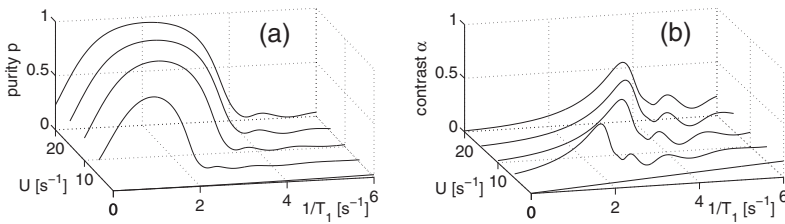
PHYSICAL REVIEW A **79**, 033621 (2009)

FIG. 13. (a) Purity p and (b) contrast α after $t=2$ s as a function of the dissipation rate $1/T_1$ for different values of the interaction strength Un calculated within the mean-field approximation. The remaining parameters are chosen as in Fig. 10(a).

VI. CONCLUSION AND OUTLOOK

In summary, we have shown that the coherence properties of a weakly and, in particular, also of a strongly interacting Bose-Einstein condensate in a double-well trap can be controlled by engineering the system's parameters and dissipation simultaneously. Surprisingly, dissipation can be used to stimulate coherence in the system rather than—as may be expected—solely reduce it.

In the weakly interacting case, the contrast of the quasi-steady-state of the system assumes a maximum for a finite value of the tunneling and the dissipation rate. This stochastic resonance effect is robust against parameter variations. A Monte Carlo wave-function simulation of the full many-body quantum dynamics shows a good agreement to the mean-field description and provides a microscopic explanation of the observed effect. Moreover, a similar effect can be observed in the case where either the tunneling or the energy bias is driven, which is conceptually even closer to the common interpretation of stochastic resonance.

In Sec. V, we have studied the effects of dissipation on the strongly interacting system. An important conclusion is that the interplay of interactions and dissipation can drive the system to a state of maximum coherence, while both pro-

cesses alone usually lead to a loss of coherence. We show that this effect can be understood from the appearance of an attractive fixed point in the mean-field dynamics reflecting the metastable behavior of the many-particle system.

Since the double-well BEC is nowadays routinely realized with nearly perfect control on atom-atom interactions and external potentials [21–23], we hope for an experimental verification of the predicted stochastic resonance effect. An interesting perspective is to lift our results to extended dissipative setups as, e.g., studied in [28,29]. Besides the general idea of controlling many-body dynamics [57], one may also investigate the possibility of dynamically engineering entanglement in similar systems as to some extent possible in state-of-the-art experiments [58].

ACKNOWLEDGMENTS

We thank M. K. Oberthaler, J. R. Anglin, and A. S. Sørensen for stimulating discussions. This work has been supported by the German Research Foundation (DFG) (Grant No. WI 3415/1) and the Heidelberg Graduate School of Fundamental Physics (Grant No. GSC 129/1), as well as the Studienstiftung des deutschen Volkes.

-
- [1] R. Benzi, A. Sutera, and A. Vulpiani, *J. Phys. A* **14**, L453 (1981).
- [2] K. Wiesenfeld and F. Moss, *Nature (London)* **373**, 33 (1995).
- [3] M. I. Dykman, D. G. Luchinsky, R. Mannella, P. V. E. McClintock, N. D. Stein, and N. G. Stocks, *Nuovo Cimento D* **17**, 661 (1995).
- [4] L. Gammaitoni, P. Hänggi, P. Jung, and F. Marchesoni, *Rev. Mod. Phys.* **70**, 223 (1998).
- [5] T. Wellens, V. Shatokhin, and A. Buchleitner, *Rep. Prog. Phys.* **67**, 45 (2004).
- [6] R. Löfstedt and S. N. Coppersmith, *Phys. Rev. Lett.* **72**, 1947 (1994).
- [7] R. Löfstedt and S. N. Coppersmith, *Phys. Rev. E* **49**, 4821 (1994).
- [8] A. Buchleitner and R. N. Mantegna, *Phys. Rev. Lett.* **80**, 3932 (1998).
- [9] T. Wellens and A. Buchleitner, *J. Phys. A* **32**, 2895 (1999).
- [10] S. F. Huelga and M. B. Plenio, *Phys. Rev. A* **62**, 052111 (2000).
- [11] H. H. Adamyán, S. B. Manvelyan, and G. Y. Kryuchkyan, *Phys. Rev. A* **63**, 022102 (2001).
- [12] S. F. Huelga and M. B. Plenio, *Phys. Rev. Lett.* **98**, 170601 (2007).
- [13] Y. Khodorkovsky, G. Kurizki, and A. Vardi, *Phys. Rev. Lett.* **100**, 220403 (2008).
- [14] Yun Li, Y. Castin, and A. Sinatra, *Phys. Rev. Lett.* **100**, 210401 (2008).
- [15] B. Kraus, H. P. Büchler, S. Diehl, A. Kantian, A. Micheli, and P. Zoller, *Phys. Rev. A* **78**, 042307 (2008).
- [16] S. Diehl, A. Micheli, A. Kantian, B. Kraus, H. P. Büchler, and P. Zoller, *Nat. Phys.* **4**, 878 (2008).
- [17] F. Verstraete, M. M. Wolf, and J. I. Cirac, e-print arXiv:0803.1447.
- [18] N. Syassen, D. M. Bauer, M. Lettner, T. Volz, D. Dietze, J. J. Garcia-Ripoll, J. I. Cirac, G. Rempe, and S. Dürr, *Science* **320**, 1329 (2008).
- [19] J. J. Garcia-Ripoll, S. Dürr, N. Syassen, D. M. Bauer, M. Lettner, G. Rempe, and J. I. Cirac, *New J. Phys.* **11**, 013053 (2009).
- [20] D. Witthaut, F. Trimborn, and S. Wimberger, *Phys. Rev. Lett.* **101**, 200402 (2008).
- [21] M. Albiez, R. Gati, J. Fölling, S. Hunsmann, M. Cristiani, and M. K. Oberthaler, *Phys. Rev. Lett.* **95**, 010402 (2005).
- [22] R. Gati, B. Hemmerling, J. Fölling, M. Albiez, and M. K. Oberthaler, *Phys. Rev. Lett.* **96**, 130404 (2006).

- [23] R. Gati, J. Estève, B. Hemmerling, T. B. Ottenstein, J. Appmeier, A. Weller, and M. K. Oberthaler, *New J. Phys.* **8**, 189 (2006).
- [24] S. Fölling, S. Trotzky, P. Cheinet, M. Feld, R. Saers, A. Widera, T. Müller, and I. Bloch, *Nature (London)* **448**, 1029 (2007).
- [25] S. Trotzky, P. Cheinet, S. Fölling, M. Feld, U. Schnorrberger, A. M. Rey, A. Polkovnikov, E. A. Demler, M. D. Lukin, and I. Bloch, *Science* **319**, 295 (2008).
- [26] T. Schumm, S. Hofferberth, L. M. Andersson, S. Wildermuth, S. Groth, I. Bar-Joseph, J. Schmiedmayer, and P. Krüger, *Nat. Phys.* **1**, 57 (2005).
- [27] J. R. Anglin, *Phys. Rev. Lett.* **79**, 6 (1997).
- [28] S. Hofferberth, I. Lesanovsky, B. Fischer, T. Schumm, and J. Schmiedmayer, *Nature (London)* **449**, 324 (2007).
- [29] S. Hofferberth, I. Lesanovsky, T. Schumm, J. Schmiedmayer, A. Imambekov, V. Gritsev, and E. Demler, *Nat. Phys.* **4**, 489 (2008).
- [30] G. J. Milburn, J. Corney, E. M. Wright, and D. F. Walls, *Phys. Rev. A* **55**, 4318 (1997).
- [31] A. Smerzi, S. Fantoni, S. Giovanazzi, and S. R. Shenoy, *Phys. Rev. Lett.* **79**, 4950 (1997).
- [32] A. Vardi and J. R. Anglin, *Phys. Rev. Lett.* **86**, 568 (2001).
- [33] J. R. Anglin and A. Vardi, *Phys. Rev. A* **64**, 013605 (2001).
- [34] F. Trimborn, D. Witthaut, and H. J. Korsch, *Phys. Rev. A* **77**, 043631 (2008).
- [35] F. Trimborn, D. Witthaut, and H. J. Korsch, *Phys. Rev. A* **79**, 013608 (2009).
- [36] J. Ruostekoski and D. F. Walls, *Phys. Rev. A* **58**, R50 (1998).
- [37] D. F. Walls and G. J. Milburn, *Phys. Rev. A* **31**, 2403 (1985).
- [38] C. W. Gardiner and P. Zoller, *Quantum Noise*, Springer Series in Synergetics (Springer, Berlin, 2004).
- [39] I. Bloch, T. W. Hänsch, and T. Esslinger, *Phys. Rev. Lett.* **82**, 3008 (1999).
- [40] F. Trimborn, D. Witthaut, and S. Wimberger, *J. Phys. B* **41**, 171001 (2008).
- [41] L. Viola, E. M. Fortunato, S. Lloyd, C.-H. Tseng, and D. G. Cory, *Phys. Rev. Lett.* **84**, 5466 (2000).
- [42] F. Bloch, *Phys. Rev.* **70**, 460 (1946).
- [43] A. J. Leggett, *Rev. Mod. Phys.* **73**, 307 (2001).
- [44] S. Wimberger, R. Mannella, O. Morsch, E. Arimondo, A. R. Kolovsky, and A. Buchleitner, *Phys. Rev. A* **72**, 063610 (2005).
- [45] P. Schlagheck and T. Paul, *Phys. Rev. A* **73**, 023619 (2006).
- [46] P. Schlagheck and S. Wimberger, *Appl. Phys. B: Lasers Opt.* **86**, 385 (2007).
- [47] Biao Wu and Qian Niu, *Phys. Rev. A* **61**, 023402 (2000).
- [48] Biao Wu and Jie Liu, *Phys. Rev. Lett.* **96**, 020405 (2006).
- [49] D. Witthaut, E. M. Graefe, and H. J. Korsch, *Phys. Rev. A* **73**, 063609 (2006).
- [50] E. M. Graefe, H. J. Korsch, and D. Witthaut, *Phys. Rev. A* **73**, 013617 (2006); E. M. Graefe, H. J. Korsch, and A. E. Niederle, *Phys. Rev. Lett.* **101**, 150408 (2008).
- [51] T. Paul, K. Richter, and P. Schlagheck, *Phys. Rev. Lett.* **94**, 020404 (2005).
- [52] K. Rapedius, D. Witthaut, and H. J. Korsch, *Phys. Rev. A* **73**, 033608 (2006).
- [53] J. Dalibard, Y. Castin, and K. Mølmer, *Phys. Rev. Lett.* **68**, 580 (1992).
- [54] K. Mølmer, Y. Castin, and J. Dalibard, *J. Opt. Soc. Am. B* **10**, 524 (1993).
- [55] H. J. Carmichael, *An Open Systems Approach to Quantum Optics* (Springer, Berlin, 1993).
- [56] M. Cristiani, O. Morsch, N. Malossi, M. Jona-Lasinio, M. Anderlini, E. Courtade, and E. Arimondo, *Opt. Express* **12**, 4 (2004).
- [57] J. Madroñero, A. Ponomarev, A. R. R. Carvalho, S. Wimberger, C. Viviescas, A. Kolovsky, K. Hornberger, P. Schlagheck, A. Krug, and A. Buchleitner, *Adv. At. Mol. Opt. Phys.* **53**, 33 (2006).
- [58] J. Estève, C. Gross, A. Weller, S. Giovanazzi, and M. K. Oberthaler, *Nature (London)* **455**, 1216 (2008).

New Journal of Physics

The open-access journal for physics

Pseudo-classical theory for directed transport at quantum resonance

Mark Sadgrove^{1,3} and Sandro Wimberger²

¹ Institute for Laser Science, The University of Electro-communication,
1-5-1 Chofugaoka, Chofu, Japan

² Institut für Theoretische Physik, Universität Heidelberg, Philosophenweg 19,
69120 Heidelberg, Germany
E-mail: mark@ils.uec.ac.jp

New Journal of Physics **11** (2009) 083027 (13pp)

Received 22 April 2009

Published 24 August 2009

Online at <http://www.njp.org/>

doi:10.1088/1367-2630/11/8/083027

Abstract. Recent studies have demonstrated that a directed current arises in kicked atom systems at quantum resonance (so-called ‘resonance ratchets’). Here, we demonstrate that this effect can be explained using a pseudo-classical model by taking classical initial conditions analogous to the initial quantum state. A corollary of our result is that a current is also expected to arise in the *actual* standard classical limit of the kicked atoms, demonstrating that the phenomenon can arise even in the absence of quantum interference. We show that in the standard classical limit, the momentum current undergoes far less saturation due to quasi-momentum spread than for the quantum resonance case. Additionally, we demonstrate that a phase-independent analytical scaling law exists for the mean momentum as a function of a single combined parameter and show that it predicts an unexpected current inversion regime.

Contents

1. Introduction	2
2. ϵ-classical map and initial conditions	3
3. ϵ-classical momentum current	4
4. The effect of quasi-momentum	6
5. Scaling law for momentum current	8
6. Conclusion	11
Acknowledgment	12
References	12

³ Author to whom any correspondence should be addressed.

1. Introduction

Dynamical systems that display directed motion in the absence of unbalanced forces are of considerable interest across scientific fields. On the one hand, physicists hope to take advantage of such effects to realize novel transport solutions at the atomic scale [1] and such studies can also improve our understanding of basic thermodynamic phenomena [2, 3]. On the other hand, biologists have an interest in studying mechanisms for movement in situations where thermal fluctuations are large compared with the forces available to propel an organism. The study of Brownian and biological motors [4] is indeed one of the driving forces behind the study of directed diffusion in general.

In the last few years, there have been a number of studies of systems where fluctuations provided by Hamiltonian chaos (rather than noise) drive a current in a system with broken symmetries [5]. The coherent nature of these noiseless ratchet realizations allows quantum effects such as current saturation and current reversal to be easily observed. Only a few realizations of such Hamiltonian ratchets have been performed experimentally [6]. However, a closely related system, which uses atoms in an initial quantum superposition of two motional states exposed to a sinusoidal potential pulsed at the quantum resonance (QR) [7] (i.e. at the Talbot time [8]) has produced readily controllable momentum currents in two separate experiments [9, 10]. In these studies, and in related studies at QR, using an asymmetric potential [11], the strictly quantum nature of the initial state along with the necessity of the wave-mechanical Talbot effect has justifiably led to the claim that this ratchet-like directed motion⁴ is *fundamentally quantum-mechanical*.

Although we do not aim to undermine the above claim, it is nonetheless clear from previous studies of the QR phenomenon that a pseudo-classical theory suffices to explain near-resonant dynamics to an excellent approximation [12]–[16]. The so-called ϵ -classical standard map (ϵ SM) and the associated scaling law for the quantum resonant peaks of the atom optics kicked rotor provide an elegant theoretical structure for understanding quantum dynamics for small detuning from resonance ϵ . Since the QR ratchets of [9, 10] rely on QR to produce a momentum current, one might expect that a pseudo-classical description of the phenomenon is also possible.

In the following, we will show that this is indeed the case. In fact, there is only one hurdle to overcome before the existing ϵ -classical theory can be adapted to the case of resonant ratchets—the identification of appropriate classical initial conditions that correspond to the initial quantum superposition state required to produce directed diffusion. Once this has been done, the phenomena documented in [9, 10] can readily be explained using the pseudo-classical theory of [13].

Along with the ϵ -classical formulation of the resonance ratchet problem come a number of interesting revelations about the system. Firstly, we find that a momentum current also exists in the semi-classical limit of vanishing kicking period. Furthermore, in this limit, the momentum current is *much less sensitive* to the initial quasi-momentum spread, and so is more useful for real transport applications. Additionally, we demonstrate that a scaling law exists for the momentum current as a function of a combined parameter of the kick strength, detuning from QR, and the kick number. This scaling law reveals that *current reversals* should occur in the resonant ratchet, not just for particular parameter values but for certain *parameter families*.

⁴ Strictly, since no ratchet potential is applied, the system does not constitute a ratchet in the normal sense. Henceforth, however, we will use ‘ratchet’ without quotation marks with the understanding that it refers to the behaviour observed in [9, 10].

Such a hitherto unnoticed phenomenon should certainly be observable in experiments at finite detuning from exact QR. Furthermore, the scaling law for the current may be expressed in a form which is *independent* of the quantum phase ϕ , raising interesting questions about the role of quantum interference in the dynamics of the atoms.

2. ϵ -classical map and initial conditions

Here we will consider the well-known atom optics quantum kicked rotor (AOQKR) system [17]. Atoms are subject to pulses from an off-resonant optical standing wave. Assuming spontaneous emission can be neglected, atomic motion is governed by the following Hamiltonian [18] in dimensionless units [12]–[14]:

$$H = \frac{\tau p^2}{2} + k \cos(\Theta) \sum_{t=1}^N \delta(t' - t), \quad (1)$$

where $\Theta = 2k_l x_{\text{phys}}$ (the ‘phys’ subscript denotes physical units as opposed to dimensionless units) is the scaled position and $p = p_{\text{phys}}/2p_{\text{rec}}$, $p_{\text{rec}} = \hbar k_l$, its conjugate momentum, with $2k_l$ being the wavenumber of the standing wave. $k = V_0 \Delta / \hbar$ is the kick strength (for an optical standing wave potential depth of V_0 pulsed on for time Δ). We also transform the kicking period T_{phys} into the dimensionless quantity $\tau = 8\omega_{\text{rec}} T_{\text{phys}}$, where $\omega_{\text{rec}} = p_{\text{rec}}^2 / (2M\hbar)$ for an atomic mass M , is the recoil frequency of the atoms in the field. Note that when the kicking period T_{phys} is an integer multiple of the QR time, then τ is an integer multiple of 2π . We also use a dimensionless continuous time variable t' and the integer kick counter t .

Classically, the system is a paradigm of chaos studies; the Hamiltonian may be replaced by a discrete map that gives discrete time atomic position x_t and momentum p_t after each δ -kick. For sufficiently large k , the system exhibits global chaos [19]. However, if the system is quantized, it is well known that two uniquely quantum behaviours can appear. Best studied is dynamical localization where atomic diffusion is halted after a certain time due to quantum interference. Also unique to the quantum system is QR (which concerns us here), which occurs when the kicking frequency is commensurate with the energy spacing of the free rotor as dictated by quantization. The primary QR of the kicked rotor occurs, then, whenever $\tau = 2\pi l$, with integer $l > 0$ [7, 13].

Starting from the quantum evolution operator over a single kick $U = \exp(-ik \cos(\Theta)) \exp(-i\tau p^2/2)$, it was shown in [13] that introducing a fictitious Planck constant $\epsilon = 2\pi l - \tau$ allowed the near resonant dynamics to be approximated by a pseudo-classical map (‘pseudo-classical’ due to the presence of a variable quantity in the role of Planck’s constant). Using appropriate definitions, the ϵ SM may be written in the same form as the usual classical map viz. [14]

$$J_{t+1} = J_t + \tilde{k} \cos(\theta_t), \quad \theta_{t+1} = \theta_t + J_t, \quad (2)$$

where J_t is a scaled momentum variable defined by $J_t = \epsilon p_t + l\pi + \tau\beta$ with β the non-integer part of the momentum or quasi-momentum and $\theta_t = \Theta_t + \pi(1 - \text{sign}(\epsilon))/2$ is the rescaled position. The effective Planck constant ϵ enters in the definition $\tilde{k} = |\epsilon|k$.

The ϵ SM reproduces the dynamics of the quantum kicked rotor near QR (i.e. when τ is a multiple of 2π) very well as was demonstrated theoretically in [12, 13] and experimentally in [14]. However, if we seek to apply it to the phenomenon of directed transport at QR as investigated experimentally in [9, 10], we run into a problem: for the derivation of the

scaling results in [13]–[16], the pseudo-classical formalism reviewed above averages over an initial momentum distribution covering the entire Brillouin zone (i.e. $0 \leq \beta \leq 1$) and uses the pendulum Hamiltonian as an approximation to the true kicked rotor Hamiltonian (see e.g. [13] for details). By symmetry of those initial conditions and of the pendulum dynamics we know that there can be no net momentum gain. Nonetheless, we will show that it is possible to adapt the usual ϵ -classical method to dynamics to describe the resonance ratchet effect by choosing classical initial conditions which are analogous (but not necessarily equivalent) to the quantum case.

Of course, in the ratchet experiments an initial quantum superposition of momentum states (and thus position states) was created, which has no direct classical analogy. Thus, our strategy is to choose initial conditions that best correspond to the quantum resonant ratchet initial conditions by considering the momentum and spatial distributions of atoms placed into the $|\psi_i\rangle = 1/\sqrt{2}(|p=0\rangle + |p=2\hbar k\rangle)$ initial state. We will show that by matching the quantum and classical distributions (both in momentum and position space) the ϵ SM may be used to describe the directed transport behaviour seen in [9, 10].

Firstly, we consider the initial momentum of the atoms. The momentum probability distribution corresponding to the initial momentum superposition state ψ_i is

$$P(p_0) = \frac{1}{2}(\delta_{p_0,0} + \delta_{p_0,1}). \quad (3)$$

We will take this to be the momentum distribution for the classical atoms as we continue below.

What about the position space distribution of atoms? If the momentum space wavefunction is ψ_i , then the position space distribution is non-trivially the Fourier transform of ψ_i . We note that for classical atoms, no such relation between the momentum and position space distributions for the atoms is actually required, given the absence of the uncertainty principle in classical physics. Writing the momentum eigenstates as δ functions in momentum space, we see that the appropriate Fourier pair is $\langle p|\psi_i\rangle = \delta(p) + \delta(p+1) \Rightarrow 1/(2\pi)(1 + \exp(i\theta))$. We can also take into account the possibility that the initial spatial distribution has a phase difference compared to the periodic potential by adding a phase term ϕ inside the complex exponential. This mimics the role of quantum phase in the pseudo-classical system. This leads to a position space probability distribution of

$$P(\theta) = |\psi(\theta)|^2 = \frac{1}{2\pi}(1 + \cos(\theta + \phi)). \quad (4)$$

3. ϵ -classical momentum current

We now show that if these probability distributions are used, the ϵ -classical map predicts the current found in the resonance ratchet system. We proceed by iterating the standard map in the usual way to find J_t dependent on particular initial conditions J_0 and θ_0 governed by the definitions of the J and θ variables along with the probability distributions given by equations (3) and (4). This gives

$$J_N = J_0 + \tilde{k} \sum_{t=0}^{N-1} \cos(\theta_t). \quad (5)$$

The mean momentum is found by averaging over initial conditions. At perfect QR, the atoms have the same value of θ modulo 2π after each iteration, we can replace θ_t with θ_0 . Thus, we

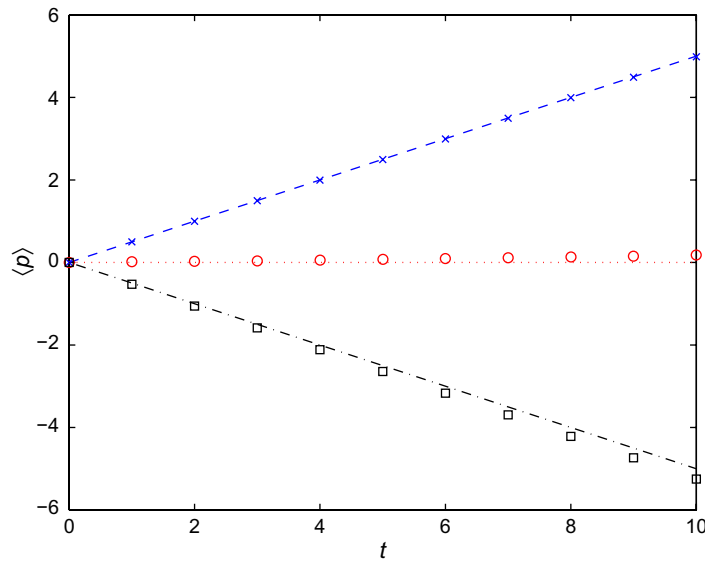


Figure 1. Simulations of the ϵ SM (discrete points) compared with the predictions of equation (8). The data sets are for $\phi = 0$ (crosses, dashed line), $\phi = \pi/2$ (circles, dotted line) and $\phi = \pi$ (squares, dash-dotted line).

have at a particular discrete time t

$$\langle J_{t,\text{res}} \rangle = \langle J_0 \rangle + \tilde{k}t \langle \cos(\theta_0) \rangle. \quad (6)$$

Finally, to find the physical mean momentum at resonance from the ϵ SM, we calculate the quantity [13]

$$\langle p_{t,\text{res}} \rangle = \frac{\langle J - J_0 \rangle}{|\epsilon|} = \frac{\tilde{k}t}{|\epsilon|} \langle \cos(\theta_0) \rangle. \quad (7)$$

For kicked rotor experiments with cold thermal atoms (i.e. atoms which still have a broad momentum spread compared with the width of the Brillouin zone of the periodic kick potential), equation (7) is trivially zero because atoms are distributed uniformly over the standing wave to a good approximation. However, in the resonant-ratchet experiments, the position space probability distribution is given by equation (4). In this case, we can show that $\langle \cos(\theta_0) \rangle = \cos(\phi)/2$. Thus, we find that

$$\langle p_{t,\text{res}} \rangle = \frac{kt}{2} \cos(\phi). \quad (8)$$

It is immediately apparent that equation (8) will reproduce the ϕ dependent momentum current seen in [9]. This is demonstrated in figure 1, where ϵ -classical simulation results are seen to be in good agreement with the predictions of equation (8).

Figure 2 shows the phase space of the resonance ratchet system for three different kick numbers for an initial phase $\phi = 0$ with initial (classical) distributions of momentum and position given by equations (3) and (4), respectively. The figures show that the phase space accumulates an imbalance in positive and negative momentum trajectories as time increases. Because the case considered here is not exactly on resonance, after a finite time (~ 400 kicks for the parameters in figure 2) the phase space becomes symmetrically filled and the current disappears. We discuss the off-resonant behaviour of the system further in section 5.

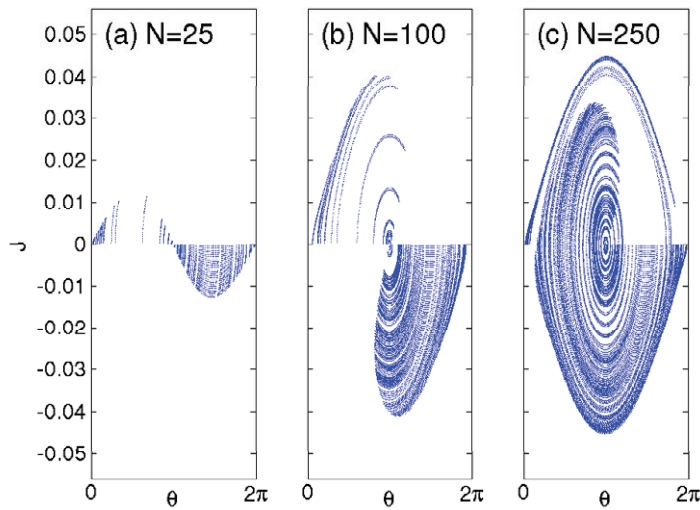


Figure 2. The ϵ -classical phase space shown for a sinusoidal initial position distribution and $\epsilon = 10^{-4}$ for a phase of 0 for total number of kicks (a) $N = 25$, (b) $N = 100$ and (c) $N = 250$ of the potential relative to the spatial density.

4. The effect of quasi-momentum

We now look at the more general case where the atoms have an initial quasi-momentum. Such an analysis is required to explain the results of the Summy group [10]. We start with the standard result from ϵ -classical theory that the momentum at QR is given by

$$\langle p_{t,\text{res}} \rangle = \lim_{\epsilon \rightarrow 0} \frac{\langle J_t - J_0 \rangle}{\epsilon} = k \left\langle \frac{\sin(tJ_0/2)}{\sin(J_0/2)} [\sin[\theta_0 + (t-1)J_0/2]] \right\rangle, \quad (9)$$

where the average is taken at fixed time t over initial conditions in momentum and position as given by equations (3) and (4). The reader may refer to [13], where a similar limit was calculated.

We proceed by computing the averages of the terms $\sin(\theta_0)$ and $\cos(\theta_0)$ over the distribution $P(\theta_0) = 1/(2\pi)[1 + \cos(\theta_0 + \phi)]$ for $\theta_0 \in [0, 2\pi]$. We find that

$$\langle \cos(\theta_0) \rangle = \frac{1}{2} \cos(\phi), \quad \langle \sin(\theta_0) \rangle = -\frac{1}{2} \sin(\phi). \quad (10)$$

Using equation (10) and trigonometric identities, and noting that by definition of J , $J_0 \rightarrow 0$ in the $\epsilon \rightarrow 0$ limit which we are considering here, we can average equation (9) over the initial conditions to give

$$\langle p_{t,\text{res}} \rangle = \frac{k \sin[(\pi l + \tau\beta)t/2]}{2 \sin[(\pi l + \tau\beta)/2]} \sin[(t-1)(\pi l + \tau\beta)/2 - \phi]. \quad (11)$$

This formula is essentially the same as equation (1) from [10], where it was derived using a purely quantum analysis. In figure 3, we show the variation of the momentum current with β for two different QRs.

The above analysis shows that an ϵ -classical treatment correctly models the behaviour of the quantum resonant ratchet. This is despite the fact that the behaviour of an atomic wavepacket subject to pulses from a standing wave at QR is fundamentally quantum in nature. The success of the ϵ -classical approach implies that the salient aspects of the quantum behaviour can be

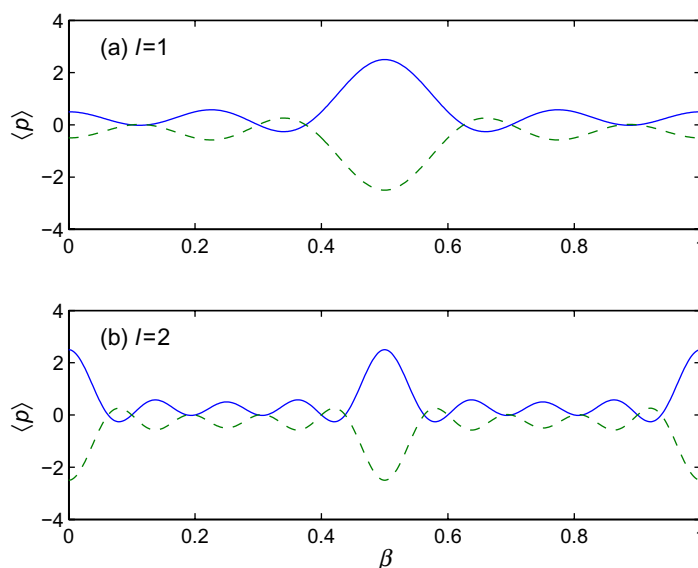


Figure 3. The momentum current as a function of β as given by equation (11) for QRs with (a) $l = 1$ and (b) $l = 2$. In each case, the solid line shows the results for $\phi = -\pi/2$ and the dashed line shows the results for $\phi = \pi/2$. The case in (a) demonstrates exactly the behaviour seen in [10].

captured in ϵ -classical correlations between the atomic position distribution and the driving field. We note that, as pointed out in [10], the actual classical mechanics for a quantum resonant pulse period do *not* exhibit a momentum current precisely because the mixing caused by classical chaos destroys the sinusoidal position distribution necessary for the ratchet effect to occur.

However, the fact that the ϵ -classical description is successful at QR suggests that there should also be a current in the semi-classical limit $\epsilon \equiv \tau \rightarrow 0$. This was established for the resonance in mean energy in [15], and its origin lies in the dependence of J on the product $\tau\beta$, which for this case tends to zero, too, as $\epsilon \rightarrow 0$.

Nonetheless, there is a very important difference between the ϵ -classical map for $l = 0$, $\epsilon \rightarrow 0$ (the semi-classical limit) and $l > 0$, $\epsilon \rightarrow 0$ which we will now comment on. The general behaviour of the resonance ratchet in the presence of an initial momentum spread, as has already been noted [10], is saturation of the momentum current at a finite kick number, rather than the unbounded momentum growth that is predicted in the absence of other limiting factors. This saturation, of course, limits the usefulness of the ratchet effect in all realistic experimental situations where a quasi-momentum spread is inevitable.

However, the effect of quasi-momentum on the system is *not* independent of the kicking period. Indeed, the longer the kicking period is, the more time there is for the system to resolve the quasi-momentum differences between atoms. For this reason, as has been noted elsewhere [15], the QR peaks in energy for the kicked rotor are narrower and taller at the $l = 0$ case than for $l > 0$. For similar reasons, when $l = 0$, the momentum current becomes insensitive to the initial momentum spread, in principle preventing saturation of the momentum current, cf, the above argument $\tau\beta = \epsilon\beta \rightarrow 0$.

Figure 4 shows the effects of an initial quasi-momentum spread for $l = 0$ and 2, with $\epsilon = 0$ in both cases. In the upper and lower plots of figure 4, solid lines show ϵ -classical

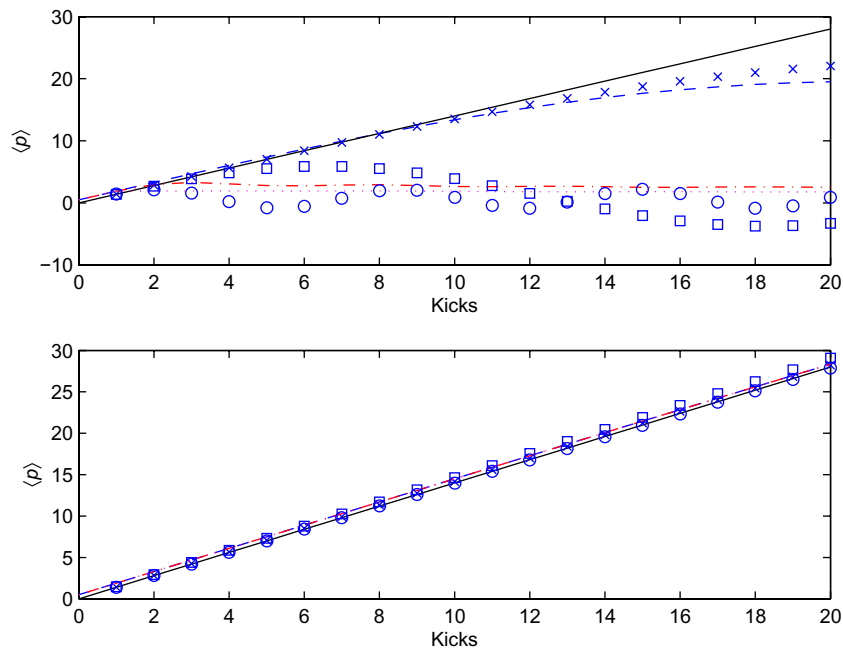


Figure 4. Simulation results for ϵ -classical simulations (lines) and quantum simulations (discrete points) showing the effect of initial momentum spread. The upper plot shows the results as a function of kick number when $l = 2$ for uniform quasi-momentum distributions of width $0\hbar k$ (solid line), $0.01 \times \hbar k$ (dashed line, crosses), $0.1 \times 2\hbar k$ (dash-dotted line, circles) and $2\hbar k$ (dotted line, squares). The lower plot shows simulations for the same values of quasi-momentum spread with the same symbols, but this time near the true classical limit (i.e. $l = 0$ in the definition of J , see around equation (2), $\tau\beta = \epsilon\beta \rightarrow 0$).

simulation results whereas discrete points are from quantum simulations. We see that as the quasi-momentum spread is increased from $0.01 \times 2\hbar k$, to $2\hbar k$, the momentum current saturates at a low kick number in the $l > 0$ case. However, in the $l = 0$ case (the semi-classical limit), $\langle p \rangle$ does not saturate.

It should not come as a surprise that in the classical limit the effect of quasi-momentum, which is an inherently quantum-mechanical quantity, becomes negligible. However, this fact is very helpful because it allows us to eliminate the principle problem with the QR ratchet—saturation due to quasi-momentum spread—while retaining the benefits of a momentum current. Of course, the flip-side to this benefit is that the control over the momentum current afforded by altering the quasi-momentum is not present in the $l = 0$ limit. This can be seen immediately by inspecting equation (11), since the quantity $\tau\beta$, which gives the variation of $\langle p \rangle$ with β is always approximately 0 in the $l = 0$ limit, for which $\tau = \epsilon \rightarrow 0$.

5. Scaling law for momentum current

So far in the study of directional momentum transport in these resonant systems, the effect of detuning from exact QR has not been considered. In general, it is not a trivial matter to calculate a closed form solution for off-resonant dynamics (representative examples of which are shown in figure 5), and the scaling functions for the atomic energy found in [13, 14] are thus considered to be important results.

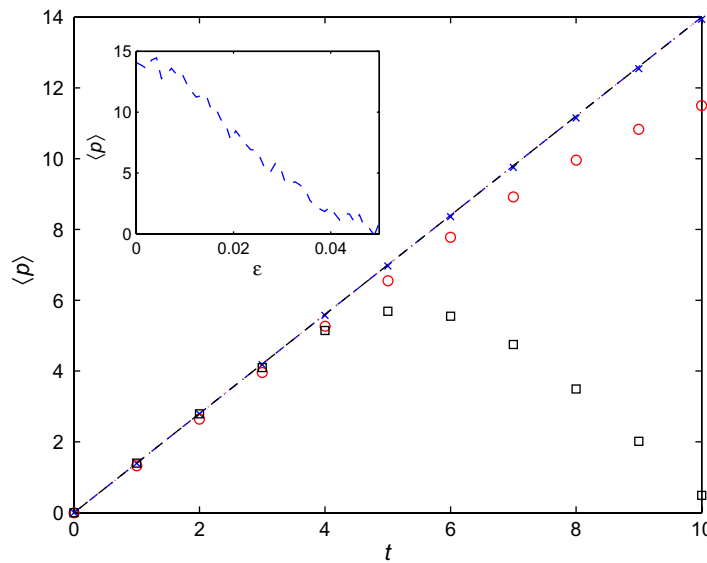


Figure 5. Momentum current as a function of kick number for $\epsilon = 0.0005$ (crosses), $\epsilon = 0.01$ (circles) and $\epsilon = 0.05$ (squares). The solid line shows linear growth for $k = 2.8$ and $\phi = 0$ for a system at perfect QR ($l = 2$). The inset shows the momentum current as a function of ϵ for the same parameters.

Before considering the possibility of a scaling law for the momentum current, we will inspect the time behaviour of the resonance ratchet as the kicking time diverges from exact resonance.

In [14] it was shown that a one parameter scaling law exists for the mean *energy* of the quantum kicked rotor near QR. In particular, the scaled energy is given by

$$\frac{E}{k^2 t} = 1 - \Phi(x) + \frac{\pi}{4x} G(x), \quad (12)$$

where $x = \sqrt{k|\epsilon|}t$ and $\Phi(x)$ and $G(x)$ are closed form functions derived by considering the topological changes in the ϵ -classical phase space as ϵ increases.

We now demonstrate that such a law also exists in the case of the momentum current. We proceed according to [13]. First, we employ the scaled variable $J' = J/(\sqrt{k|\epsilon|})$ and apply the pendulum approximation to the kicked rotor Hamiltonian [19] (in the scaled variables J' and θ). The motion is then described—in continuous time—by $H' \approx (J')^2/2 + |\epsilon|k \cos(\theta)$. Expressing the original momentum p in terms of those scaled variables, we have

$$\langle p \rangle = \frac{1}{|\epsilon|} \sqrt{k|\epsilon|} \langle J' - J'_0 \rangle. \quad (13)$$

Under the pendulum approximation, we can determine $J' = J'(\theta_0, J'_0, x)$ using solutions for the pendulum trajectories at arbitrary initial conditions. Because the definition of J' multiplies the physical momentum p by $|\epsilon|$, for small ϵ , the initial conditions for J'_0 when $p = 0$ or 1 are essentially the same. Therefore, we take the initial momentum J' to be zero and merely integrate over the (non-uniform) initial position distribution:

$$\langle J' - J'_0 \rangle = \int_{-\pi}^{\pi} d\theta_0 P(\theta_0) (J'(\theta_0, J'_0, x) - J'_0). \quad (14)$$

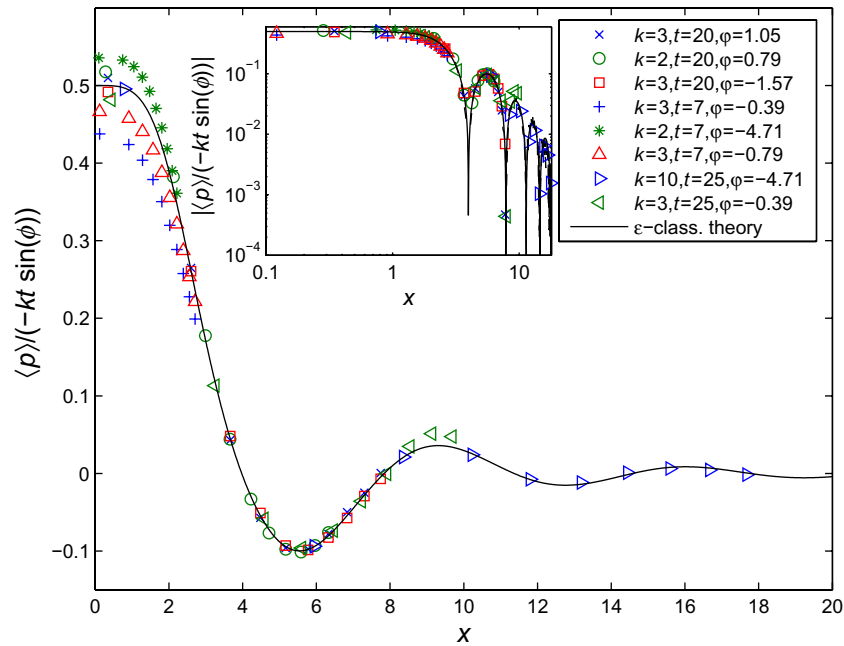


Figure 6. Scaled mean momentum $\langle p \rangle / (-kt \sin(\phi))$ plotted against the scaling variable $x = \sqrt{k|\epsilon|}t$. Discrete points show ϵ -classical (crosses) and quantum (all other symbols) simulation results for a variety of experimentally relevant parameters as indicated in the legend. The solid line shows the analytical scaling function given by equation (17). The same data are shown in the inset on logarithmic axes, where excellent agreement is found over at least two orders of magnitude on both axes.

Taking $P(\theta_0)$ as given by equation (4) and expanding the cosine term, we find that

$$\begin{aligned} \langle J' - J'_0 \rangle &= \int_{-\pi}^{\pi} d\theta_0 (J'(\theta_0, J'_0 = 0, x)) + \cos(\phi) \int_{-\pi}^{\pi} d\theta_0 \cos \theta_0 (J'(\theta_0, J'_0 = 0, x)) \\ &\quad - \sin(\phi) \int_{-\pi}^{\pi} d\theta_0 \sin \theta_0 (J'(\theta_0, J'_0 = 0, x)). \end{aligned} \quad (15)$$

Firstly, we note that by symmetry of the initial conditions, the first term on the rhs of equation (15) vanishes. Furthermore, because the solutions for J' are odd, the term in $\cos(\phi)$ also vanishes and we are left with just the sine term in ϕ . If we define $F(x) \equiv \int_{-\pi}^{\pi} d\theta_0 \sin \theta_0 (J'(\theta_0, J'_0 = 0, x))$, then substituting into equation (13) gives

$$\langle p \rangle = -\frac{\sqrt{k}}{\sqrt{|\epsilon|}} \sin(\phi) F(x). \quad (16)$$

Finally, dividing by $-kt \sin(\phi)$ gives the following new scaling law:

$$\frac{\langle p_{t,\epsilon} \rangle}{-kt \sin(\phi)} \approx R(x) \equiv \frac{F(x)}{x}. \quad (17)$$

We tested this scaling law by performing quantum simulations for a wide variety of all parameters of the system (ϕ , ϵ , t and k), and compared the results with scaled energies from an ϵ -classical simulation for a single parameter set. The results are shown in figure 6. We see very

good agreement between quantum simulations (done over a broad range of parameters) and the scaled ϵ -classical simulation (for a single parameter set with varying ϵ). For values of $k > 10$, there seems to be a breakdown in scaling, which probably results from the large spread of the wavepackets suppressing the current. However, in general, it is clear that a single parameter scaling law is valid for the momentum current over a broad parameter range, as long as time is neither too short (where our argument based on a continuous time evolution and on average momentum values fails) nor too large (where the ϵ -classical approximation would fail).

Note that the present scaling law only exists for very small spread in the initial quasi-momentum. In the case of a uniform quasi-momentum distribution, there is no momentum current because of the symmetric filling of the pseudo-classical phase space.

The most intriguing feature of the scaling function is the fact that the scaled current (and thus the unscaled current as well) becomes negative for certain x . This so-called current inversion has also been found in other quantum ratchets [1, 5], but to our knowledge this is the first prediction of current inversion due to parameter variation for the QR ratchet system (aside from the obvious dependence of the current on ϕ and β). Indeed, studies of the system up until now have focused on exactly resonant kicking. This precludes the possibility of finding the current inversion phenomenon, which requires nonzero x , and hence nonzero ϵ , or in other words off-resonant kicking. It should be a fairly simple matter to adapt current experiments to look for the scaling and current inversion effects.

Lastly, we note that we can use equation (8) to simplify the scaling function even further. Note that $\sin \phi = \pm \sqrt{1 - \cos^2 \phi} = \pm \sqrt{1 - (p_{t,\text{res}}/kt)^2}$, we may write the scaling function as

$$\frac{\text{sign}(\langle p_{t,\text{res}} \rangle) \langle p_{t,\epsilon} \rangle}{\sqrt{k^2 t^2 - \langle p_{t,\text{res}} \rangle^2}} \approx R(x) \equiv \frac{F(x)}{x}. \quad (18)$$

In equation (18) there is *no dependence* on the phase ϕ . Thus to scale experimental measurements for comparison with the scaling function, it is sufficient to know simply the resonant momentum current and the kick strength k . The exact quantum phase plays no part in determining the unique dynamics of the system.

Equation (18) underlines an intriguing feature of the work presented here. Despite the explanation of the directed transport in [9] in terms of interference of matter waves spreading from two initial wavepackets, the dynamics of the atomic ensemble may be predicted to a good approximation by a theory that takes only classical probabilities into account. We know that, in general, it is certainly not possible to replace quantum probability distributions by their classical counterparts since to do so ignores the interference terms that are responsible for uniquely quantum behaviour. However, in the present case, it is apparent that merely taking account of the spatial correlation between the atom density and the optical field intensity allows all the important features of the dynamics to be reproduced. Whether such an approach can be generalized to other systems where quantum interference is of importance is an interesting question for further research.

6. Conclusion

In the present paper, we have shown that a pseudo-classical approach may be used to describe the dynamics of QR ratchets so far studied using purely quantum methods. We first demonstrated that the pseudo-classical dynamics reproduced the main results of [9, 10], including the existence of a momentum current dependent on the quantum phase ϕ and the variation of the current as a function of the atomic quasi-momentum β .

We then demonstrated a number of surprising new facts about this system, which were illuminated by our pseudo- or ϵ -classical approach. Firstly, it follows as a simple corollary that the ratchet effect at QR *also* occurs in the limit as $\tau \rightarrow 0$. Although this does not change the fact that the ratchet effect seen when τ equals the Talbot time (i.e. equals the quantum resonant value) is purely quantum, it does show that an equivalent effect exists even for purely classical atoms.

Secondly, we demonstrated that the current suppressing effect of a nonzero quasi-momentum spread is absent in the semi-classical limit. Surprisingly, this means that the use of a vanishing kicking period is actually the best strategy to accelerate atoms using the methods developed in [9, 10]. However, in this case, we also lose the possibilities for quantum control offered by the dependence of the momentum current on the quasi-momentum.

Finally, we demonstrated the existence of a scaling law for the momentum current as a function of a combined variable $x = \sqrt{|\epsilon|kt}$. We tested the scaling law for a broad range of parameters and found good agreement between simulations and the one-parameter law so long as the kicking strength was not too large. Of particular interest was the current inversion predicted for certain x . This inversion has not yet been observed experimentally, but the advantage of the scaling law formulation is that it predicts a family of experimental parameters ϵ , k and t for which inversion should occur, allowing experimentalists freedom to find the most accessible regime in which to observe the effect.

Acknowledgment

Support within the Excellence Initiative by the DFG through the Heidelberg Graduate School of Fundamental Physics (grant no. GSC 129/1) and the detailed comments by one of our referees are gratefully acknowledged.

References

- [1] Flach S, Yevtushenko O and Zolotaryuk Y 2000 *Phys. Rev. Lett.* **84** 2358
Schiavoni M *et al* 2003 *Phys. Rev. Lett.* **90** 094101
Carlo G C *et al* 2006 *Phys. Rev. A* **74** 033617
- [2] Feynman R P 1963 *The Feynman Lectures on Physics* vol 1 (Reading, MA: Addison-Wesley) chapter 46
- [3] Thorn J J, Schoene E A, Li T and Steck D A 2008 *Phys. Rev. Lett.* **100** 240407
- [4] Astumian R D and Hänggi P 2002 *Phys. Today* **55** 33
Hänggi P and Marchesoni F 2009 *Rev. Mod. Phys.* **81** 387
- [5] Schanz H *et al* 2001 *Phys. Rev. Lett.* **87** 070601
Gong J and Brumer P 2006 *Phys. Rev. Lett.* **97** 240602
- [6] Mennerat-Robilliard C *et al* 1999 *Phys. Rev. Lett.* **82** 851
Monteiro T S *et al* 2002 *Phys. Rev. Lett.* **89** 194102
Jones P H *et al* 2007 *Phys. Rev. Lett.* **98** 073002
- [7] Izrailev F M 1990 *Phys. Rep.* **196** 299
- [8] Oskay W H, Steck D A, Milner V, Klappauf B G and Raizen M G 2000 *Opt. Commun.* **179** 137
d’Arcy M B *et al* 2001 *Phys. Rev. Lett.* **87** 074102
Duffy G J *et al* 2004 *Phys. Rev. E* **70** 056206
Ryu C *et al* 2006 *Phys. Rev. Lett.* **96** 160403
Kanem J F, Maneshi S, Partlow M, Spanner M and Steinberg A M 2007 *Phys. Rev. Lett.* **98** 083004
Lepers M, Zehnlé V and Garreau J C 2008 *Phys. Rev. A* **77** 043628

- [9] Sadgrove M, Munekazu H, Sekimura T and Nakagawa K 2007 *Phys. Rev. Lett.* **99** 043002
- [10] Dana I, Ramareddy V, Talukdar I and Summy G S 2008 *Phys. Rev. Lett.* **100** 024103
- [11] Lundh E and Wallin M 2005 *Phys. Rev. Lett.* **94** 110603
Kenfack A, Gong J and Pattanayak A 2008 *Phys. Rev. Lett.* **100** 044104
- [12] Fishman S, Guarneri I and Rebuzzini L 2002 *Phys. Rev. Lett.* **89** 084101
- [13] Wimberger S, Guarneri I and Fishman S 2003 *Nonlinearity* **16** 1381
Wimberger S, Guarneri I and Fishman S 2004 *Phys. Rev. Lett.* **92** 084102
- [14] Wimberger S, Sadgrove M, Parkins S and Leonhardt R 2005 *Phys. Rev. A* **71** 053404
- [15] Sadgrove M, Wimberger S, Parkins S and Leonhardt R 2005 *Phys. Rev. Lett.* **94** 174103
Wimberger S and Sadgrove M 2005 *J. Phys. A: Math. Gen.* **38** 10549
- [16] Sadgrove M, Wimberger S, Parkins S and Leonhardt R 2008 *Phys. Rev. E* **78** 025206(R)
- [17] Moore F L *et al* 1995 *Phys. Rev. Lett.* **75** 4598
- [18] Graham R, Schlautmann M and Zoller P 1992 *Phys. Rev. A* **45** 19(R)
- [19] Lichtenberg A L and Leiberman M A 1992 *Regular and Chaotic Dynamics* (Berlin: Springer)

PHYSICAL REVIEW E **80**, 035206(R) (2009)**Pseudoclassical theory for fidelity of nearly resonant quantum rotors**Martina Abb,¹ Italo Guarneri,^{2,3} and Sandro Wimberger¹¹*Institut für Theoretische Physik, Universität Heidelberg, Philosophenweg 19, 69120 Heidelberg, Germany*²*Center for Nonlinear and Complex Systems, Università dell'Insubria, Via Valleggio 11, 22100 Como, Italy*³*INFN, Sezione di Pavia, Via Bassi 6, 27100 Pavia, Italy*

(Received 3 July 2009; published 29 September 2009)

Using a semiclassical ansatz we analytically predict for the fidelity of δ -kicked rotors the occurrence of revivals and the disappearance of intermediate revival peaks arising from the breaking of a symmetry in the initial conditions. A numerical verification of the predicted effects is given and experimental ramifications are discussed.

DOI: [10.1103/PhysRevE.80.035206](https://doi.org/10.1103/PhysRevE.80.035206)

PACS number(s): 05.45.Mt, 37.10.Vz, 03.75.Dg

Besides entanglement in multipartite systems, it is the evolution of phases and the superposition principle which distinguishes a quantum from a classical system. Phase evolutions can be monitored in many ways, e.g., by correlation functions [1]. A quantity which has gained interest in the last decade is fidelity [2] defined as the overlap of two wave functions subjected to slightly different temporal evolutions. The temporal evolution of this quantum fidelity crucially depends on evolving relative phases. For many-particle systems, fidelity can be viewed as a Hilbert space measure to study quantum phase transitions [3] and the regular-to-chaotic transition in complex quantum systems [4]. For single-particle evolutions fidelity was measured in electromagnetic wave [5] and matter wave [6] billiards and with two different methods for periodically kicked cold atoms [7,8].

The latter system is a realization of the quantum kicked rotor (QKR), the standard model for low-dimensional quantum chaos and the occurrence of dynamical localization [9]. Great interest in the QKR has reemerged in the study of its quantum resonant motion [10–16] and related accelerator modes [17–20]. These two regimes are far from the classical limit of the QKR and, therefore, governed by distinct quantum effects. Nevertheless, close to quantum resonance the system can be described (pseudo)classically with a new Planck's constant, which is the detuning from the exact resonant value of the kicking period [10,18,21]. For the quantum resonances, the underlying pseudoclassical model is completely integrable and corresponds in good approximation to the dynamics of a classical pendulum [10,21].

In this Rapid Communication we apply well-known semiclassical methods to describe the behavior of fidelity close to the lowest-order quantum resonances of the QKR. We extend previous analytical results at exact resonance [11] to a broader parameter regime, recently measured in experiments performed by Wu and co-workers [8]. The behavior of classical [22] and quantum fidelity [23,24], in the case when classical motion is integrable, has mainly been addressed numerically so far, while our approach is both numerical and analytical. Also, the recurrences of fidelity found in [23] for the near-integrable regime of the kicked rotor are just predicted for perturbative variations around small kicking strengths. Our results are more general, allowing, e.g., for strong changes of the fidelity parameter as long as the motion remains nearly resonant. As expected, in the nearly reso-

nant regime, the temporal behavior of fidelity follows the behavior at exact resonance the longer, the smaller the detuning from resonance. Indeed, we show that the exactly resonant result predicted in [11] by quantum calculations is retrieved by pseudoclassical analysis. At large times, however, the exactly resonant fidelity and the nearly resonant one differ, as the latter displays recurrent revivals while the former steadily decays. Such revivals are approximately periodic. Their period depends on the detuning from resonance and diverges as exact resonance is approached so this noteworthy phenomenon is unrelated to quantum resonant dynamics. On the other hand, it is quite unexpected on classical grounds because the system is chaotic in the proper classical limit. Revivals of fidelity are thus a quantum effect and yet are explained by a (pseudo)classical analysis that relates them to periodic motion inside pseudoclassical resonant islands. Experimental possibilities to verify our predictions are discussed at the end of the Rapid Communication.

The dynamics of kicked atoms moving along a line in position space is described, in dimensionless units, by the Hamiltonian [10,25]

$$\mathcal{H}(t) = \frac{\tau}{2} p^2 + k \cos(x) \sum_{t'=-\infty}^{+\infty} \delta(t-t'), \quad (1)$$

where x is the position coordinate and p is its conjugate momentum. We use units in which $\hbar=1$ so the parameter τ plays the role of an effective Planck's constant; t is a continuous time variable and t' is an integer which counts the number of kicks. The evolution of the atomic wave function $\psi(x)$ from immediately after one kick to immediately after the next is ruled by the one-period Floquet operator $\hat{U}_k = \exp[-ik \cos(\hat{x})] \exp(-i\tau \hat{p}^2/2)$. Fidelity of the quantum evolution of a state ψ with respect to a change in the parameter k from a value k_1 to a value k_2 is the function of time t which for all integer t is defined by

$$F(k_1, k_2, t) = |\langle \hat{U}_{k_1}^t \psi | \hat{U}_{k_2}^t \psi \rangle|^2. \quad (2)$$

Periodicity in space of the kicking potential enforces conservation of quasimomentum β , which is just the fractional part of p thanks to $\hbar=1$. The atomic wave function decomposes into Bloch waves [10,18], which are eigenfunctions of quasimomentum, $\psi(x) = \int_0^1 d\beta e^{i\beta x} \sqrt{\rho(\beta)} \Psi_\beta(\theta)$, where

ABB, GUARNERI, AND WIMBERGER

PHYSICAL REVIEW E **80**, 035206(R) (2009)

$\theta = x \bmod(2\pi)$ and the factor $\rho(\beta)$ is introduced in order to normalize Ψ_β (it weights the initial population in the Brillouin zone of width one in our units). The dynamics at any fixed value of β is formally that of a rotor on a circle parameterized by the angle coordinate θ and described by the wave function Ψ_β . The Floquet propagator for the rotor is given by $\hat{U}_{\beta,k} = \exp[-ik \cos(\hat{\theta})] \exp[-i\tau(\hat{N} + \beta)^2/2]$, where $\hat{N} = -i \frac{d}{d\theta}$. Fidelity Eq. (2) may then be written as

$$F(k_1, k_2, t) = \left| \int_0^1 d\beta \rho(\beta) \langle \hat{U}_{\beta,k_1}^t \Psi_\beta | \hat{U}_{\beta,k_2}^t \Psi_\beta \rangle \right|^2 \quad (3)$$

so it results from averaging the scalar product under the integral sign over β with the weight $\rho(\beta)$. Note that the rotor's fidelity is the squared modulus of this quantity so the fidelity [Eq. (2)] of atomic evolution does not coincide with the β average of the rotors' fidelities, cf. [11]. Whenever $\tau = 2\pi\ell$ (ℓ integer), the evolution is explicitly solvable [10] and in particular the rotor's fidelity is determined by [11]

$$|\langle \hat{U}_{\beta,k_1}^t \Psi_\beta | \hat{U}_{\beta,k_2}^t \Psi_\beta \rangle|^2 = J_0^2(|W_t| \delta k), \quad (4)$$

where J_0 is the Bessel function of first kind and order 0, $\delta k = k_2 - k_1$, and $|W_t| = |\sin[\pi t \ell (\beta - \frac{1}{2}) \csc[\pi \ell (\beta - \frac{1}{2})]|$. If $2\beta - 1$ is an integer then a so-called QKR resonance occurs and Eq. (4) decays in time proportional to t^{-1} . When τ is close to a resonant value: $\tau = 2\pi\ell + \epsilon$, the quantum rotor dynamics may be viewed as the formal quantization of the pseudoclassical dynamics, defined by the map [10,18,21]:

$$\begin{aligned} I_{t+1} &= I_t + \tilde{k} \sin(\theta_{t+1}), \\ \theta_{t+1} &= \theta_t + I_t + \pi\ell + \tau\beta \bmod(2\pi), \end{aligned} \quad (5)$$

using ϵ as the Planck's constant, $I = \epsilon\mathcal{N}$, and $\tilde{k} = \epsilon k$. It is thus possible to investigate the quantum fidelity in the limit of small ϵ by means of standard methods of semiclassical approximation. In the limit $\epsilon \rightarrow 0$, the physical parameter k is fixed so the pseudoclassical parameter $\tilde{k} \rightarrow 0$. As a consequence, for sufficiently small ϵ , the pseudoclassical dynamics [Eq. (5)] is in the quasi-integrable regime even in cases when the classical kicked rotor dynamics is fully chaotic. It is dominated by the resonant islands at $I_{res} = (2m + \ell)\pi - \tau\beta$, with m as an integer. As we consider initial atomic states with a narrow distribution of momenta near $p=0$, we may restrict ourselves to a portion of the pseudoclassical phase space that includes the one island which is located astride $I=0$. We assume $\ell=1$ for simplicity. The pseudoclassical dynamics inside the resonant island is ruled, in continuous time, by the pendulum Hamiltonian [26] $H(\theta, I, \tilde{k}) = \frac{1}{2}(I + \tilde{\beta})^2 + \tilde{k} \cos(\theta)$, where $\tilde{\beta} = \tau(\beta - \frac{1}{2})$. We choose $\Psi_\beta(\theta) = (2\pi)^{-1/2}$ so

$$\hat{U}_{\beta,k}^t \Psi_\beta(\theta) \sim \frac{1}{\sqrt{2\pi}} \sum_s \left| \frac{\partial \theta}{\partial \theta'} \right|^{-1/2} e^{iI\epsilon\Phi_s(\theta,t) - i(\pi/2)\nu_s}, \quad (6)$$

where $\epsilon > 0$ is assumed with no limitation of generality. The sum is over all trajectories (labeled by the index s) which start with $I=0$ at time $t=0$ and reach position θ at time t . $\theta' = \theta'_s$ are their initial positions, and the function whose de-

rivative is taken in the prefactor yields θ at time t as a function of position θ' at time 0, given that the initial momentum $I'=0$. Finally, the function $\Phi_s(\theta, t) = S(\theta, \theta'_s, t)$ is the action of the s th trajectory and ν_s is the Morse-Maslov index [27]. We restrict ourselves to librational motion inside the stable island. The frequency of this motion decreases from $\omega = \sqrt{\tilde{k}}$ at the island center to $\omega=0$ at the separatrix. For times less than the minimal half period $\pi/\sqrt{\tilde{k}}$, there is a single trajectory in Eq. (6). Furthermore,

$$\begin{aligned} \frac{\partial \Phi_s(\theta, t)}{\partial t} &= \left(\frac{\partial S(\theta, \theta', t)}{\partial \theta'} \frac{\partial \theta'(\theta, t)}{\partial t} + \frac{\partial S(\theta, \theta', t)}{\partial t} \right)_{\theta'=\theta'_s} \\ &= \left(\frac{\partial S(\theta, \theta', t)}{\partial t} \right)_{\theta'=\theta'_s} = -H(\theta'_s, 0) = -\frac{\tilde{\beta}^2}{2} \\ &\quad + \tilde{k} \cos(\theta'_s). \end{aligned} \quad (7)$$

For t fixed and $\epsilon \rightarrow 0$ we use $\theta'(\theta, t) \sim \theta - \tilde{\beta}t$ in this equation so $\Phi(\theta, t) \sim -\frac{1}{2}\tilde{\beta}^2 t + \tilde{k} \int_0^t dt' \cos(\theta - \tilde{\beta}t') = -\frac{1}{2}\tilde{\beta}^2 t + 2\frac{\tilde{k}}{\tilde{\beta}} \sin(\frac{\tilde{\beta}t}{2}) \cos(\theta - \frac{\tilde{\beta}t}{2})$. Replacing all this in Eq. (3), we find for the rotor's fidelity in the limit when $\epsilon \rightarrow 0$ at constant t :

$$\begin{aligned} |\langle \hat{U}_{\beta,k_1}^t \Psi_\beta | \hat{U}_{\beta,k_2}^t \Psi_\beta \rangle|^2 &\sim \left| \frac{1}{2\pi} \int_0^{2\pi} d\theta e^{iB(\beta,t) \cos[\theta - (\tilde{\beta}t/2)]} \right|^2 \\ &= J_0^2[B(\beta, t)], \end{aligned} \quad (8)$$

where $B(\beta, t) = 2\frac{\delta k}{\tilde{\beta}} \sin(\frac{\tilde{\beta}t}{2})$. Since $B(\beta, t) \approx |W_t|$ in Eq. (4) for $\tau = 2\pi\ell$ and $\beta \approx 0.5$, we see that the pseudoclassical approximation along with the pendulum approximation well reproduce the exact quantum calculation [Eq. (4)] when $\epsilon \rightarrow 0$ at fixed t . In the final step of integrating over quasimomenta to find the fidelity for atoms (as distinct from fidelity for rotors), the pseudoclassical approximation plays no role since the particle's dynamics, unlike the rotor's, does not turn pseudoclassical in the limit $\epsilon \rightarrow 0$ [18]. Replacing Eq. (4) into Eq. (3) and computing the integral with a uniform distribution of β in $[0,1]$ shows that the complete fidelity [Eq. (3)] saturates to a nonzero value in the course of time [11].

Next we address the asymptotic regime where $\epsilon \rightarrow 0$ and $t\epsilon^{1/2} \sim \text{const}$. To this end, the exact solution of the pendulum dynamics is needed in order to compute actions; however, some major features of fidelity are accessible by exploiting the harmonic approximation of the pendulum Hamiltonian. We replace the pendulum by the quadratic Hamiltonian $H(I, \theta) = 1/2(I + \tilde{\beta})^2 + \omega^2/2\theta^2$, where $\omega = \sqrt{\tilde{k}}$ and a shift of θ by π is understood. Except at exact multiples of the period, there is one harmonic oscillator trajectory in the sum in Eq. (6); moreover, Maslov indices do not depend on the trajectory. Straightforward calculations yield $\theta'(\theta, t) = \sec(\omega t) [\theta - \tilde{\beta}\omega^{-1} \sin(\omega t)]$ and $\Phi(\theta, t) = \tilde{\beta}\theta [\sec(\omega t) - 1] - (\omega^{-1}\tilde{\beta}^2 + \omega\theta^2) \tan(\omega t)/2$, and so

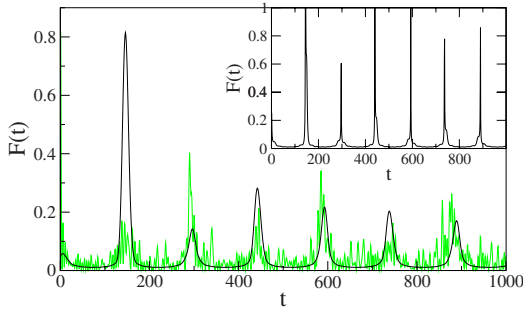


FIG. 1. (Color online) Fidelity as predicted by Eq. (12) because of the singularities of the analytical formula the curve is folded with normalized Gaussians with a standard deviation of $t \approx 6$ kicks (solid black line) and numerical data (gray/green curve) for $k_1=0.8\pi$, $k_2=0.6\pi$, and detuning $\epsilon=0.01$ from $\tau-\epsilon=2\pi$. In the inset, the non-smoothed result [Eq. (12)] is shown.

$$\langle \hat{U}_{\beta,k_1}^t \Psi_\beta | \hat{U}_{\beta,k_2}^t \Psi_\beta \rangle \sim \frac{e^{i\lambda(t)}}{2\pi \sqrt{|\cos(\omega_1 t) \cos(\omega_2 t)|}} \int_{-\pi}^{\pi} d\theta \times e^{i/2\epsilon \{A(t)\theta^2 + C(t)\bar{\beta}^2 - 2\bar{\beta}\theta B(t)\}}, \quad (9)$$

where $A(t) = \omega_2 \tan(\omega_2 t) - \omega_1 \tan(\omega_1 t)$, $B(t) = \sec(\omega_2 t) - \sec(\omega_1 t)$ and $C(t) = \omega_2^{-1} \tan(\omega_2 t) - \omega_1^{-1} \tan(\omega_1 t)$. $\lambda(t)$ is a phase factor accumulated by the Maslov indices and it just depends on time, rendering it irrelevant for our present purposes. We next insert Eq. (9) into Eq. (3) and choose for $\rho(\beta)$ a uniform distribution in some interval $[\frac{1}{2}-b, \frac{1}{2}+b]$, with $0 \leq b \leq 1/2$. It is necessary to assume that b is smaller than the halfwidth of the pseudoclassical resonant island because the harmonic approximation we have used is valid only inside that island. Then

$$F(k_1, k_2, t) \sim \frac{1}{16\pi^2 b^2 \tau^2 |\cos(\omega_1 t) \cos(\omega_2 t)|} \times \left| \int_{-\pi}^{\pi} d\theta e^{-i/2\epsilon \Lambda_1(\theta, \epsilon, t)} \int_{-\tau b}^{\tau b} d\bar{\beta} e^{-i/2\epsilon \Lambda_2(\bar{\beta}, \theta, \epsilon, t)} \right|^2, \quad (10)$$

where $\Lambda_1(\theta, \epsilon, t) = [A(t) - B(t)C(t)^{-1}] \theta^2$ and $\Lambda_2(\bar{\beta}, \theta, \epsilon, t) = [\bar{\beta} \sqrt{C(t)} - B(t)C(t)^{-1/2} \theta]^2$. As $\Lambda_2 \sim \epsilon^{-1/2}$ in the limit when $\epsilon \rightarrow 0$ and $t\sqrt{\epsilon} \sim \text{const}$, the limits in the $\bar{\beta}$ integral in Eq. (10) may be taken to $\pm\infty$:

$$\int_{-\tau b}^{\tau b} d\bar{\beta} e^{-i/2\epsilon \Lambda_2(\bar{\beta}, \theta, \epsilon, t)} \sim (2\pi)^{1/2} \epsilon^{1/2} C(t)^{-1/2} e^{-i\pi/4}.$$

Due to this approximation, Eq. (11) below is valid in the asymptotic regime where ϵ is small compared to b^2 . The remaining θ integral is dealt with similarly because the prefactor of θ^2 in Λ_1 is $\sim \epsilon^{-1/2}$. Thus finally

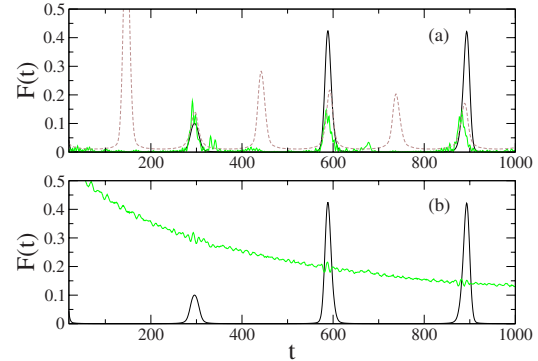


FIG. 2. (Color online) Same as in Fig. 1 for an ensemble of 5000 equidistantly chosen rotors (solid gray/green lines) with a width of (a) $\Delta\beta=0.05$ (or $\Delta\bar{\beta} \approx 0.31$) around the resonant value induced by Eq. (5) and (b) $\Delta\beta=1$ covering the full phase space, compared with the smoothed (see caption of Fig. 1) version of Eq. (11) (solid black lines). In (a) the intermediate revival peaks observed in Fig. 1 disappear as predicted by Eq. (11). The dashed line in (a) reproduces the smoothed analytic formula from Fig. 1. For β distributed over the full Brillouin zone in (b), the revivals are barely visible since the average includes many nonresonant rotors performing rotational motion in phase space, which is not described by our theory valid just for the librational island motion.

$$F(k_1, k_2, t) \sim \frac{\epsilon^2}{16\pi^2 b^2 |C(t)A(t) - B(t)^2| |\cos(\omega_1 t) \cos(\omega_2 t)|} = \frac{\epsilon^2 \omega_1 \omega_2}{8\pi^2 b^2 |4\omega_1 \omega_2 - \omega_+^2 \cos(\omega_- t) - \omega_-^2 \cos(\omega_+ t)|}, \quad (11)$$

where $\omega_{\pm} = \omega_1 \pm \omega_2$. Singularities of this expression are artifacts of the approximations used in evaluating the integrals in Eq. (10), which indeed break down when the divisor in Eq. (11) is small compared to ϵ . However, they account for the periodic “revivals” that are observed in the fidelity at large times, with the beating period $T_{12} = 2\pi/|\omega_-|$ [Fig. 2(a)]. With a quite narrow distribution of β , however, fidelity is at long times dominated by the “resonant” rotors ($\beta=0$ or $\beta=1/2$, respectively), and then revivals occur with the period $T_{12}/2$ (Fig. 1). Indeed, with the purely resonant β , Eq. (10) yields

$$F(k_1, k_2, t) \equiv F_{res}(k_1, k_2, t) \sim \frac{\epsilon}{2\pi |\omega_2 \cos(\omega_1 t) \sin(\omega_2 t) - \omega_1 \cos(\omega_2 t) \sin(\omega_1 t)|}, \quad (12)$$

which has singularities in time with the mentioned periodicity of $T_{12}/2$. This behavior of resonant rotors has a simple qualitative explanation. As the initial state of the rotor corresponds to momentum $I=0$, at that value of quasimomentum ($\beta=\frac{1}{2}$) the stationary-phase trajectories of the two harmonic oscillators, which were started at $I=0$, exactly return to $I=0$ whenever time is a multiple of the half period $T_{12}/2$ and

ABB, GUARNERI, AND WIMBERGER

PHYSICAL REVIEW E **80**, 035206(R) (2009)

so fully contribute to fidelity in spite of their angles being different by π in the case of odd multiples. At $\beta \neq 0$ this symmetry is lost. Comparing numerical data (obtained by repeated application of the Floquet operator to the initial wave function) with the analytical predictions we find excellent agreement. We observe the expected peak structure of the revivals in Fig. 1 and the loss of intermediate revival peaks at $T_{12}/2$ in Fig. 2(a). The time scale on which the revivals occur is proportional to $\epsilon^{-1/2}$ and of crucial impact to experimental measurements: conservation of coherence has been shown for up to 150 kicks (see [19]) with cold atoms, making an observation of the revivals for reasonable $\epsilon \leq 0.01$ possible. Earlier realizations of the QKR were implemented using cold atoms [7,12,14] with broad distributions in quasimomentum. Nowadays, much better control of quasimomentum is provided by using Bose-Einstein condensates (see [13,16]), which allow for a restriction in β up to 0.2% (as achieved in [16]) of the Brillouin zone. This would allow us to verify our results by conveniently reducing the intervals in quasimomentum and thus retracing the revivals with period $T_{12}/2$ to the exactly resonant and the revivals with period T_{12} to the near-resonant rotors. There exists an interesting second possibility to measure the transition from Eq. (12) to Eq. (11) with just cold atoms since the $\bar{\beta}$ we use

scales with the kicking period, i.e., $\bar{\beta} = \tau(\beta - 1/2)$. Due to this scaling, the limit $\tau \rightarrow 0$ (automatically implying also $\epsilon \rightarrow 0$, cf. [14]) permits a measurement of Eq. (12) even with an ensemble of cold atoms whose quasimomenta occupy the full Brillouin zone. Also the momentum selective interferometric measurements of fidelity [8] allow us to select narrow intervals of quasimomenta and hence would permit to check our predictions experimentally.

To summarize, we predict fidelity revivals in the QKR close to quantum resonance using a semiclassical ansatz. Our results are supported by numerical data showing the same characteristic revival peaks. Every second peak vanishes once the symmetry of the initial quasimomentum distribution on the resonance island is broken. This makes for a surprising transition that could be measured with both cold and ultracold atoms owing to the scaling of $\bar{\beta}$ or the use of momentum selective methods as described in the previous paragraph.

Support by the Excellence Initiative through the Global Networks Mobility Measures and the Heidelberg Graduate School of Fundamental Physics (DFG Grant No. GSC 129/1) and by a Short Visit Grant (DAAD) is acknowledged.

- [1] D. F. Walls and G. J. Milburn, *Quantum Optics* (Springer, New York, 2008).
- [2] T. Gorin *et al.*, *Phys. Rep.* **435**, 33 (2006).
- [3] P. Buonsante and A. Vezzani, *Phys. Rev. Lett.* **98**, 110601 (2007).
- [4] P. Plötz, M. Lubasch, and S. Wimberger, e-print arXiv:0909.4333, *Europhys. Lett.* (unpublished).
- [5] C. Dembowski *et al.*, *Phys. Rev. Lett.* **93**, 134102 (2004); R. Höhmann, U. Kuhl, and H. J. Stöckmann, *ibid.* **100**, 124101 (2008).
- [6] M. F. Andersen, A. Kaplan, T. Grunzweig, and N. Davidson, *Phys. Rev. Lett.* **97**, 104102 (2006).
- [7] S. Schlunk *et al.*, *Phys. Rev. Lett.* **90**, 054101 (2003).
- [8] S. Wu, A. Tonyushkin, and M. G. Prentiss, *Phys. Rev. Lett.* **103**, 034101 (2009).
- [9] F. M. Izrailev, *Phys. Rep.* **196**, 299 (1990); S. Fishman, in *Enrico Fermi*, edited by G. Casati *et al.* (IOS, Amsterdam, 1993).
- [10] S. Wimberger *et al.*, *Nonlinearity* **16**, 1381 (2003).
- [11] S. Wimberger and A. Buchleitner, *J. Phys. B* **39**, L145 (2006).
- [12] W. H. Oskay *et al.*, *Opt. Commun.* **179**, 137 (2000); M. B. d'Arcy, R. M. Godun, M. K. Oberthaler, D. Cassettari, and G. S. Summy, *Phys. Rev. Lett.* **87**, 074102 (2001); M. Sadgrove, S. Wimberger, S. Parkins, and R. Leonhardt, *Phys. Rev. E* **78**, 025206(R) (2008).
- [13] G. J. Duffy *et al.*, *Phys. Rev. E* **70**, 056206 (2004); I. Dana, V. Ramareddy, I. Talukdar, and G. S. Summy, *Phys. Rev. Lett.* **100**, 024103 (2008).
- [14] M. Sadgrove, S. Wimberger, S. Parkins, and R. Leonhardt, *Phys. Rev. Lett.* **94**, 174103 (2005); S. Wimberger, M. Sadgrove, S. Parkins, and R. Leonhardt, *Phys. Rev. A* **71**, 053404 (2005); S. Wimberger and M. Sadgrove, *J. Phys. A* **38**, 10549 (2005).
- [15] E. Lundh and M. Wallin, *Phys. Rev. Lett.* **94**, 110603 (2005); I. Dana and D. L. Dorofeev, *Phys. Rev. E* **74**, 045201(R) (2006); J. F. Kanem, S. Maneshi, M. Partlow, M. Spanner, and A. M. Steinberg, *Phys. Rev. Lett.* **98**, 083004 (2007); M. Lepers, V. Zehnle, and J. C. Garreau, *Phys. Rev. A* **77**, 043628 (2008); P. L. Halkyard, M. Saunders, S. A. Gardiner, and K. J. Challis, *ibid.* **78**, 063401 (2008); M. Sadgrove and S. Wimberger, *New J. Phys.* **11**, 083027 (2009).
- [16] C. Ryu *et al.*, *Phys. Rev. Lett.* **96**, 160403 (2006).
- [17] M. K. Oberthaler, R. M. Godun, M. B. d'Arcy, G. S. Summy, and K. Burnett, *Phys. Rev. Lett.* **83**, 4447 (1999).
- [18] S. Fishman, I. Guarneri, and L. Rebuzzini, *Phys. Rev. Lett.* **89**, 084101 (2002); *J. Stat. Phys.* **110**, 911 (2003).
- [19] S. Schlunk, M. B. d'Arcy, S. A. Gardiner, and G. S. Summy, *Phys. Rev. Lett.* **90**, 124102 (2003).
- [20] A. Buchleitner *et al.*, *Phys. Rev. Lett.* **96**, 164101 (2006); I. Guarneri and L. Rebuzzini, *ibid.* **100**, 234103 (2008).
- [21] S. Wimberger, I. Guarneri, and S. Fishman, *Phys. Rev. Lett.* **92**, 084102 (2004).
- [22] G. Benenti, G. Casati, and G. Veble, *Phys. Rev. E* **68**, 036212 (2003).
- [23] R. Sankaranarayanan and A. Lakshminarayan, *Phys. Rev. E* **68**, 036216 (2003).
- [24] F. Haug, M. Bienert, W. P. Schleich, T. H. Seligman, and M. G. Raizen, *Phys. Rev. A* **71**, 043803 (2005).
- [25] R. Graham, M. Schlautmann, and P. Zoller, *Phys. Rev. A* **45**, R19 (1992); F. L. Moore, J. C. Robinson, C. F. Bharucha, B. Sundaram, and M. G. Raizen, *Phys. Rev. Lett.* **75**, 4598 (1995).
- [26] A. J. Lichtenberg and M. A. Leiberman, *Regular and Chaotic Dynamics* (Springer, Berlin, 1992).
- [27] F. Haake, *Quantum Signatures of Chaos* (Springer, Berlin, 2000); L. S. Schulman, *Techniques and Applications of Path Integration* (Wiley, New York, 1981).

FAST TRACK COMMUNICATION

Collapse and revival in inter-band oscillations of a two-band Bose–Hubbard model

Patrick Plötz¹, Javier Madroño² and Sandro Wimberger¹¹ Institut für Theoretische Physik, Universität Heidelberg, Philosophenweg 19, 69120 Heidelberg, Germany² Physik Department, Technische Universität München, James-Frank-Str. 1, 85748 Garching, GermanyE-mail: ploetz@thphys.uni-heidelberg.de

Received 22 February 2010, in final form 23 February 2010

Published 23 March 2010

Online at stacks.iop.org/JPhysB/43/081001**Abstract**

We study the effect of a many-body interaction on inter-band oscillations in a two-band Bose–Hubbard model with an external Stark force. Weak and strong inter-band oscillations are observed, where the latter arise from a resonant coupling of the bands. These oscillations collapse and revive due to a weak two-body interaction between the atoms. Effective models for oscillations in and out of resonance are introduced that provide predictions for the system's behaviour, particularly for the time scales for the collapse and revival of the resonant inter-band oscillations.

(Some figures in this article are in colour only in the electronic version)

1. Introduction

Recent experiments have proven the possibility of studying the coherent dynamics of interacting many-particle systems [1–3]. Such realizations of many-body systems with ultra-cold gases in optical lattices have a short but impressive history and open immense possibilities for various fields of physics [4, 5]. The demonstration of the well-known phenomenon of collapse and revival, the latter being a pure quantum effect, with ultra-cold atoms bears witness to this coherent evolution of a many-body wavefunction [2, 6]. Additionally, the high degree of control in such experiments allows a manipulation of many system parameters and makes them particularly interesting for various fields of physics as well as future applications [5, 7]. Different ways of addressing additional degrees of freedom in such ultra-cold bosonic gases have been suggested [5].

In this fast track communication, we discuss a two-band model with an additional external force to control the coupling between the two bands. Applying a force to atoms in optical lattices leads to Bloch oscillations and is a realization of a many-body Wannier–Stark system [8]. The coupling

of the low-lying energy bands in such systems has been demonstrated in different experiments, e.g. on Landau–Zener tunnelling [8, 9], and the influence of the many-body interaction on a weak coupling of the bands has also been studied theoretically [10]. We go beyond a weak coupling of energy bands and consider an isolated two-band system with a strong external force. A closed two-band system is an idealization but can be realized approximatively with ultra-cold atoms [4] using different techniques such as, e.g., superlattices [11, 12]. Besides the possibility of experimental realization, a closed two-band model is also interesting as a simple model system. For the latter, we focus on the two lowest energy bands of interacting bosons in an optical lattice $V(x) = V_0 \cos(2k_L x)$, with the wave vector of the optical lattice $k_L = 2\pi/\lambda_L$. Then, all parameters of the model Hamiltonian just depend on this external potential. The parameters can be computed numerically (see, e.g., appendix A in [13]) and analytical approximations exist for them for not too small amplitudes V_0 [4]. Using this setup, we are able to identify regions of strong and weak inter-band coupling. A weak two-body interaction introduces new

energy scales in the coherent evolution of the many-body wavefunction, leading to a collapse of such oscillations, but the form of the interaction gives rise to subsequent revivals. We give analytical expressions for all time scales in this many-body realization of a two-band collapse and revival phenomenon, and experimental ramifications for a realization with ultra-cold bosonic gases are discussed.

2. The many-particle model

We study a two-band Bose–Hubbard model with an additional external Stark force for a strong coupling of the two bands, introduced in [13, 14],

$$\begin{aligned} \mathcal{H} = & \sum_{l=1}^L \left[\epsilon_l^- n_l^a - \frac{t_a}{2} (a_{l+1}^\dagger a_l + \text{h.c.}) + \frac{gW_a}{2} n_l^a (n_l^a - 1) \right. \\ & + \epsilon_l^+ n_l^b + \frac{t_b}{2} (b_{l+1}^\dagger b_l + \text{h.c.}) + \frac{gW_b}{2} n_l^b (n_l^b - 1) \\ & + FC_0 (b_l^\dagger a_l + \text{h.c.}) + 2gW_x n_l^a n_l^b \\ & \left. + \frac{gW_x}{2} (b_l^\dagger b_l^\dagger a_l a_l + \text{h.c.}) \right]. \end{aligned} \quad (1)$$

Here, a_l (a_l^\dagger) annihilates (creates) a particle at site l of totally L sites in the lower band and b_l (b_l^\dagger) in the upper band. The corresponding number operators are $n_l^a = a_l^\dagger a_l$, $n_l^b = b_l^\dagger b_l$. The bands are separated by a bandgap Δ and have onsite-energies $\epsilon_l^\pm = \pm\Delta/2 + lF$, respectively. We include hopping between neighbouring sites in band a, b with a hopping strength $t_a, t_b > 0$, and a repulsive interaction between particles occupying the same site in band $a(b)$ with a strength W_a (W_b). The two bands are coupled via C_0F , with the external Stark force F and a coupling constant C_0 depending on the depth of the lattice V_0 [13, 14], and also via the inter-particle interaction with a strength W_x . All parameters are measured in recoil energies $E_{\text{rec}} \equiv \hbar^2 k_L^2 / (2m)$ and we set $\hbar = 1$ throughout. Focusing on a realization with a single optical lattice rather than a superlattice, the relation between the parameters is generally: $\Delta \gg t_a, t_b$, as well as $t_a, t_b \approx W_i$ and $C_0 = \mathcal{O}(10^{-1})$. We take the external force F as a free parameter. We assume that the interaction strength can be tuned (experimentally, e.g., by the use of Feshbach resonances [4]) and include a corresponding scaling factor g to all interaction terms. To study the occupation of the upper band, we prepare the system in an initial state $|\psi(0)\rangle$, with a uniform distribution of particles in the lower band only, and evolve it in time by the many-body Schrödinger equation. The quantity we study is the (normalized) number of particles in the upper band

$$\mathcal{N}_b(t) \equiv \frac{1}{N} \langle \psi(t) | \sum_l n_l^b | \psi(t) \rangle, \quad (2)$$

where $N = \sum_l (n_l^a + n_l^b)$ is the total number of particles. We will refer to $\mathcal{N}_b(t)$ as *occupation of the upper band*.

Let us discuss the non-interacting single-particle case $\mathcal{H}_0 \equiv \mathcal{H}(g = 0)$ first. We apply the following transformation involving Bessel functions of the first kind $J_n(x)$ to our

operators, which is known to remove the hopping terms in the single-band case [15]

$$\alpha_n = \sum_{l \in \mathbb{Z}} J_{l-n}(x_a) a_l \quad \beta_n = \sum_{l \in \mathbb{Z}} J_{l-n}(x_b) b_l, \quad (3)$$

with $x_i \equiv t_i/F$, $i = a, b$. Using relations for Bessel functions, we arrive at

$$\begin{aligned} \mathcal{H}_0 = & \sum_{l \in \mathbb{Z}} \left[\epsilon_l^- \alpha_l^\dagger \alpha_l + \epsilon_l^+ \beta_l^\dagger \beta_l \right. \\ & \left. + C_0 F \sum_n J_{l-n}(\Delta x) (\alpha_l^\dagger \beta_{l+n} + \text{h.c.}) \right], \end{aligned} \quad (4)$$

where $\Delta x = x_a + x_b$ and $\epsilon_l^\pm = \pm\Delta/2 + lF$ as above. We obtain coupling between any two sites of the two different bands, weighted by Bessel functions. In (1) the coupling between different and possibly remote sites originates from an on-site coupling and subsequent hoppings. It can thus be considered a higher order process in the original basis. But in the transformed Hamiltonian (4), this coupling is now direct with a strength modified by the factor $J_{l-n}(\Delta x)$.

The Hilbert space in the many-particle problem is spanned by Fock states with fixed particle number $|n_1^a, \dots, n_L^a; n_1^b, \dots, n_L^b\rangle$ with single-particle basis a_l, b_l . The total dimension of the Fock space for a given number of atoms N and lattice sites L per band is given by $\dim \mathcal{H} = (N + 2L - 1)! / [N!(2L - 1)!]$. For numerical simulations, we change to the interaction picture with respect to the external force [16] which removes the tilt $\sum_l l n_l^{a,b} F$ and replaces $a_{l+1}^\dagger a_l \rightarrow e^{iFt} a_{l+1}^\dagger a_l$ (and likewise for $b_{l+1}^\dagger b_l$). The Hamiltonian is then time dependent with a periodicity of $T_B \equiv 2\pi/F$ and decomposes into a direct sum of operators for specific quasi-momenta κ [16]. As a consequence, the size of the Hilbert space is reduced by a factor of the order of L [13, 14, 16]. Since the different subspaces are physically equivalent, we restrain our discussion to the $\kappa = 0$ subspace of the Hilbert space [16].

For the time evolution of a given initial state, we use either a direct numerical integration (with an adaptive step-size Runge–Kutta algorithm [17]) or an eigenbasis expansion after diagonalizing the problem:

$$|\psi(mT_B)\rangle = \sum_n c_n \exp(-i\varepsilon_n mT_B) |\varepsilon_n\rangle. \quad (5)$$

Here we use the eigenstates $U_F(T_B) |\varepsilon_n\rangle = \exp(-i\varepsilon_n T_B) |\varepsilon_n\rangle$ of the Floquet–Bloch operator (\mathcal{T} denotes time ordering)

$$U_F(T_B) = \mathcal{T} \exp \left[-i \int_0^{T_B} \mathcal{H}(t) dt \right], \quad (6)$$

since the Hamiltonian is explicitly time dependent, with a periodicity T_B . In addition, this gives us the full spectrum and enables access to relevant energy scales of the problem, as well as an identification of the most important states participating in the time evolution.

3. Results

For the specific system under consideration, i.e. bosons in optical lattices, both hopping coefficients t_a, t_b are smaller than unity and (since we are interested in strong inter-band

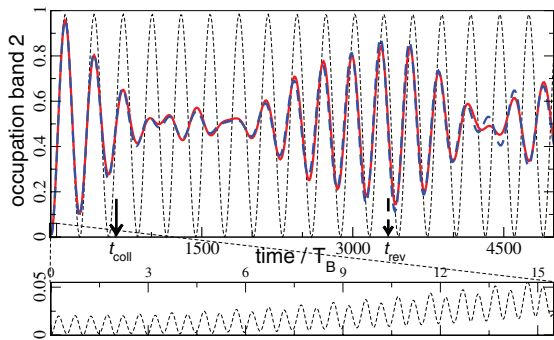


Figure 1. Occupation of the upper band as a function of time for a resonance of order $r = 2$. The following cases are shown: vanishing two-body interaction ($g = 0$, thin dashed line), weak two-body interaction ($g = 0.1$) with all interaction terms (thick line) and only one interaction term $2W_x \sum_l n_l^a n_l^b$ (thick dashed line) included. The collapse and revival times, t_{coll} and t_{rev} , are indicated by arrows. *Lower panel:* magnification of the initial oscillation showing small non-resonant oscillations of period $T_{\tilde{\Delta}}$ on top of the resonant oscillations with a much longer period T_{res} . Parameters correspond to $V_0 = 4$: $\Delta = 4.39$, $C_0 = -0.15$, $t_a = 0.062$, $t_b = 0.62$, $W_a = 0.030$, $W_b = 0.018$, $W_x = 0.012$; $N = L = 5$ and $F = 2.2207$.

coupling) we take the external Stark force F to be much larger than the hopping coefficients: $\Delta x \equiv (t_a + t_b)/F \ll 1$. The non-interacting Hamiltonian (4) now allows for simple solutions for two regimes: values of the external force F not leading to a degeneracy between energy levels of different bands (*off-resonant regime*) and values of the force F leading to such a degeneracy (*resonant regime*). For the off-resonant regime we make use of $\Delta x \ll 1$ and neglect all Bessel functions in (4) except for $J_0(\Delta x) \approx 1$. The Hamiltonian then decomposes [18] into a sum of independent two-level systems and the occupation of the upper band when initially zero follows a simple Rabi formula $\mathcal{N}_b(t) = [1 + \tilde{\Delta}^2 / (4C_0^2 F^2)]^{-1} \sin^2(\tilde{\Delta}t/2)$, where $\tilde{\Delta} \equiv \sqrt{\Delta^2 + 4C_0^2 F^2}$. This corresponds to Rabi oscillations between the bands with an amplitude much smaller than unity and a period $T_{\tilde{\Delta}} = 2\pi/\tilde{\Delta}$ of the order of the Bloch period $T_B = 2\pi/F$. An example is shown in the lower panel of figure 1 where the off-resonant contribution to the oscillations is shown.

Although the coupling from a site l to sites in the other band with different index l' is usually small (see the discussion after (4)), it is important when the two levels become degenerate in energy, i.e. for resonant values of the force F . This happens when the energy gap between both bands is close to an integer multiple of the external force $\tilde{\Delta} \approx rF$ and we refer to this regime as *resonant of order r* . In resonance, the coupling of the degenerate levels is most important and the Hamiltonian of (4) can similarly be reduced to a sum of independent two-level systems

$$\mathcal{H}_0 = \sum_{l \in Z} [\epsilon_l^- \alpha_l^\dagger \alpha_l + \epsilon_l^+ \beta_l^\dagger \beta_l + C_0 F J_{l-r}(\Delta x) (\alpha_l^\dagger \beta_{l+r} + \text{h.c.})], \quad (7)$$

and diagonalized by $\mu_l^{(r)} = \frac{1}{\sqrt{2}}(\beta_l + \alpha_{l+r})$ and $\nu_l^{(r)} = \frac{1}{\sqrt{2}}(\beta_l - \alpha_{l+r})$. The resonant oscillations (of order r) between the two bands have an amplitude of almost unity and a period given by

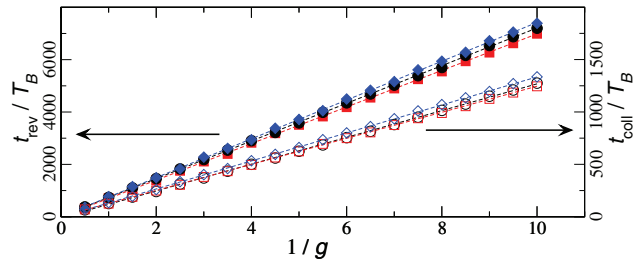


Figure 2. Collapse times (open symbols) and revival times (filled symbols) versus $1/g$ for $N, L = 5, 5$ and $V_0 = 4$: \square , $V_0 = 5$: \circ , $V_0 = 6$: \diamond . Order of the resonance: $r = 1$. The collapse time is defined via $\mathcal{N}_b(t_{\text{coll}}) = (1 + e^{-1})/2$ and the revival time is chosen as the next maximum in the oscillations after the initial decay $t > t_{\text{coll}}$, as indicated in figure 1 (upper panel).

$T_{\text{res}} = \pi/|C_0 F J_r(\Delta x)| \gg T_B$. An example of these resonant oscillations for $r = 2$ is shown as the thin dashed line in figure 1. The period predicted by the reduction to independent two-level systems is $T_{\text{res}}^{r=2} = 285 T_B$ for the parameters given there, in excellent agreement with figure 1 where the actual period is $T_{\text{res}} \approx 288 T_B$. We found equally good agreement in numerical simulations for different lattice depths and other orders r of resonance not explicitly reported here.

Let us now study the effect of the many-body interaction in the original Hamiltonian (1). Figure 1 also shows the occupation of the upper band as a function of time for the initial state $|\psi(0)\rangle = |1, \dots, 1; 0, \dots, 0\rangle$ in a weakly interacting system with $g = 0.1$. We observe a decay of the resonant oscillations followed by a major revival. At later times several minor revivals occur (not shown in figure 1). This effect is stable against variations of the system parameters (as the number of particles and lattice sites, even for fillings N/L of order but not always close to 1), with the time scales of decay and revival depending on the interaction strength g (see the following section and figure 2). We found the same phenomenon with different initial states in numerical simulations as long as the particles are mainly delocalized along the lattice and occupy only the lower band, i.e. excluding Fock states with all particles on one lattice site for instance.

The oscillatory behaviour depicted in figure 1 strongly reminds us of the collapse and revival effect known from quantum optics [19]. A specific feature in these systems is a linear dependence of the collapse and revival time on the inverse coupling strength, i.e. $t_{\text{rev}} \propto 1/g$ and $t_{\text{coll}} \propto 1/g$ where g usually denotes the coupling strength between the light field and the two-level atom in the quantum optical systems [19]. We verified numerically for our system that the observed decay and revival times obey a similar dependence with the interaction parameter g as coupling strength in our model. We define t_{coll} as the time when the difference between the maximal and average amplitude of the inter-band oscillations has fallen to $1/e$, i.e. $\mathcal{N}_b(t_{\text{coll}}) \equiv 1/2 + 1/(2e)$. The revival time is taken as the maximum of the revived oscillations. Figure 2 clearly demonstrates the linear dependence of these times on the inverse interaction strength.

To find an effective description, we try to understand the most relevant interaction processes. Clearly, the repulsive

two-body interaction disfavours double occupancy of sites since this will always cost an interaction energy $W_{a(b)}$ for two particles occupying the same site in the lower (upper) band. Starting from an initial state with population of the ground band only, the strong Stark force leads to an occupation of the upper band. Doubly occupied sites are also suppressed there, but two particles may sit at the same site in either band, i.e. ‘on top of each other’. Indeed, the most important interaction term in the time evolution is $2W_x \sum_l n_l^a n_l^b$, since it already gives a non-zero contribution when there is only one particle per site in each of the two bands. In fact, comparing the time evolution of the initial state with all interaction terms and only the one mentioned shows almost no difference (cf figure 1). We focus on fillings close to unity $\bar{n} = N/L \approx 1$ and study the time evolution of states of the form $|\psi_0\rangle = |1, 1, \dots, 1; 0, \dots, 0\rangle$, which is not an eigenstate of the system in resonance. Note that this is the most important contribution to the superfluid ground state in an expansion in our configuration state Fock basis. For large enough systems the superfluid ground state of the untilted system (and the single-occupancy state $|\psi_0\rangle$ likewise) becomes indistinguishable from a coherent state (equation (66) in [4]) that factorizes into a product of local coherent states at each site l :

$$\prod_l (e^{\sqrt{\bar{n}} a_l^\dagger} |\text{vac}\rangle_l) = \prod_l |\varphi\rangle_l \equiv |\varphi\rangle; 0. \quad (8)$$

We denote this coherent state with phase $\varphi = \sqrt{\bar{n}}$ by $|\varphi\rangle; 0$. We are now going to re-write this state in the resonant basis and determine the effect of the interaction term $2W_x \sum_l n_l^a n_l^b$ when acting on this state. We start by inserting the transformation $a_l^\dagger = (1/\sqrt{2}) \sum_n J_{l-n}(x_a) (\mu_n^\dagger - v_n^\dagger)$ into (8) to obtain

$$\begin{aligned} |\varphi\rangle; 0 &= \prod_l \exp \left[\sqrt{\frac{N}{2L}} \sum_n J_{l-n}(x_a) (\mu_n^\dagger - v_n^\dagger) \right] |\text{vac}\rangle \\ &= \prod_n e^{\sqrt{\bar{n}/2} \mu_n^\dagger} e^{-\sqrt{\bar{n}/2} v_n^\dagger} |\text{vac}\rangle, \end{aligned} \quad (9)$$

where we used $\sum_{m \in \mathbb{Z}} J_m(x) z^m = \exp[x(z - 1/z)/2]$ for $z = 1$ [20] and $[\mu_n^\dagger, v_n^\dagger] = 0$ which follows from the properties of the operators $a^{(\dagger)}, b^{(\dagger)}$. Let us denote Fock states with the single-particle basis μ_l, v_l by parentheses $|n_1^\mu, \dots, n_L^\mu; n_1^\nu, \dots, n_L^\nu\rangle$. From (9) we see that the coherent state of the lower band in resonance is a product of local coherent states for both bands in the resonance basis $\prod_l |\tilde{\varphi}\rangle; -\tilde{\varphi}\rangle_l \equiv |\tilde{\varphi}\rangle; -\tilde{\varphi}\rangle$ with $\tilde{\varphi} \equiv \varphi/\sqrt{2}$. The time evolution of this state (for the non-interacting system in resonance) is simple since it is diagonal in the eigenbasis of the Hamiltonian in resonance (7). We continue to study the phase evolution created by the most important term $2W_x \sum_l n_l^a n_l^b$ perturbatively by expressing the operators $a_l^{(\dagger)}, b_l^{(\dagger)}$ in the μ, ν -basis:

$$\begin{aligned} &\exp \left[i2g W_x t \sum_l n_l^a n_l^b \right] |\tilde{\varphi}\rangle; -\tilde{\varphi}\rangle \\ &= \exp \left[\frac{ig W_x t}{2} \sum_l \sum_{l_1, \dots, l_4} J_{l-l_1}(x_a) J_{l-l_2}(x_a) J_{l-l_3}(x_b) J_{l-l_4}(x_b) \right. \\ &\quad \left. \times (\mu_{l_1}^\dagger - v_{l_1}^\dagger) (\mu_{l_2}^\dagger - v_{l_2}^\dagger) (\mu_{l_3}^\dagger + v_{l_3}^\dagger) (\mu_{l_4}^\dagger + v_{l_4}^\dagger) \right] |\tilde{\varphi}\rangle; -\tilde{\varphi}\rangle. \end{aligned} \quad (10)$$

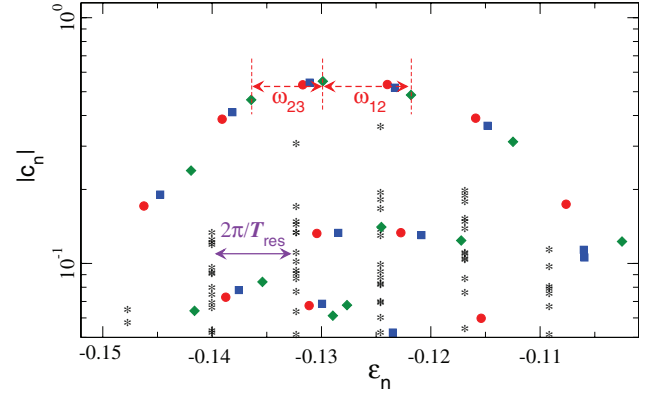


Figure 3. $|c_n|$ versus the corresponding quasi-energies ε_n in an expansion in the eigenbasis of the Floquet–Bloch operator (6). Different interaction strengths are shown: $g = 0.0$ (*), $g = 0.05$ (●), $g = 0.1$ (■), and $g = 0.2$ (◆); other parameters as in figure 1. We observe that different quasi-energies are shifted at different rates when increasing the interaction strength.

Since $|\tilde{\varphi}\rangle; -\tilde{\varphi}\rangle$ is a product of local coherent states we can ignore the sum over l and discuss the expected behaviour. First, both $x_{a,b}$ are much smaller than unity and the main contribution in the sums over l_1, \dots, l_4 will come from the zeroth-order Bessel functions J_0 . Secondly, the product of operators gives 16 different combinations of the field operators. But due to the prefactors, the combinations with equal indices are the most important. They simply give an integer number when applied to the product of local coherent states they are acting on. Taking these two points together, the time evolution of this state should show an approximate revival at

$$t_{\text{rev}} \approx \frac{4\pi}{g W_x J_0^2(x_a) J_0^2(x_b)}. \quad (11)$$

This result is valid for large systems and cannot account for the effect of non-universal properties like a limited number of particles and lattice sites, but we expect it to yield the right order of magnitude for finite systems, and in particular the correct scaling with the parameters of external potentials (cf figure 4, inset, below).

Additional finite size corrections to (11) can be understood by using the decomposition into the eigenbasis (5). The evolution of the occupation of the upper band certainly depends on the initial state, which we can take into account by studying the weights c_n of the initial state expanded in the eigenbasis. The result of a numerical diagonalization for a system in resonance is depicted in figure 3, where the absolute values of the expansion coefficients with their corresponding quasi-energies are shown. For vanishing two-body interaction strength $g = 0$, the quasi-energies from the states with different occupation numbers are degenerate as expected. The energy difference between neighbouring lines of constant quasi-energies corresponds to the time scale of the resonant inter-band oscillations and follows from the diagonalization of the resonant non-interacting system as $\Omega_{\text{res}} = 2\pi/T_{\text{res}} = 2|C_0 F J_r(\Delta x)|$. In the non-interacting system ($g = 0$), two coefficients are dominating and the difference of the quasi-energies yields a single time scale

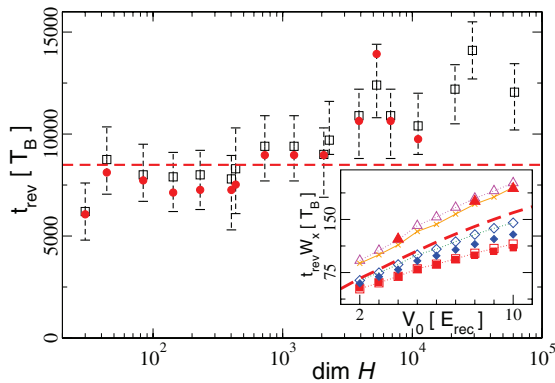


Figure 4. Comparison between estimated revival times according to (11) (---) and to (12) (●) with numerical simulations (□) for $V_0 = 8$, $r = 1$, and different system sizes, parameterized by the Hilbert space dimension of the $\kappa = 0$ subspaces. The error bars indicate the width of the revival at half maximum. *Inset:* scaling of the numerically measured revival time with the lattice depth V_0 for $r = 1$. We multiply t_{rev} by W_x since W_x also depends on V_0 to show the remaining non-trivial scaling behaviour. Shown are $N, L = 4, 4$ ($\dim \mathcal{H} = 86$, □), $N, L = 5, 5$ ($\dim \mathcal{H} = 402$, ◇), $N, L = 6, 7$ ($\dim \mathcal{H} = 3876$, △), $N, L = 7, 7$ ($\dim \mathcal{H} = 11076$, ×). Filled symbols are t_{rev} expected from (12) for the same system, and the thick dashed line again shows our universal result (11).

T_{res} . When the interaction is turned on, the weight of states with many contributions from double or higher occupancies of sites decrease significantly (since they are energetically disfavoured) and their quasi-energies are slightly shifted. But, surprisingly, only a limited number of additional coefficients c_n contributes significantly in the eigenbasis expansion even for $g \neq 0$. The observed collapse and revival signal is now determined by a few expansion coefficients that are much larger than the others. If we focus on the three largest coefficients, denoted as c_1, c_2, c_3 and sorted by their quasi-energies $\varepsilon_1, \varepsilon_2, \varepsilon_3$, we find that the latter are shifted by the interaction by different amounts. The differences between neighbouring quasi-energies, $\omega_{12} = |\varepsilon_2 - \varepsilon_1|$ and $\omega_{23} = |\varepsilon_3 - \varepsilon_2|$ (shown for the example $g = 0.2$ in figure 3), lead to a beating between two oscillations with periods $T_{12}, T_{23} \approx T_{\text{res}}$ and the revival time will thus be given by

$$t_{\text{rev}} \approx \frac{2\pi}{\omega_{23} - \omega_{12}} = \frac{T_{12}T_{23}}{T_{23} - T_{12}}. \quad (12)$$

This estimate requires a numerical diagonalization but gives a clear physical interpretation to the revival time observed in a specific realization with N atoms on L lattice sites. Thus, taking (11) and (12) together, we have an understanding of the general physical mechanism triggering the collapse and revival of the resonant two-band oscillations.

We compare our prediction for the revival time, (11) and (12), to actual numerical simulations shown in figure 4. We find that (11) gives the right order of magnitude for the revival in a specific realization, and, in particular, it shows the correct scaling behaviour with the depth of the optical lattice (shown in the inset of figure 4). Additionally, figure 4 shows that the corrections for specific sizes of the system are well accounted for by (12), which only slightly underestimate the revival times by a few per cent. This deviation could be corrected

by including more than three participating states, extending in this manner the arguments which lead to (12).

In an experimental realization, the shorter the collapse time t_{coll} , the easier it could be observed, and for an estimate we make use of the fact [19, 21] that the collapse time is proportional to the revival time

$$t_{\text{coll}} = \frac{1}{\pi(\Delta n)^2} t_{\text{rev}}, \quad (13)$$

where Δn denotes the width of the distribution of coefficients c_n necessary to expand the initial state in the eigenbasis. For the specific example of $V_0 = 5, g = 0.1, r = 1$ and $N = 5 = L$, we find $\Delta n \approx \mathcal{O}(1)$ for the width of the distribution (i.e. the $g \neq 0$ couplings include just one or very few additional states as in the derivation of (12) above), such that we estimate $t_{\text{rev}}/t_{\text{coll}} \approx 3$ compared to $t_{\text{rev}}/t_{\text{coll}} \approx 5.7 \pm 0.1$ found numerically.

In this work, we focused on realizations with ultra-cold atoms in a tilted periodic potential, and the observed effect can be manipulated by engineering the potential [1, 11] or the two-body interaction [4]. Specifically, the revival time (11) depends sensitively on parameters as the hopping strength and the external force close to the zeros of the Bessel function in (11). This is analogous to already realized manipulations by time-dependent forces as predicted by [22] and realized in [23]. The observation of Bloch oscillations over thousands of periods and a fine control on the two-body interaction have already been demonstrated experimentally [3]. Therefore, the collapse and revival of resonant inter-band oscillations predicted here should be accessible in such state-of-the-art experiments. We finally remark that the collapse and revival phenomena discussed in this section have their origin (see figure 1) in the degradation (due to interactions) of single particle *inter-band* oscillations. So, even if there are analogies to the collapses and revivals observed in other experiments [2, 6, 24], the collapse-revival oscillations reported there arise from the interaction within a single band. Therefore, in contrast to our results, those oscillations would not at all occur when the lower band interaction is suppressed, equivalent to $W_a = 0$ in the model discussed here.

4. Summary

We studied the coupling between two energy bands in a two-band Bose–Hubbard model with an additional tilting force. The force can lead to a strong coupling of the bands and we found strong resonances in the inter-band oscillations in this lattice model. Furthermore, the two-particle interaction leads to a collapse and revival of the resonant inter-band oscillations. Here, we made predictions for the relevant time scales which were verified numerically.

A closed two-band system is an idealization, but it can approximately be realized in various parameter regimes with ultra-cold atoms [4] using different techniques such as, e.g., superlattices [11]. In addition, the use of Feshbach resonances allows a complete control and fine tuning of the interaction strength [3] needed to test our predictions. Our work is an important first step in going beyond ground-band physics and accessing more degrees of freedom in bosonic ultra-cold gases.

Acknowledgments

This work was supported within the framework of the Excellence Initiative by the German Research Foundation (DFG) through the Heidelberg Graduate School of Fundamental Physics (grant number GSC 129/1), the Frontier Innovation Fonds and the Global Networks Mobility Fund. PP is grateful to Andrea Tomadin and acknowledges support from the Klaus Tschira Foundation.

References

- [1] Gustavsson M *et al* 2008 Interference of interacting matter waves arXiv:0812.4836
- [2] Will S *et al* 2009 Multi-orbital quantum phase diffusion arXiv:0911.5066
- [3] Gustavsson M *et al* 2008 *Phys. Rev. Lett.* **100** 080404
- [4] Bloch I, Dalibard J and Zwierger W 2008 *Rev. Mod. Phys.* **80** 885
- [5] Bloch I 2008 *Nature* **453** 1016
- [6] Greiner M, Mandel O, Hänsch T W and Bloch I 2002 *Nature* **6902** 51
- [7] Giovannetti V *et al* 2004 *Science* **306** 1330
Esteve J *et al* 2008 *Nature* **455** 1216–9
- [8] Morsch O and Oberthaler M 2006 *Rev. Mod. Phys.* **78** 179
Zenesini A *et al* 2008 *New J. Phys.* **10** 053038
- [9] Morsch O *et al* 2001 *Phys. Rev. Lett.* **87** 140402
- [10] Tomadin A, Mannella R and Wimberger S 2007 *Phys. Rev. Lett.* **98** 130402
- [11] Salger T *et al* 2007 *Phys. Rev. Lett.* **99** 190405
Salger T *et al* 2009 *Science* **326** 1241
- [12] Breid B M, Witthaut D and Korsch H J 2006 *New J. Phys.* **8** 110
- [13] Tomadin A, Mannella R and Wimberger S 2008 *Phys. Rev. A* **77** 013606
- [14] Tomadin A 2006 Quantum chaos with ultracold atoms in optical lattices *Master Thesis* Università di Pisa
- [15] Fukuyama H, Bari R A and Fogedby H C 1973 *Phys. Rev. B* **8** 5579–5586
- [16] Kolovsky A R and Buchleitner A 2003 *Phys. Rev. E* **68** 056213
- [17] Press W *et al* 1992 *Numerical Recipes in C* (Cambridge: Cambridge University Press)
- [18] Nakamura Y, Pashkin Y A and Tsai J S 2001 *Phys. Rev. Lett.* **87** 246601
- [19] Meystre P and Sargent M 1991 *Elements of Quantum Optics* (Berlin: Springer)
- [20] Abramowitz M and Stegun I A 1968 *Handbook of Mathematical Functions* (New York: Dover)
- [21] Buchleitner A, Delande D and Zakrzewski J 2002 *Phys. Rep.* **368** 409–547
- [22] Eckardt A, Weiss C and Holthaus M 2005 *Phys. Rev. Lett.* **95** 260404
- [23] Zenesini A *et al* 2009 *Phys. Rev. Lett.* **102** 100403
- [24] Anderlini M *et al* 2006 *J. Phys. B: At. Mol. Opt. Phys.* **39** S199
Sebby-Strabley J *et al* 2007 *Phys. Rev. Lett.* **98** 200405

Time-resolved measurement of Landau-Zener tunneling in different bases

G. Tayebirad,^{1,*} A. Zenesini,² D. Ciampini,^{3,4} R. Mannella,³ O. Morsch,⁴ E. Arimondo,^{3,4} N. Lörch,¹ and S. Wimberger¹

¹*Institut für Theoretische Physik, Universität Heidelberg, Philosophenweg 19, D-69120 Heidelberg, Germany*

²*Institut für Experimentalphysik, University of Innsbruck, Technikerstrasse 25, A-6020 Innsbruck, Austria*

³*Consorzio Nazionale Italiano di Struttura della Materia (CNISM)-Pisa, Dipartimento di Fisica, Università di Pisa, Lgo Pontecorvo 3, I-56127 Pisa, Italy*

⁴*Istituto Nazionale di Ottica (INO)-CNR, Dipartimento di Fisica, Università di Pisa, Lgo Pontecorvo 3, I-56127 Pisa, Italy*

(Received 1 June 2010; published 26 July 2010)

A comprehensive study of the tunneling dynamics of a Bose-Einstein condensate in a tilted periodic potential is presented. We report numerical and experimental results on time-resolved measurements of the Landau-Zener tunneling of ultracold atoms introduced by the tilt, which experimentally is realized by accelerating the lattice. The use of different protocols enables us to access the tunneling probability, numerically as well as experimentally, in two different bases, namely, the adiabatic basis and the diabatic basis. The adiabatic basis corresponds to the eigenstates of the lattice, and the diabatic one to the free-particle momentum eigenstates. Our numerical and experimental results are compared with existing two-state Landau-Zener models.

DOI: [10.1103/PhysRevA.82.013633](https://doi.org/10.1103/PhysRevA.82.013633)

PACS number(s): 67.85.Jk, 03.65.-w, 03.75.Lm, 03.75.Kk

I. INTRODUCTION

Quantum transport is an essential topic in solid-state physics and electronic applications. Bloch oscillations, Landau-Zener (LZ) tunneling, and Wannier-Stark ladders [1–9] are fundamental quantum effects occurring in a system of electrons moving in a periodic potential and driven by an electric field. Due to complications such as impurities, lattice vibrations, and multiparticle interactions, clean observations of these effects have been difficult [10]. In recent years, ultracold atoms and Bose-Einstein condensates in optical lattices have been increasingly used to simulate solid-state systems and the above-mentioned phenomena [6–8,11–16].

Optical lattices are easy to realize in the laboratory, and their parameters can be perfectly controlled both statically and dynamically, which makes them attractive as model systems for crystal lattices. The LZ model for transitions [1,2] between two energy states at an avoided level crossing is one of the few exactly solvable examples of time-dependent quantum mechanics. LZ transitions have been investigated for Rydberg atoms [17], molecular nanomagnets [18,19], field-driven superlattices [20], current-driven Josephson junctions [21], Cooper-pair box qubits [22], and using light waves in coupled waveguides [23–25]. While the asymptotic tunneling probability can be calculated accurately [26] and has an intuitive interpretation as a statistical mean value of experimental outcomes, the concept of tunneling time and its computation are still the subject of debate even for simple systems [21,27–31]. The tunneling time is the time required for a state to evolve into an orthogonal state.

In this paper, we present numerical as well as experimental results on the Wannier-Stark system. This system is realized with ultracold atoms, forming a Bose-Einstein condensate, in an optical lattice subjected to a static tilting force [8]. The tilt is experimentally implemented by accelerating the optical lattice [6,7,13,15,32–36]. We explore the LZ tunneling between the Bloch bands of a Bose-Einstein condensate in

such an accelerated lattice. The lattice depth controls the tunneling barrier, while its acceleration controls the time dependence of the Hamiltonian. At large accelerations, LZ tunneling leads to significant interband transitions for the condensate [15,26]. This tunneling process is detected by measuring the atomic momentum distributions.

Following our previous work, in which we presented time-resolved observations of LZ tunneling [36], in the present article we report more detailed investigations. We measure the time dependence of the tunneling probability by performing a projective quantum measurement on the eigenstates in a given basis of the Hamiltonian describing the Bose-Einstein condensate within the optical lattice. Our measurements resolve the steplike time dependence of the occupation probability. Using different numerical as well as experimental protocols, we are able to perform our calculations and experiments both in the adiabatic basis of the lattice eigenstates and in the diabatic basis of the free-particle momentum eigenstates. We present theoretical and experimental results which clearly show that the time dependence of the transition probability exhibits a steplike structure with a finite transition time and oscillations with a finite damping time, all of them depending on the choice of the measurement basis.

The paper is organized as follows. Section II collects the necessary theoretical background to describe the probability and transition time for the LZ transition tunneling. The limits one faces in applying this theory to the Wannier-Stark problem, and the essential theoretical and numerical tools to describe our time-resolved measurements are reported in Sec. III. Section IV presents numerical and experimental data. We discuss and summarize our results in Sec. V.

II. SURVIVAL PROBABILITY AND TRANSITION TIME

A. LZ theory in a nutshell

Quantum-mechanical systems having two discrete energy levels are omnipresent in nature. For crossing levels, there is a possibility of a transition if the degeneracy is lifted by a coupling and the system is forced across the resulting

*g.tayebirad@thphys.uni-heidelberg.de

avoided crossing by varying the parameter that determines the level separation. This phenomenon is known as LZ tunneling. LZ theory, developed in the early 1930s in the context of atomic scattering processes and spin dynamics in time-dependent fields [1–4], demonstrated that transitions are possible between two approaching levels as a control parameter is swept across the point of minimum energy separation. The phase accumulated between the incoming and outgoing passages varies with, e.g., the collision energy, giving rise to Stückelberg oscillations in the populations [3].

In its basic form, the LZ problem can be described by a simple two-state model and allows for a simple expression for the transition probability. The LZ Hamiltonian for a single crossing taking place at time $t = 0$ can be written as the following 2 by 2 matrix:

$$H_{\text{LZ}} = \begin{pmatrix} \alpha t & \Delta E/2 \\ \Delta E/2 & -\alpha t \end{pmatrix}. \quad (1)$$

The off-diagonal term, $\Delta E/2$, is the coupling between the two states, and α is the rate of change of the energy levels in time. The dynamics of the system can be measured in different bases: *diabatic* and *adiabatic*. The diabatic basis is the eigenbasis of the bare states of Eq. (1) when there is no off-diagonal coupling. The adiabatic basis, on the other hand, is the basis of a system with a finite $\Delta E/2$ coupling between the two states. The Hamiltonian has two adiabatic energy levels $E_{\pm} = \pm \frac{1}{2} \sqrt{(2\alpha t)^2 + \Delta E^2}$.

Assuming that the system is initially, at $t \rightarrow -\infty$, in the ground energy level E_- and if the sweeping rate is small enough, it will be exponentially likely that the system remains in its adiabatic ground state E_- at $t \rightarrow +\infty$. The limiting value of the adiabatic LZ survival probabilities (for t going from $-\infty$ to $+\infty$) is [26]

$$P_a(\infty) = 1 - \exp\left(-\frac{\pi}{\gamma}\right), \quad (2)$$

where we introduce a dimensionless parameter, the so-called adiabaticity parameter $\gamma = 4\hbar\alpha/\Delta E^2$. This survival probability is valid for both E_- and E_+ initial states, and the same equation is valid for the diabatic case. A small adiabaticity parameter corresponds to a small velocity of the state displacement along the energy scale compared to ΔE^2 , such that the system follows the adiabatic trajectory of Fig. 1.

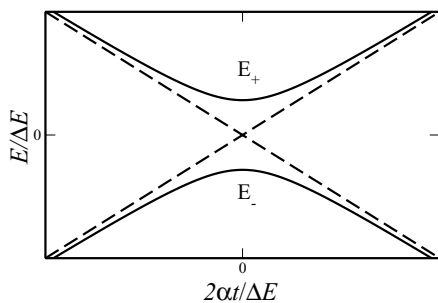


FIG. 1. Energy levels as a function of time. The dashed lines show the so-called diabatic levels, i.e., the energies of states in the absence of the interaction. The solid lines demonstrate the so-called adiabatic levels, i.e., the eigenstates of the system corresponding to the instantaneous Hamiltonian.

Thus, there is a large coupling between the diabatic states; and at the avoided crossing at $t = 0$, an almost complete transition from the initial diabatic state to the final diabatic state takes place. On the other hand, for a large value of the adiabaticity parameter γ , the coupling between the two states is small, and consequently the system remains in its initial state following the diabatic trajectories of Fig. 1.

B. Jump times

A careful study of the transition from an initial state to a final state can reveal the time required to complete the transition. Moreover, in the case of multiple level crossings, as in our experimental realization of Ref. [36], it is necessary to know whether a transition has been completed before the next avoided crossing. The LZ approach may be applied when a transition between two coupled quantum states takes place in a small time interval around the avoided crossing and successive crossings are independent from each other.

Analytical estimates for the LZ transition times have been derived in Refs. [29,30] using the two-state model of Eq. (1). In a given basis, e.g., adiabatic or diabatic, different transition times are obtained. Vitanov [29] calculated the time-dependent diabatic and adiabatic survival probability at finite times. The LZ transition times were derived in [30] using some exact and approximate results for the transition probability. Figure 2 shows a typical time dependence of the adiabatic survival probability, similar to that predicted in [29], that we measured for Bose-Einstein condensates in optical lattices for

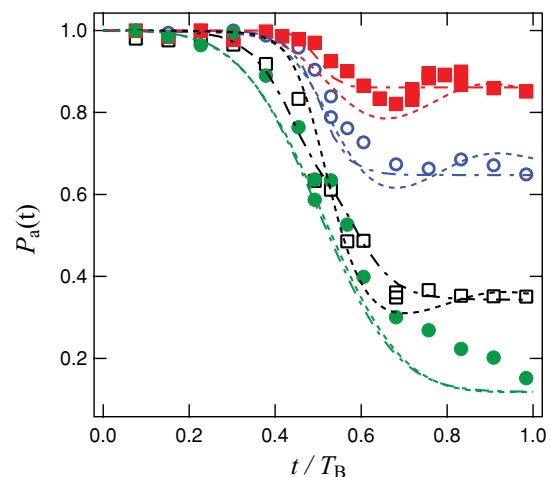


FIG. 2. (Color online) Time-resolved measurements of the adiabatic survival probability for the Bose-Einstein condensate tunneling in an optical lattice at fixed dimensionless force $F_0 = 1.197$ and different lattice depths: $V/E_{\text{rec}} = 2.3$ (filled squares), 1.8 (open circles), 1 (open squares) and 0.6 (filled circles); all parameters are introduced in detail in Sec. III A. For the Bose-Einstein condensate evolution the crossing time is $t = T_{\text{Bloch}}/2$, where the step of the survival probability is one-half of the final value. The dashed and dot-dashed lines are the results of numerical simulations using the cutoff and adiabatic method, respectively (see Sec. III C). The lattice depth for the numerical simulations was corrected by up to $\pm 15\%$ with respect to the experimentally measured values to give the best possible agreement.

experimental parameters to be discussed in Sec. IV. Notice that in the Bose-Einstein condensate case, the crossing occurs at the time $t = T_B/2$ defined below. The $t \rightarrow \infty$ asymptotic value is given by Eq. (2).

The LZ jump time in a given basis can be defined as the time after which the transition probability reaches its asymptotic value. From this definition, one can expect to observe a steplike structure, with a finite width, in the time-resolved tunneling probability, as in Fig. 2. Because the step is not very sharp, it is not straightforward to define the initial and final times for the transition. It is even less obvious how to define the jump time for both small and large couplings. Some possible choices have been used by Lim and Berry [28] and Vitanov [29,30]. The problem is even more complicated when the survival probability shows an oscillatory behavior on top of the step structure as seen in Fig. 2, which shows experimental and numerical results for a single LZ transition measured in the adiabatic basis (the numerical and experimental methods will be described in detail later in this paper). The oscillations give rise to other time scales in the system, namely, an oscillation time and a damping time of the oscillations appearing in the transition probability after the crossing. Therefore, a measurement of the tunneling time depends very much on how these times are defined and also which basis is considered.

In [29], the jump time in the diabatic and adiabatic bases is defined as

$$\tau_x^{\text{jump}} = \frac{P_x(\infty)}{P'_x(0)}. \quad (3)$$

where $x = d$ or a , and P_d (P_a) is the transition probability between the two diabatic (adiabatic) states. $P'_x(0)$ denotes the time derivative of the tunneling probability evaluated at the crossing point. The diabatic jump time $\tau_d^{\text{jump}} \approx \sqrt{2\pi\hbar/\alpha}$ is almost constant for large values of the adiabaticity parameter γ [29]. Instead, for $\gamma \ll 1$ it decreases with increasing γ , $\tau_d^{\text{jump}} \approx 2\sqrt{\hbar(\gamma\alpha)^{-1}}$ [29]. In the adiabatic basis, when γ is large, the transition probability resembles the one of the diabatic basis with an equal jump time. For a small adiabaticity parameter, because of the oscillations appearing on top of the transition probability step structure, it is not straightforward to define the initial and final times for the transition. Vitanov [29] defines the initial jump time as the time $t < 0$ at which the transition probability is very small; i.e., $P_a(\tau) = \varepsilon P_a(\infty)$, where ε is a proper small number. The final time of the transition $t > 0$ is defined as the time at which the nonoscillatory part of $P_a(\tau)$ is equal to $(1 + \varepsilon)P_a(\infty)$. Using these definitions, Vitanov derived that the transition time in the adiabatic basis depends exponentially on the adiabaticity parameter, $\tau_a^{\text{jump}} \approx (4/\varepsilon)^{1/6} \gamma^{-1/3} \exp[\pi/(6\gamma)] \sqrt{\hbar/\alpha}$, [29].

In principle, the experimental and numerical methods presented in the following could be used for a quantitative study of the tunneling time (or jump time) as a function of the parameters of the system. For the purposes of the present paper, however, we concentrate on a careful analysis of the possibilities and limitations of our methods, and in particular on measurements of LZ tunneling in different bases.

III. LZ IN AN OPTICAL LATTICE POTENTIAL

A. Wannier-Stark problem and LZ limit

We generalize the two-level LZ theory to study the temporal evolution of ultracold atoms loaded into a spatially periodic potential subjected to an additional static force in the presence of negligible atom-atom interactions, as in the experimental conditions [36]. The dynamics of ultracold atoms in a tilted optical lattice can be described by the well-known Wannier-Stark Hamiltonian [9]

$$\tilde{H} = -\frac{\hbar^2}{2M} \frac{d^2}{dx^2} + \frac{V}{2} \cos(2k_L x) + F_{LZ} x, \quad (4)$$

where M is the atomic mass, V is the depth of the optical lattice with the spatial period $d_L = \lambda_L/2$ determined by the laser wavelength λ_L , $k_L = 2\pi/\lambda_L$ is the wave number of the laser light creating the periodic potential, and F_{LZ} is the Stark force. The characteristic energy scale of the system is the recoil energy, which is defined as $E_{\text{rec}} = \pi^2 \hbar^2 / 2M d_L^2$.

The atomic motion produced by the force F_{LZ} may be interpreted in the upper left energy diagram of Fig. 3, where for the case of $F_{LZ} = 0$ the atomic energies $E(q)$ for the $n = 0, 1, 2$

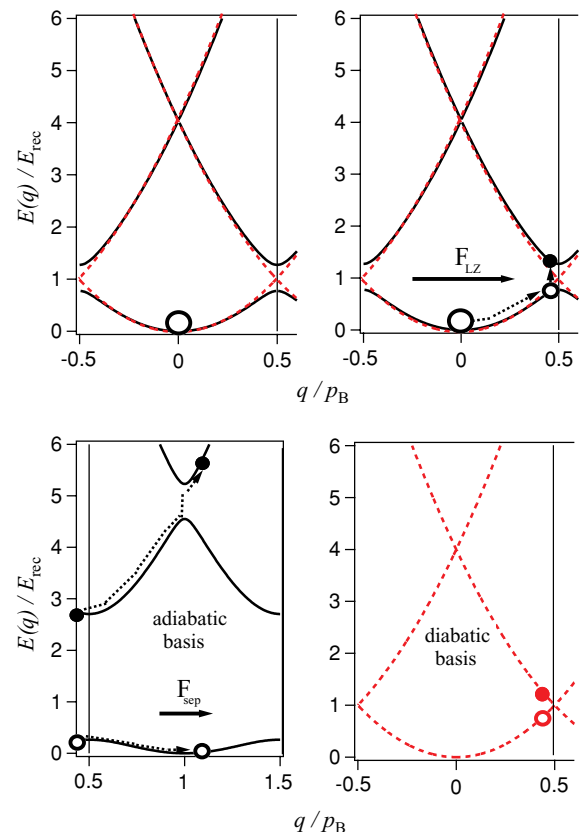


FIG. 3. (Color online) Band structure in the optical lattice potential and experimental protocols for measuring LZ dynamics in the adiabatic and diabatic bases. After the initial loading into the lattice and acceleration for a time t_{LZ} (top), measurements of the instantaneous populations in the two states are performed (bottom) as explained in the text. In the top figures, the adiabatic (solid lines) and diabatic (dashed lines) energies for an optical lattice of depth $V_0 = 1$ are shown.

lower bands are represented versus the quasimomentum q within the Brillouin zone of width $p_B = 2p_{\text{rec}} = 2\pi\hbar/d_L$ [15,32]. Under the action of a constant force F_{LZ} , the quasimomentum of a condensate initially prepared at $q = 0$ in the $n = 0$ band scans the lower band in an oscillating motion periodically with the Bloch period $T_B = 2\hbar(F_{\text{LZ}}d_L)^{-1}$. At the edge of the Brillouin zone, where a level splitting ΔE increasing with V [26] takes place, tunneling of the condensate to the $n = 1$ energy band may occur.

The Wannier-Stark Hamiltonian of Eq. (4) can be written in dimensionless units [26,37]

$$H_0 = -\frac{1}{2} \frac{\partial^2}{\partial x_0^2} + \frac{V_0}{16} \cos(x_0) + \frac{F_0 x_0}{16\pi}, \quad (5)$$

where $x_0 = 2\pi x/d_L$, and energy and time are rescaled by $H_0 = \tilde{H}/(8E_{\text{rec}})$ and $t_0 = 8tE_{\text{rec}}/\hbar$, respectively. Moreover, in dimensionless units, the lattice depth is given by $V_0 = V/E_{\text{rec}}$ and the force by $F_0 = F_{\text{LZ}}d_L/E_{\text{rec}}$. The translational symmetry of the given Hamiltonian, broken by the static force, is recovered using a gauge transformation. Substituting $\tilde{\psi}(x_0, t_0) = \exp(-iF_0 t_0 x_0/16\pi)\psi(x_0, t_0)$, the Schrödinger equation reads $i\partial\psi/\partial t_0 = H(t_0)\psi$, with $H(t_0)$ the time-dependent Hamiltonian

$$H(t_0) = \frac{1}{2} \left(\hat{p} - \frac{F_0 t_0}{16\pi} \right)^2 + \frac{V_0}{16} \cos(x_0), \quad (6)$$

and the momentum operator $\hat{p} = -i\partial/\partial x_0$. In the following, we analyze the Hamiltonian of Eq. (6) in the momentum basis. In order to decompose the Hilbert space into independent subspaces, we use the Bloch decomposition, and for that we identify the momentum eigenstates of the free particle ($V_0 = 0 = F_0$) for fixed quasimomentum q within the Brillouin zone, i.e., $p = q + n$, p and q being indices in the momentum and quasimomentum representations and $n \in \mathbb{Z}$. To calculate the time evolution of any momentum eigenstate $|p\rangle = |q + n\rangle$, we only need the Hamiltonian H_q acting on the subspace with a given quasimomentum index q , as there is no transition between states with different q , i.e.,

$$H_q = \frac{1}{2} \begin{pmatrix} \ddots & & & & 0 \\ & (\tilde{q} - 1)^2 & V_0/16 & & \\ & V_0/16 & (\tilde{q})^2 & V_0/16 & \\ & & V_0/16 & (\tilde{q} + 1)^2 & \\ 0 & & & & \ddots \end{pmatrix}, \quad (7)$$

where $\tilde{q} = q - F_0 t_0/16\pi$.

The full dynamics of the Wannier-Stark system can be locally approximated by a simple two-state model

$$h_q = \frac{1}{2} \begin{pmatrix} \tilde{q}^2 & V_0/16 \\ V_0/16 & (\tilde{q} + 1)^2 \end{pmatrix}. \quad (8)$$

h_q can be brought into the form of the Hamiltonian given by Eq. (1) by properly shifting the diagonal parts (e.g., shifting away the quadratic term in time t_0). For $q = 0$ we thus immediately obtain

$$\frac{1}{8} \begin{pmatrix} 2F_0 E_{\text{rec}} t_0 / \pi \hbar & V_0/4 \\ V_0/4 & -2F_0 E_{\text{rec}} t_0 / \pi \hbar \end{pmatrix}. \quad (9)$$

The α , ΔE , and γ introduced in the LZ model of Eq. (1) can be expressed in terms of our system parameters: $\alpha = 2F_0 E_{\text{rec}}^2 / \pi \hbar = 4E_{\text{rec}} / (\pi T_B)$, $\Delta E = V_0 E_{\text{rec}} / 2$, and $\gamma = 32F_0 / \pi V_0^2$. The LZ theory predicting the asymptotic behavior of the tunneling probability can be used as a very good approximation for our system for times far enough from the avoided crossings. However, there are some limiting cases and experimental parameters for which the simplified two-state model is not a good approximation for the Wannier-Stark system. The discrepancy is large for lattice depths larger than the energy scale E_{rec} of the system ($V_0 \gg 1$), where the gap between energy bands increases leading to quasiflat bands and localized eigenstates. Therefore, several momentum eigenstates contribute with a non-negligible amount to the lowest energy eigenstate, and one would need to take into account more components in the Hamiltonian matrix.

B. Initial conditions

Before analyzing the experiment results, we need to address an additional problem, the finite coupling duration, as in [30]: an experiment necessarily takes a finite time for the measurement, whereas the standard LZ theory assumes that the time taken for the transition runs from $-\infty$ to ∞ . The experimental finiteness of the sweep time T_B implies that for the initial state at a finite distance from the transition point, the diagonal and off-diagonal matrix elements in the system Hamiltonian are comparable. The experiment we are dealing with typically operates in the regime defined in [30] as a large time, meaning that the time intervals from the turn-on and the turn-off times to the crossing are larger than the jump time. The presence of a jump time comparable to the Bloch time may modify the temporal evolution of the survival probability for the two mechanisms discussed in the following. Because at large γ the ratio τ_d^{jump}/T_B between jump time and sweep time is given by $\pi\sqrt{F_0}/2$, large F_0 values may produce deviation from the ideal theory of [29].

At $t = -\infty$ the diabatic and adiabatic states coincide, and hence, the preparation of the system in its ground state is unambiguous. On the other hand, at a finite distance from the transition point, the diabatic and adiabatic states do not coincide. In a numerical approach any chosen initial state can be evolved given the proper Hamiltonian, but from an experimental point of view the system will be prepared in a well-defined initial state, which depends both on the parameter values and on the preparation protocol. It is not obvious that this initial state can be chosen at will: most likely, the experimental initial state will be the one corresponding to the ground state of the complete Hamiltonian, i.e., the adiabatic lower energy state, at a time equal to the time when the sweep starts. The comparison between experiments and theory performed for different initial states should clarify this issue, because the evolution for different initial states is markedly different, when observed both in the diabatic basis and in the adiabatic basis, see Figs. 4(a) and 4(b) corresponding to typical Bose-Einstein condensate experimental parameters. The results of Fig. 4 show that for experimentally accessible parameters, the two evolutions do not coincide in both the diabatic and adiabatic bases [see Figs. 4(a) and 4(b), respectively]. We have verified that the results of Fig. 4

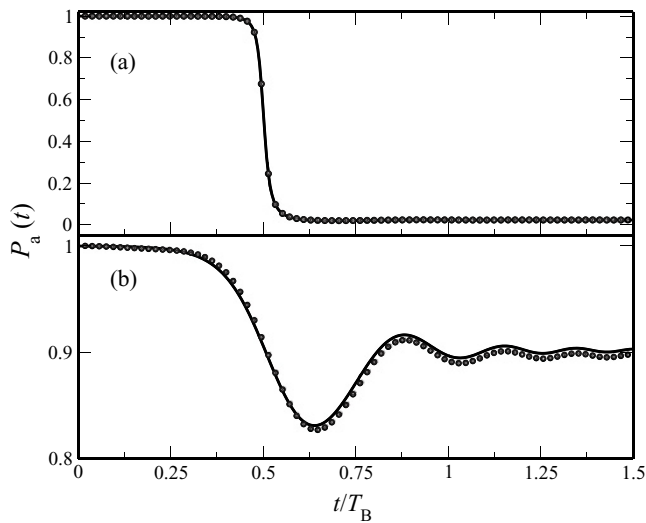


FIG. 4. Comparison between the time evolution of the Bose-Einstein condensate survival probability, in the (a) diabatic and (b) adiabatic basis, for different initial conditions, prepared at a temporal distance $\Delta t = T_B/2$ from the crossing point. The dashed line is the evolution in a possible experimental setup, i.e., the evolution following an initial preparation in the ground state of the adiabatic basis; the solid line is the evolution following an initial preparation in the ground state of the diabatic basis. Parameters are $F_0 = 1.197$ and $V_0 = 2.3$, corresponding to $\gamma = 2.3$, leading to a jump time in both adiabatic and diabatic bases 1.9 times the Bloch period T_B .

following an initial preparation in the ground state of the diabatic basis (solid lines) coincide with the finite coupling duration predictions of Ref. [30].

It is not at all obvious that an initial state chosen as the adiabatic ground state at a finite time from the transition point (which is likely to be the initial experimental state) should coincide with the state obtained evolving from $t = -\infty$, projected onto the adiabatic basis. We computed the survival probability simulating different Bose-Einstein condensate initial states, see Fig. 5. For our experimental parameter set, the discrepancy is not very large but certainly important for a precise description of the temporal evolution of the tunneling. Therefore, the approach of [29] yields some elegant theoretical results for the LZ transition, but care is needed in comparing them with the experiment due to the presence of the additional time scale connected to the finite distance between the experimental starting point and the transition point.

C. Numerical calculation

In [38] some of us have introduced an easily computable quantity to determine in a good approximation the survival probability in the adiabatic basis:

$$P_a(t) = \int_{-p_c}^{\infty} dp |\Psi(p,t)|^2, \quad (10)$$

where $\Psi(p,t)$ is the Bose-Einstein condensate wave function in momentum representation, and $p_c \geq 3p_{\text{rec}}$ is an *ad hoc* cutoff. Equation (10) can be interpreted as the projection of $\Psi(p,t)$ onto the support of the initially prepared condensate at $t = 0$ (in the presence of the optical lattice but at $F_{LZ} = 0$),

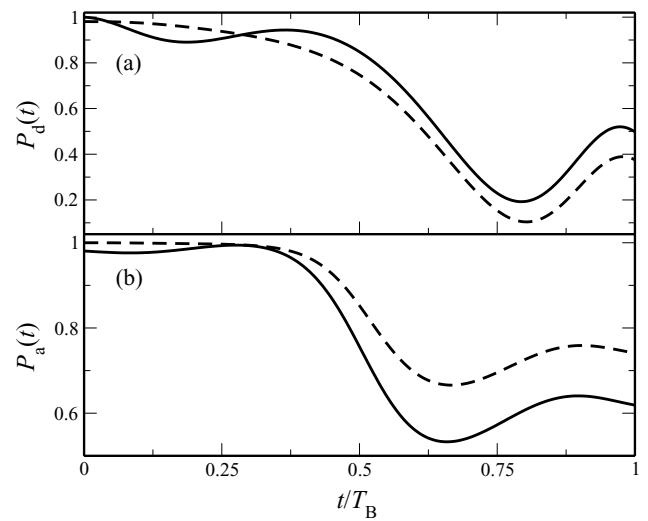


FIG. 5. Comparison between the time evolution of the Bose-Einstein condensate adiabatic survival probability, starting from initial ground states prepared at different time distances from the transition point. Survival probabilities measured for $F_0 = 1.197$ and $V_0 = 0.3$ in (a), and for $F_0 = 1.197$ and $V_0 = 3.0$ in (b). The dotted lines show the evolution obtained evolving the survival probability from the ground state in the adiabatic basis at $t = -\infty$; the solid lines illustrate the evolution obtained evolving the survival probability from the ground state which simulates a possible experimental initial state, i.e., the ground state in an adiabatic basis, at a finite time from the transition point.

which is illustrated in Fig. 6(a). Since Eq. (10) measures the decay only after the Bose-Einstein condensate wave packet $\Psi(p,t)$ has extended beyond $-p_c$ [$= -3p_{\text{rec}}$ in Fig. 6(a)], we

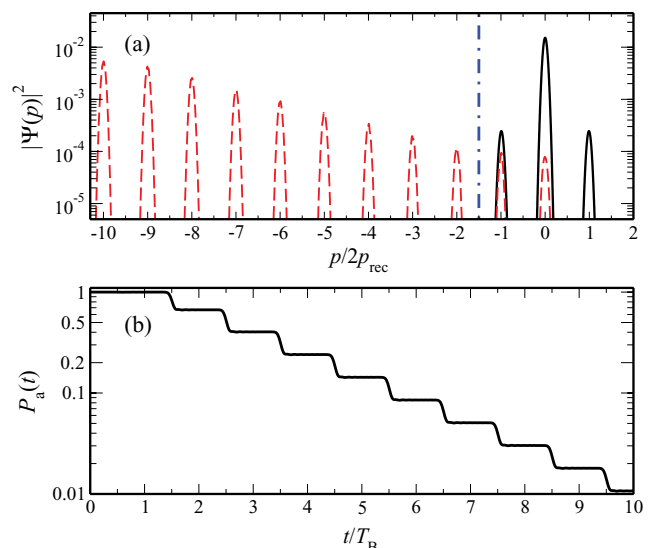


FIG. 6. (Color online) (a) Momentum distribution at time $t = 10T_B$ (dashed lines) starting from the initial momentum distribution (solid lines) under the action of a force directed toward negative p values. The vertical dash-dotted line shows the cutoff value $p_c = 3p_{\text{rec}}$ in the definition of Eq. (10). (b) Temporal evolution of the survival probability in the adiabatic basis using the mentioned definition. Simulation parameters: $V_0 = 2.07$, $F_0 = 1.197$.

must resort to the acceleration theorem [6,26] to identify time t with $t - T_B$, i.e., we must rescale time by the traversal time of the Brillouin zone T_B .

While many previous experimental results proved in very good agreement with simulations based on Eq. (10), see [34–36], a better numerical method is needed for the new generation of experiments reported here. The dash-dotted lines in Fig. 2 were produced using $P_a(t)$ of Eq. (10). These simulations well reproduce the height of the steps in agreement with the LZ prediction given in Eq. (2). They do not, however, reproduce the oscillations of the experimentally measured survival probability, due to the artificial cutoff used for evaluating $P_a(t)$. While the sequence of steps—corresponding to a sequence of LZ tunneling events—is observable in Fig. 6(b), no oscillations are visible. To reproduce the oscillatory behavior of the experimental data in Fig. 2, instead of Eq. (10) we determine $P_a(t)$ in the following way: $|\phi(n, q)\rangle$ shall denote the band solution for the ground band $n = 0$ as shown in the lower left panel of Fig. 3. Then the adiabatic survival probability is just the projection of the condensate wave function $\Psi(p, t)$ onto $\phi(n = 0, q)$ integrated over the full Brillouin zone, i.e.,

$$P_a(t) = \int_{-p_{\text{rec}}}^{p_{\text{rec}}} dq |\langle \Psi(p = q, t) | \phi(0, q) \rangle|^2. \quad (11)$$

The survival probabilities $P_a(t)$ shown in Figs. 4 and 5 have been calculated in this way.

On the other hand, following the procedure sketched in the lower right panel of Fig. 3, the survival probability determined in the diabatic basis of free-momentum eigenstates is given by

$$P_d(t) = \int_{-p_{\text{rec}}}^{p_{\text{rec}}} dq |\langle \Psi(p = q, t) | p = q \rangle|^2, \quad (12)$$

with $p = q$ within the first Brillouin zone in the notation of Sec. II A. Equation (12) is used to simulate the experimental results of Figs. 7(a) and 7(b) presented in the next section.

IV. RESULTS

In our experiments we realized the Wannier-Stark Hamiltonian of Eq. (4) with Bose-condensed rubidium atoms inside an optical lattice [13,32–36]. Initially, we created Bose-Einstein condensates of 5×10^4 ^{87}Rb atoms inside an optical dipole trap (mean trap frequency around 80 Hz). A one-dimensional optical lattice created by two counter-propagating, linearly polarized Gaussian beams was then superposed on the Bose-Einstein condensate by ramping up the power in the lattice beams in 100 ms. The wavelength of the lattice beams was $\lambda = 842$ nm, leading to a sinusoidal potential with lattice constant $d_L = \lambda/2 = 421$ nm. A small frequency offset $\Delta\nu(t)$ between the two beams could be introduced through the acousto-optic modulators in the setup, which allowed us to accelerate the lattice in a controlled fashion and hence, in the rest frame of the lattice, to subject the atoms to a force $F_{\text{LZ}} = M a_{\text{LZ}}$ with $a_{\text{LZ}} = d_L \frac{d\Delta\nu(t)}{dt}$.

In several previous experiments [32–35], we had already measured the LZ tunneling probability by first loading the Bose-Einstein condensate into a lattice, then accelerating the lattice for one Bloch period (i.e., across the zone edge and then to the center of the second Brillouin zone) and subsequently

measuring the number of atoms left in the fundamental band. This was done by accelerating the lattice further with a smaller value of a_{sep} and a larger lattice depth V_{sep} chosen such as to ensure that atoms in the fundamental band did not undergo LZ tunneling at subsequent crossing of the zone edge and that atoms in higher bands tunneled with almost 100% probability. In that way it was possible to separate atoms in the fundamental band in momentum space so that after a time of flight they could be easily measured.

The time-resolved measurements we are interested in for the purposes of the present paper initially followed the same procedure. Rather than accelerating the lattice for a full Bloch period, however, we had to interrupt the LZ tunneling event at some time $t \neq nT_B$ in general. The exact protocol then depended on whether we wanted to measure in the adiabatic or in the diabatic basis.

For measurements in the *adiabatic* basis, we proceeded as follows, see Fig. 3. After loading the Bose-Einstein condensate into the optical lattice, the lattice was accelerated with acceleration a_{LZ} for a time t_{LZ} . The lattice thus acquired a final velocity $v = a_{\text{LZ}} t_{\text{LZ}}$. At time $t = t_{\text{LZ}}$ the acceleration was abruptly reduced to a smaller value a_{sep} and the lattice depth was increased to V_{sep} in a time $t_{\text{ramp}} \ll T_B$. These values were chosen in such a way that at time $t = t_{\text{LZ}}$ the probability for LZ tunneling from the lowest to the first excited energy band dropped from between ≈ 0.1 and 0.9 (depending on the initial parameters chosen) to less than ≈ 0.01 , while the tunneling probability from the first excited to the second excited band remained high at about 0.95 . This meant that at $t = t_{\text{LZ}}$ the tunneling process was effectively interrupted, and for $t > t_{\text{LZ}}$ the measured survival probability $P(t) = N_0/N_{\text{tot}}$ (calculated from the number of atoms N_0 in the lowest band and the total number of atoms in the condensate N_{tot}) reflected the instantaneous value $P(t = t_{\text{LZ}})$.

The lattice was then further accelerated for a time t_{sep} such that $a_{\text{sep}} t_{\text{sep}} \approx 2mp_{\text{rec}}/M$ (where typically $m = 2$ or 3). In this way, atoms in the lowest band were accelerated to a final velocity $v \approx 2mp_{\text{rec}}/M$, while atoms that had undergone tunneling to the first excited band before $t = t_{\text{LZ}}$ underwent further tunneling to higher bands with a probability > 0.95 and were, therefore, no longer accelerated. At time t_{sep} the lattice and dipole trap beams were suddenly switched off and the expanded atomic cloud was imaged after 23 ms. In these time-of-flight images, the two velocity classes 0 and $2mp_{\text{rec}}/M$ were well separated and the atom numbers N_0 and N_{tot} could be measured directly. Since the populations were effectively “frozen” inside the energy bands of the lattice, which represent the adiabatic eigenstates of the total Hamiltonian of the system, this experiment measured the time dependence of the LZ survival probability P_a in the *adiabatic* basis, see Eq. (11) above.

The results of our measurements in the adiabatic basis are summarized in Fig. 2. The steplike behavior of the survival probability around $t = 0.5T_B$ is clearly visible, as well as the finite width of the step, which demonstrates that our experimental protocol does, indeed, allow us to access the dynamics of the LZ transition and the jump time associated with that transition. Also shown in the figure are the results of numerical simulations using the cutoff and the adiabatic survival methods described above in Sec. III C. As expected, both methods reproduce the step with a finite width and

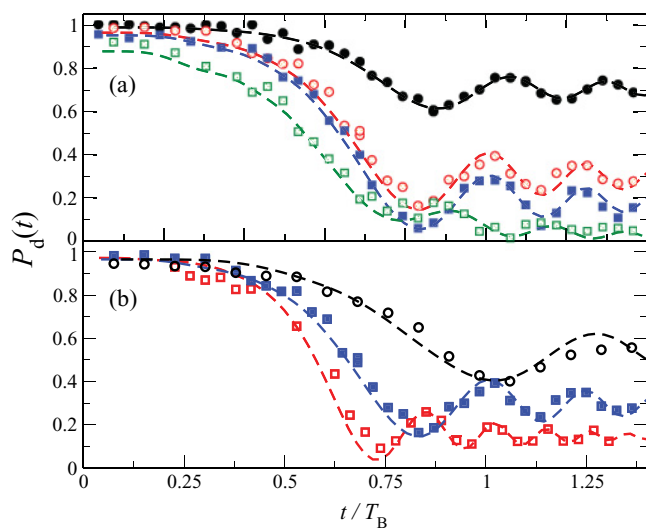


FIG. 7. (Color online) Time-resolved measurements of LZ tunneling in the diabatic basis. (a) Fixed force $F_0 = 1.197$ with different lattice depths $V_0 = 1$ (filled circles), 1.8 (open circles), 2.3 (filled squares), and 4 (open squares). (b) Fixed lattice depth $V_0 = 1.8$ with different forces: $F_0 = 2.394$ (open circles), 1.197 (filled squares), and 0.599 (open squares). The dashed lines are the results of numerical simulations based on Eq. (12), which nicely reproduce the experimental data.

the steady-state value of the survival probability for long times. The slight oscillations of the survival probability for $t > 0.5T_B$, however, are only visible in the results computed according to Eq. (11) above. In fact, the amplitude of these oscillations is larger in the numerical simulations than in our experimental data. This might indicate that our protocol for freezing the instantaneous populations in the ground and excited bands is not perfect. Indeed, we found that a delicate balance between the accelerations and lattice depths for the separation phase was necessary in order to ensure that the populations after the separation phase faithfully reproduced those at $t = t_{LZ}$, which was tested by choosing two extreme values for a_{LZ} which gave theoretical survival probabilities of approximately 0 and 1, respectively, and then verifying that these values were measured in the experiment. In practice, the parameters for the separation phase were optimized in this way for one set of the LZ parameters and then kept constant as V was varied in Fig. 2.

For measurements in the *diabatic* basis, the experimental protocol was even simpler, see Fig. 3. As in the adiabatic case, after the initial loading phase the lattice was accelerated

with acceleration a_{LZ} for a time t_{LZ} . At that point the atomic sample was projected onto the free-particle diabatic basis by instantaneously (within less than $1 \mu\text{s}$) switching off the optical lattice. After a time of flight, the number of atoms in the $v = 0$ and $v = 2p_{\text{rec}}/M$ momentum classes are measured and from these the survival probability (corresponding to the atoms remaining in the $v = 0$ velocity class relative to the total atom number) is calculated. Figure 7 shows the results of such measurements, together with numerical simulations based on Eq. (12). As in the adiabatic case, a step of the survival probability around $t = 0.5 T_B$ is clearly seen, as well as strong oscillations for $t > 0.5 T_B$. These oscillations are much stronger and visible for a wider range of parameters in the diabatic basis than in the adiabatic basis (see the results for $V_0 = 2.3$ in Fig. 2, which is confirmed by our numerical simulations).

V. CONCLUSIONS

Ultracold atoms in optical lattices provide an ideal model system for time-resolved studies of LZ tunneling. The complete control over the parameters of the lattice makes it possible to measure the tunneling dynamics in the adiabatic and diabatic bases by using different measurement methods. Our results confirm the existence of a finite temporal width for the transition in both bases and of strong oscillations of the survival probability in the diabatic basis. Both of these features are backed up by numerical simulations taking into account details of the experimental protocol.

Our findings pave the way toward more quantitative studies of the tunneling time for LZ transitions, which are of current interest in the context of optimal quantum control and the quantum speed limit [39]. Also, it should be possible to measure the tunneling dynamics in arbitrary bases by inducing a rotation of the 2×2 LZ matrix through variations in the lattice depth during the transition. With an appropriate choice of this variation, one could then, for instance, realize the superadiabatic basis proposed by Berry [28].

ACKNOWLEDGMENTS

We gratefully acknowledge funding by the EU project NAMEQUAM, the CNISM Progetto Innesco 2007, and the Excellence Initiative by the German Research Foundation (DFG) through the Heidelberg Graduate School of Fundamental Physics (Grant No. GSC 129/1) and the Global Networks Mobility Measures. G. Tayebirad thanks the Landesgraduiertenförderung Baden-Württemberg for support.

[1] L. D. Landau, *Phys. Z. Sowjet.* **2**, 46 (1932).
 [2] C. Zener, *Proc. R. Soc. A* **137**, 696 (1932).
 [3] E. C. G. Stückelberg, *Helv. Phys. Acta* **5**, 369 (1932).
 [4] E. Majorana, *Nuovo Cimento* **9**, 43 (1932).
 [5] K. Leo *et al.*, *Solid State Commun.* **84**, 943 (1992).
 [6] E. Peik, M. Ben Dahan, I. Bouchoule, Y. Castin, and C. Salomon, *Phys. Rev. A* **55**, 2989 (1997); M. Ben Dahan, E. Peik, J. Reichel, Y. Castin, and C. Salomon, *Phys. Rev. Lett.* **76**, 4508 (1996).

[7] S. R. Wilkinson, C. F. Bharucha, K. W. Madison, Q. Niu, and M. G. Raizen, *Phys. Rev. Lett.* **76**, 4512 (1996); S. R. Wilkinson *et al.*, *Nature (London)* **387**, 575 (1997).
 [8] B. P. Anderson and M. A. Kasevich, *Science* **282**, 1686 (1998).
 [9] M. Glück, A. R. Kolovsky, and H. J. Korsch, *Phys. Rep.* **366**, 103 (2002).
 [10] K. Leo, *High-Field Transport in Semiconductor Superlattices* (Springer, Berlin/Heidelberg, 2003), Vol. 187.

G. TAYEBIRAD *et al.*PHYSICAL REVIEW A **82**, 013633 (2010)

- [11] Q. Niu and M. G. Raizen, *Phys. Rev. Lett.* **80**, 3491 (1998).
- [12] G. Grynberg and C. Robilliard, *Phys. Rep.* **355**, 335 (2001).
- [13] O. Morsch, J. H. Muller, M. Cristiani, D. Ciampini, and E. Arimondo, *Phys. Rev. Lett.* **87**, 140402 (2001).
- [14] G. Roati, E. de Mirandes, F. Ferlaino, H. Ott, G. Modugno, and M. Inguscio, *Phys. Rev. Lett.* **92**, 230402 (2004).
- [15] O. Morsch and M. Oberthaler, *Rev. Mod. Phys.* **78**, 179 (2006).
- [16] I. Bloch, J. Dalibard, and W. Zwerger, *Rev. Mod. Phys.* **80**, 885 (2008).
- [17] J. R. Rubbmark, M. M. Kash, M. G. Littman, and D. Kleppner, *Phys. Rev. A* **23**, 3107 (1981).
- [18] W. Wernsdorfer and R. Sessoli, *Science* **284**, 133 (1999); *Europhys. Lett.* **50**, 552 (2000).
- [19] P. Foldi, M. G. Benedict, J. M. Pereira, and F. M. Peeters, *Phys. Rev. B* **75**, 104430 (2007).
- [20] A. Sibille, J. F. Palmier, and F. Laruelle, *Phys. Rev. Lett.* **80**, 4506 (1998).
- [21] K. Mullen, E. Ben-Jacob, and Z. Schuss, *Phys. Rev. Lett.* **60**, 1097 (1988).
- [22] W. D. Oliver, Y. Yu, J. C. Lee, K. K. Berggren, L. S. Levitov, and T. P. Orlando, *Science* **310**, 1653 (2005); M. Sillanpaa, T. Lehtinen, A. Paila, Y. Makhlin, and P. Hakonen, *Phys. Rev. Lett.* **96**, 187002 (2006).
- [23] R. Khomeriki and S. Ruffo, *Phys. Rev. Lett.* **94**, 113904 (2005).
- [24] S. Longhi, *J. Opt. B* **7**, L9 (2005).
- [25] F. Dreisow, A. Szameit, M. Heinrich, S. Nolte, A. Tunnermann, M. Ornigotti, and S. Longhi, *Phys. Rev. A* **79**, 055802 (2009).
- [26] M. Holthaus, *J. Opt. B: Quantum Semiclass. Opt.* **2**, 589 (2000).
- [27] K. Mullen, E. Ben-Jacob, Y. Gefen, and Z. Schuss, *Phys. Rev. Lett.* **62**, 2543 (1989).
- [28] M. V. Berry, *Proc. R. Soc. A* **429**, 61 (1990); R. Lim and M. V. Berry, *J. Phys. A* **24**, 3255 (1991).
- [29] N. V. Vitanov, *Phys. Rev. A* **59**, 988 (1999).
- [30] N. V. Vitanov and B. M. Garraway, *Phys. Rev. A* **53**, 4288 (1996); **54**, 5458(E) (1996).
- [31] L. S. Schulman, *Lect. Notes Phys.* **734**, 107 (2007).
- [32] M. Cristiani, O. Morsch, J. H. Muller, D. Ciampini, and E. Arimondo, *Phys. Rev. A* **65**, 063612 (2002).
- [33] M. Jona-Lasinio, O. Morsch, M. Cristiani, N. Malossi, J. H. Muller, E. Courtade, M. Anderlini, and E. Arimondo, *Phys. Rev. Lett.* **91**, 230406 (2003).
- [34] C. Sias, A. Zenesini, H. Lignier, S. Wimberger, D. Ciampini, O. Morsch, and E. Arimondo, *Phys. Rev. Lett.* **98**, 120403 (2007).
- [35] A. Zenesini *et al.*, *New J. Phys.* **10**, 053038 (2008).
- [36] A. Zenesini, H. Lignier, G. Tayebirad, J. Radogostowicz, D. Ciampini, R. Mannella, S. Wimberger, O. Morsch, and E. Arimondo, *Phys. Rev. Lett.* **103**, 090403 (2009).
- [37] S. Wimberger, P. Schlagheck, and R. Mannella, *J. Phys. B* **39**, 729 (2006).
- [38] S. Wimberger, R. Mannella, O. Morsch, E. Arimondo, A. Kolovsky, and A. Buchleitner, *Phys. Rev. A* **72**, 063610 (2005).
- [39] V. Giovannetti, S. Lloyd, and L. Maccone, *Phys. Rev. A* **67**, 052109 (2003); M. Sillanpaa, T. Lehtinen, A. Paila, Y. Makhlin, and P. Hakonen, *Phys. Rev. Lett.* **96**, 187002 (2006); T. Caneva, M. Murphy, T. Calarco, R. Fazio, S. Montangero, V. Giovannetti, and G. E. Santoro, *ibid.* **103**, 240501 (2009).

Nonlinear resonant tunneling of Bose-Einstein condensates in tilted optical lattices

K. Rapedius,^{1,2} C. Elsen,¹ D. Witthaut,³ S. Wimberger,⁴ and H. J. Korsch¹

¹*Department of Physics, Technische Universität Kaiserslautern, D-67653 Kaiserslautern, Germany*

²*Center for Nonlinear Phenomena and Complex Systems, Université Libre de Bruxelles, Code Postal 231, Campus Plaine, B-1050 Brussels, Belgium*

³*Network Dynamics Group, Max-Planck-Institute for Dynamics and Self-Organization, D-37073 Göttingen, Germany*

⁴*Institut für theoretische Physik and Center for Quantum Dynamics, Universität Heidelberg, D-69120 Heidelberg, Germany*

(Received 18 May 2010; published 3 December 2010)

We study the tunneling decay of a Bose-Einstein condensate from tilted optical lattices within the mean-field approximation. We introduce a method to calculate ground and excited resonance eigenstates of the Gross-Pitaevskii equation, based on a grid relaxation procedure with complex absorbing potentials. This algorithm works efficiently in a wide range of parameters where established methods fail. It allows us to study the effects of the nonlinearity in detail in the regime of resonant tunneling, where the decay rate is enhanced by resonant coupling to excited unstable states.

DOI: [10.1103/PhysRevA.82.063601](https://doi.org/10.1103/PhysRevA.82.063601)

PACS number(s): 03.75.Lm, 03.65.Ge, 03.65.Nk

I. INTRODUCTION

The dynamics of a quantum particle in a periodic potential subject to an external force is one of the central problems in solid-state physics. In the field free case all eigenstates are delocalized over the lattices, leading to transport [1,2]. The application of a constant force leads to a localization of the eigenstates such that transport is suppressed contrary to our intuition [3–6]. Instead, the quantum particle performs the celebrated Bloch oscillations and eventually decays by repeated Zener tunneling to higher Bloch bands [7–18]. The most detailed studies of Bloch oscillations and decay have been carried out with ultracold atoms trapped in optical lattices. These systems are particularly appealing, because the dynamics of the atoms can be recorded in situ and all parameters can be tuned precisely over a wide range. The external force can be induced by gravity [7], magnetic gradient fields [8], or accelerating the lattice [9–14]. Decay in strong fields manifests itself in the pulsed output of coherent matter waves. The dynamics is even more interesting when the atoms undergo Bose-Einstein condensation and interactions have to be taken into account. For low temperature and high densities, the dynamics of the atoms can be described by the celebrated Gross-Pitaevskii equation (GPE) with astonishing accuracy [19]. In this treatment, interactions are incorporated by a nonlinear mean-field potential, which is proportional to the condensate density. The nonlinearity of the equation alters the dynamics and in particular the decay substantially. Interactions can lead to a damping of Bloch oscillations [20], asymmetric Landau-Zener tunneling [10,21,22], or a bistability of resonance curves [23–25].

Here we study the resonance eigenstates of the GPE

$$\begin{aligned} & \left(\frac{-\hbar^2}{2m} \frac{d^2}{dx^2} + V(x) + Fx + g|\psi(x)|^2 \right) \psi(x) \\ & = (\mu - i\Gamma/2)\psi(x) \end{aligned} \quad (1)$$

with a periodic potential $V(x+d) = V(x)$ and a static force $F > 0$, which is known as a Wannier-Stark (WS) potential. The imaginary part Γ of the eigenenergy gives the decay rate of the condensate. A comprehensive review of the localized eigenstates, the WS resonances, can be found in Ref. [17]. In

the following we assume a cosine potential $V(x) = V_0 \cos(x)$ except for Sec. IV, where a bichromatic lattice is considered. Throughout this article we use scaled units defined by $\tilde{x} = 2\pi x/d$ such that the period of the potential is 2π and $\hbar = m = 1$. The energies, μ and V_0 , are then given in units of $8E_R$, where $E_R = (\hbar^2 \pi^2)/(2md^2)$ is the recoil energy. If not stated otherwise we fix the strength of the lattice as $V_0 = 1$ in scaled units.

In this article we introduce an algorithm for the computation of nonlinear resonance states based on a grid relaxation method with a complex absorbing potential (CAP). This algorithm converges in a wide parameter range and is applicable even to situations of many degenerate energy levels, such as the WS system at resonance condition (see below). It is thus capable to describe genuine nonlinear phenomena such as bistability, which pose a major difficulty to other methods as for instance nonlinear complex scaling (CS) [26–31]. In addition, it is more efficient and easier to implement and, unlike previous methods, is not restricted to ground-state calculations but can also compute excited states. Note that our approach differs from the CAP method used in Refs. [27,32] because the latter does not use a grid relaxation but relies on a basis set expansion. Although such expansions work well for simple single-well potentials, they cannot easily handle complicated problems like the Wannier-Stark system studied in the present article, which requires the use of as much as 500 basis states even in the linear (noninteracting) case [33]. Our method is applied to study the decay of a Bose-Einstein condensate in the strongly nonlinear regime. Nonlinear effects are crucial in the regime of resonantly enhanced tunneling (RET). In this case a metastable WS resonance becomes energetically degenerate with an excited, less stable state, which can increase the decay rate by orders of magnitude. This phenomenon is most pronounced in deep optical lattices and has been studied systematically for the linear case in Refs. [16,17]. The nonlinearity shifts the resonance and eventually bends the resonance peak leading to a bistable behavior.

II. COMPUTATIONAL METHOD

Linear WS resonances can be efficiently calculated with the truncated shift operator technique introduced in Ref. [33].

In the nonlinear case, the method of CS has been applied [26,28–30]. Though satisfactory from a conceptual point of view, this method has several drawbacks. The implementation is complicated as it requires switching between different basis sets as well as different time propagation methods. Furthermore, the calculation of excited states is highly nontrivial, as the method relies on an imaginary time propagation, and the convergence is quite slow, especially for weak fields and close to energetic degeneracies as present in the RET condition [28,29].

As an alternative, we propose a method based on complex absorbing potentials (CAP) performed on a finite grid $[x_-, x_+]$ in real space. We assume that the resonance wave function is mainly localized in the interval $[x_\ell, x_r]$ with $x_- < x_\ell < x_r < x_+$ and fix the normalization as $\int_{x_\ell}^{x_r} |\psi(x)|^2 dx = 1$. For $x \rightarrow -\infty$, we apply a CAP of the type

$$V_{\text{CAP}} \propto \begin{cases} -i(x/x_-)^{10} & x < 0 \\ 0 & x > 0 \end{cases}, \quad (2)$$

which only modifies the wave function in the vicinity of the grid boundary x_- making it square integrable. We choose x_- to be quite large (ca. 40 lattice periods) in order to include enough of the asymptotic behavior of the resonance. The exact size of the area of integration and the strength η of the CAP must be chosen such that the results are stable with respect to a small variation of these parameters (compare the cusp condition in Ref. [34]). On our finite grid $[x_-, x_+]$ the boundary conditions for the wave function read

$$\psi(x_-) = 0, \quad \psi(x_+) = 0, \quad \psi'(x_+) = C, \quad (3)$$

where the last condition is used to control the normalization. The algorithm starts from the linear case $g = 0$, for which all WS resonances can be computed efficiently [33]. Nonlinear WS resonances in different bands are calculated by choosing a different initial guess. The nonlinearity is then increased gradually, using the previous result as initial guess for a standard boundary value problem (BVP) solver, e.g., the MATLAB function `bvp4c`. Applying the BVP solver changes the normalization of ψ , such that the parameter C has to be adjusted according to

$$C \rightarrow C / \left(\int_{x_\ell}^{x_r} |\psi(x)|^2 dx \right)^{1/2}. \quad (4)$$

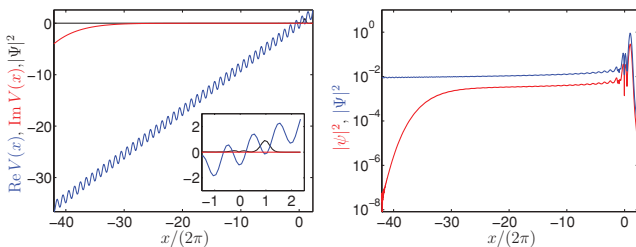


FIG. 1. (Color online) Test of the algorithm for vanishing nonlinearity $g = 0$. (Left panel) Initial solution $|\Psi|^2$ and complex potential $V(x) = \cos(x) + Fx - i\eta(x/x_\alpha)^{10}$ with $F = 0.135$. The inset shows a magnification in the vicinity of the main peak of the initial solution. (Right panel) Comparison between the initial solution $|\Psi|^2$ (blue) and the solution $|\psi|^2$ (red) obtained using a complex absorbing potential.

TABLE I. Decay rates Γ for the most stable resonance of the potential $V(x) = \cos(x)$, taken from Ref. [28] (CS method) and computed using the CAP grid relaxation method. Particularly for small decay rates the new CAP method proves more efficient than the CS technique.

g	F	Γ_{CS}	Γ_{CAP}
0	0.5	1.941×10^{-2}	1.941×10^{-2}
0.1	0.5	2.180×10^{-2}	2.180×10^{-2}
0	0.25	7.2×10^{-4}	7.104×10^{-4}
0.1	0.25	8.4×10^{-4}	8.346×10^{-4}
0.2	0.25	9.7×10^{-4}	9.688×10^{-4}
0.25	0.25	1.04×10^{-3}	1.041×10^{-3}
0.5	0.25	1.48×10^{-3}	1.476×10^{-3}
0.2	0.15	2.9×10^{-5}	2.832×10^{-5}
0.2	0.13125	5.7×10^{-5}	5.600×10^{-5}

This is repeated until the normalization converges to unity. The nonlinearity is then increased by one step.

The basic features of this algorithm and the effects of the CAPs are illustrated in Fig. 1 for a tilted cosine potential with $V_0 = 1$, $F = 0.135$, and $g = 0$. The left-hand side shows the squared magnitude $|\Psi|^2$ of the initial wave function as well as the real and imaginary part of the potential. The right panel of Fig. 1 compares the squared magnitudes of the initial wave function Ψ and the normalized wave function ψ calculated by the BVP solver for the most stable resonance. We observe a difference in the asymptotic behavior for $x \rightarrow -\infty$ which is caused by the CAP. The shift between the two functions is an artifact of a slight difference in normalization caused by the relatively coarse mesh used for the initial solution.

To demonstrate the validity of the CAP algorithm we compare the calculated decay rates for a cosine potential for several parameters to complex scaling results, which themselves were tested against a direct time propagation in Ref. [28]. The values summarized in Table I show an excellent agreement over the entire parameter range. Residual numerical errors are very small; they can mainly be attributed to the limited computation time for the CS method and reflections of the matter wave at the CAP. For a further discussion of CAPs in the simulation of few boson systems, see Ref. [35] and references therein.

III. RESONANTLY ENHANCED TUNNELING

We use the CAP method to investigate how a nonlinear interaction affects the decay of a BEC in a tilted optical lattice. In the weakly interacting regime, the scaling of the decay rate with the field strength is given by the celebrated Landau-Zener formula

$$\Gamma(F) \approx F \exp(\pi \Delta E^2 / F), \quad (5)$$

where ΔE is the energy gap between the Bloch bands of the periodic potential [2,15] and the field strength F determines the oscillation frequency in the bands [15,17]. Major differences

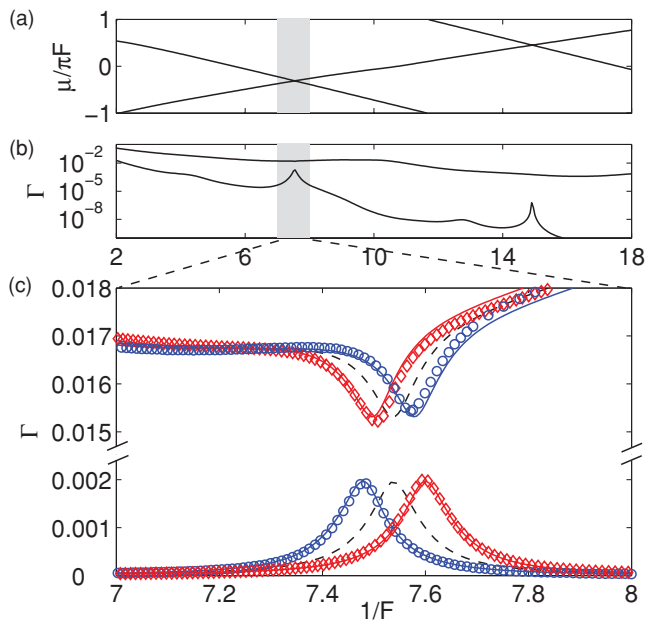


FIG. 2. (Color online) Resonantly enhanced tunneling (RET) of (non-) linear WS resonances. (a) Energies and (b) decay rates of the two most stable WS resonances in a cosine potential as a function of the inverse field strength $1/F$. (c) Shift of the RET peaks due to the nonlinear interaction of a BEC for $g = +0.02$ (\circ), $g = -0.02$ (\diamond), and $g = 0$ (- -). Numerical results (symbols) are compared to a perturbative calculation (solid lines) according to Eqs. (6) and (8).

arise in the regime of RET. In this case an eigenstate localized mainly in one of the wells of the potential becomes energetically degenerate with an excited state in another well, which can increase the decay rate by orders of magnitude [17]. In the following, we focus on the experimentally studied regime [11,12], where a modest nonlinearity strongly affects the decay of the condensate [11,12,18].

RET is illustrated in Figs. 2(a) and 2(b) for the linear case $g = 0$, showing the decay rate Γ and the chemical potential μ of the two most stable resonances as a function of F . RET is observed at $1/F \approx 7.5$, where the two energy levels $\mu(F)$ cross. The resonant coupling to the excited states leads to a pronounced RET peak of the decay rate for the most stable resonance. Coincidentally, a pronounced dip is observed for the first excited resonance, which is stabilized by the coupling to the most stable resonance [17]. The influence of a small nonlinearity is illustrated in Fig. 2(c). Three main effects are observed: a shift of the resonance peaks, an increase (decrease) of the peak decay rate in the ground state for $g > 0$ ($g < 0$), and a deformation of the peak shape.

The shift and the deformation can be qualitatively understood by a perturbative approach [28]. To first order, this predicts a shift of the real part of the eigenenergy,

$$\Delta\mu(g) \approx g \int_{x_l}^{x_r} |\psi_g|^2 |\psi_{g=0}|^2 dx \approx g \int_{x_l}^{x_r} |\psi_{g=0}|^4 dx, \quad (6)$$

which corresponds to a shift of the field strength according to

$$\Delta F(g) \approx \pm \Delta\mu(g)/(2\pi). \quad (7)$$

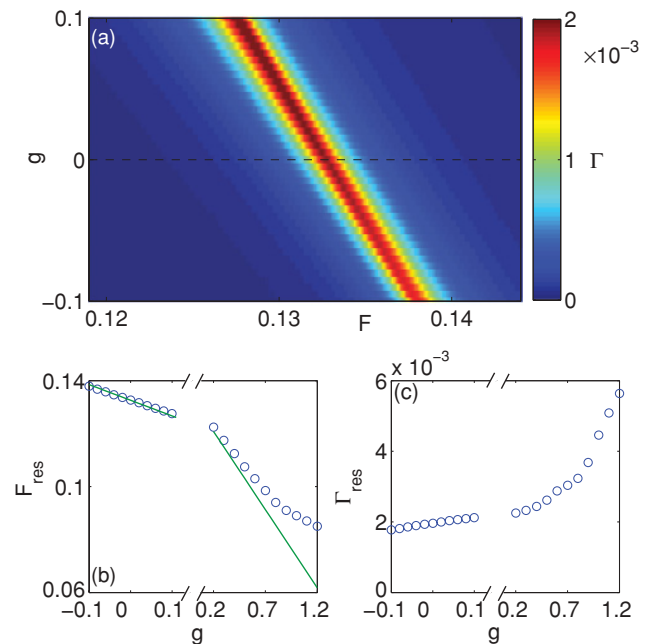


FIG. 3. (Color online) (a) Colormap plot of the decay rates of the most stable WS resonances in a cosine-potential vs. the field strength F and the interaction strength g in the vicinity of the first order RET peak. (b) Position and (c) height of the RET peak vs. the interaction strength g .

Here, the minus sign holds for the ground and the plus sign for the excited band. The nonlinear decay rate is then approximately given by

$$\Gamma_g(F) = \Gamma_0[F + \Delta F(g)]. \quad (8)$$

The shift is further investigated in Fig. 3(b), where the decay rate as well as the peak position is plotted vs. the interaction strength over a wide parameter range. The perturbative calculation (6) predicts that the peak position F_{res} is shifted with a slope $dF_{\text{res}}/dg = 0.059$ for small values of g , which is plotted as a green line in Fig. 3(b). This deviates from the numerically exact results already for small values of g , for which a linear fit yields a smaller slope of $dF_{\text{res}}/dg = 0.051$. In agreement with Ref. [28] we thus find that first-order perturbation theory is insufficient in describing the shift of the RET peaks quantitatively. Noticeably, the RET peak and the dip of the decay rate for the first excited resonance always shift into opposite directions, as shown in Fig. 2(c).

The change in the maximum decay rate is not predicted by perturbation theory but easily explained phenomenologically. It is a direct consequence of the interaction as repulsion between the particles in general leads to a destabilization, whereas attraction leads to a stabilization of both resonances and bound states (see Ref. [10] and references therein). This is further illustrated in Fig. 3(c), where the peak decay rate of the most stable resonance is plotted as a function of g over a wide parameter range. Similar effects have been investigated for several other model potentials [24,26,29,31].

The dependence of the linear and nonlinear RET peaks is further analyzed in Fig. 4. The upper panel shows the decay rate $\Gamma(F)$ for different values of the potential strength V_0 for $g = 0$.

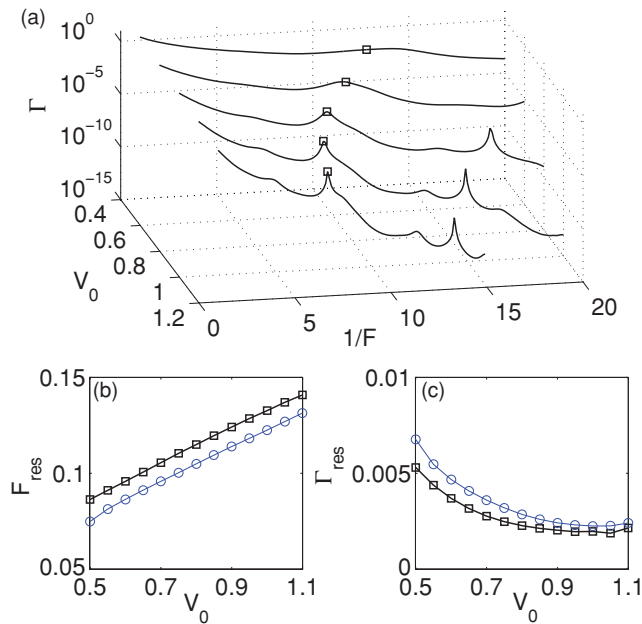


FIG. 4. (Color online) (a) Emergence of the RET peaks: Decay rate Γ as a function of the field strength F for different values of the lattice strength V_0 and $g = 0$. The primal RET peaks analyzed in the following are marked with a square (\square). [(b) and (c)] Scaling of the peak position F_{res} and the peak decay rate Γ_{res} with the strength of the optical lattice V_0 for $g = 0$ (\square) and $g = 0.2$ (\circ).

For shallow lattices, $\Gamma(F)$ decreases monotonically with $1/F$ as predicted by the celebrated Landau-Zener formula (5). As the lattice becomes deeper, Landau-Zener theory predicts that Γ vanishes exponentially with the band width ΔE . However, this is only true as long as tunneling to excited states in neighboring potential wells is not resonantly enhanced. On resonance, the decay rate Γ decreases much slower with V_0 as shown in Fig. 4(c) such that sharp RET peaks emerge. This remains true also for weak nonlinearities as shown for $g = 0.2$ in the figure. One observes a similar slow decrease of Γ_{res} with V_0 , however, the actual values of the decay rate are larger for $g > 0$. The position of the RET peaks F_{res} is plotted as a function of V_0 in Fig. 4(b). Tunneling becomes resonant when ndF matches the energy difference between the most stable and an excited, less stable resonance, where nd is an integer multiple of the lattice period. For a deep lattice this energy difference, and thus also the peak position F_{res} , is given by $\sqrt{V_0}$ [11]. This estimate agrees very well with the numerical results for the linear case $g = 0$ as shown in the figure. In the nonlinear case the RET peaks are shifted to smaller values of the field strength F according to Eq. (7); however, the general progression with the potential strength V_0 remains the same.

Another important feature observed in Fig. 2(c) is that the RET peaks become asymmetric for $g \neq 0$. For a repulsive (attractive) nonlinearity, the peak bends to higher (lower) values of F . If the nonlinearity is increased above a critical value g_{cr} , the peaks bend over and a bistable behavior emerges. The detailed shape of a bistable RET peak is plotted in Fig. 5, which also indicates how WS states are calculated numerically in the bistable regime: We have started with a small value of F which was then gradually increased, using

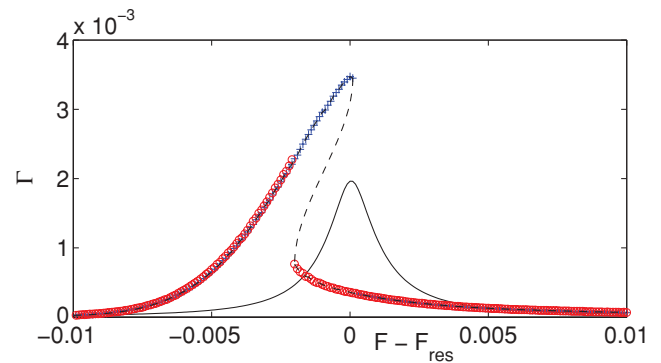


FIG. 5. (Color online) Bistability of the RET peak for strong repulsive interactions ($g = 0.8$). The decay rate was calculated for a forward sweep (blue asterisk) and a backward sweep (red circles). A spline interpolation (dashed line) is included to guide the eye. The solid line shows the linear ($g = 0$) peak shape for comparison.

every result as initial guess for the next calculation (cf. also Refs. [28,29]). After reaching a final, large value of the field strength, the procedure was reversed and F was decreased back to the initial value. Within the regime of bistability forward and backward sweep yield the upper and lower branches of the peak, respectively. The intermediate branch is generally difficult to compute as it is dynamically unstable.

The bending of the RET peak and the emergence of a bistability can be understood qualitatively by the perturbative approach introduced above. A common WS state in a deep optical lattice is strongly localized in a single potential well so its chemical potential is strongly changed according to Eq. (8). In comparison, the state corresponding to the maximum of the RET peak is delocalized because of the energetical degeneracy with an excited state in another well. Therefore its chemical potential is affected rather weakly and according to Eq. (7) also the change of the peak position ΔF is small (cf. also Refs. [11,12]). With increasing nonlinearity, the edges of a RET peak shift to smaller values of the field strength, while the maximum falls behind. The whole peak bends to the right and finally becomes bistable.

The onset of bistability is analyzed quantitatively in Fig. 6. The upper panel shows the two branches of the decay curves for $V_0 = 1$ and different values of g . The RET peaks are shifted to smaller values of F when g is increased and the peaks are bistable for $g = 0.5$ and higher. The lower panel shows the critical nonlinearity g_{cr} as a function of the lattice strength V_0 . The sharp decrease of g_{cr} for $V_0 \gtrsim 1$ can be understood from the properties of the two most stable Wannier-Stark resonance states. Generally, the critical nonlinearity for a bifurcation of a nonlinear stationary state is smallest, when the state is coupled to a second state which is energetically close—a result which has been established quantitatively for nonlinear two-state systems (see Refs. [21,30] and references therein). For $V_0 \gtrsim 1$, the optical lattice becomes deep enough such that the first excited WS resonance state becomes strongly localized and that its decay rate decreases significantly. Correspondingly, the most stable resonance is destabilized as the coupling between the two states is increased – its decay increases for $V_0 \gtrsim 1$ as shown in Fig. 4(c). Furthermore, the coupling to the first

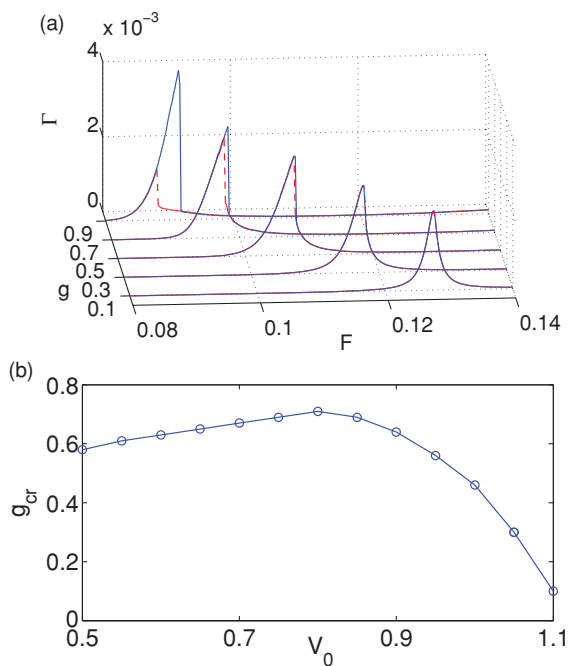


FIG. 6. (Color online) Emergence of bistability of the RET peaks in an optical lattice. (a) Decay rate Γ as a function of the field strength F for different values of the nonlinearity g . The decay rate was calculated for a forward sweep (blue solid lines) and a backward sweep (red dashed lines). (b) Critical nonlinearity g_{cr} for the onset of bistability as a function of the lattice strength V_0 . The solid line is drawn to guide the eye.

excited resonance, which is now energetically close, facilitates a bifurcation and thus the onset of bistability.

The emergence of bistability has also been analyzed for the transmission coefficient in the context of nonlinear RET through one-dimensional potential barriers [23–25]. However, in this case states corresponding to the transmission maximum are localized strongest. Thus the resonance peaks bend into the same direction as they are shifted, which is in contrast to the behavior of the WS RET peaks shown in Fig. 5.

IV. BEYOND THE RET REGIME

A new regime of RET can be explored in bichromatic optical lattices,

$$V(x) = V_0\{\cos(x) + \delta \cos(x/2 + \phi)\}. \quad (9)$$

These potentials can be realized experimentally by superimposing two incoherent optical lattices [36,37] or by combining optical potentials based on virtual two-photon and four-photon processes [38]. The introduction of an additional potential with a doubled periodicity leads to the splitting of the ground Bloch band into two minibands for $F = 0$. This distinguished feature has been used to study Landau-Zener tunneling between different minibands [39] and the interplay of tunneling and Bloch oscillations [40].

The decay rates of the WS resonance states in a bichromatic optical lattice are plotted in Fig. 7(a) as a function of the field strength F for $V_0 = 1$ and $\phi = \pi/2$. The splitting of the Bloch bands into minibands translates into a splitting

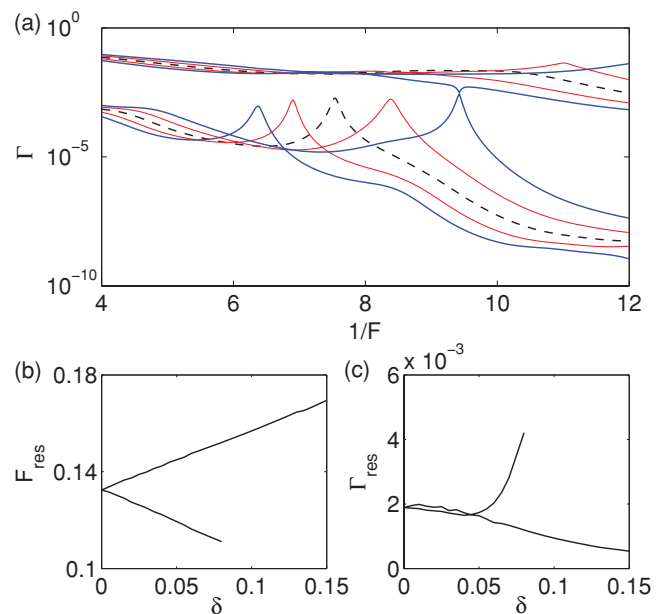


FIG. 7. (Color online) (a) The decay rate Γ of the four most stable WS resonance states in a tilted bichromatic potential (9) for $V_0 = 1$, $\phi = \pi/2$, and $\delta = 0$ (black dashed line), $\delta = 0.05$ (thin red line), and $\delta = 0.1$ (solid blue line). [(b) and (c)] Position F_{res} and height Γ_{res} of the RET peaks of the two most stable resonance states as a function of δ .

of the WS resonance states and their decay curves $\Gamma(F)$, which is most pronounced in the vicinity of the RET peaks. The position of the RET peaks changes linearly with the strength δ of the additional lattice as shown in Fig. 7(b). For $\phi = \pi/2$, the energy of the lattice wells are alternately shifted up and down in energy by an amount of $\pm\delta$. Thus also the energies of the WS resonance states shift by an amount of $\pm\delta$ and the positions of the RET peaks changes by $\Delta F_{res} = \pm 2\delta/(2\pi)$, 2π being the period of the optical lattice.

The change of the peak height Γ_{res} in a bichromatic optical lattice is much more striking as shown in Fig. 7(c). The height of one of the RET peaks increases drastically for larger values of δ . For $\delta > 0.08$ one can no longer identify a single RET peak. As argued above RET occurs when the real parts μ of the eigenenergies of two WS resonances cross, while the imaginary parts Γ anticross. For $\delta > 0.08$ the crossing scenario changes; the imaginary parts show a real crossing while the real parts anticross. The two different scenarios are commonly referred to a type I (real-parts cross) and type II crossing (imaginary parts cross), respectively [12,41,42]. The qualitative difference is also observed in the decay curves plotted in Fig. 7(a).

For both types of crossings, the eigenenergies are never fully degenerate—such a full degeneracy occurs only for isolated points in parameter space. At these exceptional points, already small nonlinearities lead to significant changes of the WS resonance states and especially their decay rates Γ . Examples are shown in Fig. 8 for $\delta = 1$ and different relative phases ϕ of the two lattices. An ordinary type II crossing is observed for $\phi = -1.7$, leading to the familiar RET peaks of the decay rates. Changing the phase slightly to $\phi = -1.6$ changes the type of the crossing scenario to type I. An exceptional point

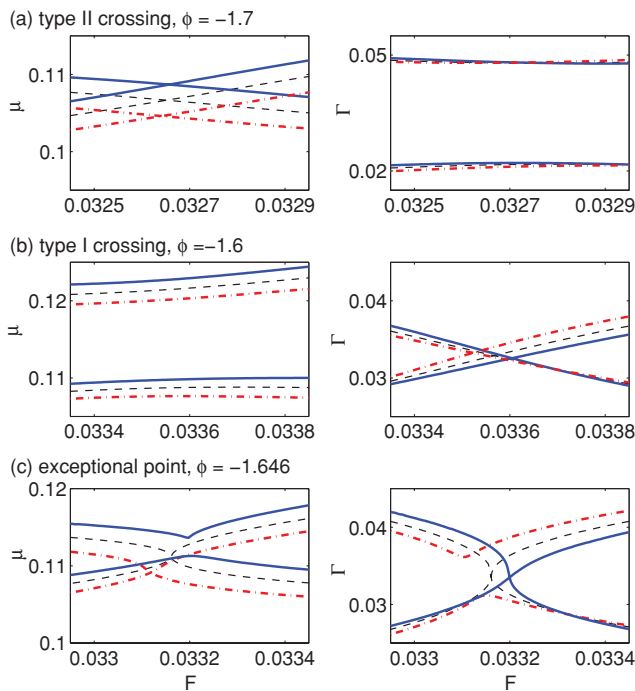


FIG. 8. (Color online) Chemical potential μ and decay rates Γ for (non-)linear WS resonances in a bichromatic optical lattice for $V_0 = 1/2$, $\delta = 1$ and (a) $\phi = -1.7$, (b) $\phi = -1.6$, (c) $\phi = -1.646$ and $g = 0$ (dashed black line), $g = +0.01$ (thick blue line), and $g = -0.01$ (dash-dotted red line).

is found for $\phi = -1.646$, as shown in Fig. 8(c). However, the degeneracy is lifted as soon as the atoms start to interact. A weak repulsive nonlinearity $g = +0.01$, turns the exceptional crossing into an ordinary type I crossing, while an attractive

nonlinearity $g = -0.01$ favors a type II crossing. This change of peak shape can have dramatic effects on the dynamics of a Bose-Einstein condensate, in particular when experimental parameters are adiabatically varied (see, e.g., Ref. [42]).

V. CONCLUSIONS

Bose-Einstein condensates in tilted optical lattices are ideal to study the decay of interacting open quantum systems. Experimentally the parameters can be tuned over a wide range and the dynamics can be recorded in situ. Here we presented an *efficient* method to calculate the decay rate in the mean-field regime also in the presence of degeneracies which also, unlike previous methods, is not restricted to ground-state calculations. The effects of the nonlinearity are strongest in the regime of resonant tunneling, where the decay rate can be enhanced by orders of magnitude by resonant coupling to unstable excited states. The interactions shift and bend the resonance peaks and eventually lead to a bistable peak shape. Even more interesting effects can be studied in tilted bichromatic lattices, where different types of level crossing scenarios emerge when the lattice parameters are tuned. These effects will be studied in detail in a future publication.

ACKNOWLEDGMENTS

We acknowledge financial support by the Deutsche Forschungsgemeinschaft (DFG) via the Graduiertenkolleg 792, the Forschergruppe 760 (Grant No. WI 3426/3-1), the Heidelberg graduate school of fundamental physics (Grant No. GSC 129/1) and the research fellowship program (Grant No. WI 3415/1-1). K.R. acknowledges support from a scholarship of the Université Libre de Bruxelles.

- [1] F. Bloch, *Z. Phys.* **52**, 555 (1929).
- [2] C. Zener, *Proc. R. Soc. London* **137**, 696 (1932).
- [3] J. Zak, *Phys. Rev. Lett.* **20**, 1477 (1968).
- [4] G. H. Wannier, *Phys. Rev.* **181**, 1364 (1969).
- [5] J. Zak, *Phys. Rev.* **181**, 1366 (1969).
- [6] J. E. Avron, J. Zak, A. Grossmann, and L. Gunther, *J. Math. Phys.* **18**, 918 (1977).
- [7] B. P. Anderson and M. A. Kasevich, *Science* **282**, 1686 (1998).
- [8] M. Gustavsson, E. Haller, M. J. Mark, J. G. Danzl, G. Rojas-Kopeinig, and H.-C. Nägerl, *Phys. Rev. Lett.* **100**, 080404 (2008).
- [9] M. Ben Dahan, E. Peik, J. Reichel, Y. Castin, and C. Salomon, *Phys. Rev. Lett.* **76**, 4508 (1996).
- [10] M. Jona-Lasinio, O. Morsch, M. Cristiani, N. Malossi, J. H. Müller, E. Courtade, M. Anderlini, and E. Arimondo, *Phys. Rev. Lett.* **91**, 230406 (2003).
- [11] C. Sias, A. Zenesini, H. Lignier, S. Wimberger, D. Ciampini, O. Morsch, and E. Arimondo, *Phys. Rev. Lett.* **98**, 120403 (2007).
- [12] A. Zenesini, C. Sias, H. Lignier, Y. Singh, D. Ciampini, O. Morsch, R. Mannella, E. Arimondo, A. Tomadin, and S. Wimberger, *New J. Phys.* **10**, 053038 (2008).
- [13] A. Zenesini, H. Lignier, G. Tayebirad, J. Radogostowicz, D. Ciampini, R. Mannella, S. Wimberger, O. Morsch, and E. Arimondo, *Phys. Rev. Lett.* **103**, 090403 (2009).
- [14] G. Tayebirad, A. Zenesini, D. Ciampini, R. Mannella, O. Morsch, E. Arimondo, N. Lörch, and S. Wimberger, *Phys. Rev. A* **82**, 013633 (2010).
- [15] M. Holthaus, *J. Opt. B: Quantum Semiclass. Opt.* **2**, 589 (2000).
- [16] M. Glück, A. R. Kolovsky, and H. J. Korsch, *J. Opt. B: Quantum Semiclass. Opt.* **2**, 694 (2000).
- [17] M. Glück, A. R. Kolovsky, and H. J. Korsch, *Phys. Rep.* **366**, 103 (2002).
- [18] S. Wimberger, R. Mannella, O. Morsch, E. Arimondo, A. R. Kolovsky, and A. Buchleitner, *Phys. Rev. A* **72**, 063610 (2005).
- [19] C. J. Pethick and H. Smith, *Bose-Einstein Condensation in Dilute Gases* (Cambridge University Press, Cambridge, 2008).
- [20] D. Witthaut, M. Werder, S. Mossmann, and H. J. Korsch, *Phys. Rev. E* **71**, 036625 (2005).
- [21] J. Liu, L. Fu, B.-Y. Ou, S.-G. Chen, D.-I. Choi, B. Wu, and Q. Niu, *Phys. Rev. A* **66**, 023404 (2002).
- [22] D. Witthaut, E. M. Graefe, and H. J. Korsch, *Phys. Rev. A* **73**, 063609 (2006).
- [23] T. Paul, K. Richter, and P. Schlagheck, *Phys. Rev. Lett.* **94**, 020404 (2005).

- [24] K. Rapedius, D. Witthaut, and H. J. Korsch, *Phys. Rev. A* **73**, 033608 (2006).
- [25] K. Rapedius and H. J. Korsch, *Phys. Rev. A* **77**, 063610 (2008).
- [26] N. Moiseyev and L. S. Cederbaum, *Phys. Rev. A* **72**, 033605 (2005).
- [27] P. Schlagheck and T. Paul, *Phys. Rev. A* **73**, 023619 (2006).
- [28] S. Wimberger, P. Schlagheck, and R. Mannella, *J. Phys. B* **39**, 729 (2006).
- [29] P. Schlagheck and S. Wimberger, *Appl. Phys. B* **86**, 385 (2007).
- [30] D. Witthaut, E. M. Graefe, S. Wimberger, and H. J. Korsch, *Phys. Rev. A* **75**, 013617 (2007).
- [31] K. Rapedius and H. J. Korsch, *J. Phys. B* **42**, 044005 (2009)
- [32] N. Moiseyev, L. D. Carr, B. A. Malomed, and Y. B. Band, *J. Phys. B* **37**, L193 (2004).
- [33] M. Glück, A. R. Kolovsky, and H. J. Korsch, *Eur. Phys. J. D* **4**, 239 (1998).
- [34] N. Moiseyev, *Phys. Rep.* **302**, 212 (1998).
- [35] A. U. J. Lode, A. I. Streltsov, O. E. Alon, H.-D. Meyer, and L. S. Cederbaum, *J. Phys. B* **42**, 044018 (2009).
- [36] A. Görlitz, T. Kinoshita, T. W. Hänsch, and A. Hemmerich, *Phys. Rev. A* **64**, 011401(R) (2001).
- [37] S. Fölling, S. Trotzky, P. Cheinet, M. Feld, R. Saers, A. Widera, T. Mueller, and I. Bloch, *Nature (London)* **448**, 1029 (2007).
- [38] G. Ritt, C. Geckeler, T. Salger, G. Cennini, and M. Weitz, *Phys. Rev. A* **74**, 063622 (2006).
- [39] T. Salger, C. Geckeler, S. Kling, and M. Weitz, *Phys. Rev. Lett.* **99**, 190405 (2007); *Science* **326**, 1241 (2009).
- [40] B. M. Breid, D. Witthaut, and H. J. Korsch, *New J. Phys.* **8**, 110 (2006); **9**, 62 (2007).
- [41] J. E. Avron, *Ann. Phys. (NY)* **143**, 33 (1982).
- [42] F. Keck, H. J. Korsch, and S. Mossmann, *J. Phys. A* **36**, 2125 (2003).

Physica A 390 (2011) 1363–1369



Contents lists available at ScienceDirect

Physica A

journal homepage: www.elsevier.com/locate/physa

Detection of avoided crossings by fidelity

Patrick Plötz^a, Michael Lubasch^{a,b}, Sandro Wimberger^{a,c,*}

^a Institut für Theoretische Physik, Philosophenweg 19, Universität Heidelberg, 69120 Heidelberg, Germany

^b Max-Planck-Institut für Quantenoptik, Hans-Kopfermann-Str. 1, 85748 Garching, Germany

^c Center for Quantum Dynamics, Philosophenweg 12, Universität Heidelberg, 69120 Heidelberg, Germany

ARTICLE INFO

Article history:

Received 25 September 2010

Received in revised form 9 November 2010

Available online 22 December 2010

Keywords:

Avoided crossings

Fidelity

Quantum chaos

Complex systems

ABSTRACT

The fidelity, defined as overlap of eigenstates of two slightly different Hamiltonians, is proposed as an efficient detector of avoided crossings in the energy spectrum. This new application of fidelity is motivated for model systems, and its value for analyzing complex quantum spectra is underlined by applying it to a random matrix model and a tilted Bose–Hubbard system.

© 2010 Elsevier B.V. All rights reserved.

1. Introduction

The progress in cooling and manipulating ultracold atomic gases in recent years has opened new perspectives on interacting many-body models from condensed matter physics [1,2]. It led to questions and opportunities beyond conventional solid-state physics, e.g., the direct experimental study of quantum phase transitions [1], the role and engineering of genuine quantum correlations [1,3], and the phenomenon of quantum chaos in systems that consist of indistinguishable particles [4–8]. In this context, it is possible to detect a quantum phase transition by the change of fidelity (modulus of the overlap between eigenstates of slightly different Hamiltonians) [9], since the ground state of a quantum system changes dramatically at a critical parameter [10].

Up until now, the temporal change of fidelity – as the overlap of the same initial states evolved by different Hamiltonians [11] – has been measured experimentally not only in wave billiards [12], but also in systems of cold atoms subject to optical potentials [13,14]. Similar techniques may be applied to measure the evolving overlap of two eigenstates where time is substituted by the change of some tunable control parameters. Often a quantum phase transition may be viewed, for finite-size realizations of a system, as an avoided crossing (AC) in parameter space which closes in the thermodynamic limit [10]. A scenario of *many* ACs with a broad distribution of widths [15–17], as a manifestation of a strong coupling of many energy levels, is naturally found in quantum chaotic systems [15]. The dynamical evolution of these systems is determined by the number and distribution of ACs present in the spectrum. The question then arises whether the applicability of fidelity can be lifted from pure ground-state analysis [18] to detect and characterize ACs in the entire spectrum of a complex quantum system. In this paper we propose to use the fidelity as a new and experimentally accessible tool to detect and characterize ACs in quantum spectra [19]. This is corroborated by analytical and numerical results for exemplary quantum systems.

* Corresponding author at: Institut für Theoretische Physik, Philosophenweg 19, Universität Heidelberg, 69120 Heidelberg, Germany. Tel.: +49 6221 54 9449; fax: +49 6221 54 9331.

E-mail address: s.wimberger@thphys.uni-heidelberg.de (S. Wimberger).

2. The fidelity measure

Given some parameter depending Hamiltonian $H(\lambda) = H_1 + \lambda H_2$, the fidelity [11] between the n th eigenstates, denoted by $|n\rangle$, of two slightly different Hamiltonians $H(\lambda)$ and $H(\lambda + \delta\lambda)$ is defined as $f_n(\lambda, \delta\lambda) \equiv |\langle n(\lambda)|n(\lambda + \delta\lambda)\rangle|$. In complex quantum systems with many degrees of freedom, many of the levels of the system are coupled to each other leading to ACs in the spectrum of the Hamiltonian when the parameter λ is changed [15]. To simplify the discussion, we assume a finite size Hilbert space \mathcal{H} , where all energy levels are never exactly degenerate. To detect and characterize an AC for a given quantum level n we study the fidelity change [9]

$$S_n(\lambda, \delta\lambda) \equiv \frac{1 - f_n(\lambda, \delta\lambda)}{(\delta\lambda)^2} \quad (1)$$

which measures the change of the state $|n\rangle$. For $\delta\lambda \ll 1$, it is independent of $\delta\lambda$, i.e. $S_n(\lambda, \delta\lambda) \approx S_n(\lambda)$, and vanishingly small everywhere except in the vicinity of an AC. The independence of $\delta\lambda$ arises from the fact that the first non-vanishing contribution to f_n in the expansion of the changed state $|n(\lambda + \delta\lambda)\rangle$ is of second order in $\delta\lambda$ [19,20]. The fidelity measure (1) also has the advantage of being applicable locally in the spectrum, where one follows a certain state $|n(\lambda)\rangle$ and its neighbors over a range of parameter values λ to study the ACs they encounter. In addition, it is well-suited for numerical computations, since λ is the only relevant parameter as long as $\delta\lambda$ is sufficiently small. The different limit of large $\delta\lambda$ and hence the coupling over a broad energy band was the focus of a recent work using another generalized fidelity [21]. In contrast, our interest here is the detection and characterization of ACs as local couplings in energy space.

2.1. Two-state model

Let us first discuss an isolated AC which can locally be described in nearly-degenerate perturbation theory as an effective two-level system. It is then represented by a Hamiltonian $H(\lambda) = \lambda\sigma_z + g\sigma_x$, with a real coupling g between the levels (σ_x and σ_z denote Pauli matrices), showing an AC at $\lambda = 0$ of width $c = 2g$. The eigenstates are easily found [15,22] and from them we calculate the fidelity for the two-level system:

$$f_{\pm}(\lambda, \delta\lambda) = \frac{g^2 + \lambda(\bar{\lambda} - \lambda) + \lambda^2 + \bar{\lambda}\sqrt{g^2 + \lambda^2} + \lambda\sqrt{g^2 + \bar{\lambda}^2} + \sqrt{[g^2 + \lambda^2][g^2 + \bar{\lambda}^2]}}{2\sqrt{[g^2 + \lambda(\lambda \pm \sqrt{g^2 + \lambda^2})][g^2 + \bar{\lambda}(\bar{\lambda} \pm \sqrt{g^2 + \bar{\lambda}^2})]}}$$

where we used the shorthand notation $\bar{\lambda} \equiv \lambda + \delta\lambda$. To obtain the fidelity change in the limit $\delta\lambda \ll 1$, we need to expand the expression for the fidelity in a power series for $\delta\lambda$ and keep only the leading term proportional to $(\delta\lambda)^2$. The final expression is the same for both eigenstates (indexed by \pm) and has the simple form:

$$S_{\pm}(\lambda) = \frac{1}{8} \left(\frac{g}{g^2 + \lambda^2} \right)^2. \quad (2)$$

This is the square of a Lorentzian and differs significantly from zero only near the AC at $\lambda = 0$. This formula already allows us a good understanding of isolated ACs, as, for example, the peak width is easily computed as $\sigma^{\text{FWHM}} = 2g\sqrt{\sqrt{2} - 1}$. On the other hand an AC can be characterized by the ratio between the local energy level curvature and the distance between the two repelling energy levels. We call the absolute value of this ratio *renormalized curvature* $C_n(\lambda)$ and find

$$C_{\pm}(\lambda) \equiv \left| \frac{1}{\Delta(\lambda)} \frac{\partial^2 E_{\pm}(\lambda)}{\partial \lambda^2} \right| = 4S_{\pm}(\lambda) \quad (3)$$

for the two-level system. For higher-dimensional systems we expand the wave function $|n(\lambda + \delta\lambda)\rangle$ in second order in $\delta\lambda$ and find

$$S_n(\lambda) = \frac{1}{2} \sum_{m \neq n} \frac{|\langle m(\lambda)|H_2|n(\lambda)\rangle|^2}{[E_n - E_m]^2} \approx \frac{|\langle n'(\lambda)|H_2|n(\lambda)\rangle|^2}{2[E_n - E_{n'}]^2},$$

where we reduced the sum near an isolated AC to the nearest neighboring level n' . Similarly, one obtains for the renormalized curvature [23]

$$C_n(\lambda) = \left| \frac{2}{\Delta(\lambda)} \sum_{m \neq n} \frac{|\langle m(\lambda)|H_2|n(\lambda)\rangle|^2}{E_n - E_m} \right| \approx 2 \frac{|\langle n'(\lambda)|H_2|n(\lambda)\rangle|^2}{[E_n - E_{n'}]^2} = 4S_n(\lambda). \quad (4)$$

The relation $C_n \approx 4S_n$ thus holds as long as the effect of other levels can be neglected close to a single AC.

2.2. Beyond the two-level approximation

ACs in higher dimensional systems are not totally isolated, but other levels can contribute to the evolution of a quantum state as the parameter λ is varied. Consider two energy levels approaching each other as $\lambda \rightarrow 0$, and a third level being well separated by a distance ϵ in energy and weakly coupled to the first two levels. A Hamiltonian model for such a situation reads

$$H(\lambda) = \begin{pmatrix} -\lambda & g & g_{13} \\ g & \lambda & g_{23} \\ g_{13} & g_{23} & \epsilon \end{pmatrix}, \quad g_{ij}, \epsilon \in \mathbb{R}, \quad (5)$$

where we limited ourselves to real couplings. Since the first two levels become nearly degenerate and are well-separated from the third one, we can write this in degenerate perturbation theory [24] close to the crossing as

$$H_{\text{PT}}(\lambda) = \begin{pmatrix} -\lambda + \frac{g_{13}^2}{\epsilon} & g + \frac{g_{13}g_{23}}{\epsilon} \\ g + \frac{g_{13}g_{23}}{\epsilon} & \lambda + \frac{g_{23}^2}{\epsilon} \end{pmatrix} + \mathcal{O}(\epsilon^{-2}). \quad (6)$$

This reduces the three-level system to an effective two-level system taking the effect of the distant level perturbatively into account. The same procedure can be applied, in principal, to higher dimensional systems. The minimal distance c between the two levels of Eq. (6) is thus changed by the influence of the distant third level in first order to

$$c_{\text{PT}} = 2|g| \sqrt{\left(1 + \frac{g_{13}g_{23}}{2g\epsilon}\right)^2 + \left(\frac{g_{23}^2 - g_{13}^2}{2g\epsilon}\right)^2} \approx 2|g| \left(1 + \frac{g_{13}g_{23}}{2g\epsilon}\right), \quad (7)$$

where we kept only the leading order behaviour. The minimal distance in an isolated AC is accordingly only slightly changed, provided that the coupling to the third level is not much larger than between the two encountering levels and that the third level is well-separated from them. We need to compute the eigenstates $|E_{\pm}(\lambda + \delta\lambda, \epsilon)\rangle$ of Eq. (6) and then take their overlap for slightly different parameter values to obtain the fidelity, i.e., $f_{\pm}(\lambda, \delta\lambda, \epsilon) = |\langle E_{\pm}(\lambda, \epsilon) | E_{\pm}(\lambda + \delta\lambda, \epsilon) \rangle|$. The fidelity change can be computed by taking the second derivative of the fidelity at $\delta\lambda = 0$. The full expression is very long and difficult to grasp. Expanding it in inverse powers of ϵ and including just the first order correction to the simple two-level system, the fidelity change under the influence of a third not too close level is then given by

$$S_{\pm}^{\text{PT}}(\lambda, \epsilon) = \frac{1}{8} \frac{g^2}{(g^2 + \lambda^2)^2} \left[1 - \frac{2(gg_{13} + \lambda g_{23})(gg_{23} - \lambda g_{13})}{g(g^2 + \lambda^2)} + \mathcal{O}(\epsilon^{-2}) \right].$$

The correction due to the third level is also λ -dependent and changes the peak height at $\lambda = 0$. Let us also include the second order correction to the fidelity change at $\lambda = 0$ here

$$S_{\pm}^{\text{PT}}(\lambda = 0, \epsilon) = \frac{1}{8g^2} \left[1 - \frac{2g_{13}g_{23}}{\epsilon} - \frac{1}{2\epsilon^2} \frac{g_{13}^4 - 8g_{13}^2g_{23}^2 + g_{23}^4}{g^2} + \mathcal{O}(\epsilon^{-3}) \right].$$

If all off-diagonal matrix elements are of similar magnitude, the effect of the third level is characterised by its inverse distance to the AC. This underlines our claim that the effect of a third level on an AC is not too strong, provided that the level is not very close. But the latter does not take place when three levels undergo a joint AC, i.e., if there were no off-diagonal matrix elements coupling the levels they would all cross in one point. Such a situation cannot be reduced to an effective two-level system. We will in the following also study numerically the behaviour of the fidelity change in exactly this case, where the third level cannot be considered a simple perturbation to the two-level system, i.e., when the approximation of an *isolated* AC breaks down.

Three crossing levels can be generated, e.g., by the following real symmetric Hamiltonian

$$H(\lambda) = \begin{pmatrix} -\lambda & a & b \\ a & 0 & c \\ b & c & \lambda \end{pmatrix}, \quad (8)$$

which generalizes the above 2×2 -model. Fig. 1 shows that the fidelity change, defined in Eq. (1), is able to detect and to distinguish two nearby ACs in this system. Furthermore it reflects specific features of an AC in the shape of its peak, i.e., depending on the coupling g , $S_n(\lambda)$ shows a narrow peak of height $S(\lambda = 0) = 1/(8g^2)$.

We see already in this simple example that the renormalized curvature captures the form of the fidelity change $S_n(\lambda)$ close to an AC, with deviations arising from the admixture of a further level, which first and foremost affects the local curvature, i.e., the numerator in Eq. (3). But it also demonstrates that the fidelity change $S(\lambda)$ itself is still effective in detecting and characterizing the ACs.

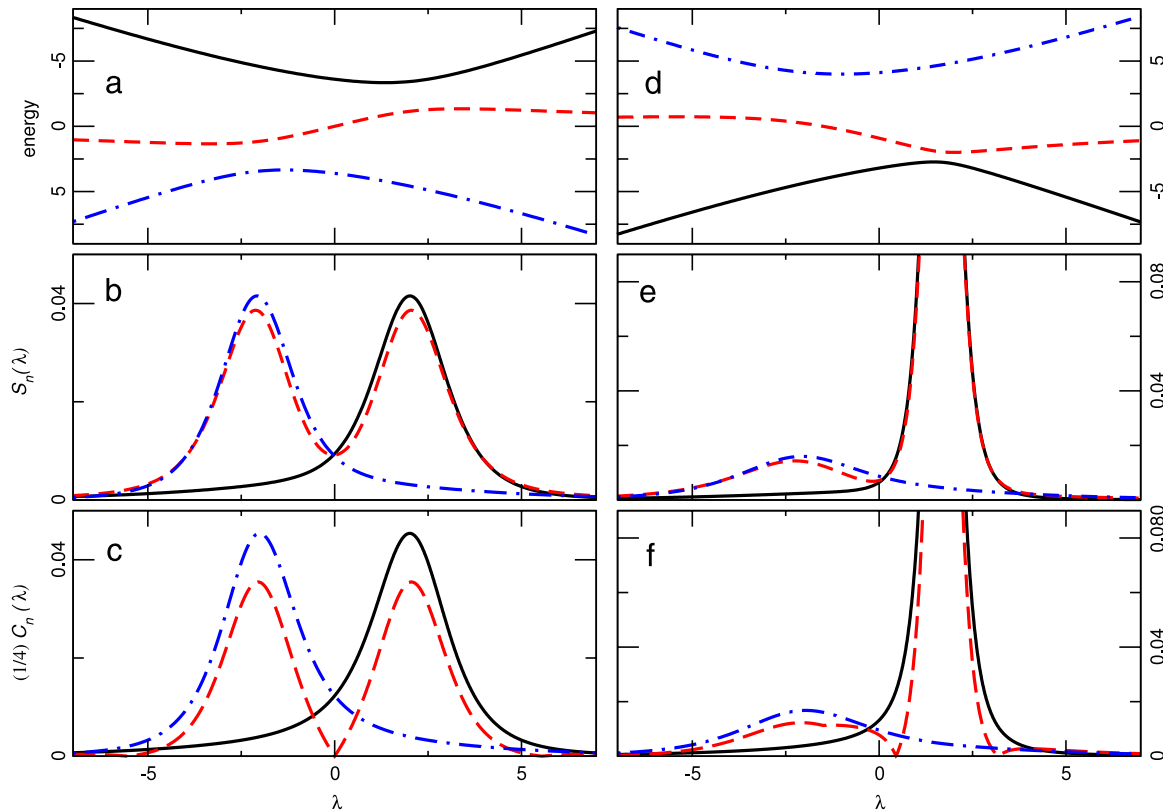


Fig. 1. (a) Energy spectrum of Eq. (8) for $a = 0$, $b = 2$, $c = 3$. All levels are coupled and the spectrum shows two close ACs; (b) fidelity change $S_n(\lambda)$ and (c) renormalized curvature $C_n(\lambda)$ for the energy levels of (a). (d) Energy spectrum for $a = 1$, $b = 2$, $c = 3$. All three levels are now directly coupled and the spectrum shows two close ACs. (e) $S_n(\lambda)$ and (f) $C_n(\lambda)$ for the energy levels of (d).

3. Application to complex systems

3.1. Quantum chaos model

A highly dense spectrum with many and possibly overlapping ACs is encountered in quantum chaotic systems as described by Random Matrix Theory (RMT) [15]. A prime example having such a dense complex spectrum is the combination of two random matrices drawn from the Gaussian orthogonal ensemble (GOE) [15]

$$H(\lambda) = \cos(\lambda)H_1 + \sin(\lambda)H_2, \quad H_1, H_2 \in \text{GOE}. \quad (9)$$

The distribution of minimal distances c at the ACs (normalized to unit mean) is then given by a Gaussian distribution $P(c) = (2/\pi) \exp[-c^2/\pi]$ [16]. Using our fidelity measure, we can directly detect the ACs in this system (by a numerical search for maxima of the S -function) and estimate also their widths. In the vicinity of a local maximum, the S -function has a Lorentzian shape as in Eq. (2) even in very dense quantum chaotic spectra. Under this assumption, we can thus extract the width of the AC as $c = 2g = 1/\sqrt{2S_{\max}}$, c.f. Eq. (2), from the local maximum S_{\max} . Averaging over many ACs, the fidelity allows the verification of the RMT prediction with high accuracy. This is demonstrated in Fig. 2 for large random matrices.

3.2. Bose–Hubbard system

To further exemplify the value of our fidelity measure, we apply it to a one-dimensional Bose–Hubbard Hamiltonian with additional Stark force [6,8,25]. This example of a many-body Wannier–Stark system can be realized with ultracold atoms in optical lattices and the relevant parameters may be changed using well-known experimental techniques [1]. This model describes N particles on L lattice sites, with hopping between adjacent sites and a local on-site interaction. As exemplified in Refs. [6,8], a gauge transformation into the force accelerated frame of reference turns a constant Stark force into a time-dependent phase $\exp(\pm iFt)$ with periodicity $T_B = 2\pi/F$ (the Bloch period). The corresponding Hamiltonian reads

$$H(t) = -\frac{J}{2} \sum_{l=1}^L (e^{iFt} a_{l+1}^\dagger a_l + \text{h.c.}) + \frac{U}{2} \sum_{l=1}^L n_l(n_l - 1), \quad (10)$$

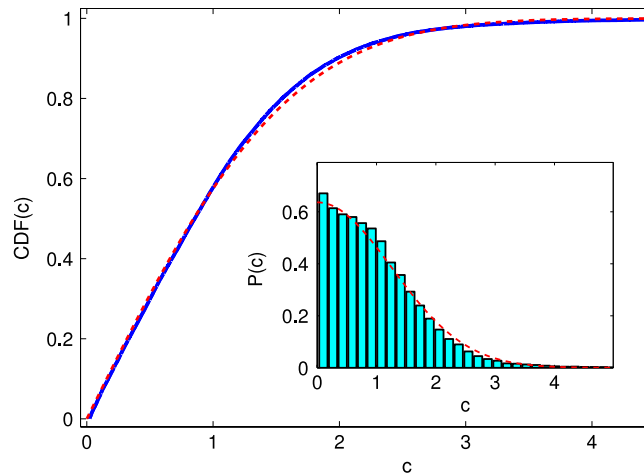


Fig. 2. Cumulative distribution of ACs determined from the fidelity change maxima for the RMT model of Eq. (9) with $\dim H_{1,2} = 1024$ and $\lambda \in [0, \pi[$ showing ca. 30,000 ACs: the numerical distribution (solid line) in excellent agreement with the RMT prediction $CDF(c) = \text{erf}(c/\sqrt{\pi})$ (dashed line). *Inset:* Distribution of widths of the ACs $P(c)$ (histogram) and the RMT prediction (dashed line).

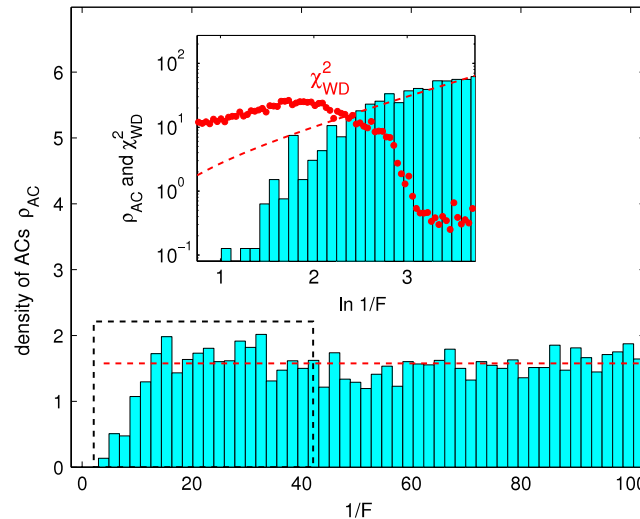


Fig. 3. Density of ACs ρ_{AC} in the quasienergy spectrum of the Floquet operator of our Bose–Hubbard model for varying F and fixed $J = 0.038$, $U = 0.032$, $N = L = 6$. The number of ACs as detected by the fidelity change increases with $1/F$ and saturates around $1/F \approx 20$ to an average value which is shown by the dashed line. *Inset:* Magnification of the region marked by the box on logarithmic scale with a comparison to a χ^2 test (with small values for good Wigner–Dyson statistics [8]).

where a_l^\dagger (a_l) creates (annihilates) a boson at site l and $n_l = a_l^\dagger a_l$ is the number of bosons at site l . The parameter J is the hopping matrix element, U the interaction energy for two atoms occupying the same site, and F the Stark force. Periodic boundary conditions are imposed for $H(t)$, such that the Hamiltonian and the one-period Floquet operator $\hat{U}_F(T_B) = \mathcal{T} \exp\left(-i \int_0^{T_B} H(t) dt\right)$ (where \mathcal{T} denotes time-ordering) decompose into a sum of operators for specific quasimomenta κ [6]. In the following, we use F as a control parameter. For $J \approx U \ll F$ the quasienergy spectrum (eigenphases of $\hat{U}_F(T_B)$) is dominated by the force F and the system is regular. Decreasing the force to $J \approx U \gtrsim F$ the quasienergy spectrum reorders and the coupling between the levels becomes more important. For fillings of order unity, e.g. $N/L \approx 1$, the system is quantum chaotic in this regime and the spectrum obeys Wigner–Dyson statistics [6,8]. As F is varied one observes an increasing number of ACs as the spectrum is changing and additionally many broad ACs once the quantum chaotic region is reached.

To illustrate the crossover between regions with few and many ACs, we study the density of ACs as detected by the fidelity change S_n , when changing the system parameter λ . In a histogram, the density $\rho_{AC}(\lambda)$ is defined via $\rho_{AC}(\lambda) \cdot d\lambda \equiv N_{AC}(\lambda) / \dim \mathcal{H}$, comparing the number of ACs $N_{AC}(\lambda)$ in the interval $[\lambda, \lambda + d\lambda]$ to the total number of energy levels $\dim \mathcal{H}$. This is shown in the main part of Fig. 3 where we observe no ACs at large F , i.e., small values of $1/F$, and an increasing number of ACs for larger values of $1/F$ that saturates around $1/F \approx 20$.

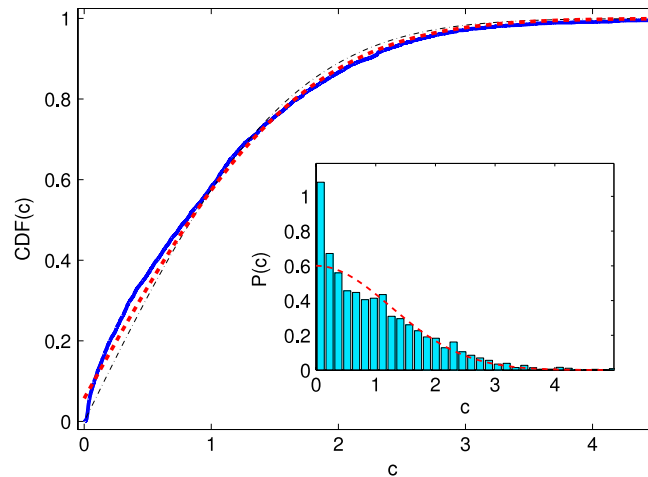


Fig. 4. Cumulative distribution of ACs determined from the fidelity change maxima for the system of Eq. (10). Shown are the numerical distribution (solid line), the best fit for a mixed RMT spectrum (thick dashed line, chaotic part $\gamma \approx 0.94$), and the RMT prediction for a purely chaotic spectrum (thin dashed-dotted line). Parameters: $N = 6$, $L = 7$, $J = 0.038$, $U = 0.032$, $F = 1/39 \dots 1/35$. *Inset:* Distribution of widths of ACs for the same model (histogram) and Eq. (11) with $\gamma \approx 0.94$ (dashed line). The enhancement close to $c = 0$ arises from regular “solitonic” states [26] in the spectrum.

The mentioned transition between regular and chaotic spectral properties for $J \approx U \gtrsim F$ and approximately integer filling in the tilted system can be visualized by comparing the actual level spacing distribution to a Wigner–Dyson distribution using a standard statistical χ^2 test [8]. This is displayed in the inset of Fig. 3 along with the density of ACs in Fig. 3. The fidelity change $S(1/F)$ detects ACs and shows the same qualitative behavior as the spectral statistics along the crossover from regular to chaotic dynamics: in regions of good Wigner–Dyson statistics we find a high density of ACs compared to a smaller number of ACs in the regular regime. The crossover beginning for $\log(1/F) \approx 2$, where the density of ACs rises above unity, i.e., on average each energy level undergoes more than one AC in the unit interval. The transition is complete for $\log(1/F) \approx 3$ where the χ^2 test saturates around a low value. However, the density of ACs alone is not able to distinguish regular from chaotic dynamics. Instead the ACs need to have a broad distribution of widths which is reflected in the distribution $P(c)$ introduced above.

By using the fidelity change in order to detect and characterize ACs, we can resolve further remarkable details in the full spectrum. With this method we are, e.g., able to detect a small number of regular states [26] traversing the chaotic sea of energy levels in the chaotic regime of the tilted Bose–Hubbard model. In this case the distribution of widths of ACs is a mixture of regular and quantum chaotic distributions:

$$P(c) = (1 - \gamma)\delta(c) + \frac{2\gamma^2}{\pi c} \exp\left[-\frac{\gamma^2 c^2}{\pi c^2}\right], \quad (11)$$

with a chaotic part of weight $0 \leq \gamma \leq 1$ [27]. A finite regular component makes itself visible as a strong enhancement of $P(c)$ close to zero, c.f., the inset of Fig. 4. We are able to estimate the size of this component by analyzing the cumulative distribution function $\text{CDF}(c) = 1 - \gamma + \gamma \text{erf}\left(\frac{\gamma c}{\sqrt{\pi}}\right)$. The result is shown in the main part of Fig. 4, where we plot the numerically obtained distribution and the best χ^2 -fit including a finite regular component. We obtain a chaotic part of $\gamma \approx 0.94$, corresponding to ca. 6% of regular levels, in good agreement with counting 7 regular levels out of 132 by direct inspection of the spectrum. Except for the identification of single regular levels [26], this has so far not been detected in the tilted Bose–Hubbard model by other statistical measures. The reported results are obtained for periodic boundary conditions applied to the Hamiltonian of Eq. (10), but we found a qualitatively similar picture for hard-wall boundary conditions, as used in Ref. [26]. Our results underline the value of fidelity as a measure for detecting ACs with high resolution in energy spectra.

4. Conclusions

We showed that quantum fidelity is perfectly suited to detect and characterize ACs in the energy spectrum. It therefore connects information about the wave function of a system with its spectrum, without direct reference to the energy levels by using only the overlap of wave functions [28]. This has been exemplified for simple models and for complex quantum systems showing many ACs. The fidelity, therefore, proves very useful to study many-body systems, also beyond their ground-state properties [9].

We expect a clear advantage of the fidelity change compared to spectral statistics in the sense that it can be applied, in principle, also just *locally* in the spectrum. This means that, if one is interested only in local spectral properties of a system, it is sufficient to follow a small number of levels to characterize the behavior of a system. For larger systems, computing

the entire spectrum and all eigenstates is in general difficult, but the fidelity allows an analysis of parts of the spectrum providing local spectral information. To make use of this advantage, one may resort to numerical algorithms optimized to access just a subset of eigenstates, e.g., the Lanczos algorithm [29]. We will pursue this interesting perspective of the fidelity proposed here in a future publication [30].

Acknowledgements

This work was supported by the HGSFP (DFG grant GSC 129/1), FOR760 (DFG grant WI 3426/3-1), the Frontier Innovation Fund, the Global Networks Mobility Measures, and the Klaus Tschira Foundation. We thank Rémy Dubertrand, Boris Fine, Andrea Tomadin, and especially Steve Tomsovic for many inspiring discussions.

References

- [1] I. Bloch, et al., *Rev. Modern Phys.* 80 (2008) 885; I. Bloch, *Nature* 453 (2008) 1016.
- [2] E. Arimondo, S. Wimberger, Tunneling of ultracold atoms in time-independent potentials, in: S. Keshavamurthy, P. Schlagheck (Eds.), *Dynamical Tunneling*, Taylor & Francis – CRC Press, Boca Raton, 2011 (in press).
- [3] D. Witthaut, et al., *Phys. Rev. Lett.* 101 (2008) 200402; M. Lubasch, et al., preprint. [arXiv:1009.4075](https://arxiv.org/abs/1009.4075).
- [4] J. Madroñero, et al., in: M. Scully, G. Rempe (Eds.), *Adv. At. Mol. Opt. Phys.*, vol. 53, Elsevier, Amsterdam, 2006, p. 33.
- [5] G. Montambaux, et al., *Phys. Rev. Lett.* 70 (1993) 497.
- [6] A.R. Kolovsky, A. Buchleitner, *Phys. Rev. E* 68 (2003) 056213.
- [7] A.R. Kolovsky, A. Buchleitner, *Europhys. Lett.* 68 (2004) 632; P. Buonsante, S. Wimberger, *Phys. Rev. A* 77 (2008) 041606(R).
- [8] A. Tomadin, et al., *Phys. Rev. Lett.* 98 (2007) 130402; A. Tomadin, et al., *Phys. Rev. A* 77 (2008) 013606.
- [9] P. Zanardi, N. Paunković, *Phys. Rev. E* 74 (2006) 031123; P. Buonsante, A. Vezzani, *Phys. Rev. Lett.* 98 (2007) 110601; S.-J. Gu, et al., *Phys. Rev. B* 77 (2008) 245109.
- [10] S. Sachdev, *Quantum Phase Transitions*, Cambridge University Press, 2001.
- [11] T. Gorin, et al., *Phys. Rep.* 435 (2006) 33; P. Jacquod, C. Petitjean, *Adv. Phys.* 58 (2009) 67.
- [12] C. Dembowsky, et al., *Phys. Rev. Lett.* 93 (2004) 134102; R. Höhmann, et al., *Phys. Rev. Lett.* 100 (2008) 124101.
- [13] S. Schlunk, et al., *Phys. Rev. Lett.* 90 (2003) 054101; M.F. Andersen, et al., *Phys. Rev. Lett.* 97 (2006) 104102; S. Wu, et al., *Phys. Rev. Lett.* 103 (2009) 034101.
- [14] S. Wimberger, A. Buchleitner, *J. Phys. B* 39 (2006) L145; M. Abb, et al., *Phys. Rev. E* 80 (2009) 035206(R).
- [15] F. Haake, *Quantum Signatures of Chaos*, Springer-Verlag, Berlin, 1991.
- [16] J. Zakrzewski, M. Kuś, *Phys. Rev. Lett.* 67 (1991) 2749.
- [17] S.-J. Wang, Q. Jie, *Phys. Rev. C* 63 (2000) 014309.
- [18] P. Giorda, P. Zanardi, *Phys. Rev. E* 81 (2010) 017203.
- [19] P. Plötz, Ph.D. Thesis, University of Heidelberg, 2010. Available online at <http://archiv.ub.uni-heidelberg.de/volltextserver/volltexte/2010/11123/>.
- [20] W.-L. You, et al., *Phys. Rev. E* 76 (2007) 022101.
- [21] M. Hiller, et al., *Phys. Rev. A* 79 (2009) 023621.
- [22] L.D. Landau, E.M. Lifshitz, *Quantum Mechanics: Non-relativistic Theory*, Pergamon Press, Oxford, 1977, §79.
- [23] P. Pechukas, *Phys. Rev. Lett.* 51 (1983) 943.
- [24] An excellent overview on this topic gives, e.g., J.H. Shirley, Interaction of a quantum system with a strong oscillating field, Ph.D. Thesis, California Institute of Technology, 1963. Available online at <http://resolver.caltech.edu/CaltechETD:etd-05142008-103758>.
- [25] P. Plötz, et al., *J. Phys. B* 43 (2010) 081001(FTC).
- [26] H. Venzl, et al., *Appl. Phys. B* 98 (2010) 647.
- [27] X. Yang, J. Burgdörfer, *Phys. Rev. A* 48 (1993) 83.
- [28] A similar connection, yet in the deep semiclassical regime, between spectral properties and fidelity is identified in H. Kohler, et al., *Phys. Rev. Lett.* 100 (2008) 190404.
- [29] C. Lanczos, *J. Res. Natl. Bur. Stand.* 45 (1950) 225; A. Buchleitner, et al., *J. Opt. Soc. Am. B* 12 (1994) 505.
- [30] C. Parra-Murillo, J. Madroñero, S. Wimberger (in preparation).

Engineering of Landau–Zener tunneling

G. Tayebirad · R. Mannella · S. Wimberger

Received: 29 June 2010 / Revised version: 30 September 2010 / Published online: 11 February 2011
© Springer-Verlag 2011

Abstract Several ways are discussed to control the Landau–Zener tunneling in the Wannier–Stark system. We focus on a realization of this system with interacting and noninteracting ultracold bosons. The tunneling from the ground band to the continuum is shown to depend crucially on the initial condition and system parameters and, more interestingly, on added time-dependent disorder—noise—on the lattice beams.

1 Introduction

Bloch oscillations, Landau–Zener (LZ) tunneling, and Wannier–Stark ladders [1–11], are fundamental quantum effects occurring in a system of electrons moving in a periodic potential and subjected to a constant electric field. Due to complications such as impurities, lattice vibrations, and multiparticle interactions, clean observations of these effects have been difficult [12]. In recent years, ultra-cold atoms and Bose–Einstein condensates in optical lattices have been increasingly used to simulate solid state systems and the above mentioned phenomena [6–10, 13–17]. Optical lattices are

nowadays easy to realize in the laboratory, and their parameters can be perfectly controlled both statically and dynamically, which makes them attractive model systems for crystal lattices. More complicated potentials can be realized by adding further lattice beams [18–24]. In fact, by superimposing laser beams from different directions and with slightly different wave-lengths, it is possible to generate many different three-dimensional lattice geometries [16, 17]. The question arises of how to control the dynamics of particles by quasi-periodic potentials (possibly time-dependent or even stochastic ones).

In this paper, we present results on the Wannier–Stark system realized with ultracold atoms, forming a Bose–Einstein condensate, in an optical lattice [6–10, 14, 25–29]. We compute the time dependence of the tunneling probability of the Bose–Einstein condensate atoms out of the ground band in which they were originally prepared. By changing the initial condition and the system parameters and introducing atom–atom interactions into the system, we are able to control the tunneling rate of the Bose–Einstein condensate to higher bands. Finally, a controlled noise added to the system will be shown to be a further handle to engineer the interband tunneling.

2 Landau–Zener tunneling in optical lattices

We study the temporal evolution of ultracold atoms loaded into a quasi one-dimensional optical lattice which can be a spatially periodic potential or a time-dependent stochastic potential, subjected to an additional static force, in the presence of weak atom–atom interactions [29]. We use the following general form of the three-dimensional Gross–Pitaevskii equation to model the temporal evolution

G. Tayebirad (✉) · S. Wimberger
Institut für Theoretische Physik, Universität Heidelberg,
Philosophenweg 19, 69120 Heidelberg, Germany
e-mail: g.Tayebirad@thphys.uni-Heidelberg.de

R. Mannella
CNR-INFM and Dipartimento di Fisica ‘E. Fermi’,
Università di Pisa, Largo Pontecorvo 3, 56127 Pisa, Italy

S. Wimberger
Center for Quantum Dynamics, Universität Heidelberg,
Heidelberg, Germany

of the atoms

$$H = -\frac{\hbar^2}{2M}\nabla_{\vec{r}}^2 + W(\vec{r}, t) + g_{3D}|\Psi(\vec{r}, t)|^2 + Fx;$$

$$W(\vec{r}, t) = V_{\text{trap}}(\vec{r}) + V_1(x) + V_2(x, t), \quad (1)$$

with lattice potentials along the longitudinal direction, x , as

$$V_1(x) = \alpha V \sin^2\left(\frac{\pi x}{d_L}\right); \quad (2a)$$

$$V_2(x, t) = \alpha V \sin^2\left(\frac{\pi x}{d'_L} + \phi(t)\right). \quad (2b)$$

M is the mass of condensate atoms and F is the Stark force. $V_1(x)$ and $V_2(x, t)$ are spatially periodic potentials with incommensurate lattice spacings d_L and d'_L , respectively. As will be shown below around (9), the noise has a tendency to average over the second lattice, and therefore the amplitudes of the two lattices should be comparable. For convenience we chose equal amplitudes αV and $d_L = 426$ nm and $d'_L = d_L(\sqrt{5} - 1)/2$ for the lattice constants. The potential $V_2(x, t)$ is a time-dependent stochastic potential with a time-dependent stochastic phase $\phi(t)$, which we will characterize further down in Sect. 2.2. The renormalization factor α is introduced to be able to compare the dynamics in the presence of the potential given by (2a) and (2b) to the dynamics of the “reference system”, i.e. the dynamics in the potential $W(\vec{r}) = V_{\text{trap}}(\vec{r}) + V \sin^2(\frac{\pi x}{d_L})$. α will be chosen in such a way that the following standard deviations are equal:

$$\left\langle \left(\sin^2\left(\frac{\pi x}{d_L}\right) - \left\langle \sin^2\left(\frac{\pi x}{d_L}\right) \right\rangle_x \right)^2 \right\rangle_x$$

$$= \left\langle \left(V_{\text{eff}}(x) - \langle V_{\text{eff}}(x) \rangle_x \right)^2 \right\rangle_x, \quad (3)$$

where the effective potential $V_{\text{eff}}(x)$ will be defined in Sect. 2.2. The average $\langle \cdot \rangle$ is an integral over space for a sufficiently large L , i.e., $\langle \cdot \rangle = 1/L \int_{-L/2}^{L/2} dx$. The third term in the Hamiltonian is the non-linearity, which makes the equation different from the Schrödinger equation. $\Psi(\vec{r}, t)$ represents the condensate wave function and $|\Psi(\vec{r}, t)|^2$ the local atomic density. $g_{3D} = \frac{4\pi\hbar^2 a_s N_0}{M}$ is the coupling constant which is proportional to the scattering length a_s and determines the strength of atom–atom interactions, where $\frac{4\pi\hbar^2 a_s}{ME_R} \approx 2.45 \times 10^{-21} \text{ m}^3$, with $a_s = 53 \times 10^{-10} \text{ m}$ and $M = 1.44 \times 10^{-25} \text{ kg}$ for rubidium 87. N_0 is the number of atoms in the condensate. The recoil energy $E_R = p_R^2/2M$ and the recoil momentum $p_R = \pi\hbar/d_L$ are the characteristic energy and momentum scales for our system. Moreover, we define $V_0 = V/E_R$ and $F_0 = Fd_L/E_R$ as dimensionless quantities in this energy unit. Experimentally, the

initial state is the relaxed condensate wave function prepared in the confining potential given by a harmonic trap $V_{\text{trap}} = \frac{1}{2}m(\omega_\rho^2 \rho^2 + \omega_x^2 x^2)$, with $\omega_x \ll \omega_\rho$ for a quasi 1D situation, and then loaded adiabatically into the optical lattice when the Stark force F equals zero. Then ω_x is either switched off or relaxed to a small value $\omega_{x,\text{rel}}$ and the Stark force F is simultaneously switched on to induce the dynamics. In the following sections we study the system in the presence/absence of different terms of the above Hamiltonian.

2.1 Noise free case

2.1.1 Linear case—Wannier–Stark problem

For zero or small $\omega_{x,\text{rel}}$ (cf., e.g., [30]) and negligible atom–atom interactions, when $V_2(x, t) = 0$ and $\alpha = 1$, the above Hamiltonian in (1) describes the dynamics of atoms in a tilted periodic potential which is the well-known single-particle Wannier–Stark problem. Without the non-linearity term, we can use the 1D version of (1) for our simulations. In the presence of F , the quasimomentum of a condensate (initially prepared at the center of the Brillouin zone in the ground band) scans the lower band in an oscillating motion periodically—so-called Bloch oscillations—with the Bloch period $T_B = 2\hbar(Fd_L)^{-1}$. At the edge of the Brillouin zone, where the gap between the ground and the first excited band ΔE of the $F = 0$ system (increasing with V_0 [31]), acquires its minimum value, a tunneling of the condensate to the first excited energy band may occur. The tunneled atoms escape from the system through successive tunneling events across the much smaller band gaps between the upper bands. This phenomenon is known as the LZ tunneling. LZ theory predicts a decay rate

$$P_{\text{LZ}} = e^{-\frac{\pi}{\gamma}}, \quad (4)$$

where γ is the adiabaticity parameter and $\gamma \approx \frac{32F_0}{\hbar V_0}$ [31].

In order to study the LZ prediction for our system we need to access the decay rate of the population from the ground band. In that respect, we compute the time dependence of the probability of the condensate to remain in the ground band in which it has been initially prepared. Such a survival probability is best measured in momentum space. From the time-dependent momentum distribution we can determine $P_{\text{sur}}(t)$ by projection of the evolved state $\tilde{\Psi}(\vec{p}, t)$ on to the support of the initial state [30, 32, 33]

$$P_{\text{sur}}(t) = \int_{-\infty}^{\infty} \int_{-\infty}^{\infty} dp_y dp_z \int_{-p_c}^{\infty} dp_x |\Psi(\vec{p}, t)|^2, \quad (5)$$

where p_c is an ad hoc cut-off momentum. In our calculation we chose $p_c = 3p_{\text{rec}}$. Then (5) starts to measure the

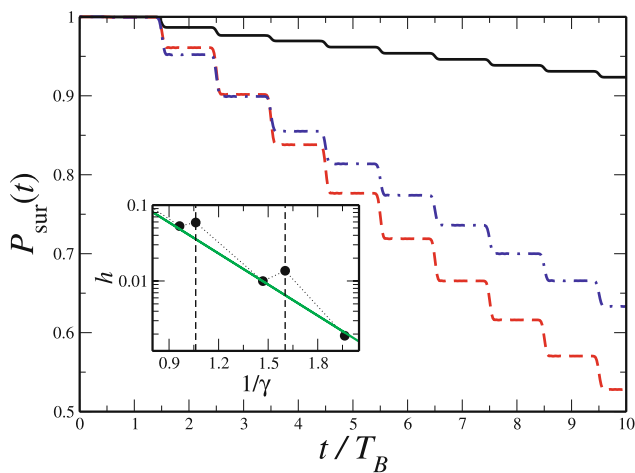


Fig. 1 Time-resolved survival probability of the BEC in the ground band, for a lattice depth $V_0 = 4$, and a narrow width of the initial momentum distribution of the BEC cloud, $\Delta p/2p_R = 0.05$ (trap frequency $\omega_x = 2\pi \times 50$ Hz), and various Stark forces. For non-RET condition: $F_0 = 1.07$ (solid line) and $F_0 = 1.63$ (dash-dotted line); for RET condition: $F_0 = 1.48$ (dashed line). Inset: height of one step (of data as shown in the main panel) for fixed $V_0 = 4$ and various γ . The step height as predicted by (4) (solid line) in comparison with the numerically obtained values (filled circles). A significant deviation from the LZ prediction can be observed at values of $1/\gamma$ corresponding to RET conditions and marked by the vertical dashed lines

wave packet leaving the ground band with an artificial delay of one Bloch period, since by the acceleration theorem the average momentum is proportional to time (more details can be found in [30, 32, 33]). A very nice step structure—local deviation from the overall exponential decay—can be seen in the survival probability (see Figs. 1 and 2). Such step structures reflect the above mentioned phenomena, i.e., Bloch oscillations and LZ tunneling. One can see that the tunneling events from the ground band to the next band occur after each Bloch period when the wave packet is at the edge of the Brillouin zone. It is possible to control the LZ tunneling of the Bose–Einstein condensate from the ground band in the linear system and in the absence of atom–atom interactions by

- Changing the system parameters, such as external force F_0 , and the amplitude of the optical lattice V_0 (see Fig. 1)
- Exploiting resonantly enhanced tunneling (RET) between degenerate Wannier–Stark states at $\Delta E \approx n \times Fd_L$ with n being an integer number (see Fig. 1) [11]
- Changing the initial condition by changing the trap frequencies and hence preparing the Bose–Einstein condensate with different widths Δp of its initial momentum distribution (see Fig. 2)

As seen in Fig. 1, increasing the tilting force leads to more and more tunneling of the atoms from the ground band. On the other hand, depending on the system parameters, one can tune into a special condition for which the rate of the tunnel-

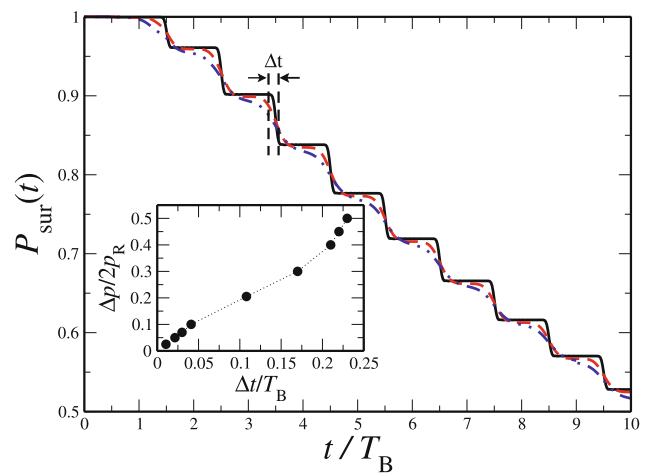


Fig. 2 The survival probability of the BEC in the ground band for a lattice depth $V_0 = 4.0$, a constant Stark force $F_0 = 1.48$, and various widths of the initial momentum distribution of the BEC cloud, $\Delta p/2p_R = 0.05$ (solid line); $\Delta p/2p_R = 0.2$ (dashed line); $\Delta p/2p_R = 0.3$ (dash-dotted line). Inset: step width Δt for several Δp (filled circles). The step width Δt is the distance between the two vertical dashed lines shown in the main panel for the case of $\Delta p/2p_R = 0.05$

ing is enhanced. This occurs when an integer multiple of the energy scale of the tilting force Fd_L matches the energy difference between the initial state and the final state, i.e., approximately the band gap ΔE . This phenomenon has been observed experimentally [27, 28] and is called resonantly enhanced tunneling (RET). A deviation from the LZ prediction is expected in this case. In order to see whether the tunneling probability given by the standard LZ tunneling probability correctly predicts the height of a step corresponding to a single tunneling event, we fit a step function to our step-like survival probability and extract the height of each step. The result and the comparison to the LZ prediction is shown in the inset of Fig. 1. When the system parameters are in the RET condition (e.g., $1/\gamma \approx 1.05$ and 1.6), the height of the steps of the survival probability increases and shows a significant deviation from the LZ prediction given in (4). This behavior is seen in Fig. 1 where the survival probability for $F_0 = 1.48$ decays much faster than for the other two cases. Since the derivation of (4) [31] does not take into account the actual Wannier–Stark level structure, which is necessary to describe the RET condition, (4) or the survival probability derived from it cannot describe the enhancement of the tunneling probability due to RET.

The other parameter which can affect the survival probability is the width Δp of the initial momentum distribution. By changing the trap frequencies ω_x and ω_p one can prepare the initial distribution with different widths. Figure 2 demonstrates the dependence of the width of the steps Δt on Δp . The steps are smooth and partly washed out since the wave packet reaches the edge of the Brillouin zone earlier

when it has a broader initial momentum distribution. Still the remnants of the steps cause a local deviation from the exponential decay of the tunneling probability. Nevertheless, the survival probability exhibits an exponential decay globally in time, i.e., on large time scales, for all the mentioned cases.

2.1.2 Non-linear case—Gross–Pitaevskii equation

In the regime of weak atom–atom interactions the effect of interactions is studied in the mean-field regime based on the Gross–Pitaevskii equation. The 3D Gross–Pitaevskii equation can describe the dynamics of the entire Bose–Einstein condensate in terms of an equation of motion for a single-particle wave function. Therefore, the following non-linear equation describes the dynamics of interacting Bose–Einstein condensate atoms in a tilted periodic potential ($V_2(x, t) = 0$) with $\alpha = 1$:

$$H = -\frac{\hbar^2}{2M}\nabla_{\vec{r}}^2 + V_{\text{trap}}(\vec{r}) + V_1(x) + g_{3D}|\Psi(\vec{r}, t)|^2 + Fx. \tag{6}$$

As mentioned in Sect. 2, g_{3D} is the coupling constant calculated from the s-wave scattering wavelength a_s and the number of atoms in the condensate N_0 . $|\Psi(\vec{r}, t)|^2$ is the local atomic density. As an estimate for the non-linear term in (6), we define $C \equiv \frac{g_{3D}|\Psi(\vec{r}, t)|^2|_{\text{peak}}}{E_R}$ at the peak density of the initial state. The following effects can be seen by increasing the strength of a repulsive non-linearity ($g_{3D} > 0$) in the system:

- Enhancement of the tunneling rate
- Deviation from mono-exponential decay
- Washed out steps (corresponding to damped Bloch oscillations)

According to our results shown in Fig. 3 for a RET case and the experimental results in [27, 28], the temporal behavior of the survival probability depends on the strength of atom–atom interactions. As can be found with more detail in [27, 30], the enhancement of decay rate is generic for repulsive interactions. The scaling of the decay rate as a function of non-linearity is yet more interesting in the RET case (see the inset of Fig. 3). We can quantify the decay rate Γ of the survival probability by globally fitting an exponential decay function to the step-like curves of the survival probability. Such rates, for various non-linearities, are depicted in the inset of Fig. 3. A repulsive interaction initially enhances the interband tunneling probability of the ultracold atoms [30]. Since the tunneling events occurring at different integer multiples of the Bloch period are correlated by the presence of the non-linearity, a clear deviation from the mono-exponential decay is observed making the definition

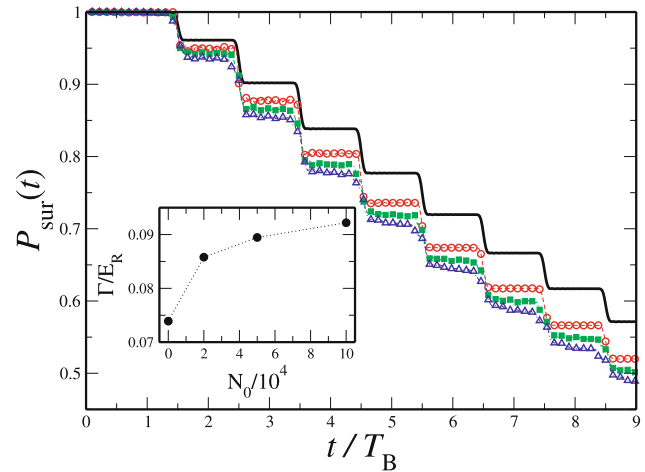


Fig. 3 Time-resolved survival probability in the ground band for the non-linear case with $V_0 = 4.0$, $F_0 = 1.48$ (RET), a narrow width of the initial momentum distribution of the BEC cloud, $\Delta p/2p_R = 0.05$, and composed of the following number of atoms prepared in a trap with $\omega_x = 2\pi \times 50$ Hz and $\omega_\rho = 2\pi \times 100$ Hz: $N_0 = 2 \times 10^4$, $C \approx 0.2$ (open circles); $N_0 = 5 \times 10^4$, $C \approx 0.32$ (filled squares); $N_0 = 1 \times 10^5$, $C \approx 0.42$ (open triangles) as compared to the linear case $g_{3D} = 0$, (solid line). Inset: Decay rate of the survival probability Γ at RET condition vs. N_0 (filled circles)

of a global decay rate Γ somewhat problematic [34]. A continuous change in the density of the condensate in time due to escaped particles from the system leads to a decreasing impact of the non-linearity. Therefore, the time local rate of decay systematically decreases as the time increases. Additionally, the non-linearity leads to a dephasing and damping of the Bloch oscillations, not discussed here, but a discussion of this phenomenon can be found in [14–16, 35, 36].

2.2 Impact of a time-dependent stochastic potential (noisy Wannier–Stark problem)

Going back to the linear system, $g_{3D} = 0$, the case of $V_2(x, t) \neq 0$ leads to a time-dependent stochastic potential where we claim that we are able to control the dynamics of the Bose–Einstein condensate atoms by changing the characteristic parameters of the time-dependent stochastic phase $\phi(t)$. α is no longer 1 and we can calculate it as defined above by (3), using the effective potential introduced below in (9). We use correlated noise for the time-dependent phase $\phi(t)$ for the second lattice. A standard example is exponentially correlated noise, which is characterized by a single correlation time. Such a noise can be obtained from linearly filtered white noise as

$$\dot{\phi} = -\frac{\phi}{\tau} + \frac{\sqrt{2D}}{\tau}\xi(t), \tag{7}$$

where ξ is a Gaussian white noise with zero mean and standard deviation equal to one. τ is the correlation time of the

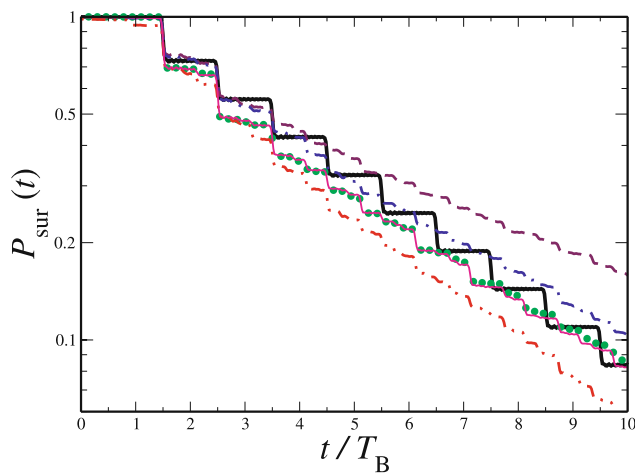


Fig. 4 Time evolution of the survival probability for $V_0 = 2.5 E_R$, $F_0 = 1.5$, and $\alpha \approx 0.82$; The thick solid line is the decay of the reference system defined by (1) with $g_{3D} = 0$, $V_2(x, t) = 0$ and $\alpha = 1$; in the presence of exponentially correlated noise with $D/\tau \approx 0.25$ and correlation times: $\tau = 10 T_B$ (dashed line), $\tau = 1 T_B$ (dot-dashed line), $\tau = 0.05 T_B$ (dot-dot-dashed line), $\tau = 0.001 T_B$ (thin solid line); results for the effective potential of (9) are shown by the filled circles

noise and the strength of the noise is given by the parameter D . The introduced noise has a zero mean ($\langle \phi(t) \rangle = 0$) and an exponential correlation function $\langle \phi(t)\phi(s) \rangle = D/\tau \exp(-|t-s|/\tau)$. τ describes the time-scale of the fluctuations and D/τ its variance. The power spectrum of the exponentially correlated noise is given by a Lorentzian function as

$$S(\omega) = \frac{D}{\pi(1 + \omega^2\tau^2)}. \tag{8}$$

Figure 4 demonstrates the survival probability of the atoms in the ground band for various correlation times τ and a fixed value of the variance $D/\tau \approx 0.25$ of the noise. The system parameters are $V_0 = 2.5 E_R$ and $F_0 = 1.5$ (non-RET condition). The solid line shows the time evolution of the survival probability for the reference system introduced by (1) with $g_{3D} = 0$, $V_2(x, t) = 0$ and $\alpha = 1$. A nice step structure similar to the ones depicted in Figures 1 and 2 is observed for this case. The other curves in Fig. 4 exhibit the time evolution of the survival probability for the temporally disordered system introduced in (1) with $g_{3D} = 0$, $V_2(x, t) \neq 0$ and $\alpha \neq 1$. As seen for all the cases the step structure is washed out. Considering the characteristic parameters of the exponentially correlated noise, different regimes of the noise are introduced. The regime of slowly varying noise is recovered when the noise has a large correlation time compared with the time scales of the system (e.g., T_B). The tunneling probability of the atoms in such a regime is suppressed (e.g., for $\tau = 10 T_B$ shown by the dashed line in Fig. 4). Decreasing the correlation time the rate of tunneling increases but, nevertheless, for $\tau \geq T_B$ the noise suppresses the tunneling compared with the reference system (see the data for

$\tau = 1 T_B$ as shown by the dot-dashed line in Fig. 4). For correlation times smaller than T_B , the noise recovers the regime of fast noise (e.g., for $\tau = 0.05 T_B$) and causes an enhancement in the tunneling rate (dot-dot-dashed line) compared with the reference system (thick solid line). Surprisingly a further decrease of the correlation time decreases the tunneling rate of the atoms (e.g., for $\tau = 0.001 T_B$ depicted by the thin solid line).

In order to understand the effect of the time-dependent stochastic potential on the system, we renormalize the potential. The time-dependent potential can be replaced by a suitable static effective potential in the limit of small τ . Such an effective potential can be calculated integrating over all possible phases giving:

$$V_{\text{eff}}(x) = \alpha V [\sin^2(\pi x/d_L) + \beta \sin^2(\pi x/d'_L)], \tag{9}$$

with a renormalization factor for the second lattice $\beta = e^{-2D/\tau}$. Equation (9) provides a time-independent potential which can be used to compute α as stated in (3). As seen in Fig. 4 the survival probability for a small $\tau = 0.001 T_B$ (thin solid line) shows perfect agreement with the results achieved using the effective potential of (9) (filled circles).

Keeping the noise parameters constant, we study the decay rate of the survival probability, Γ , of the condensate for various system parameters. The results of a scan over the Stark force are shown in Fig. 5(a). The simulations have been done for three values of the correlation time of the noise $\tau = 0.0005, 0.05, 50 T_B$, keeping the variance of the noise constant (here $D/\tau \approx 0.25$). The three correlation times are chosen from the left shoulder, the peak point and the right shoulder of curves in Fig. 5(b). The solid line depicts the decay rate of the reference system (given by (1) with $g_{3D} = 0$, $V_2(x, t) = 0$ and $\alpha = 1$). Noise in the system leads to a washing out of the RET peaks (present in the solid line of Fig. 5(a)) in the decay rate, and, dependent on the correlation time of the noise, a suppression (for very large and very small values of τ) or an enhancement of the tunneling (e.g., for $\tau \approx 0.05 T_B$) can be obtained.

We also ran a scan over the correlation time of the noise τ , again keeping the variance of the noise constant ($D/\tau \approx 0.25$). The decay rate of the survival probability for three amounts of the Stark force ($F_0 = 0.95, 1.25, 1.5$) is shown in Fig. 5(b). Comparing the symbols to the lines (which specify the decay rate in the corresponding reference system) one can realize that the decay rate is enhanced when the system parameters do *not* fulfill the RET condition, i.e., in this case for $F_0 = 0.95$ and 1.5 . For the case of $F_0 = 1.25$ (RET) the tunneling rate is suppressed, and the symbols lie always below the reference line (dot-dot-dashed line). The enhancement is pronounced in the range of $\tau \approx 0.005 \dots 0.2 T_B$, corresponding to an energy scale equal or larger to/than the band gap ΔE . On the other hand, for small values of the correlation time, the noise recovers

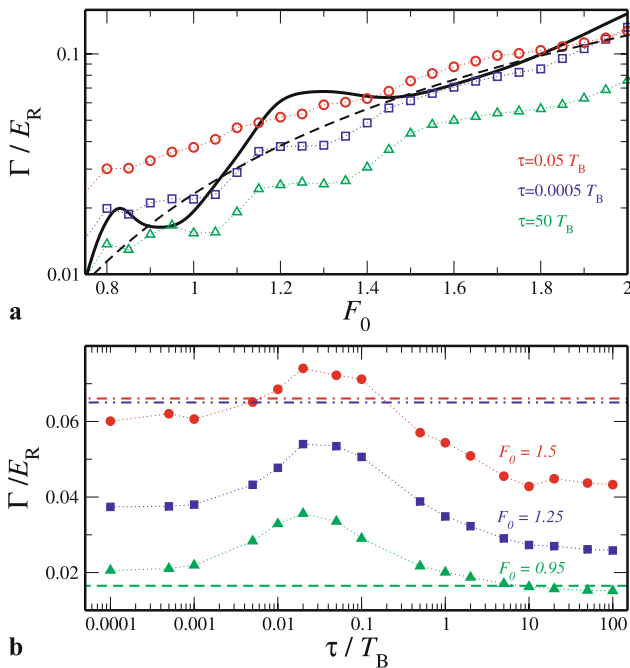


Fig. 5 The decay rate of the survival probability for $V_0 = 2.5 E_R$, and $D/\tau \approx 0.25$: **(a)** scan over F_0 for $\tau = 0.0005 T_B$ (open squares), $\tau = 0.05 T_B$ (open circles), $\tau = 50 T_B$ (open triangles), for the reference system (solid line), and the Landau–Zener exponential prediction for the reference system (dashed line); **(b)** scan over τ for $F_0 = 1.5$ (filled circles) and its reference system (dot–dot–dashed line), $F_0 = 1.25$ (filled squares) and its reference system (dot–dashed line), $F_0 = 0.95$ (filled triangles) and its reference system (dashed line)

the regime of white noise, where the effective potential describes the dynamics of the system very well, and for large values of τ , the system is in the regime of a slowly varying noise corresponding to energy scales that do not help to enhance the tunneling of atoms either.

3 Conclusion

It is possible to control the Landau–Zener (LZ) tunneling probability of the ultracold atoms from the ground band in tilted optical lattices. This control is possible by changing the system parameters such as the lattice depth and the Stark force, or by changing the initial condition which is given by the initial width of the momentum distribution of the BEC. All the mentioned parameters can be easily tuned experimentally. Furthermore, our calculations showed that atom–atom interactions affect the LZ tunneling probability and a repulsive interaction typically leads to an enhancement of the LZ tunneling of the ultracold atoms from the ground band. Most interestingly, our results demonstrate that it is also possible to control the tunneling by adding noise to the system. By changing the noise parameters, the tunneling probability can be enhanced or suppressed. The noise

can particularly enhance the tunneling probability when the system parameters are chosen far from the RET condition.

Acknowledgements We acknowledge funding by the Excellence Initiative by the German Research Foundation (DFG) through the Heidelberg Graduate School of Fundamental Physics (grant number GSC 129/1) and the Global Networks Mobility Measures. S.W. is grateful to the Heidelberg Academy of Sciences and Humanities for the Academy Award 2010 and to the Hengstberger Foundation for support by the Klaus-Georg and Sigrid Hengstberger Prize 2009. G.T. thanks the Landesgraduiertenförderung Baden-Württemberg for support.

References

1. L.D. Landau, Phys. Z. Sowjetunion **2**, 46 (1932)
2. C. Zener, Proc. R. Soc. A **137**, 696 (1932)
3. E.C.G. Stückelberg, Helv. Phys. Acta **5**, 369 (1932)
4. E. Majorana, Nuovo Cimento **9**, 43 (1932)
5. K. Leo, P.H. Bolivar, F. Brueggemann, R. Schwedler, K. Koehler, Solid State Commun. **84**, 943 (1992)
6. E. Peik, M. Ben Dahan, I. Bouchoule, Y. Castin, C. Salomon, Phys. Rev. A **55**, 2989 (1997)
7. M. Ben Dahan, E. Peik, J. Reichel, Y. Castin, C. Salomon, Phys. Rev. Lett. **76**, 4508 (1996)
8. S.R. Wilkinson, C.F. Bharucha, K.W. Madison, Q. Niu, M.G. Raizen, Phys. Rev. Lett. **76**, 4512 (1996)
9. S.R. Wilkinson, C.F. Bharucha, K.W. Madison, Q. Niu, M.G. Raizen, Nature (London) **387**, 575 (1997)
10. B.P. Anderson, M.A. Kasevich, Science **282**, 1686 (1998)
11. M. Glück, A.R. Kolovsky, H.J. Korsch, Phys. Rep. **366**, 103 (2002)
12. K. Leo, High-Field Transport in Semiconductor Superlattices (Springer, Berlin, 2003)
13. Q. Niu, M.G. Raizen, Phys. Rev. Lett. **80**, 3491 (1998)
14. O. Morsch, J.H. Müller, M. Cristiani, D. Ciampini, E. Arimondo, Phys. Rev. Lett. **87**, 140402 (2001)
15. G. Roati, E. de Mirandes, F. Ferlaino, H. Ott, G. Modugno, M. Inguscio, Phys. Rev. Lett. **92**, 230402 (2004)
16. O. Morsch, M. Oberthaler, Rev. Mod. Phys. **78**, 179 (2006)
17. I. Bloch, J. Dalibard, W. Zwerger, Rev. Mod. Phys. **80**, 885 (2008)
18. L. Santos, M.A. Baranov, J.I. Cirac, H.-U. Everts, H. Fehrmann, M. Lewenstein, Phys. Rev. Lett. **93**, 030601 (2004)
19. D. Clément, A.F. Varón, J.A. Retter, L. Sanchez-Palencia, A. Aspect, P. Bouyer, J. New, New J. Phys. **8**, 165 (2006)
20. L. Sanchez-Palencia, D. Clément, P. Lugan, P. Bouyer, A. Aspect, New J. Phys. **10**, 045019 (2008)
21. P. Lugan, D. Clément, P. Bouyer, A. Aspect, M. Lewenstein, L. Sanchez-Palencia, Phys. Rev. Lett. **98**, 170403 (2007)
22. T. Schulte, S. Drenkelforth, G. Kleine Büning, W. Ertmer, J. Arlt, M. Lewenstein, L. Santos, Phys. Rev. A **77**, 023610 (2008)
23. T. Salger, C. Geckeler, S. Kling, M. Weitz, Phys. Rev. Lett. **99**, 190405 (2007)
24. T. Salger, S. Kling, T. Hecking, C. Geckeler, L. Morales-Molina, M. Weitz, Science **326**, 1241 (2009)
25. M. Cristiani, O. Morsch, J.H. Müller, D. Ciampini, E. Arimondo, Phys. Rev. A **65**, 063612 (2002)
26. M. Jona-Lasinio, O. Morsch, M. Cristiani, N. Malossi, J.H. Müller, E. Courtade, M. Anderlini, E. Arimondo, Phys. Rev. Lett. **91**, 230406 (2003)
27. C. Sias, A. Zenesini, H. Lignier, S. Wimberger, D. Ciampini, O. Morsch, E. Arimondo, Phys. Rev. Lett. **98**, 120403 (2007)
28. A. Zenesini, C. Sias, H. Lignier, Y. Singh, D. Ciampini, O. Morsch, R. Mannella, E. Arimondo, A. Tomadin, S. Wimberger, New J. Phys. **10**, 053038 (2008)

29. A. Zenesini, H. Lignier, G. Tayebirad, J. Radogostowicz, D. Ciampini, R. Mannella, S. Wimberger, O. Morsch, E. Arimondo, *Phys. Rev. Lett.* **103**, 090403 (2009)
30. S. Wimberger, R. Mannella, O. Morsch, E. Arimondo, A.R. Kolovsky, A. Buchleitner, *Phys. Rev. A* **72**, 063610 (2005)
31. M. Holthaus, *J. Opt. B* **2**, 589 (2000)
32. G. Tayebirad, A. Zenesini, D. Ciampini, R. Mannella, O. Morsch, E. Arimondo, N. Lörch, S. Wimberger, *Phys. Rev. A* **82**, 013633 (2010)
33. G. Tayebirad, A. Zenesini, D. Ciampini, R. Mannella, O. Morsch, E. Arimondo, N. Lörch, S. Wimberger, *Phys. Rev. A* **82**, 069904 (2010)
34. P. Schlagheck, S. Wimberger, *App. Phys. B* **86**, 385 (2007)
35. M. Gustavsson, E. Haller, M.J. Mark, J.G. Danzl, G. Rojas-Kopeinig, H.-C. Nägerl, *Phys. Rev. Lett.* **100**, 080404 (2008)
36. A.R. Kolovsky, H.J. Korsch, E.-M. Graefe, *Phys. Rev. A* **80**, 023617 (2009)

Effective spin model for interband transport in a Wannier-Stark lattice system

P. Plötz^{1,a}, P. Schlagheck², and S. Wimberger¹

¹ Institut für Theoretische Physik, Universität Heidelberg, Philosophenweg 19, 69120 Heidelberg, Germany

² Département de Physique, Université de Liège, 4000 Liège, Belgium

Received 29 September 2010 / Received in final form 22 October 2010

Published online 3rd December 2010 – © EDP Sciences, Società Italiana di Fisica, Springer-Verlag 2010

Abstract. We show that the interband dynamics in a tilted two-band Bose-Hubbard model can be reduced to an analytically accessible spin model in the case of resonant interband oscillations. This allows us to predict the revival time of these oscillations which decay and revive due to inter-particle interactions. The presented mapping onto the spin model and the so achieved reduction of complexity has interesting perspectives for future studies of many-body systems.

1 Introduction

An amazing control of quantum degrees of freedom is nowadays routinely possible with the techniques of preparing and handling ultracold matter in the laboratory [1–5]. Backed by a plethora of theoretical proposals (see, e.g., [6–9]), a new direction is the coupling of such matter to additional degrees of freedom, such as provided by internal states (e.g. [10]), by external potentials (e.g. [11]), by coupling to a bath (e.g. [12]), to a continuum (e.g. [13,14]) or even to macroscopic objects (e.g. [15,16]). Such hybrid quantum systems are of high interest for applications, ranging from fundamental physics to metrology.

A major challenge in studying these systems is to reduce their inherent complexity. This is important for an understanding of both the internal dynamics as well as an extension to include a coupling to further degrees of freedom. In this paper we focus on the dynamics of atomic bosons in a two band Bose-Hubbard model. The problem is non-stationary due to an additional Stark force (or constant tilt). In particular, we describe the Rabi-like oscillations between the two bands, which are well pronounced in the case of single-particle resonant tunnelling between the levels of adjacent lattice wells [13,17]. The presence of a second band gives an additional degree of freedom – in the sense of the previous paragraph – making the full many-particle problem very rich in new phenomena, yet also very complicated in general. We show how to effectively map the original problem to a much simpler spin system for specific fillings and parameters. This new model allows us to derive an analytical formula for the revival time of the interband oscillations which decay and revive due to weak inter-particle interactions.

2 The system

2.1 The many-body model

We consider a two-band Bose-Hubbard model in one spatial dimension with an additional external force as obtained from a general many-body Hamiltonian under the assumption of a contact interaction and introduced in [18,19]. We measure all parameters of the Hamiltonian in recoil energies $E_{\text{rec}} \equiv \hbar^2 k_L^2 / (2m)$, where k_L is the wave vector of the laser creating the optical lattice and m the mass of the atoms. Setting $\hbar = 1$ throughout, the Hamiltonian reads [18,19]

$$\begin{aligned} \mathcal{H} = \sum_{l=1}^L & \left[\epsilon_l^- n_l^a - \frac{t_a}{2} (a_{l+1}^\dagger a_l + h.c.) + \frac{gW_a}{2} n_l^a (n_l^a - 1) \right. \\ & + \epsilon_l^+ n_l^b + \frac{t_b}{2} (b_{l+1}^\dagger b_l + h.c.) + \frac{gW_b}{2} n_l^b (n_l^b - 1) \\ & + FC_0 (b_l^\dagger a_l + h.c.) + 2gW_x n_l^a n_l^b \\ & \left. + \frac{gW_x}{2} (b_l^\dagger b_l^\dagger a_l a_l + h.c.) \right]. \end{aligned} \quad (1)$$

The operator a_l (a_l^\dagger) annihilates (creates) a particle at site l of totally L sites in the lower band and b_l (b_l^\dagger) in the upper band with the number operators $n_l^a = a_l^\dagger a_l$, $n_l^b = b_l^\dagger b_l$. The bands are separated by a bandgap Δ and have on-site energies $\epsilon_l^\pm = \pm \Delta / 2 + lF$. The hopping amplitudes between neighbouring sites in band a, b are denoted by $t_a, t_b > 0$, and a repulsive interaction between particles occupying the same site in band a (b) with a strength W_a (W_b) has been included. The single-particle coupling of the bands is proportional to the external Stark force F via $C_0 F$ with a coupling constant C_0 depending on the depth of the lattice V_0 [18,19]. The bands are additionally coupled via the inter-particle interactions with a

^a e-mail: ploetz@thphys.uni-heidelberg.de

strength W_x . Focusing on a realisation with a single optical lattice, the parameters fulfill generally: $\Delta \gg t_a, t_b$, as well as $t_a, t_b \approx W_i$ and $C_0 \approx -0.1$. We take the external force F as a free parameter. Additionally we assume that the interaction strength can be tuned, e.g., by the use of Feshbach resonances [3], and include a factor g to all interaction terms. For numerical simulations, we change to the interaction-picture with respect to the external force [20] which removes the tilt $\sum_l l n_l^{a,b} F$ and replaces $a_{l+1}^\dagger a_l \rightarrow e^{iFt} a_{l+1}^\dagger a_l$ (and likewise for $b_{l+1}^\dagger b_l$). The Hamiltonian is then time-dependent with a periodicity of $T_B \equiv 2\pi/F$ and allows to use periodic boundary conditions $a_{L+1} = a_1$ and $b_{L+1} = b_1$.

To study the interband transport, we prepare the system in an initial state $|\psi(0)\rangle$, with a uniform distribution of particles in the lower band only, and evolve it in time by the many-body Schrödinger equation. The quantity we study is the (normalised) number of particles in the upper band

$$\mathcal{N}_b(t) \equiv \frac{1}{N} \langle \psi(t) | \sum_l n_l^b | \psi(t) \rangle, \quad (2)$$

where $N = \langle \sum_l (n_l^a + n_l^b) \rangle$ is the total number of particles. We will refer to $\mathcal{N}_b(t)$ as *occupation of the upper band*. For the range of parameters described above, this observable shows a superposition of many sinusoidal oscillations with an amplitude of few per cent, even for strong forces [21].

2.2 Weakly interacting system in resonance

Despite the small interband oscillations described in the previous paragraph, a strong enhancement of the interband transport is possible for specific parameter values. When the force-induced tilt of the lattice is such that a lower and upper band energy level become nearly degenerate (i.e. for $\Delta \approx mF$, $m \in \mathbb{N}$), the interband oscillations of $\mathcal{N}_b(t)$ come close to 100% indicating a resonantly enhanced interband transport [21]. We refer to these specific parameter values as resonant and will focus on this resonant behaviour in the following.

To describe the non-interacting system $\mathcal{H}(g=0) = \mathcal{H}_0$ in resonance, we introduce the eigenstates of the single-band problem (the Wannier-Stark states) involving Bessel functions of the first kind $J_n(x)$ [21,22]

$$\alpha_n = \sum_{l \in \mathbb{Z}} J_{l-n}(x_a) a_l, \quad \beta_n = \sum_{l \in \mathbb{Z}} J_{l-n}(x_b) b_l, \quad (3)$$

with $x_i \equiv t_i/F$, $i = a, b$. By using $\sum_{l \in \mathbb{Z}} J_{n-l}(x) J_{n'-l}(x') = J_{n-n'}(x-x')$, one finds that the transformation removes the hopping terms from the original Hamiltonian (1) but leads to a coupling between any sites from the two different bands weighted by Bessel functions

$$\mathcal{H}_0 = \sum_{l \in \mathbb{Z}} \left[\epsilon_l^- \alpha_l^\dagger \alpha_l + \epsilon_l^+ \beta_l^\dagger \beta_l + \sum_{m \in \mathbb{Z}} C_0 F J_m(\Delta x) (\alpha_l^\dagger \beta_{l-m} + h.c.) \right], \quad (4)$$

where $\Delta x = x_a + x_b$ and $\epsilon_l^\pm = \pm \Delta/2 + lF$ as above. The resonance condition, $\Delta \approx mF$ or equivalently $\epsilon_l^- \approx \epsilon_{l-m}^+$, means that two levels from different bands become energetically degenerate. In this case, it is sufficient to keep only the direct coupling between these two sites leading to a sum of independent two-level systems

$$\mathcal{H}_0^{\text{res}} = \sum_{l \in \mathbb{Z}} \left[\epsilon_l^- \alpha_l^\dagger \alpha_l + \epsilon_l^+ \beta_l^\dagger \beta_l + C_0 F J_m(\Delta x) (\alpha_l^\dagger \beta_{l-m} + h.c.) \right]. \quad (5)$$

This approximate description of the system in resonance corresponds to lowest order nearly degenerate perturbation theory and higher order corrections are easily calculated, see e.g. [23,24]. However, the lowest order approximation, equation (5), gives already an accurate description of the non-interacting system in resonance [21,23]. The resonant contribution to the non-interacting case is thus well-described as $\mathcal{N}_b(t) = \sin^2 [C_0 F J_m(\Delta x) t]$ with a period $T_{\text{res}} = \pi / [C_0 F J_m(\Delta x)] \gg T_B$ much larger than the Bloch period.

As demonstrated in [21], the inclusion of a weak interparticle interaction leads to a dephasing of the resonant interband oscillations. The occupation of the upper band as a function of time exhibits a collapse and revival effect, with the time-scales for the collapse and revival inversely proportional to the interaction strength g [23]. An example of such oscillations under a weak repulsive interaction is given by the solid line in Figure 2. In the weakly interacting regime under consideration here, one of the interaction terms in the full Hamiltonian equation (1) is most important. We focus solely on repulsive interactions, for which the system tries to avoid double occupancy of sites in either bands. However, the system is always assumed to be at approximately integer filling and at the same time sites from different bands are nearly degenerate, such that it cannot avoid to have two particles occupying the same site in either band. Thus the dominant contribution comes from the term $2gW_x \sum_l n_l^a n_l^b$ (see [21] for further details). In the next section we derive an effective Hamiltonian that allows to study the effect of a weak interaction on the resonant interband oscillations in detail.

3 Results

3.1 Effective spin model for system in resonance

We will now derive an effective spin Hamiltonian for the interacting system in resonance. The strong reduction of complexity is possible due to the resonant behaviour of the system and the fact that the repulsive interaction suppresses higher occupation of lattice sites. The description of the non-interacting system in resonance according to equation (5) contains already the seed for an effective model. The sum of many independent two-level systems can be viewed as a system of non-interacting spins. We only need to re-order the labeling of lattice sites such that the two levels being coupled have the same site-index and the coupling operator is then proportional to

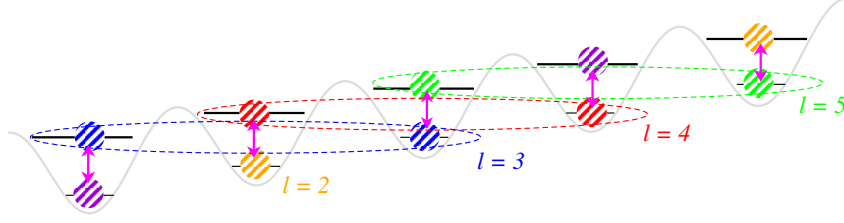


Fig. 1. (Color online) Schematic view of the effect of the interband interaction on the system in resonance of order $m = 2$. In resonance, the system is forced into a superposition of states from both bands (the sites forming a superposition are indicated by dashed ellipses). This happens on all lattice sites and the system cannot avoid an interaction of $2gW_x \sum_l n_l^a n_l^b$. A new fictitious lattice labeling scheme setting the superpositions on one site is also indicated in the figure.

the Pauli matrix σ^x . The constant of proportionality is the coupling matrix element $C_0 F J_m(\Delta x)$ from equation (5). This is simply a different way of writing the approximate Hamiltonian for the non-interacting system in resonance, equation (5), and is schematically displayed for a resonance of order $m = 2$ in Figure 1. To include the effect of the most important interaction term $2gW_x \sum_l n_l^a n_l^b$ into our effective spin model, we insert the basis transformation from equation (3) and obtain in the transformed basis

$$\begin{aligned} 2gW_x \sum_l n_l^a n_l^b &= 2gW_x \sum_{l, l_1, \dots, l_4} \left\{ J_{l-l_1}(x_a) J_{l-l_2}(x_a) \right. \\ &\quad \times J_{l-l_3}(x_b) J_{l-l_4}(x_b) \\ &\quad \left. \times \alpha_{l-l_1}^\dagger \alpha_{l-l_2} \beta_{l-l_3}^\dagger \beta_{l-l_4} \right\} \\ &\approx 2gW_x J_0^2(x_a) J_0^2(x_b) \sum_l \alpha_l^\dagger \alpha_l \beta_l^\dagger \beta_l. \end{aligned} \quad (6)$$

Here we used the fact that only one of the many different combinations of Bessel functions gives a significant contribution [21,23]. The reason is that the arguments of the Bessel functions x_a and x_b are much smaller than unity for a realisation with a single optical lattice as discussed here, and the dominant contribution is therefore given by the product of four zeroth order Bessel functions $J_0^2(x_a) J_0^2(x_b)$. We denote the interaction strength for this dominant process by

$$U \equiv 2gW_x J_0^2(x_a) J_0^2(x_b). \quad (7)$$

The introduction of the new fictitious lattice is now effectively achieved by replacing $l \rightarrow l + m$ for the sites of the upper band. It is important to note that the interband interaction was between atoms occupying the same site in different bands in the original lattice, i.e. $\propto n_l^a n_l^b$, whereas in the new lattice it connects a particle at one lattice site in the lower band $\alpha_l^\dagger \alpha_l \equiv n_l^\alpha$ with a particle at a different site in the upper band $\beta_{l+m}^\dagger \beta_{l+m} \equiv n_{l+m}^\beta$ (where we used the transformed basis α_l, β_l). We focus on unit filling $N = L$ and, since the repulsive interaction effectively suppresses higher occupation of lattice sites, we limit the occupation numbers of n_l^α and n_l^β to 0 or 1 for our effective model. This allows us to replace $n_l^{\alpha, \beta} \rightarrow \sigma_l^{\uparrow, \downarrow}$ with the projectors on a spin-up or spin-down state $\sigma_l^{\uparrow, \downarrow} = (1 \pm \sigma_l^z)/2$.

Collecting all arguments, the effective Hamiltonian (for a resonance of order m) is accordingly given by

$$\mathcal{H}_{\text{eff}} = \sum_{l=1}^L \left(V_m \sigma_l^x + U \sigma_l^\uparrow \sigma_{l+m}^\downarrow \right) \quad (8)$$

where $V_m = C_0 F J_m(\Delta x)$. Here σ_l^i denotes the Pauli matrices for a spin at site l . The first part is as in the non-interacting resonant system, which was also a sum of independent two-level systems. We only changed the ordering of the sites to bring degenerate levels close together. The second part reflects the repulsion of two particles when sitting in different bands or different spin states respectively. Since we are using spin-1/2 matrices in this effective description it can only be applied to the case of unit filling and the number of lattice sites is per definition identical with the number of spins. We expect it to be a good approximation for close-to-unit filling (as is supported by our results below, see Fig. 4). An extension to higher fillings should be possible by using larger spins than spin 1/2, since this would allow further distinction of the type non-occupied, partly occupied, or highly-occupied, but is beyond the scope of the present article. The effective Hamiltonian (8) is translational invariant as our original model, such that one could use a reduction to subspaces of fixed total quasimomentum similar to [18,20,23]. Please note, that the Hilbert space for the effective Hamiltonian has a dimension $\dim \mathcal{H}_{\text{eff}} = 2^L$ that is much smaller than the Hilbert space of the original bosonic problem, equation (1), where $\dim \mathcal{H} = (N + 2L - 1)! / [N!(2L - 1)!]$. This is advantageous for numerical computations since much larger system sizes become computable as compared to the original model.

Let us discuss the effective model of equation (8) in more detail. The parameters in the effective spin model are chosen for the particular case of the system in resonance of order m . It includes only the resonant coupling between the two sites and other non-resonant couplings are neglected. The effective model does thus not reproduce small scale oscillations which are found on top of the resonant oscillations within the full model (see [21] for an example). However, these oscillations are only weakly influenced by the interparticle interaction and are not relevant for the collapse and revival effect we want to study. Another important aspect of the effective spin model concerns the choice of the interaction term $\sigma_l^\uparrow \sigma_{l+m}^\downarrow$. Here we included

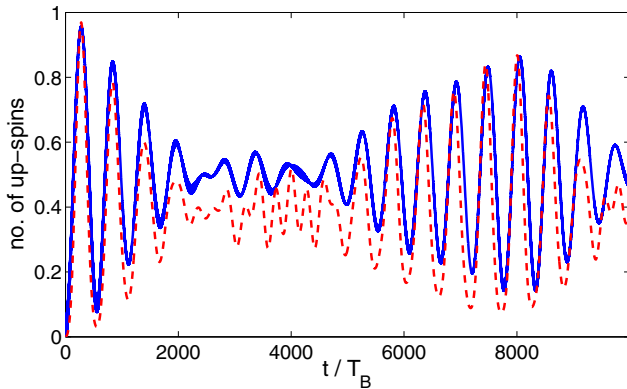


Fig. 2. (Color online) Occupation of the upper band in the full two-band Bose-Hubbard model (solid line; see [21] for details) and number of up-spins in the effective spin model (dashed line) for the same parameters. The spin model reproduces most features of the time signal, first and foremost the collapse and revival are in very good agreement between both models. Parameters correspond to $V_0 = 10$: $\Delta = 7.77$, $t_a = 0.005$, $t_b = 0.121$, $C_0 = -0.114$, $W_a = 0.040$, $W_b = 0.027$, and $W_x = 0.018$; resonance order $m = 1$, i.e. $F = 7.9804$; $g = 0.1$ and $N = 5 = L$.

only one of the four interaction terms from the original Hamiltonian, equation (1), which has the strongest effect on the resonant interband oscillations. The inclusion of the other terms is straightforward but not necessary in the present context. Furthermore we are limited to weak inter-particle interactions, $U \ll V_m$, which is, however, not a limitation of the effective model but originates from the physics of the original system: as soon as the inter-particle interaction becomes too strong, the resonant tunneling is washed out and the Rabi-like interband oscillations cease and eventually transform into an essentially structureless evolution of the band population defined in equation (2) [23].

To compare the effective model to the full problem, we computed the time-evolution of similar initial states in both models and show the resulting occupation of the upper band as a function of time with the pronounced collapse and revival effect in Figure 2. The occupation of the upper band for the full model is given by $\mathcal{N}_b(t)$, as defined by equation (2), and has been computed by direct numerical integration of the time-dependent Schrödinger equation. In the effective spin model, a state with an atom occupying the upper band is represented by a spin-up such that the corresponding observable for the spin model is given by $\mathcal{N}_\uparrow(t) = \frac{1}{L} \langle \psi(t) | \sum_l \sigma_l^\uparrow | \psi(t) \rangle$ and the initial state is of the form $|\downarrow\downarrow \dots \downarrow\rangle$. Both observables are compared in Figure 2 for a weakly interacting system of medium size. Overall, the effective spin model reproduces the occupation of the upper band very well, especially when compared to the drastic simplification from the full two-band Bose-Hubbard model to the effective model of equation (8). The good agreement is particularly surprising when taking into account that a reduction of occupation numbers to 0 or 1 is usually known as “hard-core bosons” [25,26] and valid in the limit of strong interac-

tions, whereas we are operating in exactly the opposite regime of $U \ll V_m$. Furthermore, the effective model reproduces the collapse and revival effect only when it is introduced from the transformed basis. Limiting the occupation number in the original a_l, b_l -basis by artificial constraints (such a truncation procedure was applied, e.g., in [27,28]) cannot reproduce the effect [23].

A great advantage of the effective spin model for the interband transport, equation (8), is its exact solvability. Rewriting the spin-up and -down operators in terms of Pauli matrices and applying a rotation of $\pi/2$ around the y -axis (which leads to $\sigma_x \rightarrow \sigma_z$ and $\sigma_z \rightarrow -\sigma_x$), our effective Hamiltonian takes the following form

$$\mathcal{H}_{\text{eff}} = \sum_{l=1}^L \left(V_m \sigma_l^x - \frac{1}{4} U \sigma_l^z \sigma_{l+m}^z \right) + \text{const.} \quad (9)$$

This Hamiltonian is known (for $m = 1$) as the quantum Ising model in a transverse magnetic field [29]. It describes coupled spins that tend to align in z -direction but are subjected to the force of an applied magnetic field in x -direction. It can be solved exactly by subsequent application of a Jordan-Wigner transformation [30], Fourier and Bogolyubov transformation. The final result in terms of Bogolyubov quasi-particles is [23,29]

$$\mathcal{H}_{\text{eff}} = \sum_k \epsilon(k) (d_k^\dagger d_k - 1/2). \quad (10)$$

The exact dispersion relation $\epsilon(k)$ is given by

$$\epsilon(k) = 2V_m \sqrt{1 - \frac{U}{2V_m} \cos k + \left(\frac{U}{4V_m} \right)^2} \approx 2V_m - \frac{1}{2} U \cos k \quad (11)$$

and can be approximated for our weakly interacting system $U \ll V_m$ as shown. Equation (10) is the exact solution to our effective spin model. The elementary excitations of the system are non-interacting fermions with a dispersion relation that is approximately given by a cosine. These elementary excitations correspond to magnons, i.e., to delocalised spin-flips in the original spin basis. They read explicitly

$$d_k = \cos(\theta_k/2) c_k - i \sin(\theta_k/2) c_{-k}^\dagger, \quad (12)$$

$$\tan \theta_k = \frac{\sin k}{\cos k - 4V_m/U}, \quad (13)$$

with c_k the Fourier transform of $c_l = \sigma_l^- \exp \left[i\pi \sum_{n < l} c_n^\dagger c_n \right]$, with $\sigma_l^\pm = (\sigma_l^x \pm i\sigma_l^y)/2$ and $\sigma_l^z = 2c_l^\dagger c_l - 1$.

3.2 Revival time within the effective model

The exact solution equation (10) of the effective Hamiltonian allows, e.g., the computation of various correlation functions. But in the present context, we are

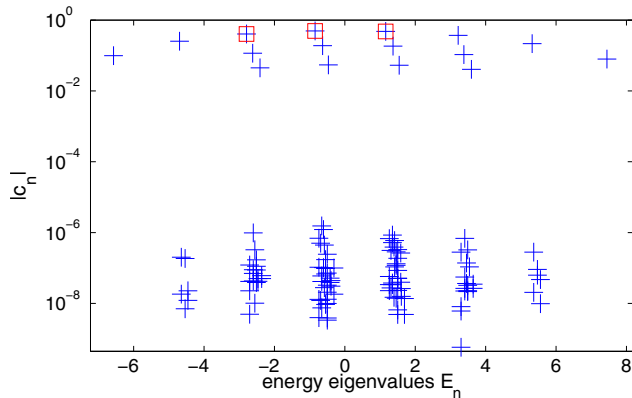


Fig. 3. (Color online) Shown are the coefficients $c_n = \langle E_n | \psi(0) \rangle$ for an eigenbasis expansion of the initial state $|\psi(0)\rangle = |\downarrow \dots \downarrow\rangle$ versus the corresponding eigenenergies (+). The three largest coefficients are marked by (\square) and highlight eigenstates with $M-1$, M , and $M+1$ magnons. Parameters: $V_m = 1$, $L = 7$, $U = 0.25$, and $F = 4.6020$. Note the logarithmic scale on the y -axis.

interested in the time-evolution of particular initial states

$$|\psi(t)\rangle = \sum_n e^{-iE_n t} c_n |E_n\rangle, \quad (14)$$

where $|E_n\rangle$ are the eigenstates of the effective model, equation (10), and $c_n = \langle E_n | \psi(0) \rangle$. In general the overlaps c_n between the given initial state and all eigenstates are needed to calculate the time-evolution. Instead of an analytical derivation of the overlaps on basis of the Jordan-Wigner transformation, we adopt a numerical approach here in order to decide which of the magnon states are relevant. In detail, it is sufficient to know which eigenstates have a significant contribution to the time-evolution to estimate the revival time of the resonant interband oscillations. Figure 3 shows the coefficients c_n for a time-evolution of the initial state $|\downarrow \dots \downarrow\rangle$ sorted by their eigenenergies. The eigenenergies appear in several bunches corresponding to eigenstates with a different number of magnon excitations ranging from 0 to L magnons. Additionally, the three coefficients with the largest amplitude have been marked by squares in Figure 3. We find that the largest coefficients in the eigenbasis expansion are from the energetically lowest eigenstates from the central bunches of the spectrum. To be more specific, we found numerically that the largest coefficients always come from the subspaces with $M-1$, M , and $M+1$ magnons, where $M = L/2$ for L even and $M = (L-1)/2$ for L odd, and are from the eigenstates with lowest energy within these subspaces. This important observation allows a simple estimate of the revival time as the time for a beating between oscillations with these three energies as frequencies.

To find the lowest eigenenergy of a state with M magnons, we use the fact that the energy of a many-body state with M magnons in the weakly interacting regime is

according to equation (11) given by

$$E_M = \sum_{l=1}^M \left(2V_m - \frac{1}{2}U \cos(k_{j_l}) \right), \quad (15)$$

where $k_{j_l} = 2\pi j_l/L$ and each j_l can take a value between $1, \dots, L$. The energies for a given number of magnons M thus arise from different choices of the momenta k_{j_l} . The state with lowest energy in this cosine dispersion is obtained by using momenta that fill the empty cosine dispersion from zero upwards. A many-magnon state with $M = L/2$ is reached when half of the possible states are filled and with $M \pm 1$ by adding or removing one magnon, respectively. This determines the momenta k_{j_l} to obtain a state with M magnons and minimal energy. We can now estimate the revival time from the difference between the energies of states with $M-1$, M , and $M+1$ magnons, i.e., we need $\Delta\omega = (E_{M+1} - E_M) - (E_M - E_{M-1}) = E_{M+1} + E_{M-1} - 2E_M$. Inserting explicitly that the energy of M magnons is proportional to the sum of M cosine functions, equation (15), with different momenta filling the possible magnon states from below, we obtain the following frequency difference

$$\begin{aligned} \Delta\omega &= -\frac{U}{2} \left(\sum_{j=1}^{M+1} \cos(k_j) + \sum_{j=1}^{M-1} \cos(k_j) - 2 \sum_{j=1}^M \cos(k_j) \right) \\ &= -\frac{U}{2} (\cos k_{M+1} - \cos k_M) \approx -\frac{\pi}{L} U, \end{aligned} \quad (16)$$

where we expanded the cosine to lowest order around its zero. Using equation (16) and our expression for U , equation (7), we find that the revival time as estimated by oscillations between the dominant frequencies is given by

$$t_{\text{rev}} = \frac{L}{2\pi} \frac{4\pi}{gW_x J_0^2(x_a) J_0^2(x_b)}. \quad (17)$$

The effective spin model predicts the revival time to be inversely proportional to the interaction strength and to a product of two Bessel functions from the basis transformation. The parameters of the original full Hamiltonian equation (1), like the hopping strengths, the gap between the two energy bands and the order of the resonance, enter via the arguments of Bessel functions $x_{a,b} = t_{a,b}/F$, where the force has to be chosen according to the order of resonance $F \approx \Delta/m$. These parameters and the revival time change when the depth of the optical lattice V_0 is varied (see Eq. (4)). Furthermore, the result equation (17) from the effective spin model additionally predicts a linear dependence of the revival time on L . Within the effective spin model this is by definition both the number of spins and lattice sites. However, within the full two-band Bose-Hubbard model the size-dependent prefactor refers to the extension of the initial state within the lattice and *not* the total number of lattice sites. Therefore, an observation of the collapse and revival effect should also be possible in an infinite lattice provided the initial state shows a limited extension. In this way, our effective model adds an additional factor of $L/2\pi$ to our earlier result [21], which has

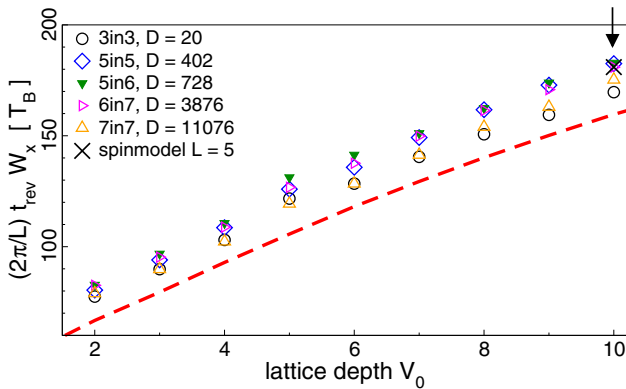


Fig. 4. (Color online) We show the revival times from different numerical simulations of the full two-band Bose-Hubbard model (the corresponding system sizes ‘ N in L ’ and the dimension of the Hilbert spaces D are indicated in the legend). The numerical values have been rescaled by the size-dependent prefactor $2\pi/L$. The data points for different system sizes coincide, with small fluctuations due to the approximation in equation (16). Our analytical prediction equation (17) (red dashed line) captures nicely the scaling with the system parameters, yet it shows a systematic offset arising from the three level approximation. The numerical result of the full spin model (cross marked by arrow), extracted from Figure 2, coincides with the full problem of equation (1).

been obtained following the arguments that led to equation (7) above, with the assumption that the initial state is comparable to a coherent state and estimating the revival time by computing the effect of the dominant interaction term on a coherent state perturbatively [21].

To compare the result from equation (17) to numerical simulations of the full two-band Bose-Hubbard model, we use the size-dependent prefactor to rescale numerical results for different system sizes. The curves for different system sizes should coincide, as is verified in Figure 4. The revival times from full many-body models with Hilbert spaces ranging over three orders of magnitude fall onto one curve and demonstrate the validity of the effective spin model equation (8) for the interband transport in the weakly interacting two-band Bose-Hubbard model. The remaining fluctuations with the system size originate in the approximation of equation (16) and decrease with growing L . The additional offset arises from taking only the three largest coefficients for the derivation of the explicit expression in equation (17). This leads to an underestimation by about 10% of the time for the maximum in the revived interband oscillations (which is our definition for the revival time). Inclusion of more than three coefficients should remove this systematic offset between the predicted and measured revival time. This has been tested by comparing the oscillation dynamics of the original model (1) with the full spin model (8) [23], and the good agreement is shown for an exemplary data point in Figure 4 (cross, extracted from the temporal evolution presented in Fig. 2 above). We finally note, that equation (17) predicts a divergence of the revival time whenever the parameters of the system are chosen such that

one of the Bessel functions in the denominator vanishes. This can be achieved, e.g., by tuning the energy gap Δ between the two bands, and the expected divergence of the revival time close to Bessel zeros was observed in numerical simulations [23], giving room for a great deal of control of the resonant interband oscillations.

4 Summary

We have shown how to reduce the complexity of the original Hamiltonian equation (1) to the exactly solvable model equation (9) for filling factors of the order one and for resonant coupling between the two energy bands. For weak inter-particle interactions the model is in good agreement with the full problem and allowed us to derive an analytical formula for the revivals of the resonant interband oscillations. Interesting future aspects to work on would be to include decay to higher energy states in the continuum part of the spectrum (e.g. by opening the model in a similar way as exercised in [18,31] for a one-band problem) and to extend the problem to atoms with internal structure. The internal degrees of freedom would become correlated with the external transport in “horizontal” – along the lattice – and “vertical” – between the bands – direction. Reductions of complex models are in general a necessary prerequisite in order to describe quantum systems with many degrees of freedom – possibly of different kind and nature. So we hope that the spirit of our approach may inspire future research in this direction.

This work was supported by the DFG FOR760. SW is especially grateful to the Hengstberger Foundation for the Klaus-Georg and Sigrid Hengstberger Prize. PP and SW acknowledge furthermore support from the Klaus Tschira Foundation, by the Helmholtz Alliance Program of the Helmholtz Association (contract HA-216 “Extremes of Density and Temperature: Cosmic Matter in the Laboratory”), and within the framework of the Excellence Initiative by the German Research Foundation (DFG) through the Heidelberg Graduate School of Fundamental Physics (grant number GSC 129/1), the Frontier Innovation Fonds and the Global Networks Mobility Measures.

References

1. O. Morsch, M. Oberthaler, *Rev. Mod. Phys.* **78**, 179 (2006)
2. J. Fortágh, C. Zimmermann, *Rev. Mod. Phys.* **79**, 235 (2007)
3. I. Bloch, J. Dalibard, W. Zwerger, *Rev. Mod. Phys.* **80**, 885 (2008)
4. S. Giorgini, L.P. Pitaevskii, S. Stringari, *Rev. Mod. Phys.* **80**, 1215 (2008)
5. C. Chin, R. Grimm, P. Julienne, E. Tiesinga, *Rev. Mod. Phys.* **82**, 1225 (2010)
6. A. Sorensen, L. Duan, J. Cirac, P. Zoller, *Nature* **409**, 63 (2001)
7. S. Diehl et al., *Nature Phys.* **4**, 878 (2008)
8. M. Singh, *Opt. Express* **17**, 2600 (2009)
9. F. Verstraete et al., *Nature Phys.* **5**, 633 (2009)

10. C. Gross, T. Zibold, E. Nicklas, J. Estève, M.K. Oberthaler, *Nature* **464**, 1165 (2010)
11. J. Estève, C. Gross, A. Weller, S. Giovanazzi, M.K. Oberthaler, *Nature* **455**, 1216 (2008)
12. S. Hofferberth, I. Lesanovsky, T. Schumm, A. Imambekov, V. Gritsev, E. Demler, J. Schmiedmayer, *Nature Phys.* **4**, 489 (2008)
13. C. Sias, A. Zenesini, H. Lignier, S. Wimberger, D. Ciampini, O. Morsch, E. Arimondo, *Phys. Rev. Lett.* **98**, 120403 (2007)
14. A. Zenesini, H. Lignier, G. Tayebirad, J. Radogostowicz, D. Ciampini, R. Mannella, S. Wimberger, O. Morsch, E. Arimondo, *Phys. Rev. Lett.* **103**, 090403 (2009)
15. D. Cano, B. Kasch, H. Hattermann, R. Kleiner, C. Zimmermann, D. Koelle, J. Fortágh, *Phys. Rev. Lett.* **101**, 183006 (2008)
16. D. Hunger, S. Camerer, T.W. Hänsch, D. König, J.P. Kotthaus, J. Reichel, P. Treutlein, *Phys. Rev. Lett.* **104**, 143002 (2010)
17. M. Glück, A.R. Kolovsky, H.J. Korsch, *Phys. Rep.* **366**, 103 (2002)
18. A. Tomadin, R. Mannella, S. Wimberger, *Phys. Rev. A* **77**, 013606 (2008)
19. A. Tomadin, Master's thesis, Università di Pisa, 2006
20. A.R. Kolovsky, A. Buchleitner, *Phys. Rev. E* **68**, 056213 (2003)
21. P. Plötz, J. Madroñero, S. Wimberger, *J. Phys. B* **43**, 081001 (2010)
22. H. Fukuyama, R.A. Bari, H.C. Fogedby, *Phys. Rev. B* **8**, 5579 (1973)
23. P. Plötz, Ph.D. thesis, Universität Heidelberg, 2010
24. J. Hausinger, M. Grifoni, *Phys. Rev. A* **81**, 022117 (2010)
25. M. Girardeau, *J. Math. Phys.* **1**, 516 (1960)
26. M. Rigol, A. Muramatsu, *Phys. Rev. A* **70**, 031603 (2004)
27. F. Schmitt, M. Hild, R. Roth, *J. Phys. B: At. Mol. Opt. Phys.* **40**, 371 (2007)
28. S.R. Clark, D. Jaksch, *New J. Phys.* **8**, 160 (2006)
29. S. Sachdev, *Quantum Phase Transitions* (Cambridge University Press, Cambridge, 2001), Chap. 4.2
30. P. Jordan, E. Wigner, *Z. Phys.* **47**, 631 (1928)
31. A. Tomadin, R. Mannella, S. Wimberger, *Phys. Rev. Lett.* **98**, 130402 (2007)

Stückelberg–Interferometry with ultra-cold atoms

Patrick Plötz and Sandro Wimberger

Institut für Theoretische Physik, Universität Heidelberg, Philosophenweg 19, 69120 Heidelberg

(Dated: December 17, 2010)

We show that and how ultra-cold atoms in an accelerated two-band lattice are a controlled realization of Landau–Zener–Stückelberg interferometry.

I. INTRODUCTION

Two-level systems subject to a strong periodic driving appear in a large variety of quantum mechanical systems and their study has a long history. They are naturally used in atomic physics when an atom is coupled to a laser-field [1], in solid state physics when describing superconducting qubits [2] or as effective models [3]. One consequence of the strong driving is the possibility for the two-level system to undergo a sequence of transitions. Each transition can be seen as an effective beam splitter and the coherent passage through several transitions leads to an accumulation of phases and interference effects known as Stückelberg oscillations (see [4] and references therein).

Recently, Stückelberg oscillations have been observed experimentally for ultra-cold atoms in accelerated optical lattices [5, 6]. This opens the route for very detailed studies of Stückelberg interferometry with cold gases. The high degree of control in these systems [7, 8] allows to explore the strong sensitivity of the phase between interband transitions on the band structure. The main goal of the present paper is to establish explicitly the connection between Stückelberg interferometry and interband transitions in optical lattices. Additionally, we provide simple analytical formulae for the interband dynamics and compute interference patterns, i.e. contour plots of transition probabilities, for realizations with a single optical lattice as experimentally used in [5] and superlattices as in [6]. The outline is as follows. In section II we are going to obtain the Landau–Zener–Stückelberg (LZS) Hamiltonian from a two-band model for ultra-cold atoms in accelerated optical lattices and study the dynamics of the interband transitions using a systematic expansion in section III. We will then compute the transition probabilities using degenerate perturbation theory and compare the results to numerical simulations. This will be followed by predictions for interference patterns in realizations with a single optical lattice and superlattices. We will close with a short summary.

II. COLD ATOM REALIZATION OF THE LANDAU–ZENER–STÜCKELBERG HAMILTONIAN

A quantum mechanical two-level system with energy bias ε_0 under strong periodic driving with amplitude A and frequency ω is modeled by the Landau–Zener–

Stückelberg Hamiltonian [4]

$$\mathcal{H}_{\text{LZS}} = -\frac{1}{2} \begin{pmatrix} \varepsilon_0 + A \sin \omega t & \Delta_T \\ \Delta_T & -\varepsilon_0 - A \sin \omega t \end{pmatrix}. \quad (1)$$

Here, Δ_T denotes the tunneling amplitude between the two levels. In the present section we are going to show explicitly how this Hamiltonian can be realized with ultra-cold atoms in accelerated optical lattices.

Using ultra-cold atoms in optical lattices it is possible to create tilted non-interacting two-band systems [6]. We make all parameters of the Hamiltonian dimensionless by measuring them in units of recoil energies $E_{\text{rec}} \equiv \hbar^2 k_L^2 / (2m)$, where k_L is the wave vector of the laser creating the optical lattice and m the mass of the atoms (we set $\hbar = 1$). The dimensionless force F is obtained by multiplication of the physical force with the lattice constant and dividing by E_{rec} . The appropriate dimensionless two-band Hamiltonian obtained from an expansion in Wannier functions of the full problem [9, 10] reads

$$\mathcal{H}_{\text{2B}} = \sum_{l \in \mathbb{Z}} \left[(lF - \frac{\Delta}{2}) a_l^\dagger a_l - \frac{J_a}{2} (a_{l+1}^\dagger a_l + \text{h.c.}) + (lF + \frac{\Delta}{2}) b_l^\dagger b_l - \frac{J_b}{2} (b_{l+1}^\dagger b_l + \text{h.c.}) + FC_0 (b_l^\dagger a_l + \text{h.c.}) \right]. \quad (2)$$

The operator a_l (a_l^\dagger) annihilates (creates) a particle at site l and b_l (b_l^\dagger) in the upper band. The bands are separated by a bandgap Δ and the whole lattice is tilted by on-site energies lF . The hopping amplitudes between neighbouring sites in band a, b are denoted by $J_a > 0$ and $J_b < 0$. The single-particle coupling of the bands is proportional to the external Stark force F via $C_0 F$ with a coupling constant C_0 depending on the optical lattice but usually of order $C_0 \approx -0.2$ [9, 10]. We take the external force F as a free parameter. The parameters of the Hamiltonian are directly computed from Wannier functions $w_l^{a,b}(x)$, which are maximally localized states centered around the l -th lattice well. They can be computed for realizations with a single optical lattice [10] $V(x) = V_0 \cos(x)$ or with a superlattice $V(x) = V_1 \cos(x) + V_2 \cos(2x + \phi)$ with a possible additional phase ϕ between the lattices [11, 12]. The parameters are then given by

$$J_{a,b} = \int w^{a,b}(x) V(x) w^{a,b}(x) dx \quad (3a)$$

$$C_0 = \int w^a(x) \cdot x \cdot w^b(x) dx. \quad (3b)$$

Here, $w_i^{a,b}(x)$ denote the Wannier functions for the lowest (a) and first excited band (b) that are computed from the Bloch functions to the potential $V(x)$. The band gap Δ is the difference between the average energy of these two lowest Bloch bands. Inter-particle interactions can be neglected under specific experimental conditions [5] and the case of weak interactions can be treated perturbatively, extending the discussion in [13, 14].

To obtain a driven time-dependent two-level system similar to eq. (1), we change to the interaction-picture with respect to the external force [15]. This removes the tilt $\sum_l l F a_l^\dagger a_l$ and replaces $a_{l+1}^\dagger a_l \rightarrow e^{iFt} a_{l+1}^\dagger a_l$ (and likewise for $b_{l+1}^\dagger b_l$). The Hamiltonian is then time-dependent with a periodicity of $T_B \equiv 2\pi/F$. Introducing Fourier components $a(k) = \sum_l e^{ilk} a_l$ and $b(k) = \sum_l e^{ilk} b_l$, we obtain the following periodic two-level Hamiltonian [16, 17]

$$\mathcal{H} = \begin{pmatrix} -\frac{\Delta}{2} - J_a \cos(k + Ft) & C_0 F \\ C_0 F & \frac{\Delta}{2} - J_b \cos(k + Ft) \end{pmatrix}. \quad (4)$$

The finite distance between the two levels, a sinusoidal driving and a constant coupling as in the LZS Hamiltonian, eq. (1), are already present now. To make the connection completely transparent, we add a periodic shift of the energy zero. The final result is then

$$\mathcal{H} = -\frac{1}{2} \begin{pmatrix} \Delta + 2J \cos(k + Ft) & -2C_0 F \\ -2C_0 F & -\Delta - 2J \cos(k + Ft) \end{pmatrix} + (J_a + J_b) \cos(k + Ft) \begin{pmatrix} 1 & 0 \\ 0 & 1 \end{pmatrix}, \quad (5)$$

where $J = J_a - J_b$. Shifting the time zero as $t \rightarrow t - k/F - \pi/2F$, we arrive exactly at the form of eq. (1). The first part of the Hamiltonian eq. (5) is the ultra-cold atom realization of the Landau-Zener-Stückelberg Hamiltonian and the second part reflects a time-dependent shift of the zero energy point, which does not concern interference effects between different phases. To simulate the LZS Hamiltonian and to perform interferometry one can use the control offered by ultra-cold atom systems in accelerated optical lattices. The role of the energy bias is taken by the average band gap between the two Bloch bands, the driving amplitude is realized as the difference in hopping strengths and the driving frequency is the Bloch frequency $\omega_B = F$ in our units. Finally, the tunneling amplitude in the ultra-cold atom realization is proportional to the external Stark Force. This correspondence between the two realizations is summarized in table I. Please note that not all parameters in the cold atom realization can be varied independently since the driving frequency $\omega_B = F$ and the interband coupling $C_0 F$ both depend on the external force. Figure 1 presents a typical LZS interferometric pattern (see [4] for many examples and a summary of different experimental results). Shown are the transition probabilities, i.e. the long-time average ($t \gg T_B$) of the occupation of the upper band, when varying the 'driving strength' J and the 'level splitting'

tilted optical lattice		Landau-Zener-Stückelberg	
band gap Δ		level splitting ε_0	
Bloch freq. $\omega_B = F$		driving freq. ω	
band coupling $2C_0 F$		level coupling $-\Delta_T/2$	
hopping $J = J_a - J_b$		field strength A	

TABLE I: Analogy between tilted optical lattices and the Landau-Zener-Stückelberg Hamiltonian. Note that the band coupling and the driving (or Bloch-) frequency are not independent in tilted optical lattices.

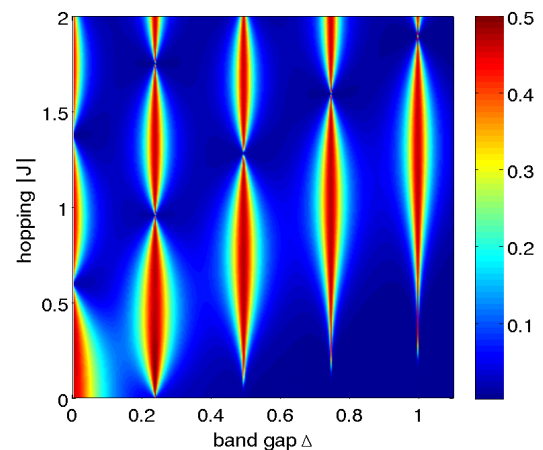


FIG. 1: (Color online) Landau-Zener-Stückelberg interferometry. Shown is the long-time average of the occupation of the upper band as a function of the band gap Δ (corresponding to the level separation in atomic systems) and the hopping difference between the bands $J = J_a - J_b$ (corresponding to the driving amplitude). Parameters: $C_0 = -0.15$ and $F = 1.0$.

Δ according to eq. (21) to be derived below. To see how these interference patterns arise in systems of cold atoms, we will derive analytical expressions for the interband dynamics.

III. STÜCKELBERG INTERFEROMETRY WITH ULTRA-COLD ATOMS

A. Dynamics of the interband transitions

To study the dynamics of the interband transition we have to solve the time-dependent Schrödinger equation. However, it can be shown to be equivalent to the Hill equation and exact analytical solutions in closed form are not possible. To obtain approximate solutions in a systematic fashion, we will use the Magnus expansion [18]. It is useful apply the following transformation in order to obtain a purely off-diagonal Schrödinger equation [16, 17]

$$\tilde{a}(k, t) = a(k, t)e^{-i\Delta \cdot t/2 - iJ_a \int_0^t \cos(k+ Ft') dt'} \quad (6a)$$

$$\tilde{b}(k, t) = b(k, t)e^{+i\Delta \cdot t/2 - iJ_b \int_0^t \cos(k+ Ft') dt'}. \quad (6b)$$

This removes the diagonal terms and we obtain an equivalent Schrödinger equation with a transformed Hamiltonian $\tilde{\mathcal{H}}(t)$ for the transformed amplitudes

$$i \frac{\partial}{\partial t} \begin{pmatrix} \tilde{a}(k, t) \\ \tilde{b}(k, t) \end{pmatrix} = \begin{pmatrix} 0 & C_0 F e^{-i\phi(k, t)} \\ C_0 F e^{i\phi(k, t)} & 0 \end{pmatrix} \begin{pmatrix} \tilde{a}(k, t) \\ \tilde{b}(k, t) \end{pmatrix}, \quad (7)$$

where $\phi(k, t) = \Delta \cdot t - (J/F)[\sin(k + Ft) - \sin(k)]$ is the phase between the two Bloch bands and $J = (J_a - J_b)$. Where the pure existence of two energy bands allows phenomena like Rabi oscillations, it is the non-trivial phase difference for the time-evolution in both bands, related to $J \neq 0$, that gives rise to Stückelberg oscillations and the complex interference phenomena. That is, the difference in the curvature $J = J_a - J_b \neq 0$ allows to collect different phases during the time evolution in the upper or lower band and excludes exact analytical solutions of the Schrödinger equation in closed form [1, 4, 17].

The idea of the Magnus expansion is to express the time evolution operator as the exponential of an infinite series $U(t) = \exp[\sum_{n=1}^{\infty} \Omega_n(t)]$, with each term containing an increasing number $(n-1)$ of nested different time commutators [18]. All orders of the Magnus expansion could be summed in a recent work for a new derivation of the transition probability in the Landau-Zener problem [19]. The first two terms of this series read explicitly (valid in both Schrödinger and interaction picture [20])

$$\Omega_1(t) = -i \int_0^t \tilde{\mathcal{H}}(t_1) dt_1 \quad (8a)$$

$$\Omega_2(t) = \frac{1}{2} \int_0^t dt_1 \int_0^{t_1} dt_2 [\tilde{\mathcal{H}}(t_1), \tilde{\mathcal{H}}(t_2)] \quad (8b)$$

To compute the terms in the Magnus expansion for our time-dependent problem, eq. (7), explicitly, we have to integrate the Hamiltonian and commutators of it over time. Without loss of generality, we restrict our discussion to $k = 0$, which can always be achieved by shifting the time zero. We will need the integral

$$\chi(t) \equiv \int_0^t e^{i\phi(t')} dt' = \int_0^t e^{i(\Delta \cdot t' - (J/F) \sin Ft')} dt'. \quad (9)$$

Using the the generating function of the Bessel function $\exp[u(\tau - 1/\tau)] = \sum_{n \in \mathbb{Z}} J_n(2u)\tau^n$ for $\tau = e^{-iFt}$, we can write the sin in the exponent as a sum over Bessel functions $\chi(t) = \sum_{n \in \mathbb{Z}} J_n(J/F) \int_0^t dt' e^{i(\Delta - nF)t'}$. After integration and minor manipulations, we obtain a closed expression with the explicit time dependence for the highly oscillatory function

$$\chi(t) = 2 \sum_{n \in \mathbb{Z}} J_n(J/F) e^{i\omega_n t/2} \frac{\sin(\omega_n t/2)}{\omega_n} \quad (10)$$

with $\omega_n = \Delta - nF$. With the explicit expression for the integral defining $\chi(t)$, the first term in the Magnus expansion is given by $\Omega_1(t) = -iC_0 F \begin{pmatrix} 0 & \chi^* \\ \chi & 0 \end{pmatrix}$ and the time evolution operator in first order reads correspondingly [11]

$$U_1(t) = \begin{pmatrix} \cos(C_0 F |\chi|) & -ie^{i \arg \chi} \sin(C_0 F |\chi|) \\ -ie^{-i \arg \chi} \sin(C_0 F |\chi|) & \cos(C_0 F |\chi|) \end{pmatrix}. \quad (11)$$

This is the result in first order and the occupation of the upper band $P_b(t) \equiv \sum_k |b(k, t)|^2$ is given by

$$P_b(t) = \sin^2 \left[2C_0 F \left| \sum_n J_n(J/F) e^{i\omega_n t/2} \frac{\sin(\omega_n t/2)}{\omega_n} \right| \right]. \quad (12)$$

This result captures resonant and non-resonant contributions of the interferometry in a single and explicit formula. Eq. (12) can be understood by treating the denominator zeros $\omega_m = 0 \Leftrightarrow \Delta = mF$ contained in $\chi(t)$ separately using $\lim_{x \rightarrow 0} \frac{\sin xt}{x} = t$. This condition $\Delta \approx mF$ corresponds to a resonant interband coupling and $\chi(t)$ can be decomposed as

$$\chi(t) = J_m(J/F) t + 2 \sum_{n \neq m} J_n(J/F) e^{i\omega_n t/2} \frac{\sin(\omega_n t/2)}{\omega_n}.$$

For large times the first term will be dominating and the overall short-time averaged occupation of the upper band shows large sinusoidal oscillations with unit amplitude $\mathcal{N}_b^{\text{res}}(t) = \sin^2[V J_m(J/F) t]$. The other high-frequency and non-resonant terms lead to small amplitude oscillations on top of this overall resonant interband oscillations.

For the second order contribution we need the commutator (where σ_z is the diagonal Pauli matrix)

$$[\tilde{\mathcal{H}}(t_1), \tilde{\mathcal{H}}(t_2)] = 2iC_0^2 F^2 \sigma_z \sin[\phi(t_2) - \phi(t_1)] \quad (13)$$

and integrate over it in time. One obtains $\Omega_2(t) = iC_0^2 F^2 \sigma_z \psi(t)$ where the required integral $\psi(t) \equiv \int_0^t dt_1 \int_0^{t_1} dt_2 \sin[\phi(t_2) - \phi(t_1)]$ can be computed by applying the same expansion as above

$$\psi(t) = \sum_{n \in \mathbb{Z}} \frac{J_n(J/F)}{\omega_n} \left\{ \sum_{m \in \mathbb{Z}} J_m(J/F) \times \left(\frac{\sin^2 \omega_m t/2}{\omega_m} - \frac{\sin^2[(m+n)Ft/2]}{(m+n)F} \right) \right\}. \quad (14)$$

The time evolution operator can again be given exactly [11] and one finds for the occupation of the upper band

$$P_b(t) = \frac{|\chi|^2}{|\chi^* \chi + C_0^2 F^2 \psi^2|} \sin^2 \left(2C_0 F \sqrt{\chi^* \chi + C_0^2 F^2 \psi^2} \right), \quad (15)$$

where we suppressed the time-dependence of the functions $\chi(t)$ and $\psi(t)$. The eqs. (12) and (15) are the central results of this section. They provide good approximations to the full interband dynamics in an explicit expression. They furthermore contain the resonant as well as non-resonant contributions to the interband dynamics.

B. Average occupation of bands

In order to determine the average occupation of the bands it is more useful to go back to the original two-band Hamiltonian eq. (2) instead of calculating the long-time average over the expressions eq. (12) and eq. (15). Introducing the Wannier–Stark states [21] $\alpha_n = \sum_{l \in \mathbb{Z}} J_{l-n}(J_a/F) a_l$ and $\beta_n = \sum_{l \in \mathbb{Z}} J_{l-n}(J_b/F) b_l$ into eq. (2), one obtains [13]

$$\mathcal{H}_{2B} = \sum_{l \in \mathbb{Z}} \left[(lF - \frac{\Delta}{2}) \alpha_l^\dagger \alpha_l + (lF + \frac{\Delta}{2}) \beta_l^\dagger \beta_l + \sum_{m \in \mathbb{Z}} C_0 F J_m(J/F) (\alpha_l^\dagger \beta_{l-m} + \text{h.c.}) \right], \quad (16)$$

where $J = J_a - J_b$ as above. This expression contains all relevant processes coupling the two bands as direct couplings weighted by Bessel functions $J_m(J/F)$. For $J/F \lesssim 1$ the dominant contribution is the on-site coupling between the bands proportional to $J_0(J/F)$. Keeping only this dominant contribution, the Hamiltonian eq. (16) is a sum of independent two-level systems and can easily be diagonalized. The resulting occupation of the upper band contains the dominant part of the non-resonant oscillations already contained in eq. (12) and reads

$$P_b(t) = \frac{4V_0^2}{\Delta^2 + 4V_0^2} \sin^2 \left(\sqrt{\Delta^2 + 4V_0^2} \cdot t/2 \right). \quad (17)$$

where $V_0 = C_0 F J_0(J/F)$. This means that the non-resonant contribution to the averaged occupation of the upper band is given by

$$\overline{P_b} = \frac{1/2}{1 + \left[\frac{\Delta/F}{2C_0 J_0(J/F)} \right]^2}. \quad (18)$$

However, in addition to this onsite coupling, the Hamiltonian eq. (16) allows a direct coupling of more remote sites. This becomes particularly important whenever a site from the lower band and a site from the upper band are energetically degenerate. The corresponding resonance condition for two levels being separated by m sites is $\Delta \approx mF$, $m \in \mathbb{N}$. We therefore apply degenerate perturbation theory [22] to the Hamiltonian eq. (16) and obtain for a resonance of order m in second order the following effective two-level system [11, 23]

$$\begin{pmatrix} \epsilon_{l-m}^+ + \sum_{i \neq l} \frac{|V_{l-m-i}|^2}{\epsilon_{l-m}^+ - \epsilon_l^-} & V_{-m} \\ V_{-m} & \epsilon_l^- + \sum_{i \neq l-m} \frac{|V_{l-i}|^2}{\epsilon_l^- - \epsilon_i^+} \end{pmatrix}, \quad (19)$$

with $\epsilon_l^\pm = lF \pm \Delta/2$ and $V_l = C_0 F J_l(J/F)$. This and higher orders allow the computation of various observables with high degree of precision [23]. For example, the resonance condition $\Delta = mF$ experiences a slight Stark

shift and the corresponding condition in second order is given by

$$\Delta = mF - 2C_0^2 F^2 \sum_{i \neq m} \frac{J_i^2(J/F)}{\Delta - iF}. \quad (20)$$

Unlike the usual LZS problem, the coupling between the bands $C_0 F$ and the driving frequency $\omega_B = F$ are not independent for atoms in optical lattices. This makes eq. (20) nonlinear and difficult to solve. However, it can be solved either numerically or by iteration. The uncorrected resonance position for a single optical lattice with $V_0 = 4$ and a resonance of order 2 is given by $F_2 = \Delta/2 = 2.195$. Solving eq. (20) numerically gives $F_2^{\text{PT}} = 2.22067$ which has a relative error of order 10^{-5} when compared to the maximum of the resonance $F = 2.22070$ from numerical simulations of the full problem eq. (4). In the same way, very high precision can be achieved by higher orders perturbation theory.

The resulting resonant contribution to the average occupation of the upper band has a Lorentzian shape [4, 17] and the total transition probability is given by the non-resonant interband coupling and the different resonant contributions

$$\overline{P_b} = \frac{1}{2} \frac{4V_0^2}{\Delta^2 + 4V_0^2} + \frac{1}{2} \sum_m \frac{4(V_m/F\Delta)^2}{(1/F - 1/F_m)^2 + 4(V_m/F\Delta)^2}. \quad (21)$$

The first term describes the direct force-induced coupling between the bands and is usually much smaller than unity. However, for $F \gg \Delta$ its contribution becomes important and grows as F^{-2} . The second part are the resonant contributions from different orders of resonance. Let us compare this result eq. (21) to numerical simulations of the full Hamiltonian eq. (2). We change to the interaction picture with respect to the external force and impose periodic boundary conditions [10, 15]. We take an initial state $|\psi_0\rangle$ which occupies only the lower band, and evolve it in time according to the Schrödinger equation $i\partial_t |\psi(t)\rangle = \mathcal{H}(t) |\psi(t)\rangle$. We compute the total occupation of the upper band $P_b(t) = \langle \psi(t) | b_l^\dagger b_l | \psi(t) \rangle$ and take the long time average. The result for a single optical lattice realization with $V_0 = 4$ is shown in fig. 2 together with our result eq. (21). We observe very good agreement even on the logarithmic scale shown in the figure. The non-resonant interband coupling and the resonant contribution as well as the resonance positions are accurately reproduced. Only the asymmetry of the resonance peaks (in particular of the high order $m = 4$ resonance at $1/F \approx 0.9$) is not captured by our present analysis since the effective model of eq. (19) should be extended to describe well such more complex peak profiles.

C. Interferometry with optical lattices

We have established the general possibility to use ultracold atoms for Stückelberg interferometry and have given

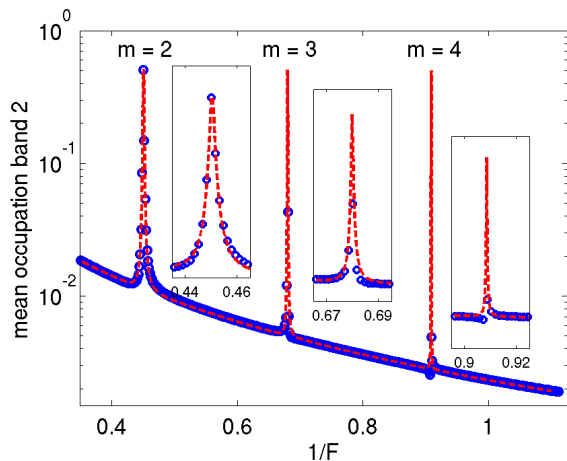


FIG. 2: (Color online) Longtime average of the occupation of the upper band from numerical simulations of the full problem (blue circles) and the theoretical prediction eq. (21) (dashed line). The insets show the resonances $m = 2, 3, 4$ on a linear scale. Parameters for a single optical lattice of depth $V_0 = 4$: $C_0 = -0.14$, $\Delta = 4.39$, and $J = -0.682$.

analytical results for the probability of interband transitions in the previous paragraphs. As already mentioned, the important parameters hopping J and band gap Δ to build the Landau–Zener–Stückelberg Hamiltonian, eq. (1), can, however, not be controlled independently in optical lattice systems. We therefore show interference patterns similar to figure 1 but with the experimentally accessible parameters varied. That is, we vary the depth of the optical (super-)lattice (and possible the phase ϕ) and compute the Wannier functions for each value of the lattice parameters. From these we obtain the relevant parameters J , Δ , and C_0 according to eq. (3). With them we obtain the transition probabilities at different forces from eq. (21). The results for realizations with a single optical lattice and a superlattice are shown in fig. 3. We clearly observe resonances of different orders as the external force is varied. The resonance position changes nonlinearly with the lattice depth since the band gap is generally a not strictly linear function of the lattice depth (in both cases of a single lattice and a superlattice). Additionally, the importance of the non-resonant background becomes more important for larger forces, i.e. for small $1/F$.

As mentioned already, the three system parameters J , Δ , and C_0 all depend on the lattice depth V_0 (or V_2/V_1) and cannot be varied independently. However, the situa-

tion is slightly advantageous for superlattices, since there are two experimental parameters, the ratio of the lattice depths V_2/V_1 and the relative phase between the lattices ϕ , that can be altered. We therefore computed the Wannier functions and the system parameters for many different combinations of these two parameters and show the resulting transition probability as a contour plot in fig. 4 for fixed external force $F = 3$. We observe a clear and broad resonance as a result of Stückelberg interference when different parts of the wave function evolve in the different bands. The complicated shape of the resonance is again a result of the nonlinear dependence of the system parameters on V_2/V_1 and ϕ . Fig. 4 is an explicit prediction for transition probabilities from multiple phase interference that should be observable with current experimental methods as in [6].

IV. SUMMARY

We have made the connection between Stückelberg interferometry and recent experiments with ultra-cold atoms. We showed explicitly how to obtain the Landau–Zener–Stückelberg Hamiltonian with cold atoms in accelerated optical lattices. More specifically, we applied the Magnus expansion to obtain analytical expressions capturing various aspects of the complicated interband dynamics. The transition probabilities for different experimental realizations with atomic quantum gases have been computed and should be experimentally accessible. We thus hope to have clarified some of the background of ongoing experiments and to stimulate further research using the high control in state-of-the-art implementations.

Acknowledgments

This work was supported by the DFG FOR760 and the Klaus Tschira Foundation. SW is especially grateful to the Hengstberger Foundation for the Klaus-Georg and Sigrid Hengstberger Prize, and acknowledges further support from the Helmholtz Alliance Program of the Helmholtz Association (contract HA-216 “Extremes of Density and Temperature: Cosmic Matter in the Laboratory”), and within the framework of the Excellence Initiative by the German Research Foundation (DFG) through the Heidelberg Graduate School of Fundamental Physics (grant number GSC 129/1), the Frontier Innovation Fonds and the Global Networks Mobility Measures.

-
- [1] M. Grifoni and P. Hänggi, *Physics Reports* **304**, 229 (1998).
 [2] W. D. Oliver, Y. Yu, J. C. Lee, K. K. Berggren, L. S. Levitov, and T. P. Orlando, *Science* **310**, 1653 (2005).
 [3] S. Longhi, *Phys. Rev. A* **81**, 022118 (2010).

- [4] S. Shevchenko, S. Ashhab, and F. Nori, *Physics Reports* **492**, 1 (2010).
 [5] A. Zenesini, D. Ciampini, O. Morsch, and E. Arimondo, arXiv:1010.2431v1 (2010).
 [6] S. Kling, T. Salger, C. Grossert, and M. Weitz, *Phys.*

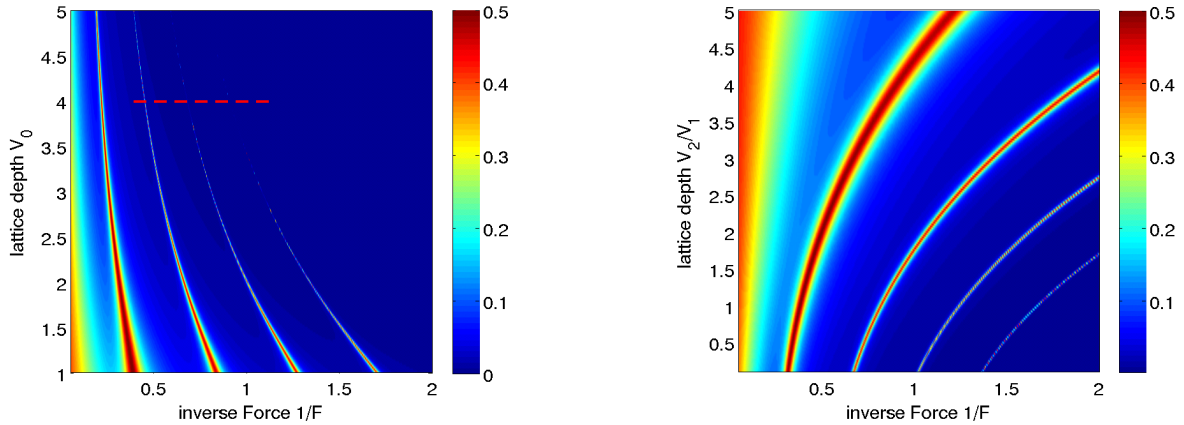


FIG. 3: (Color online) Driving interferometry, i.e. average occupation as function of the upper band as a function of the lattice depth and the external force. *Left*: Long-time average of the occupation of the upper band according to eq. (21) for a realization with a single optical lattice with depth $V(x) = V_0 \cos(x)$. The parameters $J = J_a - J_b$ and C_0 depend on the lattice depth and are determined from numerical computation of the Wannier functions and eq. (3). The dashed line marks the values shown in fig. 2. *Right*: The same as in the left panel but for a realization with a superlattice $V(x) = V_1 \cos(x) + V_2 \cos(2x + \phi)$ for $V_1 = 2$, $\phi = \pi$, and varying V_2 .

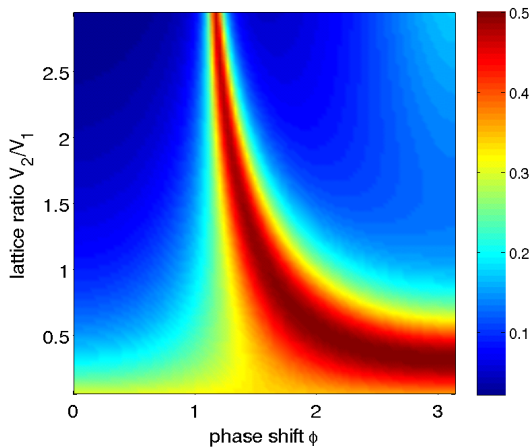


FIG. 4: (Color online) Driving interferometry, i.e. average occupation as function of the upper band as a function for a realization with a superlattice $V(x) = V_1 \cos(x) + V_2 \cos(2x + \phi)$. Shown is the average of the occupation of the upper band according to eq. (21) as a function of the accessible experimental parameters: ratio of lattice depths V_2/V_1 and phase between the lattices ϕ for fixed external force $F = 3$ and $V_1 = 2$. We observe a clear and broad resonance from phase interference. The nonlinear shape arises from the nonlinear dependence of the various system parameters on V_2/V_1 and ϕ .

Rev. Lett. **105**, 215301 (2010).

[7] O. Morsch and M. Oberthaler, Rev. Mod. Phys. **78**, 179

(2006).

- [8] I. Bloch, J. Dalibard, and W. Zwerger, Rev. Mod. Phys. **80**, 885 (2008).
- [9] A. Tomadin, R. Mannella, and S. Wimberger, Phys. Rev. A **77**, 013606 (2008).
- [10] A. Tomadin, Master's thesis, Università di Pisa (2006).
- [11] P. Plötz, Ph.D. thesis, Universität Heidelberg (2010), URL <http://archiv.ub.uni-heidelberg.de/volltextserver/volltexte/2010/11123/>.
- [12] C. Parra-Murillo, J. Madroñero, and S. Wimberger, in preparation.
- [13] P. Plötz, J. Madroñero, and S. Wimberger, J. Phys. B **43**, 081001 (2010).
- [14] P. Plötz, P. Schlagheck, and S. Wimberger, *Complex dynamics of a two-band bose-hubbard model*, in preparation.
- [15] A. R. Kolovsky and A. Buchleitner, Phys. Rev. E **68**, 056213 (2003).
- [16] X.-G. Zhao, G. A. Georgakis, and Q. Niu, Phys. Rev. B **54**, R5235 (1996).
- [17] P. Plötz, Journal of Siberian Federal University: Mathematics & Physics **3**, 381 (2010).
- [18] S. Blanes, F. Casas, J. Oteo, and J. Ros, Physics Reports **470**, 151 (2009).
- [19] A. G. Rojo, arXiv:1004.2914v1 (2010).
- [20] P. Pechukas and J. C. Light, The Journal of Chemical Physics **44**, 3897 (1966).
- [21] M. Glück, A. R. Kolovsky, and H. J. Korsch, Physics Reports **366**, 103 (2002).
- [22] J. H. Shirley, Ph.D. thesis, California Institute of Technology (1963).
- [23] J. Hausinger and M. Grifoni, Phys. Rev. A **81**, 022117 (2010).

Beyond mean-field dynamics in open Bose-Hubbard chains

D. Witthaut,^{1,*} F. Trimborn,² H. Hennig,¹ G. Kordas,³ T. Geisel,¹ and S. Wimberger³

¹*Max-Planck-Institute for Dynamics and Self-Organization, D-37073 Göttingen, Germany*

²*Institut für theoretische Physik, Leibniz Universität Hannover, D-30167 Hannover, Germany*

³*Institut für theoretische Physik and Center for Quantum Dynamics, Universität Heidelberg, D-69120 Heidelberg, Germany*

(Dated: March 19, 2012)

We investigate the effects of phase noise and particle loss on the dynamics of a Bose-Einstein condensate in an optical lattice. Starting from the many-body master equation, we discuss the applicability of generalized mean-field approximations in the presence of dissipation as well as methods to simulate quantum effects beyond mean-field by including higher-order correlation functions. It is shown that localized particle dissipation leads to surprising dynamics, as it can *suppress* decay and *restore* the coherence of a Bose-Einstein condensate. These effects can be applied to engineer coherent structures such as stable discrete breathers and dark solitons.

PACS numbers: 03.75.Lm, 03.65.Yz, 03.75.Gg

I. INTRODUCTION

Decoherence and dissipation, caused by the irreversible coupling of a quantum system to its environment, represent a major obstacle for the long-time coherent control of quantum states. However, in the last years it has been realized that dissipation can be extremely useful if it can be controlled accurately. Recent experiments have shown that strong correlations can be induced by two-body losses in ultracold quantum gases [1, 2]. Three-body losses can be tailored to generate effective three-body interactions [3] and to prepare strongly correlated states for quantum simulations of color superfluidity [4], quantum hall physics [5] or d-wave pairing [6]. Even more, dissipation can be used as a universal tool in quantum state preparation [7, 8], entanglement generation [9] and quantum information processing [10]. These concepts of controlling quantum dynamics and transport are particularly important for experiments with ultracold atoms in optical lattices, where it is possible to address the quantum system with single-site resolution [11, 12]. An even higher spatial resolution has been realized with a focussed electron beam, removing atoms one-by-one from the lattice [13, 14]. The effects of such a localized particle loss on the dynamics of a Bose-Einstein condensate (BEC) have been investigated from a nonlinear dynamics viewpoint in several papers in the last years, discussing the possibility to induce nonlinear structures such as bright breathers [15, 16], dark solitons [17] or ratchets [18]. These studies were based on a mean-field approximation, where the loss was introduced heuristically as an imaginary potential.

In this article we go beyond this approximation and investigate the quantum dynamics of ultracold atoms in a finite optical lattice with dissipation, which provides a distinguished model system for the study of open one-dimensional chains. Our analysis is based on a numer-

ical integration of the full many-body master equation and generalized mean-field methods. In section II, we present an explicit derivation of the mean-field equations of motion, which hold if the many-body state is close to a BEC, and generalize this approach to take into account higher order correlation functions [19, 20]. If particle loss is the only source of dissipation, the mean-field equations reduce to a non-hermitian Schrödinger equation applied previously [16, 17]. While such a non-hermitian description has been thoroughly studied for single particle quantum mechanics [21], the applicability to open many-body systems is an open issue.

Two important cases are studied in detail: In section III, we analyze how boundary dissipation induces localization and purifies a BEC. In section IV, we consider localized loss from a single lattice site, which creates a vacancy and leads to a fragmentation of the condensate. Remarkably, strong dissipation can suppress the decay of the condensate and a coherent dark soliton can be generated by properly engineering the dynamics. The techniques presented here can be directly applied in ongoing experiments [13, 14].

II. THE MEAN-FIELD LIMIT AND BEYOND

The coherent dynamics of ultracold atoms in optical lattices is described by the celebrated Bose-Hubbard Hamiltonian [22]

$$\hat{H} = -J \sum_j \left(\hat{a}_{j+1}^\dagger \hat{a}_j + \hat{a}_j^\dagger \hat{a}_{j+1} \right) + \frac{U}{2} \sum_j \hat{a}_j^\dagger \hat{a}_j^\dagger \hat{a}_j \hat{a}_j, \quad (1)$$

where \hat{a}_j and \hat{a}_j^\dagger are the bosonic annihilation and creation operators in mode j , J denotes the tunneling matrix element between the wells and U the interaction strength. We set $\hbar = 1$, thus measuring energy in frequency units. This model assumes that the lattice is sufficiently deep, such that the dynamics takes place in the lowest Bloch band only.

*Electronic address: witthaut@nld.ds.mpg.de

In the presence of dissipation, the dynamics is given by a master equation in Lindblad form [23],

$$\dot{\hat{\rho}} = -i[\hat{H}, \hat{\rho}] + \mathcal{L}\hat{\rho}. \quad (2)$$

Here, we are especially interested in the effects of localized particle loss, which can be implemented by an electron beam [13, 14] or by a strongly focussed resonant blast laser. Furthermore, phase noise is always present in experiments, which degrades the phase coherence between adjacent wells and heats the sample [24, 25]. These two processes are described by the Liouvillians [23, 26–28]

$$\mathcal{L}_{\text{loss}}\hat{\rho} = -\frac{1}{2} \sum_j \gamma_j \left(\hat{a}_j^\dagger \hat{a}_j \hat{\rho} + \hat{\rho} \hat{a}_j^\dagger \hat{a}_j - 2\hat{a}_j \hat{\rho} \hat{a}_j^\dagger \right), \quad (3)$$

$$\mathcal{L}_{\text{phase}}\hat{\rho} = -\frac{\kappa}{2} \sum_j \hat{n}_j^2 \hat{\rho} + \hat{\rho} \hat{n}_j^2 - 2\hat{n}_j \hat{\rho} \hat{n}_j, \quad (4)$$

where γ_j denotes the loss rate at site j and κ is the strength of the phase noise.

To derive the mean-field approximation, we start from the single particle reduced density matrix (SPDM) $\sigma_{jk} = \langle \hat{a}_j^\dagger \hat{a}_k \rangle = \text{tr}(\hat{a}_j^\dagger \hat{a}_k \hat{\rho})$ [19, 20, 29]. The equations of motion for σ_{jk} are obtained from the master equation (2),

$$\begin{aligned} i \frac{d}{dt} \sigma_{j,k} &= \text{tr} \left(\hat{a}_j^\dagger \hat{a}_k [\hat{H}, \hat{\rho}] + i \hat{a}_j^\dagger \hat{a}_k \mathcal{L} \hat{\rho} \right) \\ &= -J(\sigma_{j,k+1} + \sigma_{j,k-1} - \sigma_{j+1,k} - \sigma_{j-1,k}) \\ &\quad + U(\sigma_{kk} \sigma_{jk} + \Delta_{jkkk} - \sigma_{jj} \sigma_{jk} - \Delta_{jjjk}), \\ &\quad -i \frac{\gamma_j + \gamma_k}{2} \sigma_{j,k} - i\kappa(1 - \delta_{j,k}) \sigma_{j,k}, \end{aligned} \quad (5)$$

where we have defined the covariances

$$\Delta_{jklm} = \langle \hat{a}_j^\dagger \hat{a}_k \hat{a}_\ell^\dagger \hat{a}_m \rangle - \langle \hat{a}_j^\dagger \hat{a}_k \rangle \langle \hat{a}_\ell^\dagger \hat{a}_m \rangle. \quad (6)$$

In the mean-field limit $N \rightarrow \infty$ with $g = UN$ fixed, one can neglect the variances Δ_{jklm} in Eq. (5) in order to obtain a closed set of evolution equations. This is appropriate for a pure BEC, because the variances scale only linearly with the particle number N , while the products $\sigma_{jk} \sigma_{\ell m}$ scale as N^2 . If phase noise can be neglected, i.e. $\kappa = 0$, the equations of motion (5) are equivalent to the non-hermitian discrete nonlinear Schrödinger equation

$$i \frac{d}{dt} \psi_k = -J(\psi_{k+1} + \psi_{k-1}) + U|\psi_k|^2 \psi_k - i \frac{\gamma_k}{2} \psi_k \quad (7)$$

by the identification $\sigma_{j,k} = \psi_j^* \psi_k$. This provides a proper derivation of the non-hermitian Schrödinger equation, which has previously been applied heuristically [15–17].

The mean-field approximation assumes a pure BEC and is strictly valid only in the limit $N \rightarrow \infty$. To describe many-body effects such as quantum correlations and the depletion of the condensate for large, but finite particle numbers, we generalize the Bogoliubov backreaction (BBR) method [19] to the dissipative case, taking into account the covariances (6) explicitly. We start with

the coherent part of the master equation, which yields the following evolution equations for the four-point functions:

$$\begin{aligned} i \frac{d}{dt} \langle \hat{a}_j^\dagger \hat{a}_m \hat{a}_k^\dagger \hat{a}_n \rangle &= \text{tr} \left(\hat{a}_j^\dagger \hat{a}_m \hat{a}_k^\dagger \hat{a}_n [\hat{H}, \hat{\rho}] \right) \\ &= (\epsilon_m + \epsilon_n - \epsilon_j - \epsilon_k) \langle \hat{a}_j^\dagger \hat{a}_m \hat{a}_k^\dagger \hat{a}_n \rangle \\ &\quad - J \langle \hat{a}_j^\dagger \hat{a}_m \hat{a}_k^\dagger \hat{a}_{n+1} + \hat{a}_j^\dagger \hat{a}_m \hat{a}_k^\dagger \hat{a}_{n-1} + \hat{a}_j^\dagger \hat{a}_{m+1} \hat{a}_k^\dagger \hat{a}_n \\ &\quad + \hat{a}_j^\dagger \hat{a}_{m-1} \hat{a}_k^\dagger \hat{a}_n - \hat{a}_{j+1}^\dagger \hat{a}_m \hat{a}_k^\dagger \hat{a}_n - \hat{a}_{j-1}^\dagger \hat{a}_{m+1} \hat{a}_k^\dagger \hat{a}_n \\ &\quad - \hat{a}_j^\dagger \hat{a}_m \hat{a}_{k+1}^\dagger \hat{a}_n - \hat{a}_j^\dagger \hat{a}_m \hat{a}_{k-1}^\dagger \hat{a}_n \rangle \\ &\quad + U \langle \hat{a}_j^\dagger \hat{a}_m \hat{n}_m \hat{a}_k^\dagger \hat{a}_n + \hat{a}_j^\dagger \hat{a}_m \hat{a}_k^\dagger \hat{a}_n \hat{n}_n \\ &\quad - \hat{n}_j \hat{a}_j^\dagger \hat{a}_m \hat{a}_k^\dagger \hat{a}_n - \hat{a}_j^\dagger \hat{a}_m \hat{n}_k \hat{a}_k^\dagger \hat{a}_n \rangle. \end{aligned} \quad (8)$$

Again, the interaction hamiltonian leads to higher-order correlation functions. To obtain a closed set of evolution equations, these function are truncated according to [20]

$$\begin{aligned} \langle \hat{a}_j^\dagger \hat{a}_m \hat{a}_k^\dagger \hat{a}_n \hat{a}_r^\dagger \hat{a}_s \rangle &\approx \langle \hat{a}_j^\dagger \hat{a}_m \hat{a}_k^\dagger \hat{a}_n \rangle \langle \hat{a}_r^\dagger \hat{a}_s \rangle \\ &\quad + \langle \hat{a}_j^\dagger \hat{a}_m \hat{a}_r^\dagger \hat{a}_s \rangle \langle \hat{a}_k^\dagger \hat{a}_n \rangle + \langle \hat{a}_k^\dagger \hat{a}_n \hat{a}_r^\dagger \hat{a}_s \rangle \langle \hat{a}_j^\dagger \hat{a}_m \rangle \\ &\quad - 2 \langle \hat{a}_j^\dagger \hat{a}_m \rangle \langle \hat{a}_k^\dagger \hat{a}_n \rangle \langle \hat{a}_r^\dagger \hat{a}_s \rangle. \end{aligned} \quad (9)$$

For a BEC, the six-point function scale as N^3 , while the error introduced by this approximation increases only linearly with N . The relative error induced by the truncation thus vanishes as $1/N^2$ with increasing particle number. Close to a pure condensate, the BBR method thus provides a better description of the many-body dynamics than the simple mean-field approximation, since it includes the dynamics of higher order methods at least approximately. Using this truncation, the coherent part of the dynamics is given by

$$\begin{aligned} i \frac{d}{dt} \Delta_{jmk n} &= \\ &= -J[\Delta_{j,m,k,n+1} + \Delta_{j,m,k,n-1} + \Delta_{j,m+1,k,n} + \Delta_{j,m-1,k,n} \\ &\quad - \Delta_{j,m,k+1,n} - \Delta_{j,m,k-1,n} - \Delta_{j+1,m,k,n} - \Delta_{j-1,m,k,n}] \\ &\quad + U[\Delta_{mmkn} \sigma_{jm} - \Delta_{jjkn} \sigma_{jm} + \Delta_{jmmn} \sigma_{kn} - \Delta_{jmkk} \sigma_{kn} \\ &\quad + \Delta_{jmk n} (\sigma_{mm} + \sigma_{nn} - \sigma_{kk} - \sigma_{jj})]. \end{aligned} \quad (10)$$

Particle loss and dissipation affect the dynamics of the four-point functions as follows

$$\begin{aligned} \frac{d}{dt} \langle \hat{a}_j^\dagger \hat{a}_m \hat{a}_k^\dagger \hat{a}_n \rangle &= \text{tr} \left[\hat{a}_j^\dagger \hat{a}_m \hat{a}_k^\dagger \hat{a}_n \mathcal{L} \hat{\rho} \right] \\ &= -\frac{\gamma_j + \gamma_m + \gamma_k + \gamma_n}{2} \langle \hat{a}_j^\dagger \hat{a}_m \hat{a}_k^\dagger \hat{a}_n \rangle - \delta_{mk} \gamma_m \langle \hat{a}_j^\dagger \hat{a}_n \rangle \\ &\quad - \kappa(2 + \delta_{mn} + \delta_{jk} - \delta_{jm} - \delta_{jn} - \delta_{km} - \delta_{kn}) \\ &\quad \times \langle \hat{a}_j^\dagger \hat{a}_m \hat{a}_k^\dagger \hat{a}_n \rangle. \end{aligned}$$

In terms of the variances this yields

$$\begin{aligned} \frac{d}{dt} \Delta_{jmk n} &= -\frac{\gamma_j + \gamma_m + \gamma_k + \gamma_n}{2} \Delta_{jmk n} - \delta_{mk} \gamma_m \sigma_{jn} \\ &\quad - \kappa(\delta_{mn} + \delta_{jk} - \delta_{jn} - 2\delta_{km})(\Delta_{jmk n} + \sigma_{jm} \sigma_{kn}) \\ &\quad - \kappa(2 - \delta_{jm} - \delta_{kn}) \Delta_{jmk n}. \end{aligned} \quad (11)$$

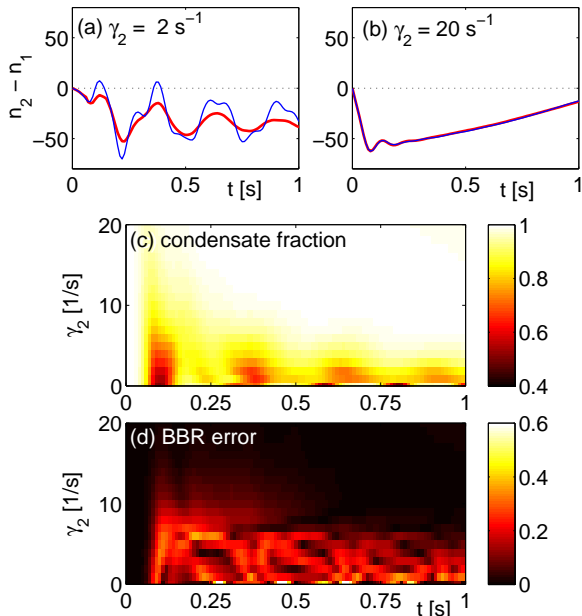


FIG. 1: (Color online) Numerical test of the BBR methods for a leaky double-well trap with loss in the second well. (a,b) Dynamics of the population imbalance $\langle \hat{n}_2 - \hat{n}_1 \rangle$ for two different values of the loss rate, comparing the BBR approximation (solid blue line) to numerically exact results (thick red line). (c) Condensate fraction λ_0/n_{tot} as a function of time and the loss rate γ_2 . (d) Trace distance (12) between the exact rescaled SPDM $\sigma(t)/n(t)$ and the respective BBR approximation. In all cases the initial state is assumed to be a pure BEC with equal population and a phase difference of π between the two modes. The remaining parameters are $J = 10 \text{ s}^{-1}$, $\kappa = 0$, $U = 0.5 \text{ s}^{-1}$ and $n(0) = 200$ atoms.

The BBR method is especially useful if the many-body state is close to, but not exactly equal to a pure BEC. In particular, it accurately predicts the onset of the depletion of the condensate mode. The number of atoms in this mode is given by the leading eigenvalue λ_0 of the SPDM $\sigma_{j,k}$, where the trace of $\sigma_{j,k}$ gives the total number of atoms n_{tot} . The ratio λ_0/n_{tot} is referred to as the condensate fraction [19, 30].

The BBR approach has been extensively tested for closed systems in [20]. Therefore, we only briefly comment on the performance of this method in the presence of dissipation. Figure 1 shows two examples of the dynamics of a BEC in a leaky double-well trap, comparing the BBR approximation (solid blue line) and numerically exact results (thick red line). The initial state is assumed to be a pure BEC with equal population and a phase difference of π between the two modes. In the case of strong dissipation, the BBR approximation predicts the correct evolution of the population imbalance $\langle \hat{n}_2 - \hat{n}_1 \rangle$ with an astonishing precision. In contrast, significant differences are observed for weak losses. This means that the presence of particle loss actually improves the performance of the BBR method, as the dissipation drives the many-

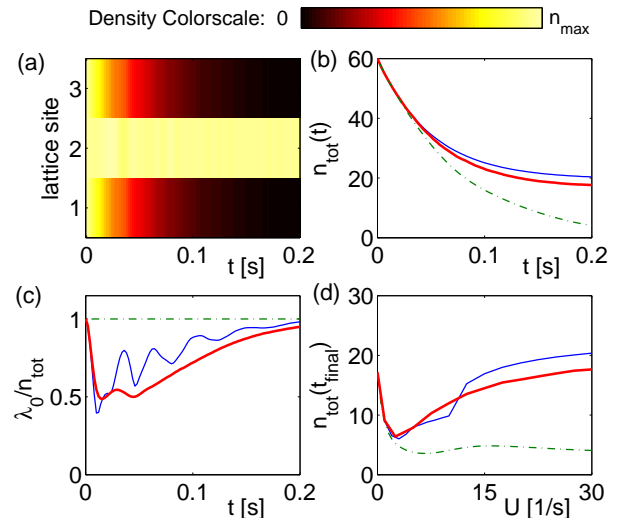


FIG. 2: (Color online) Dynamics of a BEC in a triple-well trap with boundary dissipation: (a) atomic density $\langle \hat{n}_j(t) \rangle$, (b) total particle number and (c) the condensate fraction λ_0/n_{tot} for $J = 5 \text{ s}^{-1}$, $\gamma = 20 \text{ s}^{-1}$, $\kappa = 0$, $U = 30 \text{ s}^{-1}$ and $n(0) = 60$ atoms. (d) Total particle number after a fixed propagation time $t_{\text{final}} = 0.2 \text{ s}$ as a function of the interaction strength U . Mean-field (---) and BBR (—) results are compared to numerically exact simulations with a quantum jump method averaging over 200 trajectories (thick red line).

body quantum state towards a pure BEC [36]. This is confirmed by the numerical results for the condensate fraction λ_0/n_{tot} plotted in Fig. 1 (c). A significant depletion of the condensate is only observed for small values of the loss rate γ_2 . For a further quantitative analysis of the accuracy, we compare exact and BBR results for the rescaled SPDM $\sigma(t)/n_{\text{tot}}(t)$. Figure 1 (d) shows the trace distance of the exact matrix and the matrix obtained by the BBR method,

$$d := \frac{1}{2} \text{tr}(|\sigma_{\text{BBR}}/n_{\text{BBR}} - \sigma_{\text{ex}}/n_{\text{ex}}|), \quad (12)$$

as a function of time for different values of γ_2 . For sufficiently large dissipation, one observes that the distance approximately vanishes for all times. In this regime the quantum dynamics is faithfully reproduced by the BBR approximation.

III. BOUNDARY DISSIPATION

We first analyze the effects of boundary dissipation with a focus on small systems for which numerically exact solutions of the many-particle dynamics are still possible, for instance by the quantum jump method [23, 31]. A comparison to numerically exact results for these examples provides another test of performance of the BBR approach.

We consider the decay of an initially pure, homogeneous BEC in a triple-well trap with boundary dissipation. Figure 2 (a) and (b) show the evolution of the atomic density and the total particle number for strong inter-atomic interactions $U = 30\text{s}^{-1}$. One observes a fast decay of the atoms at the outer sites while the population at the central site is remarkably stable. This is confirmed by the evolution of the total particle number, which rapidly drops to about one third of its initial value, where it saturates for a long time. This is a consequence of the dynamical formation of a discrete breather at the central site, which is an important generic feature of nonlinear lattices. Generally, discrete breathers, also called discrete solitons, are spatially localized, time-periodic, stable excitations in perfectly periodic discrete systems [32–35]. They arise intrinsically from the combination of nonlinearity and the discreteness of the system. In the presence of boundary dissipation, these excitations become attractively stable such that the quantum state of the atoms will converge to a pure BEC with a breather-like density for a wide class of initial states. Once a discrete breather is formed, it remains stable also if the dissipation is switched off. The crucial role of strong interactions is illustrated in Fig. 2 (d), where the residual atom number after $t_{\text{final}} = 0.2\text{s}$ of propagation is plotted as a function of the interaction strength. The particle number increases for large values of U to $n_{\text{tot}}(t_{\text{final}}) \approx 20$ due to the breather formation.

For strong interactions a simple mean-field approximation fails. It strongly underestimates the residual particle number as it predicts that discrete breather are formed only for stronger losses. In contrast, the BBR results agree well with the many-particle simulation even for large values of U . We thus conclude that quantum fluctuations facilitate the formation of repulsively bound structures. Furthermore, a mean-field approach cannot account for genuine many-body features of the dynamics. Figure 2 (c) shows the evolution of the condensate fraction λ_0/n_{tot} , where λ_0 is the leading eigenvalue of the SPDM [30]. In the beginning, interactions lead to a rapid depletion of the condensate. On a longer time scale, however, dissipation restores the coherence and drives the atoms to a pure BEC localized at the central lattice site [36]. The BBR approach faithfully reproduces the depletion and re-purification but additionally predicts unphysical temporal revivals. This example thus demonstrates the strength but also the limitations of this method.

The decay dynamics of the discrete breather state is further analyzed in Fig. 3. The total atom number $n_{\text{tot}}(t)$ decreases rapidly until the discrete breather is formed at $t \approx 0.2\text{s}$. Afterwards the decay is much slower and clearly non-exponential. In both regimes, one can calculate the evolution of $n_{\text{tot}}(t)$ approximately, starting from the relation $\dot{n}_{\text{tot}} = -\gamma(n_1 + n_3)$. Initially, all sites are filled homogeneously, $n_1 = n_3 = n_{\text{tot}}/3$, such that the total particle number decays as

$$n_{\text{tot}}(t) \approx n_{\text{tot}}(0)e^{-2\gamma/3t}. \quad (13)$$

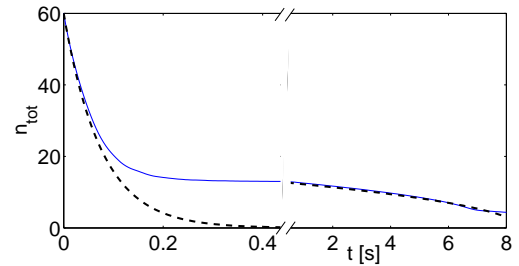


FIG. 3: (Color online) Decay of a discrete breather state for $J = 5\text{s}^{-1}$, $\gamma = 20\text{s}^{-1}$, $\kappa = 0$ and $U = 10\text{s}^{-1}$. Numerical results calculated with the BBR method (—) are compared to the analytic estimates (13) and (14), respectively (---).

When the discrete breather is formed, the population of the outer wells is given by $n_1 = n_3 = J^2/(U^2 n_{\text{tot}})$ in first order perturbation theory. The atom number then decays as

$$n_{\text{tot}}(t) \approx \sqrt{n_{\text{db}}^2 - 4\gamma J^2 t/U^2}, \quad (14)$$

where n_{db} is the number of atoms bound in the discrete breather state. Both approximations are compared to the BBR simulation results in Fig. 3, assuming a breather with $n_{\text{db}} = 13$ atoms. One observes an excellent agreement in the both regimes, i.e. an exponential decay for very short times ($t \lesssim 0.1\text{s}$) and an algebraic decay when the discrete breather is formed. The transition between the linear and nonlinear decay takes place at $t \approx 0.2\text{s}$. A deviation from the algebraic decay (14) for the discrete breather is observed only for very long times when the atom number is very small such that the simple perturbative estimate for $n_{1,3}$ is no longer valid.

IV. LOCALIZED LOSS

Recent experiments with ultracold atoms have demonstrated an enormous progress in spatial addressability using specialized optical imaging systems [11, 12] or a focussed electron beam [13, 14]. Especially the latter experiment allows to manipulate a Bose-Einstein condensate in an optical lattice dissipatively with single-site resolution. In the following, we study the quantum dynamics in a finite lattice of 11 sites with closed boundary conditions and loss occurring from the central site only, which leads to remarkably different decay as in the case of boundary dissipation studied above.

A remarkable feature of the quantum dynamics is illustrated in Figure 4, showing the results of a BBR simulation for an initially pure homogeneous BEC. For a modest loss rate $\gamma = 20\text{s}^{-1}$, atoms tunnel to the central site where they are dissipated with a rate γ , such that the BEC decays almost homogeneously. On the contrary, stronger losses ($\gamma = 100\text{s}^{-1}$) lead to a formation of a stable vacancy. The central site is rapidly depleted, but the

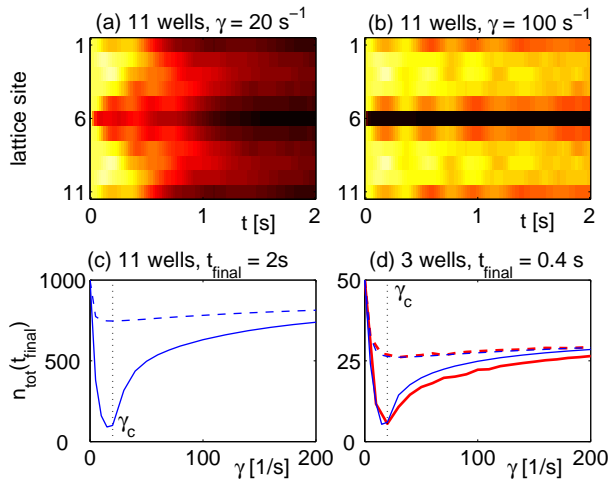


FIG. 4: (Color online) Formation of vacancies by localized loss at the central lattice site. (a,b) Evolution of the atomic density $\langle \hat{n}_j(t) \rangle$ (color scale as in Fig. 2). (c,d) Final value of the total particle number after a fixed propagation time t_{final} as a function of the loss rate γ , without (solid lines) and with strong phase noise (dashed lines, $\kappa = 50 \text{ s}^{-1}$). The remaining parameters are $J = 5 \text{ s}^{-1}$, $U = 0.2 \text{ s}^{-1}$ and $n(0) = 1000$ particles (a-c) and $U = 2 \text{ s}^{-1}$ and $n(0) = 50$ particles (d). The dynamics has been simulated with the BBR (thin blue lines) and the quantum jump method (thick red lines).

atoms in the remaining wells are mostly unaffected. Thus one faces the paradoxical situation that an increase of the loss rate can suppress the decay of the BEC. Two effects contribute to this counterintuitive behavior: (i) The absorbing potential suppresses tunneling to the leaky lattice site. This effect is present also in the linear case and can be explained by an analogy to wave optics [1]: A large mismatch of the index of refraction leads to an almost complete reflection of a wave from a surface. This is true for an imaginary index describing an absorption as well as for a real index. (ii) A dark breather stabilizes the vacancy and prevents the flow of atoms to the central site. This nonlinear structure remains stable also if the dissipation is reduced or switched off afterwards (cf. [33–35] for a discussion of the stability of breathers).

The suppressed decay of the BEC is further illustrated in Fig. 4 (c,d), where the residual atom number after a fixed propagation time is plotted as a function of the loss rate γ . The coherent output of the system, i.e. the number of lost atoms, assumes a maximum for a finite loss rate γ_c . This maximum is reminiscent of the quantum stochastic resonance discussed in [36]. In the following we will estimate the value of γ_c by determining a lower bound for γ for the dynamical breather formation. As a single (both bright and dark) breather exhibits a pronounced population imbalance between the central site and the neighboring sites, we estimate γ_c by matching the timescales of dissipation $\tau_D = 2/\gamma$ and tunneling τ_J , i.e., $\tau_D = \tau_J$. For smaller values of γ , atoms can tunnel away from the leaky lattice site again before they are

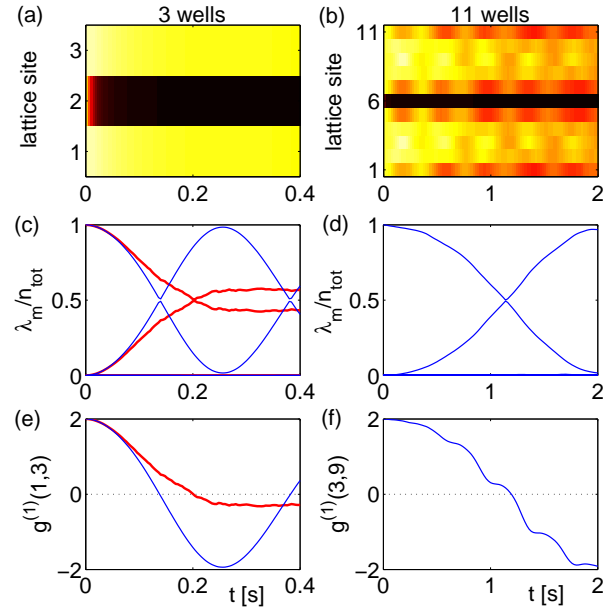


FIG. 5: (Color online) Coherence of a vacancy generated by loss from the central site: (a,b) atomic density, (c,d) scaled eigenvalues λ_m/n_{tot} of the SPDM and (e,f) phase coherence $g^{(1)}$ between the two BEC fragments. Parameters are the same as in Fig. 4 with $\gamma = 100 \text{ s}^{-1}$ and $\kappa = 0$. Results of a quantum jump simulation are plotted as thick red lines, BBR results as thin blue lines.

lost, while for larger values of γ a population imbalance can form. From Eq. (7) we read $\tau_J = 1/(2J)$ where the factor $1/2$ accounts for atoms tunneling from two sites to the leaky site. Hence, the critical loss rate is estimated as $\gamma_c = 4J$. We find good agreement of our qualitative estimate for γ_c (dotted vertical lines in Fig. 4 (c,d)) with the dip in the total particle number. An important quantity for the breather formation and stability is the effective nonlinearity of the system $\lambda = Un_{\text{tot}}(t)/2J$, which, due to particle loss, is time-dependent. Strikingly, though λ depends on the interaction strength U (which is different in Fig. 4 (c) and (d)), the fairly good estimate γ_c is independent of U .

Figure 4 (d) shows the respective results for a triple-well trap with loss from the central site. A comparison of the BBR approximation to a numerically exact many-particle simulation shows a good agreement for all values of γ . Phase noise suppresses decay as it effectively decouples the lattice sites. Thus, only the atoms initially loaded at the leaky lattice site decay as $e^{-\gamma t}$, while the other atoms remain at their initial positions. With increasing loss rate γ , the number of atoms lost from the trap approaches $\approx n(0)/M$ as shown in Fig. 4 (c,d).

The previous reasoning suggests to use dissipation as a tool to coherently engineer the quantum state of a BEC in an optical lattice. Mean-field theory predicts that dissipation can be used to efficiently create a coherent dark soliton [17], but cannot assert the coherence of the final

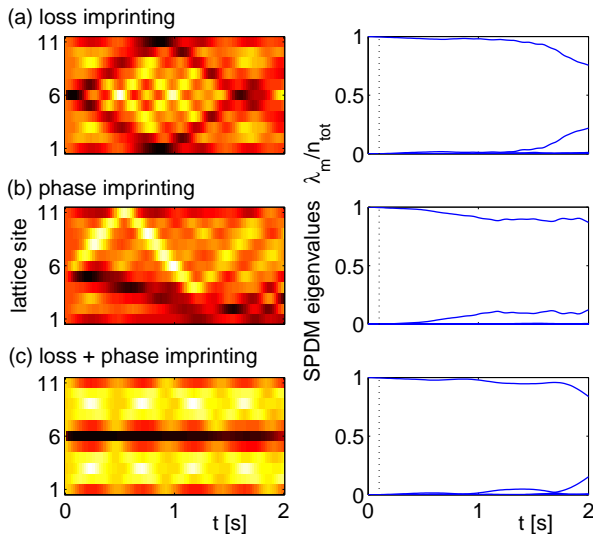


FIG. 6: (Color online) Generation of dark solitons using loss imprinting at a rate $\gamma = 100 \text{ s}^{-1}$ at the central site (a,c) and phase imprinting in the lower half of the lattice (b,c), both for times $t < 0.1 \text{ s}$ only. Shown are the atomic density (left, colorscale as in Fig. 2) and the scaled eigenvalues of the SPDM (right) calculated with the BBR method. Parameters are $J = 5 \text{ s}^{-1}$, $U = 0.1 \text{ s}^{-1}$, $\kappa = 0$ and $n(0) = 1000$ particles.

state as discussed above. The results of a BBR and a quantum jump simulation of the many-body dynamics shown in Fig. 5 reveal the limitations of the phase coherence of a soliton generated by local dissipation. The upper panels (a,b) show the rescaled eigenvalues λ_m/n_{tot} of the SPDM [30]. One observes that there are two macroscopic eigenvalues approaching $1/2$, while all remaining eigenvalues vanish approximately. This proves that the dissipation generates a fragmented BEC consisting of two incoherent parts rather than a single BEC with a solitonic wavefunction. The BBR simulations correctly describe the fragmentation of the condensate, but predict temporal revivals of the coherence which must be considered as artifacts of the approximation. Experimentally, one can test the coherence by the interference of the two fragments in a time-of-flight measurement. Figure 5 (e,f) shows the coherence

$$g^{(1)}(\ell, m) = \frac{\langle \hat{a}_\ell^\dagger \hat{a}_m + a_m^\dagger \hat{a}_\ell \rangle}{\sqrt{\langle \hat{n}_\ell \rangle \langle \hat{n}_m \rangle}} \quad (15)$$

between the wells ℓ and m . One clearly observes the breakdown of phase coherence between the two condensate fragments.

In order to overcome the loss of coherence, one can, however, engineer the many-body dynamics. Figure 6 illustrates the generation of dark solitons comparing three different strategies. If the dissipation is switched off after the generation of a vacancy at $t = 0.1 \text{ s}$, the condensate remains pure for long times. However, the vacancy is not stable but decays into two dark solitons traveling out-

wards [17], where they are reflected at the boundaries. The effects of a phase imprinting, which is an established experimental method [37], are shown in Fig. 6 (b). A local potential is applied to the lower half of the lattice for $t < 0.1 \text{ s}$ imprinting a phase difference of π . Again coherence is preserved but the generated solitons travel outwards. A coherent and stable dark soliton can be engineered by combining both methods, as shown in Fig. 6 (c). The generated dark soliton stays at its initial position and remains coherent over a long time.

V. CONCLUSION

We have discussed the influence of localized particle dissipation on the dynamics of a finite one-dimensional Bose-Hubbard chain, which describes a Bose-Einstein condensate in a deep optical lattice [13, 14]. Starting from the many-body master equation, we have derived the mean-field approximation and the dissipative Bogoliubov backreaction method, which allows a consistent calculation of the depletion of the condensate.

Two important special cases have been studied in detail. Particle loss at the *boundary* leads to localization and the formation of coherent discrete breathers. Surprisingly, dissipation together with interactions can repurify a BEC. A striking effect of *localized loss* is that strong dissipation can effectively *suppress* decay and induce stable vacancies. The decay shows a pronounced maximum for intermediate values of the loss rate, when the timescales of the dissipation and the tunneling are matched. Combined with an external potential, these effects can be used to generate stable coherent dark solitons. These examples show that engineering the dissipation is a promising approach for controlling the dynamics in complex quantum many-body systems.

Ultracold atoms provide a distinguished model system for the dynamics of interacting quantum systems, such that the effects discussed in the present paper may be observed in different systems, too. In particular, quantum transport of single excitations driven by *local* dissipation has recently been studied in a variety of physical systems ranging from spin chains [38] to light-harvesting biomolecules [39]. On the other hand, it has also been shown on the mean-field level that nonlinear excitations such as discrete breathers play an important role for quantum transport in these systems (cf. [33, 34, 40] and references therein). Thus it is of general interest to further explore the regime which interpolates between the nonlinear mean-field dynamics and the many-body quantum dynamics in the spirit of the work presented here.

Acknowledgments

We thank T. Pohl for helpful comments and M. K. Oberthaler for stimulating discussions and ideas on experimental possibilities. We acknowledge financial sup-

port by the Deutsche Forschungsgemeinschaft (DFG) via the Forschergruppe 760 (grant number WI 3426/3-1), the Heidelberg Graduate School of Fundamental Physics

(grant number GSC 129/1) and the research fellowship programme (grant number WI 3415/1-1), as well as the Studienstiftung des deutschen Volkes.

-
- [1] N. Syassen, D. M. Bauer, M. Lettner, T. Volz, D. Dietze, J. J. Garcia-Ripoll, J. I. Cirac, G. Rempe, and S. Dürr, *Science* **320**, 1329 (2008).
- [2] J. J. Garcia-Ripoll, S. Dürr, N. Syassen, D. M. Bauer, M. Lettner, G. Rempe, and J. I. Cirac, *New J. Phys.* **11**, 013053 (2009).
- [3] A. J. Daley, J. M. Taylor, S. Diehl, M. Baranov, and P. Zoller, *Phys. Rev. Lett.* **102**, 040402 (2009).
- [4] A. Kantian, M. Dalmonte, S. Diehl, W. Hofstetter, P. Zoller, and A. J. Daley, *Phys. Rev. Lett.* **103**, 240401 (2009).
- [5] M. Roncaglia, M. Rizzi, and J. I. Cirac, *Phys. Rev. Lett.* **104**, 096803 (2010).
- [6] S. Diehl, W. Yi, A. J. Daley, P. Zoller, arXiv:1007.3420v1
- [7] S. Diehl, A. Micheli, A. Kantian, B. Kraus, H. P. Büchler, and P. Zoller, *Nature Physics* **4**, 878 (2008).
- [8] B. Kraus, H. P. Büchler, S. Diehl, A. Kantian, A. Micheli, and P. Zoller, *Phys. Rev. A* **78**, 042307 (2008).
- [9] H. Krauter, C. A. Muschik, K. Jensen, W. Wasilewski, J. M. Petersen, J. I. Cirac, and E. S. Polzik, arXiv:1006.4344.
- [10] F. Verstraete, M. M. Wolf, and J. I. Cirac, *Nature Physics* **5**, 633 (2009).
- [11] W. S. Bakr, J. I. Gillen, A. Peng, S. Fölling, and M. Greiner, *Nature* **462**, 74 (2009).
- [12] J. F. Sherson, C. Weitenberg, M. Endres, M. Cheneau, I. Bloch, and S. Kuhr, *Nature* **467**, 68 (2010).
- [13] T. Gericke, P. Würtz, D. Reitz, T. Langen, and H. Ott, *Nature Physics* **4**, 949 (2008).
- [14] P. Würtz, T. Langen, T. Gericke, A. Koglbauer, and H. Ott, *Phys. Rev. Lett.* **103**, 080404 (2009).
- [15] R. Livi, R. Franzosi, and G.-L. Oppo, *Phys. Rev. Lett.* **97**, 060401 (2006).
- [16] G. S. Ng, H. Hennig, R. Fleischmann, T. Kottos, and T. Geisel, *New J. Phys.* **11**, 073045 (2009).
- [17] V. A. Brazhnyi, V. V. Konotop, V. M. Perez-Garcia, and H. Ott, *Phys. Rev. Lett.* **102**, 144101 (2009).
- [18] G. G. Carlo, G. Benenti, G. Casati, S. Wimberger, O. Morsch, R. Mannella, and E. Arimondo, *Phys. Rev. A* **74**, 033617 (2006).
- [19] A. Vardi and J. R. Anglin, *Phys. Rev. Lett.* **86**, 568 (2001), J. R. Anglin and A. Vardi, *Phys. Rev. A* **64**, 013605 (2001).
- [20] I. Tikhonenkov, J. R. Anglin, and A. Vardi, *Phys. Rev. A* **75**, 013613 (2007).
- [21] Y. V. Fyodorov, D. V. Savin, and H.-J. Sommers, *J. Phys. A.* **38**, 10731 (2005).
- [22] D. Jaksch, C. Bruder, J. I. Cirac, C. W. Gardiner, and P. Zoller, *Phys. Rev. Lett.* **81**, 3108 (1998).
- [23] H.-P. Breuer and F. Petruccione, *The theory of open quantum systems*, Oxford University Press (2002).
- [24] R. Gati, B. Hemmerling, J. Fölling, M. Albiez, and M. K. Oberthaler, *Phys. Rev. Lett.* **96**, 130404 (2006).
- [25] F. Trimborn, D. Witthaut, and H. J. Korsch, *Phys. Rev. A* **77**, 043631 (2008); *Phys. Rev. A* **79**, 013608 (2009).
- [26] J. R. Anglin, *Phys. Rev. Lett.* **79**, 6 (1997).
- [27] J. Ruostekoski and D. F. Walls, *Phys. Rev. A* **58**, R50 (1998).
- [28] H. Pichler, A. J. Daley, and P. Zoller, *Phys. Rev. A* **82**, 063605 (2010).
- [29] F. Trimborn, D. Witthaut, and S. Wimberger, *J. Phys. B: At. Mol. Opt. Phys.* **41**, 171001 (FTC) (2008).
- [30] A. J. Leggett, *Rev. Mod. Phys.* **73**, 307 (2001).
- [31] J. Dalibard, Y. Castin, and K. Mølmer, *Phys. Rev. Lett.* **68**, 580 (1992).
- [32] A. Trombettoni and A. Smerzi, *Phys. Rev. Lett.* **86**, 2353 (2001).
- [33] D. K. Campbell, S. Flach, and Y. S. Kivshar, *Phys. Today*, **57**, 43 (2004).
- [34] S. Flach and A. Gorbach, *Phys. Rep.* **467**, 1 (2008).
- [35] H. Hennig, J. Dorignac, D. K. Campbell, *Phys. Rev. A* **82**, 053604 (2010).
- [36] D. Witthaut, F. Trimborn, and S. Wimberger, *Phys. Rev. Lett.* **101**, 200402 (2008); *Phys. Rev. A* **79**, 033621 (2009).
- [37] J. Denschlag, J. E. Simsarian, D. L. Feder, C. W. Clark, L. A. Collins, J. Cubizolles, L. Deng, E. W. Hagley, K. Helmerson, W. P. Reinhardt, S. L. Rolston, B. I. Schneider, and W. D. Phillips, *Science* **287**, 97 (2000).
- [38] S. R. Clark, J. Prior, M. J. Hartmann, D. Jaksch, and M. B. Plenio, *New J. Phys.* **12**, 025005 (2010).
- [39] M. Sarovar, A. Ishizaki, G. R. Fleming, and K. B. Whaley, *Nature Phys.* **6**, 462 (2010).
- [40] Y. Zolotaryuk, S. Flach, and V. Fleurov, *Phys. Rev. B* **63**, 214422 (2001).

Kapitel 5

Eingeladene Buchbeiträge (Reviews)

- **Tunneling of ultracold atoms in time-independent potentials**
E. Arimondo and S. Wimberger,
ch. 11 in *Dynamical Tunneling*, S. Keshavamurthy and P. Schlagheck (Eds.),
(2011) 257-287 (Taylor & Francis – CRC Press, Boca Raton) 293
- **A pseudo-classical method for the atom-optics kicked rotor: from theory to experiment and back**
M. Sadgrove and S. Wimberger,
Advances in Atomic, Molecular, and Optical Physics 60 (2011) in press
(Elsevier, Amsterdam) 324

11 Tunneling of Ultracold Atoms in Time-Independent Potentials

Ennio Arimondo and Sandro Wimberger

CONTENTS

11.1 Introduction	257
11.2 Optical Lattices.....	259
11.3 Resonant Tunneling in Closed Systems	263
11.3.1 Two Levels	263
11.3.2 Three Levels	266
11.4 Tunneling in Open Systems.....	267
11.4.1 Optical Lattice without/with Tilt	267
11.4.2 Photon-Assisted Tunneling.....	268
11.4.3 RET in Optical Lattices with Tilt	271
11.4.3.1 Linear Regime and Decay Rates.....	273
11.4.3.2 Avoided Crossings	273
11.4.3.3 Nonlinearity	274
11.5 Many-Body Tunneling	276
11.5.1 Open One-Band Model.....	279
11.5.2 Closed Two-Band Model.....	280
11.6 Conclusions and Perspectives on RET	282
Acknowledgments.....	283
References.....	283

11.1 INTRODUCTION

Tunneling as a quantum mechanical effect takes place in a classically forbidden region between two regions of classically allowed motion. While the term “dynamical tunneling” typically refers to tunneling of quantum states across dynamical barriers in classical phase space [1], the original problem simply intended tunneling across a potential barrier. Both types of tunneling are addressed in this chapter, with major focus on situations in which external forces make the studied systems intrinsically time-dependent and allow for a dynamical control of tunneling through potential barriers or across band gaps which are dynamically explored by the system.

A standard example of tunneling across static barriers is the motion in a double-well potential. The two potential wells are separated by a potential barrier which is impenetrable for a low-energy classical particle. The quantum mechanical solution shows that the wave packet initially localized in one of the wells performs oscillations between the two classically allowed region. Tunneling takes place between two levels nearly degenerate in energy, and in most cases the investigated tunneling

takes place between the lowest energy states—for instance of a double well. However, in a potential configuration as the asymmetric double well shown in Figure 11.1a, an energy matching between a ground state on one side and an excited state on the other side leads to a tunneling between those states resonantly enhanced by the energy matching. In the resonantly enhanced tunneling (RET) the probability for the quantum tunneling of a particle between two potential wells is increased when the energies of the initial and final states of the process coincide. In the one-dimensional double potential barrier of Figure 11.1b, the narrow central potential well has weakly quantized (or quasistationary) bound states, of which the energies are denoted by E_1 and E_2 in Figure 11.1. If the energy E of electrons incident on the barrier coincides with these energies, the electrons may tunnel through both barriers without any attenuation. The transmission coefficient reaches unity at the electron energy $E = E_1$ or $E = E_2$. It is interesting that while the transmission coefficient of a potential barrier is always lower than one, two barriers in a row can be completely transparent for certain energies of the incident particle.

In the early 1970s, Tsu, Esaki, and Chang computed the two terminal current–voltage characteristics of a finite superlattice, and predicted that RET to be observed not only in the transmission coefficient but also in the current-voltage characteristic [2,3]. Resonant tunneling also occurs in potential profiles with more than two barriers. Technical advances led to the observation of negative differential conductance at terahertz frequencies and triggered a considerable research effort to study tunneling through multibarrier structures. Owing to the fundamental nature of this effect and the practical interest [4], in the last few years much progress has been made in constructing solid-state systems such as superlattices [5–7], quantum wells [8], and waveguide arrays [9] which enable the controlled observation and application of RET. The potential profiles required for resonant tunneling and realized in semiconductor system using heterojunctions allowed the manufacture of resonant-tunneling diodes. These devices have important applications such as in high-frequency signal generation and multivalued data storage, as reviewed in Mizuta and Tanoue (1995) [10].

In the last decade, the experimental techniques used in atom and quantum optics have made it possible to control the external and internal degrees of freedoms of ultracold atoms with a very high degree of precision. Thus, ultracold bosons or fermions loaded into the periodic optical potential created by interfering laser beams (double-well, lattices and superlattices) are optimal realizations of quantum mechanical processes and phenomena proposed and studied in other contexts of solid-state physics. Ultracold atoms and Bose–Einstein condensates (BEC), for instance, have been used

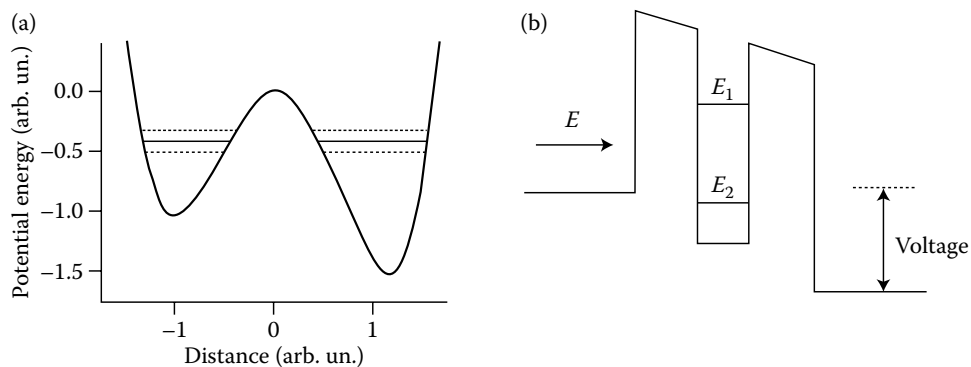


FIGURE 11.1 (a) Schematic representation of the energy levels within an asymmetric double well. The unperturbed energies within the left and right wells are indicated by the continuous lines. Because of the resonant tunneling between the ground state in the left well and the first excited one in the right well, the asymmetric and antisymmetric states are energy indicated by the dashed lines. (b) Schematic band diagram of a resonant-tunneling diode structure under a voltage bias between the incoming (left) and outgoing (right) regions.

to simulate phenomena such as Bloch oscillations in tilted periodic potentials [11–15] and to study quantum phase transitions driven by atom–atom interactions [16].

RET-like effects have been observed in a number of experiments till date. In Teo et al. (2002) [17], resonant tunneling was observed for cold atoms trapped by an optical lattice when an applied magnetic field produced a Zeeman splitting of the energy levels. Resonant tunneling has been observed in a Mott insulator within an optical lattice, where a finite amount of energy given by the on-site interaction energy is required to create a particle–hole excitation [18]. Tunneling of the atoms is therefore suppressed. If the lattice potential is tilted by application of a potential gradient, RET is allowed whenever the energy difference between neighboring lattice sites due to the potential gradient matches the on-site interaction energy. This RET control in a Mott insulator allowed Fölling et al. to observe a second-order coherence, that is, a two-atom RET [19].

Most of the quantum transport phenomena investigated with Bose–Einstein condensates within periodic optical lattices focused on the atomic motion in the ground state band of the periodic lattice. Only a few experiments examined the quantum transport associated with interband transitions “vertical” in the energy space. Interband transitions were induced by additional electromagnetic fields, as in the case of the spectroscopy of Wannier–Stark levels [20], or by quantum tunneling between the bands. Tunneling between otherwise uncoupled energy bands occurs when the bands are coupled by an additional force, which can be a static Stark force (tilting the otherwise periodic lattice) [14], or also by strong atom–atom interactions as observed for fermions in Köhl et al. (2005) [21] and discussed for bosons in Lee et al. (2007) [22]. The quantum tunneling between the ground and the first excited band is particularly pronounced in the presence of degeneracies of the single-well energy levels within the optical lattice leading to RET. In Sias et al. (2007) [23] and Zenesini et al. (2008) [24] such a type of RET was investigated for a Bose–Einstein condensate in a one-dimensional optical lattice, which allows for a high level of control on the potential depth and the lattice tilt. Those experimental investigations concentrated on the regime of parameters for which the tilting force—at RET conditions equal to the energy difference between neighboring wells—dominated the dynamics of the condensate. The RET tunneling of the ground band and the first two excited energy bands were measured in a wide range of experimental conditions. In addition the RET process is modified by the atom–atom interactions, bringing new physics to the quantum tunneling.

This chapter is organized as follows. Section 11.2 sets the stage discussing optical lattices and giving the necessary background. While Section 11.3 reports on RET in closed two- and three-well systems, Section 11.4 focuses on our main subject, the control of tunneling by RET in open quantum systems. Section 11.4 reports on our experimental data in the linear tunneling regime—that is, in the absence of atom–atom interactions, as well as on interaction induced effects. In Section 11.5, a model for many-body tunneling is introduced before we summarize the recent advances concerning RET in Section 11.6.

11.2 OPTICAL LATTICES

The investigations of tunneling for cold/ultracold atoms (Bose–Einstein condensates or Fermi degenerate gases) are based on the use of optical lattices [14,25]. For a 1D optical lattice a standing wave is created by the interference of two linearly polarized traveling waves counter-propagating along the x -axis with frequency ω_L and wave-vector λ_L . The amplitude of the generated electric field is $\mathcal{E}(r, t) = 2\mathcal{E}_0 \sin(\omega_L t) \sin(2\pi x/\lambda_L)$. When the laser detuning from the atomic transition is large enough to neglect the excited state spontaneous emission decay, the atom experiences a periodically varying conservative potential

$$V_{\text{ol}}(x) = V_0 \sin^2 \left(\frac{\pi x}{d_L} \right), \quad (11.1)$$

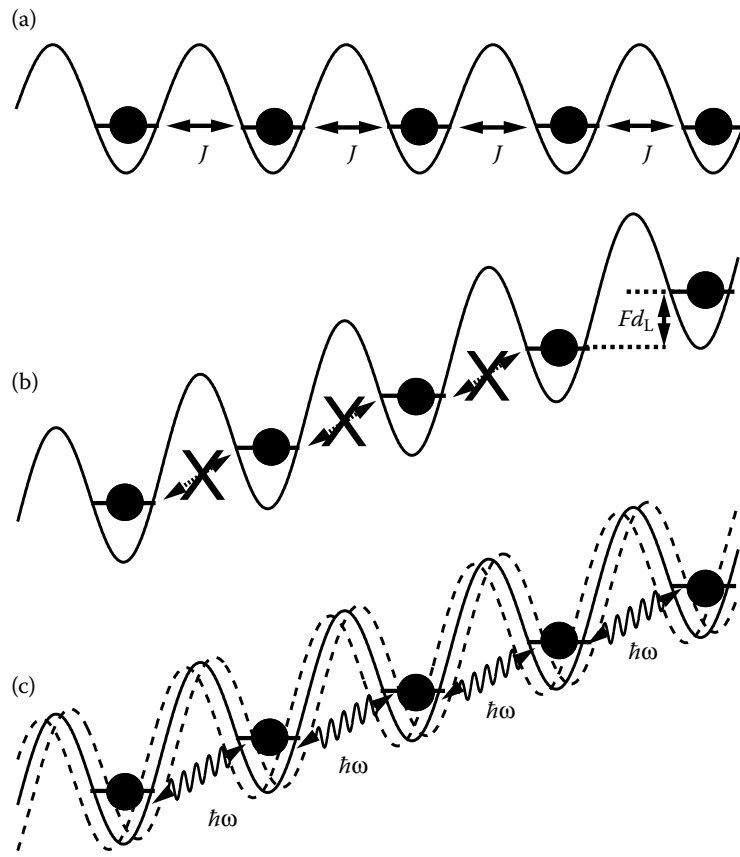


FIGURE 11.2 (a) In an optical lattice without additional external forces, the ground-state levels are resonantly coupled, leading to a tunneling energy J . (b) When a linear potential is applied, for example, by applying a force F , the levels are shifted out of resonance and tunneling is suppressed (Wannier–Stark localization). (c) If an additional potential energy oscillating at an appropriate frequency ω is applied, the levels can again be coupled through photons of energy $\hbar\omega$ and tunneling is partially restored.

schematically represented in Figure 11.2a. The amplitude V_0 depends on the laser detuning from the atomic transition and on the square of the \mathcal{E}_0 electric field amplitude [26]. The periodic potential has a spacing $d_L = \lambda_L/2$. This potential derives from the quantum mechanical interaction between atom and optical lattice photons. Therefore, the lattice quantities are linked to the recoil momentum $p_{\text{rec}} = 2\pi\hbar/\lambda_L$ acquired by an atom after the absorption or the emission of one photon. V_0 will be expressed in units of E_{rec} , the recoil energy acquired by an atom having mass M following one photon exchange

$$E_{\text{rec}} = \frac{\hbar^2}{2M\lambda_L^2}. \quad (11.2)$$

Neglecting the atom–atom interactions in a Bose–Einstein condensate, our 1D system is described by the following Hamiltonian

$$H = -\frac{\hbar^2}{2M} \frac{d^2}{dx^2} + V_0 \sin^2 \left(\frac{\pi x}{d_L} \right). \quad (11.3)$$

For this periodic potential, the associated single-particle eigenstates in the lowest band are Bloch plane waves with quasimomentum q . The energies $E_n(q)$ of the Bloch waves for the lowest bands $n = 1, 2, 3$ are plotted in Figure 11.3 versus quasimomentum. Ultracold atoms are loaded into the

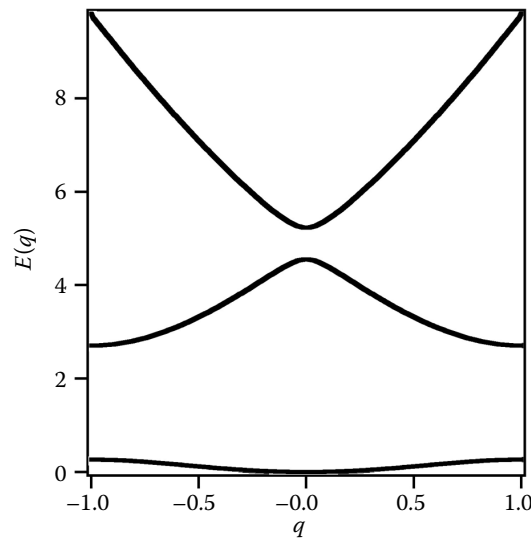


FIGURE 11.3 Plot of the energies for the energy bands $E_n(q)$ versus quasimomentum q for an optical lattice with optical depth $V_0 = 4E_{\text{rec}}$.

ground-state band having a minimum gap Δ at the edge of the Brillouin zone. The atomic evolution within that band or the excitation to a higher band is typically investigated.

If a force F is applied to the atom, as schematized in Figure 11.2b, the following Hamiltonian describes the atomic evolution neglecting for a moment atom–atom interactions in a Bose–Einstein condensate

$$H = -\frac{\hbar^2}{2M} \frac{d^2}{dx^2} + V_0 \sin^2\left(\frac{\pi x}{d_L}\right) + Fx. \quad (11.4)$$

This Hamiltonian defines the well-known Wannier–Stark problem for the electrons moving within a crystal lattice in the presence of an external electric field [27–29]. For small Stark forces F , one can picture the evolution of a momentum eigenstate induced by Equation 11.4 as an oscillatory motion in the ground energy band of the periodic lattice with Bloch period T_B [14,28,29], where

$$T_B = \frac{2\pi\hbar}{Fd_L}. \quad (11.5)$$

At stronger applied forces, a wave packet prepared in the ground band has a significant probability to tunnel at the band edge to the first excited band. This process of the quantum tunnel across an energy gap at an avoided crossing of the system’s energy levels is described by the Landau–Zener tunneling [30,31]. For a single tunneling event, the Landau–Zener tunneling probability is [29]

$$P_{\text{LZ}} = e^{-\frac{\pi^2}{8F_0} \left(\frac{\Delta}{E_{\text{rec}}}\right)^2}, \quad (11.6)$$

where we introduced the F_0 dimensionless force

$$F_0 = \frac{Fd_L}{E_{\text{rec}}}. \quad (11.7)$$

In the presence of a sequence of Landau–Zener tunneling events, the Landau–Zener rate Γ_{LZ} to the excited band is obtained by multiplying P_{LZ} with the Bloch frequency $\nu_B = 1/T_B$ [28]. By introducing the recoil frequency $\nu_{\text{rec}} = E_{\text{rec}}/h$, Γ_{LZ} may be written

$$\Gamma_{\text{LZ}} = \nu_{\text{rec}} F_0 e^{-\frac{\pi^2}{8F_0} \left(\frac{\Delta}{E_{\text{rec}}}\right)^2}. \quad (11.8)$$

For the optical lattice periodic potential, an alternative single-particle basis useful for describing the tunneling of particles among discrete lattice sites is provided by Wannier functions [16,27–29,32]. The j th Wannier function $|j\rangle$ is centered around the j lattice site, and the functions are orthonormal. In a given energy band, the Hamiltonian for free motion on the periodic lattice is determined by hopping matrix elements, which in general connect lattice sites arbitrarily spaced. However, because the hopping amplitude decreases rapidly with the distance, the tunneling Hamiltonian may include only the J tunneling hopping between neighboring lattice sites

$$H = \sum_j E_j |j\rangle\langle j| - J \sum_j (|j\rangle\langle j+1| + |j+1\rangle\langle j|), \quad (11.9)$$

where E_j defines the energy of the j th site. For ultracold atoms in an optical lattice with depth $V_0 \gg E_{\text{rec}}$, the nearest-neighbor tunneling energy J is given by [33]

$$J = \frac{4}{\sqrt{\pi}} E_{\text{rec}} \left(\frac{V_0}{E_{\text{rec}}} \right)^{3/4} \exp\left(-2\sqrt{\frac{V_0}{E_{\text{rec}}}}\right). \quad (11.10)$$

In the presence of an applied force F , supposing $E_j \equiv E_0 = 0$, the Hamiltonian becomes

$$H = F d_L \sum_j j |j\rangle\langle j| - J \sum_j (|j\rangle\langle j+1| + |j+1\rangle\langle j|). \quad (11.11)$$

However, this Hamiltonian may be used to describe the atomic evolution in the ground band only when the Landau–Zener tunneling to the excited band can be neglected. Figure 11.4 reports for a given value of the dimensionless force F_0 , the V_0 optical depth where the hopping constant J is 10 times larger than Γ_{LZ} .

The simulation of the temporal evolution of the Bose–Einstein condensate wavefunction is based either on the Gross–Pitaevskii equation based on a global mean-field description or on a many-body approach where the atomic number of the lattices sites is quantized [16,34,35]. Apart from the theoretical results reported in Section 11.5, we will concentrate here on the mean-field approach applied to describe experimental configurations and results reviewed in detail in Section 11.4. For a realistic description of those experiments, the Gross–Pitaevskii equation was used to simulate the temporal evolution of the condensate wave function $\psi(\vec{r}, t)$ subjected to the optical lattice and to a confining harmonic potential, for instance with cylindrical symmetry

$$i\hbar \frac{\partial}{\partial t} \psi(\vec{r}, t) = \left[-\frac{\hbar^2}{2M} \nabla^2 + \frac{1}{2} M (\omega_x^2 x^2 + \omega_r^2 \rho^2) + V_0 \sin^2\left(\frac{\pi x}{d_L}\right) + Fx + g |\psi(\vec{r}, t)|^2 \right] \psi(\vec{r}, t). \quad (11.12)$$

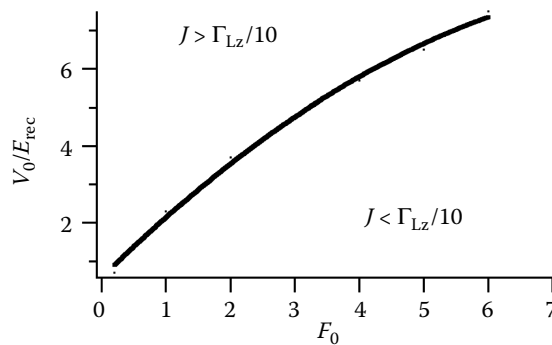


FIGURE 11.4 Plots of the line in the space of the optical lattice depth V_0 , in E_{rec} units, and the dimensionless force F_0 dividing the upper (lower) region where the interwell tunneling is ten times larger (smaller) than the Landau–Zener tunneling to the upper band.

The frequencies ω_x and ω_r characterize the longitudinal and transverse harmonic confinement. The atom–atom interactions are modeled by the nonlinear term in Equation 11.12, with the nonlinear coupling constant given by $g = 4\pi\hbar^2 a_s/M$, where a_s is the s -wave scattering length [34,35]. Morsch and Oberthaler (2006) and Cristiani et al. (2002) [14,25] introduced the \tilde{g} dimensionless nonlinearity parameter

$$\tilde{g} = \frac{gn_0}{8E_{\text{rec}}}, \quad (11.13)$$

computed from the peak density n_0 of the condensate initial state, to describe the nonlinear coupling relevant for optical lattice experiments. In the Thomas–Fermi regime of the condensate [34,35], for given ω_x and ω_r , the density n_0 , and therefore, \tilde{g} , is proportional to $N^{2/5}$ where N is the number of atoms in the condensate.

11.3 RESONANT TUNNELING IN CLOSED SYSTEMS

11.3.1 TWO LEVELS

Quantum tunneling of a two-level system takes place in the double-well potential. The quantum mechanical solution shows that the wave packet initially localized in one of the wells performs oscillations between the two classically allowed regions. The period of these oscillations is related to the inverse of the energy difference between the symmetric and antisymmetric quantum states of the double-well system, that is, to the energy corresponding to the tunneling splitting. That energy is equal to the interaction Hamiltonian between the eigenstates of the two wells. In an asymmetric double well as that shown in Figure 11.1a, an energy matching between a ground state on one side and an excited state on the other side leads to a RET between those states. The dashed lines in Figure 11.1a denote the eigenenergies for the symmetric and antisymmetric quantum superposition of the wavefunctions in left and right wells. The tunneling evolution is described by the following Hamiltonian:

$$H = \sum_{j=1,2} E_j |j\rangle\langle j| - J(|1\rangle\langle 2| + |2\rangle\langle 1|) + U \sum_{j=1,2} n_j(n_j - 1), \quad (11.14)$$

where $|1\rangle$ and $|2\rangle$ denote the wavefunctions of the resonant states in the left and right wells, $\Delta = E_1 - E_2$ is the energy difference between the two wells, and J is the tunneling energy, U is the interatomic interaction energy and n_j is the atom number in the left or right well. For the following analysis U represents a shift in energy of the left or right well. By treating at first the $U = 0$ case, the atomic wavefunction may be expanded as a superposition of the $|1, 2\rangle$ states

$$|\Psi(t)\rangle = \sum_{j=1,2} C_j(t) |j\rangle, \quad (11.15)$$

the atomic evolution is characterized by Rabi oscillations between the two wells. For instance by supposing as initial condition $C_1(0) = 1$ and $C_2(0) = 0$, the occupation probabilities of the left well at time t are given by

$$|C_2(t)|^2 = \frac{J^2}{\Delta^2 + J^2} \sin^2 \sqrt{J^2 + \frac{\Delta^2}{4}}, \quad (11.16)$$

$$|C_1(t)|^2 = 1 - |C_2(t)|^2. \quad (11.17)$$

Therefore for the $\Delta = 0$ resonance condition of RET, a complete oscillation between the two wells at frequency $2J/\hbar$ takes place. The atomic interaction term U shifting the $E_{i=1,2}$ energies of the two wells may be included into the above equations for the occupation probabilities as a contribution to the Δ energy difference. Therefore, the presence of the U interatomic energy modifies the RET condition.

Periodic double-well structures may be created in properly chosen optical lattice or superlattice geometries. For cold atoms theoretical and experimental investigations were performed by Teo et al. (2002) [17], Castin et al. (1994) [36], Dutta et al. (1999) [37], and Haycock et al. (2000) [38]. For cold atoms the coherence length of the atomic wavefunction is comparable to the extent of each double well, so that the long range periodicity of the optical lattice plays a minor role on the tunneling properties. Therefore, those investigations will be mentioned here. Those studies examined the new features appearing when the double-well potential depends on the internal atomic structure, for instance on the two electron spin states. This case was theoretically analyzed by Castin et al. (1994) [36] within the context of two dimensional Sisyphus cooling. Resonant tunneling between the adjacent potential wells of the periodic potential for the two internal states, not present in a 1D geometry, contributes with quantum processes to the cooling phenomena in optical lattices. Dutta et al. (1999) [37] studied periodic well-to-well tunneling of ^{87}Rb atoms on adiabatic potential surfaces of a 1D optical lattice. Atoms that tunnel between neighboring wells of the lattice are an excellent tool for a careful study of topological potentials associated to the optical lattice. RET-like effects have been observed in a number of experiments to date. In Teo et al. (2002) [17], resonant tunneling was observed for cold atoms trapped by an optical lattice when an applied magnetic field produced a Zeeman splitting of the energy levels. At certain values of the applied magnetic field, the states in the up-shifting and down-shifting energy levels were tuned into resonance with one another. This led to RET drastically altering the quantum dynamics of the system and producing a modulation of the magnetization and lifetime of the atoms trapped by the optical lattice. Hacock et al. (2000) [38] observed the quantum coherent dynamics of atomic spinor wave packets in the double-well potentials. With appropriate initial conditions the atomic system performed Rabi oscillations between the left and right localized states of the ground doublet, with the atomic wavepacket corresponding to a coherent superposition of these mesoscopically distinct quantum states.

For ultracold atoms, Rabi oscillations in double-well geometries have been investigated and measured by Fölling et al. (2007) [19] and Kierig et al. (2008) [39]. A highly parallel structure of double wells is created using optical lattice or optical superlattice configurations. In the superlattice configuration of [19] the periodic potentials created by two laser standing waves at wavelength λ_L and $\lambda_L/2$ are applied to create a large set of individual wells. By changing the intensity of the standing wave lasers at the two wavelengths and their relative spatial phase, any configuration of symmetric or asymmetric double wells is created. In that experiment the double-well investigation was performed with ultracold atoms in a Mott-insulator configuration having single atom occupation of the wells [16]. The modification of the optical lattice potential from a periodic structure of single wells to a periodic structure of double wells, by adiabatically raising an energy bump within each single well, allowed to produce the asymmetric loading of each double well.

Figure 11.5 summarizes experimental results obtained in Fölling et al. (2007) [19] for the RET features in symmetric and asymmetric double wells. The tunneling of the ultracold atoms was measured as a function of the energy bias Δ between the wells. The left upper inset schematizes the case of single atom tunneling. The right lower one schematizes the tunneling of one atom in the presence of an energy shift produced by the atomic interaction (U term in Equation 11.14). A conditional resonant tunneling resonance occurs, where a single atom can tunnel only in the presence of a second atom and the interaction energy U is matched by the bias. For these two cases the measured atomic Rabi-type dynamical evolution between the two wells is shown in the right upper inset. Because the presence of an atom in the left well shifts by U the level energies, a bias $\Delta = -U$ is applied in order to compensate the shift. Thus, a resonant tunneling condition is verified and the gray data denote the periodic occupation of the left well and right well, located at positions -1 and 0 , respectively. In the absence of an atom in the left well and without application of the bias, the tunneling is not resonant and the Rabi oscillations take place with a reduced amplitude and at a higher frequency, in agreement with the description of Equations 11.16 and 11.17. The left lower inset schematizes the case of a correlated atomic pair tunneling, as produced in a second-order tunneling process. The central part of that figure reports the amplitude of the Rabi oscillations versus the Δ bias for the different

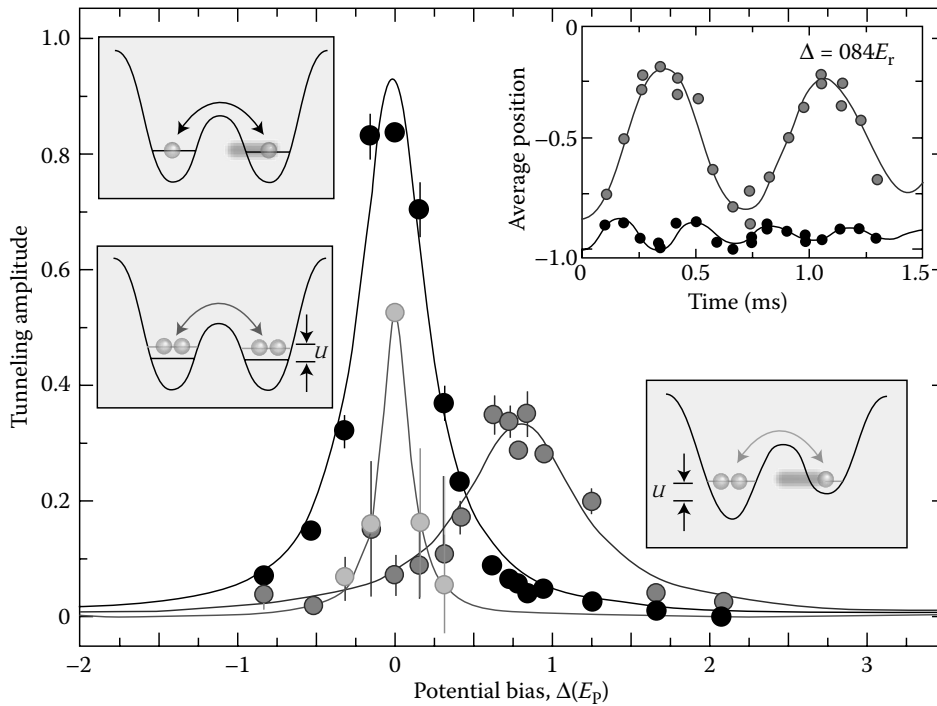


FIGURE 11.5 Tunneling configuration and experimental results for the resonant tunneling of single and double atoms in a superlattice. The periodic double-well potential for ultracold rubidium atoms was realized by superimposing two periodic potentials with periodicities of $\lambda_L = 765.0$ nm (long lattice) and $\lambda_L/2 = 382.5$ nm (short lattice), and controllable intensities and relative phase. The depth was $V_0 = 12E_{\text{rec}}$ for the short optical lattice, $V_0 = 9.5E_{\text{rec}}$ for the long lattice. The upper right, lower left and lower right insets describe the resonant tunneling configurations for one or two atoms per well. The upper left inset describes the oscillating motion of the atoms between the the two wells for the conditional resonant tunneling resonance where a single atom can tunnel only in the presence of a second atom and the interaction energy U is matched by an applied bias. In the central part the amplitude of the tunneling Rabi oscillations, and the Lorentzian fit, are shown as a function of the bias energy Δ for each of the tunneling configurations represented in the insets, black dots and Lorentzian centered at $\Delta = 0$ for upper left one, light gray dots and Lorentzian centered at $\Delta = 0$ for lower left one, and gray dots and Lorentzian centered at $\Delta = 0.78E_{\text{rec}}$ for lower right one. (From S. Fölling et al. *Nature* 448, 1029, 2007. With permission by MacMillan.)

tunneling configurations, and their fits by the Lorentzian line shapes predicted by Equation 11.16. The tunneling amplitude versus the potential bias is measured for the case of single atoms (black data points) and initially doubly occupied lattice sites (gray line and light gray data points). The gray data points and the Lorentzian fitted to the data point with center at $\Delta = 0.78(2)E_{\text{rec}}$ correspond to the conditional resonant tunneling resonance. The correlated pair tunneling (light gray circles) and the Lorentzian fit are resonant for zero bias because energies of both left and right wells are modified by the interaction energy U .

While the previous description applies to single particle tunneling, quantum tunneling of macroscopic N -body atomic systems introduces qualitatively new aspects to the quantum evolution of ultracold atoms, as investigated in Dounas-Frazer et al. (2007) [40] for Bose–Einstein condensate in a tilted multilevel double-well potential. For a double well without tilt as experimentally investigated by Albiez et al. (2005) [41], the so-called self trapping regimes is realized where the bosonic nonlinear interaction term of the equation, Equation 11.12 modifies the level energies and inhibits the resonant tunneling between the wells. Khomeriki et al. (2006) [42] demonstrated that for a double-well structure by a pulse-wise change of the intermediate barrier height, it is possible to switch between the tunneling regime and the self-trapped one.

11.3.2 THREE LEVELS

The idea of controlling the tunneling rate between two states has led several researchers to consider the effect of external forces on the tunneling oscillations. Because the tunneling rate is related to the difference in the energies of the quantum states, a number of complicated scenarios arise when one of the states undergoes interaction with a third state, and that interaction may be controlled by an external parameter, for instance a magnetic or electric field. The tunneling wavepacket is described as a linear combination of the three initial states. Their interaction can drastically affect the eigenenergies of the Hamiltonian and it would be possible to explore different regimes, from strong suppression to enhancement of tunneling.

This three-level control was theoretically investigated in Averbukh et al. (2002) [43] and Hensinger et al. (2004) [44] in connection to the dynamical tunneling produced by time-dependent potentials and for conditions as in an experiment by Raizen's group in 2001 [45] and at NIST [46]. The tunneling period in the time-dependent systems is related to the differences between quasienergies of the Floquet states, just as the tunneling period in the time-independent case has to do with the energy differences between the stationary states. The experimental and theoretical investigations considered the case of the tunneling doublet interacting with a third state associated with a chaotic region. The underlying classical phase space of the systems had a mixed regular-chaotic structure, giving the scenario of chaos-assisted [47] or, more generally speaking, of dynamical tunneling [1].

We present here the basic of the three-level tunneling in the case of time independent potentials. Figure 11.6 schematizes the dependence on an external parameter for the E_j energies for the $|j\rangle$ states, with $j = 1 \dots 3$, in the absence of interactions between them. We will discuss the modifications to those energies produced by atomic interactions between states, supposing the presence of the interactions U_{12} between states $|1\rangle$ and $|2\rangle$, and U_{23} between states $|2\rangle$ and $|3\rangle$, and supposing no interaction between states $|1\rangle$ and $|3\rangle$. Notice that these interactions modify the E_j energies in the regions close to the energy crossings, boxes 1, 2, and 3 in the Figure 11.6, and that the tunneling

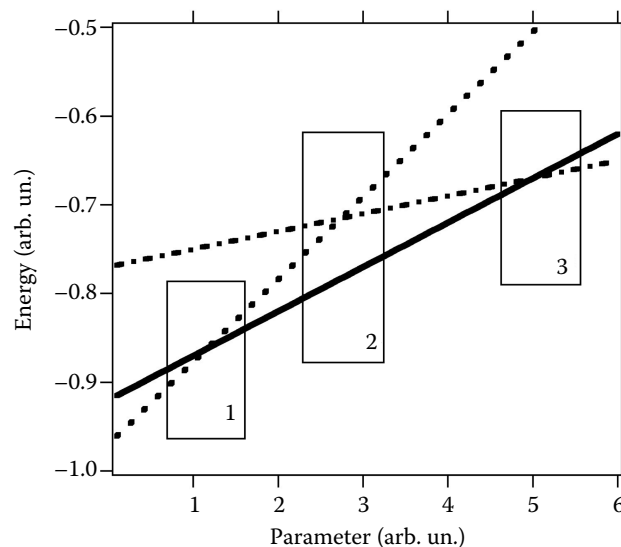


FIGURE 11.6 Unperturbed energies E_j , with $j = (1,3)$ (in arbitrary units) of three states experiencing crossings and anticrossings as a function of a parameter (also in arbitrary units). Continuous lines corresponds to state $|1\rangle$, the dotted one to state $|2\rangle$ and the dot-dashed to state $|3\rangle$. The boxes marked with 1 and 3 denote regions where the tunneling is dominated by two-state interactions. The box marked 2 denotes a region where the three-state interaction may modify the tunneling rate between state $|2\rangle$ and $|3\rangle$. In region 3 without direct interaction between states $|1\rangle$ and $|3\rangle$ a locking of tunneling, corresponding to a level crossing with $E_1 = E_3$, takes place.

frequency is determined by the splitting of the perturbed energies. In the box with number 1 the $E_1 - E_2$ energy separation, that is, the tunneling, is dominated by the interaction between states $|1\rangle$ and $|2\rangle$. In the box denoted as 2, a three-state interaction takes place and the amplitude of the interaction between states $|1\rangle$ and $|2\rangle$ may be used to enhance or suppress the tunneling frequency between the states $|2\rangle$ and $|3\rangle$. Within the region denoted as 3, in the absence of a direct interaction between the $|1\rangle$ and $|3\rangle$ states a $E_1 = E_3$ crossing point exists. This crossing produces an absence of tunneling, this configuration being indicated as locking of the wavefunction in the initial state of preparation [43].

11.4 TUNNELING IN OPEN SYSTEMS

11.4.1 OPTICAL LATTICE WITHOUT/WITH TILT

An optical lattice is composed of an infinite number of neighboring wells uniformly distributed along one direction and spacing $d_L = \lambda/2$ between the minima, where λ is the wavelength of the standing wave laser required to create the periodic potential for the atoms [14]. This configuration corresponds to Figure 11.2a. The tunneling in this system has strong similarities to the double well discussed above, when the presence of physical boundaries, as in the physical realizations, plays no role.

For a more general treatment we consider the case where an applied external force F produces an energy difference Fd_L between neighboring wells, see Figure 11.2b. The atomic evolution may be studied by considering the localized Wannier wavefunction $|i\rangle$ and the perturbations originating from the atomic occupation in neighboring sites [32]. This approximation is valid when the overlap of atomic wavefunctions introduces corrections to the localized atom picture, but they are not large enough to render the single site description irrelevant. The H Wannier–Stark Hamiltonian determining the atomic evolution in the absence of the interatomic interactions U is given by

$$H = -J \sum_j (|j\rangle\langle j+1| + |j+1\rangle\langle j|) + Fd_L \sum_j j|j\rangle\langle j|. \quad (11.18)$$

In analogy to Equation 11.15 the generic atomic wave function can be written as a superposition of the $|j\rangle$ localized wavefunctions where the sum extends over all lattice sites. The temporal evolution for the C_i coefficients under the Hamiltonian H is given by

$$i\hbar \frac{dC_j}{dt} = jFd_L C_j - J(C_{j+1} + C_{j-1}), \quad (11.19)$$

and in the following the ground state energy E_0 will be supposed to be equal to zero. The solution of these coupled equations with $t = 0$ initial condition of atomic occupation of the $i = 0$ site—that is, $C_j(t = 0) = \delta_{j=0}$, leads to [48]

$$|C_j(t)|^2 = \mathcal{J}_j^2 \left[\frac{2JT_R}{\hbar} \sin \left(\frac{\pi t}{T_R} \right) \right], \quad (11.20)$$

having introduced the Bessel functions \mathcal{J}_j of j th order. The argument of the Bessel functions in Equation 11.20 is an oscillatory function of time. T_R represents the recurrence time for the evolution of the atomic wavefunction. For the present case of the resonant tunneling modified by the presence of a force F , $T_R = T_B$ whence the recurrence time coincides with the Bloch period T_B defined in Equation 11.5 and is inversely proportional to the applied external force. The temporal recurrence of the atomic wavefunction is shown in Figure 11.7 for different times expressed in units of T_R . Notice that the parameter $2JT_R/\hbar$ of the Bessel function determines the range of lattice sites occupied by the periodic wavefunction expansion. The corresponding atomic mean-square displacement is

$$\frac{\sqrt{\langle m^2(t) \rangle}}{d_L} = \frac{2\sqrt{2}JT_R}{\pi\hbar} \left| \sin \left(\frac{\pi t}{T_R} \right) \right|. \quad (11.21)$$

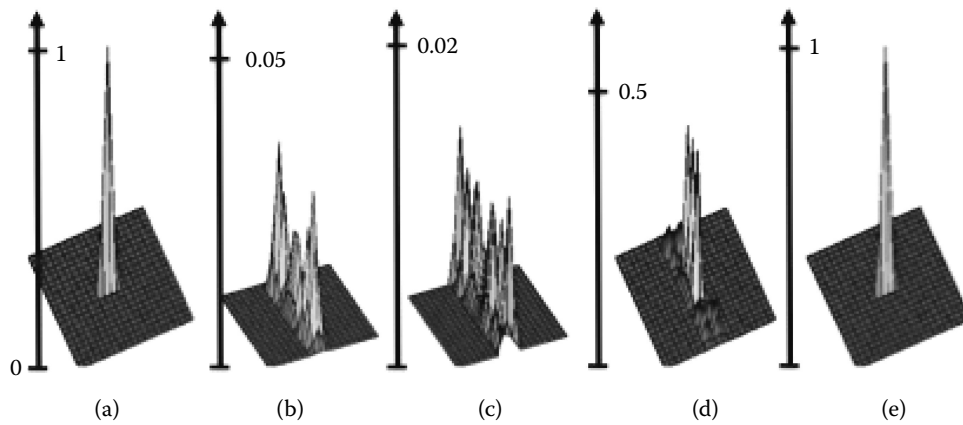


FIGURE 11.7 Temporal recurrence of the occupation probability $|C_n|^2$ versus the n position of the lattice site at different interactions times. From (a) to (e) interaction times are 0, 0.2, 0.5, 0.95, 1 measured in units of T_R . The occupation probabilities are connected by lines. Notice the reduced vertical scale at the intermediate times. The plots are obtained for the parameter $2JT_R/\hbar = 28$.

In the limit of $Fd_L \gg J$ the mean-square displacement is largely decreased because of the suppression of the resonant tunneling, as schematized in Figure 11.2b. This suppression and the related Wannier–Stark localization of the wavefunction have been intensively discussed in the solid-state physics theoretical literature [28,49]. Korsch and coworkers [50,51] have considered the case of an atomic distribution not initially concentrated on a single site, and instead described by a Gaussian distribution with root mean-square σ_0 . For that case the temporal evolution of the mean-square displacement is given by

$$\frac{\langle m^2(t) \rangle}{d_L^2} = \left(\frac{\sigma_0}{d_L} \right)^2 + 8 \left(\frac{JT_R}{\pi\hbar} \right)^2 \sin^2 \left(\frac{\pi t}{T_R} \right) \left[1 - e^{-d_L^2/2\sigma_0^2} \cos \left(\frac{2\pi t}{T_R} \right) - 2e^{-d_L^2/8\sigma_0^2} \sin^2 \left(\frac{\pi t}{T_R} \right) \right]. \quad (11.22)$$

In the absence of external force, taking the limit of $F \rightarrow 0$, we recover the result of a diffusion process for the atomic wavefunction

$$|C_j(t)|^2 = \mathcal{J}_j^2 \left[\frac{2Jt}{\hbar} \right], \quad (11.23)$$

$$\frac{\sqrt{\langle m^2 \rangle}}{d_L} = \frac{\sqrt{2Jt}}{\hbar}. \quad (11.24)$$

11.4.2 PHOTON-ASSISTED TUNNELING

The above analysis can be applied also to the photon-assisted tunneling occurring when the ground states of adjacent potential wells tuned out of resonance by the Fd_L static potential are coupled by photons at frequency ω as schematized in Figure 11.2c. When the photon energy bridges the gap created by the static potential, tunneling is (partly) restored. The resonant tunneling is restored by a photon-assisted process when the energy provided by n photons matches the separation energy Fd_L between neighboring wells. The energy resonance condition for the frequency ω_R is given by

$$n\hbar\omega_R = Fd_L, \quad (11.25)$$

with the integer n denoting the order of the photon-assisted resonance. This resonance may be expressed as $\omega_R = 2\pi\nu_B/n$ in terms of the Bloch frequency. The frequency detuning from the resonance is $\Delta\omega = \omega - \omega_R$.

In solid-state systems, the photons are typically in the microwave frequency range and the static potential is provided by an electric bias field applied to the structure. Photon-assisted tunneling has been observed in superconducting diodes [52], semiconductor superlattices [53,54], and quantum dots [55,56].

For the photon-assisted tunneling of cold and ultracold atoms, a theoretical analysis was performed by Eckardt et al. (2005) [57] and by Kolovsky and Korsch (2009) [58], with experiments performed by Sias et al. (2008) [59], Ivanov et al. (2008) [60], Alberti et al. (2009) [61], and Haller et al. (2010) [62]. In these experiments a periodic time-dependent potential was applied to the cold atoms through a periodic spatial oscillation of the optical lattice minima/maxima, to be referred to as shaking in the following. In the lattice reference frame such a backward and forward motion of the periodic potential at frequency $\omega \approx \omega_R$ along one direction is equivalent to a periodic force $F_\omega \cos(\omega t)$ applied to the atoms. Thus, using the localized Wannier wavefunction introduced above for a deep lattice the atomic evolution is determined by the following Hamiltonian:

$$H_{\text{shaking}} = -J \sum_j (|j\rangle\langle j+1| + |j+1\rangle\langle j|) + [Fd_L + K \cos(\omega t)] \sum_j |j\rangle\langle j|, \quad (11.26)$$

once again not including the U interaction term. Here $K = F_\omega d_L$, denoted as shaking amplitude, is the shaking energy difference between neighboring sites of the linear chain associated to the shaking. The theory of Eckardt et al. (2005) [57] predicts that when the driving takes place at the frequency $\omega_R \gg J/E_{\text{rec}}$ and the resonance condition of Equation 11.25 is satisfied, the shaking leads to an effective tunneling rate

$$J_{\text{eff}}(K, \omega_R) = J \mathcal{J}_n \left(\frac{K}{\hbar \omega_R} \right). \quad (11.27)$$

Therefore, a modification of the tunneling rate is obtained when the ratio of the rescaled shaking amplitude $K = F_\omega d_L$ and the shaking frequency times \hbar is varied. In the experimental realization [59] the shaking frequency was fixed and the shaking amplitude was scanned to verify the relation of Equation 11.27.

The previous analysis for the evolution of the atomic wavefunction under resonant tunneling can be applied also to the photon-assisted tunneling by using the approximation of a resonant dynamics introduced by Thommen et al. (2002) [63] or equivalently by restricting our attention to the resonant Floquet states [64]. In the presence of a driving at frequency ω and taking into account the static energy difference Fd_L between neighboring wells, we write for the atomic wavefunction

$$|\Psi(t)\rangle = \sum_{j,m} \tilde{C}_{j,m} e^{-i(jFd_L + m\hbar\omega)t/\hbar} |j\rangle, \quad (11.28)$$

where the j index labels the well and the m index the component in the Floquet spectrum. For ω close to the n th order resonance condition we may restrict the terms to the resonant ones in two sums of the above expansion

$$|\Psi(t)\rangle = \sum_j e^{-ij\Delta\omega t} \tilde{C}_j^n |j\rangle, \quad (11.29)$$

where we have simplified the notation introducing the resonant coefficients \tilde{C}_j^n .

The temporal evolution of the \tilde{C}_j^n is described by an equation similar to Equation 11.19 where J_{eff} determines the tunneling energy of the n th order resonance. Therefore, for the photon-assisted tunneling, the occupation of the j th lattice site and the mean-square displacement of the atoms are the analogs to those derived previously

$$|C_j^n(t)|^2 = \mathcal{J}_j^2 \left[\frac{2J_{\text{eff}} T_R}{\hbar} \sin \left(\frac{\pi t}{T_R} \right) \right], \quad (11.30)$$

$$\frac{\sqrt{\langle m^2 \rangle}}{d_L} = \frac{2\sqrt{2}J_{\text{eff}} T_R}{\pi \hbar} \left| \sin \left(\frac{\pi t}{T_R} \right) \right|, \quad (11.31)$$

with T_R the recurrence time for this process given by

$$T_R = 2\pi/\Delta\omega. \quad (11.32)$$

This recurrence process was named as super-Bloch oscillations in Kolovsky and Korsch (2009) [58] and Haller et al. (2010) [62]. For the resonant case $\Delta\omega = 0$, the mean-square displacement is given by Equation 11.24 and the occupation probabilities are given by Equation 11.23. Notice that for both Wannier–Stark localization and photon-assisted tunneling, the mean-square displacement and the occupation probabilities have the same functional dependence if we introduce a unifying parameter for the detuning from the resonant tunneling. This parameter is Fd_L for the case of an applied external force and $\hbar\Delta\omega$ for the case of the photon-assisted tunneling. Thus, the data of Figure 11.7 applies also to the occupation probabilities in the photon-assisted tunneling.

A few recent experiments on optical lattices have verified or made use of the theoretical predictions of this Section. In the following the experiments will be characterized by the depth V_0 of the optical lattice expressed in units E_{rec} , and the photon-assisted frequency detuning $\Delta\omega_0$.

The linear time dependence of atomic mean-square displacement predicted by Equation 11.24 in the conditions of $F = 0$ was applied by Lignier et al. (2007) [65] to measure the J tunneling energy and to verify that the experimental procedure reproduced the J dependence on the lattice depth V_0 predicted by Equation 11.10. The photon-assisted tunneling experiments [59,60] made use of that linear dependence to measure the effective tunneling rate. In these experiments, the linear dependence was tested for a total time larger than 10,000 tunneling times. Notice that in all these experimental observations the initial distribution of the atomic wavefunction was not concentrated on a single well as in our theoretical analysis and instead covered several wells. Nevertheless, a Gaussian convolution of the initial wavefunction spread and of the linearly expanding mean-square displacement represented a good fit of the experimental observations, even at earlier times where the initial width is comparable to the tunneling spread.

The Wannier–Stark localization of the atomic cloud in the presence of an applied force F was examined by Sias et al. (2008) [59] as a reduction of the mean-square displacement increasing the force amplitude at a given interrogation time. Figure 11.8a reports the temporal dependence of $\sqrt{\langle m^2 \rangle}/d_L$ as predicted by Equation 11.21, at different values of the parameter Fd_L/J scanned in that experiment within the interval (0,1). In order to provide a unified description the time is measured in units of T_B . It appears that $\sqrt{\langle m^2 \rangle}$ is periodic in time with period T_B while the

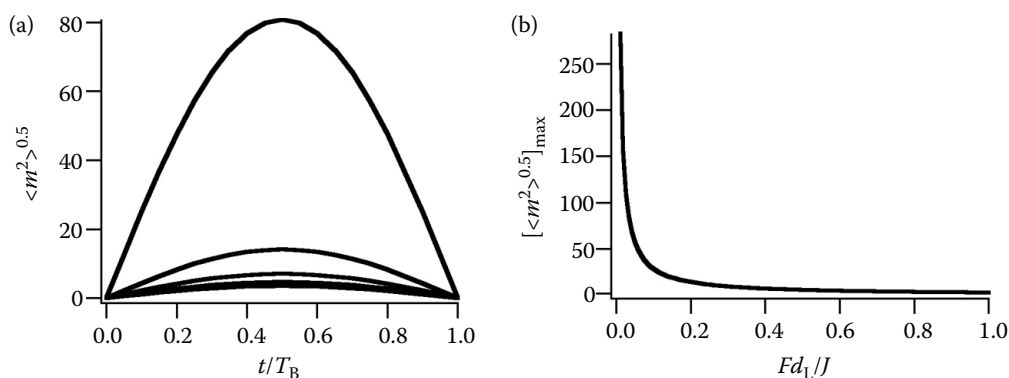


FIGURE 11.8 (a) Mean-square displacement versus time for different values of the unified RET energy mismatch, Fd_L/J for the Wannier–Stark localization and $\hbar\Delta\omega/J$ for the photon assisted tunneling. Results for values 0.2, 0.4, 0.6, 0.8, and 1.0 of the detuning parameter, with the displacement maximum decreasing at higher values. The time dependence of $\sqrt{\langle m^2 \rangle}$ is periodic in time with period T_B . In (b) the maximum of the mean-square displacement is plotted versus Fd_L/J . The mean-square displacements are measured in units of the d_L lattice spacing.

amplitude of the oscillation decreases with the force until the Wannier–Stark localization regime is reached where the atomic motion is blocked. Figure 11.8b shows the amplitude of the oscillation predicted by Equation 11.24 versus the Fd_L/J parameter. By comparing this dependence to the Lorentzian one occurring for a two-level system of the previous Section, it appears that for an infinite systems of wells the oscillation amplitude decreases more rapidly increasing Fd_L/J . For different values of the applied force, the maximum of the oscillation occurs at a different value of t . Therefore, the experiment of Sias et al. (2008) [59] that measured the oscillation amplitude at a given interaction time, obtained results similar to those of Figure 11.8b, not precisely fitted by the inverse law as sketched in Figure 11.8.

For the photon-assisted tunneling the functional dependence on time of the wavefunction spreading on the lattice and the mean-square displacement was measured in Alberti et al. (2009) [61] for a total time equivalent up to seven recurrence times in the case of a drive detuned by $\Delta\omega/2\pi = \pm 5$ Hz and up to one recurrence time for the $\Delta\omega/2\pi = \pm 0.260$ Hz detuning. The measured sinusoidal evolutions are in reasonable agreement with the sinusoidal function predicted by our model and represented in Figures 11.7 and 11.8a. Our model does not take into account the initial atomic distribution over several optical lattice sites, and in Alberti et al. (2009) [61], because the atomic de Broglie wavelength was shorter than the lattice period, the coherence degree among adjacent Wannier–Stark eigenstates was negligible. The quantum–mechanical evolution of the atomic wavefunction under the tunneling Hamiltonian described by our analysis is limited by the presence of decoherence processes, and in Alberti et al. (2009) [61] a decoherence time of 28 s was measured. It would be interesting to investigate theoretically the role of a decoherence process on the tunneling evolution.

For the photon-assisted tunneling the mean-square amplitude dependence on the detuning $\Delta\omega$ is given by Equation 11.21 with $T_R = 2\pi/\Delta\omega$. That functional dependence predicts that the full width of the resonance line-shape $\Delta\omega_{FW}$, defined by the first zeros of the sin function, is determined by the experimental interrogation time T

$$\Delta\omega_{FW} = \frac{\pi}{T}. \quad (11.33)$$

For interrogation times between 0.5 and 2 s of the experimental investigations line widths in the few Hertz range were measured. In the investigation of Ivanov et al. (2008) [60] where the external force was gravity, the measurement of the resonance frequency for the photon-assisted tunneling with the accuracy reached by the above interrogation time allowed those authors to measure the gravity acceleration with ppm resolution. This shows that sensitive RET effects have a great potential for applications, for example, for precision measurements.

The recurrence process of super-Bloch oscillations was recently investigated by Haller et al. (2010) [62] for V_0/E_{rec} values in the 3–7 range, and $\Delta\omega/2\pi$ in the 0.1 = 2 Hz range. The recurrence oscillations were measured up to 2.5 s.

11.4.3 RET IN OPTICAL LATTICES WITH TILT

In spite of the fundamental RET nature and of its practical interest, for a long time the experimental observation was restricted to the motion of electrons in superlattice structures [6]. In 2007 Sias et al. [23] observed resonant tunneling using Bose–Einstein condensates in accelerated optical lattice potentials. The nearly perfect control over the parameters of this system allowed the authors to prepare the condensates with arbitrary initial conditions and also to study the effects of nonlinearity and a loss of coherence. Such observation can be generalized to studying noise and thermal effects in resonant tunneling and underlines the usefulness of Bose–Einstein condensates in optical lattices as model systems for the solid state.

A schematic representation of RET is shown in Figure 11.9. In a tilted periodic potential, atoms can escape by tunneling to the continuum via higher-lying levels. The tilt of the potential is proportional to the applied force F acting on the atoms, and the tunneling rate Γ_{LZ} can be calcu-

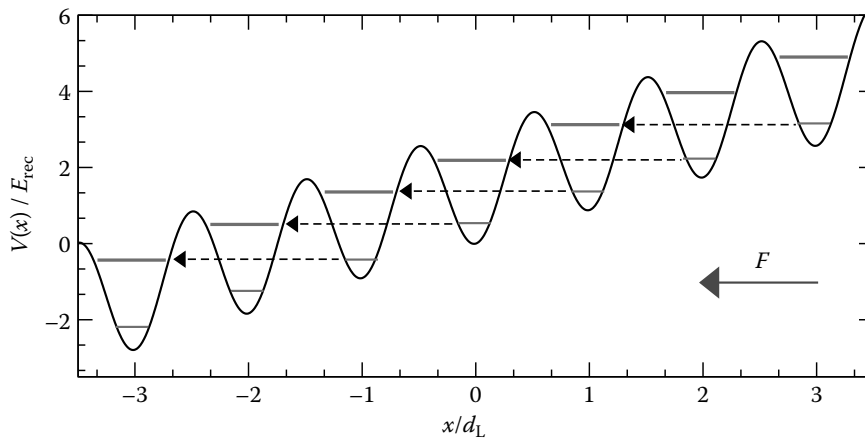


FIGURE 11.9 Schematic of the RET process between second nearest-neighbor wells, that is, for $\Delta i = 2$. The tunneling of atoms is resonantly enhanced when the energy difference between lattice wells matches the separation between the energy levels in different potential wells.

lated using the Landau–Zener formula of Equation 11.8. The actual rates can dramatically deviate from Equation 11.8 when two Wannier–Stark levels in different potentials wells are strongly coupled owing to the accidental degeneracy of Figure 11.9 where the tilt-induced energy difference between wells i and $i + \Delta i$ matches the separation between two quantized energy levels, as pointed out for cold atoms by Bharucha et al. (1997) [66]. Indeed, the tunneling probability can be enhanced by a large factor over the Landau–Zener prediction (see theoretical and experimental results of Figure 11.10).

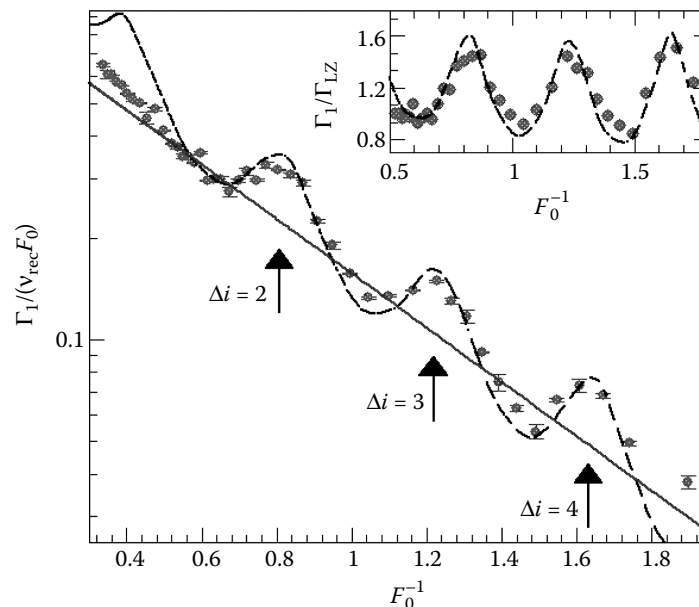


FIGURE 11.10 Resonant tunneling in the linear regime. Shown here is the tunneling rate from the lowest energy bands of the lattice as a function of the normalized inverse force F_0^{-1} for $V_0 = 2.5 E_{\text{rec}}$ lattice depth. The straight line represents the prediction of the Landau–Zener theory. Inset: Deviation from the Landau–Zener prediction of Equation 11.6. (Adapted from C. Sias et al. *Phys. Rev. Lett.* 98, 120403, 2007. Copyright 2007 of American Physical Society.)

By imposing an energy resonance between the Wannier–Stark levels in different wells of an optical lattice shifted by the potential of the external force, one finds that the energy degeneracies occur at the values F at which $F d_L \Delta i$ (Δi integer) is close to the mean band gap between two coupled bands of the $F = 0$ problem [7,28]. The actual peak positions are slightly shifted with respect to this simplified estimate, because the Wannier–Stark levels in the potential wells are only approximately defined by the averaged band gap of the $F = 0$ problem, a consequence of field-induced level shifts [28].

11.4.3.1 Linear Regime and Decay Rates

Although the finite and positive scattering length of ^{87}Rb atoms means that the linear Hamiltonian of Equation 11.4 is never exactly realized in experiments, the approximation of a noninteracting BEC is valid if the condensate density is maintained low. In that case, the interaction energy can be made much smaller than all the other energy scales of the system (recoil energy, bandwidth, gap width) and hence it is negligible for the present analysis of RET in a condensate.

Figure 11.10 shows the results of Sias et al. (2007) [23] for experimental investigations with low-density condensates and the nonlinearity parameter \tilde{g} less than $\approx 1 \times 10^{-2}$, defined as the limit of the linear regime. The tunneling rate Γ_1 out of the first band is shown as a function of F_0^{-1} . Superimposed on the overall exponential dependence of Γ_1/F_0 on F_0^{-1} , one clearly sees the resonant tunneling peaks corresponding to the various resonances $\Delta i = 1, 2, 3, 4$. Which of the resonances were visible in the experiment depended on the choice of lattice parameters and the finite experimental resolution. The limit $n = 3$ for the highest band explored in Sias et al. (2007) [23] was given by the maximum lattice depth achievable.

By measuring the positions of the $\Delta i = 1, 2, 3$ tunneling resonances for different values of the lattice depth V_0 , it appeared that the resonances were shifted according to the variation of the energy levels. For deep enough lattices, the resonance positions may be derived from a numerical simulation but can also be approximately calculated by making a harmonic approximation in the lattice wells, which predicts a separation of the two lowest energy levels ($n = 1$ and $n = 2$) of

$$\Delta E_{2-1} = 2E_{\text{rec}} \sqrt{\frac{V_0}{E_{\text{rec}}}}. \quad (11.34)$$

By imposing the resonance condition $\Delta E_{2-1} = F^{\text{res}} d_L \Delta i$, the calculated F^{res} resonance position results in good approximation with that predicted in Glück et al. (2002) [28] and Wimberger et al. (2005) [67].

11.4.3.2 Avoided Crossings

The accessibility of higher energy levels allowed an experimental measurement of the tunneling rates around RET conditions of two strongly coupled bands. The dependence of those rates on the system parameters was phrased into the frame of level crossing for states experiencing a loss rate. The modification of the level tunneling rate by the presence of a degeneracy may be described by a simple model of a two-level Hamiltonian with an energy separation ε described by an energy crossing splitting $\varepsilon = 0$ and with a single level characterized by a decay rate [68,69]. Real and imaginary parts of the Hamiltonian eigenvalues are different for $\varepsilon \neq 0$, and two different scenarios take place with crossings or anticrossings of the real and imaginary part of the Hamiltonian eigenvalues. In one case, denoted as type-I crossing, the imaginary parts of the eigenvalues cross while the real parts anticross. In the second case, denoted as type-II crossing, the eigenvalues anticross while the real parts cross. The numerical simulations of Zenesini et al. (2008) [24] pointed out that the large majority of the RET explored experimentally correspond to type-II crossings. As a consequence if a resonance takes place between the energy of the lower state and that of the decaying upper level, the tunneling rate of the lower state increases significantly. In addition the upper state experiences

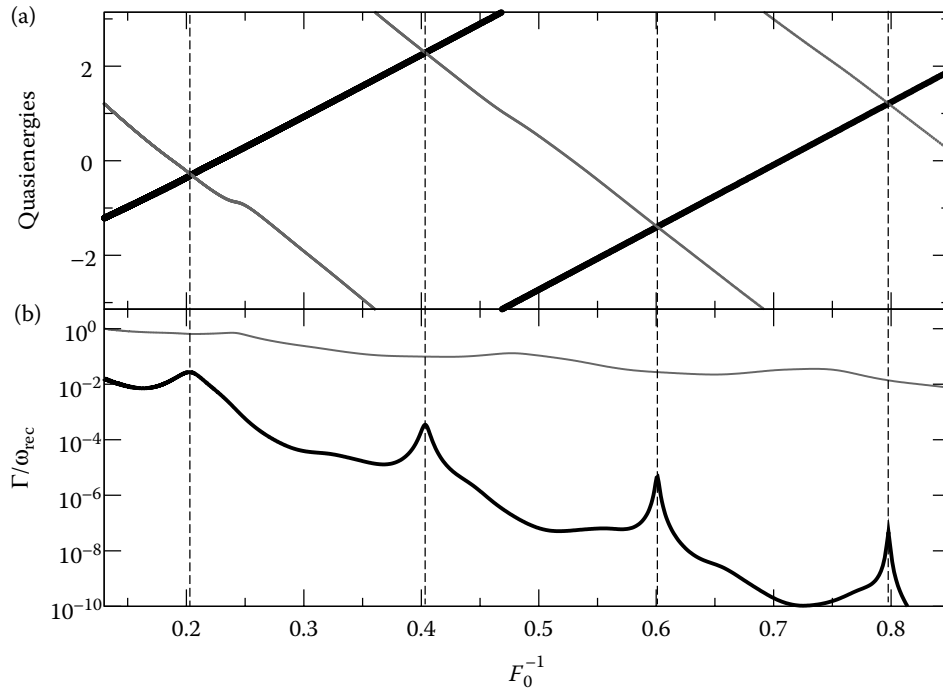


FIGURE 11.11 In (a) real parts of the eigenenergies and in (b) tunneling rate Γ in ω_{rec} units for a lattice depth of $V_0/E_{\text{rec}} = 10$ and the Hamiltonian from Equation 11.4. The eigenenergies and the tunneling rates are associated with two Wannier–Stark ladders or, equivalently, with two energy bands: ground state (thick black lines) and first excited state (thin gray lines). The maxima of the ground-state tunneling rates corresponds to $\Delta i = 1, 2, 3$, and 4. (Reproduced from A. Zenesini et al. *NJP* 10, 0530388, 2008. With permission. Copyright Institute of Physics.)

a resonantly stabilized tunneling (RST) with a decrease of its tunneling rate. Figure 11.11a shows theoretical predictions for type-II crossing and anticrossings for the real parts of the eigenenergies associated with a RET configuration investigated experimentally as a function of the experimental control parameter, the Stark force determined by the F_0 dimensionless parameter of Equation 11.7. The associated Wannier–Stark states tunneling rates are shown in Figure 11.11b as a function of F_0 . The strong modulations on top of the global exponential decrease arise from RET processes originated by the energy crossings. The resonance eigenstates and eigenenergies for the noninteracting atoms described by Equation 11.4 were obtained in Zenesini et al. (2008) [24] by diagonalizing an open version of the Hamiltonian [28,70–73].

Experimental data on anticrossings in the tunneling rates are in Figure 11.12 taken from Sias et al. (2007) [23]. Although a direct observation of the discussed anticrossing scenario in two different levels for the same set of parameters was not possible, the experimental investigation compared the ground and excited state tunneling rates Γ_1 and Γ_2 with the theoretical predictions for two different parameter sets, as shown in Figure 11.12. This figure nicely reveals the anticrossing of the corresponding tunneling rates of strongly coupled levels as a function of the control parameter F_0 around RET conditions.

11.4.3.3 Nonlinearity

This section discusses how the experimental investigation of RET in tilted optical lattices are modified by the atom–atom interactions in the Bose–Einstein condensate. We focus on a parameter regime where the Stark force essentially dominates the dynamics of the condensate. Here the

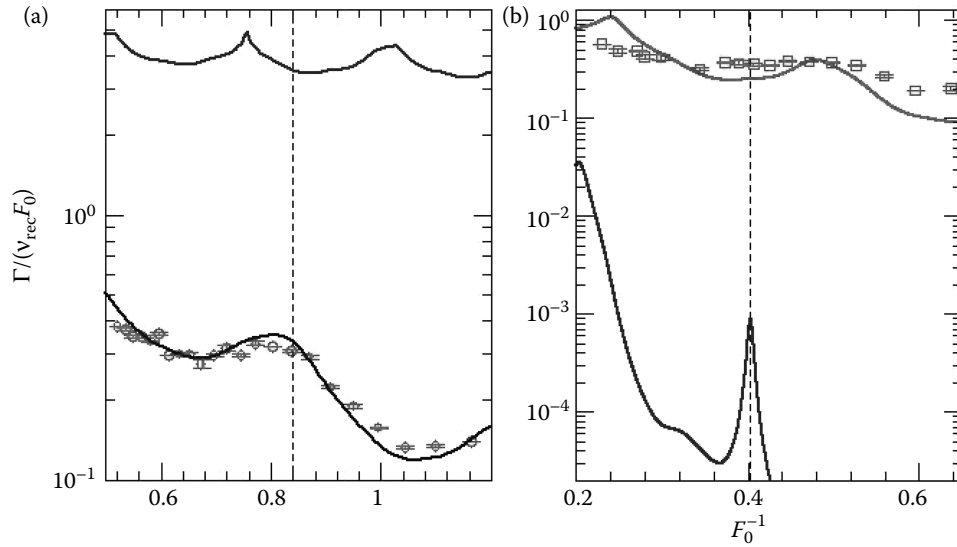


FIGURE 11.12 Anticrossing scenario of the RET rates. (a) Theoretical plot of $\Gamma_{1,2}$ for $V_0 = 2.5 E_{\text{rec}}$ with experimental points for Γ_1 . (b) Theoretical plot of $\Gamma_{1,2}$ for $V_0 = 10 E_{\text{rec}}$ with experimental points for Γ_2 . (Adapted from C. Sias et al. *Phys. Rev. Lett.* 98, 120403, 2007.)

quantum tunneling between the energy bands is significant and most easily detected experimentally. The critical field values for which such excitations are relevant can be estimated by comparing, for instance, the potential energy difference between neighboring wells, Fd_L , with the coupling parameters of the many-body Bose–Hubbard model, that is, the hopping constant J and interaction constant U [14].

Our analysis will exclude the regime of $F_0 \leq J/E_{\text{rec}} \approx U/E_{\text{rec}}$ where a quantum chaotic system is realized [74–78]. The origin of quantum chaos, that is, of the strongly force-dependent and non-perturbative mixing of energy levels can be understood as a consequence of the interaction-induced lifting of the degeneracy of the multiparticle Wannier–Stark levels in the crossover regime from Bloch to Wannier spectra, making nearby levels strongly interact, for comparable magnitudes of hopping matrix elements and Stark shifts.

For the regime of $F_0 \gg J/E_{\text{rec}}$, the effect of weak atomic interactions is just a perturbative shifting and a small splitting of many-body energy levels [71,77]. In order to access the tunneling rates measured in the experiment of Sias et al. [23], we determine the temporal evolution of the survival probability $P_{\text{sur}}(t)$ for the condensate to remain in the energy band, in which it has been prepared initially. As proposed in Wimberger et al. (2005) [67] and applied in the experimental investigation, such a survival probability is best measured in momentum space, since, experimentally, the most easily measurable quantity is the momentum distribution of the condensate obtained from a free expansion after the evolution inside the lattice. Such probability decays exponentially

$$P_{\text{sur}}(t) = P_{\text{sur}}(t=0) \exp(-\Gamma t). \quad (11.35)$$

In the absence of interatomic interactions in the Gross–Pitaevskii equation, for example, for nonlinearity parameter $g = 0$ in Equation 11.12, the individual tunneling events occurring when the condensate crosses the band edge are independent. Hence $P_{\text{sur}}(t)$ globally, that is, fitted over many Bloch periods, has a purely exponential form, apart from the $t \rightarrow 0$ limit [79]. When the nonlinear interaction term is present, the condensate density decays with time too. As a consequence, the rates Γ are at best defined locally in time, and in the presence of RET a sharp nonexponential decay may occur, as discussed in Schlagheck and Wimberger (2007) [72] and Carr et al. (2005) [80]. Nevertheless, for short evolution times and the weak nonlinear coupling strengths \tilde{g} experimentally

accessible (\tilde{g} defined in Equation 11.13, the global decay of the condensate is well fitted by an exponential law [23,81])

$$P_{\text{sur}}(t) = P_{\text{sur}}(t=0) \exp(-\Gamma_n t), \quad (11.36)$$

with rates Γ_n for the band $n = 1$ (ground band), 2 (first excited band), 3 (second excited band), in which the atoms are initially prepared.

We start our study of the tunneling rate in presence of a nonlinearity by discussing the position of RET peaks. These peaks, whose positions for the single-particle evolution are studied in the previous part of this Section 11.4.3, are affected by the nonlinear interaction term appearing in the Gross–Pitaevskii Equation 11.12 for BEC. The RET resonances originate from an exact matching of energy levels in neighboring potential wells, and hence they are very sensitive to slight perturbations. A shift of the RET peaks in energy or in the position of the Stark force, predicted in Wimberger et al. (2006) [71] for large value of the \tilde{g} parameter, is negligible for the experimental investigated nonlinearities $\tilde{g} < 0.06$, the resonance shift corresponding to the extremely small $\Delta F_0 < 5 \times 10^{-4}$ value [71].

The $\tilde{g} \gtrsim 1 \times 10^{-2}$ regime was entered by carrying out the acceleration experiments in radially tighter traps (radial frequency $\gtrsim 100\text{Hz}$) and hence at larger condensate densities. Figure 11.13a shows the $\Delta i = 2$ and $\Delta i = 3$ resonance peaks of the ground-state band ($n = 1$) for increasing values of \tilde{g} , starting from the linear case and going up to $\tilde{g} \approx 3 \times 10^{-2}$. As the nonlinearity increases, two effects occur. First, the overall (off-resonant) level of Γ_1 increases linearly with \tilde{g} . This is in agreement with earlier experiments on nonlinear Landau–Zener tunneling [82,83] and can be modeled by a condensate evolution taking place within a nonlinearity-dependent effective potential $V_{\text{eff}} = V_0/(1 + 4\tilde{g})$ [84]. Second, with increasing nonlinearity, the contrast of the RET peak is decreased and the peak eventually vanishes, as evident from the different on-resonance and off-resonance dependence of the tunneling rate as a function of the atom number N (and hence the nonlinearity) (cf. Figure 11.13b).

The critical value of \tilde{g} for which the nonlinearity affects the resonance peak is estimated by comparing the width of the RET peaks of a band n (which essentially is determined by the tunneling width Γ_{n+1} of the band into which the atoms tunnel) with the energy scale of the nonlinearity. In the experimental investigation of Sias et al. (2007) [23] atomic nonlinearities corresponding to this order-of-magnitude argument were reached. For the parameters of Figures 11.10 and 11.13a and the RET peak with $\Delta i = 2$, the typical width Γ_2 of the decaying state to which the atoms tunneling energy is of the order of $0.2 \dots 0.5 \times E_{\text{rec}}$. Since \tilde{g} reflects the nonlinearity expressed in units of $8 \times E_{\text{rec}}$, this means that substantial deviations from the linear behavior are expected when $\tilde{g} \gtrsim 0.025 \dots 0.06$. The experimental observations confirmed that this threshold is a good estimate for the onset of the destruction of the RET peak, observed to occur around $\tilde{g} = 0.02$ in Figure 11.13a.

The role of nonlinearity on the time evolution of an Wannier–Stark state localized in a single site of the optical lattice was also studied by Krimer et al. (2009) [85]. They predict that the nonlinearity strength leads to different regimes, where the nonlinearity induced shift in the energy of the lattice may enhance or inhibit RET.

11.5 MANY-BODY TUNNELING

In state-of-the-art experiments the interatomic interactions can be tuned by the transversal confinement and by Feshbach resonances [16], resulting in strong interaction-induced correlations. A good starting point for the discussion of true many-body effects is to use a lattice model, as introduced above for a single particle (cf. Equation 11.11) and widely used in the context of strongly correlated ultracold quantum gases [16]. Such a lattice description has the great advantage that the number of degrees of freedom automatically is bounded as compared to field theoretical approaches (see, e.g., Kühner and Monien (1998) [86] and Duine

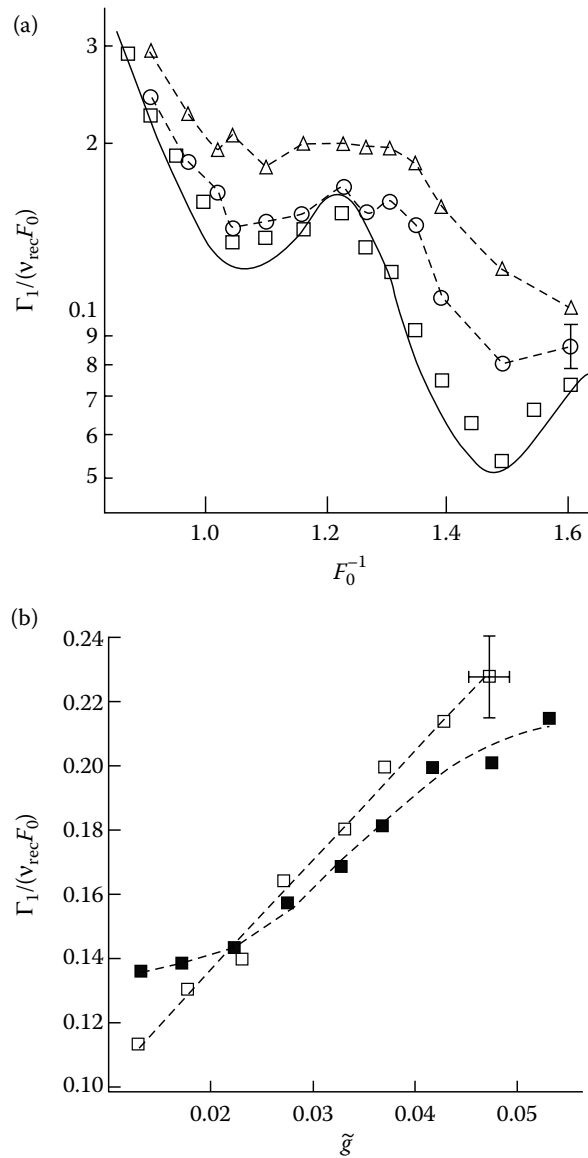


FIGURE 11.13 Resonant tunneling in the nonlinear regime. (a) The tunneling rates for $\Delta i = 3$ from the lowest energy band of the optical lattice as a function of the normalized inverse force F_0^{-1} for a lattice depth $V_0/E_{\text{rec}} = 2.5$ and different values of the nonlinearity parameter, $\tilde{g} \approx 0.01, 0.022, 0.033$ from bottom to top. The continuous line is the theoretical prediction in the linear regime. The dashed lines connect the data obtained at large \tilde{g} values. As the nonlinearity increases, the overall tunneling rate increases and the resonance peak becomes less pronounced. (b) Dependence of the tunneling rate on the nonlinearity parameter \tilde{g} at the position $F_0^{-1} = 1.21$ (solid symbols) of the RET spectrum peak and at $F_0^{-1} = 1.03$ (open symbols) at the RET spectrum local minimum, for $V_0/E_{\text{rec}} = 3.0$. (Adapted from C. Sias et al. *Phys. Rev. Lett.* 98, 120403, 2007. Copyright 2007 of American Physical Society.)

and Stoof (2003) [87] and references therein), and one can use it for practical numerical simulations.

Using a single-band model, the regime of strong correlations in the Wannier–Stark system was addressed in Buchleitner and Kolovsky (2003) [74], Tomadin et al. (2007) [76], Tomadin et al. (2008) [77], Buonsante and Wimberger (2008) [78], and Kolovsky and Buchleitner (2003) [88], revealing the sensitive dependence of the system’s dynamics on the Stark force F . The single-band

Bose–Hubbard system of Buchleitner and Kolovsky (2003) [74] and Kolovsky and Buchleitner (2003) [88] is defined by the following Hamiltonian with the creation a_l^\dagger , annihilation a_l , and number operators n_l^a for the first band of a lattice with sites $l = 1 \dots L$:

$$H_{1B} = \sum_{l=1}^L \left[F_0 E_{\text{rec}} n_l^a - \frac{J_a}{2} (a_{l+1}^\dagger a_l + \text{h.c.}) + \frac{U_a}{2} n_l^a (n_l^a - 1) + \varepsilon_a n_l^a \right], \quad (11.37)$$

where the last term describes the on-site energy.

In order to describe interband tunneling and phenomena related to those discussed in the previous Section 11.4, such a model has to be extended to include at least the equivalent of two single-particle energy bands (as plotted in Figure 11.3). In the presence of strong interatomic interactions parameterized by U terms, the single-band model of Equation 11.37 should be extended to allow for interband transitions, as for example, realized at $F_0 = 0$ in experiments with fermionic interacting atoms [21]. Doing so, Tomadin et al. [77] and Plöte et al. [89] arrived at the following full model Hamiltonian for a closed two-band system schematically sketched in Figure 11.14:

$$\begin{aligned} H(t) = & \varepsilon_a \sum_{l=1}^L n_l^a + \varepsilon_b \sum_{l=1}^L n_l^b \quad \text{onsite energy} + F_0 D E_{\text{rec}} \sum_{l=1}^L (b_l^\dagger a_l + \text{h.c.}) \quad \text{force coupling} \\ & - \frac{1}{2} J_a \sum_{l=1}^L (e^{i2\pi l/T_B} a_{l+1}^\dagger a_l + \text{h.c.}) + \frac{1}{2} J_b \sum_{l=1}^L (e^{i2\pi l/T_B} b_{l+1}^\dagger b_l + \text{h.c.}) \quad \text{hopping in the bands} \\ & + \frac{1}{2} U_a \sum_{l=1}^L n_l^a (n_l^a - 1) + \frac{1}{2} U_b \sum_{l=1}^L n_l^b (n_l^b - 1) \quad \text{onsite interaction} \\ & + 2U_x \sum_{l=1}^L n_l^a n_l^b + \frac{1}{2} U_x \sum_{l=1}^L (b_l^\dagger b_l^\dagger a_l a_l + \text{h.c.}) \quad \text{interband interaction,} \end{aligned} \quad (11.38)$$

where the b index and the b_l, b_l^\dagger creation/annihilation operators are associated to the terms of the second band. D is the “dipole” matrix element between the ground and excited single-particle states in a single lattice site (measured in $2\pi/d_L$ length units, cf. the appendix A of Tomadin et al. (2008) [77] for a detailed explanation of how parameters are computed from the physical model).

Within this full two-band system, *two* dominating mechanisms promote to the second band particles starting from the ground band. The first one is a single-particle coupling arising from the force term

$$H_1 = F_0 D E_{\text{rec}} \sum_{l=1}^L (b_l^\dagger a_l + \text{h.c.}), \quad (11.39)$$

where the dipole matrix element D depends only on the lattice depth V_0 (measured in recoil energies according to the definition above, cf. Equation 11.2). The second one is a many-body effect,

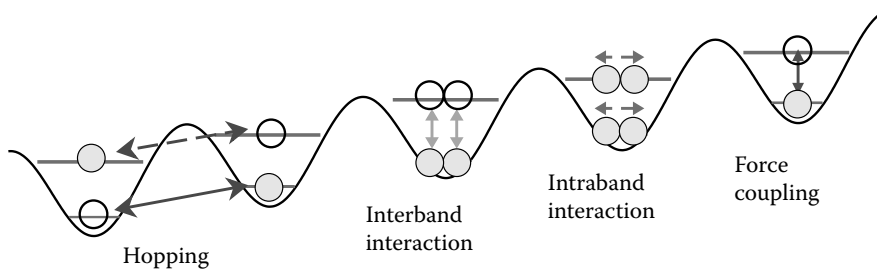


FIGURE 11.14 Sketch of most of the terms of the Hamiltonian Equation 11.38. This model can be used to *fully* describe RET, since it contains excited levels in each potential well, in contrast to the effective model of Section 11.5.1.

describing cotunneling of two particles from the first band into the second band

$$H_2 = \frac{U_x}{2} \sum_{l=1}^L \left(b_l^\dagger b_l^\dagger a_l a_l + \text{h.c.} \right). \quad (11.40)$$

In Equation 11.38 the tilting terms arising from the Stark force F_0 have been transformed into a phase factor $e^{\pm i2\pi t/T_B}$ for the hopping terms by changing into the accelerated frame of Kolovsky and Buchleitner (2003) [88]. This transformation nicely shows that the present problem is intrinsically time-dependent. Since $H(t) = H(t + T_B)$ is periodic with the Bloch period T_B , a Floquet analysis can be used to derive the eigenbasis of the one-period evolution operator generated by $H(t)$. This trick allows also the application of periodic boundary conditions, which is reasonable in order to model large experimental systems, typically extending over a large number of lattice sites. The Hamiltonian of Equation 11.38 contains hopping terms linking nearest-neighboring wells in both bands (J_a and J_b), and terms couplings different bands at a fixed lattice site l either by the force presence ($F_0 D$) or by interactions (U_x). Other terms can, in principle, be included, yet they turn out to be exponentially suppressed for sufficiently deep lattices which are well described by Bose–Hubbard like models [16].

Because of its complex form and the large number of participating many-particle states, the above Hamiltonian is hard to interpret and to treat even numerically, for reasonable numbers of atoms N and lattice sites L . Two approximate treatments will be presented in the following. Section 11.5.1 uses an effective one band model which nevertheless takes the coupling terms between the bands of Equation 11.38 into account. While this model is valid for small interband couplings, Section 11.5.2 presents analytical and numerical results for the full model Equation 11.38, which on the other hand is valid for arbitrary interband couplings but is perturbative in the atom–atom interaction terms U_a , U_b , and U_x .

11.5.1 OPEN ONE-BAND MODEL

Instead of using a numerically hardly tractable complete many-band model, we introduce here a perturbative decay of the many-particle modes in the ground band to a second energy band. This novel approach when applied to the Landau–Zener-like tunneling between the first and the second band [23,25,66,67,82,83] predicts the expected tunneling rates and their statistical distributions.

To justify this perturbative approach, it is crucial to realize that the terms of Equations 11.39 and 11.40 must be small compared with the band gap $\Delta E \equiv \varepsilon_b - \varepsilon_a$ and indeed $F_0 D, U_x \ll \Delta E$ for the parameters of Figure 11.15. As exercised in detail by Tomadin et al. [76,77], from these two coupling terms by using Fermi’s golden rule one can compute analytically the corresponding tunneling rates $\Gamma_1(s)$ and $\Gamma_2(s)$ for each basis state labeled by s . Those rates allow the computation of the total width $\Gamma(s) = \Gamma_1(s) + \Gamma_2(s)$ defined by the two analyzed coupling processes for each basis state $|s\rangle$ of the single-band problem given in Equation 11.37. The $\Gamma(s)$ are inserted as complex potentials in the diagonal of the single-band Hamiltonian matrix. Along with the statistics of the level spacings defined by the real parts of its eigenspectrum $\text{Re}\{E_j\}$ studied in Buchleitner and Kolovsky (2003) [74], Tomadin et al. (2007) [76], Tomadin et al. (2008) [77], Buonsante and Wimberger (2008) [78], and Kolovsky and Buchleitner (2003) [88], the statistical distributions of the tunneling rates $\Gamma_j = -2\text{Im}\{E_j\}$ may be analyzed, as done in Figure 11.15. For the regime where the motion of the atoms is localized along the lattice [28] that distribution is in good agreement with the expected log-normal distribution of tunneling rates (or of the similarly behaving conductance) [90]. In that regime the Stark force dominates and the system shows nearly perfect single-particle Bloch oscillations [74], the distributions agreeing with those predicted from the localization theory [90,91]. On the other hand, when the Stark force is comparable with J_a and U_a and all modes of our Bose–Hubbard model are strongly coupled, the rate distribution of Figure 11.15b follows the expected power-law for open quantum chaotic systems in the diffusive regime [91]. This regime shows strong signatures of quantum chaos [74,76–78,88], which manifest also in the rate distributions [76,77].

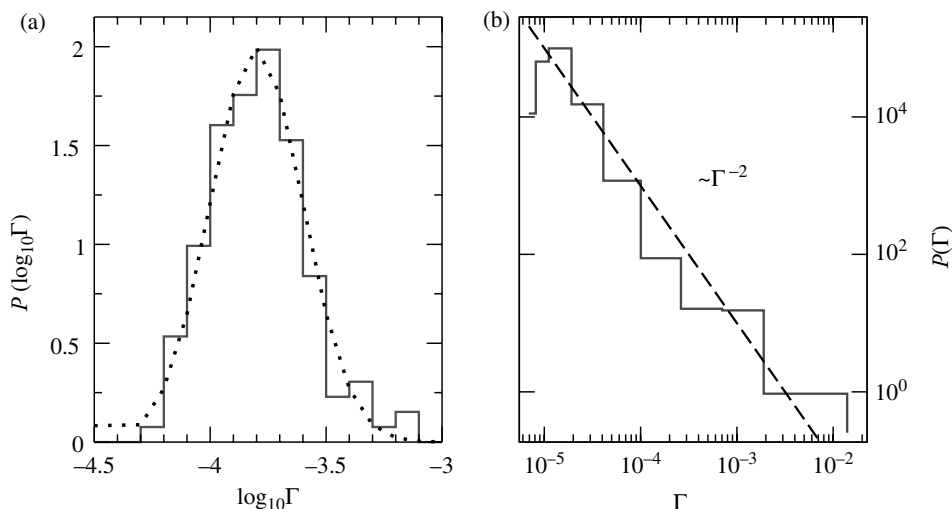


FIGURE 11.15 Rate distributions for the spectrum of an open one-band Bose–Hubbard model in (a) for $F_0 \simeq 0.47, J_a/E_{\text{rec}} = 0.22, U_a/E_{\text{rec}} = 0.2, U_x/E_{\text{rec}} \simeq 0.1$ (for system size $(N, L) = (7, 6)$) and in (b) for $F_0 \simeq 0.17, J_a/E_{\text{rec}} = 0.22, U_a/E_{\text{rec}} = 0.2, U_x/E_{\text{rec}} \simeq 0.1$ ($(N, L) = (9, 8)$). In the regime where the Stark force dominates a log-normal distribution fits well the data (dotted in (a)), whilst a power-law $P(\Gamma) \propto \Gamma^{-x}$ distribution is found with $x \simeq 2$ in the strongly coupled case (dashed line in (b)).

11.5.2 CLOSED TWO-BAND MODEL

Since the model introduced in the previous Section 11.5.1 cannot account for resonant tunneling between a ground level of one well and an excited level of another well, a different model which applies also for strong transitions between the bands was investigated by Plötz et al. (2010) [89]. This model is based on the full Hamiltonian of Equation 11.38 sketched schematically in Figure 11.14.

When the Stark force is tuned to the value where RET occurs for the single particle problem (cf. Section 11.4.3), the strong coupling of the atoms prepared in the ground band into the excited band plays an important role. Since the model is closed, that is, higher bands are neglected, there is no asymptotic tunneling as in the experimental situation described in Section 11.4.3. As a consequence, we observe an oscillation of the probability of occupying the lower and upper band, respectively, which is particularly pronounced at RET conditions. For a single particle in our lattice model, such RET oscillations can be understood easily, since in Floquet space (remembering that our Hamiltonian of Equation 11.38 is periodically time-dependent) the problem reduces to an effective two-state model of resonantly coupled states [89,92]. In this effective description, the evolution corresponds to the two-level Rabi problem of quantum optics of Plötz et al. (2010) [93]. For nonvanishing atom–atom interaction, the situation complicates, of course, and we expect a degradation of those single-particle Rabi oscillations. This is illustrated in Figure 11.16. The period of the single-particle interband oscillation is given by the following formula derived in Plötz et al. (2010) [89]:

$$\frac{t_{\text{osc}}}{T_{\text{Bloch}}} \approx \frac{1}{\left| 2DJ_{\Delta i} \left(\frac{J_b - J_a}{F_0} \right) \right|}, \quad (11.41)$$

where Δi is the resonance order introduced in Section 11.4.3 and $J_{\Delta i}$ the Bessel function of the same order.

For a Stark force F_0 not satisfying the RET conditions, the coupling to the upper band is strongly suppressed, and almost negligible at least for small particle–particle interband interactions U_x . On the other hand if U_x dominates, strong interband coupling is possible even for small forces F_0 . The

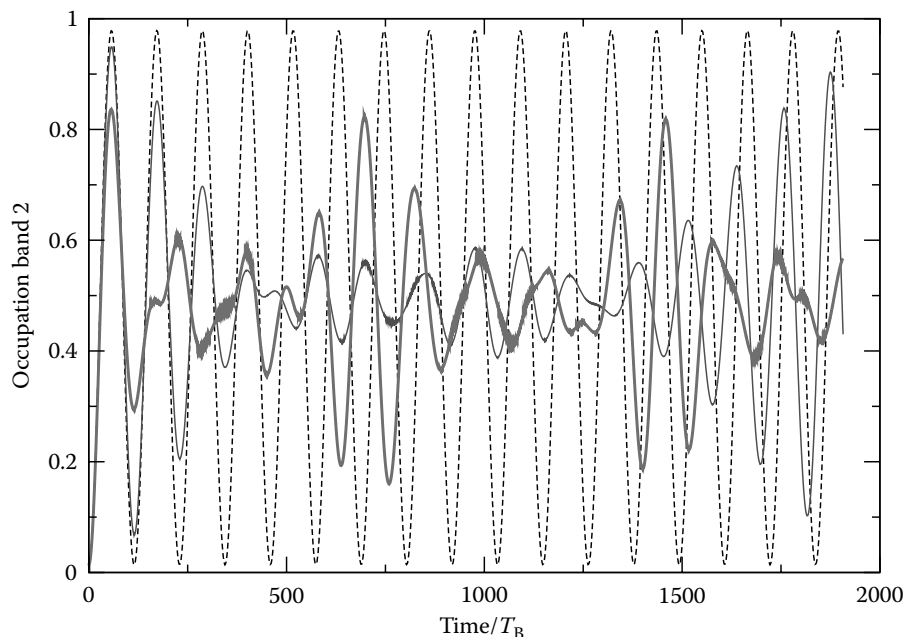


FIGURE 11.16 Population in the upper band as a function of time for the rescaling parameter $\alpha = 0$ (black dotted line), 0.2 (faint gray line) and 0.5 (gray thick line) in a closed two-band model. Clearly visible are the interaction induced collapses and revivals of the RET oscillations between the bands. Other parameters are $F_0 = 1.87$ (dominating energy scale!) and $J_a = 0.1, J_b = 0.77, U_a = 0.023, U_b = 0.014, U_x = 0.01, \varepsilon_b - \varepsilon_a = 3.38$ (all in recoil energy units) and $D = -0.16$ in length units, and $(N, L) = (5, 6)$.

latter strongly correlated regime of two energy bands is extremely hard to deal with, especially if one is searching for analytical predictions for the interband dynamics. The results shown in Figure 11.16 are just a small step in this direction. In the limit of small atom–atom interactions, the observed collapse and revival times can be determined analytically in good approximation. We quantify small interactions by artificially rescaling the parameters U_a, U_b, U_x , which would be obtained by a given scattering length and a given depth of the optical lattice potential [16], by a constant factor $0 < \alpha < 1$. From the results of Figure 11.16, α was chosen to be zero (black dotted line), 0.2 (faint gray line) and 0.5 (gray thick line). The analogy with the Rabi oscillation problem even carries over to those values of interaction strength, since we observe a collapse and later on a revival of the periodic oscillation of the population. Collapse and revival timescale inversely proportional with the strength factor α , as shown in Figure 11.17, where the revival time is well approximated by the formula derived in Plötz et al. (2010) [89]

$$\frac{t_{\text{revival}}}{T_{\text{Bloch}}} \approx \frac{2F_0}{\alpha U_x J_0^2 \left(\frac{J_a}{F_0} \right) J_0^2 \left(\frac{J_b}{F_0} \right)}, \quad (11.42)$$

with the zeroth-order Bessel function J_0 . This formula arises from a perturbative calculation of the effect of atom–atom interactions for small $\alpha U_{a,b,x} \ll F_0$ starting from the single-particle solution, which itself is known within the effective two-state model, and assuming a delocalized initial state along the lattice. From Equation 11.42 the collapse time was estimated in Meystre and Sargent (2007) [93] as $t_{\text{collapse}} \approx t_{\text{revival}} / (\pi \sigma_s)$, with the effective number σ_s of additionally coupled many-particle states as compared to the single-particle two-state model. This collapse is analogous to that of the Rabi oscillations in the presence of atomic interactions, or to the collapse arising whenever the phase evolution of each s basis state is nonlinear in the particle number. Notice that the collapse

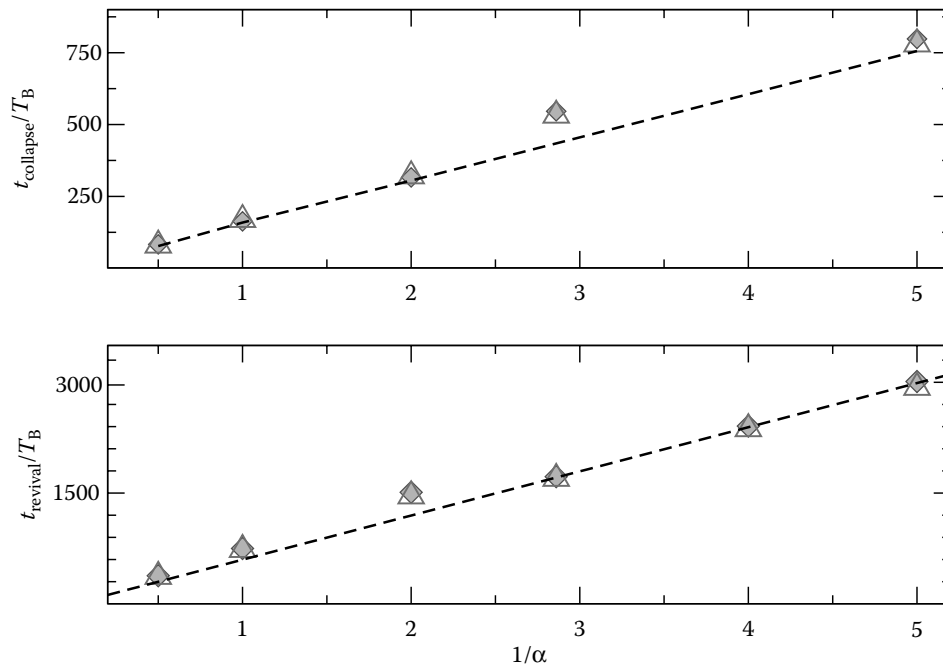


FIGURE 11.17 Collapse and revival times extracted from data (symbols for two different system parameter sets) as shown in Figure 11.16 versus the inverse of the atom–atom interaction rescaling factor α . As expected for a two-state Rabi problem perturbed by a coupling to additional states, both times scale inverse proportionally to α . The dashed lines should guide the eye.

and revival phenomena of Figure 11.16 stem from a degradation (arising from interactions) of single particle *interband* oscillations (with original period given by Equation 11.41 which just depends on the force F_0). So, even if there are analogies to the collapses and revivals observed in BEC [18, 94–96], their origins are different. In the BEC investigations the collapse-revival oscillations were produced by the interaction within a single-band (in Will et al. (2009) [96] by atomic interactions depending on higher power of the well occupation number). Therefore, those oscillations would *not* at all occur when the lower band nonlinear interaction(s) is (are) suppressed, equivalent to $U_a = 0$ in the model here discussed.

The above steps may be expanded in different directions within the realm of true many-body dynamics and tunneling, with great perspectives for many-body induced RET effects. Remaining questions are, for instance, the study of the strongly correlated regime of strong particle and strong interband interactions simultaneously, and the enlargement of our closed two band model in order to allow for a realistic description of experiments similar to the ones reported in Section 11.4.3 now carried over into the realm of strong many-body interactions.

11.6 CONCLUSIONS AND PERSPECTIVES ON RET

This chapter has presented and discussed the RET investigations performed with cold and ultracold atoms. Owing to the reached high level of control on the atom initial preparation and on the realization of potentials with arbitrary shapes, the atomic physics community has reproduced and analyzed basic quantum mechanics phenomena well established, and with important applications, within the solid-state physics community. An important feature associated to the investigations on the atoms, compared to those on electrons in a solid, is the absence of decoherence phenomena. Therefore, quantum interference phenomena may play an enormous role on the tunneling temporal evolution of the cold atoms. For the ultracold atoms an additional characteristic is the presence of inter-

atomic interactions, that modify the position of the energy levels and therefore greatly influence the RET. In more complex configurations the atomic interactions lead to a very complex Hamiltonian whose action on the atoms requires large computational efforts or analyses based on perturbation approaches.

Our analysis was restricted to potentials which are either not explicitly time-dependent or lead to a temporal evolution of the atomic wavefunction corresponding to an adiabatic evolution of the atomic system. Tunneling processes produced by a nonadiabatic atomic evolution are described in other chapters of this volume.

Macroscopic quantum tunneling is an important direction of research well investigated by the solid-state physics community. Up to now no clear evidence of that tunneling was reported by the BEC community even if configurations for the occurrence of macroscopic quantum tunneling in Bose–Einstein condensates have been proposed by different authors. Ueda and Leggett [97,98] examined the instability of a collective mode in a BEC with attractive interaction induced by macroscopic tunneling. Thus, a collective variable, the spatial width of BEC is analyzed as a tunneling variable. Carr et al. [80] studied BEC in a potential of finite depth, harmonic for small radii and decaying as a Gaussian for large radii, which supports both bound and quasibound states. The atomic nonlinearity transforming bound states into quasibound ones, leads to macroscopic quantum tunneling. The experimental observation of such macroscopic tunneling would enlarge the quantum simulation configurations explored with ultracold atoms.

ACKNOWLEDGMENTS

Ennio Arimondo thanks the IFRAF, Paris (France), for the financial support at the École Normale Supérieure where this work was initiated. We also gratefully acknowledge the support from the Project NAMEQUAM of the Future and Emerging Technologies (FET) programme within the Seventh Framework Programme for Research of the European Commission (FET-Open grant number: 225187), the PRIN Project of the MIUR of Italy, and the Excellence Initiative by the German Research Foundation (DFG) through the Heidelberg Graduate School of Fundamental Physics (Grant No. GSC 129/1), the Frontier Innovation Funds and the Global Networks Mobility Measures of the University of Heidelberg. Sandro Wimberger is especially grateful to the Heidelberg Academy of Sciences and Humanities for the Academy Award 2010 and to the Hengstberger Foundation for support by the Klaus-Georg and Sigrid Hengstberger Prize 2009. This review was stimulated by the tunneling experiments performed in Pisa by D. Ciampini, H. Lignier, O. Morsch, C. Sias, and A. Zenesini, and we thank all of them for the continuous valuable discussions. Finally, we would like to thank our theory collaborators, G. Tayebirad, N. Lörch, A. Tomadin, P. Schlagheck, A. Kolovsky, P. Plötz, D. Witthaut, J. Madroñero, and R. Mannella for their help in pushing forward this work.

REFERENCES

1. M. J. Davis and E. J. Heller, Quantum dynamical tunneling in bound states. *J. Chem. Phys.* 75, 246, 1981.
2. R. Tsu and L. Esaki, Tunneling in a finite superlattice. *Appl. Phys. Lett.* 22, 562, 1973.
3. L. L. Chang, L. Esaki, and R. Tsu, Resonant tunneling in semiconductor double barriers. *Appl. Phys. Lett.* 24, 593, 1974.
4. L. L. Chang, E. E. Mendez, and C. Tejedor, eds., *Resonant Tunneling in Semiconductors*, Plenum Press, Amsterdam, 1991.
5. L. Esaki, A bird's-eye view on the evolution of semiconductor superlattices and quantum wells. *IEEE J. Quant. Electr.* QE-22, 1611, 1986.
6. K. Leo, *High-Field Transport in Semiconductor Superlattices*, Springer-Verlag, Berlin, 2003.
7. S. Glutsch, Nonresonant and resonant Zener tunneling. *Phys. Rev. B* 69, 235317, 2004.

8. M. Wagner and H. Mizuta, Complex-energy analysis of intrinsic lifetimes of resonances in biased multiple quantum wells. *Phys. Rev. B* 48, 14393, 1993.
9. B. Rosam, K. Leo, M. Glück, F. Keck, H. J. Korsch, F. Zimmer, and K. Köhler, Lifetime of Wannier-Stark states in semiconductor superlattices under strong Zener tunneling to above-barrier bands. *Phys. Rev. B* 68, 125301, 2003.
10. H. Mizuta and T. Tanoue, *The Physics and Applications of Resonant Tunneling Diodes*, Cambridge University Press, Cambridge, UK, 1995.
11. M. Ben Dahan, E. Peik, J. Reichel, Y. Castin, and C. Salomon, Oscillations of atoms in an optical potential. *Phys. Rev. Lett.* 76, 4508, 1996.
12. M. Raizen, C. Salomon, and Q. Niu, New light on quantum transport. *Phys. Today* 50, 30, 1997.
13. G. Roati, E. de Mirandes, F. Ferlaino, H. Ott, G. Modugno, and M. Inguscio, Atom interferometry with trapped Fermi gases. *Phys. Rev. Lett.* 92, 230402, 2004.
14. O. Morsch and M. Oberthaler, Dynamics of Bose–Einstein condensates in optical lattices. *Rev. Mod. Phys.* 78, 179, 2006.
15. M. Gustavsson, E. Haller, M. J. Mark, J. G. Danzl, G. Rojas-Kopeinig, and H.-C. Nägerl, Control of interaction-induced dephasing of Bloch oscillations. *Phys. Rev. Lett.* 100, 080404, 2008.
16. I. Bloch, J. Dalibard, and W. Zwerger, Many-body physics with ultracold gases. *Rev. Mod. Phys.* 80, 885, 2008.
17. B. K. Teo, J. R. Guest, and G. Raithel, Tunneling resonances and coherence in an optical lattice. *Phys. Rev. Lett.* 88, 173001, 2002.
18. M. Greiner, O. Mandel, T. Esslinger, T. W. Hänsch, and I. Bloch, Quantum phase transition from a superfluid to a Mott insulator in a gas of ultracold atoms. *Nature* 415, 39, 2002.
19. S. Fölling, S. Trotzky, P. Cheinet, M. Feld, R. Saers, A. Widera, T. Müller, and I. Bloch, Direct observation of second-order atom tunnelling. *Nature* 448, 1029, 2007.
20. S. R. Wilkinson, C. F. Bharucha, K. W. Madison, Q. Niu, and M. G. Raizen, Observation of atomic Wannier-Stark ladders in an accelerating optical potential. *Phys. Rev. Lett.* 76, 4512, 1996.
21. M. Köhl, H. Moritz, T. Stöferle, K. Günter, and T. Esslinger, Fermionic atoms in a three dimensional optical lattice: Observing Fermi surfaces, dynamics, and interactions. *Phys. Rev. Lett.* 94, 080403, 2005.
22. C. Lee, E. A. Ostrovskaya, and Y. Kivshar, Nonlinearity-assisted quantum tunnelling in a matter-wave interferometer. *J. Phys. B: At. Mol. Opt. Phys.* 40, 4235, 2007.
23. C. Sias, A. Zenesini, H. Lignier, S. Wimberger, D. Ciampini, O. Morsch, and E. Arimondo, Resonantly enhanced tunneling of Bose-Einstein condensates in periodic potentials. *Phys. Rev. Lett.* 98, 120403, 2007.
24. A. Zenesini, C. Sias, H. Lignier, Y. Singh, D. Ciampini, O. Morsch, R. Mannella, E. Arimondo, A. Tomadin, and S. Wimberger, Resonant tunneling of Bose-Einstein condensates in optical lattices. *NJP* 10, 0530388, 2008.
25. M. Cristiani, O. Morsch, J. H. Müller, D. Ciampini, and E. Arimondo, Experimental properties of Bose-Einstein condensates in one-dimensional optical lattices: Bloch oscillations, Landau-Zener tunneling, and mean-field effects. *Phys. Rev. A* 65, 063612, 2002.
26. R. Grimm, M. Weidemüller, and Y. B. Ovchinnikov, Optical dipole traps for neutral atoms. *Adv. At. Mol. Opt. Phys.* 42, 95, 2000.
27. G. Nenciu, Dynamics of band electrons in electric and magnetic fields: Rigorous justification of the effective Hamiltonians. *Rev. Mod. Phys.* 63, 91, 1991.
28. M. Glück, A. R. Kolovsky, and H. J. Korsch, Wannier-Stark resonances in optical and semiconductor superlattices. *Phys. Rep.* 366, 103, 2002.
29. M. Holthaus, Bloch oscillations and Zener breakdown in an optical lattice. *J. Opt. B: Quant. Semicl. Opt.* 2, 589, 2000.
30. L. Landau, On the theory of transfer of energy at collisions II. *Phys. Z. Sowjetunion* 2, 46, 1932.
31. C. Zener, Non-adiabatic crossing of energy levels. *Proc. R. Soc. London, Ser. A* 137, 696, 1932.
32. N. Aschcroft and N. Mermin, *Solid State Physics*, Saunders College, Philadelphia, 1976.
33. W. Zwerger, Mott–Hubbard transition of cold atoms in optical lattices. *J. Opt. B: Quantum Semicl. Opt.* 5, S9, 2003.
34. C. J. Pethick and H. Smith, *Bose–Einstein Condensation in Dilute Gases*, Cambridge University Press, Cambridge, UK, 2002.
35. L. Pitaevskii and S. Stringari, *Bose–Einstein Condensation*, Oxford University Press, Oxford, UK, 2003.

36. Y. Castin, K. Berg-Sørensen, J. Dalibard, and K. Mølmer, Two-dimensional Sisyphus cooling. *Phys. Rev. A* 50, 5092, 1994.
37. S. K. Dutta, B. K. Teo, and G. Raithel, Tunneling dynamics and gauge potentials in optical lattices. *Phys. Rev. Lett.* 83, 1934, 1999.
38. D. L. Haycock, P. M. Alsing, I. H. Deutsch, J. Grondalski, and P. S. Jessen, Mesoscopic quantum coherence in an optical lattice. *Phys. Rev. Lett.* 85, 3365, 2000.
39. E. Kierig, U. Schnorrberger, A. Schietinger, J. Tomkovic, and M. K. Oberthaler, Single-particle tunneling in strongly driven double-well potentials. *Phys. Rev. Lett.* 100, 190405, 2008.
40. D. R. Dounas-Frazer, A. M. Hermundstad, and L. D. Carr, Ultracold bosons in a tilted multilevel double-well potential. *Phys. Rev. Lett.* 99, 200402, 2007.
41. M. Albiez, R. Gati, J. Fölling, S. Hunsmann, M. Cristiani, and M. K. Oberthaler, Direct observation of tunneling and nonlinear self-trapping in a single bosonic Josephson junction. *Phys. Rev. Lett.* 95, 010402, 2005.
42. R. Khomeriki, S. Ruffo, and S. Wimberger, Driven collective quantum tunneling of ultracold atoms in engineered optical lattices. *Europhys. Lett.* 77, 40005, 2006.
43. V. Averbukh, S. Osovski, and N. Moiseyev, Controlled tunneling of cold atoms: From full suppression to strong enhancement. *Phys. Rev. Lett.* 89, 253201, 2002.
44. W. K. Hensinger, A. Mouchet, P. S. Julienne, D. Delande, N. R. Heckenberg, and H. Rubinsztein-Dunlop, Analysis of dynamical tunneling experiments with a Bose–Einstein condensate. *Phys. Rev. A* 70, 013408, 2004.
45. D. A. Steck, W. H. Oskay, and M. G. Raizen, Observation of chaos-assisted tunneling between islands of stability. *Science* 293, 274, 2001.
46. W. Hensinger, H. Haffner, A. Browaeys, N. Heckenberg, K. Helmerson, C. McKenzie, G. Milburn, W. Phillips, S. Rolston, H. Rubinsztein-Dunlop, and B. Uppcroft, Dynamical tunnelling of ultracold atoms. *Nature* 412, 52, 2001.
47. O. Bohigas, S. Tomsovic, and D. Ullmo, Manifestations of classical phase space structures in quantum mechanics. *Phys. Rep.* 223, 43, 1993.
48. D. H. Dunlap and V. M. Kenkre, Dynamic localization of a charged particle moving under the influence of an electric field. *Phys. Rev. B* 34, 3625, 1986.
49. F. Rossi, Coherent phenomena in semiconductors. *Semicon. Sci. Technol.* 13, 147, 1998.
50. H. J. Korsch and S. Mossmann, An algebraic solution of driven single band tight binding dynamics. *Phys. Lett. A* 317, 54, 2003.
51. A. Klumpp, D. Witthaut, and H. J. Korsch, Quantum transport and localization in biased periodic structures under bi- and polychromatic driving. *J. Phys. A: Math. Theor.* 40, 2299, 2007.
52. P. K. Tien and J. P. Gordon, Multiphoton process observed in the interaction of microwave fields with the tunneling between superconductor films. *Phys. Rev.* 129, 647, 1963.
53. B. J. Keay, S. J. Allen, J. Galán, J. P. Kaminski, K. L. Campman, A. C. Gossard, U. Bhattacharya, and M. J. W. Rodwell, Photon-assisted electric field domains and multiphoton-assisted tunneling in semiconductor superlattices. *Phys. Rev. Lett.* 75, 4098, 1995.
54. B. J. Keay, S. Zeuner, S. J. Allen, K. D. Maranowski, A. C. Gossard, U. Bhattacharya, and M. J. W. Rodwell, Dynamic localization, absolute negative conductance, and stimulated, multiphoton emission in sequential resonant tunneling semiconductor superlattices. *Phys. Rev. Lett.* 75, 4102, 1995.
55. L. P. Kouwenhoven, S. Jauhar, J. Orenstein, P. L. McEuen, Y. Nagamune, J. Motohisa, and H. Sakaki, Observation of photon-assisted tunneling through a quantum dot. *Phys. Rev. Lett.* 73, 3443, 1994.
56. T. H. Oosterkamp, L. P. Kouwenhoven, A. E. A. Koolen, N. C. van der Vaart, and C. J. P. M. Harmans, Photon sidebands of the ground state and first excited state of a quantum dot. *Phys. Rev. Lett.* 78, 1536, 1997.
57. A. Eckardt, C. Weiss, and M. Holthaus, Superfluid-insulator transition in a periodically driven optical lattice. *Phys. Rev. Lett.* 95, 260404, 2005.
58. A. R. Kolovsky and H. J. Korsch, Dynamics of interacting atoms in driven tilted optical lattices in Bose-Einstein condensates in optical lattices. *J. Sib. Fed. Un.: Math, Phys*, 3, 211, 2010.
59. C. Sias, H. Lignier, Y. P. Singh, A. Zenesini, D. Ciampini, O. Morsch, and E. Arimondo, Observation of photon-assisted tunneling in optical lattices. *Phys. Rev. Lett.* 100, 040404, 2008.
60. V. V. Ivanov, A. Alberti, M. Schioppo, G. Ferrari, M. Artoni, M. L. Chiofalo, and G. M. Tino, Coherent delocalization of atomic wave packets in driven lattice potentials. *Phys. Rev. Lett.* 100, 043602, 2008.

61. A. Alberti, V. Ivanov, G. Tino, and G. Ferrari, Engineering the quantum transport of atomic wavefunctions over macroscopic distances. *Nat. Phys.* 5, 547, 2009.
62. E. Haller, R. Hart, M. J. Mark, J. Danzl, L. Reichsöllner, and H. Nägerl, Inducing transport in a dissipation-free lattice with super Bloch oscillations. *Phys. Rev. Lett.* 104, 200403, 2010.
63. Q. Thommen, J. C. Garreau, and V. Zehnle, Theoretical analysis of quantum dynamics in one-dimensional lattices: Wannier–Stark description. *Phys. Rev. A* 65, 053406, 2002.
64. A. Eckardt and M. Holthaus, Dressed matter waves. *J. Phys.: Conf. Ser.* 99, 012007, 2008.
65. H. Lignier, C. Sias, D. Ciampini, Y. Singh, A. Zenesini, O. Morsch, and E. Arimondo, Dynamical control of matter-wave tunneling in periodic potentials. *Phys. Rev. Lett.* 99, 220403, 2007.
66. C. F. Bharucha, K. W. Madison, P. R. Morrow, S. R. Wilkinson, B. Sundaram, and M. G. Raizen, Observation of atomic tunneling from an accelerating optical potential. *Phys. Rev. A* 55, R857, 1997.
67. S. Wimberger, R. Mannella, O. Morsch, E. Arimondo, A. R. Kolovsky, and A. Buchleitner, Nonlinearity-induced destruction of resonant tunneling in the Wannier–Stark problem. *Phys. Rev. A* 72, 063610, 2005.
68. J. E. Avron, The lifetime of Wannier ladder states. *Ann. Phys.* 143, 33, 1982.
69. F. Keck, H. J. Korsch, and S. Mossmann, Unfolding a diabolic point: A generalized crossing scenario. *J. Phys. A: Math. Gen.* 36, 2125, 2003.
70. M. Glück, A. R. Kolovsky, and H. J. Korsch, Lifetime of Wannier–Stark states. *Phys. Rev. Lett.* 83, 891, 1999.
71. S. Wimberger, P. Schlagheck, and R. Mannella, Tunnelling rates for the nonlinear Wannier–Stark problem. *J. Phys. B: At. Mol. Opt. Phys.* 39, 729, 2006.
72. P. Schlagheck and S. Wimberger, Nonexponential decay of Bose–Einstein condensates: A numerical study based on the complex scaling method. *Appl. Phys. B: Lasers Opt.* 86, 385, 2007.
73. D. Witthaut, E. M. Graefe, S. Wimberger, and H. J. Korsch, Bose–Einstein condensates in accelerated double-periodic optical lattices: Coupling and crossing of resonances. *Phys. Rev. A* 75, 013617, 2007.
74. A. Buchleitner and A. R. Kolovsky, Interaction-induced decoherence of atomic Bloch oscillations. *Phys. Rev. Lett.* 91, 253002, 2003.
75. Q. Thommen, J. C. Garreau, and V. Zehnlé, Classical chaos with Bose–Einstein condensates in tilted optical lattices. *Phys. Rev. Lett.* 91, 210405, 2003.
76. A. Tomadin, R. Mannella, and S. Wimberger, Many-body interband tunneling as a witness of complex dynamics in the Bose–Hubbard mode. *Phys. Rev. Lett.* 98, 130402, 2007.
77. A. Tomadin, R. Mannella, and S. Wimberger, Many-body Landau–Zener tunneling in the Bose–Hubbard mode. *Phys. Rev. A* 77, 013606, 2008.
78. P. Buonsante and S. Wimberger, Engineering many-body quantum dynamics by disorder. *Phys. Rev. A* 77, 041606(R), 2008.
79. S. R. Wilkinson, C. F. Bharucha, M. C. Fischer, K. W. Madison, P. R. Morrow, Q. Niu, B. Sundaram, and M. G. Raizen, Observation of atomic Wannier-Stark ladders in an accelerating optical potential. *Nature* 387, 575, 1997.
80. L. D. Carr, M. J. Holland, and B. A. Malomed, Macroscopic quantum tunnelling of Bose–Einstein condensates in a finite potential well. *J. Phys. B: At. Mol. Opt. Phys.* 38, 3217, 2005.
81. S. Wimberger, D. Ciampini, O. Morsch, R. Mannella, and E. Arimondo, Engineered quantum tunnelling in extended periodic potentials. *J. Phys.: Conf. Ser.* 67, 012060, 2007.
82. O. Morsch, J. H. Müller, M. Cristiani, D. Ciampini, and E. Arimondo, Bloch oscillations and mean-field effects of Bose–Einstein condensates in 1D optical lattices. *Phys. Rev. Lett.* 87, 140402, 2001.
83. M. Jona-Lasinio, O. Morsch, M. Cristiani, N. Malossi, J. H. Müller, E. Courtade, M. Anderlini, and E. Arimondo, Asymmetric Landau–Zener tunneling in a periodic potential. *Phys. Rev. Lett.* 91, 230406, 2003; *ibidem* (93), 119903(E), 2004.
84. D.-I. Choi and Q. Niu, Bose–Einstein condensates in an optical lattice. *Phys. Rev. Lett.* 82, 2022, 1999.
85. D. O. Krimer, R. Khomeriki, and S. Flach, Delocalization and spreading in a nonlinear Stark ladder. *Phys. Rev. E* 80, 036201, 2009.
86. T. D. Kühner and H. Monien, Phases of the one-dimensional Bose–Hubbard model. *Phys. Rev. B* 58, R14741, 1998.
87. R. A. Duine and H. T. C. Stoof, Many-body aspects of coherent atom-molecule oscillations. *Phys. Rev. Lett.* 91, 150405, 2003.

88. A. R. Kolovsky and A. Buchleitner, Floquet-Bloch operator for the Bose–Hubbard model with static field. *Phys. Rev. E* 68, 056213, 2003.
89. P. Plötz, J. Madroñero, and S. Wimberger, Collapse and revival in inter-band oscillations of a two-band Bose–Hubbard mode. *J. Phys. B: At. Mol. Opt. Phys.* 43, 081001, 2010.
90. C. W. J. Beenakker, Random-matrix theory of quantum transport. *Rev. Mod. Phys.* 69, 731, 1997.
91. T. Kottos, Statistics of resonances and delay times in random media: Beyond random matrix theory. *J. Phys. A: Math. General* 38, 10761, 2005.
92. Y. Nakamura, Y. A. Pashkin, and J. S. Tsai, Rabi oscillations in a Josephson-junction charge two-level system. *Phys. Rev. Lett.* 87, 246601, 2001.
93. P. Meystre and M. I. Sargent, *Elements of Quantum Optics*, Springer-Verlag, Heidelberg, 2007.
94. M. Anderlini, J. Sebby-Strabley, J. Kruse, J. V. Porto, and W. Phillips, Controlled atom dynamics in a double-well optical lattice. *J. Phys. B: At. Mol. and Opt. Phys.* 39, S199, 2006.
95. J. Sebby-Strabley, B. L. Brown, M. Anderlini, P. J. Lee, W. D. Phillips, J. V. Porto, and P. R. Johnson, Preparing and probing atomic number states with an atom interferometer. *Phys. Rev. Lett.* 98, 200405, 2007.
96. S. Will, T. Best, U. Schneider, L. Hackermüller, D.-S. Lühmann, and I. Bloch, Multi-orbital quantum phase diffusion. *Nature* 465, 197, 2010.
97. M. Ueda and A. J. Leggett, Macroscopic quantum tunneling of a Bose–Einstein condensate with attractive interaction. *Phys. Rev. Lett.* 80, 1576, 1998.
98. M. Ueda and A. J. Leggett, Ueda and Leggett reply. *Phys. Rev. Lett.* 81, 1343, 1998.

A Pseudo-classical Method for the Atom-Optics Kicked Rotor: From Theory to Experiment and back

Mark Sadgrove¹ and Sandro Wimberger²

¹*Institute for Laser Science, The University of Electro-communication, 1-5-1
Chofugaoka, Chofu, Japan*

²*Institut für Theoretische Physik, Universität Heidelberg, Philosophenweg 19,
69120 Heidelberg, Germany*

Contents

1	Introduction	3
1.1	The quantum kicked rotor	3
1.2	The atom-optics realization of the quantum kicked rotor	4
2	The pseudo-classical method for nearly resonant quantum motion	12
2.1	Dynamical localization and quantum resonances	12
2.2	Exact results at quantum resonance	13
2.3	Pseudo-classical theory for principal quantum resonances	15
3	Application of the pseudo-classical method	22
3.1	Scaling functions for mean energy of the AKOR	22
3.2	Comparison of near-resonant method with the standard semi-classical limit	26
3.3	Noise and decoherence	30
3.4	Directed transport at quantum resonance	39
3.5	Fidelity as a measure of stability	44
3.6	Pseudo-classical theory for fidelity	47
4	Conclusions and outlook	50
4.1	Review of the state of the art	50
4.2	Future perspectives for the pseudo-classical method	52
5	Acknowledgements	53

Abstract

We review the concept and applications of a semi-classical (ϵ -classical or pseudo-classical) approximation to the resonant dynamics of an atom “kicked” by a pulsed, periodic potential. This powerful method allows us to derive analytical results in the

deep quantum limit of the kicked rotor. Additionally, classical phase space portraits may be used to represent the dynamics even though the system is fundamentally quantum mechanical. The technique has been successfully adapted for systems including noise and decoherence, as well as systems for which the initial state is a nontrivial quantum superposition (leading to directed transport at quantum resonance). For almost a decade, theoretical investigations and experimental investigations have been proceeding hand-in-hand in this field, which has been stimulated regularly by experimental progress in controlling driven dynamical systems. Here we review both theoretical and experimental advances, which in turn may inspire future applications of the presented pseudo-classical method.

Key words: Semi-classical methods, quantum kicked rotor, nonlinear dynamics, (ultra)cold atoms, noise and decoherence

Notation

M	atomic mass
k_L	laser wavevector
T	laser pulse period
ω_{rec}	recoil angular frequency
p	atomic momentum in $2\hbar k_L$ units
β	rescaled atomic quasimomentum
τ	kicking period in dimensionless units
t	total number of kicks and kick total time in units of τ
k	kicking strength in dimensionless units
ϵ	detuning from resonance value
	$\tilde{k} \equiv \epsilon k$
	$\omega = \sqrt{\tilde{k}}$

1 Introduction

1.1 *The quantum kicked rotor*

The kicked rotor is a model system in the study of chaos. It is physically embodied by a “Gedankenexperiment” in which a rigid pendulum is subject to periodic, sharp pulses from gravity (referred to as momentum “kicks”) and evolves freely between those pulses. Its formal classical description is known as the *standard map* (Chirikov, 1979), and it is arguably the simplest Hamiltonian system in which to study the onset of chaotic dynamics (Lichtenberg and Leiberman, 1992).

Given its status as a paradigm system, it is natural that studies of the *quantum* dynamics of chaotic systems (vulgo *quantum chaos*) have focused heavily on the quantized standard map or, equivalently, the quantum kicked rotor (QKR). It became apparent in early numerical studies of the QKR that quantization of the system produced two particularly notable divergences from the classical dynamics of the standard map. Most well known is the appearance of *dynamical localization* (DL) in the generic quantum dynamics, that is, the freezing of diffusive energy growth after a characteristic quantum break time (Casati et al., 1979; Fishman, 1993; Izrailev, 1990). It was later demonstrated that the quantized standard map could be mapped onto a disordered tight-binding model in solid-state physics, demonstrating a link between the DL effect in the QKR and spatial Anderson localization in disordered solids (Fishman et al., 1982). Recently, this analogy between the QKR and solid-state systems was used to demonstrate a dynamical analog of the famous metal-insulator transition using cold atoms (Chabé et al., 2008; Lemarié et al., 2010).

Aside from the celebrated phenomenon of DL, the quantization of the standard map produces another notable qualitative difference between the classical and quantum dynamics. Quantization of the rotor momentum introduces a natural time scale to the system which is absent in the usual standard map. As the strength of the kicks is increased in the classical picture, chaos results and finally all invariant tori in phase space are completely destroyed by this strong perturbation of the pendulum dynamics. Among other things, this global chaos prevents the possibility of resonant driving by the kicks. However, in the quantum system, even in this chaotic limit, momentum quantization guarantees that the kick frequency remains an independent parameter along with the kick strength. This allows for resonant driving of discrete quantized states at certain kick periods, realizing the so-called *quantum resonances* (QRs) of the QKR (Izrailev, 1990; Izrailev and Shepelyansky, 1979, 1980; Guarneri, 2009; Dana and Dorofeev, 2006; Tian and Altland, 2010). In the present review, we will concern ourselves with the properties of the most prominent QRs (the

so-called principal QRs) and, more precisely, with the dynamics of ensembles of cold atoms in the close vicinity of those resonances.

For a system rich enough to encompass dynamics analogous to Anderson-localization (Anderson, 1958; Lee and Ramakrishnan, 1985), it is not surprising that analytical results predicting the behaviour of the QKR are few and far between. Kick-to-kick correlations remain analytically tractable only for small times (Shepelyansky, 1987; Daley and Parkins, 2002), and DL itself has only recently been rigorously demonstrated to exist for the QKR (Bourgain, 2002; Jitomirskaya, 2002). Whilst numerical simulations of the system are relatively easy to perform, they usually provide little insight. In this review, we will detail one of the few approaches to the QKR that simplifies understanding and generates true physical insight about the system, in this case in the vicinity of the principal QRs. The so-called ϵ -classical method that we study accomplishes this insight by taking advantage of the fundamental periodicities of the quantum system to produce a *pseudo-classical* model for the near-resonant dynamics. The first insight this allows is that due to the pseudo-classical phase space description, we can simply illustrate the dynamics of the system near to the QRs. The second insight, which stems from these phase space portraits, is the existence of closed form analytical *scaling functions*. The derivation of these scaling functions marks one of the few analytical and, at the same time, experimentally useful results available for the QKR. Furthermore, the simplest of these scaling functions (in the absence of noise and external perturbations) is given as a function of a single parameter which combines time, detuning from resonance and strength of the kicks, providing a unified understanding of the effect of parameter changes on the quantum dynamics.

Since the original derivation of the ϵ -classical standard map (Fishman et al., 2002; Wimberger et al., 2004), it has been adapted to provide analytical theories for the QKR with decoherence (Wimberger et al., 2003), amplitude fluctuations (Sadgrove et al., 2008), for highly non-classical initial states (Sadgrove and Wimberger, 2009) (as in the directed diffusion experiments discussed in section 3.4), and also for the stability of wavepackets with respect to deterministic variations of the kick strength (via fidelity) (Abb et al., 2009). In each case, as we will discuss, understanding comes from first examining the ϵ -classical phase space and its changes when varying parameters, and then adapting the theory to take account of those changes.

1.2 The atom-optics realization of the quantum kicked rotor

Aside from the addition of elegant analytical results to the canon of quantum chaos, the principle interest of the pseudo-classical method which we review here is that it was developed in response to and alongside experiments. Indeed,

the initial development of the theory in refs. (Fishman et al., 2002; Wimberger et al., 2004, 2003) was in response to experimentally observed phenomena (Oberthaler et al., 1999; d’Arcy et al., 2001). It is therefore necessary to give a brief account of the experimental setup in which observations of the kicked rotor typically take place (Raizen, 1999).

The QKR was first realized experimentally using cold noninteracting sodium atoms exposed to a pulsed optical standing wave (with spatial period π/k_L , k_L being the wavevector of the laser creating the potential), far detuned from the nearest atomic transition (Moore et al., 1995; Latka and West, 1995). Before this publication, DL had been studied in the context of driven Rydberg atoms (Casati et al., 1988; Krug et al., 2003; Galvez et al., 1988; Bayfield et al., 1989; Arndt et al., 1991) and atoms in a modulated standing wave potential (Moore et al., 1994). However, in (Moore et al., 1995), the realization of effective δ -like pulses (i.e. pulses much shorter than the pulsing period T) created a very good experimental realization of the standard map. This realization became known as the *atom optics kicked rotor* (AOKR). Although the atom-optics setting swaps angular for linear momentum, it still makes the unique aspects of the QKR more clear. The atomic system may be represented by the following scaled Hamiltonian (Graham et al., 1992)

$$H(t') = \frac{p^2}{2} + k \cos(z) \sum_{j=0}^{t-1} \delta(t' - j\tau), \quad (1)$$

where p is the atomic momentum in units of $2\hbar k_L$, z is the atomic position scaled by $2k_L = 4\pi/\lambda$, t' is time. t is an integer which counts the total number of kicks, and in units of the kicking period τ it represents the total time. The scaled kicking period τ is defined by $\tau = 8\omega_{\text{rec}}T$, where $\omega_{\text{rec}} = E_{\text{rec}}/\hbar = \hbar k_L^2/2M$ is the angular recoil frequency for atoms of mass M and E_{rec} the recoil energy. The kicking strength k is proportional to the optical standing wave intensity. An important time scale when studying QRs is defined by the Talbot time $T_T = \pi\hbar/(2E_{\text{rec}})$, since QRs can be seen to arise from nothing other than the Talbot effect (Talbot, 1836; Dubetsky and Berman, 1997; Deng et al., 1999; Lepers et al., 2008) (albeit in the time domain) for atomic matterwaves diffracted from the “grating” induced by the flashed periodic potential. We will motivate this analogy further in Section 2.1. The state evolution of an atom from one kick to immediately after the next kick is determined by the unitary one-cycle Floquet operator (Wimberger et al., 2003):

$$\hat{\mathcal{U}}_{\beta,k} = e^{-ik \cos(\hat{\theta})} e^{-i\frac{\tau}{2}(\hat{\mathcal{N}}+\beta)^2}, \quad (2)$$

where $\theta \equiv z \bmod 2\pi$. The Floquet operator of Eq. (2) differs from the Floquet operator of the original model of the QKR by the phase β , which represents the rescaled quasi-momentum of the atom moving along a line in contrast

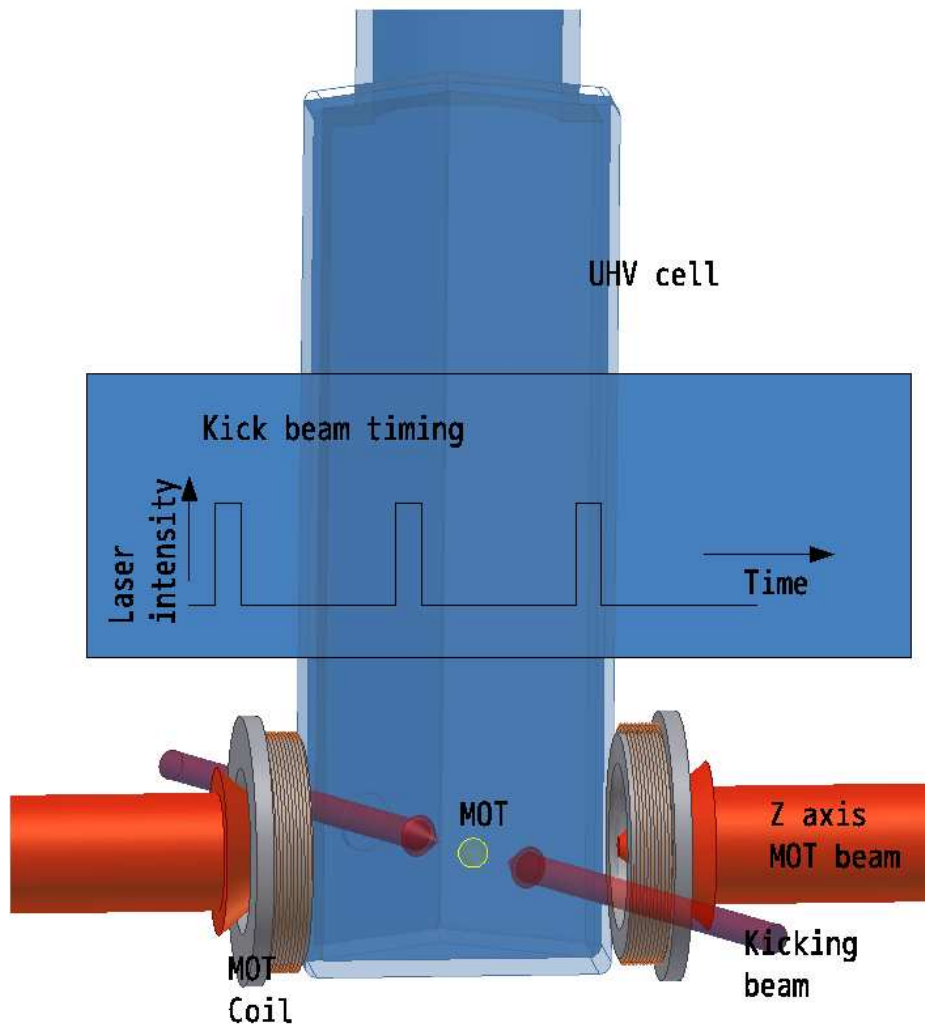


Fig. 1. Diagram of the most basic experimental configuration of the atom-optics kicked rotor. Thin arrows represent counter-propagating, co-polarized laser beams which intersect with a sample of cold atoms which are released from a magneto-optical trap (MOT). (Note that only two of the six MOT beams are shown in this diagram). The laser beams are periodically gated to create a pulsed potential with a form controlled precisely by the experimenter.

to a rotor which would move on a circle. By translational invariance of the potential, quasi-momentum is conserved for all times and, therefore, it acts just as a continuous index defined by the fractional part of the real momentum p (Wimberger et al., 2003). \hat{N} then corresponds to the integer part of p and can be interpreted as an angular momentum operator in the θ -representation, $\hat{N} = -id/d\theta$, with periodic boundary conditions.

As shown schematically in Fig. 1, all AOKR experiments using cold atoms follow roughly the same common sequence, first realized in (Moore et al., 1995): (1) A sample of atoms is laser cooled in a magneto-optical trap (MOT), (2)

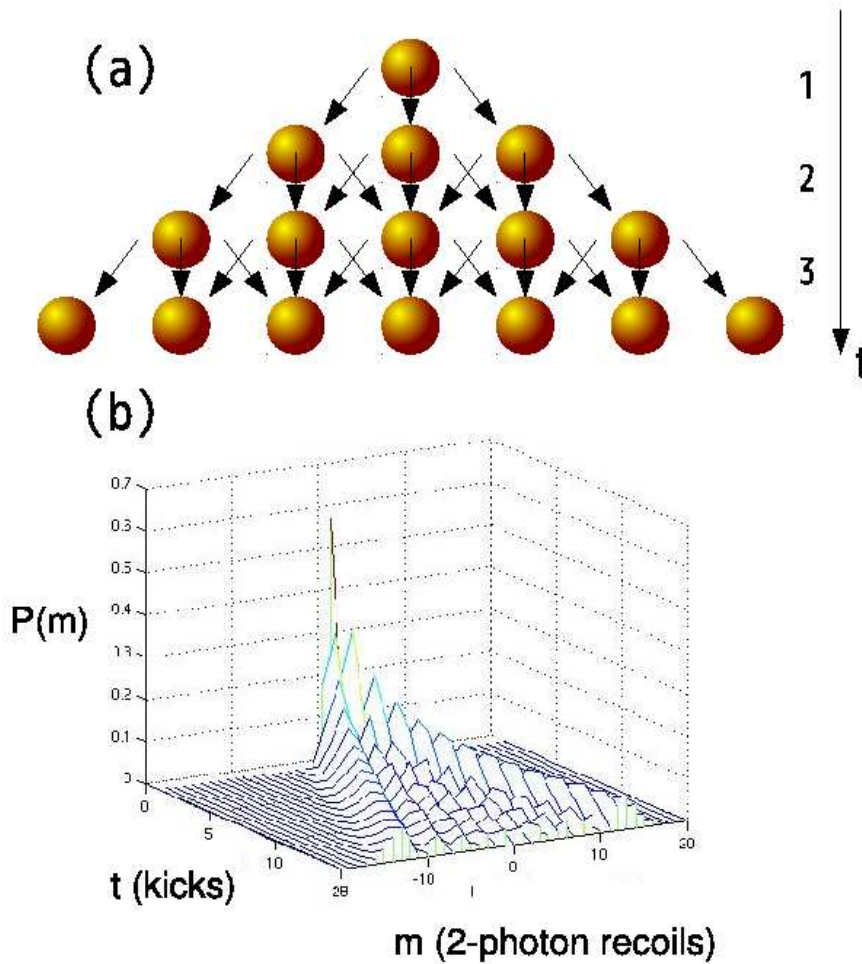


Fig. 2. (a) Schematic depiction of the atom diffraction over a few kicks from the intersected optical standing wave, following just first order diffraction into momentum eigenstates separated by $2\hbar k$ (from an initial zero momentum eigenstate). Each ball represents a momentum eigenstate with value m in units of $2\hbar k$. The importance of interference effects (whenever two lines intersect in the diagram) becomes clear, and the difficulty of making analytical predictions in the general case is thus apparent. (b) shows the predicted momentum distribution over 15 successive kicks for an atom starting from an initial zero momentum state and kicked at QR.

the cooled atomic sample is released from the trap (all optical and magnetic fields are turned off), (3) the released atoms are subject to a number of periodic pulses (“kicks”) from an optical standing wave which intersects with the sample and (4) the kicked atoms are allowed to expand for some milli-seconds before being exposed to near resonant light and having the consequent fluorescence distribution imaged on a charge coupled device (CCD) camera. This recipe gives access to the atoms’ momentum distribution after t kicks, as shown in Fig. 2. The mean energy of the atomic ensemble may be inferred by calculating the second moment of the momentum distribution. Since the first realization of the AOKR in (Moore et al., 1995), however, a number of variations on steps (1-3) in the experiment have been implemented including the use of a diluted Bose-Einstein condensate (BEC) as the initial state (Duffy et al., 2004b; Ryu et al., 2006; Currivan et al., 2009), kicking of trapped samples (Duffy et al., 2004a) and non-periodic kicking fields (Monteiro et al., 2002; Jones et al., 2007), amongst other innovations as we will discuss now briefly.

One of the earliest variations on the AOKR experiment was the addition of noise in various forms in order to observe decoherence effects. In (Ammann et al., 1998), a controllable, non-zero spontaneous emission rate was introduced leading to the destruction of DL. Experiments with a randomly fluctuating standing wave amplitude (Klappauf et al., 1998; Milner et al., 2000) or temporal period between kicks (Oskay et al., 2003; Sadgrove et al., 2004) demonstrated similar decoherence effects, seen in the changing lineshape of atomic momentum distributions. However, when the effects of spontaneous emission were tested at QR in (d’Arcy et al., 2001), it was found that rather than destroying the quantum energy resonances, the addition of spontaneous emission *enhanced* their visibility. This unusual result, similar to behaviour noticed in other investigations (Daley et al., 2002), was explained in (d’Arcy et al., 2004), and also in (Wimberger et al., 2003) using ϵ -classical theory as we will explain in detail in Section 3.3.1. The unusual response of the QR peaks to noise was confirmed in (Sadgrove et al., 2004), where the robustness of the QR peak structure in the presence of amplitude fluctuations was demonstrated and explained in terms of ϵ -classical stability of the near-resonant dynamics. More recently, the stability of the resonance behaviour has been quantified more rigorously in experiments where *fidelity* of quantum states was measured directly (Tonyushkin et al., 2009; Wu et al., 2009).

Another fruitful variation on the kicked rotor is the kicked *accelerator*, where the standing wave is oriented in the vertical direction. This allows so-called accelerator modes to emerge – narrow momentum classes of atoms which gain energy in a resonant fashion from the pulsed standing wave (Oberthaler et al., 1999). These accelerator modes and their stability (Schlunk et al., 2003a) inspired the first ϵ -classical treatment of kicked atoms in (Fishman et al., 2002), and investigations of this rich system have also extended to higher

order accelerator modes (Guarneri and Rebuzzini, 2008; Ramareddy et al., 2010), accelerator mode decay (Sheinman et al., 2006), and to study so-called Arnol'd Tongues (Guarneri et al., 2006). At this point, however, we note that the present review is concerned only with the “horizontal kicking” system as used in the original kicked rotor experiments (Moore et al., 1995). The behaviour found when the kicks are administered in the vertical direction and acceleration due to gravity is non-negligible is an interesting topic worthy of review in its own right.

Perhaps the single greatest experimental advance in the investigation of kicked atoms involved the use of atoms sourced from a degenerate quantum gas rather than a thermal MOT source. The first such experiments using a dilute BEC (for which atom-atom interactions can be neglected (Wimberger et al., 2005a)) subject to standing wave pulses were performed at NIST in Gaithersburg in a strictly atom-optics setting (Deng et al., 1999). Both atom diffraction into discrete orders and the time-domain Talbot effect were demonstrated in these early studies. Other investigations probed QR and the opposite regime of anti-resonance (at which the system oscillates between states instead of absorbing energy (Izrailev, 1990)) more carefully using a BEC (Duffy et al., 2004b) and also investigated the kicking of a BEC in situ with the magnetic trap still on (Duffy et al., 2004a). BEC studies of the AOKR, along with nondegenerate ultra-cold samples (Kanem et al., 2007), also finally allowed such central predictions about QR as ballistic energy growth and some fractional resonances to be successfully demonstrated in the laboratory (Ryu et al., 2006).

In Fig. 3, manifestations of QR behaviour are shown in two different atom optics settings. Fig. 3(a) and (b) show raw absorption images of a dilute BEC subject to anti-resonant (half-Talbot time) and resonant (Talbot-time) kicking respectively. When the time between pulses equals half of the Talbot time, we see oscillations in the atomic energy from one kick to the next (seen here as alternate expansion and contraction of the atomic momentum distribution), whilst when the period matches the Talbot time, ballistic growth is seen and the momentum distribution expands with each kick. Fig. 3(c) shows mean energies for a kicked atomic ensemble for which the initial momentum distribution is much larger than $2\hbar k$. In this case, individual momentum orders are not resolvable and the effect of resonant kicking on the atomic momentum distribution is more subtle. However, a strong signature of QR is still seen in the mean energies at integer or half integer multiples of the Talbot time. It is interesting to note that these energy peaks are indistinguishable between the anti-resonant and resonant cases, due to the fact that the broad quasi-momentum distribution allows resonant transport in both cases. In both of the experimental situations shown in Fig. 3, ultra-cold atoms were kicked by standing-wave pulses which satisfied the *Raman-Nath* condition (Nath, 1936), which, physically speaking, requires that the pulse time is short compared to the time it takes for atoms to traverse a single period of the standing wave.

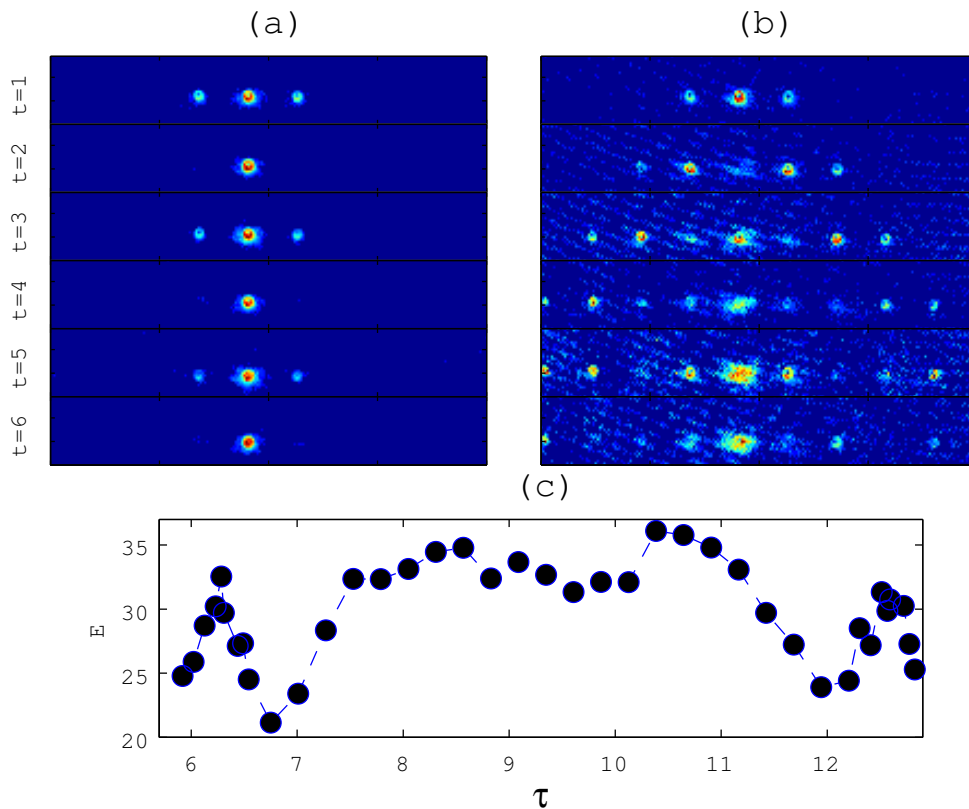


Fig. 3. Manifestations of QR phenomena in cold atom experiments. (a) ($\tau \approx 2\pi$) and (b) ($\tau \approx 4\pi$) show absorption images for a kicked Bose-Einstein condensate demonstrating the clearly distinguishable cases of anti-resonance and resonance respectively. This behaviour is seen for an atomic ensemble with an initial momentum width $\sigma \ll 2\hbar k_L$. The absorption images reproduce the atomic momentum distribution after t kicks, schematically introduced in Fig. 2(a). At anti-resonance, atoms oscillate between 0 and non-zero energy from kick to kick. At resonance, the atoms gain energy quadratically as the kick number increases. (c) shows the case for atoms where $\sigma \gg 2\hbar k_L$. In this case, we see peaks in the mean energy (on the y-axis) near the resonance *and* anti-resonance values at $\tau = 4\pi$ and 2π respectively in (c).

Outside the Raman-Nath regime, momentum transfer to atoms is curtailed (Bharucha et al., 1999; Vant et al., 1999; Blümel et al., 1986), the extreme case being an optical lattice in which the standing wave is always on and the atoms do not absorb energy as from a flashed lattice. We also note in passing that the half-Talbot time effect was recently used to demonstrate fidelity decay in cold atoms perturbed by standing wave kicks (Wu et al., 2009). We will have more to say on the topic of fidelity later in this review (see Section 3.5).

Still further intriguing variations on the basic AOKR experiment are possible when deviations from strict periodicity of the kicking are introduced. Double kicks were first used to probe the dynamics of atoms in the presence of classical phase space structures (Vant et al., 1999), but the introduction of multiple kicking frequencies yielded more surprising results in (Lemarié et al., 2010). In these experiments, resonances were found depending on the ratio between two kicking frequencies. These resonances were further shown to possess a *sub-Fourier* nature, suggesting possible applications to signal processing. The QRs were later shown to possess a similar sub-Fourier narrowing of the mean energy with time, as will be discussed below in Section 3.1. Interestingly, an analysis of the fidelity overlap of two states kicked with slightly different periods shows such a sub-Fourier scaling, which is yet another manifestation of the stability of QR motion useful for applications (see the recent papers (McDowall et al., 2009; Talukdar et al., 2010)).

Finally, at the intersection between non-periodic driving and studies performed with a BEC, investigations of directed transport have recently taken place. The goal to create a Hamiltonian ratchet (Flach et al., 2000; Schanz et al., 2001; Hänggi and Marchesoni, 2009) using a variant of the kicked rotor system was first investigated using thermal atoms (Monteiro et al., 2002; Jones et al., 2007) but a more surprising variation on ratchet motion was found using a BEC prepared in an initial superposition of momentum eigenstates and subjected to kicking at QR (Sadgrove et al., 2007; Dana et al., 2008; Lundh and Wallin, 2005; Gong and Brumer, 2006). It is also interesting to note that in the first true “ratchet” for cold atoms, achieved using an approximate saw-tooth potential combined with modulation of the standing wave, a significant current was only observed when the modulation frequency was close to QR (Salger et al., 2009).

Historically, the motivation to study the QKR experimentally was to observe DL, thus demonstrating the restriction on chaotic motion expected in quantum systems arising from a stabilizing interference effect. However, as the AOKR was extended to different initial conditions and driving fields, the QRs have become more compelling phenomena of study, due to the possible applications to precision measurements, atomic transport and stable quantum behaviour that they represent (Madroñero et al., 2006). Thus, we believe it is timely

to review the tools provided by the pseudo-classical description of the quasi-resonant regime embodied by the ϵ -classical theory of QR. For reasons of compactness, we restrict our overview to the principal QRs of the QKR and mainly, but not exclusively, discuss our own research work on the topic.

2 The pseudo-classical method for nearly resonant quantum motion

This Section introduces the theoretical concepts of the pseudo-classical method which has proven very useful for the description of experiments and applications such as those detailed in the following Section 3. We start out with a short review of the dynamical regimes of the QKR, in particular, the QR regime at which the rotor maximally absorbs energy from the kicking field, essentially because of a revival of its wave function in momentum space in-between two kicks. The reported pseudo-classical method (see Section 2.3) allows us to characterize the QKR and its experimental realization by kicked cold or ultra-cold noninteracting atoms (see Section 1) in the vicinity of these QRs.

2.1 Dynamical localization and quantum resonances

As mentioned in the introduction, the QKR – at first glance a system seemingly too simple to be of practical use – became famous because it reproduces in a clear way the predictions made by P.W. Anderson on the transport of single-particles wave packets across disordered samples (Anderson, 1958; Lee and Ramakrishnan, 1985). While the original idea of Anderson – recently verified in an ingenious experiment by Billy et al. (2008) – describes transport in real space, the QKR realizes the same situation in momentum space (Fishman et al., 1982; Fishman, 1993). Kicking the system with periods such that $\tau/4\pi$ is sufficiently far from a rational number leads to what is known as “dynamical localization” (DL) of a spreading wave packet, stressing its dynamical origin¹. DL, as a purely quantum effect, suppresses the classically expected diffusion in systems such as the QKR which have a classically chaotic counterpart. It is a ubiquitous effect which also occurs in other periodically driven quantum chaotic systems, such as microwave driven hydrogen or alkali Rydberg states of electronic wave packets (Casati et al., 1988; Wimberger and Buchleitner,

¹ The notion dynamic or dynamical localization is unfortunately also used in different contexts, one example being the suppression of tunneling by a periodic driving force (Dunlap and Kenkre, 1986), for experimental realizations of this effect see, e.g. (Lignier et al., 2007; Kierig et al., 2008).

2001) (for which DL was indeed observed for the very first time in the laboratory (Galvez et al., 1988; Bayfield et al., 1989; Arndt et al., 1991)). While for driven Rydberg states the effect of localization manifests itself only indirectly in the measurable ionization yield, the experimental realization of the QKR allowed the observation of localized momentum space wave functions in situ along with the extraction of the average energy of the kicked atoms (Moore et al., 1995; Bharucha et al., 1999) (i.e. the second moment of the wave packet in momentum space) long before its real space analogue could be directly observed (Billy et al., 2008). Since we aim at describing motion close to QR for the QKR, here we provide only an intuitive description of DL: for $\tau/4\pi$ irrational, the phases of the free part of the QKR evolution in momentum representation, i.e. from $\exp(-i\tau n^2/2)$ (see Eq. (2) for $\beta = 0$), in-between two kicks are essentially randomly distributed between the different momentum classes. Even if deterministically defined, these phases have a pseudo-random character, which is discussed, e.g., in (Brenner and Fishman, 1992). This pseudo-randomness substitutes the spatial disorder in the real-space Anderson problem, and it essentially leads to a destructive interference in the temporal evolution of the QKR hindering the spread of the wave packet in momentum space (after some transient time which is known as the “break time” (Shepelyansky, 1987)).

The above mentioned phases $\exp(-i\tau n^2/2)$ allow us to understand the origin of quantum resonant motion as well. QRs occur for rational values of $\tau/4\pi$ leading to a complete (i.e. for all momenta n) or partial (i.e. for a subset of momenta) phase revivals in-between two successive kicks. Those revivals are analogous to the Talbot effect or the fractional Talbot effect, respectively, of interfering light or matter waves diffracted and recombined at a series of gratings, see, e.g., (Talbot, 1836; Dubetsky and Berman, 1997) for a discussion of this constructive interference effect. In the following we concentrate on the *principal QRs of the QKR* at which a complete revival happens, i.e., $\exp(-i\tau n^2/2) \equiv 1$ for all $n \in \mathbb{Z}$, or for real atoms moving along a line, $\exp(-i\tau(n + \beta)^2/2) \equiv 1$, which occurs at $\tau = 2\pi\ell$ (ℓ a positive integer) and $\beta = 1/2 + j/\ell \pmod{1}$, $j = 0, \ell, \dots, \ell - 1$ (Wimberger et al., 2003).

2.2 Exact results at quantum resonance

The existence of QRs in the QKR was noticed by Izrailev and Shepelyansky (Izrailev and Shepelyansky, 1979, 1980) shortly after the discovery of DL. They obtained the exact quasi-momentum spectrum for some major resonances. This spectrum must be continuous in order to support unlimited ballistic growth with the number of kicks t for the mean energy of the QKR, i.e. $E(t) = E(t = 0) + \alpha t + \gamma t^2$, for appropriate values of the α and γ constants (Izrailev, 1990; Guarneri, 2009). For the principal QR at $\tau = 4\pi$ and $\beta = 0$,

one can immediately see from Eq. (2) that the spectrum is given by $e(\theta) = k \cos(\theta)$ for $\theta \in [0, 2\pi)$. Hence it is a continuous function of the θ angle variable of the rotor. Nevertheless exact results at QR have been rare until recently (Izrailev, 1990; Guarneri, 2009; Tian and Altland, 2010), not least because the resonances were regarded as a rather peculiar property of the QKR. Inspired by experiments by d’Arcy et al. (2001), new theoretical as well as experimental progress has been made over the last decade. As a background for the pseudo-classical theory introduced in the next Subsection, we review briefly some aspects of this theoretical progress at exact QR for δ -kicked noninteracting atoms having a flat uniform distribution $f(\beta)$ of quasimomenta $\beta \in [0, 1)$. As derived in detail in (Wimberger et al., 2003), the average energy of such an atomic ensemble at $\tau = 2\pi\ell$ ($\ell \in \mathbb{N}$) increases linearly with the number of kicks t

$$\langle E(n_0, \beta, t) \rangle_{n_0, \beta} \sim \langle E(\beta, t = 0) \rangle_{n_0, \beta} + \frac{k^2 t}{4}, \quad (3)$$

where n_0 are the integer parts of the atomic momenta at time $t = 0$. For the momentum distribution of the kicked ensemble we have the asymptotic result valid at large $t \rightarrow \infty$ and for $n \gg n_0$

$$P(n) \sim \frac{4k}{\pi^3 n^2}. \quad (4)$$

In essence, the contribution of many nonresonant rotors or nonresonant values of β and very few resonant ones (see end of previous Subsection) averages to a linear increase of the mean energy. This continued increase of the energy means that higher and higher momentum classes become populated with increasing time. This builds up the algebraic distribution of momenta (which, at finite t , shows a time-dependent cutoff momentum $n_{\text{cut}} \approx \pi kt/2$ up to which Eq. (4) faithfully describes the actual distribution (Wimberger et al., 2003)).

The experimental possibilities to add noise to the system (d’Arcy et al., 2001; Ammann et al., 1998; Klappauf et al., 1998; Milner et al., 2000; Oskay et al., 2003; Sadgrove et al., 2004; d’Arcy et al., 2004) inspired a number of theoretical treatments yielding exact results, which typically are rare for noisy dynamical systems. Here we quickly review two interesting cases of noise which will be extended later on in Sections 3.3.2 and 3.3.1 for values of τ not exactly but close to QR condition. The first of these results at exact QR describes the effect of amplitude noise in the kick pulse on the dynamical evolution of the atoms (Sadgrove et al., 2008; Brouard and Plata, 2003). It predicts a linear increase of the average energy of an atomic ensemble under the same assumptions as made

above (now averaged over the ensemble and over many noise realizations):

$$\langle E(n_0, \beta, t) \rangle_{n_0, \beta, \delta k} \sim \langle E(\beta, t = 0) \rangle_{n_0, \beta} + \frac{k^2 t}{4} \left(1 + \frac{L^2}{12} \right), \quad (5)$$

where the actual kick strength is $k + \delta k$, with δk uniformly distributed in $[-L/2, L/2]$. The second term on the right side of the equation is now corrected with respect to Eq. (3) by the standard deviation of the noise $L^2/12$. Since the conditions for QRs do not depend on the kick strength but just on τ and β , this case of amplitude noise is still fairly simple to analyze.

More work is needed to extend the above Eqs. (3) and (4) to a perturbation arising from spontaneous emission acting on the kicked atoms. For the specific realization of such an experiment at Oxford by d’Arcy et al. (2001, 2004), spontaneous emission was induced in a very controlled way by an additional light field independently of the kicking laser. It was then shown in Wimberger et al. (2003) that this kind of spontaneous emission acts as additional kicks (with random distributions of kick strengths) on the atoms, which occur in-between successive δ -kicks of the original model. The result is that the average energy of an ensemble (averaged over many realizations of the random spontaneous emission events) again increases linearly in time. The momentum distribution approaches a Gaussian form with zero mean and a standard deviation $k^2 t/2 + Dt$ (as long as the initial – at $t = 0$ – momentum distribution of the atoms is symmetric around zero), where D is now the diffusion constant given by the mean square momentum change per period τ due to spontaneous emission. These results are based on exact proofs to be found in Wimberger et al. (2003), but one may intuitively understand them as describing a diffusive process in momentum space driven by the random kicks from spontaneous emission.

2.3 Pseudo-classical theory for principal quantum resonances

This Subsection presents the essentials of the pseudo-classical theory which has proven very powerful for describing the QKR and its experimental realizations in the vicinity of the QRs. This method allows us to extend our theoretical understanding to a regime for which direct quantum calculations would be extremely difficult in general. The pseudo-classical approach is inspired by a rescaling usually done for the standard semi-classical limit of the QKR. The latter is obtained by *simultaneously* letting the kick period $\tau \rightarrow 0$ and the kick strength $k \rightarrow \infty$ but keeping their product $K_s \equiv \tau k$ fixed. Fixing the “stochasticity parameter” K_s fixes also the classical phase space structure

described by the standard map, the classical correspondence of the QKR:

$$I_{t+1} = I_t + K_s \sin(\theta_{t+1}), \quad \theta_{t+1} = \theta_t + I_t \pmod{2\pi}. \quad (6)$$

Here the momentum I is rescaled with respect to the physical momentum p $I = \tau p$, just as the kick strength above. In the standard semi-classical limit, the quantum version of the rotor now has less and less time for free phase evolutions while the kicks dominate more and more over these phases, c.f. the Floquet operator in Eq. (2). Nevertheless, the classical phase space is not at all affected since K_s is kept constant, and it can either describe regular (for sufficiently small $K_s \ll 1$), chaotic (for $K_s \gtrsim 5$), or mixed regular-chaotic motion (for intermediate values of K_s).

The same idea of rescaling variables can now be applied for kick periods which are not at all small, i.e. far away from the standard classical limit, but for $\tau = 2\pi\ell + \epsilon$ ($\ell \in \mathbb{N}$ and ϵ small) in the vicinity of the QR condition on τ . The crucial difference to the scaling for the standard semi-classical limit is that the scaling factor is not directly τ but $\epsilon = \tau - 2\pi\ell$, the detuning from the exact resonant value (Hogg and Huberman, 1983). As we will see below, this gives a pseudo-classical map which is always integrable in the limit $\epsilon \rightarrow 0$, even if the system has a completely chaotic classical analogue in the unscaled coordinates p and θ . Rescaling $I \equiv |\epsilon|N$ (for $p = N + \beta$) and $\tilde{k} \equiv |\epsilon|k$, we can rewrite the Floquet operator of the quantum map, c.f. Eq. (2), in the following way:

$$\hat{\mathcal{U}}_{\beta,k}(t) = e^{-\frac{i}{|\epsilon|}\tilde{k}\cos(\hat{\theta})} e^{-\frac{i}{|\epsilon|}\hat{\mathcal{H}}_{\beta}}, \quad (7)$$

with

$$\hat{\mathcal{H}}_{\beta}(\hat{I}, t) = \frac{1}{2}\text{sign}(\epsilon)\hat{I}^2 + \hat{I}(\pi\ell + \tau\beta). \quad (8)$$

To arrive at Eq. (7) we have just rewritten the free evolution part of the Floquet operator for the β -rotor given in Eq. (2) as follows:

$$e^{-i\frac{\tau}{2}(n+\beta)^2} = e^{-i\pi\ell n^2} e^{-i\frac{\epsilon}{2}n^2} e^{-i\tau n\beta} e^{-i\frac{\tau}{2}\beta^2} = e^{-i\pi\ell\frac{I}{|\epsilon|}} e^{-i\text{sign}(\epsilon)\frac{I^2}{2|\epsilon|}} e^{-i\tau\beta\frac{I}{|\epsilon|}} e^{-i\frac{\tau}{2}\beta^2}, \quad (9)$$

where the last factor does not depend on I and may be omitted.

If $|\epsilon|$ is now regarded as the Planck constant, then Eq. (7) formally defines just the quantized version of either of the following classical maps:

$$I_{t+1} = I_t + \tilde{k} \sin(\theta_{t+1}), \quad \theta_{t+1} = \theta_t \pm I_t + \pi\ell + \tau\beta \pmod{2\pi}, \quad (10)$$

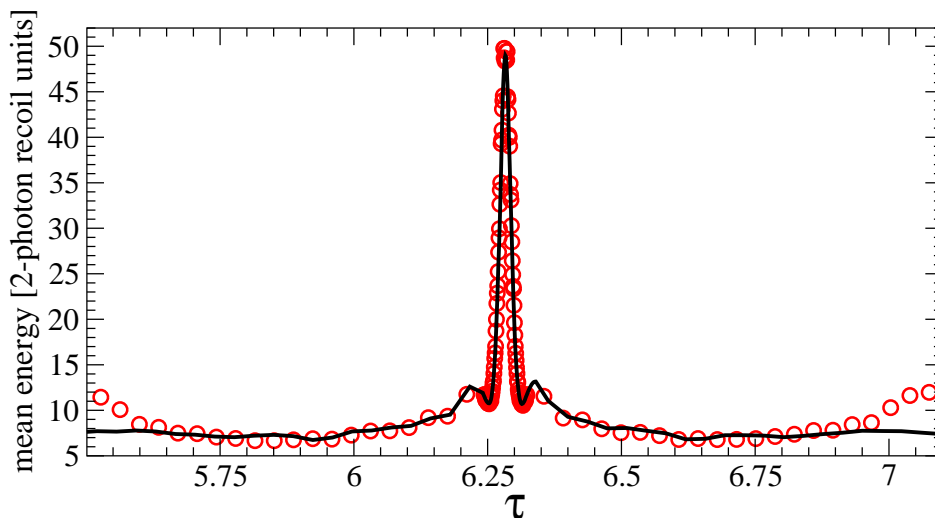


Fig. 4. Atomic mean energy vs. τ , after $t = 30$ kicks, for $k = 0.8\pi$ near the QR at $\tau = 2\pi$. Quantum data (solid lines) are compared with ϵ -classical results (circles) for the same initial momentum distribution.

where \pm has to be chosen according to the sign of ϵ . We stress that “classical” here is not related to the $\tau \rightarrow 0$ limit but to the limit $\epsilon \rightarrow 0$ instead. The small- $|\epsilon|$ asymptotics of the quantum β -rotor is thus equivalent to a quasi-classical approximation based on the “classical” dynamics given by Eq. (10), that has been dubbed ϵ -classical in (Fishman et al., 2002; Wimberger et al., 2003). Changing variables to $J = \pm I + \pi\ell + \tau\beta$, $\vartheta = \theta + \pi(1 - \text{sign}(\epsilon))/2$ turns the maps in Eq. (10) into a single standard map (c.f. Eq. (6)), known as the ϵ -classical standard map (ϵ SM), independent of the value of β :

$$J_{t+1} = J_t + \tilde{k} \sin(\vartheta_{t+1}), \quad \vartheta_{t+1} = \vartheta_t + J_t. \quad (11)$$

As we have already noted above, the semi-classical limit of the ϵ SM is quite different from the one for the usual standard map of Eq. (6). Eq. (11) *always* describes a completely integrable system for $\epsilon \rightarrow 0$, since the effective kick strength $\tilde{k} \propto \epsilon$ also tends to zero in this limit.

To get a feeling for how powerful the method just introduced actually is, we compare in Fig. 4 the average energies of an ensemble of rotors as a function of τ in a neighbourhood of the QR at $\tau = 2\pi$. All data are obtained from numerical simulations of the quantum map, Eq. (2), and the ϵ -classical map, Eq. (10), respectively, for the same initial ensemble of momenta and quasimomenta. For any given particle in the initial ensemble, the map in Eq. (10), with β equal to the quasi-momentum of the particle, was used to compute a set of trajectories started at $I = n_0|\epsilon|$ with uniformly distributed $\theta_0 \in [0, 2\pi)$. The final energies $\epsilon^{-2}I_t^2/2$ at $t = 30$ of the individual trajectories were averaged over θ_0, β, n_0 with the appropriate weights. This is equivalent to using the ϵ SM in all cases, with different initial ensembles $J_0 = \text{const} = \pm n_0|\epsilon| + \pi\ell + \tau\beta$.

The main qualitative features emerging of Fig. 4 are: (i) on a larger scale along the τ axis, the curves are shaped in the form of a basin with a high, narrow spike in the centre, closely flanked by a much smaller peak on either side. (ii) quantum and ϵ -classical curves agree very well at small $|\epsilon|$, in particular the structure of the spike is the same. Their behaviour at large $|\epsilon|$, i.e. for $\tau \gtrsim 6.6$ and $\tau \lesssim 6$ is qualitatively similar but quantitatively different. This overall behaviour may be explained in ϵ -classical terms, and an approximate scaling law for the t, k, ϵ dependence of the average energy close to the QRs can be obtained, as shown in the Section 3.1. The ϵ -classical standard map is different from the map obtained in the classical limit proper $\tau \propto \hbar \rightarrow 0$. In particular, if $\tau k > 1$, then the classical and the ϵ -classical dynamics are at sharp variance whenever $\tilde{k} < 1$. In the former unbounded diffusion occurs, while in the latter the dynamics is quasi-integrable instead. In this quasi-integrable system, the ϵ -classical trajectories remain trapped forever in-between impenetrable phase space barriers, which survive small perturbations according to the Kolmogorov-Arnold-Moser (KAM) theorem (Lichtenberg and Lieberman, 1992). It is exactly the change occurring in the ϵ -classical phase space (see Fig. 5) as τ is varied at constant k that accounts for the energy vs. τ dependence at fixed time (Fig. 4).

In the following, we show that the introduced ϵ -classical technique allows us to fully recover the exact quantum result for the average energy reviewed above, see Eq. (3), at exact QR. We assume for simplicity an initially flat distribution of $p_0 \in [0, 1)$; then $I_0 = 0$, and $J_0 = \pi\ell + \tau\beta_0$ with β_0 uniformly distributed in $[0, 1)$ and $n_0 = 0$. Without loss of generality we only consider $\ell = 1$. Hence if $|\epsilon| \ll 1$ then J_0 is practically uniformly distributed over one period (in action) $(\pi, 3\pi)$ of the ϵ SM. Since $J_t = \pm I_t + \pi + \tau\beta$, and $I_0 = 0$, the mean energy of the rotor after a titak number of kicks t is:

$$\langle E_{t,\epsilon} \rangle = \epsilon^{-2} \langle I_t^2 \rangle / 2 = \frac{\langle (\delta J_t)^2 \rangle}{2\epsilon^2}, \quad \text{with } \delta J_t = J_t - J_0. \quad (12)$$

The exact QR at $\epsilon = 0$ corresponds to the integrable limit of the ϵ SM, where $\delta J_t = 0$. However, $\langle E_{t,\epsilon} \rangle$ is scaled by ϵ^{-2} , so in order to compute it at $\epsilon = 0$ one has to compute δJ_t at first order in ϵ . This is done by substituting the 0-th ϵ -order of the second part of Eq. (11), i.e. $\vartheta_t \simeq \vartheta_0$, into the first part of Eq. (11). This leads to

$$\delta J_t = |\epsilon|k \sum_{s=0}^{t-1} \sin(\theta_0 + J_0 s) + r(\epsilon, t), \quad (13)$$

where $r(\epsilon, t) = O(\epsilon)$ as $\epsilon \rightarrow 0$ at any fixed t . The energy at time t is found from Eq. (13) by taking squares, averaging over θ_0, J_0 , dividing by $2|\epsilon|^2$, and finally letting $\epsilon \rightarrow 0$:

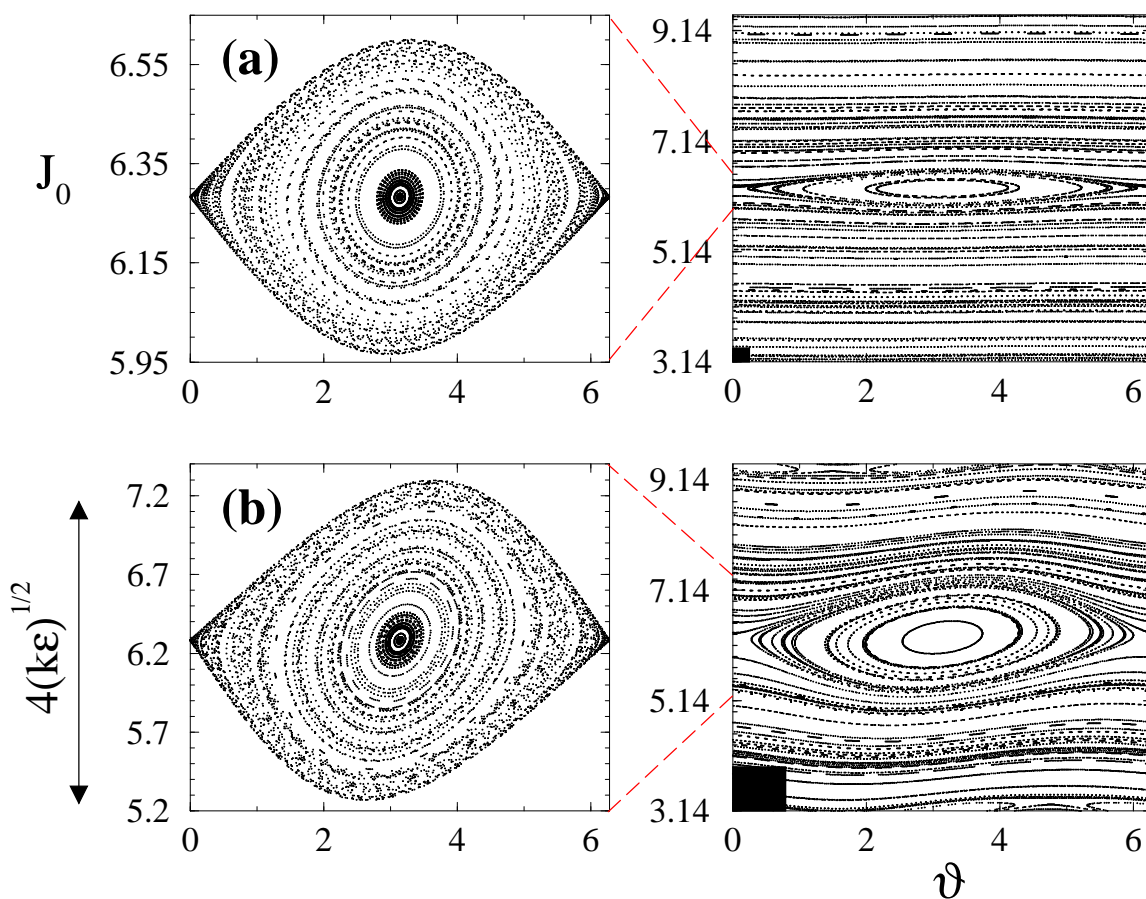


Fig. 5. Poincaré surfaces of section for the standard map of Eq. (11), and $k = 0.8\pi$, $\epsilon = 0.01$ (a), $\epsilon = 0.1$ (b). As ϵ increases, the invariant curves (right panels) become more and more distorted, with a primary resonance island (left panels) having a width of $\delta J_{\text{res}} \approx 4(\tilde{k})^{1/2}$. The black boxes in the right panels represent the Planck cell of area $2\pi|\epsilon|$.

$$\begin{aligned} \langle E_{t,\epsilon} \rangle &= \frac{1}{8\pi^2} \int_0^{2\pi} d\theta_0 \int_{\pi}^{3\pi} dJ_0 \frac{(\delta J_t)^2}{\epsilon^2} \xrightarrow{\epsilon \rightarrow 0} \\ \frac{k^2}{8\pi^2} \int_0^{2\pi} d\theta_0 \int_{\pi}^{3\pi} dJ_0 \left(\sum_{s=0}^{t-1} \sin(\theta_0 + J_0 s) \right)^2 &= \frac{k^2}{8\pi} \int_{\pi}^{3\pi} dJ_0 \frac{\sin^2(J_0 t/2)}{\sin^2(J_0/2)}. \end{aligned} \quad (14)$$

With the help of $\int_0^{2\pi} dx \sin^2(tx)/\sin^2(x) = 2\pi t$, this yields:

$$\langle E_{t,0} \rangle = \langle E(\beta, t=0) \rangle_{\beta} + \frac{k^2}{4} t, \quad (15)$$

where we have added in the first term on the right hand side the small contribution of the initial quasimomenta in energies which we had neglected so far. Eq. (15) reproduces the quantum behaviour at exact QR, given by Eq. (3) of Section 2.2.

The integral over J_0 in Eq. (14) collects contributions from all the invariant curves $J_0 = \text{const}$ of the ϵ SM at $\epsilon = 0$. Of these, the one at $J_0 = 2\pi$ leads to quadratic energy growth because it consists of (period 1) fixed points (Lichtenberg and Lieberman, 1992). This is called a classical nonlinear resonance and it can be seen clearly in Fig. 5. It is responsible for the linear growth of energy in Eq. (15), because the main contribution to the integral in Eq. (14) comes from a small interval $\sim 2\pi/t$ of actions around $J_0 = 2\pi$. Note that $J_0 = 2\pi$ corresponds to $\beta_0 = 1/2$, the resonant value of quasi-momentum at the QR at $\tau = 2\pi$. It is hence seen that the ϵ - or pseudo-classical approximation explains the *quantum* resonances of the QKR in terms of the principal *classical* resonance of a quasi-integrable standard map.

Before we come to actual applications of the pseudo-classical method, we briefly discuss its range of validity. The ϵ -quasi-classical approximation is exact at all times for $\epsilon = 0$, as shown above. At nonzero ϵ , it is valid when the number of kicks t is not too large, and in the long run it is spoiled by quantum, non ϵ -classical effects. At $|\epsilon| < |\epsilon|_{cr}$ the ϵ -classical motion is bounded by KAM curves, so the main quantum mechanism leading to non- ϵ -classical behaviour is tunnelling across the regular regions. Estimating the related time scales is not at all easy, because the 2π -periodicity in action of the ϵ -classical phase space may enhance tunnelling, and even result in delocalisation, depending on the degree of commensuration between 2π and the ‘‘Planck constant’’ $|\epsilon|$. For instance, if $|\epsilon|/2\pi$ is rational, then the quantum motion will be ballistic at some stage asymptotically in time (it would just realize a high-order QR). In order that such a resonance with $|\epsilon| = 4\pi s/q$ exists at $|\epsilon|$ less than some $|\epsilon_0|$, it is necessary that the order q of the QR obeys $q > 4\pi/|\epsilon_0|$. It will show up after a time roughly estimated by $|\epsilon|$ times the inverse bandwidth of the continuous quasienergy spectrum at this QR (Guarneri, 2009). The bandwidth is estimated to decrease faster than exponentially at large q (Izrailev, 1990;

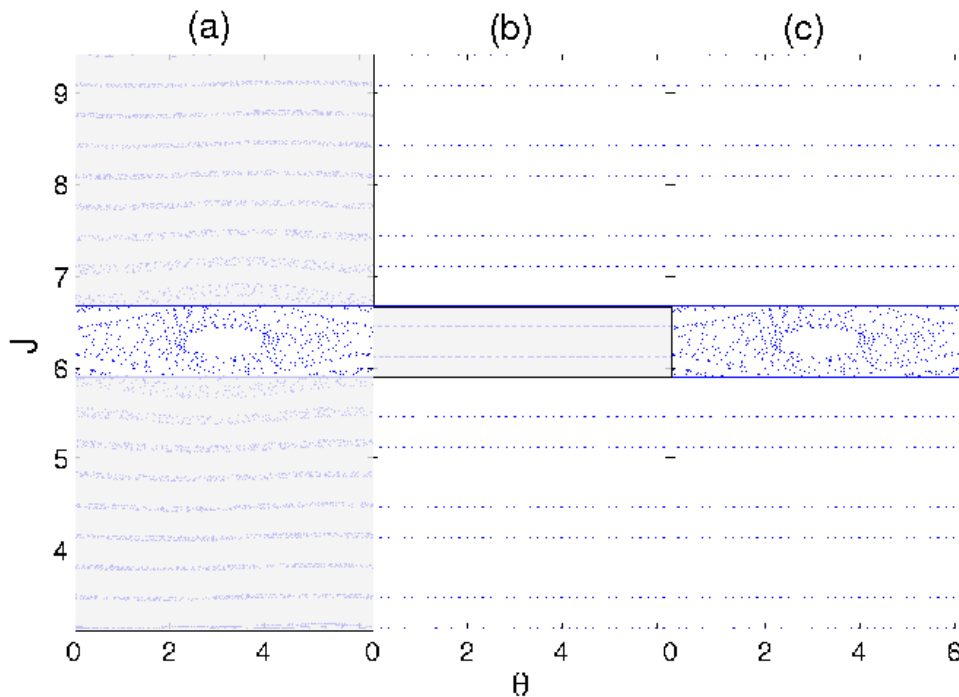


Fig. 6. A depiction of the construction of the ϵ -classical scaling function in phase space. In (a), the entire phase space is shown as generated by iterating the ϵ SM of Eq. (11). The regions outside the influence of the central nonlinear resonance are shaded grey. The dynamics in the unshaded region where the dynamical resonance is seen are well modelled by the function G introduced in Eq. 18 which calculates the mean energy due of the analogous pendulum trajectories. On the other hand, (b) shows the “flat” phase space when the rotor is perfectly on resonance and the mean energy is simply $(k^2/4)t$ as given by Eq. (15). The shaded region in (b) shows the area which will be affected by the nonlinear resonance for the parameters used in (a). The energy in this shaded region is represented by the Φ function introduced in Eq. 16. The figure (c) shows an approximation to the true phase space (a) found by taking (b), subtracting the shaded region and adding in the unshaded region (i.e. the resonance portion) of (a). This is the graphical equivalent of Eq. (16) which is used to derive the scaling function.

Guarneri, 2009), so one may infer that the time of validity of the ϵ -quasi-classical approximation is at least exponentially increasing with $1/|\epsilon|$ as the exact resonance at $\epsilon = 0$ is approached. At $|\epsilon| > |\epsilon|_{cr}$ the ϵ -classical motion is unbounded, and the difference between ϵ -classical and quantum energy curves vs. τ is basically set by various quantum localization effects, including localization by cantori close to the $|\epsilon|_{cr}$ (Grepel et al., 1984; Fishman et al., 1987). As a consequence, if t is large enough, then the ϵ -classical curve lies higher than the quantum one (see Fig. 4 at the very right and left).

3 Application of the pseudo-classical method

3.1 Scaling functions for mean energy of the AKOR

Having reviewed the fundamentals of the ϵ -classical method, we now turn to one of the most useful corollaries of the theory. By approximating the near-resonant quantum dynamics of the AOKR with a classical standard map of small kicking strength, the ϵ -classical model allows a *pendulum approximation* (Lichtenberg and Lieberman, 1992) to the dynamics to be made. It turns out that the near resonant quantum dynamics can be captured by a single parameter description, so long as appropriate scaling of the momentum or energy is made - a fact which has been confirmed experimentally (Wimberger et al., 2005b). We now derive this so-called *scaling law* with emphasis on a heuristic explanation which arises from inspection of the ϵ -classical phase space (see Fig. 6).

We start by considering the difference in the phase space for on-resonant and off-resonant kicked rotors. Fig. 6(b) shows the on - resonant ($\epsilon = 0$) phase space - a continuum of flat “orbits” which give rise to the maximum energy at quantum resonance. In contrast, away from resonance ($|\epsilon| > 0$) a nonlinear resonance island disturbs the phase space as shown in Fig. 6(a). Inspecting the change in the phase space structure as $|\epsilon|$ is increased suggests the following relation between the off-resonant energy $E_{\epsilon,t}$ and the on-resonant energy $\langle E_{\epsilon=0,t} \rangle = k^2t/4$:

$$\langle E_{\epsilon,t} \rangle \approx \frac{k^2t}{4} - \Phi(t) + \langle E_t \rangle_{\text{res}}, \quad (16)$$

where the term $\Phi(t)$ corresponds to the energy associated with the *shaded* region in Fig. 6(b). (Note that we neglect any initial energy of the atoms in the above treatment; initial momentum does not change the periodic structure of the phase space, and the relevant energy can simply be added on to the final result, or subtracted from experimental and simulation results before comparison with theory). Off-resonance, this region is destroyed by the phase space island and so the $\Phi(t)$ term must be subtracted from the resonant energy and replaced with a term which gives the energy in the portion of phase space disturbed by the island. This term is $\langle E_t \rangle_{\text{res}}$ - the energy associated with the resonance island itself in Fig. 6(a). In fact, the approximation in Eq. (16) can be seen as corresponding to the approximation of the off-resonant phase space as shown in Fig. 6(a) by adding the unshaded portions of Fig. 6(b) and Fig. 6(a) to give Fig. 6(c).

We can extract analytic expressions for $\Phi(t)$ and $\langle E_t \rangle_{\text{res}}$ from considerations of

the portion of the entire phase space cell the island occupies and the solutions to the pendulum equations of motion. The latter solutions describe *continuous* time motion induced by the pendulum Hamiltonian

$$H_{\text{res}} = \frac{1}{2}(J')^2 + \tilde{k} \cos(\vartheta) , \quad (17)$$

in the canonical variable J' and ϑ of Eq. (11), where J' measures the deviation from the island centre. The resonance width of the principal nonlinear island δJ_{res} is estimated by the separation (in action) between the separatrices of the pendulum motion (Lichtenberg and Lieberman, 1992). The period of the small pendulum oscillations is $2\pi t_{\text{res}}$ where $t_{\text{res}} = \tilde{k}^{-1/2}$ (Lichtenberg and Lieberman, 1992), so t_{res} defines a characteristic time scale for the elliptic motion in the resonant zone. One may altogether remove $|\epsilon|$ from Hamilton's equations as induced by Eq. (17), by scaling momentum and time by factors $\tilde{k}^{-1/2} = 4/\delta J_{\text{res}}$, $\tilde{k}^{1/2} = 1/t_{\text{res}}$ respectively. Therefore,

$$\langle (\delta J_t)^2 \rangle = \langle (J'_t - J'_0)^2 \rangle \sim \tilde{k} G(t\sqrt{\tilde{k}}) , \quad (18)$$

for an ensemble of orbits started inside the resonant zone, where $G(\cdot)$ is a parameter-free function, whose explicit expression involves elliptic integrals. $G(\cdot)$ represents the average energy contribution from trajectories in the primary island of the ϵ SM. Hence, this function results from averaging over nonlinear pendulum motions with a continuum of different periods, so it saturates to a constant value when its argument $\gg 1$. At small values ($\ll 1$) of the argument, it behaves quadratically. This behaviour is illustrated in Fig. 7 below, where G is plotted vs. the scaled variable $x \equiv t/t_{\text{res}}$. The contribution to the total energy is then obtained on multiplying Eq. (18) by $|\epsilon|^{-2} \delta J_{\text{res}} / (4\pi)$, because only a fraction $\sim \delta J_{\text{res}} / (2\pi)$ of the initial ensemble is trapped in the resonant zone. As a result

$$\langle E_{t,\epsilon} \rangle_{\text{res}} \sim \frac{\delta J_{\text{res}}}{4\pi} \frac{\langle (\delta J_t)^2 \rangle}{2\epsilon^2} \sim \frac{k^2}{\pi \tilde{k}} G\left(t\sqrt{\tilde{k}}\right) . \quad (19)$$

Furthermore, if we divide through by the peak energy $k^2 t / 4$ (c.f. Eqs. (3) and (15)), it turns out the right hand side of Eq. (16) can be written solely as a function of the scaled time variable x , as we expect given the scaling property of the pendulum. The scaling function we finally arrive at is

$$\frac{\langle E_{\epsilon,t} \rangle}{\langle E_{t,0} \rangle} \approx H(x) \equiv 1 - \Phi_0(x) + \frac{4}{\pi x} G(x) . \quad (20)$$

Explicit expressions for $\Phi_0(x)$ and $G(x)$ may be found in refs. (Wimberger et al., 2003; Wimberger, 2004; Sadgrove, 2005; Sadgrove et al., 2005) together

with methods for calculating these functions.

To gain an appreciation for the convenience of the scaling function formu-

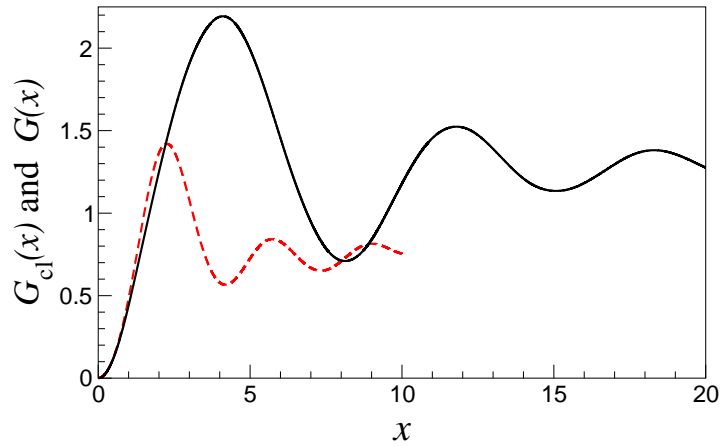


Fig. 7. $G(x)$ used in Eq. (20) (solid line) is shown along with G_{cl} from Eq. (26) (dashed line). The differences between the two scaling functions arise due to the different initial conditions in phase space in the classical and ϵ -classical limits.

lation from an experimental point of view, consider the experimental data

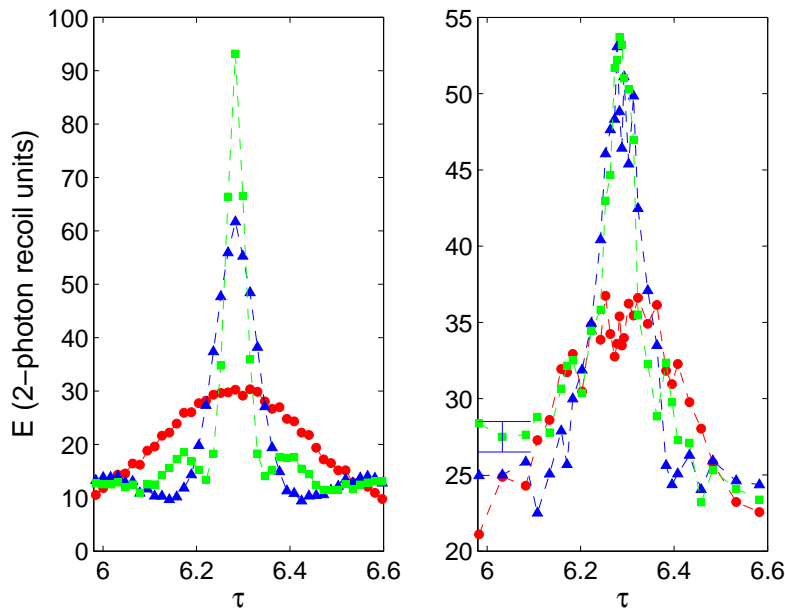


Fig. 8. ϵ -classical simulation energies (left panel) and experimental results (right panel) demonstrating the change in the QR peaks as the total number of kicks is increased from 5 (circles), 10 (triangles) to 15 (squares) for similar values of kicking strength. Note both the narrowing of the peak and the appearance of small peaks to the side of the main resonance. In the right panel we show a representative error bar which gives the standard error of the mean over five experimental runs. (Adapted figure from Wimberger et al. (2005b)).

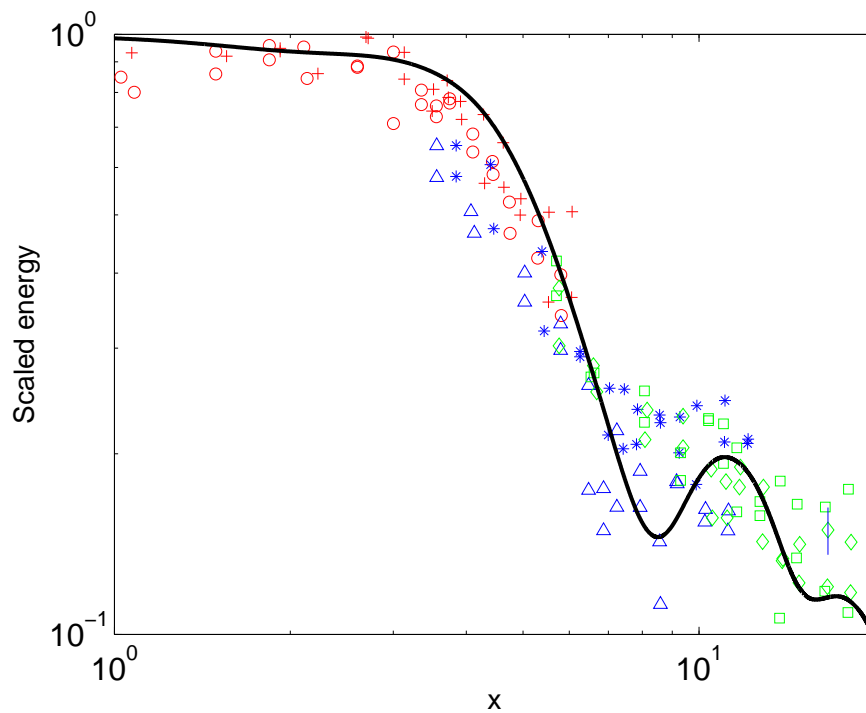


Fig. 9. Experimental (discrete points) and analytical results (solid) for the scaled data near the first and second QRs. The plus, star and diamond symbols show points taken near the first primary QR at $\tau = 2\pi$ for 5, 10 and 15 kicks respectively. Circles, triangles and squares show data near $\tau = 4\pi$ for the same respective kick numbers as the $\tau = 2\pi$ case. Note again the representative error bar as explained in Fig. 8. (Adapted figure from Wimberger et al. (2005b).)

shown in Fig. 8 (Wimberger et al., 2005b). In the left panel, simulation energies are shown, and in the right panel experimental energies were measured for 3 different kick numbers. Both simulations and experimental results make clear that the peaks have different widths and even different structures, with side-peaks flanking the main quantum resonance being visible in the case of 15 kicks. Nonetheless, the three different experimental data sets, when scaled by the peak energy, all collapse onto a single curve as shown in Fig. 9².

Considering that comparison of experimental data with theory typically requires the estimation of the theoretical parameter k along with time-consuming quantum simulations, for all values of t and ϵ used in the experiment, the scaling function can immediately be seen to be a huge boon for experimentalists, who now need only compare data with a single analytical function of one variable.

3.2 Comparison of near-resonant method with the standard semi-classical limit

We now consider an intuitive question regarding the ϵ -classical standard map: Since it describes the pseudo-classical limit near exact quantum resonance so well, can it also describe dynamics in the standard semi-classical limit, that is, when $\epsilon = \tau \rightarrow 0$? As might be expected, the answer is indeed “yes”. However, there are some interesting differences between the dynamics in the ϵ -classical and standard semi-classical limit.

To investigate the regime of vanishing τ , we can use the ϵ -classical standard map as derived in Section 2 with $\ell = 0$ (i.e. choosing the “zeroth” quantum resonance) and setting $\epsilon = \tau$. The appropriate map is then again given by Eq. (11), but now with $\tilde{k} = k\tau = K_s$. Plotting the phase space of the map of Eq. 11 for various values of $\epsilon = \tau$, as done in Fig. 10, immediately reveals differences with the standard ϵ -classical phase space. In particular, we note that all trajectories are now contained within the central phase space island. This means that in calculating the off resonant energy, only the kinetic energy from the pendulum approximation to the motion within the island needs to be considered and not that due to the regular phase space outside the island. We proceed to find a version of the scaling function as follows: Scaling momentum by $1/t_{\text{res}} = 1/\sqrt{\tau k}$ as before, the mean energy due to the nonlinear resonance

² Because of imperfect experimental detection, the wings of momentum distributions where resonant atoms are concentrated are inevitably underestimated in measurements, leading to deviation from the exact theory for very small $|\epsilon|$. When comparing to the scaling function, we typically suppress these points as in Wimberger et al. (2005b).

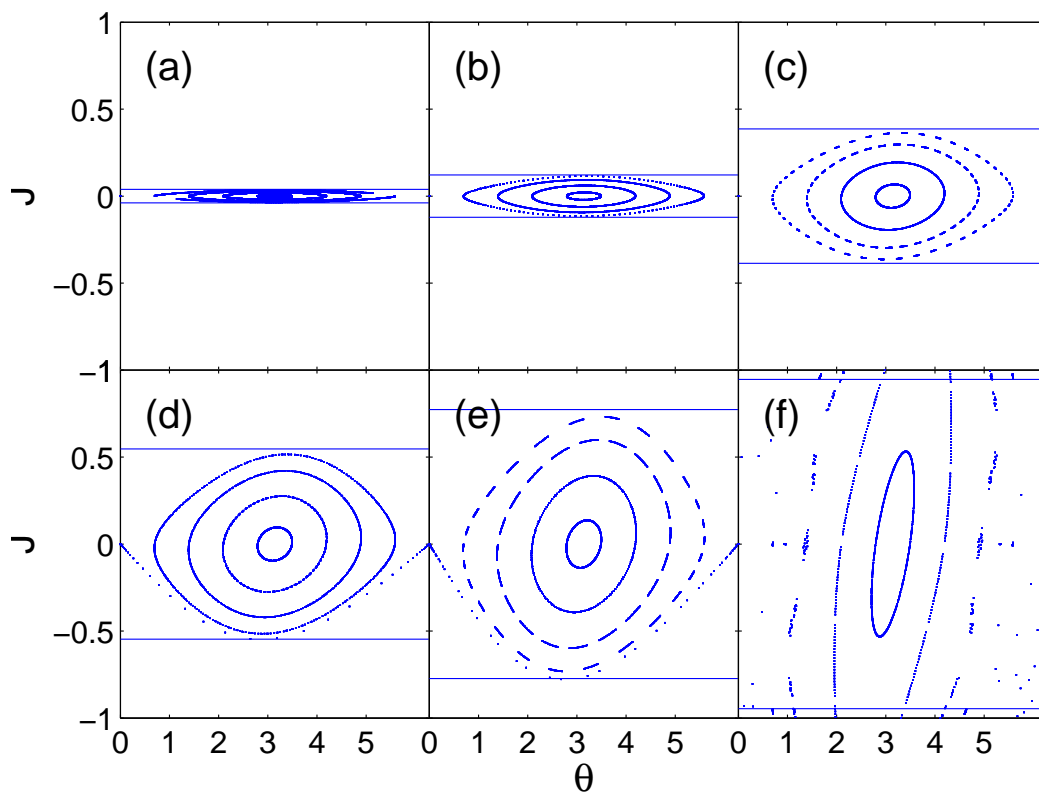


Fig. 10. Phase space diagrams for the ϵ SM with $\ell = 0$ and $\tau = \epsilon =$ (a) 0.0001, (b) 0.001, (c) 0.01, (d) 0.02 (e) 0.04 and (f) 0.06. The solid horizontal lines show the resonance width $\pm 2\sqrt{\tau k}$ in each case.

island may be written as

$$\langle E_t \rangle_{\text{res,cl}} = \frac{\langle (J'_t - J'_0)^2 \rangle}{2\tau^2} = k \frac{G_{\text{cl}}(t\sqrt{\tau k})}{2\tau}, \quad (21)$$

where the subscript “cl” denotes “classical” and the G_{cl} function depends weakly on the ratio of τ and k . As $\tau \rightarrow 0$, G_{cl} tends to

$$G_{\text{cl},\tau=0}(x) = \frac{1}{2\pi} \int_0^{2\pi} d\vartheta_0 J'(x, \vartheta_0, J'_0 = 0)^2, \quad (22)$$

for $x = t\sqrt{\tau k}$.

In the limits of small and “large τ ”, two interesting results can be derived for the mean energy (Sadgrove et al., 2005). Firstly, as shown in Fig. 7, as $\tau \rightarrow 0$, $G_{\text{cl}}(x) \approx x^2/2$ and thus the energy in this limit is

$$\langle E_{t,\tau \rightarrow 0} \rangle = \frac{k^2 t^2}{4}, \quad (23)$$

that is, the energy grows *quadratically* with the number of kicks t . Such ballistic energy growth occurs in this case just as it does for quantum resonance for an ideal kicked rotor in an initial momentum eigenstate. This growth is much faster than the linear increase predicted for the quantum resonance peaks for the same broad initial momentum distribution. From Fig. 7, it may be seen that ballistic growth occurs only for $x \lesssim 1$ which implies that

$$t_{\text{ball.}} \lesssim \frac{1}{\sqrt{\tau k}} = t_{\text{res}}, \quad (24)$$

which shows that ballistic energy growth may occur so long as t is less than the characteristic resonance period of the pendulum approximation.

Additionally, for large τ , Fig. 7 shows that $G_{\text{cl}}(x)$ saturates to a value $\alpha \approx 0.75$. Thus the mean energy is

$$\langle E_{t,\tau \gg 0} \rangle \simeq \frac{k}{2\tau} \alpha. \quad (25)$$

This result implies that, after gaining energy in the first kick, the kicked rotor ensemble ceases to absorb energy from subsequent kicks – energy growth is frozen. This result is as one would expect in the presence of DL except here we have a completely classical explanation for the frozen energy growth (Sadgrove et al., 2005).

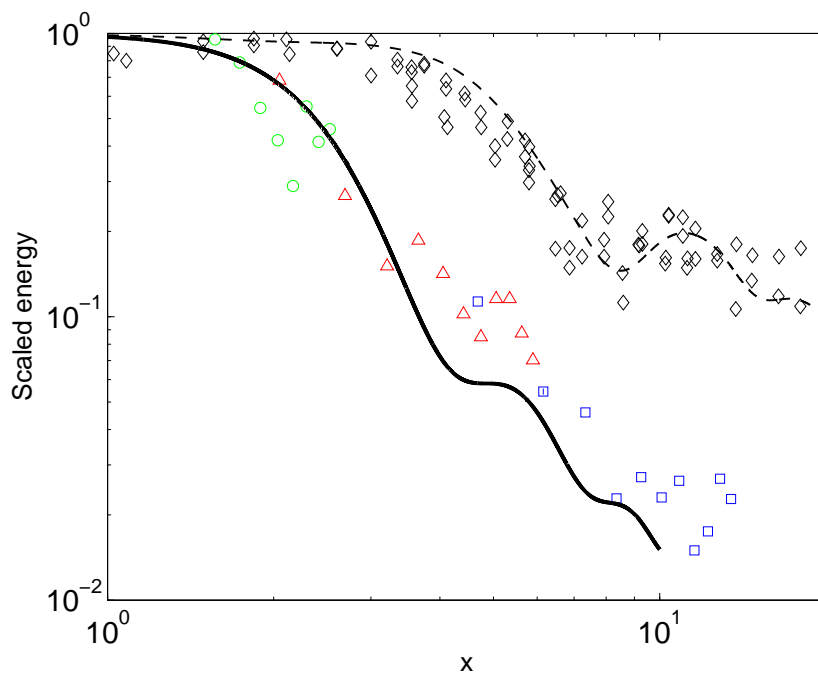


Fig. 11. Experimental (symbols) and analytical results (solid line) for the scaled data near the semi-classical limit. The data shown is for 5 kicks (circles), 10 kicks (triangles) and 15 kicks (squares). Experimental data (diamonds) and theory (dashed line) for the first primary quantum resonance are reproduced from Fig. 9 for comparison. (Adapted figure from Wimberger et al. (2005b).)

Finally, ignoring the small τ dependence of the G_{cl} function, a scaling function for the $\tau \rightarrow 0$ resonance may be written as for the quantum resonance peaks:

$$\frac{\langle E_{t,\tau} \rangle}{\langle E_{t,\tau=0} \rangle} \approx R(x) \equiv \frac{2G_{\text{cl}}(x)}{x^2}. \quad (26)$$

Fig. 11 shows experimental data (discrete points) and theory for the standard ϵ -classical and the $\tau \rightarrow 0$ limit cases (Wimberger et al., 2005b). The experimental data for the two different limits clearly lie on different curves and in particular are in good agreement with their respective theoretical scaling functions.

Once again, we would like to emphasize that extending the scaling function to a new domain is not an inconsequential theoretical exercise; rather it can reveal new physics “hiding” in the opaque quantum formulation, such as the ballistic and frozen growth regimes seen in the semi-classical limit.

3.3 Noise and decoherence

Surprisingly, the pseudo-classical description and the scaling of the mean energy introduced in Section 3.1 works in the presence of perturbations of the quantum evolution as well. In the following we show this for two special cases where noise acts on the kicking strength (amplitude noise) and, even more interestingly, mainly on the phase evolution of the free rotational parts of the Floquet operator (i.e. on the second factor on the right hand side of Eq. (2)). We start out with the latter in the next Subsection.

3.3.1 Spontaneous emission

Early experiments which perturbed the phase evolution of kicked cold atoms in a controlled manner used a kicking beam closer to resonance with the internal atomic transition of the atoms. This enhanced the spontaneous emission (SE) rate of the atoms, leading to random momentum kicks in addition to the conservative part of the potential (Ammann et al., 1998; Daley et al., 2002). Better control on the impact of SE is obtained by separating both effects, the kicks and the SE events. This was implemented at Oxford some time ago, using a second laser (again closer to resonance than the kick laser) to induce SE events after each kick and in a short time interval compared to the kicking period (d’Arcy et al., 2001, 2004). Such SE events not only lead to a dephasing of the unperturbed quantum evolution of the kicked particle, but also to a heating of its centre of mass motion (since they correspond to additional kicks). Both can be taken into account in an amended version of the classical mapping describing the evolution close to quantum resonance (i.e. small ϵ). The amended mapping is given by

$$\begin{aligned} I_{t+1} &= I_t + |\epsilon| \delta_{t+1} + \tilde{k} \sin(\theta_{t+1}) , \\ \theta_{t+1} &= \theta_t \pm I_t + \pi\ell + 2\pi\ell\eta_t , \\ \eta_{t+1} &= \eta_t + \delta_{t+1} \quad \text{with} \quad \eta_0 = \frac{\tau\beta}{2\pi\ell} . \end{aligned} \tag{27}$$

β is the initial quasi-momentum which is effectively shifted by the SE events (see third equation). Also the momenta I_t (corresponding to the ϵ -rescaled integer parts of momentum in the original physical system) are affected which is taken into account by the term $|\epsilon|\delta_{t+1}$ in the first equation. The δ_t describe the sum of momentum changes arising from SE up to the number of kicks t and they are independent random variables, whose distribution is determined by the statistics of SE. Numerical simulations using Eq. (27) are shown in Fig. 12, and the results are found to match the true quantum evolution very well at small $|\epsilon|$. Under the substitution $J_t = \pm I_t + \pi\ell + 2\pi\ell\eta_t$, the map of Eq. 27 reduces to a noisy pseudo-classical standard map, which differs from Eq. (11)

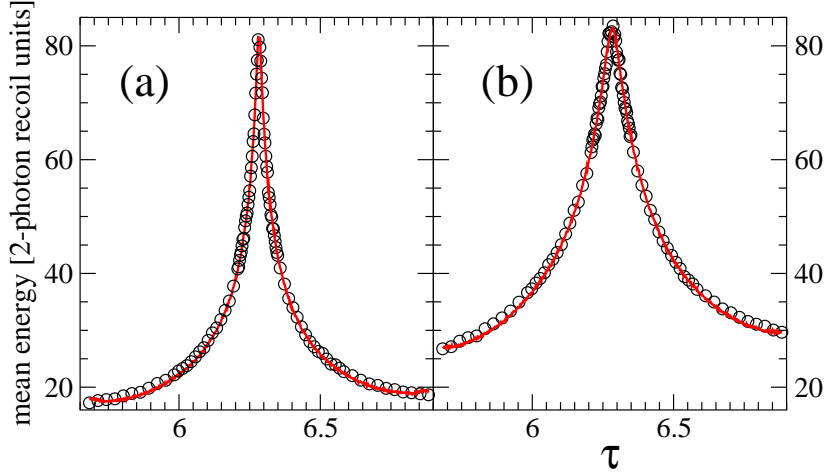


Fig. 12. Mean energies of the same initial ensemble of atoms as shown in Fig. 4 as a function of the kicking period τ scanned over the quantum resonance at $\tau = 2\pi$; for $k = 0.8\pi$ and in the presence of SE. Results of full quantum calculations (circles) and of ϵ -classical ones using the map of Eq. (27) (solid lines) are compared for different SE rates (a) $n_{\text{SE}} \approx 0.1, t = 50$ and (b) $n_{\text{SE}} \approx 0.2, t = 50$. We note the asymmetry of the peaks which is best visible for larger n_{SE} . Its origin has not yet been discussed in the literature but it certainly lies in the asymmetry of the initial ensemble in the pseudo-classical phase space with respect to the sign of ϵ , which enters into the term $\tau\beta$ of the mappings of Eqs. (10) and (27).

by a random shift $\tau\delta_t$ of the action J at each step. The scaling law of Eq. (20) shows that the only relevant time scale for the evolution of the quantum motion sufficiently near to $\tau = 2\pi\ell$ ($\ell \in \mathbb{N}$) is given by $t_{\text{res}} = 1/\sqrt{\tilde{k}}$. The noisy time evolution brings an additional time scale into play that characterises the strength of the noise. In the following, we indeed find an equivalent of the scaling law of Eq. 20 in the presence of SE, which is based on the two time scales t_{res} and t_c , where t_c is the mean waiting time between two SE events. Then, the structure of the resonance peak in the mean energy in the presence of SE may be analytically studied, using essentially the same ideas developed above in Section 3.1.

Let us assume an initially uniform quasi-momentum distribution. At any SE event, the distribution of the ensemble in the phase space of the pseudo-classical standard map is reshuffled by the random action change. Under the assumption of homogeneous distribution of single SEs in an interval of integer length (in units of two photon recoils), the resulting distribution of $J \bmod(2\pi)$ is approximately homogeneous over the unit cell of the map of Eq. (11). Such randomisation may be assumed to wash out correlations between the past and the subsequent random dynamics. Hence the scaling of Eq. (20) may be used to write the energy after a number of kicks t as

$$\langle E_{t,\epsilon} \rangle \sim \frac{k^2}{4} \left\langle \sum_{j=0}^{N_t-1} \Delta_j H(\Delta_j/t_{\text{res}}) \right\rangle + \frac{1}{2} D n_{\text{SE}} t, \quad (28)$$

where $\langle \cdot \rangle$ stands for the average over all realisations of the times of SE events and N_{t-1} is the number of SE events up to a number of kicks $t-1$. n_{SE} is the average number of SE per period, and $D = n_{\text{SE}}^{-1} \langle \delta_t^2 \rangle$ is the mean square momentum imparted by a single SE. For an individual realisation, Eq. (28) states that the energy is given by the sum of the SE-free scaling function H of the evolutions over time intervals Δ_j . The SE resets the evolution after each event at times Δ_j , apart from the momentum shift contained in the second term in Eq. (28). If t_c is sufficiently large compared to 1, one may replace the random process of SE events by a continuous time Poisson process with the characteristic time $t_c = 1/n_{\text{SE}}$ (Wimberger et al., 2003). This process has delays Δ distributed with density $t_c^{-1} \exp(-\Delta/t_c)$. Its statistic reduces to that of the unit Poisson process (with $t_c = 1$) by just rescaling all times by the factor $1/t_c$. This reasoning allows the following approximation

$$\left\langle \sum_{j=0}^{N_{t-1}} \Delta_j H(\Delta_j/t_{\text{res}}) \right\rangle \approx 4t_c Q(t/t_c, t_c/t_{\text{res}}), \quad (29)$$

where

$$Q(u, v) \equiv \frac{1}{4} \left\langle \sum_{j=0}^{N_u^1} \Delta_j^1 H(\Delta_j^1 v) \right\rangle. \quad (30)$$

The superscript 1 specifies that the average is now over the realisations of the unit Poisson process: each realisation has a continuous time interval $[0, u]$ divided in subintervals Δ_j^1 by a random number N_u^1 of Poisson events. We are hence led to the following scaling law:

$$\langle E_{t,\epsilon} \rangle \sim D' \frac{t}{2t_c} + k^2 t_c Q\left(\frac{t}{t_c}, \frac{t_c}{t_{\text{res}}}\right) \quad (31)$$

or, equivalently introducing $u = t/t_c$, $v = t_c/t_{\text{res}}$,

$$\frac{2\langle E_{t,\epsilon} \rangle - D't/t_c}{2k^2 t_c} \sim Q(u, v). \quad (32)$$

The scaling function $Q(u, v)$ may be explicitly written in terms of the function $H(x)$. This is shown in detail in appendix D of Wimberger et al. (2003) and it gives:

$$4Q(u, v) = uH(uv)e^{-u} + \int_0^u dx e^{-x} x H(xv)(2 + u - x). \quad (33)$$

Limiting behaviours of the scaling function $Q(u, v)$ immediately follow from this equation, or from Eq. (30) itself. On one hand, for $u = t/t_c \gg 1$ the right-hand side in Eq. (30) is a sum of a large number $\sim t/t_c$ of terms. In that limit, such terms are weakly correlated and can be averaged independently which gives

$$u \gg 1 : \quad Q(u, v) \sim \frac{1}{4} u \int_0^{\infty} dx H(vx) x e^{-x} . \quad (34)$$

On the other hand, for $t/t_c \ll 1$, the sum reduces to the single term $j = 0$, with $\Delta_0^1 = t/t_c$; hence

$$u \ll 1 : \quad Q(u, v) \sim \frac{1}{4} u H(uv) . \quad (35)$$

In particular, Eq. (35) shows that Eq. (31) coincides with Eq. (20) in the SE-free limit $t_c \rightarrow \infty$. In the opposite limit, Eq. (34) shows that, if k is fixed, then the width in ϵ of the resonant peak will not shrink any more with time when $t \gg t_c$, and its width thereafter scales like $(t_c^2 k)^{-1}$. The spike is therefore erased (i.e. it is absorbed in the background) in the strong noise limit $t_c \sim 1$. In the latter limit, the method developed above breaks down, because on average after each kick an SE event happens, which does not let the time evolution recover for some time interval. The result is then a completely random motion which does not depend on the system specific dynamics, and hence not on the chosen value of the kicking period τ .

The spreading of the resonance peaks with increasing noise, as can be seen in Fig. 12, explains why they are more stable and easier to observe experimentally than in the case without noise for broadly distributed initial momenta of the atoms (d'Arcy et al., 2001, 2004). An intuitive argument for the spreading of the resonance peaks is that for a fixed value of ϵ , due to SE there is an enhanced chance to find a quasi-momentum β , such that the free evolution part of the Floquet operator is approximately the identity. This is the condition for quantum resonant motion.

Numerical simulations in Fig. 13 support the scaling law of Eq. (31). Data were obtained in a similar manner to the case without SE; however, one of the parameters u, v is varied, while keeping fixed either the other parameter or the ratio u/v . The theoretical scaling function $Q(u, v)$ was calculated numerically using in Eq. (33) the function $H(x)$ introduced above in Section 3.1.

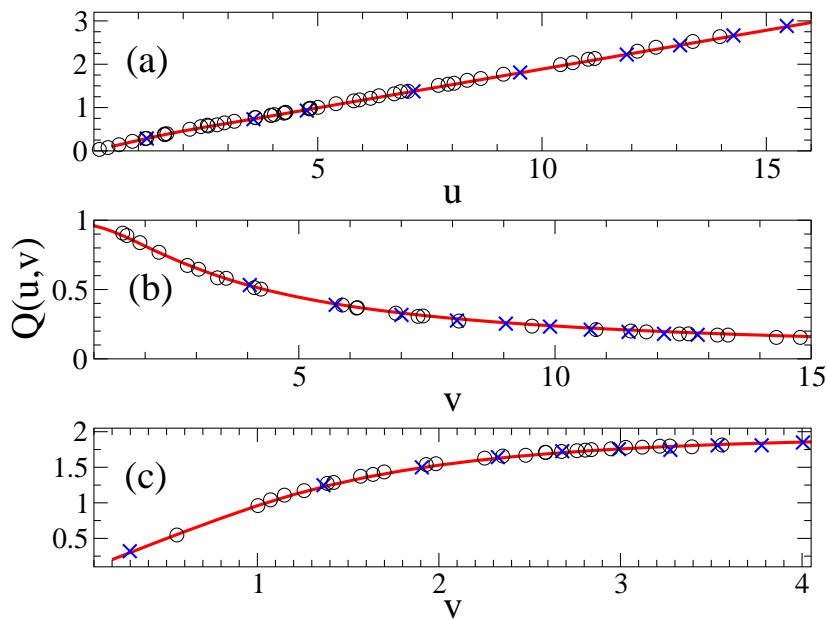


Fig. 13. Demonstrating the scaling law of Eq. (31) in a right neighbourhood of $\tau = 2\pi$. In (a), (b) the $Q(u, v)$ quantity on the left-hand side of Eq. (32) is plotted vs. one of the parameters $u = t/t_c$ or $v = t_c/t_{\text{res}}$ while keeping the other fixed: (a) $v = 2$, (b) $u = 4$. In (c) the ratio $u/v = 4$ is fixed. Open circles correspond to different values of the parameters t, t_c, k, ϵ , randomly generated in the ranges $1 < t < 200$, $5 < t_c < 60$, $0.001 < \epsilon < 0.1$, $0.1 < k < 20$, with the constraints $0.001 < k\epsilon < 0.2$ and $t_c\sqrt{k\epsilon} = 2$ in (a), $t/t_c = 4$ in (b), $t = 4t_c^2\sqrt{k\epsilon}$ in (c). In each case an ensemble of 2×10^6 ϵ -classical rotors was used, with a uniform distribution of initial momenta in $[0, 1)$ and a uniform distribution of initial θ in $[0, 2\pi)$. The random momentum shifts at each step of the ϵ -classical evolution of Eq. (27) were generated from the uniform distribution in $[-1/2, 1/2]$. Crosses represent the results of quantum simulations for $k = 0.8\pi$, and $\epsilon = 0.01$ in (a), $\epsilon = 0.05$ in (c), and $t = 50$ and $t = 100$ in (b). The solid lines correspond to the theoretical prediction of Eq. (33). Adapted figure from Wimberger et al. (2003).

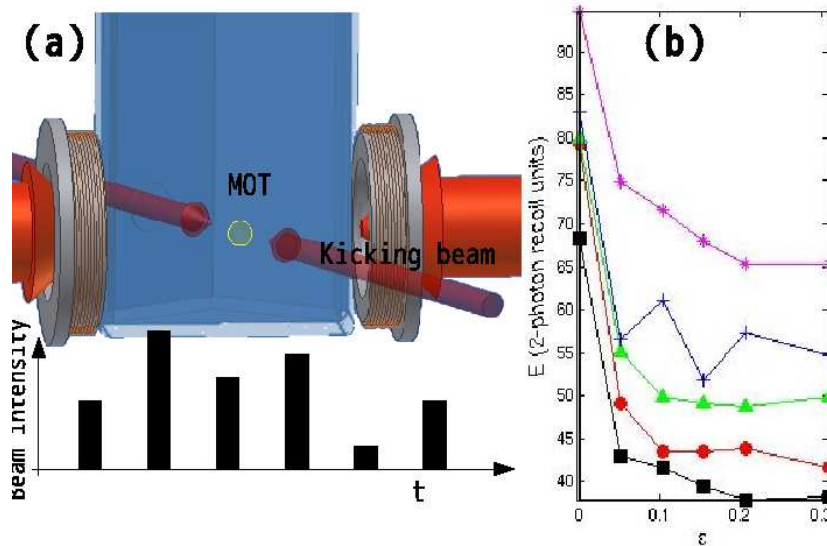


Fig. 14. In (a) diagram illustrating the experimental setup used for amplitude noise experiments. The important difference in comparison to the system of Fig. 1 is the time varying pulse amplitudes. In (b) experimental measurements for the E atomic mean kinetic energy (y axis) vs. the ϵ detuning from quantum resonance(x axis) demonstrating QR peaks broadened under the influence of amplitude noise. The noise level ranged from 0 (squares), 0.5 (circles), 1.0 (triangles), 1.5 (plus sign) and 2.0 (stars). (Adapted figure with permission from Sadgrove et al. (2008). Copyright 2008 of the American Physical Society.)

3.3.2 Amplitude noise

Spontaneous emission is a dissipative noise process directly altering the momentum of individual atoms, and thus altering the otherwise coherent dynamics associated with the AOKR. But other types of noise processes are also present in experimental implementations of the kicked rotor – particularly noise in the kicking parameters themselves. An example of some interest is caused by fluctuating laser power which gives rise to so-called *amplitude noise* – that is noise due to the strength of kicking fluctuating randomly.

In order to analyse the effects of this non-dissipative noise, fluctuations are typically added in a controlled manner using a random number generator along with an optical attenuator to create a pulse amplitude with any desired noise distribution and noise strength. In studies up to now, it has been typical to use a uniform noise distribution and vary the noise from 0 to 200% – the latter indicating that pulses can vary in strength from 0 to twice the nominal kicking strength. Fig. 14(a) depicts a kicked rotor experiment for which pulses with amplitude noise are applied.

The ϵ -classical method was coopted for use in amplitude noise studies in order to explain the following puzzling observation: although in general the

amplitude noise was found to completely destroy the AOKR quantum correlations (Klappauf et al., 1998; Milner et al., 2000), Sadgrove et al. (2004) demonstrated that in the vicinity of the quantum resonance, the peak structure is not destroyed even by maximum noise, as shown in Fig. 14(b). One intuitive interpretation of this phenomenon is to note that quantum resonance is dependent on the frequency of the applied pulses, and not their amplitude, and so the resonance condition itself is robust against amplitude fluctuations. This does not, however, explain why for a range of kicking frequencies which are merely *close* to quantum resonance, the effect of amplitude noise is minimal.

To explain the stability of the peak, we modify the ϵ -classical map as follows. Given a uniform noise level $L \in [0, 2]$, we introduce a stochastic parameter R_t which is drawn from $[-L/2, +L/2]$ for each pulse as labelled by the discrete time (i.e. the total number of kicks) t . We then simply multiply the kicking strength k by $(1 + R_t)$ to give uniform random fluctuations in the kicking strength about a mean of k . The modified ϵ SM is then

$$J_{t+1} = J_t + \epsilon k(1 + R_t) \sin(\theta_{t+1}), \quad \theta_{t+1} = \theta_t + J_t. \quad (36)$$

From this map, we can immediately plot the phase space for various ϵ and look for answers regarding the stability of the quantum resonance in the changing phase space structure. Fig 15(a) shows the phase space away from resonance for a high level of noise – specifically for $L = 1.5$ (150% amplitude noise). The important thing to note is that even away from perfect quantum resonance ($\epsilon = 0$) the broad structure of the phase space is undamaged by noise, meaning that an energy peak is still present even at high noise levels.

We can formalize this intuition regarding the phase space and the associated stability of quantum correlations near resonance by seeking to extend the ϵ -classical scaling function to the amplitude noise case. Fig 15(b) shows the pendulum phase space which approximates the phase space in Fig 15(a). The shaded gray area marks the region of the phase space around the separatrix which is most affected by the noise, as calculated by considering the fluctuations in k which directly determines the separatrix position (Sadgrove et al., 2008). Modification of trajectories near the separatrix has the largest effect on the near resonant energy since stable librations may become higher energy rotation orbits if the separatrix becomes transparent. Applying this reasoning, an approximate scaling law for the AOKR quantum resonances in the presence of amplitude noise can be derived, specifically (Sadgrove et al., 2008):

$$\langle E_{t,\epsilon} \rangle \approx 1 + \frac{L^2}{12} - [1 - L/(8\pi)]\Phi_0(x) + \frac{4}{\pi x}G(x), \quad (37)$$

where the average is taken over the initial conditions in the pseudo-classical

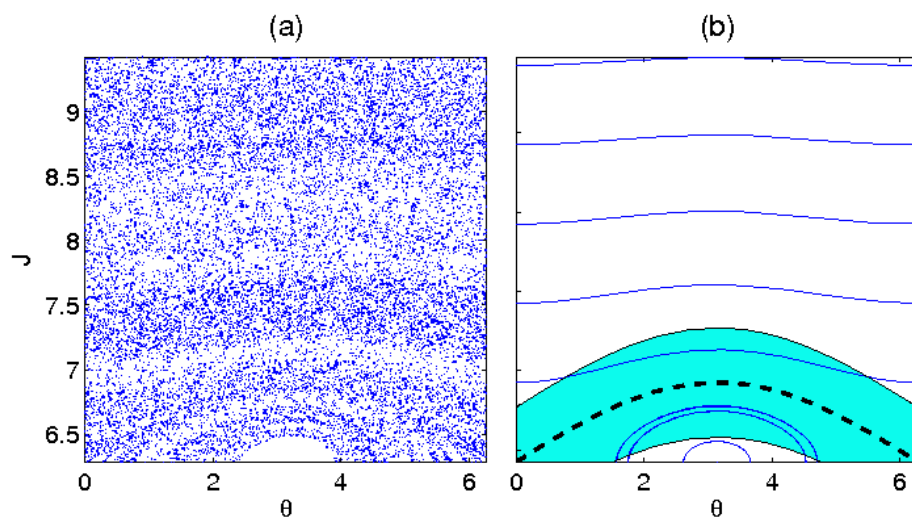


Fig. 15. (a) The ϵ -classical phase space in the presence of amplitude noise. (Compare with Fig. 6(c)). (b) Shows the pendulum phase space approximation to (a) with the area around the separatrix shaded. It is trajectories in this area (for a noise level $L = 1.5$ in (b)) which have the most effect on the energy when amplitude noise is added to the system. (Adapted figure with permission from Sadgrove et al. (2008). Copyright 2008 of the American Physical Society.)

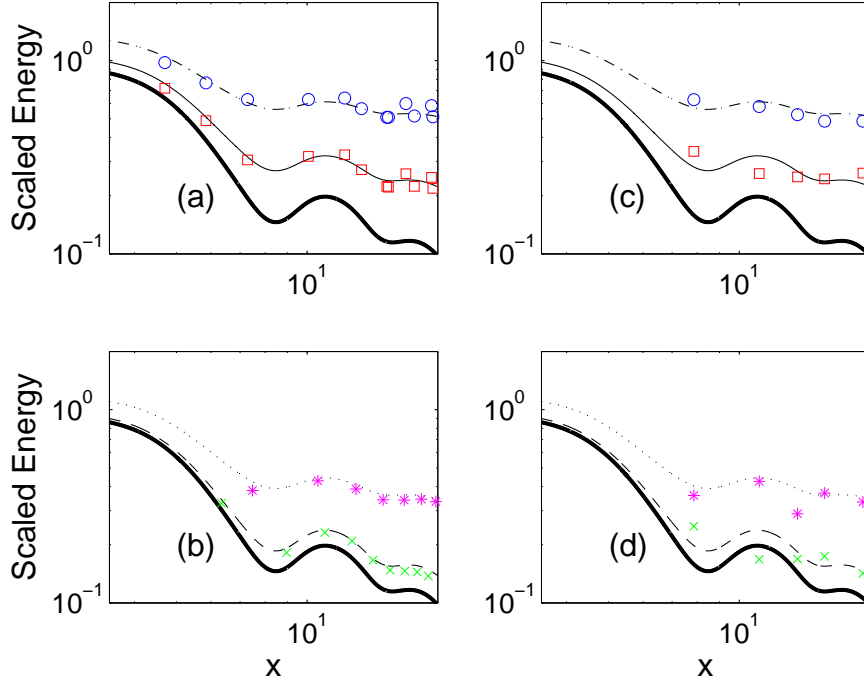


Fig. 16. The ϵ -classical scaling function is compared with simulation data (a,c) and experimental data (b,d). In (a) simulation data for $L = 1$ (squares) and $L = 2$ (circles) are compared to the scaling functions (solid line, dash-dotted line) for the same respective noise values. (c) Experimental data, and scaling functions, using the same symbols for the same parameters as in (a). In (b), simulation data for $L = 0.5$ (crosses) and $L = 1.5$ (stars) are compared to the scaling functions (dashed line, dotted line) for the same respective noise values. In (d), experimental data and scaling functions with the same symbols corresponding to the same parameters as in (b). The scaling function in this case is augmented by additional terms dependent on the noise level L , although to a good approximation the energy contribution from the nonlinear resonance (the last term on the right hand side of Eq. (37)) is not affected. Note that in all figures, the thick black line shows the standard (zero-noise) scaling function for comparison.

phase space.

In Fig. 16 the modified scaling law is compared with experimental data (left column) and simulation results (right column) showing good agreement. Thus, with the addition of an additional parameter L , we find that the stability of the quantum resonances in the presence of amplitude noise may be characterised by a scaling law as in the noise free case, and all of the usual benefits of a scaling law for data analysis and consolidation of experimental parameters are still available even in the noisy system.

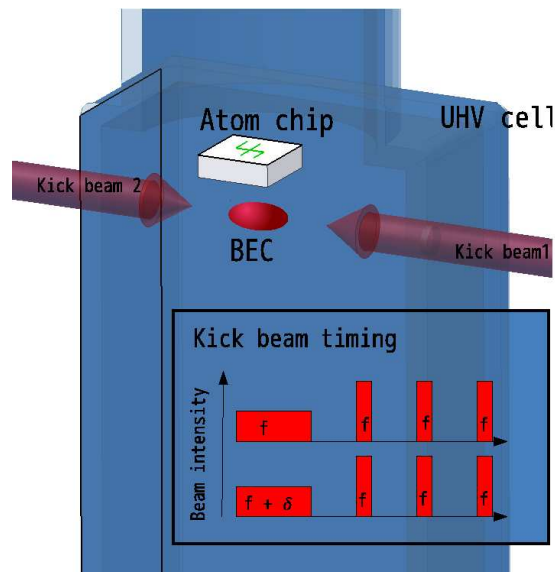


Fig. 17. Depiction of the experimental system used to realize directed motion at QR. A BEC is created and split into two momentum components by an initial Bragg pulse, where counter-propagating beams have a frequency difference δ . After a phase evolution period, standard kicks (where both beams have frequency f) are applied giving rise to a momentum current.

3.4 Directed transport at quantum resonance

This Subsection and the following one present new theoretical results which have not all been tested experimentally yet. Specifically, in the present Subsection, we consider a scaling function explanation for the results published in (Sadgrove et al., 2007; Dana et al., 2008), but we also use the pseudo-classical theory to predict new effects (Sadgrove and Wimberger, 2009).

Numerous reasons exist for studying directed transport due to non-biased forcing in quantum systems. These range from the motivation to explore fundamental physics (in particular thermodynamics which Feynman famously used as a motivator for the study of the ratchet and pawl system (Feynman, 1963)) to the more practical desire to find new ways to transport atoms and other quantum objects. Reviews of the broad area of ratchet dynamics are available (see, e.g., (Reimann, 2002; Hänggi and Marchesoni, 2009)). Here we will restrict our discussion to cold atom ratchet systems and focus in particular on the “resonance ratchet” system (Sadgrove et al., 2007; Dana et al., 2008) where ϵ -classical techniques may be used.

The resonance ratchet system, as realized in refs. (Sadgrove et al., 2007; Dana et al., 2008) uses ultra-cold atoms (so far sourced from a BEC) which are initially coherently split into two momentum components using a momentum conserving Bragg pulse. The quantum phase between the two components may be adjusted by allowing a free evolution period after the Bragg pulse. After

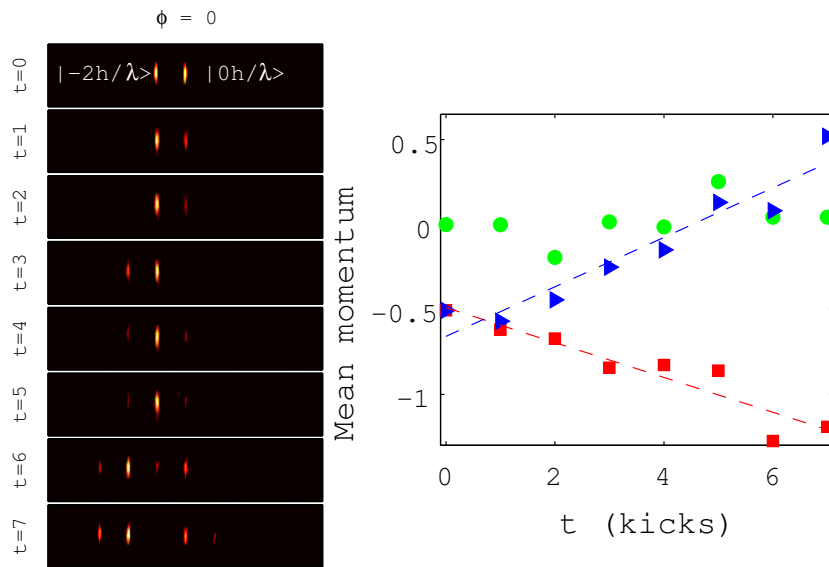


Fig. 18. Left panel: Absorption images for the momentum components of a Bose-Einstein condensate following a resonance ratchet experiment. In this case the momentum components show a momentum current towards negative momentum. For each sub-panel the total number of kicks t , is indicated on the y axis. Initially, a coherent atomic superposition of the $p = 0$ and $p = -2\hbar k = -2h/\lambda$ momentum components was created using a Bragg pulse. In this initial absorption image (at $t = 0$) that superposition appears as two “spots” with the momentum components labelled. The experimental data were taken at exact quantum resonance and with $\phi = 0$. The right panel shows experimentally measured mean momenta for the same experiment for two different phases 0 (triangles) and π (squares) which give opposite momentum currents. Dashed lines show linear fits to the data. The circles show measured mean momenta for a standard AOKR experiment (i.e. with no initial superposition). The results are for a kicking strength $k \approx 0.1$. (Adapted figure with permission from Sadgrove et al. (2007). Copyright 2007 of the American Physical Society.)

this preparation phase, kicks are delivered to the atoms with period equal to the Talbot time. Fig. 17 depicts the experimental setup used in Sadgrove et al. (2007), where a BEC was created on an “atom chip” before being exposed to an optical standing wave giving rise to the ratchet effect.

Unlike the usual case for the kicked rotor, where atoms are always found to gain energy symmetrically about zero momentum, in the resonance ratchet configuration the mean momentum of the atoms increases linearly with each kick with a direction and coefficient determined by the phase between the two initial momentum components. Fig. 18 shows the ratchet behaviour as a function of the number of pulses applied to the split condensate with both

the raw data (left panel) and the measured mean momentum clearly showing a momentum current (right panel). With this brief background on the effect, we now turn to the ϵ -classical analysis of the resonance ratchet phenomenon, and show what additional light the method can shed on the conditions for and nature of the momentum current.

Because the ratchet effect takes place at or very near to quantum resonance, the system may be analysed using an ϵ -classical treatment with a focus on the mean momentum of the atoms rather than their energy. There is, however, an important point to consider before diving into the analysis: how should we represent the initial momentum superposition state in the ϵ -classical formalism. Strictly, this is a problem without a clear answer: the difference between quantum mechanics and classical mechanics arises precisely because of the existence of classically impermissible superpositions in the quantum theory, and the ϵ -classical theory which contains no operators and treats atoms as classical particles cannot accommodate the quantum initial state any better than a standard classical treatment could. For now we delay discussion of this issue and simply present our method which produces useful ϵ -classical results in agreement with quantum simulations.

After the initial Bragg pulse, the atomic wavefunction is split into two momentum components. We can represent such an initial condition classically (i.e. non-coherently) by the distribution

$$P(p_0) = \frac{1}{2}(\delta_{p_0,0} + \delta_{p_0,1}). \quad (38)$$

where, as in Subsection 1.2, $\theta \equiv z \bmod 2\pi$. Fourier transforming the momentum space wavefunction gives the position space wavefunction. For the ϵ -classical atoms, we can choose the position space distribution to be the norm squared of this quantum wavefunction:

$$P(\theta) = |\psi(\theta)|^2 = \frac{1}{2\pi}(1 + \cos(\theta + \phi)). \quad (39)$$

Note that the role of the quantum phase is captured by adding the phase ϕ in the cosine term of Eq. (39), physically signifying a phase difference between the (classical) atomic density distribution and the sinusoidal driving field.

Having made these choices, we now proceed as in Section 2.3, arriving at the on-resonance result (this time for momentum rather than energy) averaged over the initial conditions given in Eqs. (39) and (38)

$$\langle p_{t,\epsilon} \rangle = \frac{kt}{2|\epsilon|} \cos(\phi). \quad (40)$$

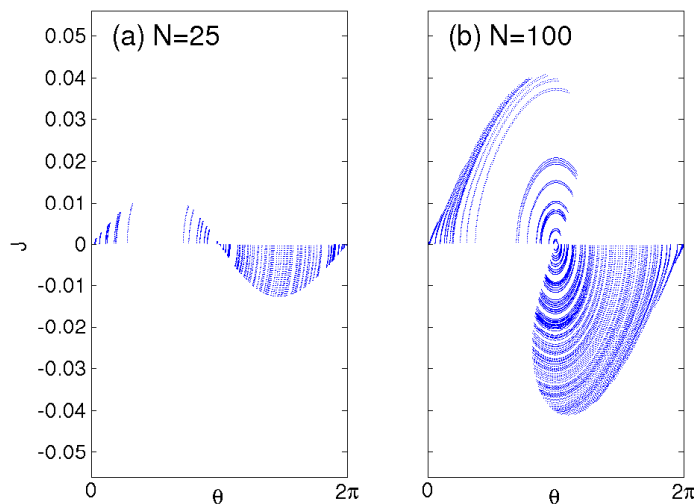


Fig. 19. ϵ -classical phase space for the ratchet system at 25 and 100 kicks with $k = 1$ and $\epsilon = 5 \times 10^{-4}$. The asymmetry in the phase space gives rise to the momentum current. (Adapted figure with permission from Sadgrove and Wimberger (2009). Copyright 2009 of the New Journal of Physics.)

This result agrees with the purely quantum expressions found in (Sadgrove et al., 2007; Dana et al., 2008). Furthermore, the result can also be modified to predict the effects of an arbitrary initial quasi-momentum, as explored experimentally in (Dana et al., 2008). The emergence of a momentum current is seen in the ϵ -classical phase space (see Fig. 19) as an asymmetry in the trajectories at finite times.

Next, we consider a question which has not yet been experimentally investigated: what happens to the momentum current if the pulse rate moves off-resonance? Once again, we proceed as in Section 3.1, and with our new initial conditions. Intriguingly, we find that the off-resonant momentum scales just as the energy does as a function of the scaled time $x = t/t_{\text{res}}$.

Fig. 20 shows the ϵ -classical scaling function for the momentum which is arrived at by dividing Eq. (40) by $-kt \cos(\phi)$ to give a single parameter scaling law on the RHS:

$$\frac{\langle p_{t,\epsilon} \rangle}{-kt \sin(\phi)} \approx A(x)/x, \quad (41)$$

where $A(x)$ is a function derived from the average momentum over general solutions of the pendulum dynamics (Sadgrove and Wimberger, 2009). More explicitly, it is given by the expression

$$A(x) = \frac{1}{2\pi} \int_{-\pi}^{\pi} d\theta_0 [\sin(\theta_0) \times J'(\theta_0, J'_0 = 0, x)]. \quad (42)$$

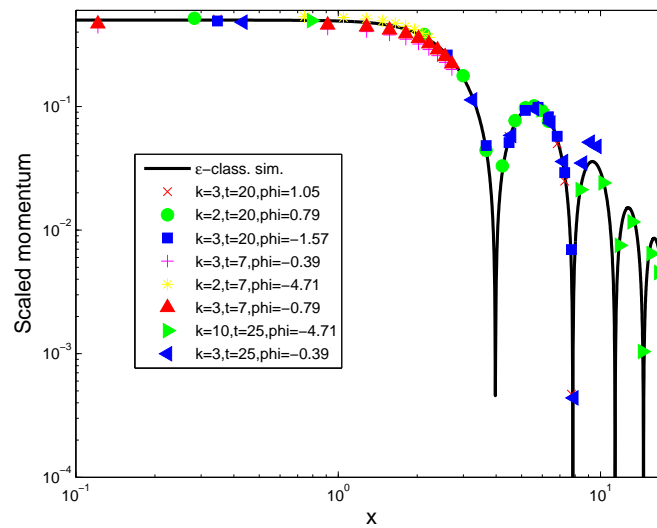


Fig. 20. The absolute value of the ϵ -classical scaling function (solid line) from Eq. (41). Here we compare the theory with simulation results for a range of parameters (symbols) as indicated in the legend. (Adapted figure with permission from Sadgrove and Wimberger (2009). Copyright 2009 of the New Journal of Physics.)

The one parameter scaling may be seen to capture the full dynamics of the resonance ratchet system. Indeed, Eq. (41) reveals a non-trivial feature of the off-resonant dynamics: current reversal (that is a negative mean momentum) is possible for certain parameter regimes *independent of the quantum phase ϕ* . This intriguing prediction has yet to be tested experimentally.

We now briefly return to the question of why replacing quantum superposition states with their associated classical probability distributions was a successful strategy here, when typically it would lead to a loss of the very quantum effects that are being modelled. One answer arises from a consideration of the role that momentum plays in ϵ -classical formalism. Say we start by setting the classical atomic position distribution to Eq. (39), as above. The problem is that with no uncertainty principle in play, the fixing of the position space distribution does not constrain the momentum distribution in the ϵ -classical system, as it does in the quantum system (according to the Fourier transform). Thus our choice of Eq. (38) is rather arbitrary. However, when the quasi-momentum distribution is very narrow (or $\tau \rightarrow 0$) and, more importantly, when ϵ is small, the precise details of the momentum distribution are unimportant in the ϵ -classical model, as inspection of Eq. (11) along with the definition of $I = |\epsilon|N$ shows. Thus, our choice of the classical analog to the quantum position distribution rewards us by successfully capturing position space correlations important to the ratchet dynamics, and the ϵ -classical formalism's indifference to the exact details of the momentum distribution mean that we do not have to pay any price for its ill-defined nature.

3.5 Fidelity as a measure of stability

In this Section we present a further tool to characterize the stability of the QR and near QR motion of the QKR, supporting our results in Sections 3.1–3.3.

Entanglement measures or witnesses have become modern tools of correlation analysis in multipartite quantum systems (Horodecki et al., 2009). For single-particle systems some correlations can only build up during their temporal evolution, just like the kick-to-kick correlations for the QKR (see Section 1.1). It is then the evolution of relative phases and the superposition principle which distinguish quantum from classical dynamics. Correlation functions may be used to monitor phase evolutions (Walls and Milburn, 2008). A related quantity which has gained much interest in the last decade is fidelity (Gorin et al., 2006), defined as the overlap of two wavefunctions subjected to slightly different temporal evolutions. The temporal evolution of this quantum fidelity crucially depends on evolving relative phases. For many-particle systems, fidelity can be viewed as a Hilbert space measure to study quantum phase transitions (Buonsante and Vezzani, 2007) or local and global spec-

tral properties (Plötz et al., in press). Fidelity was introduced originally as a measure for the stability of quantum motion with respect to changes in some control parameter of the Hamiltonian (Peres, 1984). In our case this parameter will be the kicking strength. The predicted saturation of fidelity at exact QR (Wimberger and Buchleitner, 2006) reported in the following Subsection has only recently been confirmed experimentally (Wu et al., 2009), while our predictions for finite detunings (Abb et al., 2009) of Subsection 3.6 still await experimental verification.

3.5.1 Fidelity at exact quantum resonance

Using the kick-to-kick operator from Eq. (2), the fidelity can be written (Wimberger, 2004; Wimberger and Buchleitner, 2006)

$$F(k_1, k_2, t) = \left| \int_0^1 d\beta \rho(\beta) \langle \hat{\mathcal{U}}_{\beta, k_1}^t \Psi_\beta | \hat{\mathcal{U}}_{\beta, k_2}^t \Psi_\beta \rangle \right|^2, \quad (43)$$

where we note that the kick-to-kick operator is applied t times, and the kicking strengths k_1 and k_2 have distinct values, their difference giving the strength of the relative perturbation under the two time evolutions. The fidelity results from averaging the scalar product under the integral sign over β with the weight $\rho(\beta)$. Note that the rotor's fidelity is the squared modulus of this quantity, so the fidelity of Eq. (43) of atomic evolution does not coincide with the β -average of the rotors' fidelities (Wimberger and Buchleitner, 2006). In good approximation of experiments, the initial rotor states Ψ_β can be taken to be plane waves. $\Psi_\beta(\theta) = (2\pi)^{-1/2}$ if only the zero momentum class is initially populated (which we will assume in the following discussion). For kicking periods at exact QR, i.e. $\tau = 2\pi\ell$ ($\ell \in \mathbb{N}$), the fidelity may be derived analytically to be $\left| \langle \hat{\mathcal{U}}_{\beta, k_1}^t \Psi_\beta | \hat{\mathcal{U}}_{\beta, k_2}^t \Psi_\beta \rangle \right|^2 = J_0^2(|W_t|\Delta k)$, where J_0 is the Bessel function of 1st kind and order 0, $\Delta k = k_2 - k_1$ and $|W_t| = |\sin(\pi t \ell (\beta - \frac{1}{2})) \csc(\pi \ell (\beta - \frac{1}{2}))|$ (Wimberger et al., 2003; Wimberger and Buchleitner, 2006). With $|W_t| = t$ for resonant quasimomenta β and using the asymptotic expansion formula [9.2.1] from (Abramowitz and Stegun, 1972) for Bessel function J_0 , one further arrives at $F_{\beta_{\text{res}}}(t) \simeq \frac{2}{\pi \Delta k t} \cos^2\left(\Delta k t - \frac{\pi}{4}\right)$. This shows that the fidelity decay is very slow obeying a power law $\propto 1/t$ for the resonant β -states. For an ensemble of initial atoms representing a broad quasi-momentum distribution with $\rho(\beta) = 1$, an interesting freeze or saturation of fidelity occurs, typically already after a small number of kicks which immediately made this result accessible to experiments performed by the Harvard group (Wu et al., 2009):

$$F(k_1, k_2, t \rightarrow \infty) \rightarrow F^*(\Delta k) \equiv \frac{1}{(2\pi)^2} \left(\int_0^{2\pi} dy J_0^2\left(\frac{\Delta k}{2 \sin(y)}\right) \right)^2. \quad (44)$$

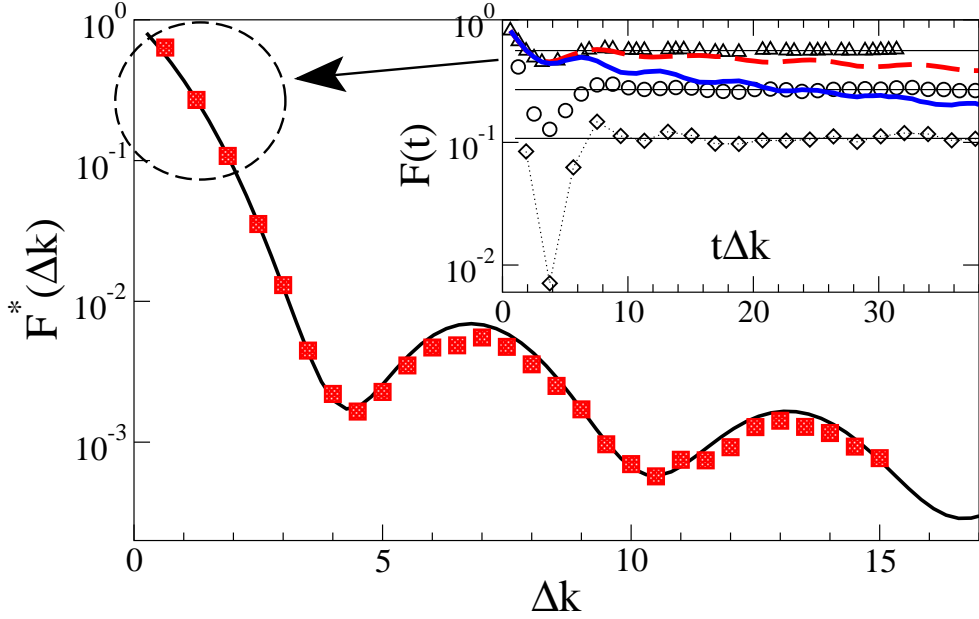


Fig. 21. $F^*(\Delta k)$ from Eq. (44) (solid line), compared with numerical data (red squares) obtained by evolving ensembles of 10^4 β -rotors with an initially uniform momentum distribution in $[0, 1)$, at $\tau = 2\pi$ and $t = 50$. Inset: numerically computed fidelity ($F(t) \equiv F(k_1, k_2, t)$) vs. $t\Delta k$ for $\tau = 2\pi$, $k_1 = 0.8\pi$, and fixed $\Delta k = 0.6283$ (triangles), 1.257 (circles), 1.885 (diamonds). The position of the minima corresponds to the time $3.83/\Delta k$. The fidelity saturates for times $t\Delta k \gtrsim 20$ at Δk -dependent, constant values, indicated by the thin horizontal lines. Data for finite detunings $\epsilon = 0.025$ (red dashed) and 0.1 (blue thick solid line) are shown for $\Delta k = 0.6283$. (Figure adapted from Wimberger and Buchleitner (2006)).

This result is strictly true only in the limit of a large number of kicks, but practically the saturation is reached after $t \sim \Delta k^{-1}$ kicks. This follows from the minima in the inset in Fig. 21 which are found by differentiating the time-dependent fidelity with respect to Δk . Then, the first zero of the 1st order Bessel function $J_1(t\Delta k)$ at $t\Delta k \simeq 3.83$ is essentially responsible for the observed minima. Interestingly, $F^*(\Delta k)$ oscillates quasiperiodically rather than dropping monotonically as a function of the perturbation Δk , another feature which highlights the stability of the QR dynamics of the QKR. The aforementioned features are all illustrated in Fig. 21 which also shows that strict saturation is destroyed by arbitrarily small detunings $\epsilon \equiv 2\pi\ell - \tau$ from resonance. However, the temporal decay of the fidelity depends continuously on ϵ and is again slow for small ϵ . This implies that the predicted saturation is an *experimentally robust* observable (Wu et al., 2009). In the following Subsection, we will use the pseudo-classical approach of Section 2.3 to compute the long-time behaviour of fidelity for near resonant rotors.

3.6 Pseudo-classical theory for fidelity

We have seen above in Section 2.3 that the resonant rotor dynamics essentially corresponds to the pseudo-classical motion astride a nonlinear resonance island, provided ϵ is sufficiently small. We consider from now on only initial atomic states with a narrow distribution of momenta near $p = 0$. This means that we restrict ourselves to a portion of the pseudo-classical phase space that contains only the principal resonance island which is located at $J = 2\pi$ or $I = 0$ (assuming $\ell = 1$ for the rest of this Subsection). At the centre of that island we have a stable elliptic fixed point of the pseudo-classical standard map, and the motion around it can be locally approximated by a simple harmonic oscillator Hamiltonian

$$H(I, \theta) = \frac{1}{2}(I + \bar{\beta})^2 + \frac{\omega^2}{2}\theta^2, \quad (45)$$

where $\omega \equiv \sqrt{\tilde{k}}$, $\bar{\beta} \equiv \tau\beta - \pi \approx \tau(\beta - 0.5)$, and a shift of θ by π is understood. Using this approximation of the dynamics along the nonlinear resonance island, we can directly compute the fidelity using semi-classical wavefunctions of the form

$$\hat{\mathcal{U}}_{\beta,k}^t \Psi_{\beta}(\theta) \sim \frac{1}{\sqrt{2\pi}} \sum_s \left| \frac{\partial\theta}{\partial\theta'} \right|_{\theta'=\theta'_s}^{-1/2} e^{i\epsilon\Phi_s(\theta,t) - i\frac{\pi}{2}\nu_s}, \quad (46)$$

where we chose as initial state a zero momentum plane wave $\Psi_{\beta}(\theta) = (2\pi)^{-1/2}$ and $\epsilon > 0$ is assumed with no limitation of generality. The sum is over all trajectories (labeled by the index s) which start with $I = 0$ at $t = 0$ and reach position θ at after a number of kicks t . $\theta' = \theta'_s$ are their initial positions, and the function whose derivative is taken in the pre-factor yields θ at time t as a function of position θ' at $t = 0$, given that the initial momentum $I' = 0$. Finally, the function $\Phi_s(\theta, t) = S(\theta, \theta'_s, t)$ is the action of the s -th trajectory and ν_s is the Morse-Maslov index (Haake, 2000; Schulman, 1981). Except at exact multiples of the period, there is one harmonic oscillator trajectory in the sum in Eq. (46); moreover, Maslov indices do not depend on the trajectory in this case. Straightforward calculation of the action integral (Abb, 2009) yields $\theta'(\theta, t) = \sec(\omega t)(\theta - \bar{\beta}\omega^{-1}\sin(\omega t))$ and $\Phi(\theta, t) = \bar{\beta}\theta(\sec(\omega t) - 1) - (\omega^{-1}\bar{\beta}^2 + \omega\theta^2)\tan(\omega t)/2$, giving

$$\langle \hat{\mathcal{U}}_{\beta,k_1}^t \Psi_{\beta} | \hat{\mathcal{U}}_{\beta,k_2}^t \Psi_{\beta} \rangle \sim \frac{e^{i\lambda(t)}}{2\pi\sqrt{|\cos(\omega_1 t)\cos(\omega_2 t)|}} \int_{-\pi}^{\pi} d\theta e^{\frac{i}{2\epsilon}\{A(t)\theta^2 + C(t)\bar{\beta}^2 - 2\bar{\beta}\theta B(t)\}}, \quad (47)$$

where $\omega_{1,2} \equiv \sqrt{\tilde{k}_{1,2}}$. Additionally, we have defined $A(t) = \omega_2 \tan(\omega_2 t) - \omega_1 \tan(\omega_1 t)$, $B(t) = \sec(\omega_2 t) - \sec(\omega_1 t)$, and $C(t) = \omega_2^{-1} \tan(\omega_2 t) - \omega_1^{-1} \tan(\omega_1 t)$. $\lambda(t)$ is a phase factor accumulated by the Maslov indices which depends only on time, rendering it irrelevant to the computation of fidelity. We next insert Eq. (47) in Eq. (43) and choose for $\rho(\beta)$ a uniform distribution in some interval $[\frac{1}{2} - b, \frac{1}{2} + b)$, with $0 \leq b \leq 1/2$. It is necessary to assume that b is smaller than the halfwidth of the pseudo-classical resonant island, because the harmonic approximation we have started from is, of course, valid just inside the island. Then

$$F(k_1, k_2, t) \sim \frac{\left| \int_{-\pi}^{\pi} d\theta e^{-\frac{i}{2\epsilon} \Lambda_1(\theta, \epsilon, t)} \int_{-\tau b}^{\tau b} d\bar{\beta} e^{-\frac{i}{2\epsilon} \Lambda_2(\bar{\beta}, \theta, \epsilon, t)} \right|^2}{16\pi^2 b^2 \tau^2 |\cos(\omega_1 t) \cos(\omega_2 t)|}, \quad (48)$$

where $\Lambda_1(\theta, \epsilon, t) = (A(t) - B^2(t)C(t)^{-1})\theta^2$ and $\Lambda_2(\bar{\beta}, \theta, \epsilon, t) = (\bar{\beta}\sqrt{C(t)} - B(t)C(t)^{-1/2}\theta)^2$. As $\Lambda_2 \sim \epsilon^{-1/2}$ in the limit when $\epsilon \rightarrow 0$ and $t\sqrt{\epsilon} \sim \text{const.}$, the limits in the $\bar{\beta}$ -integral in Eq. (48) can be taken to $\pm\infty$ to yield

$$\int_{-\tau b}^{\tau b} d\bar{\beta} e^{-\frac{i}{2\epsilon} \Lambda_2(\bar{\beta}, \theta, \epsilon, t)} \sim (2\pi)^{1/2} \epsilon^{1/2} C(t)^{-1/2} e^{-i\pi/4}.$$

Due to this approximation, Eq. (49) below is valid in the regime where ϵ is small compared to b^2 . The remaining θ -integral is dealt with similarly, because the pre-factor of θ^2 in Λ_1 is $\sim \epsilon^{-1/2}$. Thus finally

$$\begin{aligned} F(k_1, k_2, t) &\sim \frac{\epsilon^2}{16\pi^2 b^2 |C(t)A(t) - B(t)^2| |\cos(\omega_1 t) \cos(\omega_2 t)|} \\ &= \frac{\epsilon^2 \omega_1 \omega_2}{8\pi^2 b^2 |4\omega_1 \omega_2 - \omega_+^2 \cos(\omega_- t) - \omega_-^2 \cos(\omega_+ t)|}, \end{aligned} \quad (49)$$

where $\omega_{\pm} = \omega_1 \pm \omega_2$. Singularities of this expression are artifacts of the approximations used in evaluating the integrals in Eq. (48), which indeed break down when the divisor in Eq. (49) is small compared to ϵ . However, they account for the ‘‘revivals’’ of the fidelity occurring periodically with the beating period $T_{12} = 2\pi/|\omega_-|$. For purely resonant rotors (here $\beta = 1/2$), the revivals occur with the period $T_{12}/2$. This can be seen by evaluating Eq. (48) with just one, the purely resonant β , to arrive at

$$\begin{aligned} F(k_1, k_2, t) &\equiv F_{res}(k_1, k_2, t) \\ &\sim \frac{\epsilon/(2\pi)}{|\omega_2 \cos(\omega_1 t) \sin(\omega_2 t) - \omega_1 \cos(\omega_2 t) \sin(\omega_1 t)|}, \end{aligned} \quad (50)$$

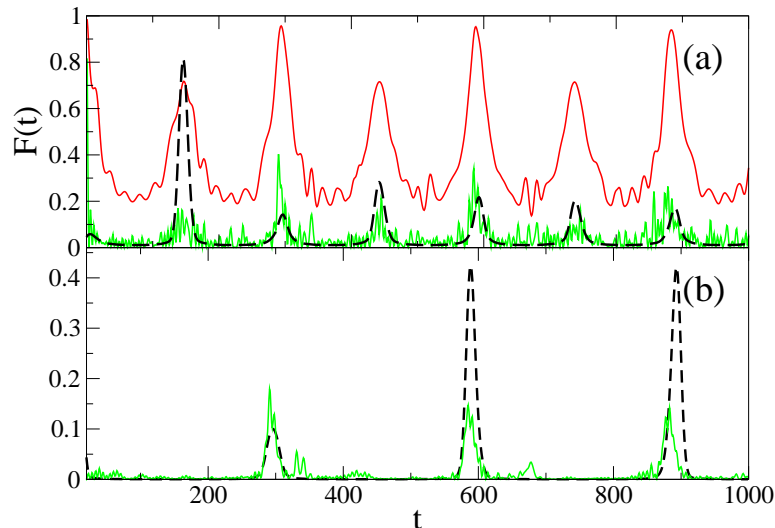


Fig. 22. (a) Fidelity as predicted by Eq. (50) – because of the singularities of the analytical formula the curve is folded with normalized Gaussians with a standard deviation of $t \approx 6$ kicks (dashed black line) – and numerical data for a single resonant rotor (grey/green curve) and a coherent initial state built up for fixed resonant $\beta = 1/2$ and centred at the elliptic fixed point of the island (solid red/dark line), for $k_1 = 0.8\pi$, $k_2 = 0.6\pi$ and detuning $\epsilon = 0.01$ from $\tau - \epsilon = 2\pi$. The coherent state shows almost perfect revivals at T_{12} and slightly smaller ones at the intermediate peaks. (b) Same as in (a) for an ensemble of 5000 equidistantly chosen rotors (grey/green curve) with a width of $\Delta\beta = 0.05$ (or $\Delta\bar{\beta} \approx 0.31$) around the resonant value, covering half the width of the resonance island in the phase space induced by Eq. (11) compared with the smoothed version of Eq. (49) (dashed black line). The intermediate revival peaks observed in (a) disappear as predicted by Eq. (49).

which has singularities with the mentioned periodicity of $T_{12}/2$. This behaviour of resonant rotors has a simple qualitative explanation. The stationary-phase trajectories of the two harmonic oscillators, which were started at $I = 0$, exactly return to $I = 0$ whenever time is a multiple of the half-period $T_{12}/2$, and so fully contribute to fidelity, in spite of their angles being different by π in the case of odd multiples. At $\beta \neq 0$ this symmetry is lost, which suppresses each second revival according to Eq. (49).

Comparing numerical data (obtained by repeated application of the Floquet operator to the initial wavefunction) with the analytical predictions we find fairly good agreement. We observe the expected peak structure of the revivals in Fig. 22(a) and the loss of intermediate revival peaks at $T_{12}/2$ in Fig. 22(b). An experimental observation of these revivals is quite challenging since a good control over a narrow initial distribution of quasimomenta and a stable experiment over a relatively large number of kicks are both required. The time scale on which the revivals occur is proportional to $\epsilon^{-1/2}$ and of crucial impact to experimental measurements. A conservation of coherence has been shown for up to 150 kicks (see e.g. ref. (Schlunk et al., 2003b)) with cold atoms, making

an observation of the revivals for reasonable $\epsilon \lesssim 0.01$ possible. Earlier realizations of the QKR were implemented using cold atoms (Moore et al., 1995; Ammann et al., 1998; Bharucha et al., 1999; d’Arcy et al., 2001; Sadgrove et al., 2005; d’Arcy et al., 2004) with broad distributions in quasi-momentum. Nowadays, much better control of quasi-momentum is provided by using BECs (see (Duffy et al., 2004b; Ryu et al., 2006; Ramareddy et al., 2010)), which allows for a restriction in β up to 0.2 % of the Brillouin zone (as achieved, e.g., in (Ryu et al., 2006)). This would allow the verification of our results by reducing the intervals in quasi-momentum and thus retracing the revivals with period $T_{12}/2$ to the exactly resonant and the revivals with period T_{12} to the near-resonant rotors. There exists a second possibility to measure the transition from Eq. (50) to Eq. (49) with just cold atoms, since the $\bar{\beta}$ we use scales with the kicking period, i.e. $\bar{\beta} \approx \tau(\beta - 1/2)$. Due to this scaling, the limit $\tau \rightarrow 0$ (automatically implying also $\epsilon \rightarrow 0$, c.f. Section 3.2) permits a measurement of Eq. (50), even with an ensemble of cold atoms whose quasimomenta occupy the full Brillouin zone. This Subsection exclusively focused on the evolution of fidelity corresponding to librational motion within the nonlinear resonance island of the pseudo-classical phase space. Ongoing research is currently extending our understanding to non-resonant values of quasi-momentum corresponding to rotational orbits in phase space (Probst, 2010). It remains to combine these two classes of motion in order to provide a full account of the behaviour seen in the inset of Fig. 21 for finite ϵ .

4 Conclusions and outlook

4.1 Review of the state of the art

While the principle aim of this review is to introduce the ϵ -classical method to a wider audience, we would also like to think that it serves to illustrate the way that physics progresses in a microcosm. The interplay between theory and experiment in this particular field has driven the method well beyond the tasks for which it was originally conceived. At times, the desire to verify new details turned up by the theory has been the driving force of investigations. Just as often, the observation of new phenomena, or the modification of an experiment has motivated the extension of the theory.

Below, we recap the uses to which the ϵ -classical theory has so far been put in list form:

- (1) **Analysis of quantum accelerator modes.** Although outside the scope of this review, we note that these studies marked the invention of the ϵ -classical map (Fishman et al., 2002).

- (2) **Reduction of near-resonant quantum dynamics to a one-parameter scaling law.** The quantum kicked rotor until very recently remained a theoretically opaque system in that quantum correlations between kicks could only be evaluated precisely up to $N \sim 5$ and the exact behaviour was sensitive to three principle parameters – kick strength, kick number, and the period of the kicks. The application of a pendulum approximation to the ϵ -classical approximation allowed the entire problem to be reduced to a one parameter scaling function for the dynamics near to resonance.

New features predicted and measured by the scaling law. The ϵ -classical scaling law for dynamics of the AOKR near QR predicted some features which had not been noticed before in experimental or numerical studies. In particular, side peaks around the quantum resonance were predicted and measured, and anomalous behaviour including frozen and ballistic energy growth near the actual semi-classical limit were predicted and observed experimentally. The observation of these effects also served to demonstrate that quantum resonance peaks exhibit sub-Fourier narrowing with respect to the applied pulse train – a phenomenon predicted clearly by the scaling law for the resonances.

- (3) **Modelling of the effect of spontaneous emission near quantum resonance.** The study of spontaneous emission in the kicked rotor near quantum resonance showed that the effect on the dynamics of a decoherence process could be captured using a quasi-classical model.
- (4) **Explanation of stability of QR against large amplitude fluctuations.** The puzzle of why amplitude fluctuations destroy some quantum coherent effects (notably dynamical localization) but leave near resonant dynamics largely unchanged was solved by modifying the ϵ -classical map to include amplitude fluctuations. However, such fluctuations have little effect on the phase space, explaining why the quantum resonance peaks are robust.

Scaling law in the presence of amplitude fluctuations. An explanation of the stability of the QR peaks in the presence of amplitude noise was finally given in terms of a scaling law. By observing that the noise changed the phase space predominantly around the separatrix, an approximate scaling law was derived, extending analytical results to the system in the presence of a common source of decoherence.

- (5) **Scaling law for directed transport experiments (quantum resonance ratchets).** Choosing the appropriate classical initial conditions allows the pseudo-classical method to be extended to the case where the initial state is a quantum superposition of momentum states. Once again, extending the scaling law to this variant of the kicked rotor predicts new dynamics such as current reversal for slight detunings from exact QR.
- (6) **Fidelity of kicked rotors described pseudo-classically.** Although the concept of fidelity is inherently quantum mechanical, the pseudo-classical method was once again extended to describing the evolution of

the phase sensitive fidelity in the AOKR near QR.

4.2 *Future perspectives for the pseudo-classical method*

The state of the art in AOKR experiments is arguably represented by experiments on atoms with very narrow initial momentum distributions (typically sourced from a BEC) and indeed for the last two topics listed above, a BEC would be necessary to fully test the new phenomena suggested by the theory. We note that, of course, there are topics outside of quantum resonance where studies of the kicked rotor are being extended and even thermal atoms still allow the measurement of very interesting new results (such as the metal-insulator transition reported in Chabé et al. (2008)). Such studies are outside the scope of the present review.

However, we tend to believe that the quantum resonance phenomenon in the AOKR provides the most fertile ground for new applications of cold atoms in time dependent optical lattices. It is interesting to note, for example, that the momentum current in the first “atom motor” (i.e. Hamiltonian quantum ratchet) experiment was sharply peaked around quantum resonance (Salger et al., 2009). Additionally, the extension of the pseudo-classical method to quantum fidelity and the fact that the Talbot effect has been used to perform factorization (Bigourd et al., 2008; Mack et al., 2002) suggests that the ϵ -classical method might be applicable in quantum information settings.

Slightly more prosaically, it should be noted that the extension of the ϵ -classical theory to fractional quantum resonances still represents a challenge (c.f. results in this direction for the accelerator modes in the amended QKR (Guarneri and Rebuzzini, 2008)), even though the fractional resonances have been measured carefully in both ultra-cold by Ryu et al. (2006) and cold atom settings by Kanem et al. (2007). That this task represents more of a challenge than extending the theory to some of the interesting variants of the AOKR explored above, serves as a reminder that the derivation of analytical results in the AOKR system is still not a trivial task in general.

Qualitatively new directions of research would include the effects of either atom-atom interactions (Rebuzini et al., 2005, 2007; Monteiro et al., 2009; Wimberger et al., 2005a) or the dissipative opening of kicked atomic systems (Carlo et al., 2006; Benenti et al., 2001; Schomerus and Tworzydło, 2004; Tomadin et al., 2006; Facchini et al., 2007; Romanelli, 2009). For instance, the stability of QR motion with respect to typical values of a mean-field non-linearity arising from atom-atom interactions in a BEC was numerically predicted in Wimberger et al. (2005a) and experimentally tested in Ryu et al. (2006), yet an extension to near resonant motion is desirable, in particular by

analytical means. New ideas based on the pseudo-classical method may allow us to take into account such complications in a more or less rigorous way.

5 Acknowledgements

The work reported in this review was supported by the Alexander von Humboldt Foundation, the Heidelberg Centre for Quantum Dynamics, the Excellence Initiative by the German Research Foundation (DFG) through the Heidelberg Graduate School of Fundamental Physics (Grant No. GSC 129/1), the Frontier Innovation Fonds and the Global Networks Mobility Measures of the University of Heidelberg. We are indebted to Ken'ichi Nakagawa and the staff of the Institute for Laser Science for their support and hospitality. S.W. is grateful to the Heidelberg Academy of Sciences and Humanities for the Academy Award 2010 and to the Hengstberger Foundation for support by the Klaus-Georg and Sigrid Hengstberger Prize 2009. Finally, we would like to warmly thank our collaborators, Andreas Buchleitner, Italo Guarneri, Shmuel Fishman, Scott Parkins, Rainer Leonhardt, Terry Mullins, Andrew Hilliard, Roberto Artuso, Michael d'Arcy, Gil Summy, Riccardo Mannella, Andrea Tomadin, Angelo Facchini, Martina Abb, Benedikt Probst, and Remy Dubertrand, for their help in pushing forward research based on the AOKR system.

References

- Abb, M., 2009. Fidelity for kicked atoms at nearly resonant driving. Master's thesis, University of Heidelberg.
- Abb, M., Guarneri, I., Wimberger, S., Sep 2009. Pseudoclassical theory for fidelity of nearly resonant quantum rotors. *Phys. Rev. E* 80 (3), 035206.
- Abramowitz, M., Stegun, I. A., 1972. Handbook of mathematical functions. Dover, New York.
- Ammann, H., Gray, R., Shvarchuck, I., Christensen, N., May 1998. Quantum delta-kicked rotor: Experimental observation of decoherence. *Phys. Rev. Lett.* 80 (19), 4111–4115.
- Anderson, P. W., Mar 1958. Absence of diffusion in certain random lattices. *Phys. Rev.* 109 (5), 1492–1505.
- Arndt, M., Buchleitner, A., Mantegna, R. N., Walther, H., Oct 1991. Experimental study of quantum and classical limits in microwave ionization of rubidium rydberg atoms. *Phys. Rev. Lett.* 67 (18), 2435–2438.
- Bayfield, J. E., Casati, G., Guarneri, I., Sokol, D. W., Jul 1989. Localization of classically chaotic diffusion for hydrogen atoms in microwave fields. *Phys. Rev. Lett.* 63 (4), 364–367.

- Benenti, G., Casati, G., Guarneri, I., Terraneo, M., Jun 2001. Quantum fractal fluctuations. *Phys. Rev. Lett.* 87 (1), 014101.
- Bharucha, C. F., Robinson, J. C., Moore, F. L., Sundaram, B., Niu, Q., Raizen, M. G., Oct 1999. Dynamical localization of ultracold sodium atoms. *Phys. Rev. E* 60 (4), 3881–3895.
- Bigourd, D., Chatel, B., Schleich, W. P., Girard, B., Jan 2008. Factorization of numbers with the temporal talbot effect: Optical implementation by a sequence of shaped ultrashort pulses. *Phys. Rev. Lett.* 100 (3), 030202.
- Billy, J., Josse, V., Zuo, Z., Bernard, A., Hambrecht, B., Lugan, P., Clément, D., L. Sanchez-Palencia, P. B., Aspect, A., 2008. Direct observation of anderson localization of matter waves in a controlled disorder. *Nature* 453, 891.
- Blümel, R., Fishman, S., Smilansky, U., 1986. Excitation of molecular rotation by periodic microwave pulses – a testing ground for anderson localization. *J. Chem. Phys.* 84, 2604.
- Bourgain, J., 2002. Estimates on green’s functions, localization and the quantum kicked rotor model. *Ann. Math.* 156, 249.
- Brenner, N., Fishman, S., 1992. Pseudo-randomness and localization. *Nonlinearity* 5 (1), 211.
- Brouard, S., Plata, J., 2003. Quantum -kicked rotor: the effect of amplitude noise on the quantum resonances. *Journal of Physics A: Mathematical and General* 36 (13), 3745.
- Buonsante, P., Vezzani, A., Mar 2007. Ground-state fidelity and bipartite entanglement in the bose-hubbard model. *Phys. Rev. Lett.* 98 (11), 110601.
- Carlo, G. G., Benenti, G., Casati, G., Wimberger, S., Morsch, O., Mannella, R., Arimondo, E., Sep 2006. Chaotic ratchet dynamics with cold atoms in a pair of pulsed optical lattices. *Phys. Rev. A* 74 (3), 033617.
- Casati, G., Chirikov, B., Ford, J., Izrailev, F., 1979. *Stochastic Behavior in Classical and Quantum Hamiltonian Systems*. Springer, Berlin, Ch. Stochastic Behavior of A Quantum Pendulum Under Periodic Perturbation.
- Casati, G., Guarneri, I., Shepelyansky, D., 1988. Hydrogen atom in monochromatic field: chaos and dynamical photonic localization. *IEEE J. Quantum Electron.* 24, 1420.
- Chabé, J., Lemarié, G., Grémaud, B., Delande, D., Szriftgiser, P., Garreau, J. C., 2008. Experimental observation of the anderson metal-insulator transition with atomic matter waves. *Phys. Rev. Lett.* 101, 255702.
- Chirikov, B. V., 1979. A universal instability of many-dimensional oscillator systems. *Physics Reports* 52 (5), 263 – 379.
- Curri van, J.-A., Ullah, A., Hoogerland, M. D., 2009. The initial velocity dependence of the quantum resonance in the delta-kicked rotor. *Europhys. Lett.* 85, 3005.
- Daley, A. J., Parkins, A., Leonhardt, R., Tan, S. M., 2002. Diffusion resonances in action space for an atom optics kicked rotor with decoherence. *Phys. Rev. E* 65, 035201(R).
- Daley, A. J., Parkins, A. S., Nov 2002. Early time diffusion for the quan-

- tum kicked rotor with narrow initial momentum distributions. *Phys. Rev. E* 66 (5), 056210.
- Dana, I., Dorofeev, D. L., Oct 2006. Fluctuations and transients in quantum-resonant evolution. *Phys. Rev. E* 74 (4), 045201.
- Dana, I., Ramareddy, V., Talukdar, I., Summy, G. S., Jan 2008. Experimental realization of quantum-resonance ratchets at arbitrary quasimomenta. *Phys. Rev. Lett.* 100 (2), 024103.
- d’Arcy, M. B., Godun, R. M., Oberthaler, M. K., Cassettari, D., Summy, G. S., Jul 2001. Quantum enhancement of momentum diffusion in the delta-kicked rotor. *Phys. Rev. Lett.* 87 (7), 074102.
- d’Arcy, M. B., Godun, R. M., Summy, G. S., Guarneri, I., Wimberger, S., Fishman, S., Buchleitner, A., Feb 2004. Decoherence as a probe of coherent quantum dynamics. *Phys. Rev. E* 69 (2), 027201.
- Deng, L., Hagley, E. W., Denschlag, J., Simsarian, J. E., Edwards, M., Clark, C. W., Helmerson, K., Rolston, S. L., Phillips, W. D., Dec 1999. Temporal, matter-wave-dispersion talbot effect. *Phys. Rev. Lett.* 83 (26), 5407–5411.
- Dubetsky, B., Berman, P. R., 1997. Atomic interferometry. *Adv. At. Mol. Phys.* 37, 407, suppl. 3.
- Duffy, G. J., Mellish, A. S., Challis, K. J., Wilson, A. C., Oct 2004a. Nonlinear atom-optical δ -kicked harmonic oscillator using a bose-einstein condensate. *Phys. Rev. A* 70 (4), 041602.
- Duffy, G. J., Parkins, S., Müller, T., Sadgrove, M., Leonhardt, R., Wilson, A. C., Nov 2004b. Experimental investigation of early-time diffusion in the quantum kicked rotor using a bose-einstein condensate. *Phys. Rev. E* 70 (5), 056206.
- Dunlap, D. H., Kenkre, V. M., Sep 1986. Dynamic localization of a charged particle moving under the influence of an electric field. *Phys. Rev. B* 34 (6), 3625–3633.
- Facchini, A., Wimberger, S., Tomadin, A., 2007. Multifractal fluctuations in the survival probability of an open quantum system. *Physica A: Statistical Mechanics and its Applications* 376, 266 – 274.
- Feynman, R. P., 1963. *The Feynman Lectures on Physics*. Vol. 1. Addison-Wesley, ch. 46.
- Fishman, S., 1993. *Quantum Chaos*. IOS – North Holland, Amsterdam, Ch. Quantum Localization, school “E. Fermi” CXIX.
- Fishman, S., Grempel, D. R., Prange, R. E., Aug 1982. Chaos, quantum recurrences, and anderson localization. *Phys. Rev. Lett.* 49 (8), 509–512.
- Fishman, S., Grempel, D. R., Prange, R. E., Jul 1987. Temporal crossover from classical to quantal behavior near dynamical critical points. *Phys. Rev. A* 36 (1), 289–305.
- Fishman, S., Guarneri, I., Rebuzzini, L., Aug 2002. Stable quantum resonances in atom optics. *Phys. Rev. Lett.* 89 (8), 084101.
- Flach, S., Yevtushenko, O., Zolotaryuk, Y., 2000. Directed current due to broken time-space symmetry. *Phys. Rev. Lett.* 84, 2358.
- Galvez, E. J., Sauer, B. E., Moorman, L., Koch, P. M., Richards, D., Oct 1988.

- Microwave ionization of h atoms: Breakdown of classical dynamics for high frequencies. *Phys. Rev. Lett.* 61 (18), 2011–2014.
- Gong, J., Brumer, P., Dec 2006. Generic quantum ratchet accelerator with full classical chaos. *Phys. Rev. Lett.* 97 (24), 240602.
- Gorin, T., Prosen, T., Seligman, T. H., Znidaric, M., 2006. Dynamics of loschmidt echoes and fidelity decay. *Physics Reports* 435 (2-5), 33 – 156.
- Graham, R., Schlautmann, M., Zoller, P., Jan 1992. Dynamical localization of atomic-beam deflection by a modulated standing light wave. *Phys. Rev. A* 45 (1), R19–R22.
- Grepel, D. R., Fishman, S., Prange, R. E., Sep 1984. Finite-planck’s-constant scaling at stochastic transitions of dynamical systems. *Phys. Rev. Lett.* 53 (13), 1212–1215.
- Guarneri, I., 2009. On the spectrum of the resonant quantum kicked rotor. *Annales Henri Poincare* 10, 1097.
- Guarneri, I., Rebuzzini, L., Jun 2008. Quantum accelerator modes near higher-order resonances. *Phys. Rev. Lett.* 100 (23), 234103.
- Guarneri, I., Rebuzzini, L., Fishman, S., 2006. Arnol’d tongues and quantum accelerator modes. *Nonlinearity* 19 (5), 1141.
- Haake, F., 2000. *Quantum signatures of chaos*. Springer, Berlin.
- Hänggi, P., Marchesoni, F., Mar 2009. Artificial brownian motors: Controlling transport on the nanoscale. *Rev. Mod. Phys.* 81 (1), 387–442.
- Hogg, T., Huberman, B., 1983. Quantum dynamics and nonintegrability. *Phys. Rev. A* 28.
- Horodecki, R., Horodecki, P., Horodecki, M., Horodecki, K., Jun 2009. Quantum entanglement. *Rev. Mod. Phys.* 81 (2), 865–942.
- Izrailev, F., Shepelyansky, D., 1979. Quantum resonance for a rotator in a nonlinear periodic field. *Sov. Phys. Dokl.* 24, 996.
- Izrailev, F., Shepelyansky, D., 1980. Quantum resonance for a rotator in a nonlinear periodic field. *Theor. Math. Phys.* 43, 353.
- Izrailev, F. M., 1990. Simple models of quantum chaos: Spectrum and eigenfunctions. *Physics Reports* 196 (5-6), 299 – 392.
- Jitomirskaya, S., 2002. Non-perturbative localization. *Proceedings of the ICM* 3, 445, arXiv:math-ph/0304044.
- Jones, P. H., Goonasekera, M., Meacher, D. R., Jonckheere, T., Monteiro, T. S., Feb 2007. Directed motion for delta-kicked atoms with broken symmetries: Comparison between theory and experiment. *Phys. Rev. Lett.* 98 (7), 073002.
- Kanem, J. F., Maneshi, S., Partlow, M., Spanner, M., Steinberg, A. M., Feb 2007. Observation of high-order quantum resonances in the kicked rotor. *Phys. Rev. Lett.* 98 (8), 083004.
- Kierig, E., Schnorrberger, U., Schietinger, A., Tomkovic, J., Oberthaler, M. K., May 2008. Single-particle tunneling in strongly driven double-well potentials. *Phys. Rev. Lett.* 100 (19), 190405.
- Klappauf, B. G., Oskay, W. H., Steck, D. A., Raizen, M. G., Aug 1998. Observation of noise and dissipation effects on dynamical localization. *Phys.*

- Rev. Lett. 81 (6), 1203–1206.
- Krug, A., Wimberger, S., Buchleitner, A., 2003. Decay, interference, and chaos: How simple atoms mimic disorder. *Eur. Phys. J. D* 26, 21.
- Latka, M., West, B., 1995. Nature of quantum localization in atomic momentum transfer experiments. *Phys. Rev. Lett.* 75, 4202.
- Lee, P. A., Ramakrishnan, T. V., Apr 1985. Disordered electronic systems. *Rev. Mod. Phys.* 57 (2), 287–337.
- Lemarié, G., Lignier, H., Delande, D., Szriftgiser, P., Garreau, J. C., 2010. Critical state of the anderson transition: Between a metal and an insulator. *Phys. Rev. Lett.* 105, 090601.
- Lepers, M., Zehnlé, V., Garreau, J. C., Apr 2008. Kicked-rotor quantum resonances in position space. *Phys. Rev. A* 77 (4), 043628.
- Lichtenberg, A., Lieberman, M., 1992. *Regular and Chaotic Dynamics*. Springer, Berlin.
- Lignier, H., Sias, C., Ciampini, D., Singh, Y., Zenesini, A., Morsch, O., Arimondo, E., Nov 2007. Dynamical control of matter-wave tunneling in periodic potentials. *Phys. Rev. Lett.* 99 (22), 220403.
- Lundh, E., Wallin, M., Mar 2005. Ratchet effect for cold atoms in an optical lattice. *Phys. Rev. Lett.* 94 (11), 110603.
- Mack, H., Bienert, M., Haug, F., Straub, F. S., Freyberger, M., Schleich, W. P., 2002. H. mack and m. bienert and f. haug and f. s. straub and m. freyberger and w. p. schleich, arXiv:quant-ph/0204040v1.
- Madroñero, J., Ponomarev, A., Carvalho, A., Wimberger, S., Viviescas, C., Kolovsky, A., Hornberger, K., Schlagheck, P., Krug, A., Buchleitner, A., 2006. Quantum chaos, transport, and control - in quantum optics. *Adv. At. Mol. Opt. Phys.* 53, 33, elsevier.
- McDowall, P., Hilliard, A., McGovern, M., Grünzweig, T., Andersen, M. F., 2009. A fidelity treatment of near-resonant states in the atom-optics kicked rotor. *New Journal of Physics* 11 (12), 123021.
- Milner, V., Steck, D. A., Oskay, W. H., Raizen, M. G., Jun 2000. Recovery of classically chaotic behavior in a noise-driven quantum system. *Phys. Rev. E* 61 (6), 7223–7226.
- Monteiro, T. S., Dando, P. A., Hutchings, N. A. C., Isherwood, M. R., Oct 2002. Proposal for a chaotic ratchet using cold atoms in optical lattices. *Phys. Rev. Lett.* 89 (19), 194102.
- Monteiro, T. S., Rançon, A., Ruostekoski, J., Jan 2009. Nonlinear resonances in δ -kicked bose-einstein condensates. *Phys. Rev. Lett.* 102 (1), 014102.
- Moore, F. L., Robinson, J. C., Bharucha, C., Williams, P. E., Raizen, M. G., Nov 1994. Observation of dynamical localization in atomic momentum transfer: A new testing ground for quantum chaos. *Phys. Rev. Lett.* 73 (22), 2974–2977.
- Moore, F. L., Robinson, J. C., Bharucha, C. F., Sundaram, B., Raizen, M. G., Dec 1995. Atom optics realization of the quantum δ -kicked rotor. *Phys. Rev. Lett.* 75 (25), 4598–4601.
- Nath, N. S. N., 1936. The diffraction of light by high-frequency sound waves:

- Generalized theory. Proc. Indian Acad. Sci. 4, 222.
- Oberthaler, M. K., Godun, R. M., d'Arcy, M. B., Summy, G. S., Burnett, K., Nov 1999. Observation of quantum accelerator modes. Phys. Rev. Lett. 83 (22), 4447–4451.
- Oskay, W. H., Steck, D. A., Raizen, M. G., 2003. Timing noise effects on dynamical localization. Chaos, Solitons and Fractals 16 (3), 409 – 416.
- Peres, A., Oct 1984. Stability of quantum motion in chaotic and regular systems. Phys. Rev. A 30 (4), 1610–1615.
- Plötz, P., Lubasch, M., Wimberger, S., in press. Detection of avoided crossings by fidelity. Physica A ArXiv:0909.4333.
- Probst, B., 2010. The pendulum approximation for fidelity in quantum kicked rotor systems. Master's thesis, University of Heidelberg.
- Raizen, M., 1999. Quantum chaos with ultra-cold atoms. Adv. At. Mol. Phys. 41, 43.
- Ramareddy, V., Behinaein, G., Talukdar, I., Ahmadi, P., Summy, G. S., 2010. High-order resonances of the quantum -kicked accelerator. EPL (Europhysics Letters) 89 (3), 33001.
- Rebuzzini, L., Artuso, R., Fishman, S., Guarneri, I., Sep 2007. Effects of atomic interactions on quantum accelerator modes. Phys. Rev. A 76 (3), 031603.
- Rebuzzini, L., Wimberger, S., Artuso, R., Mar 2005. Delocalized and resonant quantum transport in nonlinear generalizations of the kicked rotor model. Phys. Rev. E 71 (3), 036220.
- Reimann, P., 2002. Brownian motors: noisy transport far from equilibrium. Physics Reports 361 (2-4), 57 – 265.
- Romanelli, A., 2009. Decoherence without classicality in the resonant quantum kicked rotor. Phys. Rev. A 80, 022102.
- Ryu, C., Andersen, M. F., Vaziri, A., d'Arcy, M. B., Grossman, J. M., Helmerston, K., Phillips, W. D., Apr 2006. High-order quantum resonances observed in a periodically kicked bose-einstein condensate. Phys. Rev. Lett. 96 (16), 160403.
- Sadgrove, M., 2005. Resonant quantum transport for kicked atoms. Ph.D. thesis, University of Auckland.
- Sadgrove, M., Hilliard, A., Mullins, T., Parkins, S., Leonhardt, R., Sep 2004. Observation of robust quantum resonance peaks in an atom optics kicked rotor with amplitude noise. Phys. Rev. E 70 (3), 036217.
- Sadgrove, M., Horikoshi, M., Sekimura, T., Nakagawa, K., Jul 2007. Rectified momentum transport for a kicked bose-einstein condensate. Phys. Rev. Lett. 99 (4), 043002.
- Sadgrove, M., Wimberger, S., 2009. Pseudo-classical theory for directed transport at quantum resonance. New Journal of Physics 11 (8), 083027.
- Sadgrove, M., Wimberger, S., Parkins, S., Leonhardt, R., May 2005. Ballistic and localized transport for the atom optics kicked rotor in the limit of a vanishing kicking period. Phys. Rev. Lett. 94 (17), 174103.
- Sadgrove, M., Wimberger, S., Parkins, S., Leonhardt, R., Aug 2008. Scaling

- law and stability for a noisy quantum system. *Phys. Rev. E* 78 (2), 025206.
- Salger, T., Kling, S., Hecking, T., Geckeler, C., Morales-Molina, L., Weitz, M., 2009. Directed Transport of Atoms in a Hamiltonian Quantum Ratchet. *Science* 326 (5957), 1241–1243.
- Schanz, H., Otto, M.-F., Ketzmerick, R., Dittrich, T., Jul 2001. Classical and quantum hamiltonian ratchets. *Phys. Rev. Lett.* 87 (7), 070601.
- Schlunk, S., d’Arcy, M. B., Gardiner, S. A., Cassettari, D., Godun, R. M., Summy, G. S., Feb 2003a. Signatures of quantum stability in a classically chaotic system. *Phys. Rev. Lett.* 90 (5), 054101.
- Schlunk, S., d’Arcy, M. B., Gardiner, S. A., Summy, G. S., Mar 2003b. Experimental observation of high-order quantum accelerator modes. *Phys. Rev. Lett.* 90 (12), 124102.
- Schomerus, H., Tworzydło, J., Oct 2004. Quantum-to-classical crossover of quasibound states in open quantum systems. *Phys. Rev. Lett.* 93 (15), 154102.
- Schulman, L. S., 1981. *Techniques and applications of path integration*. Wiley, New York.
- Sheinman, M., Fishman, S., Guarneri, I., Rebuzzini, L., May 2006. Decay of quantum accelerator modes. *Phys. Rev. A* 73 (5), 052110.
- Shepelyansky, D., 1987. Localization of diffusive excitation in multi-level systems. *Physica D* 28, 103.
- Talbot, H. F., 1836. Facts relating to optical science. *Philos. Mag.* 9, 401.
- Talukdar, I., Shrestha, R., Summy, G. S., Jul 2010. Sub-fourier characteristics of a δ -kicked-rotor resonance. *Phys. Rev. Lett.* 105 (5), 054103.
- Tian, C., Altland, A., 2010. Theory of localization and resonance phenomena in the quantum kicked rotor. *New Journal of Physics* 12 (4), 043043.
- Tomadin, A., Mannella, R., Wimberger, S., 2006. Can quantum fractal fluctuations be observed in an atom-optics kicked rotor experiment? *Journal of Physics A: Mathematical and General* 39 (10), 2477.
- Tonyushkin, A., Wu, S., Prentiss, M., May 2009. Demonstration of a multi-pulse interferometer for quantum kicked-rotor studies. *Phys. Rev. A* 79 (5), 051402.
- Vant, K., Ball, G., Ammann, H., Christensen, N., Mar 1999. Experimental evidence for the role of cantori as barriers in a quantum system. *Phys. Rev. E* 59 (3), 2846–2852.
- Walls, D. F., Milburn, G. J., 2008. *Quantum Optics*. Springer, Berlin.
- Wimberger, S., 2004. *Chaos and localisation: Quantum transport in periodically driven atomic systems*. Ph.D. thesis, Ludwig-Maximilians-Universität Munich and Università degli Studi dell’Insubria, available online at <http://edoc.ub.uni-muenchen.de/archive/00001687>.
- Wimberger, S., Buchleitner, A., 2001. Signatures of anderson localization in the ionization rates of periodically driven rydberg states. *Journal of Physics A: Mathematical and General* 34 (36), 7181.
- Wimberger, S., Buchleitner, A., 2006. Saturation of fidelity in the atom-optics kicked rotor. *Journal of Physics B: Atomic, Molecular and Optical Physics*

- 39 (7), L145.
- Wimberger, S., Guarneri, I., Fishman, S., 2003. Quantum resonances and decoherence for -kicked atoms. *Nonlinearity* 16 (4), 1381.
- Wimberger, S., Guarneri, I., Fishman, S., Feb 2004. Classical scaling theory of quantum resonances. *Phys. Rev. Lett.* 92 (8), 084102.
- Wimberger, S., Mannella, R., Morsch, O., Arimondo, E., Apr 2005a. Resonant nonlinear quantum transport for a periodically kicked bose condensate. *Phys. Rev. Lett.* 94 (13), 130404.
- Wimberger, S., Sadgrove, M., Parkins, S., Leonhardt, R., May 2005b. Experimental verification of a one-parameter scaling law for the quantum and “classical” resonances of the atom-optics kicked rotor. *Phys. Rev. A* 71 (5), 053404.
- Wu, S., Tonyushkin, A., Prentiss, M. G., Jul 2009. Observation of saturation of fidelity decay with an atom interferometer. *Phys. Rev. Lett.* 103 (3), 034101.

Kapitel 6

Nicht enthaltene Veröffentlichungen

Im Folgenden sind die weiteren Veröffentlichungen des Autors aufgeführt, die seit dem Jahr 2005 (d.h. nach der Promotion) erschienen sind bzw. noch erscheinen werden, aber in der vorliegenden Schrift nicht abgedruckt sind.

Editierte Sonderausgabe einer Fachzeitschrift

- **Hybrid quantum systems: new perspectives on quantum state control**
S. Wimberger (Herausgeber eines “Topical Issue”),
European Physical Journal D (2011) to be published

Populärwissenschaftliche Arbeit

- **Kalt, kälter, am kältesten**
S. Wimberger and T. Paul,
Forschungsmagazin Ruperto Carola 2 (2009) 44-45 (Universität Heidelberg)

Eingeladene Konferenzberichte

- **Decay of a Bose-Einstein condensate in a dissipative lattice: the mean-field approximation and beyond**
F. Trimborn, D. Witthaut, H. Hennig, G. Kordas, T. Geisel, and S. Wimberger,
European Physical Journal D (2011) submitted
- **Nonlinear dynamics in double square well potentials**
R. Khomeriki, J. Leon, S. Ruffo, and S. Wimberger,
Theoretical and Mathematical Physics 152 (2007) 1122-1131
- **Engineering quantum tunneling in extended periodic potentials**
S. Wimberger, D. Ciampini, O. Morsch, R. Mannella, and E. Arimondo,
in: “DICE 2006 - Quantum mechanics between decoherence and determinism”,
ed. by L. Diosi, H.-T. Elze, and G. Vitiello,
Journal of Physics: Conference Series 67 (2007) 012060

Wissenschaftliche Arbeiten zu anderen Themen

- **Saturation of fidelity in the atom-optics kicked rotor**
S. Wimberger and A. Buchleitner,
Journal of Physics B: Atomic, Molecular and Optical Physics 39 (2006) L145-L151
- **Quantum chaos, transport and control – in quantum optics**
J. Madroñero, A. Ponomarev, A. R. Ribeiro de Carvalho, S. Wimberger, C. Viviescas, A. Kolovsky, K. Hornberger, P. Schlagheck, A. Krug, and A. Buchleitner, M. Scully and G. Rempe (Eds.), Advances in Atomic, Molecular, and Optical Physics 53 (2006) 33-73 (Elsevier, Amsterdam)
- **Resonance-assisted decay of nondispersive wave packets**
S. Wimberger, P. Schlagheck, C. Eltschka, and A. Buchleitner,
Physical Review Letters 97 (2006) 043001
- **Transient localization in the kicked Rydberg atom**
E. Persson, S. Führthauer, S. Wimberger, and J. Burgdörfer,
Physical Review A 74 (2006) 053417
- **Phase-selected momentum transport in ultra-cold atoms**
M. Sadgrove, S. Wimberger, and K. Nakagawa,
Physical Review A (2011) submitted
- **Two-photon driven nonlinear dynamics and entanglement of an atom in a nonuniform cavity**
L. Chotorlishvili, Z. Toklikishvili, S. Wimberger, and J. Berakdar,
Physical Review A (2011) submitted
- **Induced delocalization by correlation and interaction in the one-dimensional Anderson model**
C. Albrecht and S. Wimberger,
Physical Review B (2011) submitted

Literaturverzeichnis

- [1] O. Morsch and M. Oberthaler, *Dynamics of Bose-Einstein condensates in optical lattices*, Rev. Mod. Phys. **78**, 179 (2006).
- [2] I. Bloch, J. Dalibard, and W. Zwerger, *Many-body physics with ultracold gases*, Rev. Mod. Phys. **80**, 885 (2008).
- [3] D. Jaksch and P. Zoller, *The cold atom Hubbard toolbox*, Annals of Physics **315**, 52 (2005).
- [4] M. Lewenstein, A. Sanpera, V. Ahufinger, B. Damski, A. Send, and U. Sen, *Ultracold atomic gases in optical lattices: mimicking condensed matter physics and beyond*, Adv. Phys. **56**, 243 (2007).
- [5] S. Diehl, A. Micheli, A. Kantian, B. Kraus, H. P. Büchler, and P. Zoller, *Quantum States and Phases in Driven Open Quantum Systems with Cold Atoms*, Nature Physics **4**, 878 (2008).
- [6] D. Witthaut, F. Trimborn, and S. Wimberger, *Dissipation Induced Coherence of a Two-Mode Bose-Einstein Condensate*, Phys. Rev. Lett. **101**, 200402 (2008).
- [7] F. Verstraete, M. M. Wolf, and J. I. Cirac, *Quantum computation and quantum-state engineering driven by dissipation*, Nature Physics **5**, 633 (2009).
- [8] V. A. Brazhnyi, V. V. Konotop, V. M. Pérez-García, and H. Ott, *Dissipation-Induced Coherent Structures in Bose-Einstein Condensates*, Phys. Rev. Lett. **102**, 144101 (2009).
- [9] *Special issue: Quantum control theory for coherence and information dynamics*, Journal of Physics B: Atomic, Molecular and Optical Physics (in print July 2011).
- [10] K. Tordrup and K. Mølmer, *Quantum computing with a single molecular ensemble and a Cooper-pair box*, Phys. Rev. A **77**, 020301 (2008).
- [11] D. Hunger, S. Camerer, T. W. Hänsch, D. König, J. P. Kotthaus, J. Reichel, and P. Treutlein, *Resonant Coupling of a Bose-Einstein Condensate to a Micromechanical Oscillator*, Phys. Rev. Lett. **104**, 143002 (2010).
- [12] J. Verdú, H. Zoubi, C. Koller, J. Majer, H. Ritsch, and J. Schmiedmayer, *Strong Magnetic Coupling of an Ultracold Gas to a Superconducting Waveguide Cavity*, Phys. Rev. Lett. **103**, 043603 (2009).
- [13] K. Henschel, J. Majer, J. Schmiedmayer, and H. Ritsch, *Cavity QED with an ultracold ensemble on a chip: Prospects for strong magnetic coupling at finite temperatures*, Phys. Rev. A **82**, 033810 (2010).

- [14] S. Wimberger, R. Mannella, O. Morsch, and E. Arimondo, *Resonant Nonlinear Quantum Transport for a Periodically Kicked Bose Condensate*, Phys. Rev. Lett. **94**, 130404 (2005).
- [15] M. Sadgrove, S. Wimberger, S. Parkins, and R. Leonhardt, *Ballistic and Localized Transport for the Atom Optics Kicked Rotor in the Limit of a Vanishing Kicking Period*, Phys. Rev. Lett. **94**, 174103 (2005).
- [16] L. Rebuzzini, S. Wimberger, and R. Artuso, *Delocalized and resonant quantum transport in nonlinear generalizations of the kicked rotor model*, Phys. Rev. E **71**, 036220 (2005).
- [17] S. Wimberger, M. Sadgrove, S. Parkins, and R. Leonhardt, *Experimental verification of a one-parameter scaling law for the quantum and “classical” resonances of the atom-optics kicked rotor*, Phys. Rev. A **71**, 053404 (2005).
- [18] S. Wimberger, R. Mannella, O. Morsch, E. Arimondo, A. R. Kolovsky, and A. Buchleitner, *Nonlinearity-induced destruction of resonant tunneling in the Wannier-Stark problem*, Phys. Rev. A **72**, 063610 (2005).
- [19] S. Wimberger and M. Sadgrove, *The role of quasi-momentum in the resonant dynamics of the atom-optics kicked rotor*, Journal of Physics A: Mathematical and General **38**, 10549 (2005).
- [20] A. Tomadin, R. Mannella, and S. Wimberger, *Can quantum fractal fluctuations be observed in an atom-optics kicked rotor experiment?*, Journal of Physics A: Mathematical and General **39**, 2477 (2006).
- [21] S. Wimberger, P. Schlagheck, and R. Mannella, *Tunnelling rates for the nonlinear Wannier-Stark problem*, Journal of Physics B: Atomic, Molecular and Optical Physics **39**, 729 (2006).
- [22] G. G. Carlo, G. Benenti, G. Casati, S. Wimberger, O. Morsch, R. Mannella, and E. Arimondo, *Chaotic ratchet dynamics with cold atoms in a pair of pulsed optical lattices*, Phys. Rev. A **74**, 033617 (2006).
- [23] C. Sias, A. Zenesini, H. Lignier, S. Wimberger, D. Ciampini, O. Morsch, and E. Arimondo, *Resonantly Enhanced Tunneling of Bose-Einstein Condensates in Periodic Potentials*, Phys. Rev. Lett. **98**, 120403 (2007).
- [24] A. Tomadin, R. Mannella, and S. Wimberger, *Many-Body Interband Tunneling as a Witness of Complex Dynamics in the Bose-Hubbard Model*, Phys. Rev. Lett. **98**, 130402 (2007).
- [25] R. Khomeriki, S. Ruffo, and S. Wimberger, *Driven collective quantum tunneling of ultracold atoms in engineered optical lattices*, EPL (Europhysics Letters) **77**, 40005 (2007).
- [26] D. Witthaut, E. M. Graefe, S. Wimberger, and H. J. Korsch, *Bose-Einstein condensates in accelerated double-periodic optical lattices: Coupling and crossing of resonances*, Phys. Rev. A **75**, 013617 (2007).
- [27] A. Facchini, S. Wimberger, and A. Tomadin, *Multifractal fluctuations in the survival probability of an open quantum system*, Physica A: Statistical Mechanics and its Applications **376**, 266 (2007).

- [28] P. Schlagheck and S. Wimberger, *Nonexponential decay of Bose-Einstein condensates: a numerical study based on the complex scaling method*, Applied Physics B: Lasers and Optics **86**, 385 (2007).
- [29] A. Tomadin, R. Mannella, and S. Wimberger, *Many-body Landau-Zener tunneling in the Bose-Hubbard model*, Phys. Rev. A **77**, 013606 (2008).
- [30] P. Buonsante and S. Wimberger, *Engineering many-body quantum dynamics by disorder*, Phys. Rev. A **77**, 041606 (2008).
- [31] A. Zenesini, C. Sias, H. Lignier, Y. Singh, D. Ciampini, O. Morsch, R. Mannella, E. Arimondo, A. Tomadin, and S. Wimberger, *Resonant tunneling of Bose-Einstein condensates in optical lattices*, New Journal of Physics **10**, 053038 (2008).
- [32] F. Trimborn, D. Witthaut, and S. Wimberger, *Mean-field dynamics of a two-mode Bose-Einstein condensate subject to noise and dissipation*, Journal of Physics B: Atomic, Molecular and Optical Physics **41**, 171001 (2008).
- [33] M. Sadgrove, S. Wimberger, S. Parkins, and R. Leonhardt, *Scaling law and stability for a noisy quantum system*, Phys. Rev. E **78**, 025206 (2008).
- [34] A. Zenesini, H. Lignier, G. Tayebirad, J. Radogostowicz, D. Ciampini, R. Mannella, S. Wimberger, O. Morsch, and E. Arimondo, *Time-Resolved Measurement of Landau-Zener Tunneling in Periodic Potentials*, Phys. Rev. Lett. **103**, 090403 (2009).
- [35] D. Witthaut, F. Trimborn, and S. Wimberger, *Dissipation-induced coherence and stochastic resonance of an open two-mode Bose-Einstein condensate*, Phys. Rev. A **79**, 033621 (2009).
- [36] M. Sadgrove and S. Wimberger, *Pseudo-classical theory for directed transport at quantum resonance*, New Journal of Physics **11**, 083027 (2009).
- [37] M. Abb, I. Guarneri, and S. Wimberger, *Pseudoclassical theory for fidelity of nearly resonant quantum rotors*, Phys. Rev. E **80**, 035206 (2009).
- [38] M. Lubasch, F. Mintert, and S. Wimberger, *Dynamical enhancement of spatial entanglement in massive particles*, Phys. Rev. Lett., submitted (2011), preprint: arXiv:1009.4075.
- [39] P. Plötz, J. Madroñero, and S. Wimberger, *Collapse and revival in inter-band oscillations of a two-band Bose-Hubbard model*, Journal of Physics B: Atomic, Molecular and Optical Physics **43**, 081001 (2010).
- [40] G. Tayebirad, A. Zenesini, D. Ciampini, R. Mannella, O. Morsch, E. Arimondo, N. Lörch, and S. Wimberger, *Time-resolved measurement of Landau-Zener tunneling in different bases*, Phys. Rev. A **82**, 013633 (2010).
- [41] G. Tayebirad, A. Zenesini, D. Ciampini, R. Mannella, O. Morsch, E. Arimondo, N. Lörch, and S. Wimberger, *Erratum: Time-resolved measurement of Landau - Zener tunneling in different bases [Phys. Rev. A 82, 013633 (2010)]*, Phys. Rev. A **82**, 069904 (2010).

- [42] K. Rapedius, C. Elsen, D. Witthaut, S. Wimberger, and H. J. Korsch, *Nonlinear resonant tunneling of Bose-Einstein condensates in tilted optical lattices*, Phys. Rev. A **82**, 063601 (2010).
- [43] P. Plötz, M. Lubasch, and S. Wimberger, *Detection of avoided crossings by fidelity*, Physica A: Statistical Mechanics and its Applications **390**, 1363 (2011).
- [44] G. Tayebirad, R. Mannella, and S. Wimberger, *Engineering of Landau-Zener tunneling*, Applied Physics B: Lasers and Optics **102**, 489 (2011).
- [45] G. Tayebirad, R. Mannella, and S. Wimberger, *Engineering interband transport by time-dependent disorder*, Phys. Rev. Lett., submitted (2011).
- [46] P. Plötz, P. Schlagheck, and S. Wimberger, *Effective spin model for interband transport in a Wannier-Stark lattice system*, Eur. Phys. J. D, in press (2011), online at: DOI: 10.1140/epjd/e2010-10554-7.
- [47] P. Plötz and S. Wimberger, *Stückelberg-Interferometry with ultra-cold atoms*, Eur. Phys. J. D, submitted (2011), preprint: arXiv:1012.3690.
- [48] D. Witthaut, F. Trimborn, H. Hennig, G. Kordas, T. Geisel, and S. Wimberger, *Beyond mean-field dynamics in open Bose-Hubbard chains*, Phys. Rev. A, submitted (2011).
- [49] E. Arimondo and S. Wimberger, in *Dynamical Tunneling*, edited by S. Keshavamurthy and P. Schlagheck (Taylor and Francis – CRC Press, Boca Raton, 2011), pp. 257–287.
- [50] M. Sadgrove and S. Wimberger, *A pseudo-classical method for the atom-optics kicked rotor: from theory to experiment and back*, Adv. At. Mol. Opt. Phys. **60**, (2011), in press.
- [51] C. Cohen-Tannoudji, J. Dupont-Roc, and G. Grynberg, *Atom-Photon Interactions, Basic Processes and Applications* (John Wiley & Sons, New York, 1992).
- [52] R. Grimm, M. Weidemüller, and Y. B. Ovchinnikov, *Optical dipole traps for neutral atoms*, Adv. At. Mol. Opt. Phys. **42**, 95 (2000).
- [53] P. Meystre, *Atom Optics* (Springer-Verlag, New York, 2001).
- [54] C. J. Foot, *Atomic Physics* (Oxford Univ. Press, Oxford, 2005).
- [55] M. Glück, A. R. Kolovsky, and H. J. Korsch, *Wannier-Stark resonances in optical and semiconductor superlattices*, Phys. Rep. **366**, 103 (2002).
- [56] M. Raizen, *Quantum chaos with ultra-cold atoms*, Adv. At. Mol. Phys. **41**, 43 (1999).
- [57] M. G. Raizen, V. Milner, W. H. Oskay, and D. A. Steck, in *New Directions in Quantum Chaos, Proceedings of the International School of Physics ‘E. Fermi’*, edited by G. Casati, I. Guarneri, and U. Smilansky (IOS Press, Amsterdam, 2000), Vol. Course CXLIII, p. 299.
- [58] H. J. Metcalf and P. van der Straten, *Laser cooling and trapping, Graduate texts in contemporary physics* (Springer-Verlag, New York, 1999).

- [59] M. B. d’Arcy, R. M. Godun, M. K. Oberthaler, G. S. Summy, K. Burnett, and S. A. Gardiner, *Approaching Classicality in Quantum Accelerator Modes through Decoherence*, Phys. Rev. E **64**, 056233 (2001).
- [60] S. Wimberger, I. Guarneri, and S. Fishman, *Quantum resonances and decoherence for δ -kicked atoms*, Nonlinearity **16**, 1381 (2003).
- [61] M. B. d’Arcy, R. M. Godun, G. S. Summy, I. Guarneri, S. Wimberger, S. Fishman, and A. Buchleitner, *Decoherence as a probe of coherent quantum dynamics*, Phys. Rev. E **69**, 027201 (2004).
- [62] M. Sadgrove, A. Hilliard, T. Mullins, S. Parkins, and R. Leonhardt, *Observation of robust quantum resonance peaks in an atom optics kicked rotor with amplitude noise*, Phys. Rev. E **70**, 036217 (2004).
- [63] E. A. Cornell and C. E. Wieman, *Nobel Lecture: Bose-Einstein condensation in a dilute gas, the first 70 years and some recent experiments*, Rev. Mod. Phys. **74**, 875 (2002).
- [64] W. Ketterle, *Nobel Lecture: When atoms behave as waves: Bose-Einstein condensation and the atom laser*, Rev. Mod. Phys. **74**, 1131 (2002).
- [65] A. J. Leggett, *Bose-Einstein condensation in the alkali gases: Some fundamental concepts*, Rev. Mod. Phys. **73**, 307 (2001).
- [66] C. J. Pethick and H. Smith, *Bose-Einstein Condensation in Dilute Gases* (Cambridge Univ. Press, Cambridge, 2002).
- [67] L. Pitaevskii and S. Stringari, *Bose-Einstein Condensation* (Oxford Univ. Press, Oxford, 2003).
- [68] O. E. Alon, A. I. Streltsov, and L. S. Cederbaum, *Multiconfigurational time-dependent Hartree method for bosons: Many-body dynamics of bosonic systems*, Phys. Rev. A **77**, 033613 (2008).
- [69] J. C. Slater, *A Soluble Problem in Energy Bands*, Phys. Rev. **87**, 807 (1952).
- [70] W. Kohn, *Construction of Wannier Functions and Applications to Energy Bands*, Phys. Rev. B **7**, 4388 (1973).
- [71] N. Marzari and D. Vanderbilt, *Maximally localized generalized Wannier functions for composite energy bands*, Phys. Rev. B **56**, 12847 (1997).
- [72] M. P. A. Fisher, P. B. Weichman, G. Grinstein, and D. S. Fisher, *Boson localization and the superfluid-insulator transition*, Phys. Rev. B **40**, 546 (1989).
- [73] A. Tomadin, *Quantum Chaos with Ultracold Atoms in Optical Lattices*, Master’s thesis, Università degli Studi di Pisa, Pisa (2006).
- [74] M. Abb, *Fidelity for Kicked Atoms at nearly Resonant Driving*, Master’s Thesis, University of Heidelberg (2009).
- [75] M. Lubasch, *Quantum Chaos and Entanglement in the Bose-Hubbard Model*, Master’s thesis, University of Heidelberg (2009).

- [76] C. Albrecht, *Induced Delocalization by Correlation and Interaction in the 1D Anderson Model*, Master's Thesis, University of Heidelberg (2010).
- [77] B. Probst, *The Pendulum Approximation for Fidelity in Quantum Kicked Rotor Systems* (2010).
- [78] N. Lörch, *A Study of Open Quantum Systems*, Master's thesis, University of Heidelberg (2010).
- [79] P. Plötz, *Complex Dynamics of Ultracold Atoms*, Ph.D. thesis, University of Heidelberg (2010).
- [80] G. Tayebirad, *Engineering the Landau-Zener Tunneling of Ultracold Atoms in Tilted Potentials*, Ph.D. thesis, University of Heidelberg (2011).
- [81] A. J. Lichtenberg and M. A. Lieberman, *Regular and Chaotic Dynamics*, Vol. 38 of *Applied Mathematical Sciences* (Springer-Verlag, Berlin, 1992).
- [82] B. V. Chirikov, *A universal instability of many-dimensional oscillator systems*, Phys. Rep. **52**, 263 (1979).
- [83] G. Casati, B. V. Chirikov, J. Ford, and F. M. Izrailev, in *Stochastic Behavior in Classical and Quantum Hamiltonian Systems*, Vol. 93 of *Lecture Notes in Physics*, edited by G. Casati and J. Ford (Springer-Verlag, Berlin, 1979), p. 334.
- [84] F. M. Izrailev, *Simple Models of Quantum Chaos: Spectrum and Eigenfunctions*, Phys. Rep. **196**, 299 (1990).
- [85] S. Fishman, in *Quantum Chaos*, Vol. Course CXIX of *Proceedings of the International School of Physics 'E. Fermi'*, edited by G. Casati, I. Guarneri, and U. Smilansky (North Holland, Amsterdam, 1993), p. 187.
- [86] S. Fishman, D. R. Grempel, and R. E. Prange, *Chaos, Quantum Recurrences, and Anderson Localization*, Phys. Rev. Lett. **49**, 509 (1982).
- [87] F. Haake, *Quantum Signatures of Chaos*, Vol. 54 of *Springer Series in Synergetics* (Springer-Verlag, Berlin, 1991).
- [88] P. W. Anderson, *Absence of Diffusion in Certain Random Lattices*, Phys. Rev. **109**, 1492 (1958).
- [89] B. Kramers and A. MacKinnon, *Localization: theory and experiment*, Rep. Prog. Phys. **56**, 1469 (1993).
- [90] R. Graham, M. Schlautmann, and P. Zoller, *Dynamical localization of atomic-beam deflection by a modulated standing light wave*, Phys. Rev. A **45**, R15 (1992).
- [91] N. S. N. Nath, *The diffraction of light by high-frequency sound waves: Generalized theory*, Proc. Indian Acad. Sci. **4**, 222 (1936).
- [92] R. W. Boyd, *Nonlinear optics* (Academic Press, San Diego, 1992).
- [93] P. Szriftgiser, J. Ringot, D. Delande, and J. C. Garreau, *Observation of Sub-Fourier Resonances in a Quantum-Chaotic System*, Phys. Rev. Lett. **89**, 224101 (2002).

- [94] J. Chabé, H. Lignier, H. Cavalcante, D. Delande, P. Szriftgiser, and J. C. Garreau, *Quantum Scaling Laws in the Onset of Dynamical Delocalization*, Phys. Rev. Lett. **97**, 264101 (2006).
- [95] J. Chabé, G. Lemarié, B. Grémaud, D. Delande, P. Szriftgiser, and J. C. Garreau, *Experimental Observation of the Anderson Metal-Insulator Transition with Atomic Matter Waves*, Phys. Rev. Lett. **101**, 255702 (2008).
- [96] G. Lemarié, H. Lignier, D. Delande, P. Szriftgiser, and J. C. Garreau, *Critical State of the Anderson Transition: Between a Metal and an Insulator*, Phys. Rev. Lett. **105**, 090601 (2010).
- [97] F. M. Izrailev and D. L. Shepelyansky, *Quantum resonance for the rotor in a non-linear periodic field*, Dok. Akad. Nauk SSSR **249**, 1103 (1979).
- [98] V. V. Sokolov, O. V. Zhirov, D. Alonso, and G. Casati, *Quantum Resonances of the Kicked Rotor and the $SU(q)$ Group*, Phys. Rev. Lett. **84**, 3566 (2000).
- [99] M. K. Oberthaler, R. M. Godun, M. B. d'Arcy, G. S. Summy, and K. Burnett, *Observation of Quantum Accelerator Modes*, Phys. Rev. Lett. **83**, 4447 (1999).
- [100] S. Fishman, I. Guarneri, and L. Rebuzzini, *Stable Quantum Resonances in Atom Optics*, Phys. Rev. Lett. **89**, 084101 (2002).
- [101] S. Wimberger, I. Guarneri, and S. Fishman, *Classical Scaling Theory of Quantum Resonances*, Phys. Rev. Lett. **92**, 084102 (2004).
- [102] S. Wimberger, *Chaos and Localisation: Quantum Transport in Periodically Driven Atomic Systems*, Ph.D. thesis, Ludwig-Maximilians-Universität München and Università degli Studi dell'Insubria, Como (2004), available online at <http://edoc.ub.uni-muenchen.de/archive/00001687>.
- [103] I. Guarneri, L. Rebuzzini, and S. Fishman, *Arnol'd tongues and quantum accelerator modes*, Nonlinearity **19**, 1141 (2006).
- [104] I. Guarneri and L. Rebuzzini, *Quantum Accelerator Modes Near Higher-Order Resonances*, Phys. Rev. Lett. **100**, 234103 (2008).
- [105] C. F. Bharucha, J. C. Robinson, F. L. Moore, B. Sundaram, Q. Niu, and M. G. Raizen, *Dynamical localization of ultracold sodium atoms*, Phys. Rev. E **60**, 3881 (1999).
- [106] W. H. Oskay, D. A. Steck, V. Milner, B. G. Klappauf, and M. G. Raizen, *Ballistic peaks at quantum resonance*, Opt. Commun. **179**, 137 (2000).
- [107] M. B. d'Arcy, R. M. Godun, M. K. Oberthaler, D. Cassettari, and G. S. Summy, *Quantum Enhancement of Momentum Diffusion in the Delta-Kicked Rotor*, Phys. Rev. Lett. **87**, 074102 (2001).
- [108] C. Ryu, M. F. Andersen, A. Vaziri, M. B. d'Arcy, J. M. Grossman, K. Helmerson, and W. D. Phillips, *High-Order Quantum Resonances Observed in a Periodically Kicked Bose-Einstein Condensate*, Phys. Rev. Lett. **96**, 160403 (2006).
- [109] G. Behinaein, V. Ramareddy, P. Ahmadi, and G. S. Summy, *Exploring the Phase Space of the Quantum δ -Kicked Accelerator*, Phys. Rev. Lett. **97**, 244101 (2006).

- [110] J. F. Kanem, S. Maneshi, M. Partlow, M. Spanner, and A. M. Steinberg, *Observation of High-Order Quantum Resonances in the Kicked Rotor*, Phys. Rev. Lett. **98**, 083004 (2007).
- [111] V. Ramareddy, G. Behinaein, I. Talukdar, P. Ahmadi, and G. S. Summy, *High-order resonances of the quantum δ -kicked accelerator*, EPL (Europhysics Letters) **89**, 33001 (2010).
- [112] G. J. Duffy, S. Parkins, T. Müller, M. Sadgrove, R. Leonhardt, and A. C. Wilson, *Experimental investigation of early-time diffusion in the quantum kicked rotor using a Bose-Einstein condensate*, Phys. Rev. E **70**, 056206 (2004).
- [113] G. J. Duffy, A. S. Mellish, K. J. Challis, and A. C. Wilson, *Nonlinear atom-optical δ -kicked harmonic oscillator using a Bose-Einstein condensate*, Phys. Rev. A **70**, 041602 (2004).
- [114] D. L. Shepelyansky, *Delocalization of quantum chaos by weak nonlinearity*, Phys. Rev. Lett. **70**, 1787 (1993).
- [115] S. Fishman, Y. Krivolapov, and A. Soffer, *Perturbation Theory for the Nonlinear Schrödinger Equation with a random potential*, Nonlinearity **22**, 2861 (2009).
- [116] C. F. Bharucha, K. W. Madison, P. R. Morrow, S. R. Wilkinson, B. Sundaram, and M. G. Raizen, *Observation of atomic tunneling from an accelerating optical potential*, Phys. Rev. A **55**, R857 (1997).
- [117] S. Brouard and J. Plata, *Quantum δ -kicked rotor: the effect of amplitude noise on the quantum resonances*, J. Phys. A **36**, 3745 (2003).
- [118] V. Milner, D. A. Steck, W. H. Oskay, and M. G. Raizen, *Recovery of classically driven behavior in a noise-driven quantum system*, Phys. Rev. E **61**, 7223 (2000).
- [119] D. A. Steck, V. Milner, W. H. Oskay, and M. G. Raizen, *Quantitative study of amplitude noise effects on dynamical localization*, Phys. Rev. E **62**, 3461 (2000).
- [120] A. Peres, *Stability of quantum motion in chaotic and regular systems*, Phys. Rev. A **30**, 1610 (1984).
- [121] T. Gorin, T. Prosen, T. H. Seligman, and M. Znidaric, *Dynamics of Loschmidt echoes and fidelity decay*, Physics Reports **435**, 33 (2006).
- [122] P. Jacquod and C. Petitjean, *Decoherence, entanglement and irreversibility in quantum dynamical systems with few degrees of freedom*, Adv. Phys. **58**, 67 (2009).
- [123] Y. Krivolapov, S. Fishman, E. Ott, and T. M. Antonsen, *Quantum chaos of a mixed open system of kicked cold atoms*, Phys. Rev. E **83**, 016204 (2011).
- [124] E. Lundh and M. Wallin, *Ratchet Effect for Cold Atoms in an Optical Lattice*, Phys. Rev. Lett. **94**, 110603 (2005).
- [125] E. Lundh, *Directed transport and Floquet analysis for a periodically kicked wave packet at a quantum resonance*, Phys. Rev. E **74**, 016212 (2006).

- [126] I. Dana and V. Roitberg, *Quantum resonances and ratchets in free-falling frames*, Phys. Rev. E **76**, 015201 (2007).
- [127] A. Kenfack, J. Gong, and A. K. Pattanayak, *Controlling the Ratchet Effect for Cold Atoms*, Phys. Rev. Lett. **100**, 044104 (2008).
- [128] M. Sadgrove, M. Horikoshi, T. Sekimura, and K. Nakagawa, *Rectified Momentum Transport for a Kicked Bose-Einstein Condensate*, Phys. Rev. Lett. **99**, 043002 (2007).
- [129] I. Dana, V. Ramareddy, I. Talukdar, and G. S. Summy, *Experimental Realization of Quantum-Resonance Ratchets at Arbitrary Quasimomenta*, Phys. Rev. Lett. **100**, 024103 (2008).
- [130] S. Flach, O. Yevtushenko, and Y. Zolotaryuk, *Directed Current due to Broken Time-Space Symmetry*, Phys. Rev. Lett. **84**, 2358 (2000).
- [131] P. Reimann, *Brownian motors: noisy transport far from equilibrium*, Physics Reports **361**, 57 (2002).
- [132] P. Hänggi and F. Marchesoni, *Artificial Brownian motors: Controlling transport on the nanoscale*, Rev. Mod. Phys. **81**, 387 (2009).
- [133] G. G. Carlo, G. Benenti, G. Casati, and D. L. Shepelyansky, *Quantum Ratchets in Dissipative Chaotic Systems*, Phys. Rev. Lett. **94**, 164101 (2005).
- [134] T. S. Monteiro, P. A. Dando, N. A. C. Hutchings, and M. R. Isherwood, *Proposal for a Chaotic Ratchet Using Cold Atoms in Optical Lattices*, Phys. Rev. Lett. **89**, 194102 (2002).
- [135] T. Salger, C. Geckeler, S. Kling, and M. Weitz, *Atomic Landau-Zener Tunneling in Fourier-Synthesized Optical Lattices*, Phys. Rev. Lett. **99**, 190405 (2007).
- [136] T. Salger, S. Kling, T. Hecking, C. Geckeler, L. Morales-Molina, and M. Weitz, *Directed Transport of Atoms in a Hamiltonian Quantum Ratchet*, Science **326**, 1241 (2009).
- [137] M. Kasevich, D. S. Weiss, E. Riis, K. Moler, S. Kasapi, and S. Chu, *Atomic velocity selection using stimulated Raman transitions*, Phys. Rev. Lett. **66**, 2297 (1991).
- [138] J.-L. Pichard, N. Zanon, Y. Imry, and A. D. Stone, *Theory of random multiplicative transfer matrices and its implications for quantum transport*, J. Phys. (Paris) **51**, 587 (1990).
- [139] G. Benenti, G. Casati, I. Guarneri, and M. Terraneo, *Quantum Fractal Fluctuations*, Phys. Rev. Lett. **87**, 014101 (2001).
- [140] G. Casati, J. Ford, I. Guarneri, and F. Vivaldi, *Search for randomness in the kicked quantum rotor*, Phys. Rev. A **34**, 1413 (1986).
- [141] A. M. García-García and J. Wang, *Anderson Transition in Quantum Chaos*, Phys. Rev. Lett. **94**, 244102 (2005).

- [142] G. H. Wannier, *Wave Functions and Effective Hamiltonian for Bloch Electrons in an Electric Field*, Phys. Rev. **117**, 432 (1960).
- [143] J. E. Avron, *The Lifetime of Wannier Ladder States*, Ann. Phys. **143**, 33 (1981).
- [144] M. Ben Dahan, E. Peik, J. Reichel, Y. Castin, and C. Salomon, *Bloch Oscillations of Atoms in an Optical Potential*, Phys. Rev. Lett. **76**, 4508 (1996).
- [145] S. R. Wilkinson, C. F. Bharucha, K. W. Madison, Q. Niu, and M. G. Raizen, *Observation of Atomic Wannier-Stark Ladders in an Accelerating Optical Potential*, Phys. Rev. Lett. **76**, 4512 (1996).
- [146] B. P. Anderson and M. A. Kasevich, *Macroscopic Quantum Interference from Atomic Tunnel Arrays*, Science **282**, 1686 (1998).
- [147] O. Morsch, J. H. Müller, M. Cristiani, D. Ciampini, and E. Arimondo, *Bloch Oscillations and Mean-Field Effects of Bose-Einstein Condensates in 1D Optical Lattices*, Phys. Rev. Lett. **87**, 140402 (2001).
- [148] G. Roati, E. de Mirandes, F. Ferlaino, H. Ott, G. Modugno, and M. Inguscio, *Atom Interferometry with Trapped Fermi Gases*, Phys. Rev. Lett. **92**, 230402 (2004).
- [149] M. Gustavsson, E. Haller, M. J. Mark, J. G. Danzl, G. Rojas-Kopeinig, and H.-C. Nägerl, *Control of Interaction-Induced Dephasing of Bloch Oscillations*, Phys. Rev. Lett. **100**, 080404 (2008).
- [150] T. Köhler, K. Góral, and P. S. Julienne, *Production of cold molecules via magnetically tunable Feshbach resonances*, Rev. Mod. Phys. **78**, 1311 (2006).
- [151] N. Moiseyev and L. S. Cederbaum, *Resonance solutions of the nonlinear Schrödinger equation: Tunneling lifetime and fragmentation of trapped condensates*, Phys. Rev. A **72**, 033605 (2005).
- [152] P. Schlagheck and T. Paul, *Complex-scaling approach to the decay of Bose-Einstein condensates*, Phys. Rev. A **73**, 023619 (2006).
- [153] E. M. Graefe, H. J. Korsch, and D. Witthaut, *Mean-field dynamics of a Bose-Einstein condensate in a time-dependent triple-well trap: Nonlinear eigenstates, Landau-Zener models, and stimulated Raman adiabatic passage*, Phys. Rev. A **73**, 013617 (2006).
- [154] R. Tsu and L. Esaki, *Tunneling in a finite superlattice*, Appl. Phys. Lett **22**, 562 (1973).
- [155] S. Wilkinson, C. Bharucha, M. Fischer, K. Madison, Q. Niu, B. Sundaram, and M. Raizen, *Experimental Evidence for Non-Exponential Decay in Quantum Tunneling*, Nature **387**, 575 (1997).
- [156] A. Zenesini, D. Ciampini, O. Morsch, and E. Arimondo, *Observation of Stückelberg oscillations in accelerated optical lattices*, Phys. Rev. A **82**, 065601 (2010).
- [157] S. Kling, T. Salger, C. Grossert, and M. Weitz, *Atomic Bloch-Zener Oscillations and Stückelberg Interferometry in Optical Lattices*, Phys. Rev. Lett. **105**, 215301 (2010).

- [158] L. D. Carr, M. J. Holland, and B. A. Malomed, *Macroscopic quantum tunneling of Bose-Einstein condensates in a finite potential well*, Journal of Physics B: Atomic, Molecular and Optical Physics **38**, 3217 (2005).
- [159] G. Roati, C. D'Errico, L. Fallani, M. Fattori, C. Fort, M. Zaccanti, G. Modugno, M. Modugno, and M. Inguscio, *Anderson localization of a non-interacting Bose-Einstein condensate*, Nature **453**, 895 (2008).
- [160] B. Deissler, M. Zaccanti, G. Roati, C. D'Errico, M. Fattori, M. Modugno, G. Modugno, and M. Inguscio, *Delocalization of a disordered bosonic system by repulsive interactions*, Nature Physics **6**, 354 (2010).
- [161] S. Aubry and G. André, *Analyticity breaking and Anderson localization in incommensurate lattices*, Ann. Isr. Phys. Soc. **3**, 133 (1980).
- [162] M. Albert and P. Leboeuf, *Localization by bichromatic potentials versus Anderson localization*, Phys. Rev. A **81**, 013614 (2010).
- [163] A. Buchleitner and A. R. Kolovsky, *Interaction-Induced Decoherence of Atomic Bloch Oscillations*, Phys. Rev. Lett. **91**, 253002 (2003).
- [164] A. R. Kolovsky and A. Buchleitner, *Floquet-Bloch operator for the Bose-Hubbard model with static field*, Phys. Rev. E **68**, 056213 (2003).
- [165] H. Venzl, A. J. Daley, F. Mintert, and A. Buchleitner, *Statistics of Schmidt coefficients and the simulability of complex quantum systems*, Phys. Rev. E **79**, 056223 (2009).
- [166] V. W. Scarola and S. Das Sarma, *Quantum Phases of the Extended Bose-Hubbard Hamiltonian: Possibility of a Supersolid State of Cold Atoms in Optical Lattices*, Phys. Rev. Lett. **95**, 033003 (2005).
- [167] A. Isacsson and S. M. Girvin, *Multiflavor bosonic Hubbard models in the first excited Bloch band of an optical lattice*, Phys. Rev. A **72**, 053604 (2005).
- [168] J. Larson, A. Collin, and J.-P. Martikainen, *Multiband bosons in optical lattices*, Phys. Rev. A **79**, 033603 (2009).
- [169] S. Fölling, *Probing Strongly Correlated States of Ultracold Atoms in Optical Lattices*, Ph.D. Thesis, University of Mainz (2008).
- [170] M. Terraneo and I. Guarneri, *Distribution of resonance widths in localized tight-binding models*, The European Physical Journal B - Condensed Matter and Complex Systems **18**, 303 (2000).
- [171] T. Kottos, *Statistics of resonances and delay times in random media: beyond random matrix theory*, Journal of Physics A: Mathematical and General **38**, 10761 (2005).
- [172] G. Casati, L. Molinari, and F. Izrailev, *Scaling properties of band random matrices*, Phys. Rev. Lett. **64**, 1851 (1990).
- [173] M. Greiner, O. Mandel, T. W. Hänsch, and I. Bloch, *Collapse and revival of the matter wave field of a Bose-Einstein condensate*, Nature **419**, 51 (2002).

- [174] S. Will, T. Best, U. Schneider, L. Hackermüller, D.-S. Lühmann, and I. Bloch, *Time-resolved observation of coherent multi-body interactions in quantum phase revivals*, Nature **465**, 197 (2010).
- [175] O. Bohigas, M. J. Giannoni, and C. Schmit, *Characterization of Chaotic Quantum Spectra and Universality of Level Fluctuation Laws*, Phys. Rev. Lett. **52**, 1 (1984).
- [176] M. L. Mehta, *Random Matrices* (Academic Press, Boston, 1991).
- [177] J. Zakrzewski and M. Kuś, *Distributions of avoided crossings for quantum chaotic systems*, Phys. Rev. Lett. **67**, 2749 (1991).
- [178] A. R. Kolovsky and A. Buchleitner, *Quantum chaos in the Bose-Hubbard model*, EPL (Europhysics Letters) **68**, 632 (2004).
- [179] P. Buonsante and A. Vezzani, *Ground-State Fidelity and Bipartite Entanglement in the Bose-Hubbard Model*, Phys. Rev. Lett. **98**, 110601 (2007).
- [180] M. M. Rams and B. Damski, *Quantum Fidelity in the Thermodynamic Limit*, Phys. Rev. Lett. **106**, 055701 (2011).
- [181] P. Zanardi and N. Paunković, *Ground state overlap and quantum phase transitions*, Phys. Rev. E **74**, 031123 (2006).
- [182] C. Parra-Murillo, J. Madroñero, and S. Wimberger, in preparation.
- [183] J. Javanainen, *Oscillatory exchange of atoms between traps containing Bose condensates*, Phys. Rev. Lett. **57**, 3164 (1986).
- [184] G. J. Milburn, J. Corney, E. M. Wright, and D. F. Walls, *Quantum dynamics of an atomic Bose-Einstein condensate in a double-well potential*, Phys. Rev. A **55**, 4318 (1997).
- [185] A. Smerzi, S. Fantoni, S. Giovanazzi, and S. R. Shenoy, *Quantum Coherent Atomic Tunneling between Two Trapped Bose-Einstein Condensates*, Phys. Rev. Lett. **79**, 4950 (1997).
- [186] I. Zapata, F. Sols, and A. J. Leggett, *Josephson effect between trapped Bose-Einstein condensates*, Phys. Rev. A **57**, R28 (1998).
- [187] S. Raghavan, A. Smerzi, S. Fantoni, and S. R. Shenoy, *Coherent oscillations between two weakly coupled Bose-Einstein condensates: Josephson effects, π oscillations, and macroscopic quantum self-trapping*, Phys. Rev. A **59**, 620 (1999).
- [188] F. Meier and W. Zwerger, *Josephson tunneling between weakly interacting Bose-Einstein condensates*, Phys. Rev. A **64**, 033610 (2001).
- [189] M. Albiez, R. Gati, J. Fölling, S. Hunsmann, M. Cristiani, and M. K. Oberthaler, *Direct Observation of Tunneling and Nonlinear Self-Trapping in a Single Bosonic Josephson Junction*, Phys. Rev. Lett. **95**, 010402 (2005).
- [190] R. Gati and M. K. Oberthaler, *A bosonic Josephson junction*, Journal of Physics B: Atomic, Molecular and Optical Physics **40**, R61 (2007).

- [191] T. Zibold, E. Nicklas, C. Gross, and M. K. Oberthaler, *Classical Bifurcation at the Transition from Rabi to Josephson Dynamics*, Phys. Rev. Lett. **105**, 204101 (2010).
- [192] L. Amico, R. Fazio, A. Osterloh, and V. Vedral, *Entanglement in many-body systems*, Rev. Mod. Phys. **80**, 517 (2008).
- [193] R. Horodecki, P. Horodecki, M. Horodecki, and K. Horodecki, *Quantum entanglement*, Rev. Mod. Phys. **81**, 865 (2009).
- [194] C. E. Creffield, *Quantum Control and Entanglement using Periodic Driving Fields*, Phys. Rev. Lett. **99**, 110501 (2007).
- [195] A. Eckardt and M. Holthaus, *Avoided-Level-Crossing Spectroscopy with Dressed Matter Waves*, Phys. Rev. Lett. **101**, 245302 (2008).
- [196] C. Kollath, A. Iucci, T. Giamarchi, W. Hofstetter, and U. Schollwöck, *Spectroscopy of Ultracold Atoms by Periodic Lattice Modulations*, Phys. Rev. Lett. **97**, 050402 (2006).
- [197] C. Weiss and N. Teichmann, *Differences between Mean-Field Dynamics and N -Particle Quantum Dynamics as a Signature of Entanglement*, Phys. Rev. Lett. **100**, 140408 (2008).
- [198] L. Gammaitoni, P. Hänggi, P. Jung, and F. Marchesoni, *Stochastic resonance*, Rev. Mod. Phys. **70**, 223 (1998).
- [199] T. Wellens, V. Shatokhin, and A. Buchleitner, *Stochastic resonance*, Reports on Progress in Physics **67**, 45 (2004).
- [200] C. Kittel, *Einführung in die Festkörperphysik* (Oldenbourg Verlag, München – Wien, 1996).
- [201] B. T. Seaman, M. Krämer, D. Z. Anderson, and M. J. Holland, *Atomtronics: Ultracold-atom analogs of electronic devices*, Phys. Rev. A **75**, 023615 (2007).
- [202] R. A. Pepino, J. Cooper, D. Meiser, D. Z. Anderson, and M. J. Holland, *Open quantum systems approach to atomtronics*, Phys. Rev. A **82**, 013640 (2010).
- [203] A. Vardi and J. R. Anglin, *Bose-Einstein Condensates beyond Mean Field Theory: Quantum Backreaction as Decoherence*, Phys. Rev. Lett. **86**, 568 (2001).
- [204] I. Tikhonenkov, J. R. Anglin, and A. Vardi, *Quantum dynamics of Bose-Hubbard Hamiltonians beyond the Hartree-Fock-Bogoliubov approximation: The Bogoliubov back-reaction approximation*, Phys. Rev. A **75**, 013613 (2007).
- [205] Y. Meir and N. S. Wingreen, *Landauer formula for the current through an interacting electron region*, Phys. Rev. Lett. **68**, 2512 (1992).
- [206] A. Recati, P. O. Fedichev, W. Zwerger, J. von Delft, and P. Zoller, *Atomic Quantum Dots Coupled to a Reservoir of a Superfluid Bose-Einstein Condensate*, Phys. Rev. Lett. **94**, 040404 (2005).
- [207] G. Kordas, A. Komnik, and S. Wimberger, in preparation.